ORGANISATION EUROPÉENNE POUR LA RECHERCHE NUCLÉAIRE

CERN EUROPEAN ORGANIZATION FOR NUCLEAR RESEARCH

Handbook of LHC Higgs cross sections:
3. Higgs Properties

Report of the LHC Higgs Cross Section Working Group

Editors: S. Heinemeyer
C. Mariotti
G. Passarino
R. Tanaka

GENEVA
2013

Conveners

Gluon-fusion process: Y. Gao, D. de Florian, B. di Micco, K. Melnikov, F. Petriello

Vector-boson-fusion process: A. Denner, P. Govoni, C. Oleari, D. Rebuzzi

WH/ZH *production mode*: S. Dittmaier, G. Ferrera, J. Olsen, G. Piacquadio, A. Rizzi

ttH *process*: C. Neu, C. Potter, L. Reina, A. Rizzi, M. Spira

Light Mass Higgs A. David, A. Denner, M. Dührssen, C. Grojean, M. Grazzini, K. Prokofiev, M. Schumacher, G. Weiglein, M. Zanetti

MSSM Higgs: M. Flechl, M. Krämer, S. Lehti, R. Harlander, P. Slavich, M. Spira, M. Vazquez Acosta, T. Vickey

Heavy Higgs and BSM S. Bolognesi, S. Diglio, C. Grojean, M. Kadastik, H. E. Logan, M. Mühlleitner, K. Peters

Branching ratios: S. Heinemeyer, A. Mück, I. Puljak, D. Rebuzzi

Jets: B. Mellado, D. Del Re, G. P. Salam, F. Tackmann

NLO MC: F. Krauss, F. Maltoni, P. Nason

PDF: S. Forte, J. Huston, R. Thorne

This Report should be cited as:

LHC Higgs Cross Section Working Group, S. Heinemeier, C. Mariotti, G. Passarino, R. Tanaka (Eds.), *Handbook of LHC Higgs Cross Sections: 3. Higgs Properties*, CERN–2013–004 (CERN, Geneva, 2013), DOI: 10.5170/CERN–2013–004

Abstract

This Report summarizes the results of the activities in 2012 and the first half of 2013 of the LHC Higgs Cross Section Working Group. The main goal of the working group was to present the state of the art of Higgs Physics at the LHC, integrating all new results that have appeared in the last few years. This report follows the first working group report *Handbook of LHC Higgs Cross Sections: 1. Inclusive Observables* (CERN-2011-002) and the second working group report *Handbook of LHC Higgs Cross Sections: 2. Differential Distributions* (CERN-2012-002). After the discovery of a Higgs boson at the LHC in mid-2012 this report focuses on refined prediction of Standard Model (SM) Higgs phenomenology around the experimentally observed value of $125 - 126$ GeV, refined predictions for heavy SM-like Higgs bosons as well as predictions in the Minimal Supersymmetric Standard Model and first steps to go beyond these models. The other main focus is on the extraction of the characteristics and properties of the newly discovered particle such as couplings to SM particles, spin and CP-quantum numbers etc.

We, the authors, would like to dedicate this Report to the memory of
Ken Wilson.

S. Heinemeyer[1], C. Mariotti[2], G. Passarino[2,3] and R. Tanaka[4] (eds.);
J. R. Andersen[5], P. Artoisenet[6], E. A. Bagnaschi[7], A. Banfi[8], T. Becher[9], F. U. Bernlochner[10],
S. Bolognesi[11], P. Bolzoni[12], R. Boughezal[13], D. Buarque[14], J. Campbell[15], F. Caola[11],
M. Carena[15,16,17], F. Cascioli[18], N. Chanon[19], T. Cheng[20], S. Y. Choi[21], A. David[22,23],
P. de Aquino[24], G. Degrassi[25], D. Del Re[26], A. Denner[27], H. van Deurzen[28], S. Diglio[29],
B. Di Micco[25], R. Di Nardo[30], S. Dittmaier[8], M. Dührssen[22], R. K. Ellis[15], G. Ferrera[31],
N. Fidanza[32], M. Flechl[8], D. de Florian[32], S. Forte[31], R. Frederix[33], S. Frixione[34], S. Gangal[35],
Y. Gao[36], M. V. Garzelli[37], D. Gillberg[22], P. Govoni[38], M. Grazzini[18,†], N. Greiner[28], J. Griffiths[39],
A .V. Gritsan[11], C. Grojean[40,22], D. C. Hall[41], C. Hays[41], R. Harlander[42], R. Hernandez-Pinto[32],
S. Höche[43], J. Huston[44], T. Jubb[5], M. Kadastik[45], S. Kallweit[18], A. Kardos[38], L. Kashif[46],
N. Kauer[47], H. Kim[39], R. Klees[48], M. Krämer[48], F. Krauss[5], A. Laureys[14], S. Laurila[49], S. Lehti[49],
Q. Li[50], S. Liebler[42], X. Liu[51], H. E. Logan[52], G. Luisoni[28], M. Malberti[22], F. Maltoni[14],
K. Mawatari[24], P. Maierhöfer[18], H. Mantler[42], S. Martin[53], P. Mastrolia[28,54], O. Mattelaer[55],
J. Mazzitelli[32], B. Mellado[56], K. Melnikov[11], P. Meridiani[26], D. J. Miller[57], E. Mirabella[28],
S. O. Moch[12], P. Monni[18], N. Moretti[18], A. Mück[48], M. Mühlleitner[58], P. Musella[22], P. Nason[38],
C. Neu[59], M. Neubert[60], C. Oleari[38], J. Olsen[61], G. Ossola[62] T. Peraro[28], K. Peters[22],
F. Petriello[13,51], G. Piacquadio[22], C. T. Potter[63], S. Pozzorini[18], K. Prokofiev[64], I. Puljak[65],
M. Rauch[58], D. Rebuzzi[66], L. Reina[67], R. Rietkerk[33], A. Rizzi[68], Y. Rotstein-Habarnau[32],
G. P. Salam[34,7,‡], G. Sborlini[32], F. Schissler[58], M. Schönherr[5], M. Schulze[13], M. Schumacher[8],
F. Siegert[8], P. Slavich[7], J. M. Smillie[69], O. Stål[70], J. F. von Soden-Fraunhofen[28], M. Spira[71],
I. W. Stewart[72], F. J. Tackmann[35], P. T. E. Taylor[29], D. Tommasini[73], J. Thompson[5], R. S. Thorne[74],
P. Torrielli[18], F. Tramontano[75], N. V. Tran[36], Z. Trócsányi[76,73], M. Ubiali[48], P. Vanlaer[77],
M. Vazquez Acosta[78], T. Vickey[56,41], A. Vicini[31], W. J. Waalewijn[79], D. Wackeroth[80],
C. Wagner[13,16,17], J. R. Walsh[81], J. Wang[77], G. Weiglein[35], A. Whitbeck[11], C. Williams[15], J. Yu[39]
G. Zanderighi[41], M. Zanetti[72], M. Zaro[14], P. M. Zerwas[35], C. Zhang[14], T. .J .E. Zirke[42], and
S. Zuberi[81].

[1] Instituto de Física de Cantabria (IFCA), CSIC-Universidad de Cantabria, Santander, Spain

[2] INFN, Sezione di Torino, Via P. Giuria 1, 10125 Torino, Italy

[3] Dipartimento di Fisica Teorica, Università di Torino, Via P. Giuria 1, 10125 Torino, Italy

[4] Laboratoire de l'Accélérateur Linéaire, CNRS/IN2P3, F-91898 Orsay CEDEX, France

[5] Institute for Particle Physics Phenomenology, Department of Physics, University of Durham,
    Durham DH1 3LE, UK

[6] Nikhef Theory Group, Science Park 105, 1098 XG Amsterdam, The Netherlands

[7] Laboratoire de Physique Théorique et Hautes Energies (LPTHE), CNRS et Université Paris 6, 4
    Place Jussieu, F-75252 Paris CEDEX 05, France

[8] Physikalisches Institut, Albert-Ludwigs-Universität Freiburg, D-79104 Freiburg, Germany

[9] Universität Bern - Albert Einstein Center for Fundamental Physics,
    Institute for Theoretical Physics Sidlerstrasse 5, CH-3012 Bern, Switzerland

[10] University of Victoria, Victoria, British Columbia, V8W 3P, Canada

[11] Johns Hopkins University, Baltimore, Maryland. 410-516-8000, USA

[12] II. Institut für Theoretische Physik, Universität Hamburg,
    Luruper Chaussee 149, D-22761 Hamburg, Germany

[13] High Energy Physics Division, Argonne National Laboratory, Argonne, IL 60439, USA

[14] Centre for Cosmology, Particle Physics and Phenomenology (CP3),
    Université Catholique de Louvain, B-1348 Louvain-la-Neuve, Belgium

[15] Theoretical Physics Department, Fermi National Accelerator Laboratory,
    MS 106, Batavia, IL 60510-0500, USA

[16] University of Chicago - Enrico Fermi Institute,
5640 S. Ellis Avenue, RI-183, Chicago, IL 60637, USA

[17] University of Chicago - Kavli Institute for Cosmological Physics,
Lab. for Astrophys. Space Res. (LASR), 933 East 56th St., Chicago, IL 60637, USA

[18] Institute for Theoretical Physics, University of Zurich,
Winterthurerstrasse 190, CH-8057 Zurich, Switzerland

[19] Institute for Particle Physics, ETH Zurich,
Schafmattstrasse 16, CH-8093, Zurich, Switzerland

[20] University of Florida, 215 Williamson Hall, P.O. Box 118440 Gainesville, FL 32611, USA

[21] Chunbuk National University, Physics Department, Jeonju 561-756, South Korea

[22] CERN, CH-1211 Geneva 23, Switzerland

[23] Laboratório de Instrumentação e Física Experimental de Partículas, LIP-Lisboa, Portugal

[24] Theoretische Natuurkunde and IIHE/ELEM, Vrije Universiteit Brussel,
and International Solvay Institutes, Pleinlaan 2, B-1050 Brussels, Belgium

[25] Università degli Studi di "Roma Tre" Dipartimento di Fisica,
Via Vasca Navale 84, Rome, Italy

[26] Università di Roma "Sapienza" and INFN Sezione di Roma, Italy

[27] Institut für Theoretische Physik und Astrophysik, Universität Würzburg,
Emil-Hilb-Weg 22, D-97074 Würzburg, Germany

[28] Max-Planck-Institut für Physik, Werner-Heisenberg-Institut,
Föhringer Ring 6, D-80805 München, Germany

[29] School of Physics, University of Melbourne, Victoria, Australia

[30] INFN Laboratori Nazionali di Frascati, Frascati, Italy

[31] Dipartimento di Fisica, Università degli Studi di Milano and INFN,
Sezione di Milano, Via Celoria 16, I-20133 Milan, Italy

[32] Departamento de Física, Facultad de Ciencias Exactas y Naturales,
Universidad de Buenos Aires, Pabellon I, Ciudad Universitaria (1428),
Capital Federal, Argentina

[33] Institute for Theoretical Physics, University of Amsterdam,
Science Park 904, 1090 GL Amsterdam, The Netherlands

[34] PH Department, TH Unit, CERN, CH-1211 Geneva 23, Switzerland

[35] DESY, Notkestrasse 85, D-22607 Hamburg, Germany

[36] Fermi National Accelerator Laboratory, MS 106, Batavia, IL 60510-0500, USA

[37] University of Nova Gorica, Laboratory for Astroparticle Physics,
SI-5000 Nova Gorica, Slovenia

[38] Università di Milano-Bicocca and INFN, Sezione di Milano-Bicocca,
Piazza della Scienza 3, 20126 Milan, Italy

[39] Department of Physics, Univ. of Texas at Arlington, SH108, University of Texas,
Arlington, TX 76019, USA

[40] ICREA at IFAE, Universitat Autònoma de Barcelona, Bellaterra, Spain

[41] Department of Physics, University of Oxford, Denys Wilkinson Building,
Keble Road, Oxford OX1 3RH, UK

[42] Bergische Universität Wuppertal, D-42097 Wuppertal, Germany

[43] SLAC National Accelerator Laboratory, Menlo Park, CA 94025, USA

[44] Department of Physics and Astronomy, Michigan State University,
East Lansing, MI 48824, USA

[45] National Institute of Chemical Physics and Biophysics, Tallinn, Estonia

[46] Univ. of Wisconsin, Dept. of Physics, High Energy Physics,
2506 Sterling Hall 1150 University Ave, Madison, WI 53706, USA

[47] Department of Physics, Royal Holloway, University of London, Egham TW20 0EX, UK

[48] Institut für Theoretische Teilchenphysik und Kosmologie, RWTH Aachen University,
D-52056 Aachen, Germany

[49] Helsinki Institute of Physics, P.O. Box 64, FIN-00014 University of Helsinki, Finland

[50] School of Physics, and State Key Laboratory of Nuclear Physics and Technology,
Peking University, China

[51] Department of Physics & Astronomy, Northwestern University, Evanston, IL 60208, USA

[52] Ottawa-Carleton Institute for Physics (OCIP), Ottawa, Ontario K1S 5B6, Canada

[53] Northern Illinois University (NIU) - Department of Physics DeKalb, IL 60115, USA

[54] Dipartimento di Fisica e Astronomia, Università di Padova, and INFN Sezione di Padova,
via Marzolo 8, 35131 Padova, Italy

[55] Department of Physics, University of Illinois at Urbana-Champaign, Urbana, IL 61801, USA

[56] School of Physics, University of the Witwatersrand, Private Bag 3,
Wits 2050, Johannesburg, South Africa

[57] SUPA, School of Physics and Astronomy, University of Glasgow, Glasgow, G12 8QQ, UK

[58] Institute for Theoretical Physics, Karlsruhe Institute of Technology, 76128 Karlsruhe, Germany

[59] University of Virginia, Charlottesville, VA 22906, USA

[60] Johannes Gutenberg-Universität Mainz (JGU) - Institut für Physik (IPH),
Staudingerweg 7, 55128 Mainz, Germany

[61] Department of Physics, Princeton University, Princeton, NJ 08542, USA

[62] New York City College of Technology, City University of New York,
300 Jay Street, Brooklyn NY 11201, USA
and The Graduate School and University Center, City University of New York,
365 Fifth Avenue, New York, NY 10016, USA

[63] Department of Physics, University of Oregon, Eugene, OR 97403-1274, USA

[64] Department of Physics, New York University, New York, NY, USA

[65] University of Split, FESB, R. Boskovica bb, 21 000 Split, Croatia

[66] Università di Pavia and INFN, Sezione di Pavia, Via A. Bassi, 6, 27100 Pavia, Italy

[67] Physics Department, Florida State University, Tallahassee, FL 32306-4350, USA

[68] Università and INFN of Pisa, via F. Buonarotti, PIsa, Italy

[69] School of Physics and Astronomy, University of Edinburgh,
Mayfield Road, Edinburgh EH9 3JZ, UK

[70] The Oskar Klein Centre, Deptartment of Physics Stockholm University,
SE-106 91 Stockholm, Sweden

[71] Paul Scherrer Institut, CH–5232 Villigen PSI, Switzerland

[72] Massachusetts Institute of Technology,
77 Massachusetts Avenue, Cambridge, MA 02139-4307, USA

[73] Institute of Physics, University of Debrecen, H-4010 Debrecen P.O.Box 105, Hungary

[74] Department of Physics and Astronomy, University College London,
Gower Street, London WC1E 6BT, UK

[75] Università di Napoli Federico II Dipartimento di Scienze Fisiche, via Cintia I-80126 Napoli, Italy

[76] Institute of Nuclear Research of the Hungarian Academy of Sciences, Hungary

[77] Univ. Libre de Bruxelles, B-1050 Bruxelles, Belgium

[78] Physics Dept., Blackett Laboratory, Imperial College London,
Prince Consort Rd, London SW7 2BW, UK

[79] Department of Physics, University of California at San Diego, La Jolla, CA 92093, USA

[80] Department of Physics, SUNY at Buffalo, Buffalo, NY 14260-1500, USA

[81] Lawrence Berkeley National Laboratory (LBNL) - Physics Division,
1 Cyclotron Road, 50R4049, Berkeley, CA 94720-8153, USA

[†] On leave of absence from INFN, Sezione di Firenze, Italy

[‡] On leave from Department of Physics, Princeton University, Princeton, NJ 08544, USA

Contents

[1]S. Heinemeyer, C. Mariotti, G. Passarino and R. Tanaka.

[2]S. Heinemeyer, A. Mück, I. Puljak, D. Rebuzzi (eds.); A. Denner, S. Dittmaier, M. Spira, M. Mühlleitner.

[3]D. de Florian, B. Di Micco (eds.); R. Boughezal, F. Caola, N. Chanon, R. Di Nardo, G. Ferrera, N. Fidanza, M. Grazzini, D.C. Hall, C. Hays, J. Griffiths, R. Hernandez-Pinto, N. Kauer, H. Kim, S. Martin, J. Mazzitelli, K. Melnikov, F. Petriello, Y. Rotstein-Habarnau, G. Sborlini, M. Schulze, D. Tommasini and J. Yu

[4]D. de Florian, M. Grazzini

[5]R. Boughezal, F. Caola, K. Melnikov, F. Petriello, M. Schulze

[6]D. de Florian, G. Ferrera, M. Grazzini, D. Tommasini

[7]B. Di Micco, R.Di Nardo, H. Kim, J. Griffiths, D. C. Hall, C. Hays and J. Yu

[8]A. Denner, P. Govoni, C. Oleari, D. Rebuzzi (eds.); P. Bolzoni, S. Dittmaier, S. Frixione, F. Maltoni, C. Mariotti, S.-O. Moch, A. Mück, P. Nason, M. Rauch, P. Torrielli, M. Zaro.

[9]S. Dittmaier, G. Ferrera, A. Rizzi, G. Piacquadio (eds.); A. Denner, M. Grazzini, R.V. Harlander, S. Kallweit, A. Mück, F. Tramontano and T.J.E. Zirke.

[10]C. Neu, C. Potter, L. Reina, A. Rizzi, M. Spira, (eds.); P. Artoisenet, F. Cascioli, R. Frederix, M. V. Garzelli, S. Hoeche, A. Kardos, F. Krauss, P. Maierhöfer, O. Mattelaer, N. Moretti, S. Pozzorini, R. Rietkerk, J. Thompson, Z. Trócsányi, D. Wackeroth

[11]S. Forte, J. Huston, R. Thorne

---

[12]D. Del Re, B. Mellado, G. P. Salam, F. J. Tackmann (eds.); A. Banfi, T. Becher, F.U. Bernlochner, S. Gangal, D. Gillberg, X. Liu, M. Malberti, P. Meridiani, P. Monni, P. Musella, M. Neubert, F. Petriello, I. W. Stewart, J. R. Walsh, G. Zanderighi, S. Zuberi

[13]A. Banfi, T. Becher, P. Monni, M. Neubert, G. P. Salam, I. W. Stewart, F. J. Tackmann, J. R. Walsh, G. Zanderighi, S. Zuberi

[14]X. Liu, F. Petriello

[15]F. U. Bernlochner, S. Gangal, D. Gillberg, F. J. Tackmann

[16]F. Krauss, F. Maltoni, P. Nason (eds.); Jeppe R. Andersen, F. Cascioli, H. van Deurzen, N. Greiner, S. Höche, T. Jubb, G. Luisoni, P. Maierhoefer, P. Mastrolia, E. Mirabella, C. Oleari, G. Ossola, T. Peraro, S. Pozzorini, M. Schönherr, F. Siegert, J. M. Smillie, J. F. von Soden-Fraunhofen, F. Tramontano

[17]A. David, A. Denner, M. Dührssen, M. Grazzini, C. Grojean, K. Prokofiev, G. Weiglein, M. Zanetti (eds.); S. Dittmaier, G. Passarino, M. Spira.

[18]G. Cacciapaglia, C. Contino, A. Deandrea, B. Dobrescu, G. Drieu La Rochelle, J.R. Espinosa, A. Falkowski, E. Feng, J.B. Flament, M. Ghezzi, S. Heinemeyer, M. Mühlleitner, G. Petrucciani, R. Rattazzi, M. Schumacher, R. Sundrum, M. Trott, A. Vicini, D. Zeppenfeld are thanked for useful discussions and active participations in the working group activities.

[19]A. David, A. Denner, M. Dührssen, M. Grazzini, C. Grojean, K. Prokofiev, G. Weiglein, M. Zanetti (eds.); S. Bolognesi, S.Y. Choi, P. de Aquino, Y.Y Gao, A.V. Gritsan, K. Mawatari, K. Melnikov, D.J. Miller, M.M. Mühlleitner, M. Schulze, M. Spira, N.V. Tran, A. Whitbeck, P. Zerwas

[20]S. Bolognesi, S. Diglio, M. Kadastik, H.E. Logan, M. Muhlleitner, K. Peters (eds.); D. Buarque, J. Campbell, R.K. Ellis, S. Frixione, L. Kashif, N. Kauer, A. Laureys, Q. Li, F. Maltoni, G. Passarino, M. Rauch, F. Schissler, P.T.E. Taylor, J. Wang, C. Williams, C. Zhang

[21]S. Bolognesi, S. Diglio, C. Grojean, M. Kadastik, H.E. Logan, M. Muhlleitner K. Peters (eds.)

---

[22]M. Flechl, R. Harlander, M. Krämer, S. Lehti, P. Slavich, M. Spira, M. Vazquez Acosta, T. Vickey (eds.); E. Bagnaschi, M. Carena, G. Degrassi, S. Dittmaier, S. Heinemeyer, R. Klees, S. Laurila, S. Liebler, H. Mantler, O. Stål, M. Ubiali, A. Vicini, C. Wagner, G. Weiglein

[23]S. Heinemeyer, C. Mariotti, G. Passarino, R. Tanaka

1 Introduction[1]

The 4th of July 2012 ATLAS and CMS announced that they had discovered a new particle with a mass around 125 GeV [1, 2]. This came after only a bit more than one year of data taken at center of mass energies of 7 and 8 TeV. The discovery has been made while searching for the Higgs boson, the particle linked to the Brout-Englert-Higgs mechanism [3–8]. The outstanding performance of the LHC in 2012 delivered in total four times as much 8 TeV data as was used in the discovery analyses. The experiments were able thus to present new preliminary results confirming the existence of the particles and measuring the properties. The new particle is a boson, since it decays into two photons, $2\,Z$ and $2\,W$ bosons, and it could possibly be the Standard Model (SM) Higgs boson. More data and new theoretical approaches will help us in the future to establish the nature of this particle and, more important, if there is new physics around the corner.

At the Moriond conference this year, 2013, ATLAS and CMS presented the results on five main decay modes: $H \to 2\gamma$, $H \to ZZ \to 4\ell$, $H \to WW \to \ell\nu\ell\nu$, $H \to \tau\tau$, and $H \to \overline{b}b$ channels, with an integrated luminosities of up to 5 fb^{-1} at $\sqrt{s} = 7$ TeV and up to 21 fb^{-1} at $\sqrt{s} = 8$ TeV. The $H \to 2\gamma$ and $H \to ZZ \to 4\ell$ channels allow to measure the mass of the boson with very high precision. ATLAS measures $125.5 \pm 0.2(\text{stat.})^{+0.5}_{-0.6}(\text{syst.})$ GeV [9], CMS measures a mass of $125.7 \pm 0.3(\text{stat.}) \pm 0.3(\text{syst.})$ GeV [10]. Figure 1 shows the signal strength for the various decay channels for ATLAS and CMS. For ATLAS the combined signal strength is determined to be $\mu = 1.30 \pm 0.13(\text{stat.}) \pm 0.14(\text{syst.})$ at the measured mass value [11]. For CMS the combined signal strength is determined to be $\mu = 0.80 \pm 0.14$ at the measured mass value [10].

Whether or not the new particle is a Higgs boson is demonstrated by how it interacts with other particles and its own quantum properties. For example, a Higgs boson is postulated to have no spin and in the SM its parity, a measure of how its mirror image behaves, should be positive. ATLAS and CMS have compared a number of alternative spin-parity (J^P) assignments for this particle and, in pairwise hypothesis tests, the hypothesis of no spin and positive parity (0^+) is consistently favored against the alternative hypotheses [10, 12].

This report presents improved inclusive cross section calculation at 7 and 8 TeV in the SM and its minimal supersymmetric extension, together with the calculation of the relevant decay channels, in particular around the measured mass value of $125 - 126$ GeV. Results and extensive discussions are also presented for a heavy (SM-like) Higgs boson, including the correct treatment via the Complex Pole Scheme (CPS) as well as interference effects in particular in the WW and ZZ channels.

In view of the newly discovered particle the property determination becomes paramount. This report presents the interim recommendation to extract couplings as well as the spin and the parity of the new particle. For the determination of the coupling strength factors the correlated uncertainties for the decay calculations have to be taken into account and corresponding descriptions and results for the uncertainties at the level of partial widths are included in this report.

The report furthermore includes the state-of-the-art description of the relevant Monte Carlo generators, in particular for the difficult task of simulating the Higgs production together with (two) jets in gluon gluon fusion as compared to vector boson fusion. The treatment of jet bin uncertainties is also discussed.

This report tries to lay the path towards a further exploration of the Higgs sector of the (yet to be determined) underlying model. First, this includes the (re)quest for even more refined calculations of inclusive and differential cross sections in the SM, for heavy (SM-like) Higgs bosons, as well as in as many BSM models as possible. Dedicated efforts are needed to match the required accuracy in the SM, the MSSM and other BSM models. Methods for a reliable estimate of remaining uncertainties are needed. Second, this includes prescriptions for the correct extraction of the properties of the newly

---
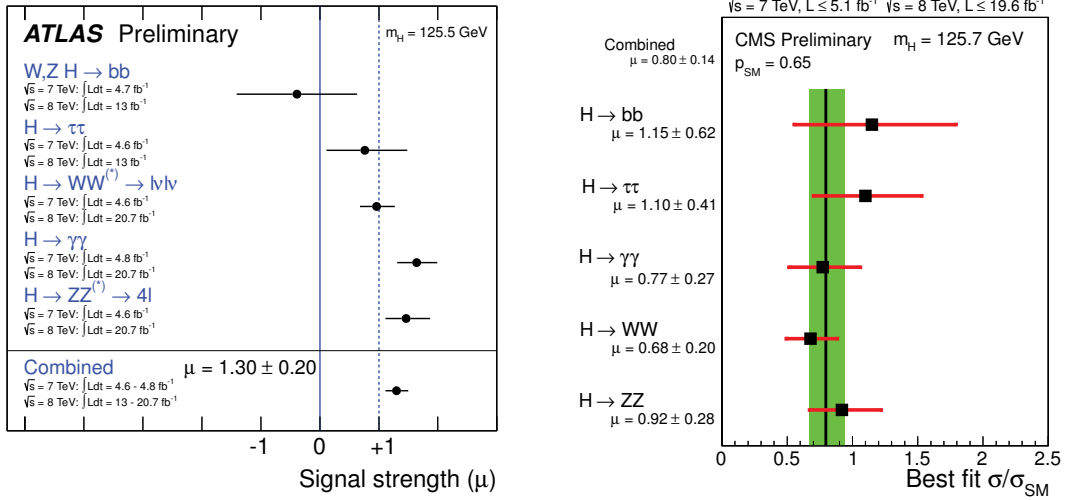
**Fig. 1:** The signal strength for the individual channel and their combination. The values of μ are given for $M_H = 125.5$ GeV for ATLAS and for $M_H = 125.7$ GeV for CMS.

discovered particle. While we report on substantial progress on these topics, it also becomes clear that a lot of dedicated effort will be needed to match the challenges electroweak symmetry breaking holds for us.

2 Branching Ratios [2]

For a correct interpretation of experimental data, precise calculations not only of the various production cross sections, but also for the relevant decay widths are essential, including their respective uncertainties. Concerning the SM Higgs boson, in Ref. [13] a first precise prediction of the branching ratios (BR) was presented. In Ref. [14,15] the BR predictions were supplemented with an uncertainty estimate including parametric uncertainties as well as the effects of unknown higher-order corrections. In Section 2.1, we update these predictions with a fine step size around the mass of the newly discovered Higgs-like particle at ATLAS [1] and CMS [2]. We also present the error estimates in a form which is suitable for taking error correlations into account. In Section 2.2, we discuss differential distributions for four-fermion final states. We show that interference effects (already at LO) and higher-order corrections distort the shapes of distributions at the level of 10%. For the lightest Higgs boson in the MSSM in Ref. [14] first results for $\mathrm{BR}(\mathrm{H} \to \tau^+\tau^-)$ ($\phi = \mathrm{h, H, A}$) were given in the $m_\mathrm{h}^\mathrm{max}$ scenario [16]. In Section 2.3 we present a first prediction for all relevant decay channels of the charged Higgs bosons in the $m_\mathrm{h}^\mathrm{max}$ scenario. We also provide first results for the BRs of all MSSM Higgs bosons in the newly presented benchmark scenarios.

2.1 SM Branching Ratios

In this section we update the SM BR calculations presented in Refs. [13–15]. The strategy and the calculational tools are unchanged with respect to Ref. [14]. Here, we focus on more detailed results for the BRs and the corresponding uncertainties for a SM Higgs boson around the mass of the newly discovered Higgs-like particle, i.e. around $M_\mathrm{H} = 126$ GeV, and correct small inconsistencies in the tabulated error estimates in Ref. [14]. The BRs as well as the corresponding uncertainties are a crucial ingredient entering the phase of precision measurements in order to compare the properties of the new resonance to a SM Higgs boson in a reliable way. Moreover, for a Higgs mass around 126 GeV, we give detailed results on the different parametric uncertainties (PU) and theoretical uncertainties (THU), as introduced in Refs. [14,15], of the relevant partial Higgs decay widths. The given results facilitate the combination of Higgs measurements including error correlations in the BRs. First, in Section 2.1.1, we briefly review the evaluation of the decay widths, the BRs, and the relevant uncertainties. More details can be found in Refs. [13–15]. Results are presented for the total width, Γ_H, and the BRs for the decay modes $\mathrm{H} \to \mathrm{bb}$, $\mathrm{H} \to \mathrm{c\bar{c}}$, $\mathrm{H} \to \tau^+\tau^-$, $\mathrm{H} \to \mu^+\mu^-$, $\mathrm{H} \to \mathrm{gg}$, $\mathrm{H} \to \gamma\gamma$, $\mathrm{H} \to \mathrm{Z}\gamma$, $\mathrm{H} \to \mathrm{WW}$, and $\mathrm{H} \to \mathrm{ZZ}$ (including detailed results also for the various four-fermion final states) in Section 2.1.2. For large Higgs masses also the decay mode $\mathrm{H} \to \mathrm{t\bar{t}}$ has been analyzed. The various PUs and THUs on the level of the partial widths are presented in Section 2.1.3 for selected Higgs masses.

2.1.1 Strategy and input for Branching Ratio Calculations

In this section we briefly summarize the strategy for the BR calculations for the updates in this report. The calculations are performed in exactly the same setup as the BR predictions in Ref. [14]. A detailed description can be found there.

We use HDECAY [17–19] and PROPHECY4F [20–22] to calculate all the partial widths with the highest accuracy available. The included higher-order corrections and the remaining THUs have been discussed in detail in Section 2.1.3.2 of Ref. [14]. For the detailed results in the low-mass region, the total uncertainties in Table 2 of Ref. [14] are used as THUs for the different Higgs-boson decay modes. The uncertainty for the total width is derived by adding the uncertainties for the partial widths linearly. Concerning the BRs, the variations of all branching ratios are calculated for each individual partial width being varied within the corresponding relative error keeping all other partial widths fixed at their central value (since each branching ratio depends on all partial widths, scaling a single partial width modifies all branching ratios). Hence, there is an individual THU of each branching ratio due to the THU of each partial width. We assume only all $\mathrm{H} \to \mathrm{WW/ZZ} \to 4f$ decays to be correlated and, hence, only

3

consider the simultaneous scaling of all 4-fermion partial widths. The derived individual THUs for each branching ratios are added linearly to obtain the corresponding total THU.

For our calculations, the input parameter set as defined in Appendix A of Ref. [13] has been used (for quark masses see comments below). From the given PDG values of the gauge-boson masses, we derive the pole masses $M_Z = 91.15349$ GeV and $M_W = 80.36951$ GeV which are used as input. The gauge-boson widths have been calculated at NLO from the other input parameters resulting in $\Gamma_Z = 2.49581$ GeV and $\Gamma_W = 2.08856$ GeV. It should be noted again that for our numerical analysis we have used the one-loop pole masses for the charm and bottom quarks and their uncertainties, since these values do not exhibit a significant dependence on the value of the strong coupling constant α_s in contrast to the $\overline{\text{MS}}$ masses [23]. To be precise, we use $M_b = 4.49$ GeV, $M_c = 1.42$ GeV, and $M_s = 0.10$ GeV. The small shifts with respect to the charm- and strange-quark masses used in Ref. [14] do not affect the BRs significantly at all.

Concerning the parametric uncertainties, we take only into account the uncertainties of the input parameters α_s, m_c, m_b, and m_t as given in Table 1 of Ref. [14], where also the detailed reasoning leading to this specific choice is given. Using these uncertainties, for each parameter $p = \alpha_s, m_c, m_b, m_t$ we have calculated the Higgs branching ratios for p, $p + \Delta p$ and $p - \Delta p$ keeping all the other parameters fixed at their central values. The resulting error on each BR is then given by

$$
\begin{aligned}
\Delta_+^p \text{BR} &= \max\{\text{BR}(p + \Delta p), \text{BR}(p), \text{BR}(p - \Delta p)\} - \text{BR}(p), \\
\Delta_-^p \text{BR} &= \text{BR}(p) - \min\{\text{BR}(p + \Delta p), \text{BR}(p), \text{BR}(p - \Delta p)\},
\end{aligned} \tag{1}
$$

which may lead to asymmetric errors. The total PUs have been obtained by adding the calculated errors due to the four parameters in quadrature. In analogy, the uncertainties of the partial and total decay widths are given by

$$
\begin{aligned}
\Delta_+^p \Gamma &= \max\{\Gamma(p + \Delta p), \Gamma(p), \Gamma(p - \Delta p)\} - \Gamma(p), \\
\Delta_-^p \Gamma &= \Gamma(p) - \min\{\Gamma(p + \Delta p), \Gamma(p), \Gamma(p - \Delta p)\},
\end{aligned} \tag{2}
$$

where Γ denotes the partial decay width for each considered decay channel or the total width, respectively. The total PUs have been calculated again by adding the individual PUs in quadrature.

The total uncertainties on the BRs, i.e. combining PUs and THUs, are derived by adding linearly the total parametric uncertainties and the total theoretical uncertainties. To allow for taking into account correlations in the errors of the different BRs, we provide also the uncertainties for the different partial widths in Section 2.1.3 for selected Higgs masses.

For completeness, we repeat that the Higgs total width resulting from HDECAY has been modified according to the prescription

$$
\Gamma_H = \Gamma^{\text{HD}} - \Gamma_{ZZ}^{\text{HD}} - \Gamma_{WW}^{\text{HD}} + \Gamma_{4f}^{\text{Proph.}}, \tag{3}
$$

where Γ_H is the total Higgs width, Γ^{HD} the Higgs width obtained from HDECAY, Γ_{ZZ}^{HD} and Γ_{WW}^{HD} stand for the partial widths to ZZ and WW calculated with HDECAY, while $\Gamma_{4f}^{\text{Proph.}}$ represents the partial width of H $\to$ 4f calculated with PROPHECY4F. The latter can be split into the decays into ZZ, WW, and the interference,

$$
\Gamma_{4f}^{\text{Proph.}} = \Gamma_{H \to W^* W^* \to 4f} + \Gamma_{H \to Z^* Z^* \to 4f} + \Gamma_{WW/ZZ - \text{int.}}, \tag{4}
$$

where the individual contributions are defined in terms of partial widths with specific final states according to

$$
\Gamma_{H \to W^* W^* \to 4f} = 9 \cdot \Gamma_{H \to \nu_e e^+ \mu \bar{\nu}_\mu} + 12 \cdot \Gamma_{H \to \nu_e e^+ d \bar{u}} + 4 \cdot \Gamma_{H \to u \bar{d} s \bar{c}},
$$

4

$$
\begin{aligned}
\Gamma_{H \to Z^*Z^* \to 4f} = {} & 3 \cdot \Gamma_{H \to \nu_e \bar{\nu}_e \nu_\mu \bar{\nu}_\mu} + 3 \cdot \Gamma_{H \to ee^+ \mu\mu^+} + 9 \cdot \Gamma_{H \to \nu_e \bar{\nu}_e \mu\mu^+} \\
& + 3 \cdot \Gamma_{H \to \nu_e \bar{\nu}_e \nu_e \bar{\nu}_e} + 3 \cdot \Gamma_{H \to ee^+ ee^+} \\
& + 6 \cdot \Gamma_{H \to \nu_e \bar{\nu}_e u \bar{u}} + 9 \cdot \Gamma_{H \to \nu_e \bar{\nu}_e d \bar{d}} + 6 \cdot \Gamma_{H \to u \bar{u} ee^+} + 9 \cdot \Gamma_{H \to d \bar{d} ee^+} \\
& + 1 \cdot \Gamma_{H \to u \bar{u} c \bar{c}} + 3 \cdot \Gamma_{H \to d \bar{d} s \bar{s}} + 6 \cdot \Gamma_{H \to u \bar{u} s \bar{s}} + 2 \cdot \Gamma_{H \to u \bar{u} u \bar{u}} \\
& + 3 \cdot \Gamma_{H \to d \bar{d} d \bar{d}} \, , \\
\Gamma_{WW/ZZ-\text{int.}} = {} & 3 \cdot \Gamma_{H \to \nu_e e^+ e \bar{\nu}_e} - 3 \cdot \Gamma_{H \to \nu_e \bar{\nu}_e \mu\mu^+} - 3 \cdot \Gamma_{H \to \nu_e e^+ \mu \bar{\nu}_\mu} \\
& + 2 \cdot \Gamma_{H \to u \bar{d} d \bar{u}} - 2 \cdot \Gamma_{H \to u \bar{u} s \bar{s}} - 2 \cdot \Gamma_{H \to u \bar{d} s \bar{c}} \, .
\end{aligned}
$$

2.1.2 BR Results for Higgs masses

In this section we provide results for the BRs of the SM Higgs boson, using a particularly fine grid of mass points close to $M_H = 126$ GeV. The results are generated and presented in complete analogy to the predictions in Refs. [14], including the error estimates for each BR. In the error estimates, we have identified and removed inconsistencies in the calculation of the numbers presented in Refs. [14]. The corresponding changes in the error estimate are at the level of one percent for $m_H > 135$ GeV. For $m_H > 500$ GeV the changes increase for some decay modes, in particular for H $\to$ t$\bar{\text{t}}$. The central values of the BRs are not affected.

The fermionic decay modes are shown in Table A.1 to Table A.7. The bosonic decay modes together with the total width are given in Table A.8 to Table A.14. The same information (including the full uncertainty) is also presented graphically in Figure 2 for the low-mass region (left) and for the full mass range (right).
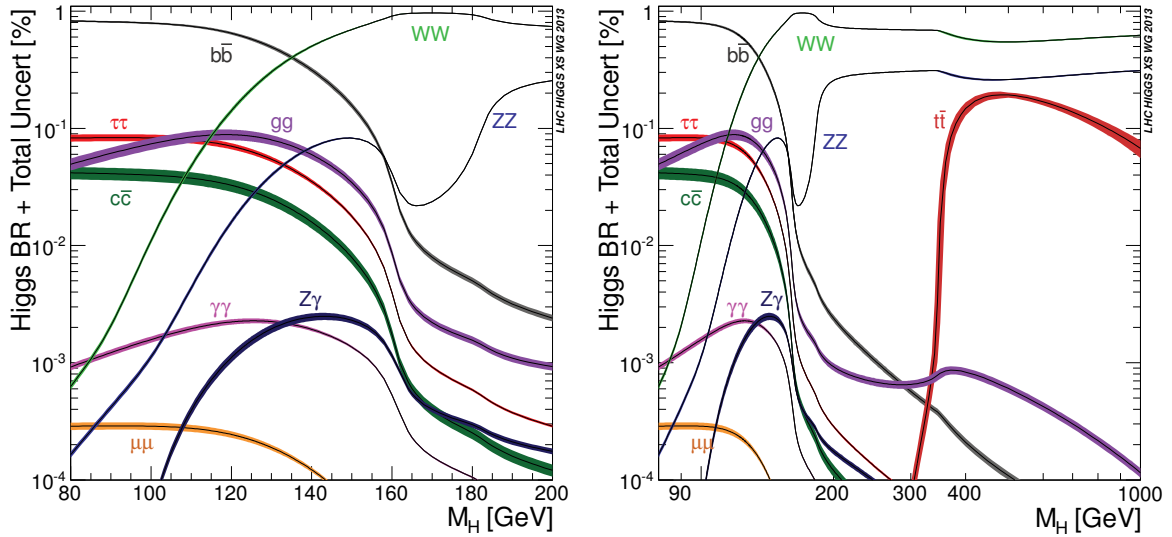
Fig. 2: Higgs branching ratios and their uncertainties for the low mass range (left) and for the full mass range (right).

2.1.3 BR Correlations for Higgs masses close to 126 GeV

In this section, we focus on the error correlations for the different BRs. The reason for the correlations is two-fold: Varying the input parameters within their error bands will induce shifts of the different partial widths and the resulting BRs in a correlated way. Moreover, there is trivial correlation between the BRs

because all the BRs have to add up to one. The shift in a single partial width will shift all BRs in a correlated way.

In Table 3 of Ref. [14], focusing on the errors of the BRs, we showed how the PUs for each input parameter and the THUs affect the final BR predictions. To take correlations into account, it is beneficial to present the same information directly on the level of the partial widths. For the partial widths, the THUs can be assumed to be uncorrelated. Moreover, the correlated effect on each partial width from varying a parameter within its errors is disentangled from the additional trivial correlation when calculating the BRs. We show the results for the partial widths in Table 1 for $M_H = 122$ GeV, 126 GeV, and 130 GeV. For each relevant partial width, we show the THU and the different PUs evaluated as before according to (2).

To be even more precise, as in Table 3 of Refs. [14], for each input parameter we show the induced shift on each partial width for the maximal and minimal choice of the input parameter as upper and lower entry in the table, respectively. Hence, the table allows to read off the correlation in the variation of the different partial widths. The associated error bands are slightly asymmetric. However, it is a good approximation to symmetrize the error band and assume a Gaussian probability distribution for the corresponding prediction.

The THUs on the partial widths of all the four-fermion final-states can be considered to be fully correlated. All other THUs are considered to be uncorrelated. Hence, for the BRs only the trivial correlation is present. However, it should be stressed again that in contrast to the PUs theory errors cannot be assumed to be Gaussian errors. Assuming a Gaussian distribution and, hence, effectively adding THUs to the PUs in quadrature will in general lead to underestimated errors. According to the recommendations in Section 12 of Ref. [13], the THUs should be considered to have a flat probability distribution within the given range. Alternatively, the envelope of extreme choices for the theory prediction on the partial widths should be used as an error estimate. (For all the presented errors on the BRs, we have added PUs and THUs of the resulting BRs linearly, as discussed in Section 2.1.1 before. Thereby we provide the envelope for each resulting BR, however, correlation is lost on the level of BRs.)

In total, there are four input parameters to be varied corresponding to the PUs and one has to include eight uncorrelated THUs for the various partial widths. Analyzing in detail the most interesting region around $M_H = 126$ GeV, the different uncertainties are of different importance. Aiming for a given accuracy, some uncertainties may be safely neglected, as can be inferred from Table 1. Even sizeable uncertainties for a given partial width can be unimportant if the decay mode has a small BR and does not contribute significantly to combined measurements.

Concerning the PUs, the variation of α_s and the bottom quark mass impact the BR predictions at the few percent level each. The charm quark mass is only relevant for $H \to c\bar{c}$ and affects other BRs only at the few per mille level. The dominant THU for most relevant channels is the one for $H \to b\bar{b}$. The THU for $H \to \gamma\gamma$ amounts to 1% and is needed at this level of precision. The THU for $H \to WW/ZZ \to 4f$ is estimated at 0.5% and thus also quite small. The THU for $H \to c\bar{c}$, $H \to gg$, $H \to Z\gamma$, $H \to \mu^+\mu^-$, and $H \to \tau^+\tau^-$ only has sizeable effects if a measurement of the corresponding channel is included or errors of a few per mille are important.

2.2 Differential prediction for the final state $H \to WW/ZZ \to 4f$

In this section, we discuss differential distributions for $H \to WW/ZZ \to 4f$ as calculated with PROPHECY4F for a SM Higgs boson with mass $M_H = 126$ GeV. It is not our goal to provide an analysis of the role of differential distributions in the measurement of Higgs-boson properties as done in other chapters of this report. Here, we merely want to emphasize the impact of NLO corrections and in particular the impact of interference effects on distributions. These interference effects have already been discussed for the branching rations in Ref. [14]. They arise when the final-state fermions can pair up in more than one way to form intermediate vector bosons. Therefore, they are not included in any ap-

6

Table 1: SM Higgs partial widths and their relative parametric (PU) and theoretical (THU) uncertainties for a selection of Higgs masses. For PU, all the single contributions are shown. For these four columns, the upper percentage value (with its sign) refers to the positive variation of the parameter, while the lower one refers to the negative variation of the parameter.

Channel	M_H [GeV]	Γ [MeV]	$\Delta\alpha_s$	Δm_b	Δm_c	Δm_t	THU
$H \to bb$	122	2.30	−2.3% +2.3%	+3.2% −3.2%	+0.0% −0.0%	+0.0% −0.0%	+2.0% −2.0%
	126	2.36	−2.3% +2.3%	+3.3% −3.2%	+0.0% −0.0%	+0.0% −0.0%	+2.0% −2.0%
	130	2.42	−2.4% +2.3%	+3.2% −3.2%	+0.0% −0.0%	+0.0% −0.0%	+2.0% −2.0%
$H \to \tau^+\tau^-$	122	$2.51{\cdot}10^{-1}$	+0.0% +0.0%	+0.0% −0.0%	+0.0% −0.0%	+0.0% −0.1%	+2.0% −2.0%
	126	$2.59{\cdot}10^{-1}$	+0.0% +0.0%	+0.0% −0.0%	−0.0% −0.0%	+0.1% −0.1%	+2.0% −2.0%
	130	$2.67{\cdot}10^{-1}$	+0.0% +0.0%	+0.0% −0.0%	+0.0% −0.0%	+0.1% −0.1%	+2.0% −2.0%
$H \to \mu^+\mu^-$	122	$8.71{\cdot}10^{-4}$	+0.0% +0.0%	+0.0% −0.0%	+0.0% −0.0%	+0.1% −0.1%	+2.0% −2.0%
	126	$8.99{\cdot}10^{-4}$	+0.0% +0.0%	+0.0% −0.0%	−0.1% −0.0%	+0.0% −0.1%	+2.0% −2.0%
	130	$9.27{\cdot}10^{-4}$	+0.1% +0.0%	+0.0% −0.0%	+0.0% −0.0%	+0.1% −0.0%	+2.0% −2.0%
$H \to c\bar{c}$	122	$1.16{\cdot}10^{-1}$	−7.1% +7.0%	−0.1% −0.1%	+6.2% −6.0%	+0.0% −0.1%	+2.0% −2.0%
	126	$1.19{\cdot}10^{-1}$	−7.1% +7.0%	−0.1% −0.1%	+6.2% −6.1%	+0.0% −0.1%	+2.0% −2.0%
	130	$1.22{\cdot}10^{-1}$	−7.1% +7.0%	−0.1% −0.1%	+6.3% −6.0%	+0.1% −0.1%	+2.0% −2.0%
$H \to gg$	122	$3.25{\cdot}10^{-1}$	+4.2% −4.1%	−0.1% −0.1%	+0.0% −0.0%	−0.2% +0.2%	+3.0% −3.0%
	126	$3.57{\cdot}10^{-1}$	+4.2% −4.1%	−0.1% −0.1%	+0.0% −0.1%	−0.2% +0.2%	+3.0% −3.0%
	130	$3.91{\cdot}10^{-1}$	+4.2% −4.1%	−0.1% −0.2%	+0.0% −0.0%	−0.2% +0.2%	+3.0% −3.0%
$H \to \gamma\gamma$	122	$8.37{\cdot}10^{-3}$	+0.0% −0.0%	+0.0% −0.0%	+0.0% −0.0%	+0.0% −0.0%	+1.0% −1.0%
	126	$9.59{\cdot}10^{-3}$	+0.0% −0.0%	+0.0% −0.0%	+0.0% −0.0%	+0.0% −0.0%	+1.0% −1.0%
	130	$1.10{\cdot}10^{-2}$	+0.1% −0.0%	+0.0% −0.0%	+0.0% −0.0%	+0.0% −0.0%	+1.0% −1.0%
$H \to Z\gamma$	122	$4.74{\cdot}10^{-3}$	+0.0% −0.1%	+0.0% −0.0%	+0.0% −0.0%	+0.0% −0.1%	+5.0% −5.0%
	126	$6.84{\cdot}10^{-3}$	+0.0% −0.0%	+0.0% −0.0%	+0.0% −0.1%	+0.0% −0.1%	+5.0% −5.0%
	130	$9.55{\cdot}10^{-3}$	+0.0% −0.0%	+0.0% −0.0%	+0.0% −0.0%	+0.0% −0.0%	+5.0% −5.0%
$H \to WW$	122	$6.25{\cdot}10^{-1}$	+0.0% −0.0%	+0.0% −0.0%	+0.0% −0.0%	+0.0% −0.0%	+0.5% −0.5%
	126	$9.73{\cdot}10^{-1}$	+0.0% −0.0%	+0.0% −0.0%	+0.0% −0.0%	+0.0% −0.0%	+0.5% −0.5%
	130	1.49	+0.0% −0.0%	+0.0% −0.0%	+0.0% −0.0%	+0.0% −0.0%	+0.5% −0.5%
$H \to ZZ$	122	$7.30{\cdot}10^{-2}$	+0.0% −0.0%	+0.0% −0.0%	+0.0% −0.0%	+0.0% −0.0%	+0.5% −0.5%
	126	$1.22{\cdot}10^{-1}$	+0.0% −0.0%	+0.0% −0.0%	+0.0% −0.0%	+0.0% −0.0%	+0.5% −0.5%
	130	$1.95{\cdot}10^{-1}$	+0.0% −0.0%	+0.0% −0.0%	+0.0% −0.0%	+0.0% −0.0%	+0.5% −0.5%

proximation which relies on factorizing the Higgs decays into a decay to vector bosons $H \to WW/ZZ$, where the vector bosons have definite momenta, and successive vector-boson decays $W/Z \to 2f$. In contrast, they are included in PROPHECY4F which is based on the full $H \to 4f$ matrix elements including all interferences between different Feynman diagrams. To anticipate the results of this section, NLO corrections become important at the level of 5% accuracy, while the (LO) interference effects can distort distributions by more than 10%.

To be specific, we exemplarily analyze the following differential distributions for a Higgs decay with four charged leptons in the final state, for which the Higgs-boson rest frame is assumed to be reconstructed:

– In the Higgs-boson rest frame, we investigate $\cos\theta_{f^-f^-}$, where $\theta_{f^-f^-}$ is the angle between the two negatively charged leptons. This angle is unambiguously defined in any of the final states $H \to 4e$, $H \to 4\mu$, and $H \to 2\mu2e$ so that interference effects can be easily studied.

- In the Higgs-boson rest frame, we investigate the angle $\phi\prime$ between the two decay planes of the vector bosons, where

$$\cos\phi\prime = \frac{(\mathbf{k}_{12} \times \mathbf{k}_1) \cdot (\mathbf{k}_{12} \times \mathbf{k}_3)}{|\mathbf{k}_{12} \times \mathbf{k}_1||\mathbf{k}_{12} \times \mathbf{k}_3|} \quad , \quad \mathrm{sgn}(\sin\phi\prime) = \mathrm{sgn}(\mathbf{k}_{12} \cdot [(\mathbf{k}_{12} \times \mathbf{k}_1) \times (\mathbf{k}_{12} \times \mathbf{k}_3)]),$$

and $\mathbf{k}_{12} = \mathbf{k}_1 + \mathbf{k}_2$. In turn, $\mathbf{k}_{1,2}$ are the three-momenta of the fermions forming the fermion pair which is closest in invariant mass to an on-shell Z-boson. Moreover, $\mathbf{k}_1$ and $\mathbf{k}_3$ correspond to the momenta of the negatively charged fermions. For $H \rightarrow 2\mu 2e$, the fermion momenta could, of course, be associated to intermediate Z bosons unambiguously without kinematic information simply according to their flavour. However, only the kinematic selection is possible for $H \rightarrow 4e$ and $H \rightarrow 4\mu$. Since we want to compare the different channels to investigate interference effects, we use the kinematic identification for all channels.
- For the fermion pair that is closest in invariant mass to an on-shell Z boson, we investigate $\cos\Theta_{Vf^-}$, where Θ_{Vf^-} is the angle between the vector boson momentum (the sum of the momenta of the fermion pair) in the Higgs rest frame and the momentum of the negatively charged fermion associated to the vector boson in the vector-boson rest frame.

For a Higgs decay with 2 charged leptons and two neutrinos in the final state the Higgs rest frame is not reconstructable. However, we assume that the transverse momentum of the Higgs boson is known so that one can boost into the frame with vanishing transverse momentum. In this frame, we investigate

- the angle between the two charged leptons $\phi_{f^-f^+,T}$ in the transverse plane, i.e.

$$\cos\phi_{f^-f^+,T} = \frac{\mathbf{k}_{f^+,T} \cdot \mathbf{k}_{f^-,T}}{|\mathbf{k}_{f^+,T}||\mathbf{k}_{f^-,T}|} \quad \text{and} \quad \mathrm{sgn}(\sin\phi_{f^-f^+,T}) = \mathrm{sgn}(\mathbf{e}_z \cdot (\mathbf{k}_{f^+,T} \times \mathbf{k}_{f^-,T})),$$

where $\mathbf{k}_{f^\pm,T}$ denote the transverse momentum vectors of the charged fermions and $\mathbf{e}_z$ is the unit vector along one of the beams in the lab frame.

Similar differential distributions have been analyzed with PROPHECY4F already in Ref. [20] where additional discussions can be found. In Figure 3 (left column), we show the distributions, normalized to the corresponding partial width, with four charged leptons in the final state for a Higgs-boson mass $M_H = 126$ GeV at NLO accuracy for $H \rightarrow 4e$ and $H \rightarrow 2\mu 2e$. The electrons and positrons in $H \rightarrow 4e$ can form intermediate Z bosons in two different ways and the corresponding amplitudes interfere. The interference contributions are absent for fermion pairs of different flavour. Concerning final states with neutrinos, we show the results for the decay channels $H \rightarrow \nu_e e^+ \bar{\nu}_e e^-$ (with interference contributions) and $H \rightarrow \nu_e e^+ \bar{\nu}_\mu \mu$ (without interference contributions).

Also in Figure 3 (middle column), we show the relative NLO corrections δ to the different distributions (not to the normalized distributions to also show the overall effects on the partial width). To be precise, in the presence of bremsstrahlung photons, the fermion momenta are defined after recombination with the photon if the invariant mass of the lepton–photon pair is smaller than 5 GeV. We use the invariant mass as a criterion for recombination because it is independent of the lab frame which depends on the Higgs-production process. The results are similar to the NLO corrections shown in Ref. [20] for different Higgs-boson masses. It is also evident that the NLO corrections for channels with and without interference are similar.

Finally, in the right column of Figure 3, the relative difference

$$\Delta = \left(\frac{1}{\Gamma^{\mathrm{LO}}_{\mathrm{w.int.}}} \frac{\mathrm{d}\Gamma^{\mathrm{LO}}_{\mathrm{w.int.}}}{\mathrm{d}\mathcal{O}} - \frac{1}{\Gamma^{\mathrm{LO}}_{\mathrm{wo int.}}} \frac{\mathrm{d}\Gamma^{\mathrm{LO}}_{\mathrm{wo int.}}}{\mathrm{d}\mathcal{O}} \right) \Big/ \left(\frac{1}{\Gamma^{\mathrm{LO}}_{\mathrm{wo int.}}} \frac{\mathrm{d}\Gamma^{\mathrm{LO}}_{\mathrm{wo int.}}}{\mathrm{d}\mathcal{O}} \right)$$

between the channels with interference $\Gamma^{\mathrm{LO}}_{\mathrm{w int.}}$ and without interference $\Gamma^{\mathrm{LO}}_{\mathrm{wo int.}}$ is shown for the various observables $\mathcal{O}$ introduced above. To stress, that the interference is already present at LO, we show the
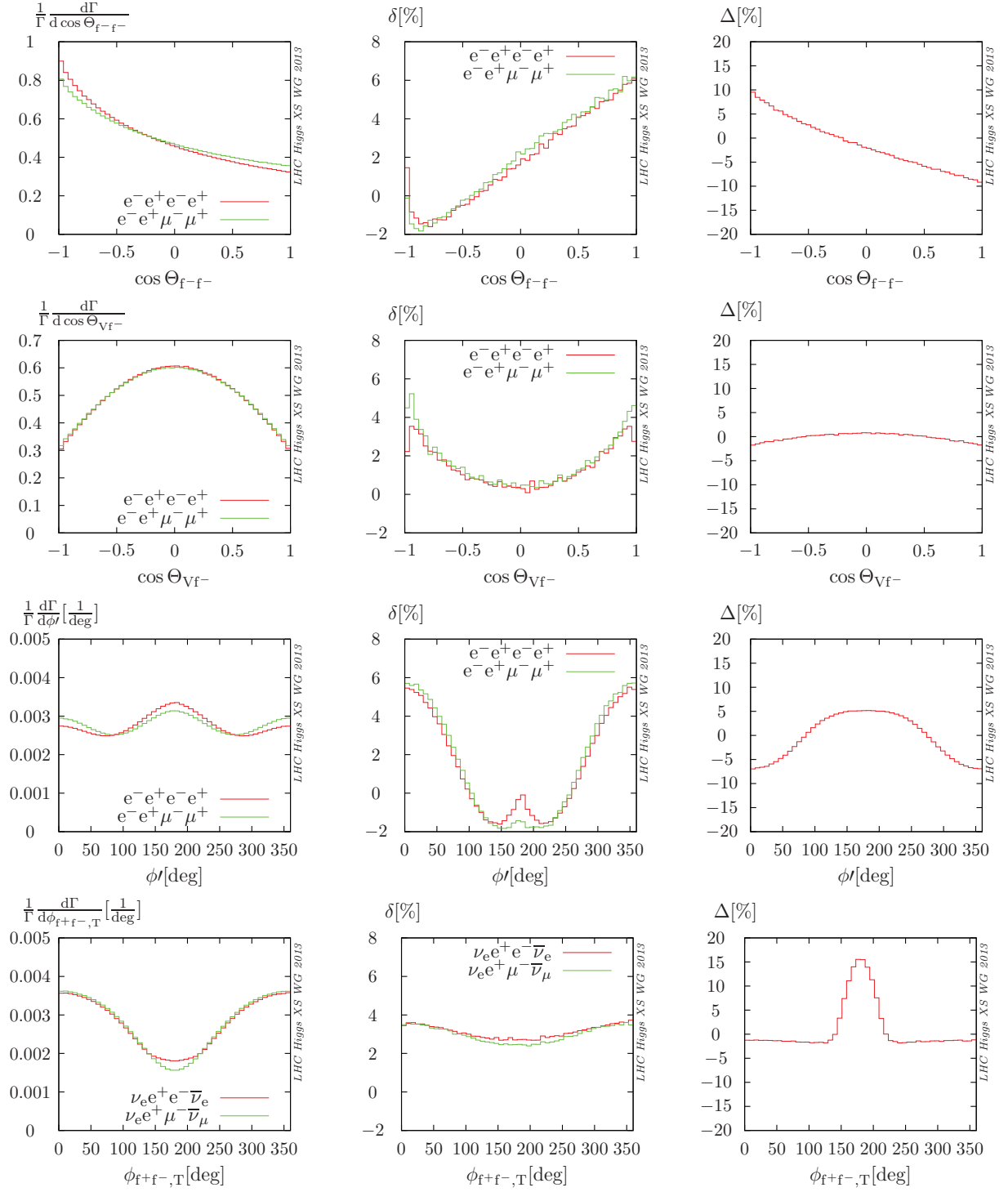
Fig. 3: The normalized distributions for different observables (left column) is shown together with the relative NLO corrections to the unnormalized distributions (middle column) and the relative difference of the two investigated channels Δ due to interference effects (right column) for $M_H = 126$ GeV (calculated with PROPHECY4F).

9

relative difference between the channels at LO. However, the difference at NLO would hardly differ as can be seen from the similarity of the NLO corrections in the middle column.

When aiming at an accuracy at the 10% level, the interference effects cannot be neglected any more. In particular, any approximation to the full process based on intermediate vector-bosons which neglects interference effects, must fail at this level of accuracy for final states like H → 4e and H → $\nu_e e^+ \overline{\nu}_e e$. Note that the interference effects as well as the NLO corrections distort the distributions and could be mistaken for anomalous couplings in precision measurements if they are not taken into account in the predictions.

2.3 MSSM Branching Ratios

In the MSSM the evaluation of cross sections and of branching ratios have several common issues as outlined in Section 14.1 (see also Sect. 12.1 in Ref. [14]). It was discussed that *before* any branching ratio calculation can be performed in a first step the Higgs-boson masses, couplings and mixings have to be evaluated from the underlying set of (soft SUSY-breaking) parameters. For the case of real parameters in the MSSM the code (FEYNHIGGS [24–28] was selected for the evaluations in this report. (The case with complex parameters has not been investigated so far.) The results for Higgs-boson masses and couplings can be provided to other codes (especially HDECAY [17–19]) via the SUSY Les Houches Accord [29, 30].

In the following subsections we describe how the relevant codes for the calculation of partial decay widths, FEYNHIGGS and HDECAY, are combined to give the most precise result for the Higgs-boson branching ratios in the MSSM. Numerical results are shown for all MSSM Higgs bosons (including the charged Higgs) within the updated benchmark scenarios [31], see Section 14.2. It should be stressed that it would be desirable to interpret the model-independent results of various Higgs-boson searches at the LHC also in other benchmark models, see for instance Ref. [32]. While we show exemplary plots for the branching ratios of A and H$^\pm$ for $\tan\beta = 10, 50$, detailed results for all Higgs BRs for $\tan\beta = 0.5 \ldots 60$ and $M_A = 90$ GeV $\ldots 1000$ GeV can be found in the working group web page [33].

2.3.1 Combination of calculations

After the calculation of Higgs-boson masses and mixings from the original SUSY input the branching ratio calculation has to be performed. Here we concentrate on the MSSM with real parameters. We combine the results from HDECAY and FEYNHIGGS on various decay channels to obtain the most accurate result for the branching ratios currently available. In a first step, all partial widths have been calculated as accurately as possible. Then the branching ratios have been derived from this full set of partial widths. Concretely, we used FEYNHIGGS for the evaluation of the Higgs-boson masses and couplings from the original input parameters, including corrections up to the two-loop level. The status of the various evaluations in FEYNHIGGS and HDECAY are detailed in Ref. [14]. The total decay width of the neutral Higgs bosons is calculated as,

$$\Gamma_\phi = \Gamma^{\mathrm{FH}}_{\mathrm{H}\to\tau^+\tau^-} + \Gamma^{\mathrm{FH}}_{\mathrm{H}\to\mu^+\mu^-} + \Gamma^{\mathrm{FH/P4f}}_{\mathrm{H}\to\mathrm{W}^{(*)}\mathrm{W}^{(*)}} + \Gamma^{\mathrm{FH/P4f}}_{\mathrm{H}\to\mathrm{Z}^{(*)}\mathrm{Z}^{(*)}}$$
$$+ \Gamma^{\mathrm{HD}}_{\mathrm{H}\to\mathrm{b}\overline{\mathrm{b}}} + \Gamma^{\mathrm{HD}}_{\mathrm{H}\to\mathrm{t}\overline{\mathrm{t}}} + \Gamma^{\mathrm{HD}}_{\mathrm{H}\to\mathrm{c}\overline{\mathrm{c}}} + \Gamma^{\mathrm{HD}}_{\mathrm{H}\to\mathrm{gg}} + \Gamma^{\mathrm{HD}}_{\mathrm{H}\to\gamma\gamma} + \Gamma^{\mathrm{HD}}_{\mathrm{H}\to\mathrm{Z}\gamma} \,, \tag{5}$$

followed by a corresponding evaluation of the respective branching ratio. Decays to strange quarks or other lighter fermions have been neglected. Due to the somewhat different calculation compared to the SM case in Section 2.1.1 no full decoupling of the decay widths and branching ratios of the light MSSM Higgs to the respective SM values can be expected.

The total decay width of the charged Higgs boson is calculated as,

$$\Gamma_{\mathrm{H}^\pm} = \Gamma^{\mathrm{FH}}_{\mathrm{H}^\pm\to\tau\nu_\tau} + \Gamma^{\mathrm{FH}}_{\mathrm{H}^\pm\to\mu\nu_\mu} + \Gamma^{\mathrm{FH}}_{\mathrm{H}^\pm\to\mathrm{hW}} + \Gamma^{\mathrm{FH}}_{\mathrm{H}^\pm\to\mathrm{HW}} + \Gamma^{\mathrm{FH}}_{\mathrm{H}^\pm\to\mathrm{AW}}$$

$$+ \Gamma^{HD}_{H^\pm \to tb} + \Gamma^{HD}_{H^\pm \to ts} + \Gamma^{HD}_{H^\pm \to td} + \Gamma^{HD}_{H^\pm \to cb} + \Gamma^{HD}_{H^\pm \to cs} + \Gamma^{HD}_{H^\pm \to cd}$$

$$+ \Gamma^{HD}_{H^\pm \to ub} + \Gamma^{HD}_{H^\pm \to us} + \Gamma^{HD}_{H^\pm \to ud} \, , \tag{6}$$

followed by a corresponding evaluation of the respective branching ratio.

2.3.2 Results in the new benchmark scenarios

The procedure outlined in the previous subsection can be applied to arbitrary points in the MSSM parameter space. Here we show representative results for the decay of the neutral MSSM Higgs bosons in the (updated) m_h^{max}, m_h^{mod+}, m_h^{mod-}, light stop, light stau, and τ-phobic scenario in Figure 4 - 9, respectively. Shown are the branching ratios for the h in the upper row, for the H in the middle row and for the A in the lower row with $\tan\beta = 10(50)$ in the left (right) column. The results for the charged Higgs boson are given in Figure 10, (11). The first plot shows the m_h^{max} (upper row), m_h^{mod+} (middle row) and m_h^{mod-} (lower row) scenario, while the second plot contains the light stop (upper row), light stau (middle row) and τ-phobic Higgs (lower row) scenario.

The branching ratios of the light Higgs boson, h, exhibit a strong variation at low M_A, while for large M_A the SM limit is reached. The corresponding values of the light Higgs boson mass, M_h, are indicated in the corresponding plots in Section 14.2. In particular in the τ-phobic scenario a reduction in the $h \to bb$ and $h \to \tau^+\tau^-$ channel can be observed, as analyzed in Ref. [31].

The branching ratios of the H and A boson follow the same pattern in all scenarios. For very low values of M_A the $H \to WW$ channel contributes, but overall the $H \to bb$ channel is dominant, about 10 times larger than the $H \to \tau^+\tau^-$ channel, which in turn is about 200 times larger than the $H \to \mu^+\mu^-$ channel. The size of the $H \to t\bar{t}$ channel, above the $t\bar{t}$ threshold is somewhat above the $H \to \tau^+\tau^-$ channel for $\tan\beta = 10$, but stays below even the $A \to \mu^+\mu^-$ channel for $\tan\beta = 50$ due to the suppression of the Higgs top coupling. The same pattern, except the decay to W^+W^- can be observed for the A boson. It should be noted that the decays of the heavy Higgs bosons to charginos and neutralinos, while taken into account in the BR evaluation, are not shown. However, their effects are visible at the kinks in the lines of the other channels, in particular for $\tan\beta = 10$ (see also Ref. [31]).

The branching ratios of the $H^\pm$, shown as a function of $M_{H^\pm}$, are also very similar in the various scenarios. At low values only the channels $H^\pm \to \tau\nu_\tau$, $H^\pm \to cs$ and $H^\pm \to \mu\nu_\mu$ are open. At $\sim 180\,\text{GeV}$ the channel $H^\pm \to tb$ opens up and becomes dominant, while $BR(H^\pm \to cs)$ and $BR(H^\pm \to \mu\nu_\mu)$ are very similar in size and more than two orders of magnitude smaller than $BR(H^\pm \to \tau\nu_\tau)$. The decays of the charged Higgs boson to charginos and neutralinos, again while taken into account in the BR evaluation, are not shown. However, their effects are visible as for the neutral Higgs bosons at the kinks in the lines of the other channels, in particular for $\tan\beta = 10$.
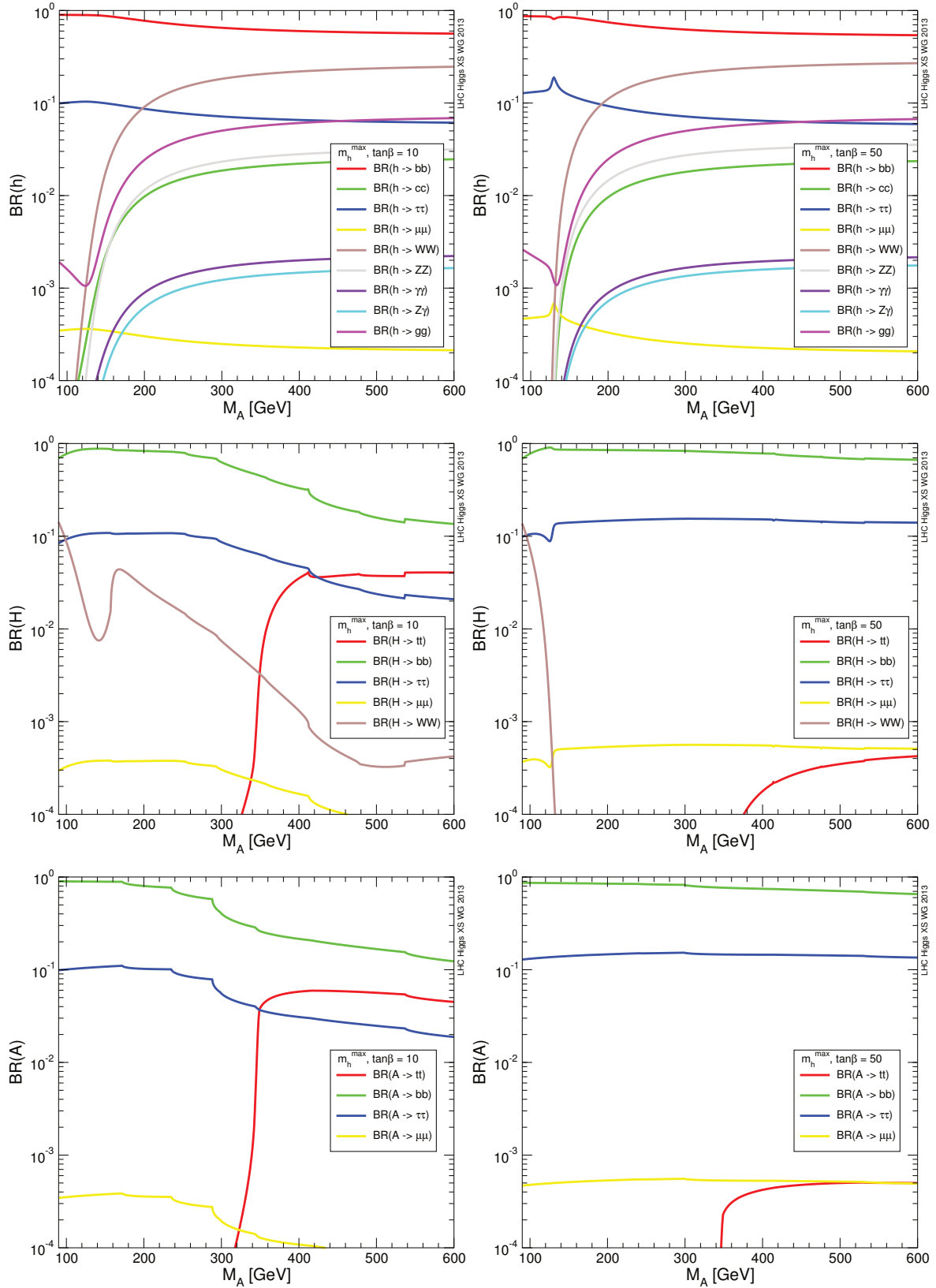
Fig. 4: Branching ratios of the MSSM Higgs bosons h (upper row), H (middle row) and A (lower row) in the m_h^{max} scenario as a function of M_A. The left (right) column shows the results for $\tan\beta = 10(50)$.
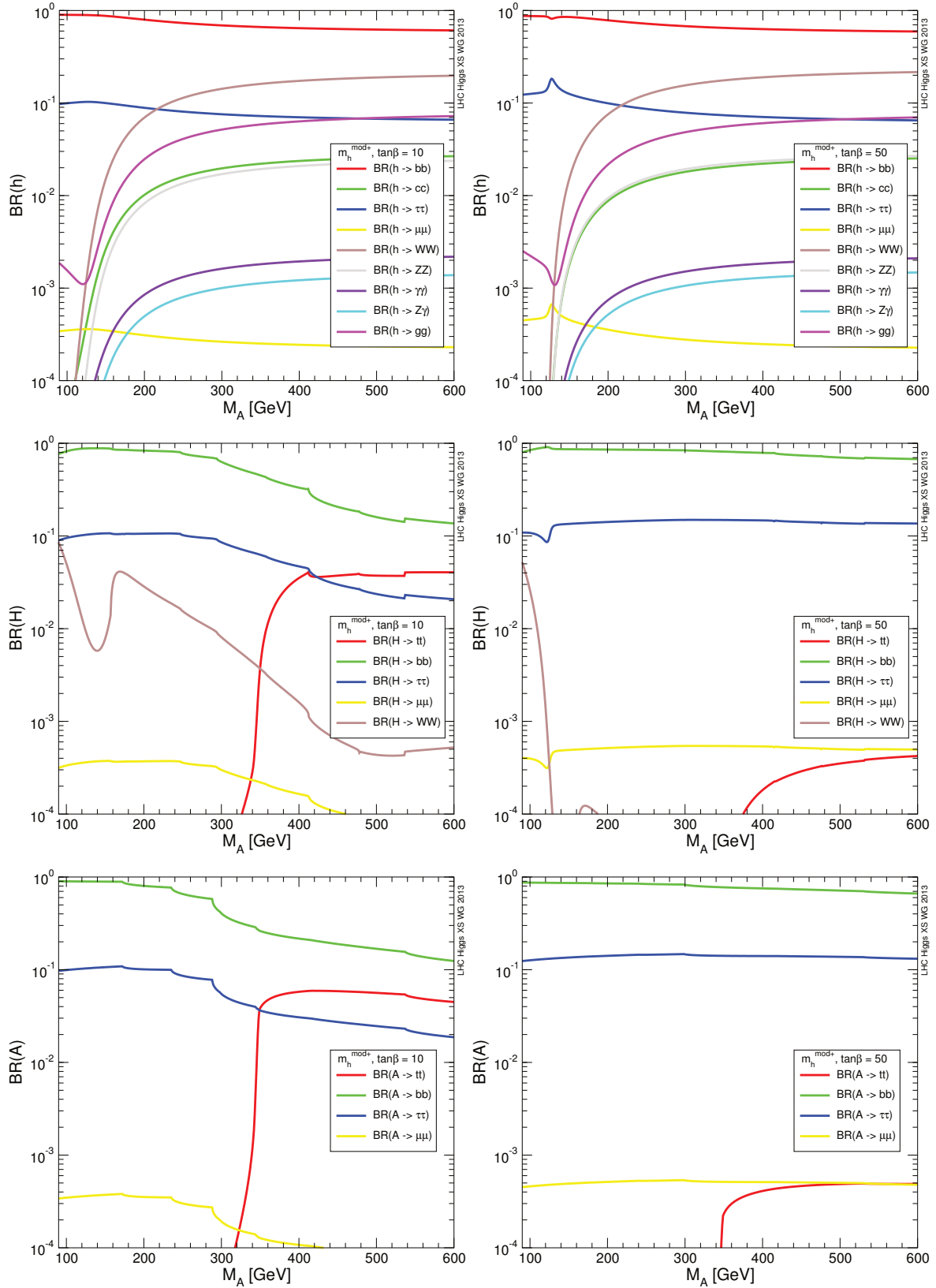
Fig. 5: Branching ratios of the MSSM Higgs bosons h (upper row), H (middle row) and A (lower row) in the $m_h^{\text{mod}+}$ scenario as a function of M_A. The left (right) column shows the results for $\tan\beta = 10(50)$.
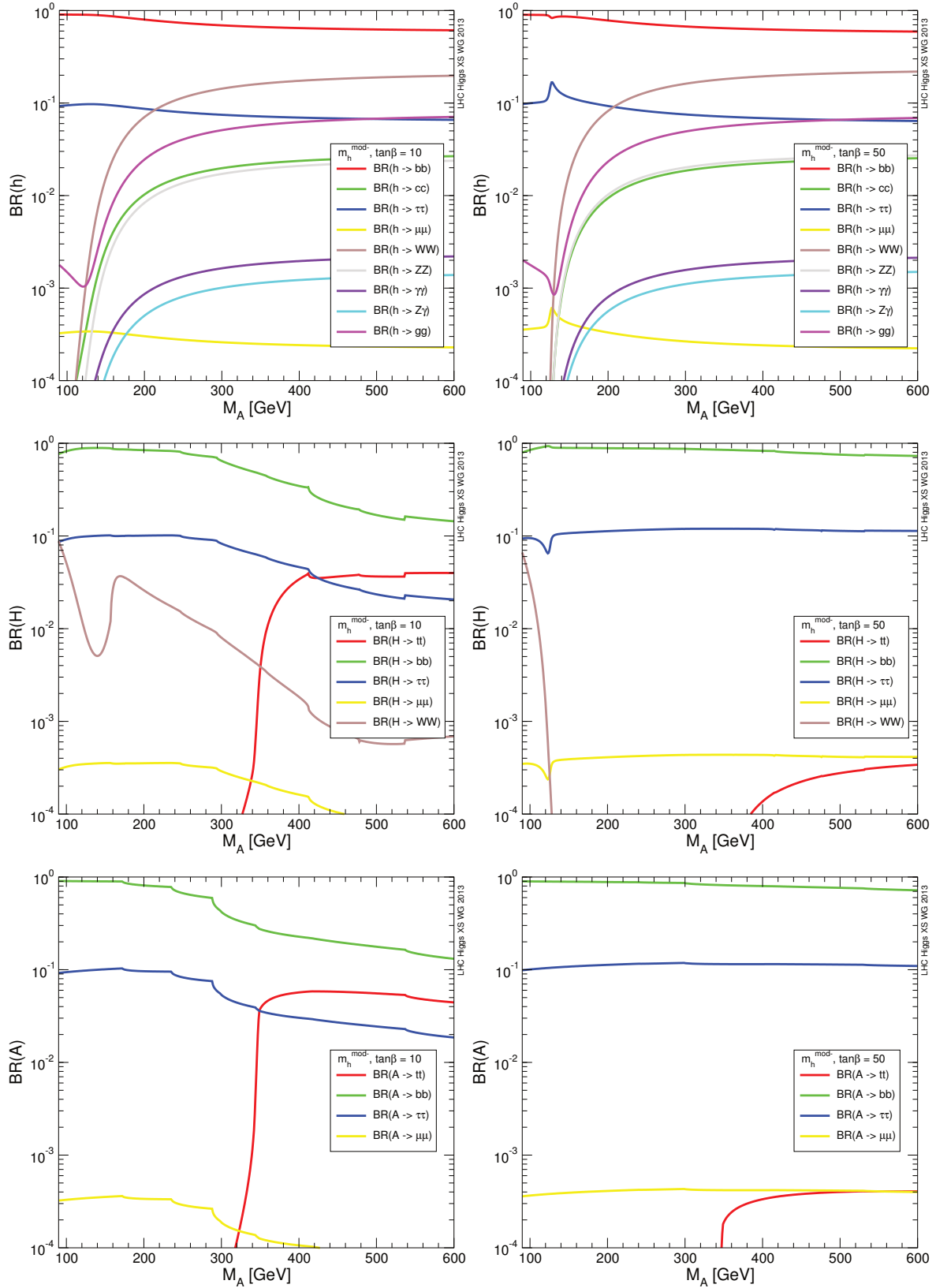
Fig. 6: Branching ratios of the MSSM Higgs bosons h (upper row), H (middle row) and A (lower row) in the $m_h^{\mathrm{mod}-}$ scenario as a function of M_A. The left (right) column shows the results for $\tan\beta = 10(50)$.
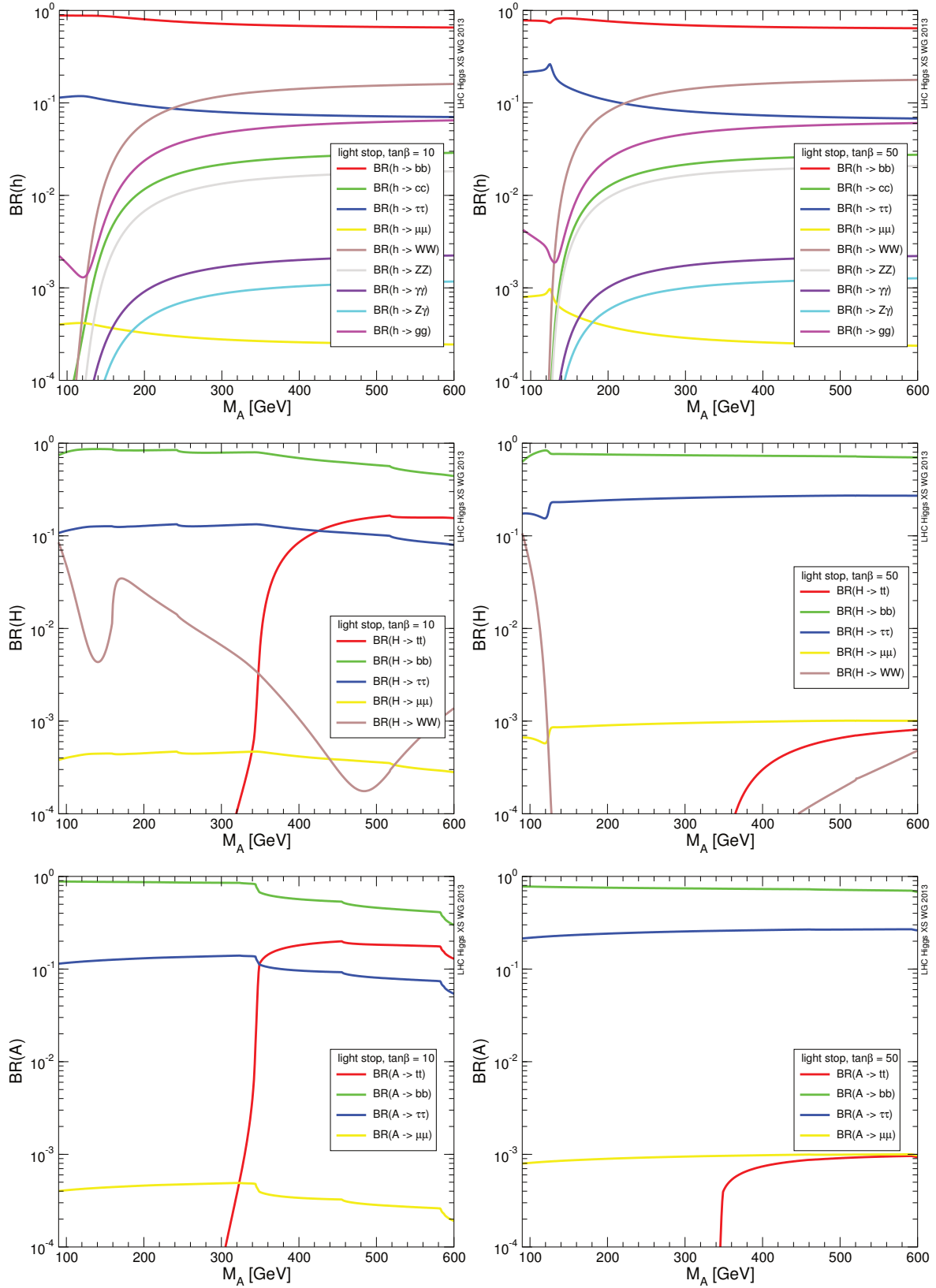
Fig. 7: Branching ratios of the MSSM Higgs bosons h (upper row), H (middle row) and A (lower row) in the light stop scenario as a function of M_A. The left (right) column shows the results for $\tan\beta = 10(50)$.
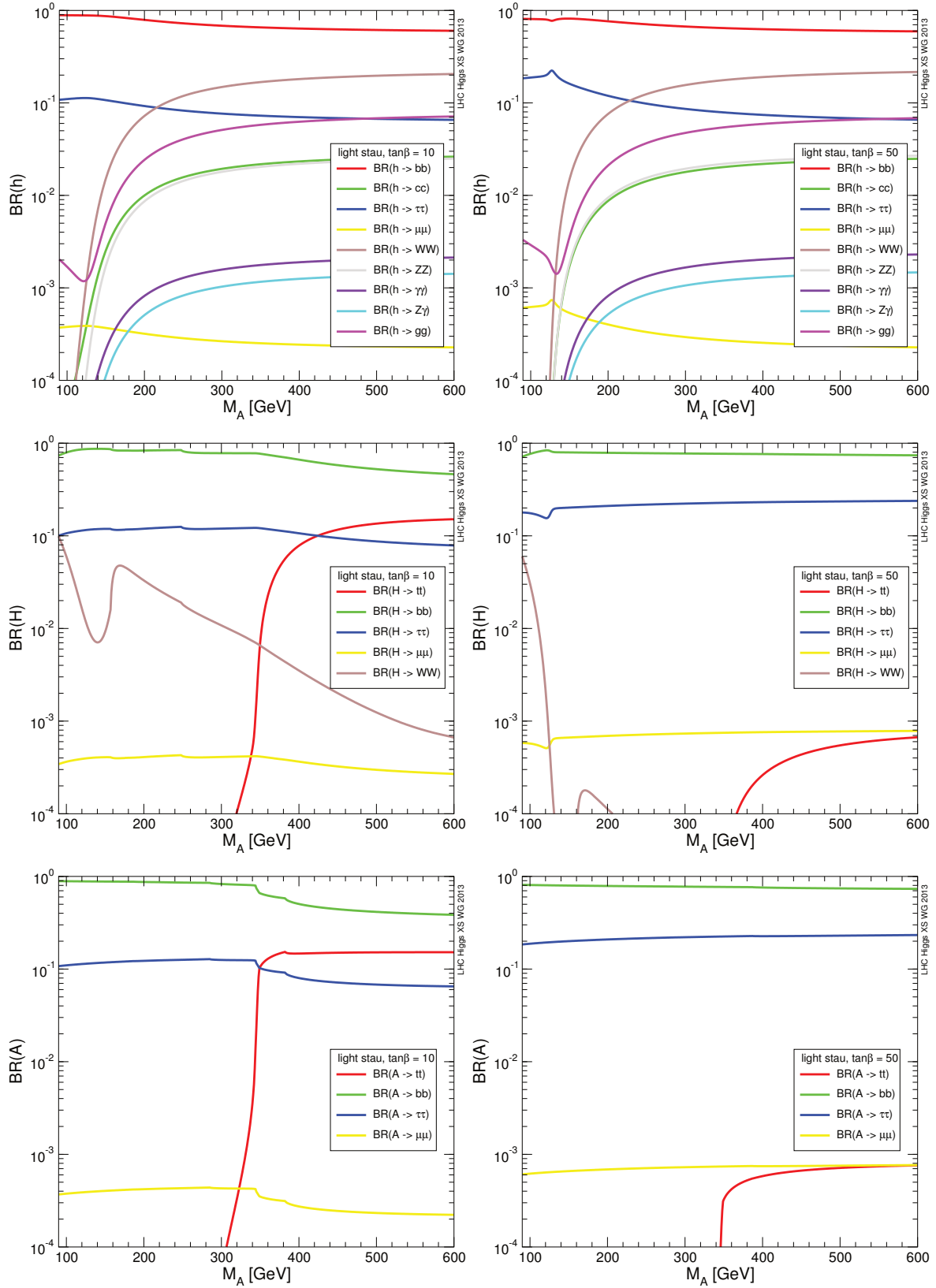
Fig. 8: Branching ratios of the MSSM Higgs bosons h (upper row), H (middle row) and A (lower row) in the light stau scenario as a function of M_A. The left (right) column shows the results for $\tan\beta = 10(50)$.
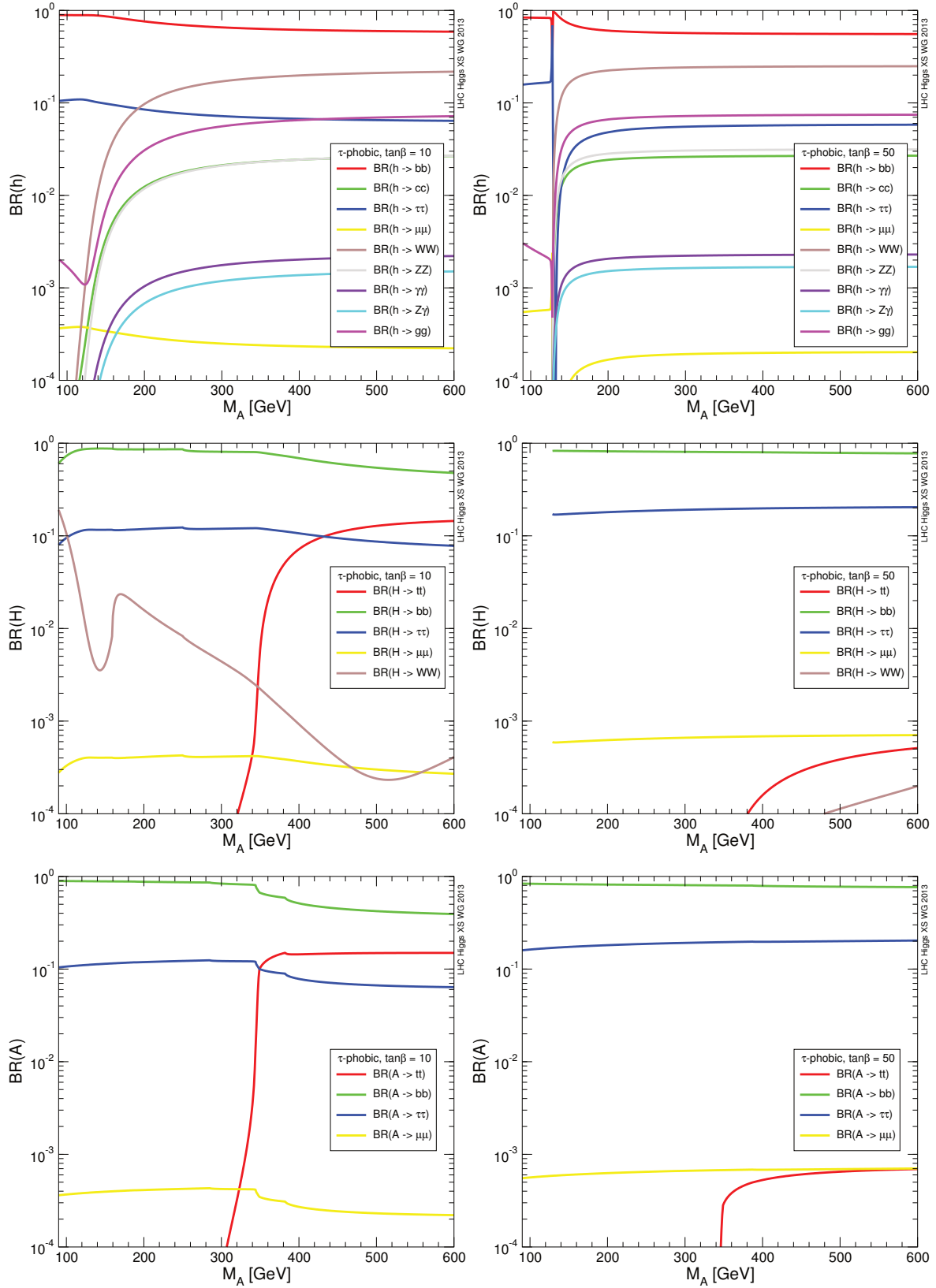
Fig. 9: Branching ratios of the MSSM Higgs bosons h (upper row), H (middle row) and $A^{\pm}$ (lower row) in the τ-phobic scenario as a function of M_A. The left (right) column shows the results for $\tan\beta = 10(50)$.
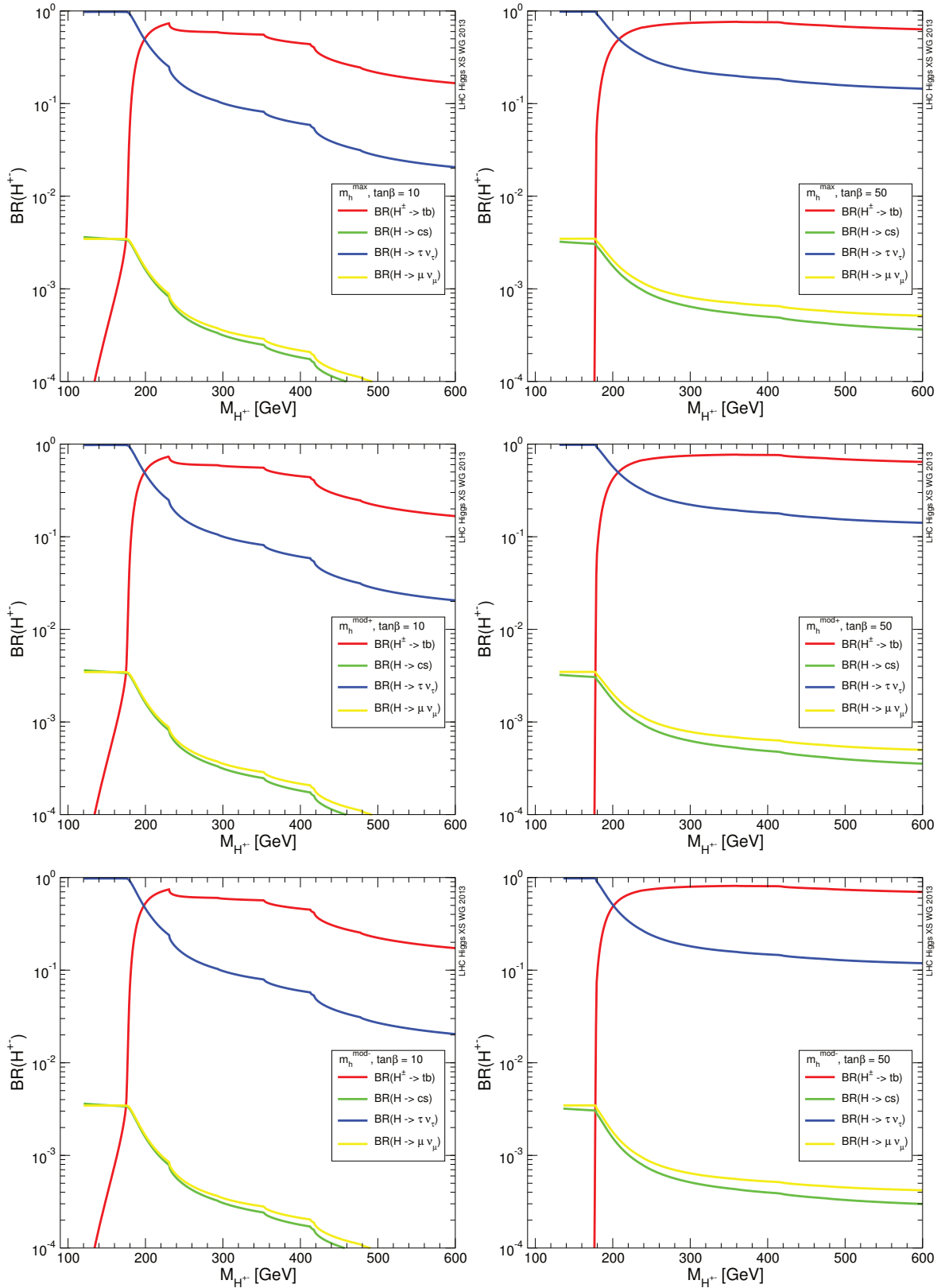
Fig. 10: Branching ratios of the charged MSSM Higgs boson in the m_h^{max} (upper row), $m_h^{\mathrm{mod+}}$ (middle row) and the $m_h^{\mathrm{mod-}}$ (lower row) scenario as a function of $M_{H^\pm}$. The left (right) column shows the results for $\tan\beta = 10(50)$.
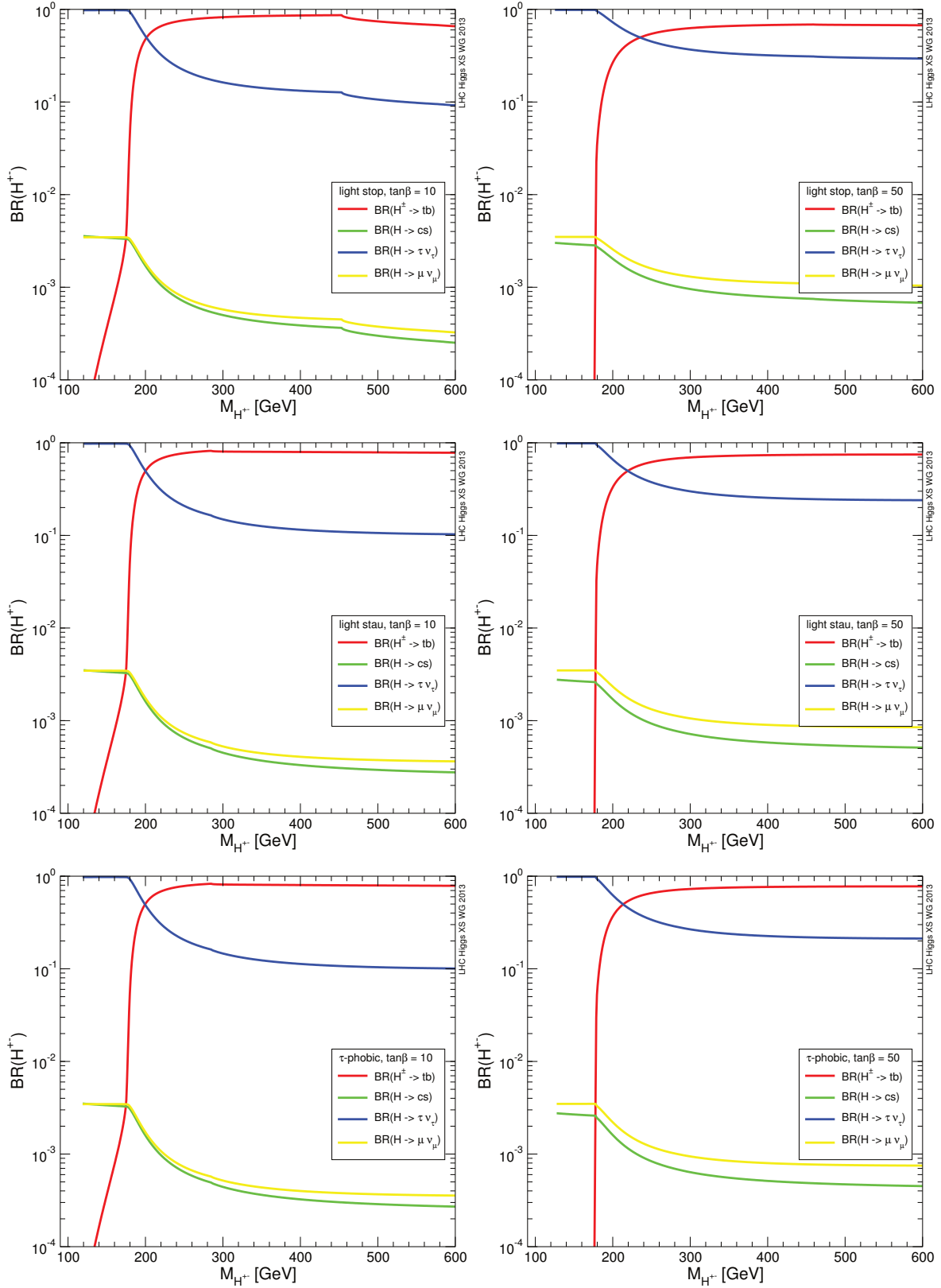
Fig. 11: Branching ratios of the charged MSSM Higgs boson in the light stop (upper row), light stau (middle row) and the τ-phobic (lower row) scenario as a function of $M_{H^\pm}$. The left (right) column shows the results for $\tan\beta = 10(50)$.

3 Gluon-gluon fusion production mode[3]

The first two volumes of this Handbook [13, 14] summarized the status of the inclusive and differential cross section for Higgs production in gluon fusion, respectively. Our goal in this volume is two-folded: we present an update on some of the relevant cross sections described in the previous volumes and continue the research on a number of issues relevant for Higgs boson production at the LHC.

The section is organised as follows. In Section 3.1 we present the state of the art in the inclusive cross section for Higgs production. Section 3.2 presents the first calculation for H+jet production at second order in perturbation theory with phenomenological results arising from the gluon fusion channel. In Sections 3.3-3.4 we compare the Higgs transverse momentum distribution outcome from different generators. Section 3.5 summarizes recent findings on the interference effects in light Higgs VV modes. Finally, Section 3.6 discusses theoretical uncertainties on the $pp \rightarrow WW$ estimation in the Higgs search.

3.1 Update on the inclusive Higgs boson production by gluon-gluon fusion[4]

The dominant mechanism for SM Higgs boson production at hadron colliders is gluon-gluon fusion [34], through a heavy-quark loop. The QCD radiative corrections to the total cross section have been computed at the next-to-leading order (NLO) in Refs. [35–37] and at the next-to-next-to-leading order (NNLO accuracy) in [38–40]. NNLO results at the exclusive level can be found in Refs. [41–44].

The main features of the different calculations for the inclusive cross section were discussed in Ref. [13]. For the 7 TeV run, both LHC experiments based their analysis on the combination [13] of the predictions of Anastasiou, Boughezal, Petriello and Stoeckli (ABPS) [45] and de Florian and Grazzini (dFG) [46]. Since the presentation of the First Yellow Report [13] a number of advancements, including a better treatment of the effect of heavy quark masses and the Higgs boson line-shape were discussed. Considering that the ABPS and dFG agree within $1 - 2\%$, and that the improvements reported below were applied only to the calculation of dFG, here we focus on the improvements presented in [47], which represented the theoretical prediction being used nowadays by the LHC collaborations.

The calculation of dFG is based on the resummation of soft-gluon contributions to next-to-next-to-leading logarithmic accuracy (NNLL) [48], as a way to improve state of the art fixed-order predictions with the dominant effect from higher-order corrections. The implementation requieres the knowledge of the Sudakov radiative factor, which depends only on the dynamics of soft gluon emission from the initial state partons and the hard coefficient (Cgg) which includes terms arising from both soft and hard gluon emission. The hard coefficient depends on the details of the coupling to the Higgs boson and, therefore, on the masses of the heavy quarks in the loop. Ref. [47] presented the *exact* expression for this coefficient up to next-to-leading logarithmic accuracy (NLL) with the explicit dependence on the heavy-quark masses in the loop, matching the precision reached in the fixed order calculation. Furthermore, the usually neglected contribution form the charm quark is also taken into account up to that order. Corrections beyond NL accuracy are treated in the infinite quark mass limit, accounting only for the top quark contribution. The inclusion of the exact dependence on the top- and bottom-quark masses up to NLL accuracy results in a decrease of the cross section ranging from about 1.5% at $M_H = 125$ GeV, to about 6% at $M_H = 800$ GeV. The usually neglected charm-quark contribution further decreases the cross section by about 1% for a light Higgs, being very small in the high-mass region.

The second improvement with respect to the work of Ref. [46] regards the treatment of the Higgs boson width. While the Zero Width Approximation (ZWA) can be considered sufficiently accurate for the evaluation of the *inclusive* cross section for a light Higgs boson, the increase of the Higgs boson width at large masses requires a proper implementation of the corresponding line-shape. We rely on the

---

[3]D. de Florian, B. Di Micco (eds.); R. Boughezal, F. Caola, N. Chanon, R. Di Nardo, G. Ferrera, N. Fidanza, M. Grazzini, D.C. Hall, C. Hays, J. Griffiths, R. Hernandez-Pinto, N. Kauer, H. Kim, S. Martin, J. Mazzitelli, K. Melnikov, F. Petriello, Y. Rotstein-Habarnau, G. Sborlini, M. Schulze, D. Tommasini and J. Yu

[4]D. de Florian, M. Grazzini

OFFP scheme described in Ref. [49] as an effective implementation of the complex-pole scheme. The calculation in Ref. [49] provides a realistic estimate of the complex-pole width γ_H above the ZZ threshold but might introduce an artificial effect at low masses. In order to recover the ZWA for light Higgs we use an extrapolation of the value of γ_H towards the on-shell decay width $\Gamma(M_H)$ below $M_H = 200$ GeV. The inclusion of finite-width effects results in an increase of the cross section with respect to the ZWA of about $\mathcal{O}(10\%)$ at $M_H = 800$ GeV. The use of a naive Breit Wigner would give a smaller cross section with respect to the result in the complex-pole scheme, the difference ranging from -3.5% for $M_H = 300$ GeV to -18% at $M_H = 600$ GeV, to -27% at $M_H = 800$ GeV.

As discussed in Ref. [13], the ensuing result is finally corrected for two-loop electro-weak (EW) contributions [50–52] as evaluated in [49] in the *complete factorization* scheme.

Uncertainties are estimated as in Ref. [13]. The updated numbers for the cross section at 7 TeV and 8 TeV are presented in Tables B.1-B.7 and Tables B.8-B.14, respectively.

These results can be compared to those presented in Ref. [53], where the impact of finite-width effects is also included. For a light Higgs boson, the main difference with the computation of dFG arises from the evaluation of higher-order QCD corrections, which are computed up to NNLO but choosing the factorization and renormalization scales $\mu_F = \mu_R = M_H/2$, as an attempt to reproduce effects beyond NNLO, that, in the dFG calculation, are instead estimated through soft-gluon resummation. For example, at $M_H = 125$ GeV the result of Ref. [53] is about 7% higher that the one of dFG, but still well within the corresponding uncertainty bands. Larger differences are observed in the high mass region, due to the different implementation of finite-width effects. In Ref. [53] a Breit-Wigner with running width is used as the default implementation of the line-shape. At $M_H = 400$ GeV, the result of Ref. [53] turns out to be about 16% smaller than the one of dFG.

3.2 Higgs+jet at NNLO [5]

We describe in this section a first calculation of Higgs-boson production in association with a jet at next-to-next-to-leading order in perturbative QCD [54]. This result is urgently needed in order to reduce the theoretical uncertainties hindering a precise extraction of the Higgs properties at the LHC. Currently, the theoretical errors in the one-jet bin comprise one of the largest systematic errors in Higgs analyses, particularly in the WW final state. There are two theoretical methods one can pursue to try to reduce these uncertainties. The first is to resum sources of large logarithmic corrections to all orders in QCD perturbation theory. An especially pernicious source of large logarithmic corrections comes from dividing the final state into bins of exclusive jet multiplicities. An improved theoretical treatment of these terms has been pursued in both the zero-jet [55–59] and one-jet [60, 61] bins (see Section 8). The second, which we discuss here, is to compute the higher-order corrections to the next-to-next-to-leading order (NNLO) in perturbative QCD. Both are essential to produce the reliable results necessary in experimental analyses. In this contribution we give a brief overview of the calculational framework that was used to obtain the NNLO calculation for Higgs plus jet production, and present initial numerical results arising from gluon-fusion.

3.2.1 *Notation and setup*

We begin by presenting the basic notation needed to describe our calculation. We use the QCD Lagrangian, supplemented with a dimension-five non-renormalizable operator that describes the interaction of the Higgs boson with gluons in the limit of very large top quark mass:

$$\mathcal{L} = -\frac{1}{4}G_{\mu\nu}^{(a)}G^{(a)\mu\nu} - \lambda_{\mathrm{Hgg}}\mathrm{H}G_{\mu\nu}^{(a)}G^{(a)\mu\nu}. \tag{7}$$

---

[5]R. Boughezal, F. Caola, K. Melnikov, F. Petriello, M. Schulze

Here, $G_{\mu\nu}^{(a)}$ is the field-strength tensor of the gluon field and H is the Higgs-boson field. Matrix elements computed with the Lagrangian of Eq. (7) need to be renormalized. Two renormalization constants are required to do so: one which relates the bare and renormalized strong coupling constants, and another which ensures that matrix elements of the Hgg dimension-five operator are finite. The expressions for these quantities are given in Ref. [54]. We note that the Lagrangian of Eq. (7) neglects light fermions, as will the initial numerical results presented. We comment on the phenomenological impact of this approximation later in this section.

Renormalization of the strong coupling constant and of the effective Higgs-gluon coupling removes ultraviolet divergences from the matrix elements. The remaining divergences are of infrared origin. To remove them, we must both define and compute infrared-safe observables, and absorb the remaining collinear singularities by renormalizing parton distribution functions. Generic infrared safe observables are defined using jet algorithms. For the calculation described here we employ the k_{T}-algorithm.

Collinear singularities associated with gluon radiation by incoming partons must be removed by additional renormalization of parton distribution functions. We describe how to perform this renormalization in what follows. We denote the ultraviolet-renormalized partonic cross section by $\bar{\sigma}(x_1, x_2)$, and the collinear-renormalized partonic cross section by $\sigma(x_1, x_2)$. Once we know $\sigma(x_1, x_2)$, we can compute the hadronic cross sections by integrating the product of σ and the gluon distribution functions over x_1 and x_2:

$$\sigma(\mathrm{p}+\mathrm{p} \to \mathrm{H}+j) = \int \mathrm{d}x_1 \mathrm{d}x_2 \, g(x_1) g(x_2) \, \sigma(x_1, x_2). \tag{8}$$

The relation between σ and $\bar{\sigma}$ is given by the following formula:

$$\sigma = \Gamma^{-1} \otimes \bar{\sigma} \otimes \Gamma^{-1}, \tag{9}$$

where the convolution sign stands for

$$[f \otimes g](x) = \int_0^1 \mathrm{d}z \, \mathrm{d}y \delta(x - yz) f(y) g(z). \tag{10}$$

The collinear counterterm can be expanded in the strong coupling constant as

$$\Gamma = \delta(1 - x) - \left(\frac{\alpha_{\mathrm{s}}}{2\pi}\right) \Gamma_1 + \left(\frac{\alpha_{\mathrm{s}}}{2\pi}\right)^2 \Gamma_2. \tag{11}$$

We write the ultraviolet-renormalized partonic cross section through NNLO as

$$\bar{\sigma} = \bar{\sigma}^{(0)} + \left(\frac{\Gamma(1+\epsilon)\alpha_{\mathrm{s}}}{2\pi}\right) \bar{\sigma}^{(1)} + \left(\frac{\Gamma(1+\epsilon)\alpha_{\mathrm{s}}}{2\pi}\right)^2 \bar{\sigma}^{(2)}, \tag{12}$$

and the collinear-renormalized partonic cross section as

$$\sigma = \sigma^{(0)} + \left(\frac{\alpha_{\mathrm{s}}}{2\pi}\right) \sigma^{(1)} + \left(\frac{\alpha_{\mathrm{s}}}{2\pi}\right)^2 \sigma^{(2)}. \tag{13}$$

Using these results, we can solve to find the following results for the finite cross section expanded in α_{s}:

$$\sigma^{(0)} = \bar{\sigma}^{(0)}, \qquad \sigma^{(1)} = \bar{\sigma}^{(1)} + \frac{\Gamma_1 \otimes \sigma^{(0)}}{\Gamma(1+\epsilon)} + \frac{\sigma^{(0)} \otimes \Gamma_1}{\Gamma(1+\epsilon)},$$

$$\sigma^{(2)} = \bar{\sigma}^{(2)} - \frac{\Gamma_2 \otimes \sigma^{(0)}}{\Gamma(1+\epsilon)^2} - \frac{\sigma^{(0)} \otimes \Gamma_2}{\Gamma(1+\epsilon)^2} - \frac{\Gamma_1 \otimes \sigma^{(0)} \otimes \Gamma_1}{\Gamma(1+\epsilon)^2} + \frac{\Gamma_1 \otimes \sigma^{(1)}}{\Gamma(1+\epsilon)} + \frac{\sigma^{(1)} \otimes \Gamma_1}{\Gamma(1+\epsilon)}. \tag{14}$$

We note that although finite, the $\sigma^{(i)}$ still depend on unphysical renormalization and factorization scales because of the truncation of the perturbative expansion. In the following, we will consider for simplicity the case of equal renormalization and factorization scales , $\mu_{\mathrm{R}} = \mu_{\mathrm{F}} = \mu$. The residual μ dependence is easily determined by solving the renormalization-group equation order-by-order in α_{s}.

3.2.2 Calculational framework

It follows from the previous section that in order to obtain $\sigma^{(2)}$ at a generic scale, apart from lower-order results we need to know the NNLO renormalized cross section $\bar{\sigma}^{(2)}$ and convolutions of NLO and LO cross sections with the various splitting functions which appear in the collinear counterterms. Up to terms induced by the renormalization, there are three contributions to $\bar{\sigma}^{(2)}$ that are required:

- the two-loop virtual corrections to $gg \rightarrow Hg$;
- the one-loop virtual corrections to $gg \rightarrow Hgg$;
- the double-real contribution $gg \rightarrow Hggg$.

We note that helicity amplitudes for all of these processes are available in the literature. The two-loop amplitudes for $gg \rightarrow Hg$ were recently computed in Ref. [62]. The one-loop corrections to $gg \rightarrow Hgg$ and the tree amplitudes for $gg \rightarrow Hggg$ are also known, and are available in the form of a Fortran code in the program MCFM [63].

Since all ingredients for the NNLO computation of $gg \rightarrow H + jet$ have been available for some time, it is interesting to understand what has prevented this calculation from being performed. The main difficulties with NNLO calculations appear when one attempts to combine the different contributions, since integration over phase space introduces additional singularities if the required number of jets is lower than the parton multiplicity. To perform the phase-space integration, we must first isolate singularities in tree- and loop amplitudes.

The computational method that we will explain shortly is based on the idea that relevant singularities can be isolated using appropriate parameterizations of phase space and expansions in plus-distributions. To use this approach for computing NNLO QCD corrections, we need to map the relevant phase space to a unit hypercube in such a way that extraction of singularities is straightforward. The correct variables to use are the re-scaled energies of unresolved partons and the relative angles between two unresolved collinear partons. However, the problem is that different partons become unresolved in different parts of the phase space. It is not immediately clear how to switch between different sets of coordinates and cover the full phase space.

We note that for NLO QCD computations, this problem was solved in Ref. [64], where it was explained that the full phase space can be partitioned into sectors in such a way that in each sector only one parton (i) can produce a soft singularity and only one pair of partons (ij) can produce a collinear singularity. In each sector, the proper variables are the energy of the parton i and the relative angle between partons i and j. Once the partitioning of the phase space is established and proper variables are chosen for each sector, we can use an expansion in plus-distributions to construct relevant subtraction terms for each sector. With the subtraction terms in place, the Laurent expansion of cross sections in ϵ can be constructed, and each term in such an expansion can be integrated over the phase space independently. Therefore, partitioning of the phase space into suitable sectors and proper parameterization of the phase space in each of these sectors are the two crucial elements needed to extend this method to NNLO. It was first suggested in Ref. [65] how to construct this extension for double real-radiation processes at NNLO. We give a brief overview of this technique in the next section.

3.2.3 An example: double-real emission corrections

We briefly present the flavor of our calculational methods by outlining how the double-real emission corrections are handled. To start, we follow the logic used at NLO in Ref. [64] and partition the phase space for the $g(p_1)g(p_2) \rightarrow Hg(p_3)g(p_4)g(p_5)$ process into separate structures that we call 'pre-sectors' where only a given set of singularities can occur:

$$\frac{1}{3!} dLips_{12 \rightarrow H345} = \sum_\alpha dLips^{(\alpha)}_{12 \rightarrow H345}, \tag{15}$$

Here, α is a label which denotes which singularities can occur, and dLIPS denotes the standard Lorentz-invariant phase space. At NNLO we can have at most two soft singularities and two collinear singularities in each pre-sector, so as an example there will be an α labeling where p_4 and p_5 can be soft, and where both can be collinear to p_1. Within this particular pre-sector, which we label as a 'triple-collinear' pre-sector, it is clear that the appropriate variables to describe the phase space are the energies of gluons p_4 and p_5, and the angles between these gluons and the direction of p_1.

Our goal in introducing a parameterization is to have all singularities appear in the following form:

$$I(\epsilon) = \int\limits_0^1 \mathrm{d}x \, x^{-1-a\epsilon} F(x), \tag{16}$$

where the function $F(x)$ has a well-defined limit $\lim\limits_{x \to 0} F(x) = F(0)$. Here, the $F(x)/x$ structure comes from the matrix elements, while the $x^{-a\epsilon}$ comes from the phase space. When such a structure is obtained, we can extract singularities using the plus-distribution expansion

$$\frac{1}{x^{1+a\epsilon}} = -\frac{1}{a\epsilon}\delta(x) + \sum_{n=0}^{\infty} \frac{(-\epsilon a)^n}{n!}\left[\frac{\ln^n(x)}{x}\right]_+, \tag{17}$$

so that

$$I(\epsilon) = \int\limits_0^1 \mathrm{d}x \left(-\frac{F(0)}{a\epsilon} + \frac{F(x)-F(0)}{x} - a\epsilon\frac{F(x)-F(0)}{x}\ln(x) + ...\right). \tag{18}$$

The above equation provides the required Laurent expansion of the integral $I(\epsilon)$. We note that each term in such an expansion can be calculated numerically, and independently from the other terms.

Unfortunately, no phase-space parameterization for double-real emission processes can immediately achieve the structure of Eq. (16). Each pre-sector must be further divided into a number of sectors using variable changes designed to produce the structure of Eq. (16) in each sector. Following Ref. [65], we further split the triple-collinear pre-sector mentioned above into five sectors so that all singularities in the matrix elements appear in the form of Eq. (16). Explicit details for these variables changes, and those for all other pre-sectors needed for the NNLO calculation of Higgs plus jet, are presented in Ref. [54].

Once we have performed the relevant variables changes, we are left with a set of integrals of the form shown in Eq. (18). We now discuss how we evaluate the analogs of the $F(x)$ and $F(0)$ terms that appear in the full calculation. When all x_i variables that describe the final-state phase space are non-zero, we are then evaluating the $gg \to Hggg$ matrix elements with all gluons resolved. The helicity amplitudes for this process are readily available, as discussed above, and can be efficiently evaluated numerically. When one or more of the x_i vanish, we are then in a singular limit of QCD. The factorization of the matrix elements in possible singular limits appearing in double-real emission corrections in QCD has been studied in detail [66], and we can appeal to this factorization to evaluate the analogs of the $F(0)$. For example, one singular limit that appears in all pre-sectors is the so-called 'double-soft' limit, in which both gluons p_4 and p_5 have vanishingly small energies. The matrix elements squared factorize in this limit in the following way in terms of single $S_{ij}(p)$ and double $S_{ij}(p,q)$ universal eikonal factors [66]:

$$\begin{aligned}
|\mathcal{M}_{g_1 g_2 \to H g_3 g_4 g_5}|^2 \approx C_A^2 g_s^4 &\left[\left(\sum_{ij \in S_p} S_{ij}(p_4) \right) \left(\sum_{kn \in S_p} S_{kn}(p_5) \right) \right. \\
&\left. + \sum_{ij \in S_p} S_{ij}(p_4, p_5) - \sum_{i=1}^3 S_{ii}(p_4, p_5) \right] |\mathcal{M}_{g_1 g_2 \to H g_3}|^2.
\end{aligned} \tag{19}$$

The advantage of using this factorization is that all structures on the right-hand side of Eq. (19) are readily available in the literature and can be efficiently evaluated numerically; as discussed the helicity amplitudes for $\text{gg} \to \text{Hg}$ are known, and the S_{ij} eikonal factors which appear are also well-known functions. Using this and other such relations, the analogs of the integrals in Eq. (18) appearing in the full theory can be calculated using known results. Similar techniques can be used to obtain the other structures needed for the NNLO computation of Higgs plus jet production. For a discussion of all relevant details, we refer the reader to Ref. [54].

3.2.4 Numerical results

We present here initial numerical results for Higgs production in association with one or more jets at NNLO, arising from the dominant gluon-fusion subprocess. A detailed series of checks on the presented calculation were performed in Ref. [54], and we do not repeat this discussion here. We compute the hadronic cross section for the production of the Higgs boson in association with one or more jets at the 8 TeV LHC through NNLO in perturbative QCD. We reconstruct jets using the k_{T}-algorithm with $\Delta R = 0.5$ and $p_{\text{T}}^j = 30$ GeV. The Higgs mass is taken to be $M_{\text{H}} = 125$ GeV and the top-quark mass $m_{\text{t}} = 172$ GeV. We use the latest NNPDF parton distributions [67,68] with the number of active fermion flavors set to five, and numerical values of the strong coupling constant α_{s} at various orders in QCD perturbation theory as provided by the NNPDF fit. We note that in this case $\alpha_{\text{s}}(M_{\text{Z}}) = [0.130, 0.118, 0.118]$ at leading, next-to-leading and next-to-next-to-leading order, respectively. We choose the central renormalization and factorization scales to be $\mu = \mu_{\text{R}} = \mu_{\text{F}} = M_{\text{H}}$.

In Fig. 12 we show the partonic cross section for $\text{gg} \to \text{H} + j$ multiplied by the gluon luminosity through NNLO in perturbative QCD:

$$\beta \frac{\text{d}\sigma_{\text{had}}}{\text{d}\sqrt{s}} = \beta \frac{\text{d}\sigma(s, \alpha_{\text{s}}, \mu_{\text{R}}, \mu_{\text{F}})}{\text{d}\sqrt{s}} \times \mathcal{L}(\frac{s}{s_{\text{had}}}, \mu_{\text{F}}),$$ (20)

where β measures the distance from the partonic threshold,

$$\beta = \sqrt{1 - \frac{E_{\text{th}}^2}{s}}, \qquad E_{\text{th}} = \sqrt{M_{\text{H}}^2 + p_{\perp,j}^2} + p_{\perp,j} \approx 158.55 \text{ GeV}.$$ (21)

The partonic luminosity $\mathcal{L}$ is given by the integral of the product of two gluon distribution functions

$$\mathcal{L}(z, \mu_{\text{F}}) = \int_z^1 \frac{\text{d}x}{x} g(x, \mu_{\text{F}}) g\left(\frac{z}{x}, \mu_{\text{F}}\right).$$ (22)

It follows from Fig. 12 that NNLO QCD corrections are significant in the region $\sqrt{s} < 500$ GeV. In particular, close to partonic threshold $\sqrt{s} \sim E_{\text{th}}$, radiative corrections are enhanced by threshold logarithms $\ln \beta$ that originate from the incomplete cancellation of virtual and real corrections. There seems to be no significant enhancement of these corrections at higher energies, where the NNLO QCD prediction for the partonic cross section becomes almost indistinguishable from the NLO QCD one.

We now show the integrated hadronic cross sections in the all-gluon channel. We choose to vary the renormalization and factorization scale in the range $\mu = \mu_{\text{R}} = \mu_{\text{F}} = M_{\text{H}}/2, M_{\text{H}}, 2M_{\text{H}}$. After convolution with the parton luminosities, we obtain

$$\sigma_{\text{LO}}(\text{pp} \to \text{H}j) = 2713^{+1216}_{-776} \text{ fb},$$
$$\sigma_{\text{NLO}}(\text{pp} \to \text{H}j) = 4377^{+760}_{-738} \text{ fb},$$ (23)
$$\sigma_{\text{NNLO}}(\text{pp} \to \text{H}j) = 6177^{+204}_{-242} \text{ fb}.$$

We note that NNLO corrections are sizable, as expected from the large NLO K−factor, but the perturbative expansion shows marginal convergence. We also evaluated PDF errors using the full set of NNPDF
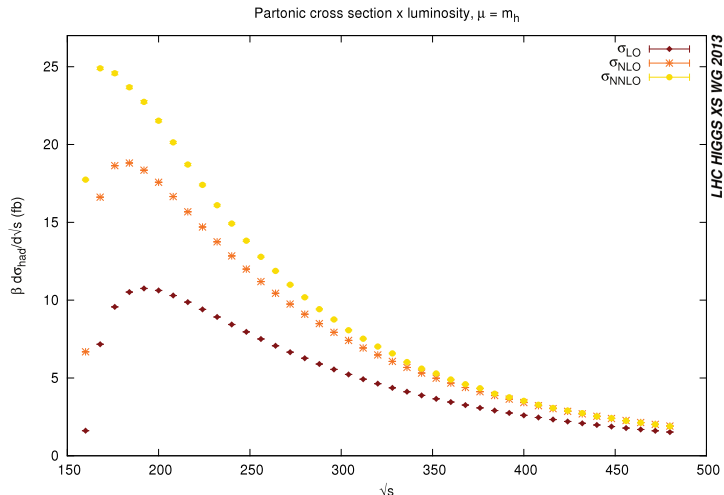
Fig. 12: Results for the product of partonic cross sections gg → H + jet and parton luminosity in consecutive orders in perturbative QCD at $\mu = \mu_{\mathrm{R}} = \mu_{\mathrm{F}} = M_{\mathrm{H}} = 125$ GeV. See the text for explanation.

replicas, and found it to be of order 5% at LO, and of order $1 - 2\%$ at both NLO and NNLO, similarly to the inclusive Higgs case [68]. The cross section increases by about sixty percent when we move from LO to NLO and by thirty percent when we move from NLO to NNLO. It is also clear that by accounting for the NNLO QCD corrections we reduce the dependence on the renormalization and factorization scales in a significant way. The scale variation of the result decreases from almost 50% at LO, to 20% at NLO, to less than 5% at NNLO. We also note that a perturbatively-stable result is obtained for the scale choice $\mu \approx M_{\mathrm{H}}/2$. In this case the ratio of the NNLO over the LO cross section is just 1.5, to be compared with 2.3 for $\mu = M_{\mathrm{H}}$ and 3.06 for $\mu = 2M_{\mathrm{H}}$, and the ratio of NNLO to NLO is 1.2. A similar trend was observed in the calculation of higher-order QCD corrections to the Higgs boson production cross section in gluon fusion. The reduced scale dependence is also apparent from Fig. 13, where we plot total cross section as a function of the renormalization and factorization scale μ in the region $p_{\mathrm{T}}^{j} < \mu < 2M_{\mathrm{H}}$.

Finally, we comment on the phenomenological relevance of the results for the cross sections and K-factors reported here that refer only to the Higgs production through gluon-gluon collisions. We note that at leading and next-to-leading order, quark-gluon collisions increase the H + j production cross section by about 30 percent, for the input parameters that we use in this paper. At the same time, the NLO K-factors for the full H + j cross section are smaller by about $10-15\%$ than the 'gluons-only' K-factors, presumably because quark color charges are smaller than the gluon ones. Therefore, we conclude that the gluon-only results can be used for reliable phenomenological estimates of perturbative K-factors but adding quark channels will be essential for achieving precise results for the H + j cross section.

3.3 Higgs boson production by the gluon-gluon fusion and decay in the electroweak channels in the HRES code [6]

3.3.1 Introduction

In the section we introduce the HRES [69] Monte Carlo program implementing the Higgs boson production by gluon-gluon fusion channel (at the NNLL+NNLO accuracy) and the electroweak decay modes H → γγ, H → WW → $l\nu_{l}l\nu_{l}$ and H → ZZ → $4l$. In the latter case the user can choose between H → ZZ → $\mu^{+}\mu e^{+}e$ and H → ZZ → $e^{+}ee^{+}e$, which includes the appropriate interference contribution. This HRES numerical program embodies the features of both the HNNLO [43, 44] and HQT [70]

---

[6]D. de Florian, G. Ferrera, M. Grazzini, D. Tommasini
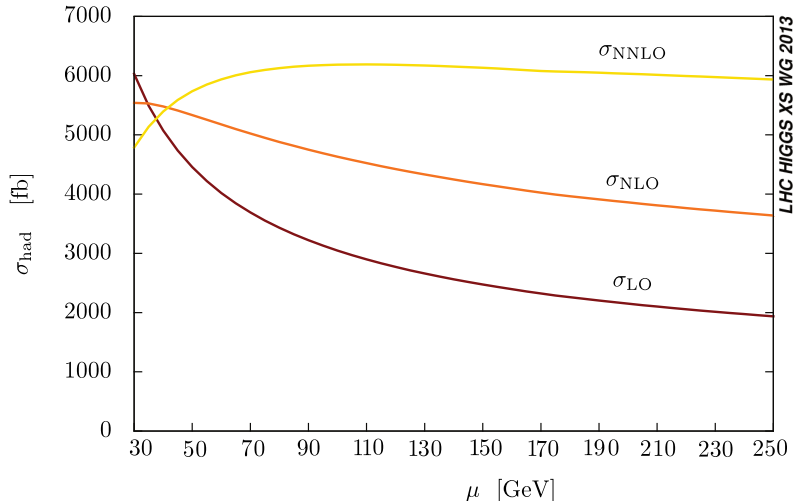
Fig. 13: Scale dependence of the hadronic cross section in consecutive orders in perturbative QCD. See the text for details.

numerical codes. Here we compare some selected results with the fixed order ones, up to the NNLO accuracy, obtained with the HNNLO. The program can be downloaded from [71], together with some accompanying notes.

3.3.2 HRES *example with the* γγ *decay channel*

We present selected numerical results for the signal cross section at the LHC ($\sqrt{s} = 8$ TeV), by using explicative cuts that can be applied in current Higgs boson searches by the ATLAS and CMS collaborations. We consider the production of a SM Higgs boson with mass $M_H = 125$ GeV and the decay channel into γγ, but analogous studies can be performed by the other decay channels (see Ref. [69]).

For each event, we classify the photon transverse momenta according to their minimum and maximum value, $p_{T\min}$ and $p_{mathrmTmax}$. We apply the following cuts on the photons: they are required to be in the central rapidity region, $|\eta| < 2.5$, with $p_{T\min,\gamma} > 25$ GeV and $p_{T\max,\gamma} > 40$ GeV. The corresponding inclusive cross sections are reported in Table 2, where we show the resummed results obtained through the HRES code, and we compare them with the fixed order predictions obtained with the HNNLO code. We see that the NLL+NLO (NNLL+NNLO) inclusive cross section agrees with the NLO (NNLO) result to better than 1%. We recall that the resummation does not affect the total cross section for the Higgs boson production, but when geometrical cuts are applied, their effect can act in a different way on fixed order and resummed calculations. In Table 2 we compare the accepted cross sections, obtained by the fixed order and resummed calculations, and the corresponding efficiencies. The numeri-

Table 2: Fixed order and resummed cross sections for pp $\rightarrow$ H + X $\rightarrow$ γγ + X at the LHC, before and after geometrical acceptance cuts.

Cross section	NLO	NLL+NLO	NNLO	NNLL+NNLO
Total [fb]	30.65 ± 0.01	30.79 ± 0.03	38.47 ± 0.15	38.41 ± 0.06
With cuts [fb]	21.53 ± 0.02	21.55 ± 0.01	27.08 ± 0.08	26.96 ± 0.04
Efficiency [%]	70.2	70.0	70.4	70.2

cal errors estimate the statistical uncertainty of the Monte Carlo integration. Comparing resummed and

fixed order predictions, we see that there are no substantial differences on the accepted cross section, due to the fact that the integration is performed over a wide kinematical range. It is also possible to study the accepted cross section for different choices of the scales. After selection cuts, by varying the scales $2Q = \mu_F = \mu_R$ in the range $M_H/2 \leq 2Q \leq 2M_H$, the scale uncertainty is about $\pm 15\%$ ($\pm 18\%$) at NLL+NLO (NLO) and $\pm 9\%$ ($\pm 10\%$) at NNLL+NNLO (NNLO).

In Fig. 14-left we plot the photon $p_T^{\min,\gamma}$ distribution (the $p_T^{\max,\gamma}$ distribution has similar features). These distribution are enhanced when going from LO to NLO to NNLO according to the increase of the total cross section. We note that, as pointed out in Ref. [43], the shape of these distributions sizeable differs when going from LO to NLO and to NNLO. In particular, at the LO the two photons are emitted with the same p_T^γ because the Higgs boson is produced with zero transverse momentum, hence the LO $p_T^{\min,\gamma}$ and $p_T^{\max,\gamma}$ are exactly identical. Furthermore the LO distribution has a kinematical boundary at $p_T^\gamma = M_H/2$ (Jacobian peak), which is due to the use of the narrow width approximation. Such condition is released once extra radiation is accounted for. Thus higher order predictions suffer of perturbative instabilities, i.e. each higher-order perturbative contribution produces (integrable) logarithmic singularities in the vicinity of that boundary, as explained in Ref. [72]. The same $p_T^{\min,\gamma}$ predictions are shown in
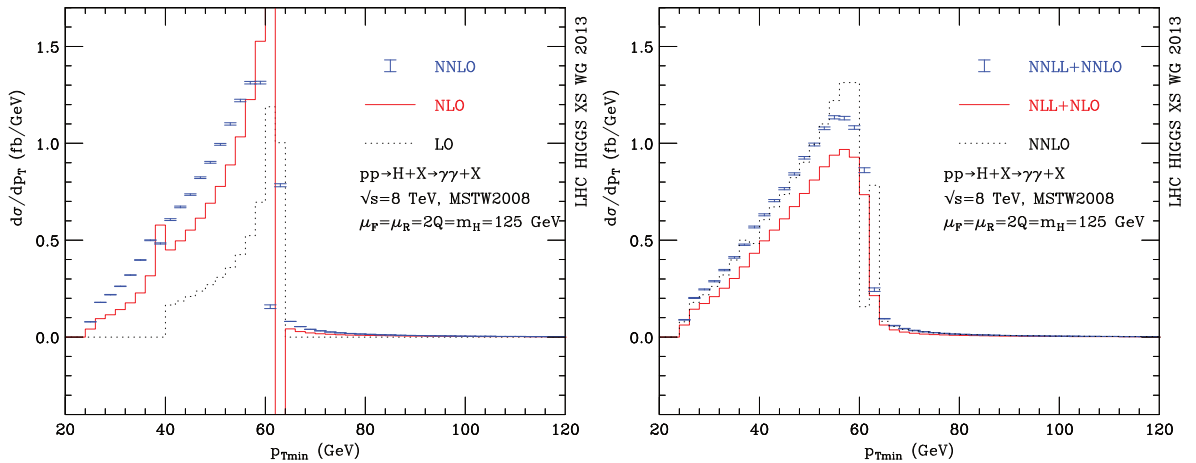
Fig. 14: Distribution $p_T^{\max,\gamma}$ for the H $\rightarrow \gamma\gamma$ signal at the LHC, obtained by resummed (right plot) calculations and fixed order (left plot) for comparison.

Fig. 14(right); in this case the NNLO result is compared with the resummed result at the NLL+NLO and NNLL+NNLO accuracy. As expected [72], resummed results do not suffer of such instabilities in the vicinity of the LO kinematical boundary; the resummed distributions are smooth and the shape is rather stable when going from NLL+NLO to NNLL+NNLO.

The HRES code provides all the momenta of final state particles and studies on other variables can be performed. For example a variable that is often studied is $\cos(\theta^*)$, where θ^* is the polar angle of one of the photons with respect to the beam axis in the Higgs boson rest frame. A cut on the photon transverse momentum p_T^γ implies a maximum value for $\cos(\theta^*)$ at LO. For example for $M_H = 125$ GeV and $p_T^\gamma \geq 40$ GeV we obtain $|\cos(\theta^*)| \leq |\cos(\theta_{\mathrm{cut}}^*)| \simeq 0.768$. At the NLO and NNLO the Higgs transverse momentum is non vanishing and events with $|\cos(\theta^*)| > |\cos(\theta_{\mathrm{cut}}^*)|$ are kinematically allowed. In the region of the kinematical boundary higher-order perturbative distributions suffer of logarithmic singularities. As expected [72], resummed results do not suffer of such instabilities in the vicinity of the LO kinematical boundary; the resummed distributions are smooth and the shape is rather stable when going from NLL+NLO to NNLL+NNLO. In Fig. 2 we report both the distributions (normalized to unity) obtained by fixed order and the resummed calculations. We see that the resummed results are smooth in the region around the kinematical boundary. Away from such region, fixed order and resummed results show perfect agreement.
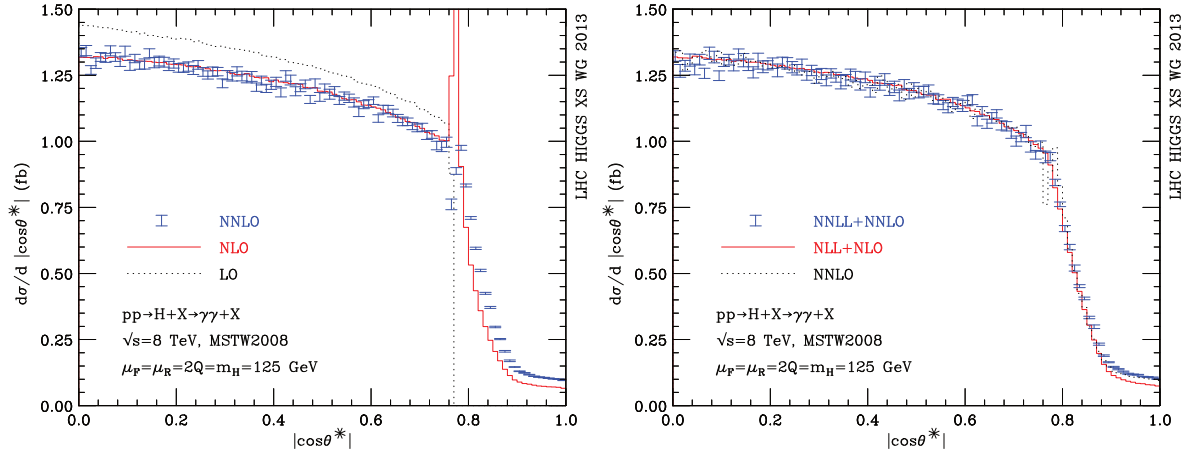
Fig. 15: Normalized $\cos\theta^*$ distribution at the LHC. On the left: LO, NLO and NNLO results. On the right: resummed predictions at NLL+NLO and NNLL+NNLO accuracy are compared with the NNLO result.

3.4 Higgs p_T distribution using different generators

3.4.1 Comparison among HRES, POWHEG, MADGRAPH, AMC@NLO, SHERPA without Heavy Quark mass effect [7]

Results of Higgs boson searches performed at 7 TeV were using POWHEG as main generator for the gluon fusion process. In both CMS and ATLAS collaborations the Higgs boson p_T was reweighted event by event to match the NNLO+NNLL p_T spectrum predicted by HqT. Higgs boson searches performed at 8 TeV are using POWHEG where the dampening factor *hfact* was tuned to reproduce HqT spectrum, therefore no reweighting was needed. In this section we perform a comparison of different generators able to generate the gluon fusion process, with the following setup.

We consider a Higgs boson mass of 125 GeV. HRES predictions are computed with a factorization and renormalization scales set to 125 GeV, and resummation scale set to 62.5 GeV, using the PDF set MSTW2008. The theory uncertainty bands are computed by multiplying/dividing by 2 the renormalization and factorization scales independently. HRES spectrum was cross-checked against HqT and found to be identical. POWHEG predictions are computed at NLO with *hfact*= $M_H/1.2$ [14, 73] and the showering is performed with PYTHIA 6. MADGRAPH 5 predictions are computed with up to 3 extra jets using PYTHIA 6 shower, the PDF set CTEQ6L1 is used and the matching scale, obtained by looking at the differential jet rate which needs to be smoothed, was found to be $Q_{\rm cut} = 26$ GeV. We also compare two generators with matching/merging of extra-jets at NLO. aMC@NLO predictions are performed on sample of matched and merged 0/1/2 jets at NLO and the third jet at LO with herwig6 shower, the PDF used is MSTW2008 and the matching scale is set to 50 GeV. Sherpa predictions are performed with a matched/merged sample of 0/1 jets at NLO, the second jet a LO, with hadronization and MPI, the PDF set used is CT10 and the matching scale is set to 30 GeV. Generated samples are compared inclusively (no further selection is applied). All are normalized to the cross-section computed with HRES with central renormalization and factorization scales.

The Higgs boson p_T distribution zoomed in the range [0,50] GeV is shown Fig. 16. As previously noted and shown on Fig. 16, the p_T spectrum of POWHEG with *hfact* tuned is slightly harder than the one predicted with HRES. It can also be observed that Madgraph has a somehow softer p_T than POWHEG. On the other hand, aMC@NLO seems to predict a mildly harder p_T. A larger range of p_T is shown on Fig. 17 along with the Higgs boson rapidity. Decay to photons was included in all generators but Sherpa. We show on Fig. 18 the distributions of $\Delta\phi(\gamma,\gamma)$ and $p_{T\gamma}$.

---

[7]N. Chanon
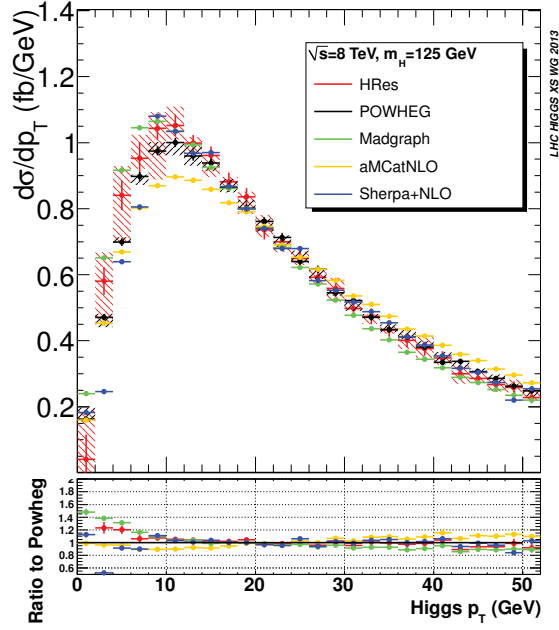
Fig. 16: Distribution of Higgs p_T for different generators for Higgs boson of $M_\mathrm{H} = 125$ GeV at 8 TeV.
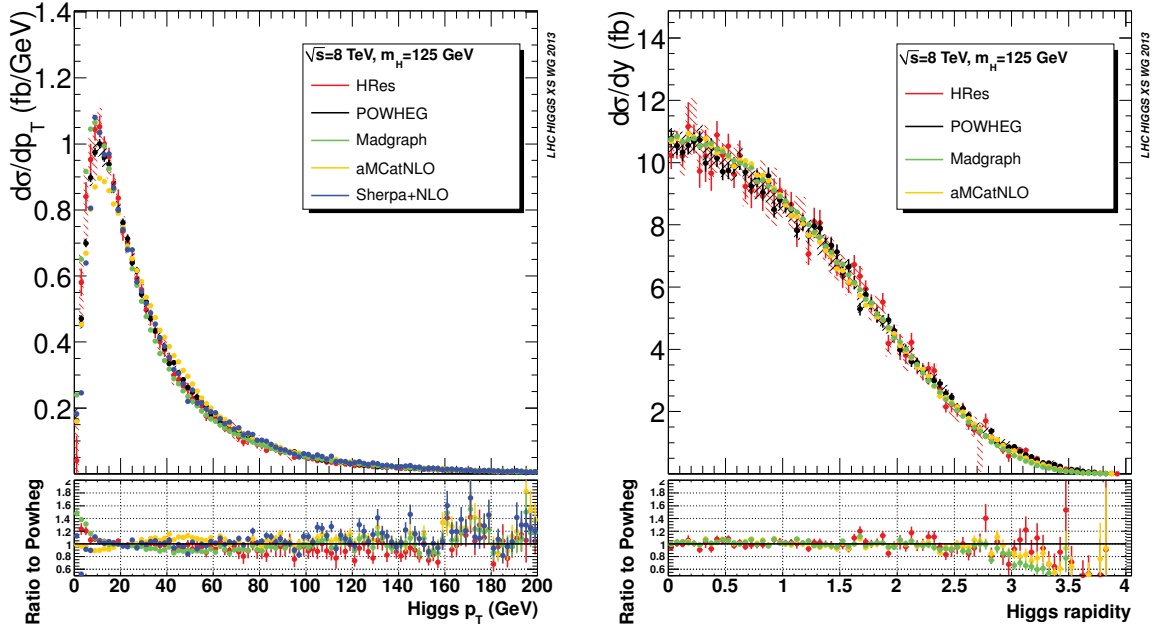
Fig. 17: Distribution of Higgs p_T (left) and rapidity (right) for different generators for Higgs boson of $M_\mathrm{H} = 125$ GeV at 8 TeV.
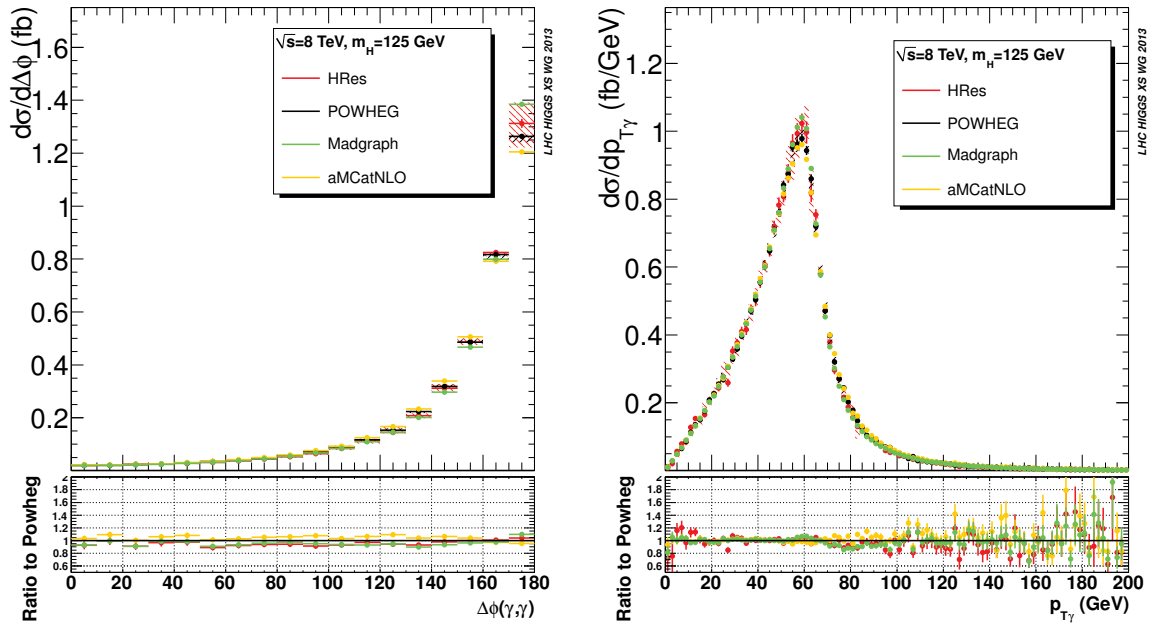
Fig. 18: Distribution of diphoton $\Delta\phi(\gamma,\gamma)$ and $p_{T,\gamma}$ for different generators for Higgs boson of $M_\mathrm{H} = 125$ GeV at 8 TeV.
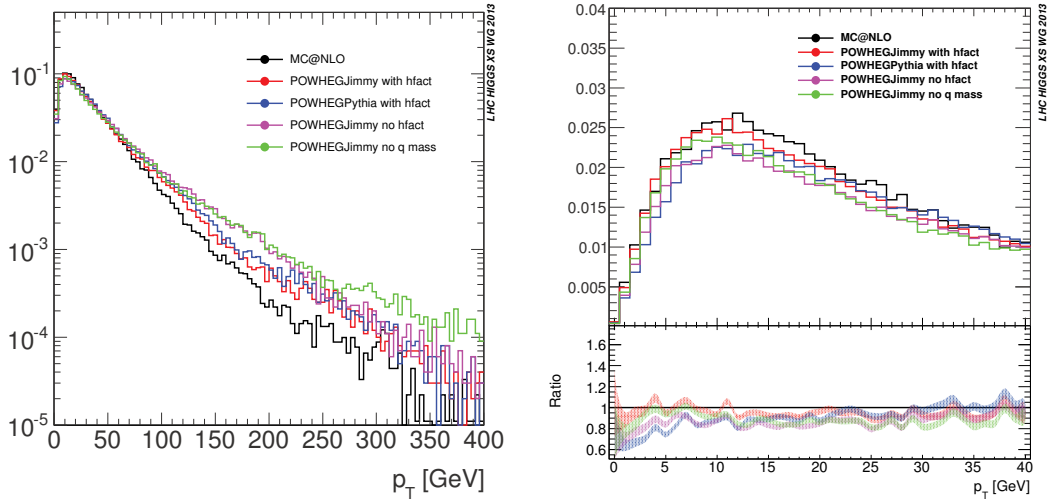
Fig. 19: Higgs p_T distribution using different MC generators and parton shower configurations. POWHEGPythia indicates POWHEG + PYTHIA8, POWHEGJimmy indicates POWHEG + HERWIG6 and JIMMY for the underlying event simulation. The *no q mass* distribution corresponds to a configuration where both *hfact* and the Heavy Quark mass effect are switched off.

3.4.2 *Higgs p_T distribution, MC@NLO-Powheg comparison using finite HQ mass effect* [8]

In the search of the Higgs boson and the measurement of the Higgs boson production yield in the H → γγ and H → ZZ* → 4l channel, the Higgs transverse momentum is of particular interest because it affects the signal acceptance due to the cuts applied on the photon and lepton momenta. Moreover the signal purity can be increased by cutting on the transverse momentum of the di-boson system that is on average larger in the Higgs decay than the non resonant background due to the higher jet activity in the Higgs gluon fusion production process than the di-photon and ZZ non resonant backgrounds. Such techniques are applied in the H → γγ search [74] and under study in the H → ZZ → 4l and H → ττ searches. It is therefore important to understand the impact of several contributions to the Higgs p_T and how they affect the p_T spectrum predicted by the MC generators.

In the present section we show a comparison of the Higgs p_T distribution between MC@NLO 4.09 [75], using HERWIG 6.5 [76] for the showering, and POWHEG [77–80] that has been showered with both PYTHIA8 [81, 82] and HERWIG 6.5. The signal process is pp → H → ZZ* at the mass $M_H = 125.5$ GeV. This value has been chosen being the last ATLAS best fit value [9]. HERWIG 6.5 has been interfaced to JIMMY [83] for the underlying event simulation. The ATLAS AUET2 [84] tune using the CTEQ 10 NLO pdfs in the showering algorithm has been used. Both MC@NLO 4.09 and POWHEG include the heavy quark mass effect in the gluon gluon loop for the Higgs p_T determination. The contribution is available for t,b and c quarks in POWHEG and for the t and b quarks in MC@NLO. In the present section the contribution from the c quark has been switched off in POWHEG so that the quark mass effects refer to the contribution from the top and bottom quarks. The p_T dampening factor *hfact* has been set to $m_H/1.2$ in the POWHEG case. A configuration without the *hfact* has also been studied. The top mass has been set at $m_t = 172.5$ GeV and the bottom quark mass at $m_b = 4.75$ GeV. The generation has been performed using the CT10 pdf set.

In Fig. 19 the Higgs p_T distribution is shown with different configurations. In the range, $0 - 400$ GeV, we observe that the MC@NLO spectrum is softer than the POWHEG + PYTHIA8 one. Comparing POWHEG+HERWIG with POWHEG + PYTHIA8 is possible to see that the parton shower doesn't

---

[8]B. Di Micco, R. Di Nardo

affect the high Higgs p_T tail as expected. The use of the *hfact* dampening factor makes the POWHEG spectrum closer to the MC@NLO one at high p_T but still significantly harder. The heavy quark mass effect has been switched off in the POWHEG + HERWIG sample in order to estimate the size of the effect. The contribution is visible in the very high p_T tail ($p_\mathrm{T} > 250$ GeV) but doesn't seem responsible for the main high p_T behaviour. In order to compare the generators at low p_T the same figure has been zoomed in the range 0-40 GeV. For $p_\mathrm{T} < 15$ GeV differences between the HERWIG and PYTHIA8 showering are visible and in the very low p_T region ($p_\mathrm{T} < 10$ GeV), MC@NLO + HERWIG and POWHEG + HERWIG with the *hfact* are compatible while both the PYTHIA8 showering and the *no hfact* configuration are different from the MC@NLO prediction. This shows that at low p_T the parton shower has a relevant role but the dampening factor correction is still important and brings the POWHEG + HERWIG spectrum in agreement with MC@NLO 4.09.

3.5 Interference in light Higgs VV modes

Interferences between signal and background amplitudes are known to be relevant for heavy Higgs production. However, they can play a significant role also for a light Higgs, by considerably modifying the cross section and eventually contributing to a shift in the signal peak. In this section we analyse the interference effects for the WW, ZZ and $\gamma\gamma$ channels.

In Section 3.5.1, the findings of Ref. [85] about the inadequacy of zero-with approximation and importance of signal-background interference are summarised. In Sections 3.5.2 and 3.5.3, results for $\mathrm{gg}\,(\to \mathrm{H}) \to 4$ leptons including Higgs-continuum interference effects calculated with GG2VV [86] are presented. The complex-pole scheme [87] with $M_\mathrm{H} = 125$ GeV and $\Gamma_\mathrm{H} = 4.434$ MeV is used.

Sections 3.5.4 and 3.5.5 summarize the recent findings of [88, 89] about the effect on the diphoton invariant mass shift due to the inclusion of the contribution from the gq and $\overline{\mathrm{q}}$q channels in the signal-background interference. Section 3.5.4 considers the case of inclusive $\gamma\gamma$ production while Section 3.5.5 discusses the effect on $\gamma\gamma$ + jet production.

3.5.1 *Inadequacy of zero-with approximation and importance of signal-background interference* [9]

For the SM Higgs boson with $M_\mathrm{H} \approx 125$ GeV, one has $\Gamma_\mathrm{H}/M_\mathrm{H} < 10^{-4}$, which suggests an excellent accuracy of the zero-width approximation (ZWA). However, as shown in Ref. [85] for inclusive cross sections and cross sections with experimental selection cuts, the ZWA is in general not adequate and the error estimate $\mathcal{O}(\Gamma_\mathrm{H}/M_\mathrm{H})$ is not reliable for a light Higgs boson. The inclusion of off-shell contributions is essential to obtain an accurate Higgs signal normalisation at the 1% precision level as well as correct kinematic distributions. ZWA deviations are particularly large for $\mathrm{H} \to \mathrm{VV}^*$ processes (V = W, Z). To be more specific, without optimised selection cuts they are of $\mathcal{O}(5-10\%)$. The ZWA caveat also applies to Monte Carlos that approximate off-shell effects with an ad hoc Breit-Wigner reweighting of the on-shell propagator, as can be seen by comparing the $\mathrm{H_{ZWA}}$ and $\mathrm{H_{offshell}}$ distributions in Figure 20. The ZWA limitations are also relevant for the extraction of Higgs couplings, which is initially being performed using the ZWA. The findings of Ref. [85] make clear that off-shell effects have to be included in future Higgs couplings analyses.

The unexpected off-shell effect can be traced back to the dependence of the decay matrix element on the Higgs invariant mass $\sqrt{q^2}$. For $\mathrm{H} \to \mathrm{VV}^*$ decay modes one finds that the q^4 dependence of the decay matrix element for $q^2 > (2M_\mathrm{V})^2$ compensates the q^2-dependence of the Higgs propagator, which causes a strongly enhanced off-shell cross section in comparison to the ZWA up to invariant masses of about 600 GeV (see Figure 20). The total $\mathrm{gg} \to \mathrm{H} \to \mathrm{VV}^*$ cross section thus receives an $\mathcal{O}(10\%)$ off-shell correction. Furthermore, in the region above $2M_\mathrm{V}$ the Higgs signal is affected by $\mathcal{O}(10\%)$ signal-background interference effects, which, due to the enhanced off-shell tail, can have a significant impact also for $M_\mathrm{H} \ll 2M_\mathrm{V}$. On the other hand, in the vicinity of the Higgs resonance finite-width

---

[9]N. Kauer
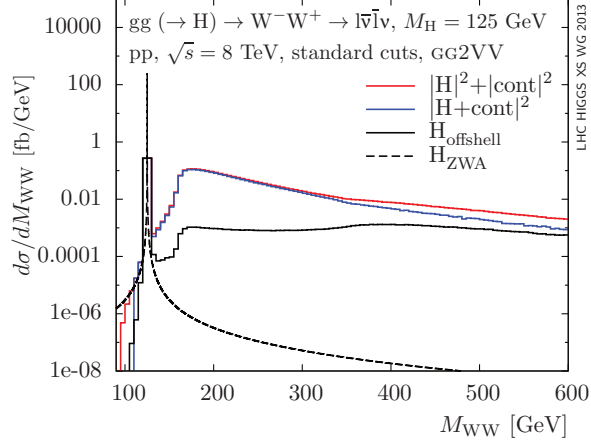
Fig. 20: M_{WW} distributions for gg $(\to H) \to W^-W^+ \to l\bar{\nu}\bar{l}\nu$ in pp collisions at $\sqrt{s} = 8$ TeV for $M_H = 125$ GeV. The ZWA distribution (black, dashed) as defined in Eq. (3.2) in Ref. [85], the off-shell Higgs distribution (black, solid), the $d\sigma(|\mathcal{M}_H + \mathcal{M}_{cont}|^2)/dM_{WW}$ distribution (blue) and the $d\sigma(|\mathcal{M}_H|^2 + |\mathcal{M}_{cont}|^2)/dM_{WW}$ distribution (red) are shown. Standard cuts are applied: $p_{T1} > 20$ GeV, $|\eta_l| < 2.5$, $\not{p}_T > 30$ GeV, $M_{ll} > 12$ GeV. No flavour summation is carried out for charged leptons or neutrinos.

and Higgs-continuum interference effects are negligible if $M_H \ll 2M_V$. For weak boson decays that permit the reconstruction of the Higgs invariant mass, the experimental procedure focuses on the Higgs resonance region and for $M_H \ll 2M_V$ the enhanced off-shell region is thus typically excluded. For $H \to VV^*$ channels that do not allow to reconstruct the Higgs invariant mass, the tail can nevertheless be effectively excluded by applying a $M_T < M_H$ cut on a suitable transverse mass observable M_T which approximates the Higgs invariant mass. Finally, in addition to gluon fusion the $H \to VV^*$ modes in other Higgs production channels also exhibit an enhanced off-shell tail, since the effect is caused by the decay matrix element.

3.5.2 WW*/ZZ* *interference in* gg $(\to H) \to l\bar{\nu}_l\bar{l}\nu_l$

In this section, ZZ* corrections (including γ^* contributions) to gg $(\to H) \to WW^* \to l\bar{\nu}_l\bar{l}\nu_l$ with same-flavour final state in pp collisions at 8 TeV are studied for $M_H = 125$ GeV including WW*/ZZ* interference. To quantify the signal-background interference effect the $S+B$-inspired measure R_1 and $S/\sqrt{B}$-inspired measure R_2 are used:

$$R_1 = \frac{\sigma(|\mathcal{M}_H + \mathcal{M}_{cont}|^2)}{\sigma(|\mathcal{M}_H|^2) + \sigma(|\mathcal{M}_{cont}|^2)} , \quad R_2 = \frac{\sigma(|\mathcal{M}_H|^2 + 2\,\mathrm{Re}(\mathcal{M}_H\mathcal{M}_{cont}^*))}{\sigma(|\mathcal{M}_H|^2)} , \quad (24)$$

where $\mathcal{M}_H$ and $\mathcal{M}_{cont}$ are the gg $\to H \to l\bar{\nu}_l\bar{l}\nu_l$ and gg $\to l\bar{\nu}_l\bar{l}\nu_l$ amplitudes, respectively. Off-shell Higgs contributions are included. The selection cuts choice (see Table 3) follows Ref. [85]. A cut on the transverse mass

$$M_T = \sqrt{(M_{T,ll} + \not{p}_T)^2 - (\mathbf{p}_{T,ll} + \not{p}_T)^2} \quad \text{with} \quad M_{T,ll} = \sqrt{p_{T,ll}^2 + M_{ll}^2} \quad (25)$$

is applied.

Results with ZZ* contribution including WW*/ZZ* interference are given in Table 3. To assess the importance of including the ZZ* contribution for the same-flavour final state, for the observables in Table 3 the ratio with/without ZZ* correction (including interference) is displayed in Table 4. It shows that the cross sections are affected by the ZZ* correction at the few percent level, but the interference measures $R_{1,2}$ are essentially unchanged.

Table 3: Cross sections in fb for $gg \, (\to H) \, \to \, WW^*/ZZ^* \, \to \, l\bar{\nu}_l \bar{l} \nu_l$ (same flavour) in pp collisions at 8 TeV for $M_H = 125$ GeV. Results are given for signal ($|H|^2$), gg continuum background ($|cont|^2$) and signal+background+interference ($|H+cont|^2$). Off-shell Higgs contributions are included. $R_{1,2}$ as defined in Eq.(24) are also displayed. Standard cuts as in Figure 20. Higgs search cuts: standard cuts and $M_{ll} < 50$ GeV, $\Delta\phi_{ll} < 1.8$. M_T is defined in Eq.(25). No flavour summation is carried out for charged leptons or neutrinos. The integration error is given in brackets.

selection cuts	$|H|^2$	$|cont|^2$	$|H+cont|^2$	R_1	R_2
standard cuts	3.225(4)	11.42(5)	12.95(8)	0.884(6)	0.47(3)
Higgs search cuts	1.919(3)	2.711(7)	4.438(8)	0.958(3)	0.900(6)
$+(0.75 M_H < M_T < M_H)$	1.736(2)	0.645(2)	2.335(4)	0.981(2)	0.974(3)

Table 4: As Table 3, but the ratio with/without ZZ^* correction (including interference) is shown for cross sections and $R_{1,2}$. The results without ZZ^* correction are taken from Table 4 in Ref. [85].

selection cuts	$|H|^2$	$|cont|^2$	$|H+cont|^2$	R_1	R_2
standard cuts	1.000(2)	1.088(5)	1.058(7)	0.991(7)	0.88(6)
Higgs search cuts	0.969(2)	1.002(3)	0.987(2)	0.998(3)	0.994(6)
$+(0.75 M_H < M_T < M_H)$	0.976(2)	1.001(3)	0.980(2)	0.997(3)	0.996(3)

3.5.3   H → ZZ* *invariant mass peak shift due to signal-background interference*

The prediction of a $\mathcal{O}(-100\,\mathrm{MeV})$ Higgs invariant mass peak shift in $gg \to H \to \gamma\gamma$ for $M_H = 125$ GeV in Ref. [90] raises the question if a similar effect occurs in the $gg \to H \to ZZ^*$ mode. That the deformation of the $H \to ZZ^*$ Breit-Wigner peak at $M_H = 125$ GeV due to Higgs-continuum interference is negligible at parton level can, for example, be seen in Figure 17 in Ref. [85], which displays the M_{ZZ} distribution in the range $M_H \pm 3\Gamma_H$ for the process $gg \to H \to ZZ^* \to l\bar{l}\nu\bar{\nu}$ in pp collisions at 8 TeV. No difference is perceptible between the signal and signal+interference+background distributions. At $M_H \approx 125$ GeV, the SM Higgs width is several orders of magnitude smaller than the M_{ZZ} resolution. Hence, detector resolution effects need to be taken into account to obtain a realistic prediction. For $gg \to H \to ZZ^* \to l\bar{l}l'\bar{l}'$ in pp collisions at 8 TeV with $M_H = 125$ GeV, one obtains the M_{ZZ} distributions shown in Figure 21 when a Gaussian smearing of $\Delta E_l/E_l = 0.02$ is applied to the charged lepton momenta. Figure 21 demonstrates that any shift between the signal and signal+interference distribution is tiny compared to the histogram bin width of 167 MeV. That the peak shift effect is much smaller for $H \to ZZ^*$ than for $H \to \gamma\gamma$ can be traced back to the tree-level-enhanced Higgs decay process and suppressed background process for a ZZ^* versus $\gamma\gamma$ final state.

3.5.4   *Interference effects in* γγ [10]

The resonance observed in the reconstruction of the diphoton invariant mass in proton proton collisions at the LHC turns out to be one of the main discovery channels and, therefore, requests precise theoretical calculations for the corresponding cross section.

The high precision achieved for the signal in gluon-gluon fusion $gg \to H$, the main production mechanism, is discussed in detail in Section 3.1. The rare decay $H \to \gamma\gamma$ is also mediated by loops.

---

[10]D. de Florian, N. Fidanza, R. Hernandez-Pinto, J. Mazzitelli, Y. Rotstein-Habarnau, G. Sborlini
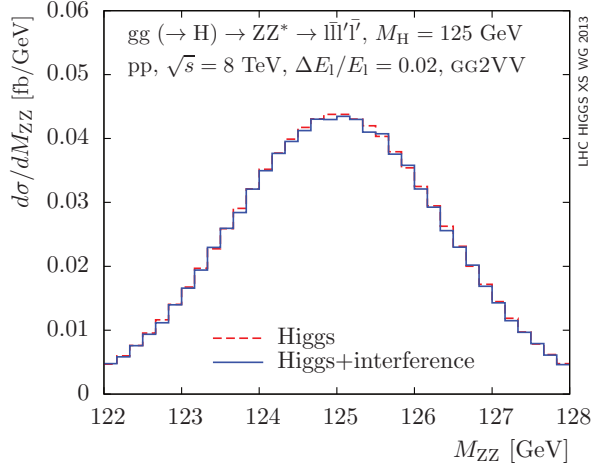
Fig. 21: $H \to ZZ^*$ invariant mass peak shift due to signal-background interference.

Corrections for the corresponding branching ratio are known to NLO accuracy for both QCD [37, 91–96] and electroweak [49] cases. Missing higher orders are estimated to be below 1%.

The corresponding background for diphoton production has been recently computed also up to NNLO [97], but the interference between *signal* and *background* has not been evaluated to such level of accuracy yet.

The interference of the resonant process $ij \to X + H \to \gamma\gamma$ with the continuum QCD background $ij \to X + \gamma\gamma$ induced by quark loops can be expressed at the level of the partonic cross section as:

$$
\begin{aligned}
\delta\hat{\sigma}_{ij \to X+H \to \gamma\gamma} &= -2(\hat{s} - M_H^2) \frac{\mathrm{Re}\left(\mathcal{A}_{ij \to X+H} \mathcal{A}_{H \to \gamma\gamma} \mathcal{A}_{\mathrm{cont}}^*\right)}{(\hat{s} - M_H^2)^2 + M_H^2 \Gamma_H^2} \\
&\quad -2M_H \Gamma_H \frac{\mathrm{Im}\left(\mathcal{A}_{ij \to X+H} \mathcal{A}_{H \to \gamma\gamma} \mathcal{A}_{\mathrm{cont}}^*\right)}{(\hat{s} - M_H^2)^2 + M_H^2 \Gamma_H^2} \,,
\end{aligned}
\tag{26}
$$

where $\hat{s}$ is the partonic invariant mass, M_H and Γ_H are the Higgs mass and decay width respectively [11].

As pointed out in [98, 99], given that the contribution arising from the real part of the amplitudes is odd in $\hat{s}$ around M_H, its effect on the total $\gamma\gamma$ rate is subdominant. For the gluon-gluon partonic subprocess, Dicus and Willenbrock [99] found that the imaginary part of the corresponding one-loop amplitude has a quark mass suppression for the relevant helicity combinations. Dixon and Siu [98] computed the main contribution of the interference to the cross-section, which originates on the two-loop imaginary part of the continuum amplitud $gg \to \gamma\gamma$. Recently, Martin [90] showed that even though the real part hardly contributes at the cross-section level, it has a quantifiable effect on the position of the diphoton invariant mass peak, producing a shift of about $\mathcal{O}(100 \text{ MeV})$ towards lower mass region once the smearing effect of the detector is taken into account.

The gg interference channel considered in [90] is not the only $\mathcal{O}(\alpha_s^2)$ contribution that has to be considered for a full understanding of the interference term, since other partonic subprocesses initiated by gq and q$\overline{\text{q}}$ can contribute at the same order. At variance with the gg subprocess that necessarily requests at least a one-loop amplitude for the background, the contribution from the remaining channels arises from tree-level amplitudes and can therefore only contribute to the real part of the interference in Eq.26 [12].

---

[11]The details on the implementation of the lineshape [87] have a very small effect on the light Higgs discussed in this section. We rely here on a naive Breit-Wigner prescription.

[12]Apart from a small imaginary part originated on the heavy-quark loops.
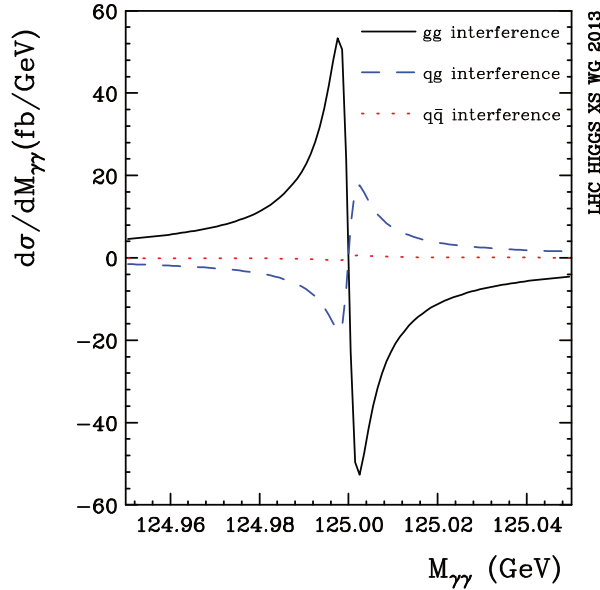
Fig. 22: Diphoton invariant mass distribution for the interference terms. The solid line is the gg channel contribution, the dotted one the gq channel, and dashed the $\overline{q}q$.

In this section we present the results obtained for the remaining gq → qγγ and qq → gγγ channels, finalizing a full (lowest order) $\mathcal{O}(\alpha_s^2)$ calculation of the interference between Higgs diphoton decay amplitude and the corresponding continuum background [88]. We concentrate on the effect of the new interference channels on the position of the diphoton invariant mass peak.

It is worth noticing that, compared to the gg → γγ subprocess, there is one more parton in the final state in the new channels. This parton has to be integrated out to evaluate the impact on the cross section and its appearance might provide the wrong impression that the contribution is next-to-leading order-like. However, since signal and background amplitudes develop infrared singularities in different kinematical configurations, the interference is finite after phase space integration and behave as a true tree-level contribution, with exactly the same power of the coupling constant as the one arising from gluon-gluon interference channel.

For a phenomenological analysis of the results, we need to perform a convolution of the partonic cross-section with the parton density functions. We use the MSTW2008 LO set [100] (five massless flavours are considered), and the one-loop expression of the strong coupling constant, setting the factorization and renormalization scales to the diphoton invariant mass $\mu_\mathrm{F} = \mu_\mathrm{R} = M_{\gamma\gamma}$. For the sake of simplicity, the production amplitudes are computed within the effective Lagrangian approach for the ggH coupling (relying in the infinite top mass limit), approximation known to work at the few percent level for the process of interest. The decay into two photons is treated exactly and we set $\alpha = 1/137$. For the Higgs boson we use $M_\mathrm{H} = 125$ GeV and $\Gamma_\mathrm{H} = 4.2$ MeV. For all the histograms we present in this section, an asymmetric cut is applied to the transverse momentum of the photons: $p_{T,\gamma}^{hard(soft)} \geq 40(30)$ GeV. Their pseudorapidity is constrained to $|\eta\gamma| \leq 2.5$. We also implement the standard isolation prescription for the photons, requesting that the transverse hadronic energy deposited within a cone of size $R = \sqrt{\Delta\phi^2 + \Delta\eta^2} < 0.4$ around the photon should satisfy $p_{T,had} \leq 3$ GeV. Furthermore, we reject all the events with $R_{\gamma\gamma} < 0.4$.

In Figure 22 we show the three contributions to the full signal-background interference as a function of the diphoton invariant mass $M_{\gamma\gamma}$ after having implemented all the cuts mentioned above. The gg term (solid line) represents the dominant gg channel, while the gq contribution (dashed) is about 3 times
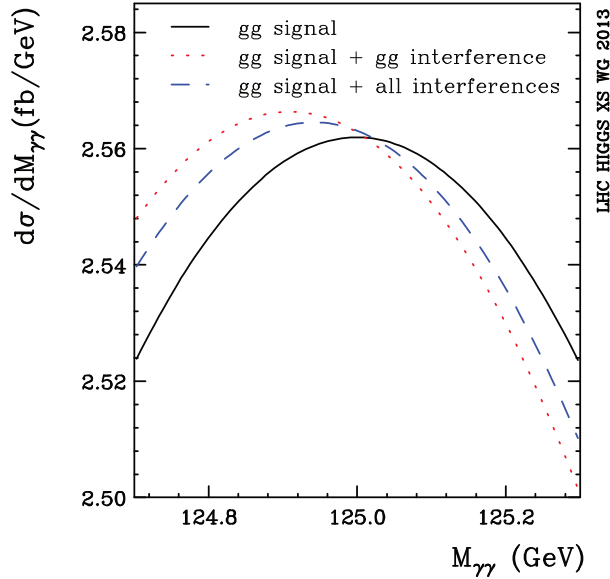
Fig. 23: Diphoton invariant mass distribution including the smearing effects of the detector (Gaussian function of width 1.7 GeV). The solid line corresponds to the signal-only contribution. The dotted line corresponds to the distribution after adding the gg interference term, and the dashed line represents the complete Higgs signal plus all three interference contributions (gg, gq and $\overline{q}q$).

smaller in absolute magnitude, but as we can observe, has the same shape but opposite sign to the gg channel. The $\overline{q}q$ contribution (dotted) is a couple of orders of magnitude smaller than the gg one. The position of the maximum and minimum of the distribution are located near $M_{\gamma\gamma} = H \pm \Gamma_H/2$, with a shift at this level that remains at $\mathcal{O}(1 \text{ MeV})$.

To simulate the smearing effects introduced by the detector, we convolute the cross-section with a Gaussian function of mass resolution width $\sigma_{MR} = 1.7$ GeV following the procedure Ref. [90].

In order to quantify the physical effect of the interferences in the diphoton invariant mass spectrum, we present in Figure 23 the corresponding results after adding the Higgs signal. The solid curve corresponds to the signal cross-section, without the interference terms, but including the detector smearing effects. As expected, the (signal) Higgs peak remains at $M_{\gamma\gamma} = 125$ GeV. When adding the gg interference term, we observe a shift on the position of the peak of about 90 MeV towards a lower mass (dotted), as found in Ref. [90]. If we also add the gq and $\overline{q}q$ contributions (dashed), the peak is shifted around 30 MeV back towards a higher mass region because of the opposite sign of the amplitudes.

Given the fact that $\overline{q}q$ and gq channels involve one extra particle in the final state, one might expect their contribution to be even more relevant for the corresponding interference in the process $pp \to H(\to \gamma\gamma) + jet$, since the *usually dominant* gg channel [101] starts to contribute at the next order in the strong coupling constant for this observable.

It is worth noticing that the results presented here are plain LO in QCD. Given the fact that very large K-factors are observed in both the signal and the background, one might expect a considerable increase in the interference as well. While reaching NNLO accuracy for the interference looks impossible at the present time, a prescription to estimate the uncertainty on the evaluation of the interference and a way to combine it with more precise higher order computations for signal and background for $gg \to ZZ$ was recently presented in [102]. The procedure can be easily extended to the case presented here by including all possible initial state channels.

Finally, we would like to emphasize that a more realistic simulation of the detector effects should

be performed in order to obtain reliable predictions and allow for a direct comparison with the experimental data.

3.5.5 *Interference effects in γγ + jet* [13]

The Higgs diphoton signal at the LHC is in principle affected by interference between the Higgs resonant amplitudes and the continuum background amplitudes with the same initial and final states. Because the continuum amplitude $gg \rightarrow \gamma\gamma$ is of one-loop order while the resonant amplitude $gg \rightarrow H \rightarrow \gamma\gamma$ is effectively of two-loop order, the interference need not be negligible. It was shown in [98, 99] that the effect on the cross-section is very small at leading order, but the imaginary part of the two-loop amplitude leads to a suppression of the diphoton rate of order a few per cent for H near 126 GeV [98]. The interference also produces a shift in the position of the diphoton mass peak. The diphoton lineshape can be written in the form

$$\frac{d\sigma_{\text{pp}\rightarrow\gamma\gamma+X}}{d(\sqrt{h})} \;\; = \;\; C(h) + \frac{1}{D(h)}\left[P(h) + (h - \text{H}^2)I(h)\right]. \tag{27}$$

Here, $h = M_{\gamma\gamma}^2$, and $C(h)$, $P(h)$, and $I(h)$ are smooth functions of h near the resonance, and the Breit-Wigner function $D(h) \equiv (h - \text{H}^2)^2 + \text{H}^2\Gamma_{\text{H}}^2$ defines the Higgs mass H. The function $C(h)$ comes from the pure continuum amplitudes not containing the Higgs, and $P(h)$ comes mainly from the pure Higgs-mediated contribution, while $I(h)$ comes from the interference. The integral of the $I(h)$ term over the whole lineshape nearly vanishes. However, at leading order it produces an excess of events below the Higgs mass H, and a corresponding deficit above, that is potentially observable Ref. [90].

The magnitude of the mass shift is potentially larger than the eventual experimental uncertainty in the mass. It is important to note that this shift will be different for different final states. For example, the interference should be much smaller for the $ZZ \rightarrow 4\ell$ final state; this makes the shift observable. For the diphoton case, it is reasonable to expect that the shift will be greatly affected by higher order effects, and a full NLO calculation (at least) should be done. As a precursor to this, in [88] and [89] the interference has been evaluated for the case of a final state including an extra jet, $\text{pp} \rightarrow j\gamma\gamma$. This follows from the parton-level subprocesses $gg \rightarrow g\gamma\gamma$ and $Qg \rightarrow Q\gamma\gamma$ (together with $\overline{Q}g \rightarrow \overline{Q}\gamma\gamma$) and a numerically very small contribution from $Q\overline{Q} \rightarrow g\gamma\gamma$. As was pointed out in [88], the shift for the processes involving quarks has the opposite sign from the leading order, while in [89] it was shown that the gg-initiated process shift has the same sign, but smaller relative magnitude, than the leading order. The combined effects of this are shown in Figure 24, for cuts p_{T}^{γ}(leading, sub-leading) $> (40, 30)$ GeV, $|\eta_{\gamma}| < 2.5$, $|\eta_j| < 3.0$, and $\Delta R_{\gamma\gamma}, \Delta R_{j\gamma} > 0.4$. The cut on the transverse momentum of the jet is varied, and used as the horizontal axis of the plot. For an experimentally reasonable cut $p_{T,\text{cut}}^{j} > 25$ GeV, the magnitude of the mass shift is much less than at leading order and is positive. This is in contrast to the negative shift of about $(-95, -125, -155)$ MeV for $\sigma_{\text{MR}} = (1.3, 1.7, 2.4)$ GeV from the leading order $\text{pp} \rightarrow \gamma\gamma$ case with no jet. The plot also shows the calculated shift for very low values of $p_{T,\text{cut}}^{j}$, where the process $gg \rightarrow g\gamma\gamma$ dominates due to logarithmically enhanced soft gluons attached to the leading order diagrams. The shift in the limit of extremely small $p_{T,\text{cut}}^{j}$ therefore approaches the leading order case.

The fact that $\Delta M_{\gamma\gamma}$ depends on the transverse momentum of the diphoton system is potentially useful, because it allows a measurement of the effect entirely within the sample of diphoton events, which have different systematics from the $ZZ \rightarrow 4\ell$. So far, the interference effects of genuine virtual corrections has not been done, and a full NLO analysis would be interesting.

---

[13]S. Martin
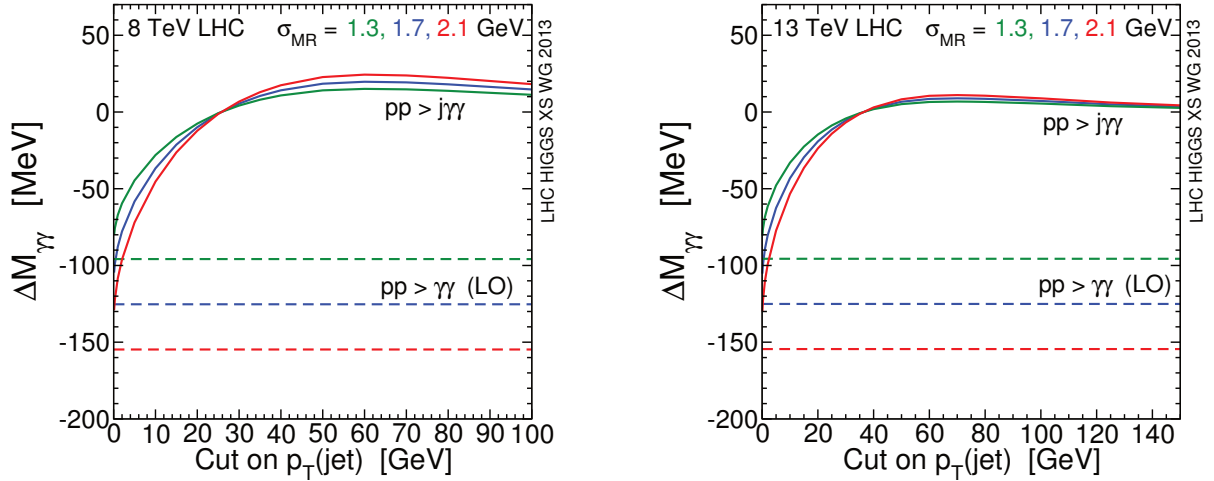
Fig. 24: The solid lines show the shifts in the diphoton mass peak, $\Delta M_{\gamma\gamma} \equiv M_{\gamma\gamma}^{\text{peak}} - H$, for pp $\to j\gamma\gamma$, as a function of the cut on the transverse momentum of the jet, $p_{\text{T,cut}}^{j}$, for $\sigma_{\text{MR}} = 1.3, 1.7$ GeV, and 2.1 GeV (from top to bottom on the left). The dashed lines shows the results for pp $\to \gamma\gamma$ at leading order without a jet requirement, again for $\sigma_{\text{MR}} = 1.3, 1.7$ GeV, and 2.1 GeV (from top to bottom). The left (right) panel is for $\sqrt{s} = 8(13)$ TeV. From Ref. [89].

3.6 Theoretical uncertainties on the pp $\to$ WW estimation in the Higgs search [14]

The most relevant background to the $H \to W^+W^- \to l\nu_l l\nu_l$ channel is the non resonant pp $\to$ $W^+W^- \to l\nu_l l\nu_l$ process.

In the decay of the Higgs boson to W pairs, W bosons have opposite spin orientation, since the Higgs has spin zero. In the weak decay of the W boson, due to the V-A nature of the interaction, the positive lepton is preferably emitted in the direction of the W^+ spin and the negative lepton in the opposite direction of the W^- spin. Therefore the two leptons are emitted close to each other and their invariant mass m_{ll} is small. This feature is used in the ATLAS [103] analysis to define a low-signal control region (CR) through a cut on m_{ll} of $50-100$ GeV. The event yield of the WW background is computed in the control region and extrapolated to the signal regions. The signal region is divided in two m_{ll} bins when the outcoming leptons belong to different families (different flavour in the following), each one defining one signal region (SR1,2 in the following), while if the outcoming leptons belong to the same family only one signal region (SR) is defined.

The WW yield in the signal regions is therefore:

$$
\begin{aligned}
N_{\text{SR}(1,2)}^{\text{WW0j}} &= \alpha_{0j}^{1,2} N_{\text{CR}}^{\text{WW0j}}, \\
N_{\text{SR}(1,2)}^{\text{WW1j}} &= \alpha_{1j} N_{\text{CR}}^{\text{WW1j}}
\end{aligned}
$$

where alpha is the ratio (evaluated with the MC simulation) of expected events in the signal region and the WW control region. The uncertainty on α is dominated by theoretical uncertainties, since it is defined using only well-measured charged-lepton quantities. There are two separate WW production processes to consider: $\bar{q}q \to$ WW and $gg \to$ WW. Since the $\bar{q}q \to$ WW process contributes $95\%(93\%)$ of the total WW background in the 0-jet (1-jet) channel, uncertainties on this process are the most important and are evaluated in Sec. 3.6.1.

---

[14]B. Di Micco, R.Di Nardo, H. Kim, J. Griffiths, D. C. Hall, C. Hays and J. Yu

Table 5: Definition of the preselection cuts for the WW studies.

	Different flavour	Same flavour
Exactly 2 leptons	**lepton:** $p_T > 15$ GeV, $|\eta| < 2.47$	
Leading lepton p_T	> 25 GeV	
m_{ll}	> 10 GeV	> 12 GeV
E_T^{miss}	> 25 GeV	> 45 GeV
Jet binning	**jet:** $p_T > 25$ GeV, $|\eta| < 4.5$	
p_T^{ll} (0 jet only)	> 30 GeV	

Table 6: Definitions of the signal regions (SR), control regions (CR), and validation region (VR). The cuts are in addition to the preselection cuts described in Table 5. Note that, for both the different-flavour and same-flavour analyses, the CR is always defined in the different flavour channel.

	m_{ll}	$\Delta\phi_{ll}$
SR1 (DF)	$12 - 30$ GeV	< 1.8
SR2 (DF)	$30 - 50$ GeV	< 1.8
SR (SF)	$12 - 50$ GeV	< 1.8
CR (DF 0j)	$50 - 100$ GeV	–
CR (DF 1j)	> 80 GeV	–
VR (DF 0j)	> 100 GeV	–

3.6.1 Uncertainties for the 0-jet and 1-jet analyses

The WW background is estimated using event counts in a control region (CR) defined using cuts on the m_{ll} variable. In Table 5 we describe the preselection cuts, and in Table 6 we show the cuts used to define the signal regions (SR) and the WW CR. Note that for both the different flavour (DF) and same flavour (SF) analyses, a DF CR is used to normalise to data.

The parameter α defined by:

$$\alpha_{WW} = \frac{N_{WW}^{SR/VR}}{N_{WW}^{CR}} \tag{28}$$

is used to predict the amount of WW background in each signal or validation region (VR) from the data counts in the control region. The Validation Region is a signal free region non overlapping with the WW CR, this region is used to test the validity of the extrapolation procedure on data. The α parameters are evaluated independently for the 0-jet and 1-jet bins, the same-flavor and different-flavor analyses, and in the two signal regions in the different-flavor analysis.

The non resonant $pp \to WW^{(*)}$ process is simulated with the POWHEG Monte Carlo program interfaced to PYTHIA8 for parton showering. POWHEG computes the process $pp \to WW^{(*)} \to lv_l lv_l$ at NLO including off-shell contributions. The calculation includes the "single-resonant" process where the process $l \to Wv_l$, $W \to lv_l$ happens from a lepton of a "single resonant" Z boson decay. Uncertainties on the α parameters arise from PDF modelling, missing orders in the perturbative calculation, parton shower modelling, and the merging of the fixed-order calculation with the parton-shower model.

3.6.2 PDF uncertainties

In order to evaluate the PDF uncertainties, we used 90% C.L. CT10 PDF eigenvectors and the PDF parametrizations from MSTW2008 and NNPDF2.3. The last two are significantly smaller than the CT10

Table 7: The α parameters for the standard analysis computed using different PDF sets and the spread obtained using the CT10 error set. The signs indicate the difference with respect to the CT10 central value and show the correlated differences in the different regions.

	CT10 error set	MSTW2008	NNPDF2.3
α_{0j}^{DF} (SR1)	1.4%	0.01%	-0.5%
α_{0j}^{DF} (SR2)	1.0%	-0.02%	-0.4%
α_{0j}^{SF}	1.1%	-0.01%	-0.4%
α_{1j}^{DF} (SR1)	1.8%	0.6%	-0.5%
α_{1j}^{DF} (SR2)	1.6%	0.5%	-0.4%
α_{1j}^{SF}	1.6 %	0.5%	-0.4%

Table 8: The α parameters for the low p_{T} analysis computed using different PDF sets and the spread obtained using the CT10 error set.

	CT10 error set	MSTW2008	NNPDF2.3
α_{0j}^{DF} (SR1)	1.7%	0.00%	-0.6%
α_{0j}^{DF} (SR2)	1.2%	0.04%	-0.4%
α_{0j}^{SF}	1.4%	0.01%	-0.6%
α_{1j}^{DF} (SR1)	1.9%	0.4%	-0.5%
α_{1j}^{DF} (SR2)	1.7%	0.6%	-0.4%
α_{1j}^{SF}	1.7%	0.4%	-0.6%

uncertainty. We take the quadrature sum of the CT10 uncertainties and the differences with respect to other parametrizations as the PDF uncertainty. A summary of α values and uncertainties are shown in Table 7. This methods gives uncertainty bands close enough to the envelope method but allows to compute the spread respect to the central PDF set that is used in the full MC simulation. The envelope method cannot be applied because it is not possible to generate a sample with a PDF set that exactly matches the central value.

3.6.3 Renormalization and factorization scales

The uncertainty from the missing higher-order terms in the calculation of the production process can affect the p_{T} distribution of the WW^* pair and the α values. The MCFM generator was used to estimate their effect producing samples with renormalisation (μ_{R}) and factorisation (μ_{F}) scale variations. The renormalisation scales are defined as $\mu_{\mathrm{R}} = \xi_{\mathrm{R}}\mu_0$ and $\mu_{\mathrm{F}} = \xi_{\mathrm{F}}\mu_0$, where μ_0 is a dynamic scale defined as $\mu_0 = m_{\mathrm{WW}}$.

The scale variations were calculated using 20 million 'virtual' integrations and ≈ 100 million 'real' integrations. In order to obtain an estimate of the statistical uncertainty on the α value produced by each scale variation, each sample was used individually to give an estimate of α and the central limit theorem was used to evaluate the uncertainty on the mean value. This gives a statistical uncertainty of around 0.4% for the 0-jet case (the 1 jet case has negligible statistical uncertainty).

The nominal scale is obtained with $\xi_{\mathrm{R}} = \xi_{\mathrm{F}} = 1$ and the scale uncertainties are obtained by varying ξ_{R} and ξ_{F} in the range $1/2 - 2$ while keeping $\xi_{\mathrm{R}}/\xi_{\mathrm{F}}$ between $1/2$ and 2; the maximum deviation from the nominal value is then taken as the scale uncertainty. The scale uncertainties on α are shown in Table 19, where we summarize also the PDF, parton-shower, and modelling uncertainties. The correlation between the α parameters of the 0-jet and 1-jet analyses is also evaluated in the calculation and their values are found to be fully correlated.

Table 9: Values of $\alpha_{0\mathrm{j}}^{\mathrm{DF}}$ (SR1) as the renormalisation scale (columns) and factorisation scale (rows) were varied. Statistical uncertainties in these vales are also shown.

	$\mu_0/2$	$3\mu_0/2$	μ_0	$3\mu_0/2$	$2\mu_0$
$\mu_0/2$	$0.2261 \pm 0.21\%$	$0.2250 \pm 0.26\%$	$0.2248 \pm 0.17\%$	–	–
$3\mu_0/2$	$0.2274 \pm 0.67\%$	$0.2250 \pm 0.42\%$	$0.2244 \pm 0.22\%$	$0.2242 \pm 0.36\%$	–
μ_0	$0.2264 \pm 0.32\%$	$0.2254 \pm 0.26\%$	$0.2247 \pm 0.22\%$	$0.2243 \pm 0.26\%$	$0.2232 \pm 0.23\%$
$3\mu_0/2$	–	$0.2248 \pm 0.24\%$	$0.2255 \pm 0.48\%$	$0.2237 \pm 0.19\%$	$0.2233 \pm 0.19\%$
$2\mu_0$	–	–	$0.2249 \pm 0.21\%$	$0.2240 \pm 0.43\%$	$0.2239 \pm 0.24\%$

Table 10: Values of $\alpha_{0\mathrm{j}}^{\mathrm{DF}}$ (SR2) as the renormalisation scale (columns) and factorisation scale (rows) were varied. Statistical uncertainties in these vales are also shown.

	$\mu_0/2$	$3\mu_0/4$	μ_0	$3\mu_0/2$	$2\mu_0$
$\mu_0/2$	$0.3846 \pm 0.22\%$	$0.3816 \pm 0.19\%$	$0.3828 \pm 0.23\%$	–	–
$3\mu_0/4$	$0.3856 \pm 0.64\%$	$0.3839 \pm 0.40\%$	$0.3821 \pm 0.29\%$	$0.3801 \pm 0.37\%$	–
μ_0	$0.3849 \pm 0.24\%$	$0.3819 \pm 0.42\%$	$0.3833 \pm 0.24\%$	$0.3805 \pm 0.30\%$	$0.3810 \pm 0.24\%$
$3\mu_0/2$	–	$0.3810 \pm 0.28\%$	$0.3823 \pm 0.41\%$	$0.3805 \pm 0.32\%$	$0.3794 \pm 0.24\%$
$2\mu_0$	–	–	$0.3848 \pm 0.43\%$	$0.3808 \pm 0.45\%$	$0.3826 \pm 0.24\%$

Table 11: Values of $\alpha_{0\mathrm{j}}^{\mathrm{SF}}$ as the renormalisation scale (columns) and factorisation scale (rows) were varied. Statistical uncertainties in these vales are also shown.

	$\mu_0/2$	$3\mu_0/4$	μ_0	$3\mu_0/2$	$2\mu_0$
$\mu_0/2$	$0.4694 \pm 0.45\%$	$0.4665 \pm 0.43\%$	$0.4675 \pm 0.39\%$	–	–
$3\mu_0/4$	$0.4713 \pm 0.63\%$	$0.4667 \pm 0.43\%$	$0.4650 \pm 0.42\%$	$0.4640 \pm 0.42\%$	–
μ_0	$0.4698 \pm 0.40\%$	$0.4675 \pm 0.47\%$	$0.4689 \pm 0.52\%$	$0.4645 \pm 0.39\%$	$0.4657 \pm 0.48\%$
$3\mu_0/2$	–	$0.4663 \pm 0.39\%$	$0.4659 \pm 0.44\%$	$0.4647 \pm 0.37\%$	$0.4639 \pm 0.40\%$
$2\mu_0$	–	–	$0.4674 \pm 0.41\%$	$0.4655 \pm 0.59\%$	$0.4659 \pm 0.40\%$

In order to ensure that we are not missing a localised large deviation in α on the $\mu_{\mathrm{R}} - \mu_{\mathrm{F}}$ plane and hence underestimating the scale uncertainty, we used the MCFM to simulate cases where ξ_R and ξ_F were equal to $3/4$ and $3/2$, but still fulfilling the same requirements as mentioned previously. This corresponded to 12 more points in the $\mu_{\mathrm{R}} - \mu_{\mathrm{F}}$ plane, and for each point we generated 5 files with the same number of events as before. Although this resulted in maximum deviations that were slightly larger than in the nominal variations, these deviations are within the statistical uncertainty evaluated using the central limit theorem. Table 9, 10 and 11 summarise the results.

Scale uncertainties were alternatively evaluated with the AMC@NLO generator varying ξ_{R} and ξ_{F} in the range $1/2 - 2$ while keeping $\xi_{\mathrm{R}}/\xi_{\mathrm{F}}$ between $1/2$. These uncertainties are summarized in Table 12 and are statistically consistent with those of MCFM.

3.6.4 Generator modelling

The α predictions using various generators was studied to get a range encompassing different orders of perturbative calculation and different models of parton showering and the associated merging with the fixed-order calculation. We conservatively assign a modelling uncertainty on the difference in α predicted between the best available pair of generators in terms of the fixed-order calculation. POWHEG + PYTHIA8 and MCFM have been compared for this study. MCMF is a pure parton level MC that is not matched to a parton showering algorithm. However, other effects included in this uncertainty might

Table 12: The uncertainty on the WW extrapolation parameters, α, calculated by varying the renormalisation and factorisation scales with the aMC@NLO generator. The statistical uncertainty is included as an uncertainty on the uncertainty.

	Maximum Deviation
α_{0j}^{DF} (SR1)	$1.7 \pm 0.7\%$
α_{0j}^{DF} (SR2)	$0.6 \pm 0.6\%$
α_{0j}^{SF}	$1.0 \pm 0.5\%$
α_{1j}^{DF} (SR1)	$3.4 \pm 1.1\%$
α_{1j}^{DF} (SR2)	$1.4 \pm 0.9\%$
α_{1j}^{SF}	$2.3 \pm 0.8\%$

Table 13: The WW extrapolation parameters, α, calculated using POWHEG + PYTHIA 8 and MCFM. The 0-jet and 1-jet, different-flavour (DF) and same-flavour (SF) values are each calculated.

	POWHEG + Pythia 8	MCFM	$\delta\alpha$
α_{0j}^{DF} (SR1)	0.2277	0.225	-1.2%
α_{0j}^{DF} (SR2)	0.3883	0.383	-1.4%
α_{0j}^{SF}	0.4609	0.469	+1.7%
α_{1j}^{DF} (SR1)	0.1107	0.105	-5.1%
α_{1j}^{DF} (SR2)	0.1895	0.180	-5.0%
α_{1j}^{SF}	0.2235	0.217	-3.1%

Table 14: The WW extrapolation parameters, α, calculated using POWHEG + HERWIG and AMC@NLO. The 0-jet and 1-jet, different-flavour (DF) and same-flavour (SF) values are each calculated.

	POWHEG + Herwig	aMC@NLO	$\delta\alpha$
α_{0j}^{DF} (SR1)	0.2277	0.2274	-0.4%
α_{0j}^{DF} (SR2)	0.3914	0.3845	-1.7%
α_{0j}^{SF}	0.4623	0.4581	-0.9%
α_{1j}^{DF} (SR1)	0.1113	0.1064	-4.3%
α_{1j}^{DF} (SR2)	0.1904	0.1840	-3.4%
α_{1j}^{SF}	0.2247	0.2122	-5.6%

involve e.g. different renormalisation and factorisation scales, or different electroweak schemes. The differences in α between the generators and the assigned uncertainties are shown in Table 13.

The modelling uncertainties were computed also for the extrapolation from the signal region to an higher m_{ll} region (validation region) used to test the uncertainty prescription. The validation region is defined by $m_{ll} > 100$ GeV after preselection. The results are shown in Table 15.

The uncertainty in the shape of the m_T distribution in the signal region arising from higher order corrections was estimated by varying the renormalisation and factorisation scales in MCFM, in a similar fashion to that used when calculating the uncertainty in α. In addition, the uncertainty in the shape of the m_T distribution due to the underlying event and parton showering is evaluated by comparing events generated with POWHEG and showered with PYTHIA8 to those same events showered with HERWIG. These shape systematics are shown in Figures 25, 26, and 27. The largest systematics are at low m_T and at high m_T, on the tails of the distribution, while the core part and in particular the region around the Higgs mass $m = 125$ GeV is not affected by large systematics.

Table 15: The WW extrapolation parameters, α, calculated for the validation region using POWHEG + PYTHIA8 and MCFM. The 0 jet and 1 jet, different flavour (DF) values are each calculated.

	POWHEG + PYTHIA 8	MCFM	$\delta\alpha$
α_{0j}^{DF} (VR)	0.9420	0.961	2.0%

Table 16: The WW extrapolation parameters, α, calculated with respect to the validation region using POWHEG + HERWIG and AMC@NLO. The 0 jet and 1 jet, different flavour (DF) values are each calculated.

	POWHEG + Herwig	aMC@NLO	$\delta\alpha$
α_{0j}^{DF} (VR)	0.9177	0.9738	6.1%

Various additional generators have been used to investigate the modelling of the WW background, Events generated with POWHEG are compared to those generated with Sherpa, MC@NLO + HERWIG, and MCFM. Between those generators, some differences are existing. The generators have the following features:

– POWHEG: NLO calculation matched to Sudakov factor for first emission
– MCFM: NLO calculation with no parton shower
– MC@NLO + HERWIG: NLO calculation with parton shower but no "singly resonant" diagrams
– Sherpa: LO calculation with parton shower

These studies offer insight into the effect of including NLO contributions, single-resonant diagrams, or the parton shower in the model.

The events are generated at a center of mass energy of 7 TeV using CTEQ 6.6 parton distribution functions (CTEQ 6.1 for Sherpa). Figure 28 shows the m_T distribution in the signal region.

The ratio of the MC@NLO to MCFM m_T distributions is taken as an uncertainty in the final m_T shape fit (the uncertainty is symmetrized).
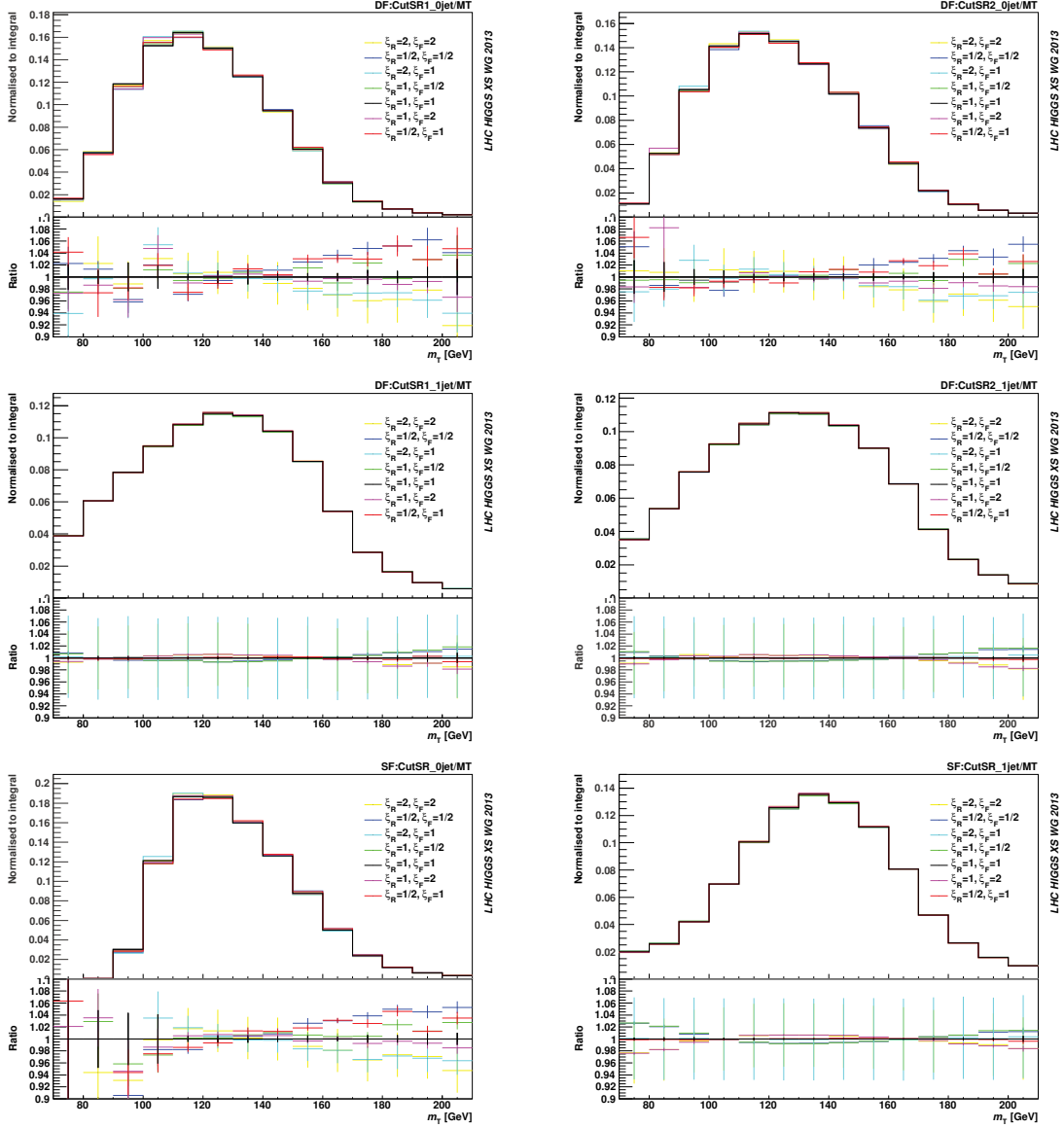
Fig. 25: Scale uncertainties in the m_T distribution in (top left) SR1 in DF 0j analysis, (top right) SR2 in DF 0j analysis, (middle left) SR1 in DF 1j analysis, (middle right) SR2 in DF 1j analysis, (bottom left) SR in SF 0j analysis, and (bottom right) SR in SF 1j analysis.
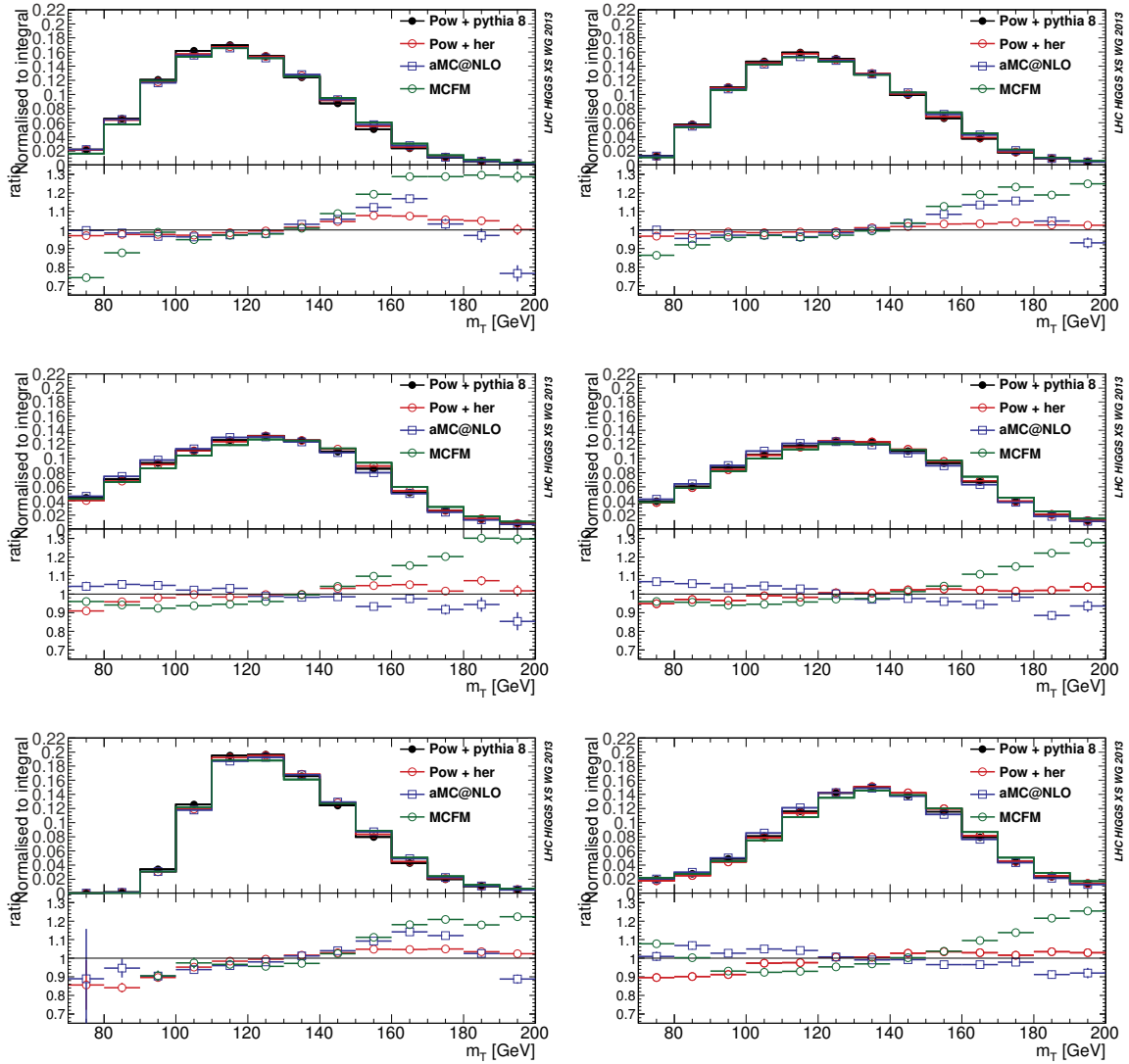
Fig. 26: Parton showering/modelling uncertainties in the m_T distribution in (top left) SR1 in DF 0j analysis, (top right) SR2 in DF 0j analysis, (middle left) SR1 in DF 1j analysis, (middle right) SR2 in DF 1j analysis, (bottom left) SR in SF 0j analysis, and (bottom right) SR in SF 1j analysis. POWHEG + PYTHIA8/HERWIG is shown along with MCFM. All ratios are with respect to POWHEG + PYTHIA8.
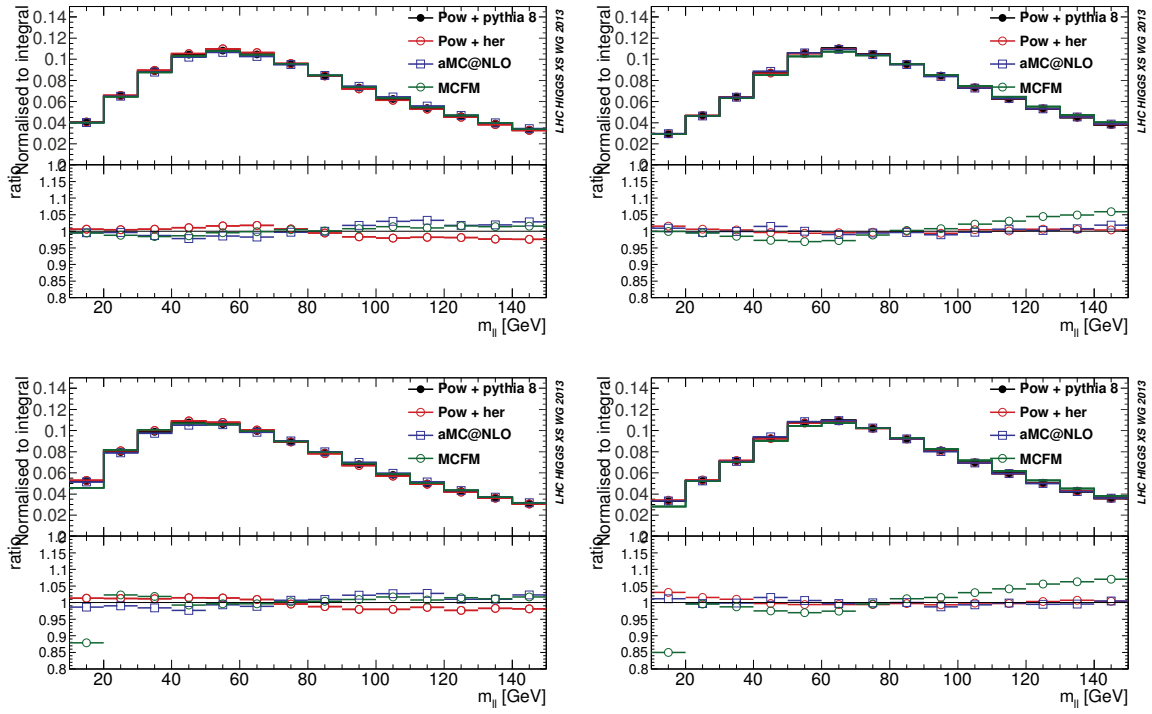
**Fig. 27:** Parton showering/modelling uncertainties in the m_{ll} distribution in (top left) SR1/2 in DF 0j analysis, (top right) SR1/2 in DF 1j analysis, (bottom left) SR in SF 0j analysis, and (bottom right) SR in SF 1j analysis. POWHEG + PYTHIA8/HERWIG is shown along with MCFM. All ratios are with respect to POWHEG + PYTHIA8.
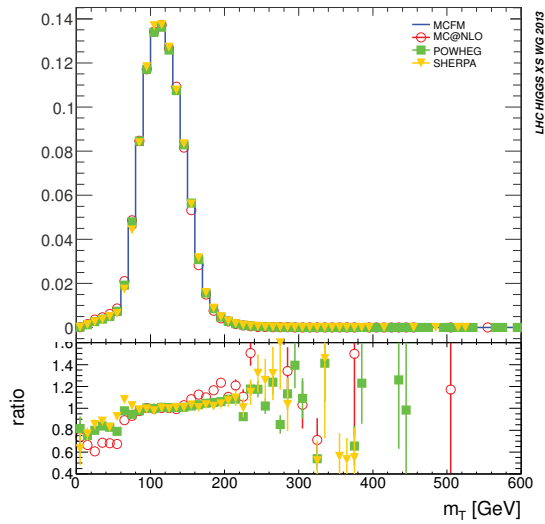

Fig. 28: Distributions of m_T in the signal region for the four generators considered.

3.6.5 Parton shower modelling

Parton showering effect is studied by comparing the measured α values (eqn. 28) when using the nominal matrix element event generator, POWHEG, interfaced with either PYTHIA8, PYTHIA6, or HERWIG. One million events were generated with POWHEG in each of the WW $\to$ ee/$\mu\mu$/eμ/μe final states, yielding a total of 4 million events. The α values are computed in both the same flavor and different flavor analyses separately for 0, 1, and ≥ 2 jet events. The jet multiplicity distributions after preselection for the different generators are shown in Fig. 29.
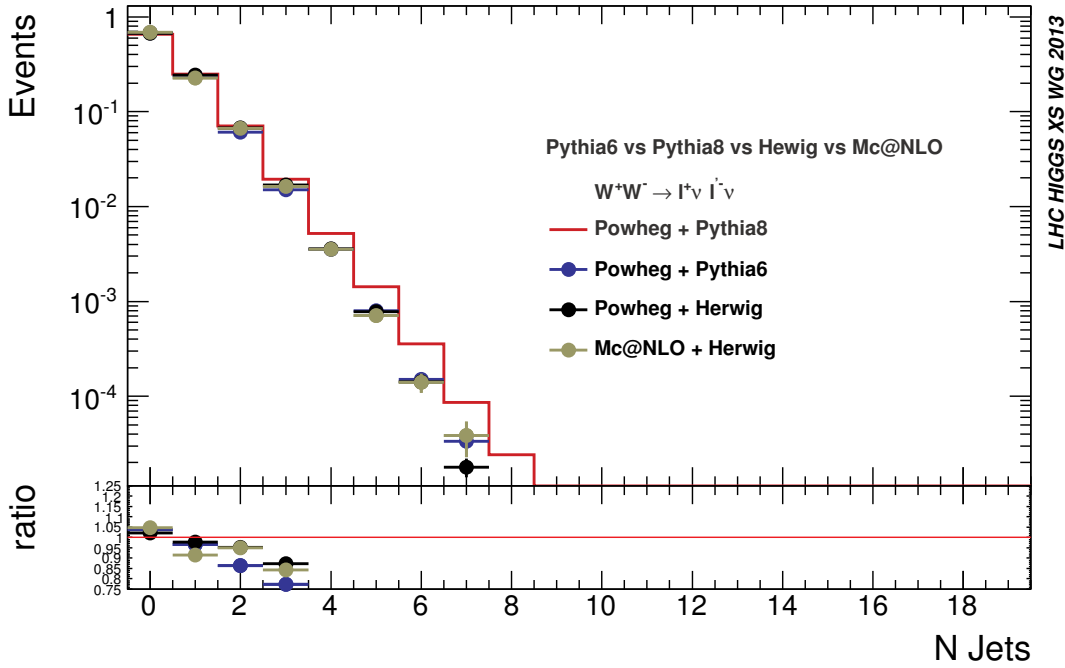
Fig. 29: The jet multiplicity distributions for the four generators considered.

Table 17 shows the measured alpha values for each showering program split into the two jet bins for both the same flavor and opposite flavor analyses. Table 18 shows the relative difference between each showering program and the nominal, PYTHIA8. In general, PYTHIA8 and PYTHIA6 are consistent with each other. The measured systematic uncertainties for choice of parton showering is determined from the difference between PYTHIA8 and HERWIG. For both analyses, the observed shift is about 4.5% for the 0-jet bin, while for the other jet bins, the observed shift is consistent with zero (except for the ≥ 2-jet bin in the opposite flavor analysis). We conservatively take 4.5% as a correlated uncertainty for both 0-jet and 1-jet bins, since further study is required to appropriately assess the uncertainty in the 1-jet bin.

3.6.6 Summary

The theoretical uncertainties on the normalization in the signal and validation regions are summarized in Tables 19 and 20. The modelling uncertainty has been checked with aMC@NLO; the differences between POWHEG and aMC@NLO are generally smaller than, or the same within uncertainties, those between POWHEG and MCFM.

Table 17: The α_{WW} values for POWHEG generated events showered with PYTHIA6, PYTHIA8, or HERWIG are shown. The values are shown both for same flavor and opposite flavor analyses in either the 0, 1, or ≥ 2 jet-bins. For reference, the α value is also shown in events generated with MC@NLO and showered with HERWIG.

SR vs CR	UEPS	DF		SF
		SR1	SR2	
0-jet	POWHEG+PYTHIA6	0.2275 ± 0.0006	0.3877 ± 0.0008	0.4602 ± 0.0009
	POWHEG+PYTHIA8	0.2277 ± 0.0003	0.3883 ± 0.0004	0.4609 ± 0.0004
	POWHEG+HERWIG	0.2277 ± 0.0003	0.3914 ± 0.0004	0.4623 ± 0.0004
	MC@NLO+HERWIG	0.229 ± 0.003	0.385 ± 0.004	0.4597 ± 0.0043
1-jet	POWHEG+PYTHIA6	0.1098 ± 0.0004	0.1895 ± 0.0006	0.2232 ± 0.0007
	POWHEG+PYTHIA8	0.1107 ± 0.0002	0.1895 ± 0.0003	0.2235 ± 0.0003
	POWHEG+HERWIG	0.1113 ± 0.0002	0.1904 ± 0.0003	0.2247 ± 0.0003
	MC@NLO+HERWIG	0.1071 ± 0.0021	0.179 ± 0.003	0.211 ± 0.003

Table 18: Systematic uncertainty between nominal (POWHEG + PYTHIA8) vs. the other PDF showering tools and MC@NLO+HERWIG. The systematic uncertainty is computed by subtracting PYTHIA6 or HERWIG from PYTHIA8 and then dividing the difference by PYTHIA8.

SR vs CR	UEPS	DF		SF
		SR1	SR2	
0-jet	POWHEG+PYTHIA6	$0.1 \pm 0.3\%$	$0.2 \pm 0.2\%$	$0.14 \pm 0.2\%$
	POWHEG+HERWIG	$-0.02 \pm 0.2\%$	$-0.8 \pm 0.1\%$	$-0.3 \pm 0.1\%$
	MC@NLO+HERWIG	$-0.3 \pm 1.2\%$	$0.8 \pm 1.0\%$	$0.3 \pm 0.9\%$
1-jet	POWHEG+PYTHIA6	$0.8 \pm 0.4\%$	$-0.1 \pm 0.4\%$	$0.1 \pm 0.3\%$
	POWHEG+HERWIG	$-0.5 \pm 0.3\%$	$-0.5 \pm 0.2\%$	$-0.6 \pm 0.2\%$
	MC@NLO+HERWIG	$3.2 \pm 2.0\%$	$5.8 \pm 1.6\%$	$5.6 \pm 1.5\%$

Table 19: Scale, PDF, parton-shower/underlying event, and modelling uncertainties on the WW extrapolation parameters α for the NLO $\overline{q}q, qg \rightarrow WW$ processes; the errors are taken to be fully correlated between the 0-jet and 1-jet bins. The correlations in the parton-shower and modelling variations are shown explicitly by including the signed difference in the comparison.

	Scale	Parton-shower	PDFs	Modelling
α_{0j}^{DF} (SR1)	0.9%	+0.2 %	1.5%	-1.2%
α_{0j}^{DF} (SR2)	0.9%	+0.8%	1.1%	-1.4%
α_{0j}^{SF}	1.0%	+0.3%	1.1%	1.7%
α_{1j}^{DF} (SR1)	1.6%	+0.5%	2.0%	-5.1%
α_{1j}^{DF} (SR2)	1.5%	+0.5%	1.8%	-5.0%
α_{1j}^{SF}	1.4%	+0.6%	1.7%	-3.1%
$\alpha_{\mathrm{WW}}^{0j}, \alpha_{\mathrm{WW}}^{1j}$ correlation		1		

Table 20: Scale, PDF, parton-shower/underlying event, and modelling uncertainties on the WW extrapolation parameters α calculated relative to the validation region for the NLO $qq, qg \rightarrow WW$ processes.

	scale	parton-shower	PDFs	modelling
α_{0j}^{DF} (VR)	1.0%	2.6%	2.2%	2.0%

4 VBF production mode[15]

4.1 Programs and Tools

4.1.1 HAWK

HAWK is a parton-level event generator for Higgs production in vector-boson fusion [104–106], $pp \to Hjj$, and Higgs-strahlung [107], $pp \to WH \to \nu_l l H$ and $pp \to ZH \to l^- l^+ H / \nu_l \bar{\nu}_l H$. Here we summarize its most important features for the VBF channel. HAWK includes the complete NLO QCD and EW corrections and all weak-boson fusion and quark–antiquark annihilation diagrams, i.e. t-channel and u-channel diagrams with VBF-like vector-boson exchange and s-channel Higgs-strahlung diagrams with hadronic weak-boson decay, as well as all interferences. External fermion masses are neglected and the renormalization and factorization scales are set to M_W by default. Recently also anomalous Higgs-boson–vector-boson couplings have been implemented.

For the results presented below, s-channel contributions have been switched off. These contributions are at the level of a few per mille once VBF cuts are applied [105]. Interferences between t- and u-channel diagrams are included at LO and NLO, while contributions of b-quark parton distribution functions (PDFs) and final-state b quarks, which can amount to about 2%, are taken into account at LO. Contributions from photon-induced processes, which are part of the real EW corrections and at the level of $1-2\%$, can be calculated by HAWK as well, but have not been included, since photon PDFs are not supported by the PDF sets used. HAWK allows for an on-shell Higgs boson or for an off-shell Higgs boson (with optional decay into a pair of gauge singlets). For an off-shell Higgs boson, besides the fixed-width scheme [see Eq. (31)] the complex-pole scheme (CPS) [87, 108, 109] is supported with a Higgs propagator of the form

$$\frac{1}{\pi} \frac{M \, \Gamma_H(M)}{\left(M^2 - M_H^2\right)^2 + (M_H \Gamma_H)^2},$$

(29)

where M_H and Γ_H are the Higgs mass and width in the complex-mass scheme and $\Gamma_H(M)$ is the Higgs width for the off-shell mass M as taken from the tables in Ref. [13].

4.1.2 VBFNLO

VBFNLO [110–112] is a parton-level Monte Carlo event generator which can simulate vector-boson fusion, double and triple vector-boson production in hadronic collisions at next-to-leading order in the strong coupling constant, as well as Higgs-boson plus two jets and double vector-boson production via gluon fusion at the one-loop level. For Higgs-boson production via VBF, both the NLO QCD and EW corrections to the t-channel can be included in the SM (and also in the (complex) MSSM), and the NLO QCD corrections are included for anomalous couplings between the Higgs and a pair of vector bosons.

VBFNLO can also simulate the Higgs decays $H \to \gamma\gamma, \mu^+\mu^-, \tau^+\tau^-, b\bar{b}$ in the narrow-width approximation, either calculating the appropriate branching ratios internally at LO (or, in the case of the MSSM not considered in this section, taking them from an input SLHA file). The Higgs-boson decays $H \to W^+W^- \to l^+\nu_l l^-\bar{\nu}_l$ and $H \to ZZ \to l^+l^-l^+l^-, l^+l^-\nu_l\bar{\nu}_l$ are calculated using a Breit–Wigner distribution for the Higgs boson and the full LO matrix element for the $H \to 4f$ decay. Initial- and final-state b quarks can be included at NLO QCD for the neutral-current diagrams, where no external top quarks appear. For PDF sets which support photon PDFs, their effects are automatically included as well. As the used PDF sets do not include photon PDFs, this does however not play any role here. Interference effects between VBF-Higgs and continuum production in leptonic or semi-leptonic W^+W^- or ZZ VBF processes are contained in VBFNLO as part of the di-boson VBF processes.

For the results presented here, a modified version of VBFNLO was used, that simulates off-shell Higgs boson using the complex-pole scheme (see Eq. 29).

---

[15]A. Denner, P. Govoni, C. Oleari, D. Rebuzzi (eds.); P. Bolzoni, S. Dittmaier, S. Frixione, F. Maltoni, C. Mariotti, S.-O. Moch, A. Mück, P. Nason, M. Rauch, P. Torrielli, M. Zaro.

4.1.3 POWHEG

The POWHEG method is a prescription for interfacing NLO calculations with parton-shower generators, like HERWIG and PYTHIA. It was first presented in Ref. [78] and was described in great detail in Ref. [79]. In Ref. [113], Higgs-boson production in VBF has been implemented in the framework of the POWHEG BOX [80], a computer framework that implements in practice the theoretical construction of Ref. [79].

All the details of the implementation can be found in Ref. [113]. Here we briefly recall that, in the calculation of the partonic matrix elements, all partons have been treated as massless. This gives rise to a different treatment of quark flavors for diagrams where a Z boson or a W boson is exchanged in the t-channel. In fact, for all Z-exchange contributions, the b quark is included as an initial and/or final-state massless parton. For the (dominant) W-exchange contributions, no initial b quark has been considered, since it would have produced mostly a t quark in the final state, which would have been misleadingly treated as massless. The Cabibbo–Kobayashi–Maskawa (CKM) matrix V_{CKM} elements can be assigned by the user. The default setting used to compute the results in this section is

$$
V_{\mathrm{CKM}} = \begin{array}{c} \\ \mathrm{u} \\ \mathrm{c} \\ \mathrm{t} \end{array} \begin{array}{ccc} \mathrm{d} & \mathrm{s} & \mathrm{b} \\ \begin{pmatrix} 0.9748 & 0.2225 & 0.0036 \\ 0.2225 & 0.9740 & 0.041 \\ 0.009 & 0.0405 & 0.9992 \end{pmatrix} \end{array} . \tag{30}
$$

We point out that, as long as no final-state hadronic flavor is tagged, this is practically equivalent to the result obtained using the identity matrix, due to unitarity.

The Higgs-boson virtuality M^2 can be generated according to three different schemes:

1. the fixed-width scheme

$$
\frac{1}{\pi} \frac{M_{\mathrm{H}} \Gamma_{\mathrm{H}}}{\left(M^2 - M_{\mathrm{H}}^2\right)^2 + M_{\mathrm{H}}^2 \Gamma_{\mathrm{H}}^2} , \tag{31}
$$

   with fixed decay width Γ_{H},

2. the running-width scheme

$$
\frac{1}{\pi} \frac{M^2 \, \Gamma_{\mathrm{H}}/M_{\mathrm{H}}}{\left(M^2 - M_{\mathrm{H}}^2\right)^2 + (M^2 \, \Gamma_{\mathrm{H}}/M_{\mathrm{H}})^2} , \tag{32}
$$

3. the complex-pole scheme, as given in Eq. (29).

As a final remark, we recall that the renormalization μ_{R} and factorization μ_{F} scales used in the calculation of the POWHEG $\bar{B}$ function (i.e. the function that is used to generate the underlying Born variables to which the POWHEG BOX attaches the radiation ones) are arbitrary and can be set by the user. For the results in this section, they have been taken equal to M_{W}. The renormalization scale for the evaluation of the strong coupling associated to the radiated parton is set to its transverse momentum, as the POWHEG method requires. The transverse momentum of the radiated parton is taken, in the case of initial-state radiation, as exactly equal to the transverse momentum of the parton with respect to the beam axis. For final-state radiation one takes instead

$$
p_{\mathrm{T}}^2 = 2E^2(1 - \cos \theta), \tag{33}
$$

where E is the energy of the radiated parton and θ the angle it forms with respect to the final-state parton that has emitted it, both taken in the partonic centre-of-mass frame.

4.1.4 VBF@NNLO

VBF@NNLO [114, 115] computes VBF total Higgs cross sections at LO, NLO, and NNLO in QCD via the structure-function approach. This approach [116] consists in considering VBF process as a double deep-inelastic scattering (DIS) attached to the colorless pure electroweak vector-boson fusion into a Higgs boson. According to this approach one can include NLO QCD corrections to the VBF process employing the standard DIS structure functions $F_i(x, Q^2)$; $i = 1, 2, 3$ at NLO [117] or similarly the corresponding structure functions at NNLO [118–121].

The effective factorization underlying the structure-function approach does not include all types of contributions. At LO an additional contribution arises from the interferences between identical final-state quarks (e.g., $uu \to Huu$) or between processes where either a W or a Z can be exchanged (e.g., $ud \to Hud$). These LO contributions have been added to the NNLO results presented here, even if they are very small. Apart from such contributions, the structure-function approach is exact also at NLO. At NNLO, however, several types of diagrams violate the underlying factorization. Their impact on the total rate has been computed or estimated in Ref. [115] and found to be negligible. Some of them are color suppressed and kinematically suppressed [122–124], others have been shown in Ref. [125] to be small enough not to produce a significant deterioration of the VBF signal.

At NNLO QCD, the theoretical QCD uncertainty is reduced to less than 2%. Electroweak corrections, which are at the level of 5%, are not included in VBF@NNLO. The Higgs boson can either be produced on its mass-shell, or off-shell effects can be included in the complex-pole scheme.

4.1.5 aMC@NLO

The aMC@NLO generator [126, 127] is a program that implements the matching of a generic NLO QCD computation to parton-shower simulations according to the MC@NLO formalism [128]; its defining feature is that all ingredients of such matching and computation are fully automated. The program is developed within the MADGRAPH5 [129] framework and, as such, it does not necessitate of any coding by the user, the specification of the process and of its basic physics features (such as particle masses or phase-space cuts) being the only external informations required: the relevant computer codes are then generated on-the-fly, and the only practical limitation is represented by CPU availability.

aMC@NLO is based on different building blocks, each devoted to the generation and evaluation of a specific contribution to an NLO-matched computation. MADFKS [130] deals with the Born and real-emission terms, and in particular it performs in a general way the analytical subtraction of the infrared singularities that appear in the latter matrix elements according to the FKS prescription [64, 131]; moreover, it is also responsible for the process-independent generation of the so-called Monte Carlo subtraction terms, namely the contributions ensuring the avoidance of double-counting in the MC@NLO cross sections; MADLOOP [132] computes the finite part of the virtual contributions, based on the OPP [133] one-loop integrand-reduction method and on its implementation in CUTTOOLS [134].

The first applications of aMC@NLO[16] have been presented in Refs. [136–141], and a novel technique for merging different multiplicities of NLO-matched samples has been developed in the aMC@NLO environment and documented in Ref. [142].

As the MC@NLO method is Monte-Carlo dependent (through the Monte Carlo subtraction terms), a different subtraction has to be performed for each parton shower one wants to interface a computation to. So far this has been achieved in aMC@NLO for the HERWIG6 and HERWIG++ event generators (which amounts to the automation of the implementations detailed in Refs. [128, 143], respectively), and for the virtuality-ordered version of PYTHIA6 (the proof of concept of which was given in Ref. [144]). The present publication is the first in which aMC@NLO results are presented for PYTHIA6 in a process involving final-state radiation, and for HERWIG++.

---

[16]These results were still based on version 4 of MADGRAPH [135].

In the AMC@NLO framework, t-channel VBF can be generated with NLO accuracy in QCD. A $V_{\text{CKM}} = 1$ is employed, as there is no flavor tagging in our analysis. This computation includes all interferences between t- and u-channel diagrams, such as those occurring for same-flavor quark scattering and for partonic channels that can be obtained by the exchange of either a Z or a W boson (e.g. u d > h u d). Only vertex loop-corrections are included (the omitted loops are however totally negligible [105]). The Les-Houches parton-level event file thus generated also contains the necessary information for the computation of scale and PDF uncertainties without the need of extra runs [138]. The Higgs boson is considered as stable.

4.2 VBF Parameters and Cuts

The numerical results presented in Section 4.3 have been computed using the values of the EW parameters given in Appendix A of Ref. [13]. The electromagnetic coupling is fixed in the G_F scheme, to be

$$\alpha_{G_F} = \sqrt{2} G_F M_{\text{W}}^2 (1 - M_{\text{W}}^2/M_{\text{Z}}^2)/\pi = 1/132.4528\ldots. \tag{34}$$

The weak mixing angle is defined in the on-shell scheme,

$$\sin^2 \theta_{\text{w}} = 1 - M_{\text{W}}^2/M_{\text{Z}}^2 = 0.222645\ldots. \tag{35}$$

The renormalization and factorization scales are set equal to the W-boson mass,

$$\mu_{\text{R}} = \mu_{\text{F}} = M_{\text{W}}, \tag{36}$$

and both scales are varied independently in the range $M_{\text{W}}/2 < \mu < 2M_{\text{W}}$.

In the calculation of the inclusive cross sections, we have used the MSTW2008 [100], CT10 [145], and NNPDF2.1 [146] PDFs, for the calculation of the differential distributions we employed MSTW2008nlo PDFs [100].

Contributions from s-channel diagrams and corresponding interferences have been neglected throughout.

For the differential distributions presented in Section 4.3.2 the following reconstruction scheme and cuts have been applied. Jets are constructed according to the anti-k_{T} algorithm, with the rapidity–azimuthal angle separation $\Delta R = 0.5$, using the default recombination scheme (E scheme). Jets are subject to the cuts

$$p_{\text{T}j} > 20\,\text{GeV}, \qquad |y_j| < 4.5, \tag{37}$$

where y_j denotes the rapidity of the (massive) jet. Jets are ordered according to their p_{T} in decreasing progression. The jet with highest p_{T} is called leading jet, the one with next highest p_{T} subleading jet, and both are the tagging jets. Only events with at least two jets are kept. They must satisfy the additional constraints

$$|y_{j_1} - y_{j_2}| > 4, \qquad m_{jj} > 600\,\text{GeV}. \tag{38}$$

4.3 Results

4.3.1 Inclusive Cross Sections with CPS

In the following we present results for VBF inclusive cross sections at 7 TeV (for Higgs-boson masses below 300 GeV) and 8 TeV (over the full Higgs-boson mass range) calculated in the CPS, as described above.

Tables B.15–B.21 list the VBF inclusive cross sections at 7 TeV as a function of the Higgs-boson mass, while Tables B.22–B.28 display results at 8 TeV. The pure NNLO QCD results (second column), obtained with VBF@NNLO, the relative NLO EW corrections (fourth column), obtained with HAWK, and the combination of NNLO QCD and NLO EW corrections (third column) are given, together with
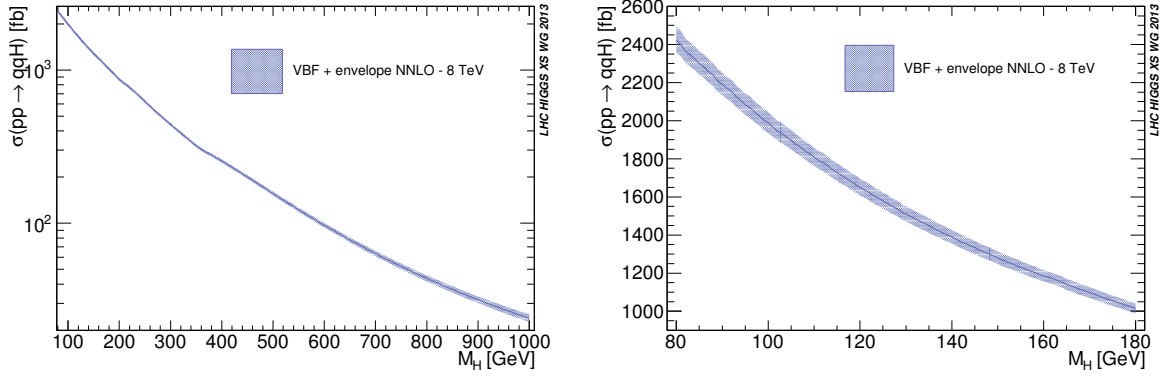
Fig. 30: VBF inclusive cross sections at the LHC at 8 TeV for the full (left) and low (right) Higgs-boson mass range. The uncertainty band represents the PDF + $\mathcal{O}(\alpha_s)$ envelope estimated according to the PDF4LHC prescription [147].

uncertainties from PDF + $\mathcal{O}(\alpha_s)$ and from QCD scale variations. The combination has been performed under the assumption that QCD and EW corrections factorize completely, i.e.

$$\sigma^{\text{NNLO+EW}} = \sigma^{\text{NNLO}}_{\text{VBF@NNLO}} \times (1 + \delta^{\text{EW}}_{\text{HAWK}}), \tag{39}$$

where $\sigma^{\text{NNLO}}_{\text{VBF@NNLO}}$ is the NNLO QCD result and $\delta^{\text{EW}}_{\text{HAWK}}$ the relative EW correction determined in the limit $\alpha_s = 0$.

Figure 30 summarizes the VBF results at 8 TeV for the full and for the low mass range. The inclusive cross section including the combined NNLO QCD and NLO EW corrections are shown as a function of the Higgs-boson mass. The band represents the PDF + $\mathcal{O}(\alpha_s)$ uncertainties, calculated from the envelope of the three PDF sets, CT10, MSTW2008, and NNPDF2.1, according to the PDF4LHC prescription.

In Table 22 we compare the predictions for the Higgs cross section in VBF from different calculations at NLO QCD and including EW corrections at 8 and 13 TeV. Using MSTW2008 PDFs, results are presented at NLO from VBF@NNLO, HAWK, and VBFNLO. The NLO QCD corrections agree within 0.6% between HAWK and VBF@NLO. The NLO EW corrections amount to -5% while the NNLO QCD corrections are below 0.3%.

All results are obtained in the CPS. Note that for Higgs-boson masses in the range $120-130$ GeV the cross section calculated in the complex-pole scheme is larger than the one for an on-shell Higgs boson by $\sim 1.4\%$ at 8 TeV and $\sim 2.2\%$ at 13 TeV. The presented results in the CPS assume that the Higgs distribution is integrated over all kinematically allowed invariant Higgs masses. If cuts on the invariant mass are applied, the cross section decreases down to the on-shell value.

4.3.2 Differential Distributions

In this section we present results relevant to the production of a 125 GeV Standard Model Higgs boson through a VBF mechanism at the 8 TeV LHC. These have been obtained with AMC@NLO [148] and POWHEG [80,113]. As AMC@NLO and POWHEG perform the NLO matching with parton showers by means of two different prescriptions (see Refs. [128] and [78,79], respectively), the comparison of the two allows one to assess the matching systematic that affects VBF Higgs production; it also constitutes a non-trivial validation of the public, fully-automated code AMC@NLO. Our predictions are obtained with the MSTW2008nlo68cl PDF set [100], and by setting the renormalization and factorization scales equal to the W-boson mass M_W. Matching with HERWIG6 [76], virtuality-ordered PYTHIA6 [81],
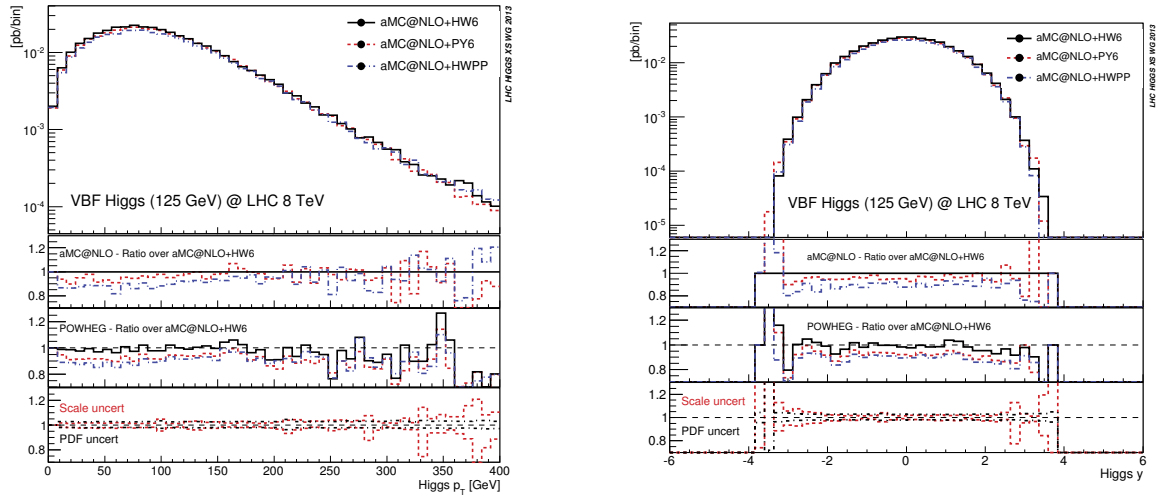
Fig. 31: Higgs-boson transverse-momentum (left) and rapidity (right) distributions. Main frame and upper inset: AMC@NLO results; middle inset: ratio of POWHEG results over AMC@NLO+HERWIG6; lower inset: AMC@NLO+HERWIG6 scale and PDF variations.

and HERWIG++ [149] has been considered in both schemes with default settings for such event generators; the only exception is for AMC@NLO+PYTHIA6, where `PARP(67)` and `PARP(71)` have been set to `1D0`. No simulation of the underlying event has been performed.

Plots for the most relevant distributions are shown using the following pattern. The curves in the main frame represent AMC@NLO matched with HERWIG6 (solid, black), PYTHIA6 (dashed, red), and HERWIG++ (dot-dashed, blue). The upper inset carries the same information as the main frame, displayed as ratio of the three AMC@NLO curves (with the same colors and patterns as described above) over AMC@NLO+HERWIG6. The middle inset contains the ratio of the POWHEG events showered with the three Monte Carlos (again, using the same colors and patterns) over AMC@NLO +HERWIG6. Finally, the lower inset displays the PDF (dot-dashed, black) and scale (dashed, red) uncertainties obtained automatically [138] after the AMC@NLO+HERWIG6 run. The scale band is the envelope of the nine curves corresponding to $(\mu_R, \mu_F) = (\kappa_R, \kappa_F) M_W$, with κ_R and κ_F varied independently in the range $\{1/2, 1, 2\}$. The parton-distribution band is obtained by following the asymmetric Hessian prescription given by the PDF set in Ref. [100]. We remind the reader that all results presented in this section are obtained by imposing the cuts introduced in Section 4.2.

In Figure 31 the transverse-momentum and rapidity distributions of the Higgs boson are shown. These observables are mildly affected by extra QCD radiation, essentially because they are genuinely NLO (in the sense that they are non-trivial in their full kinematical ranges already at the Born level $\mathcal{O}(\alpha_s^0)$). This explains why there is a general good agreement (in terms of shape) among the results obtained with different parton showers (main frame and upper inset), and between those obtained with AMC@NLO and POWHEG (middle inset). The discrepancy in the normalization of the various curves is due to the impact of the VBF cuts on the radiation generated by the different showers, as can be deduced by looking at the numbers reported in Table 21. The scale and PDF bands are fairly constant and both of the order of $\pm 3\%$, with a marginal increase of the former at large rapidities and transverse momentum.

Figures 32, 33, and the left panel of Fig. 34 display quantities related to the two hardest (tagging) jets, namely their transverse momenta, the pair invariant mass and azimuthal distance, and the absolute value of their rapidity difference, respectively. In spite of their being directly related to QCD radiation, these observables are described at the NLO, which translates in the overall agreement, up to the normal-

Table 21: Cross section after VBF cuts normalized to AMC@NLO+HERWIG6.

|	HERWIG6	PYTHIA6	HERWIG++
AMC@NLO	1.00	0.96	0.90
POWHEG	0.99	0.93	0.90
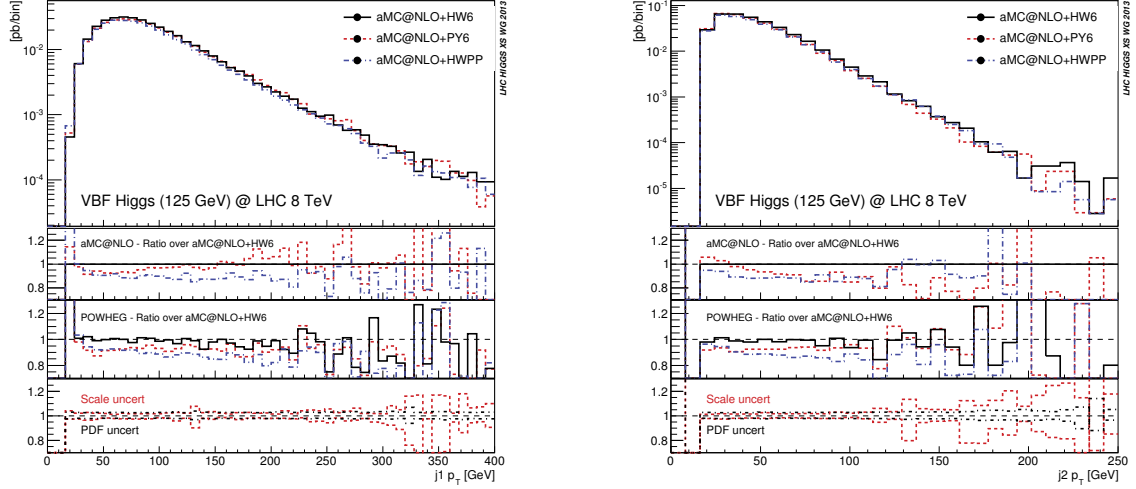
Fig. 32: Transverse-momentum distributions for the hardest (left) and next-to-hardest (right) jets. Main frame and upper inset: AMC@NLO results; middle inset: ratio of POWHEG results over AMC@NLO+HERWIG6; lower inset: AMC@NLO+HERWIG6 scale and PDF variations.

ization effect discussed above, of the results. Predictions obtained with PYTHIA6 tend to be marginally harder with respect to the two HERWIG curves for the first-jet transverse momentum both in POWHEG and in AMC@NLO, while the second-jet transverse momentum is slightly softer in AMC@NLO. The theoretical-uncertainty bands are constant with a magnitude of about $\pm 3\%$ for all observables, with the exceptions of a slight increase at large pair invariant mass ($\pm 5\%$), and of a more visible growth, up to $\pm 10-15\%$, towards the upper edge of the rapidity-difference range. For the parton distributions, this is due to the larger uncertainties in the high-x region, while the growth in the scale error may be related to $M_{\rm W}$ not being a representative scale choice for such extreme kinematical configurations.

The right panel Fig. 34 shows the exclusive jet-multiplicity. This observable is described with NLO accuracy in the 2-jet bin, and at the LO in the 3-jet bin. For the 2-jet bin, the pattern displayed in the upper and middle inset closely follows that of Table 21, while in the 3-jet bin discrepancies are of the order of $10-20\%$, with POWHEG predicting less events than AMC@NLO. Consistently with this picture, and with the formal accuracy of the two bins, scale uncertainties are $\pm 3\%$ and $\pm 10\%$, respectively. The differences between POWHEG and AMC@NLO, of the same order of (or slightly larger than) the scale variations, can be considered as an independent way of estimating the theoretical uncertainty associated with higher-order corrections.

From the 4-jet bin onwards, the description is completely driven by the leading-logarithmic (LL) accuracy of the showers, and by the tunes employed, which is reflected in the large differences that can be observed in the predictions given by the different event generators (for both AMC@NLO and POWHEG). For such jet multiplicities, theoretical-uncertainty bands are completely unrepresentative.

The left panel of Fig. 35 shows the transverse-momentum distribution of the third-hardest jet, which is a LO variable that can be affected by the different radiation patterns produced by the Monte Carlos. This is indeed what can be observed in the plot. In particular the AMC@NLO results display a $10-15\%$ dependence on the parton shower adopted. The POWHEG curves are slightly closer to
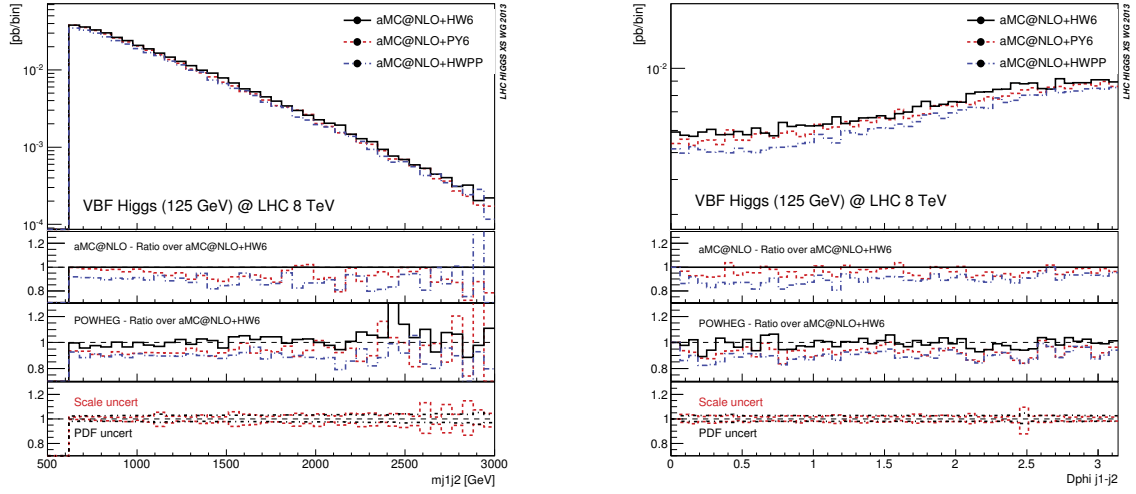
Fig. 33: Invariant mass (left) and azimuthal separation (right) of the two tagging jets. Main frame and upper inset: AMC@NLO results; middle inset: ratio of POWHEG results over AMC@NLO+HERWIG6; lower inset: AMC@NLO+HERWIG6 scale and PDF variations.
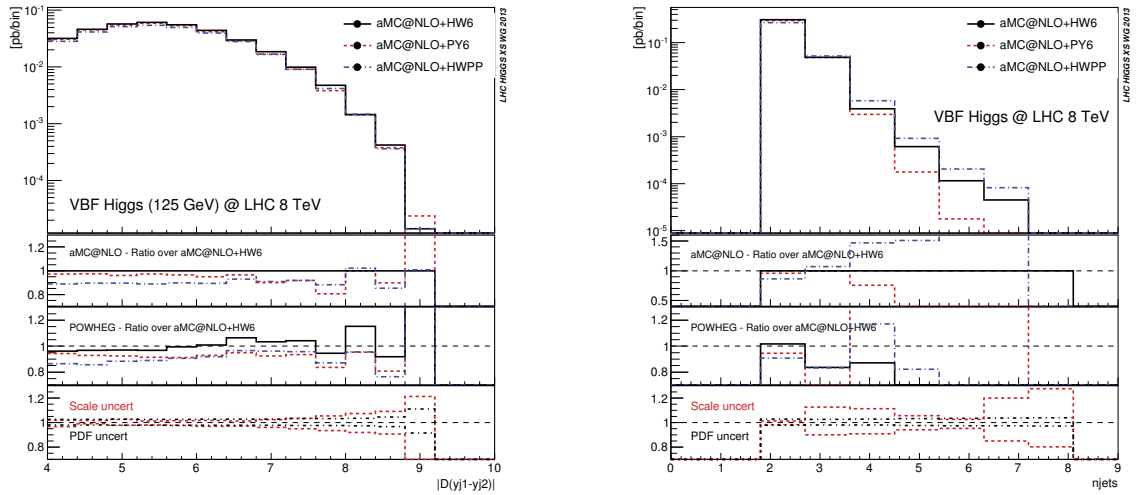
Fig. 34: Rapidity separation of the two tagging jets (left) and exclusive jet-multiplicity (right). Main frame and upper inset: AMC@NLO results; middle inset: ratio of POWHEG results over AMC@NLO+HERWIG6; lower inset: AMC@NLO+HERWIG6 scale and PDF variations.

each other, since in this case the hardest extra emission (the most relevant for quantities related to the overall third-hardest jet) is performed independently of the actual Monte Carlo employed. Furthermore, the two matching schemes differ quite sizably for this observable, up to $\pm 20-25\%$ at large transverse momentum, with POWHEG predicting a softer spectrum with respect to AMC@NLO. This discrepancy is consistent with the normalizations of the 3-jet bin in the right panel of Fig. 34. Different settings in PYTHIA6 have been checked to induce a variation in the curves within the previously mentioned discrepancy range, which is thus to be considered as a measure of the matching systematics affecting the prediction of this quantity. Scale uncertainties are quite large, compatibly with the LO nature of this observable, and growing from $\pm 10\%$ to $\pm 25\%$ with increasing transverse momentum. The rapidity distribution of the third-hardest jet, shown in the right panel of Fig. 35 has similar features, with the POWHEG samples more central than the AMC@NLO ones.
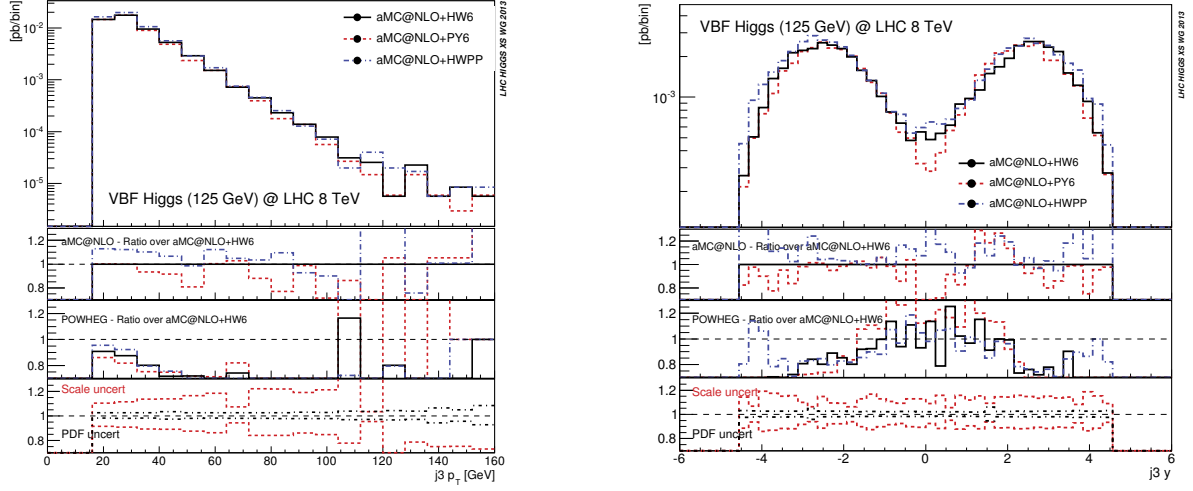
Fig. 35: Third-hardest jet transverse momentum (left) and rapidity (right) distributions. Main frame and upper inset: AMC@NLO results; middle inset: ratio of POWHEG results over AMC@NLO+HERWIG6; lower inset: AMC@NLO+HERWIG6 scale and PDF variations.
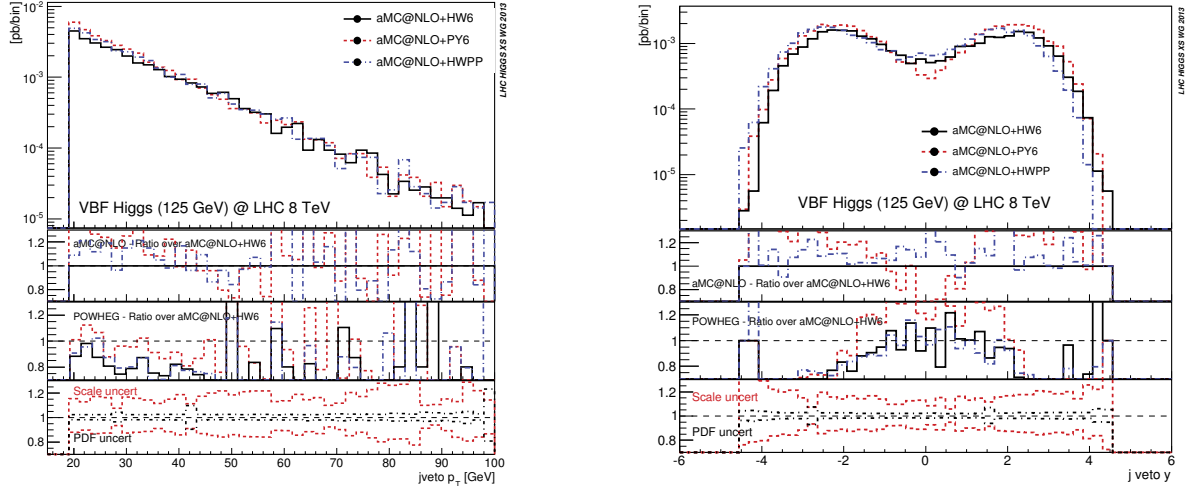
Fig. 36: Veto-jet transverse momentum (left) and rapidity (right) distributions. Main frame and upper inset: AMC@NLO results; middle inset: ratio of POWHEG results over AMC@NLO+HERWIG6; lower inset: AMC@NLO+HERWIG6 scale and PDF variations.

Fig. 36 displays features of the veto jet, defined as the hardest jet with rapidity ($y_{j_{\text{veto}}}$) lying between those (y_{j_1} and y_{j_2}) of the two tagging jets:

$$\min\left(y_{j_1}, y_{j_2}\right) < y_{j_{\text{veto}}} < \max\left(y_{j_1}, y_{j_2}\right). \tag{40}$$

This definition implies that the more central the third jet, the larger the probability that it be the veto jet. Since POWHEG predicts a more central third jet with respect to AMC@NLO, the veto condition has the effect that the two predictions for the veto jet are closer to each other than for the third jet; this is interesting in view of the fact that the differences between the two approaches can to a large extent be interpreted as matching systematics.
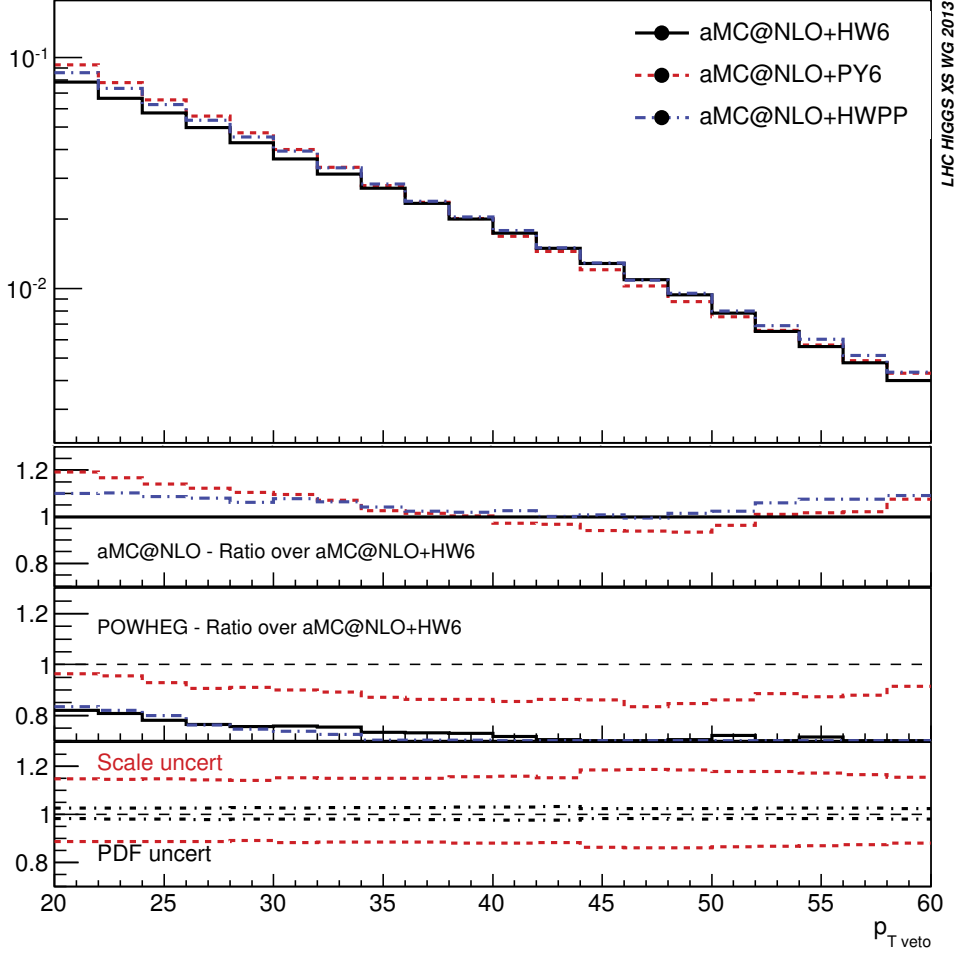
Fig. 37: Veto probability. Main frame and upper inset: AMC@NLO results; middle inset: ratio of POWHEG results over AMC@NLO+HERWIG6; lower inset: AMC@NLO+HERWIG6 scale and PDF variations.

To further investigate this point, Fig. 37 shows the veto probability $P_{\text{veto}}(p_{\text{T,veto}})$, defined as

$$P_{\text{veto}}(p_{\text{T,veto}}) = \frac{1}{\sigma_{\text{NLO}}} \int_{p_{\text{T,veto}}}^{\infty} \mathrm{d}p_{\text{T}} \frac{\mathrm{d}\sigma}{\mathrm{d}p_{\text{T}}}, \tag{41}$$

where $\sigma_{\text{NLO}} = (0.388 \pm 0.002)$ pb is the (fixed-order) NLO cross section within VBF cuts [17].
The excess of events between $p_{\text{T}} \sim 20$ GeV and $p_{\text{T}} \sim 40$ GeV in AMC@NLO matched to PYTHIA6 and HERWIG++ translates in a slightly larger cumulative probability of passing the veto cut. The POWHEG curves are lower, with up to $20-25\%$ discrepancy with respect to AMC@NLO at medium-high transverse momentum. Scale variation are compatible with a LO prediction, with a fairly constant magnitude of $\pm 15\%$.

---

[17]The AMC@NLO+HERWIG6 cross section within VBF cuts is 0.361 pb. The cross sections relevant to the other parton showers and to POWHEG can be deduced using the ratios in Table 21.

Table 22: VBF inclusive cross sections at 8 and 13 TeV calculated using MSTW2008NLO PDF set. Comparison among different calculations at NLO QCD for a selected number of Higgs-boson masses. The t–u-channel interferences and the b-quark contributions are included in the computation.

$M_{\rm H}$ [GeV]	$\sigma_{\rm VBF@NNLO}^{\rm NLOQCD}$ [fb]	$\sigma_{\rm HAWK}^{\rm NLOQCD}$ [fb]	$\sigma_{\rm HAWK}^{\rm NLOQCD+NLOEW}$ [fb]	$\sigma_{\rm VBFNLO}^{\rm NLOQCD}$ [fb]
8 TeV				
120	1737 ± 0.6	1732 ± 0.8	1651 ± 0.9	1743 ± 0.5
122	1706 ± 0.6	1701 ± 0.7	1623 ± 0.8	1711 ± 0.5
124	1675 ± 0.5	1671 ± 0.7	1594 ± 0.8	1681 ± 0.5
126	1646 ± 0.5	1641 ± 0.7	1566 ± 0.8	1651 ± 0.5
128	1617 ± 0.5	1613 ± 0.7	1539 ± 0.8	1622 ± 0.5
130	1588 ± 0.5	1585 ± 0.7	1513 ± 0.8	1593 ± 0.5
13 TeV				
120	4164 ± 2.5	4162 ± 2.2	3938 ± 2.5	4168 ± 2.1
122	4096 ± 2.1	4098 ± 2.2	3878 ± 2.5	4103 ± 2.0
124	4034 ± 1.8	4035 ± 2.2	3820 ± 2.4	4040 ± 1.8
126	3975 ± 2.0	3974 ± 2.2	3762 ± 2.4	3979 ± 1.8
128	3914 ± 2.3	3913 ± 2.3	3705 ± 2.4	3919 ± 1.7
130	3854 ± 1.6	3857 ± 2.0	3651 ± 2.2	3860 ± 1.6

5 WH/ZH production mode[18]

5.1 Theoretical developments

In the previous two working group reports [13] and [14] the state-of-the-art predictions for pp → WH/ZH were summarized and numerically discussed for the total and differential cross sections, respectively, taking into account all available higher-order corrections of the strong and electroweak interactions. The remaining uncertainties in the cross-section predictions, originating from missing higher orders and parametric errors in α_s and PDFs, were estimated to be smaller than 5% for integrated quantities, with somewhat larger uncertainties for differential distributions. In the meantime the predictions have been refined and supplemented upon including further higher-order corrections that are relevant at this level of accuracy as well. In the following we, thus, update the cross-section predictions accordingly.

Current state-of-the-art predictions are based on the following ingredients:

– QCD corrections are characterized by the similarity of WH/ZH production to the Drell–Yan process. While the NLO QCD corrections to these two process classes are analytically identical, the NNLO QCD corrections to WH/ZH production also receive contributions that have no counterparts in Drell–Yan production. The Drell–Yan-like contributions comprise the bulk of the QCD corrections of $\sim 30\%$ and are completely known to NNLO both for integrated [150] and fully differential [151, 152] observables for the WH and ZH channels, where the NNLO corrections to the differential ZH cross section were not yet available in Ref. [14].

QCD corrections beyond NLO that are not of Drell–Yan type are widely known only for total cross sections. The most prominent contribution of this kind comprises ZH production via gluon fusion which is mediated via quark loops. This part shows up first at the NNLO level [150] where it adds $\sim 3\%(5\%)$ to the total cross section at 7 TeV (14 TeV) for $M_H = 126$ GeV with a significant scale uncertainty of $\sim 30-60\%$. This uncertainty has been reduced recently [153] upon adding the NLO corrections to the gg channel in the heavy-top-quark limit (which is the dominant contribution of NNNLO to the pp cross section). This contribution, which roughly doubles the impact of the gg channel[19] and mildly reduces its scale uncertainty to $\sim 20-30\%$, was not yet taken into account in the predictions documented in Ref. [13], but is included in the results on total cross sections below.

Both WH and ZH production receive non-Drell–Yan-like corrections in the quark/antiquark-initiated channels at the NNLO level where the Higgs boson is radiated off a top-quark loop. After the completion of report [13], they were calculated in Ref. [154] and amount to $1-2\%$ for a Higgs-boson mass of $M_H \lesssim 150$ GeV. These effects are taken into account in the total-cross-section predictions below.

– Electroweak corrections, in contrast to QCD corrections, are quite different from the ones to Drell–Yan processes already at NLO and, in particular, distinguish between the various leptonic decay modes of the $W^\pm$ and Z bosons. The NLO corrections to total cross sections already revealed EW effects of the size of $-7\%(-5\%)$ for WH (ZH) production [155], almost independent from the collider energy for $M_H = 126$ GeV. The NLO EW corrections to differential cross sections [107], which were calculated with the HAWK Monte Carlo program [104–106] for the full processes pp → WH → ν_llH and pp → ZH → l^-l^+H/$\nu_l\bar{\nu}_l$H, i.e. including the W/Z decays, get even more pronounced in comparison to the ones for the total cross sections. Requiring a minimal transverse momentum of the Higgs boson of 200 GeV in the so-called "boosted-Higgs regime" leads to EW corrections of about $-(10-15)\%$ with a trend of further increasing in size at larger transverse momenta.

---

[18]S. Dittmaier, G. Ferrera, A. Rizzi, G. Piacquadio (eds.); A. Denner, M. Grazzini, R.V. Harlander, S. Kallweit, A. Mück, F. Tramontano and T.J.E. Zirke.

[19]The fact that this 100% correction exceeds the above-mentioned scale uncertainty of $\sim 60\%$ is similar to the related well-known situation observed for gg → H, where the LO scale uncertainty underestimates the size of missing higher-order corrections as well.

The EW corrections depend only very weakly on the hadronic environment, i.e. on the PDF choice and factorization scale, which suggests to include them in the form of relative corrections factors to QCD-based predictions as detailed below.

The following numerical results are based on the same input parameters as used for the total and differential cross sections in Refs. [13] and [14], respectively, if not stated otherwise. The same applies to the theoretical setup of the calculations, such as the EW input parameter scheme, scale choices, etc.

5.2 Predictions for total cross sections

The following numerical results for the total cross sections are obtained with the program VH@NNLO [156], which includes the full QCD corrections up to NNLO, the NLO corrections to the gg channel, and the NLO EW corrections (with the latter taken from Ref. [155] in parametrized form). In detail the QCD and EW corrections are combined as follows,

$$\sigma_{\text{VH}} = \sigma_{\text{VH}}^{\text{NNLO QCD(DY)}} \times (1 + \delta_{\text{VH,EW}}) + \sigma_{\text{VH}}^{\text{NNLO QCD(NON-DY)}}, \tag{42}$$

i.e. the EW corrections are incorporated as relative correction factor to the NNLO QCD cross section based on Drell–Yan-like corrections, $\sigma_{\text{VH}}^{\text{NNLO QCD(DY)}}$. Electroweak corrections induced by initial-state photons, which are at the level of 1% (see below), are not included here.

Tables B.29–B.34 and B.35–B.40 display numerical values for the WH production cross section as evaluated according to (42). Note that the cross sections for W^+H and W^-H production are added here. The scale uncertainty is obtained by varying the renormalization and the factorization scale independently within the interval $[Q/3, 3Q]$, where $Q \equiv \sqrt{Q^2}$ is the invariant mass of the VH system. The PDF uncertainties are calculated by following the PDF4LHC recipe, using MSTW2008 [100], CT10 [145], and NNPDF2.3 [68]; the total uncertainties are just the linear sum of the PDF and the scale uncertainties.

Similarly, Tables B.41–B.46 and B.47–B.52 show up-to-date results for ZH production. The gluon-fusion channel $\sigma_{\text{gg}\to\text{ZH}}$ is listed separately in the last column. It is obtained by calculating the radiative correction factor of this channel through order α_s^3 in the heavy-top limit, and multiplying it with the exact LO result, as described in Ref. [153]. The scale uncertainty of $\sigma_{\text{gg}\to\text{ZH}}$ is obtained by varying the renormalization and the factorization scales of the NLO term simultaneously by a factor of three around $\sqrt{Q^2}$. The PDF uncertainty of $\sigma_{\text{gg}\to\text{ZH}}$ is evaluated only at LO, and its total uncertainty is simply the sum of the scale and the PDF uncertainty. The uncertainties arising from all terms except for gluon fusion are obtained in analogy to the WH process, see above. The sum of all scale and PDF uncertainties are listed in columns "Scale" and "PDF". Adding them linearly results in column "Total". The second columns in Tables B.41–B.46 and B.47–B.52 contain the cross section including all available radiative corrections.

Note that the uncertainties are symmetrized around the central values which in turn are obtained with the MSTW2008 PDF set and by setting the central renormalization and the factorization scales equal to Q, the invariant mass of the VH system.

5.3 Predictions for differential cross sections

We first briefly recall the salient features in the definition of the cross sections with leptonic W/Z decays. A detailed description can be found in Section 7.2 of Ref. [14]. All results are given for a specific leptonic decay mode without summation over lepton generations. For charged leptons l in the final state we distinguish two different treatments of photons that are collinear to those leptons. While the "bare" setup assumes perfect isolation of photons and leptons, which is reasonable only for muons, in the "rec" setup we mimic electromagnetic showers in the detector upon recombining photons and leptons to "quasi-leptons" for $R_{l\gamma} < 0.1$, where $R_{l\gamma}$ is the usual distance in the plane spanned by rapidity and the

azimuthal angle in the transverse plane. After the eventual recombination procedure the following cuts are applied if not stated otherwise,

$$p_{T,l} > 20 \text{ GeV}, \qquad |y_l| < 2.5, \qquad p_{T,\text{miss}} > 25 \text{ GeV}, \qquad (43)$$

$$p_{T,H} > 200 \text{ GeV}, \qquad p_{T,W/Z} > 190 \text{ GeV}, \qquad (44)$$

where p_T is the transverse momentum of the respective particle and $p_{T,\text{miss}}$ the total transverse momentum of the involved neutrinos.

Similar to the procedure for the total cross section, QCD-based predictions are dressed with relative EW correction factors,

$$\sigma = \sigma^{\text{NNLO QCD(DY)}} \times \left(1 + \delta_{\text{EW}}^{\text{bare/rec}}\right) + \sigma_\gamma, \qquad (45)$$

where $\sigma^{\text{NNLO QCD(DY)}}$ is the NNLO QCD cross-section prediction of Refs. [151, 152] and $\delta_{\text{EW}}^{\text{bare/rec}}$ the EW correction factor obtained with HAWK [104–107]. Note that the relative EW correction is not included on an event-by-event basis during the phase-space integration, but used as reweighting factor in the histograms bin by bin. The contribution σ_γ, which is induced by processes with photons in the initial state, also delivered by HAWK, is found to be at the level of 1% (see Refs. [14, 107]). All cross-section predictions of this section are based on the MSTW2008 NNLO PDF set [100], but the EW correction factor hardly depends on the PDF choice. We recall that the non-Drell–Yan-like corrections, which are included in the predictions for total cross sections (see previous section), are not (yet) available for differential quantities.

Figure 38 shows the distributions for the various VH production channels at the LHC with a CM energy of 8 TeV for a Higgs-boson mass of $M_H = 126$ GeV in the boosted-Higgs scenario, where the cuts (44) on the Higgs and W/Z transverse momenta are applied. The only differences to the results shown in Fig. 56 of Ref. [14] concerns the new value of M_H and the transition from NLO QCD to NNLO QCD for ZH production. Qualitatively the results look very similar, so that the discussion presented in Ref. [14] still holds. This applies, in particular, to the respective EW corrections which are depicted in Figure 39 for the "bare" and "rec" treatments of radiated photons. The smallness of the difference between the two variants, which is about $1-3\%$, shows that the bulk of the EW corrections, which are typically $-(10-15)\%$, is of pure weak origin. While the EW corrections to rapidity distributions are flat and resemble the ones to the respective integrated cross sections, the corrections to p_T distributions show the typical tendency to larger negative values with increasing p_T (weak Sudakov logarithms). Finally, for comparison we show the EW corrections in the boosted-Higgs regime, where the transverse momenta of the Higgs and W/Z bosons are $\gtrsim 200$ GeV, to the scenario of Figure 40 where only basic isolation cuts are kept, i.e. the cuts (44) on $p_{T,H}$ and $p_{T,W/Z}$ are dropped. As already noted in Ref. [14], switching from the basic cuts to the boosted-Higgs scenario increases the size of the EW corrections by about 5% in the negative direction.

In spite of the theoretical improvement by the transition from NLO QCD to NNLO QCD in the ZH channel, the estimate of the relative uncertainties shown in Table 19 of Ref. [14] remains valid, because in the predictions for the differential cross sections the contribution of the $gg \to ZH$ channel are not (yet) included. The change from $M_H = 120$ GeV to $M_H = 126$ GeV leaves the error estimate untouched as well.
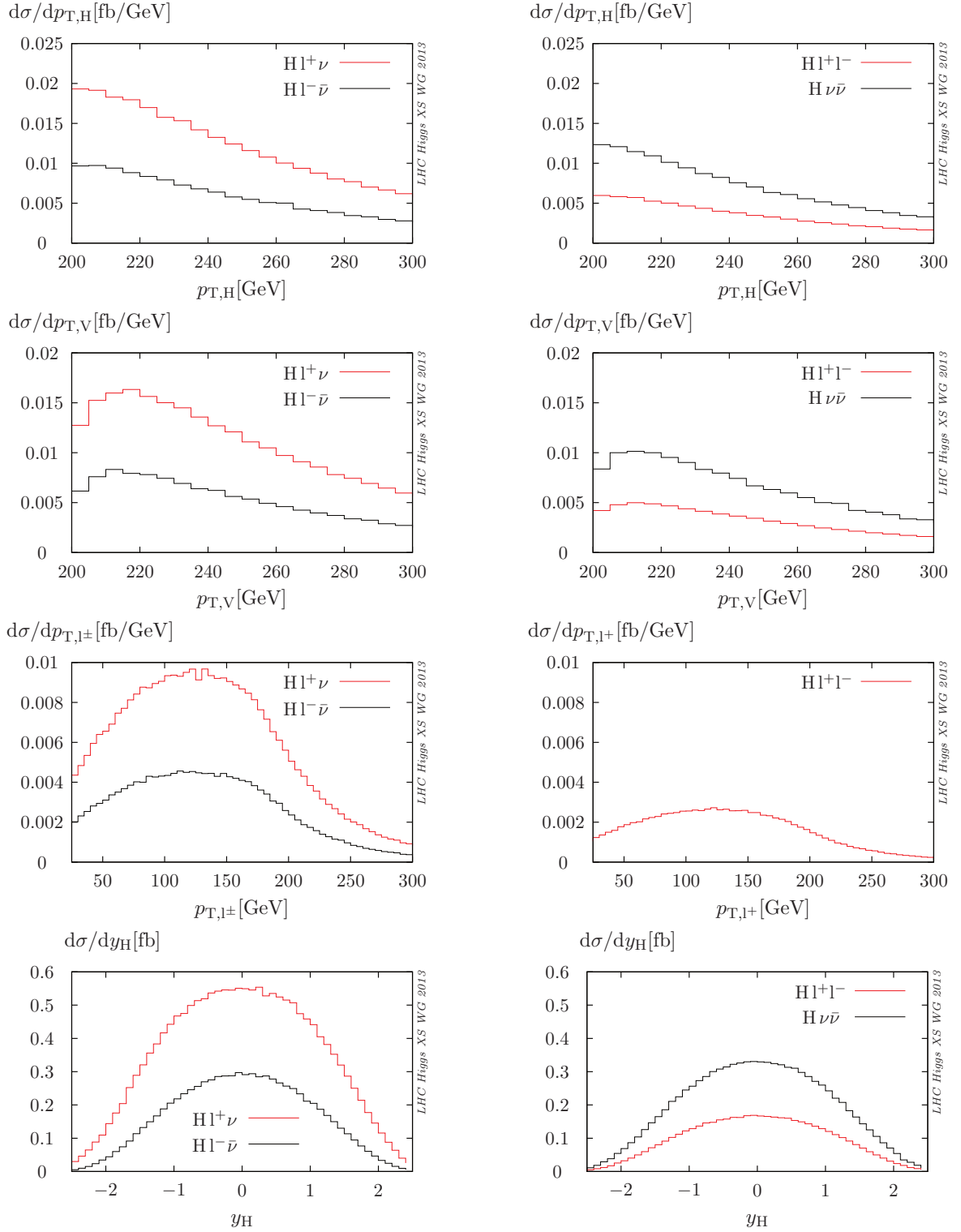
Fig. 38: Predictions for the $p_{\mathrm{T,H}}$, $p_{\mathrm{T,V}}$, $p_{\mathrm{T,l}}$, and y_{H} distributions (top to bottom) for Higgs strahlung off W bosons (left) and Z bosons (right) for boosted Higgs bosons at the 8 TeV LHC for $M_{\mathrm{H}} = 126$ GeV.
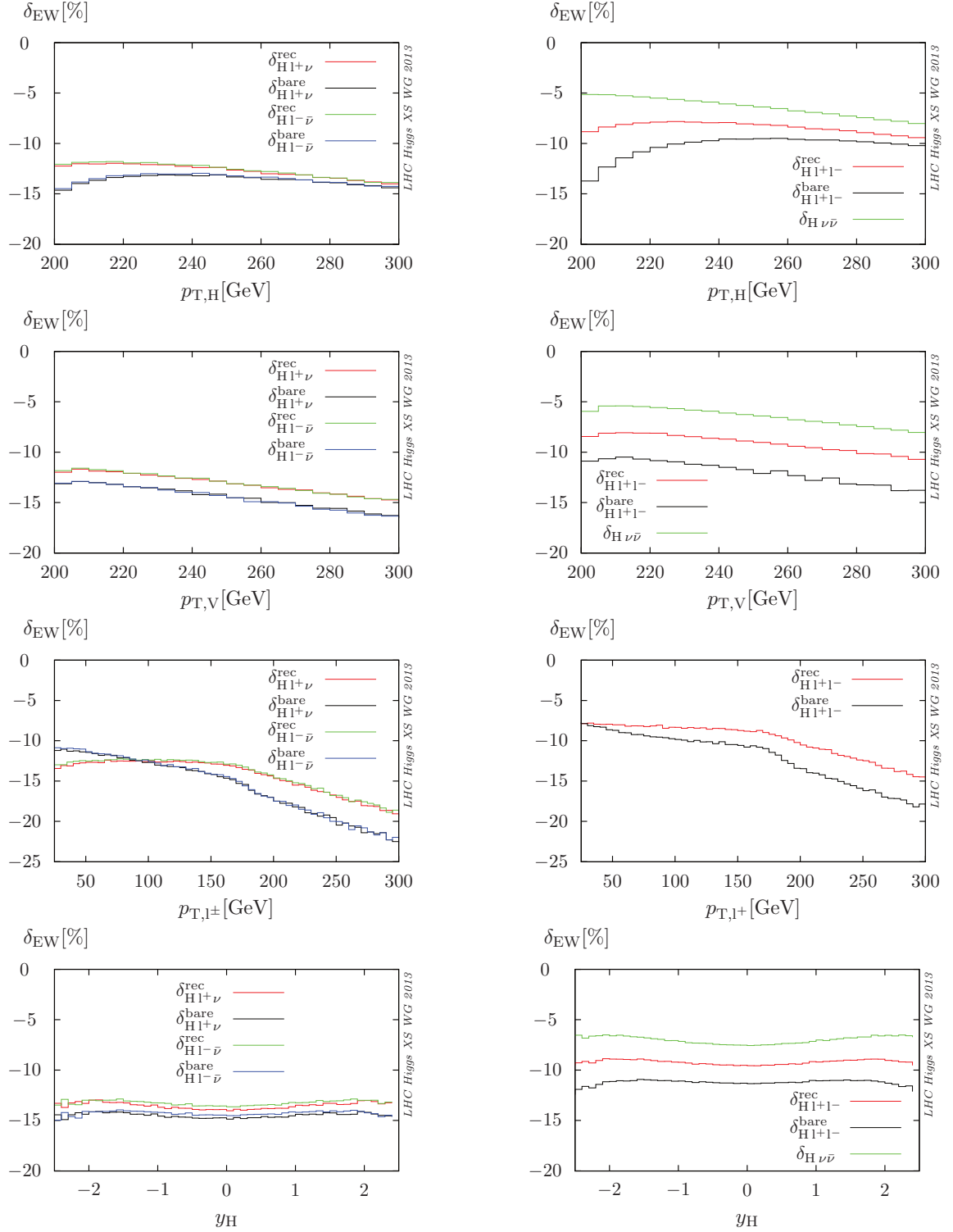
Fig. 39: Relative EW corrections for the $p_{T,H}$, $p_{T,V}$, $p_{T,l}$, and y_H distributions (top to bottom) for Higgs strahlung off W bosons (left) and Z bosons (right) for boosted Higgs bosons at the 8 TeV LHC for $M_H = 126$ GeV.
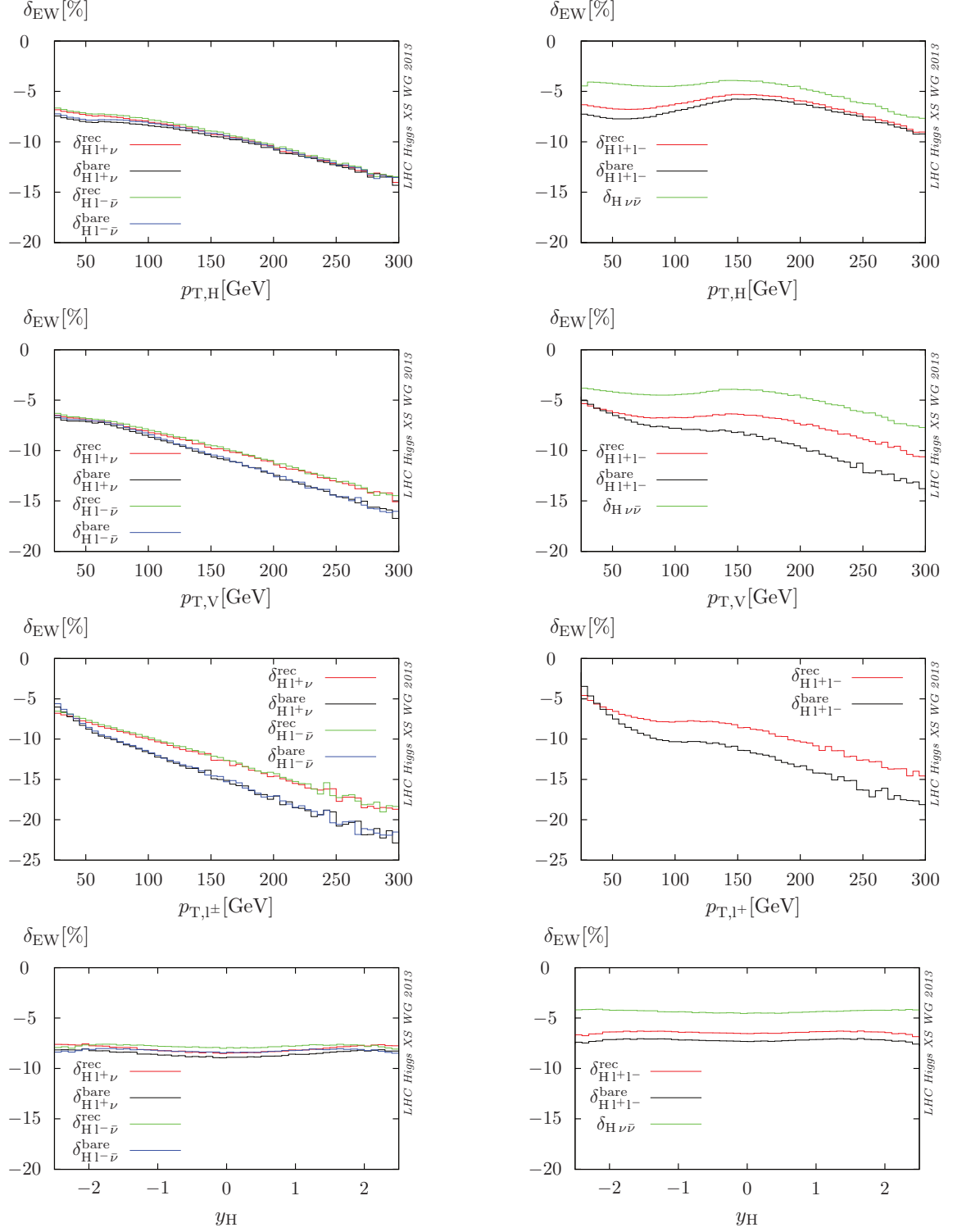
Fig. 40: Relative EW corrections for the $p_{\mathrm{T,H}}$, $p_{\mathrm{T,V}}$, $p_{\mathrm{T,l}}$, and y_{H} distributions (top to bottom) for Higgs strahlung off W bosons (left) and Z bosons (right) for the basic cuts at the 8 TeV LHC for $M_{\mathrm{H}} = 126$ GeV.

6 $t\bar{t}H$ process [20]

The experimental discovery of a Higgs boson with mass around $125 - 126$ GeV casts new light on the role played by the associated production of a Higgs boson with a pair of top quarks, i.e. $q\bar{q}/gg \to Ht\bar{t}$. Detailed studies of the properties of the discovered Higgs boson will be used to confirm or exclude the Higgs mechanism of electroweak symmetry breaking as minimally implemented in the SM. In this context, the measurement of the $t\bar{t}H$ production rate can provide direct information on the top-Higgs Yukawa coupling, probably the most crucial coupling to fermions.

Using the NLO codes developed Refs. [157–160], in a previous report [13] we studied the inclusive $t\bar{t}H$ production at both $\sqrt{s} = 7$ and 14 TeV and we provided a breakdown of the estimated theoretical error from renormalization- and factorization-scale dependence, from α_s, and from the choice of Parton Distribution Functions (PDFs). The total theoretical errors were also estimated combining the uncertainties from scale dependence, α_s dependence, and PDF dependence according to the recommendation of the LHC Higgs Cross Section Working Group [13]. For low Higgs-boson masses, the theoretical errors typically amount to $10 - 15\%$ of the corresponding cross sections. In Sect. 6.1 we will repeat the same exercise for $\sqrt{s} = 8$ TeV using finer Higgs-mass steps, in particular around $125 - 126$ GeV and adding some steps above 300 GeV.

In the context of this workshop, we continued the study of the $t\bar{t}H$ signal and provided in a second report [14] a thorough study of the interface of the NLO QCD calculation of $t\bar{t}H$ with parton shower Monte Carlo programs (PYTHIA and HERWIG). We compared results obtained using the MC@NLO method via AMC@NLO [136] and results obtained using the POWHEG method via POWHEL [161]. The two implementations were found to be in very good agreement and should be considered as the state-of-the-art tools to obtain theoretical predictions and theoretical uncertainties on total and differential cross sections for $t\bar{t}H$ production that also include experimental cuts and vetos on the final-state particles and their decay products.

In this report we expand on the studies presented in [14] by presenting in Section 6.2 a new study of parton-shower uncertainty obtained by interfacing the NLO calculation of Ref. [159, 160] with the SHERPA Monte-Carlo program [162], and in Section 6.3 a novel implementation of the decay of heavy resonances in NLO Monte-Carlo events as implemented in AMC@NLO via the MADSPIN [163] framework.

Finally, we focus on one of the main backgrounds for $t\bar{t}H$ production, namely $t\bar{t}b\bar{b}$ production and we present two dedicated studies. In Section 6.4 we present new parton-level NLO predictions for $t\bar{t}b\bar{b}$ production at 8 TeV, obtained within OPENLOOPS [164] and SHERPA [162, 165, 166]. On the other hand, in Section 6.5 the NLO calculation of $t\bar{t}b\bar{b}$ is for the first time consistently interfaced with the PYTHIA parton-shower Monte Carlo using the POWHEL framework [167] and compared with the $t\bar{t}H$ signal at 14 TeV.

6.1   Theoretical uncertainty on the parton level $t\bar{t}H$ total cross section at 7 and 8 TeV

In this section we provide results for the inclusive NLO signal cross section at $\sqrt{s} = 7$ and 8 TeV for different values of Higgs masses. The mass steps have been chosen following the recommendation of the Higgs Cross Section Working Group, up to $M_H = 400$ GeV. For consistency, we have kept the same setup used in Ref. [13] where analogous results for $\sqrt{s} = 7$ and 14 TeV were presented. In summary, we used the on-shell top-quark mass fixed at $m_t = 172.5$ GeV and did not include the parametric uncertainties due to the experimental error on the top-quark mass. Loop diagrams with a bottom-quark loop were calculated using the b-quark pole mass. The top-quark Yukawa coupling was set to $y_t = m_t(\sqrt{2}G_F)^{1/2}$. The central scale has been chosen as $\mu_R = \mu_F = \mu_0 = m_t + M_H/2$.

We have used the MSTW2008 [100, 168], CTEQ6.6 [169] and NNPDF2.0 [170] sets of parton density functions. The central values of the strong coupling constant have been implemented according to the corresponding PDFs for the sake of consistency.

The uncertainties due to scale variations of a factor of two around the central scale μ_0 as well as the 68% CL uncertainties due to the PDFs and the strong coupling α_s have been calculated and are given explicitly in Table B.53 to Table B.58 for $\sqrt{s} = 7$ TeV and in Table B.59 to Table B.64 for $\sqrt{s} = 8$ TeV. We exhibit the central values and the PDF+α_s uncertainties according to the envelope method of the PDF4LHC recommendation and the relative scale variations using MSTW2008 PDFs.

6.2 Theory uncertainties in the simulation of $t\bar{t}H$

In this section we discuss the estimate of the theoretical uncertainties on $t\bar{t}H$ production at the 8 TeV LHC, using the example of a few key distributions. We consider the case in which the top quarks decay semi-leptonically and the Higgs boson decays into a $b\bar{b}$ pair. For the simulation of the process at the hadron level we use the SHERPA event generator [162], and NLO matrix elements from [159, 160], which we also cross-checked with those from OPENLOOPS [164]. The latter uses loop integrals provided by the COLLIER library which implements the numerically stable reduction methods of Refs. [171, 172] and the scalar integrals of Ref. [173]. They are connected with the SHERPA parton shower [174], based on Catani-Seymour splitting kernels [175, 176], through an MC@NLO-type matching [128] in the fully color-correct version of [177]. Spin correlations have been included in the full chain of production and decays, where the former is treated at NLO accuracy and the latter is treated at LO accuracy. In addition, we employ the following conventions and settings for the simulation.

- We use $m_t = 172$ GeV, $m_H = 125$ GeV, and $m_W = 80.4$ GeV. The b quark is treated as massive with an on-shell mass of $m_b = 4.79$ GeV. The 4-flavor MSTW2008 set of PDF [100] is being used.

- We use a dynamical renormalization and factorization scale of

$$\mu_R = \mu_F = \frac{m_{T,t} + m_{T,\bar{t}} + m_H}{2}, \qquad (46)$$

which also fixes the parton-shower starting scale μ_Q.

- In order to estimate the theoretical uncertainty we vary μ_R and μ_F in parallel by a factor of 2 up and down. A full estimate of the theoretical uncertainty from parton showering should also consider the independent variation of μ_Q, but we do not include it in the present study.

- PDF uncertainties and those related to other perturbative parameters such as $\alpha_s(M_Z)$ or particle masses are ignored.

- Similarly, uncertainties related to hadronization and the underlying events are not taken into account.

For the simulation, cuts similar to the ones typically used in ongoing analyses have been implemented in a RIVET [178] analysis, namely:

- one isolated lepton with $p_T \geq 25$ GeV and $|\eta| \leq 2.5$. The isolation criterion requires the summed p_T of tracks within $\Delta R = 0.3$ not to exceed 0.1 of the lepton p_T. In addition, all further visible particles within $\Delta R = 0.2$ of the lepton deposit less transverse momentum than 0.1 of the lepton p_T.

- For events with electrons, $\not{E}_T \geq 35$ GeV, while for event with muons, $\not{E}_T \geq 20$ GeV.

- Anti-k_T jets with $R = 0.4$ are reconstructed using FastJet [179] with a minimum p_T of 20 GeV in $|\eta| \leq 2.5$.

- Jets containing at least one b-hadron are considered b-jets.
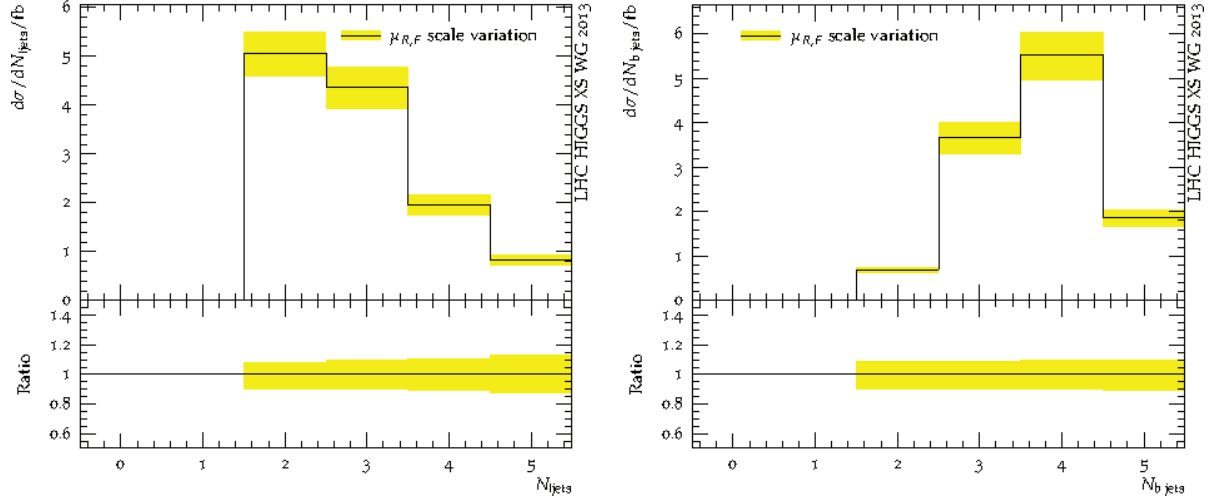
Fig. 41: The number of light (left panel) and b jets (right panel) in the acceptance region for $t\bar{t}H$ events at the 8 TeV LHC. Uncertainties due to renormalization and factorization scale variations (yellow band) as given in an MC@NLO simulation are also indicated.

Typically at least two light and two b jets are required in addition to an isolated lepton and missing transverse momentum in order to reconstruct the $t\bar{t}$ system, plus further jets related to the Higgs boson. The tops are reconstructed by first finding the hadronic W from the light jets, and combining it with the b-tagged jet giving the best mass for the resulting top quark. Then the leptonic W is reconstructed from the lepton and the missing transverse momentum, the degeneracy is resolved through combination with the remaining b jets and picking the best mass of the resulting top quark. It is only then that the Higgs-boson candidate is reconstructed from the remaining jets. The distribution of light and b jets and their uncertainties are displayed in Fig. 41. In all further plots shown here we will concentrate on events with 4 b jets and at least two light jets. In Fig. 42 we display inclusive observables such as H_T, the scalar sum of the transverse momenta of all hard objects – isolated lepton, $\slashed{E}_T$, and jets – and the transverse momentum of the overall $t\bar{t}H$ system as reconstructed from its decay products. In Fig. 43 we focus on the $t\bar{t}$ system and depict the distance of the two reconstructed top quarks in rapidity, azimuthal angle, and in R (distance in the rapidity-azimuthal angle plane). Finally, in Fig. 44 we show observables related to the two b jets not associated with top-quark decays, namely the invariant mass of the pair of jets and their joint transverse momentum. The emerging picture of the uncertainties is consistent:

– the traditional scale variation of a factor of 2 applied in parallel to both renormalization and factorization scale to the NLO matrix element impact distributions at the level of $10\% - 20\%$. It is interesting to note that also observables like the transverse momentum of the produced (and reconstructed) $t\bar{t}H$ system or the number of light jets, which are sensitive to further QCD radiation, are fairly stable under these variations, which may indicate that a parallel shift in the scales could underestimate the actual scale uncertainty.

– The picture will certainly change somewhat when considering variations in the parton shower starting scale, which also defines the hard regime of radiation where no K factor is applied to the configurations. In addition, uncertainties due to the underlying event will impact the tagging of b jets and, through varying QCD activity have an effect on, for instance, the overall acceptance.
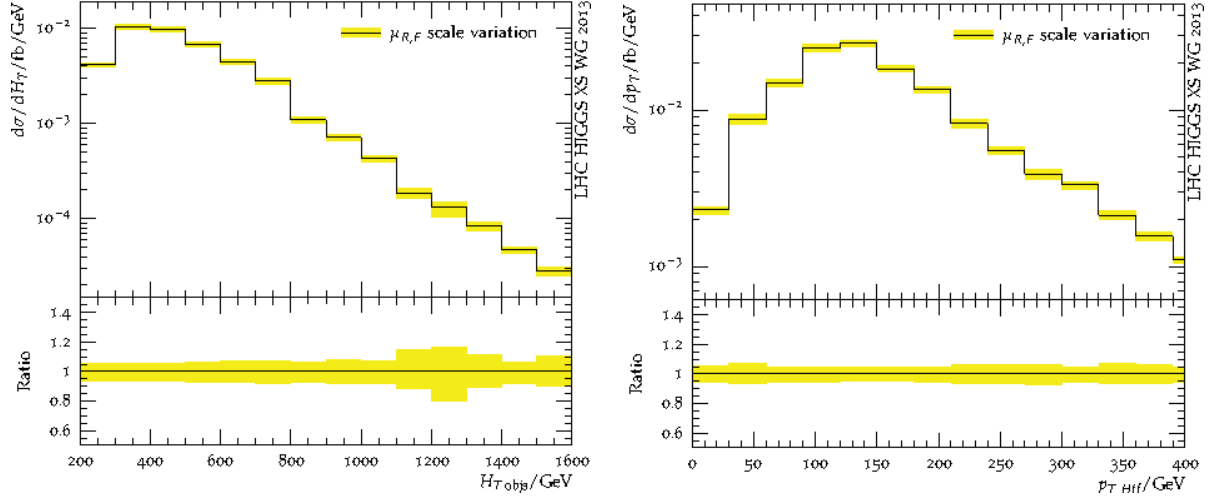
Fig. 42: H_T(left panel) and $p_T^{t\bar{t}H}$ (right panel) distribution in the acceptance region for $t\bar{t}H$ events at the 8 TeV LHC. Uncertainties due to renormalization and factorization scale variations (yellow band) as given in an MC@NLO simulation are also indicated.
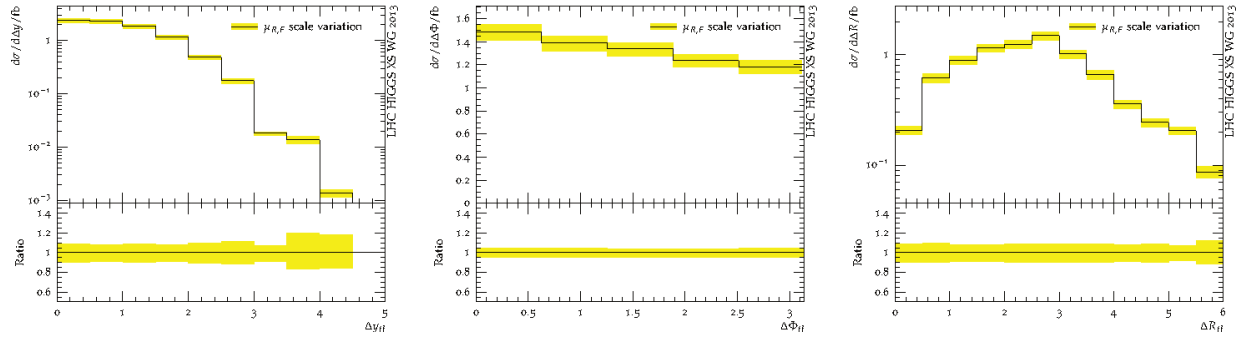
Fig. 43: Distance of the two reconstructed top quarks in rapidity (left panel), azimuthal angle (central panel), and R (right panel) for $t\bar{t}H$ events at the 8 TeV LHC. Uncertainties due to renormalization and factorization scale variations (yellow band) as given in an MC@NLO simulation are also indicated.

6.3 Spin correlation effects in $t\bar{t}H$ using MADSPIN

Monte Carlo generators have now entered the era of fully automated NLO event generators [80,136,177], which open several perspectives in hadron collider phenomenology by allowing the simulation of a new class of processes at next-to-leading-order accuracy. Even though these automated NLO Monte Carlo generators feature, in principle, no restrictions on complexity of the process and particle multiplicity, in practice the CPU cost becomes enormous for high-multiplicity final states. Most of the current tools cannot simulate the full production and decay at NLO accuracy in a reasonable amount of time; only the generation of undecayed events at next-to-leading order is feasible.

In this context a generic framework dubbed MADSPIN [163] has recently been proposed to decay heavy resonances in next-to-leading-order Monte Carlo events. The method includes not only *decay* spin correlation effects (which induce angular correlations among the final-state particles inside a given decay branch) but also *production* spin correlation effects (which induce angular correlations among the particles from distinct decay branches) by unweighting decay configurations with tree-level matrix elements associated with the decayed process. Generating the decay of a specific event typically requires
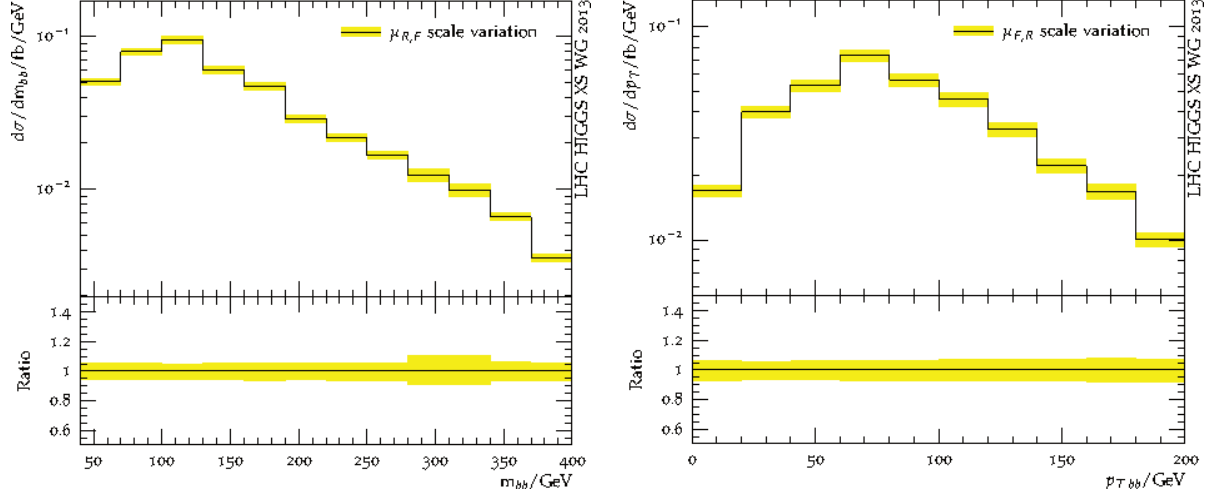
Fig. 44: Invariant mass (left panel) and transverse momentum (right panel) distribution of the pair of b jets not associated with top decays in the acceptance region for $t\bar{t}H$ events at the 8 TeV LHC. Uncertainties due to renormalization and factorization scale variations (yellow band) as given in an MC@NLO simulation are also indicated.

only a few evaluations of matrix elements, so that the algorithm is in general very fast. Although only tree-level matrix elements are used to unweight the decay configurations, for specific processes this procedure was shown to capture essentially all spin correlation effects as predicted by a full next-to-leading-order calculation.

The approach in MADSPIN is based on the narrow-width approximation, as the production of events is factorized from the decay. However, off-shell effects are partly recovered by smearing the mass of each resonance in undecayed events according to a Breit-Wigner distribution, and by applying the unweighting procedure also with respect to the generated virtualities of the resonances. The other momenta in undecayed events are reshuffled in an optimal way with the use of diagram-based information of the tree-level scattering amplitude associated with the undecayed events.

In order to illustrate the capabilities of the tool, we apply it to the case of top-quark pair production in association with a light Higgs boson at the LHC (running at 8 TeV), considering both the scalar and pseudo-scalar hypotheses for the Higgs boson. Due to the large irreducible QCD background, any search strategy for this Higgs production process relies strongly on the accuracy of the Monte-Carlo predictions. QCD correction to these processes has been analysed by two groups [136,161] and a comparison between these independent calculations has appeared in Ref. [14]. In these works it was shown that the NLO corrections are very mild, in particular on shapes of distributions.

To the best of our knowledge, the problem of retaining spin-correlation effects in events generated at NLO accuracy has not been addressed yet for these processes. This problem is trivially solved using the scheme proposed in this section: NLO parton-level events are generated with AMC@NLO, (LHC at 8 TeV, PDF set = MSTW2008(n)lo68cl [100], $M_H = M_A = 125$ GeV, $\mu_R = \mu_F = (m_T(H/A)m_T(t)m_T(\bar{t}))^{(1/3)}$, no cuts) and then decayed with MADSPIN before they are passed to HERWIG for showering and hadronization. In this illustration, top and anti-top quarks are decayed semi-leptonically, whereas the Higgs is decayed into a pair of b quarks.

Figure 45 shows the normalized distribution of events with respect to $\cos(\phi)$ (where ϕ is the angle between the direction of flight of l^+ in the t rest frame and l^- in the $\bar{t}$ rest frame), and with respect to the transverse momentum of the hardest positively-charged lepton. Although spin-correlation effects significantly distort the distribution of events with respect to $\cos(\phi)$, their impact on the p_T spectrum of the leptons is milder, except at large transverse momentum. The relatively larger effect in the tail of this
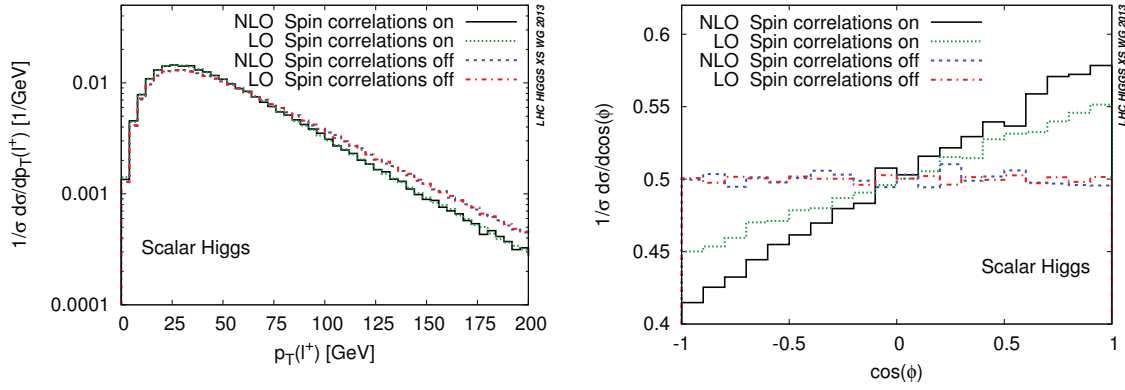
Fig. 45: Next-to-leading-order cross sections differential in $p_T(l^+)$ (left panel) and in and $\cos\phi$ (right panel) for $t\bar{t}H$ events with or without spin correlation effects. For comparison, also the leading-order results without spin-correlation effects are shown. Events were generated with AMC@NLO, then decayed with MADSPIN, and finally passed to HERWIG for parton showering and hadronization.

distribution can easily be understood from the fact that the inclusion of the spin correlations is a unitary procedure: a small change at low p_T, where the cross section is large, needs to be compensated by a larger (relative) effect at high p_T.

It is interesting that spin correlations have a much more dramatic influence on the shape of these distributions than NLO corrections: the leading order results fall directly on top of the NLO results for these normalized distributions (both without spin correlations), as can be seen by comparing the dotted blue and dash-dotted red curves. We can therefore conclude that preserving spin correlations is more important than including NLO corrections for these observables. Naturally, the inclusion of both, as is done here, is preferred: it retains the good features of a NLO calculation, i.e., reduced uncertainties due to scale dependence (not shown), while keeping the correlations between the top-quark decay products.
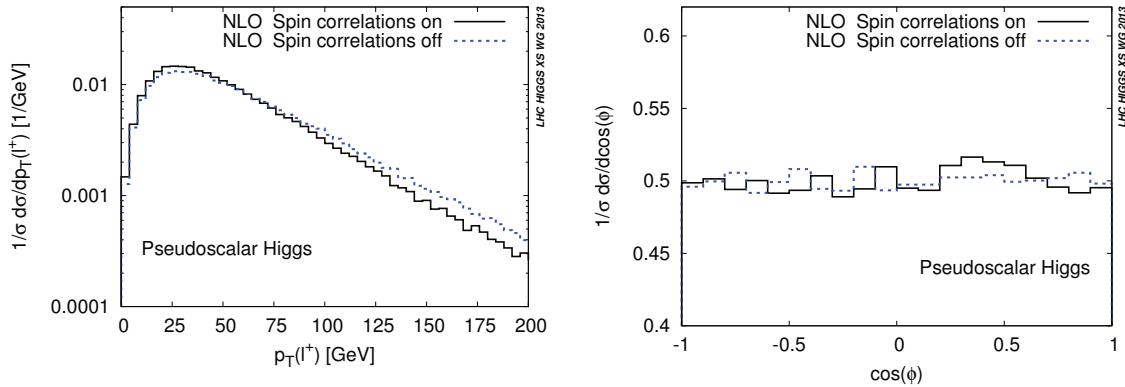
Fig. 46: Next-to-leading-order cross sections differential in $p_T(l^+)$ (left panel) and in and $\cos(\phi)$ (right panel) for $t\bar{t}A$ events with or without spin-correlation effects. Events were generated with AMC@NLO, then decayed with MADSPIN, and finally passed to HERWIG for parton showering and hadronization.

The results for the pseudoscalar Higgs boson are shown in Figure 46. The effects of the spin correlations on the transverse momentum of the charged lepton are similar as in the case of a scalar Higgs boson: about 10% at small p_T, increasing to about 40% at $p_T = 200$ GeV. On the other hand, the $\cos(\phi)$ does not show any significant effect from the spin-correlations. Therefore this observable could possibly help in determining the CP nature of the Higgs boson, underlining the importance of the

inclusion of the spin correlation effects.

6.4 NLO parton-level predictions for $t\bar{t}b\bar{b}$ production at 8 TeV

The experimental observation of $t\bar{t}H(b\bar{b})$ production is notoriously very challenging due to large QCD backgrounds and the non-trivial signature, involving at least four b-jets. The selection of $H \rightarrow b\bar{b}$ candidates is contaminated by more than 70% combinatorial background, where one of the selected b-jets is a top-quark decay product or a misidentified light jet. As a consequence, the Higgs-boson mass peak is strongly diluted and contaminated by QCD backgrounds. The dominant background contributions are given by $t\bar{t}b\bar{b}$ and $t\bar{t}jj$ production. The reducible $t\bar{t}jj$ component constitutes more than 95% of the background cross section and can be estimated using a data-driven approach. Moreover, $t\bar{t}jj$ can be strongly suppressed by means of b-tagging. In contrast, the lack of sufficiently distinctive kinematic features and the much smaller cross section do not permit to determine the normalization of the irreducible $t\bar{t}b\bar{b}$ background in a signal-free control region. Thus theory predictions play a key role in the modeling of $t\bar{t}b\bar{b}$ production.

The $t\bar{t}H(b\bar{b})$ searches by ATLAS [180] and CMS [181, 182] are based on a simultaneous fit of signal and backgrounds in $t\bar{t}$+jets sub-samples with different light-jet and b-jet multiplicities. The $t\bar{t}b\bar{b}$ background enters only the sub-samples with high $t\bar{t}H$ sensitivity, where it can not be separated from the signal, and experimental data are fitted using LO $t\bar{t}b\bar{b}$ predictions assuming an *ad hoc* theory error of 50% [180, 182]. This uncertainty, which lies between the typical scale dependence of LO and NLO $t\bar{t}b\bar{b}$ predictions, constitutes the dominant systematic error of $t\bar{t}H(b\bar{b})$ searches. The use of state-of-the art theory predictions and error estimates for $t\bar{t}b\bar{b}$ (and $t\bar{t}jj$) production is thus a key prerequisite to improve the sensitivity to $t\bar{t}H(b\bar{b})$.

Parton-level NLO studies of $t\bar{t}b\bar{b}$ [183–186] and $t\bar{t}jj$ [187,188] production at 14 TeV indicate that NLO corrections reduce scale uncertainties in a drastic way. In the case of $t\bar{t}b\bar{b}$ production at 14 TeV, the scale dependence goes down from roughly 80% at LO to 20-30% at NLO, depending on the central-scale choice. In order to further increase the accuracy of theory predictions and render them applicable to the experimental analyses, various major improvements are needed. Apart from updating existing calculations to 7 and 8 TeV, it will be crucial to include top-quark decays, match NLO predictions to parton showers, and merge $t\bar{t}$+jets final states with different jet multiplicities at NLO. Also finite b-quark mass effects and the relevance of b-quark induced contributions at NLO should be considered.

Thanks to recent developments in NLO automation, these goals are now within reach. To illustrate progress in this direction, in the following new NLO predictions for $pp \rightarrow t\bar{t}b\bar{b}$ at 8 TeV, obtained with OPENLOOPS [164] and SHERPA [162, 165, 166], are presented. The OPENLOOPS program is a fully automated generator of one-loop QCD corrections to SM processes. Loop amplitudes are evaluated with a numerical recursion that guarantees high CPU efficiency for many-particle processes. Tensor integrals are computed with the COLLIER library, which implements the numerically stable reduction methods of Refs. [171, 172] and the scalar integrals of Ref. [173]. OPENLOOPS and SHERPA are interfaced in a fully automated way, which allows to steer NLO simulations via standard SHERPA run cards. Matching to parton shower within the MC@NLO framework [128, 177] and multi-jet merging at NLO [189] are also fully supported within SHERPA.2.0.

6.4.1 Input parameters and selection cuts

Parton-level NLO results for $pp \rightarrow t\bar{t}b\bar{b}$ at $\sqrt{s} = 8$ TeV are presented for stable top quarks with mass $m_t = 173.2$ GeV. Top-quark decays will be addressed in a forthcoming study. In NLO (LO) QCD the LHAPDF implementation of the MSTW2008NLO (LO) parton distributions [100] and the corresponding running α_s are employed. Contributions from initial-state b quarks are discarded, otherwise the five-flavor scheme with massless b quarks is consistently used. Top-quark loops are included in the virtual corrections but decoupled from the running of α_s via zero-momentum subtraction. All massless QCD

Table 23: Cross sections for $pp \to t\bar{t}b\bar{b}$ at $\sqrt{s} = 8$ TeV with loose (S1) or signal (S2) selection cuts. Predictions with fixed ($\mu_0 = m_t$) and dynamical ($\mu_0 = \mu_{dyn}$) scales are compared. The upper and lower uncertainties correspond to scale variations $\mu/\mu_0 = 0.5$ and 2, respectively. Statistical errors are given in parenthesis. The K factor, $K = \sigma_{NLO}/\sigma_{LO}$, is evaluated at $\mu = \mu_0$. While σ_{LO} is computed with LO α_s and PDFs, $\tilde{\sigma}_{LO}$ is obtained with NLO inputs, and the corresponding K factor is denoted as $\tilde{K} = \sigma_{NLO}/\tilde{\sigma}_{LO}$.

cuts	μ_0	σ_{LO} [fb]	$\tilde{\sigma}_{LO}$ [fb]	σ_{NLO} [fb]	K	$\tilde{K}$
$S1$	m_t	$503(1)^{+84\%}_{-42\%}$	$342(1)^{+74\%}_{-39\%}$	$671(3)^{+33\%}_{-28\%}$	1.34	1.96
$S1$	μ_{dyn}	$861(1)^{+95\%}_{-45\%}$	$556(1)^{+83\%}_{-42\%}$	$900(2)^{+23\%}_{-27\%}$	1.04	1.62
$S2$	m_t	$37.35(2)^{+86\%}_{-43\%}$	$25.33(2)^{+76\%}_{-40\%}$	$45.5(1)^{+29\%}_{-26\%}$	1.22	1.79
$S2$	μ_{dyn}	$54.9(1)^{+94\%}_{-45\%}$	$36.0(1)^{+82\%}_{-42\%}$	$54.3(2)^{+17\%}_{-24\%}$	0.99	1.50

partons (including b quarks) are recombined into IR-safe jets using the anti-k_T algorithm [190] with jet-resolution parameter $R = 0.5$. The jet algorithm is not applied to top quarks.

Similarly as in the ATLAS and CMS $t\bar{t}H(b\bar{b})$ analyses, $t\bar{t}b\bar{b}$ events are selected that contain

(S1) 2 b jets with $p_T, b > 20$ GeV and $|\eta_b| < 2.5$.

In addition to these rather inclusive cuts, to investigate NLO effects in the Higgs-signal region an invariant-mass window around the Higgs resonance is considered,

(S2) $|m_{b\bar{b}} - M_H| < \Delta M$, with $M_H = 126$ GeV and $\Delta M = 15$ GeV.

The width ΔM is taken of the order of the the experimental $m_{b\bar{b}}$ resolution, and $m_{b\bar{b}}$ is identified with the invariant mass of the $b\bar{b}$ Higgs candidate, i.e., of the two b jets that do not arise from top decays. From the experimental viewpoint this selection is unrealistic, since the large combinatorial background resulting from incorrect b-jet assignments is not taken into account. Nevertheless, it is instructive to quantify the background contamination of the signal region in the ideal limit of exact b-jet combinatorics. On the one hand, this permits to assess the potential sensitivity improvement that might be achieved with a strong reduction of the combinatorial background. On the other hand, it is interesting to investigate if NLO corrections feature significance differences in the S1 and S2 regions.

6.4.2 Cross section results at $\sqrt{s} = 8$ TeV

Cross section predictions for $pp \to t\bar{t}b\bar{b}$ at 8 TeV with loose cuts (S1) and in the signal region (S2) are shown in Table 23. Perturbative uncertainties are estimated by uniform factor-two variations of the renormalization and factorization scales, $\mu_R = \mu_F = \xi\mu_0$ with $\xi = 0.5, 1, 2$.[21] For the central scale μ_0 two different options are compared:

(i) a fixed scale choice $\mu_0^2 = m_t^2$;

(ii) the dynamical scale $\mu_0^2 = \mu_{dyn}^2 = m_t \sqrt{p_{T,b} p_{T,\bar{b}}}$, introduced in Ref. [185].

Here $p_{T,b}$ and $p_{T,\bar{b}}$ are the transverse momenta of the two b jets that do not originate from top decays. Absolute LO and NLO cross sections are complemented by respective K factors, $K = \sigma_{NLO}/\sigma_{LO}$,

---

[21]Antipodal rescalings with $\mu_F = \mu_0/\xi$ are not considered, since at 14 TeV it was shown that they induce smaller variations than uniform rescalings [185].
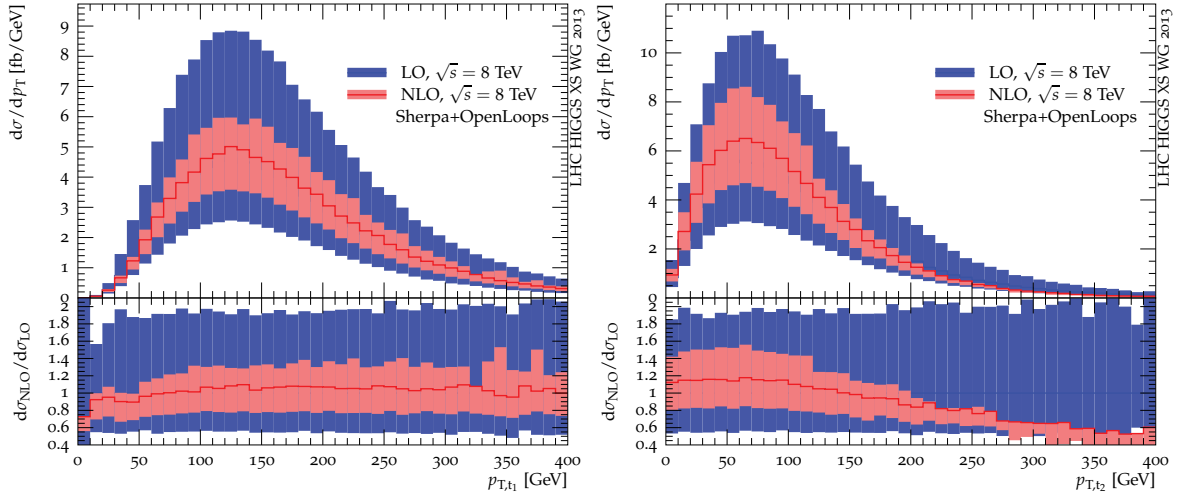
Fig. 47: Distributions in the transverse momenta of the harder (left) and softer (right) top quark in $pp \rightarrow t\bar{t}b\bar{b}$ at $\sqrt{s} = 8$ TeV. Predictions at LO (blue) and NLO (red) are evaluated at the dynamical scale $\mu_0 = \mu_{\mathrm{dyn}}$. The respective bands correspond to variations of the renormalization and factorization scales by a factor of 2 around the central value μ_0. In the lower frame, LO and NLO bands are normalized to LO results at the central scale. The S1 selection is applied.

which might be employed to correct the normalization of LO event samples used in experimental studies. In this respect it is important to keep in mind that K factors can be applied to LO cross sections only if both are computed at the same scale. This is crucial since K factors feature a similarly large scale dependence as LO quantities. Another issue, relevant for the consistent rescaling of LO quantities by K factors, is that LO cross sections can be computed using PDFs and α_{s} either in LO or NLO approximation, depending on the convention. Obviously, combining LO predictions and K factors based on different conventions leads to inconsistent results. To point out the quantitative importance of a consistent combination, in Table 23 we show results corresponding to both conventions: LO cross sections based on NLO inputs and related K factors are denoted as $\tilde{\sigma}_{\mathrm{LO}}$ and $\tilde{K} = \sigma_{\mathrm{NLO}}/\tilde{\sigma}_{\mathrm{LO}}$, while the standard notation is used when LO quantities are computed with LO inputs as usual.

LO results in Table 23 feature a huge scale dependence, which results from the α_{s}^4-scaling of the $t\bar{t}b\bar{b}$ cross section and can reach 95%. The LO cross sections corresponding to different scale choices ($m_{\mathrm{t}}, \mu_{\mathrm{dyn}}$) and conventions ($\sigma_{\mathrm{LO}}, \tilde{\sigma}_{\mathrm{LO}}$) can differ by even more than 100%. These sizable effects are clearly visible also in the differences between the respective K and $\tilde{K}$ factors. An inconsistent combination of K factors and LO predictions, as discussed above, can induce errors of tens of percent.

The impact of NLO corrections turns out to be rather mild as compared to 14 TeV [184–186]. Using $\mu_0 = \mu_{\mathrm{dyn}}$ results in a K factor very close to one and a residual scale dependence of about 25%. This applies to both kinematic regions and is consistent with the good perturbative convergence observed at 14 TeV with dynamical scale choice. As already pointed out in Ref. [185], a hard fixed scale $\mu_0 = m_{\mathrm{t}}$ is less adequate to the multi-scale nature of $t\bar{t}b\bar{b}$ production and results in a slower convergence. In fact corrections and scale uncertainties turn out to be larger with $\mu_0 = m_{\mathrm{t}}$. Results based on the dynamical scale and respective uncertainties can thus be regarded as better predictions. The goodness of this scale choice is also supported by the fairly little K-factor differences in the S1 and S2 regions.

6.4.3 Differential distributions

Various top-quark and b-jet distributions relevant for the $t\bar{t}H$ analyses at 8 TeV are shown in Figures 47–51. Predictions at LO and NLO are based on PDFs and α_{s} at the respective perturbative order, and the
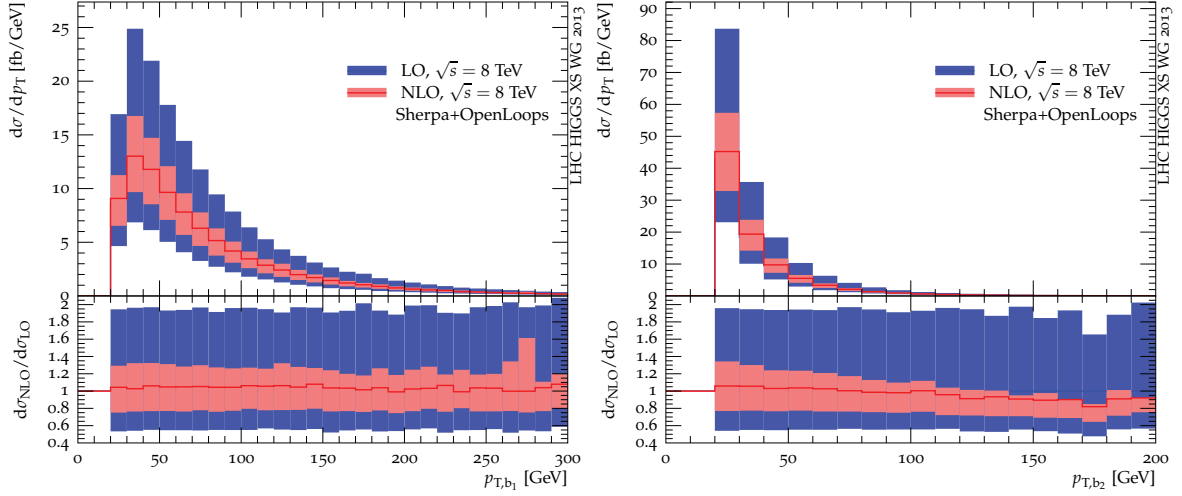
Fig. 48: Distributions in the transverse momenta of the harder (left) and softer (right) b jet in $pp \rightarrow t\bar{t}b\bar{b}$ at $\sqrt{s} = 8$ TeV. Same setup and conventions as in Figure 47.

dynamical scale $\mu_0 = \mu_{dyn}$ is used. The $S1$ selection is applied. Variations of the renormalization and factorization scales by a factor of 2 around the central value μ_0 are displayed as uncertainty bands. In the lower frames, LO and NLO bands are normalized to LO results at the central scale.

In general the size of the corrections as well as the NLO scale dependence turn out to be fairly stable with respect to all considered kinematical variables. The most noticeable exception is given by the top-quark transverse-momentum distributions. In particular, shape distortions in the tail of the p_T distribution of the softer top quark (Figure 47b) reach up to 40%. These corrections might be reduced by using the top-quark transverse mass instead of m_t in μ_{dyn}. Non-negligible 10%-level distortions are visible also in the $p_{T,b\bar{b}}$ and in the $m_{b\bar{b}}$ distributions (Figure 49), while the $\Delta\phi_{b\bar{b}}$ and $\Delta R_{b\bar{b}}$ distributions receive somewhat larger shape corrections, up to $15 - 20\%$ (Figure 51).

In summary, we have presented new NLO results for $t\bar{t}b\bar{b}$ production at 8 TeV, which confirm that the dynamical scale introduced in Ref. [185] guarantees a stable perturbative description of this irreducible background to $t\bar{t}H(b\bar{b})$. The K factor turns out to be surprisingly close to one, both for loose cuts and in the $t\bar{t}H(b\bar{b})$ signal region, while, similarly to what originally seen at $\sqrt{s} = 14$ TeV, NLO corrections reduce the factorization and renormalization scale uncertainty to about 25%. Typical transverse-momentum, invariant-mass, and angular distributions receive moderate but non-negligible shape corrections, which do not exceed $15 - 20\%$ in general. More pronounced kinematic distortions are found only at large top-quark transverse momenta.

6.5 $t\bar{t}H$ vs. $t\bar{t}b\bar{b}$: predictions by POWHEL plus Shower Monte Carlo

The $t\bar{t}b\bar{b}$ and $t\bar{t}jj$ hadroproduction processes represent important backgrounds to $t\bar{t}H$ production at the LHC, when the Higgs particle decays hadronically.

In order to allow for realistic phenomenological studies we have started the effort of studying both signal ($t\bar{t}H$) and background ($t\bar{t}b\bar{b}$ and $t\bar{t}jj$) at the hadron level, interfacing the corresponding NLO QCD calculations with Parton Shower generators in the POWHEL framework. In a previous Working Group report [14], predictions at the hadron level for $t\bar{t}H$ hadroproduction at the NLO QCD + Parton Shower accuracy were presented by considering both a SM scalar Higgs boson and a pseudoscalar one at $\sqrt{s} = 7$ TeV. While predictions at the parton level for $t\bar{t}b\bar{b}$ and $t\bar{t}jj$ production at the NLO QCD accuracy have been presented in the literature [183, 184, 186–188] and in Section 6.4 of this report , yet
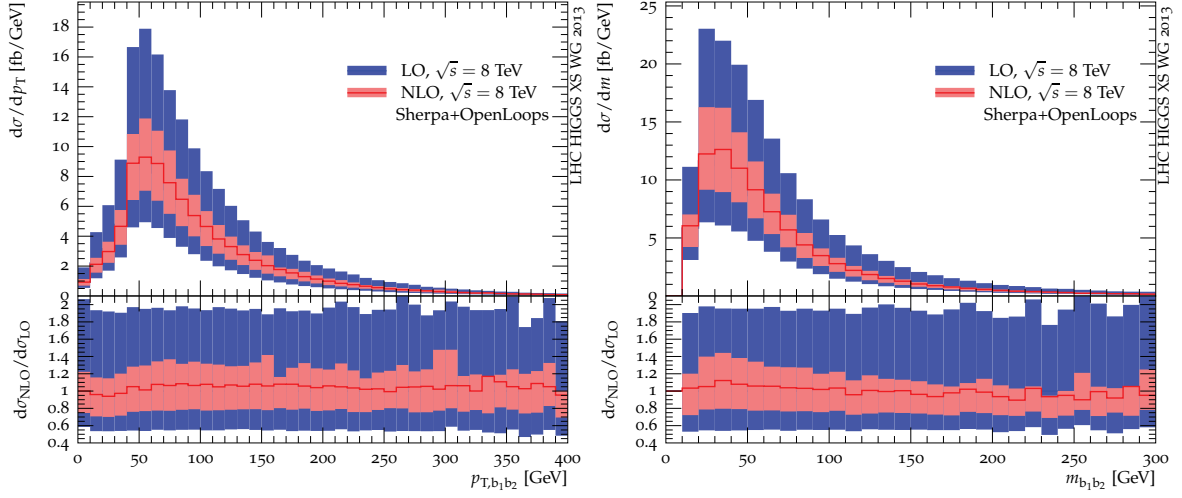
Fig. 49: Distributions in the total transverse momentum (left) and the invariant mass (right) of the b-jet pair in pp → t$\bar{\text{t}}$b$\bar{\text{b}}$ at $\sqrt{s}$ = 8 TeV. Same setup and conventions as in Figure 47.
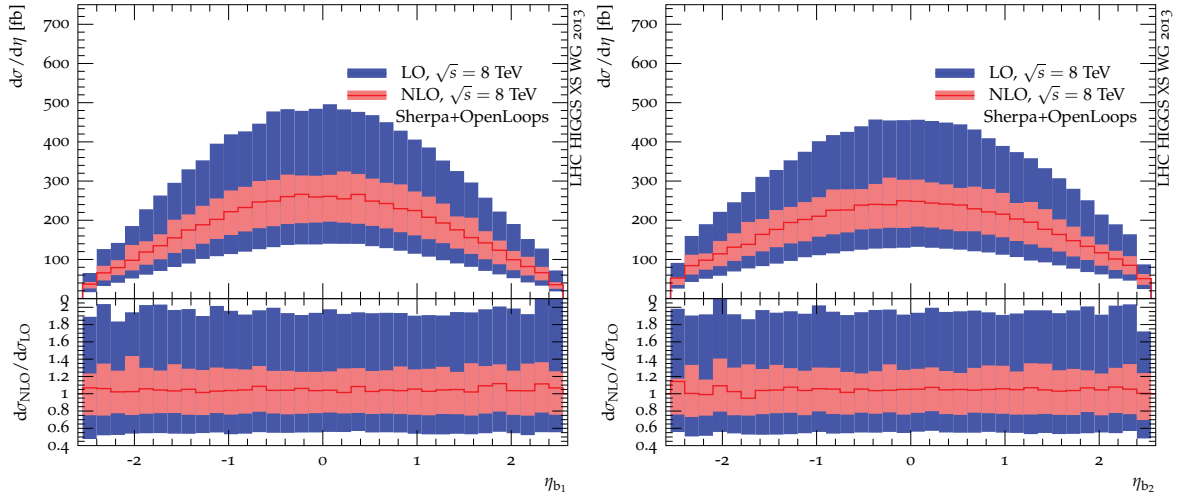
Fig. 50: Distributions in pseudo-rapidity of the harder (left) and softer (right) b jet in pp → t$\bar{\text{t}}$b$\bar{\text{b}}$ at $\sqrt{s}$ = 8 TeV. Same setup and conventions as in Figure 47.

the extension of these computations to the hadron level, by a proper NLO matching to a Parton Shower approach, is a highly non-trivial task. This section presents the status of our efforts in this direction, based on developments in the POWHEL event generator.

POWHEL is an event generator resulting from the interface of the HELAC-NLO set of codes [191, 192], that are publicly available to compute various SM processes at the NLO QCD accuracy, and POWHEG-BOX [80], a publicly available computer framework to match NLO QCD calculations to shower Monte-Carlo (SMC) programs using the POWHEG method [78, 79]. In POWHEL, we use the HELAC-NLO set of codes to produce all matrix elements required as input in POWHEG-BOX. The SMC codes are used to compute all shower emissions except the hardest one, already generated according to the POWHEG matching formalism, and to simulate hadronization and hadron-decay effects. Thus POWHEL can be used to produce both predictions at the parton level, retaining NLO accuracy, and at the hadron level. In particular, one of the possible outputs of POWHEL are Les Houches event (LHE)
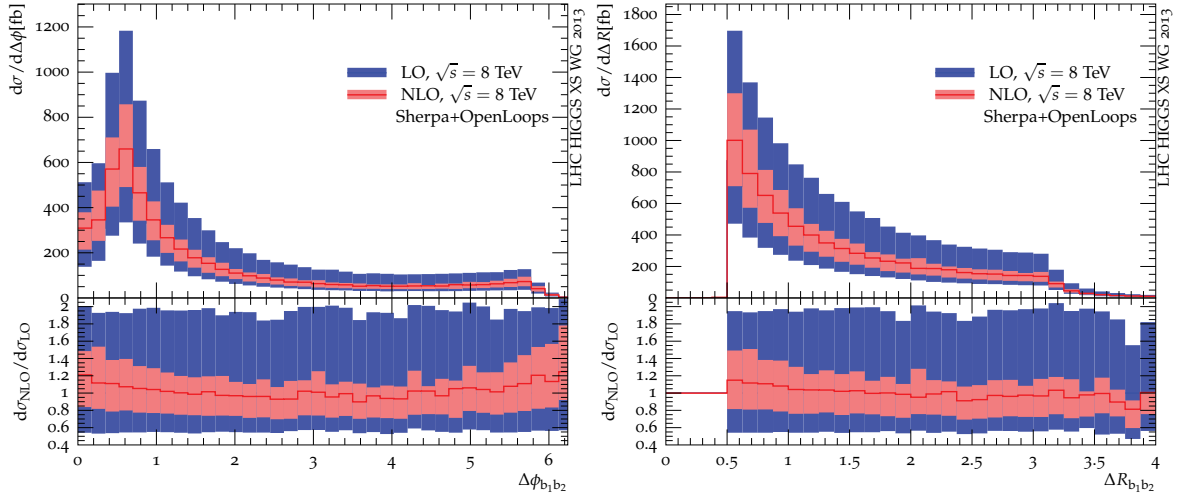
Fig. 51: Distributions in azimuthal-angle (left) and R separation (right) of the b-jet pair in $pp \rightarrow t\bar{t}b\bar{b}$ at $\sqrt{s} = 8$ TeV. Same setup and conventions as in Figure 47.

files [193], at the first radiation emission level, ready to be further showered by SMC. So far, POWHEL (+ SMC) has been used to produce predictions for several processes involving the production of a $t\bar{t}$ pair in association with a third hard object ($t\bar{t}$+ jet [194], $t\bar{t}$H [161], $t\bar{t}$Z [195], $t\bar{t}$W [196]), accompanied by the corresponding sets of LHE files publicly available on our web-site [197].

As for $t\bar{t}$H, a very recent update consisted in the production of POWHEL events at both $\sqrt{s} = 8$ and 14 TeV, for different values of M_H. At present, our LHE files at both 7 and 8 TeV are used by the ATLAS collaboration. Here we present predictions for 14 TeV collider energy including a preliminary comparison to the $t\bar{t}b\bar{b}$ background, simulated using massless b-quarks. More complete phenomenological analysis will be published elsewhere. At 14 TeV, predictions for $t\bar{t}b\bar{b}$ at the NLO QCD accuracy are known [184, 186]. For the sake of comparison, we consider the same configuration as in Ref. [184] and we verify that POWHEL predictions at NLO accuracy agree with those published in [184]. This is a non-trivial check, also taking into account that POWHEL, like HELAC-NLO, uses the OPP method [133, 134] complemented by rational terms of kind R_2 [198] to compute one-loop amplitudes, whereas the authors of [184] rely on tensor-reduction techniques.

As a further step, we used POWHEL to produce $t\bar{t}b\bar{b}$ events and predictions at the first-radiation emission and at the SMC level. The delicate issues in this respect are the following:

1. the choice of a set of technical cuts, that we have to implement for the generation of LHE events in POWHEG-BOX, given that the $t\bar{t}b\bar{b}$ process with massless b-quarks is already singular at LO; in particular, for b quarks, we impose a cut on the minimum transverse momenta of the b-quarks and on the minimum invariant mass of the b-quark pair, $p_{T,b}$, $p_{T,\bar{b}}$, $m_{b\bar{b}} > 2$ GeV;

2. the choice of suitable suppression factors to suppress the phase-space regions less interesting from the physical point of view (i.e. the regions that will be cut by the selection cuts);

3. the correct estimate of the contribution of the remnants, taking into account that in POWHEG-BOX the phase space of the real emission is split in two parts (singular and remnant regions);

4. the stability of the computation, that requires the use of higher than double precision in a non-negligible fraction of the phase space points;

5. the computing time: on the one hand, the high number of final-state particles at the parton level, and, as a consequence, the complexity of the virtual and real correction diagrams, and on the other, the use of higher than double-precision arithmetic, requires intensive CPU resources.

79

We discuss these points in detail in Ref. [167].

For the predictions shown in this section, we adopted the parameters of Ref. [184], in the generation of both the signal and background events: the CTEQ6M PDF set [169] available in the LHAPDF interface [199], with 5 active flavors and a 2-loop running α_s, $m_t = 172.6$ GeV, $M_W = 80.385$ GeV, $M_Z = 91.1876$ GeV, $m_b = 0$. We use $M_H = 125$ GeV, close to the measured mass of the newly discovered boson at the LHC [200, 201]. The factorization and renormalization scales were set equal, $\mu_F = \mu_R \equiv \mu_0$ and chosen to be $\mu_0 = m_t + M_H/2$ for the signal and $\mu_0 = m_t$ for the background.

As for SMC, we used PYTHIA-6.4.26. The masses of heavy bosons in PYTHIA were set to be the same as in POWHEL. For simplicity the contribution of photon emission from leptons was switched off and B-hadron stability was enforced, whereas all other particles and hadrons were assumed to be stable or to decay according to the PYTHIA default implementation. This implies that both top quarks and the Higgs boson were allowed to decay in all possible channels available in the SMC. The effect of multiple interactions was neglected.

We produced predictions for both $t\bar{t}H$ and $t\bar{t}b\bar{b}$, by applying the following selection cuts at the hadron level:

1. All hadronic tracks with $|\eta| < 5$ were used to build jets, by means of the anti-$k_\perp$ algorithm [190], with a recombination parameter $R = 0.4$, as implemented in FASTJET-3.0.3 [179].
2. We required at least six jets with $p_{T,j} > 20$ GeV and $|\eta_j| < 5$. Jets not satisfying these constraints were not considered.
3. Among the jets we identify b-jets by tagging them according to the MCTRUTH information and we required at least four b-jets (two tagged with b and two with $\bar{b}$) with $|\eta_b| < 2.7$. Jets not satisfying the $|\eta_b|$ constraint were classified as non-b jets.
4. We required at least one isolated lepton with $p_{T,\ell} > 20$ GeV and $|\eta_\ell| < 2.5$. The lepton was isolated from all jets by requiring a minimum separation in the pseudorapidity-azimuthal angle plane $\Delta R = 0.4$.
5. We required an event missing energy $p_\perp^{\text{miss}} > 15$ GeV.

The aim of these cuts is selecting $t\bar{t}H$ and $t\bar{t}b\bar{b}$ events with H decaying in $b\bar{b}$ and with a $t\bar{t}$ pair decaying semileptonically.

The total cross-section of the signal after cuts is 34 fb and that for the background is about 18 times larger than that of the signal. The differential distributions for $t\bar{t}H$ always lie below those for $t\bar{t}b\bar{b}$. It is thus important to look for differences in their shapes, to understand if it is possible to disentangle effects of the signal in the cumulative contribution of the signal and background. Here we concentrate on the distributions where a difference of shape between signal and background turned out to be more evident. In Figure 52 we show the invariant masses of all possible pairings of the four b-jets with one b- and one $\bar{b}$-tagged jet in the pair: (a) the hardest b- and $\bar{b}$-tagged jets, (b) the hardest b- and second hardest $\bar{b}$-tagged jets, (c) the second hardest b- and hardest $\bar{b}$-tagged jets, and (d) the second hardest b- and $\bar{b}$-tagged jets. On each plot, the solid histogram is the signal and the shaded one is the background (both based on about 200 k events). The signal is also shown added to the background cumulatively. In all cases, a peak in vicinity of m_H is clearly visible in the distributions from $t\bar{t}H$, whereas it is absent in case of $t\bar{t}b\bar{b}$. We emphasize that this is true not only for the pair of the hardest b-jets, but also for the other combinations. It is interesting to see how the effects of shower and hadronization do not eliminate the presence of the $t\bar{t}H \to t\bar{t}b\bar{b}$ peak, at least when our selection cuts are applied. Seeing this peak in the experimental analysis requires good reconstruction of the b-jets, with a low mistagging probability.

Other interesting distributions are the ΔR-distributions of the b-jet pairs with one b- and one $\bar{b}$-tagged jet in the pair. In particular, when looking at the shape of the ΔR-distribution between the two second-hardest b-jets, shown in Figure 53.b, we see an almost flat distribution in the region $\Delta R \in [0.4, 3]$
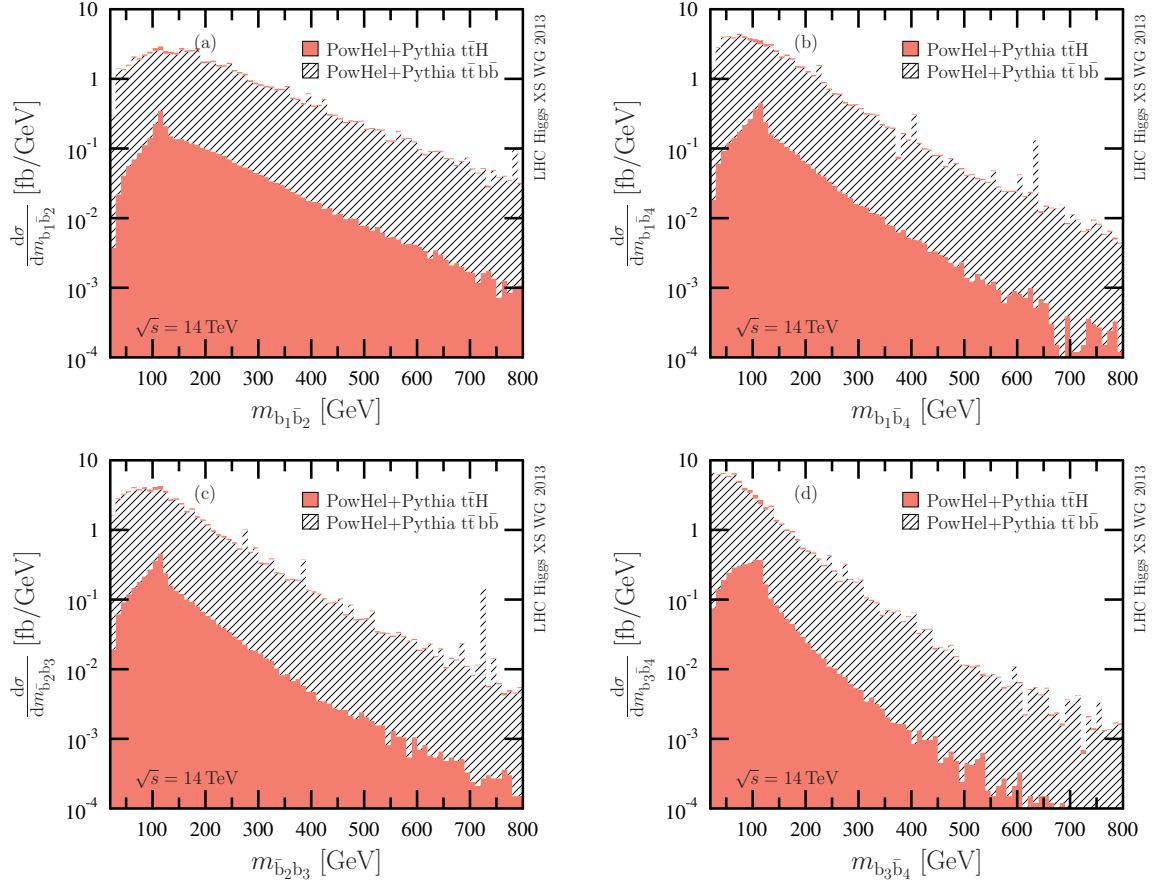
Fig. 52: Invariant mass of the four possible b-jet pairs with one b- and one $\overline{\text{b}}$-tagged jet in the pairs. The $t\bar{t}H$ and the $t\bar{t}b\bar{b}$ distributions after POWHEL+PYTHIA are shown by pink and shaded black histograms, respectively. Peaks around the Higgs mass are visible in the $t\bar{t}H$ distributions.

in the case of the background, as opposed to a growing behavior in the case of the signal. However, when observing this same plot in non-log scale, it is not easy to disentangle the $t\bar{t}H$ contribution from the $t\bar{t}b\bar{b}$ one due to the large difference in the cross-sections. The ΔR-distribution between the two hardest b-jets, shown in Figure 53.a, has a different shape, and previous conclusions do not apply. The differences between Figure 53.a and Figure 53.b show that the ΔR-distributions can be quite sensitive to the experimental b-jet reconstruction procedures and to the precision of the b-tagging algorithms.

As for the p_T- and η-distributions of single b-jets and single leptons, our simulations do not bring evidence of big changes of shape when comparing $t\bar{t}H$ and $t\bar{t}b\bar{b}$. Analyses under different systems of cuts are also under way.

Besides looking for systems of cuts that allow to increase the signal/background ratio, further developments of this work will consist in providing estimates of the theoretical uncertainties on our predictions at the hadron level. In this respect, it is important to assess the role of renormalization and factorization scale and pdf variation, as well as to provide an estimate of the uncertainties intrinsic to the NLO+PS matching. A first step in this direction, when dealing with the POWHEG matching scheme, as implemented in the `POWHEG-Box` (and also in `PowHel`), is quantifying the impact of the variation of the starting scale for SMC emissions. In the `POWHEG-Box`, this information is encoded in a prescription for the choice of the `SCALUP` value of each event. The original `POWHEG-Box`, prescription, also applied in this section, fixes the `SCALUP` value to the relative transverse momentum of the first radiation emission, with respect to the emitting particle. Recently, a modification of this prescription has
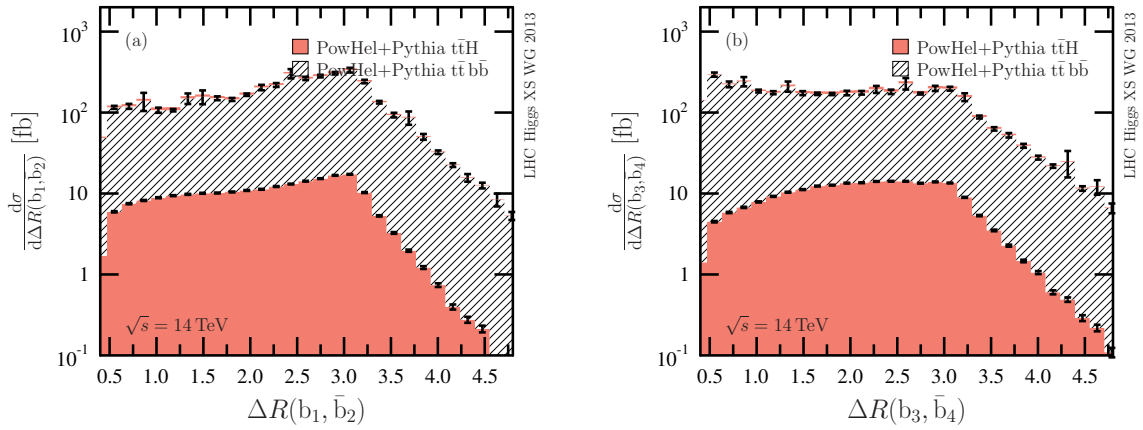
Fig. 53: ΔR distance in the pseudorapidity–azimuthal angle plane between the two hardest b-jet pairs, and between the two second-hardest b-jet pairs with one b- and one $\overline{\mathrm{b}}$-tagged jet in the pairs. The $\mathrm{t}\overline{\mathrm{t}}\mathrm{H}$ and the $\mathrm{t}\overline{\mathrm{t}}\mathrm{b}\overline{\mathrm{b}}$ distributions after POWHEL+PYTHIA are shown by pink and shaded black histograms, respectively. When comparing the two panels a difference in the shape of the distributions is clearly visible. The error bars represent the statistical uncertainty of the events.

been proposed in Ref. [202]. This can be optionally applied during the analysis of the LHE files created by POWHEG-BOX and PowHel. The application of the new prescription has no effect on predictions for $\mathrm{t}\overline{\mathrm{t}}\mathrm{H}$, whereas our preliminary studies show an uncertainty of about 20 % of the $\mathrm{t}\overline{\mathrm{t}}\mathrm{b}\overline{\mathrm{b}}$ differential cross-sections presented in this contribution (decrease of the cross-sections after SMC for hadroproduction of $\mathrm{t}\overline{\mathrm{t}}\mathrm{b}\overline{\mathrm{b}}$ events), whose exact amount depends on the system of cuts. A complete quantitative study of the uncertainties will be presented elsewhere.

7 PDF [22]

Several of the PDF sets (at both NLO and NNLO) discussed in the previous Yellow Reports [13,14], and specifically some of those recommended for inclusion in the PDF4LHC prescription [147, 203] for the computation of central value and uncertainty of a process have been updated. Furthermore, a number of relevant studies and results from PDF groups have become available in the last year.

The NNLO CT10 PDFs have become available [204]. These PDFs use essentially the same data sets as in the already existing CT10 NLO PDFs [145]. In this new analysis, the effects of finite quark masses have been implemented in the S-ACOT-χ scheme (see e.g. Ref. [205], Sect. 22 for a review) at NNLO accuracy. A similar quality of agreement with the fitted experimental data sets is obtained at NNLO as at NLO. At low x ($<10^{-2}$), the NNLO gluon distribution is found to be suppressed, while the quark distributions increase, compared to the same distributions at NLO. The GM-VFN scheme used in the NNLO fit yields in changes to both the charm and bottom quark distributions.

Two of the MSTW group [206] have investigated the generation of their PDFs as a Monte Carlo set obtained from fits to data replicas (as done by NNPDF, see e.g. Ref. [13], Sect. 8.2.2), rather than the Hessian eigenvector approach used by default. For given $\Delta\chi^2$ the results are compatible with the eigenvector approach. Furthermore, it was shown that Monte Carlo PDF sets could also be generated starting from PDF determined using the Hessian approach. This has the advantage that it is then possible to determine combined uncertainties from different PDF sets by merging Monte Carlo sets. Also, it is then possible to use for all sets the reweighting approach for estimating the effect of new data on PDFs introduced by NNPDF [207, 208]. In Ref. [209], the MSTW group also presented in new PDF sets based on a modification and extension of their standard parameterization to one using Chebyshev polynomials (MSTW2008CP) (and also including modified deuteron corrections - MSTW08CPdeut), and studied the effect of LHC data on the MSTW2008 PDFs [100] and the new PDFs using the reweighting procedure. The modifications to the PDFs result in a change to the low-x valence quark distributions, and improves the comparison to data for central rapidity lepton asymmetry from W decays. Little else of significance is changed, including $\alpha_s(M_Z)$, and for the overwhelming majority of processes a new PDF release would be redundant.

NNPDF have presented a new set, NNPDF2.3 [68] at NLO and NNLO, which, besides introducing some small methodological improvements, is the first set to fully include available LHC data. It turns out, however, that the impact of LHC data is only moderate for the time being, and thus differences in comparison to the previous NNPDF2.1 set [67, 210] are small (consequently, the LO NNPDF2.1 set has not been updated and its usage together with NNPDF2.3 NLO and NNLO is recommended by NNPDF). The only significant impact is that of the CMS W asymmetry data on the up-down separation, which leads to a slightly more accurate prediction of the W^+/W^- cross section ratio, besides of course more precise predictions for the W asymmetry itself. This is in agreement with the findings of Ref. [100], and indeed the prediction for the up-down valence ratio in the $x \sim 0.001$ region obtained using reweighted MSTW08 PDFs is in much better agreement with NNPDF2.3 (and also NNPDF2.1) [211]. NNPDF has also presented a first PDF determination using only collider data (hence avoiding both nuclear target and lower-energy data): whereas these PDFs are less subject to theoretical uncertainties related to nuclear an higher twist corrections, their statistical uncertainties are still not competitive. A similar conclusion, though based on studies without the recent LHC data appeared in [206].

The updated PDF sets to be used with the NLO PDF4LHC prescriptions are thus currently CT10, MSTW08, and NNPDF2.3.

A new NLO and NNLO set, ABM11, has been made available by the ABM group [212], and a benchmarking exercise performed. As well as updating for the combined HERA data [213] this fit uses the $\overline{\text{MS}}$ renormalization scheme for heavy quark masses. In all important respects these PDFs remain similar to those of ABKM09 [214], though the gluon distribution is a little larger at small x. As before

---

[22]S. Forte, J. Huston, R. Thorne

Tevatron jet data is not included directly in the fit, though a comparison to this data is presented by the same authors in [215]. The authors make the PDFs available for a wide variety of $\alpha_s(M_Z)$ values, though the extracted value, which is recommended by the authors, is $\alpha_s(M_Z) = 0.1134 \pm 0.0011$ at NNLO.

The HERAPDF collaboration have released the HERAPDF1.5 NLO and NNLO PDF set [216, 217], which in addition to the combined HERA-I dataset uses the inclusive HERA-II data from H1 [218] and ZEUS [219] (though the PDF set is partially based on a yet-unpublished combined data set).

Furthermore, within the HERAPDF-HERAFITTER framework [213], the ATLAS collaboration performed [220] a study of the impact on the strange quark PDF of the inclusion of their data on differential W and Z production [221]. This implied a significant increase of the strange quark contribution to the sea. However, NNPDF2.3 instead finds that whereas the ATLAS do tend to pull the strange distribution upwards, the effect is negligible withing current uncertainties; MSTW find similar results. There is also a study of the sensitivity W and Z production to the strange quark distribution in [222], but no explicit examination of the effect of the published data.

A variety of studies of theoretical uncertainties on PDFs have recently appeared. As mentioned above, the study of extended parameterizations in Ref. [209] has been generalized to include variation and optimization of the nuclear corrections to deuteron structure functions. Hence, a further modified version of the MSTW08 set, MSTW2008CPdeut was obtained. A study of nuclear corrections using CTEQ PDFs has also been presented [223], with broadly similar conclusions, i.e. a slight increase (and increased uncertainty) on the high-x down quark. An increase of the d/u ratio at the one-sigma level for $0.1 \lesssim x \lesssim 0.5$ as a consequence of the inclusion of deuterium corrections was similarly found in Ref. [224], where it was also shown that their impact is however otherwise negligible (and in particular negligible for larger x) in the scale of current PDF uncertainties.

In [225] it was shown that there can be sensitivity to input scale for PDFs, though this will always depend on the flexibility of the input parameterization. In [226] the uncertainty associated with choices of general mass variable flavour number scheme (GM-VFNS) was studied. At NLO this can be a couple of percent, but as with other scheme choices it diminishes at increasing order and becomes $< 1\%$ at NNLO. These changes were less than those obtained in using either the zero mass approximation or using fixed flavour number scheme (FFNS). There were implications that the differences in PDFs and the value of $\alpha_s(M_Z)$ obtaining using either (GM-VFNS) and FFNS can be significant, and this requires further (ongoing) study. Similar conclusions were reached in Ref. [224], where it was shown that use of a FFN scheme affects significantly the total quark and gluon PDFs, and leads to significant loss in fit quality, especially to difficulties in reproducing the high Q^2, low x HERA data. In the same Ref. it was also shown that higher twist corrections to the DIS data included in the NNPDF PDF determination have a negligible impact on all PDFs, similar to previous conclusions by MRST [227] and more recent studies involving MSTW PDFs.

Largely as a part of the work on CT10 NNLO, a number of theoretical uncertainties related to the treatment of jet cross sections has been examined, notably those that may have impact on processes involving gluon scattering. A benchmark comparison of NLO computations for inclusive jet production constraining the gluon PDF has been performed [228, 229]. A new version of the program EKS for NLO jet cross sections was developed [228, 230] that is entirely independent from NLOJET++ [231] as well as APPLGRID [232] and FASTNLO [233] programs that interpolate the NLOJET++ input. Specific input settings that produce agreement of all these codes were identified, and uncertainties in the gluon PDFs associated with fitting the jet data were examined. It was pointed out, for example, that correlated systematic errors published by the jet experiments are interpreted differently by the various PDF fitting groups, which leads to non-negligible differences between the PDF sets. This issue is not widely known and will be considered in the future to avoid biases in PDF fits.

Hence, overall, although there have been a significant number of important and interesting updates, there has been no dramatic change in PDFs in the past year, mainly because it is clear that LHC data so far published do not add add a great deal of extra constraint. A comparison of results using NLO PDFs

would be little different to a year ago. However, especially in the quark sector, there is some gradual improvement in agreement between the sets included in the PDF4LHC prescription, which follows prior improvement at the time of the previous report [14] since the original prescription [147].

Also, a more complete comparison of results using NNLO PDFs is now possible. Therefore, in this section, we compare NNLO PDF luminosities (and their uncertainties) from five PDF fitting groups, i.e. those that are made available for a variety of $\alpha_s(M_Z)$ values including those similar to the world average, and the resulting predictions for both standard model and Higgs boson cross sections at 8 TeV at the LHC. We follow the recent benchmarking exercise in [229].

Following Ref. [234], we define the parton luminosity for production of a final state with mass M_X as

$$\Phi_{ij}\left(M_X^2\right) = \frac{1}{s} \int_\tau^1 \frac{dx_1}{x_1} f_i\left(x_1, M_X^2\right) f_j\left(\tau/x_1, M_X^2\right) , \tag{47}$$

where $f_i(x, M^2)$ is a PDF at a scale M^2, and $\tau \equiv M_X^2/s$.

In Fig. 54, the gluon-gluon (top) and gluon-quark (bottom) parton luminosities from five PDF groups are plotted for the production of a state of mass M_X (GeV), as a ratio to the PDF luminosity of NNPDF2.3. For these comparisons, a common value of $\alpha_s(M_Z)$ of 0.118 has been used. In the region of the Higgs mass (125 GeV), the gg luminosities (and uncertainties) of NNPDF2.3, CT10 and MSTW2008 are reasonably close, with the error bands overlapping, but the total uncertainty range, defined from the bottom of the CT10 error band to the top of the NNPDF2.3 error band, is of the order of 8%. This is approximately twice the size of the error bands of either CT10 or MSTW2008 (and a bit more than twice that of NNPDF2.3). The gg luminosities of HERAPDF1.5 and ABM11 are similar to the three PDFs sets discussed above in the Higgs mass range, although the gg PDF luminosity for ABM11 falls faster with mass than any of the other PDFs. The HERAPDF PDF uncertainty is larger, due to the more limited data sets included in the fit.

The gq PDF luminosity error bands overlap very well for CT10, MSTW2008 and NNPDF2.3 in the Higgs mass range, and indeed at all masses except, to some extent, well above 1 TeV. Again the HERAPDF1.5 uncertainty band is larger. The $\overline{q}q$ (top) and qq (bottom) PDF luminosity comparisons are shown in Fig. 55. For both $\overline{q}q$ and qq, there is a very good overlap of the CT10, MSTW2008 and NNPDF2.3 error bands. The central predictions of HERAPDF1.5 also agree well, with the uncertainty band again being somewhat larger. The ABM11 luminosities are somewhat higher in the low to medium mass range and fall more quickly at high mass.

In the PDF4LHC report [147], published at a time when NNLO PDFs were not available from either CT or NNPDF, the recommendation at NNLO was to use the MSTW2008 central prediction, and to multiply the MSTW2008 PDF uncertainty by a factor of 2. This factor of 2 appears to be an overestimate in this new comparison of the three global PDFs, for $\overline{q}q$, qq and gq initial states, but is still needed for gg initial states. A direct comparison of the parton luminosity uncertainties is shown in Fig. 56 for $\overline{q}q$ (top) and gg (bottom), where the points made previously about the relative size of the uncertainties can be more easily observed.

In Fig. 57, we show predictions for Higgs production at 8 TeV in various channels, for $\alpha_s(M_Z)$ values of 0.117 (left) and 0.119 (right) for the 5 different PDFs being considered. As expected, the cross section predictions follow the trends discussed for the PDF luminosities. The strongest disagreements, perhaps, are from the ABM11 predictions for VBF and associated (VH) Higgs production, though if the ABM11 PDFs with $\alpha_s(M_Z) = 0.1134$ are used the disagreement in these channels is reduced, but increases for the gluon fusion channel.

Cross section predictions for Higgs production (in the gg channel at 8 TeV, for values of $\alpha_s(M_Z)$ of 0.117 and 0.119) are shown in Fig. 58 and Fig. 59 for CTEQ, MSTW and NNPDF PDFs. In Fig. 58, the predictions are at NLO, but using the PDFs available in 2010 (left) and in 2012 (right). In Fig. 59, the
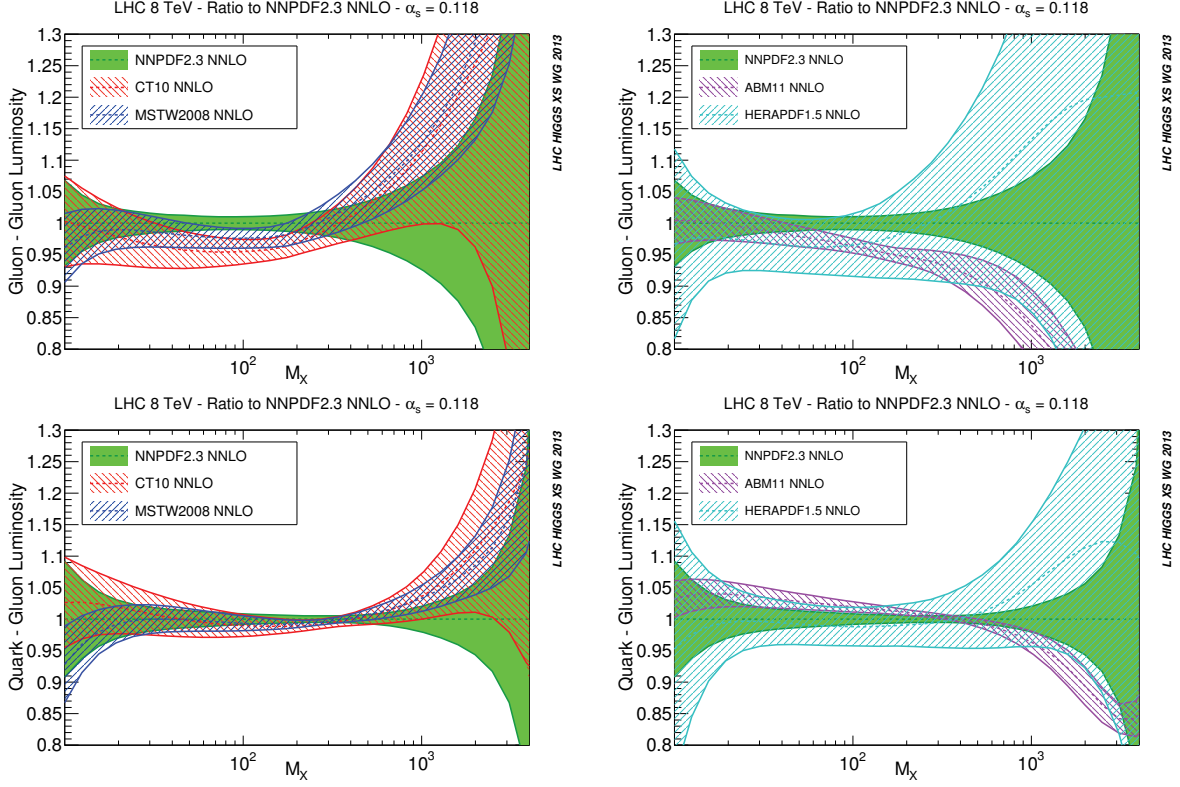
Fig. 54: The gluon-gluon (upper plots) and quark-gluon (lower plots) luminosities, Eq. (47), for the production of a final state of invariant mass M_X (in GeV) at LHC 8 TeV. The left plots show the comparison between NNPDF2.3, CT10 and MSTW08, while in the right plots we compare NNPDF2.3, HERAPDF1.5 and MSTW08. All luminosities are computed at a common value of $\alpha_s(M_Z) = 0.118$.

cross sections are plotted using the 2012 NNLO PDFs. Here, we estimate the PDF+$\alpha_s(M_Z)$ uncertainty using a small variation of the original PDF4LHC rubric; we take the envelope of the predictions from CT/CTEQ, MSTW and NNPDF including their PDF uncertainties, and using values of $\alpha_s(M_Z)$ of 0.117 and 0.119. The uncertainty bands are given by the dashed lines. There is little change at NLO with the evolution from CTEQ6.6 and NNPDF2.0 to CT10 and NNPDF2.3, and the uncertainty at NNLO is very similar to the uncertainty estimated for NLO.

As a contrast, we show in Fig. 60 predictions for W^+ production based on the 2010 NLO and 2012 NNLO PDFs from CT/CTEQ, MSTW and NNPDF. The relative PDF+$\alpha_s(M_Z)$ uncertainty estimated with the same prescription used for Higgs production has a sizable decrease from the 2010 NLO predictions to the 2012 NNLO predictions. Similar improvements should be expected for all quark-initiated processes, including those involved in Higgs production.

Finally, we demonstrate that although the previous proposal in the PDF4LHC recommendation to use the envelope of the predictions using three PDF sets does not strictly have a solid statistical basis, it certainly produces sensible results. Using the techniques for generating random PDFs sets in [206] it was shown in section 4.1.3 of [211] that similar results are obtained from combining the results from 100 random sets from MSTW2008, NNPDF2.3 and CT10 as from taking the envelopes. The results are shown in Fig. 61. The envelope procedure can be seen to be a little more conservative, and becomes more-so in comparison to the combination of random sets as any discrepancy between sets becomes more evident. However, for predictions using these three PDF sets there is generally not much differences between the two methods of calculation. In order to maintain a conservative uncertainty the continuation
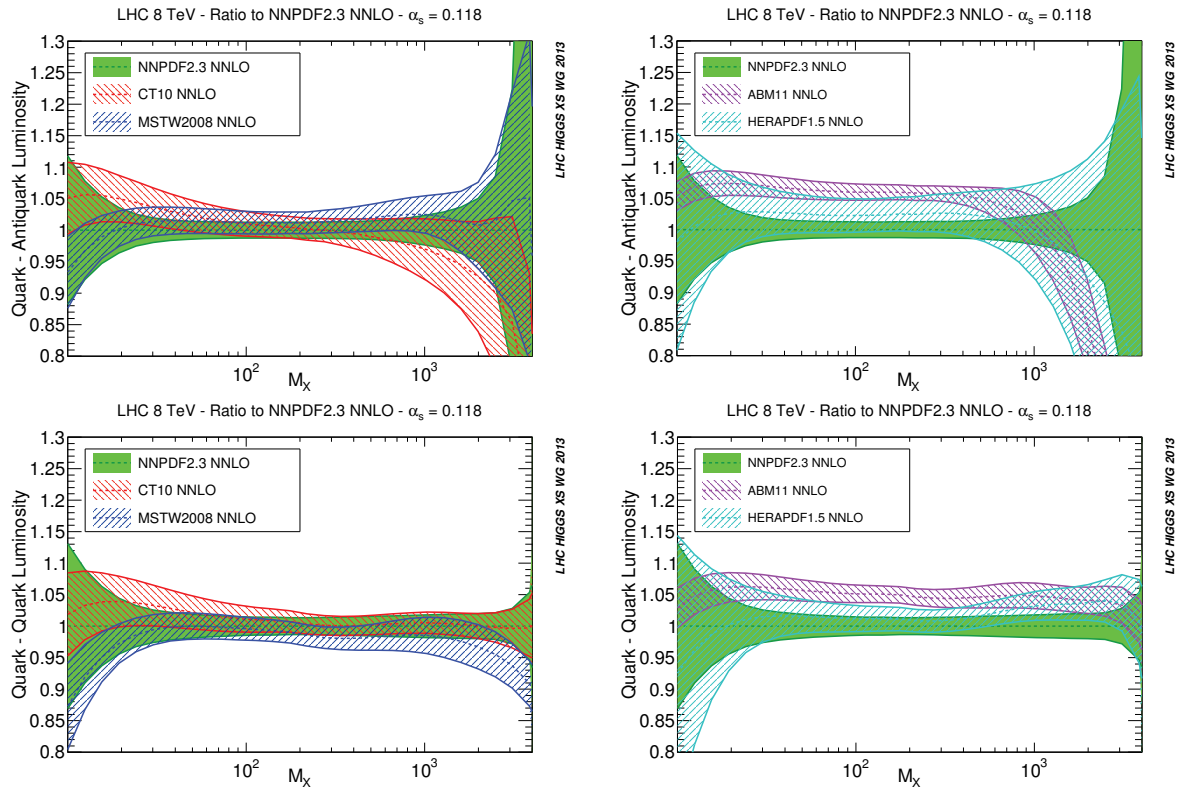
Fig. 55: The same as Fig. 54 for the quark-antiquark (upper plots) and quark-quark (lower plots) luminosities.

of the envelope method is probably preferred.
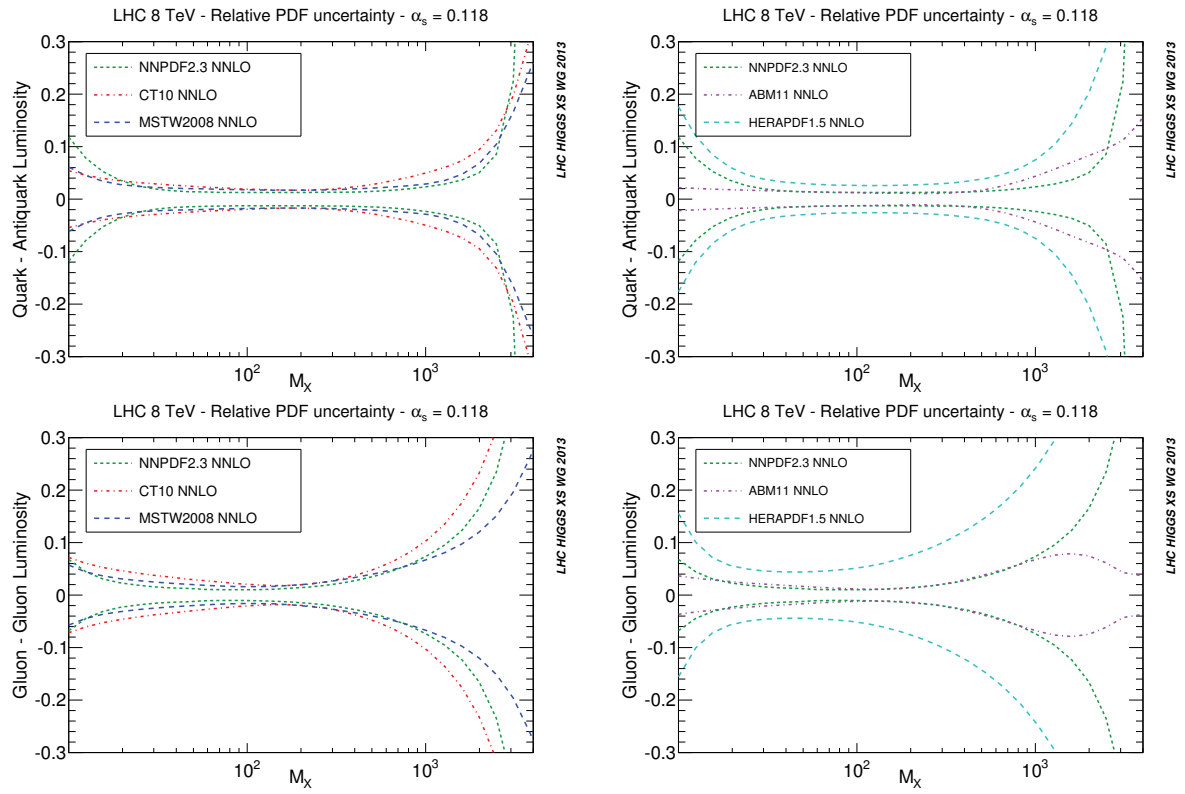
Fig. 56: The relative PDF uncertainties in the quark-antiquark luminosity (upper plots) and in the gluon-gluon luminosity (lower plots), for the production of a final state of invariant mass M_X (in GeV) at the LHC 8 TeV. All luminosities are computed at a common value of $\alpha_s = 0.118$.
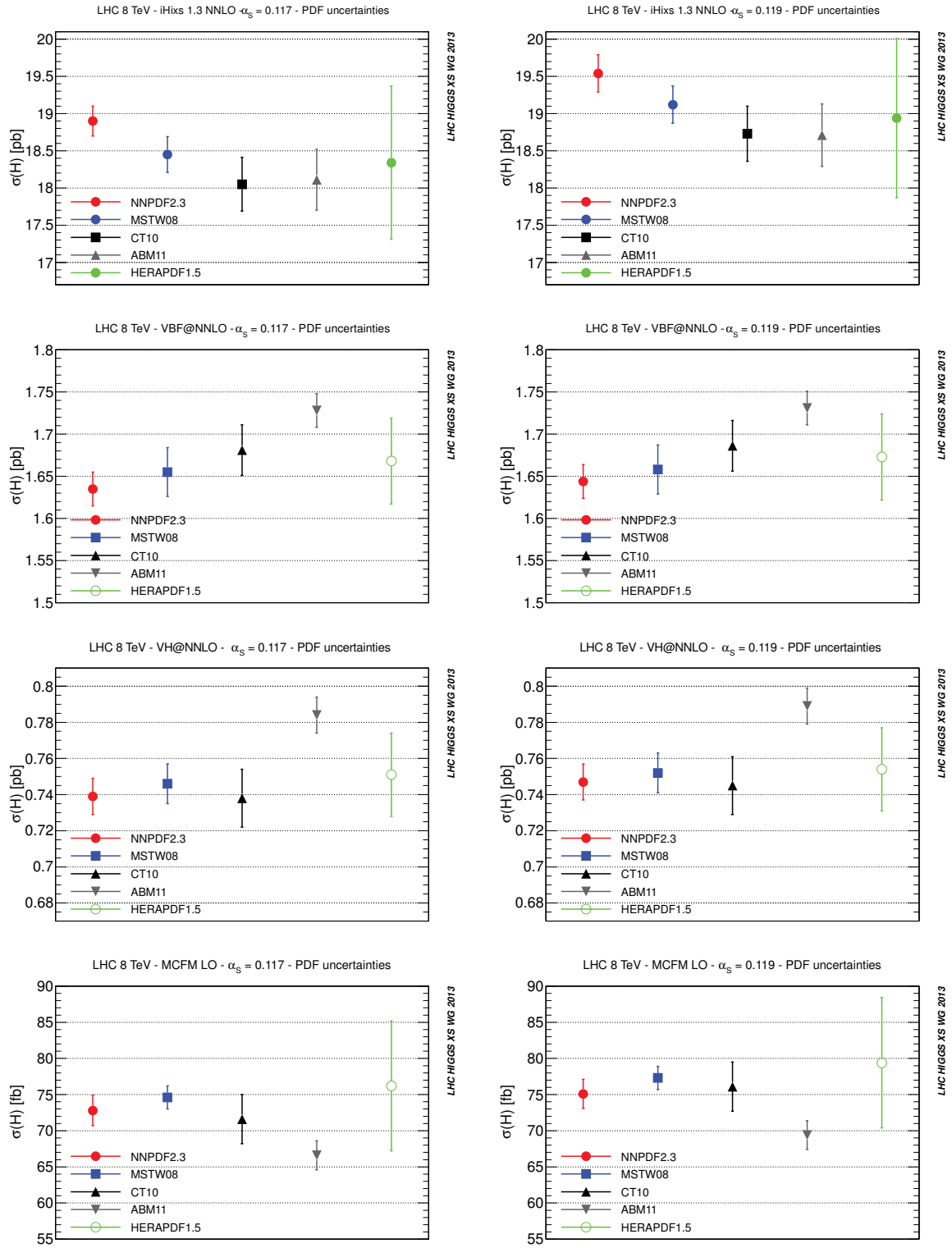
Fig. 57: Comparison of the predictions for the LHC Standard Model Higgs boson cross sections at 8 TeV obtained using various NNLO PDF sets. From top to bottom we show gluon fusion, vector boson fusion, associated production (with W), and associated production with a $\overline{t}t$ pair. The left hand plots show results for $\alpha_s(M_Z) = 0.117$, while on the right we have $\alpha_s(M_Z) = 0.119$.
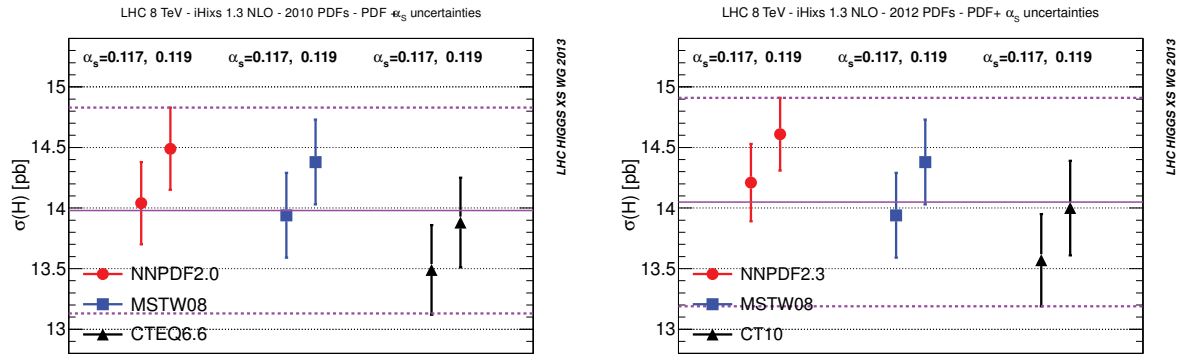
Fig. 58: The Higgs boson production cross section in the gluon fusion channel using the NLO PDF sets included in the PDF4LHC prescription for $\alpha_s(M_Z) = 0.117$ and 0.119. The left plot has been computed with 2010 PDFs and the right plot with 2012 PDF sets. The envelope (dashed violet horizontal lines) is defined by the upper and lower values of the predictions from all the three PDF sets and the two values of α_s. The solid violet horizontal line is the midpoint of the envelope.
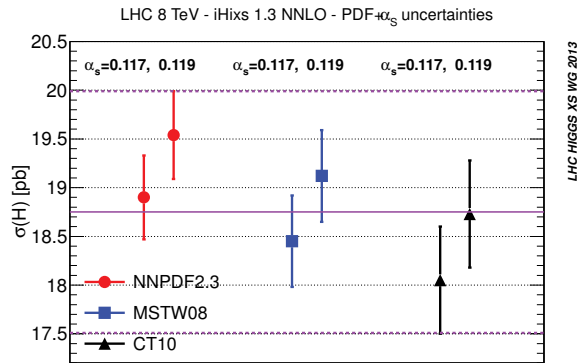
Fig. 59: The same as Fig. 58, but using 2012 NNLO PDFs.
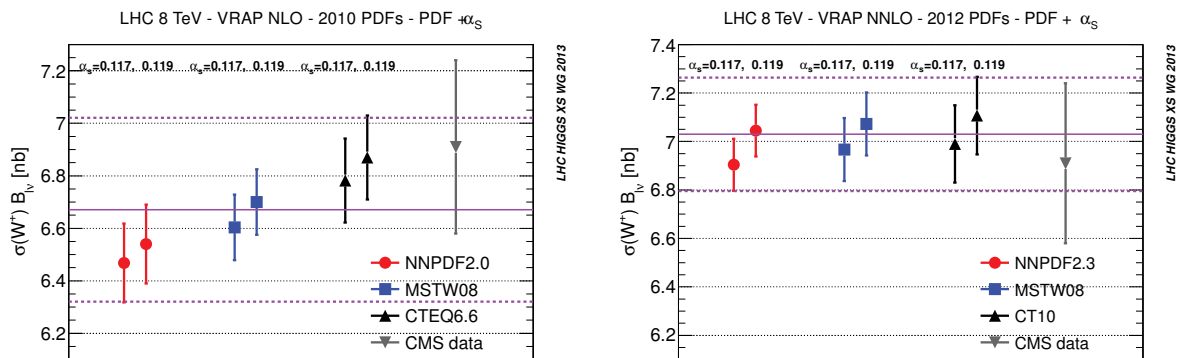
Fig. 60: The W^+ production cross sections determined using the same PDFs and envelope as in Figs. 58fig:h8nnlo. The left plot shows 2010 NLO PDFs, the right plot 2012 NNLO PDFs. The recent 8 TeV CMS measurement is also shown.
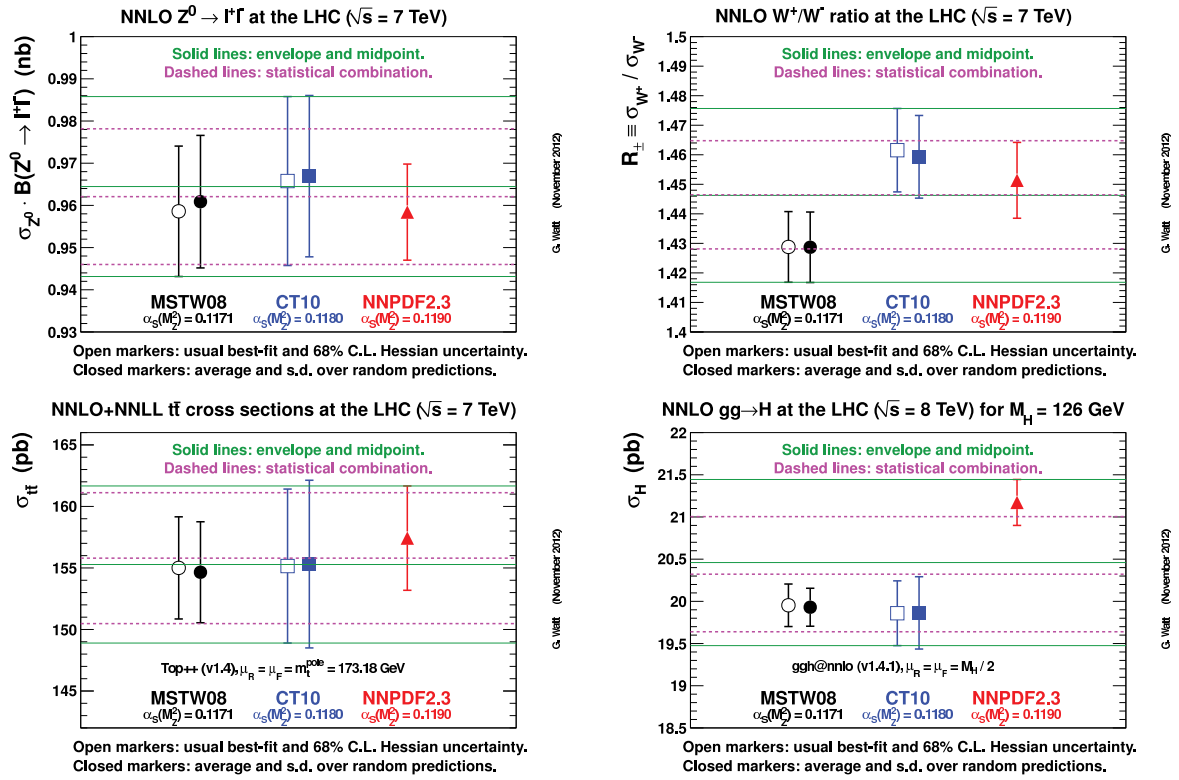
Fig. 61: NNLO (a) Z, (b) W^+/W, (c) $\bar{t}t$ and (d) $gg \rightarrow H$ cross sections from MSTW08, CT10 and NNPDF2.3, combined either by taking the envelope of the three predictions, or from the statistical combination of 100 random predictions from each group (from Ref. [211]).

8 Jets in Higgs physics[23]

Jets are relevant in multiple contexts in Higgs studies. The separation of the data into "jet bins", each with a specific number of jets in the final state, can be useful to help discriminate Higgs production from backgrounds. Cuts on the kinematics of jets can also help to separate different Higgs production mechanisms. This is of particular importance for discriminating between vector-boson fusion, which tends to be accompanied by two forward jets, from gluon fusion. Finally, jets may be produced from the fragmentation of Higgs decay products, as in the search for $H \to b\bar{b}$, or in analyses of $H \to VV$ when one of the vector bosons decays hadronically.

The main type of question that we address in this section is how we can reliably estimate cross sections for a given jet bin and the kinematic distributions used to discriminate between different signal production mechanisms. We consider uncertainties in fixed-order predictions, their potential reduction with the help of resummations, and non-perturbative uncertainties from the underlying event.

8.1 Resummation for Higgs production with a jet veto [24]

In the study of $H \to WW$, with leptonic W decays, it is customary to distinguish events according to their number of jets. In particular, selecting events with zero jets, i.e. imposing a jet veto, significantly reduces the background from $\bar{t}t$ production. To relate experimental observations with the jet veto to the total Higgs production cross section, one must then be able to evaluate the expected number of signal events that pass the jet veto requirement.

In practice the transverse-momentum threshold for identifying jets, $p_{T,\mathrm{min}} \simeq 25\text{–}30$ GeV, is substantially smaller than the Higgs mass, M_{H}. As a result, perturbative calculations of the cross section with the jet veto [41, 44, 235] involve terms enhanced by up to two powers of $\ln M_{\mathrm{H}}/p_{T,\mathrm{min}}$ for each power of α_{s} beyond the leading-order cross section. A large value for the logarithm degrades the convergence of the perturbative series. Currently the experiments account for the resulting additional perturbative uncertainty in the fixed-order, NNLO, calculations via the Stewart–Tackmann procedure [236]. In the results with the full 2012 dataset [103], the theoretical uncertainty in $H \to W^+W^-$ results is comparable to the statistical error from a single experiment, and significantly larger than the experimental systematic uncertainty.

The use of fixed-order predictions in the presence of large logarithms is known not to be optimal, and one can usually obtain significantly improved predictions by resumming the large logarithms to all orders. Previous work in this context [237–239] considered resummations for related cases, such as the Higgs boson p_{T} spectrum (the p_{T} resummations themselves can be found in Ref. [70, 240–245]) or a global jet veto using beam thrust [55, 246], and using Monte Carlo generators to establish the relation with the experimental jet veto.

In the past year substantial progress has been made in carrying out a resummation directly for a veto based explicitly on a jet algorithm. Ref. [56] presented a calculation at next-to-leading logarithmic (NLL) accuracy,[25] where it was observed that the resummation structure at this order is simple and reduces to a Sudakov form factor. It also derived the subset of NNLL terms associated with the jet radius (R) dependence, for the generalized-k_{T} family of jet algorithms [190, 247–250], which includes the anti-k_{T} algorithm used experimentally. Subsequently, in Ref. [57] a calculation at next-to-next-to-leading logarithmic (NNLL) order was presented, incorporating the R-dependent NNLL corrections of Ref. [56], but relying on an extrapolation of these results to large R. In addition, it proposed an all-order factorization theorem for the cross section in Soft Collinear Effective Theory (SCET) Refs. [251–256].

---

[23]D. Del Re, B. Mellado, G. P. Salam, F. J. Tackmann (eds.); A. Banfi, T. Becher, F.U. Bernlochner, S. Gangal, D. Gillberg, X. Liu, M. Malberti, P. Meridiani, P. Monni, P. Musella, M. Neubert, F. Petriello, I. W. Stewart, J. R. Walsh, G. Zanderighi, S. Zuberi

[24]A. Banfi, T. Becher, P. Monni, M. Neubert, G. P. Salam, I. W. Stewart, F. J. Tackmann, J. R. Walsh, G. Zanderighi, S. Zuberi

[25]Terminology for resummation accuracies differs according to the context. Here, N^pLL accuracy is defined to mean that in the *logarithm* of the jet veto efficiency, one accounts for terms $\alpha_{\mathrm{s}}^n \ln^{n+1-p} M_{\mathrm{H}}/p_{T,\mathrm{min}}$ for all n.

Ref. [58] discussed questions related to the all-order factorization theorem. In addition, it pointed out that logarithms of the jet radius R can lead to sizable corrections for the moderately small values, $R = 0.4$–0.5, used experimentally. If these $\ln R$ terms are included in the logarithmic counting, then they would constitute an NLL contribution, which is not resummed at present. Ref. [59] took a complementary approach to the derivation of the full NNLL resummation, accompanied by cross checks of the NNLL terms at orders α_s^2 and α_s^3 (relative to the total cross section), obtained with MCFM [257–259]. While the results of Ref. [57] and Ref. [59] are identical in structure at NNLL accuracy, initially one of the coefficients differed by a numerically relevant term. The difference was traced in Ref. [59] to an extra term which spoils the extrapolation used in Ref. [57]. Subsequent discussions between the groups have led to a consensus that the NNLL terms are as given in Ref. [59].

Numerically, Ref. [59] found that the resummation, matched with the NNLO calculation, had only a small (percent-level) impact on the predicted jet-veto efficiency relative to the pure NNLO prediction, but with a reduction in the perturbative uncertainty from about 15% to 9%. The remaining uncertainty is partially associated with the choice of prescription for matching the resummed and NNLO results. The code to reproduce these results is available in the form of the JETVHETO program Ref. [260]. A further reduction appears to be possible if one uses a jet radius R of order 1, rather than the smaller values currently in use experimentally, an observation that is consistent with the discussion in Ref. [58].

Numerical results from the authors of Ref. [57] and [58] are currently available in preliminary form and are expected to be published soon. We look forward to comparisons between all three sets of results in the near future and also to the experiments taking advantage of the corresponding reduced uncertainties.

8.2 Resummation for exclusive Higgs plus 1-jet production[26]

In this section we study the resummation of a class of large Sudakov logarithms affecting Higgs boson production in the exclusive one-jet bin at the LHC. These large logarithms occur when the Higgs signal cross section is divided into bins of exclusive jet multiplicity. This division is an experimental necessity; for example, in the zero-jet bin of the WW final state the background is dominated by continuum WW production, while in the one-jet and two-jet bins, top-pair production becomes increasingly important. The optimization of this search requires cuts dependent on the number of jets observed, and therefore also on theoretical predictions for exclusive jet multiplicities.

The theoretical community has invested significant recent effort in resumming jet-veto logarithms to all orders in perturbation theory in order to more accurately model the LHC Higgs signal. As summarized in Section 8.1, a significant reduction of the residual theoretical uncertainties is obtained in the zero-jet bin by resumming the jet-veto logarithms. Given that the theoretical uncertainties are currently one of the largest systematic errors affecting the one-jet bin analyses of the Higgs-like particle properties, it is desirable to formulate the resummation when final-state jets are also present. (Inclusion of the NNLO Higgs+1-jet prediction, calculated recently for the purely gluonic contributions to the process [54] and described in Section 3.2 can also be expected to bring an improvement.)

The specific logarithms that we address in this section occur when the transverse momenta of the hard jet in the exclusive one-jet bin is larger than the veto scale. We calculate contributions through next-to-leading order in the exponent of the Sudakov form factor and include the full one-loop functions describing hard, soft, and collinear emissions. This implies that we correctly obtain the first three logarithmic corrections at each order in the QCD coupling constant: $\alpha_s L^2$, $\alpha_s L$ and α_s; $\alpha_s^2 L^4$, $\alpha_s^2 L^3$, and $\alpha_s^2 L^2$; $\alpha_s^3 L^6$, $\alpha_s^3 L^5$, $\alpha_s^3 L^4$; and so on. We have set $L = \ln(Q/p_T^{veto})$, where $Q \sim M_H$ denotes any hard scale in the problem. We match the results to fixed-order to obtain a NLL$'$ + NLO prediction (using the order counting of Ref. [55]), and present numerical results for use in LHC analyses. We first demonstrate that the region of phase space where the leading-jet transverse momentum is of order the

---

[26]X. Liu, F. Petriello

93

Higgs mass accounts for nearly half of the error in the fixed-order NLO prediction for Higgs plus one jet, and is therefore a prime candidate for an improved theoretical treatment. We then perform a detailed study of the residual theoretical uncertainties using our prediction that accounts for the variation of all unphysical scales remaining in the prediction. Even with a very conservative treatment of the errors, a significant reduction of the residual uncertainty as compared to the fixed-order estimate is found; the estimated uncertainties decrease by up to a quarter of their initial values. The results, and the improvements in the zero-jet bin obtained previously, should form the basis for future theoretical error estimates in experimental analyses of Higgs properties. In this section we briefly review the salient features of our formalism, and present numerical results for use in LHC searches. Further details can be found in Ref. [60, 61].

8.2.1 *Review of the formalism*

We use effective-field theory techniques to derive a factorization theorem for exclusive Higgs plus jet production. The factorization of the cross section into separate hard, soft, and collinear sectors is complicated by the presence of the jet algorithm needed to obtain an infrared-safe observable. Following the experimental analyses, we use the anti-k_T algorithm [190] to define jets. We demand that the final state contain only a single jet with $p_T^J > p_T^{veto} \sim 25 - 30$ GeV. Other jets with a transverse momentum above this threshold are vetoed. Since p_T^{veto} is usually substantially lower than the partonic center-of-mass energy $\hat{s}$, such that $\lambda \equiv p_T^{veto}/\sqrt{\hat{s}} \ll 1$, the vetoed observables are usually very sensitive to soft and collinear emissions. We will make the following assumptions in order to proceed in our analysis:

$$p_T^J \sim M_H \sim \sqrt{\hat{s}}, \qquad 1 \gg R^2 \gg \lambda^2, \qquad \frac{\alpha_s}{2\pi} \ln^2 R \ll 1. \tag{48}$$

Given that $p_T^{veto} \approx 25 - 30$ GeV and $R \approx 0.4 - 0.5$, when the leading jet $p_T^J \sim M_H$, the second two assumptions are justified. The first assumption restricts us to specific region of phase space, which we later show contributes roughly half of the uncertainty in the full one-jet bin.

We are able to utilize an effective-theory framework because of how the anti-k_T algorithm clusters soft and collinear emissions. The initial clustering combines the final-state hard emissions into a jet, so that the soft radiation sees only the jet direction and does not probe its internal structure. The mixing between the soft and beam sectors is power-suppressed, as is the mixing between the beam and jet sectors. Denoting the measurement function that imposes the jet clustering and vetoing as $\hat{\mathcal{M}}$, these facts imply that we can factor the full $\hat{\mathcal{M}}$ into the product of individual measurement functions acting separately on the soft ($\hat{\mathcal{M}}_S$), jet ($\hat{\mathcal{M}}_J$), and the two beam sectors ($\hat{\mathcal{M}}_a$ and $\hat{\mathcal{M}}_b$),

$$\hat{\mathcal{M}} = \hat{\mathcal{M}}_J \hat{\mathcal{M}}_S \hat{\mathcal{M}}_a \hat{\mathcal{M}}_b, \tag{49}$$

up to power-suppressed corrections in p_T^{veto} and R [57, 58]. For more details we refer the reader to Ref. [60, 61].

The remaining steps in the derivation of the factorization theorem are presented in detail in Ref. [60]. The final result for the cross section for exclusive Higgs plus one-jet production takes the following form:

$$d\sigma_{NLL'} = d\Phi_H d\Phi_J \, \mathcal{F}(\Phi_H, \Phi_J) \sum_{a,b} \int dx_a dx_b \frac{1}{2\hat{s}} (2\pi)^4 \delta^4 (q_a + q_b - q_J - q_H)$$

$$\times \sum_{spin} \sum_{color} \text{Tr}(H \cdot S) \, (\mathcal{I}_{a,i_a j_a} \otimes f_{j_a})(x_a) \, (\mathcal{I}_{b,i_b j_b} \otimes f_{j_b})(x_b) J_J(R). \tag{50}$$

Here, H, S, and J_J denote hard, soft, and final-state jet functions. The convolutions $(\mathcal{I}_{ij} \otimes f_j)(x)$ give the initial-state beam functions for beams a and b in terms of the usual PDFs, f_j, with i, j labeling the incoming parton types. We have denoted explicitly by the subscript that we will evaluate this cross section to the NLL' level, in the language of Ref. [55]. We again remind the reader that this implies

that we correctly obtain the leading three logarithmic corrections in the cross section at each order in the strong coupling constant. $d\Phi_H$ and $d\Phi_{j_i}$ are the phase space measures for the Higgs and the massless jet J, respectively. $\mathcal{F}(\Phi_{H_c}, \Phi_J)$ includes all additional phase-space cuts other than the p_T veto acting on the Higgs boson and the hard jet. H is the hard function that comes from matching full QCD onto the effective theory, and S describes soft final-state emissions. The trace is over the color indices. The functions $\mathcal{I}$ and J describe collinear emissions along the beam axes and along the final-state jet direction, respectively. The measured jet p_T^J should be much larger than p_T^{veto}. For more details on this formula and the objects contained within, we refer the reader to Ref. [60, 61].

We briefly comment here on non-global logarithms [261] that first occur at the NLL$'$ level. Although they are not included in our current factorization theorem, to estimate their numerical effect we use the large-N_c resummation of these terms derived in Ref. [261]. We include them as a multiplicative correction to our factorization formula. Their numerical effect is small, at or below one percent of the total exclusive Higgs plus one-jet production rate for the relevant values of M_H and p_T^{veto}. To check the robustness of this result we vary the hard scale appearing in these corrections by a factor of two around their nominal value of M_H, and find similarly small corrections. We therefore believe that it is numerically safe to neglect these terms in our NLL$'$ result, although they should be further investigated in the future.

8.2.2   Matching NLL$'$ with NLO

We begin our presentation of the numerical results by matching our resummed expression with the fixed-order NLO result to obtain a NLL$'$+NLO prediction. We use the NLO predictions for Higgs plus one-jet contained in MCFM [63]. We obtain our prediction by setting

$$\sigma_{\text{NLL}'+\text{NLO}} = \sigma_{\text{NLL}'} + \sigma_{\text{NLO}} - \sigma_{\text{NLL}'}^{\text{exp}}. \tag{51}$$

In this equation, σ_{NLO} is the fixed-order NLO cross section obtained from MCFM, and σ'_{NLL} is the resummed cross section up to NLL$'$ accuracy presented in Eq. (50). $\sigma_{\text{NLL}'}^{\text{exp}}$ captures the singular features of σ_{NLO}, and is obtained by expanding $\sigma_{\text{NLL}'}$ with all scales set to a common value μ. Schematically, we have

$$\begin{aligned}
\sigma_{\text{NLL}'} &= \sigma_{\text{LO}} \left(1 + \alpha_s g_0\right) e^{-Lg_{\text{LL}}(\alpha_s L) - g_{\text{NLL}}(\alpha_s L)} \\
\sigma_{\text{NLL}'}^{\text{exp}} &= \sigma_{\text{LO}} \left(1 + \alpha_s \left[-g_2 L^2 - g_1 L + g_0\right]\right),
\end{aligned} \tag{52}$$

where $L\, g_{\text{LL}}$ and g_{NLL} resum the leading and next-to-leading logarithms, respectively. The difference between σ_{NLO} and the expanded NLL$'$ result $\sigma_{\text{NLL}'}^{\text{exp}}$ only contains power-suppressed contributions for large values of Q:

$$\sigma_{\text{non-singular}} \equiv \sigma_{\text{NLO}} - \sigma_{\text{NLL}'}^{\text{exp}} \sim \mathcal{O}\left(R^2 L, \frac{p_T^{\text{veto}}}{Q} L, \frac{p_T^{\text{veto}}}{Q} \ln R, \cdots\right), \tag{53}$$

with $L = \ln\left(Q/p_T^{\text{veto}}\right)$, and Q stands for any kinematic quantity of order M_H. Since the scale QR is used to define the jet mode, the $R^2 L$ terms are regarded as power suppressed. We have demonstrated explicitly in Ref. [61] that our formalism correctly captures the singular terms at NLO as $L \to 0$.

8.2.3   Validity of the effective theory

We comment here briefly on the expected range of validity of our effective theory approach. In our derivation of the factorization theorem, we assumed that the signal jet p_T^J is of order M_H. This configuration contributes a non-negligible fraction, roughly 30%, of the experimentally-interesting total cross section for $p_T^{\text{veto}} \sim 30$ GeV and $p_T^J > p_T^{\text{veto}}$. Our factorization theorem holds for $p_T^{\text{veto}} \ll p_T^J \sim Q$, but breaks down when $p_T^J \sim p_T^{\text{veto}} \ll M_H$. Additional large logarithms of the form $\ln^2 M_H/p_T^J$ and

$L \times p_{\mathrm{T}}^{\mathrm{veto}}/p_{\mathrm{T}}^{\mathrm{J}}$ are not resummed in our formalism. We describe these terms only as well as a fixed NLO calculation. A different effective theory is needed for this regime to correctly sum the large logarithms. We do not consider this theory in this contribution; our goal here is to consistently apply the currently available formalism at $\mathrm{NLL}' + \mathrm{NLO}$ to see to what extent we can reduce the theoretical uncertainty.

Interestingly, the $p_{\mathrm{T}}^{\mathrm{J}} \sim M_{\mathrm{H}}$ region contributes roughly 50% of the uncertainty in the one-jet bin, larger than might be expected. We show this by computing the NLO cross section for an example parameter choice. We set $M_{\mathrm{H}} = 126$ GeV and $p_{\mathrm{T}}^{\mathrm{veto}} = 25$ GeV, and divide the Higgs plus one-jet cross section, whose inclusive value is $\sigma_{\mathrm{NLO}}^{1j} = 5.75^{+2.03}_{-2.66}$ pb, into two bins: the first with $p_{\mathrm{T}}^{\mathrm{J}} < M_{\mathrm{H}}/2$, and the second with $p_{\mathrm{T}}^{\mathrm{J}} > M_{\mathrm{H}}/2$. As explained in detail later in Section 8.2.4, we use the fixed-order cross section in the first bin since our effective-theory analysis does not hold, and turn on resummation in the second bin. Computing the cross section at NLO in each bin, and estimating the uncertainties as described in detail in Section 8.2.4, we find

$$\sigma_{\mathrm{NLO}}^{1j}(p_{\mathrm{T}}^{\mathrm{J}} < M_{\mathrm{H}}/2) = 4.74^{+1.31}_{-1.29} \text{ pb} \,,$$
$$\sigma_{\mathrm{NLO}}^{1j}(p_{\mathrm{T}}^{\mathrm{J}} > M_{\mathrm{H}}/2) = 1.01^{+0.85}_{-1.51} \text{ pb} \,. \tag{54}$$

The central values have been obtained using the scale choice for $\mu = M_{\mathrm{H}}/2$.[27] Although it accounts for less than 25% of the cross section, the region where our effective-theory analysis can improve the uncertainties contributes roughly half of the error in the full one-jet bin.

8.2.4 Scale choices and uncertainty estimation

Since the resummation holds only for $p_{\mathrm{T}} \sim M_{\mathrm{H}}$, we wish to turn it off and recover the fixed-order NLO result as $p_{\mathrm{T}}^{\mathrm{J}}$ becomes small. To do so, we note that the fixed order cross section σ_{NLO} and the expanded NLL' cross section $\sigma_{\mathrm{NLL}'}^{\mathrm{exp}}$ depend only on the scale $\mu_{\mathrm{R}} = \mu_{\mathrm{F}} = \mu$, while $\sigma_{\mathrm{NLL}'}$ also depends on the various scales $\mu_{\mathrm{H}}, \mu_{\mathrm{J}}, \mu_{\mathrm{B}}, \mu_{\mathrm{S}}, \nu_{\mathrm{B}}$ and ν_{S} at which the hard, jet, beam, and soft functions are evaluated. The optimal choice for each scale can be determined by minimizing the higher order corrections to each separate component. These functions are then RG-evolved from their respective starting scales μ_i and ν_i to the common scales μ and ν. Consequently, the resummation can be turned off by setting all scales to μ, so that the full $\mathrm{NLL}' + \mathrm{NLO}$ result reduces to the NLO one. We adopt a conservative scheme to turn off the resummation as soon as possible, as suggested in Ref. [55]. In the region where $p_{\mathrm{T}}^{\mathrm{J}} \gg p_{\mathrm{T}}^{\mathrm{veto}}$, we keep the resummation on. When $p_{\mathrm{T}}^{\mathrm{J}} \sim p_{\mathrm{T}}^{\mathrm{veto}}$, we switch off the resummation by setting all scales to μ, which leads to the fixed-order prediction. We interpolate between these two regions smoothly using

$$\mu_i^{\mathrm{int.}} = \mu + (\mu_i - \mu) \left[1 + \tanh \left(\kappa \left(p_{\mathrm{T}}^{\mathrm{J}} - p_{\mathrm{off}} \right) \right) \right]/2 \,, \tag{55}$$

where the index $i = \{\mathrm{H}, \mathrm{J}, \mathrm{B}, \mathrm{S}\}$ runs over all appearing scales. We use similar expressions for the ν's. Our numerical predictions are obtained using the $\mu_i^{int.}$ expressions in our code. When $p_{\mathrm{T}}^{\mathrm{J}} < p_{\mathrm{off}}$, the resummation starts to vanish. We set $p_{\mathrm{off}} = \max(2p_{\mathrm{T}}^{\mathrm{veto}}, \frac{M_{\mathrm{H}}}{2})$ to be the default value.[28] When making uncertainty estimations, we vary each scale separately. In the resummation region, the cross section is relatively insensitive to the variation of μ. In the fixed-order range, it is insensitive to μ_i and ν_i. The slope κ controls how smoothly we turn off the resummation. We find that the interpolated cross section is insensitive to the choice of κ. Varying κ in a reasonable range from 0.04 to 0.2, the effect on the cross section is much smaller than our estimated uncertainties.

To derive the uncertainties in both the fixed-order and RG-improved results, we vary all scales appearing in the cross section around their central values by factors of two in both directions in order to estimate the theoretical error. To avoid an underestimate of the uncertainty of the fixed-order calculation,

---

[27]We note that using a larger central scale choice leads to the same conclusions regarding the relative uncertainties of the two bins.

[28]The reason for this choice is that our EFT is valid when $p_{\mathrm{T}}^{\mathrm{J}}$ is located in the hard domain whose lower boundary is estimated to be $M_{\mathrm{H}}/2$, and it entirely breaks down when $p_{\mathrm{T}}^{\mathrm{J}}$ falls into the "soft" regime whose upper boundary is roughly $2p_{\mathrm{T}}^{\mathrm{veto}}$.

we follow the procedure suggested by Stewart and Tackmann [236]. We split the exclusive one-jet cross section into the difference of one-jet inclusive and two-jet inclusive results:

$$\sigma_{1j} = \sigma_{\geq 1j} - \sigma_{\geq 2j} \,. \tag{56}$$

We estimate the scale uncertainty for each piece separately and add them in quadrature to obtain the scale uncertainty for the exclusive cross section:

$$\delta_{1j,\mathrm{NLO}}^2 = \delta_{\geq 1j,\mathrm{NLO}}^2 + \delta_{\geq 2j,\mathrm{NLO}}^2 \,. \tag{57}$$

For the $\mathrm{NLL}' + \mathrm{NLO}$ result, the uncertainty is derived by adding in quadrature the separate variations of all scales which enter [236]:

$$\delta_{1j}^2 = \delta_{\mathrm{non-singular},\mu}^2 + \delta_{\mathrm{NLL}',\mu}^2 + \delta_{\mathrm{NLL}',\mu_\mathrm{H}}^2 + \delta_{\mathrm{NLL}',\mu_\mathrm{J}}^2 + \delta_{\mathrm{NLL}',\mu_\mathrm{B},\nu_\mathrm{B}}^2 + \delta_{\mathrm{NLL}',\mu_\mathrm{S},\nu_\mathrm{S}}^2 \,. \tag{58}$$

Before continuing we comment briefly on the structure of Eq. (58). In order to perform the matching to fixed order in Eq. (51), we RG-evolve the NLL' result so that all scales are set to the common scale μ. We then add on the non-singular NLO terms via the difference between the full NLO cross section and the expanded NLL' results. This explains the first two contributions to the above equations. As the hard and jet functions live at the scales $\sqrt{M_\mathrm{H} p_\mathrm{T}^\mathrm{J}}$ and $p_\mathrm{T}^\mathrm{J} R$ respectively [60], these scale variations are treated as uncorrelated in Eq. (58). Finally, the variations of beam and soft functions, which live at the scale $p_\mathrm{T}^\mathrm{veto}$, are added to this.

When we apply this formalism and assume actual LHC kinematic cuts, a large fraction of the cross section comes from the low-p_T^J regime where $p_\mathrm{T}^\mathrm{J} < p_\mathrm{off}$, and the fixed-order calculation dominates. In this situation, we split the cross section into two regions, one with $p_\mathrm{T}^\mathrm{veto} < p_\mathrm{T}^\mathrm{J} < p_\mathrm{off}$ and the other with $p_\mathrm{T}^\mathrm{J} > p_\mathrm{off}$. For the former region, we use Eq. (57) to estimate the uncertainty and for the latter one, we utilize Eq. (58). We combine these two linearly to estimate the scale dependence for the RG-improved cross section:

$$\delta_{1j}(p_\mathrm{T}^\mathrm{J} > p_\mathrm{T}^\mathrm{veto}) = \delta_{1j,\mathrm{NLO}}(p_\mathrm{T}^\mathrm{J} < p_\mathrm{off}) + \delta_{1j}(p_\mathrm{T}^\mathrm{J} > p_\mathrm{off}) \,. \tag{59}$$

Since the resummation in the result used for $p_\mathrm{T}^\mathrm{J} > p_\mathrm{off}$ is turned off quickly by using the interpolation in Eq. (55), and the uncertainty of the fixed-order cross section used for $p_\mathrm{T}^\mathrm{J} < p_\mathrm{off}$ is obtained using the Stewart-Tackmann prescription, we believe that this leads to a very conservative estimate of the theoretical error after performing our RG-improvement.

8.2.5 Numerics for the LHC

We now present predictions and uncertainty estimates for use in LHC analyses. For the following numerical results, and those shown above, we use the MSTW 2008 parton distribution functions [168] at NLO. We assume an 8 TeV LHC, and $M_\mathrm{H} = 126$ GeV unless stated otherwise. We demand that the leading jet be produced with rapidity $|y_\mathrm{J}| < 4.5$, and veto all other jets with $p_\mathrm{T} > p_\mathrm{T}^\mathrm{veto}$ over the entire rapidity range. The following central values are used for the scales which appear:

$$\begin{aligned}
\mu &= \sqrt{(m_\mathrm{H}^\mathrm{T})_\mathrm{min}(p_T^\mathrm{J})_\mathrm{min}}, &\qquad \mu_\mathrm{H} &= \sqrt{m_\mathrm{H}^\mathrm{T} p_T^\mathrm{J}}, \\
\mu_\mathrm{J} &= p_\mathrm{T}^\mathrm{J} R, &\qquad \mu_\mathrm{B} &= \mu_\mathrm{S} = p_\mathrm{T}^\mathrm{veto}, \\
\nu_{B_{a,b}} &= x_{a,b}\sqrt{s}, &\qquad \nu_\mathrm{S} &= p_\mathrm{T}^\mathrm{veto} \,.
\end{aligned} \tag{60}$$

where $m_\mathrm{H}^\mathrm{T} = \sqrt{M_\mathrm{H}^2 + p_\mathrm{T}^{\mathrm{J},2}}$. We note that these central scale values, as well as the variations up and down by a factor of two, are used as the μ_i on the right-hand side of Eq. (55). The actual numerical scale

Table 24: Shown are the central values and uncertainties for the NLO cross section, the resummed cross section, and the event fractions in the one-jet bin using both the fixed-order and the resummed results. Numbers are given for several Higgs masses and for $p_T^{\text{veto}} = 25, 30$ GeV.

M_H (GeV)	p_T^{veto} (GeV)	σ_{NLO} (pb)	$\sigma_{\text{NLL}'+\text{NLO}}$ (pb)	f_{NLO}^{1j}	$f_{\text{NLL}'+\text{NLO}}^{1j}$
124	25	$5.92^{+35\%}_{-46\%}$	$5.62^{+29\%}_{-30\%}$	$0.299^{+38\%}_{-49\%}$	$0.283^{+33\%}_{-34\%}$
125	25	$5.85^{+34\%}_{-46\%}$	$5.55^{+29\%}_{-30\%}$	$0.300^{+37\%}_{-49\%}$	$0.284^{+33\%}_{-33\%}$
126	25	$5.75^{+35\%}_{-46\%}$	$5.47^{+30\%}_{-30\%}$	$0.300^{+38\%}_{-49\%}$	$0.284^{+34\%}_{-33\%}$
124	30	$5.25^{+31\%}_{-41\%}$	$4.83^{+29\%}_{-29\%}$	$0.265^{+35\%}_{-43\%}$	$0.244^{+33\%}_{-33\%}$
125	30	$5.19^{+32\%}_{-41\%}$	$4.77^{+30\%}_{-29\%}$	$0.266^{+35\%}_{-43\%}$	$0.244^{+33\%}_{-33\%}$
126	30	$5.12^{+32\%}_{-41\%}$	$4.72^{+30\%}_{-29\%}$	$0.266^{+35\%}_{-43\%}$	$0.246^{+33\%}_{-32\%}$

choices used in the code are the $\mu_i^{int.}$ appearing on the left-hand side of Eq. (55). We use $\kappa = 0.2$ to produce all numerical results, although we have checked that their dependence on κ is negligible.

We show in Fig. 62 the cross section as a function of the lower cut on p_T^J for a fixed $p_T^{\text{veto}} = 30$ GeV. The solid line and blue band show the NLL$'$ + NLO result together with its perturbative uncertainty, which can be compared with the dashed line and yellow band showing the fixed NLO result with its uncertainty. Even for values of the lower p_T^J cut near p_T^{veto}, a sizeable reduction of the uncertainty occurs when the NLL$'$ + NLO result is used. The reason for this is discussed in Section 8.2.3; roughly half of the uncertainty comes from the high-p_T^J region, which is exactly the parameter space improved by our effective-theory description.
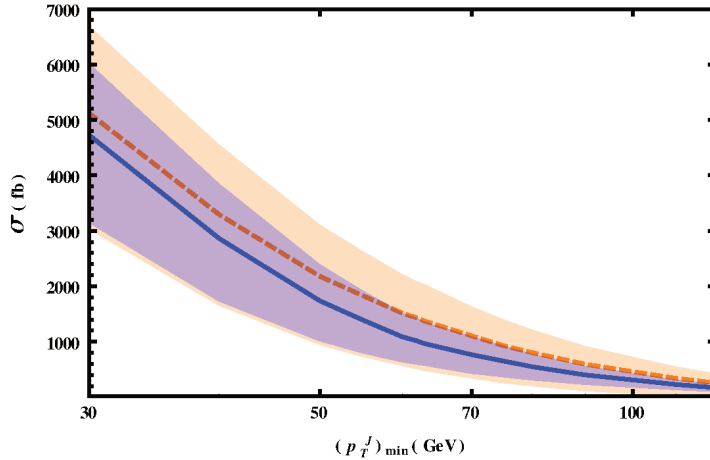
Fig. 62: Shown are the NLL$'$ + NLO (blue band) and NLO (yellow band) cross sections for fixed $p_T^{\text{veto}} = 30$ GeV as a function of the lower cut on p_T^J.

We present in Table 24 numerical results for both the cross sections and the fraction of events in the one-jet bin, f^{1j}. We define the event fraction as

$$f_x^{1j} = \frac{\sigma_x}{\sigma_{\text{inc}}}, \tag{61}$$

where x denotes either the NLO or the NLL$'$ + NLO cross section in the one-jet bin. We note that our values for f_{NLO}^{1j} are consistent with those obtained by the ATLAS collaboration, which provides a cross-check of our results. The total cross section σ_{inc}, as well as its estimated uncertainty, is taken from the LHC Higgs cross section working group. The uncertainties shown are calculated as discussed

in Section 8.2.4. Results are given for $M_H = 124 - 126$ GeV, and for $p_T^{\text{veto}} = 25$ and 30 GeV. The reductions of the uncertainties are significant for both values of p_T^{veto}. Symmetrizing the error for this discussion, the estimated uncertainty on the cross section improves from $\pm 40\%$ at NLO to $\pm 30\%$ at NLL$'$ + NLO, a reduction of one quarter of the initial value. The one-jet fraction uncertainty decreases from $\pm 44\%$ to $\pm 34\%$. For $p_T^{\text{veto}} = 30$ GeV, the error on the cross section decreases from $\pm 36\%$ to $\pm 29\%$ when resummation is included, while the error on f^{1j} decreases from $\pm 39\%$ to $\pm 33\%$. We note that these are extremely conservative error estimates, as discussed in Section 8.2.4. We default to the Stewart-Tackmann prescription over a large region of the relevant parameter space, and turn off the resummation at a relatively high value of p_T^J. Enough of the error comes from the high p_T^J region that our RG-improvement is effective in taming the uncertainty.

8.3 Perturbative uncertainties in the Higgs plus 2-jet VBF selection[29]

With the typical kinematic cuts used by the ATLAS and CMS collaborations to select events from vector-boson fusion (VBF), the VBF sample is contaminated by a $\sim 25\%$ fraction from Higgs + 2 jet production via gluon fusion (ggF). In this section we discuss the perturbative uncertainties in this contribution, which tend to be sizable and therefore require a reliable estimate. Typical VBF selections include indirect restrictions or explicit vetoes on additional jet activity, primarily to reduce non-Higgs backgrounds but also to reduce the amount of contamination from ggF. Such exclusive restrictions constitute a nontrivial jet binning, where the inclusive Higgs plus 2-jet cross section is effectively divided into an exclusive 2-jet bin and a remaining inclusive 3-jet bin. With such a jet binning one has to account for two sources of perturbative uncertainties: In addition to the absolute yield uncertainty which is correlated between the jet bins, there is also a migration uncertainty which is anticorrelated and drops out in the sum of the bins. This migration uncertainty is associated with the additional perturbative uncertainty induced by the exclusive binning cut. In practice, the experimentally relevant region typically lies inside a transition region between the fully inclusive region (no binning) and the extreme exclusive region (very tight binning). In this region, fixed-order perturbation theory can still be applied however since the logarithms in the perturbative series induced by the binning are already sizeable their effect on the migration uncertainty must be taken into account. This can be achieved using the Stewart-Tackmann (ST) method [236].

We discuss in detail the application of the ST method to estimate the perturbative uncertainties in the fixed NLO predictions for pp $\rightarrow$ H + 2 jets via ggF from MCFM [258, 259][30]. To be specific we will concentrate on the VBF selection of the current H $\rightarrow \gamma\gamma$ analyses. Qualitatively, our results apply equally to other decay channels with similar VBF selection cuts. After reviewing the general setup in Section 8.3.1 and the jet-binning uncertainties in Section 8.3.2, we first discuss the fixed-order perturbative uncertainties in a cut-based setup closely following Ref. [262]. In Section 8.3.6 we then discuss a simple method to propagate the theory uncertainties into a multivariate selection.

8.3.1 Setup and inclusive 2-jet cross section

We use MCFM [258, 259] to compute the NLO cross section, with the ggH effective vertex in the infinite top mass limit, and then rescale the cross section with the exact m_t dependence of the total LO cross section, $\sigma_{\text{LO}}(m_t)/\sigma_{\text{LO}}(\infty) = 1.0668$ for $M_H = 125$ GeV. We take $\sqrt{s} = 8$ TeV, $M_H = 125$ GeV, and use the MSTW2008 [168] NLO PDFs with their corresponding value of $\alpha_s(m_Z) = 0.12018$. In our analysis we implement the 2-jet selection and VBF selection cuts from the current ATLAS and CMS H $\rightarrow \gamma\gamma$ analyses (summarized in Table 25 below). However, note that we consider the cross section for the production of an on-shell Higgs boson, without including any branching ratios or cuts on the Higgs decay products.

---

[29]F. U. Bernlochner, S. Gangal, D. Gillberg, F. J. Tackmann

[30]For simplicity we denote the process as gg $\rightarrow$ H + 2j below, where a sum over all possible partonic channels with a ggF vertex is implied.
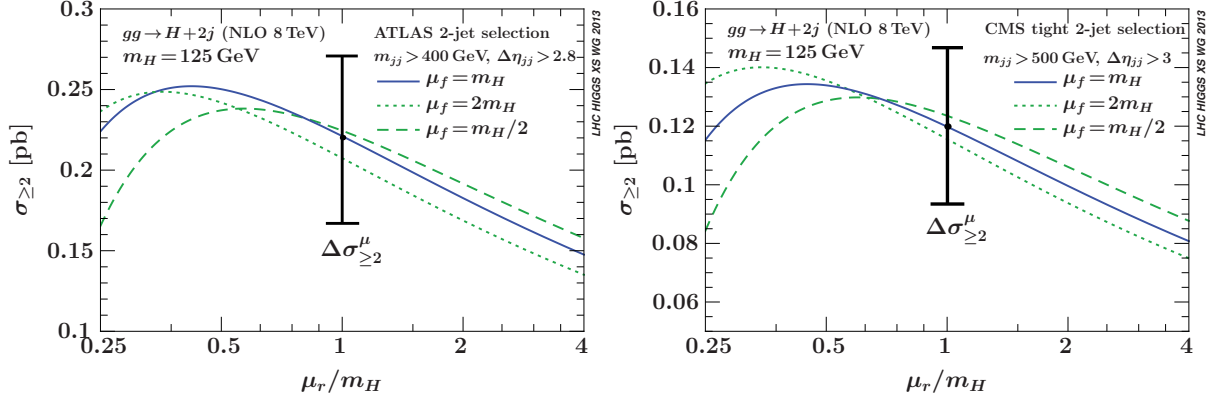
Fig. 63: Inclusive 2-jet cross section over a range of μ_R/M_H for ATLAS VBF selection (left panel) and CMS tight selection (right panel). The three curves show different values of μ_F. The blue solid, green dotted, and green dashed curves correspond to $\mu_F = M_H$, $\mu_F = 2M_H$, and $\mu_F = M_H/2$, respectively. The uncertainty bars show the inclusive 2-jet scale variation uncertainty.

For all our central value predictions we use $\mu_R = \mu_F = M_H$, which was also used in Ref. [258, 259]. In Figure 63, we show the scale dependence of the inclusive 2-jet cross section, $\sigma_{\geq 2}$, where we plot it over a range of $1/4 < \mu_R/M_H < 4$ for three different values of μ_F. To estimate the scale uncertainty we consider the range $0.5 \leq \mu_R/M_H \leq 2$. The maximum deviation from the central value is given by the green dotted curve for $\mu_F = \mu_R = 2M_H$. We use this maximum variation to construct a symmetric scale uncertainty for the inclusive 2-jet cross section, denoted as $\Delta\sigma_{\geq 2}^\mu$, and shown by the uncertainty bar in Figure 63. It corresponds to a relative uncertainty at NLO of 21%, which is similar to what was found in earlier studies [258, 259] where a somewhat looser VBF selection was used. We also require scale uncertainties for the inclusive 3-jet cross section, $\Delta\sigma_{\geq 3}^\mu$, for which we symmetrize the scale variation by taking half of the difference between the $\mu = M_H/2$ and $\mu = 2M_H$ variations, as discussed in Ref. [262].

8.3.2 Review of jet binning uncertainties

We consider the *inclusive* N-jet cross section, $\sigma_{\geq N}$, for some process containing at least N jets, and assume that $\sigma_{\geq N}$ is a sufficiently inclusive quantity such that it can be computed in fixed-order perturbation theory. We are interested in the case where $\sigma_{\geq N}$ is divided up into a corresponding *exclusive* N-jet cross section, σ_N, and a remainder $\sigma_{\geq N+1}$,

$$\sigma_{\geq N} = \sigma_N(\text{excl. cut}) + \sigma_{\geq N+1}(\text{inverse excl. cut}). \tag{62}$$

All three cross sections here have the *same* selection cuts applied that identify the leading N signal jets. What defines σ_N to be "exclusive" is that the additional exclusive cut applied to it restricts the phase space of additional emissions in such a way that σ_N is dominated by configurations close to the N-parton Born kinematics. In particular, at leading order (LO) in perturbation theory $\sigma_{\geq N}^{\text{LO}} = \sigma_N^{\text{LO}}$, while relative to these $\sigma_{\geq N+1}$ is suppressed by $\mathcal{O}(\alpha_s)$. In other words, $\sigma_{\geq N+1}$ requires at least one additional emission to be non-vanishing. Hence, we can consider it an inclusive $(N + 1)$-jet cross section with at least $N + 1$ jets.[31]

In the simplest case, $\sigma_{\geq N}$ is divided into the two jet bins σ_N and $\sigma_{\geq N+1}$ by using a fixed cut on some kinematic variable, p_{N+1}, which characterizes additional emissions, with $p_{N+1} = 0$ for a tree-level N-parton state. (Two examples we will consider are p_{THjj} and $\Delta\phi_{H-jj}$, defined below.) The two jet

---

[31]Note that that $\sigma_{\geq N+1}$ is defined by inverting the exclusive cut that defines σ_N and so (as in the examples we consider) does not necessarily require the explicit identification of another well-separated jet via a jet algorithm.

bins then correspond to the integrals of the differential spectrum $\mathrm{d}\sigma/\mathrm{d}p_{N+1}$ above and below some cut,

$$\sigma_{\geq N} = \int_0^{p^{\mathrm{cut}}} \mathrm{d}p_{N+1} \frac{\mathrm{d}\sigma_{\geq N}}{\mathrm{d}p_{N+1}} + \int_{p^{\mathrm{cut}}} \mathrm{d}p_{N+1} \frac{\mathrm{d}\sigma_{\geq N}}{\mathrm{d}p_{N+1}} \equiv \sigma_N(p^{\mathrm{cut}}) + \sigma_{\geq N+1}(p^{\mathrm{cut}})\,. \tag{63}$$

In general, the jet bin boundary can be a much more complicated function of phase space, as in the multivariate analysis considered in Section 8.3.6.

We are interested in the uncertainties involved in the binning. The covariance matrix for $\{\sigma_N, \sigma_{\geq N+1}\}$ is a symmetric 2×2 matrix with three independent parameters. A convenient and general parameterization is to write it in terms of two components,

$$C = \begin{pmatrix} (\Delta_N^{\mathrm{y}})^2 & \Delta_N^{\mathrm{y}}\,\Delta_{\geq N+1}^{\mathrm{y}} \\ \Delta_N^{\mathrm{y}}\,\Delta_{\geq N+1}^{\mathrm{y}} & (\Delta_{\geq N+1}^{\mathrm{y}})^2 \end{pmatrix} + \begin{pmatrix} \Delta_{\mathrm{cut}}^2 & -\Delta_{\mathrm{cut}}^2 \\ -\Delta_{\mathrm{cut}}^2 & \Delta_{\mathrm{cut}}^2 \end{pmatrix}. \tag{64}$$

Here, the first term is an absolute "yield" uncertainty, denoted with a superscript "y", which (by definition) is 100% correlated between the two bins σ_N and $\sigma_{\geq N+1}$. The second term is a "migration" uncertainty between the bins and corresponds to the uncertainty introduced by the binning cut. It has the same absolute size, Δ_{cut}, for both bins and is 100% anticorrelated between them, such that it drops out when the two bins are added. Hence, the total uncertainty for each bin is given by

$$\Delta_N^2 = (\Delta_N^{\mathrm{y}})^2 + \Delta_{\mathrm{cut}}^2\,, \qquad \Delta_{\geq N+1}^2 = (\Delta_{\geq N+1}^{\mathrm{y}})^2 + \Delta_{\mathrm{cut}}^2\,, \tag{65}$$

while the total uncertainty on their sum, i.e. on $\sigma_{\geq N}$, is given by the total yield uncertainty,

$$\Delta_{\geq N} = \Delta_{\geq N}^{\mathrm{y}} = \Delta_N^{\mathrm{y}} + \Delta_{\geq N+1}^{\mathrm{y}}\,. \tag{66}$$

Considering the perturbative uncertainties, the basic question is how each of the uncertainties in Eq.(64) can be evaluated. The fixed-order prediction provides us with two independent pieces of information, namely the variations obtained by the standard scale variations, which we denote as $\Delta_{\geq N}^{\mu}$, Δ_N^{μ}, $\Delta_{\geq N+1}^{\mu}$, and which satisfy $\Delta_{\geq N}^{\mu} = \Delta_N^{\mu} + \Delta_{\geq N+1}^{\mu}$. The usual assumption that the standard fixed-order scale variations can be used to obtain a reliable estimate of the total uncertainties in the *inclusive* cross sections imposes the two conditions

$$\Delta_{\geq N} = \Delta_{\geq N}^{\mu}\,, \qquad \Delta_{\geq N+1} = \Delta_{\geq N+1}^{\mu}\,. \tag{67}$$

Together with Eqs.(65) and (66) these lead to

$$\begin{aligned} \text{i)} && \Delta_{\geq N}^{\mu} &= \Delta_N^{\mathrm{y}} + \Delta_{\geq N+1}^{\mathrm{y}}\,, \\ \text{ii)} && (\Delta_{\geq N+1}^{\mu})^2 &= (\Delta_{\geq N+1}^{\mathrm{y}})^2 + \Delta_{\mathrm{cut}}^2\,. \end{aligned} \tag{68}$$

Thus, the basic question is how to divide up $\Delta_{\geq N+1}^{\mu}$ between $\Delta_{\geq N+1}^{\mathrm{y}}$ and Δ_{cut} in order to satisfy condition ii). Condition i) then determines Δ_N^{y}. The nontrivial effect Δ_{cut} can have is on the size of Δ_N as well as on the off-diagonal entries in Eq.(64), which determine the correlation between Δ_N and $\Delta_{\geq N+1}$.

Clearly, the simplest is to neglect the effect of Δ_{cut} altogether and to directly use the scale variations to estimate the uncertainties, i.e., to take

$$\Delta_N^{\mathrm{y}} = \Delta_{\geq N}^{\mu} - \Delta_{\geq N+1}^{\mu} \equiv \Delta_N^{\mu}\,, \quad \Delta_{\geq N+1}^{\mathrm{y}} = \Delta_{\geq N+1}^{\mu}\,, \quad \Delta_{\mathrm{cut}} = 0\,. \tag{69}$$

which leads to

$$\text{direct:} \qquad C = \begin{pmatrix} (\Delta_N^{\mu})^2 & \Delta_N^{\mu}\,\Delta_{\geq N+1}^{\mu} \\ \Delta_N^{\mu}\,\Delta_{\geq N+1}^{\mu} & (\Delta_{\geq N+1}^{\mu})^2 \end{pmatrix}. \tag{70}$$

Note that since $\sigma_{\geq N+1}$ starts at higher order in perturbation theory than $\sigma_{\geq N}$, its relative uncertainty $\Delta^\mu_{\geq N+1}/\sigma_{\geq N+1}$ will typically be (much) larger than $\sigma_{\geq N}$'s relative uncertainty $\Delta^\mu_{\geq N}/\sigma_{\geq N}$. This means one cannot simply apply the latter as the relative yield uncertainty in each bin, which means one *cannot* take $\Delta^y_i = (\Delta^\mu_{\geq N}/\sigma_{\geq N})\sigma_i$, as this would violate the condition $\Delta_{\geq N+1} = \Delta^\mu_{\geq N+1}$. This point has already been emphasized in earlier studies [238].

The direct scale variation choice is reasonable as long as the effect of $\Delta_{\rm cut}$ is indeed negligible. It is certainly justified if numerically $\Delta^\mu_{\geq N} \gg \Delta^\mu_{\geq N+1}$, since any uncertainty due to migration effects can be at most as large as $\Delta^\mu_{\geq N+1}$ (by virtue of condition ii) above). This can happen, for example, when $\Delta^\mu_{\geq N}$ is sizable due to large perturbative corrections in $\sigma_{\geq N}$ and/or the binning cut is very loose (i.e., is cutting out only a small fraction of phase space) such that $\sigma_{\geq N+1}$ is numerically small to begin with.

In perturbation theory, the effect of the binning cut is to introduce Sudakov double logarithms in the perturbative series of σ_N and $\sigma_{\geq N+1}$, which have opposite sign and cancel in the sum of the two bins, schematically

$$\sigma_{\geq N} \simeq \sigma_{\rm B}[1 + \alpha_{\rm s} + \alpha_{\rm s}^2 + \mathcal{O}(\alpha_{\rm s}^3)]\,,$$
$$\sigma_{\geq N+1} \simeq \sigma_{\rm B}[\alpha_{\rm s}(L^2 + L + 1) + \alpha_{\rm s}^2(L^4 + L^3 + L^2 + L + 1) + \mathcal{O}(\alpha_{\rm s}^3 L^6)]\,,$$
$$\sigma_N = \sigma_{\geq N} - \sigma_{\geq N+1}\,, \tag{71}$$

where $\sigma_{\rm B}$ denotes the Born cross section and L is a Sudakov logarithm, e.g. for Eq.(63) $L = \ln(p^{\rm cut}/Q)$ where $Q \sim M_{\rm H}$ is a typical hard scale. The perturbative migration uncertainty $\Delta_{\rm cut}$ can be directly associated with the perturbative uncertainty in the logarithmic series induced by the binning, and so should not be neglected once the logarithms have a noticeable effect. In particular, as demonstrated in Ref. [236], the simple choice in Eqs.(69) and (70) can easily lead to an underestimate of Δ_N in the region where there are sizable numerical cancellations between the two series in $\sigma_{\geq N}$ and $\sigma_{\geq N+1}$. Since in this region the dominant contribution to $\sigma_{\geq N+1}$ comes from the logarithmic series, varying the scales in $\sigma_{\geq N+1}$ directly tracks the size of the logarithms, which means we can use $\Delta_{\rm cut} = \Delta^\mu_{\geq N+1}$ as an estimate for the binning uncertainty, as proposed in Ref. [236]. From Eq.(68), we then find

$$\Delta^y_N = \Delta^\mu_{\geq N}\,, \qquad \Delta^y_{\geq N+1} = 0\,, \qquad \Delta_{\rm cut} = \Delta^\mu_{\geq N+1}\,, \tag{72}$$

such that

$$\text{ST:} \quad C = \begin{pmatrix} (\Delta^\mu_{\geq N})^2 + (\Delta^\mu_{\geq N+1})^2 & -(\Delta^\mu_{\geq N+1})^2 \\ -(\Delta^\mu_{\geq N+1})^2 & (\Delta^\mu_{\geq N+1})^2 \end{pmatrix}\,. \tag{73}$$

Since $\Delta^\mu_{\geq N+1}$ is now used as $\Delta_{\rm cut}$, the effective outcome is that one treats $\Delta^\mu_{\geq N}$ and $\Delta^\mu_{\geq N+1}$ as uncorrelated. More generally, we can introduce a parameter $0 \leq \rho \leq 1$, which controls the fraction of $\Delta^\mu_{\geq N+1}$ assigned to $\Delta^y_{\geq N+1}$, such that

$$\Delta^y_N = \Delta^\mu_{\geq N} - \rho\,\Delta^\mu_{\geq N+1}\,, \qquad \Delta^y_{\geq N+1} = \rho\,\Delta^\mu_{\geq N+1}\,, \qquad \Delta_{\rm cut} = \sqrt{1-\rho^2}\,\Delta^\mu_{\geq N+1}\,, \tag{74}$$

which leads to

$$\text{ST}(\rho): \quad C = \begin{pmatrix} (\Delta^\mu_{\geq N})^2 + (\Delta^\mu_{\geq N+1})^2 - 2\rho\,\Delta^\mu_{\geq N}\Delta^\mu_{\geq N+1} & (\rho\,\Delta^\mu_{\geq N} - \Delta^\mu_{\geq N+1})\Delta^\mu_{\geq N+1} \\ (\rho\,\Delta^\mu_{\geq N} - \Delta^\mu_{\geq N+1})\Delta^\mu_{\geq N+1} & (\Delta^\mu_{\geq N+1})^2 \end{pmatrix}\,. \tag{75}$$

From this one can easily see that ρ corresponds the correlation between $\Delta^\mu_{\geq N}$ and $\Delta^\mu_{\geq N+1}$. The choice $\rho = 1$ would be equivalent to the case in Eq.(70), while $\rho = 0$ reproduces Eqs.(72) and (73). Hence, from the above arguments one should take ρ to be small. The dependence on ρ was explored in Ref. [262] where it was found that for $\rho \lesssim 0.4$ the results are not very sensitive to the precise value of ρ, so we take $\rho = 0$ as our default choice.

Another prescription to obtain fixed-order uncertainty estimates for exclusive jet cross section, which is based on using veto efficiencies, was applied in Ref. [56] to the 0-jet case at NNLO. We will
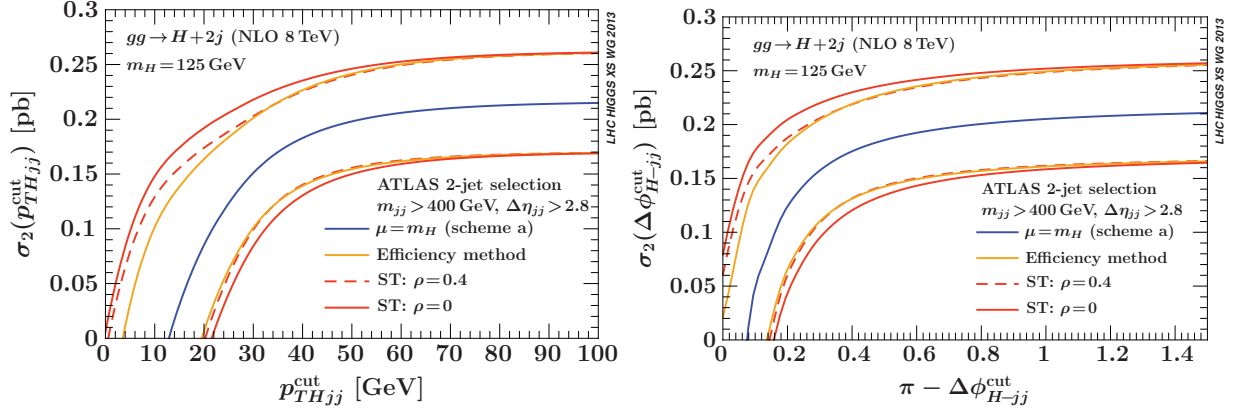
Fig. 64: Comparison of the ST method with the efficiency method for p_{THjj}^{cut} (left panel) and $\pi - \Delta\phi_{\text{H}-jj}^{\text{cut}}$ (right panel) using the ATLAS VBF selection. The exclusive scale uncertainties from both methods are consistent with each other. The uncertainties from the efficiency method are very close to those from the ST method with $\rho = 0.4$.

refer to it as "efficiency method". In Ref. [239] it was shown that for the case of H + 0 jets at NNLO the ST and efficiency methods yield very similar uncertainties, providing a good cross check on both methods. The starting point in the efficiency method is to write the exclusive jet cross section in terms of the corresponding inclusive jet cross section times the corresponding exclusive efficiency, i.e., applied to the $N = 2$ case, one has

$$\sigma_2 = \sigma_{\geq 2}\Big(1 - \frac{\sigma_{\geq 3}}{\sigma_{\geq 2}}\Big) \equiv \sigma_{\geq 2} \times \epsilon_2, \qquad \sigma_{\geq 3} = \sigma_{\geq 2}\left(1 - \epsilon_2\right). \tag{76}$$

The basic assumption made in Ref. [56] is to treat the perturbative uncertainties in $\sigma_{\geq 2}$ and ϵ_2 as uncorrelated. Since the 2-jet efficiency $\epsilon_2 = 1 - \sigma_{\geq 3}/\sigma_{\geq 2}$ is still an exclusive quantity, similar cancellations between the two perturbative series for $\sigma_{\geq 2}$ and $\sigma_{\geq 3}$ can happen in their ratio rather than in their difference, so the direct scale variation for ϵ_2 might not provide a reliable uncertainty estimate. To circumvent this, the perturbative uncertainty in ϵ_2 is instead estimated by using three different schemes for how to write the perturbative result for ϵ_2, which differ by uncontrolled higher-order terms in α_{s}, as follows:[32]

$$\text{Scheme (a):} \qquad \epsilon_2^{(a)} = 1 - \frac{\sigma_{\geq 3}}{\sigma_{\geq 2}} = 1 - \frac{\alpha_{\text{s}}\sigma_{\geq 3}^{(0)}}{\sigma_{\geq 2}^{(0)} + \alpha_{\text{s}}\sigma_{\geq 2}^{(1)}} + \mathcal{O}(\alpha_{\text{s}}^2),$$

$$\text{Scheme (b):} \qquad \epsilon_2^{(b)} = 1 - \alpha_{\text{s}}\frac{\sigma_{\geq 3}^{(0)}}{\sigma_{\geq 2}^{(0)}} + \mathcal{O}(\alpha_{\text{s}}^2),$$

$$\text{Scheme (c):} \qquad \epsilon_2^{(c)} = 1 - \alpha_{\text{s}}\frac{\sigma_{\geq 3}^{(0)}}{\sigma_{\geq 2}^{(0)}}\left(1 - \alpha_{\text{s}}\frac{\sigma_{\geq 2}^{(1)}}{\sigma_{\geq 2}^{(0)}}\right) + \mathcal{O}(\alpha_{\text{s}}^2), \tag{77}$$

where we expanded the inclusive 2-jet and 3-jet cross sections as

$$\sigma_{\geq 2} = \alpha_{\text{s}}^2\big[\sigma_{\geq 2}^{(0)} + \alpha_{\text{s}}\,\sigma_{\geq 2}^{(1)} + \alpha_{\text{s}}^2\,\sigma_{\geq 2}^{(2)} + \mathcal{O}(\alpha_{\text{s}}^3)\big],$$

$$\sigma_{\geq 3} = \alpha_{\text{s}}^2\big[\alpha_{\text{s}}\sigma_{\geq 3}^{(0)} + \alpha_{\text{s}}^2\,\sigma_{\geq 3}^{(1)} + \mathcal{O}(\alpha_{\text{s}}^3)\big]. \tag{78}$$

In Figure 64 we compare the results of the ST and efficiency methods for the exclusive 2-jet cross section σ_2 using cuts on p_{THjj} and $\Delta\phi_{\text{H}-jj}$ for the ATLAS VBF selection (see Section 8.3.3 below).

---

[32] As originally motivated in Ref. [56] in scheme (c) one strictly re-expands the ratio of cross section to a given order in α_{s}, which at NLO yields the same result as scheme (b). To produce another expression with differing higher order terms, the analog to scheme (c) we use here is to keep the $\mathcal{O}(\alpha_{\text{s}}^2)$ cross term that comes from expanding the denominator.

The blue solid curve shows the default NLO central value (equivalent to the scheme (a) central value). The light orange solid curves are the uncertainties obtained in the efficiency method. They are obtained by combining in quadrature the inclusive scale uncertainties $\Delta^{\mu}_{\geq 2}$ with the direct scale variations in $\epsilon^{(a)}_{2}$ treating both as uncorrelated. (Here, the values for ϵ_2 in schemes (b) and (c) lie within the scheme (a) scale variations, so we use the latter as uncertainty estimate.) The dark orange solid curves show the ST uncertainties for $\rho = 0$, which are slightly larger. The dashed lines show the ST uncertainties for $\rho = 0.4$, which are in close agreement with the efficiency method. This can be understood by noting that by varying the scales in ϵ_2 one effectively varies the scales correlated in $\sigma_{\geq 2}$ and $\sigma_{\geq 3}$, which has the effect of reintroducing a certain amount of correlation between $\Delta^{\mu}_{\geq 2}$ and $\Delta^{\mu}_{\geq 3}$ when computing σ_2, which is also what a nonzero value of ρ does. Overall, the good consistency between the various methods gives us confidence in the reliability of our uncertainty estimates.

8.3.3 Cut-based analyses

We now study the uncertainties in the exclusive $H + 2$ jet cross section as a function of two kinematic variables, p_{THjj} and $\Delta\phi_{H-jj}$. Here, p_{THjj} is the magnitude of the total transverse momentum of the Higgs-dijet system,

$$p_{THjj} = |\vec{p}_{Tj1} + \vec{p}_{Tj2} + \vec{p}_{TH}| \,. \tag{79}$$

At Born level, $p_{THjj} = 0$ and so applying a cut $p_{THjj} < p^{\text{cut}}_{THjj}$ restricts the phase space to the exclusive 2-jet region, and induces Sudakov logarithms of the form $L = \ln(p^{\text{cut}}_{THjj}/M_H)$ in the perturbative series of σ_2 and $\sigma_{\geq 3}$. At NLO p_{THjj} is equivalent to the p_T of the third jet, so it is a useful reference variable for a p_T-veto on additional emissions, such as the central jet vetoes applied in the $H \rightarrow WW$ and $H \rightarrow \tau\tau$ VBF analyses. The VBF category in the $H \rightarrow \gamma\gamma$ analyses by ATLAS and CMS includes a cut $\Delta\phi_{H-jj} > \Delta\phi^{\text{cut}}_{H-jj}$. Taking the beam direction along the z-axes, $\Delta\phi_{H-jj}$ is defined as

$$\cos\Delta\phi_{H-jj} = \frac{(\vec{p}_{Tj1} + \vec{p}_{Tj2}) \cdot \vec{p}_{TH}}{|\vec{p}_{Tj1} + \vec{p}_{Tj2}||\vec{p}_{TH}|} \,, \tag{80}$$

with the Higgs momentum given by the total momentum of the diphoton system. Events with only two jets always have $\Delta\phi_{H-jj} \approx \pi$, so the constraint $\Delta\phi_{H-jj} > \Delta\phi^{\text{cut}}_{H-jj}$ forces the kinematics into the exclusive 2-jet region and restricts additional emissions. Hence, it behaves similar to p^{cut}_{THjj} and for $\pi - \Delta\phi^{\text{cut}}_{H-jj} \rightarrow 0$ induces large logarithms in the perturbative series. The exclusive 2-jet bins defined in terms of these variables are written as

$$\sigma_2(p_{THjj} < p^{\text{cut}}_{THjj}) = \sigma_{\geq 2} - \sigma_{\geq 3}(p_{THjj} > p^{\text{cut}}_{THjj})$$
$$\sigma_2(\Delta\phi_{H-jj} > \Delta\phi^{\text{cut}}_{H-jj}) = \sigma_{\geq 2} - \sigma_{\geq 3}(\Delta\phi_{H-jj} < \Delta\phi^{\text{cut}}_{H-jj}) \,, \tag{81}$$

where in all cross sections the remaining VBF selection cuts in Table 25 are applied (excluding the cut on $\Delta\phi_{H-jj}$ in case of p_{THjj}).

In Figure 65 we plot the result for the exclusive 2-jet cross section as a function of p^{cut}_{THjj} and $\Delta\phi^{\text{cut}}_{H-jj}$ for the ATLAS and CMS tight VBF selections. In these plots, the blue central line shows the central-value prediction obtained from $\mu = M_H$, while the orange solid lines show our uncertainty estimate. For reference, the green dashed and dotted curves show the direct scale variation for $\mu = M_H/2$ and $\mu = 2M_H$, respectively. For large values of p^{cut}_{THjj} or $\pi - \Delta\phi^{\text{cut}}_{H-jj}$, the cross section $\sigma_{\geq 3}$ that is cut away becomes small and so the effect of Δ^{cut} is negligible. In this limit the uncertainties reproduce those in the inclusive 2-jet cross section. On the other hand, in the transition region, once the exclusive cut starts to impact the cross section, the direct scale variations cannot be used any longer to estimate uncertainties, which is exhibited by the crossing of the lines. The ST method takes into account the migration uncertainty which becomes important in this region as the exclusive cut gets tighter, thus providing robust uncertainties for all values of p^{cut}_{THjj} or $\Delta\phi^{\text{cut}}_{H-jj}$.

Table 25: VBF selection cuts we use, corresponding to the H → γγ analyses by ATLAS [74, 263] and CMS [264] (as of last year). The cut on $\Delta\phi_{H-jj}$ in the last row is treated special as an exclusive binning cut.

	ATLAS	CMS tight
2-jet selection	anti-k_T $R = 0.4$ $p_{Tj} > 25$ GeV for $|\eta_j| < 2.5$ $p_{Tj} > 30$ GeV for $2.5 < |\eta_j| < 4.5$	anti-k_T $R = 0.5$ $p_{Tj} > 30$ GeV, $|\eta_j| < 4.7$
$\Delta\eta_{jj} = |\eta_{j1} - \eta_{j2}|$	> 2.8	> 3.0
m_{jj}	> 400 GeV	> 500 GeV
$|\eta_H - (\eta_{j1} + \eta_{j2})/2|$	-	< 2.5
$\Delta\phi_{H-jj}$	> 2.6	> 2.6

(a) ATLAS VBF selection

(b) ATLAS VBF selection

(c) CMS tight VBF selection

(d) CMS tight VBF selection
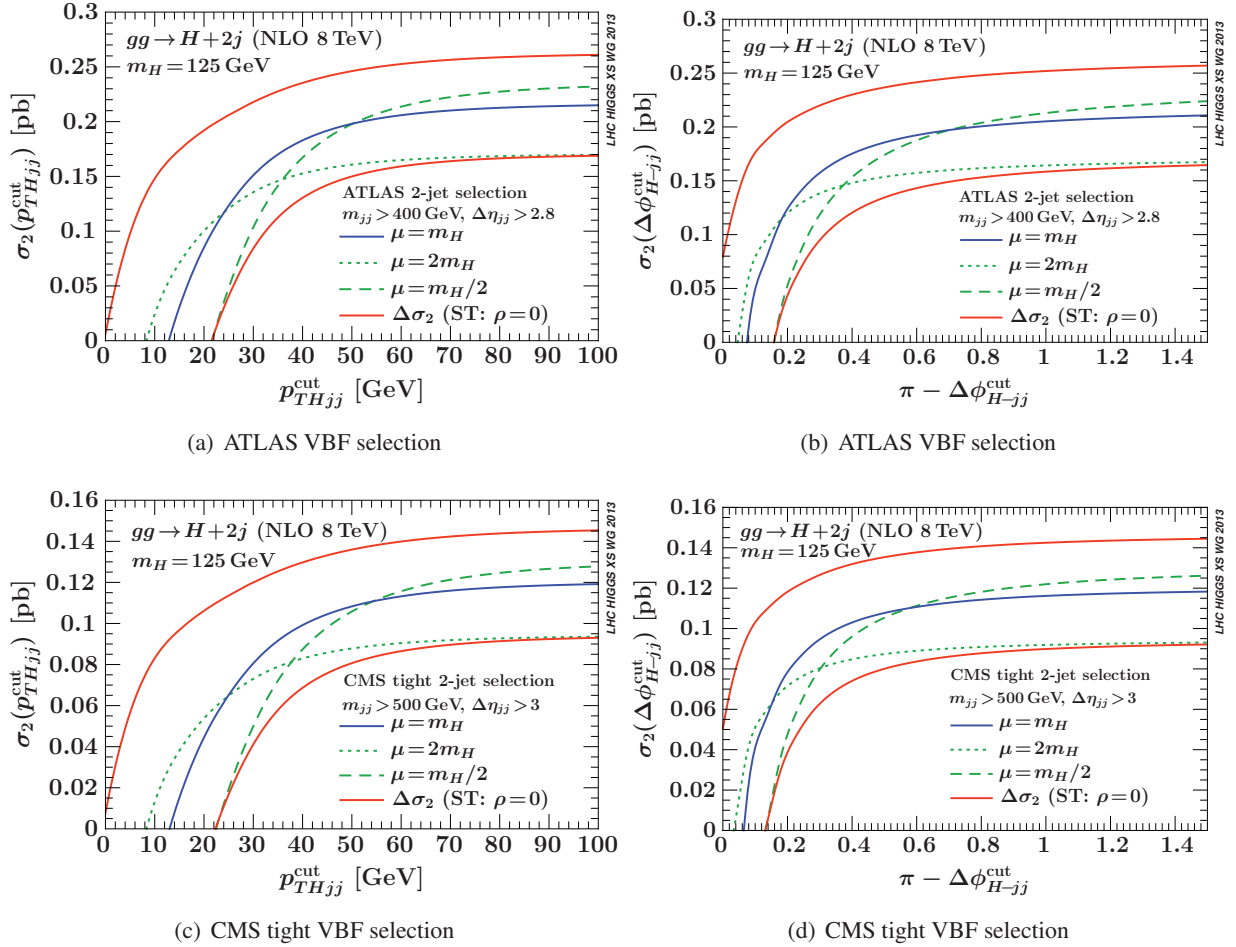
Fig. 65: Exclusive pp → H + 2 jet cross section via ggF at NLO for as function of p_{THjj}^{cut} (left panels) and $\pi - \Delta\phi_{H-jj}^{cut}$ (right panels) for both ATLAS and CMS VBF selections.

In Table 26 we quote the results for the cross sections and their percentage uncertainties for a few specific cuts. For $\Delta\phi_{H-jj}$ we use the experimental value $\Delta\phi_{H-jj} > 2.6$. Compared to the 21% in the inclusive 2-jet cross section with VBF cuts ($\sigma_{\geq 2}$), we see a moderate increase in the uncertainty in $\sigma_2(\Delta\phi_{H-jj} > 2.6)$ to 26% for ATLAS and CMS tight. For p_{THjj} we use a representative value of $p_{THjj} < 30$ GeV, for which the uncertainties increase substantially to 44% and 49% for ATLAS and CMS tight respectively. Note that for a fixed exclusive cut the uncertainties increase somewhat with a tighter VBF selection, which is expected.

Table 26: Perturbative uncertainties at NLO in the exclusive $pp \to H + 2$ jet cross section via gluon fusion for cuts on p_{THjj} and $\Delta\phi_{H-jj}$ for the ATLAS and CMS tight VBF selections given in Table 25.

Selection	σ [pb]	Direct scale variation		Combined incl. uncertainties
	$\mu = M_H$	$\mu = 2M_H$	$\mu = M_H/2$	ST ($\rho = 0$)
ATLAS				
$\sigma_{\geq 2}$	0.21			$\pm 21\%$
$\sigma_2(p_{THjj} < 30\,\text{GeV})$	0.15	-8%	-29%	$\pm 44\%$
$\sigma_2(\Delta\phi_{H-jj} > 2.6)$	0.19	-17%	-4%	$\pm 26\%$
CMS tight				
$\sigma_{\geq 2}$	0.12			$\pm 21\%$
$\sigma_2(p_{THjj} < 30\,\text{GeV})$	0.08	-8%	-35%	$\pm 49\%$
$\sigma_2(\Delta\phi_{H-jj} > 2.6)$	0.10	-19%	-1%	$\pm 26\%$

An important source of theoretical uncertainty in the extraction of the VBF signal is the large perturbative uncertainty in the ggF contribution. After subtracting the non-Higgs backgrounds (which are of course another source of uncertainty), the measured cross section for Higgs production after implementing the VBF selection is given by

$$\sigma_2^{\text{measured}}(\Delta\phi_{H-jj}^{\text{cut}}) = \sigma_2^{\text{VBF}}(\Delta\phi_{H-jj}^{\text{cut}}) + \sigma_2^{\text{ggF}}(\Delta\phi_{H-jj}^{\text{cut}}). \tag{82}$$

For the purpose of extracting the VBF cross section one effectively subtracts the theory prediction for $\sigma_2^{\text{ggF}}(\Delta\phi_{H-jj}^{\text{cut}})$ from $\sigma_2^{\text{measured}}(\Delta\phi_{H-jj}^{\text{cut}})$, and therefore, the relevant figure of merit is $\Delta\sigma_2^{\text{ggF}}(\Delta\phi_{H-jj}^{\text{cut}})/\sigma_2^{\text{VBF}}(\Delta\phi_{H-jj}^{\text{cut}})$, i.e., the theory uncertainty in σ_2^{ggF} measured relative to the expected VBF cross section, σ_2^{VBF}. In Figure 66 we show this quantity over a range of p_{THjj}^{cut} and $\Delta\phi_{H-jj}^{\text{cut}}$ for the ATLAS VBF selection. The results for the CMS selection are very similar. Here, the solid orange curve shows our results for the NLO perturbative uncertainties (corresponding to the orange lines in Figure 65). For comparison, the green dotted curve shows a fixed 20% uncertainty in the ggF cross section, i.e., taking $\Delta\sigma_2^{\text{ggF}} = 0.2\,\sigma_2^{\text{ggF}}$, which for example could be due to PDF and α_s parametric uncertainties. In the dashed blue lines, both uncertainty contributions are added in quadrature. In the region of low p_{THjj}^{cut} or $\pi - \Delta\phi_{H-jj}^{\text{cut}}$, the relative uncertainty coming from the ggF contribution quickly increases below $p_{THjj} \lesssim 30\,\text{GeV}$ and $\pi - \Delta\phi_{H-jj} \lesssim 0.4$. Hence, care must be taken when implementing and optimizing either indirect restrictions on additional radiation, like $\Delta\phi_{H-jj}$, or explicit p_T-vetoes like p_{THjj} or a central jet veto, and also in applying more general cuts which restrict to the exclusive 2-jet region as in the case of MVAs.

8.3.4 *Generalization to arbitrary number of cuts*

The formalism of Eq.(63) can be extended to further divide $\sigma_{\geq N+1}$ into an arbitrary number of bins,

$$\sigma_{\geq N} = \int_0^{p^{\text{cut 1}}} dp_{N+1} \frac{d\sigma_{\geq N}}{dp_{N+1}} + \int_{p^{\text{cut 1}}}^{p^{\text{cut 2}}} dp_{N+1} \frac{d\sigma_{\geq N}}{dp_{N+1}} + \cdots + \int_{p^{\text{cut } n-1}}^{p^{\text{cut } n}} dp_{N+1} \frac{d\sigma_{\geq N}}{dp_{N+1}}$$
$$\equiv \sigma_N(p^{\text{cut 1}}) + \sigma_{\geq N+1}(p^{\text{cut 1}}, p^{\text{cut 2}}) + \cdots + \sigma_{\geq N+1}(p^{\text{cut } n-1}, p^{\text{cut } n}). \tag{83}$$

This splitting divides the inclusive N-jet cross section, $\sigma_{\geq N}$, into n bins, whose uncertainties and correlations can be described by a symmetric $n \times n$ covariance matrix with $n(n+1)/2$ independent parameters. To construct this covariance matrix we use the boundary conditions that the inclusive cross sections $\sigma_{\geq N}$ and $\sigma_{\geq N+1}(p^{\text{cut}}, \infty)$ are uncorrelated, which implements the ST procedure for a given p^{cut}. This is not sufficient to determine the complete matrix. For the remaining entries, a simple linear correlation model
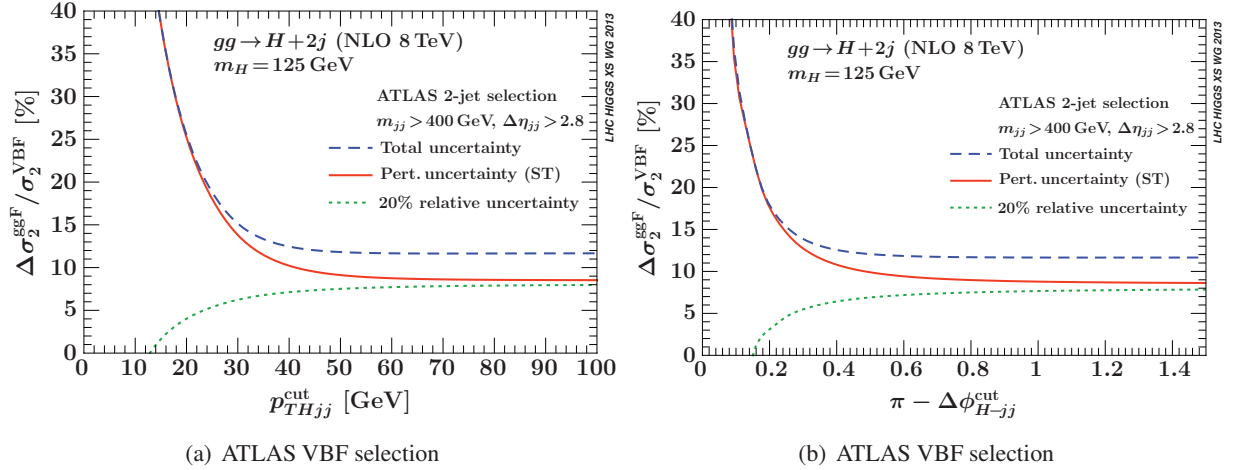
Fig. 66: Theoretical uncertainties of the ggF contribution relative to the VBF cross section as function of p_{THjj}^{cut} (left) and $\Delta\phi_{\text{H}-jj}^{\text{cut}}$ (right) for the ATLAS VBF selection.

is used, where the correlation κ_{ij} between $\sigma_{\geq N+1}(p^{\text{cut}\, i}, \infty)$ and $\sigma_{\geq N+1}(p^{\text{cut}\, j}, \infty)$ is given by

$$\kappa_{ij} = 1 - (1 - \kappa)\frac{|p^{\text{cut}\, i} - p^{\text{cut}\, j}|}{p^{\text{cut}\, n} - p^{\text{cut}\, 1}}. \tag{84}$$

The parameter κ determines the strength of the correlations between the inclusive $N+1$-jet cross sections for different p^{cut}. The dependence on this underlying correlation model is tested below by using the three different values $\kappa = \{50\%, 90\%, 99\%\}$. As we will see, the obtained uncertainty estimates are very insensitive to the precise choice of κ.

In the following, the above procedure is demonstrated using $\Delta\phi_{\text{H}-jj}$ as the underlying IR sensitive binning variable. Here, the first bin, which encloses the IR sensitive region, must be chosen large enough to ensure that MCFM can still be used to estimate its uncertainties using the ST procedure. Based on Figure 65(b) and Figure 65(d) we choose the first bin as $\left(\pi - \Delta\phi_{\text{H}-jj}\right) \in [0, 0.2]$.

For their most recent results, ATLAS and CMS use POWHEG gg $\rightarrow$ H + 0 jets at NLO [78–80] to model the hard scattering process, interfaced with PYTHIA8 [82] for modeling of underlying event, parton showering, and hadronization. In the left panel of Figure 67 we compare the normalized cumulative cross section for different values of $\Delta\phi_{\text{H}-jj}^{\text{cut}}$ between POWHEG+PYTHIA8 and MCFM. For both generators, the anti-k_{T} algorithm with $R = 0.4$ is used to reconstruct the jets, excluding the Higgs decay products, and a typical VBF phase space selection is applied. The cumulant shapes are in good agreement, also when the POWHEG+PYTHIA8 VBF selection is varied. When applying an exclusive 2-jet selection based on $\Delta\phi_{\text{H}-jj}$, the uncertainty of the event yield N_2 from POWHEG+PYTHIA8 can be estimated from

$$(\Delta N_2)^2 = \sum_{i,j} \widehat{C}_{ij}\, n_i\, n_j, \qquad \widehat{C}_{ij} = \frac{1}{\sigma_i \sigma_j} C_{ij}, \qquad N_2 = \sum_i n_i, \tag{85}$$

where C_{ij} denotes the covariance matrix, σ_i the predicted cross section in the interval of the ith bin, n_i denotes the event yield of the Monte Carlo prediction in the ith bin, and the sum runs over all bins that define the exclusive 2-jet phase space one is interested in. To construct C_{ij}, we use the MCFM uncertainties of Figure 65(b) as inputs to the procedure described above. The right panel of Figure 67 compares the relative uncertainties calculated from Eq.(85) for POWHEG+PYTHIA8 for different correlation models, showing a good agreement with the input MCFM uncertainties. Note in particular that the 2-jet inclusive cross section uncertainty is recovered when calculating the cumulant over the full range
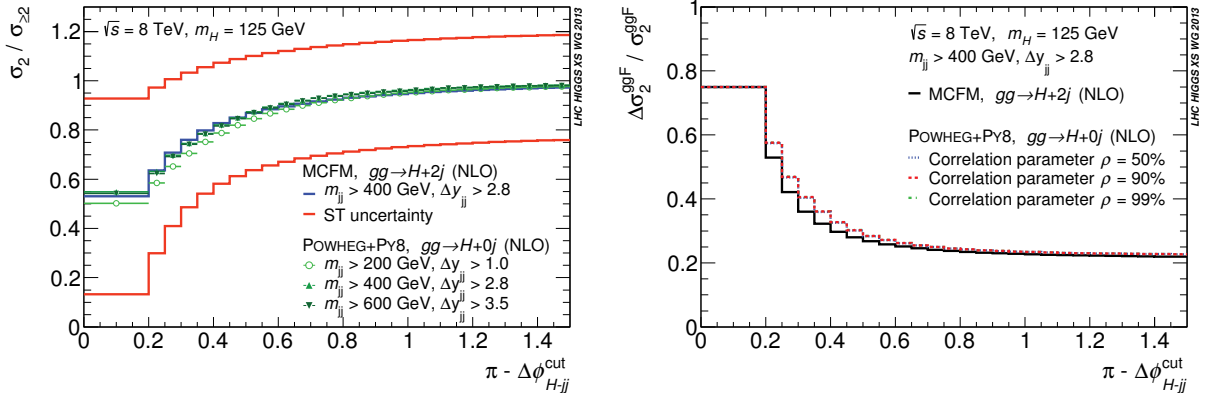
Fig. 67: Comparison of the exclusive $pp \to H + 2$ jet cross section via ggF from MCFM and POWHEG+PYTHIA8 $H + 0$ jets as a function of $\pi - \Delta\phi_{H-jj}^{cut}$ (where the cut value is given by the upper bin edges). Left: The normalized cumulant $\sigma_2/\sigma_{\geq 2}$. The histograms show the fixed-order results from MCFM, corresponding to Figure 65(b). The data points show POWHEG+PYTHIA8 results for different VBF selections, which only depend weakly on the precise VBF selection and agree well with MCFM. Right: The relative ST uncertainties from MCFM (black solid histogram) are compared to the resulting uncertainties (dotted histograms) after propagation to the POWHEG+PYTHIA8 prediction using Eq.(85). The resulting uncertainties closely agree with the MCFM input uncertainties and do not depend on the correlation model assumed in the propagation.
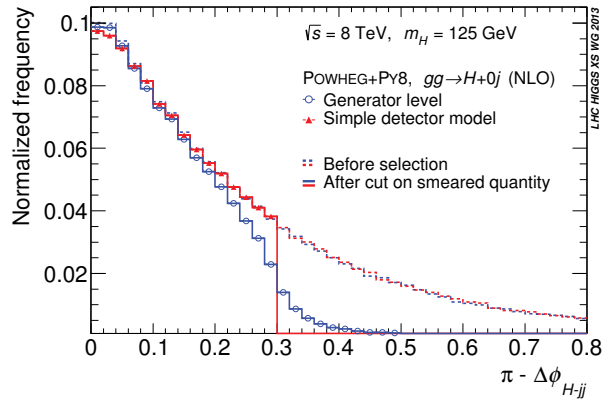
Fig. 68: Illustration of the effect of finite reconstruction resolution on $\Delta\phi_{H-jj}$. The solid blue histogram shows the generator level $\Delta\phi_{H-jj}$ distribution after a cut on the reconstructed $\Delta\phi_{H-jj}^{reco}$ show in red. The resolution results in a nonlinear selection cut for the generator level $\Delta\phi_{H-jj}$.

of $\Delta\phi_{H-jj}$. Eq.(85) is used in the following two sections to derive uncertainties for nonlinear cuts on $\Delta\phi_{H-jj}$ due to resolution effects and for selections based on a multivariate classifier.

8.3.5 Detector smearing

The photon and jet four momenta used in an actual physics measurement are degraded due to the energy and angular resolution smearing and reconstruction inefficiency of the detector. As a consequence, a cut applied on a reconstructed quantity in a physics analysis causes migration above and below the cut value when looking at the same variable calculated at the generator level. This is illustrated for a selection on $\Delta\phi_{H-jj}$ in Figure 68, where the energy resolution is modeled using a simple normal

Table 27: Relative perturbative uncertainties at NLO for $gg \to H + 2$ jets after applying a VBF selection defined by $m_{jj} > 400$ GeV, $\Delta\eta_{jj} > 2.8$, and various different cuts on $\Delta\phi_{H-jj}$. This selection is applied separately at the generator (truth) level (for jets reconstructed from stable particles from the MC event record) and after applying a simple detector smearing. The uncertainty is calculated using generator level $\Delta\phi_{H-jj}$ and detector level $\Delta\phi_{H-jj}$ using the linear correlation model with $\kappa = 90\%$.

$\pi - \Delta\phi^{\text{cut}}_{H-jj}$	0.25	0.3	0.4	0.5	no cuts
Generator level	57.1%	46.2%	35.3%	29.4%	21.0%
Detector level	54.2%	45.2%	34.8%	29.3%	21.0%

distributed resolution.[33] For photons, the angular resolution and the reconstruction efficiency is also roughly modeled (depending on p_T and η with a typical value of 80%). The cut on $\Delta\phi^{\text{reco}}_{H-jj}$ results in a nonlinear selection on $\Delta\phi_{H-jj}$. The impact on the cross section uncertainty from this smearing is studied using Eq.(85) and is summarized in Table 27. For a loose selection, the results are very similar, but as the cut is tightened the impact of the detector resolution gets more important and tends to result in slightly smaller uncertainties.

8.3.6 Multivariate analyses

In the context of a multivariate analysis, the effective cuts on $\Delta\phi_{H-jj}$ and p_{THjj} introduced by the nonlinear selection of phase space have to be studied carefully. In particular, if either of the variables are used directly as learning input for the multivariate classifier, one has to make sure that the final classification does not cut arbitrarily close into the infrared sensitive regions, i.e. $\Delta\phi_{H-jj} \to \pi$ and $p_{THjj} \to 0$. This can be prevented by transforming either variable into an infrared safe form,

$$\Delta\phi'_{H-jj} = \begin{cases} \Delta\phi_{H-jj} & \text{if } \Delta\phi_{H-jj} < \Delta\phi^{\text{cut}}_{H-jj}, \\ \Delta\phi^{\text{cut}}_{H-jj} & \text{if } \Delta\phi_{H-jj} \geq \Delta\phi^{\text{cut}}_{H-jj}, \end{cases} \quad p'_{THjj} = \begin{cases} p_{THjj} & \text{if } p_{THjj} > p^{\text{cut}}_{THjj}, \\ p^{\text{cut}}_{THjj} & \text{if } p_{THjj} \leq p^{\text{cut}}_{THjj}, \end{cases} \quad (86)$$

allowing the multivariate algorithm only to exploit the normalization difference in the infrared sensitive region of phase space.

The procedure of deriving the exclusive 2-jet cross section uncertainties is illustrated in the following using a multivariate selection based on a boosted decision tree trained using the software of Ref. [265][34]. The decision tree was trained to distinguish VBF like events in $H \to \gamma\gamma$ and to reject prompt diphoton background. As input for background, simulated prompt diphoton decays by SHERPA are used. The signal was simulated using POWHEG+PYTHIA8 for VBF and ggF decays, both simulated at NLO. To all samples resolution effects were added using the same simple normal resolution model as above. Six typical variables often used in VBF analyses were chosen to train the decision tree[35].

Figure 69(a) shows the distribution in $\Delta\phi_{H-jj}$ for the simulated background and signal decays. VBF events produce a topology which causes the Higgs and dijet system to be more back-to-back than background and ggF events. The multivariate method will make use of this to select a signal enriched region of phase space, and cut into this distribution. Figure 69(b) depicts the $m_{\gamma\gamma}$ invariant mass distribution before and after a cut on the multivariate classifier, illustrating the effect of the smearing model. Figure 69(c) shows the classifier $\mathcal{O}_{\text{MVA}}$: VBF signal peaks near the positive values, and background and ggF accumulates near negative values. Finally, Figure 69(d) depicts the ggF $\Delta\phi_{H-jj}$ spectrum for a

---

[33] A scale factor applied to the four momenta is sampled from $\text{Gaus}(1, \sigma)$ where σ is p_T and η dependent with a typical value of 0.02 and 0.1 for photons and jets respectively.

[34] The specific configuration used is: 1000 trees, a shrinkage factor of 0.1, a gradient bagging fraction of 0.5, and maximally five nodes, for more details and definitions see Ref. [265].

[35] The transverse projection of the Higgs p_T on the axis orthogonal to the thrust axis defined by the two photons; the invariant mass of the leading dijet system; the difference in rapidity of the two leading jets, the rapidities of the two leading jets, and the infrared safe version of $\Delta\phi_{H-jj}$ defined in Eq.(86) using a cutoff of $\Delta\phi^{\text{cut}}_{H-jj} = 2.94$.

Table 28: Relative perturbative uncertainties at NLO for $gg \rightarrow H + 2$ jets after applying a selection on the multivariate classifier $\mathcal{O}_{MVA}$. The uncertainty is calculated using generator level $\Delta\phi_{H-jj}$.

Cut	$\Delta\sigma_2/\sigma_2$ ($\kappa = 50\%$)	$\Delta\sigma_2/\sigma_2$ ($\kappa = 90\%$)	$\Delta\sigma_2/\sigma_2$ ($\kappa = 99\%$)
no cut	21.0%	21.0%	20.9%
$\mathcal{O}_{MVA} > 0.2$	26.6%	26.8%	26.9%
$\mathcal{O}_{MVA} > 0.6$	34.3%	34.6%	34.7%
$\mathcal{O}_{MVA} > 0.8$	40.8%	41.1%	41.1%

progression of cuts on the classifier. The curves were normalized to have the same number of events in the region of $0 - 0.2$, which corresponds to the cutoff value used in Eq.(86).

Cutting on the classifier separates the inclusive 2-jet cross section into an exclusive 2-jet and an inclusive 3-jet part, similar as with a rectangular cut on $\Delta\phi_{H-jj}$ or p_{THjj}. In Table 28 we list the uncertainties calculated from Eq.(85) for a progression of cuts and different slopes for the linear correlation model: Harder cuts on the classifier translate into a tighter nonlinear selection in $\Delta\phi_{H-jj}$ phase space. As expected, this increases the exclusive 2-jet cross section uncertainty. The progressive harder cuts have a flat efficiency in $\Delta\phi_{H-jj}$ above the threshold of 0.2 (i.e. cut into this region without changing its shape), which is important to obtain reliable uncertainties from Eq.(85). The dependence on the actual details on the linear correlation model is small: Changing the bin-by-bin correlations of the inclusive 3-jet cross section phase space by varying κ from 50% to 99% has a practically negligible effect on the estimated uncertainty.

The method described here was used in the latest ATLAS $H \rightarrow \gamma\gamma$ measurement [266], to determine the uncertainties for the two used VBF MVA selections. The uncertainties found there were 28.3% and 48.4% for the loose and tight MVA category, respectively. The same approach applied to the CMS MVA analysis [267] at reconstruction level gives an uncertainty for the tight category of about 40%, which is similar to the ATLAS result. The effect for the loose category is larger, about 48%. This difference can be due to multiple sources: limited statistics (after the full selection, only $\mathcal{O}(500)$ events survive), different tune (Z2* [268]), and looser selection for the di-jet loose category compared to ATLAS.

8.4 Underlying event uncertainties in the Higgs plus 2-jet VBF selection

The simulation of the underlying event for the most recent experimental results is done by either PYTHIA6 [81] (CMS) or PYTHIA8 [82] (ATLAS). The hard scattering process is simulated separately using a dedicated NLO generator, i.e., POWHEG [78–80] interfaced to PYTHIA for the modeling of underlying event, hadronization, and showering. In Pythia the underlying event is simulated using a multipartonic interaction (MPI) model [269, 270], that is tuned on underlying event or minimal bias data. In the following the impact of the underlying event on the Higgs plus two-jet VBF selection is studied by comparing simulated gluon-gluon-fusion and vector-boson-fusion production mechanisms with and without PYTHIA's multipartonic interaction.

The following are guidelines for the estimation of UE related uncertainties in ggF and VBF processes:

– Turn UE on/off for the nominal default tune
– Cross check on/off effect for alternative tunes
– Cross checks can include the use of tunes performed within a common framework but using different PDFs (eg. NLO v. LO, as is the case with AU2-CT10 and AU2-CTEQ6L1)

(a) Signal and background $\Delta\phi_{H-jj}$

(b) Signal and background $m_{\gamma\gamma}$

(c) Multivariate classifier

(d) ggF $\Delta\phi_{H-jj}$ for a progression of cuts
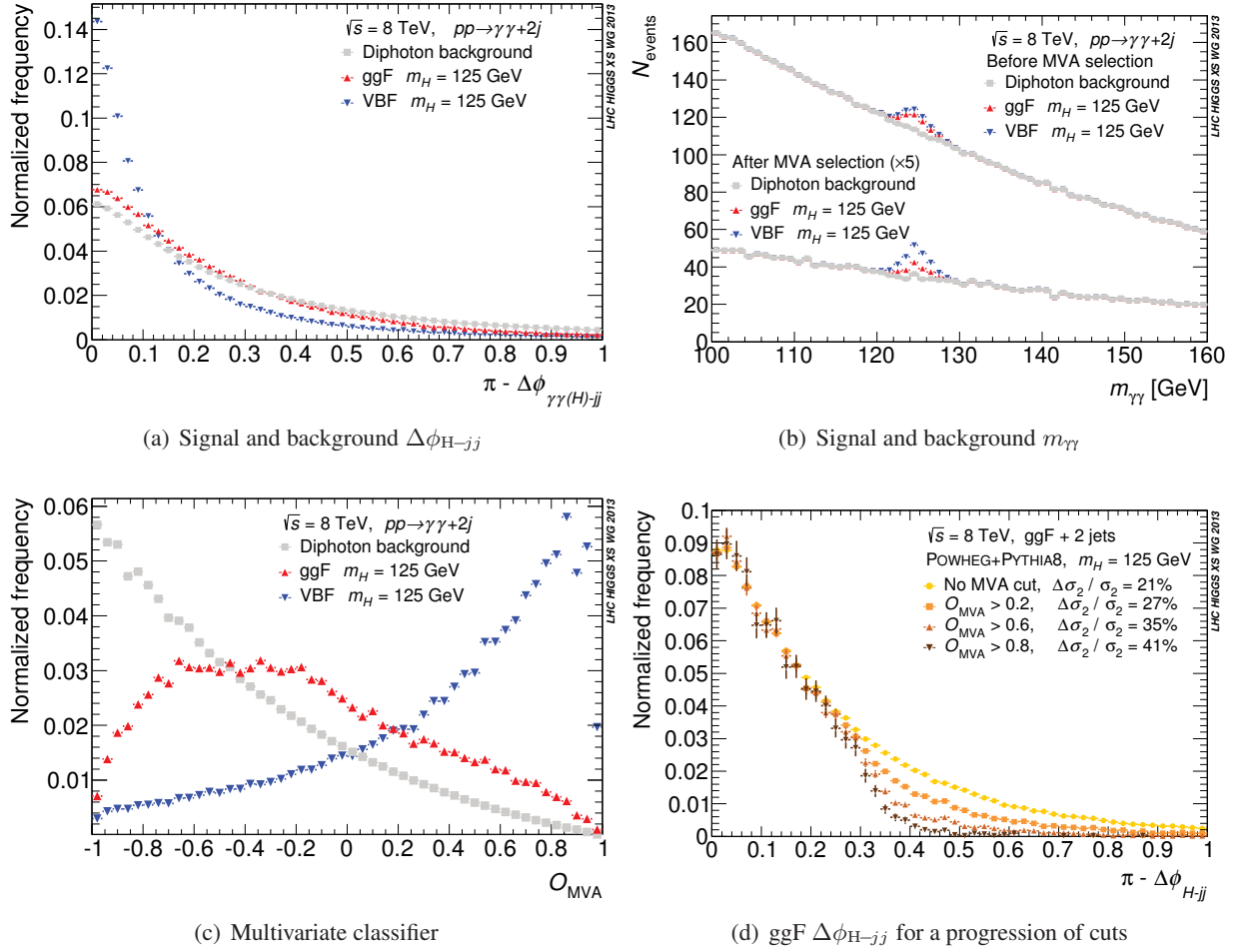
Fig. 69: Signal and Background distributions of the multivariate selection: Figure 69(a) shows $\Delta\phi_{H-jj}$ for background and VBF signal; Figure 69(b) depicts the invariant diphoton mass spectrum for diphoton background (grey), ggF (red), and VBF (blue) before and after an arbitrary cut on the multivariate classifier. Figure 69(c) depicts the multivariate classifier constructed from the six input variables for background, ggF, and VBF following the same color code. Figure 69(d) shows the $\Delta\phi_{H-jj}$ distribution without any cut, and a progression of cuts on the multivariate classifier, also quoting the uncertainties on the integral obtained using Eq.(85).

8.4.1 Comparative multipartonic interaction study [36]

In the following the impact on the Higgs plus two-jet VBF selection with and without PYTHIA's underlying event model are investigated. In the first study performed, three tunes of the MPI model parameters for three parton distribution functions (PDF) are studied: CTEQ10 [145], CTEQ6L1 [169], and MSTW2008 [206], which are NLO, LO, and LO PDFs, respectively. The initial hard scattering process are ggF + 0 jets and VBF at NLO, simulated by POWHEG with CTEQ10 as the PDF. Jets are reconstructed from stable particles using the anti-k_T algorithm with $R = 0.4$ and are required to have $p_{Tj} > 25$ GeV for $|\eta_j| < 2.5$ and $p_{Tj} > 30$ GeV for $2.5 < |\eta_j| < 4.5$. Additional requirements are applied to isolate the VBF signal: $m_{jj} > 400$ GeV, $\Delta\eta_{jj} > 2.8$ and $\Delta\phi_{H-jj} > 2.6$ rad.

Figure 70 shows the distribution of $\Delta\phi$ between the Higgs and the dijet system for ggF for the CTEQ10 (AU2-CT10) and CTEQ6L1 (AU2-CTEQ6L1) tunes [271]. Switching off MPI results in overall less hadronic activity and a reduction in the number of selected events. Figure 71 shows $\Delta\phi_{H-jj}$ for VBF for the same tunes: the effect here is much smaller, since the dijet system originates most of the time from

---

[36]F. U. Bernlochner, D. Gillberg, M. Malberti, P. Meridiani, P. Musella, G. Salam
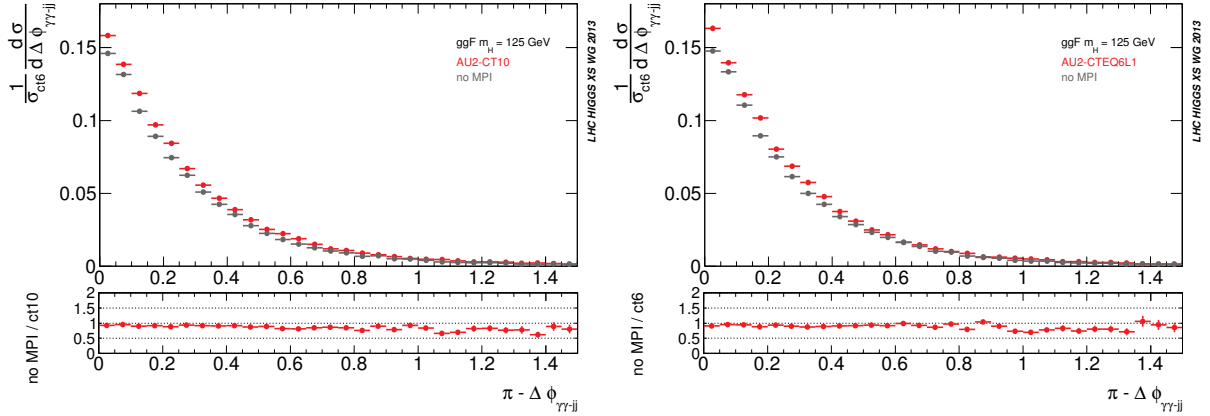
Fig. 70: The effect of switching off multi-partonic interaction for $gg \to H + 0$ jets at NLO for $\Delta\phi_{H-jj}$ is shown: CTEQ10 with the ATLAS AU2-CT10 tune (left) and CTEQ6L1with the ATLAS AU2-CTEQ6L1 tune (right). The no MPI histogram was scaled to account for the change in the two jet selection efficiency. The hard scatter for both was simulated using POWHEG using the CTEQ10 NLO PDF.

the hard scatter alone, and little additional hadronic activity in the rapidity gap between the dijet system is produced in the VBF topology. Table 29 summarizes the relative difference in percent without MPI for AU2-CT10, AU2-CTEQ6L1, and the MSTW2008 PDF tune AU2-MSTW2008 [271]: the relative shifts in the yields of the two-jet selection and a typical VBF phase space selection are quoted. The overall effect of the MPI on selected cross sections is about 10% in ggF and 4% in VBF. In the tails of distributions it can be sometimes larger.

The comparisons using AU2-CTEQ6L1 and AU2-MSTW2008, although illustrative, might be considered somewhat inconsistent, since the hard-scatter uses a different PDF from the showering and MPI. As a cross check, the MPI-induced variations in the selected cross sections have been studied (based on stable particles) also in the Pythia 6 DW [272], Pythia 6 Perugia 2011 [273] and Pythia 8 4C [274] tunes. Again, the effects are of the order of 10% for ggF.

In the second study five different PYTHIA6 tunes are used, either based on a MPI model with p_T ordered showers like Z2* (CMS default) [268], Pro-PT0 [275] and P0 [273], or with virtuality ordered showers, Pro-Q20 [275] and D6T [272]. The main motivation to look at this set of tunes is in the data/MC comparison that CMS made using 36 pb^{-1} of 7 TeV data of the forward energy flow and the central charged multiplicity in hard-scattering W and Z events [276]. It was found that none of the considered tunes was able to simultaneously describe the central charged multiplicity and the forward energy flow, and, particularly, their correlations.

This study is based on fully simulated and reconstructed events. The simulation of the CMS detector is done with GEANT4 and the reconstruction uses the official CMS software. Reconstructed quantities allow for a better determination of the effect of MPI uncertainty on the final observables, given that jet resolution and mis-reconstruction are properly taken into account. On the other hand, because of the small detector efficiency, only a tiny number of selected events ($\mathcal{O}(500)$) for the ggF samples are available (from an initial sample of about 100k fully simulated events). This implies that the following numbers are affected by a somewhat large statistical uncertainty. For each tune, the MPI is switched on and off and the difference in selection efficiency times acceptance for the CMS H $\to \gamma\gamma$ VBF analyses [267] is estimated. Results are summarized in Table 30. The uncertainty associated to the MPI is defined as the largest variation in the on/off ratio over the 5 tunes. The uncertainty is split in two parts: the overall VBF selection efficiency and the migration between the tight and loose categories. The migration is evaluated as the ratio between the number of events in the tight category and the one in the tight and loose categories together. The effect is below 10% for both ggF and VBF.
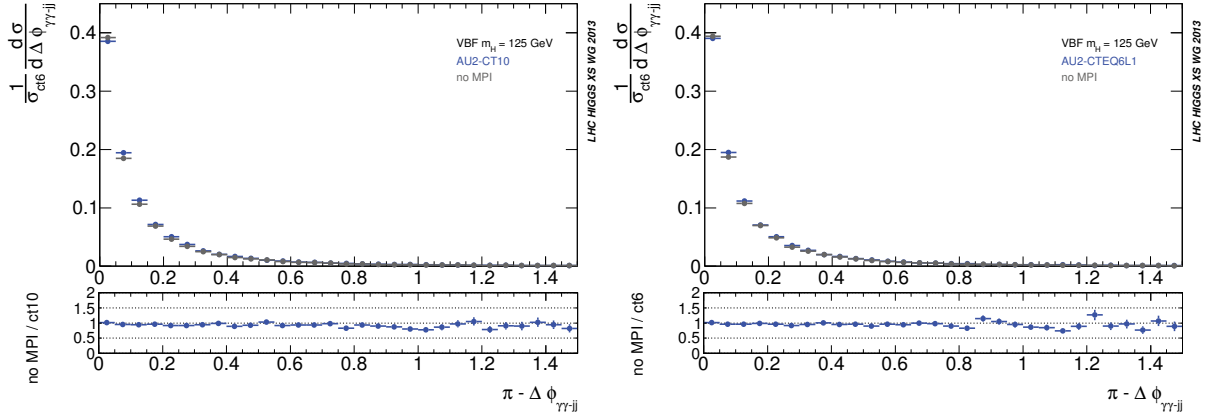
Fig. 71: The effect of switching off multi-partonic interaction for $qq \to H + 0$ jets at NLO for $\Delta\phi_{H-jj}$ is shown: CTEQ10 with the ATLAS AU2-CT10 tune (left) and CTEQ6L1with the ATLAS AU2-CTEQ6L1 tune (right).

Table 29: The uncertainties for the underlying event evaluated in % of the nominal yields from switching the multi-partonic interaction off for the 2-jet selection, and a VBF-type selection ($m_{jj} > 400$ GeV, $\Delta\eta_{jj} > 2.8$, $\Delta\phi_{H-jj} > 2.6$) are listed.

Tune / ggF	2-jet selection	VBF selection
AU2-CT10	9.8%	8.8%
AU2-CTEQ6L1	8.9%	5.3%
AU2-MSTW2008	8.2%	6.0%

Tune / VBF	2-jet selection	VBF selection
AU2-CT10	3.0%	3.5%
AU2-CTEQ6L1	2.1%	1.8%
AU2-MSTW2008	2.6%	3.1%

Table 30: The uncertainties for the underlying event evaluated in % of the nominal yields from switching the multi-partonic interaction off for the CMS VBF-type cut-based selection, as described in [267]. The numbers in the second column are related to the effect on the tight and loose VBF categories together, while the third column reports the migration between the two categories.

Tune / ggF	tight + loose	migration
TuneProQ20	2.4%	0.6%
TuneZ2Star	0.3%	2.1%
TuneProPT0	6.6%	1.2%
TuneP0	0.4%	0.8%
TuneD6T	0.7%	0.4%
Maximum variation	6.6%	2.1%

Tune / VBF	tight + loose	migration
TuneProQ20	8.7%	2.4%
TuneZ2Star	0.3%	1.5%
TuneProPT0	3.2%	0.3%
TuneP0	2.7%	0.6%
TuneD6T	8.3%	2.2%
Maximum variation	8.7%	2.4%

9 NLO MC [37]

In this section, some recent studies related to the dominant Higgs boson production mode, gluon fusion, are presented with a focus on the issue of additional jets in this class of processes.

In Sec. 9.1, various fixed order results at next-to leading order in the strong coupling constant for the production of a Higgs boson in association with two jets are compared to results from Monte Carlo event generators. They treat jet emission at leading or next-to leading order, but resumming different types of potentially large logarithms. In this study, some interesting differences when going to the kinematically more extreme weak boson fusion region emerge, with clear consequences on the projected accuracy for the important gluon fusion background to this important production mode.

In Sec. 9.2 a careful analysis of jet multiplicities and the associated errors is presented for the irreducible background to Higgs boson production in gluon fusion and its subsequent decays into two leptons and two neutrinos. In this calculation all interferences are taken into account, and the fixed order parton level includes next-to leading order accuracy for the 0 and 1 jet bins.

Finally, in Sec. 9.3 first steps towards the calculation of next-to leading order QCD corrections to the production of $H + 3$ jets in gluon fusion are reported.

9.1 Jet studies in gluon-fusion production

This section reports on an ongoing study concerning the gluon fusion contribution to Higgs boson production in association with at least two jets. Both rather inclusive cuts and cuts specific for the weak-boson fusion (WBF) regime are applied and results compared between various approaches to the description of higher-order corrections. The WBF region covers a notoriously difficult regime of QCD radiation, where the perturbative stability of the calculations are being put to a new test. It is therefore not surprising that while the various approach agree well in the inclusive region, some significant differences show up within the WBF cuts. The study here represents merely a snapshot of the current findings, which definitely deserve further studies to better understand similarities and differences between the approaches and to quantify their intrinsic uncertainties.

The two kinematic regimes are defined as follows:

– Inclusive Selection:
  – All jets are defined by the anti-k_T algorithm [190] ($R = 0.4$) and counted if their transverse momentum is greater than 20 GeV and their absolute rapidity is less than 5.0.
  – At least two hard jets above 25 GeV are required.
– WBF Selection:
  – Furthermore require $|\eta_{j_1} - \eta_{j_2}| > 2.8$, $m_{j1,j2} > 400$ GeV.

9.1.1 Monte-Carlo generators

In this section the physics input of the Monte-Carlo generators used is described and their setup, scale choices, etc. is detailed[38]. For this study, which focuses on the multi-jet descriptions, all predictions are obtained with no restrictions on the the Higgs boson momentum or decay channel.

---

[37]F. Krauss, F. Maltoni, P. Nason (eds.); Jeppe R. Andersen, F. Cascioli, H. van Deurzen, N. Greiner, S. Höche, T. Jubb, G. Luisoni, P. Maierhoefer, P. Mastrolia, E. Mirabella, C. Oleari, G. Ossola, T. Peraro, S. Pozzorini, M. Schönherr, F. Siegert, J. M. Smillie, J. F. von Soden-Fraunhofen, F. Tramontano

[38]The beginning stages of this study displayed results also from aMC@NLO [139] using the multijet-merging algorithm at NLO presented in [142]

9.1.1.1 HEJ

High Energy Jets (HEJ) gives a description to all orders and all multiplicities of the effects of hard, wide-angle (high energy-) emissions, by utilizing an approximation to the hard scattering amplitudes [277–279], which in this limit ensures leading logarithmic accuracy for both real and virtual corrections. These logarithmic corrections are dominant in the region of large partonic center of mass energy compared to the typical transverse momentum. The resummation obtained is matched with a merging procedure to full tree-level accuracy for multiplicities up to and including three jets [280–282].

The predictions of HEJ depend principally on the choice of factorization and renormalization scale, and on the pdf set (MSTW2008nlo [100]). For this study, we allow different scales for individual occurrences of the strong coupling. We choose to evaluate two powers of the strong coupling at a scale given by the Higgs mass, and all remaining scales are identified with the transverse momentum of the hardest jet. Therefore, for n jets,

$$\alpha_s^{n+2}(\mu_R) = \alpha_s^2(M_H) \cdot \alpha_s^n(p_\perp^{\text{hardest}}) \,. \tag{87}$$

The merging scale is set to 20 GeV, the minimum transverse momentum of the jets.

9.1.1.2 MCFM

For the purpose of this comparison MCFM [259,283] was used to provide a fixed-order description of the observables in question. The transverse mass of the Higgs boson $m_{T,H}^2 = M_H^2 + p_{T,H}^2$ has been used as the factorization and renormalization scale. The CTEQ6.6 parton distribution functions [284] were used in conjunction with its accompanying value and evolution of the strong coupling constant. The effective ggH vertex is calculated in the $m_t \to \infty$ limit.

9.1.1.3 PowhegBox

The POWHEGBOX generators for Higgs (H), Higgs plus one jet (HJ) and Higgs plus two jets (HJJ) have appeared in Refs. [285] and [73]. For the present work, the HJJ generator has been augmented with the MiNLO method [286, 287]. As shown in these references, when using the MiNLO method, the HJ and HJJ generators also maintain some level of validity when used to compute inclusive quantities that do not require the presence of jets. More specifically, the HJ generator remains valid also for describing the Higgs inclusive cross section, and the HJJ generator remains valid for describing the Higgs plus one jet, and the Higgs inclusive cross section. This is achieved without introducing any unphysical matching scale. The generators become smoothly consistent with the generators of lower multiplicities when the emitted parton become unresolvable. The level of accuracy that they maintain is discussed in detail in Ref. [287]. By the arguments given there one can show that the MiNLO procedure can be implemented in such a way that the HJ generator maintains NLO accuracy when the emitted parton becomes unresolved. The HJJ generator, at present, maintains only LO accuracy when emitted partons become unresolvable.

In Table 31 we show the inclusive production rates obtained with the different generators according to the standard cuts described in this report. Furthermore, we show the standard set of distributions obtained with the HJJ generator interfaced with PYTHIA6 [81], without hadronization.

9.1.1.4 Sherpa

The SHERPA [162] predictions are calculated using the MEPS@NLO method [189, 288]. It combines multiple NLOPS [78, 79, 128, 177] matched calculations of successive jet multiplicity into an inclusive sample such that both the fixed order accuracy of every subsample is preserved and the resummation properties of the parton shower w.r.t. the inclusive sample are restored.

For the purpose of this study the subprocesses $pp \to h + 0, 1$ jets are calculated at next-to-leading order accuracy using a variant of the MC@NLO method [177], while the subprocesses $pp \to h + 2, 3$

Table 31: Total rates for the H generator (H), the HJ generator with MiNLO (HJ), the HJ generator with MiNLO improved according to [287] (HJ-N) and the MiNLO improved HJJ generator.

	Inclusive	2 jets, $p_T > 25, |y| < 5$	$+ \eta_{jj} < 2.8, m_{jj} > 400\,\text{GeV}$
H	13.2	1.61	0.177
HJ	16.2	2.04	0.202
HJ-N	13.3	2.10	0.209
HJJ	17.8	2.41	0.239

jets are calculated at leading order accuracy. Further emissions are effected at parton shower accuracy only. The $\text{pp} \to \text{H}$ and $\text{pp} \to \text{H} + 1$ jet virtual matrix elements are taken from [36, 289–291]. While not included in this study, the subprocess $\text{pp} \to \text{H} + 2$ jets can also be calculated at next-to-leading order accuracy by interfacing GOSAM [292] through the Binoth-Les Houches accord [293] interface, see also the description in the following section, 9.3. The effective ggh vertices are computed in the $m_t \to \infty$ limit.

Scales are chosen in the usual way of MEPS merging [294], i.e. they are set to the relative transverse momenta of parton splittings reconstructed through backwards clustering the respective final states using inverted parton shower kinematics and splitting probabilities. Thus,

$$\alpha_s^{n+k}(\mu_R) = \alpha_s^k(\mu_0) \cdot \prod_{i=1}^{n} \alpha_s(\mu_i) \,, \tag{88}$$

wherein the μ_i are in the individual splitting scales and μ_0 is the scale of the underlying $\text{pp} \to \text{H}$ production process, here $\mu_0 = M_H$, $k = 2$. This plays an integral part in restoring the overall resummation properties. The CT10 [295] parton distributions, with the respective value and evolution of the strong coupling, are used throughout. The merging scale is set to $Q_{\text{cut}} = 20$ GeV.

9.1.2 Comparison

Figures 72–73 exhibit important jet distributions in the inclusive regime. Results of HEJ, MCFM, POWHEGBOX, and SHERPA agree fairly well for distributions of the individual two hardest jets, like for instance rapidity distributions (Fig. 72). The notable exception is the fixed-order calculation. However, this is easily understood by the renormalization scales in the NLO calculation, which tends to pick higher scales for all strong couplings and therefore leads to a smaller cross section. Interestingly enough, though, this does not lead to large visible shape differences in the inclusive rapidity distributions of the two jets, *cf.* Fig. 72. This picture somewhat changes when considering observables sensitive to the kinematics of both leading jets, like their invariant mass or rapidity distance (Fig. 73). Again, the fixed-order result is below the two DGLAP-type resummations provided by the parton showers and Sudakov form factors in the POWHEGBOX and SHERPA, with only minor, but now more visible differences in shape. Again, this can be attributed to different choices for the renormalization and factorization scales. On the other hand, for the invariant mass and rapidity difference distributions of the two leading jets now the shape of the results from HEJ start to strongly deviate. This may be understood from the Regge-type suppression factors systematically resummed in HEJ, but which are not present in the other approaches, but it definitely deserves further and more detailed studies. These effects disfavor large empty rapidity gaps, see Fig. 73.

Fig. 73 also illustrates how the HEJ cross section in the WBF regime will deviate from the other Monte Carlos, since the region of large rapidity separation between the two hardest jets is suppressed. This is further quantified in Table 32. The relative effect of imposing the WBF cuts is largest for the predictions from HEJ.
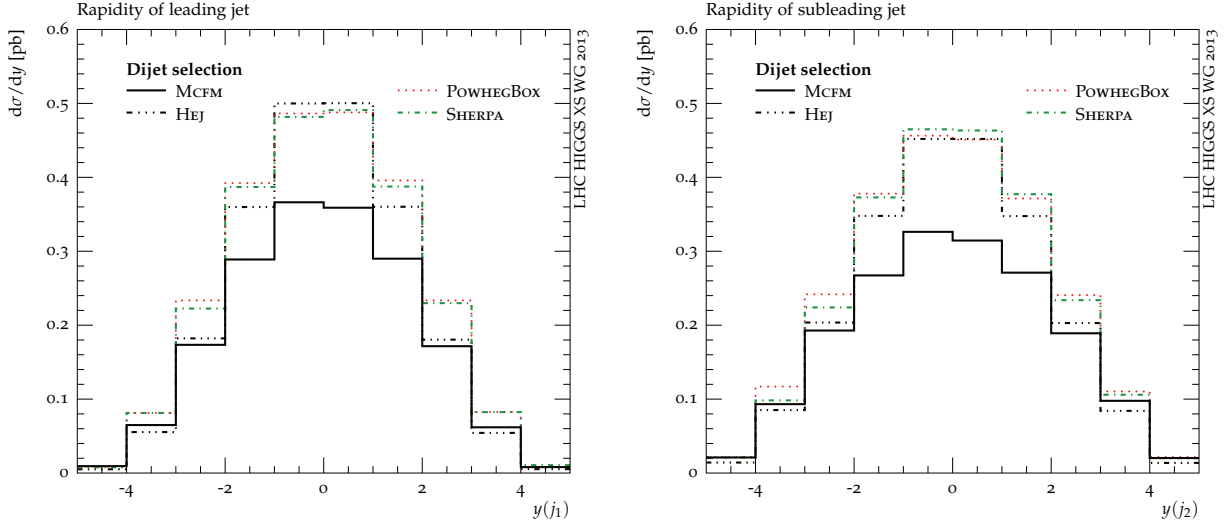
Fig. 72: Rapidity of the leading (left) and subleading (right) jets in the dijet selection.
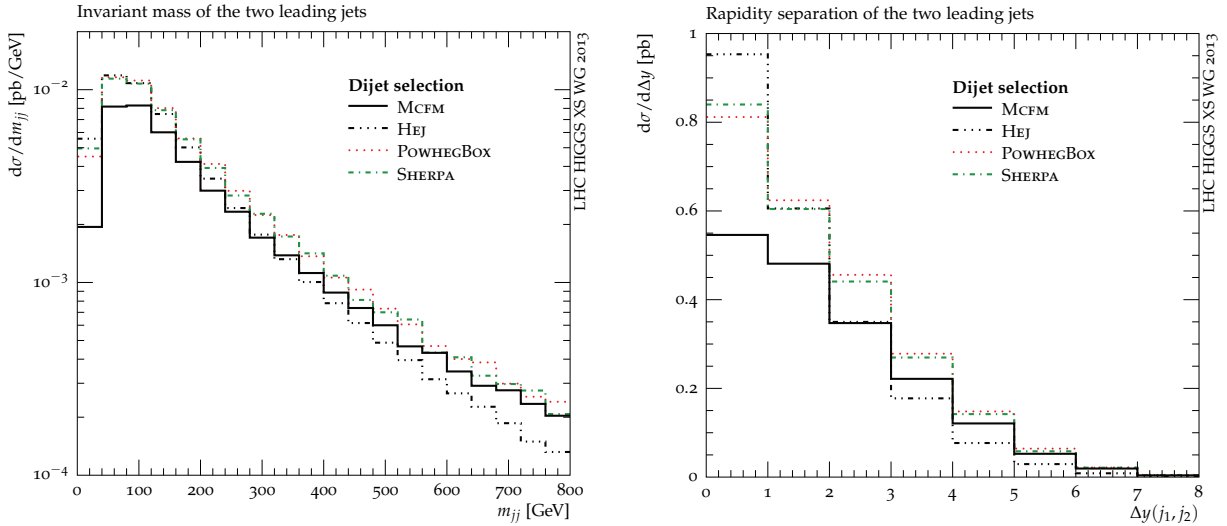
Fig. 73: Invariant mass (left) and rapidity separation (right) of the leading jets in the dijet selection.

An interesting difference, apart from the overall normalization, can be seen in the shape of the rapidity distribution of the leading jet after WBF cuts: HEJ has a much less developed dip at central rapidities; the leading jet is typically more central in rapidity than in the other approaches, cf. Figure 74. Such aspects of the QCD radiation pattern for large rapidity separations are currently investigated also experimentally, and a better understanding could be used to further discriminate QCD and WBF production.

A similar trend is observed in the transverse momentum distributions of the two leading jets exhibited in Fig. 75, where HEJ exhibits differences in normalization and shape, with slightly harder spectrum for the two hardest jets. Conversely, the rapidity of the third hardest jet displayed in the left panel of Fig. 76, tends to be a bit wider at tree-level (from MCFM) and in HEJ than in the parton-shower based approaches. This, however, is an observable which for all approaches is given at leading order only, potentially supported by some resummation. It is thus not a surprise that here the largest differences between different approaches show up.

The right panel of Fig. 76 shows the difference in the azimuthal angle of the two leading jets.

Table 32: Cross sections predicted by the individual generators for the dijet and WBF selections and the predicted relative reduction in cross section by applying WBF selection.

	Dijet selection	WBF selection	Effect of WBF cut
MCFM	1.73 pb	0.192 pb	0.111
HEJ	2.20 pb	0.127 pb	0.058
POWHEGBOX	2.41 pb	0.237 pb	0.098
SHERPA	2.38 pb	0.225 pb	0.094
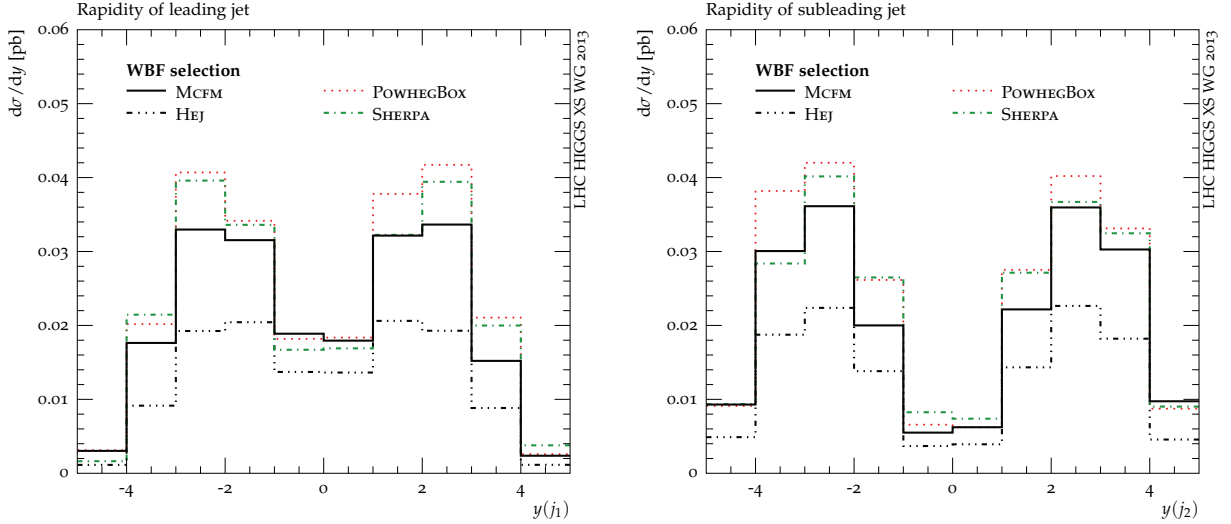
Fig. 74: Rapidity of the leading (left) and subleading (right) jets in the WBF selection.

SHERPA exhibits a visible shape difference for small angles, while the other approaches are more similar. HEJ shows a slightly reduced correlation of the two hardest jets, possibly caused by a larger jet radiation activity than in the shower-based approaches [296].

9.1.3 Outlook

The results presented here tend to open more questions than to provide answers, with differences between approaches being somewhat larger than expected. Further studies are clearly important, since the gluon fusion background to WBF production of a Higgs boson will mostly be estimated from Monte Carlo techniques and a Monte Carlo driven extrapolation from control to signal regions. In this respect the apparent similarity of approaches for the inclusive selection and the visible and sometimes even large differences in the WBF region necessitates a much better understanding of the QCD radiation pattern in the extreme phase space region of the WBF selection. In addition to an understanding on the level of central values, it will also be of utmost importance to gain a well-defined handle on the theory uncertainties related to the extrapolation. This will be the subject of ongoing and further studies.

9.2 Irreducible background to $H \rightarrow WW^*$ in exclusive 0- and 1-jets bins with MEPS@NLO

Final states involving four leptons played an important role in the discovery of the Higgs-like boson in 2012 and will continue to be crucial in the understanding of its coupling structure. By far and large, there are two classes of final states of interest, namely those consistent with decays $H \rightarrow ZZ^*$ yielding four charged leptons and those related to $H \rightarrow WW^*$ resulting in two charged leptons and two neutrinos. They have quite different backgrounds, and for the latter, the dominant and large top-pair production and
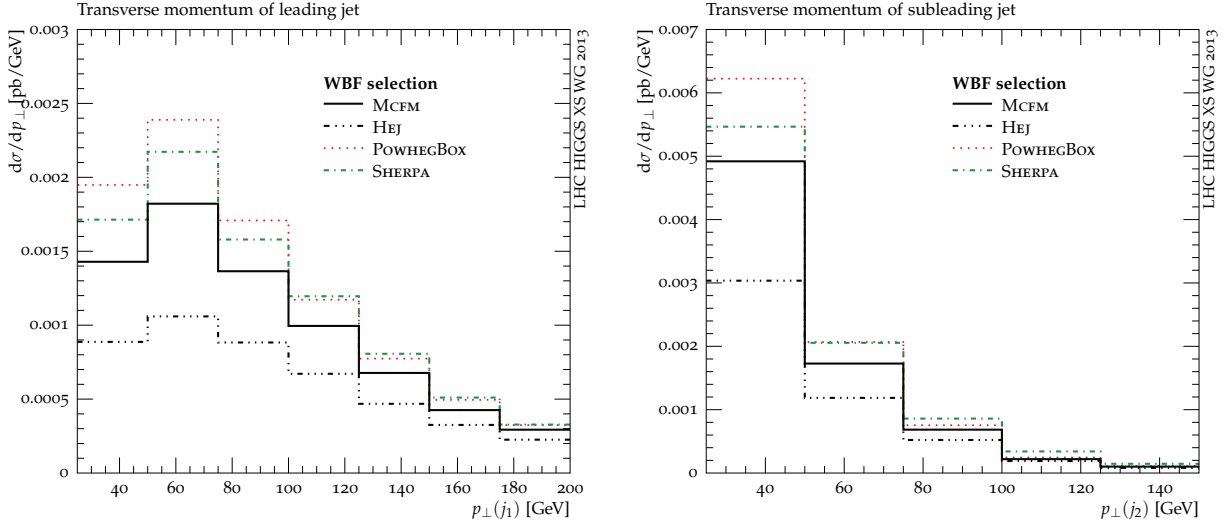
Fig. 75: Transverse momenta of the leading (left) and subleading (right) jets in the WBF selection.
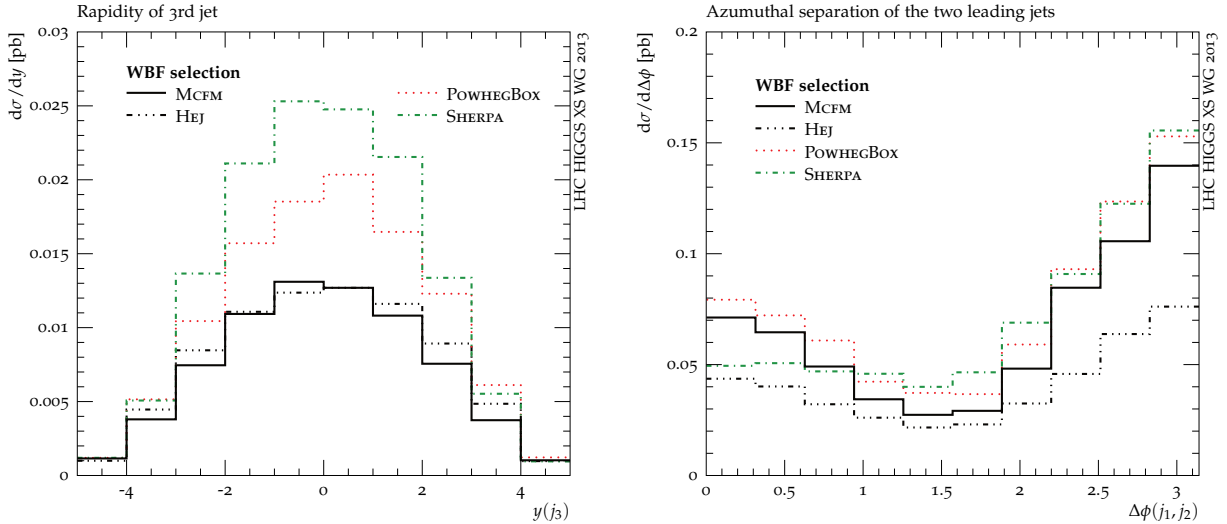
Fig. 76: Rapidity of the third jet (left) and azimuthal separation of the two leading jets (right) in the WBF selection.

decay background necessitates the introduction of jet vetoes to render the signal visible. In addition, in order to study the weak-boson fusion production channel of the Higgs boson, it is important to understand jet production in association with the Higgs boson in the gluon-fusion channel as well, a topic discussed in Section 9.1 of this report. In this section, rather than focusing on the signal, the irreducible background to $H \to WW^*$ in the exclusive 0-jets and 1-jet bins will be discussed.

9.2.1 *Monte Carlo samples*

As the tool of choice the SHERPA event generator [162] is employed, using the recently developed multijet merging at next-to-leading order accuracy [189, 288]. Predictions obtained with this MEPS@NLO technology will be contrasted with inclusive MC@NLO and parton-level NLO results for the production of four leptons plus 0 or 1 jets, all taken from the corresponding implementations within SHERPA. While the latter guarantee NLO accuracy in the 0- and 1-jets bins, but do not resum the potentially large Sudakov logarithms arising in the presence of jet vetos, inclusive MC@NLO simulations provide a better description of such Sudakov logarithms in the 0-jet bin, but are only LO or leading-log accurate in bins with 1 or

more jets. This is overcome by the new MEPS@NLO algorithm, which effectively combines MC@NLO-type simulations [128] in the fully color-correct algorithm of [177, 297] for increasing jet multiplicities, preserving both the NLO accuracy of the contributions in the individual jet bins and the logarithmic accuracy of the parton shower. Result for four-lepton final states obtained with this formalism are presented for the first time here.

Virtual corrections are computed with OPENLOOPS [164], an automated generator of NLO QCD amplitudes for SM processes, which uses the COLLIER library for the numerically stable evaluation of tensor integrals [171, 172] and scalar integrals [173]. Thanks to a fully flexible interface of SHERPA with OPENLOOPS, the entire generation chain – from process definition to collider observables – is fully automated and can be steered through SHERPA run cards.

The results presented below refer to $\text{pp} \to \mu^+ \nu_\mu \text{e}^- \bar{\nu}_\text{e} + X$ at a centre-of-mass energy of 8 TeV and are based on a SHERPA 2.0 pre-release version[39]. The multijet merging is performed with a merging parameter of $Q_\text{cut} = 20$ GeV, and also LO matrix elements for $\text{pp} \to \mu^+ \nu_\mu \text{e}^- \bar{\nu}_\text{e} + 2$ jets are included in the merged sample. Gluon-gluon induced contributions resulting from squared loop amplitudes are discarded. All matrix elements are evaluated in the complex mass scheme and include all interference and off-shell effects. Masses and widths of the gauge bosons have been adjusted to yield the correct branching ratios into leptons at NLO accuracy and are given by

$$
\begin{aligned}
M_\text{W} &= 80.399 \, \text{GeV} \,, \quad \Gamma_\text{W} = 2.0997 \, \text{GeV} \,, \\
M_\text{Z} &= 91.1876 \, \text{GeV} \,, \quad \Gamma_\text{Z} = 2.5097 \, \text{GeV} \,,
\end{aligned}
\tag{89}
$$

while the electroweak mixing angle is a complex number given by the ratio of the complex W and Z masses, and

$$
G_F = 1.16637 \cdot 10^{-5} \, \text{GeV}^{-2} \quad \text{and} \quad 1/\alpha_\text{QED} = 132.348905 \,,
\tag{90}
$$

in the G_F-scheme. The five-flavor CT10 NLO [145] parton distributions with the respective running strong coupling α_s has been employed throughout. Contributions with external b-quarks are not included to trivially avoid any overlap with $\bar{\text{t}}\text{t}$ production. As a default renormalization (μ_R), factorization (μ_F) and resummation (μ_Q) scale we adopt the total invariant mass of the $\ell\ell'\nu\nu'$ final state, $\mu_0 = m_{\ell\ell'\nu\nu'}$. In the NLO parton-level predictions all α_s factors are evaluated at the same scale $\mu_\text{R} = \mu_\text{F} = \mu_0$, while μ_Q is irrelevant. In MEPS@NLO predictions the scale μ_0 is used only in tree and loop contributions to the $\text{pp} \to \mu^+ \nu_\mu \text{e}^- \bar{\nu}_\text{e}$ core process, after clustering of hard jet emission. For α_s factors associated with additional jet emissions a CKKW scale choice is applied. In fact, in contrast to the original proposal for such a choice for NLO merging presented in Ref. [189], the nodal k_T-scales for NLO parts of the simulation are implemented through

$$
\alpha_\text{s}(k_\text{T}) = \alpha_\text{s}(\mu_0) \left[1 - \frac{\alpha_\text{s}(\mu_0)}{2\pi} \beta_0 \log \frac{k_\text{T}^2}{\mu_0^2} \right] \,,
\tag{91}
$$

because preliminary studies suggest that this choice indeed further minimizes the effect of Q_cut variations.

There are various theoretical uncertainties entering the simulation of hadronic observables:

– renormalization and factorization scale uncertainties are assessed by an independent variation of μ_R and μ_F by factors of two excluding in both directions only the two opposite combinations. Note that the renormalization scale is varied in all α_s terms that arise in matrix elements or from the shower;

– resummation scale uncertainties are evaluated by varying the starting scale of the parton shower μ_Q by a factor of $\sqrt{2}$ in both directions;

---

[39]This pre-release version corresponds to SVN revision 21340 (25 Mar 2013) and the main difference with respect to the final SHERPA 2.0 release version is the tuning of parton shower, hadronization and multiple parton interactions to experimental data.

- PDF – and, related to them – $\alpha_\mathrm{s}(M_\mathrm{Z})$ uncertainties, which are both ignored here;
- non-perturbative uncertainties, which broadly fall into two categories: those related to the hadronization, which could be treated by retuning the hadronization to LEP data and allowing/enforcing a deviation of for example 5% or one charged particle in the mean charged particle multiplicity at the Z-pole, and those related to the underlying event, which could be evaluated by allowing the respective tunes to typical data to yield a 10% variation in the plateau region of the mean transverse momentum flow in the transverse regions of jet events. Both have been ignored here and will be presented in a forthcoming study.

Quantifying the resummation scale uncertainty is crucial for a realistic study of theory uncertainties in jet distributions and other observables sensitive to details of the QCD radiation pattern. As such, they certainly impact also on the cross sections in different jet bins. They can be assessed through μ_Q variations in the MEPs@Nlo approach, which provide some sensitivity to subleading – but potentially large – Sudakov logarithms resulting from jet vetoes. In contrast, the usual μ_R and μ_F variations alone are not sensitive to Sudakov logarithms or the scales entering them and are thus not sufficient for a reliable assessment of theory errors in jet bins. The consistent implementation of all these effects in ongoing, but preliminary studies suggest that the μ_Q variation is fairly suppressed compared to the standard μ_R and μ_F variation.

9.2.2 Experimental setups and cuts

The results presented here correspond to the cuts of the two relevant analyses by the ATLAS [103] and CMS [298] collaborations for $\mathrm{H} \to \mathrm{WW}^* \to \mu^+\nu_\mu \mathrm{e}^- \bar{\nu}_\mathrm{e}$ in the exclusive 0- and 1-jet bins. The various cuts are listed in Table 33[40]. Lepton isolation is implemented at the particle level to be close to the experimental definitions of both ATLAS and CMS. The scalar sum of the transverse momenta of all visible particles within a $R = 0.3$ cone around the lepton candidate is not allowed to exceed 15% of the lepton p_T. After a preselection (**S1**), additional cuts are applied that define a signal (**S2s**) and a control (**S2c**) region. The latter is exploited to normalize background simulations to data in the experimental analyses in each jet bin. In the ATLAS analysis, different cuts are applied in the 0- and 1-jet bins.

9.2.3 Results

Predictions and theoretical errors[41] for exclusive jet cross sections in the signal and control regions, as well as their ratios, are displayed in Tables 34 and 35 for the ATLAS and CMS analyses, respectively. Comparing Nlo, Mc@Nlo and MEPs@Nlo results at the same central scale we observe that deviations between Nlo and MEPs@Nlo predictions amount to only 0.5% and $1-3\%$ in the 0-jets and 1-jet bins, respectively. The differences between Mc@Nlo and MEPs@Nlo results are larger and reach The sizable deficit of the Mc@Nlo simulation in the 1-jet bin is not surprising given the limited (LO) accuracy of this approximation for exclusive 1-jet final states.

Differences between the Nlo, Mc@Nlo and MEPs@Nlo approximations are fairly similar in the various analyses and kinematic regions, and the agreement between the various approximations is at

---

[40]Definition of some kinematical quantities in Table 33:

†: The quantity $\displaystyle{\not}E_\mathrm{T}^{(\mathrm{proj})}$ is given by

$$\not{E}_\mathrm{T}^{(\mathrm{proj})} = \not{E}_\mathrm{T} \cdot \sin\left(\min\{\Delta\phi_\mathrm{near}, \pi/2\}\right) ,$$

where $\Delta\phi_\mathrm{near}$ denotes the angle between the missing transverse momentum $\not{E}_\mathrm{T}$ and the nearest lepton in the transverse plane.

‡: ATLAS and CMS have different definitions for m_T, namely

$$m_\mathrm{T}^2 = \begin{cases} \left(\sqrt{p_{\perp,\ell\ell'}^2 + m_{\ell\ell'}^2} + \not{E}_\mathrm{T}\right)^2 - \left|p_{\perp,\ell\ell'} + \not{E}_\mathrm{T}\right|^2 & \text{for} \quad \text{ATLAS} \\ 2|p_{\perp,\ell\ell'}|\,|\not{E}_\mathrm{T}|\,(1 - \cos\Delta\phi_{\ell\ell',\not{E}_\mathrm{T}}) & \text{for} \quad \text{CMS.} \end{cases}$$

[41]Scale variations in Mc@Nlo predictions are not considered.

Table 33: Jet definitions and selection cuts in the ATLAS [103] and CMS [298] analyses of H $\to$ WW* $\to$ $\mu^+\nu_\mu$e$^-\bar{\nu}_e$ at 8 TeV. Partons are recombined into jets using the anti-k_T algorithm [190]. The cuts refer to various levels and regions, namely event preselection (**S1** cuts), the signal region (**S1** and **S2s** cuts) and the control region (**S1** and **S2c** cuts). All cuts have been implemented in form of a RIVET [178] analysis.

anti-k_T jets		ATLAS		CMS	
R	=	0.4		0.5	
$p_{\perp,j}(|\eta_j|)$	>	25 GeV	$(|\eta_j| < 2.4)$	30 GeV	$(|\eta_j| < 4.7)$
		30 GeV	$(2.4 < |\eta_j| < 4.5)$		
S1		**ATLAS**		**CMS**	
$p_{\perp,\{\ell_1,\ell_2\}}$	>	25, 15 GeV		20, 10 GeV	
$|\eta_{\{e,\mu\}}|$	<	2.47, 2.5		2.5, 2.4	
$|\eta_e|$	$\notin$	[1.37, 1.57]			
$p_{\perp,\ell\ell'}$	>	see **S2s**, **S2c**		30 GeV	
$m_{\ell\ell'}$	>	10 GeV		12 GeV	
$\slashed{E}_T^{(\mathrm{proj})}$	>	25 GeV		20 GeV [†]	
S2s		**ATLAS**		**CMS**	
$\Delta\phi_{\ell\ell',\slashed{E}_T}$	>	$\pi/2$	(0 jets only)		
$p_{\perp,\ell\ell'}$	>	30 GeV	(0 jets only)		
$\Delta\phi_{\ell\ell'}$	<	1.8 rad			
$m_{\ell\ell'}$	<	50 GeV		200 GeV	
m_T	$\in$			[60 GeV, 280 GeV] [‡]	
S2c		**ATLAS**		**CMS**	
$\Delta\phi_{\ell\ell',\slashed{E}_T}$	>	$\pi/2$	(0 jets only)		
$p_{\perp,\ell\ell'}$	>	30 GeV	(0 jets only)		
$m_{\ell\ell'}$		$\in [50, 100]$ GeV	(0 jets only)	> 100 GeV	
		> 80 GeV	(1 jet only)		

the $0.5-3\%$ level in the $\sigma_{\mathrm{S2s}}/\sigma_{\mathrm{S2c}}$ ratios. The interpretation of this result as theoretical uncertainty in the extrapolation from control to signal regions requires a careful analysis of shape uncertainties, where also the (un)correlation of scale choices in the various predictions should be considered. These subtle issues are beyond the scope of the present study. We thus refrain from assigning theoretical uncertainties to the individual signal-to-control ratios. In contrast, scale variations of the absolute MEPS@NLO cross sections in the various regions and jet bins can be regarded as a realistic estimate of perturbative theory errors. Adding (μ_R, μ_F) and μ_Q variations in quadrature[42] we find a combined MEPS@NLO uncertainty of $3-4\%$ in both jet bins. The dominant contribution arises from renormalization and factorization scale variations, which turn out to be fairly consistent but slightly different from the scale variations of the parton-level NLO calculation. The observed (minor) differences can be attributed to the variation of extra α_s terms originating from the shower, the CKKW scale choice in the MEPS@NLO method, and the merging of different jet multiplicities, which opens gluon-initiated channels also in the 0-jets bin. Moreover, MEPS@NLO uncertainties might be slightly overestimated due to statistical fluctuations at 1% level.

Resummation scale variations of MEPS@NLO cross sections turn out to be rather small. This

---

[42]Variations of (μ_R, μ_F) and μ_Q can be regarded as uncorrelated and thus added in quadrature. Another natural way of combining these two sources of uncertainty is to consider simultaneous variations of (μ_R, μ_F, μ_Q), excluding rescalings in opposite directions as usual. The variations resulting from this alternative approach are likely to be even smaller than those obtained by adding QCD and resummation scale uncertainties in quadrature.

Table 34: Exclusive 0-jet and 1-jet bin cross sections in the signal (S2s) and control (S2c) regions for the ATLAS analysis at 8 TeV. The production of $\mu^+\nu_\mu e^-\bar{\nu}_e + 0, 1$ jets is described with NLO, MC@NLO (inclusive), and MEPS@NLO accuracy as described in the text. Results at NLO for the N-jet bin correspond to $\mu^+\nu_\mu e^-\bar{\nu}_e + N$ jets production. Variations of the (μ_R, μ_F) and μ_Q scales are labeled as Δ_{QCD} and Δ_{res}, respectively. Statistical errors are given in parenthesis.

0-jets bin	NLO $\pm\Delta_{\text{QCD}}$	MC@NLO	MEPS@NLO $\pm\Delta_{\text{QCD}} \pm\Delta_{\text{res}}$
σ_{S2s} [fb]	$35.08(9)\,^{+2.0\%}_{-1.9\%}$	$33.33(8)$	$35.21(15)\,^{+1.8\%\ +1.7\%}_{-3.3\%\ -0.6\%}$
σ_{S2c} [fb]	$57.05(9)\,^{+2.1\%}_{-2.0\%}$	$53.76(9)$	$56.76(17)\,^{+2.3\%\ +1.9\%}_{-3.6\%\ -0.3\%}$
$\sigma_{\text{S2s}}/\sigma_{\text{S2c}}$	0.615	0.620	0.620
1-jet bin	**NLO $\pm\Delta_{\text{QCD}}$**	**MC@NLO**	**MEPS@NLO $\pm\Delta_{\text{QCD}} \pm\Delta_{\text{res}}$**
σ_{S2s} [fb]	$9.43(3)\,^{+1.8\%}_{-4.7\%}$	$7.43(4)$	$9.23(9)\,^{+3.5\%\ +0.9\%}_{-1.9\%\ -0\%}$
σ_{S2c} [fb]	$29.14(6)\,^{+1.6\%}_{-4.7\%}$	$22.59(7)$	$28.80(21)\,^{+3.1\%\ +1.4\%}_{-2.5\%\ -1.7\%}$
$\sigma_{\text{S2s}}/\sigma_{\text{S2c}}$	0.324	0.329	0.320

Table 35: Exclusive 0-jet and 1-jet bin cross sections in the signal (S2s) and control (S2c) regions for the CMS analysis at 8 TeV, with the same structure and conventions as in Table 34.

0-jets bin	NLO $\pm\Delta_{\text{QCD}}$	MC@NLO	MEPS@NLO $\pm\Delta_{\text{QCD}} \pm\Delta_{\text{res}}$
σ_{S2s} [fb]	$159.34(18)\,^{+1.8\%}_{-1.7\%}$	$150.6(2)$	$160.3(3)\,^{+2.6\%\ +1.4\%}_{-3.8\%\ -0.5\%}$
σ_{S2c} [fb]	$60.08(15)\,^{+1.5\%}_{-1.4\%}$	$56.60(11)$	$60.31(22)\,^{+3.6\%\ +0.7\%}_{-3.5\%\ -0.2\%}$
$\sigma_{\text{S2s}}/\sigma_{\text{S2c}}$	2.65	2.66	2.66
1-jet bin	**NLO $\pm\Delta_{\text{QCD}}$**	**MC@NLO**	**MEPS@NLO $\pm\Delta_{\text{QCD}} \pm\Delta_{\text{res}}$**
σ_{S2s} [fb]	$45.01(7)\,^{+1.3\%}_{-2.6\%}$	$34.75(9)$	$44.88(23)\,^{+3.0\%\ +0.1\%}_{-2.7\%\ -0.3\%}$
σ_{S2c} [fb]	$22.09(5)\,^{+1.2\%}_{-3.2\%}$	$17.41(7)$	$22.30(18)\,^{+3.0\%\ +0.5\%}_{-2.7\%\ -0.4\%}$
$\sigma_{\text{S2s}}/\sigma_{\text{S2c}}$	2.04	2.00	2.01

suggests that higher-order subleading Sudakov logarithms, which are beyond the accuracy of the shower, are quite suppressed. The rather good agreement between NLO and MEPS@NLO predictions indicates that also leading-logarithmic resummation effects have a quantitatively small impact on the considered observables.

In Figures 77–79 distributions for the transverse mass m_{T} and the dilepton mass $m_{\ell\ell'}$ are displayed for the ATLAS analysis at 8 TeV. Similar plots for the CMS analysis are shown in Figures 80–82. These observables provide high sensitivity to the Higgs signal. They are depicted separately in the exclusive 0- and 1-jet bins in the signal (**S1** and **S2s** cuts) and control (**S1** and **S2c** cuts) regions. In the lower frames, the various predictions are normalized to MEPS@NLO results at the central scale. Scale variations are given only for the MEPS@NLO case. Specifically, the individual (μ_R, μ_F) and μ_Q variations and their combination in quadrature are displayed as three separate color-additive bands.

Comparing NLO, MC@NLO and MEPS@NLO distributions, agreement on the few-percent level in the 0-jet is found, while in the 1-jet bin discrepancies between MC@NLO and MEPS@NLO on the 20% level appear. This is consistent with the results in Table 34 and Table 35. In the case of both m_{T} and $m_{\ell\ell'}$ distributions, also some shape distortions emerge. However, as could be anticipated they are fairly moderate in the 0-jet bins and reach up to about 20% in the hard region of the 1-jet bins. In the tails of some distributions scale-variation bands are distorted by statistical fluctuations. These features are
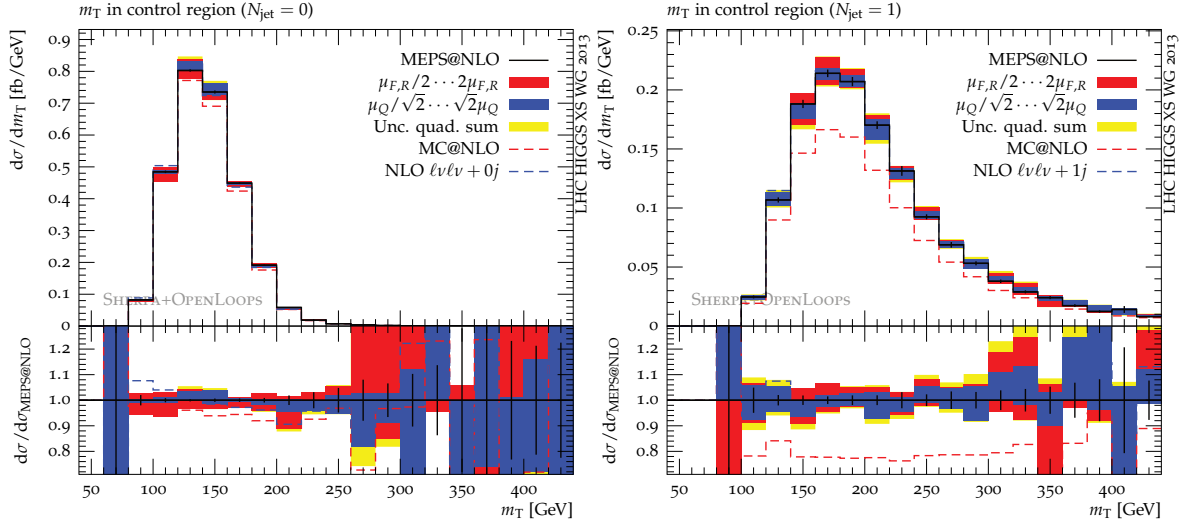
Fig. 77: Control region of the ATLAS analysis at 8 TeV: transverse-mass distribution in the 0-jets (left) and 1-jet (right) bins. MEPS@NLO (black solid), inclusive MC@NLO (red dashed), and NLO (blue dashed) predictions at the central scale $\mu_R = \mu_F = \mu_Q = m_{\ell\ell'\nu\nu'}$. In the lower panel, showing the deviations and uncertainties, results are normalized to the central MEPS@NLO predictions. The factor-2 variations of μ_R and μ_F (red band), and factor-$\sqrt{2}$ variations of μ_Q (blue band), are combined in quadrature (yellow band). Scale variation bands are color additive, i.e., yellow+blue=green, yellow+red=orange, and yellow+red+blue=brown.
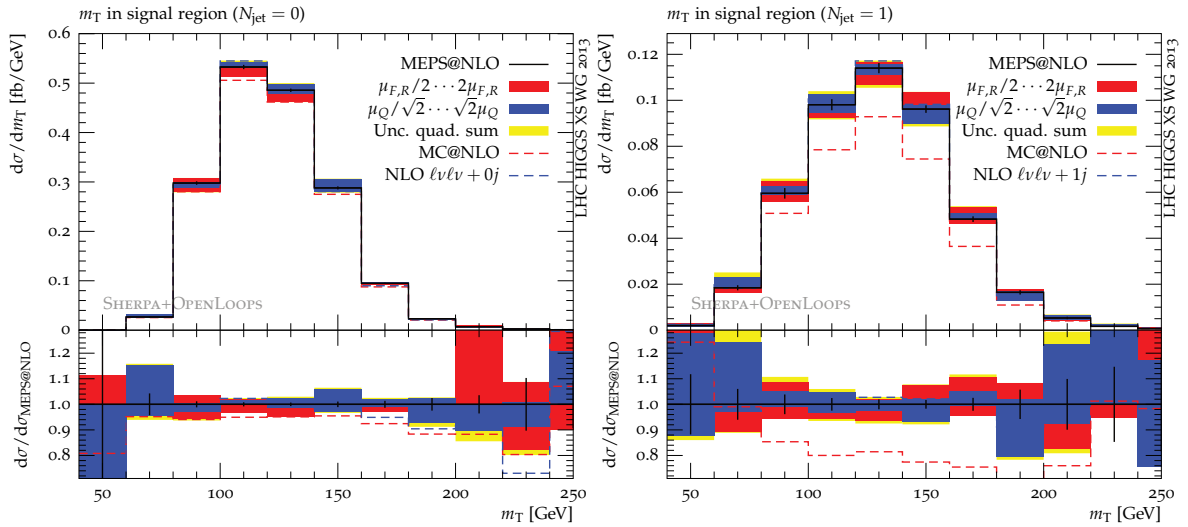
Fig. 78: Signal region of the ATLAS analysis at 8 TeV: transverse-mass distribution in the 0-jets (left) and 1-jet (right) bins. Same approximations and conventions as in Figure 77.

qualitatively similar in the ATLAS and CMS setups.

9.2.4 Conclusion and outlook

The findings of this contribution can be summarized as follows:

– Analyzing the leptonic observables m_T and $m_{\ell\ell'}$ only moderate shape distortions emerge between MC@NLO and MEPS@NLO predictions, which reach up to about 20% only in the hard tails of the leptonic system.
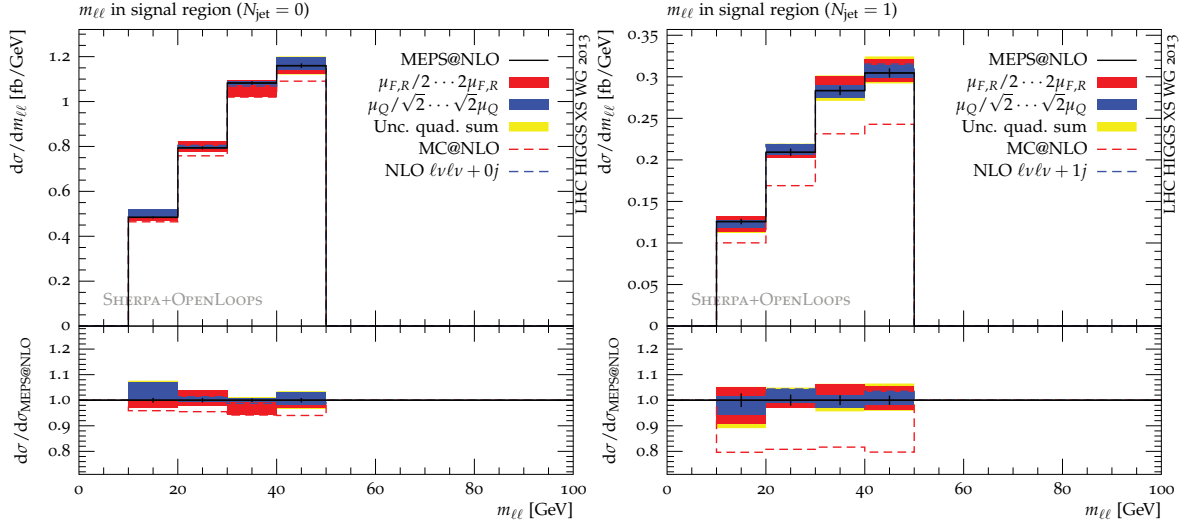
Fig. 79: Signal region of the ATLAS analysis at 8 TeV: dilepton invariant-mass distribution in the 0-jets (left) and 1-jet (right) bins. Same approximations and conventions as in Figure 77.
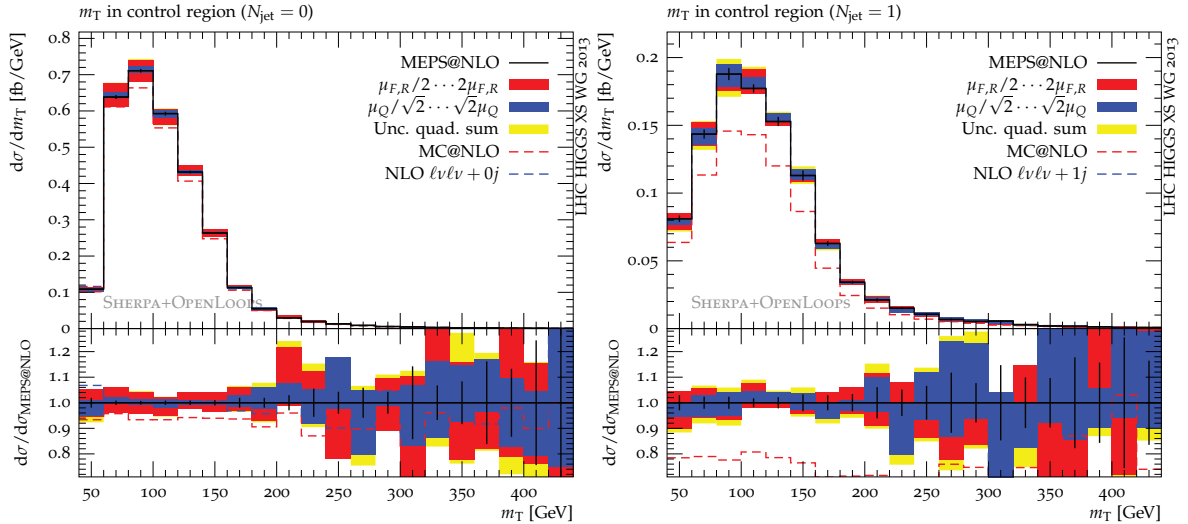
Fig. 80: Control region of the CMS analysis at 8 TeV: transverse-mass distribution in the 0-jets (left) and 1-jet (right) bins. Same approximations and conventions as in Figure 77.

- The picture changes when discussing the cross sections in the different jet bins, where sizable differences of up to about 20% emerge between MC@NLO and MEPS@NLO predictions. They are well understood and reflect the fact that the 1-jet contribution in MEPS@NLO is evaluated at logarithmically improved NLO accuracy, while in MC@NLO the fixed order accuracy is LO only. It can be expected that this trend will also continue, and probably become more pronounced, when studying the 2-jet bin, relevant for the weak boson fusion channel. This is left for further investigations.

- Comparing MEPS@NLO and NLO predictions one finds only small deviations at 0.5% and 3% level in the 0- and 1-jet bin cross sections, respectively.

- The combined theoretical uncertainties, as estimated through renormalization-, factorization- and resummation-scale variations in the MEPS@NLO approach, amount to $3-4\%$, both in the 0- and 1-jets bins. Resummation scale variations turn out to be rather small, suggesting that subleading
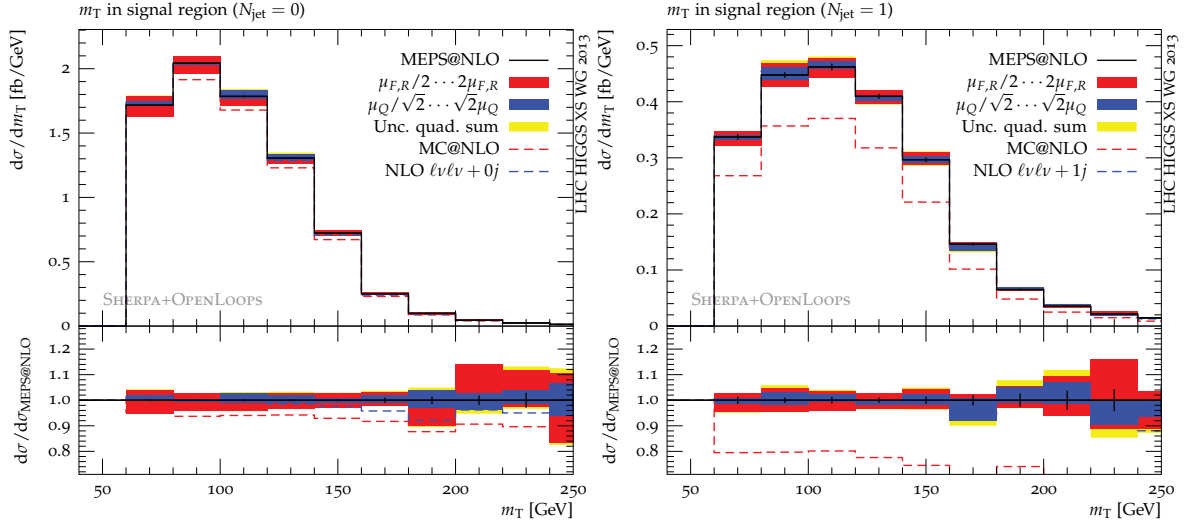
Fig. 81: Signal region of the CMS analysis at 8 TeV: transverse-mass distribution in the 0-jets (left) and 1-jet (right) bins. Same approximations and conventions as in Figure 77.
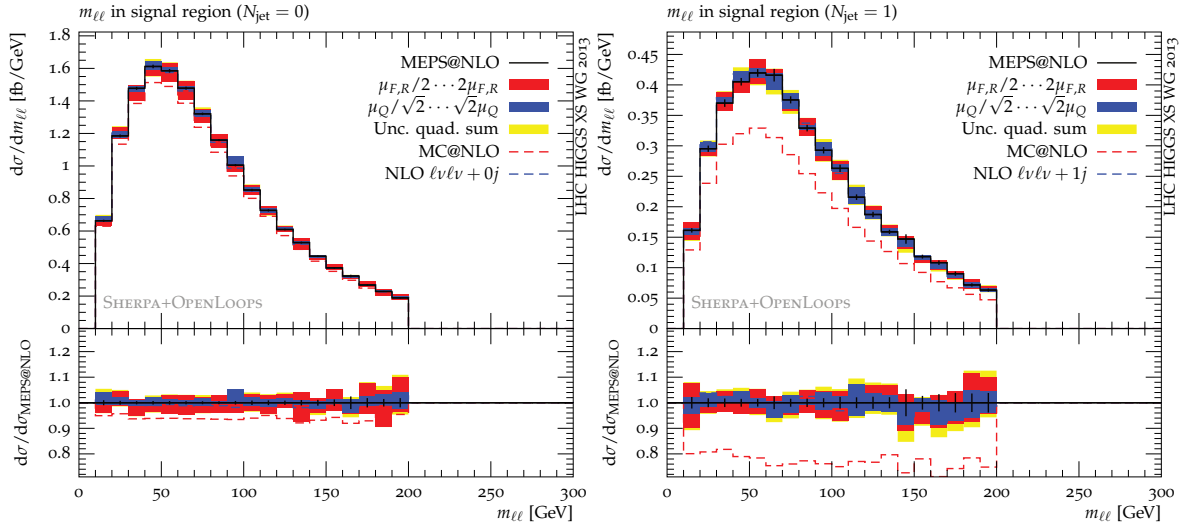

Fig. 82: Signal region of the CMS analysis at 8 TeV: dilepton invariant-mass distribution in the 0-jets (left) and 1-jet (right) bins. Same approximations and conventions as in Figure 77.

logarithms beyond the shower accuracy are not important. The few-percent level agreement between NLO and MEPS@NLO cross sections in both jet bins indicates that also leading-log effects beyond NLO are rather small.

– Although the effect of hadronization and the underlying event have not been investigated here, it is clear that the former will not lead to uncertainties that are comparable in size to the ones already present. This is not quite so clear for the underlying event, which will influence the observable cross sections in two ways. First of all, a varying hadronic activity will lead to varying acceptance of isolated leptons. At the same time, variations in the underlying event activity or hardness may also lead to differences in the jet multiplicity distribution. The quantification of such effects will be left to further studies.

9.3 NLO QCD corrections to the production of Higgs boson plus two and three jets in gluon fusion

In this section, we illustrate the recent computation of the NLO contributions to Higgs plus two jets production at the LHC in the large top-mass limit [292], and for the first time also provide results for the one-loop virtual contribution to Higgs plus three jets production.

The results are obtained by using a fully automated framework for fixed order NLO QCD calculations based on the interplay of the packages GOSAM [299] and SHERPA [162]. For the computation of the virtual corrections we use a code generated by the program package GOSAM, which combines automated diagram generation and algebraic manipulation with integrand-level reduction techniques [133, 300, 301]. More specifically, the virtual corrections are evaluated using the d-dimensional integrand-level decomposition implemented in the SAMURAI library [302], which allows for the combined determination of both cut-constructible and rational terms at once. Moreover, the presence of effective couplings in the Lagrangian requires an extended version [303] of the integrand-level reduction, of which the present calculation is a first application. For the calculation of tree-level contributions we use SHERPA [162], which computes the LO and the real radiation matrix elements [165], regularizes the IR and collinear singularities using the Catani-Seymour dipole formalism [166], and carries out the phase space integrations as well. The code that evaluates the virtual corrections, generated by GOSAM, is linked to SHERPA via the Binoth-Les-Houches Accord (BLHA) [293] interface, which allows for a direct communication between the two codes at running time.

9.3.1 Results for $\mathrm{pp} \rightarrow \mathrm{H}jj$ with GOSAM-SHERPA

For Hjj production, GOSAM identifies and generates the following minimal set of processes $\mathrm{gg} \rightarrow \mathrm{Hgg}$, $\mathrm{gg} \rightarrow \mathrm{H\overline{q}q}$, $\mathrm{\overline{q}q} \rightarrow \mathrm{H\overline{q}q}$, $\mathrm{\overline{q}q} \rightarrow \mathrm{Hq'\overline{q}'}$. The other processes are obtained by performing the appropriate symmetry transformation. The ultraviolet (UV), the infrared, and the collinear singularities are regularized using dimensional reduction (DRED). UV divergences have been renormalized in the $\overline{\mathrm{MS}}$ scheme. Our results are in agreement with [304] and MCFM (v6.4) [259].

As an illustration of possible analyses that can be performed with the GOSAM-SHERPA automated setup, in Fig. 83 we present the distribution of the transverse momentum p_{T} of the Higgs boson and its pseudorapidity η, for proton-proton collisions at the LHC at $\sqrt{s} = 8$ TeV. Both of them show a K-factor between the LO and the NLO distribution of about $1.5 - 1.6$ and a decrease of the scale uncertainty of about 50%. These results are obtained using the parameters $M_{\mathrm{H}} = 125\mathrm{Gev}$,
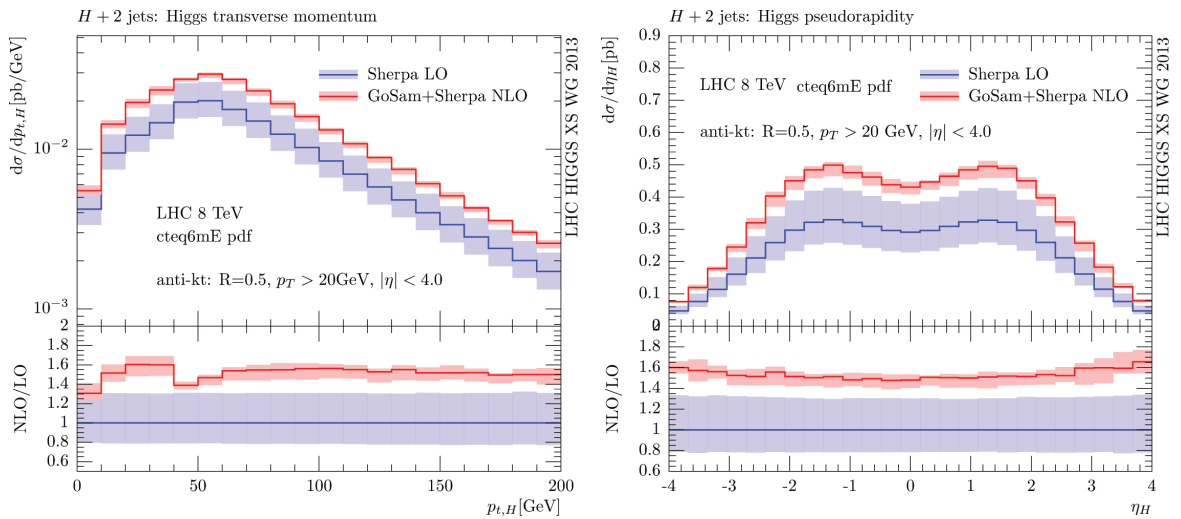

Fig. 83: Transverse momentum p_{T} and pseudorapidity η of the Higgs boson.

127

$G_F = 1.16639 \cdot 10^{-5} \, \mathrm{Gev}^{-2}$, $\alpha_s^{\mathrm{LO}}(M_Z) = 0.129783$, and $\alpha_s^{\mathrm{NLO}}(M_Z) = 0.117981$. We use the CTEQ6L1 and CTEQ6mE [169] parton distribution functions (PDF) for the LO and NLO, respectively. The jets are clustered by using the anti-k_T algorithm provided by the FastJet package with the following setup: $p_{t,j} \geq 20 \mathrm{Gev}$, $|\eta_j| \leq 4.0$, $R = 0.5$. The Higgs boson is treated as a stable on-shell particle, without including any decay mode. To fix the factorization and the renormalization scale we define $\hat{H}_t = \sqrt{M_\mathrm{H}^2 + p_{t,H}^2} + \sum_j p_{t,j}$, where $p_{t,H}$ and $p_{t,j}$ are the transverse momenta of the Higgs boson and the jets. The nominal value for the two scales is defined as $\mu = \mu_\mathrm{R} = \mu_\mathrm{F} = \hat{H}_t$, whereas theoretical uncertainties are assessed by varying simultaneously the factorization and renormalization scales in the range $\frac{1}{2}\hat{H}_t < \mu < 2\hat{H}_t$. The error is estimated by taking the envelope of the resulting distributions at the different scales.

Within our framework, we find the following total cross sections for the process $\mathrm{pp} \to \mathrm{H}jj$ in gluon fusion:

$$\sigma_\mathrm{LO} = 1.90^{+0.58}_{-0.41} \, \mathrm{pb}, \quad \sigma_\mathrm{NLO} = 2.90^{+0.05}_{-0.20} \, \mathrm{pb}.$$

9.3.2 *Virtual corrections to* $\mathrm{pp} \to \mathrm{H}jjj$

All independent processes contributing to $\mathrm{H}jjj$ can be obtained by adding one extra gluon to the final state of the processes listed in the case of $\mathrm{H}jj$. Accordingly, we generate the codes for the virtual corrections to the processes $\mathrm{gg} \to \mathrm{Hggg}$, $\mathrm{gg} \to \mathrm{H}\overline{\mathrm{q}}\mathrm{qg}$, $\overline{\mathrm{q}}\mathrm{q} \to \mathrm{H}\overline{\mathrm{q}}\mathrm{qg}$, $\mathrm{q}\overline{\mathrm{q}} \to \mathrm{Hq}'\overline{\mathrm{q}}'\mathrm{g}$. Some representative one-loop diagrams are depicted in Fig. 84.
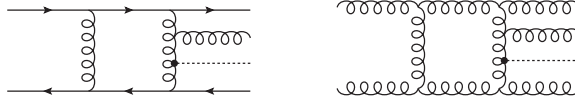
Fig. 84: Sample hexagon diagrams which enter in the six-parton one-loop amplitudes for $\overline{\mathrm{q}}\mathrm{q} \to \mathrm{H}\overline{\mathrm{q}}\mathrm{qg}$ and $\mathrm{gg} \to \mathrm{Hggg}$. The dot represents the effective ggH vertex.

To display our results for the virtual matrix elements of the various subprocesses, we choose an arbitrary phase space point, with the momenta of the initial partons along the z-axis. Then, we create new momentum configurations by rotating the final state through an angle θ about the y-axis. For each subprocess, we plot in Figure 85 the behavior of the finite part a_0 of the amplitudes defined as

$$\frac{2\mathfrak{Re}\left\{\mathcal{M}^{\mathrm{tree\text{-}level}*}\mathcal{M}^{\mathrm{one\text{-}loop}}\right\}}{(4\pi\alpha_s)\left|\mathcal{M}^{\mathrm{tree\text{-}level}}\right|^2} \equiv \frac{a_{-2}}{\epsilon^2} + \frac{a_{-1}}{\epsilon} + a_0 \,,$$

when the final external momenta are rotated from $\theta = 0$ to $\theta = 2\pi$. We verified that the values of the double and the single poles conform to the universal singular behavior of dimensionally regulated one-loop amplitudes.
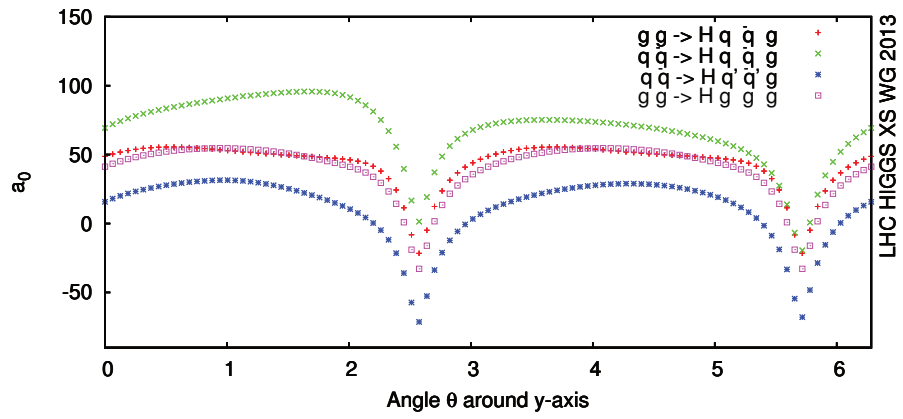
Fig. 85: Finite-term of the virtual matrix elements for $gg \rightarrow H\overline{q}qg$ (red), $\overline{q}q \rightarrow H\overline{q}qg$ (green), $\overline{q}q \rightarrow Hq'\overline{q}'g$ (red), $gg \rightarrow Hggg$ (purple).

10 Higgs properties: couplings[43] [44]

10.1 Introduction

The recent observation of a new massive neutral boson by ATLAS and CMS [1, 2], as well as evidence from the Tevatron experiments [305], opens a new era where characterization of this new object is of central importance.

The SM, as any renormalizable theory, makes very accurate predictions for the coupling of the Higgs boson to all other known particles. These couplings directly influence the rates and kinematic properties of production and decay of the Higgs boson. Therefore, measurement of the production and decay rates of the observed state as well as its angular correlations yields information that can be used to probe whether data are compatible with the SM predictions for the Higgs boson.

While coarse features of the observed state can be inferred from the information that the experiments have made public, only a consistent and combined treatment of the data can yield the most accurate picture of the coupling structure. Such a treatment must take into account all the systematic and statistical uncertainties considered in the analyses, as well as the correlations among them.

At the LHC a SM-like Higgs boson is searched for mainly in four exclusive production processes: the predominant gluon fusion $gg \to H$, the vector boson fusion $qq' \to qq'H$, the associated production with a vector boson $q\overline{q} \to WH/ZH$ and the associated production with a top-quark pair $q\overline{q}/gg \to t\overline{t}H$. The main search channels are determined by five decay modes of the Higgs boson, the $\gamma\gamma$, $ZZ^{(*)}$, $WW^{(*)}$, $b\overline{b}$ and $\tau^+\tau^-$ channels.

In 2011, the LHC delivered an integrated luminosity of slightly less than 6 fb^{-1} of proton–proton (pp) collisions at a centre-of-mass energy of 7 TeV to the ATLAS and CMS experiments. In 2012, the LHC delivered approximately 23 fb^{-1} of pp collisions at a centre-of-mass energy of 8 TeV to both experiments. For this dataset, the instantaneous luminosity reached record levels of approximately $7 \cdot 10^{33}$ cm^{-2} s^{-1}, almost double the peak luminosity of 2011 with the same 50 ns bunch spacing.

The ATLAS and CMS experiments have reported compatible measurements of the mass of the observed narrow resonance yielding:

$$125.5 \pm 0.2(\text{stat.}) \, {}^{+0.5}_{-0.6}(\text{syst.}) \text{ GeV (ATLAS [9]),}$$
$$125.7 \pm 0.3(\text{stat.}) \pm 0.3(\text{syst.}) \text{ GeV (CMS [10]).}$$

In Sections 10.2 and 10.3 we present and extend the interim framework and benchmarks [306] for the measurements of Higgs couplings. With increasing precision of the measurements, this framework eventually has to be replaced by one that allows for a fully consistent inclusion of higher-order corrections. Such a framework is provided by an effective Lagrangian formalism. To start with, we define in Section 10.4 effective Lagrangians for Higgs interactions to be used in future calculations and experimental determinations of Higgs couplings. Methods for the measurement of the spin and the CP properties of the Higgs boson are described in Section 11.

10.2 Interim framework for the analysis of Higgs couplings

This subsection outlines an interim framework to explore the coupling structure of the recently observed state. The framework proposed in this recommendation should be seen as a continuation of the earlier studies of the LHC sensitivity to the Higgs couplings initiated in Refs. [307–310], and has been influenced by the works of Refs. [109, 311–317]. It follows closely the methodology proposed in the

recent phenomenological works of Refs. [318–320] which have been further extended in several directions [321–408] along the lines that are formalized in the present recommendation. While the interim framework is not final, it has an accuracy that matches the statistical power of the datasets that the LHC experiments have collected until the end of the 2012 LHC run and is an explicit attempt to provide a common ground for the dialogue in the, and between the, experimental and theoretical communities.

Based on that framework, a series of benchmark parameterizations are presented in Section 10.3. Each benchmark parameterization allows to explore specific aspects of the coupling structure of the new state. The parameterizations have varying degrees of complexity, with the aim to cover the most interesting possibilities that can be realistically tested with the LHC 7 and 8 TeV datasets. On the one hand, the framework and benchmarks were designed to provide a recommendation to experiments on how to perform coupling fits that are useful for the theory community. On the other hand the theory community can prepare for results based on the framework discussed in this document.

10.2.1 *Idea and underlying assumptions*

The idea behind this framework is that all deviations from the SM are computed assuming that there is only one underlying state at ~ 125 GeV. It is assumed that this state is a Higgs boson, i.e. the excitation of a field whose vacuum expectation value (VEV) breaks electroweak symmetry, and that it is SM-like, in the sense that the experimental results so far are compatible with the interpretation of the state in terms of the SM Higgs boson. No specific assumptions are made on any additional states of new physics (and their decoupling properties) that could influence the phenomenology of the 125 GeV state, such as additional Higgs bosons (which could be heavier but also lighter than 125 GeV), additional scalars that do not develop a VEV, and new fermions and/or gauge bosons that could interact with the state at 125 GeV, giving rise, for instance, to an invisible decay mode.

The purpose of this framework is to either confirm that the light, narrow, resonance indeed matches the properties of the SM Higgs, or to establish a deviation from the SM behavior, which would rule out the SM if sufficiently significant. In the latter case the next goal in the quest to identify the nature of EWSB would obviously be to test the compatibility of the observed patterns with alternative frameworks of EWSB.

In investigating the experimental information that can be obtained on the coupling properties of the new state near 125 GeV from the LHC data collected so far the following assumptions are made[45]:

– The signals observed in the different search channels originate from a single narrow resonance with a mass near 125 GeV. The case of several, possibly overlapping, resonances in this mass region is not considered.

– The width of the assumed Higgs boson near 125 GeV is neglected, i.e. the zero-width approximation for this state is used. Hence the signal cross section can be decomposed in the following way for all channels:

$$(\sigma \cdot \mathrm{BR}) \left(ii \rightarrow \mathrm{H} \rightarrow ff \right) = \frac{\sigma_{ii} \cdot \Gamma_{ff}}{\Gamma_{\mathrm{H}}} \tag{92}$$

where σ_{ii} is the production cross section through the initial state ii, Γ_{ff} the partial decay width into the final state ff and Γ_{H} the total width of the Higgs boson.

Within the context of these assumptions, in the following a simplified framework for investigating the experimental information that can be obtained on the coupling properties of the new state is outlined. In general, the couplings of the assumed Higgs state near 125 GeV are "pseudo-observables", i.e. they cannot be directly measured. This means that a certain "unfolding procedure" is necessary to extract information on the couplings from the measured quantities like cross sections times branching ratios (for specific experimental cuts and acceptances). This gives rise to a certain model dependence of the

---

[45]The experiments are encouraged to test the assumptions of the framework, but that lies outside the scope of this document.

extracted information. Different options can be pursued in this context. One possibility is to confront a specific model with the experimental data. This has the advantage that all available higher-order corrections within this model can consistently be included and also other experimental constraints (for instance from direct searches or from electroweak precision data) can be taken into account. However, the results obtained in this case are restricted to the interpretation within that particular model. Another possibility is to use a general parameterization of the couplings of the new state without referring to any particular model. While this approach is clearly less model-dependent, the relation between the extracted coupling parameters and the couplings of actual models, for instance the SM or its minimal supersymmetric extension (MSSM), is in general non-trivial, so that the theoretical interpretation of the extracted information can be difficult. It should be mentioned that the results for the signal strengths of individual search channels that have been made public by ATLAS and CMS, while referring just to a particular search channel rather than to the full information available from the Higgs searches, are nevertheless very valuable for testing the predictions of possible models of physics beyond the SM.

In the SM, once the numerical value of the Higgs mass is specified, all the couplings of the Higgs boson to fermions, bosons and to itself are specified within the model. It is therefore in general not possible to perform a fit to experimental data within the context of the SM where Higgs couplings are treated as free parameters. While it is possible to test the overall compatibility of the SM with the data, it is not possible to extract information about deviations of the measured couplings with respect to their SM values.

A theoretically well-defined framework, as outlined in Section 10.4, for probing small deviations from the SM predictions — or the predictions of another reference model — is to use the state-of-the-art predictions in this model (including all available higher-order corrections) and to supplement them with the contributions of additional terms in the Lagrangian, which are usually called "anomalous couplings". In such an approach and in general, not only the coupling strength, i.e. the absolute value of a given coupling, will be modified, but also the tensor structure of the coupling. For instance, the HW^+W^- LO coupling in the SM is proportional to the metric tensor $g^{\mu\nu}$, while anomalous couplings will generally also give rise to other tensor structures, however required to be compatible with the $SU(2) \times U(1)$ symmetry and the corresponding Ward-Slavnov-Taylor identities. As a consequence, kinematic distributions will in general be modified when compared to the SM case.

Since the reinterpretation of searches that have been performed within the context of the SM is difficult if effects that change kinematic distributions are taken into account and since not all the necessary tools to perform this kind of analysis are available yet, the following additional assumption is made in this simplified framework:

– Only modifications of couplings strengths, i.e. of absolute values of couplings, are taken into account, while the tensor structure of the couplings is assumed to be the same as in the SM prediction. This means in particular that the observed state is assumed to be a CP-even scalar.

As mentioned above, the described framework assumes that the observed state is SM-like. In case a large discrepancy from SM-like behavior is established, this framework would still be useful for assessing the level of compatibility of the SM predictions with the data. The interpretation of the physical origin of such a discrepancy, on the other hand, would most likely require to go beyond this framework.

10.2.2 Definition of coupling scale factors

In order to take into account the currently best available SM predictions for Higgs cross sections, which include higher-order QCD and EW corrections [13, 14, 409], while at the same time introducing possible deviations from the SM values of the couplings, the predicted SM Higgs cross sections and partial decay widths are dressed with scale factors κ_i. The scale factors κ_i are defined in such a way that the cross sections σ_{ii} or the partial decay widths Γ_{ii} associated with the SM particle i scale with the factor κ_i^2

when compared to the corresponding SM prediction. Table 36 lists all relevant cases. Taking the process $gg \rightarrow H \rightarrow \gamma\gamma$ as an example, one would use as cross section:

$$(\sigma \cdot BR)(gg \rightarrow H \rightarrow \gamma\gamma) = \sigma_{SM}(gg \rightarrow H) \cdot BR_{SM}(H \rightarrow \gamma\gamma) \cdot \frac{\kappa_g^2 \cdot \kappa_\gamma^2}{\kappa_H^2} \quad (93)$$

where the values and uncertainties for both $\sigma_{SM}(gg \rightarrow H)$ and $BR_{SM}(H \rightarrow \gamma\gamma)$ are taken from Ref. [409] for a given Higgs mass hypothesis.

By definition, the currently best available SM predictions for all $\sigma \cdot BR$ are recovered when all $\kappa_i = 1$. In general, this means that for $\kappa_i \neq 1$ higher-order accuracy is lost. Nonetheless, NLO QCD corrections essentially factorize with respect to coupling rescaling, and are accounted for wherever possible. This approach ensures that for a true SM Higgs boson no artificial deviations (caused by ignored NLO corrections) are found from what is considered the SM Higgs boson hypothesis. The functions $\kappa_{VBF}^2(\kappa_W, \kappa_Z, m_H)$, $\kappa_g^2(\kappa_b, \kappa_t, m_H)$, $\kappa_\gamma^2(\kappa_b, \kappa_t, \kappa_\tau, \kappa_W, m_H)$, $\kappa_{(Z\gamma)}^2(\kappa_b, \kappa_t, \kappa_\tau, \kappa_W, m_H)$ and $\kappa_H^2(\kappa_i, m_H)$ are used for cases where there is a non-trivial relationship between scale factors κ_i and cross sections or (partial) decay widths, and are calculated to NLO QCD accuracy. The functions are defined in the following sections and all required input parameters as well as example code can be found in Ref. [409]. As explained in Sec. 10.2.3 below, the notation in terms of the partial widths $\Gamma_{WW^{(*)}}$ and $\Gamma_{ZZ^{(*)}}$ in Table 36 is meant for illustration only. In the experimental analysis the 4-fermion partial decay widths are taken into account.

10.2.2.1 Scaling of the VBF cross section

κ_{VBF}^2 refers to the functional dependence of the VBF[46] cross section on the scale factors κ_W^2 and κ_Z^2:

$$\kappa_{VBF}^2(\kappa_W, \kappa_Z, m_H) = \frac{\kappa_W^2 \cdot \sigma_{WF}(m_H) + \kappa_Z^2 \cdot \sigma_{ZF}(m_H)}{\sigma_{WF}(m_H) + \sigma_{ZF}(m_H)} \quad (110)$$

The W- and Z-fusion cross sections, σ_{WF} and σ_{ZF}, are taken from Refs. [112, 410]. The interference term is $< 0.1\%$ in the SM and hence ignored [105].

In Table 37 one can find the approximate values to be inserted in Eq. (110) for $m_H = 125$ GeV.

10.2.2.2 Scaling of the gluon fusion cross section and of the $H \rightarrow gg$ decay vertex

κ_g^2 refers to the scale factor for the loop-induced production cross section σ_{ggH}. The decay width Γ_{gg} is not observable at the LHC, however its contribution to the total width is also considered.

Gluon fusion cross-section scaling
As NLO QCD corrections factorize with the scaling of the electroweak couplings with κ_t and κ_b, the function $\kappa_g^2(\kappa_b, \kappa_t, m_H)$ can be calculated in NLO QCD:

$$\kappa_g^2(\kappa_b, \kappa_t, m_H) = \frac{\kappa_t^2 \cdot \sigma_{ggH}^{tt}(m_H) + \kappa_b^2 \cdot \sigma_{ggH}^{bb}(m_H) + \kappa_t \kappa_b \cdot \sigma_{ggH}^{tb}(m_H)}{\sigma_{ggH}^{tt}(m_H) + \sigma_{ggH}^{bb}(m_H) + \sigma_{ggH}^{tb}(m_H)} \quad (111)$$

Here, σ_{ggH}^{tt}, σ_{ggH}^{bb} and σ_{ggH}^{tb} denote the square of the top-quark contribution, the square of the bottom-quark contribution and the top-bottom interference, respectively. The interference term (σ_{ggH}^{tb}) is

---

[46]Vector Boson Fusion is also called Weak Boson Fusion, as only the weak bosons W and Z contribute to the production.

Table 36: LO coupling scale factor relations for Higgs boson cross sections and partial decay widths relative to the SM. For a given m_H hypothesis, the smallest set of degrees of freedom in this framework comprises κ_W, κ_Z, κ_b, κ_t, and κ_τ. For partial widths that are not detectable at the LHC, scaling is performed via proxies chosen among the detectable ones. Additionally, the loop-induced vertices can be treated as a function of other κ_i or effectively, through the κ_g and κ_γ degrees of freedom which allow probing for BSM contributions in the loops. Finally, to explore invisible or undetectable decays, the scaling of the total width can also be taken as a separate degree of freedom, κ_H, instead of being rescaled as a function, $\kappa_H^2(\kappa_i, m_H)$, of the other scale factors.

Production modes

$$\frac{\sigma_{ggH}}{\sigma_{ggH}^{SM}} = \begin{cases} \kappa_g^2(\kappa_b, \kappa_t, m_H) \\ \kappa_g^2 \end{cases} \quad (94)$$

$$\frac{\sigma_{VBF}}{\sigma_{VBF}^{SM}} = \kappa_{VBF}^2(\kappa_W, \kappa_Z, m_H) \quad (95)$$

$$\frac{\sigma_{WH}}{\sigma_{WH}^{SM}} = \kappa_W^2 \quad (96)$$

$$\frac{\sigma_{ZH}}{\sigma_{ZH}^{SM}} = \kappa_Z^2 \quad (97)$$

$$\frac{\sigma_{t\bar{t}H}}{\sigma_{t\bar{t}H}^{SM}} = \kappa_t^2 \quad (98)$$

Detectable decay modes

$$\frac{\Gamma_{WW^{(*)}}}{\Gamma_{WW^{(*)}}^{SM}} = \kappa_W^2 \quad (99)$$

$$\frac{\Gamma_{ZZ^{(*)}}}{\Gamma_{ZZ^{(*)}}^{SM}} = \kappa_Z^2 \quad (100)$$

$$\frac{\Gamma_{b\bar{b}}}{\Gamma_{b\bar{b}}^{SM}} = \kappa_b^2 \quad (101)$$

$$\frac{\Gamma_{\tau^-\tau^+}}{\Gamma_{\tau^-\tau^+}^{SM}} = \kappa_\tau^2 \quad (102)$$

$$\frac{\Gamma_{\gamma\gamma}}{\Gamma_{\gamma\gamma}^{SM}} = \begin{cases} \kappa_\gamma^2(\kappa_b, \kappa_t, \kappa_\tau, \kappa_W, m_H) \\ \kappa_\gamma^2 \end{cases} \quad (103)$$

Currently undetectable decay modes

$$\frac{\Gamma_{t\bar{t}}}{\Gamma_{t\bar{t}}^{SM}} = \kappa_t^2 \quad (104)$$

$$\frac{\Gamma_{gg}}{\Gamma_{gg}^{SM}} : \quad \text{see Section 10.2.2}$$

$$\frac{\Gamma_{c\bar{c}}}{\Gamma_{c\bar{c}}^{SM}} = \kappa_t^2 \quad (105)$$

$$\frac{\Gamma_{s\bar{s}}}{\Gamma_{s\bar{s}}^{SM}} = \kappa_b^2 \quad (106)$$

$$\frac{\Gamma_{\mu^-\mu^+}}{\Gamma_{\mu^-\mu^+}^{SM}} = \kappa_\tau^2 \quad (107)$$

$$\frac{\Gamma_{Z\gamma}}{\Gamma_{Z\gamma}^{SM}} = \begin{cases} \kappa_{(Z\gamma)}^2(\kappa_b, \kappa_t, \kappa_\tau, \kappa_W, m_H) \\ \kappa_{(Z\gamma)}^2 \end{cases} \quad (108)$$

Total width

$$\frac{\Gamma_H}{\Gamma_H^{SM}} = \begin{cases} \kappa_H^2(\kappa_i, m_H) \\ \kappa_H^2 \end{cases} \quad (109)$$

Table 37: Approximate numerical values for resolving the VBF production cross-section according to Eq. (110) assuming $m_H = 125$ GeV.

$\sqrt{s}$	σ_{WF} (pb)	σ_{ZF} (pb)
7 TeV	0.938	0.321
8 TeV	1.210	0.417

negative for a light mass Higgs, $m_H < 200$ GeV. Within the LHC Higgs Cross Section Working Group (for the evaluation of the MSSM cross section) these contributions were evaluated, where for σ_{ggH}^{bb} and σ_{ggH}^{tb} the full NLO QCD calculation included in HIGLU [411] was used. For σ_{ggH}^{tt} the NLO QCD result of HIGLU was supplemented with the NNLO corrections in the heavy-top-quark limit as implemented in *GGH@NNLO* [38], see Ref. [13, Sec. 6.3] for details.

In Table 38 one can find the approximate values to be inserted in Eq. (111) for $m_H = 125$ GeV.

$\sqrt{s}$	σ_{ggH}^{tt} (pb)	σ_{ggH}^{bb} (pb)	σ_{ggH}^{tb} (pb)
7 TeV	4.355	0.09528	-0.8970
8 TeV	18.31	0.1206	-1.125

Table 38: Approximate numerical values for resolving the gluon-fusion production cross-section according to Eq. (111) assuming $m_H = 125$ GeV.

Partial width scaling

In a similar way, NLO QCD corrections for the H $\rightarrow$ gg partial width are implemented in HDECAY [17, 19, 412]. This allows to treat the scale factor for Γ_{gg} as a second order polynomial in κ_b and κ_t:

$$\frac{\Gamma_{gg}}{\Gamma_{gg}^{SM}(m_H)} = \frac{\kappa_t^2 \cdot \Gamma_{gg}^{tt}(m_H) + \kappa_b^2 \cdot \Gamma_{gg}^{bb}(m_H) + \kappa_t \kappa_b \cdot \Gamma_{gg}^{tb}(m_H)}{\Gamma_{gg}^{tt}(m_H) + \Gamma_{gg}^{bb}(m_H) + \Gamma_{gg}^{tb}(m_H)} \tag{112}$$

The terms Γ_{gg}^{tt}, Γ_{gg}^{bb} and Γ_{gg}^{tb} are defined like the σ_{ggH} terms in Eq. (111). The Γ_{gg}^{ii} correspond to the partial widths that are obtained for $\kappa_i = 1$ and all other $\kappa_j = 0, j \neq i$. The cross-term Γ_{gg}^{tb} can then be derived by calculating the SM partial width by setting $\kappa_b = \kappa_t = 1$ and subtracting Γ_{gg}^{tt} and Γ_{gg}^{bb} from it.

In Table 39 one can find the approximate values to be used in Eq. (112) for $m_H = 125, 126$ GeV.

Table 39: Approximate numerical values for resolving the gluon-fusion decay partial width according to Eq. (112).

m_H	Γ_{gg}^{tt} (keV)	Γ_{gg}^{bb} (keV)	Γ_{gg}^{tb} (keV)
125 GeV	380.8	3.96	-42.1
126 GeV	389.6	3.95	-42.7

Effective treatment

In the general case, without the assumptions above, possible non-zero contributions from additional particles in the loop have to be taken into account and κ_g^2 is then treated as an effective coupling scale factor parameter in the fit: $\sigma_{ggH}/\sigma_{ggH}^{SM} = \kappa_g^2$. The effective scale factor for the partial gluon width Γ_{gg} should behave in a very similar way, so in this case the same effective scale factor κ_g is used: $\Gamma_{gg}/\Gamma_{gg}^{SM} = \kappa_g^2$. As the contribution of Γ_{gg} to the total width is <10% in the SM, this assumption is believed to have no measurable impact.

10.2.2.3 Scaling of the $H \rightarrow \gamma\gamma$ *partial decay width*

Like in the previous section, κ_γ^2 refers to the scale factor for the loop-induced $H \rightarrow \gamma\gamma$ decay. Also for the $H \rightarrow \gamma\gamma$ decay NLO QCD corrections exist and are implemented in HDECAY. This allows to treat the scale factor for the $\gamma\gamma$ partial width as a second order polynomial in κ_b, κ_t, κ_τ, and κ_W:

$$\kappa_\gamma^2(\kappa_b, \kappa_t, \kappa_\tau, \kappa_W, m_H) = \frac{\sum_{i,j} \kappa_i \kappa_j \cdot \Gamma_{\gamma\gamma}^{ij}(m_H)}{\sum_{i,j} \Gamma_{\gamma\gamma}^{ij}(m_H)} \tag{113}$$

where the pairs (i, j) are $bb, tt, \tau\tau, WW, bt, b\tau, bW, t\tau, tW, \tau W$. The $\Gamma_{\gamma\gamma}^{ii}$ correspond to the partial widths that are obtained for $\kappa_i = 1$ and all other $\kappa_j = 0, (j \neq i)$. The cross-terms $\Gamma_{\gamma\gamma}^{ij}, (i \neq j)$ can then be derived by calculating the partial width by setting $\kappa_i = \kappa_j = 1$ and all other $\kappa_l = 0, (l \neq i, j)$, and subtracting $\Gamma_{\gamma\gamma}^{ii}$ and $\Gamma_{\gamma\gamma}^{jj}$ from them.

In Table 40 one can find the approximate values to be used in Eq. (113) for $m_H = 125, 126$ GeV.

Table 40: Approximate numerical values for resolving the di-photon decay partial width according to Eq. (113). All values are given in eV.

m_H	$\Gamma_{\gamma\gamma}^{tt}$	$\Gamma_{\gamma\gamma}^{bb}$	$\Gamma_{\gamma\gamma}^{WW}$	$\Gamma_{\gamma\gamma}^{tb}$	$\Gamma_{\gamma\gamma}^{tW}$	$\Gamma_{\gamma\gamma}^{bW}$	$\Gamma_{\gamma\gamma}^{\tau\tau}$	$\Gamma_{\gamma\gamma}^{t\tau}$	$\Gamma_{\gamma\gamma}^{b\tau}$	$\Gamma_{\gamma\gamma}^{\tau W}$
125 GeV	662.84	0.18	14731.86	-16.39	-6249.93	77.42	0.21	-17.69	0.40	83.59
126 GeV	680.39	0.18	15221.98	-16.62	-6436.35	78.78	0.22	-17.94	0.40	85.05

Effective treatment

In the general case, without the assumption above, possible non-zero contributions from additional particles in the loop have to be taken into account and κ_γ^2 is then treated as an effective coupling parameter in the fit.

10.2.2.4 Scaling of the $H \rightarrow Z\gamma$ *decay vertex*

Like in the previous sections, $\kappa_{(Z\gamma)}^2$ refers to the scale factor for the loop-induced $H \rightarrow Z\gamma$ decay. This allows to treat the scale factor for the $Z\gamma$ partial width as a second order polynomial in κ_b, κ_t, κ_τ, and κ_W:

$$\kappa_{(Z\gamma)}^2(\kappa_b, \kappa_t, \kappa_\tau, \kappa_W, m_H) = \frac{\sum_{i,j} \kappa_i \kappa_j \cdot \Gamma_{Z\gamma}^{ij}(m_H)}{\sum_{i,j} \Gamma_{Z\gamma}^{ij}(m_H)} \tag{114}$$

where the pairs (i, j) are $bb, tt, \tau\tau, WW, bt, b\tau, bW, t\tau, tW, \tau W$. The $\Gamma_{Z\gamma}^{ij}$ are calculated in the same way as for Eq. (113). NLO QCD corrections have been computed and found to be very small [413], and thus ignored here.

In Table 41 one can find the approximate values to be inserted in Eq. (114) for $m_H = 125, 126$ GeV.

Effective treatment

In the general case, without the assumption above, possible non-zero contributions from additional particles in the loop have to be taken into account and $\kappa_{(Z\gamma)}^2$ is then treated as an effective coupling parameter in the fit.

Table 41: Approximate numerical values for resolving the H → Zγ decay partial width according to Eq. (114). All values are given in eV.

m_H	$\Gamma^{tt}_{(Z\gamma)}$	$\Gamma^{bb}_{(Z\gamma)}$	$\Gamma^{WW}_{(Z\gamma)}$	$\Gamma^{tb}_{(Z\gamma)}$	$\Gamma^{tW}_{(Z\gamma)}$	$\Gamma^{bW}_{(Z\gamma)}$	$\Gamma^{\tau\tau}_{(Z\gamma)}$	$\Gamma^{t\tau}_{(Z\gamma)}$	$\Gamma^{b\tau}_{(Z\gamma)}$	$\Gamma^{\tau W}_{(Z\gamma)}$
125 GeV	21.74	0.019	7005.6	−1.11	−780.4	19.90	1.5×10^{-5}	−0.033	0.0010	0.594
126 GeV	23.51	0.020	7648.4	−1.19	−848.1	21.47	1.6×10^{-5}	−0.035	0.0011	0.640

10.2.2.5 Scaling of the total width

The total width Γ_H is the sum of all Higgs partial decay widths. Under the assumption that no additional BSM Higgs decay modes (into either invisible or undetectable final states) contribute to the total width, Γ_H is expressed as the sum of the scaled partial Higgs decay widths to SM particles, which combine to a total scale factor κ^2_H compared to the SM total width Γ^{SM}_H:

$$\kappa^2_H(\kappa_i, m_H) = \sum_{\substack{j = WW^{(*)}, ZZ^{(*)}, b\bar{b}, \tau^-\tau^+, \\ \gamma\gamma, Z\gamma, gg, t\bar{t}, c\bar{c}, s\bar{s}, \mu^-\mu^+}} \frac{\Gamma_j(\kappa_i, m_H)}{\Gamma^{SM}_H(m_H)} \tag{115}$$

Effective treatment

In the general case, additional Higgs decay modes to BSM particles cannot be excluded and the total width scale factor κ^2_H is treated as free parameter.

The total width Γ_H for a light Higgs with $m_H \sim 125$ GeV is not expected to be directly observable at the LHC, as the SM expectation is $\Gamma_H \sim 4$ MeV, several orders of magnitude smaller than the experimental mass resolution [13]. There is no indication from the results observed so far that the natural width is broadened by new physics effects to such an extent that it could be directly observable. Furthermore, as all LHC Higgs channels rely on the identification of Higgs decay products, there is no way of measuring the total Higgs width indirectly within a coupling fit without using assumptions. This can be illustrated by assuming that all cross sections and partial widths are increased by a common factor $\kappa^2_i = r > 1$. If simultaneously the Higgs total width is increased by the square of the same factor $\kappa^2_H = r^2$ (for example by postulating some BSM decay mode) the experimental visible signatures in all Higgs channels would be indistinguishable from the SM.

Hence without further assumptions only ratios of scale factors κ_i can be measured at the LHC, where at least one of the ratios needs to include the total width scale factor κ^2_H. Such a definition of ratios absorbs two degrees of freedom (e.g. a common scale factor to all couplings and a scale factor to the total width) into one ratio that can be measured at the LHC.

Assumptions for absolute coupling scale factor measurements

In order to go beyond the measurement of ratios of coupling scale factors to the determination of absolute coupling scale factors κ_i additional assumptions are necessary to remove one degree of freedom. Possible assumptions are:

1. No new physics in Higgs decay modes (Eq. (115)).
2. $\kappa_W \leq 1$, $\kappa_Z \leq 1$ [307, 309, 377]. This assumption is theoretically well motivated in the sense that it holds in a wide class of models. In particular, it is valid in any model with an arbitrary number of Higgs doublets, with and without additional Higgs singlets. The assumption is also justified in certain classes of composite Higgs models, while on the other hand it may be violated for instance in Little Higgs models, in particular in the presence of an isospin-2 scalar multiplet [414].

If one combines this assumption with the fact that all Higgs partial decay widths are positive definite and the total width is bigger than the sum of all (known) partial decay widths, this is sufficient to give a lower and upper bound on all κ_i and also determine a possible branching ratio $\mathrm{BR_{inv.,undet.}}$ into final states invisible or undetectable at the LHC. This is best illustrated with the $\mathrm{VH(H \to VV)}$ process:

$$\sigma_{\mathrm{VH}} \cdot \mathrm{BR(H \to VV)} = \frac{\kappa_V^2 \cdot \sigma_{\mathrm{VH}}^{\mathrm{SM}} \cdot \kappa_V^2 \cdot \Gamma_V^{\mathrm{SM}}}{\Gamma_{\mathrm{H}}}$$

$$\text{and} \qquad \Gamma_{\mathrm{H}} > \kappa_V^2 \cdot \Gamma_V^{\mathrm{SM}} \qquad (116)$$

$$\text{give combined:} \qquad \sigma_{\mathrm{VH}} \cdot \mathrm{BR(H \to }VV) < \frac{\kappa_V^2 \cdot \sigma_{\mathrm{VH}}^{\mathrm{SM}} \cdot \kappa_V^2 \cdot \Gamma_V^{\mathrm{SM}}}{\kappa_V^2 \cdot \Gamma_V^{\mathrm{SM}}}$$

$$\implies \qquad \kappa_V^2 > \frac{\sigma_{\mathrm{VH}} \cdot \mathrm{BR(H \to VV)}}{\sigma_{\mathrm{VH}}^{\mathrm{SM}}} \qquad (117)$$

If more final states are included in Eq. (116), the lower bounds become tighter and together with the upper limit assumptions on κ_W and κ_Z, absolute measurements are possible. However, uncertainties on all κ_i can be very large depending on the accuracy of the $b\bar{b}$ decay channels that dominate the uncertainty of the total width sum for a SM-like Higgs.

3. $\kappa_j = $ constant. If at least one coupling scale factor κ_j is known either from an external measurement or through theory assumptions, the total width and the branching ratio $\mathrm{BR_{inv.,undet.}}$ into final states invisible or undetectable at the LHC can be determined. An example is given in the benchmark model in Section 10.3.5, where the assumption $\kappa_Z = \kappa_W = \kappa_\tau = \kappa_b = \kappa_t = 1$ is used to determine $\mathrm{BR_{inv.,undet.}}$.

In the benchmark parameterizations in Section 10.3 three versions are given, unless otherwise stated: one without assumptions on the total width (effective treatment of κ_H), one assuming no beyond SM Higgs decay modes (Option 1. above) and one assuming bounds on the gauge coupling scale factors (Option 2. above).

10.2.3 Further assumptions

10.2.3.1 Theoretical uncertainties

The quantitative impact of theory uncertainties in the Higgs production cross sections and decay rates is discussed in detail in Ref. [13].

Such uncertainties will directly affect the determination of the scale factors. When one or more of the scaling factors differ from 1, the uncertainty from missing higher-order contributions will in general be larger than what was estimated in Ref. [13].

In practice, the cross section predictions with their uncertainties as tabulated in Ref. [13] are used as such so that for $\kappa_i = 1$ the recommended SM treatment is recovered. Without a consistent electroweak NLO calculation for deviations from the SM, electroweak corrections and their uncertainties for the SM prediction ($\sim 5\%$ in gluon fusion production and $\sim 2\%$ in the di-photon decay) are naively scaled together. In the absence of explicit calculations this is the currently best available approach in a search for deviations from the SM Higgs prediction.

10.2.3.2 Limit of the zero-width approximation

Concerning the zero-width approximation (ZWA), it should be noted that in the mass range of the narrow resonance the width of the Higgs boson of the Standard Model (SM) is more than four orders of

magnitude smaller than its mass. Thus, the zero-width approximation is in principle expected to be an excellent approximation not only for a SM-like Higgs boson below ~ 150 GeV but also for a wide range of BSM scenarios which are compatible with the present data. However, it has been shown in Ref. [85] that this is not always the case even in the SM. The inclusion of off-shell contributions is essential to obtain an accurate Higgs signal normalization at the 1% precision level. For $gg (\rightarrow H) \rightarrow VV$, $V = W, Z$, $\mathcal{O}(10\%)$ corrections occur due to an enhanced Higgs signal in the region $M_{VV} > 2\,M_V$, where also sizeable Higgs-continuum interference occurs. However, with the accuracy anticipated to be reached in the 2012 data these effects play a minor role.

10.2.3.3 *Signal interference effects*

A possible source of uncertainty is related to interference effects in $H \rightarrow 4$ fermion decay. For a light Higgs boson the decay width into 4 fermions should always be calculated from the complete matrix elements and not from the approximation

$$\text{BR}(H \rightarrow VV) \cdot \text{BR}^2(V \rightarrow f\bar{f}), \; (V = Z, W) \,. \tag{118}$$

This approximation, based on the ZWA for the gauge boson V, neglects both off-shell effects and interference between diagrams where the intermediate gauge bosons couple to different pairs of final-state fermions. As shown in Chapter 2 of Ref. [14], the interference effects not included in Eq. (118) amount to 10% for the decay $H \rightarrow e^+e^-e^+e^-$ for a 125 GeV Higgs. Similar interference effects of the order of 5% are found for the $e^+\nu_e e^-\bar{\nu}_e$ and $q\bar{q}q\bar{q}$ final states.

The experimental analyses take into account the full NLO 4-fermion partial decay width [20–22]. The partial width of the 4-lepton final state (usually described as $H \rightarrow ZZ^{(*)} \rightarrow 4l$) is scaled with κ_Z^2. Similarly, the partial width of the 2-lepton, 2-jet final state (usually described as $H \rightarrow ZZ^{(*)} \rightarrow 2l2q$) is scaled with κ_Z^2. The partial width of the low mass 2-lepton, 2-neutrino final state (usually described as $H \rightarrow WW^{(*)} \rightarrow l\nu\,l\nu$, although a contribution of $H \rightarrow Z^{(*)}Z \rightarrow ll\,\nu\nu$ exists and is taken into account) is scaled with κ_W^2.

10.2.3.4 *Treatment of $\Gamma_{c\bar{c}}$, $\Gamma_{s\bar{s}}$, $\Gamma_{\mu^-\mu^+}$ and light fermion contributions to loop-induced processes*

When calculating $\kappa_H^2(\kappa_i, m_H)$ in a benchmark parameterization, the final states $c\bar{c}$, $s\bar{s}$ and $\mu^-\mu^+$ (currently unobservable at the LHC) are tied to κ_i scale factors which can be determined from the data. Based on flavor symmetry considerations, the following choices are made:

$$\frac{\Gamma_{c\bar{c}}}{\Gamma_{c\bar{c}}^{\text{SM}}(m_H)} \;=\; \kappa_c^2 = \kappa_t^2 \tag{119}$$

$$\frac{\Gamma_{s\bar{s}}}{\Gamma_{s\bar{s}}^{\text{SM}}(m_H)} \;=\; \kappa_s^2 = \kappa_b^2 \tag{120}$$

$$\frac{\Gamma_{\mu^-\mu^+}}{\Gamma_{\mu^-\mu^+}^{\text{SM}}(m_H)} \;=\; \kappa_\mu^2 = \kappa_\tau^2 \tag{121}$$

Following the rationale of Ref. [13, Sec. 9], the widths of e^-e^+, $u\bar{u}$, $d\bar{d}$ and neutrino final states are neglected.

Through interference terms, these light fermions also contribute to the loop-induced $gg \rightarrow H$ and $H \rightarrow gg, \gamma\gamma, Z\gamma$ vertices. In these cases, the assumptions $\kappa_c = \kappa_t$, $\kappa_s = \kappa_b$ and $\kappa_\mu = \kappa_\tau$ are made.

Once sensitivity to the $H \rightarrow \mu^-\mu^+$ final state is reached in the experiments, a separate coupling scale factor κ_μ should be used where appropriate.

10.2.3.5 Approximation in associated ZH *production*

When scaling the associated ZH production mode, the contribution from gg → ZH through a top-quark loop is neglected. This is estimated to be around 5% of the total associated ZH production cross section [13, Sec. 4.3].

10.3 Benchmark parameterizations based on the interim framework

In putting forward a set of benchmark parameterizations based on the framework described in the previous section several considerations were taken into account. One concern is the stability of the fits which typically involve several hundreds of nuisance parameters. With that in mind, the benchmark parameterizations avoid quotients of parameters of interest. Another constraint that heavily shapes the exact choice of parameterization is consistency among the uncertainties that can be extracted in different parameterizations. Some coupling scale factors enter linearly in loop-induced photon and gluon vertices. For that reason, all scale factors are defined at the same power, leading to what could appear as an abundance of squared expressions. Finally, the benchmark parameterizations are chosen such that some potentially interesting physics scenarios can be probed and the parameters of interest are chosen so that at least some are expected to be determined.

For every benchmark parameterization, unless otherwise stated, three variations are provided (see Section 10.2.2 for details):

1. The total width is scaled assuming that there are no invisible or undetected widths. In this case $\kappa_H^2(\kappa_i, m_H)$ is a function of the free parameters as defined in Eq. (115).
2. The total width scale factor is treated as a free parameter, but an assumption of $\kappa_W < 1$ and $\kappa_Z < 1$ on the gauge coupling scale factors is applied together with the condition $\kappa_H^2 > \kappa_H^2(\kappa_i)$.
3. The total width scale factor is treated as a free parameter. In this case no assumption is made and there will be a parameter of the form $\kappa_{ij} = \kappa_i \cdot \kappa_j / \kappa_H$ contributing to all Higgs boson rates.

The benchmark parameterizations are given in tabular form where each cell corresponds to the scale factor to be applied to a given combination of production and decay mode.

For every benchmark parameterization, a list of the free parameters and their relation to the framework parameters is provided. To reduce the amount of symbols in the tables, m_H is omitted throughout. In practice, m_H can either be fixed to a given value or profiled together with other nuisance parameters.

10.3.1 One common scale factor

The simplest way to look for a deviation from the predicted SM Higgs coupling structure is to leave the overall signal strength μ as a free parameter.

In order to perform the same fit in the context of the coupling scale factor framework, the only difference is that $\mu = \kappa^2 \cdot \kappa^2 / \kappa^2 = \kappa^2$, where the three terms κ^2 in the intermediate expression account for production, decay and total width scaling, respectively (Table 42).

This parameterization, despite providing the highest experimental precision, has several clear shortcomings, such as ignoring that the role of the Higgs boson in providing the masses of the vector bosons is very different from the role it has in providing the masses of fermions.

10.3.2 Scaling of vector boson and fermion couplings

In checking whether an observed state is compatible with the SM Higgs boson, one obvious question is whether it fulfills its expected role in EWSB which is intimately related to the coupling to the vector bosons (W, Z).

Table 42: The simplest possible benchmark parameterization where a single scale factor applies to all production and decay modes.

Common scale factor				
Free parameter: $\kappa(=\kappa_t = \kappa_b = \kappa_\tau = \kappa_W = \kappa_Z)$.				
Dependent parameters: $\kappa_\gamma = \kappa$, $\kappa_g = \kappa$, $\kappa_H = \kappa$.				
$H \to \gamma\gamma$ $H \to ZZ^{(*)}$ $H \to WW^{(*)}$ $H \to b\bar{b}$ $H \to \tau^-\tau^+$				
ggH				
$t\bar{t}$H				
VBF		κ^2		
WH				
ZH				

Therefore, assuming that the SU(2) custodial symmetry holds, in the simplest case two parameters can be defined, one scaling the coupling to the vector bosons, $\kappa_V(=\kappa_W = \kappa_Z)$, and one scaling the coupling common to all fermions, $\kappa_f(=\kappa_t = \kappa_b = \kappa_\tau)$. Loop-induced processes are assumed to scale as expected from the SM structure.

In this parameterization, presented in Table 43, the gluon vertex loop is effectively a fermion loop and only the photon vertex loop requires a non-trivial scaling, given the contributions of the top and bottom quarks, of the τ lepton, of the W-boson, as well as their (destructive) interference.

This parameterization, though exceptionally succinct, makes a number of assumptions, which are expected to be object of further scrutiny with the accumulation of data at the LHC. The assumptions naturally relate to the grouping of different individual couplings or to assuming that the loop amplitudes are those predicted by the SM.

10.3.3   Probing custodial symmetry

One of the best motivated symmetries in case the new state is responsible for electroweak symmetry breaking is the one that links its couplings to the W and Z bosons. Since $SU(2)_V$ or custodial symmetry is an approximate symmetry of the SM (e.g. $\Delta\rho \neq 0$), it is important to test whether data are compatible with the amount of violation allowed by the SM at NLO.

In this parameterization, presented in Table 44, $\lambda_{WZ}(=\kappa_W/\kappa_Z)$ is of particular interest for probing custodial symmetry. Though providing interesting information, both κ_Z and κ_f can be thought of as nuisance parameters when performing this fit. In addition to the photon vertex loop not having a trivial scaling, in this parameterization also the individual W and Z boson fusion contributions to the vector boson fusion production process need to be resolved.

In Table 44 the explicit parameterization using the assumption $\kappa_W < 1$ and $\kappa_Z < 1$ is omitted for this benchmark, as an independent test of custodial symmetry under assumptions on the gauge couplings themselves is difficult. If wanted, this table can be obtained from the first parameterization in Table 44 using the replacement $\kappa_H^2(\kappa_i) \to \kappa_H^2$.

As the photon vertex loop is very sensitive to BSM physics contributions, this benchmark is given in Table 45 as a second variant where a potential deviation in the $H \to \gamma\gamma$ decay mode is decoupled from the λ_{WZ} measurement by using the effective photon coupling scale factor κ_γ as additional degree of freedom.

10.3.4   Probing the fermion sector

In many extensions of the SM the Higgs bosons couple differently to different types of fermions.

Given that the gluon-gluon fusion production process is dominated by the top-quark coupling,

Table 43: A benchmark parameterization where custodial symmetry is assumed and vector boson couplings are scaled together (κ_V) and fermions are assumed to scale with a single parameter (κ_f).

Boson and fermion scaling assuming no invisible or undetectable widths

Free parameters: $\kappa_V(=\kappa_W=\kappa_Z)$, $\kappa_f(=\kappa_t=\kappa_b=\kappa_\tau)$

Dependent parameters: $\kappa_\gamma=\kappa_\gamma(\kappa_f,\kappa_f,\kappa_f,\kappa_V)$, $\kappa_g=\kappa_f$, $\kappa_H=\kappa_H(\kappa_i)$.

	$H\to\gamma\gamma$	$H\to ZZ^{(*)}$ $H\to WW^{(*)}$	$H\to b\overline{b}$ $H\to\tau^-\tau^+$
ggH ttH̄	$\dfrac{\kappa_f^2\cdot\kappa_\gamma^2(\kappa_f,\kappa_f,\kappa_f,\kappa_V)}{\kappa_H^2(\kappa_i)}$	$\dfrac{\kappa_f^2\cdot\kappa_V^2}{\kappa_H^2(\kappa_i)}$	$\dfrac{\kappa_f^2\cdot\kappa_f^2}{\kappa_H^2(\kappa_i)}$
VBF WH ZH	$\dfrac{\kappa_V^2\cdot\kappa_\gamma^2(\kappa_f,\kappa_f,\kappa_f,\kappa_V)}{\kappa_H^2(\kappa_i)}$	$\dfrac{\kappa_V^2\cdot\kappa_V^2}{\kappa_H^2(\kappa_i)}$	$\dfrac{\kappa_V^2\cdot\kappa_f^2}{\kappa_H^2(\kappa_i)}$

Boson and fermion scaling assuming $\kappa_V<1$

Free parameters: $\kappa_V(=\kappa_W=\kappa_Z)$, $\kappa_f(=\kappa_t=\kappa_b=\kappa_\tau)$, κ_H, with conditions $\kappa_V<1$ and $\kappa_H^2>\kappa_H^2(\kappa_i)$

Dependent parameters: $\kappa_\gamma=\kappa_\gamma(\kappa_f,\kappa_f,\kappa_f,\kappa_V)$, $\kappa_g=\kappa_f$.

	$H\to\gamma\gamma$	$H\to ZZ^{(*)}$ $H\to WW^{(*)}$	$H\to b\overline{b}$ $H\to\tau^-\tau^+$
ggH ttH̄	$\dfrac{\kappa_f^2\cdot\kappa_\gamma^2(\kappa_f,\kappa_f,\kappa_f,\kappa_V)}{\kappa_H^2}$	$\dfrac{\kappa_f^2\cdot\kappa_V^2}{\kappa_H^2}$	$\dfrac{\kappa_f^2\cdot\kappa_f^2}{\kappa_H^2}$
VBF WH ZH	$\dfrac{\kappa_V^2\cdot\kappa_\gamma^2(\kappa_f,\kappa_f,\kappa_f,\kappa_V)}{\kappa_H^2}$	$\dfrac{\kappa_V^2\cdot\kappa_V^2}{\kappa_H^2}$	$\dfrac{\kappa_V^2\cdot\kappa_f^2}{\kappa_H^2}$

Boson and fermion scaling without assumptions on the total width

Free parameters: $\kappa_{VV}(=\kappa_V\cdot\kappa_V/\kappa_H)$, $\lambda_{fV}(=\kappa_f/\kappa_V)$.

Dependent parameters: $\kappa_\gamma=\kappa_\gamma(\lambda_{fV},\lambda_{fV},\lambda_{fV},1)$, $\lambda_{gV}=\lambda_{fV}$.

	$H\to\gamma\gamma$	$H\to ZZ^{(*)}$ $H\to WW^{(*)}$	$H\to b\overline{b}$ $H\to\tau^-\tau^+$
ggH ttH̄	$\kappa_{VV}^2\cdot\lambda_{fV}^2\cdot\kappa_\gamma^2(\lambda_{fV},\lambda_{fV},\lambda_{fV},1)$	$\kappa_{VV}^2\cdot\lambda_{fV}^2$	$\kappa_{VV}^2\cdot\lambda_{fV}^2\cdot\lambda_{fV}^2$
VBF WH ZH	$\kappa_{VV}^2\cdot\kappa_\gamma^2(\lambda_{fV},\lambda_{fV},\lambda_{fV},1)$	κ_{VV}^2	$\kappa_{VV}^2\cdot\lambda_{fV}^2$

$$\kappa_i^2=\Gamma_{ii}/\Gamma_{ii}^{SM}$$

and that there are two decay modes involving fermions, one way of splitting fermions that is within experimental reach is to consider up-type fermions (top quark) and down-type fermions (bottom quark and tau lepton) separately. In this parameterization, presented in Table 46, the most relevant parameter of interest is $\lambda_{du}(=\kappa_d/\kappa_u)$, the ratio of the scale factors of the couplings to down-type fermions, $\kappa_d=\kappa_\tau(=\kappa_\mu)=\kappa_b(=\kappa_s)$, and up-type fermions, $\kappa_u=\kappa_t(=\kappa_c)$.

Alternatively one can consider quarks and leptons separately. In this parameterization, presented in Table 47, the most relevant parameter of interest is $\lambda_{lq}(=\kappa_l/\kappa_q)$, the ratio of the coupling scale factors to leptons, $\kappa_l=\kappa_\tau(=\kappa_\mu)$, and quarks, $\kappa_q=\kappa_t(=\kappa_c)=\kappa_b(=\kappa_s)$.

One further combination of top-quark, bottom-quark and tau-lepton, namely scaling the top-quark and tau-lepton with a common parameter and the bottom-quark with another parameter, can be envisaged and readily parametrized based on the interim framework but is not put forward as a benchmark.

10.3.5 *Probing the loop structure and invisible or undetectable decays*

New particles associated with physics beyond the SM may influence the partial width of the gluon and/or photon vertices.

In this parameterization, presented in Table 48, each of the loop-induced vertices is represented

Table 44: A benchmark parameterization where custodial symmetry is probed through the λ_{WZ} parameter.

Probing custodial symmetry assuming no invisible or undetectable widths

Free parameters: κ_Z, $\lambda_{WZ}(=\kappa_W/\kappa_Z)$, $\kappa_f(=\kappa_t=\kappa_b=\kappa_\tau)$.

Dependent parameters: $\kappa_\gamma=\kappa_\gamma(\kappa_f,\kappa_f,\kappa_f,\kappa_Z\lambda_{WZ})$, $\kappa_g=\kappa_f$, $\kappa_H=\kappa_H(\kappa_i)$.

	$H\to\gamma\gamma$	$H\to ZZ^{(*)}$	$H\to WW^{(*)}$	$H\to b\bar{b}$ $H\to\tau^-\tau^+$
ggH $t\bar{t}H$	$\dfrac{\kappa_f^2\cdot\kappa_\gamma^2(\kappa_f,\kappa_f,\kappa_f,\kappa_Z\lambda_{WZ})}{\kappa_H^2(\kappa_i)}$	$\dfrac{\kappa_f^2\cdot\kappa_Z^2}{\kappa_H^2(\kappa_i)}$	$\dfrac{\kappa_f^2\cdot(\kappa_Z\lambda_{WZ})^2}{\kappa_H^2(\kappa_i)}$	$\dfrac{\kappa_f^2\cdot\kappa_f^2}{\kappa_H^2(\kappa_i)}$
VBF	$\dfrac{\kappa_{VBF}^2(\kappa_Z,\kappa_Z\lambda_{WZ})\cdot\kappa_\gamma^2(\kappa_f,\kappa_f,\kappa_f,\kappa_Z\lambda_{WZ})}{\kappa_H^2(\kappa_i)}$	$\dfrac{\kappa_{VBF}^2(\kappa_Z,\kappa_Z\lambda_{WZ})\cdot\kappa_Z^2}{\kappa_H^2(\kappa_i)}$	$\dfrac{\kappa_{VBF}^2(\kappa_Z,\kappa_Z\lambda_{WZ})\cdot(\kappa_Z\lambda_{WZ})^2}{\kappa_H^2(\kappa_i)}$	$\dfrac{\kappa_{VBF}^2(\kappa_Z,\kappa_Z\lambda_{WZ})\cdot\kappa_f^2}{\kappa_H^2(\kappa_i)}$
WH	$\dfrac{(\kappa_Z\lambda_{WZ})^2\cdot\kappa_\gamma^2(\kappa_f,\kappa_f,\kappa_f,\kappa_Z\lambda_{WZ})}{\kappa_H^2(\kappa_i)}$	$\dfrac{(\kappa_Z\lambda_{WZ})^2\cdot\kappa_Z^2}{\kappa_H^2(\kappa_i)}$	$\dfrac{(\kappa_Z\lambda_{WZ})^2\cdot(\kappa_Z\lambda_{WZ})^2}{\kappa_H^2(\kappa_i)}$	$\dfrac{(\kappa_Z\lambda_{WZ})^2\cdot\kappa_f^2}{\kappa_H^2(\kappa_i)}$
ZH	$\dfrac{\kappa_Z^2\cdot\kappa_\gamma^2(\kappa_f,\kappa_f,\kappa_f,\kappa_Z\lambda_{WZ})}{\kappa_H^2(\kappa_i)}$	$\dfrac{\kappa_Z^2\cdot\kappa_Z^2}{\kappa_H^2(\kappa_i)}$	$\dfrac{\kappa_Z^2\cdot(\kappa_Z\lambda_{WZ})^2}{\kappa_H^2(\kappa_i)}$	$\dfrac{\kappa_Z^2\cdot\kappa_f^2}{\kappa_H^2(\kappa_i)}$

Probing custodial symmetry without assumptions on the total width

Free parameters: $\kappa_{ZZ}(=\kappa_Z\cdot\kappa_Z/\kappa_H)$, $\lambda_{WZ}(=\kappa_W/\kappa_Z)$, $\lambda_{fZ}(=\kappa_f/\kappa_Z)$.

Dependent parameters: $\kappa_\gamma=\kappa_\gamma(\lambda_{fZ},\lambda_{fZ},\lambda_{fZ},\lambda_{WZ})$, $\lambda_{gZ}=\lambda_{fZ}$.

	$H\to\gamma\gamma$	$H\to ZZ^{(*)}$	$H\to WW^{(*)}$	$H\to b\bar{b}$ $H\to\tau^-\tau^+$
ggH $t\bar{t}H$	$\kappa_{ZZ}^2\lambda_{fZ}^2\cdot\kappa_\gamma^2(\lambda_{fZ},\lambda_{fZ},\lambda_{fZ},\lambda_{WZ})$	$\kappa_{ZZ}^2\lambda_{fZ}^2$	$\kappa_{ZZ}^2\lambda_{fZ}^2\cdot\lambda_{WZ}^2$	$\kappa_{ZZ}^2\lambda_{fZ}^2\cdot\lambda_{fZ}^2$
VBF	$\kappa_{ZZ}^2\kappa_{VBF}^2(1,\lambda_{WZ}^2)\cdot\kappa_\gamma^2(\lambda_{fZ},\lambda_{fZ},\lambda_{fZ},\lambda_{WZ})$	$\kappa_{ZZ}^2\kappa_{VBF}^2(1,\lambda_{WZ}^2)$	$\kappa_{ZZ}^2\kappa_{VBF}^2(1,\lambda_{WZ}^2)\cdot\lambda_{WZ}^2$	$\kappa_{ZZ}^2\kappa_{VBF}^2(1,\lambda_{WZ}^2)\cdot\lambda_{fZ}^2$
WH	$\kappa_{ZZ}^2\lambda_{WZ}^2\cdot\kappa_\gamma^2(\lambda_{fZ},\lambda_{fZ},\lambda_{fZ},\lambda_{WZ})$	$\kappa_{ZZ}^2\cdot\lambda_{WZ}^2$	$\kappa_{ZZ}^2\lambda_{WZ}^2\cdot\lambda_{WZ}^2$	$\kappa_{ZZ}^2\lambda_{WZ}^2\cdot\lambda_{fZ}^2$
ZH	$\kappa_{ZZ}^2\cdot\kappa_\gamma^2(\lambda_{fZ},\lambda_{fZ},\lambda_{fZ},\lambda_{WZ})$	κ_{ZZ}^2	$\kappa_{ZZ}^2\cdot\lambda_{WZ}^2$	$\kappa_{ZZ}^2\cdot\lambda_{fZ}^2$

$$\kappa_i^2=\Gamma_{ii}/\Gamma_{ii}^{SM}$$

Table 45: A benchmark parameterization where custodial symmetry is probed through the λ_{WZ} parameter, but the $H \to \gamma\gamma$ decay mode is decoupled from the measurement of κ_W by using the effective photon scale factor κ_γ as additional degree of freedom.

Probing custodial symmetry decoupled from $H \to \gamma\gamma$, assuming no invisible or undetectable widths

Free parameters: κ_Z, $\lambda_{WZ}(=\kappa_W/\kappa_Z)$, $\kappa_f(=\kappa_t=\kappa_b=\kappa_\tau)$, κ_γ.

Dependent parameters: $\kappa_g = \kappa_f$, $\kappa_H = \kappa_H(\kappa_i)$.

	$H \to \gamma\gamma$	$H \to ZZ^{(*)}$	$H \to WW^{(*)}$	$H \to b\bar{b}$ $H \to \tau^-\tau^+$
ggH $t\bar{t}$H	$\dfrac{\kappa_f^2 \cdot \kappa_\gamma^2}{\kappa_H^2(\kappa_i)}$	$\dfrac{\kappa_f^2 \cdot \kappa_Z^2}{\kappa_H^2(\kappa_i)}$	$\dfrac{\kappa_f^2 \cdot (\kappa_Z\lambda_{WZ})^2}{\kappa_H^2(\kappa_i)}$	$\dfrac{\kappa_f^2 \cdot \kappa_f^2}{\kappa_H^2(\kappa_i)}$
VBF	$\dfrac{\kappa_{VBF}^2(\kappa_Z,\kappa_Z\lambda_{WZ}) \cdot \kappa_\gamma^2}{\kappa_H^2(\kappa_i)}$	$\dfrac{\kappa_{VBF}^2(\kappa_Z,\kappa_Z\lambda_{WZ}) \cdot \kappa_Z^2}{\kappa_H^2(\kappa_i)}$	$\dfrac{\kappa_{VBF}^2(\kappa_Z,\kappa_Z\lambda_{WZ}) \cdot (\kappa_Z\lambda_{WZ})^2}{\kappa_H^2(\kappa_i)}$	$\dfrac{\kappa_{VBF}^2(\kappa_Z,\kappa_Z\lambda_{WZ}) \cdot \kappa_f^2}{\kappa_H^2(\kappa_i)}$
WH	$\dfrac{(\kappa_Z\lambda_{WZ})^2 \cdot \kappa_\gamma^2}{\kappa_H^2(\kappa_i)}$	$\dfrac{(\kappa_Z\lambda_{WZ})^2 \cdot \kappa_Z^2}{\kappa_H^2(\kappa_i)}$	$\dfrac{(\kappa_Z\lambda_{WZ})^2 \cdot (\kappa_Z\lambda_{WZ})^2}{\kappa_H^2(\kappa_i)}$	$\dfrac{(\kappa_Z\lambda_{WZ})^2 \cdot \kappa_f^2}{\kappa_H^2(\kappa_i)}$
ZH	$\dfrac{\kappa_Z^2 \cdot \kappa_\gamma^2}{\kappa_H^2(\kappa_i)}$	$\dfrac{\kappa_Z^2 \cdot \kappa_Z^2}{\kappa_H^2(\kappa_i)}$	$\dfrac{\kappa_Z^2 \cdot (\kappa_Z\lambda_{WZ})^2}{\kappa_H^2(\kappa_i)}$	$\dfrac{\kappa_Z^2 \cdot \kappa_f^2}{\kappa_H^2(\kappa_i)}$

Probing custodial symmetry decoupled from $H \to \gamma\gamma$ and without assumptions on the total width

Free parameters: $\kappa_{ZZ}(=\kappa_Z \cdot \kappa_Z/\kappa_H)$, $\lambda_{WZ}(=\kappa_W/\kappa_Z)$, $\lambda_{fZ}(=\kappa_f/\kappa_Z)$, $\lambda_{\gamma Z}(=\kappa_\gamma/\kappa_Z)$.

Dependent parameters: $\lambda_{gZ} = \lambda_{fZ}$.

	$H \to \gamma\gamma$	$H \to ZZ^{(*)}$	$H \to WW^{(*)}$	$H \to b\bar{b}$ $H \to \tau^-\tau^+$
ggH $t\bar{t}$H	$\kappa_{ZZ}^2\lambda_{fZ}^2 \cdot \lambda_{\gamma Z}^2$	$\kappa_{ZZ}^2\lambda_{fZ}^2$	$\kappa_{ZZ}^2\lambda_{fZ}^2 \cdot \lambda_{WZ}^2$	$\kappa_{ZZ}^2\lambda_{fZ}^2 \cdot \lambda_{fZ}^2$
VBF	$\kappa_{ZZ}^2\kappa_{VBF}^2(1,\lambda_{WZ}^2) \cdot \lambda_{\gamma Z}^2$	$\kappa_{ZZ}^2\kappa_{VBF}^2(1,\lambda_{WZ}^2)$	$\kappa_{ZZ}^2\kappa_{VBF}^2(1,\lambda_{WZ}^2) \cdot \lambda_{WZ}^2$	$\kappa_{ZZ}^2\kappa_{VBF}^2(1,\lambda_{WZ}^2) \cdot \lambda_{fZ}^2$
WH	$\kappa_{ZZ}^2\lambda_{WZ}^2 \cdot \lambda_{\gamma Z}^2$	$\kappa_{ZZ}^2 \cdot \lambda_{WZ}^2$	$\kappa_{ZZ}^2\lambda_{WZ}^2 \cdot \lambda_{WZ}^2$	$\kappa_{ZZ}^2\lambda_{WZ}^2 \cdot \lambda_{fZ}^2$
ZH	$\kappa_{ZZ}^2 \cdot \lambda_{\gamma Z}^2$	κ_{ZZ}^2	$\kappa_{ZZ}^2 \cdot \lambda_{WZ}^2$	$\kappa_{ZZ}^2 \cdot \lambda_{fZ}^2$

$$\kappa_i^2 = \Gamma_{ii}/\Gamma_{ii}^{SM}$$

by an effective scale factor, κ_g and κ_γ. On the other hand, the couplings to the known SM particles are assumed to be as in the SM: $\kappa_Z = \kappa_W = \kappa_\tau = \kappa_b = \kappa_t = 1$.

Particles not predicted by the SM may also give rise to invisible or undetectable decays. In order to probe this possibility, instead of absorbing the total width into another parameter or leaving it free, a different parameter is introduced, $BR_{inv.,undet.}$. The assumption of the fixed coupling couplings to SM particles allows to determine $BR_{inv.,undet.}$ from the LHC data. The definition of $BR_{inv.,undet.}$ is relative to the rescaled total width, $\kappa_H^2(\kappa_i)$, and can thus be interpreted as the invisible or undetectable fraction of the total width.

Invisible decays might show up as a missing transverse energy (MET) signature and can be measured at the LHC with dedicated analyses. An example of an undetectable final state would be a multi-jet signature that cannot be separated from QCD backgrounds at the LHC and hence not detected. With sufficient data it can be envisaged to disentangle the invisible and undetectable components by splitting into two parameters $BR_{inv.}$ and $BR_{undet.}$, where $BR_{inv.}$ is determined by the direct searches for invisible Higgs decay signatures.

One particularity of this benchmark parameterization is that it should allow theoretical predictions involving new particles to be projected into the $(\kappa_g, \kappa_\gamma)$ or $(\kappa_g, \kappa_\gamma, BR_{inv.,undet.})$ spaces.

It can be noted that the benchmark parameterization including $BR_{inv.,undet.}$ can be recast in a form that allows for an interpretation in terms of a tree-level scale factor and the loop-induced scale factors with the following substitutions: $\kappa_j \to \kappa_j'/\kappa_{tree}$ (with $j = g, \gamma$) and $(1 - BR_{inv.,undet.}) \to \kappa_{tree}^2$.

Once the $H \to Z\gamma$ decay mode reaches sufficient sensitivity, a natural extension for this benchmark is to fit an extra degree of freedom in the form of the parameter $\kappa_{(Z\gamma)}$ for the $Z\gamma$ final state.

10.3.6 *A minimal parameterization without assumptions on new physics contributions*

The following parameterization gathers the most important degrees of freedom considered before, namely κ_g, κ_γ, κ_V, κ_f. The parameterization, presented in Table 49, is chosen such that some parameters are expected to be reasonably constrained by the LHC data in the near term, while other parameters are not expected to be as well constrained in the same time frame.

It should be noted that this is a parameterization which only includes trivial scale factors.

With the presently available analyses and data, $\kappa_{gV}^2 = \kappa_g^2 \cdot \kappa_V^2/\kappa_H^2$ seems to be a good choice for the common κ_{ij} parameter, but all choices are equivalent when considering the full 4-dimensional probability distribution.

10.3.7 *Most general parameterization for all gauge bosons and third generation fermion couplings*

Table 50 presents the relations in a fit only with simple scale factors, making no assumptions on identical coupling scale factors for different particles beyond these necessary for first and second generation fermions as discussed in Section 10.2.3.

Several choices are possible for κ_{ij}. With the currently available channels, $\kappa_{gZ} = \kappa_g \cdot \kappa_Z/\kappa_H$ seems most appropriate, as shown in table 50. The more appealing choices using vector boson scattering $\kappa_{WW} = \kappa_W \cdot \kappa_W/\kappa_H$ or $\kappa_{ZZ} = \kappa_Z \cdot \kappa_Z/\kappa_H$ will have lower sensitivity until more data is accumulated, but are completely equivalent when looking at the full 7-dimensional probability distribution of all parameters.

From all benchmarks discussed in this section, the last parameterization in table 50 is the most general parameterization that needs no assumptions beyond those stated in the definition of the framework.

Once the $H \to \mu^-\mu^+$ and $H \to Z\gamma$ decay modes reach sufficient sensitivity, a natural extension for this benchmark is to fit extra degrees of freedom in the form of the parameters κ_μ and $\kappa_{(Z\gamma)}$ for these two final states.

10.3.8   *General parameterization assuming no beyond SM particles*

Table 51 presents the relations to be used in a fit where the loop-induced ggH and $H \rightarrow \gamma\gamma$ processes and the total width are expressed in terms of the SM gauge- and Yukawa coupling scale factors (κ_W, κ_Z, κ_b, κ_t, κ_τ), assuming no beyond SM particle contributions. This benchmark makes full use of Eqs.(111), (113), (115) and has the highest sensitivity in an independent fit of the SM gauge- and Yukawa-coupling scale factors.

Once the $H \rightarrow \mu^-\mu^+$ and $H \rightarrow Z\gamma$ decay modes reach sufficient sensitivity, a natural extension for this benchmark is to fit an extra degree of freedom in the form of the parameter κ_μ, while resolving the $H \rightarrow Z\gamma$ decay mode using Eq.(114).

Table 46: A benchmark parameterization where the up-type and down-type symmetry of fermions is probed through the λ_{du} parameter.

Probing up-type and down-type fermion symmetry assuming no invisible or undetectable widths

Free parameters: $\kappa_V (= \kappa_Z = \kappa_W)$, $\lambda_{du} (= \kappa_d/\kappa_u)$, $\kappa_u (= \kappa_t)$.

Dependent parameters: $\kappa_\gamma = \kappa_\gamma(\kappa_u\lambda_{du}, \kappa_u, \kappa_u\lambda_{du}, \kappa_V)$, $\kappa_g = \kappa_g(\kappa_u\lambda_{du}, \kappa_u)$, $\kappa_H = \kappa_H(\kappa_i)$.

	$H \to \gamma\gamma$	$H \to ZZ^{(*)}$ $H \to WW^{(*)}$	$H \to b\overline{b}$ $H \to \tau^-\tau^+$
ggH	$\dfrac{\kappa_g^2(\kappa_u\lambda_{du},\kappa_u)\cdot\kappa_\gamma^2(\kappa_u\lambda_{du},\kappa_u,\kappa_u\lambda_{du},\kappa_V)}{\kappa_H^2(\kappa_i)}$	$\dfrac{\kappa_g^2(\kappa_u\lambda_{du},\kappa_u)\cdot\kappa_V^2}{\kappa_H^2(\kappa_i)}$	$\dfrac{\kappa_g^2(\kappa_u\lambda_{du},\kappa_u)\cdot(\kappa_u\lambda_{du})^2}{\kappa_H^2(\kappa_i)}$
t$\overline{t}$H	$\dfrac{\kappa_u^2\cdot\kappa_\gamma^2(\kappa_u\lambda_{du},\kappa_u,\kappa_u\lambda_{du},\kappa_V)}{\kappa_H^2(\kappa_i)}$	$\dfrac{\kappa_u^2\cdot\kappa_V^2}{\kappa_H^2(\kappa_i)}$	$\dfrac{\kappa_u^2\cdot(\kappa_u\lambda_{du})^2}{\kappa_H^2(\kappa_i)}$
VBF WH ZH	$\dfrac{\kappa_V^2\cdot\kappa_\gamma^2(\kappa_u\lambda_{du},\kappa_u,\kappa_u\lambda_{du},\kappa_V)}{\kappa_H^2(\kappa_i)}$	$\dfrac{\kappa_V^2\cdot\kappa_V^2}{\kappa_H^2(\kappa_i)}$	$\dfrac{\kappa_V^2\cdot(\kappa_u\lambda_{du})^2}{\kappa_H^2(\kappa_i)}$

Probing up-type and down-type fermion symmetry assuming $\kappa_V < 1$

Free parameters: $\kappa_V (= \kappa_Z = \kappa_W)$, $\lambda_{du} (= \kappa_d/\kappa_u)$, $\kappa_u (= \kappa_t)$, κ_H, with conditions $\kappa_V < 1$ and $\kappa_H^2 > \kappa_H^2(\kappa_i)$.

Dependent parameters: $\kappa_\gamma = \kappa_\gamma(\kappa_u\lambda_{du}, \kappa_u, \kappa_u\lambda_{du}, \kappa_V)$, $\kappa_g = \kappa_g(\kappa_u\lambda_{du}, \kappa_u)$.

	$H \to \gamma\gamma$	$H \to ZZ^{(*)}$ $H \to WW^{(*)}$	$H \to b\overline{b}$ $H \to \tau^-\tau^+$
ggH	$\dfrac{\kappa_g^2(\kappa_u\lambda_{du},\kappa_u)\cdot\kappa_\gamma^2(\kappa_u\lambda_{du},\kappa_u,\kappa_u\lambda_{du},\kappa_V)}{\kappa_H^2}$	$\dfrac{\kappa_g^2(\kappa_u\lambda_{du},\kappa_u)\cdot\kappa_V^2}{\kappa_H^2}$	$\dfrac{\kappa_g^2(\kappa_u\lambda_{du},\kappa_u)\cdot(\kappa_u\lambda_{du})^2}{\kappa_H^2}$
t$\overline{t}$H	$\dfrac{\kappa_u^2\cdot\kappa_\gamma^2(\kappa_u\lambda_{du},\kappa_u,\kappa_u\lambda_{du},\kappa_V)}{\kappa_H^2}$	$\dfrac{\kappa_u^2\cdot\kappa_V^2}{\kappa_H^2}$	$\dfrac{\kappa_u^2\cdot(\kappa_u\lambda_{du})^2}{\kappa_H^2}$
VBF WH ZH	$\dfrac{\kappa_V^2\cdot\kappa_\gamma^2(\kappa_u\lambda_{du},\kappa_u,\kappa_u\lambda_{du},\kappa_V)}{\kappa_H^2}$	$\dfrac{\kappa_V^2\cdot\kappa_V^2}{\kappa_H^2}$	$\dfrac{\kappa_V^2\cdot(\kappa_u\lambda_{du})^2}{\kappa_H^2}$

Probing up-type and down-type fermion symmetry without assumptions on the total width

Free parameters: $\kappa_{uu}(= \kappa_u \cdot \kappa_u/\kappa_H)$, $\lambda_{du}(= \kappa_d/\kappa_u)$, $\lambda_{Vu}(= \kappa_V/\kappa_u)$.

Dependent parameters: $\kappa_\gamma = \kappa_\gamma(\lambda_{du}, 1, \lambda_{du}, \lambda_{Vu})$, $\kappa_g = \kappa_g(\lambda_{du}, 1)$.

	$H \to \gamma\gamma$	$H \to ZZ^{(*)}$ $H \to WW^{(*)}$	$H \to b\overline{b}$ $H \to \tau^-\tau^+$
ggH	$\kappa_{uu}^2\kappa_g^2(\lambda_{du},1)\cdot\kappa_\gamma^2(\lambda_{du},1,\lambda_{du},\lambda_{Vu})$	$\kappa_{uu}^2\kappa_g^2(\lambda_{du},1)\cdot\lambda_{Vu}^2$	$\kappa_{uu}^2\kappa_g^2(\lambda_{du},1)\cdot\lambda_{du}^2$
t$\overline{t}$H	$\kappa_{uu}^2\cdot\kappa_\gamma^2(\lambda_{du},1,\lambda_{du},\lambda_{Vu})$	$\kappa_{uu}^2\cdot\lambda_{Vu}^2$	$\kappa_{uu}^2\cdot\lambda_{du}^2$
VBF WH ZH	$\kappa_{uu}^2\lambda_{Vu}^2\cdot\kappa_\gamma^2(\lambda_{du},1,\lambda_{du},\lambda_{Vu})$	$\kappa_{uu}^2\lambda_{Vu}^2\cdot\lambda_{Vu}^2$	$\kappa_{uu}^2\lambda_{Vu}^2\cdot\lambda_{du}^2$

$$\kappa_i^2 = \Gamma_{ii}/\Gamma_{ii}^{SM}, \kappa_d = \kappa_b = \kappa_\tau$$

Table 47: A benchmark parameterization where the quark and lepton symmetry of fermions is probed through the λ_{lq} parameter.

Probing quark and lepton fermion symmetry assuming no invisible or undetectable widths

Free parameters: $\kappa_V(=\kappa_Z=\kappa_W)$, $\lambda_{\mathrm{lq}}(=\kappa_l/\kappa_q)$, $\kappa_q(=\kappa_t=\kappa_b)$.

Dependent parameters: $\kappa_\gamma=\kappa_\gamma(\kappa_q,\kappa_q,\kappa_q\lambda_{\mathrm{lq}},\kappa_V)$, $\kappa_g=\kappa_q$, $\kappa_H=\kappa_H(\kappa_i)$.

	$H\to\gamma\gamma$	$H\to ZZ^{(*)}$	$H\to WW^{(*)}$	$H\to b\bar{b}$	$H\to\tau^-\tau^+$
ggH $t\bar{t}H$	$\dfrac{\kappa_q^2\cdot\kappa_\gamma^2(\kappa_q,\kappa_q,\kappa_q\lambda_{\mathrm{lq}},\kappa_V)}{\kappa_H^2(\kappa_i)}$	$\dfrac{\kappa_q^2\cdot\kappa_V^2}{\kappa_H^2(\kappa_i)}$		$\dfrac{\kappa_q^2\cdot\kappa_q^2}{\kappa_H^2(\kappa_i)}$	$\dfrac{\kappa_q^2\cdot(\kappa_q\lambda_{\mathrm{lq}})^2}{\kappa_H^2(\kappa_i)}$
VBF WH ZH	$\dfrac{\kappa_V^2\cdot\kappa_\gamma^2(\kappa_q,\kappa_q,\kappa_q\lambda_{\mathrm{lq}},\kappa_V)}{\kappa_H^2(\kappa_i)}$	$\dfrac{\kappa_V^2\cdot\kappa_V^2}{\kappa_H^2(\kappa_i)}$		$\dfrac{\kappa_V^2\cdot\kappa_q^2}{\kappa_H^2(\kappa_i)}$	$\dfrac{\kappa_V^2\cdot(\kappa_q\lambda_{\mathrm{lq}})^2}{\kappa_H^2(\kappa_i)}$

Probing quark and lepton fermion symmetry assuming $\kappa_V<1$

Free parameters: $\kappa_V(=\kappa_Z=\kappa_W)$, $\lambda_{\mathrm{lq}}(=\kappa_l/\kappa_q)$, $\kappa_q(=\kappa_t=\kappa_b)$, κ_H, with conditions $\kappa_V<1$ and $\kappa_H^2>\kappa_H^2(\kappa_i)$.

Dependent parameters: $\kappa_\gamma=\kappa_\gamma(\kappa_q,\kappa_q,\kappa_q\lambda_{\mathrm{lq}},\kappa_V)$, $\kappa_g=\kappa_q$.

	$H\to\gamma\gamma$	$H\to ZZ^{(*)}$	$H\to WW^{(*)}$	$H\to b\bar{b}$	$H\to\tau^-\tau^+$
ggH $t\bar{t}H$	$\dfrac{\kappa_q^2\cdot\kappa_\gamma^2(\kappa_q,\kappa_q,\kappa_q\lambda_{\mathrm{lq}},\kappa_V)}{\kappa_H^2}$	$\dfrac{\kappa_q^2\cdot\kappa_V^2}{\kappa_H^2}$		$\dfrac{\kappa_q^2\cdot\kappa_q^2}{\kappa_H^2}$	$\dfrac{\kappa_q^2\cdot(\kappa_q\lambda_{\mathrm{lq}})^2}{\kappa_H^2}$
VBF WH ZH	$\dfrac{\kappa_V^2\cdot\kappa_\gamma^2(\kappa_q,\kappa_q,\kappa_q\lambda_{\mathrm{lq}},\kappa_V)}{\kappa_H^2}$	$\dfrac{\kappa_V^2\cdot\kappa_V^2}{\kappa_H^2}$		$\dfrac{\kappa_V^2\cdot\kappa_q^2}{\kappa_H^2}$	$\dfrac{\kappa_V^2\cdot(\kappa_q\lambda_{\mathrm{lq}})^2}{\kappa_H^2}$

Probing quark and lepton fermion symmetry without assumptions on the total width

Free parameters: $\kappa_{qq}(=\kappa_q\cdot\kappa_q/\kappa_H)$, $\lambda_{\mathrm{lq}}(=\kappa_l/\kappa_q)$, $\lambda_{Vq}(=\kappa_V/\kappa_q)$.

Dependent parameters: $\kappa_\gamma=\kappa_\gamma(1,1,\lambda_{\mathrm{lq}},\lambda_{Vq})$, $\kappa_g=\kappa_q$.

	$H\to\gamma\gamma$	$H\to ZZ^{(*)}$	$H\to WW^{(*)}$	$H\to b\bar{b}$	$H\to\tau^-\tau^+$
ggH $t\bar{t}H$	$\kappa_{qq}^2\cdot\kappa_\gamma^2(1,1,\lambda_{\mathrm{lq}},\lambda_{Vq})$	$\kappa_{qq}^2\cdot\lambda_{Vq}^2$		κ_{qq}^2	$\kappa_{qq}^2\cdot\lambda_{\mathrm{lq}}^2$
VBF WH ZH	$\kappa_{qq}^2\lambda_{Vq}^2\cdot\kappa_\gamma^2(1,1,\lambda_{\mathrm{lq}},\lambda_{Vq})$	$\kappa_{qq}^2\lambda_{Vq}^2\cdot\lambda_{Vq}^2$		$\kappa_{qq}^2\cdot\lambda_{Vq}^2$	$\kappa_{qq}^2\lambda_{Vq}^2\cdot\lambda_{\mathrm{lq}}^2$

$$\kappa_i^2=\Gamma_{ii}/\Gamma_{ii}^{\mathrm{SM}},\ \kappa_l=\kappa_\tau$$

Table 48: A benchmark parameterization where effective vertex couplings are allowed to float through the κ_g and κ_γ parameters. Instead of absorbing κ_H, explicit allowance is made for a contribution from invisible or undetectable widths via the $\mathrm{BR}_{\mathrm{inv.,undet.}}$ or $\mathrm{BR}_{\mathrm{inv.}}$ and $\mathrm{BR}_{\mathrm{undet.}}$ parameters.

Probing loop structure assuming no invisible or undetectable widths

Free parameters: κ_g, κ_γ.

Dependent parameters: $\kappa_H = \kappa_H(\kappa_i)$. Fixed parameters $\kappa_Z = \kappa_W = \kappa_\tau = \kappa_b = \kappa_t = 1$.

	$H \to \gamma\gamma$	$H \to ZZ^{(*)}$	$H \to WW^{(*)}$	$H \to b\bar{b}$	$H \to \tau^-\tau^+$
ggH	$\dfrac{\kappa_g^2 \cdot \kappa_\gamma^2}{\kappa_H^2(\kappa_i)}$		$\dfrac{\kappa_g^2}{\kappa_H^2(\kappa_i)}$		
ttH					
VBF	$\dfrac{\kappa_\gamma^2}{\kappa_H^2(\kappa_i)}$		$\dfrac{1}{\kappa_H^2(\kappa_i)}$		
WH					
ZH					

Probing loop structure allowing for invisible or undetectable widths

Free parameters: κ_g, κ_γ, $\mathrm{BR}_{\mathrm{inv.,undet.}}$.

Dependent parameters: $\kappa_H = \kappa_H(\kappa_i)$. Fixed parameters $\kappa_Z = \kappa_W = \kappa_\tau = \kappa_b = \kappa_t = 1$.

	$H \to \gamma\gamma$	$H \to ZZ^{(*)}$	$H \to WW^{(*)}$	$H \to b\bar{b}$	$H \to \tau^-\tau^+$
ggH	$\dfrac{\kappa_g^2 \cdot \kappa_\gamma^2}{\kappa_H^2(\kappa_i)/(1-\mathrm{BR}_{\mathrm{inv.,undet.}})}$		$\dfrac{\kappa_g^2}{\kappa_H^2(\kappa_i)/(1-\mathrm{BR}_{\mathrm{inv.,undet.}})}$		
ttH					
VBF	$\dfrac{\kappa_\gamma^2}{\kappa_H^2(\kappa_i)/(1-\mathrm{BR}_{\mathrm{inv.,undet.}})}$		$\dfrac{1}{\kappa_H^2(\kappa_i)/(1-\mathrm{BR}_{\mathrm{inv.,undet.}})}$		
WH					
ZH					

Probing loop structure allowing for separate invisible and undetectable widths

Free parameters: κ_g, κ_γ, $\mathrm{BR}_{\mathrm{inv.}}$, $\mathrm{BR}_{\mathrm{undet.}}$, with condition $\mathrm{BR}_{\mathrm{inv.}} + \mathrm{BR}_{\mathrm{undet.}} \leq 1$.

Dependent parameters: $\kappa_H = \kappa_H(\kappa_i)$. Fixed parameters $\kappa_Z = \kappa_W = \kappa_\tau = \kappa_b = \kappa_t = 1$.

	$H \to \gamma\gamma$	$H \to ZZ^{(*)}$	$H \to WW^{(*)}$	$H \to b\bar{b}$	$H \to \tau^-\tau^+$
ggH	$\dfrac{\kappa_g^2 \cdot \kappa_\gamma^2}{\kappa_H^2(\kappa_i)/(1-\mathrm{BR}_{\mathrm{inv.}}-\mathrm{BR}_{\mathrm{undet.}})}$		$\dfrac{\kappa_g^2}{\kappa_H^2(\kappa_i)/(1-\mathrm{BR}_{\mathrm{inv.}}-\mathrm{BR}_{\mathrm{undet.}})}$		
ttH					
VBF	$\dfrac{\kappa_\gamma^2}{\kappa_H^2(\kappa_i)/(1-\mathrm{BR}_{\mathrm{inv.}}-\mathrm{BR}_{\mathrm{undet.}})}$		$\dfrac{1}{\kappa_H^2(\kappa_i)/(1-\mathrm{BR}_{\mathrm{inv.}}-\mathrm{BR}_{\mathrm{undet.}})}$		
WH					
ZH					

$$\kappa_i^2 = \Gamma_{ii}/\Gamma_{ii}^{\mathrm{SM}}$$

Table 49: A benchmark parameterization where effective vertex couplings are allowed to float through the κ_g and κ_γ parameters and the gauge and fermion couplings through the unified parameters κ_V and κ_f.

Probing loops while allowing other couplings to float assuming no invisible or undetectable widths

Free parameters: κ_g, κ_γ, $\kappa_V(=\kappa_W=\kappa_Z)$, $\kappa_f(=\kappa_t=\kappa_b=\kappa_\tau)$.

Dependent parameters: $\kappa_H = \kappa_H(\kappa_i)$.

	$H \to \gamma\gamma$	$H \to ZZ^{(*)}$ $\quad H \to WW^{(*)}$		$H \to b\bar{b}$	$H \to \tau^-\tau^+$
ggH	$\dfrac{\kappa_g^2 \cdot \kappa_\gamma^2}{\kappa_H^2(\kappa_i)}$	$\dfrac{\kappa_g^2 \cdot \kappa_V^2}{\kappa_H^2(\kappa_i)}$		$\dfrac{\kappa_g^2 \cdot \kappa_f^2}{\kappa_H^2(\kappa_i)}$	
t$\bar{\text{t}}$H	$\dfrac{\kappa_f^2 \cdot \kappa_\gamma^2}{\kappa_H^2(\kappa_i)}$	$\dfrac{\kappa_f^2 \cdot \kappa_V^2}{\kappa_H^2(\kappa_i)}$		$\dfrac{\kappa_f^2 \cdot \kappa_f^2}{\kappa_H^2(\kappa_i)}$	
VBF WH ZH	$\dfrac{\kappa_V^2 \cdot \kappa_\gamma^2}{\kappa_H^2(\kappa_i)}$	$\dfrac{\kappa_V^2 \cdot \kappa_V^2}{\kappa_H^2(\kappa_i)}$		$\dfrac{\kappa_V^2 \cdot \kappa_f^2}{\kappa_H^2(\kappa_i)}$	

Probing loops while allowing other couplings to float assuming $\kappa_V < 1$

Free parameters: κ_g, κ_γ, $\kappa_V(=\kappa_W=\kappa_Z)$, $\kappa_f(=\kappa_t=\kappa_b=\kappa_\tau)$, κ_H, with conditions $\kappa_V < 1$ and $\kappa_H^2 > \kappa_H^2(\kappa_i)$.

	$H \to \gamma\gamma$	$H \to ZZ^{(*)}$ $\quad H \to WW^{(*)}$		$H \to b\bar{b}$	$H \to \tau^-\tau^+$
ggH	$\dfrac{\kappa_g^2 \cdot \kappa_\gamma^2}{\kappa_H^2}$	$\dfrac{\kappa_g^2 \cdot \kappa_V^2}{\kappa_H^2}$		$\dfrac{\kappa_g^2 \cdot \kappa_f^2}{\kappa_H^2}$	
t$\bar{\text{t}}$H	$\dfrac{\kappa_f^2 \cdot \kappa_\gamma^2}{\kappa_H^2}$	$\dfrac{\kappa_f^2 \cdot \kappa_V^2}{\kappa_H^2}$		$\dfrac{\kappa_f^2 \cdot \kappa_f^2}{\kappa_H^2}$	
VBF WH ZH	$\dfrac{\kappa_V^2 \cdot \kappa_\gamma^2}{\kappa_H^2}$	$\dfrac{\kappa_V^2 \cdot \kappa_V^2}{\kappa_H^2}$		$\dfrac{\kappa_V^2 \cdot \kappa_f^2}{\kappa_H^2}$	

Probing loops while allowing other couplings to float allowing for invisible or undetectable widths

Free parameters: $\kappa_{gV}(=\kappa_g \cdot \kappa_V/\kappa_H)$, $\lambda_{Vg}(=\kappa_V/\kappa_g)$, $\lambda_{\gamma V}(=\kappa_\gamma/\kappa_V)$, $\lambda_{fV}(=\kappa_f/\kappa_V)$.

	$H \to \gamma\gamma$	$H \to ZZ^{(*)}$ $\quad H \to WW^{(*)}$		$H \to b\bar{b}$	$H \to \tau^-\tau^+$
ggH	$\kappa_{gV}^2 \cdot \lambda_{\gamma V}^2$	κ_{gV}^2		$\kappa_{gV}^2 \cdot \lambda_{fV}^2$	
t$\bar{\text{t}}$H	$\kappa_{gV}^2 \lambda_{Vg}^2 \lambda_{fV}^2 \cdot \lambda_{\gamma V}^2$	$\kappa_{gV}^2 \lambda_{Vg}^2 \lambda_{fV}^2$		$\kappa_{gV}^2 \lambda_{Vg}^2 \lambda_{fV}^2 \cdot \lambda_{fV}^2$	
VBF WH ZH	$\kappa_{gV}^2 \lambda_{Vg}^2 \cdot \lambda_{\gamma V}^2$	$\kappa_{gV}^2 \lambda_{Vg}^2$		$\kappa_{gV}^2 \lambda_{Vg}^2 \cdot \lambda_{fV}^2$	

$$\kappa_i^2 = \Gamma_{ii}/\Gamma_{ii}^{\text{SM}}, \quad \kappa_V = \kappa_W = \kappa_Z, \quad \kappa_f = \kappa_t = \kappa_b = \kappa_\tau$$

Table 50: A benchmark parameterization without further assumptions and maximum degrees of freedom.

General parameterization allowing all gauge and third generation fermion couplings to float assuming no invisible or undetectable widths

Free parameters: κ_g, κ_γ, κ_W, κ_Z, κ_b, κ_t, κ_τ.

Dependent parameters: $\kappa_H = \kappa_H(\kappa_i)$.

	$H \to \gamma\gamma$	$H \to ZZ^{(*)}$	$H \to WW^{(*)}$	$H \to b\bar{b}$	$H \to \tau^-\tau^+$
ggH	$\dfrac{\kappa_g^2 \cdot \kappa_\gamma^2}{\kappa_H^2(\kappa_i)}$	$\dfrac{\kappa_g^2 \cdot \kappa_Z^2}{\kappa_H^2(\kappa_i)}$	$\dfrac{\kappa_g^2 \cdot \kappa_W^2}{\kappa_H^2(\kappa_i)}$	$\dfrac{\kappa_g^2 \cdot \kappa_b^2}{\kappa_H^2(\kappa_i)}$	$\dfrac{\kappa_g^2 \cdot \kappa_\tau^2}{\kappa_H^2(\kappa_i)}$
$t\bar{t}H$	$\dfrac{\kappa_t^2 \cdot \kappa_\gamma^2}{\kappa_H^2(\kappa_i)}$	$\dfrac{\kappa_t^2 \cdot \kappa_Z^2}{\kappa_H^2(\kappa_i)}$	$\dfrac{\kappa_t^2 \cdot \kappa_W^2}{\kappa_H^2(\kappa_i)}$	$\dfrac{\kappa_t^2 \cdot \kappa_b^2}{\kappa_H^2(\kappa_i)}$	$\dfrac{\kappa_t^2 \cdot \kappa_\tau^2}{\kappa_H^2(\kappa_i)}$
VBF	$\dfrac{\kappa_{VBF}^2(\kappa_Z,\kappa_W) \cdot \kappa_\gamma^2}{\kappa_H^2(\kappa_i)}$	$\dfrac{\kappa_{VBF}^2(\kappa_Z,\kappa_W) \cdot \kappa_Z^2}{\kappa_H^2(\kappa_i)}$	$\dfrac{\kappa_{VBF}^2(\kappa_Z,\kappa_W) \cdot \kappa_W^2}{\kappa_H^2(\kappa_i)}$	$\dfrac{\kappa_{VBF}^2(\kappa_Z,\kappa_W) \cdot \kappa_b^2}{\kappa_H^2(\kappa_i)}$	$\dfrac{\kappa_{VBF}^2(\kappa_Z,\kappa_W) \cdot \kappa_\tau^2}{\kappa_H^2(\kappa_i)}$
WH	$\dfrac{\kappa_W^2 \cdot \kappa_\gamma^2}{\kappa_H^2(\kappa_i)}$	$\dfrac{\kappa_W^2 \cdot \kappa_Z^2}{\kappa_H^2(\kappa_i)}$	$\dfrac{\kappa_W^2 \cdot \kappa_W^2}{\kappa_H^2(\kappa_i)}$	$\dfrac{\kappa_W^2 \cdot \kappa_b^2}{\kappa_H^2(\kappa_i)}$	$\dfrac{\kappa_W^2 \cdot \kappa_\tau^2}{\kappa_H^2(\kappa_i)}$
ZH	$\dfrac{\kappa_Z^2 \cdot \kappa_\gamma^2}{\kappa_H^2(\kappa_i)}$	$\dfrac{\kappa_Z^2 \cdot \kappa_Z^2}{\kappa_H^2(\kappa_i)}$	$\dfrac{\kappa_Z^2 \cdot \kappa_W^2}{\kappa_H^2(\kappa_i)}$	$\dfrac{\kappa_Z^2 \cdot \kappa_b^2}{\kappa_H^2(\kappa_i)}$	$\dfrac{\kappa_Z^2 \cdot \kappa_\tau^2}{\kappa_H^2(\kappa_i)}$

General parameterization allowing all gauge and third generation fermion couplings to float assuming $\kappa_V < 1$

Free parameters: κ_g, κ_γ, κ_W, κ_Z, κ_b, κ_t, κ_τ, κ_H, with conditions $\kappa_W < 1$, $\kappa_Z < 1$ and $\kappa_H^2 > \kappa_H^2(\kappa_i)$.

	$H \to \gamma\gamma$	$H \to ZZ^{(*)}$	$H \to WW^{(*)}$	$H \to b\bar{b}$	$H \to \tau^-\tau^+$
ggH	$\dfrac{\kappa_g^2 \cdot \kappa_\gamma^2}{\kappa_H^2}$	$\dfrac{\kappa_g^2 \cdot \kappa_Z^2}{\kappa_H^2}$	$\dfrac{\kappa_g^2 \cdot \kappa_W^2}{\kappa_H^2}$	$\dfrac{\kappa_g^2 \cdot \kappa_b^2}{\kappa_H^2}$	$\dfrac{\kappa_g^2 \cdot \kappa_\tau^2}{\kappa_H^2}$
$t\bar{t}H$	$\dfrac{\kappa_t^2 \cdot \kappa_\gamma^2}{\kappa_H^2}$	$\dfrac{\kappa_t^2 \cdot \kappa_Z^2}{\kappa_H^2}$	$\dfrac{\kappa_t^2 \cdot \kappa_W^2}{\kappa_H^2}$	$\dfrac{\kappa_t^2 \cdot \kappa_b^2}{\kappa_H^2}$	$\dfrac{\kappa_t^2 \cdot \kappa_\tau^2}{\kappa_H^2}$
VBF	$\dfrac{\kappa_{VBF}^2(\kappa_Z,\kappa_W) \cdot \kappa_\gamma^2}{\kappa_H^2}$	$\dfrac{\kappa_{VBF}^2(\kappa_Z,\kappa_W) \cdot \kappa_Z^2}{\kappa_H^2}$	$\dfrac{\kappa_{VBF}^2(\kappa_Z,\kappa_W) \cdot \kappa_W^2}{\kappa_H^2}$	$\dfrac{\kappa_{VBF}^2(\kappa_Z,\kappa_W) \cdot \kappa_b^2}{\kappa_H^2}$	$\dfrac{\kappa_{VBF}^2(\kappa_Z,\kappa_W) \cdot \kappa_\tau^2}{\kappa_H^2}$
WH	$\dfrac{\kappa_W^2 \cdot \kappa_\gamma^2}{\kappa_H^2}$	$\dfrac{\kappa_W^2 \cdot \kappa_Z^2}{\kappa_H^2}$	$\dfrac{\kappa_W^2 \cdot \kappa_W^2}{\kappa_H^2}$	$\dfrac{\kappa_W^2 \cdot \kappa_b^2}{\kappa_H^2}$	$\dfrac{\kappa_W^2 \cdot \kappa_\tau^2}{\kappa_H^2}$
ZH	$\dfrac{\kappa_Z^2 \cdot \kappa_\gamma^2}{\kappa_H^2}$	$\dfrac{\kappa_Z^2 \cdot \kappa_Z^2}{\kappa_H^2}$	$\dfrac{\kappa_Z^2 \cdot \kappa_W^2}{\kappa_H^2}$	$\dfrac{\kappa_Z^2 \cdot \kappa_b^2}{\kappa_H^2}$	$\dfrac{\kappa_Z^2 \cdot \kappa_\tau^2}{\kappa_H^2}$

General parameterization allowing all gauge and third generation fermion couplings to float allowing for invisible or undetectable widths

Free parameters: $\kappa_{gZ}(= \kappa_g \cdot \kappa_Z/\kappa_H)$, $\lambda_{\gamma Z}(= \kappa_\gamma/\kappa_Z)$, $\lambda_{WZ}(= \kappa_W/\kappa_Z)$, $\lambda_{bZ}(= \kappa_b/\kappa_Z)$, $\lambda_{\tau Z}(= \kappa_\tau/\kappa_Z)$, $\lambda_{Zg}(= \kappa_Z/\kappa_g)$, $\lambda_{tg}(= \kappa_t/\kappa_g)$.

	$H \to \gamma\gamma$	$H \to ZZ^{(*)}$	$H \to WW^{(*)}$	$H \to b\bar{b}$	$H \to \tau^-\tau^+$
ggH	$\kappa_{gZ}^2 \cdot \lambda_{\gamma Z}^2$	κ_{gZ}^2	$\kappa_{gZ}^2 \cdot \lambda_{WZ}^2$	$\kappa_{gZ}^2 \cdot \lambda_{bZ}^2$	$\kappa_{gZ}^2 \cdot \lambda_{\tau Z}^2$
$t\bar{t}H$	$\kappa_{gZ}^2 \lambda_{tg}^2 \cdot \lambda_{\gamma Z}^2$	$\kappa_{gZ}^2 \lambda_{tg}^2$	$\kappa_{gZ}^2 \lambda_{tg}^2 \cdot \lambda_{WZ}^2$	$\kappa_{gZ}^2 \lambda_{tg}^2 \cdot \lambda_{bZ}^2$	$\kappa_{gZ}^2 \lambda_{tg}^2 \cdot \lambda_{\tau Z}^2$
VBF	$\kappa_{gZ}^2 \lambda_{Zg}^2 \kappa_{VBF}^2(1,\lambda_{WZ}) \cdot \lambda_{\gamma Z}^2$	$\kappa_{gZ}^2 \lambda_{Zg}^2 \kappa_{VBF}^2(1,\lambda_{WZ})$	$\kappa_{gZ}^2 \lambda_{Zg}^2 \kappa_{VBF}^2(1,\lambda_{WZ}) \cdot \lambda_{WZ}^2$	$\kappa_{gZ}^2 \lambda_{Zg}^2 \kappa_{VBF}^2(1,\lambda_{WZ}) \cdot \lambda_{bZ}^2$	$\kappa_{gZ}^2 \lambda_{Zg}^2 \kappa_{VBF}^2(1,\lambda_{WZ}) \cdot \lambda_{\tau Z}^2$
WH	$\kappa_{gZ}^2 \lambda_{Zg}^2 \lambda_{WZ}^2 \cdot \lambda_{\gamma Z}^2$	$\kappa_{gZ}^2 \lambda_{Zg}^2 \lambda_{WZ}^2$	$\kappa_{gZ}^2 \lambda_{Zg}^2 \lambda_{WZ}^2 \cdot \lambda_{WZ}^2$	$\kappa_{gZ}^2 \lambda_{Zg}^2 \lambda_{WZ}^2 \cdot \lambda_{bZ}^2$	$\kappa_{gZ}^2 \lambda_{Zg}^2 \lambda_{WZ}^2 \cdot \lambda_{\tau Z}^2$
ZH	$\kappa_{gZ}^2 \lambda_{Zg}^2 \cdot \lambda_{\gamma Z}^2$	$\kappa_{gZ}^2 \lambda_{Zg}^2$	$\kappa_{gZ}^2 \lambda_{Zg}^2 \cdot \lambda_{WZ}^2$	$\kappa_{gZ}^2 \lambda_{Zg}^2 \cdot \lambda_{bZ}^2$	$\kappa_{gZ}^2 \lambda_{Zg}^2 \cdot \lambda_{\tau Z}^2$

$$\kappa_i^2 = \Gamma_{ii}/\Gamma_{ii}^{SM}$$

Table 51: A benchmark parameterization expressing all processes in terms of the SM gauge- and Yukawa-coupling scale factors, assuming no beyond SM particle contributions.

General parameterization assuming no beyond SM particles

Free parameters: κ_W, κ_Z, κ_b, κ_t, κ_τ.

Dependent parameters: $\kappa_g = \kappa_g(\kappa_b, \kappa_t)$, $\kappa_\gamma = \kappa_\gamma(\kappa_b, \kappa_t, \kappa_\tau, \kappa_W)$, $\kappa_H = \kappa_H(\kappa_i)$.

	$H \to \gamma\gamma$	$H \to ZZ^{(*)}$	$H \to WW^{(*)}$	$H \to b\bar{b}$	$H \to \tau^-\tau^+$
ggH	$\dfrac{\kappa_g^2(\kappa_b,\kappa_t)\cdot\kappa_\gamma^2(\kappa_b,\kappa_t,\kappa_\tau,\kappa_W)}{\kappa_H^2(\kappa_i)}$	$\dfrac{\kappa_g^2(\kappa_b,\kappa_t)\cdot\kappa_Z^2}{\kappa_H^2(\kappa_i)}$	$\dfrac{\kappa_g^2(\kappa_b,\kappa_t)\cdot\kappa_W^2}{\kappa_H^2(\kappa_i)}$	$\dfrac{\kappa_g^2(\kappa_b,\kappa_t)\cdot\kappa_b^2}{\kappa_H^2(\kappa_i)}$	$\dfrac{\kappa_g^2(\kappa_b,\kappa_t)\cdot\kappa_\tau^2}{\kappa_H^2(\kappa_i)}$
$t\bar{t}H$	$\dfrac{\kappa_t^2\cdot\kappa_\gamma^2(\kappa_b,\kappa_t,\kappa_\tau,\kappa_W)}{\kappa_H^2(\kappa_i)}$	$\dfrac{\kappa_t^2\cdot\kappa_Z^2}{\kappa_H^2(\kappa_i)}$	$\dfrac{\kappa_t^2\cdot\kappa_W^2}{\kappa_H^2(\kappa_i)}$	$\dfrac{\kappa_t^2\cdot\kappa_b^2}{\kappa_H^2(\kappa_i)}$	$\dfrac{\kappa_t^2\cdot\kappa_\tau^2}{\kappa_H^2(\kappa_i)}$
VBF	$\dfrac{\kappa_{VBF}^2(\kappa_Z,\kappa_W)\cdot\kappa_\gamma^2(\kappa_b,\kappa_t,\kappa_\tau,\kappa_W)}{\kappa_H^2(\kappa_i)}$	$\dfrac{\kappa_{VBF}^2(\kappa_Z,\kappa_W)\cdot\kappa_Z^2}{\kappa_H^2(\kappa_i)}$	$\dfrac{\kappa_{VBF}^2(\kappa_Z,\kappa_W)\cdot\kappa_W^2}{\kappa_H^2(\kappa_i)}$	$\dfrac{\kappa_{VBF}^2(\kappa_Z,\kappa_W)\cdot\kappa_b^2}{\kappa_H^2(\kappa_i)}$	$\dfrac{\kappa_{VBF}^2(\kappa_Z,\kappa_W)\cdot\kappa_\tau^2}{\kappa_H^2(\kappa_i)}$
WH	$\dfrac{\kappa_W^2\cdot\kappa_\gamma^2(\kappa_b,\kappa_t,\kappa_\tau,\kappa_W)}{\kappa_H^2(\kappa_i)}$	$\dfrac{\kappa_W^2\cdot\kappa_Z^2}{\kappa_H^2(\kappa_i)}$	$\dfrac{\kappa_W^2\cdot\kappa_W^2}{\kappa_H^2(\kappa_i)}$	$\dfrac{\kappa_W^2\cdot\kappa_b^2}{\kappa_H^2(\kappa_i)}$	$\dfrac{\kappa_W^2\cdot\kappa_\tau^2}{\kappa_H^2(\kappa_i)}$
ZH	$\dfrac{\kappa_Z^2\cdot\kappa_\gamma^2(\kappa_b,\kappa_t,\kappa_\tau,\kappa_W)}{\kappa_H^2(\kappa_i)}$	$\dfrac{\kappa_Z^2\cdot\kappa_Z^2}{\kappa_H^2(\kappa_i)}$	$\dfrac{\kappa_Z^2\cdot\kappa_W^2}{\kappa_H^2(\kappa_i)}$	$\dfrac{\kappa_Z^2\cdot\kappa_b^2}{\kappa_H^2(\kappa_i)}$	$\dfrac{\kappa_Z^2\cdot\kappa_\tau^2}{\kappa_H^2(\kappa_i)}$

$$\kappa_i^2 = \Gamma_{ii}/\Gamma_{ii}^{SM}$$

10.4 Effective Lagrangians for Higgs interactions

The "interim framework" described in Section 10.2 was proposed as a first step for exploring the coupling structure of the recently observed state, making use of the data taken until the end of 2012. In future, however, one should aim at a more general analysis where besides possible deviations in the absolute values of the couplings from their SM values also possible deviations in the tensor structure of the couplings are taken into account. This implies that the exploration of the couplings and of the spin and CP properties have to be treated together within a coherent framework.

In the following we use effective Lagrangians as an approach towards such a coherent framework. An effective Lagrangian can be understood to arise from integrating out heavy degrees of freedom, such that the different terms in the Lagrangian are obtained from a systematic expansion in inverse power of a heavy scale. The effective Lagrangian provides in this way a parameterization of possible deviations from the SM predictions. In the tools providing the theoretical predictions for the relevant observables that are confronted with the experimental data those parameterizations of possible deviations from the SM can then be used to supplement the most accurate theoretical predictions within the SM, including the known higher-order corrections.

It should be noted, however, that such an effective Lagrangian approach does not cover possible effects of light BSM particles in loops. In order to investigate the latter type of effects it seems preferable to resort to specific models. Such a model-specific approach for exploring the coupling structure of the recently observed state is complementary to the model-independent approach based on effective Lagrangians, on which we will focus below.

The description of BSM physics based on an effective Lagrangian in terms of the SM fields has been pioneered by Buchmüller and Wyler [415], who provided a list of operators of dimensions 5 and 6 in the linear parameterization of the Higgs sector with a Higgs doublet. In the sequel various authors considered subsets of this operator basis or introduced different sets of operators adapted to specific goals. Recently a complete minimal basis of dimension-6 operators has been presented in Ref. [416]. For the analysis of Higgs interactions different authors prefer to use different sets of operator bases [311, 315, 346, 359, 375, 403, 417–422]. The purpose of this section is to propose a suitable set of operators to be used for the future analysis of the Higgs sector based on the most accurate predictions for the relevant observables within the SM which are supplemented by a parameterization of possible deviations from the SM. The effects of the dimension-6 operators on the Higgs decay ratios are implemented in the code EHDECAY [403], a modified version of HDECAY [17], including some radiative corrections beyond the leading order. We consider two versions of effective Lagrangians, namely a linear parameterization involving a Higgs doublet and a parameterization where the EW symmetry is non-linearly realized.

10.4.1 Linear parameterization with a Higgs doublet

In this section we define an effective Lagrangian based on a linear representation of the electroweak gauge symmetry with a Higgs-doublet field. We follow closely the framework introduced in Ref. [415] and further developed in Ref. [416]. We restrict ourselves to dimension-6 operators relevant for Higgs physics. The effective Lagrangian has the general form

$$\mathcal{L}_{\text{eff}} = \mathcal{L}_{\text{SM}}^{(4)} + \frac{1}{\Lambda^2} \sum_k \alpha_k \mathcal{O}_k, \tag{122}$$

where $\mathcal{L}_{\text{SM}}^{(4)}$ is the usual SM Lagrangian, $\mathcal{O}_k \equiv \mathcal{O}_k^{d=6}$ denotes dimension-6 operators and α_k the corresponding Wilson coefficients. Since the effective Lagrangian must be hermitian, in Eq.(122) for each non-hermitian operator $\mathcal{O}_k$ the hermitian conjugate operator $\mathcal{O}_k^\dagger$ appears with the complex conjugate Wilson coefficient α_k^*.

Using $\alpha = 1, 2, 3$, $i = 1, 2$, and $p = 1, 2, 3$ for color, weak isospin, and flavor indices, respectively, the matter fields of the SM are left-handed lepton doublets l^i_p, right-handed charged leptons e_p, left-handed quark doublets $q^{\alpha i}_p$, right-handed quarks u^α_p, d^α_p, and the Higgs doublet Φ^i with hypercharges $Y = -1/2, -1, 1/6, 2/3, -1/3, 1/2$, respectively. Right-handed neutrinos are not included. The charge-conjugate Higgs field is given by $\widetilde{\Phi}^i = \varepsilon^{ij}(\Phi^j)^*$ with ε^{ij} antisymmetric and $\varepsilon^{12} = 1$.

The SM Lagrangian reads

$$
\begin{aligned}
\mathcal{L}^{(4)}_{\text{SM}} = \; & -\frac{1}{4}G^A_{\mu\nu}G^{A\mu\nu} - \frac{1}{4}W^I_{\mu\nu}W^{I\mu\nu} - \frac{1}{4}B_{\mu\nu}B^{\mu\nu} \\
& + (D_\mu\Phi)^\dagger(D^\mu\Phi) + m^2\Phi^\dagger\Phi - \frac{1}{2}\lambda(\Phi^\dagger\Phi)^2 \\
& + \mathrm{i}\bar{l}\slashed{D}l + \mathrm{i}\bar{e}\slashed{D}e + \mathrm{i}\bar{q}\slashed{D}q + \mathrm{i}\bar{u}\slashed{D}u + \mathrm{i}\bar{d}\slashed{D}d \\
& - (\bar{l}\,\Gamma_e e\Phi + \bar{q}\,\Gamma_u u\widetilde{\Phi} + \bar{d}\,\Gamma_d d\Phi + \text{h.c.}),
\end{aligned}
\tag{123}
$$

where flavor, color, and weak-isospin indices have been suppressed in the matter parts. The field-strength tensors are given by

$$
\begin{aligned}
G^A_{\mu\nu} &= \partial_\mu G^A_\nu - \partial_\nu G^A_\mu - g_s f^{ABC}G^B_\mu G^C_\nu, \quad A = 1,\dots,8, \\
W^I_{\mu\nu} &= \partial_\mu W^I_\nu - \partial_\nu W^I_\mu - g\varepsilon^{IJK}W^J_\mu W^K_\nu, \quad I = 1,2,3, \qquad B_{\mu\nu} = \partial_\mu B_\nu - \partial_\nu B_\mu \,, \quad (124)
\end{aligned}
$$

in terms of the gauge fields G^A_μ, W^I_μ, B_μ of the gauge group $SU(3) \times SU(2) \times U(1)$ and the corresponding gauge couplings g_s, g, g'. The covariant derivative acting on $SU(2)$ doublets reads

$$
D_\mu = \partial_\mu + \mathrm{i}g_s\frac{\lambda^A}{2}G^A_\mu + \mathrm{i}g\frac{\tau^I}{2}W^I_\mu + \mathrm{i}g'Y B_\mu
\tag{125}
$$

with the Gell-Mann matrices λ^A acting on color indices, the Pauli matrices τ^I acting on $SU(2)$ indices and the hypercharge operator Y. The terms with λ^A and τ^I are absent for color and $SU(2)$ singlets, respectively. The quantities Γ_f, $f = e, u, d$ are matrices in flavor space.

Furthermore, we define dual tensors by

$$
\widetilde{X}_{\mu\nu} = \frac{1}{2}\varepsilon_{\mu\nu\rho\sigma}X^{\rho\sigma}, \quad X = G^A, W^I, B \quad \text{and} \quad \varepsilon_{0123} = +1,
\tag{126}
$$

and introduce hermitian derivatives

$$
\Phi^\dagger\mathrm{i}\overleftrightarrow{D}_\mu\Phi = \mathrm{i}(\Phi^\dagger D_\mu\Phi - (D_\mu\Phi)^\dagger\Phi), \qquad \Phi^\dagger\mathrm{i}\overleftrightarrow{D}^I_\mu\Phi = \mathrm{i}(\Phi^\dagger\tau^I D_\mu\Phi - (D_\mu\Phi)^\dagger\tau^I\Phi)\,,
\tag{127}
$$

and $\sigma^{\mu\nu} = \mathrm{i}(\gamma^\mu\gamma^\nu - \gamma^\nu\gamma^\mu)/2$.

For the dimension-6 operators we choose the minimal complete basis[47] defined in Ref. [416], but restrict ourselves here to operators that involve Higgs or gauge-boson fields, see Table 52.[48] In addition to the operators in Table 52 for each non-hermitian operator its hermitian conjugate must be included. The Wilson coefficients of these operators are in general complex, whereas those of the hermitian operators are real. In order to avoid flavor-changing neutral currents, the flavor matrices appearing in dimension-6 operators involving left-handed doublets and right-handed singlets ($\psi^2 X\Phi$ terms) have been fixed to the same matrices Γ_f that are present in the Yukawa couplings, i.e. we assume minimal flavor violation.

---

[47] A minimal complete basis can be constructed by writing down all dimension-6 operators that can be built from the SM fields and using the equations of motion to eliminate all redundant operators.

[48] In a complete analysis all 59 independent operators of Ref. [416], including 25 four-fermion operators, have to be considered in addition to the 34 operators of Table 52.

Table 52: Dimension-6 operators involving Higgs doublet fields or gauge-boson fields. For all $\psi^2\Phi^3$, $\psi^2 X\Phi$ operators and for $\mathcal{O}_{\Phi\mathrm{ud}}$ the hermitian conjugates must be included as well.

Φ^6 and $\Phi^4 D^2$	$\psi^2\Phi^3$	X^3
$\mathcal{O}_\Phi = (\Phi^\dagger\Phi)^3$	$\mathcal{O}_{\mathrm{e}\Phi} = (\Phi^\dagger\Phi)(\bar{l}\,\Gamma_e e\Phi)$	$\mathcal{O}_G = f^{ABC}G_\mu^{A\nu}G_\nu^{B\rho}G_\rho^{C\mu}$
$\mathcal{O}_{\Phi\Box} = (\Phi^\dagger\Phi)\Box(\Phi^\dagger\Phi)$	$\mathcal{O}_{\mathrm{u}\Phi} = (\Phi^\dagger\Phi)(\bar{q}\,\Gamma_u u\widetilde{\Phi})$	$\mathcal{O}_{\widetilde{G}} = f^{ABC}\widetilde{G}_\mu^{A\nu}G_\nu^{B\rho}G_\rho^{C\mu}$
$\mathcal{O}_{\Phi D} = (\Phi^\dagger D^\mu\Phi)^*(\Phi^\dagger D_\mu\Phi)$	$\mathcal{O}_{\mathrm{d}\Phi} = (\Phi^\dagger\Phi)(\bar{q}\,\Gamma_d d\Phi)$	$\mathcal{O}_W = \varepsilon^{IJK}W_\mu^{I\nu}W_\nu^{J\rho}W_\rho^{K\mu}$
		$\mathcal{O}_{\widetilde{W}} = \varepsilon^{IJK}\widetilde{W}_\mu^{I\nu}W_\nu^{J\rho}W_\rho^{K\mu}$

$X^2\Phi^2$	$\psi^2 X\Phi$	$\psi^2\Phi^2 D$
$\mathcal{O}_{\Phi G} = (\Phi^\dagger\Phi)G_{\mu\nu}^A G^{A\mu\nu}$	$\mathcal{O}_{\mathrm{u}G} = (\bar{q}\sigma^{\mu\nu}\tfrac{\lambda^A}{2}\Gamma_u u\widetilde{\Phi})G_{\mu\nu}^A$	$\mathcal{O}_{\Phi l}^{(1)} = (\Phi^\dagger i\overset{\leftrightarrow}{D}_\mu\Phi)(\bar{l}\gamma^\mu l)$
$\mathcal{O}_{\Phi\widetilde{G}} = (\Phi^\dagger\Phi)\widetilde{G}_{\mu\nu}^A G^{A\mu\nu}$	$\mathcal{O}_{\mathrm{d}G} = (\bar{q}\sigma^{\mu\nu}\tfrac{\lambda^A}{2}\Gamma_d d\Phi)G_{\mu\nu}^A$	$\mathcal{O}_{\Phi l}^{(3)} = (\Phi^\dagger i\overset{\leftrightarrow}{D}_\mu^I\Phi)(\bar{l}\gamma^\mu\tau^I l)$
$\mathcal{O}_{\Phi W} = (\Phi^\dagger\Phi)W_{\mu\nu}^I W^{I\mu\nu}$	$\mathcal{O}_{\mathrm{e}W} = (\bar{l}\sigma^{\mu\nu}\Gamma_e e\tau^I\Phi)W_{\mu\nu}^I$	$\mathcal{O}_{\Phi e} = (\Phi^\dagger i\overset{\leftrightarrow}{D}_\mu\Phi)(\bar{e}\gamma^\mu e)$
$\mathcal{O}_{\Phi\widetilde{W}} = (\Phi^\dagger\Phi)\widetilde{W}_{\mu\nu}^I W^{I\mu\nu}$	$\mathcal{O}_{\mathrm{u}W} = (\bar{q}\sigma^{\mu\nu}\Gamma_u u\tau^I\widetilde{\Phi})W_{\mu\nu}^I$	$\mathcal{O}_{\Phi q}^{(1)} = (\Phi^\dagger i\overset{\leftrightarrow}{D}_\mu\Phi)(\bar{q}\gamma^\mu q)$
$\mathcal{O}_{\Phi B} = (\Phi^\dagger\Phi)B_{\mu\nu}B^{\mu\nu}$	$\mathcal{O}_{\mathrm{d}W} = (\bar{q}\sigma^{\mu\nu}\Gamma_d d\tau^I\Phi)W_{\mu\nu}^I$	$\mathcal{O}_{\Phi q}^{(3)} = (\Phi^\dagger i\overset{\leftrightarrow}{D}_\mu^I\Phi)(\bar{q}\gamma^\mu\tau^I q)$
$\mathcal{O}_{\Phi\widetilde{B}} = (\Phi^\dagger\Phi)\widetilde{B}_{\mu\nu}B^{\mu\nu}$	$\mathcal{O}_{\mathrm{e}B} = (\bar{l}\sigma^{\mu\nu}\Gamma_e e\Phi)B_{\mu\nu}$	$\mathcal{O}_{\Phi u} = (\Phi^\dagger i\overset{\leftrightarrow}{D}_\mu\Phi)(\bar{u}\gamma^\mu u)$
$\mathcal{O}_{\Phi WB} = (\Phi^\dagger\tau^I\Phi)W_{\mu\nu}^I B^{\mu\nu}$	$\mathcal{O}_{\mathrm{u}B} = (\bar{q}\sigma^{\mu\nu}\Gamma_u u\widetilde{\Phi})B_{\mu\nu}$	$\mathcal{O}_{\Phi d} = (\Phi^\dagger i\overset{\leftrightarrow}{D}_\mu\Phi)(\bar{d}\gamma^\mu d)$
$\mathcal{O}_{\Phi\widetilde{W}B} = (\Phi^\dagger\tau^I\Phi)\widetilde{W}_{\mu\nu}^I B^{\mu\nu}$	$\mathcal{O}_{\mathrm{d}B} = (\bar{q}\sigma^{\mu\nu}\Gamma_d d\Phi)B_{\mu\nu}$	$\mathcal{O}_{\Phi\mathrm{ud}} = i(\widetilde{\Phi}^\dagger D_\mu\Phi)(\bar{u}\gamma^\mu\Gamma_{\mathrm{ud}}d)$

Moreover, in all dimension-6 operators involving neutral currents (first seven $\psi^2\Phi^2 D$ terms) the flavor matrices have been chosen to be equal to the unit matrix. In the operator $\mathcal{O}_{\Phi\mathrm{ud}}$ leading to right-handed flavor-changing charged currents we kept a general flavor matrix Γ_{ud}. The generalization to more general flavor schemes is straightforward.

In weakly interacting theories the dimension-6 operators of Table 52 involving field strengths can only result from loops, while the others also result from tree diagrams [423]. The operators involving dual field strengths tensors or complex Wilson coefficients violate CP.

10.4.1.2 Alternative basis

In the previous basis, the $O(p^2)$ EW oblique corrections, i.e., the S and T parameters, are captured in terms of $\psi^2\Phi^2 D$ operators. An alternative basis, see Table 53, is often used [315, 403] where these oblique corrections are now described by purely bosonic operators:

$$\mathcal{L}_{\mathrm{eff}} = \mathcal{L}_{\mathrm{SM}}^{(4)} + \frac{1}{\Lambda^2}\sum_k \alpha_k' \mathcal{O}_k', \tag{128}$$

The two basis representations are related with the following relations obtained by integration by parts:

$$\frac{g}{2}\mathcal{O}_{\mathrm{DW}}' - \frac{g'}{2}\mathcal{O}_{\mathrm{DB}}' + g'\mathcal{O}_{D\Phi B}' - g\mathcal{O}_{D\Phi W}' - \frac{g'^2}{4}\mathcal{O}_{\Phi B}' = -\frac{g^2}{4}\mathcal{O}_{\Phi W}, \tag{129}$$

$$\frac{g'}{2}\mathcal{O}_{\mathrm{DB}}' - g'\mathcal{O}_{D\Phi B}' + \frac{g'^2}{4}\mathcal{O}_{\Phi B}' = -\frac{gg'}{4}\mathcal{O}_{\Phi WB}. \tag{130}$$

Actually, the two linear combinations of the $\psi^2\Phi^2 D$ operators that correspond to the S and T oblique parameters have to be omitted in the counting of the number of independent operators thanks to the two

Table 53: Alternative basis of dimension-6 operators involving Higgs doublet fields or gauge-boson fields.

$\Phi^6 \quad \text{and} \quad \Phi^4 D^2$	$\psi^2\Phi^3$	X^3
$\mathcal{O}'_6 = (\Phi^\dagger\Phi)^3$	$\mathcal{O}'_{e\Phi} = (\Phi^\dagger\Phi)(\bar{l}\,\Gamma_e e\Phi)$	$\mathcal{O}'_G = f^{ABC}G_\mu^{A\nu}G_\nu^{B\rho}G_\rho^{C\mu}$
$\mathcal{O}'_\Phi = \partial_\mu(\Phi^\dagger\Phi)\partial^\mu(\Phi^\dagger\Phi)$	$\mathcal{O}'_{u\Phi} = (\Phi^\dagger\Phi)(\bar{q}\,\Gamma_u u\widetilde{\Phi})$	$\mathcal{O}'_{\widetilde{G}} = f^{ABC}\widetilde{G}_\mu^{A\nu}G_\nu^{B\rho}G_\rho^{C\mu}$
$\mathcal{O}'_T = (\Phi^\dagger\overleftrightarrow{D}_\mu\Phi)(\Phi^\dagger\overleftrightarrow{D}^\mu\Phi)$	$\mathcal{O}'_{d\Phi} = (\Phi^\dagger\Phi)(\bar{q}\,\Gamma_d d\Phi)$	$\mathcal{O}'_W = \varepsilon^{IJK}W_\mu^{I\nu}W_\nu^{J\rho}W_\rho^{K\mu}$
		$\mathcal{O}'_{\widetilde{W}} = \varepsilon^{IJK}\widetilde{W}_\mu^{I\nu}W_\nu^{J\rho}W_\rho^{K\mu}$

$X^2\Phi^2$	$\psi^2 X\Phi$	$\psi^2\Phi^2 D$
$\mathcal{O}'_{DW} = \left(\Phi^\dagger\tau^I\mathrm{i}\overleftrightarrow{D^\mu}\Phi\right)(D^\nu W_{\mu\nu})^I$	$\mathcal{O}'_{uG} = (\bar{q}\sigma^{\mu\nu}\frac{\lambda^A}{2}\Gamma_u u\widetilde{\Phi})G_{\mu\nu}^A$	$\mathcal{O}'^{(1)}_{\Phi l} = (\Phi^\dagger\mathrm{i}\overleftrightarrow{D}_\mu\Phi)(\bar{l}\gamma^\mu l)$
$\mathcal{O}'_{DB} = \left(\Phi^\dagger\mathrm{i}\overleftrightarrow{D^\mu}\Phi\right)(\partial^\nu B_{\mu\nu})$	$\mathcal{O}'_{dG} = (\bar{q}\sigma^{\mu\nu}\frac{\lambda^A}{2}\Gamma_d d\Phi)G_{\mu\nu}^A$	$\mathcal{O}'^{(3)}_{\Phi l} = (\Phi^\dagger\mathrm{i}\overleftrightarrow{D}_\mu^I\Phi)(\bar{l}\gamma^\mu\tau^I l)$
$\mathcal{O}'_{D\Phi W} = \mathrm{i}(D^\mu\Phi)^\dagger\tau^I(D^\nu\Phi)W_{\mu\nu}^I$	$\mathcal{O}'_{eW} = (\bar{l}\sigma^{\mu\nu}\Gamma_e e\tau^I\Phi)W_{\mu\nu}^I$	$\mathcal{O}'_{\Phi e} = (\Phi^\dagger\mathrm{i}\overleftrightarrow{D}_\mu\Phi)(\bar{e}\gamma^\mu e)$
$\mathcal{O}'_{D\Phi\widetilde{W}} = \mathrm{i}(D^\mu\Phi)^\dagger\tau^I(D^\nu\Phi)\widetilde{W}_{\mu\nu}^I$	$\mathcal{O}'_{uW} = (\bar{q}\sigma^{\mu\nu}\Gamma_u u\tau^I\widetilde{\Phi})W_{\mu\nu}^I$	$\mathcal{O}'^{(1)}_{\Phi q} = (\Phi^\dagger\mathrm{i}\overleftrightarrow{D}_\mu\Phi)(\bar{q}\gamma^\mu q)$
$\mathcal{O}'_{D\Phi B} = \mathrm{i}(D^\mu\Phi)^\dagger(D^\nu\Phi)B_{\mu\nu}$	$\mathcal{O}'_{dW} = (\bar{q}\sigma^{\mu\nu}\Gamma_d d\tau^I\Phi)W_{\mu\nu}^I$	$\mathcal{O}'^{(3)}_{\Phi q} = (\Phi^\dagger\mathrm{i}\overleftrightarrow{D}_\mu^I\Phi)(\bar{q}\gamma^\mu\tau^I q)$
$\mathcal{O}'_{D\Phi\widetilde{B}} = \mathrm{i}(D^\mu\Phi)^\dagger(D^\nu\Phi)\widetilde{B}_{\mu\nu}$	$\mathcal{O}'_{eB} = (\bar{l}\sigma^{\mu\nu}\Gamma_e e\Phi)B_{\mu\nu}$	$\mathcal{O}'_{\Phi u} = (\Phi^\dagger\mathrm{i}\overleftrightarrow{D}_\mu\Phi)(\bar{u}\gamma^\mu u)$
$\mathcal{O}'_{\Phi B} = (\Phi^\dagger\Phi)B_{\mu\nu}B^{\mu\nu}$	$\mathcal{O}'_{uB} = (\bar{q}\sigma^{\mu\nu}\Gamma_u u\widetilde{\Phi})B_{\mu\nu}$	$\mathcal{O}'_{\Phi d} = (\Phi^\dagger\mathrm{i}\overleftrightarrow{D}_\mu\Phi)(\bar{d}\gamma^\mu d)$
$\mathcal{O}'_{\Phi\widetilde{B}} = (\Phi^\dagger\Phi)B_{\mu\nu}\widetilde{B}^{\mu\nu}$	$\mathcal{O}'_{dB} = (\bar{q}\sigma^{\mu\nu}\Gamma_d d\Phi)B_{\mu\nu}$	$\mathcal{O}'_{\Phi ud} = \mathrm{i}(\widetilde{\Phi}^\dagger D_\mu\Phi)(\bar{u}\gamma^\mu\Gamma_{ud}d)$
$\mathcal{O}'_{\Phi G} = \Phi^\dagger\Phi G_{\mu\nu}^A G^{A\mu\nu}$		
$\mathcal{O}'_{\Phi\widetilde{G}} = \Phi^\dagger\Phi G_{\mu\nu}^A \widetilde{G}^{A\mu\nu}$		

relations that hold up to total derivative terms:

$$\mathcal{O}'^{(1)}_{\Phi l} - \frac{1}{3}\mathcal{O}'^{(1)}_{\Phi q} + 2\mathcal{O}'_{\Phi e} - \frac{4}{3}\mathcal{O}'_{\Phi u} + \frac{2}{3}\mathcal{O}'_{\Phi d} = -\mathcal{O}'_T + \frac{2}{g'}\mathcal{O}'_{DB}\,, \tag{131}$$

$$2(\mathcal{O}'_{u\Phi} + \mathcal{O}'_{d\Phi} + \mathcal{O}'_{e\Phi} + \text{h.c.}) + \mathcal{O}'^{(3)}_{\Phi q} + \mathcal{O}'^{(3)}_{\Phi l} = 3\mathcal{O}'_\Phi - 4\lambda\mathcal{O}'_6 + 4m^2(\Phi^\dagger\Phi)^2 - \frac{2}{g}\mathcal{O}'_{DW}\,. \tag{132}$$

A convenient choice of the two redundant operators to drop are $\mathcal{O}'^{(1)}_{\Phi l}$ and $\mathcal{O}'^{(3)}_{\Phi l}$.

Another advantage of the new operator basis is that it offers a simple power-counting to estimate the size the Wilson coefficients under the assumptions that the New Physics sector is characterized by a single scale and a single coupling and that the photon does not couple to electrically neutral particles at tree-level: starting from the SM Lagrangian, any additional power of Φ is suppressed by a factor $g_*/M \equiv 1/f$, where g_* denotes the coupling between the Higgs boson and the New Physics states and M is the overall mass scale of the New Physics sector; any additional derivative instead costs a factor $1/M$. According to the power counting of Ref. [315], one naively estimates ($\psi = \mathrm{u},\mathrm{d},\mathrm{l},\mathrm{q},L$)

$$\alpha'_H, \alpha'_T, \frac{\alpha'_6}{\lambda}, \alpha'_{\psi\Phi} \sim O\left(\frac{\Lambda^2}{f^2}\right), \quad \frac{\alpha'_{DW}}{g}, \frac{\alpha'_{DB}}{g'} \sim O\left(\frac{\Lambda^2}{M^2}\right), \tag{133}$$

$$\frac{\alpha'_{D\Phi W}}{g}, \frac{\alpha'_{D\Phi B}}{g'}, \frac{\alpha'_{\Phi B}}{g'^2}, \frac{\alpha'_{\Phi G}}{g_s^2} \sim O\left(\frac{\Lambda^2}{16\pi^2 f^2}\right), \quad \frac{\alpha'_{\psi W}}{g}, \frac{\alpha'_{\psi B}}{g'}, \frac{\alpha'_{\psi G}}{g_s} \sim O\left(\frac{\Lambda^2}{16\pi^2 f^2}\right), \tag{134}$$

$$\alpha'_{\Phi e}, \alpha'_{\Phi u}, \alpha'_{\Phi d}, \alpha'^{(1)}_{\Phi q}, \alpha'^{(1)}_{\Phi l}, \alpha'^{(3)}_{\Phi q}, \alpha'^{(3)}_{\Phi l} \sim O\left(\frac{\lambda_\psi^2}{g_*^2}\frac{\Lambda^2}{f^2}\right), \quad \alpha'_{\Phi ud} \sim O\left(\frac{\lambda u \lambda d}{g_*^2}\frac{\Lambda^2}{f^2}\right), \tag{135}$$

where λ_ψ denotes the coupling of a generic SM fermion ψ to the New Physics sector. Notice the additional factors $(g_*^2/16\pi^2)$ in $\alpha'_{D\Phi B}, \alpha'_{D\Phi W}, \alpha'_{\Phi B}$ and $\alpha'_{\Phi G}$ as the corresponding operators contribute to the coupling of on-shell photons and gluons to neutral particles and correct the W gyromagnetic ratio, which in most models of New Physics are effects occurring only at the loop-level.

10.4.1.3 Translation to the physical basis

In order to perform calculations it is useful to express the effective Lagrangian introduced above in terms of properly normalized physical fields and physical parameters. In the SM the Higgs doublet field can be parametrized as[49]

$$\Phi = \begin{pmatrix} \phi^+_{\rm SM} \\ \frac{1}{\sqrt{2}}(v_{\rm SM} + H_{\rm SM} + {\rm i}\phi^0_{\rm SM}) \end{pmatrix}, \qquad \widetilde{\Phi} = \begin{pmatrix} \frac{1}{\sqrt{2}}(v_{\rm SM} + H_{\rm SM} - {\rm i}\phi^0_{\rm SM}) \\ -\phi^-_{\rm SM} \end{pmatrix}, \qquad \phi^-_{\rm SM} = (\phi^+_{\rm SM})^*, \tag{136}$$

where H is the Higgs field and $\phi^\pm$ and ϕ^0 the would-be Goldstone-boson fields. In the SM without dimension-6 operators the vacuum expectation value $v_{\rm SM}$ of the Higgs field is in LO obtained as

$$v_{\rm SM} = \frac{\sqrt{2}m}{\sqrt{\lambda}}, \tag{137}$$

and the Higgs-boson mass reads

$$M_{\rm H,SM} = \sqrt{\lambda}v_{\rm SM}. \tag{138}$$

The physical gauge-boson fields are given by

$$\begin{aligned} W^\pm_{{\rm SM}\mu} &= \frac{1}{\sqrt{2}}({\rm W}^1_\mu \mp {\rm i}{\rm W}^2_\mu), \\ Z_{{\rm SM}\mu} &= c_{\rm w,SM}{\rm W}^3_\mu - s_{\rm w,SM}{\rm B}_\mu, \qquad A_{{\rm SM}\mu} = s_{\rm w,SM}{\rm W}^3_\mu + c_{\rm w,SM}{\rm B}_\mu \end{aligned} \tag{139}$$

with

$$c_{\rm w,SM} = \frac{g}{\sqrt{g^2 + g'^2}}, \qquad s_{\rm w,SM} = \frac{g'}{\sqrt{g^2 + g'^2}}. \tag{140}$$

The masses of the gauge bosons are obtained as

$$M_{\rm W,SM} = \frac{1}{2}gv_{\rm SM}, \qquad M_{\rm Z,SM} = \frac{1}{2}\sqrt{g^2 + g'^2}v_{\rm SM}, \tag{141}$$

and the electromagnetic coupling reads

$$e_{\rm SM} = \frac{gg'}{\sqrt{g^2 + g'^2}}. \tag{142}$$

The physical fermion fields $f_{{\rm SM}p}$, corresponding to the mass eigenstates, are obtained by diagonalizing the Yukawa-coupling matrices $\Gamma_{\rm f}$,

$$f_{{\rm SM}p} = U^{\rm f}_{pq}f_q, \quad f = l_i, e, q_i, u, d. \tag{143}$$

resulting in diagonal fermion-mass matrices

$$m_{\rm f,SM} = \frac{1}{\sqrt{2}}U^{\hat{\rm f}}\Gamma_{\rm f}U^{{\rm f},\dagger}v_{\rm SM}, \tag{144}$$

---

[49]We use the index "SM" to denote fields and parameters in the SM without dimension-6 operators.

where $\hat{f} = q_1, q_2, e_1, e_2$ for $f = u, d, e, \nu_l$, respectively. The matrices U^f give rise to the appearance of the quark-mixing matrix

$$V_{pq} = (U^{q_1} U^{q_2\dagger})_{pq} \tag{145}$$

in charged-current interactions. The electric charges of fermions result from the relation

$$Q = I_3 + Y, \tag{146}$$

where I_3 is the third component of the weak isospin.

The presence of the dimension-6 operators modifies the quadratic part of the Lagrangian. Consequently, the fields have to be redefined such that the free part has the canonical normalization and the SM parameters get extra contributions. Moreover the vacuum expectation value of the Higgs field is shifted to

$$v^2 = v_{\text{SM}}^2 \left(1 + \frac{3}{2} \alpha_\Phi \frac{v_{\text{SM}}^2}{\lambda \Lambda^2} \right) = \frac{2m^2}{\lambda} \left(1 + \frac{3}{2} \alpha_\Phi \frac{v_{\text{SM}}^2}{\lambda \Lambda^2} \right). \tag{147}$$

Canonically normalized kinetic terms for the bosonic fields can be restored in the presence of dimension-6 operators upon redefining the fields as follows:

$$
\begin{aligned}
H_{\text{SM}} &= \text{H} \left[1 - \frac{v^2}{4\Lambda^2} (\alpha_{\Phi D} - 4\alpha_{\Phi \Box}) \right] + \frac{3}{4} v\alpha_\Phi \frac{v^2}{\lambda\Lambda^2}, \\
\phi_{\text{SM}}^0 &= \phi^0 \left[1 - \frac{v^2}{4\Lambda^2} \alpha_{\Phi D} \right], \qquad \phi_{\text{SM}}^\pm = \phi^\pm, \\
W_{\text{SM}\mu}^\pm &= \text{W}_\mu \left[1 + \frac{v^2}{\Lambda^2} \alpha_{\Phi W} \right], \qquad Z_{\text{SM}\mu} = \text{Z}_\mu \left[1 + \frac{v^2}{\Lambda^2} \alpha_{ZZ} \right], \\
A_{\text{SM}\mu} &= \text{A}_\mu \left[1 + \frac{v^2}{\Lambda^2} \alpha_{AA} \right] + \text{Z}_\mu \left[1 + \frac{v^2}{\Lambda^2} \alpha_{AZ} \right], \qquad G_{\text{SM}\mu}^A = G_\mu^A \left[1 + \frac{v^2}{\Lambda^2} \alpha_{\Phi G} \right], \quad (148)
\end{aligned}
$$

where

$$
\begin{aligned}
\alpha_{ZZ} &= c_{\text{w,SM}}^2 \alpha_{\Phi W} + s_{\text{w,SM}}^2 \alpha_{\Phi B} + c_{\text{w,SM}} s_{\text{w,SM}} \alpha_{\Phi WB}, \\
\alpha_{AA} &= s_{\text{w,SM}}^2 \alpha_{\Phi W} + c_{\text{w,SM}}^2 \alpha_{\Phi B} - c_{\text{w,SM}} s_{\text{w,SM}} \alpha_{\Phi WB}, \\
\alpha_{AZ} &= 2c_{\text{w,SM}} s_{\text{w,SM}} (\alpha_{\Phi W} - \alpha_{\Phi B}) + (s_{\text{w,SM}}^2 - c_{\text{w,SM}}^2) \alpha_{\Phi WB},
\end{aligned}
\tag{149}
$$

and analogous definitions hold for $\alpha_{Z\widetilde{Z}}$, $\alpha_{A\widetilde{Z}}$, and $\alpha_{A\widetilde{A}}$. Since we have chosen the flavor-mixing matrix in the $\psi^2 \Phi^3$ terms to be identical to the one in the Yukawa couplings, the physical fermionic fields stay the same as in the SM. We denote them by f in the following (the individual physical fermion fields u, d, and l should not to be confused with the same symbols used in (123) for the fields in the symmetric basis).

In terms of the redefined fields the quadratic part of the Lagrangian reads after adding a 't Hooft–Feynman gauge-fixing term and dropping total derivatives and a constant

$$
\begin{aligned}
\mathcal{L}_{\text{SM}}^{(4)} &= -\frac{1}{2}(\partial_\mu G_\nu^A)(\partial^\mu G^{A\nu}) - (\partial_\mu \text{W}_\nu^+)(\partial^\mu \text{W}^{-\nu}) - \frac{1}{2}(\partial_\mu \text{Z}_\nu)(\partial^\mu \text{Z}^\nu) - \frac{1}{2}(\partial_\mu \text{A}_\nu)(\partial^\mu \text{A}^\nu) \\
&\quad + M_\text{W}^2 \text{W}_\mu^+ \text{W}^{-\mu} + \frac{1}{2} M_\text{Z}^2 \text{Z}_\mu \text{Z}^\mu + \frac{1}{2}(\partial_\mu \text{H})(\partial^\mu \text{H}) - \frac{1}{2} M_\text{H}^2 \text{H}^2 \\
&\quad + (\partial_\mu \phi^+)(\partial^\mu \phi^-) - M_\text{W}^2 \phi^+ \phi^- + \frac{1}{2}(\partial_\mu \phi^0)(\partial^\mu \phi^0) - \frac{1}{2} M_\text{Z}^2 (\phi^0)^2 \\
&\quad + \sum_{f=l,u,d} \bar{\text{f}}(i\slashed{\partial} - m_\text{f})\text{f} + \bar{\nu}_\text{e} i\slashed{\partial}\nu_\text{e}
\end{aligned}
\tag{150}
$$

with the physical mass parameters

$$
\begin{aligned}
M_{\mathrm{W}}^2 &= \frac{1}{4}g^2 v^2 \left[1 + 2\frac{v^2}{\Lambda^2}\alpha_{\Phi\mathrm{W}}\right], \\
M_{\mathrm{Z}}^2 &= \frac{1}{4}(g^2 + g'^2)v^2 \left[1 + \frac{v^2}{2\Lambda^2}\left(4\alpha_{\mathrm{ZZ}} + \alpha_{\Phi D}\right)\right], \\
M_{\mathrm{H}}^2 &= \lambda v^2 \left[1 + \frac{v^2}{2\Lambda^2}\left(4\alpha_{\Phi\Box} - \frac{6}{\lambda}\alpha_\Phi - \alpha_{\Phi D}\right)\right], \\
m_{\mathrm{f}} &= \frac{1}{\sqrt{2}}U^{\hat{\mathrm{f}}}\Gamma_{\mathrm{f}}U^{\mathrm{f},\dagger}v\left[1 - \frac{1}{2}\frac{v^2}{\Lambda^2}\alpha_{\mathrm{f}\phi}\right].
\end{aligned}
\tag{151}
$$

In (150) we have used the usual 't Hooft–Feynman gauge-fixing term

$$
\mathcal{L}_{\mathrm{fix}} = -C_+ C_- - \frac{1}{2}(C_{\mathrm{Z}})^2 - \frac{1}{2}(C_{\mathrm{A}})^2 - \frac{1}{2}C_G^A C_G^A
\tag{152}
$$

with

$$
C_G^A = \partial_\mu G^{A\mu}, \qquad C_{\mathrm{A}} = \partial_\mu \mathrm{A}^\mu, \qquad C_{\mathrm{Z}} = \partial_\mu \mathrm{Z}^\mu + M_{\mathrm{Z}}\phi^0, \qquad C_\pm = \partial_\mu \mathrm{W}^{\pm\mu} \pm \mathrm{i}M_{\mathrm{W}}\phi^\pm
\tag{153}
$$

in terms of the physical fields and parameters, which gives rise to the same propagators as in the SM.

In the following, the abbreviations c_{w} and s_{w} are defined via the physical masses

$$
c_{\mathrm{w}} = \frac{M_{\mathrm{W}}}{M_{\mathrm{Z}}}, \qquad s_{\mathrm{w}} = \sqrt{1 - c_{\mathrm{w}}^2}.
\tag{154}
$$
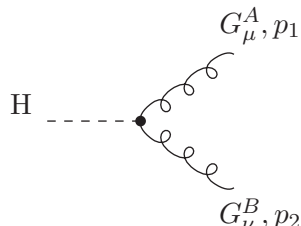
The parameters of the SM Lagrangian g, g', λ, m^2, and Γ_{f} keep their meaning in the presence of dimension-6 operators.

10.4.2 Higgs vertices

Here we list the most important Feynman rules for vertices involving exactly one physical Higgs boson. These are given in terms of the above-defined physical fields and parameters. In the coefficients of dimension-6 couplings we replaced v^2 by the Fermi constant via $v^2 = 1/(\sqrt{2}G_F)$.
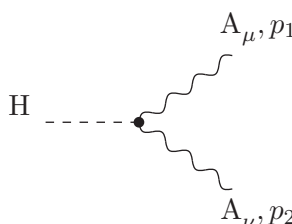
The triple vertices involving one Higgs boson read:

Hgg coupling:
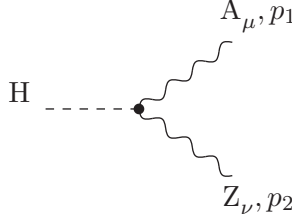
$$
= \mathrm{i}\frac{2g}{M_{\mathrm{W}}}\frac{1}{\sqrt{2}G_F\Lambda^2}\left[\alpha_{GG}(p_{2\mu}p_{1\nu} - p_1 p_2 g_{\mu\nu}) + \alpha_{G\widetilde{G}}\varepsilon_{\mu\nu\rho\sigma}p_1^\rho p_2^\sigma\right]\delta^{AB},
$$

(155)

HAA coupling:
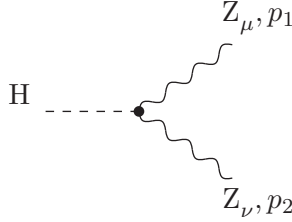
$$
= \mathrm{i}\frac{2g}{M_{\mathrm{W}}}\frac{1}{\sqrt{2}G_F\Lambda^2}\left[\alpha_{\mathrm{AA}}(p_{2\mu}p_{1\nu} - p_1 p_2 g_{\mu\nu}) + \alpha_{\mathrm{A}\widetilde{\mathrm{A}}}\varepsilon_{\mu\nu\rho\sigma}p_1^\rho p_2^\sigma\right], \tag{156}
$$

159
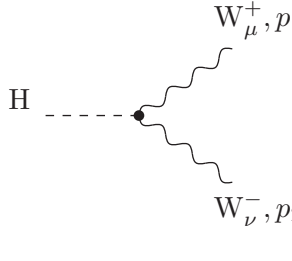
HAZ coupling:

$$= \mathrm{i}\frac{g}{M_{\mathrm{W}}}\frac{1}{\sqrt{2}G_F\Lambda^2}\left[\alpha_{\mathrm{AZ}}(p_{2\mu}p_{1\nu}-p_1p_2 g_{\mu\nu})+\alpha_{\mathrm{A}\widetilde{\mathrm{Z}}}\varepsilon_{\mu\nu\rho\sigma}p_1^\rho p_2^\sigma\right],\qquad(157)$$

HZZ coupling:
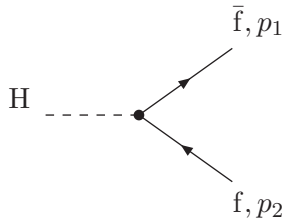
$$= \mathrm{i}g\frac{M_{\mathrm{Z}}}{c_{\mathrm{w}}}g_{\mu\nu}\left[1+\frac{1}{\sqrt{2}G_F\Lambda^2}\left(\alpha_{\Phi\mathrm{W}}+\alpha_{\Phi\square}+\frac{1}{4}\alpha_{\Phi D}\right)\right]$$
$$+\,\mathrm{i}\frac{2g}{M_{\mathrm{W}}}\frac{1}{\sqrt{2}G_F\Lambda^2}\left[\alpha_{\mathrm{ZZ}}(p_{2\mu}p_{1\nu}-p_1p_2 g_{\mu\nu})+\alpha_{\mathrm{Z}\widetilde{\mathrm{Z}}}\varepsilon_{\mu\nu\rho\sigma}p_1^\rho p_2^\sigma\right],\qquad(158)$$

HWW coupling:

$$= \mathrm{i}gM_{\mathrm{W}}g_{\mu\nu}\left[1+\frac{1}{\sqrt{2}G_F\Lambda^2}\left(\alpha_{\Phi\mathrm{W}}+\alpha_{\Phi\square}-\frac{1}{4}\alpha_{\Phi D}\right)\right]$$
$$+\,\mathrm{i}\frac{2g}{M_{\mathrm{W}}}\frac{1}{\sqrt{2}G_F\Lambda^2}\left[\alpha_{\Phi\mathrm{W}}(p_{2\mu}p_{1\nu}-p_1p_2 g_{\mu\nu})+\alpha_{\Phi\widetilde{\mathrm{W}}}\varepsilon_{\mu\nu\rho\sigma}p_1^\rho p_2^\sigma\right],$$
$$(159)$$

Hff coupling:
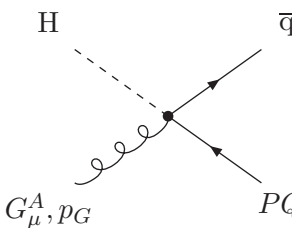
$$= -\mathrm{i}\frac{g}{2}\frac{m_{\mathrm{f}}}{M_{\mathrm{W}}}\left[1+\frac{1}{\sqrt{2}G_F\Lambda^2}\left(\alpha_{\Phi\mathrm{W}}+\alpha_{\Phi\square}-\frac{1}{4}\alpha_{\Phi D}-\alpha_{\mathrm{f}\phi}\right)\right],\qquad(160)$$

where $\mathrm{f}=\mathrm{e},\mathrm{u},\mathrm{d}$.

The quadruple vertices involving one Higgs field, one gauge boson and a fermion–antifermion pair are given by ($\mathrm{q}=\mathrm{u},\mathrm{d}$, $\mathrm{f}=\mathrm{u},\mathrm{d},\nu_{\mathrm{l}},\mathrm{e}$, and $\hat{\mathrm{f}}=\mathrm{q}$ for $\mathrm{f}=\mathrm{u},\mathrm{d}$ and $\hat{\mathrm{f}}=\mathrm{l}$ for $\mathrm{f}=\mathrm{e}$):

Hgq$\overline{\mathrm{q}}$ coupling:

$$= \mathrm{i}g\frac{m_q}{M_{\mathrm{W}}}\mathrm{i}p_{G\nu}\sigma^{\mu\nu}\frac{\lambda^A}{2}\left[\frac{1+\gamma_5}{2}\alpha_{\mathrm{q}G}+\frac{1-\gamma_5}{2}\alpha_{\mathrm{q}G}^*\right],\qquad(161)$$

HAff̄ coupling:
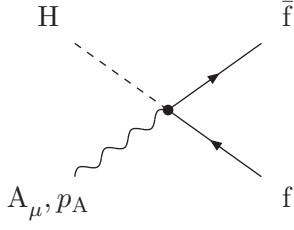
$$
\begin{aligned}
= \mathrm{i}g\frac{m_f}{M_\mathrm{W}}\mathrm{i}p_{A\nu}\sigma^{\mu\nu}\Bigg[& \frac{1+\gamma_5}{2}(\alpha_\mathrm{fB}c_\mathrm{w}+2I_3^f\alpha_\mathrm{fW}s_\mathrm{w}) \\
& +\frac{1-\gamma_5}{2}(\alpha_\mathrm{fB}^*c_\mathrm{w}+2I_3^f\alpha_\mathrm{fW}^*s_\mathrm{w})\Bigg],
\end{aligned}
\tag{162}
$$

HZff̄ coupling:
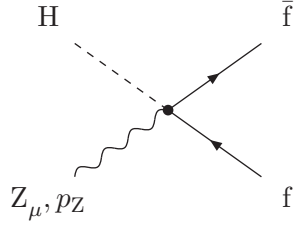
$$
\begin{aligned}
= \mathrm{i}g\frac{m_f}{M_\mathrm{W}}\mathrm{i}p_{Z\nu}\sigma^{\mu\nu}\Bigg[& \frac{1+\gamma_5}{2}(2I_3^\mathrm{f}\alpha_\mathrm{fW}c_\mathrm{w}-\alpha_\mathrm{fB}s_\mathrm{w}) \\
& +\frac{1-\gamma_5}{2}(2I_3^\mathrm{f}\alpha_\mathrm{fW}^*c_\mathrm{w}-\alpha_\mathrm{fB}^*s_\mathrm{w})\Bigg] \\
& +\mathrm{i}2M_\mathrm{Z}\gamma^\mu\left[\frac{1-\gamma_5}{2}\left(\alpha_{\Phi\hat{\mathrm{f}}}^{(1)}-2I_3^\mathrm{f}\alpha_{\Phi\hat{\mathrm{f}}}^{(3)}\right)+\frac{1+\gamma_5}{2}\alpha_{\Phi\mathrm{f}}\right],
\end{aligned}
\tag{163}
$$

HW$^+$dū coupling:
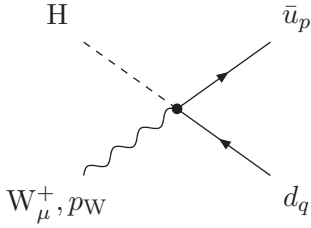
$$
\begin{aligned}
= \mathrm{i}g\frac{\sqrt{2}}{M_\mathrm{W}}\mathrm{i}p_{\mathrm{W}\nu}\sigma^{\mu\nu}V_{pq}\left[\frac{1+\gamma_5}{2}m_\mathrm{d}\alpha_\mathrm{dW}+\frac{1-\gamma_5}{2}m_\mathrm{u}\alpha_\mathrm{uW}^*\right] \\
-\mathrm{i}\sqrt{2}M_\mathrm{W}\gamma^\mu\left[\frac{1-\gamma_5}{2}2\alpha_{\Phi\mathrm{q}}^{(3)}V_{pq}+\frac{1+\gamma_5}{2}(\Gamma_\mathrm{ud})_{pq}\alpha_{\Phi\mathrm{ud}}\right],
\end{aligned}
\tag{164}
$$

HW$^-$ud̄ coupling:
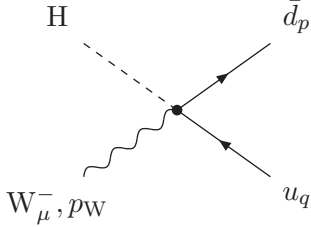
$$
\begin{aligned}
= \mathrm{i}g\frac{\sqrt{2}}{M_\mathrm{W}}\mathrm{i}p_{\mathrm{W}\nu}\sigma^{\mu\nu}V_{pq}^\dagger\left[\frac{1+\gamma_5}{2}m_\mathrm{u}\alpha_\mathrm{uW}+\frac{1-\gamma_5}{2}m_\mathrm{d}\alpha_\mathrm{dW}^*\right] \\
-\mathrm{i}\sqrt{2}M_\mathrm{W}\gamma^\mu\left[\frac{1-\gamma_5}{2}2\alpha_{\Phi\mathrm{q}}^{(3)}V_{pq}^\dagger+\frac{1+\gamma_5}{2}(\Gamma_\mathrm{ud}^\dagger)_{pq}\alpha_{\Phi\mathrm{ud}}^*\right],
\end{aligned}
\tag{165}
$$
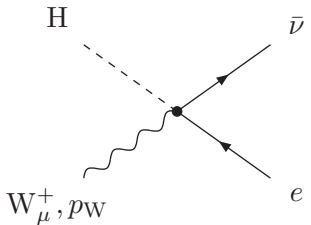
HW$^+$eν̄$_\mathrm{e}$ coupling:

$$
= \mathrm{i}g\frac{\sqrt{2}}{M_\mathrm{W}}\mathrm{i}p_{\mathrm{W}\nu}\sigma^{\mu\nu}\frac{1+\gamma_5}{2}m_\mathrm{e}\alpha_\mathrm{eW}-\mathrm{i}\sqrt{2}M_\mathrm{W}\gamma^\mu\frac{1-\gamma_5}{2}2\alpha_{\Phi l}^{(3)},
\tag{166}
$$

HW$^-$ν$_\mathrm{e}$e$^+$ coupling:
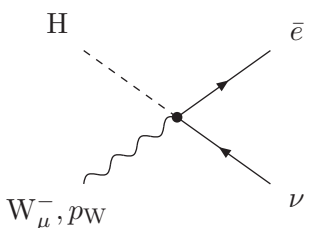
$$
= \mathrm{i}g\frac{\sqrt{2}}{M_\mathrm{W}}\mathrm{i}p_{\mathrm{W}\nu}\sigma^{\mu\nu}\frac{1-\gamma_5}{2}m_\mathrm{e}\alpha_\mathrm{eW}^*-\mathrm{i}\sqrt{2}M_\mathrm{W}\gamma^\mu\frac{1-\gamma_5}{2}2\alpha_{\Phi l}^{(3)}.
\tag{167}
$$

The flavor matrix Γ_{ud} appearing in the above Feynman rules has now to be understood in the mass eigenstate basis for the quarks, and V denotes the usual quark-mixing matrix. For neutrinos the terms involving α_{fW}, α_{fB}, and $\alpha_{\Phi\mathrm{f}}$ in Eqs. (162) and Eq. (163) are absent.

There are additional vertices involving one Higgs field together with three or four vector-boson fields resulting from the $X^2\Phi^2$ operators, and the operators $\psi^2 X\Phi$ give rise to vertices involving a fermion–antifermion pair and a vector-boson pair along with a single Higgs field. Additional vertices involve more than one Higgs-boson field.

The Feynman rules above are given in terms of the weak coupling g. Choosing M_{Z}, M_{W}, and G_F as input, g can be written as

$$g = 2M_{\mathrm{W}}\sqrt{\sqrt{2}G_F}\left(1 - \frac{1}{\sqrt{2}G_F\Lambda^2}\left(\alpha_{\Phi\mathrm{W}} + \alpha_{\phi\mu}^{(3)}\right)\right). \tag{168}$$

Inserting this into the Feynman rules with SM contributions leads to the replacement

$$g\left(1 + \frac{1}{\sqrt{2}G_F\Lambda^2}\left(\alpha_{\Phi\mathrm{W}}\right)\right) \to 2M_{\mathrm{W}}\sqrt{\sqrt{2}G_F}\left(1 - \frac{1}{\sqrt{2}G_F\Lambda^2}\left(\alpha_{\phi\mu}^{(3)}\right)\right). \tag{169}$$

We note that for $\Lambda \approx 5$ TeV we have $1/(\sqrt{2}G_F\Lambda^2) \approx g^2/(4\pi)$, i.e. the contributions of dimension-6 operators are generically of the order of loop effects. For higher scales, loop contributions tend to be more important than dimension-6 operators.

In the basis of Table 52, the scaling of the SM Higgs–vector-boson couplings is parametrized by $\alpha_{\Phi\Box}$, the difference between the HZZ and HWW couplings by $\alpha_{\Phi D}$, and the Higgs-fermion coupling by $\alpha_{\mathrm{f}\phi}$. Additional overall factors depend on the input-parameter scheme. The new coupling structures appearing in the Higgs–gauge-boson couplings are parametrized by $\alpha_{\Phi\mathrm{W}}$, $\alpha_{\Phi\mathrm{B}}$, and $\alpha_{\Phi\mathrm{WB}}$ for the CP-conserving part and by $\alpha_{\Phi\widetilde{\mathrm{W}}}$, $\alpha_{\Phi\widetilde{\mathrm{B}}}$, and $\alpha_{\Phi\mathrm{W}\widetilde{\mathrm{B}}}$ for the CP-violating part. In the HVVBf$\bar{\mathrm{f}}$ vertices all coefficients of the $\psi^2 X^2\Phi$ and $\psi^2\Phi^2 D$ operators enter. Since these coefficients also enter the gauge-boson–fermion couplings they are constrained by results from LEP and on anomalous moments (see for instance Ref. [403]).

10.4.3 Nonlinear parameterization

In the unitary gauge and in the basis of fermion mass eigenstates, the effective Lagrangian relevant for Higgs physics reads as follows [403, 424]

$$\begin{aligned}
\mathcal{L} = &\frac{1}{2}\partial_\mu\mathrm{H}\,\partial^\mu\mathrm{H} - \frac{1}{2}M_{\mathrm{H}}^2\mathrm{H}^2 - c_3\frac{1}{6}\left(\frac{3M_{\mathrm{H}}^2}{v_{\mathrm{SM}}}\right)\mathrm{H}^3 - \sum_{\mathrm{f=u,d,l}}m_{\mathrm{f}}\,\bar{\mathrm{f}}\mathrm{f}\left(1 + c_{\mathrm{f}}\frac{\mathrm{H}}{v_{\mathrm{SM}}} + \dots\right) \\
&+ M_{\mathrm{W}}^2\,\mathrm{W}_\mu^+\mathrm{W}^{-\mu}\left(1 + 2c_{\mathrm{W}}\frac{\mathrm{H}}{v_{\mathrm{SM}}} + \dots\right) + \frac{1}{2}M_{\mathrm{Z}}^2\,\mathrm{Z}_\mu\mathrm{Z}^\mu\left(1 + 2c_{\mathrm{Z}}\frac{\mathrm{H}}{v_{\mathrm{SM}}} + \dots\right) + \dots \\
&+ \left(c_{\mathrm{WW}}\,\mathrm{W}_{\mu\nu}^+\mathrm{W}^{-\mu\nu} + \frac{c_{\mathrm{ZZ}}}{2}\,\mathrm{Z}_{\mu\nu}\mathrm{Z}^{\mu\nu} + c_{\mathrm{Z}\gamma}\,\mathrm{Z}_{\mu\nu}\mathrm{A}^{\mu\nu} + \frac{c_{\gamma\gamma}}{2}\,\mathrm{A}_{\mu\nu}\mathrm{A}^{\mu\nu} + \frac{c_{\mathrm{gg}}}{2}\,G_{\mu\nu}^A G^{A\mu\nu}\right)\frac{\mathrm{H}}{v_{\mathrm{SM}}} \\
&+ \left(c_{\mathrm{W}\partial\mathrm{W}}\left(\mathrm{W}_\nu^- D_\mu\mathrm{W}^{+\mu\nu} + \mathrm{h.c.}\right) + c_{\mathrm{Z}\partial\mathrm{Z}}\,\mathrm{Z}_\nu\partial_\mu\mathrm{Z}^{\mu\nu} + c_{\mathrm{Z}\partial\gamma}\,\mathrm{Z}_\nu\partial_\mu\mathrm{A}^{\mu\nu}\right)\frac{\mathrm{H}}{v_{\mathrm{SM}}} \\
&+ \left(\tilde{c}_{\mathrm{WW}}\,\mathrm{W}_{\mu\nu}^+\widetilde{\mathrm{W}}^{-\mu\nu} + \frac{\tilde{c}_{\mathrm{ZZ}}}{2}\,\mathrm{Z}_{\mu\nu}\widetilde{\mathrm{Z}}^{\mu\nu} + \tilde{c}_{\mathrm{Z}\gamma}\,\mathrm{Z}_{\mu\nu}\widetilde{\mathrm{A}}^{\mu\nu} + \frac{\tilde{c}_{\gamma\gamma}}{2}\,\mathrm{A}_{\mu\nu}\widetilde{\mathrm{A}}^{\mu\nu} + \frac{\tilde{c}_{\mathrm{gg}}}{2}\,G_{\mu\nu}^A\widetilde{G}^{A\mu\nu}\right)\frac{\mathrm{H}}{v_{\mathrm{SM}}} + \dots
\end{aligned} \tag{170}$$

where $v_{\mathrm{SM}} = 1/\sqrt{\sqrt{2}G_F}$ and where $\dots$ denote operators with more than a Higgs field or with more than four derivatives. We have shown only terms involving up to three bosonic fields. Table 54 reports the

relations between the couplings appearing in Eq. (170) and the coefficients of the dimension-6 operators in Eq. (128). It is worth noting that the same Lagrangian (170) applies identically to the case in which the electroweak symmetry $SU(2)_L \times U(1)_Y$ is non-linearly realized and H is a generic scalar, singlet of the custodial symmetry, not necessarily connected with the EW symmetry breaking. Reference [403] (and references therein) explains how to write the Lagrangian (170) in a manifestly $SU(2)_L \times U(1)_Y$ gauge invariant form. Assuming that the New Physics sector is invariant under custodial symmetry, several relations hold among the 22 free parameters c_i appearing in the Lagrangian (169), as for instance $c_W = c_Z$, see Ref. [403] for a detailed discussion. Notice that the operators proportional to $\tilde{c}_i$ are not invariant under CP (at the p^2 level, there are 5 such operators but one linear combination vanishes if the New Physics sector is invariant under the custodial symmetry).

The advantage of the chiral Lagrangian (170) is that it does not assume that H is part of an EW doublet and it can thus be used to describe a more generic Higgs-like particle, like for instance a dilaton, as well as a resonance that would correspond to a mixing of a state belonging to an EW doublet with an EW singlet state. Furthermore the linear Lagrangian (128) is based on a triple expansion in the SM couplings, in powers of E/M and also in powers of Φ/Λ, therefore it implicitly assumes that all the Higgs coupling relative deviations are bounded by $v_{\rm SM}^2/\Lambda^2$ while the chiral Lagrangian (170) allows one to explore larger deviations. However, it is more complicated to calculate higher order corrections using the chiral parameterization than with the linear Lagrangian (128), see e.g. Ref. [403] for a detailed discussion.

Table 54: Relations between the linear and the non-linear parameterization of the Higgs couplings (adapted from Ref. [403]). The CP-violating couplings, $\tilde{c}_i$, are obtained by similar relations with the simple exchange $\alpha'_k \to \alpha'_{\tilde{k}}$ (notice that the Bianchi identities forbid any operator equivalent to $O_{V\partial V}$ in the CP-odd sector).

Higgs couplings	Linear realization
c_W	$1 - \alpha'_\Phi\, v_{SM}^2/\Lambda^2$
c_Z	$1 - (\alpha'_\Phi + 4\alpha'_T)\, v_{SM}^2/\Lambda^2$
c_f (f = u, d, l)	$1 - (\alpha'_\Phi + \alpha'_f)\, v_{SM}^2/\Lambda^2$
c_3	$1 + (2\alpha'_6 - 3\alpha'_\Phi)\, v_{SM}^2/\Lambda^2$
c_{gg}	$8\,(\alpha_s/\alpha_2)\,\alpha'_g\, M_W^2/\Lambda^2$
$c_{\gamma\gamma}$	$8\sin^2\theta_W\,\alpha'_\gamma\, M_W^2/\Lambda^2$
$c_{Z\gamma}$	$\left(\alpha'_{\Phi B} - \alpha'_{\Phi W} - 8\,\alpha'_\gamma \sin^2\theta_W\right) \tan\theta_W\, M_W^2/\Lambda^2$
c_{WW}	$-2\,\alpha'_{\Phi W}\, M_W^2/\Lambda^2$
c_{ZZ}	$-2\left(\alpha'_{\Phi W} + \alpha'_{\Phi B}\tan^2\theta_W - 4\alpha'\gamma\tan^2\theta_W\sin^2\theta_W\right) M_W^2/\Lambda^2$
$c_{W\partial W}$	$-2(2\alpha'_W + \alpha'_{\Phi W})\, M_W^2/\Lambda^2$
$c_{Z\partial Z}$	$-2(2\alpha'_W + \alpha'_{\Phi W}) - 2\left(2\alpha'_B + \alpha'_{\Phi B}\right)\tan^2\theta_W\, M_W^2/\Lambda^2$
$c_{Z\partial\gamma}$	$2\left(2\alpha'_B + \alpha'_{\Phi B} - 2\alpha'_W - \alpha'_{\Phi W}\right)\tan\theta_W\, M_W^2/\Lambda^2$

11 Higgs properties: spin/CP[50]

11.1 Introduction

Since a clear signal for a resonance consistent with the long sought Higgs boson has been established [1,2], the next step is a detailed study of its properties. In this Section we focus on the spin/CP properties of the new resonance, and review the strategies to determine whether the Higgs-like boson is consistent with the spin zero particle predicted in the SM, with $J^{CP} = 0^+$, and the extent to which it could be a mixture of different CP eigenstates. We recall that, as discussed in Section 10.4, going beyond the interim framework for coupling studies presented in Section 10.2 will require the analysis of couplings and spin/CP properties to be treated in a common framework. Nonetheless, to the purpose of presentation, we discuss here the spin/CP properties in a separate section.

The observation of the new resonance in the decay modes H → γγ [266,267], H → ZZ [425,426] and H → WW [103,298] allows multiple independent tests of the spin/CP properties. Thanks to the Landau-Yang theorem [427,428], the observation in the H → γγ mode already rules out the possibility that the new resonance has spin 1, and, barring C violating effects in the Higgs sector, fixes $C = +1$.

Having ruled out the $J = 1$ possibility[51], the case $J = 2$ is of course the first one that should be tested. This possibility turns out to be extremely challenging from a theoretical view point. The naive coupling of a massive spin-2 field with a $U(1)$ gauge field leads to the Velo-Zwanziger problem [429, 430], and the model develops modes that travel superluminally and other pathological features. Detailed studies have shown that such models have an intrinsic cut off of the order of the mass of the spin-2 resonance [431]. A consistent effective description could be obtained by interpreting the spin 2 particle as a Kaluza Klein (KK) graviton. However, one should then explain why analogous KK excitations of the SM gauge bosons have never been observed. Moreover, a recent study [432] has shown that a graviton-like massive spin 2 boson would have too small couplings to WW and ZZ with respect to γγ, and that in many models with a compactified extra dimension the massive spin 2 boson would have equal coupling to gg and γγ, thus leading to $\Gamma(H \to gg) \sim 8\Gamma(H \to \gamma\gamma)$, which seems to be in contradiction to the observed data.

The strategies to determine the properties of a resonance through its decays to gauge bosons date back to more than 50 years ago. Photon polarization in $\pi^0 \to \gamma\gamma$ decay can be used to measure the pion parity [428] but it turns out to be easier to use the orientation of the decay planes in the $\pi^0 \to e^+e^-e^+e^-$ [433] decay. Analogously, the H → ZZ → 4l decay mode, allowing full control on the event kinematics, is an excellent channel to study spin, parity and tensor structure of the coupling of the Higgs-like resonance. As discussed in detail in Section 11.3, the invariant mass distribution of the off shell gauge boson in H → VV* is proportional to the velocity $d\Gamma/dM_* \sim \beta \sim \sqrt{(m_H - m_V)^2 - M_*^2}$ (where M_* denotes the invariant mass of the off-shell gauge boson) and therefore features a characteristic steep behavior with M_* just below the kinematical threshold. This behavior is related to the spin-zero nature of the SM Higgs boson and will rule out other spin assignments with the exception of the 1^+ and 2^- cases, which can be ruled out through angular correlations. The pseudoscalar case 0^- can be instead discriminated against the SM 0^+ by studying the distribution in the azimuthal angle ϕ between the two Z decay planes [434,435]. It should be noted, however, that in many models of physics beyond the SM there is no lowest-order coupling between a pseudoscalar and a pair of gauge bosons, so that the decay A → ZZ → 4l can be heavily suppressed compared to the decay H → ZZ → 4l. For a state that is an admixture between CP-even and CP-odd components the decay into ZZ essentially projects to the CP-even part in such a case, so that the angular distributions would show a pure CP-even pattern

---

[51]Note that there are two caveats to this argument. The first is that the Landau-Yang theorem strictly applies to an on-shell resonance. This means that the $J = 1$ hypothesis can be excluded only by making an additional small-width assumption. The second is that in principle the decay product could consist of 2 pairs of boosted photons each misinterpreted as a single photon.

although the state in fact has a sizable CP-odd component. See section Section 11.2 for a more detailed discussion of this issue.

More generally, instead of relying on specific kinematical variables, one can try to exploit the full information on the event. The *matrix element method* uses the tree level amplitude to construct a likelihood to isolate a signal over a background, or to discriminate between two different signal hypothesis. The construction of the matrix element can be carried out by using two different strategies: the *effective Lagrangian* (see Section 10.4 and Section 11.5) and *anomalous couplings* (see Section 11.4: 'generic parameterizations') approaches. The former implies to write the most general effective Lagrangian compatible with Lorentz and gauge invariance. The latter implies to write the most general *amplitude* compatible with Lorentz and gauge invariance, but does not assume a hierarchy in the scales, and thus the couplings become momentum dependent form factors. The effective Lagrangian approach has the advantage that it can be extended beyond LO. The anomalous coupling approach is restricted to LO but somewhat more general, since it is valid also in the case in which new light degrees of freedom are present and circulate in the loops. The effective Lagrangian approach is being pursued by the MAD-GRAPH team (see Section 11.5). The anomalous coupling approach has been used to perform studies on the spin/CP properties of the Higgs boson [436], and its most widely used implementation is so called MELA approach[52] [437], described in Section 11.4 (see also MEKD [438]).

Here we note that the matrix element method is *maximally* model dependent, since it allows to exclude various specific models one by one. An issue which is important to understand is the extent to which the discrimination of a given spin and CP hypothesis depends on the production model assumed. The results for the $H \to \gamma\gamma$ channel recently presented by the ATLAS collaboration [439] show that the spin-2 hypothesis can be discriminated only by assuming a gg fusion production mode. This is somewhat related to the fact that the $H \to \gamma\gamma$ channel offers essentially only one angular variable, the polar angle θ^* of the photons in the Higgs rest frame. The situation is different in the $H \to WW$ decay mode, where a discrimination against the 2^+ hypothesis is possible [440], although, thanks to spin correlations, the discriminating power is maximum if the Higgs is produced in the $q\bar{q}$ channel. As discussed above, it is the $H \to ZZ \to 4l$ channel that offers the maximum amount of information. Here, the dependence on the production model is present but the experimental results [425] show that the discrimination power is essentially independent on the production model. This is consistent with what is shown in Section 11.4, and is due to the fact that, as observed in Ref. [436], the selection cuts *sculpt* the angular distributions making the dependence on the production model rather marginal.

Another channel that can be used to test the CP structure of the HVV vertex is the HV associated production of the Higgs boson with a vector boson ($V = W^{\pm}, Z$). In Ref. [441] it has been noted that the invariant mass distribution of the VH system would be very different in the 0^+, 0^- and 2^+ hypotheses, thus providing a fast track indicator on Higgs spin and CP properties. We point out that these differences in the invariant mass distribution, together with analogous differences in other kinematical distributions [442, 443], are related to the fact that such spin/CP assignments lead to interactions with the vector bosons that are mediated by higher dimensional operators.

The Higgs CP properties and the structure of the HVV vertex can also be studied in vector boson fusion (VBF), by looking at the azimuthal separation of the two tagging jets [444]. Recent studies on the determination of Higgs Spin/CP properties in VBF are presented in Refs. [443, 445, 446]. When more data will be available, the VBF channel will nicely complement the information obtained in the inclusive Higgs production modes.

The experimental analyses of the CP properties have so far mainly focused on discriminating between the distinct hypotheses of a pure CP-even and a pure CP-odd state. First studies towards dealing with an admixture of CP-even and CP-odd components have recently been presented by the CMS collaboration [426]. As mentioned above, however, angular distributions in $H \to ZZ$ and $H \to WW$ decays

---

[52]ATLAS uses also the BDT method.

as well as invariant mass distributions and azimuthal distributions in VH and VBF production will have a limited sensitivity for discriminating between a pure CP-even state and a mixed state if the coupling of the CP-odd component to VV is suppressed compared to the HVV coupling. The couplings of the Higgs boson to fermions offer a more democratic test of its CP nature, since in this case the CP even and odd components can have the same magnitude. In this respect, if the $\mathrm{Ht\bar{t}}$ channel can be exploited sufficiently well this would offer a good opportunity to study Higgs CP properties [447–449].

The remainder of this Section is organized as follows. In Section 11.2 an overview is given about the coupling of a pseudoscalar to gauge bosons in different models of physics beyond the SM. In Section 11.3 the theoretical basis for spin and parity studies at the LHC is reviewed. In Section 11.4 the matrix element approach based on the JHU generator is briefly reviewed. In Section 11.5 the effective Lagrangian approach implemented by the MADGRAPH group is presented, together with a comparison with JHU results.

11.2 Pseudoscalar couplings to gauge bosons

As discussed above, the present analyses of the CP properties of the new state are based in particular on the investigation of angular distributions of the decays H → ZZ → 4l and H → WW → 4l, of the azimuthal separation of the two tagging jets in VBF and of the invariant mass distributions of the WH and ZH production processes. It should be noted that all the above processes involve the coupling of the new state to two gauge bosons, HVV, where V = W, Z (this coupling also plays an important role for the processes H → γγ and H → Zγ via the W loop contribution).

The angular and kinematic distributions in these processes will only provide sensitivity for a discrimination between CP-even and CP-odd properties if a possible CP-odd component A of the new state couples with sufficient strength to WW and ZZ. If however the AVV coupling is heavily suppressed compared to the coupling of the CP-even component, the difference between a pure CP-even state and a state that is a mixture of CP-even and CP-odd components would merely manifest itself as a modification of the total rate (which could at least in principle also be caused by other effects). The angular distributions in this case, on the other hand, would show no deviations from the expectations for a pure CP-even state, even if the state had a sizable CP-odd component.

The extent to which the above analyses will be able to reveal effects of a CP-odd component of the new state therefore crucially depends on the coupling strength AVV in comparison to the coupling of the CP-even component to gauge bosons. In the following we will briefly discuss this issue for different kinds of models of physics beyond the SM.

While the coupling of a CP-even scalar to VV is present in lowest order in renormalizable gauge theories, no such coupling exists for a CP-odd scalar. In general pseudoscalar states A couple to gauge bosons via dimension 5 operators,

$$\mathcal{L}_{\mathrm{AVV}} = \frac{c_{\mathrm{V}}}{\Lambda} \, A \, V^{a\mu\nu} \tilde{V}^a_{\mu\nu} \tag{171}$$

with $\tilde{V}^a_{\mu\nu} = \frac{1}{2}\epsilon_{\mu\nu\rho\sigma}V^{a\rho\sigma}$ denoting the dual field strength tensor (the same structure also holds for couplings to photons and gluons). In the effective operator given in Eq. (171) c_{V} denotes the coupling strength emerging from the theory at the scale Λ. These couplings can either arise via loop effects in renormalizable weakly-interacting models as e.g. extensions of the Higgs sector or supersymmetric models, or they can occur in non-perturbative models as e.g. expanded versions of technicolor [450–452] with a typical cut-off scale Λ.

11.2.1 Weakly interacting models

In weakly interacting models the pseudoscalar coupling to gauge bosons is mediated by loop effects (dominantly top loops in many models) such that the coupling c_{V} of Eq. (171) is related to the contributing Yukawa couplings of the underlying model and Λ to the masses of the fermions involved in the

corresponding contribution to the chiral anomaly.

This loop-induced coupling turns out to be heavily suppressed in several classes of BSM models. In particular, in the minimal supersymmetric extension of the SM (MSSM) the production times decay rates for purely pseudoscalar Higgs boson states are typically suppressed by three orders of magnitude or more (see e.g. the analysis in [453] and the case of a CP-violating scenario discussed in [454]). Within the MSSM, the detection of any pseudoscalar component of a mixed scalar-pseudoscalar via the above analyses at the LHC therefore does not look feasible. The same holds for the pseudo-axion states in Little Higgs models [455–457].

The situation may be somewhat better in other extensions of the SM. In [453] a general type II 2HDM was investigated. Based on a scan over the relevant parameters it was found that rates for pseudoscalar production and decay can reach a detectable level at the LHC for small values of $\tan\beta$ (i.e. $\tan\beta < 1$), where the pseudoscalar rates can get close to or even exceed the rates for a SM Higgs in some cases. In regions of significant and observable rates at the LHC the pseudoscalar Higgs boson is predominantly produced via gluon fusion $gg \to A$ which is enhanced by the larger top quark contribution than for the SM Higgs boson. The loop-induced decays into gauge bosons also involve the relatively large coupling of the top quark to the pseudoscalar for small values of $\tan\beta$. The main difference to the MSSM is that small values of $\tan\beta$ are still allowed within the type II 2HDM, while the MSSM is strongly constrained by the direct MSSM Higgs searches so that such small values of $\tan\beta$ are excluded [458].

11.2.2 Strongly interacting models

Turning now to strongly interacting models involving non-perturbative effects, effective couplings of pseudoscalar states to gauge bosons naturally arise in technicolor models [450–452], where the pseudoscalar pseudo-Nambu-Goldstone bosons (PNGB) couple to the respective chiral anomalies and the associated axial vector currents [459–461]. Moreover, these types of couplings can be generated by instanton effects in the framework of these models. The cut-off scale Λ of the novel underlying strong interactions is related to the corresponding pseudoscalar decay constant F_A defined by the associated PNGB couplings to the axial vector currents via PCAC,

$$\langle 0|j_5^\mu|A(p)\rangle = iF_A p^\mu \tag{172}$$

where j_5^μ denotes the axial vector current emerging from the novel techni-fermions and p^μ the four-momentum of the pseudoscalar field A. The coupling of the PNGB A to gauge bosons can be derived from the corresponding coupling to the divergence of the axial vector current,

$$\mathcal{L}_A = \frac{A}{F_A}\partial_\mu j_5^\mu \tag{173}$$

Even for massless techni-fermions the divergence of the axial vector current develops an anomalous contribution, the Adler–Bell–Jackiw-anomaly (ABJ-anomaly) [462, 463],

$$\partial_\mu j_5^\mu = -S_V \frac{g_V^2}{16\pi^2} V^{a\mu\nu}\tilde{V}_{\mu\nu}^a \tag{174}$$

where S_V is the associated anomaly coefficient of the corresponding gauge group and g_V its gauge coupling to the techni-fermions. Finally one obtains the effective PNGB couplings to gauge bosons [459–461]

$$\mathcal{L}_{AVV} = -S_V \frac{g_V^2}{16\pi^2 F_A} A\, V^{a\mu\nu}\tilde{V}_{\mu\nu}^a \tag{175}$$

Depending on the size of the anomaly coefficient S_V and the PNGB decay constant F_A these effective couplings can imply production and decay processes of these pseudoscalar states at the LHC which can reach similar orders of magnitude as for SM Higgs bosons. For CP-non-conserving technicolor models

in general large admixtures of scalar and pseudoscalar components are possible which could lead to sizeable deviations of e.g. the angular distributions in final states with 4 charged leptons.

A rigorous analysis of PNGB production and decay at the LHC has been performed in the framework of top-color assisted technicolor models [464]. These models introduce two separate strongly interacting sectors in order to explain electroweak symmetry breaking (EWSB) and the large top quark mass at the same time. Techni-fermion condensates generate most of the EWSB but contribute only little to the top mass. The latter is induced by the condensation of top-antitop pairs which eventually generates a large Yukawa coupling of the techni-pion to top quarks. The top condensate makes only a small contribution to EWSB. Within this class of models pseudoscalar rates of the order of the SM Higgs rates can be reached in a large part of the available parameter space [453]. In contrast to the top quark case the much smaller Yukawa coupling of the pseudoscalar top-pion state to bottom quarks is induced by extended technicolor as well as top-color instanton effects. As before the pseudoscalar couplings to gauge bosons are generated by the ABJ-anomaly. At the LHC a discrimination between scalar and pseudoscalar components at the level of $\mathcal{O}(10\%)$ could help to put constraints on possible mixing between scalar and pseudoscalar fields within these models.

11.3 Basis of Higgs Spin/Parity measurements at the LHC

11.3.1 Projection

The spin/parity quantum numbers of the Higgs-like resonance can be analyzed systematically in decay processes and production channels by studying the associated helicity amplitudes[53]. Measurements allow the determination of necessary and sufficient conditions for assigning the J^{CP} quantum numbers of pure states but also reveal the nature of mixed CP-even/odd states. Such analyses were comprehensively performed for Z^*Z decays followed by leptonic Z^* and Z decays in Refs. [435–437, 465, 466], $\gamma\gamma$ decays in Refs. [467–470], and CP-violating decays in Refs. [471–475], including appropriate production channels of gluon and vector boson fusion [444, 476], and Higgs-strahlung/associated Higgs-vector production in Refs. [442, 477, 478]. The flow of helicities in a representative amplitude for production and decay of the general state H_m^J can be written as

$$g_\mu g_{\mu'} \to H_m^J \to Z_\lambda^* Z_{\lambda'} \quad : \quad \langle Z_\lambda^* Z_{\lambda'} | H_m^J | g_\mu g_{\mu'} \rangle = \mathcal{T}_{\lambda\lambda'} \, d_{m,\lambda-\lambda'}^J(\Theta) \, \delta_{m,\mu-\mu'} \, \mathcal{G}_{\mu\mu'} \tag{176}$$

with $d(\Theta)$ denoting the Wigner rotation functions [479]. $\mathcal{G}$ and $\mathcal{T}$ are the reduced helicity amplitudes for the production and the decay processes, $gg(VV) \to H^J$ and $H^J \to Z^*Z$, respectively. All the relevant angles are mapped in Figures 86(a) and (b) in the rest frame of the Higgs boson.

Angular distributions in unpolarized particle decays to Z^*Z vector pairs allow the measurement of four independent helicity amplitudes. Combined with the analysis of threshold excitation in $H^J \to Z^*Z$, this set is sufficient to determine the spin up to $J = 2$ and the parity. In addition to strongly constrained angular correlations, scalar Higgs decays exhibit only phase-space suppression proportional to the velocity β. In contrast, higher spins can be probed, and eventually excluded, by studying threshold effects in $H^J \to Z^*Z$, predicted for $J > 2$ to behave at least as β^{2J-3} and carrying the power ≥ 3. Alternatively the angular distribution in the joint process of production plus decay can be exploited. The final-state axis in $gg \to H^J \to Z^*Z, \gamma\gamma$ is distributed isotropically for spin = 0 but non-trivially modified by terms up to $\cos^{2J} \Theta$ for any higher spin J.

Some aspects have been studied already in earlier reports [434, 480–485]. A large number of reports on Higgs properties has been published in particular recently in response to the discovery of the "125 GeV Higgs boson"; a partial list of references is recorded in Refs. [20, 468, 486–500], including also analyses like WW decay channels which are theoretically closely related to the channels described here.

---

[53]We point out that the methods we describe here are based on leading-order expressions. Nonetheless, we expect that NLO corrections will not change the picture dramatically.
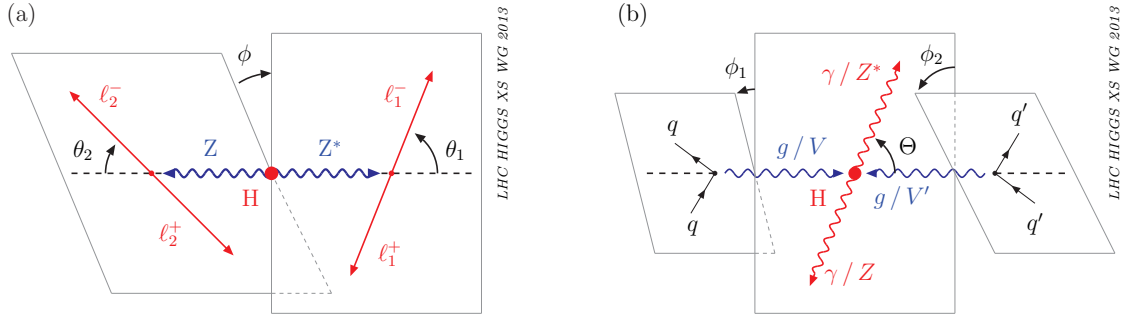
Figure 86: (a) Kinematics of the decay $H^J \to Z^*Z \to (\ell_1^- \ell_1^+)(\ell_2^- \ell_2^+)$ in the rest frame of the Higgs boson. The angles $\theta_{1,2}$ denote the polar angles of the leptons $\ell_{1,2}^-$ in the rest frame of the virtual Z^* and real Z bosons; (b) Higgs production in gluon collisions and subsequent $\gamma\gamma$ and Z^*Z decays, also in the Higgs rest frame. If the gluons are replaced by electroweak gauge bosons, $\phi = \phi_1 - \phi_2 \,(\mathrm{mod}\,2\pi) \in [0, 2\pi)$ corresponds to the azimuthal angle between the two initial qV and $q'V'$ emission planes [476].

11.3.2 Higgs Decay into Virtual/Real Z Bosons

Denoting the polar angles of the leptons $\ell_{1,2}^-$ in the rest frame of the virtual Z^* and real Z bosons by $\theta_{1,2}$ (see Fig. 86(a)), the forward-backward symmetric differential decay distributions of the polar angles for pure-spin/parity unpolarized boson states H^J decaying into $Z_\lambda^* Z_{\lambda'}$ final states can be expressed in terms of four independent helicity amplitudes [435]:

$$
\frac{1}{\Gamma}\frac{d\Gamma}{d\cos\theta_1 d\cos\theta_2} = \mathcal{N}^{-1}\left[\sin^2\theta_1\sin^2\theta_2\,|\mathcal{T}_{00}|^2 + \frac{1}{2}(1+\cos^2\theta_1)(1+\cos^2\theta_2)[|\mathcal{T}_{11}|^2 + |\mathcal{T}_{1,-1}|^2]\right.
$$
$$
\left. + (1+\cos^2\theta_1)\sin^2\theta_2\,|\mathcal{T}_{10}|^2 + \sin^2\theta_1(1+\cos^2\theta_2)\,|\mathcal{T}_{01}|^2\right] \tag{177}
$$

for fixed M_*^2 and suppressing the quartic terms involving the P-violating parameters, $\eta_{1,2}$, which are very small ~ 0.15 for leptonic Z decays, see also Ref. [501]. The distribution is normalized to unity by the coefficient $\mathcal{N}$. Other helicity amplitudes are related by parity and Bose symmetry of the state: $\mathcal{T}_{\lambda\lambda'} = n_H \mathcal{T}_{-\lambda,-\lambda'}$ and $\mathcal{T}_{\lambda\lambda'}[Z, Z^*] = (-1)^J \mathcal{T}_{\lambda'\lambda}[Z^*, Z]$, respectively, the normality given by $n_H = P(-1)^J$. The amplitude $\mathcal{T}_{00}$ vanishes specifically for negative-parity states. The corresponding azimuthal distribution of the Z-decay planes can be expressed by helicity amplitudes as

$$
\frac{1}{\Gamma}\frac{d\Gamma}{d\phi} = \frac{1}{2\pi}\left[1 + n_H\,|\zeta_1|\cos 2\phi\right] \quad \text{with} \quad |\zeta_1| = |\mathcal{T}_{11}|^2 / \left[2\sum|\mathcal{T}_{\lambda\lambda'}|^2\right] \tag{178}
$$

suppressing the small P-violating $\eta_{1,2}$-dependent parts again. (The full expressions of the polar and azimuthal distributions, (177) and (178), can be found in Ref. [435].) The sign of the ϕ modulation is uniquely determined by the normality of the Higgs state. The characteristic behavior of the azimuthal angle between the two Z decay planes is illustrated in Figure 87(a) for spin-zero of positive (SM) and negative parity. Distributions of positive and negative parity decays are mutually anti-cyclic. This will also be observed in jet-jet correlations of electroweak-boson and gluon fusion [441, 443–446, 476, 502].

The spin averaged distribution applies to all configurations in which the orientation of the Z^*Z event axis in the rest frame is summed over so that the decay state is effectively unpolarized.

The functional form of the angular correlations among the Z decay products is not specific to the spin of the decaying boson for $J \geq 2$. These spins cannot be discriminated anymore by such
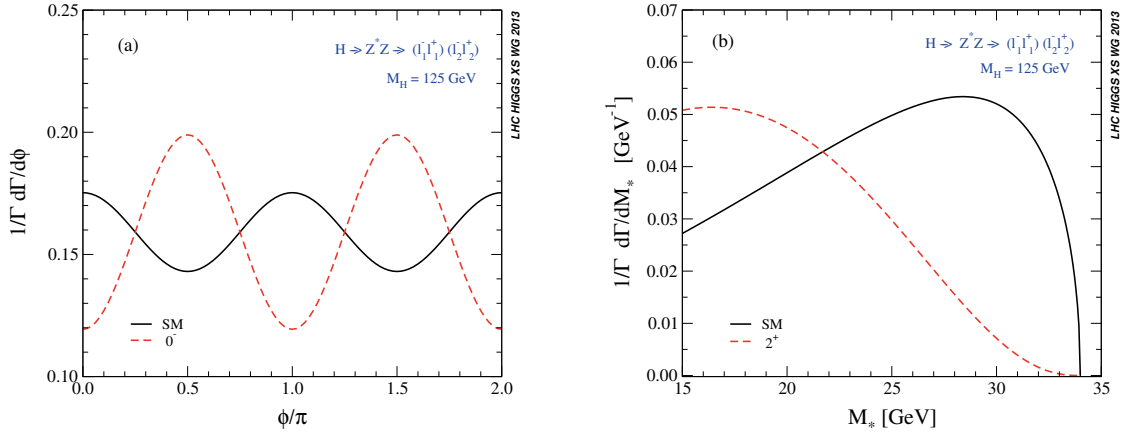
Figure 87: (a) Oscillations of the azimuthal angle between the two Z decay planes for spin = 0 with positive parity in the SM compared with negative parity; (b) Threshold behavior of the decay width $H^J \to Z^*Z$ for the SM and spin-2 ($c_i = 0$ except $c_2 = 1/M_H^2$, c_i defined in Table 55) even normality bosons, with a Higgs boson mass of 125 GeV.

generic analyses. However, angular correlations supplemented by threshold suppression can resolve the ambiguities. After solving for the case $J = 2$ specifically, the analysis is quite general and transparent for $J > 2$ since the tensor structure of these decay amplitudes leads to a characteristic signature of the spin. The $(J + 2)$-tensor structure enforces the amplitude $\mathcal{T}$ for $J > 2$ to rise at least $\sim \beta^{J-2}$ and the decay width correspondingly with $\sim \beta^{2J-3}$. In the absence of the $(1 + \cos \theta_1^2) \sin^2 \theta_2$ and $\sin^2 \theta_1 (1 + \cos^2 \theta_2)$ polar-angle correlations, the pronounced difference of the threshold behavior is exemplified for the spin = 0 SM and spin = 2 even normality bosons with identical 4ℓ angular correlations in Figure 87(b).

Alternatively the measurement of the polar angular distribution of the Z^*Z axis in the production process $gg \to H^J \to Z^*Z$ can be exploited to analyze spin states of any value J. This method can also be applied in $\gamma\gamma$ decays which, since technically simpler, will be described in detail later.

11.3.3 Standard Model

The SM Higgs boson with $J^P = 0^+$ predicts by angular momentum conservation only two non-vanishing $H \to Z^*Z$ decay helicity amplitudes, $\mathcal{T}_{00} = (M_H^2 - M_*^2 - M_Z^2)/(2M_*M_Z)$ and $\mathcal{T}_{11} = -1$. The angular distributions can therefore be cast into the transparent form [435, 477]:

$$\frac{1}{\Gamma_H} \frac{d\Gamma_H}{d\cos\theta_1 \cos\theta_2} = \frac{9}{16} \frac{1}{\gamma^4 + 2} \left[\gamma^4 \sin^2 \theta_1 \sin^2 \theta_2 + \frac{1}{2}(1 + \cos^2 \theta_1)(1 + \cos^2 \theta_2) \right] \quad (179)$$

$$\frac{1}{\Gamma_H} \frac{d\Gamma_H}{d\phi} = \frac{1}{2\pi} \left[1 + \frac{1}{2} \frac{1}{\gamma^4 + 2} \cos 2\phi \right] \quad (180)$$

where $\gamma^2 = (M_H^2 - M_*^2 - M_Z^2)/(2M_*M_Z)$. These angular distributions will come with the Z^*Z threshold rise [435, 477]

$$\frac{d\Gamma[H \to Z^*Z]}{dM_*^2} \Rightarrow \beta \sim \sqrt{(M_H - M_Z)^2 - M_*^2}/M_H \quad \text{for} \quad M_* \Rightarrow M_H - M_Z \quad (181)$$

The observation of the angular distributions associated with the helicity amplitudes, $\mathcal{T}_{00}$, $\mathcal{T}_{11}$ and of the threshold rise $\sim \beta$ are necessary conditions for the zero-spin character of the SM Higgs boson. They

prove also sufficient by noting that any other spin/parity assignment necessarily generates, for any pure state, a different combination of angular correlations and threshold power.

The analysis applies analogously to Higgs bosons in generalized scenarios, like supersymmetric theories, in which the couplings to vector bosons are non-derivative, in conformity with generating masses through the Higgs mechanism.

11.3.4 Alternative J^P Assignments

To prove the unique 0^+ assignment to the SM Higgs boson, it must be demonstrated that the observed signals discussed above are characteristically different for other assignments so that any spin/parity confusion is avoided. The most general Lorentz bases are summarized in Table 55 for spin $J = 0$ and 2. The elements are introduced Bose symmetric to leading order in the momenta, and they exhibit all the characteristics relevant for the general analyses.

Table 55: The most general tensor couplings of the Bose symmetric $H^J Z^* Z$ vertex and the corresponding helicity amplitudes for Higgs bosons of spin $= 0$ and 2 satisfying the relation $\mathcal{T}_{\lambda\lambda'}[M_*, M_Z] = (-1)^J \mathcal{T}_{\lambda'\lambda}[M_Z, M_*]$. Here $p = k_1 + k_2$ and $k = k_1 - k_2$, where k_1 and k_2 are the 4-momenta of the Z^* and the Z bosons, respectively.

J^P	$H^J Z^* Z$ Coupling	Helicity Amplitudes	Threshold
0^+	$a_1 g^{\mu\nu} + a_2 p^\mu p^\nu$	$\mathcal{T}_{00} = [2a_1(M_H^2 - M_*^2 - M_Z^2) + a_2 M_H^4 \beta^2]/(4M_* M_Z)$	1
		$\mathcal{T}_{11} = -a_1$	1
2^+	$c_1 (g^{\mu\beta_1} g^{\nu\beta_2} + g^{\mu\beta_2} g^{\nu\beta_1})$ $+ c_2 g^{\mu\nu} k^{\beta_1} k^{\beta_2}$ $+ c_3 [(g^{\mu\beta_1} p^\nu - g^{\nu\beta_1} p^\mu)k^{\beta_2}$ $+ (\beta_1 \leftrightarrow \beta_2)]$ $+ c_4 p^\mu p^\nu k^{\beta_1} k^{\beta_2}$	$\mathcal{T}_{00} = \Big\{ -c_1 (M_H^4 - (M_Z^2 - M_*^2)^2)/M_H^2 + M_H^2 \beta^2 [c_2 (M_H^2 - M_Z^2 - M_*^2)$ $+ 2c_3 M_H^2 + \frac{1}{2}c_4 M_H^4 \beta^2] \Big\}/(\sqrt{6}M_Z M_*)$	1
		$\mathcal{T}_{01} = -[c_1(M_H^2 - M_Z^2 + M_*^2) - c_3 M_H^4 \beta^2]/(\sqrt{2}M_* M_H)$	1
		$\mathcal{T}_{10} = -[c_1(M_H^2 - M_*^2 + M_Z^2) - c_3 M_H^4 \beta^2]/(\sqrt{2}M_Z M_H)$	1
		$\mathcal{T}_{11} = -\sqrt{2/3}\,(c_1 + c_2 M_H^2 \beta^2)$	1
		$\mathcal{T}_{1,-1} = -2\,c_1$	1
0^-	$a_1 \epsilon^{\mu\nu\rho\sigma} p_\rho k_\sigma$	$\mathcal{T}_{00} = 0$	
		$\mathcal{T}_{11} = i\,\beta\,M_H^2\,a_1$	β
2^-	$c_1 \epsilon^{\mu\nu\beta_1\rho} p_\rho k^{\beta_2}$ $+ c_2 \epsilon^{\mu\nu\rho\sigma} p_\rho k_\sigma k^{\beta_1} k^{\beta_2}$ $+ (\beta_1 \leftrightarrow \beta_2)$	$\mathcal{T}_{00} = 0$	
		$\mathcal{T}_{01} = i\,\beta\,c_1\,(M_H^2 + M_*^2 - M_Z^2)M_H/(\sqrt{2}M_*)$	β
		$\mathcal{T}_{10} = i\,\beta\,c_1\,(M_H^2 + M_Z^2 - M_*^2)M_H/(\sqrt{2}M_Z)$	β
		$\mathcal{T}_{11} = i\,\beta\,2\sqrt{2/3}\,(c_1 + c_2 M_H^2 \beta^2)M_H^2$	β
		$\mathcal{T}_{1,-1} = 0$	

11.3.4.1 Pseudoscalar

Pure pseudoscalar/CP-odd states $H^J = A$ with $J^P = 0^-$ may have a significant branching ratio for decays into Z-boson pairs, though not guaranteed in general [453], as manifest in supersymmetric theories. The pseudoscalar A is the state of minimal complexity as the helicity amplitude $\mathcal{T}_{00} = 0$ by parity invariance and the only non-zero amplitude is $\mathcal{T}_{11} = -\mathcal{T}_{-1,-1}$. As a result, the polar and azimuthal angular distributions are independent of any free parameter [435, 477]:

$$\frac{1}{\Gamma_A} \frac{d\Gamma_A}{d\cos\theta_1 \cos\theta_2} = \frac{9}{64}(1 + \cos^2\theta_1)(1 + \cos^2\theta_2) \tag{182}$$

$$\frac{1}{\Gamma_A} \frac{d\Gamma_A}{d\phi} = \frac{1}{2\pi}\left[1 - \frac{1}{4}\cos 2\phi\right] \tag{183}$$

172

The negative-parity decays are distinctly different from decays of the SM Higgs boson. In particular, the $\cos 2\phi$ term, proportional to the normality n_H, flips sign when the parity is switched, cf. Fig. 87(a). First experimental analyses [12, 425, 426] exclude the negative-parity assignment at more than the 3σ level.

It may be read off Table 55 that the decay amplitude is suppressed near the threshold so that the width rises as β^3, in contrast to β in the SM.

If the branching ratio for A → Z*Z decays is small, initial-final state correlations in γγ as well as jet-jet correlations in gluon fusion build up a set of necessary and sufficient analyses of the spin/parity quantum numbers:

– The angular distribution of the photons in gg → A → γγ is isotropic for spin = 0 in the A rest frame while behaving as a polynomial up to $\cos^{2J} \Theta$ for higher spins.

– The jets in gluon fusion gg → A + gg are anti-correlated in the azimuthal distribution $\cos 2\phi$ for pseudoscalar states [476], opposite to correlated pairs for scalars. Parity signals follow from the correlation $\vec{\epsilon}_1 \times \vec{\epsilon}_2$ of the linear gluon polarization vectors for A, and $\vec{\epsilon}_1 \cdot \vec{\epsilon}_2$ for H, with the polarization vectors concentrated in the gluon-emission planes.

11.3.4.2 Higher Spin States $J > 0$

Vector/Axialvector $J^P = 1^{\mp}$: Vector states of both parities cannot decay into di-photon final states by virtue of the Landau-Yang theorem [427, 428]. Independently of the theorem it may be noted that vector decays into Z*Z pairs can be ruled out experimentally by analyses parallel to those for spin-2 states, which will be described next.

2-Tensors $J^P = 2^{\pm}$: Tensor decays into Z*Z pairs with negative parity are suppressed with the third power β^3 in the velocity near the threshold. Tensor decays with positive parity are also suppressed, if correlations $(1 + \cos^2 \theta_1) \sin^2 \theta_2$ *et v.v.*, absent also in scalar decays, are not observed. This case is nicely illustrated by the "tensor assignment" as studied in Graviton-related Kaluza-Klein scenarios [436, 437, 465–469].

Spin $J \geq 3$: Spin states $J \geq 3$ generate the same generic angular correlations in decays of unpolarized particles as $J = 2$, though with different coefficients. However, the threshold rise, at least $\sim \beta^{2J-3}$, is characteristically reduced compared to the SM Higgs boson as explained in Section 11.1. (In addition, characteristic initial-final state correlations would signal the production of a spin ≥ 3 state.)

11.3.5 Di-Photon Final States

A prominent decay mode of Higgs bosons are H → γγ decays [503]. They can be exploited to study the spin quantum number of the particle [436, 437, 465–470], supplementing the decays into electroweak gauge bosons.

The Landau–Yang theorem [427, 428], based on Lorentz invariance, electromagnetic gauge invariance and Bose symmetry, forbids spin-1 particles to decay into photon pairs. This theorem can easily be extended to odd-spin states of negative parity [428, 470]. From the isotropic decay of spinless states it follows that the parity cannot be measured in on-shell di-photon decays [427, 470]. However, this problem can be solved by gluon fusion gg → H, A + jj with γγ decays of the Higgs bosons and jets in the final state [476].

Information on any spin of the Higgs boson can be derived from combining the production with the decay process. The information is carried in gluon fusion, cf. Fig. 87(b), by the angle Θ of the decay photons with respect to the axis of the incoming partons in the rest frame of the Higgs boson (see Figure 86(b)):

$$gg \to H^J \to \gamma\gamma. \tag{184}$$

Initial and final states carry helicities $\mu - \mu', \lambda - \lambda' = 0$ and ± 2, added up incoherently in the differential

cross section

$$\frac{1}{\sigma}\frac{d\sigma[\mathrm{gg}\to\mathrm{H}^J\to\gamma\gamma]}{d\cos\Theta} = (2J+1)\left[\mathcal{X}_0\mathcal{Y}_0\mathcal{D}_{00}^J + \mathcal{X}_0\mathcal{Y}_2\mathcal{D}_{02}^J + \mathcal{X}_2\mathcal{Y}_0\mathcal{D}_{20}^J + \mathcal{X}_2\mathcal{Y}_2\mathcal{D}_{22}^J\right] \quad (185)$$

with the angular-symmetric squared Wigner functions $\mathcal{D}_{m\lambda}^J = \frac{1}{2}\{[d_{m\lambda}^J(\Theta)]^2 + [d_{m,-\lambda}^J(\Theta)]^2\}$. The probabilities for production $\mathcal{X}_{0,2}$ and decay $\mathcal{Y}_{0,2}$ are built up by the $\mathrm{gg}\to\mathrm{H}^J$ production and $\mathrm{H}^J\to\gamma\gamma$ decay helicity amplitudes. Quite generally they rise up to the non-trivial maximum power of

$$\mathcal{D}^J \sim \cos^{2J}\Theta, \quad (186)$$

independently of the helicity indices 0 or 2. Thus a characteristic signal of the Higgs spin involved is provided by the angular distribution of the photon axis, singling out the isotropic spin = 0 very clearly [470].

While scalar/pseudoscalar Higgs production in the SM is isotropic, any other spin assignment gives rise to non-trivial polar angular distributions as manifest in Fig. 88. In particular, the SM Higgs angular distribution $\{0;00\}$, coming with $\mathcal{D}_{00}^0(\Theta) = 1$ for $\mathcal{X}_0 = \mathcal{Y}_0 = 1$, is compared with the spin-2 distributions for the 'scalar assignment' $\{2;00\}$ and the 'tensor assignment' $\{2;22\}$. For example, the angular distribution for spin-2 graviton-like states is described [467–470] by $\mathcal{D}_{22}^2(\Theta) = (\cos^4\Theta + 6\cos^2\Theta + 1)/16$ for $\mathcal{X}_2 = \mathcal{Y}_2 = 1$. The spin/parity states, which are probed by observing the squared Wigner functions $\mathcal{D}^J$ in $\gamma\gamma$ decays, are listed in Table 56.

Whenever a $\gamma\gamma$ final state is observed as demanded for a Higgs boson, the polar angular distribution can be exploited to measure the spin of the decaying particle and eventually rule out any non-zero spin decay.
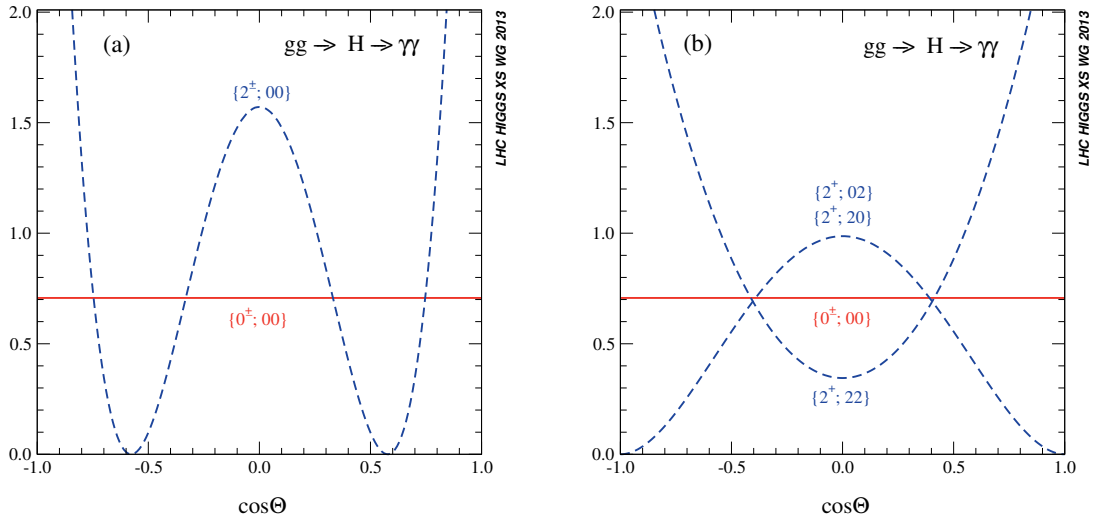
Figure 88: Polar-angle distributions of the $\gamma\gamma$ axes in the rest frame of the subprocesses: the flat Higgs signal compared with potential spin-2 distributions; (a) the 'scalar assignment' $\{2;00\}$ and (b) the 'tensor assignment' $\{2;22\}$ and the 'mixed assignments', $\{2;02\}$ and $\{2;20\}$ (all distributions normalized over the interval $|\cos\Theta| \leq 1/\sqrt{2}$). The upper indices refer to the allowed parity associated with the distributions in $\gamma\gamma$ decays.

An analogous experimental analysis can be carried out for $\mathrm{Z}^*\mathrm{Z}$ final states if the angular distribution of the $\mathrm{Z}^*\mathrm{Z}$ axis is measured.

In contrast to the correlation analyses of polarization-averaged Higgs states in the final states, the measurement of this polar angle Θ is affected by the boost from the laboratory frame to the Higgs

Table 56: Selection rules for Higgs spin/parity following from observing the polar angular distribution of a spin-J Higgs state in the process $gg \rightarrow H \rightarrow \gamma\gamma$, cf. Ref. [470].

$P \setminus J$	0	1	$2, 4, \cdots$	$3, 5, \cdots$
even	1	forbidden	$\mathcal{D}^J_{00}$ $\mathcal{D}^J_{02}$	$\mathcal{D}^J_{22}$
			$\mathcal{D}^J_{20}$ $\mathcal{D}^J_{22}$	
odd	1	forbidden	$\mathcal{D}^J_{00}$	forbidden

rest frame. A simple technique is provided by boosting the reference frame along the 3-momentum of the Higgs boson in the proton-proton-Higgs production plane, leaving the orthogonal space coordinate unchanged. The corresponding vector is known experimentally since the Higgs decay final states, $\gamma\gamma, Z^*Z \rightarrow 4\ell$ allow the explicit reconstruction of this vector.

11.3.6 *Vector-boson Fusion*

The production of Higgs bosons in *electroweak vector-boson fusion $VV' \rightarrow H$* offers another powerful check of the Higgs parity [444, 476]. Radiating the vector bosons off the quark lines, as depicted in Fig. 86(b), the azimuthal correlation between the two radiation planes is sensitive to this quantum number. The two planes are spanned by the proton-proton axis combined with any of the two final quark jets. The correlations of the planes in gluon fusion to Higgs + two jets can be exploited in parallel.

The differential cross sections can be written as a straightforward generalization of the cross sections derived above, for the forward-backward symmetric combination with the transversal and longitudinal degrees of freedom of V, V' and Z^*, Z (from the decay of the Higgs boson into Z^*Z) summed up.

Electroweak vector-boson fusion is supplementary in several facets to Higgs-boson decays, and we will focus on the new elements in *gluon fusion* [476, 504],

$$qq \rightarrow H, A + qq \quad \text{and} \quad q \rightarrow \bar{q}, g \,. \tag{187}$$

By producing the Higgs bosons in gluon fusion, followed by di-photon decays, this mechanism allows the determination of the parity of the pseudoscalar A in scenarios for which A does not decay into Z pairs with sufficiently large branching ratio.

Radiating gluons off quarks or gluons the daughter gluons are polarized to a high degree P in the emission plane [476, 505] as opposed to the perpendicular plane,

$$q \rightarrow qg \quad : \quad P(q; z) = 2(1-z)/(2-2z+z^2) \tag{188}$$

$$g \rightarrow gg \quad : \quad P(g; z) = (1-z)^2/(1-z+z^2)^2 \tag{189}$$

where z denotes the energy fraction transferred to the daughter gluon in the fragmentation process $q \rightarrow qg$ or $g \rightarrow gg$ in the collinear and massless parton limit. Since parity-even Higgs bosons H are produced preferentially for parallel gluon polarization $\sim \vec{\epsilon}_1 \cdot \vec{\epsilon}_2$, while parity-odd Higgs bosons A demand perpendicular polarization $\sim \vec{\epsilon}_1 \times \vec{\epsilon}_2$, the azimuthal modulation of the parton-level production cross sections is uniquely predicted [476] as

$$\frac{1}{\sigma} \frac{d\sigma}{d\phi} = \frac{1}{2\pi} \left[1 \pm |\zeta| \cos 2\phi \right] \quad \text{for} \quad H, A \,. \tag{190}$$

The angle ϕ is the azimuthal angle between the two emission planes $q \rightarrow q\,g$ and/or $g \rightarrow g\,g$, and the polarization parameters $|\zeta|$

$$|\zeta| = P(u; z_1) \, P(v; z_2) \quad \text{with} \quad u, v = q, g \quad \text{for} \quad qq/qg/gg \tag{191}$$

measures the size of the correlation/anti-correlation of the two planes for H/A production [476]. In the limit of soft gluon radiation the degrees of polarization approach unity. Since the recoil quarks are emitted at small but non-vanishing transverse momenta, the planes formed each by quark and proton axis can be determined experimentally. The description of quantitative analyses is deferred to the proper analysis group.

11.3.7 Addenda

Higgs-strahlung : This process in e^+e^- collisions has been proposed quite early [477, 478] as a tool for measuring Higgs spin/parity, and invites investigating $q\bar{q} \rightarrow Z/W + H$ at the LHC [441–443, 445, 446, 502]. The threshold behavior can be exploited in the same way as described in the Higgs decay into virtual Z bosons. A linear rise in the invariant mass distribution rules out the states $0^-, 1^-, 2^-$, while to rule out $1^+, 2^+$ one also requires the angular correlations in the leptonic Z boson decay products. A linear rise in the mass distribution and non-observation of the non-trivial $[1 + \cos^2 \theta] \sin^2 \theta_*$ and $\sin^2 \theta [1 + \cos^2 \theta_*]$ correlations rules out $1^+, 2^+$ (θ denoting the polar angle in $H^J Z$ production and θ_* the fermion polar angle in the Z rest frame with respect to the Z flight direction in the laboratory frame). Any higher spin assignment above spin-2 is ruled out by a rise in the invariant mass distribution with a power ≥ 3.

Fermion Final States : There are scenarios, in particular in supersymmetric theories [506–508], in which CP-odd (pseudoscalar) Higgs particles decay, though not forbidden in principle, into pairs of vector bosons only with perturbatively small branching ratio. This problem can be approached in fermion decays of the Higgs boson [485, 509–511], which may be illustrated by two examples, specific for moderate and large masses:

(i) The angular correlation of the light $0^\pm$ Higgs decay H, A $\rightarrow \tau^- \tau^+ \rightarrow \pi^- \pi^+...$ can be written [474, 475, 485] as

$$\frac{1}{\Gamma} \frac{d\Gamma[H, A \rightarrow \pi^- \pi^+...]}{d\cos \theta_1 d\cos \theta_2 d\phi} = \frac{1}{8\pi} \left[1 - \cos \theta_1 \cos \theta_2 \mp \sin \theta_1 \sin \theta_2 \cos \phi \right] , \tag{192}$$

modulated characteristically opposite for positive and negative parities.

(ii) The process H, A $\rightarrow \bar{t} t$ followed by the 2-particle decay $t \rightarrow Wb$ for heavy Higgs bosons can be analyzed in the same way as the τ chain; the b-jet and the $W^\pm$ angular distribution read identically [474, 475, 485]:

$$\frac{1}{\Gamma} \frac{d\Gamma[H, A \rightarrow \bar{t} t \rightarrow \bar{b} b...]}{d\cos \theta_1 d\cos \theta_2 d\phi} = \frac{1}{8\pi} \left[1 - \kappa_W^2 (\cos \theta_1 \cos \theta_2 \pm \sin \theta_1 \sin \theta_2 \cos \phi) \right] \tag{193}$$

with the polarization-resolving factor $\kappa_W = (m_t^2 - 2M_W^2)/(m_t^2 + 2M_W^2) \sim 2/5$.

11.3.8 *CP mixing in the spin-zero Higgs system*

CP violation in the Higgs system can arise from two different sources which of course influence each other at second order in the perturbative expansion. CP violation can be either indirect and implanted in the Higgs mass matrix [27, 512–515], or direct and effective in the interaction mechanisms with other particles, or both sources may act in parallel.

Combining the CP-mixed Higgs states H$'$ with CP-violating interactions, an effective H$'ZZ$ vertex with complex coefficients can be defined,

$$V_{H'ZZ}^{\mu\nu} = ig_Z M_Z \left[a\, g^{\mu\nu} + b \frac{p^\mu p^\nu}{M_{H'}^2} + c\, \epsilon^{\mu\nu\rho\sigma} \frac{p_\rho k_\sigma}{M_{H'}^2} \right] , \tag{194}$$

176

in the same notation for the 4-momenta as in Table 55. Neglecting any small interference effects, the SM-type parameter a can be taken real. CP is violated if at the same time in addition to c the couplings a and/or b do not vanish simultaneously [473]. Note that these parameters can in general be momentum-dependent form factors obtained from integrating out new physics at some large scale Λ. As the momentum dependence involves ratios of typical momenta in the process to Λ, in a first approximation the scale dependence can be neglected and only the constant part is kept.

The SM is characterized by the set $a = 1$ and $b = c = 0$. Of particular interest is the subgroup $a \neq 0$, $b = 0$ and $c \neq 0$, with c being either real or complex. This subgroup is realized in scenarios in which CP-violation is rooted in the coherent superposition of CP-even H and CP-odd A components of the Higgs wave function. It will provide transparent illustrations of CP-violation effects.

The five general parameters of the $H'ZZ$ vertex, $\{a, \mathrm{Re}(b), \mathrm{Im}(b), \mathrm{Re}(c), \mathrm{Im}(c)\}$, can be measured by five independent observables, $\{\mathcal{O}_1, \cdots, \mathcal{O}_5\}$. CP-violation proper can be observed by isolating the $\sin 2\phi$ observable [471, 472],

$$\mathcal{O}_4 = \sin^2\theta_1 \sin^2\theta_2 \sin 2\phi \tag{195}$$

which can be accessed by a pure measurement of $d\Gamma/d\phi \sim \beta\, \mathrm{Re}(ac^*)$.

In a first step CP-violation may solely be associated with the wave function of the Higgs boson, which is built up by the superposition of CP-even H and CP-odd A spinless components [516, 517]:

$$\mathrm{H}' = \cos\chi\,\mathrm{H} + \sin\chi\,e^{i\xi}\,A\,. \tag{196}$$

Apart from the wave function we assume the $\mathrm{Z}^*\mathrm{Z}$ vertex to be identified with the SM parameters so that in the notation introduced above $a = \cos\chi$, $b = 0$ and $c = \rho_\mathrm{Z} \sin\chi\, e^{i\xi}$, with the real parameter ρ_Z denoting the magnitude of the CP-conserving AZZ coupling, potentially suppressed relative to the HZZ coupling.

The CP-violating $\mathrm{H}' \to \mathrm{Z}^*\mathrm{Z}$ decay helicity amplitudes are built up by the basic $\mathrm{HZ}^*\mathrm{Z}$ and $\mathrm{AZ}^*\mathrm{Z}$ amplitudes and their parity mirrors. Suppressing the very small $\eta_{1,2}$-dependent terms for leptonic Z decays, the width can be cast into the form

$$\frac{1}{\Gamma}\frac{d\Gamma}{d\cos\theta_1 d\cos\theta_2} = \frac{9}{16\mathcal{N}}\left[\gamma^4 c_\chi^2 \sin^2\theta_1 \sin^2\theta_2 + \frac{1}{2}(c_\chi^2 + \rho_\mathrm{Z}^2\beta^2 s_\chi^2)(1 + \cos^2\theta_1)(1 + \cos^2\theta_2)\right]$$

$$\frac{1}{\Gamma}\frac{d\Gamma}{d\phi} = \frac{1}{2\pi}\left[1 + \frac{1}{2}\left\{(c_\chi^2 - \rho_\mathrm{Z}^2\beta^2 s_\chi^2)\cos 2\phi + \rho_\mathrm{Z}\beta s_{2\chi}c_\xi \sin 2\phi\right\}/\mathcal{N}\right] \tag{197}$$

using the normalization $\mathcal{N} = (2 + \gamma^4)c_\chi^2 + 2\rho_\mathrm{Z}^2\beta^2 s_\chi^2$ with the abbreviations $c_\chi = \cos\chi$, etc., and the boosts-related factor $\gamma^2 = (M_{\mathrm{H}'}^2 - M_*^2 - M_\mathrm{Z}^2)/(2M_* M_\mathrm{Z})$, and β accounting for the standard phase space suppression in massive decays.

The original H and A contributions, coming with c_χ^2 and s_χ^2 can easily be recognized in the $\cos\theta_1 \cos\theta_2$ and $\cos 2\phi$ distributions. The novel CP-violating H/A interference term is proportional to $\sin 2\chi \cos\xi$. It is uniquely isolated from the CP-conserving terms by the angular dependence $\sin 2\phi$. When the angle χ moves from 0 to $\pi/2$, the system moves continuously from the pure 0^+ SM Higgs state through CP-mixed states to the pure 0^- state. This transition is demonstrated in Fig. 89(a) in which the modifications of the helicity coefficients compared with the SM are displayed as a function of χ with $\rho_\mathrm{Z} = 1$ and $\xi = 0$. As shown in Fig. 89(b), the azimuthal modulation for a non-trivial CP-violating phase $\chi = 2\pi/5$ is distinctly different from that for the SM case with $\chi = 0$. The size of the admixture ρ_Z is crucial for observing the mixed state experimentally (where for small $\rho\mathrm{Z}$ the ϕ distribution moves back to the SM oscillation, independent of χ).

For $M_{\mathrm{H}'} = 125$ GeV a maximum value of the asymmetry $\mathcal{A}_4 = [\Gamma(O_4 > 0) - \Gamma(O_4 < 0)]/\Gamma$ of the observable $\mathcal{O}_4$ of 0.10 is obtained for $\mathrm{Re}(c)/a = 2.7$ (reduced only to 0.06 for the ratio set to 1.0). A rough theoretical estimate based on the numbers for signal and background at 7 and 8 TeV taken from
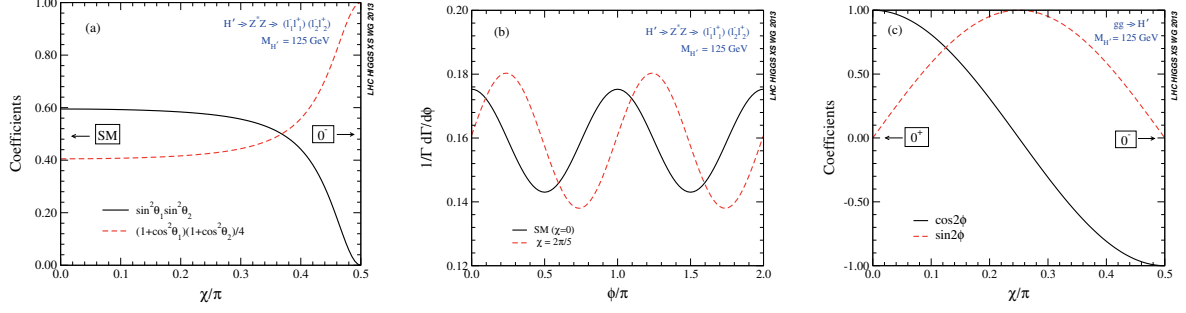
Figure 89: (a) The CP-even and CP-odd coefficients in the correlated polar-angle distribution with respect to the H/A mixing angle χ and (b) the correlated azimuthal-angle distribution in the process $H' \to Z^*Z \to 4\ell$ for the SM case ($\chi = 0$) and a CP-violating case with $\chi = 2\pi/5$; (c) the CP-even and CP-odd coefficients in the correlated azimuthal-angle distribution of the two initial two-jet emission planes with respect to the CP-mixing angle χ. The H$'$ mass $M_{H'}$ is set to be 125 GeV. In addition, the ratios $\rho_Z = \rho_g = 1$, the phase $\xi = 0$ and the polarization parameter $|\zeta| = 1$ are taken for illustration.

Ref. [425] yields for $\mathcal{A}_4$ a significance of 0.45, where we have assumed that both the Higgs coupling to Z and W bosons is CP-violating. We have calculated the significance according to the formula given in Ref. [473]. With the signal and background numbers from CMS [12] we have a significance of 0.50. At 14 TeV, extrapolating the numbers for signal and background from Ref. [310], the significance increases to 0.74 for an integrated luminosity of 100 fb^{-1} and to 1.28 for 300 fb^{-1}.

For small AZZ couplings, gluon fusion $gg \to H' + gg$ followed by $H' \to \gamma\gamma$ decays offers a viable alternative. The Hgg and Agg vertices are combined to

$$V_{H'gg} = \cos\chi V_{Hgg} + \sin\chi e^{i\xi} V_{Agg} \tag{198}$$

Denoting the ratio of Agg/Hgg couplings by ρ_g, the superposition of the $\pm$ parities modifies the azimuthal angular modulation of the two jets to

$$\frac{1}{\sigma}\frac{d\sigma}{d\phi} = \frac{1}{2\pi}\left[1 + |\zeta|\left\{\left(c_\chi^2 - \rho_g^2 s_\chi^2\right)\cos 2\phi + \rho_g s_{2\chi} c_\xi \sin 2\phi\right\}/\mathcal{N}'\right] \tag{199}$$

with the polarization parameters $|\zeta|$ defined in Eq. (191) and the normalization $\mathcal{N}' = c_\chi^2 + \rho_g^2 s_\chi^2$. The two coefficients are illustrated in Fig. 89(c) for $\xi = 0$, the admixture parameter $\rho_g = 1$ and the polarization parameter $|\zeta| = 1$.

Fermion decays: Other observables for studying the CP-violating mixing effects experimentally are the polarization of the τ leptons and top quarks, cf. Ref. [518–522]. The correlations are built up by the dot and cross products of the transverse polarization vectors, $\mathcal{C}_{\parallel}$ and $\mathcal{C}_{\perp}$, respectively, coming with coefficients $\cos\phi$ and $\sin\phi$ in the azimuthal decay distributions.

11.4 Spin, parity and tensor couplings with JHUGEN and MELA

Studies of spin, parity, and couplings of the Higgs-like boson may employ either effective Lagrangians or generic parameterizations of scattering amplitudes. The two approaches are fully equivalent. Effective Lagrangians typically lead to smaller number of tensor couplings by restricting dimensions of contributing operators; this makes the spin-parity analyses more tractable. Generic parameterizations of scattering amplitudes contain all possible tensor structures consistent with assumed symmetries and Lorentz invariance without assigning relative significance to different contributions. Therefore, if the

goal is to maximize the variety of scenarios that can be explored for a given hypothesis, generic parameterizations of amplitudes is a reasonable choice.

We split studies of the new boson properties, such as spin, parity, and couplings, into two groups

– tests of discrete spin/parity/coupling hypotheses of the new particle;

– identification and measurement of various types of tensor couplings that are consistent with assumed symmetries and Lorentz invariance, for a given spin assignment.

11.4.1 Parameterization of amplitudes for spin-zero, spin-one, and spin-two bosons

To introduce our notation, we follow Ref. [437], and write the general scattering amplitude that describes the interaction of the Higgs-like boson with the gauge bosons, such as ZZ, WW, Zγ, γγ, or gg

$$
A(\mathrm{X}_{J=0} \to \mathrm{VV}) = v^{-1} \left(g_1 m_V^2 \epsilon_1^* \epsilon_2^* + g_2 f_{\mu\nu}^{*(1)} f^{*(2),\mu\nu} + g_3 f^{*(1),\mu\nu} f_{\mu\alpha}^{*(2)} \frac{q_\nu q^\alpha}{\Lambda^2} + g_4 f_{\mu\nu}^{*(1)} \tilde{f}^{*(2),\mu\nu} \right),
$$
(200)

where $f^{(i),\mu\nu} = \epsilon_i^\mu q_i^\nu - \epsilon_i^\nu q_i^\mu$ is the field strength tensor of a gauge boson with momentum q_i and polarization vector ϵ_i; $\tilde{f}_{\mu\nu}^{(i)}$ is the conjugate field strength tensor. Parity-conserving interaction of a pseudo-scalar corresponds to g_4, of a scalar to g_1, g_2, and g_3. The SM Higgs coupling at tree level (to ZZ and WW) is described by the g_1 term, while the g_2 term appears in the loop-induced processes, such as Zγ, γγ, or gg, and as a small contribution due to radiative corrections in the ZZ and WW couplings. The g_3 term can be absorbed into the g_2 term if the constants are allowed to be momentum-dependent [437]. Moreover, this term is supposed to be small since it corresponds to a dimension-seven operator in an effective Lagrangian. We therefore neglect the g_3 term in the following discussion, but we note that it can be easily included in our framework if necessary.

Next, we write the general scattering amplitude that describes the interaction of the Higgs-like boson with the fermions, such as $\tau^+\tau^-$, $\mu^+\mu^-$, $b\bar{b}$, and $t\bar{t}$. We assume that the chiral symmetry is exact in the limit when fermion masses vanish

$$
A(\mathrm{X}_{J=0} \to f\bar{f}) = \frac{m_\mathrm{f}}{v} \bar{u}_2 \left(\rho_1 + \rho_2 \gamma_5 \right) v_1 ,
$$
(201)

where m_f is the fermion mass and $\bar{u}$ and v are the Dirac spinors. The two constants ρ_1 and ρ_2 correspond to the scalar and pseudoscalar couplings.

For more exotic spin assignments of the new boson, a large variety of tensor couplings is possible. For completeness, we write down the amplitudes that describe the coupling of this particle to the vector bosons, cf. Ref. [437],

$$
A(\mathrm{X}_{J=1} \to \mathrm{VV}) = g_1^{(1)} \left[(\epsilon_1^* q)(\epsilon_2^* \epsilon_\mathrm{X}) + (\epsilon_2^* q)(\epsilon_1^* \epsilon_\mathrm{X}) \right] + g_2^{(1)} \epsilon_{\alpha\mu\nu\beta} \epsilon_\mathrm{X}^\alpha \epsilon_1^{*,\mu} \epsilon_2^{*,\nu} \tilde{q}^\beta ,
$$
(202)

$$
A(\mathrm{X}_{J=2} \to \mathrm{VV}) = \Lambda^{-1} \left[2 g_1^{(2)} t_{\mu\nu} f^{*1,\mu\alpha} f^{*2,\nu\alpha} + 2 g_2^{(2)} t_{\mu\nu} \frac{q_\alpha q_\beta}{\Lambda^2} f^{*1,\mu\alpha} f^{*2,\nu,\beta} \right.
$$

$$
+ g_3^{(2)} \frac{\tilde{q}^\beta \tilde{q}^\alpha}{\Lambda^2} t_{\beta\nu} (f^{*1,\mu\nu} f_{\mu\alpha}^{*2} + f^{*2,\mu\nu} f_{\mu\alpha}^{*1}) + g_4^{(2)} \frac{\tilde{q}^\nu \tilde{q}^\mu}{\Lambda^2} t_{\mu\nu} f^{*1,\alpha\beta} f_{\alpha\beta}^{*(2)}
$$

$$
+ m_V^2 \left(2 g_5^{(2)} t_{\mu\nu} \varepsilon_1^{*\mu} \varepsilon_2^{*\nu} + 2 g_6^{(2)} \frac{\tilde{q}^\mu q_\alpha}{\Lambda^2} t_{\mu\nu} (\varepsilon_1^{*\nu} \varepsilon_2^{*\alpha} - \varepsilon_1^{*\alpha} \varepsilon_2^{*\nu}) + g_7^{(2)} \frac{\tilde{q}^\mu \tilde{q}^\nu}{\Lambda^2} t_{\mu\nu} \varepsilon_1^* \varepsilon_2^* \right)
$$

$$
+ g_8^{(2)} \frac{\tilde{q}_\mu \tilde{q}_\nu}{\Lambda^2} t_{\mu\nu} f^{*1,\alpha\beta} \tilde{f}_{\alpha\beta}^{*(2)} + g_9^{(2)} t_{\mu\alpha} \tilde{q}^\alpha \epsilon_{\mu\nu\rho\sigma} \epsilon_1^{*\nu} \epsilon_2^{*\rho} q^\sigma
$$

$$
\left. + \frac{g_{10}^{(2)} t_{\mu\alpha} \tilde{q}^\alpha}{\Lambda^2} \epsilon_{\mu\nu\rho\sigma} q^\rho \tilde{q}^\sigma (\epsilon_1^{*\nu}(q\epsilon_2^*) + \epsilon_2^{*\nu}(q\epsilon_1^*)) \right] ,
$$
(203)

and to the fermions

$$A(\mathrm{X}_{J=1} \to \mathrm{f\bar{f}}) = \epsilon^{\mu} \bar{u}_1 \left(\gamma_{\mu} \left(\rho_1^{(1)} + \rho_2^{(1)} \gamma_5 \right) + \frac{m_q \tilde{q}_{\mu}}{\Lambda^2} \left(\rho_3^{(1)} + \rho_4^{(1)} \gamma_5 \right) \right) v_2, \tag{204}$$

$$A(\mathrm{X}_{J=2} \to \mathrm{f\bar{f}}) = \frac{1}{\Lambda} t^{\mu\nu} \bar{u}_1 \left(\gamma_{\mu} \tilde{q}_{\nu} \left(\rho_1^{(2)} + \rho_2^{(2)} \gamma_5 \right) + \frac{m_q \tilde{q}_{\mu} \tilde{q}_{\nu}}{\Lambda^2} \left(\rho_3^{(2)} + \rho_4^{(2)} \gamma_5 \right) \right) v_2. \tag{205}$$

The $g_1^{(1)}$ ($g_2^{(1)}$) coupling corresponds to parity-conserving interaction of a vector (pseudo-vector). The $g_1^{(2)}$ and $g_5^{(2)}$ couplings correspond to parity-conserving interaction of a spin-two tensor with the minimal couplings. We note that both spin-one and spin-two assignments for the Higgs-like boson are rather exotic and, at the same time, require large number of couplings to fully parametrize the $\mathrm{X} \to \mathrm{VV}$ amplitude. Moreover, since existing evidence already disfavors exotic spin assignments [12, 298, 425, 426, 439, 440, 523], the complete measurement of the tensor couplings for both of these cases is not particularly motivated. Nevertheless, further checks of some spin-two scenarios against available data and the development of robust methods to exclude certain spin-parity assignments in a model-independent way are important and should be pursued.

11.4.2 Tensor couplings in the spin-zero case

As we already mentioned above, there is a significant evidence that the Higgs-like boson is in fact a spin-zero particle whose properties are very similar to that of the SM Higgs boson. Taking this as a starting point, we need to focus on the Higgs-like boson precision phenomenology. One of the important questions we should address is how to determine and/or put constraints on all the different couplings of the spin-zero Higgs-like boson that appear in Eqs. (200) and (201).

To set up a framework for couplings determination, we consider the case of three independent complex couplings g_1, g_2, and g_4 for each type of a vector boson $(\mathrm{Z}, \gamma, \mathrm{W}, \mathrm{g})$ and two independent complex couplings ρ_1 and ρ_2 for each type of a fermion, under the spin-zero assignment. Therefore, we require four independent real numbers to describe bosonic process and two real numbers to describe fermionic process provided that the overall rate is treated separately and one overall complex phase is not measurable. For a vector boson coupling, we can represent the four independent parameters by two fractions (f_{g2} and f_{g4}) and two phases (ϕ_{g2} and ϕ_{g4}), defined as

$$f_{gi} = \frac{|g_i|^2 \sigma_i}{|g_1|^2 \sigma_1 + |g_2|^2 \sigma_2 + |g_4|^2 \sigma_4}; \qquad \phi_{gi} = \arg\left(\frac{g_i}{g_1}\right).$$

We note that σ_i is the effective cross-section of the process corresponding to $g_i = 1, g_{j\neq i} = 0$. The parameter f_{g4} is equivalent to the parameter f_{a3} as introduced by CMS [426] under the assumption $g_2 = 0$, and is the fraction of a CP-violating contribution.

Based on Eq. (201), we can define two parameters describing mixing in the fermion couplings, $f_{\rho2}$ and $\phi_{\rho2}$, equivalent to the boson coupling parameters defined above. We note that the fractions and phases can be defined independently for each type of boson or fermion couplings or they can be related to each other by further assumptions about the electroweak quantum numbers of the Higgs-like boson. The advantage of introducing fractions f_{g_i} to parametrize different couplings is that they are uniquely defined and have a clear experimental interpretation as effective fractions of yields of events corresponding to each independent scattering amplitude. We note that contributions that originate from the interference of different amplitudes can be easily described using the parameterization introduced above.

11.4.3 Monte Carlo Simulation

Dedicated simulation programs can be used to describe various di-boson final states in the production and decay to two vector bosons of the spin-zero, spin-one, and spin-two resonances in hadron-hadron

collisions. Implementation of the processes $gg/q\bar{q} \to X \to ZZ$ and $WW \to 4f$, as well as $gg/q\bar{q} \to X \to \gamma\gamma$, into a Monte Carlo program JHU generator, is described in Ref. [524]. The JHU generator incorporates the general couplings of the X particle to gluons and quarks in production and to vector bosons in decay and includes all spin correlations and interferences of all contributing amplitudes. The program can be interfaced to parton shower simulation as well as full detector simulation through the Les Houches Event file format [193]. The program also allows interfacing the decay of a spin-zero particle with the production simulated by other Monte Carlo programs. This makes it possible to include NLO QCD effects in the production through event generators such as POWHEG [78–80].

The JHU generator can be used to develop ideas and tools for the study of the Higgs-like boson with experimental data. To illustrate this point, we show in Table 57 several scenarios that can be explored. Of course, any combination of the above scenarios with proper interferences of amplitudes can be tested as well using the JHU generator. An example of interference study is shown in Figure 91.

Table 57: List of representative scenarios for the analysis of the production and decay of an exotic X particle with quantum numbers J^P. The subscripts m (minimal couplings) and h (couplings with higher-dimension operators) distinguish different scenarios, as discussed in the last column.

scenario	X production	X → VV decay	comments
0_m^+	$gg \to X$	$g_1^{(0)} \neq 0$ in Eq. (200)	SM Higgs boson scalar
0_h^+	$gg \to X$	$g_2^{(0)} \neq 0$ in Eq. (200)	scalar with higher-dim. operators
0^-	$gg \to X$	$g_4^{(0)} \neq 0$ in Eq. (200)	pseudo-scalar
1^+	$\bar{q}q \to X$	$g_2^{(1)} \neq 0$ in Eq. (202)	exotic pseudo-vector
1^-	$\bar{q}q \to X$	$g_1^{(1)} \neq 0$ in Eq. (202)	exotic vector
2_m^+	$g_1^{(2)} \neq 0$ in Eq. (203)	$g_1^{(2)} = g_5^{(2)} \neq 0$ in Eq. (203)	graviton-like tensor with min. couplings
2_h^+	$g_4^{(2)} \neq 0$ in Eq. (203)	$g_4^{(2)} \neq 0$ in Eq. (203)	tensor with higher-dimension operators
2_h^-	$g_8^{(2)} \neq 0$ in Eq. (203)	$g_8^{(2)} \neq 0$ in Eq. (203)	"pseudo-tensor"

11.4.4 Approaches to mixture and spin measurements

The basic idea behind any spin-parity measurement is that various spin-parity assignments restrict allowed types of interactions between the Higgs-like boson and other particles. This feature manifests itself in various kinematic distributions of either the decay products of the Higgs-like particle or particles produced in association with it. Let us first discuss the three processes which would allow the complete determination of the tensor couplings in Eq. (200) for the HZZ interaction vertex. These are illustrated in Figure 90 and can be described as follows

  – production of a Higgs boson (in any process) and decay H → ZZ → 4l, see Figure 90 (left);
  – Z* production and radiation of a Higgs boson (with decay into any final state), see Figure 90 (middle).
  – VBF production of a Higgs boson in Z boson fusion (with decay into any final state), see Figure 90 (right).

In all cases, the spin-zero H assignment leads to an isotropic distribution of $\cos\theta^*$ and Φ_1 regardless of the H production or decay mechanism. The weak vector boson fusion process VBF can be used to determine HWW and HZZ couplings in production on LHC using jet information [446], though this measurement relies stronger on dynamic distributions and does not allow to separate HWW and HZZ couplings.

The ultimate goal of the analysis should be the experimental determination of all amplitudes that involve the new boson and two gauge bosons or fermions. The techniques discussed in Ref. [437]
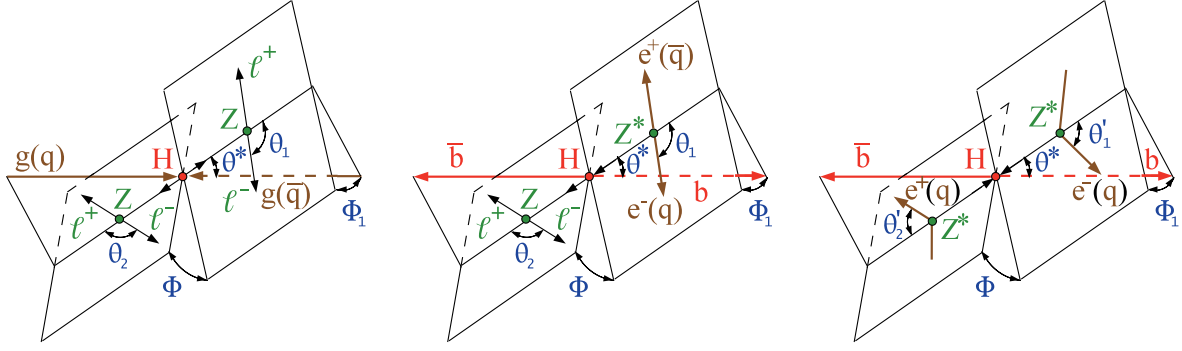
Figure 90: Illustration of an H particle production and decay in pp collision $gg/\overline{q}q \rightarrow H \rightarrow ZZ \rightarrow 4\ell^{\pm}$, $q\bar{q} \rightarrow Z^* \rightarrow ZH \rightarrow \ell^+\ell^-b\bar{b}$, or $qq' \rightarrow qq'V^*V^* \rightarrow qq'H \rightarrow qq'b\bar{b}$. Five angles fully characterize orientation of the decay chain and are defined in the corresponding particle rest frames. Both spin-zero and exotic spin assignments of H are considered. The e^+e^- production is shown for comparison with the production modes on LHC.

are suited for such measurements since parameters in the angular and mass distributions become fit parameters in analysis of data. However, such multi-parameter fits require large samples of the signal events. Therefore, there are two steps in understanding the tensor couplings and the spin of the Higgs-like boson:

– discrete hypothesis testing;

– fit of all coupling parameters.

For the first step, a simplified, but still optimal, analysis approach can be developed that employs just one observable to differentiate between the two hypotheses, as we explain in the next section (a second observable can be used for signal-to-background separation). The second step requires a complete multi-dimensional fit of all coupling parameters using a complete set of kinematic observables which is the ultimate goal of this research program. In the remainder of this note we concentrate on the $H \rightarrow ZZ \rightarrow 4l^{\pm}$ process in Figure 90 and other processes can be studied by analogy [437, 446].

11.4.5 Discrete hypothesis testing

For discrete hypothesis testing one can create a kinematic discriminant (MELA approach) [2] which is constructed from the ratio of probabilities for the SM signal and alternative signal J_x^P hypotheses

$$D_{J_x^P} = \left[1 + \frac{\mathcal{P}_{J_x^P}(m_{4\ell}; m_1, m_2, \vec{\Omega})}{\mathcal{P}_{\text{SM}}(m_{4\ell}; m_1, m_2, \vec{\Omega})} \right]^{-1}. \tag{206}$$

Here $\mathcal{P}$ are the probabilities, as a function of masses m_i and angular observables $\vec{\Omega}$, as defined in Figure 90 and discussed in Ref. [437]. The separation power depends on information contained in kinematic distributions. All this information is combined in an optimal way in the $D_{J_x^P}$ observable. The expected [437] and observed separation with LHC data [12, 298, 425, 426, 439, 440, 523] indicates that most of the hypotheses listed in Table 57 are strongly disfavored, both with gg and q$\bar{q}$ production mechanisms of the spin-two particle. The typical distributions for the 0^- analysis are shown in Figure 91. Consistency between the data and the two spin-parity models could be judged from the observed and expected distribution of $-2\ln(\mathcal{L}_1/\mathcal{L}_2)$ with the likelihood $\mathcal{L}_k$ evaluated for two models based on distributions of D_{0^-}.
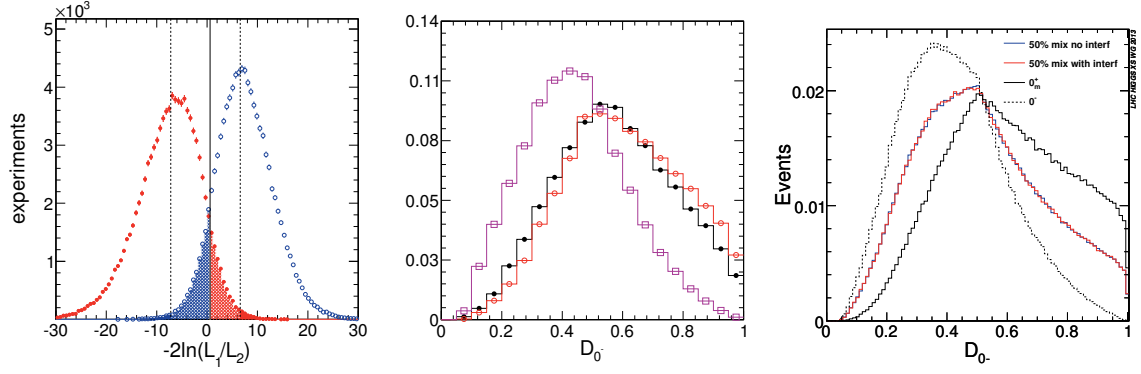
Figure 91: Left: Distributions of $-2\ln(\mathcal{L}_1/\mathcal{L}_2)$ with the likelihood $\mathcal{L}_k$ evaluated for two models and shown for a large number of generated experiments in the analysis [437]. Middle: Distributions of D_{0^-} in the X $\to$ ZZ analysis for the non-resonant ZZ background (black solid circles), and two signal hypotheses: SM Higgs boson (red open circles), 0^- (magenta squares) [437]. Right: Distribution of D_{0^-} for event samples with generated $f_{g4} = 0.5$ with and without interference of the g_1 and g_4 terms included, and compared to the two pure cases of 0_m^+ and 0^-.

The above approach exploits in the optimal way the maximum available kinematic information but at the expense of testing very specific models. With increasing data-sample, we can afford loosening some requirements with the advantage of gaining generality. For instance, while the production mechanism for the spin-one boson is q$\bar{\text{q}}$ annihilation, the production of the spin-two bosons receives contributions from both gg and q$\bar{\text{q}}$ initial states in a composition that is model-dependent and a priori unknown. Since a particular type of production mechanism for a non-zero-spin state may influence the kinematics of the decay products of the Higgs-like boson, any spin-hypothesis test may strongly depend on the production model.

It is desirable to extend the above hypothesis testing approach in a way that does not depend on the production model. This feature can be easily achieved by considering the unpolarized X-boson production by either averaging over the spin degrees of freedom of the produced X-boson or, equivalently, integrating over the two production angles $\cos\theta^*$ and Φ_1, defined in Figure 90, in the J_x^P probability expectation $\mathcal{P}_{J_x^P}$ [437]. This leads to the spin-averaged matrix element squared for the X-decay as the probability $\mathcal{P}$ in the kinematic discriminant

$$D_{J_x^P}^{\text{decay}} = \left[1 + \frac{\int d\Phi_1 d\cos\theta^* \, \mathcal{P}_{J_x^P}(m_{4\ell}; m_1, m_2, \vec{\Omega})}{\mathcal{P}_{\text{SM}}(m_{4\ell}; m_1, m_2, \vec{\Omega})}\right]^{-1}. \tag{207}$$

This method applies to any possible hypothesis with non-zero spin. The spin-zero kinematics is already independent of the production mechanism due to lack of spin correlations for any spin-zero particle; as the result $\cos\theta^*$ and Φ_1 distributions are isotropic for any production model.

Below we illustrate this approach with the example of spin-two, where we compare two production models, $2_{m\,\bar{\text{q}}\text{q}}^+$ and $2_{m\,\text{gg}}^+$. The distribution of the most optimal discriminant (which includes production and decay variables) is different depending on the mixture of q$\bar{\text{q}}$ annihilation and gluon-gluon fusion production mechanisms, as shown in Figure 92. As expected, the discriminant built for a specific production mechanism has different distributions depending on the production process of the sample (being sub-optimal if the production mechanism is different from the one for which the discriminant is built). The new discriminant $D_{2_m^+}^{\text{decay}}$ from Eq. (207) does not depend on the production mechanism, as shown in Figure 92 (right) at the expense of having somewhat less separation power between the SM and the alter-

native spin hypothesis. The production-dependent information (the two production angles, as well as the transverse momentum distribution of the boson) can still have a second order effect on the discriminant distribution through the detector acceptance effects. However, this effect is found to be small in the fully reconstructed $H \rightarrow ZZ \rightarrow 4l^{\pm}$ process.

Finally we would like to point out that while discrete hypothesis testing allows us to quickly exclude the most plausible models, complete exclusion of all models with exotic spin requires more time. Such tests may see decreasing level of interest as more and more exotic models are tested. Nonetheless, it should still be possible to exclude all possibilities eventually, assuming all tests remain consistent with the spin-zero particle. For example, in the spin-one case, only two couplings are present and it is relatively easy to span the continuous spectrum of couplings. The situation with spin-two is less trivial, but it might be possible to come up with the most pessimistic scenario (kinematics closest to the SM Higgs boson) excluding which could bring us to the situation when the full spectrum of exotic-spin models can be excluded. Production-model-independent test discussed above is an important step in that direction.

11.4.6   *Continuous hypothesis testing of mixing structure*

As discussed above, the ultimate approach requires a complete multi-dimensional fit of all coupling parameters using a complete set of kinematic observables. However, first we would like to note an interesting feature in the fit for the f_{g4} parameter, as introduced by the CMS experiment with the f_{a3} measurement [426]. The distribution of the D_{0-} observable for a fraction $f_{g4} = 0.5$ of 0_m^+ (g_1) and 0^- (g_4) contributions is independent of the interference effects between the two amplitudes as shown in Figure 91 (right). Distributions appear nearly identical for any phase of the mixture ϕ_{g4} and also for the case when the interference contribution is neglected altogether. The same feature is observed for other fractions of f_{g4}. This leads to a simplified but still optimal analysis to determine f_{g4} from measuring the shape of the D_{0-} observable. The CMS experiment estimates a current expected precision on f_{g4} of about 0.40 at 68% CL [12, 298, 425, 426, 439, 440, 523]. This translates to about 0.08 expected precision with $300\,\mathrm{fb}^{-1}$ at 14 TeV run of LHC. As long as only a limit is set on f_{g4} and this limit is not much smaller than the above expectation, such an analysis may be sufficient for setting a limit on the *CP*-violating contribution to the HZZ coupling.

For a more complete treatment, for example if a non-zero value of f_{g4} is measured, we follow the
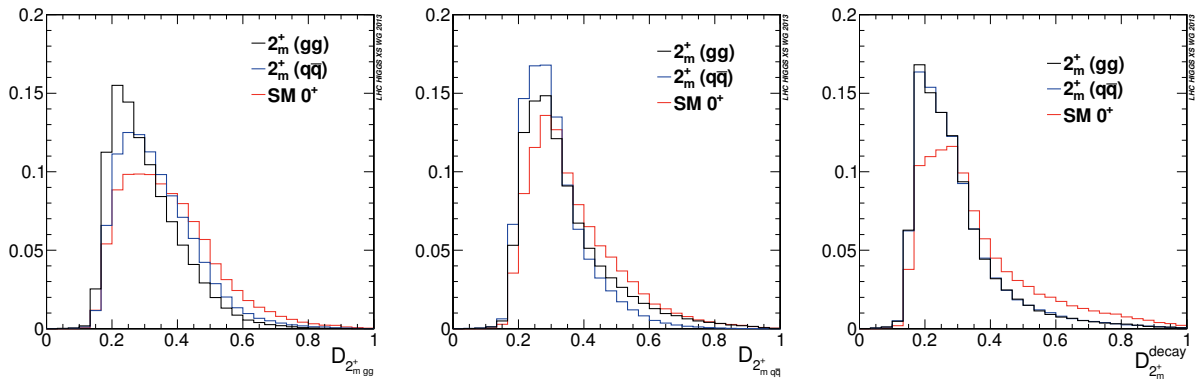
Figure 92: Distribution of the discriminants $D_{2_m^+ \mathrm{gg}}$ (left), $D_{2_m^+ \overline{\mathrm{q}}\mathrm{q}}$ (middle), $D_{2_m^+}^{\mathrm{decay}}$ (right) evaluated with three different samples: SM Higgs boson, spin-two produced through gluon-gluon fusion and produced through $\overline{\mathrm{q}}\mathrm{q}$ annihilation.

notation of Ref. [437] for the likelihood function for N candidate events

$$\mathcal{L} = \exp\left(-\sum_{J=0}^{2} n_J - n_{\mathrm{bkg}}\right) \prod_{i}^{N} \left(\sum_{J=0}^{2} n_J \times \mathcal{P}_J(\vec{x}_i;\ \vec{\zeta}_J;\ \vec{\xi}) + n_{\mathrm{bkg}} \times \mathcal{P}_{\mathrm{bkg}}(\vec{x}_i;\ \vec{\xi})\right), \qquad (208)$$

where n_J is the number of signal events for each resonance spin J, n_{bkg} is the number of background events and $\mathcal{P}(\vec{x}_i;\vec{\zeta};\vec{\xi})$ is the probability density function for signal or background. It is assumed that only one resonance is observed in a given mass window and the three yields, n_J, allow one to test different hypotheses. Each event candidate i is characterized by a set of eight observables $\vec{x}_i = \{m_{4\ell},\ m_1,\ m_2,\ \cos\theta^*,\ \Phi_1,\ \cos\theta_1,\ \cos\theta_2,\ \Phi\}_i$. The number of observables can be extended or reduced, depending on the desired fit. The signal polarization parameters f_{gi} and ϕ_{gi} are collectively denoted by $\vec{\zeta}_J$, and the remaining parameters by $\vec{\xi}$.

The advantage of the maximum likelihood fit approach is that the likelihood $\mathcal{L}$ in Eq. (208) can be maximized for a large set of parameters in the most optimal way without losing information. The disadvantage is the difficulty to describe the detector response in the eight-dimensional space. The latter can be achieved with certain approximations and may become the future direction of hypothesis testing in multi-parameter models with increasing samples of signal events.

11.5 Higgs characterization with FEYNRULES and MADGRAPH 5

In this section we introduce a complete framework, based on an effective field theory description, that allows to perform characterization studies of a new boson in all relevant channels in a consistent, systematic and accurate way.

In the following we present the implementation of an effective Lagrangian featuring bosons $X(J^P)$ with various assignments of spin/parity $J^P = 0^+, 0^-, 1^+, 1^-, 2^+, 2^-$ that can be used to test the nature of the recently-discovered new boson with mass around 125 GeV at the LHC [1, 2]. The new states can couple to Standard Model particles via interactions of the minimal (and next-to-minimal) dimensions. The implementation of the Lagrangian is done in FEYNRULES [525] and the corresponding model named *Higgs Characterization model*. It extends and completes an earlier version used in Ref. [446] and it is publicly accessible at [526]. It is therefore available to all matrix element generators featuring an UFO interface [527]. For our study we have employed MADGRAPH 5 [129]. Results at the NLO accuracy in QCD can be automatically (or semi-automatically) obtained via AMC@NLO [130, 132].

There are several advantages in having a first principle implementation in terms of an effective Lagrangian which can be automatically interfaced to a matrix element generator (and then to an event generator). First and most important, all relevant production and decay modes can be studied within the same model, from gluon-gluon fusion to VBF as well as VH and $\bar{t}t$ associated productions can be considered and the corresponding processes automatically generated within minutes. Second, it is straightforward to modify the model implementation to extend it further in case of need, by adding further interactions, for example of higher-dimensions. Finally, higher-order effects can be easily accounted for, by generating multi-jet merged samples or computing NLO corrections with automatic frameworks. All the detailed demonstration and analyses are currently in progress [528].

In the following we first write down the effective Lagrangian explicitly and then show comparison plots with JHU results as presented in Ref. [465] which are currently employed by both ATLAS and CMS collaborations. We remind here that, even though we list several cases of interest in a simple conversion table as a dictionary between JHU and our *Higgs Characterization model* [528], in general the two approaches will be different. Our implementation is based on an effective theory approach valid up to the scale Λ, while JHU describes the interaction between the new state and SM particles in terms of anomalous couplings.

11.5.1 The effective Lagrangian

Table 58: Model parameters.

parameter	default value	description
Λ [GeV]	10^3	cutoff scale
$c_\alpha (\equiv \cos\alpha)$	1	mixing between 0^+ and 0^-
κ_i	1 or 0	dimensionless coupling parameter

11.5.1.1 Spin 0

The spin-0 X interaction Lagrangian with fermions and vector-bosons are given by

$$\mathcal{L}_0^{\mathrm{f}} = -\left[c_\alpha\kappa_{\mathrm{Hff}}g_{\mathrm{Hff}}\,\bar{\psi}_{\mathrm{f}}\psi_{\mathrm{f}} + s_\alpha\kappa_{\mathrm{Aff}}g_{\mathrm{Aff}}\,\bar{\psi}_{\mathrm{f}}i\gamma_5\psi_{\mathrm{f}}\right]\mathrm{X}_0, \tag{209}$$

and

$$
\begin{aligned}
\mathcal{L}_0^{\mathrm{V}} = \Bigg[& c_\alpha\kappa_{\mathrm{SM}}\Big[\tfrac{1}{2}g_{\mathrm{HZZ}}\,\mathrm{Z}_\mu\mathrm{Z}^\mu + g_{\mathrm{HWW}}\,\mathrm{W}^{+\mu}\mathrm{W}^{-\mu}\Big] \\
& -\frac{1}{4}\big[c_\alpha\kappa_{\mathrm{H\gamma\gamma}}g_{\mathrm{H\gamma\gamma}}\,\mathrm{A}_{\mu\nu}\mathrm{A}^{\mu\nu} + s_\alpha\kappa_{\mathrm{A\gamma\gamma}}g_{\mathrm{A\gamma\gamma}}\,\mathrm{A}_{\mu\nu}\widetilde{\mathrm{A}}^{\mu\nu}\big] \\
& -\frac{1}{2}\big[c_\alpha\kappa_{\mathrm{HZ\gamma}}g_{\mathrm{HZ\gamma}}\,\mathrm{Z}_{\mu\nu}\mathrm{A}^{\mu\nu} + s_\alpha\kappa_{\mathrm{AZ\gamma}}g_{\mathrm{AZ\gamma}}\,\mathrm{Z}_{\mu\nu}\widetilde{\mathrm{A}}^{\mu\nu}\big] \\
& -\frac{1}{4}\big[c_\alpha\kappa_{\mathrm{Hgg}}g_{\mathrm{Hgg}}\,G_{\mu\nu}^a G^{a,\mu\nu} + s_\alpha\kappa_{\mathrm{Agg}}g_{\mathrm{Agg}}\,G_{\mu\nu}^a \widetilde{G}^{a,\mu\nu}\big] \\
& -\frac{1}{4}\frac{1}{\Lambda}\big[c_\alpha\kappa_{\mathrm{HZZ}}\,\mathrm{Z}_{\mu\nu}\mathrm{Z}^{\mu\nu} + s_\alpha\kappa_{\mathrm{AZZ}}\,\mathrm{Z}_{\mu\nu}\widetilde{\mathrm{Z}}^{\mu\nu}\big] \\
& -\frac{1}{2}\frac{1}{\Lambda}\big[c_\alpha\kappa_{\mathrm{HWW}}\,\mathrm{W}_{\mu\nu}^+\mathrm{W}^{-\mu\nu} + s_\alpha\kappa_{\mathrm{AWW}}\,\mathrm{W}_{\mu\nu}^+\widetilde{\mathrm{W}}^{-\mu\nu}\big]\Bigg]\mathrm{X}_0,
\end{aligned}
\tag{210}
$$

where the (reduced) field strength tensors are

$$V_{\mu\nu} = \partial_\mu V_\nu - \partial_\nu V_\mu \quad (V = \mathrm{A,Z,W^\pm}), \tag{211}$$

$$G_{\mu\nu}^a = \partial_\mu G_\nu^a - \partial_\nu G_\mu^a + g_s f^{abc}G_\mu^b G_\nu^c, \tag{212}$$

and the dual tensor is

$$\widetilde{V}_{\mu\nu} = \frac{1}{2}\epsilon_{\mu\nu\rho\sigma}V^{\rho\sigma}. \tag{213}$$

The model parameters in the Lagrangian that are possible to be modified are listed in Table 58. This parameterization allows to describe the mixing between CP-even and CP-odd states and correspondingly to give an effective description of a reasonably ample range of CP-violating scenarios, such as those arising in SUSY or in a generic 2HDM.

The dimensionful couplings are set so as to reproduce a SM Higgs in the case $c_\alpha = 1$ and a pseudo scalar in a 2HDM with $\tan\beta = 1$ for the default values of κ_i, e.g. $g_{\mathrm{Hff}} = m_{\mathrm{f}}/v$ and $g_{\mathrm{HVV}} = 2m_{\mathrm{V}}^2/v$ as well as $g_{\mathrm{Hgg}} = -\alpha_s/3\pi v$ in the heavy top loop limit.

11.5.1.2 Spin 1

The spin-1 X interaction Lagrangian with fermions is

$$\mathcal{L}_1^{\mathrm{f}} = \sum_{f=\mathrm{u,d}} \bar{\psi}_{\mathrm{f}}\gamma_\mu(\kappa_{f_a}a_{\mathrm{f}} - \kappa_{f_b}b_{\mathrm{f}}\gamma_5)\psi_{\mathrm{f}}\mathrm{X}_1^\mu, \tag{214}$$

where u and d denote the up-type and down-type quarks, respectively. The a_f and b_f are the SM couplings, i.e.

$$a_\mathrm{u} = \frac{g}{2c_\mathrm{w}}\left(\frac{1}{2} - \frac{4}{3}s_\mathrm{w}^2\right), \quad b_\mathrm{u} = \frac{g}{2c_\mathrm{w}}\frac{1}{2}, \tag{215}$$

$$a_\mathrm{d} = \frac{g}{2c_\mathrm{w}}\left(-\frac{1}{2} + \frac{2}{3}s_\mathrm{w}^2\right), \quad b_\mathrm{d} = -\frac{g}{2c_\mathrm{w}}\frac{1}{2}. \tag{216}$$

The XWW interaction at the lowest dimension is in general [529]

$$\begin{aligned}
\mathcal{L}_1^\mathrm{W} = &+ i\kappa_{\mathrm{V}_1} g_\mathrm{WWZ}(\mathrm{W}^+{}_{\mu\nu}\mathrm{W}^{-\mu} - \mathrm{W}^-{}_{\mu\nu}\mathrm{W}^{+\mu})\mathrm{X}_1^\nu \\
&+ i\kappa_{\mathrm{V}_2} g_\mathrm{WWZ}\mathrm{W}^+{}_\mu\mathrm{W}^-{}_\nu\mathrm{X}_1^{\mu\nu} \\
&- \kappa_{\mathrm{V}_3}\mathrm{W}^+{}_\mu\mathrm{W}^-{}_\nu(\partial^\mu\mathrm{X}_1^\nu + \partial^\nu\mathrm{X}_1^\mu) \\
&+ i\kappa_{\mathrm{V}_4}\mathrm{W}^+{}_\mu\mathrm{W}^-{}_\nu\widetilde{\mathrm{X}}_1^{\mu\nu} \\
&- \kappa_{\mathrm{V}_5}\epsilon_{\mu\nu\rho\sigma}[\mathrm{W}^{+\mu}(\partial^\rho\mathrm{W}^{-\nu}) - (\partial^\rho\mathrm{W}^{+\mu})\mathrm{W}^{-\nu}]\mathrm{X}_1^\sigma, \tag{217}
\end{aligned}$$

where $g_\mathrm{WWZ} = e\cot\theta_\mathrm{w}$. Similarly, the XZZ interaction is given by [491]

$$\mathcal{L}_1^\mathrm{Z} = - \kappa_{\mathrm{V}_3}\mathrm{X}_1^\mu(\partial^\nu\mathrm{Z}_\mu)\mathrm{Z}_\nu \tag{218}$$

$$- \kappa_{\mathrm{V}_5}\epsilon_{\mu\nu\rho\sigma}\mathrm{X}_1^\mu\mathrm{Z}^\nu(\partial^\rho\mathrm{Z}^\sigma). \tag{219}$$

For $\mathrm{X}_1 = 1^-$ in parity-conserving scenarios:

$$\kappa_{f_a,\mathrm{V}_1,\mathrm{V}_2,\mathrm{V}_3} \neq 0. \tag{220}$$

For $\mathrm{X}_1 = 1^+$ in parity-conserving scenarios:

$$\kappa_{f_b,V_4,V_5} \neq 0. \tag{221}$$

11.5.1.3 Spin 2

The spin-2 X interaction Lagrangian starts from the dimension-five terms [446, 468, 530, 531]:

$$\mathcal{L}_2^\mathrm{f} = -\frac{1}{\Lambda}\sum_{f=\mathrm{q},\ell}\kappa_f\, T_{\mu\nu}^f\mathrm{X}_2^{\mu\nu}, \tag{222}$$

and

$$\begin{aligned}
\mathcal{L}_2^\mathrm{V} = &- \frac{1}{\Lambda}\kappa_\mathrm{V}\, T_{\mu\nu}^V\mathrm{X}_2^{\mu\nu} \\
&- \frac{1}{\Lambda}\kappa_\gamma\, T_{\mu\nu}^\gamma\mathrm{X}_2^{\mu\nu} \\
&- \frac{1}{\Lambda}\kappa_\mathrm{g}\, T_{\mu\nu}^\mathrm{g}\mathrm{X}_2^{\mu\nu}, \tag{223}
\end{aligned}$$

where $V = \mathrm{Z}, \mathrm{W}^\pm$ and $T_{\mu\nu}^i$ is the energy-momentum tensor of the SM fields; see e.g. [532] for the explicit forms. The even higher dimensional terms [465], dimension-seven, are also implemented as

$$\begin{aligned}
\mathcal{L}_2^{V_\mathrm{HD}} = &- \frac{1}{4}\frac{1}{\Lambda^3}\kappa_{\mathrm{V}_1}(\partial_\nu(\partial_\mu(\mathrm{Z}_{\rho\sigma}\mathrm{Z}^{\rho\sigma} + 2\mathrm{W}^+_{\rho\sigma}\mathrm{W}^{-\rho\sigma})))\mathrm{X}_2^{\mu\nu} \\
&- \frac{1}{4}\frac{1}{\Lambda^3}\kappa_{\mathrm{V}_2}(\partial_\nu(\partial_\mu(\mathrm{Z}_{\rho\sigma}\widetilde{\mathrm{Z}}^{\rho\sigma} + 2\mathrm{W}^+_{\rho\sigma}\widetilde{\mathrm{W}}^{-\rho\sigma})))\mathrm{X}_2^{\mu\nu}
\end{aligned}$$

$$-\frac{1}{4}\frac{1}{\Lambda^3}\kappa_{\gamma_1}(\partial_\nu(\partial_{mu}A_{\rho\sigma}A^{\rho\sigma}))X_2^{\mu\nu}$$

$$-\frac{1}{4}\frac{1}{\Lambda^3}\kappa_{\gamma_2}(\partial_\nu(\partial_{mu}A_{\rho\sigma}\widetilde{A}^{\rho\sigma}))X_2^{\mu\nu}$$

$$-\frac{1}{4}\frac{1}{\Lambda^3}\kappa_{g_1}(\partial_\nu(\partial_\mu G_{\rho\sigma}G^{\rho\sigma}))X_2^{\mu\nu}$$

$$-\frac{1}{4}\frac{1}{\Lambda^3}\kappa_{g_2}(\partial_\nu(\partial_\mu G_{\rho\sigma}\widetilde{G}^{\rho\sigma}))X_2^{\mu\nu}, \tag{224}$$

where $V_{\mu\nu} = \partial_\mu V_\nu - \partial_\nu V_\mu$, etc, are the reduced field strength tensor.

For $X_2 = 2^+$ in the RS-like graviton scenario:

$$\kappa_f = \kappa_V = \kappa_\gamma = \kappa_g \neq 0. \tag{225}$$

For $X_2 = 2^+$ with the higher-dimensional operator in parity-conserving scenarios:

$$\kappa_{V_1}, \kappa_{\gamma_1}, \kappa_{g_1} \neq 0. \tag{226}$$

For $X_2 = 2^-$ with the higher-dimensional operator in parity-conserving scenarios:

$$\kappa_{V_2}, \kappa_{\gamma_2}, \kappa_{g_2} \neq 0. \tag{227}$$

11.5.2 Comparison plots with JHU

In this section we show comparison plots with JHU results in Ref. [465] for $pp \to X \to VV^* \to 4\ell$.

11.5.2.1 Event generation

50K events with $mX = 125$ GeV at the 8TeV-LHC were generated for each spin state with the MG5 (v1.5.9). Note that all the kinematical cuts for leptons are removed. We note that we remove photons for diagram generation for spin-2, while the X_0-Z-γ contribution for spin-0 can be removed by setting $\kappa_{HZ\gamma} = \kappa_{AZ\gamma} = 0$. We also note that the spin-2 case has seven diagrams, one double-V resonant diagram and six single-V diagrams including the four point X_2-V-ℓ-ℓ diagrams. Those single resonant contributions can be removed by setting $\kappa_\ell = 0$.

11.5.2.2 Distributions

The translation of the notation for the kinematical variables to JHU is

$$\phi_1 \to \Phi_1, \quad \phi_1 - \phi_2 \to \Phi. \tag{228}$$

Note also that the azimuthal angles are defined from 0 to 2π here, while $-\pi$ to π in the JHU paper. The parameter set for the JHU comparison are listed in Table 59.

As shown in Figs. 93 and 94, all the distributions agree with the JHU ones. Moreover, the lowest dimensional spin-2 is consistent with the RS model in MG5. The comparison for the higher dimensional terms for spin-2 is in progress and will be reported elsewhere [528].

spin-0   spin-1   spin-2
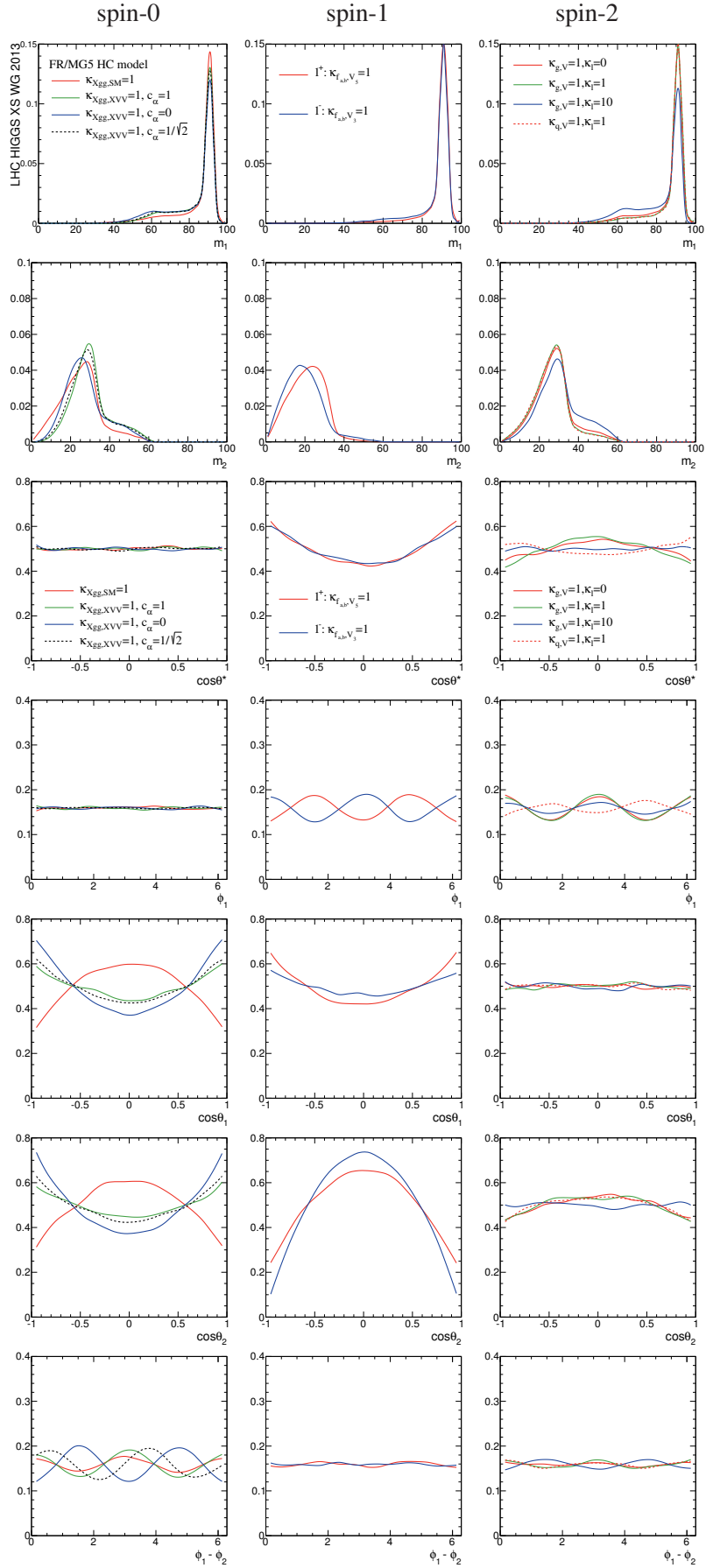
Figure 93: Distributions of the X → ZZ analysis; see also JHU Figs. 11 and 12 [465].

Table 59: Parameter set for the JHU comparison; see also Table I in the JHU implementation [465].

JHU scenario	HC parameter choice
0_m^+	$\kappa_{\mathrm{Hgg}} \neq 0,\ \kappa_{\mathrm{SM}} \neq 0,\ c_\alpha = 1$
0_h^+	$\kappa_{\mathrm{Hgg}} \neq 0,\ \kappa_{HVV} \neq 0,\ c_\alpha = 1$
0^-	$\kappa_{\mathrm{Agg}} \neq 0,\ \kappa_{\mathrm{AVV}} \neq 0,\ c_\alpha = 0$
1^+	$\kappa_{fu_a} = \kappa_{fu_b} = \kappa_{fd_a} = \kappa_{fd_b} \neq 0,\ \kappa_{V_5} \neq 0$
1^-	$\kappa_{fu_a} = \kappa_{fu_b} = \kappa_{fd_a} = \kappa_{fd_b} \neq 0,\ \kappa_{V_3} \neq 0$
2_m^+	$\kappa_{\mathrm{g}} \neq 0,\ \kappa_{\mathrm{V}} \neq 0$
2_h^+	$\kappa_{\mathrm{g}_1} \neq 0,\ \kappa_{\mathrm{V}_1} \neq 0$
2_h^-	$\kappa_{\mathrm{g}_2} \neq 0,\ \kappa_{\mathrm{V}_2} \neq 0$
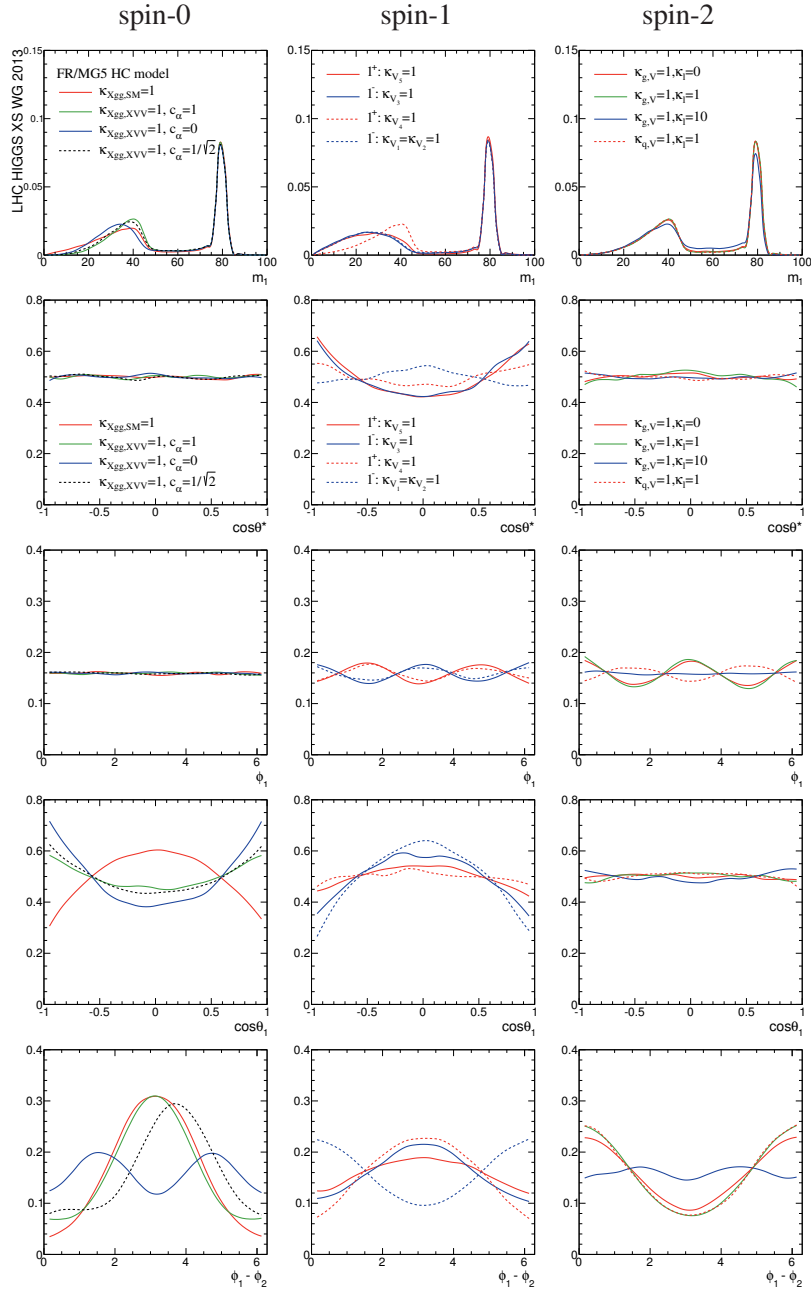
Figure 94: Distributions of the X → WW analysis; see also JHU Fig. 13 [465].

12 Heavy Higgs search [54]

The search for an heavy Higgs with mass greater than 400 GeV assuming Standard Model (SM) properties is well motivated by the necessity to directly explore all the available mass range up to 1 TeV without having any prejudice on the nature of the more recently discovered 125 GeV resonance, and by the possibility to use these searches as a starting point for specific Beyond the Standard Model (BSM) extensions which can be studied by simply rescaling SM analysis. This will be extensively discussed in Section 13.

The main differences between low and high mass regions will be discussed in Section 12.1, the available Monte Carlo generators will be presented in Section 12.2 and the studies performed by using these generators and specific tools developed for the high mass region searches will be summarized in Section 12.3. Finally the Vector Boson Fusion case will be discussed in Section 12.4.

12.1 Lineshape and signal/background interference in $gg \rightarrow VV$

The lineshape of an unstable particle is usually described at NLO in Monte Carlo generators with a Breit-Wigner distribution. This approximation has an accuracy of the order Γ/m, where Γ is the width and m is the nominal mass of the particle, but it breaks down at high Higgs mass due to the very large Higgs width: $M_H \gtrsim 450$ GeV gives $\Gamma_H/M_H \gtrsim 10\%$.

The problem has been discussed in details in Ref. [87] and a more correct approach to describe the Higgs lineshape has been proposed, known as Complex Pole Scheme (CPS). The corresponding complete calculation of the lineshape in the $gg \rightarrow H \rightarrow VV$ process with assessment of the theoretical uncertainties is presented in Section 12.1.1.

An alternative general approach to describe the lineshape based on effective Lagrangian is presented in Section 12.1.3.

Another important effect that becomes very large with the increase of the Higgs mass is the interference between the signal and the $gg \rightarrow VV$ non resonant background, as recently discussed in Ref. [102]. In Section 12.1.2, this effect is addressed with a proposal to compute the theoretical uncertainties due to missing higher order perturbation terms in the current available interference estimation.

12.1.1 CPS - scheme

The general formalism for describing unstable particles in QFT was developed long ago, see Refs. [533–537]. For an implementation of the formalism in gauge theories we refer to the work of Refs. [538–541], for complex poles in general to Refs. [542–544].

We can summarize by saying that unstable particles are described by irreducible, non-unitary representations of the Poincare group, corresponding to the complex eigenvalues of the four-momentum p^μ satisfying the condition $p^2 = -\mu^2 + i\,\mu\gamma$.

A complete implementation of the Higgs-boson complex pole (within the SM) can be found in the work of Refs. [87, 108, 545].

In this Section we summarize the status of theoretical uncertainties (THU) associated with the Higgs boson lineshape. The recent observation of a new massive neutral boson by ATLAS and CMS opens a new era where characterization of this new object is of central importance. The search for the coupling structure of the light Higgs-like particle, as well as for new heavy states, will continue. The huge uncertainty used so far for the heavy Higgs searches [13] $(1.5\,(M_H/\,\mathrm{TeV})^3$ uncertainty on the

---

cross-section) was supposed to cover both the effect of the incorrect treatment of the lineshape and the missing interference. However, this uncertainty forced ATLAS and CMS to stop the search at 600 GeV, where the uncertainty is 30%.

In the following we will review recent improvements on estimating the THU. We do not discuss uncertainties coming from QCD scale variations[55] and from PDF $+\alpha_s$ [13].

Until recently, the Higgs boson invariant mass distribution (Higgs-boson-lineshape) has received little attention. In the work of Refs. [87, 108] we have made an attempt to resolve the problem by comparing different theoretical inputs to the off-shellness of the Higgs boson. There is no question at all that the zero-width approximation should be avoided, especially in the high-mass region where the on-shell width becomes of the same order as the on-shell mass, or higher. We have shown evidence that only the Dyson-resummed propagator should be used, leading to the introduction of the H complex pole, a gauge-invariant property of the S-matrix. It is convenient to describe the Complex-Pole scheme (CPS) as follows: the signal cross-section for the process $ij \to$ F can be written as

$$\sigma_{ij \to H \to F}(s) = \frac{1}{\pi} \sigma_{ij \to H} \frac{s^2}{\left| s - s_H \right|^2} \frac{\Gamma_H^{\text{tot}}(\sqrt{s})}{\sqrt{s}} BR(H \to F), \quad \Gamma_H^{\text{tot}}(\sqrt{s}) = \sum_F \Gamma_{H \to F}(\sqrt{s}). \quad (229)$$

where s is the Higgs virtuality, s_H is the Higgs complex pole and we have introduced a sum over all final states.

Note that the complex pole describing an unstable particle is conventionally parametrized as $s_i = \mu_i^2 - i\,\mu_i\,\gamma_i$. It would we desirable to include two- and three-loop contributions in γ_H and for some of these contributions only on-shell results have been computed so far. Therefore, it is very useful to give a rough estimate of the missing orders. Following the authors of Ref. [546] (as explained in Sect. 7 of Ref. [87]) we can estimate that the leading uncertainty in γ_H is roughly given by

$$\delta_H = 0.350119 \frac{G_F\,\mu_H^2}{2\sqrt{2}\pi^2}. \quad (230)$$

Uncertainty estimates in γ_H range from 2.3% at 400 GeV to 9.4% at 750 GeV. In general, we do not see very large variations up to 1 TeV with a breakdown of the perturbative expansion around 1.74 TeV. Therefore, using $\gamma_H (1 \pm \delta_H)$ we can give a rough but reasonable estimate of the remaining uncertainty on the lineshape. To summarize our estimate of the theoretical uncertainty associated to the signal: the remaining uncertainty on the production cross-section is typically well reproduced by $(\delta_H + 1)[\%]$, σ_{max} (the peak cross-section) changes approximately with the naive expectation, $2\,\delta_H[\%]$.

The factor $\Gamma_H^{\text{tot}}(\sqrt{s})$ in Eq.(229) deserves a separate discussion. It represents the "on-shell" decay of an Higgs boson of mass $\sqrt{s}$ and we have to quantify the corresponding uncertainty. The staring point is Γ^{tot} computed by PROPHECY4F [22] which includes two-loop leading corrections in $G_F M_H^2$, where M_H is now the on-shell mass. Next we consider the on-shell width in the Higgs-Goldstone model, discussed in [546, 547]. We have

$$\left. \frac{\Gamma_H}{\sqrt{s}} \right|_{HG} = \sum_{n=1}^{3} a_n \lambda^n = X_{HG}, \qquad \lambda = \frac{G_F s}{2\sqrt{2}\pi^2}. \quad (231)$$

Let $\Gamma_p = X_p \sqrt{s}$ the width computed by PROPHECY4F, we redefine the total width as

$$\frac{\Gamma_{\text{tot}}(\sqrt{s})}{\sqrt{s}} = \left(X_p - X_{HG} \right) + X_{HG} = \sum_{n=0}^{3} a_n \lambda^n, \quad (232)$$

193

where now $a_0 = X_{\mathrm{p}} - X_{\mathrm{HG}}$. As long as λ is not too large we can define a $p\% < 80\%$ credible interval (see the work of Ref. [548] for details) as (following from $a_{2,3} < a_1$)

$$\Gamma_{\mathrm{tot}}(\sqrt{s}) = \Gamma_{\mathrm{p}}(\sqrt{s}) \pm \Delta\Gamma, \qquad \Delta\Gamma = \frac{5}{4}\, \max\{|\, a_0\, |, a_1\}\, p\%\, \lambda^4\, \sqrt{s}. \tag{233}$$

The CPS has been recently implemented within the POWHEG-BOX Monte Carlo generator [80].

12.1.2 Interference signal - background

In the current experimental analysis there are additional sources of uncertainty, e.g. background and Higgs interference effects [549–553]. As a matter of fact, this interference is partly available and should not be included as a theoretical uncertainty; for a discussion and results we refer to Refs. [554–556].

Here we will examine the channel $\mathrm{gg} \to \mathrm{ZZ}$ and discuss the associated THU. The background (continuum $\mathrm{gg} \to \mathrm{ZZ}$) and the interference are only known at leading order (LO, one-loop) [557]. Here we face two problems, a missing NLO calculation of the background (two-loop) and the NLO and NNLO signal at the amplitude level, without which there is no way to improve upon the present LO calculation[56].

A potential worry, already addressed in Ref. [554], is: should we simply use the full LO calculation or should we try to effectively include the large (factor two) K-factor to have effective NNLO observables? There are different opinions since interference effects may be as large or larger than NNLO corrections to the signal. Therefore, it is important to quantify both effects. Let us consider any distribution D, i.e.

$$D = \frac{d\sigma}{dx} \quad x = M_{\mathrm{ZZ}} \quad \text{or} \quad x = p_\perp^{\mathrm{Z}} \quad \text{etc.} \tag{234}$$

where M_{ZZ} is the invariant mass of the ZZ-pair and $p_\perp^{\mathrm{Z}}$ is the transverse momentum. We introduce the following options, see Ref. [102] (S, B and I are shorthands for signal, background and interference):

– **additive** where one computes

$$\frac{d\sigma_{\mathrm{eff}}^{\mathrm{NNLO}}}{dx} = \frac{d\sigma^{\mathrm{NNLO}}}{dx}(S) + \frac{d\sigma^{\mathrm{LO}}}{dx}(I) + \frac{d\sigma^{\mathrm{LO}}}{dx}(B) \tag{235}$$

– **multiplicative** where one computes

$$\frac{d\sigma_{\mathrm{eff}}^{\mathrm{NNLO}}}{dx} = K_{\mathrm{D}}\left[\frac{d\sigma^{\mathrm{LO}}}{dx}(S) + \frac{d\sigma^{\mathrm{LO}}}{dx}(I)\right] + \frac{d\sigma^{\mathrm{LO}}}{dx}(B), \qquad K_{\mathrm{D}} = \frac{\frac{d\sigma^{\mathrm{NNLO}}}{dx}(S)}{\frac{d\sigma^{\mathrm{LO}}}{dx}(S)}, \tag{236}$$

where K_{D} is the differential K-factor for the distribution. Note that K_{D} accounts for both QCD and EW higher order effects in the production and in the decay.

– **intermediate** It is convenient to define

$$K_{\mathrm{D}} = K_{\mathrm{D}}^{\mathrm{gg}} + K_{\mathrm{D}}^{\mathrm{rest}}, \qquad K_{\mathrm{D}}^{\mathrm{gg}} = \frac{\frac{d\sigma^{\mathrm{NNLO}}}{dx}\big(\mathrm{gg} \to \mathrm{H(g)} \to \mathrm{ZZ(g)}\big)}{\frac{d\sigma^{\mathrm{LO}}}{dx}\big(\mathrm{gg} \to \mathrm{H} \to \mathrm{ZZ}\big)}, \tag{237}$$

$$\frac{d\sigma_{\mathrm{eff}}^{\mathrm{NNLO}}}{dx} = K_{\mathrm{D}}\frac{d\sigma^{\mathrm{LO}}}{dx}(S) + \left(K_{\mathrm{D}}^{\mathrm{gg}}\right)^{1/2}\frac{d\sigma^{\mathrm{LO}}}{dx}(I) + \frac{d\sigma^{\mathrm{LO}}}{dx}(B)\,. \tag{238}$$

Our recipe for estimating the theoretical uncertainty in the effective NNLO distribution is as follows: the intermediate option gives the *central value*, while the band between the multiplicative and the additive options gives the uncertainty. Note that the difference between the intermediate option and the

---

[56]There is, however, a recent and promising attempt to go beyond leading-order in Ref. [558].

median of the band is always small if not far away from the peak where, in any case, all options become questionable.

For an inclusive quantity the effect of the interference, with or without the NNLO K-factor for the signal, is almost negligible. For distributions this is radically different; referring to the ZZ invariant mass distribution we can say that, close to $M_{\rm ZZ} = \mu_{\rm H}$, the uncertainty is small but becomes large in the rest of the search window $[\mu_{\rm H} - \gamma_{\rm H}\,,\,\mu_{\rm H} + \gamma_{\rm H}]$. The effect of the LO interference, w.r.t. LO $S + B$, reaches a maximum before the peak (e.g. $+16\%$ at $\mu_{\rm H} = 700$ GeV) while our estimate of the scaled interference (always w.r.t. LO $S + B$) is $86^{+7}_{-3}\%$ in the same region, showing that NNLO signal effects are not negligible[57].

EW corrections to $\rm gg \to H$ *and* $\rm H \to VV$

The NLO EW corrections to gluon fusion have been computed in Refs. [49, 560]. The original results have been produced up to a Higgs invariant mass of 1 TeV. If one is interested in the lineshape corresponding to a Higgs mass of 600 GeV- 1 TeV there will be some non-negligible fraction of events with invariant mass up to 2 TeV. In this case extrapolation will give wrong results; for this reason we have provided additional values for the NLO EW correction factor to the inclusice cross-section: $\delta_{\rm W} = +19.37\%(+34.53\%, +53.90\%)$ for $\mu_{\rm H} = 1.5$ TeV$(2$ TeV$, 2.5$ TeV$)$[58]. Also $\Gamma_{\rm H}^{\rm tot}$ of Eq.(229) needs some attention. The best results available are from Ref. [13] where, however, tables stop at 1 TeV. If one wants to go above this value extrapolation should be avoided and it is better to include few additional points in the grid, e.g. we have included $\Gamma_{\rm H}^{\rm tot} = 3.38(15.8)$ TeV for $\mu_{\rm H} = 1.5(2)$ TeV. Note that, at 2 TeV, one has $\Gamma({\rm H} \to {\rm ZZ}) = 5.25$ TeV and $\Gamma({\rm H} \to {\rm WW}) = 10.52$ TeV. Finally, mention should be made of the very recent estimate of the $\rm N^3LO$ QCD corrections, see Ref. [563].

---

[57]Complete set of results, including results for the THU discussed in Section 12.1.1, and a code for computing the SM Higgs complex pole can be found at [559].

[58]A complete grid up to 2.5 TeV (see Refs. [49, 560, 561]) and a program for a cubic interpolating spline incorporating the grid can be found at [562].

12.1.3 Effective lineshape

The phenomenology of a new resonance, including searches and exclusion limits at the LHC, depends significantly on the lineshape. When large, i.e., comparable to the mass, off-shell effects becomes relevant and the very same quantum field theoretic definition of width becomes non trivial. Taking a heavy Higgs boson as an example, we propose a new formulation of the lineshape obtained via an effective field theory approach. Our method leads to amplitudes that are gauge invariant, respect unitarity and it can be thought of as a generalization of the complex mass scheme. We consider applications to the phenomenology of a heavy SM-like scalar that are relevant for the LHC.

12.1.3.1 Introduction

In this work we tackle the problem from an Effective Field Theory (EFT) point of view. We propose to systematically include width effects via a set of gauge invariant higher dimensional terms to the SM Lagrangian, along the lines of what was first proposed in Refs. [564, 565]. Such new operators systematically encapsulate higher order terms coming from the self-energy and naturally allow a running and physical width for the Higgs in a gauge invariant way. As we will show in the following, our scheme is consistent at higher orders and it can be considered a generalization of the CMS(Complex Mass Scheme) as it reduces to it in the limit where the dependence on the virtuality of the Higgs self-energy is neglected.

12.1.3.2 Setting up the stage

The two-point Green's function for the Higgs boson is

$$\Delta_{\mathrm{H}}(s) = s - M_{\mathrm{H},0}^2 + \Pi_{\mathrm{HH}}(s) , \tag{239}$$

where $M_{\mathrm{H},0}$ is the bare mass, and $\Pi_{\mathrm{HH}}(s)$ is the Higgs self-energy. In the conventional on-shell definition, the mass and width are given by

$$M_{\mathrm{H},\mathrm{OS}}^2 = M_{\mathrm{H},0}^2 - \mathrm{Re}\Pi(M_{\mathrm{H},\mathrm{OS}}^2) , \tag{240}$$

$$M_{\mathrm{H},\mathrm{OS}}\Gamma_{\mathrm{H},\mathrm{OS}} = \frac{\mathrm{Im}\Pi(M_{\mathrm{H},\mathrm{OS}}^2)}{1 + \mathrm{Re}\Pi'(M_{\mathrm{H},\mathrm{OS}}^2)} . \tag{241}$$

These definitions become gauge-dependent at order $\mathcal{O}(g^4)$.

In order to avoid the divergence of the tree-level propagator $D(s) = i/(s - M_{\mathrm{H},OS}^2)$, one performs the Dyson resummation to obtain

$$D(s) = \frac{i}{s - M_{\mathrm{H},\mathrm{OS}}^2 + iM_{\mathrm{H},\mathrm{OS}}\Gamma_{\mathrm{H},\mathrm{OS}}} . \tag{242}$$

To include the running effects of the width, one can further approximate the propagator by

$$D(s) = \frac{i}{s - M_{\mathrm{H},\mathrm{OS}}^2 + i\mathrm{Im}\Pi(s)} , \tag{243}$$

where the imaginary part of $\Pi(s)$ is related to the Higgs-boson width. The consistency of the above treatments of the Higgs propagator with the equivalence theorem and unitarity has been discussed in Refs. [566, 567].

Alternatively, as shown in a series of papers [540–542, 568–574] a consistent, convenient and resilient definition of mass μ and width γ up to two loops, is obtained by setting $s_{\mathrm{H}} \equiv \mu^2 - i\mu\gamma$ and then solving the implicit equation

$$s_{\mathrm{H}} - M_{\mathrm{H},0}^2 + \Pi_{\mathrm{HH}}(s_{\mathrm{H}}) = 0 \tag{244}$$

in terms of s_H. This gives a gauge independent definition to all orders [538, 539, 575] (independent of the gauge choice present in the computation of $\Pi_{HH}(s_H)$) and in addition avoids unphysical threshold singularities [576].

The above definition is also consistent with the use of the CMS. In this scheme the propagator is $\Delta_H^{-1}(s) = s - s_H$. By definition this approach can give a good approximation of the full propagator

$$\Delta_H^{-1}(s) = \frac{1}{s - s_H + \Pi_{HH}^R(s)} \tag{245}$$

only close to the pole or, equivalently, for a small width, $\gamma/\mu \ll 1$. Here $\Pi_{HH}^R(s)$ is the renormalized self energy, satisfying the following renormalization conditions:

$$\Pi_{HH}^R(s_H) = 0 \,, \quad \Pi_{HH}'^R(s_H) = 0 \,. \tag{246}$$

A natural improvement would consist in including the full resummed propagator in explicit calculations. This, however, leads to gauge violation already at the tree level. The reason being that in perturbation theory gauge invariance is guaranteed order by order while the presence of a width implies the resummation of a specific subset of higher order contributions, the self-energy corrections. This results in a mixing of different orders of perturbation theory. In particular, the following issues need to be addressed:

1. In general $\Pi_{HH}(s)$ explicitly depends on the gauge-fixing parameter (GFP). To resum the self-energy correction to all orders, $\Pi_{HH}(s)$ must be extracted in a physically meaningful way.
2. The resummed propagator spoils the gauge cancellation among different diagrams, and eventually leads to the violation of Goldstone-boson equivalence theorem and unitarity bound.

Both issues can be tackled by the so-called Pinch Technique (PT) [577–580]. In the PT framework, a modified one-loop self-energy for the Higgs boson can be constructed by appending to the conventional self energy additional propagator-like contributions concealed inside vertices and boxes. For the application of PT in resonant transition amplitude, and in particular, the extraction of a physical self energy, we refer to Refs. [581–585].

The modified self-energy correction for the Higgs is GFP-independent, and reflects properties generally associated with physical observables. At the one loop level, we have the following expressions [584, 586]

$$\Pi_{HH}^{(WW)}(s) = \frac{\alpha_w}{16\pi} \frac{M_H^4}{M_W^2} \left[1 + 4\frac{M_W^2}{M_H^2} - 4\frac{M_W^2}{M_H^4}(2s - 3M_W^2) \right] B_0(s, M_W^2, M_W^2) \,, \tag{247}$$

$$\Pi_{HH}^{(ZZ)}(s) = \frac{\alpha_w}{32\pi} \frac{M_H^4}{M_W^2} \left[1 + 4\frac{M_Z^2}{M_H^2} - 4\frac{M_Z^2}{M_H^4}(2s - 3M_Z^2) \right] B_0(s, M_Z^2, M_Z^2) \,, \tag{248}$$

$$\Pi_{HH}^{(ff)}(s) = \frac{3\alpha_w}{8\pi} \frac{m_f^2}{M_W^2} \left(s - 4m_f^2 \right) B_0(s, m_f^2, m_f^2) \,, \tag{249}$$

$$\Pi_{HH}^{(HH)}(s) = \frac{9\alpha_w}{32\pi} \frac{M_H^4}{M_W^2} B_0(s, M_H^2, M_H^2) \,, \tag{250}$$

where the superscripts denote the contributions from the W, Z, fermions and Higgs loops, and

$$B_0(p^2, m_1^2, m_2^2)$$
$$\equiv (2\pi\mu)^{4-d} \int \frac{d^d k}{i\pi^2} \frac{1}{(k^2 - m_1^2)[(k+p)^2 - m_2^2]} \tag{251}$$

is the normal Passarino-Veltman function [587, 588]. These results are independent of the GFP. Note that the expressions in Eqs. (247–250) coincide with the $\xi = 1$ result obtained in the background-field gauge [589–591].

In addition, the gauge cancellation among different amplitudes can be restored, by including certain vertex corrections obtained via the PT [586, 592]. This is because in this framework the Green's functions satisfy the tree-level-like Ward Identities (WI), which are crucial for ensuring the gauge invariance of the resummed amplitude.
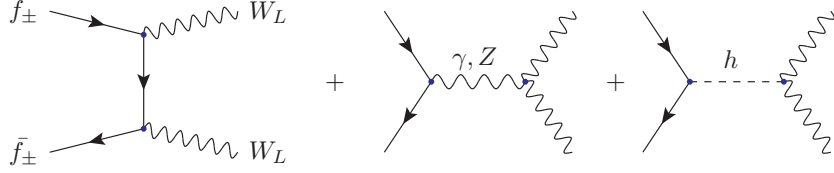
Figure 95: Diagrams contributing to fermion anti-fermion scattering into longitudinal W's.

As an example, let us consider the Higgs-mediated part of same helicity fermion scattering into longitudinal W's, $f_\pm \bar{f}_\pm \to W^+_L W^-_L$. There are contributions from s-channel and t-channel diagrams, as is shown in Fig. 95. The contributions from t-channel and Higgs diagram to the amplitudes coming from longitudinal components of the W's and same helicity fermions (in the high energy limit) read [59]

$$\mathcal{M}^L_h \equiv \mathcal{M}^{\mu\nu}_s \frac{k_{1\mu} k_{2\nu}}{M^2_W}$$

$$= \frac{-igm_f}{2M_W} \bar{v}(p_2) u(p_1) \frac{i}{\Delta_H(s)} \Gamma^{\text{HWW},\mu\nu}(q, k_1, k_2) \frac{k_{1\mu} k_{2\nu}}{M^2_W}$$

$$\mathcal{M}^L_t \equiv \mathcal{M}^{\mu\nu}_{t,Z} \frac{k_{1\mu} k_{2\nu}}{M^2_W}$$

$$= -\frac{ig^2 m_f}{4M^2_W} \bar{v}(p_2) u(p_1) + \cdots \tag{252}$$

where $\Gamma^{\text{HWW}}_{\mu\nu}(q, k_1, k_2)$ is the HW^+W^- vertex. The ellipsis in $\mathcal{M}^L_t$ denotes terms that are not related to the Higgs exchange diagram. These terms come from the contribution of opposite helicity fermions, and are supposed to cancel the bad high-energy behavior of the γ/Z mediated diagrams.

Without the Higgs contribution $\mathcal{M}^L$ grows with energy and eventually violates unitarity. The cancellation of the bad high-energy behavior of each amplitude, and the equivalence theorem, are guaranteed by the following WI:

$$k^\mu_+ k^\nu_- \Gamma^{\text{HWW}}_{\mu\nu}(q, k_+, k_-) =$$
$$- M^2_W \Gamma^{\text{H}\phi^+\phi^-}(q, k_+, k_-) + \frac{igM_W}{2} \Delta_H(q^2), \tag{253}$$

where $\phi^\pm$ are Nambu-Goldstone bosons. Only the leading terms at high energy are included. The relation above explicitly shows that the inclusion of higher order terms in the imaginary part of $\Delta_H(q^2)$ has to be related to the EW corrections of $\Gamma^{\text{HWW}}_{\mu\nu}$ and three scalar vertex. Only if both $\Delta_H(s)$ and $\Gamma^{\text{HWW}}_{\mu\nu}$ are computed in one-loop via the PT, then the WI remains valid, and the gauge-cancellation, as well as the equivalence theorem, are not spoiled. Besides, $\mathcal{M}^L_{t,Z}$ is not affected by the Higgs width and therefore the tree-level relations can be used. Thus the resummed propagator can be consistently included with the one-loop correction to $\Gamma^{\text{HWW}}_{\mu\nu}$ via the PT.

---

[59]Here we assume $\epsilon^\mu_{1,2} \approx k^\mu_{1,2}/M_W$ at high energy region.

Even though correct, the solution outlined above for $f\bar{f} \to W^+_L W^-_L$ is not a general one. In $W^+_L W^-_L \to Z_L Z_L$, for example, it is not sufficient to include only the HWW and HZZ corrections. The triple and quartic vector-boson vertices at one-loop are also required to cancel the bad high-energy behavior of the Higgs-mediated amplitude and the overall procedure of analyzing the full set of WI's becomes more and more involved. The goal of this work is to present a simple method to generate the needed corrections to the vertices and propagators so that the WI's are automatically satisfied and unitarity automatically ensured.

12.1.3.3 The EFT approach

As explained above, we aim at finding a systematic approach to improve the Higgs propagator without breaking either gauge invariance or unitarity. In other words we are looking for a mechanism that guarantees the constraints imposed by the WI to be satisfied at any order in perturbation theory.

At one loop, the full calculation via the PT certainly provides an exact solution valid at NLO. The challenge is to achieve the same keeping the calculation at leading order, including only the necessary ingredients coming from NLO and resumming them into the propagator via a Dyson-Schwinger approach. The idea is to associate the corrections to an ad hoc constructed gauge-invariant operator and match the operator to the one-loop two-point function $\Delta_H(s)$ calculated via the PT. In so doing one aims at obtaining the exact resummed propagator already at the leading order and, *at the same time*, the interactions modified to automatically satisfy the WI's. The latter desired result ensures the gauge-invariance of the amplitudes, and it can be considered as an approximation to a full one-loop calculation in PT.

To this aim, we consider the Taylor expansion of the function $\Pi(s) = \Pi^R_{HH}(s)$

$$\Pi(s) = \sum_{i=0}^{\infty} c_i s^i, \tag{254}$$

where c_i are dimensionful constants and, as first attempt, we add the following infinite set of operators to the Lagrangian:

$$\mathcal{O}_\Pi = \sum_{i=0}^{\infty} c_i \phi^\dagger (-D^2)^i \phi$$
$$\equiv \phi^\dagger \Pi(-D^2)\phi \tag{255}$$

where ϕ is the Higgs doublet, and D^μ is the covariant derivative. It is straightforward to check that $\mathcal{O}_\Pi$ modifies the Higgs propagator as desired: the two ϕ's contribute two Higgs fields, and each $-D^2$ contributes an s leading to

$$\Pi(s) = \Pi^R_{HH}(s), \tag{256}$$

as desired. Note that in principle, $\mathcal{O}_\Pi$ is a non-local operator, yet by expanding it, we re-express it in terms of an infinite series of local operators.[60]

We remark that while very similar in spirit , our approach differs from that of Ref. [564]: the operator chosen there does not contain gauge fields, and it is therefore not sufficient to restore the gauge cancellation and fix the bad high-energy behavior in vector-vector scattering.

Eq. (255) leads to the correct expression for the propagator. However, the first term $\Pi(0)\phi^\dagger\phi$ in the expansion corresponds to a tadpole contribution. This can be avoided if this term is replaced by

$$\Pi(0)\phi^\dagger\phi \to \frac{\Pi(0)}{2v^2}\left[(\phi^\dagger\phi) - \frac{v^2}{2}\right]^2,$$

---

[60]In general, inclusion of higher-order derivatives in the Lagrangian leads to very peculiar quantum field theories, aka Lee-Wick theories, see [593] for a recent analysis and references. As we are going to see later, in our approach, we only use the imaginary part of $\Pi(s)$ and therefore the real part of the propagator is not affected.
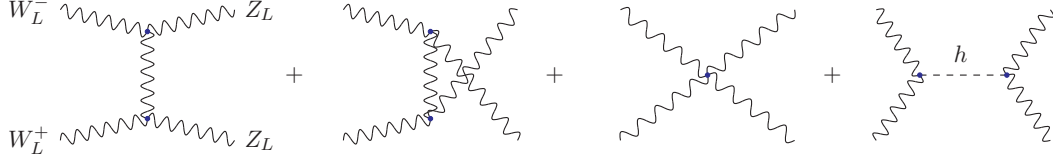
Figure 96: Diagrams contributing to $W^+_L W^-_L \to Z_L Z_L$

i.e., the Higgs-self interaction is suitably modified. As one can easily check, such a modification leaves the relation of Eq. (256) unchanged. The final form of the operator, which we dub $\tilde{\mathcal{O}}_\Pi$, is

$$\tilde{\mathcal{O}}_\Pi = \phi^\dagger [\Pi(-D^2) - \Pi(0)]\phi + \frac{\Pi(0)}{2v^2}\left[(\phi^\dagger\phi) - \frac{v^2}{2}\right]^2 . \tag{257}$$

The addition of this operator to the SM leads to several changes, which we now consider in detail. First of all, by construction, it gives rise to the propagator in Eq. (245), and a resummed propagator with the full one-loop self energy via the PT at tree level is obtained. Second it leads to modifications of the other interactions, in such a way that gauge invariance is maintained. For example, the W and Z two-point functions are modified by the addition of

$$i\Delta\Pi^{\mu\nu}_{WW}(q^2) = i\left(\frac{gv}{2}\right)^2 \left[\Pi'(0)g^{\mu\nu} + \Pi''(q^2)q^\mu q^\nu\right] ,$$

$$i\Delta\Pi^{\mu\nu}_{ZZ}(q^2) = i\left(\frac{gv}{2c_{\rm w}}\right)^2 \left[\Pi'(0)g^{\mu\nu} + \Pi''(q^2)q^\mu q^\nu\right] ,$$

where v is the Higgs vev, and

$$\Pi'(x) \equiv \frac{\Pi(x) - \Pi(0)}{x}, \qquad \Pi''(x) \equiv \frac{\Pi'(x) - \Pi'(0)}{x} . \tag{258}$$

The values for the W and Z masses are shifted

$$M_{\rm W}^2 = \left(\frac{gv}{2}\right)^2 (1 + \Pi'(0))$$

$$M_Z^2 = \left(\frac{gv}{2c_{\rm w}}\right)^2 (1 + \Pi'(0)), \tag{259}$$

as well as the propagators

$$\frac{i}{q^2 - m_{W,Z}^2}\left[-g^{\mu\nu} + \frac{\left(1 + \frac{m_{W,Z}^2 \Pi''(q^2)}{1+\Pi'(0)}\right)q^\mu q^\nu}{m_{W,Z}^2 + q^2 \frac{m_{W,Z}^2 \Pi''(q^2)}{1+\Pi'(0)}}\right] . \tag{260}$$

Let us first consider $f\bar{f} \to W^+_L W^-_L$ in the EFT approach. The operator modifies the HW^+W^- and the $Hf\bar{f}$ interactions. The combined effect is a factor of $1 + \Pi'(s)$. Therefore in this process the EFT approach is equivalent to the following substitution of the Higgs propagator:

$$\Delta_{\rm H}^{-1}(s) = \frac{1 + \Pi'(s)}{s - s_{\rm H} + \Pi(s)} , \tag{261}$$

which behaves like $1/s$ at large energy, and therefore exactly cancels the high-energy behavior from $\mathcal{M}_t^L$. It is also interesting to note that, if $\Pi(s)$ has a linear dependence on s, i.e.,

$$\Pi(s) = i(s - \mu^2)\frac{\gamma}{\mu} , \tag{262}$$

200

the above equation becomes

$$\Delta_{\mathrm{H}}^{-1}(s) = \frac{1 + i\frac{\gamma}{\mu}}{s - \mu^2 + is\frac{\gamma}{\mu}} \,, \tag{263}$$

and the EFT approach coincides with the scheme proposed by Seymour [594]. This could be expected because in the Seymour scheme the vector boson pair self energy also has a linear dependence on s. In our scheme we see that the numerator of Seymour's propagator comes from the modified $\mathrm{HW^+W^-}$ vertex, as required by the WI.

We now turn to vector-vector scattering and in particular to $\mathrm{W^+_L W^-_L \to Z_L Z_L}$. This process features a pure gauge and a Higgs-mediated s-channel contribution, Fig. 96. Both contributions do contain terms that grow as s at high energy, whose cancellation is guaranteed by gauge-invariance. To calculate $\mathrm{W^+_L W^-_L \to Z_L Z_L}$ amplitude in the EFT we need to extract the Feynman rules from $\tilde{\mathcal{O}}_\Pi$, i.e., the contributions that need to be added to the usual SM rules. This is straightforward and gives (all momenta incoming):

$$H(q)W^{+\mu}(k_1)W^{-\nu}(k_2): \qquad ig\frac{M_{\mathrm{W}}}{\sqrt{1+\Pi'(0)}}\Pi'(q^2)g^{\mu\nu} + \cdots$$

$$Z^\mu(k_1)W^{+\nu}(k_2)W^{-\rho}(k_3): \qquad i\frac{g}{c_{\mathrm{w}}}\frac{M_{\mathrm{W}}^2}{1+\Pi'(0)}s_{\mathrm{w}}^2\left[\Pi''(k_3^2)g^{\mu\nu}k_3^\rho - \Pi''(k_2^2)g^{\mu\rho}k_2^\nu\right] + \cdots$$

$$Z^\mu(k_1)Z^\nu(k_2)W^{+\rho}(k_3)W^{-\sigma}(k_4): \qquad ig^2\frac{M_{\mathrm{Z}}^2}{1+\Pi'(0)}\left[\Pi''(s)g^{\mu\nu}g^{\rho\sigma} + s_{\mathrm{w}}^4(\Pi''(t)g^{\mu\rho}g^{\nu\sigma} + \Pi''(u)g^{\mu\sigma}g^{\nu\rho})\right] + \cdots$$

$$H\phi^+\phi^-, \ H\phi^0\phi^0: \qquad -i\frac{g[M_{\mathrm{H}}^2-\Pi(0)]}{2M_{\mathrm{W}}}\sqrt{1+\Pi'(0)}$$

$$\phi^+\phi^-\phi^0\phi^0: \qquad -i\frac{g^2[M_{\mathrm{H}}^2-\Pi(0)]}{4M_{\mathrm{W}}^2}[1+\Pi'(0)]$$

$$\tag{264}$$

where ellipsis denotes terms vanishing on shell and $s = (k_1 + k_2)^2$, $t = (k_1 + k_3)^2$, and $u = (k_1 + k_4)^2$. These Feynman rules are sufficient to calculate both $\mathrm{W^+_L W^-_L \to Z_L Z_L}$ and $\phi^+\phi^- \to \phi^0\phi^0$. At the leading order in $\frac{M_{\mathrm{W}}^2}{s}$ and $\frac{M_{\mathrm{W}}^2}{M_{\mathrm{H}}^2}$, we find for $\mathrm{W^+_L W^-_L \to Z_L Z_L}$,

$$\mathcal{M}_{\mathrm{H}}^{\mathrm{LLLL}} = -\frac{ig^2}{4M_{\mathrm{W}}^2}\frac{s^2[1+\Pi'(s)]^2}{[s - M_{\mathrm{H}}^2 + \Pi(s)][1+\Pi'(0)]} \tag{265}$$

$$\mathcal{M}_{\mathrm{gauge}}^{\mathrm{LLLL}} = \frac{ig^2}{4M_{\mathrm{W}}^2}s\frac{1+\Pi'(s)}{1+\Pi'(0)} \tag{266}$$

and for $\phi^+\phi^- \to \phi^0\phi^0$,

$$\mathcal{M}_G = -\frac{ig^2}{4M_{\mathrm{W}}^2}\frac{s + \Pi(s) - \Pi(0)}{s - M_{\mathrm{H}}^2 + \Pi(s)}\left[M_{\mathrm{H}}^2 - \Pi(0)\right]\left[1 + \Pi'(0)\right] \tag{267}$$

so that

$$\mathcal{M}_{\mathrm{H}}^{\mathrm{LLLL}} + \mathcal{M}_{\mathrm{gauge}}^{\mathrm{LLLL}} = -\frac{ig^2}{4M_{\mathrm{W}}^2}\frac{s + \Pi(s) - \Pi(0)}{s - M_{\mathrm{H}}^2 + \Pi(s)}\frac{M_{\mathrm{H}}^2 - \Pi(0)}{1 + \Pi'(0)}$$

$$= \frac{\mathcal{M}_G}{[1+\Pi'(0)]^2} \,. \tag{268}$$

As expected, $\mathcal{M}_{\mathrm{H}}^{\mathrm{LLLL}} + \mathcal{M}_{\mathrm{gauge}}^{\mathrm{LLLL}}$ does not grow with s and the equivalence theorem is recovered, up to a factor $[1 + \Pi'(0)]^2$, which exactly amounts to the wave function renormalization of the Goldstone fields.

An interesting feature of our approach is that in the limit where the dependence of $\Pi(s)$ on s is neglected, $\Pi(s) \equiv \Pi$ is a constant, then $\Pi'(s) = \Pi''(s) = 0$. The only effect of the operator is a shift

in λ, the coupling of the Higgs-boson self interaction. If M_H is the on-shell mass, this amounts to the replacement

$$M_H^2 \to M_H^2 - \Pi,\tag{269}$$

i.e., given that Π can be a complex number, it is equivalent to the CMS.

The advantage of the EFT approach is the possibility of using "arbitrary" functional form of the self energy. We have shown that with special choices of $\Pi(s)$, the EFT approach can reduce to the Seymour scheme and the CMS scheme in certain cases. For example, there is no need for spurious non-zero width for t-channel propagators as this can be easily imposed by always maintaining gauge invariance. Finally, we note that despite the restoration of gauge-invariance and equivalence theorem is a general feature of our approach, one has to be careful in choosing the appropriate operator. For example, the following operator

$$\mathcal{O}'_\Pi = \frac{1}{2v^2}\left(\phi^\dagger\phi - v^2\right)\Pi(-\partial^2)\left(\phi^\dagger\phi - v^2\right)\tag{270}$$

introduced in Ref. [564], gives rise to the correct self energy and the resummed propagator, but it does not modify the gauge contribution, so in $W^+_L W^-_L \to Z_L Z_L$ the gauge cancellation between the s-channel Higgs-mediated amplitude and the gauge amplitude is not restored. On the other hand, it modifies the Goldstone amplitude in a way so that the equivalence theorem is satisfied. As a result, both $W^+_L W^-_L \to Z_L Z_L$ and $\phi^+\phi^- \to \phi^0\phi^0$ have bad high-energy behavior, and eventually break unitarity bounds. In general, adding higher dimensional operators to the Lagrangian leads to unitarity violation at some scale. We are going to show in the next sections that the operators we use do not have this problem.

Though the above operator $\mathcal{O}'_\Pi$ solely does not treat the HZZ and HW$^+$W$^-$ correctly at high energy, when combined with $\mathcal{O}_\Pi$, we can adjust them in a certain way to improve this method. We will discuss this in Section 12.1.3.6.

12.1.3.4 Unitarity

Adding operators of dimension $n > 4$ to the SM Lagrangian

$$\mathcal{L}_{\text{EFT}} = \mathcal{L}_{\text{SM}} + \sum_i c_i \frac{\mathcal{O}_i[n]}{\Lambda^{n-4}},\tag{271}$$

is equivalent to recast the SM in terms of an effective field theory valid up to scales of order Λ [595], beyond which the theory is not unitary. It is therefore mandatory to check whether this is the case for the operator $\tilde{\mathcal{O}}_\Pi$. In fact, as we will see in the following section, a consistent perturbation theory implies that the same operator needs to also appear as a counterterm at higher orders. Overall we do not modify the theory and our procedure amounts to a reorganization of the perturbative expansion. However, we still need to make sure that neither unitarity is violated nor double counting happens at any given order in the perturbation theory. In this section we consider the first of these issues by showing that in sample calculations, $f\bar{f} \to VV$ and $VV \to VV$, at tree-level the operator in Eq. (257) does not break unitarity at large energy.

In $f_\pm \bar{f}_\pm \to VV$ the change in HVV vertex cancels the change in H propagator at high s, independently of the helicities of VV, so the s-channel Higgs diagram does not lead to any bad high-energy behavior. The scattering of opposite helicity fermions does not entail the s-channel Higgs diagram and is the same as in the SM.

As we have already verified, in $W^+W^- \to ZZ$ the longitudinal amplitude does not break unitarity, because the modification to the corresponding Goldstone interaction is finite (vertices involving Goldstones are modified by factors of $1 - \Pi(0)/MH^2$ and $1 + \Pi'(0)$). We now check the transverse amplitude $++ \to --$, $00 \to ++$, $++ \to 00$, $++ \to ++$, in the limit

$$s \sim |t| \sim |u| \gg M_W^2, \quad M_H^2 \gg M_W^2.\tag{272}$$

(Note that $+-$, $+0$, -0 configurations do not feature a Higgs in the s-channel and therefore are left unchanged.) An explicit calculation for $W^+{}_+W^-{}_+ \to Z_-Z_-$ gives

$$\mathcal{M}_{\mathrm{H}}^{++--} = \mathcal{M}_{\mathrm{H}}^{\mathrm{LLLL}} \frac{4M_{\mathrm{W}}^4}{s^2 c_{\mathrm{w}}^2} + \mathcal{O}(M_{\mathrm{W}}^4) \tag{273}$$

$$\mathcal{M}_{\mathrm{gauge}}^{++--} = \mathcal{M}_{\mathrm{gauge}}^{\mathrm{LLLL}} \frac{4M_{\mathrm{W}}^4}{s^2 c_{\mathrm{w}}^2} + \mathcal{O}(M_{\mathrm{W}}^4)\,, \tag{274}$$

where M^{LLLL} indicates the amplitude with four longitudinal vectors. For $W^+{}_{\mathrm{L}}W^-{}_{\mathrm{L}} \to Z_+Z_+$ we obtain

$$\mathcal{M}_{\mathrm{H}}^{\mathrm{LL}++} = \mathcal{M}_{\mathrm{H}}^{\mathrm{LLLL}} \frac{-2M_{\mathrm{W}}^2}{s c_{\mathrm{w}}^2} + \mathcal{O}(M_{\mathrm{W}}^2) \tag{275}$$

$$\mathcal{M}_{\mathrm{gauge}}^{\mathrm{LL}++} = \mathcal{M}_{\mathrm{gauge}}^{\mathrm{LLLL}} \frac{-2M_{\mathrm{W}}^2}{s c_{\mathrm{w}}^2} + \mathcal{O}(M_{\mathrm{W}}^2)\,, \tag{276}$$

and for $W^+{}_+W^-{}_+ \to Z_{\mathrm{L}}Z_{\mathrm{L}}$ we obtain

$$\mathcal{M}_{\mathrm{H}}^{++\mathrm{LL}} = \mathcal{M}_{\mathrm{H}}^{\mathrm{LLLL}} \frac{-2M_{\mathrm{W}}^2}{s} + \mathcal{O}(M_{\mathrm{W}}^2) \tag{277}$$

$$\mathcal{M}_{\mathrm{gauge}}^{++\mathrm{LL}} = \mathcal{M}_{\mathrm{gauge}}^{\mathrm{LLLL}} \frac{-2M_{\mathrm{W}}^2}{s} + \mathcal{O}(M_{\mathrm{W}}^2)\,, \tag{278}$$

These results vanish faster than the longitudinal amplitude at large s. Finally for $W^+{}_+W^-{}_+ \to Z_+Z_+$, we obtain

$$\mathcal{M}_{\mathrm{H}}^{++++} = -ig^2 M_{\mathrm{Z}}^2 \frac{[1 + \Pi'(s)]^2}{[s - M_{\mathrm{H}}^2 + \Pi(s)][1 + \Pi'(0)]} + \mathcal{O}(M_{\mathrm{W}}^4)$$

$$\approx \frac{-ig^2 M_{\mathrm{Z}}^2}{1 + \Pi'(0)} \Pi''(s) \sim s^{-1} \quad \text{at large } s, \tag{279}$$

$$\mathcal{M}_{\mathrm{gauge}}^{++++} = i8g^2 c_{\mathrm{w}}^2 \frac{s^2}{4tu} + \mathcal{O}(M_{\mathrm{W}}^2)\,. \tag{280}$$

so at large energy the inclusion of $\tilde{\mathcal{O}}_\Pi$ does not lead to any bad high energy behavior.

12.1.3.5 The EFT approach at higher orders

Starting at order α_{w}, the operator $\tilde{\mathcal{O}}_\Pi$ is allowed in any leading order computation. At next-to-leading order in EW interactions, however, this is not necessarily consistent and possibly leads to double counting. In this section we argue that this is not a fundamental problem and can be dealt with by simply subtracting the same operator in a NLO as a counterterm, in full analogy to the procedure used in the CMS [596, 597].

In the CMS, an imaginary part is added to the real mass, and then subtracted as counterterm at NLO. One can prove that this procedure does not spoil the WI's, despite the fact that only a special class of higher order terms is resummed. As the EFT approach can be viewed as a generalization to the CMS, the same approach can be followed. The operator $\tilde{\mathcal{O}}_\Pi$ corresponds to the imaginary part of the mass. It includes some of the higher-order contribution, and provides an improved solution to the WI's. It enters the resummed propagator and other Feynman rules, and needs to be subtracted at higher orders. The main difference is that in the CMS the propagator describes an unstable particle with a fixed width, while in the EFT approach one can resum an arbitrary part of the self-energy correction. This difference may

be important when the width of the unstable particle is large, as in the case of a heavy Higgs, and the actual functional form of $\Pi(s)$ becomes important.

In the pole-mass renormalization scheme, the two-point function of the Higgs can be written as

$$\Delta_H(s) = s - s_H + \Pi^R_{HH}(s) \tag{281}$$

where s_H is the pole and $\Pi^R_{HH}(s)$ is the one-loop PT self-energy correction renormalized in the pole-mass scheme. We can now define the EFT approach by adding the operator in Eq. (257) and subtracting it as a counterterm:

$$\mathcal{L}_{SM} \to \mathcal{L}_{SM} + \tilde{\mathcal{O}}_\Pi - \tilde{\mathcal{O}}_\Pi \,. \tag{282}$$

In so doing the theory is exactly the same as before. Now Eq. (281) can be rewritten as

$$\begin{aligned}\Delta_H(s) =&s - s_H + \Pi(s) \\ &+ [\Pi^R_{HH}(s) - \Pi(s)]\end{aligned} \tag{283}$$

where the first line starts at leading order, while the second line starts at order α_w. The EFT approach then amounts to choose $\Pi(s)$ in a way to capture the important part of (if not all of) $\Pi^R_{HH}(s)$, so that this part of the self-energy correction is included at the leading order, and will be resummed. In practice, one does not have to choose the exact PT self energy, and gauge invariance is always guaranteed. In particular, choosing $\Pi(s) = 0$ corresponds to the CMS scheme.

In our scheme, EW NLO calculations are obviously more involved. The resummed propagator (245) and the modified Feynman rules do require extra work. However, one can also always employ a standard CMS at NLO and only include the full propagators and vertices in the LO result. In this way we can consistently have leading order calculated in the EFT approach, and NLO in CMS but with counterterms from $\tilde{\mathcal{O}}_\Pi$.

12.1.3.6 Applications

The treatment of the propagator of the Higgs is of immediate relevance for the LHC. As simple testing ground of our proposal and comparisons to the conventional methods, we consider three processes of particular phenomenological importance at the LHC for a scalar boson (which for brevity, we identify with an hypothetical heavy Higgs): vector boson scattering, $\bar{t}t$ production via vector boson fusion and Higgs production via gluon fusion. We have compared the effective approach described above in Eqs. (259), (260) and (264), with two other schemes:

1. A naive inclusion of the self energy, i.e., using the following propagator

$$\frac{i}{\Delta_H(s)} = \frac{i}{s - s_H + \Pi_R(s)} \,, \tag{284}$$

   without changing anything else. Here $s_H = \mu^2 - i\mu\gamma$.

2. The CMS scheme,

$$\frac{i}{\Delta_H(s)} = \frac{i}{s - s_H} \,. \tag{285}$$

As mentioned in Section 12.1.3.3, we improve our operator by combining it with $\mathcal{O}'_\Pi$ given in Eq. (270). More specifically, we define

$$\bar{\mathcal{O}}_\Pi = \mathcal{O}_{\Pi_1} + \mathcal{O}'_{\Pi_2} \,, \tag{286}$$

$$\mathcal{O}_{\Pi_1} = \phi^\dagger \Pi_1(-D^2)\phi \,, \tag{287}$$

$$\mathcal{O}'_{\Pi_2} = \frac{1}{2v^2} \left(\phi^\dagger \phi - v^2 \right) \Pi_2(-\partial^2) \left(\phi^\dagger \phi - v^2 \right) \,. \tag{288}$$

where the functions Π_1 and Π_2 are determined by requiring $\Pi_1(s) + \Pi_2(s) = \Pi(s)$, and that the operator $\bar{\mathcal{O}}_\Pi$ gives (the imaginary part of) the exact one-loop PT HZZ vertex. We use the operator $\bar{\mathcal{O}}_\Pi$ in the following analysis.

A modified version of MADGRAPH [129], with the implementation of the effective Lagrangian approach and the naive propagator with the PT self energy is used to generate events. As SM input parameters we take:

$$M_Z = 91.188 \text{GeV} \tag{289}$$

$$G_F = 1.16639 \times 10^{-5} \text{GeV}^{-2} \tag{290}$$

$$\alpha^{-1} = 132.507 \tag{291}$$

$$m_t = 173 \, \text{GeV} \,. \tag{292}$$

The Higgs pole mass is

$$\mu = 800 \, \text{GeV} \,, \tag{293}$$

and $\Pi_R(s)$ is the imaginary part of the PT self energy renormalized in the pole scheme. The factorization scale is set as the default dynamical scale of MADGRAPH and the PDF set is CTEQ6l1 [169].

– Vector Boson Scattering

In $PVBV \to PVBV$ scattering processes, the effective description allows one to achieve a complete description of the Higgs line-shape at the resonance region and at the same time it corrects the bad high-energy behavior originated from the momenta dependent part of the self energy. In addition, we show that our definition avoids the need for including spurious t-channel widths which occur in the complex-mass scheme also affecting the high energy behavior of the scattering amplitudes.

In Fig. 97 we show the energy behavior of the ZZ $\to$ ZZ scattering amplitude summed over helicities, $\sum_{\text{hel}} |\mathcal{M}(s, t, u)|^2$, at scattering angle $\cos \theta = 0$. The fixed width scheme, Eq. (285), naive propagator, Eq. (284), the effective description and a case in which the width is set to zero are presented. The agreement between the effective scheme and the naive propagator at the resonance region is pretty good. The difference with respect to the fixed width scheme is evident. At high energy, the naive propagator diverges, while the effective description behaves correctly. Similar comments can be made about $W^+W^- \to W^+W^-$ amplitude, shown in Fig. 98.

The fact that in both ZZ $\to$ ZZ and $W^+W^- \to W^+W^-$ the fixed width scheme differs from the effective approach at the high energy region indicates that the spurious t-channel width gives a non-negligible contribution. This fact can be verified by comparing the different schemes with the no-width case. Moreover, in the case of $W^\pm W^\pm \to W^\pm W^\pm$, shown in Fig. 99, the effective description and naive propagator are equivalent to the no-width case and the excess observed in the amplitudes in the fixed width scheme comes from the spurious width in the t and u-channels. At the LHC, the differences shown above may become important for a broad resonance. Despite the fact that a light Higgs has been observed, there is still room for new heavy and eventually broad resonances, e.g. The VV scattering are embedded in more complex processes of the form qq $\to$ qqVV, where the two final state jets are emitted with high energy in the forward-backward region of the detectors and the vector bosons decay into two fermions with high p_T through the central region. We study the processes uc $\to$ ucZZ and us $\to$ dcW$^+$W$^-$ assuming the nominal energy of LHC, $E_{CM} = 14$ TeV.

In Figs. 100 and 101, the distribution of the invariant mass of the Z Z-system is shown. In Fig. 100, the resonant region is shown. A basic set of selection cuts to enhance vector boson scattering contribution, listed in the left column of Table 60, have been applied. The effective description fits well with the running behavior of the Higgs propagator. In Fig. 101, the high-energy region is put in evidence. To better appreciate the differences between schemes at LHC energy, a further set of cuts has been added (right column of Table 60). As expected, the effective approach gives a well behaved distribution at such
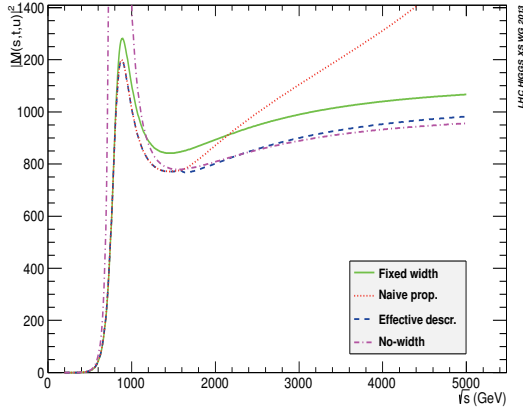
Figure 97: $\sum_{hel}|M(\mathrm{ZZ}\to\mathrm{ZZ})|^2$ with scattering angle, $\theta=\pi/2$. The curves correspond to: fixed width scheme, Eq. (285), naive propagator, Eq. (284), the effective description and the no-width, in which the width is set to zero.
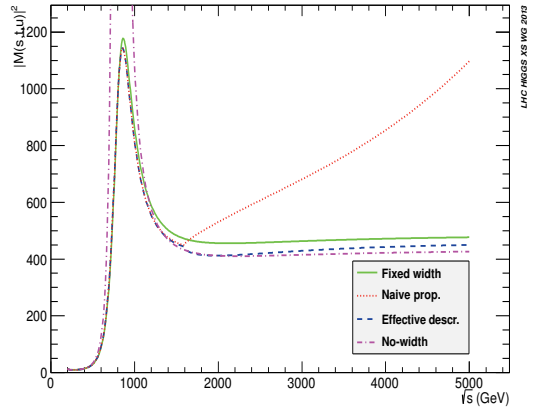
Figure 98: $\sum_{hel}|M(\mathrm{W}^+\mathrm{W}^-\to\mathrm{W}^+\mathrm{W}^-)|^2$ with scattering angle, $\theta=\pi/2$. The curves correspond to: fixed width scheme, Eq. (285), naive propagator, Eq. (284), the effective description and the no-width, in which the width is set to zero.
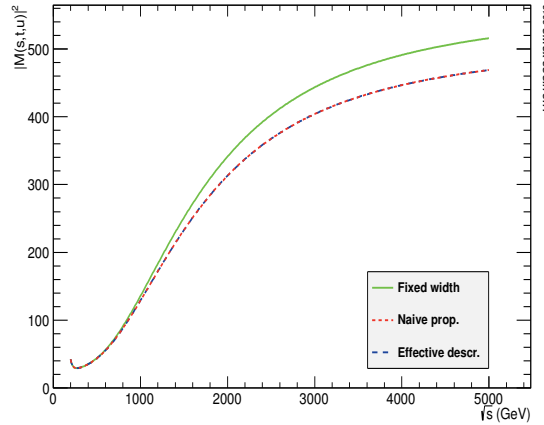
Figure 99: $\sum_{hel}|M(\mathrm{W}^+\mathrm{W}^+\to\mathrm{W}^+\mathrm{W}^+)|^2$ with scattering angle, $\theta=\pi/2$. The curves correspond to: fixed width scheme, Eq. (285), naive propagator, Eq. (284) and the effective description. The no-width case is equivalent to the last two.

energies contrary to the naive propagator and with a rate about 10% lower than the fixed width scheme. This difference amounts to the t-channel spurious contribution present in the fixed width case. Similar conclusions can be drawn from Figs. 102 and 103, where the reconstructed WW-system invariant mass distribution for the us $\to$ dcW$^+$W$^-$ process is shown.

– W$^+$W$^+\to$ H $\to\bar{\mathrm{t}}$t production

In $\bar{\mathrm{t}}$t production, we can observe a similar behavior with respect to ZZ $\to$ ZZ vector boson scattering. We have concentrated on the process $us\to dc\bar{\mathrm{t}}$t, in which the Higgs in produced by W$^+$W$^-$ fusion and decayed to a pair of top quarks. The energy in the center of mass is set to 14 TeV. In Fig. 104, the invariant mass distribution of $\bar{\mathrm{t}}$t at the resonant region is presented. The cuts shown in the left column
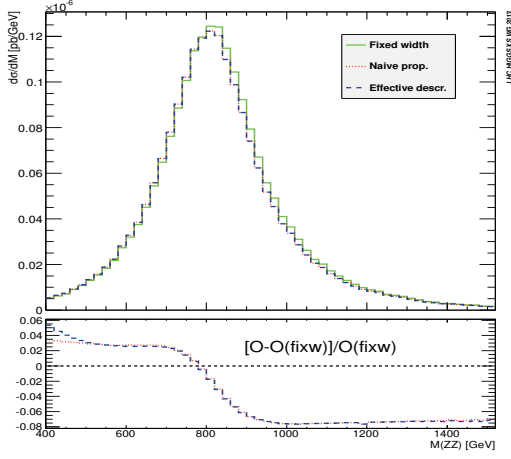
Figure 100: Mass distribution of ZZ-system in the process uc → ucZZ around the resonance peak. The cuts listed in the left column of Table 60 have been applied.
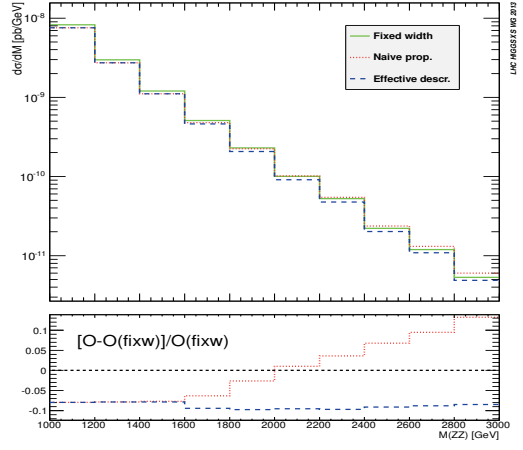
Figure 101: Mass distribution of ZZ-system in the process uc → ucZZ at the high energy region. All cuts listed in Table 60 have been applied.
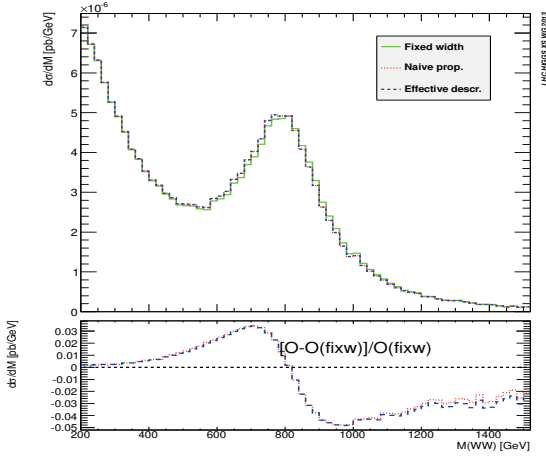
Figure 102: Mass distribution of WW-system in the process us → dcWW around the peak. The cuts listed in the left column of Table 60 have been applied.
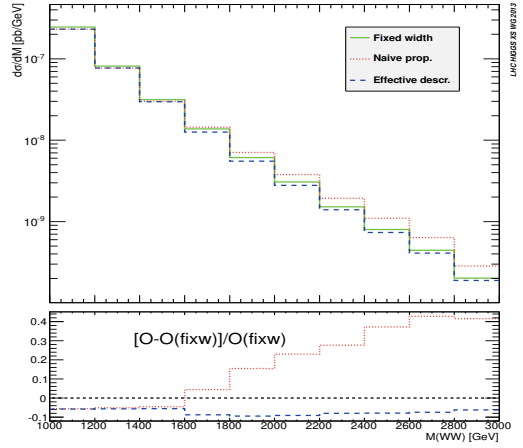
Figure 103: Mass distribution of WW-system in the process us → dcW^+W^- at the high energy region. All cuts listed in Table 60 have been applied.

Table 60: Cuts to enhance vector boson fusion. Basic ones on the left column and the extra ones on the right column.

Basic	Extra
$p_T(j) > 10$ GeV	$p_T(V) > 400$ GeV
$2 < \eta(j) < 10$	$\Delta\eta(jj) > 4.8$
$\Delta R(j,j) > 4$	$\eta(V) < 2$
$M(jj) > 100$ GeV	$M(jj) > 1000$ GeV
	$\Delta\eta(V,j) > 1$

of Table 60 have been applied in order to enhance the vector boson fusion contribution. Here again, the effective description describes the functional form of the propagator, which can go up to 5% of difference

w.r.t the fixed width scheme. As seen in Fig. 105, in the high mass region, the effective description is dumped down by the effective WWH vertex and does not grow with energy as is the case in which the naive propagator is adopted. The extra cuts shown in the right-hand column of Table 60 have been added in order to highlight the differences better.
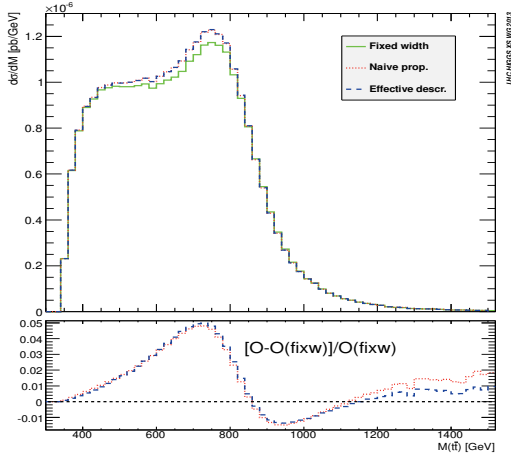
Figure 104: Mass distribution of $\overline{t}t$-system in the process us $\rightarrow$ dc$\overline{t}t$ around the resonance peak. The cuts listed in the left column of Table 60 have been applied.
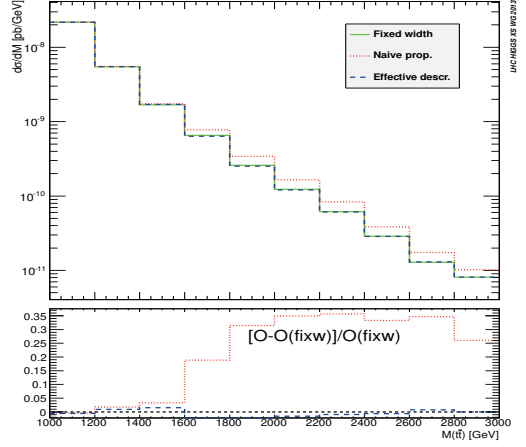
Figure 105: Mass distribution of $\overline{t}t$-system in the process us $\rightarrow$ dc$\overline{t}t$ at the high energy region. All cuts listed in Table 60 have been applied.

– Gluon-gluon Fusion

For the study of a heavy Higgs produced via gluon-gluon fusion and decayed to a W-boson pair, gg $\rightarrow$ W^+W^-, it is very important to consider the complete set of diagrams due to delicate gauge cancellations that control the high energy behavior. For this purpose we have relied on MCFM [283] for evaluation of the matrix elements, taking into account all diagrams contributing at leading order (yet one loop) to the process gg $\rightarrow$ W^+W^-, with Ws decaying to leptons. Phase space integration and unweighted event generation have been carried out within the MADGRAPH framework. The selection cuts shown in Table 61 have been applied. The mass distribution of WW-system in the three schemes considered if

Table 61: Cuts applied for gg $\rightarrow$ W^+W^- on the second one.

$p_T(\ell) > 2$ GeV
$\not{E}_T > 2$ GeV
$\eta(\ell) < 3$
$\Delta R(\ell\ell) > 0.5$

shown in Fig. 106 and Fig. 107. In Fig. 106 we can see that the effective scheme and the naive propagator description present the same behavior around the resonance region, while the fixed width scheme shows a typical slightly harder resonance. At high energy, the naive propagator diverges and the effective scheme and fixed width scheme are well behaved.

12.1.3.7 Conclusions

We have argued that it is possible to consistently and efficiently include running width effects for a heavy Higgs-like boson employing an EFT method. We can summarize the main points of our approach as follows:
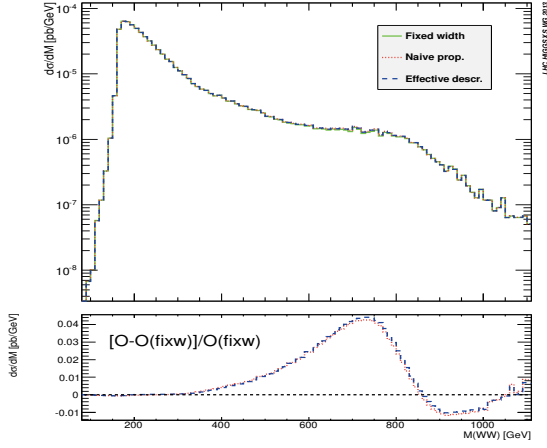
Figure 106: Mass distribution of the reconstructed WW-system in the process gg $\to$ W$^+$W$^-$ $\to$ e$^+\nu_e\mu\nu_\mu$, around the resonance peak. The cuts listed in Table 61 have been applied.
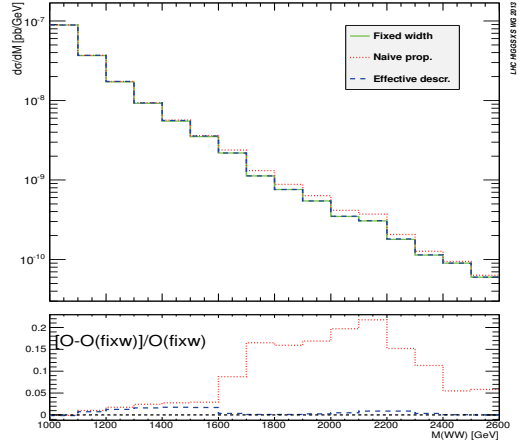
Figure 107: Mass distribution of the reconstructed WW-system in the process gg $\to$ W$^+$W$^-$ at the high energy region. The cuts listed in Table 61 have been applied.

– Introducing a width for an unstable particle amounts to a rearrangement of the perturbative expansion where the corrections to the two-point function are resummed in the propagator. The addition of the operator $\bar{\mathcal{O}}_\Pi$ defined in Eq. (286) allows to effectively perform such resummation in a gauge invariant and unitary way while keeping the full virtuality dependence of the self-energy. We have shown that in the limit where such dependence can be neglected our scheme is equivalent to the CMS.

– At leading order, one has the freedom to choose the functional form of $\Pi(s)$. We propose to use the exact one-loop PT self-energy correction. The rationale is that such self-energies are gauge invariant and by exploiting the WI's, we demand $\tilde{\mathcal{O}}_\Pi$ to mimic the most important one-loop corrections as much as possible. In practice, however, using any other form of $\Pi(s)$ does not break either gauge invariance or unitarity. In particular, one could avoid the need for a spurious non-zero width for t-channel propagators.

– EW higher-order corrections can be still performed in the CMS, without loss of accuracy or double counting issues. In practice, one can include the running width effects via the EFT at the leading order and neglect the virtuality dependence at NLO, i.e., employ the usual CMS for the NLO term.

In conclusion, in this work we have considered the case of how to consistently define a running width in the case of a heavy SM Higgs. The same approach can be used, for example, in the context of a Two-Higgs-Doublet model and applied to the current searches for new scalar states at the LHC. Extension to gauge vectors and heavy fermion states, on the other hand, are not straightforward and need further investigation.

12.2 Monte Carlo lineshape and interference implementations

An overview of the Monte Carlo tools available to describe the heavy mass $gg \to H$ lineshape and the $gg \to VV$ signal-background interference is presented.

12.2.1 Signal-background interference studies for $H \to ZZ$ searches with GG2VV

In this section, the impact of Higgs-continuum interference on $H \to ZZ$ searches at the LHC for a heavy SM Higgs boson is studied with GG2VV [86]. GG2VV is a parton-level integrator and event generator for all $gg (\to H) \to VV \to 4$ leptons processes ($V = W, Z/\gamma^*$) [85, 556, 598, 599]. It can be used to calculate integrated and differential cross sections with scale and PDF uncertainties and to produce unweighted events in LHEF format. GG2VV takes into account the complete, fully off-shell $gg \to 4$ leptons loop-induced LO matrix element with full spin correlations. Finite top and bottom quark mass effects are included. Amplitude evaluation is facilitated by FEYNARTS/FORMCALC [600, 601]. MC integration is facilitated by DVEGAS [602], which was developed in the context of Refs. [603, 604].

The following input parameters and settings have been used to calculate the results presented in Sections 12.2.1.1 and 12.2.1.2. They also apply to the light Higgs results presented in Sections 3.5.2 and 3.5.3. The input-parameter set of Ref. [13], App. A, is used with NLO $\Gamma_{W,Z}$ and G_μ scheme. Top and bottom quark mass effects are taken into account, while lepton masses are neglected. The renormalization and factorization scales are set to $M_H/2$. In Section 3.5.2 (Section 12.2.1.1) [Sections 3.5.3 and 12.2.1.2], the PDF set MSTW2008 NNLO (MSTW2008 LO) [CT10 NNLO] with 3(1)[3]-loop running for $\alpha_s(\mu^2)$ and $\alpha_s(M_Z^2) = 0.11707$ (0.13939) [0.1180] is used. The complex-pole scheme [87] with $\Gamma_H = 29.16$ (103.9) [416.1] GeV for $M_H = 400$ (600) [1000] GeV is used for the Higgs resonance. The fixed-width prescription is used for W and Z propagators. The CKM matrix is set to the unit matrix, which causes a negligible error [555]. No flavor summation is carried out for charged leptons (l) or neutrinos. A $p_{TV} > 1$ GeV cut is applied to prevent that numerical instabilities spoil the amplitude evaluation.

12.2.1.1 Signal-background interference in $gg (\to H) \to ZZ \to l\bar{l}l'\bar{l}'$

To illustrate signal-background interference effects for a heavy SM Higgs boson, integrated cross sections and differential distributions for $gg (\to H) \to ZZ \to l\bar{l}l'\bar{l}'$ in pp collisions at 7 TeV for $M_H = 400$ GeV are presented in Table 62 and Figures 108 and 109, respectively. Results are given for Higgs signal, gg continuum background and the sum with (without) interference. To quantify the signal-background interference effect, the $S+B$-inspired measure R_1 and $S/\sqrt{B}$-inspired measure R_2 defined in Eq.(24) are used. When standard cuts ($p_{Tl} > 20$ GeV, $|\eta_l| < 2.5$, 76 GeV $< M_{l\bar{l}}, M_{l'\bar{l}'} < 106$ GeV) are applied, interference effects of about 2% are obtained at 7 TeV, which increase to 3–5% when the collision energy is increased to 14 TeV (see Table 63). As shown in Figure 108, the Higgs-continuum interference is negative (positive) for M_{ZZ} larger (smaller) than M_H. A compensation between negative and positive interference will typically occur for integrated cross sections. Applied selection cuts will in general reduce this cancellation, as seen in Figure 109 for the charged-lepton azimuthal opening angle $\Delta\phi_{l\bar{l}}$, and should be taken into account to get a reliable estimate for the interference effect. Since the Higgs invariant mass can be reconstructed, it is suggestive to apply a $|M_{ZZ} - M_H| < \Gamma_H$ cut in addition to the standard cuts to reduce the background (Higgs search cuts). Such a cut further improves the cancellation of positive and negative interference, due to the change of sign at M_H. As seen in Tables 62 and 63, the interference measures $R_{1,2} - 1$ are reduced to the 1% level, when Higgs search cuts are applied.

12.2.1.2 ZZ/WW interference in $gg (\to H) \to l\bar{l}\nu_l\bar{\nu}_l$

In Section 12.2.1.1, the key features of signal-background interference in $H \to ZZ$ searches were elucidated using the "golden mode." In this section, WW corrections are studied that occur when the

Table 62: Cross sections in fb for gg $(\to \mathrm{H}) \to \mathrm{ZZ} \to \mathrm{l\bar{l}l'\bar{l}'}$ in pp collisions at 7 TeV for $M_\mathrm{H} = 400$ GeV. Results are given for signal ($|\mathrm{H}|^2$), gg continuum background ($|\mathrm{cont}|^2$) and signal+background+interference ($|\mathrm{H+cont}|^2$). $R_{1,2}$ as defined in Eq.(24) are also displayed. Standard cuts: $p_{\mathrm{Tl}} > 20$ GeV, $|\eta| < 2.5$, 76 GeV $< M_{\mathrm{l\bar{l}}}, M_{\mathrm{l'\bar{l}'}} <$ 106 GeV. Higgs search cuts: standard cuts and $|M_{\mathrm{ZZ}} - M_\mathrm{H}| < \Gamma_\mathrm{H}$ with $\Gamma_\mathrm{H} = 29.16$ GeV. No flavor summation is carried out. The integration error is given in brackets.

selection cuts	$|\mathrm{H}|^2$	$|\mathrm{cont}|^2$	$|\mathrm{H+cont}|^2$	R_1	R_2
standard cuts	0.3654(4)	0.3450(4)	0.7012(8)	0.987(2)	0.975(3)
Higgs search cuts	0.2729(3)	0.01085(2)	0.2867(3)	1.010(2)	1.011(2)

Table 63: As Table 62, but for $\sqrt{s} = 14$ TeV.

selection cuts	$|\mathrm{H}|^2$	$|\mathrm{cont}|^2$	$|\mathrm{H+cont}|^2$	R_1	R_2
standard cuts	1.893(3)	1.417(2)	3.205(5)	0.969(2)	0.945(3)
Higgs search cuts	1.377(2)	0.0531(1)	1.445(2)	1.011(2)	1.011(3)
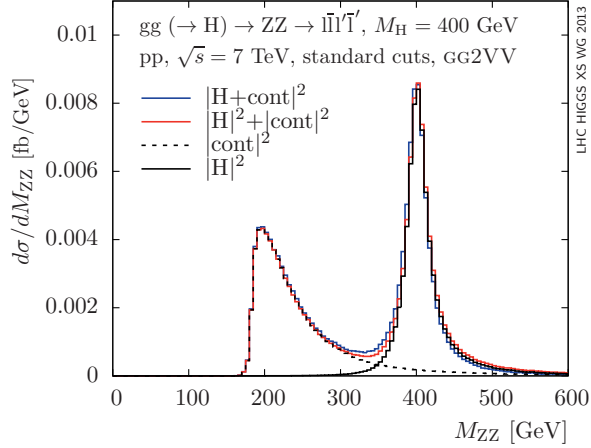
Figure 108: M_{ZZ} distributions for gg $(\to \mathrm{H}) \to \mathrm{ZZ} \to \mathrm{l\bar{l}l'\bar{l}'}$ in pp collisions at 7 TeV for $M_\mathrm{H} = 400$ GeV. Distributions for signal ($|\mathrm{H}|^2$), gg continuum background ($|\mathrm{cont}|^2$), signal+background ($|\mathrm{H}|^2+|\mathrm{cont}|^2$), and signal+background+interference ($|\mathrm{H+cont}|^2$) are shown. Standard cuts and other details as in Table 62.

same-flavor final state $\mathrm{l\bar{l}\nu_l\bar{\nu}_l}$ is produced.[61] Results obtained with a minimal $M_{\mathrm{l\bar{l}}} > 4$ GeV cut are shown in Tables 64 and 65 for $M_\mathrm{H} = 600$ GeV and $M_\mathrm{H} = 1$ TeV, respectively, at $\sqrt{s} = 8$ TeV. Cross sections when only either the WW or ZZ intermediate state is included are also given. As above, results for Higgs signal, gg continuum background and the sum with interference as well as the interference measures $R_{1,2}$ are displayed. Without search cuts, S/B decreases significantly with increasing heavy Higgs mass. Consequently, the interference measure $R_2 - 1$ increases substantially when going from $M_\mathrm{H} = 600$ GeV to $M_\mathrm{H} = 1$ TeV, namely from $\mathcal{O}(20\%)$ to $\mathcal{O}(2)$. In addition to signal-background in-

---

[61]See also Section 3.5.2.
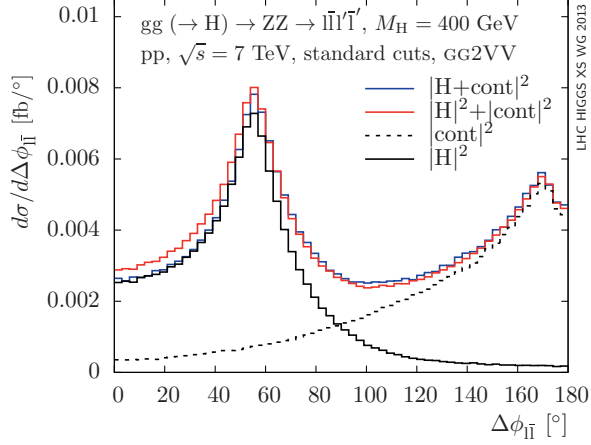
Figure 109: Azimuthal opening angle $\Delta\phi_{l\bar{l}}$ distributions for gg $(\to H) \to ZZ \to l\bar{l}l'\bar{l}'$ in pp collisions at 7 TeV for $M_H = 400$ GeV. Other details as in Figure 108.

Table 64: Cross sections in fb for gg $(\to H) \to WW, ZZ \to l\bar{l}\nu_l\bar{\nu}_l$ (same flavor) in pp collisions at 8 TeV for $M_H = 600$ GeV. Cross sections when only either the WW or ZZ intermediate state is included are also given. A minimal $M_{l\bar{l}} > 4$ GeV cut is applied. Other details as in Table 62.

VV	$|H|^2$	$|\text{cont}|^2$	$|H+\text{cont}|^2$	R_1	R_2
WW	1.44(1)	12.29(3)	14.10(5)	1.027(4)	1.26(4)
ZZ	0.261(2)	1.590(5)	1.896(6)	1.024(4)	1.17(3)
WW, ZZ	1.69(2)	12.98(6)	15.00(8)	1.022(7)	1.19(6)

Table 65: As Table 64, but for $M_H = 1$ TeV.

VV	$|H|^2$	$|\text{cont}|^2$	$|H+\text{cont}|^2$	R_1	R_2
WW	0.0772(5)	10.50(3)	10.72(3)	1.013(4)	2.8(5)
ZZ	0.01426(9)	1.353(4)	1.387(4)	1.015(4)	2.4(4)
WW, ZZ	0.0914(6)	11.02(6)	11.30(8)	1.017(9)	3(1)

terference, the interference between WW and ZZ contributions is also of interest. For the gg continuum background, one finds $\sigma(|WW + ZZ|^2)/\sigma(|WW|^2 + |ZZ|^2) = 0.935(5)$, while for the signal this ratio agrees with 1 at the sub-percent level for $M_H = 600$ GeV and 1 TeV. The $\mathcal{O}(5\%)$ WW/ZZ interference for the gg continuum background has to be compared to the negligible WW/ZZ interference found in Ref. [605] for the quark-induced continuum background.

We now investigate the impact of H $\to$ ZZ search cuts on the signal-background interference. To be specific, we consider the cuts $|M_{l\bar{l}} - M_Z| < 15$ GeV, $\not{E}_T > 110$ GeV, $M_T > 325$ GeV. The

Table 66: Cross sections in fb for $\text{gg} (\to \text{H}) \to \text{WW}, \text{ZZ} \to \text{l}\bar{\text{l}}\nu_l\bar{\nu}_l$ (same flavor) in pp collisions at 8 TeV for $M_\text{H} = 600$ GeV. $\text{H} \to \text{ZZ}$ search cuts are applied: $|M_{\text{l}\bar{\text{l}}} - M_\text{Z}| < 15$ GeV, $\not{E}_\text{T} > 110$ GeV, $M_\text{T} > 325$ GeV. M_T is defined in Eq.(294). Other details as in Table 64.

VV	$|\text{H}|^2$	$|\text{cont}|^2$	$|\text{H+cont}|^2$	R_1	R_2
ZZ	0.2175(8)	0.0834(2)	0.3150(8)	1.047(4)	1.065(6)
ZZ, WW	0.2220(8)	0.1020(2)	0.3406(8)	1.051(4)	1.075(6)

Table 67: As Table 66, but for $M_\text{H} = 1$ TeV.

VV	$|\text{H}|^2$	$|\text{cont}|^2$	$|\text{H+cont}|^2$	R_1	R_2
ZZ	0.01265(5)	0.0687(2)	0.0927(2)	1.140(3)	1.90(2)
ZZ, WW	0.01278(5)	0.0846(3)	0.1090(2)	1.119(3)	1.91(3)

transverse mass is defined as

$$M_\text{T} = \sqrt{\left(M_{\text{T},\text{l}\bar{\text{l}}} + \not{M}_\text{T}\right)^2 - (\mathbf{p}_{\text{T},\text{l}\bar{\text{l}}} + \not{\mathbf{p}}_\text{T})^2} \quad \text{with} \quad \not{M}_\text{T} = \sqrt{\not{p}_\text{T}^2 + M_{\text{l}\bar{\text{l}}}^2}. \tag{294}$$

Results for $M_\text{H} = 600$ GeV and 1 TeV are shown in Tables 66 and 67, respectively. Since the Higgs search cuts suppress the background while retaining the signal, one can expect that with search cuts R_2 deviates less from 1 than when only minimal cuts are applied. This is confirmed by the shown results: For $M_\text{H} = 600$ GeV (1 TeV), $R_2 - 1$ decreases from $\mathcal{O}(20\%)$ $(\mathcal{O}(2))$ to $\mathcal{O}(7\%)$ $(\mathcal{O}(1))$.

12.2.2 Heavy Higgs implementation in MCFM

This section provides an overview of the implementation of Higgs boson production and background processes in MCFM. Further details can be found in Refs. [554,606]. MCFM contains NLO predictions for a variety of processes. For studies of heavy Higgs bosons the most relevant signal processes are Higgs production through gluon fusion and vector-boson-fusion, with subsequent decays to massive vector bosons. The SM background production of the direct diboson final state themselves. In addition to the standard NLO predictions for the diboson processes, MCFM includes the contributions from gluon induced initial states. Although formally $\mathcal{O}(\alpha_\text{s}^2)$ (and hence NNLO) the large gluon flux at LHC operating energies enhances these pieces beyond the naive NNLO power counting. The current status (as of MCFM v6.4) of these processes is as follows. For the $\text{gg} \to \text{WW}$ process all three families of quarks are included in the loops, with the exact dependence on the top mass m_t kept and all other quarks considered massless. For the ZZ process only the first five massless flavors are implemented.

One of the most interesting phenomenological features of a heavy Higgs boson is its large width and the corresponding impact of the interference term with the SM production of VV pairs. Since the interference pattern is often not accounted for in event generator simulations and higher order corrections, we focus on its impact on phenomenology in this report.

In order to study the interference between the SM production of W pairs and Higgs decay to WW we introduce the following definitions,

$$\sigma_\text{B} \longrightarrow |\mathcal{A}_\text{box}|^2, \qquad \mathcal{A}_\text{box} = 2\mathcal{A}_\text{massless} + \mathcal{A}_\text{massive},$$

213

$$\sigma_{\mathrm{H}} \longrightarrow |\mathcal{A}_{\mathrm{Higgs}}|^2 \; ,$$
$$\sigma_i \longrightarrow 2\mathrm{Re}\left(\mathcal{A}_{\mathrm{Higgs}}\mathcal{A}_{\mathrm{box}}^{\star}\right) \; ,$$
$$\sigma_{\mathrm{H},i} = \sigma_{\mathrm{H}} + \sigma_i \; . \tag{295}$$

Here σ_{B} represents the background production of WW pairs, (proceeding through the $\mathcal{A}_{\mathrm{box}}$ amplitude which is made up of massless and massive fermion loops) and σ_{H} represents signal squared cross section associated with the LO production of a Higgs boson through gluon fusion, with a subsequent decay to WW. Note that this LO processes proceeds through a top quark loop. Finally σ_i represents the interference between the signal and background amplitudes.

The interference pattern contains two terms, which are extracted by removing the Higgs propagator from the amplitude (with the new stripped amplitude referred to as $\tilde{A}_{\mathrm{Higgs}}$). The imaginary part of the Higgs propagator couples to the imaginary part of the product, $\tilde{A}_{\mathrm{Higgs}}\mathcal{A}_{\mathrm{box}}^*$. Hence this piece is proportional to the Higgs width. The real part of the Higgs propagator couples to the real part of $\tilde{A}_{\mathrm{Higgs}}\mathcal{A}_{\mathrm{box}}^*$. The resulting interference cross section is thus of the form,

$$\delta\sigma_i = \frac{(\hat{s} - M_{\mathrm{H}}^2)}{(\hat{s} - M_{\mathrm{H}}^2)^2 + M_{\mathrm{H}}^2\Gamma_{\mathrm{H}}^2}\,\mathrm{Re}\left(2\tilde{\mathcal{A}}_{\mathrm{Higgs}}\mathcal{A}_{\mathrm{box}}^*\right) + \frac{M_{\mathrm{H}}\Gamma_{\mathrm{H}}}{(\hat{s} - M_{\mathrm{H}}^2)^2 + M_{\mathrm{H}}^2\Gamma_{\mathrm{H}}^2}\,\mathrm{Im}\left(2\tilde{\mathcal{A}}_{\mathrm{Higgs}}\mathcal{A}_{\mathrm{box}}^*\right) \; , \tag{296}$$

The first piece of this expression is an odd function in $\hat{s}$ about M_{H} and therefore, for well resolved final states (such as ZZ^* and $\gamma\gamma$) in which the Higgs signal can be localized in $\hat{s}$, the interference effects from this piece approximately cancel over the integration of the $\hat{s}$ bin. In these cases the interference phenomenology is dominated by the width effects (which for a heavy Higgs will be sizeable). For Higgs decays which are not fully reconstructed (such as WW) both terms contribute. Since the Higgs boson is a unitarizing particle the interference is destructive at large $\hat{s}$. Thus, since the function is odd the interference in the corresponding region $\hat{s} < M_{\mathrm{H}}$ is constructive. Since the background cross section is typically larger in this region the net effect of the interference is constructive for most Higgs masses.
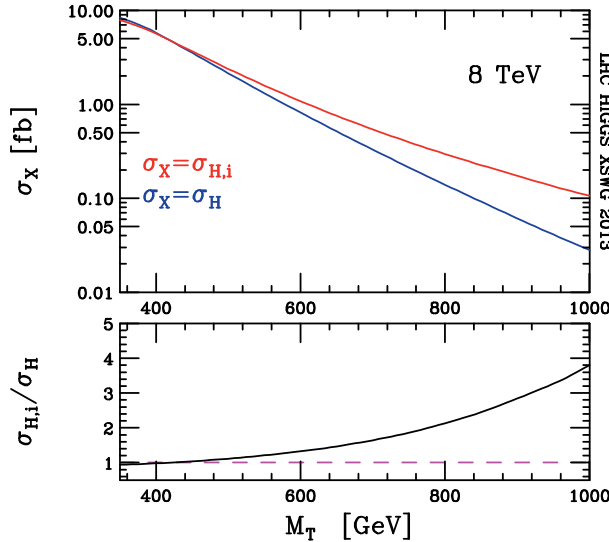
Figure 110: Inclusive $H \to WW \to \ell\nu\ell'\nu'$ cross section at the LHC8. The standard signal squared σ_{H} is shown in blue, whilst the signal squared plus interference cross sections are shown in red. The lower panel shows the ratio of these two cross sections.

Fig. 110 presents the net contribution of the interference for the inclusive $H \to WW \to \ell\nu\ell'\nu'$ cross section at LHC operating energies (8 TeV), focusing on the heavy Higgs region. The renormalization and factorization scales have been set equal to the Higgs mass. It is clear that the interference

becomes the dominant part of the Higgs production cross section as the Higgs mass grows. This is primarily since the Higgs cross section is a rapidly falling function in M_H, hence the term linear in the signal amplitude (the interference) dominates over the quadratic piece (the signal squared).
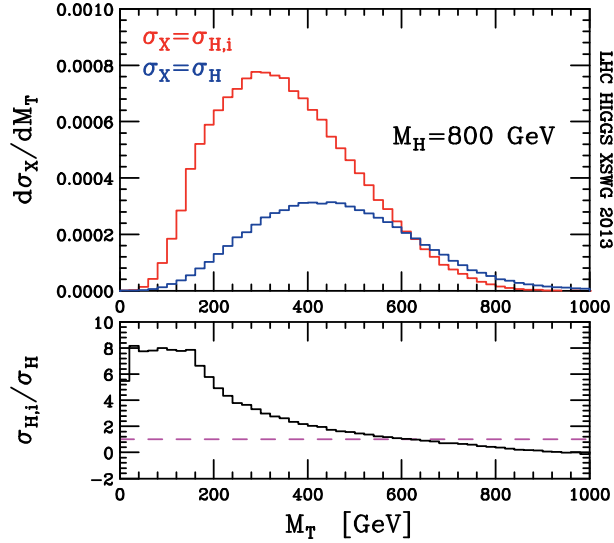
Figure 111: The transverse mass distribution for a Higgs boson with mass 800 GeV at the 8 TeV LHC. The upper panel shows the prediction for the differential distribution with and without including the interference terms, the lower panel provides the ratio of these predictions.

It is also interesting to consider the impact of the interference pieces on more differential quantities. One such relevant quantity is the transverse mass of the missing transverse energy plus leptons final state. The MCFM prediction for the transverse mass spectrum for a Higgs mass of 800 GeV is shown in Fig. 111. The pattern predicted by Eq.(296) is manifest. The interference is large and constructive in the region ($\hat{s} < M_H \implies m_T < M_H$), whilst in the large $\hat{s}$ region the interference is destructive. The enhancement in the low m_T region is significant and can be around an order of magnitude compared to the naive signal prediction. Therefore inclusion of the interference effects are vital in order to simulate the phenomenological impact of the heavy Higgs.

Since it is clear that the contributions from the interference effects are important, it is interesting to look at possible mechanisms for modifying the Higgs propagator in order to simulate the impact of the interference. If such a modification can mimic the interference terms then use of this propagator in higher order codes (for example the NNLO code of ref. [109]) can enhance these predictions. MCFM provides an excellent testing environment for these techniques, since it is possible to modify the Higgs propagator as desired and compare it to the full signal plus interference prediction at LO. One such modification is the improved $s-$channel approximation (ISA) due to Seymour [594]. In this setup one replaces the fixed-width propagator with the following,

$$\frac{is}{s - M_H^2 + i\Gamma_H M_H} \rightarrow \frac{iM_H^2}{s - M_H^2 + i\Gamma_H(M_H)\frac{s}{M_H}}. \tag{297}$$

The dependence on $\hat{s}$ in the width piece modifies the corresponding Higgs boson lineshape. We illustrate these differences in Fig. 112. In order to ensure the invariant mass distribution is positive definite we also include the prediction for gg $\rightarrow$ WW, σ_B. It is clear that by modifying the propagator we have significantly altered the resulting lineshape of the Higgs. The ISA has captured the form of the interference prediction, namely enhancing the differential cross section in the region $\hat{s} < M_H$ and decreasing it in the

high mass tail. Whilst the ISA is an improvement over the fixed width approximation it fails to capture the true impact of the destructive interference and overestimates the rate at small $m_{4\ell}$.
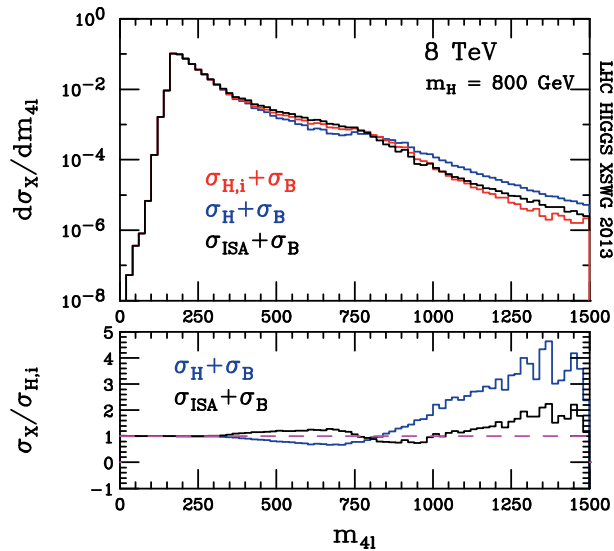
Figure 112: Comparison of the improved s-channel approximation and the full LO signal plus interference prediction for the invariant mass of the four lepton final state. For reference the naive signal squared prediction is also plotted. The background production of $gg \rightarrow WW$ is also included.

Summary

MCFM provides a range of predictions relevant for searches for a heavy Higgs boson. The most relevant being the signal production cross sections and many of the irreducible background processes. Since the width of a heavy Higgs boson is very large interference effects between signal and background dominate the lineshape of the Higgs. MCFM includes a full treatment of this interference at LO for the WW decay modes, allowing the user to test systematic uncertainties in other codes which may not model these interactions.

12.2.3 Signal-background interference implementation in aMC@NLO

At LO the cross section for $gg \to VV$ can be written as

$$\sigma_{\text{S+i+B}}^{\text{LO}} = |\mathcal{M}_{\text{S}}|^2 + 2\,\text{Re}(\mathcal{M}_{\text{S}}\mathcal{M}_{\text{B}}^*) + |\mathcal{M}_{\text{B}}|^2\,, \tag{298}$$

where the signal S features a triangle loop and the Higgs propagation in the s-channel while the background B proceeds via $gg \to VV$ boxes. At high partonic energy $\hat{s}$, there is a cancellation between the $pp \to H \to VV$ diagram and the S-wave massive contribution of the non-resonant ones [557], each growing as $m_{\text{q}}^2/m_{\text{V}}^2 \log^2 \hat{s}/m_{\text{q}}^2$ where q is the heavy quark running in the loop. This contribution is proportional to the axial part of the vector boson coupling to the quarks and it is basically due to the non-conservation of the axial current for massive quarks. Such a cancellation ensures the unitarity of the standard model up to arbitrary large scales. Note that the width scheme has also an impact on the unitarity of the theory.

In absence of a complete NLO computation for the full process $pp \to VV$ a scheme for combining the signal $pp \to H \to VV$ at NLO (or NNLO), the background at LO and the interference between them is needed. Different methods have been proposed and discussed, see, .e.g., [102], which make different approximations and can broadly divided in multiplicative or additive. In essence the main difference stems from how the signal-background interference is treated: in the additive scheme it is taken at the LO, i.e., it corresponds exactly to the accuracy to which is presently known, while in the multiplicative scheme a guess for the NLO (or NNLO) interference is made, which is obtained by multiplying the LO results by a K-factor, overall or differential based on a pivot distribution. The former scheme is the only possible one for a MC generator, yet it violates unitarity at NLO in α_{s}, while the latter is better suited for analytical calculations, does not violate unitarity, yet it is just a guess for an unknown quantity.

In our approach, we therefore employ an additive scheme,

$$\sigma^{\text{MC}}(pp \to VV) = \sigma_{\text{S}}^{\text{NLO}} + \sigma_{\text{i+B}}^{\text{LO}} = \sigma_{\text{S}}^{\text{NLO}} + 2\,\text{Re}(\mathcal{M}_{\text{S}}\mathcal{M}_{\text{B}}^*) + |\mathcal{M}_{\text{B}}|^2\,. \tag{299}$$

Events corresponding to the first term are generated with MC@NLO v.4.09 [128], which features real (one-loop) and virtual (two-loop) matrix elements with the exact m_{b} and m_{t} dependence (taken from Ref. [607, 608]). Such calculation is for on-shell Higgs production. Introducing the Higgs propagation and decay, and therefore the Higgs width, needs special care especially for a heavy Higgs in order to maintain gauge invariance and unitarity, as discussed at length in the literature and this report. In MC@NLO given a final state in terms of leptons, this is achieved by the replacement:

$$\delta(\hat{s} - M_{\text{H}}^2) \to \frac{1}{\pi} \frac{\sqrt{\hat{s}} \cdot \Gamma(H(\hat{s}) \to \text{final state})}{(\hat{s} - M_{\text{H}}^2)^2 + M_{\text{H}}^2 \Gamma_{\text{H}}^2}\,, \tag{300}$$

where the partial width into the final state is calculated at corresponding virtuality and Γ_{H} is the total Higgs width. Such a replacement exactly corresponds to a complex-pole scheme for the Higgs if Γ_{H} is calculated accordingly [87].

The second and third terms in Eq. (299) are generated via dedicated implementations, whose loop matrix elements are automatically obtained via MADLOOP [132] and checked, when possible, with MCFM [554]. The corresponding codes are publicly available at the AMC@NLO web page (`http://amcatnlo.cern.ch`). In our calculation all six flavor run in the background boxes for $gg \to VV$ and quark mass effects are accounted for exactly.

Samples corresponding to different leptonic final states, $\ell^+\nu_\ell\ell'^-\bar{\nu}_{\ell'}(W^+W^-)$, $\ell^+\ell^-\nu_{\ell'}\bar{\nu}_{\ell'}(ZZ)$ and $\ell^+\ell^-\ell'^+\ell'^-(Z/\gamma^*Z/\gamma^*)$ can be obtained. In Fig. 113 the invariant mass of the four leptons in the $e^+e\nu_\mu\bar{\nu}_\mu$ and $e^+e\mu^+\mu$ final states for two different Higgs masses are shown. Only minimal acceptance cuts have been applied. The blue (low lying) curve show the full LO result. the black (dotted) curve the NLO signal plus the background, while the red curve is the combined result corresponding to Eq. (299).

The first important result is that NLO effects for the signal are very important around the Higgs mass, as expected, and cannot be neglected. The interference gives an enhancement of the cross section before the peak and a depletion (corresponding to the cancellation of the bad high-energy behavior) at large invariant masses. Such effects, while certainly visible already for a Higgs of $M_H = 500-600$ GeV, give a small contributions overall as the high-energy tail is strongly suppressed by the gluon PDF's.
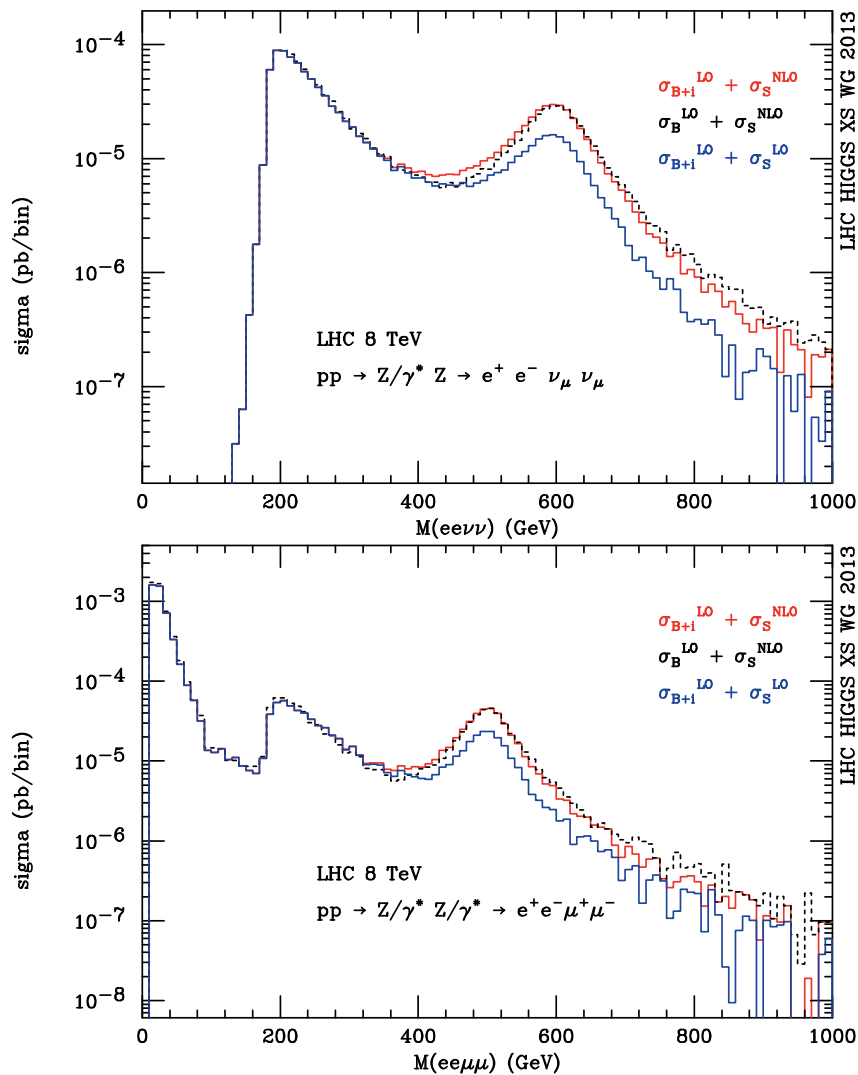
Figure 113: Invariant mass distributions for pp $\rightarrow 4\ell$ in different channels as obtained from MC@NLO for the signal S and MADLOOP for the background and interference $B + i$. Basic acceptance cuts applied.

12.3 Reweighting studies

In this section the effect of reweighting distributions to account for the interference effect in several final states by using different Monte Carlo generators and tools will be presented.

12.3.1 Comparison with MCFM: gg->WW->lνjj

For a light Higgs with mass near 125 GeV, the interference effect is at percent level between the signal $gg \rightarrow H \rightarrow WW$ and the continuum background $gg \rightarrow WW$. With increasing Higgs mass, the interference effect becomes more and more crucial. As shown in Ref. [554], the effect on LO total cross sections can already be over 30% for $M_H \gtrsim 600 GeV$. Moreover, it changes much the M_{WW} spectrum, with constructive behavior at $M_{WW} \lesssim M_H$ while destructive at $M_{WW} \gtrsim M_H$.

One usually can include the interference effects by reweighting the signal's M_{WW} spectrum (S) with the M_{WW} binned scale factor R_2

$$S_{\text{Reweight}} \equiv R_2 \times S. \tag{301}$$

However, one needs then to validate this method by examining additional distributions other than M_{WW}, especially those exploited in the data analysis [609]. Moreover, one should also provide a conservative yet appropriate estimation on theoretical uncertainties from R_2.

In the CMS study of searching Higgs via the $WW \rightarrow lv_1 jj$ channel [609], we evaluate R_2 with the LO results of signal and interference terms got from the MCFM v6.3 (without any cuts applied). We then exploit the method proposed in Ref. [102] to estimate the reweighting uncertainty with 3 kinds of factors (k) applied on top of R_2 by $1 + k \times (R_2 - 1)$, inspired by higher order QCD corrections:

$$k = 1, \ \sqrt{K_{\text{gg}}/K_{\text{NNLO}}}, \ \text{and} \ 1/K_{\text{NNLO}}, \tag{302}$$

where the K-factors K_{gg} and K_{NNLO} are read from the $H \rightarrow ZZ$ numbers in Ref. [102], as the ones for $H \rightarrow WW$ are not ready yet and meanwhile the K-factors should not depend on final states between $gg \rightarrow H \rightarrow WW$ and ZZ.

In Fig. 114, we show our reweighting results for $gg \rightarrow H \rightarrow WW \rightarrow lv_1 jj$ at the generator level, for $M_H = 700$ GeV at the 8 TeV LHC, with the factorization and renormalization scales fixed to M_H and CTEQ6L1 PDF exploited, and $p_T^l > 30$ GeV, $p_T^j > 30$ GeV, MET> 30 GeV, $|\eta_{l,j}| < 2.4$. The effects of the interference on several crucial kinematic variables are studied, listed as following:

- the four body mass m_{WW},
- the two body mass of the hadronic decayed W, m_W,
- the rapidity of the hadronic decayed W, η_W,
- the transverse momentum of the lepton, p_T^l,
- the minimal azimuthal opening angle between the lepton and jets, ϕ_{1j},
- the azimuthal opening angle between the jets, ϕ_{jj}.

The blue curves in Fig. 114 are for signal process, the red ones are for the signal plus continuum background, while the yellow bands correspond to the reweighted signal uncertainties). As one can see from Fig. 114, the reweighting scheme mentioned above based on M_{WW} spectrum, turns out to describe well other distributions: the reweigthed curves differ a lot from the Signal curves while lie mostly inside the the interference uncertainty bands.

12.3.2 Comparison with MCFM: gg->WW->lνlν

For the $WW \rightarrow lv_1 lv_1$ channel (with $l = e, \mu$), the effect of the interference between $gg \rightarrow H \rightarrow WW$ and continuum $gg \rightarrow WW$ production becomes increasingly important as the mass of the resonance increases.

(a) M_{WW}

(b) M_W

(c) η_W

(d) PT_l

(e) ϕ_{lj}

(f) ϕ_{jj}
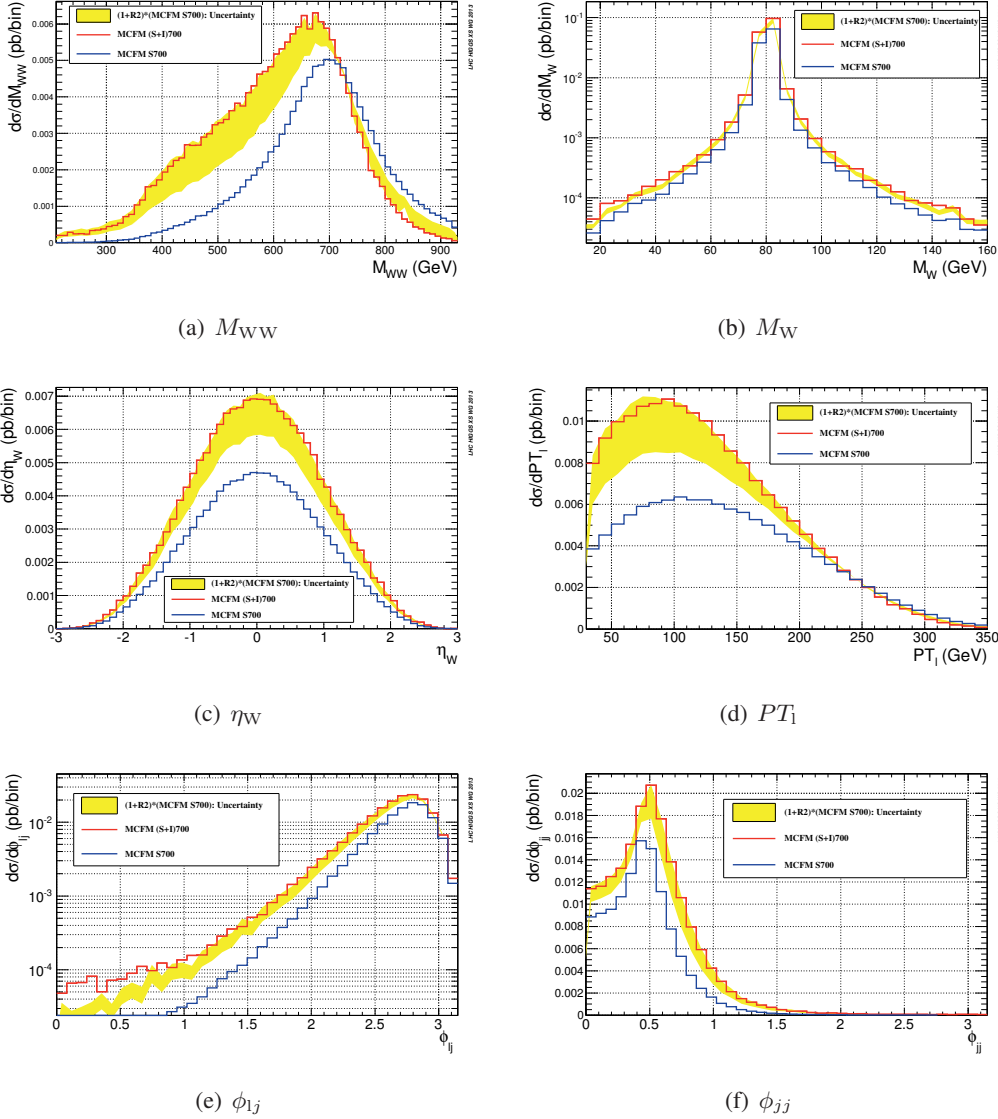
Figure 114: Reweighting MCFM $gg \rightarrow H \rightarrow WW \rightarrow l\nu_l jj$ results to take into account interference effects at the generator level, for $M_H = 700$ GeV at the 8 TeV LHC, with $p_T^l > 30$ GeV, $p_T^j > 30$ GeV, MET> 30 GeV, and $|\eta_{l,j}| < 2.4$. Blue curves are for signal process, the red ones are for the signal plus continuum background, while the yellow bands correspond to the reweighted signal uncertainties Eqs.(301) and (302).

Fig. 115 shows the LO Feynman diagrams for the two processes.

In ATLAS, a study of the effect of the interference on key kinematic variables has been performed using the MCFM [283] Monte Carlo program. The study uses MCFM 6.2, the processes being generated at a centre-of-mass (CM) energy of 8 TeV, with no cuts on the generation. Events MCFM processes 121 and 122 are respectively used to generate distributions for the pure $H \rightarrow WW \rightarrow l\nu_l l\nu_l$ process and the process including the effect of the interference. Both processes are calculated to leading order accuracy in QCD. This requires a reweighting procedure to account for higher-order corrections. This procedure has been described in section 12.1.1. Distributions are generated for six different resonance masses $M_H : 400, 500, 600, 700, 800$ and 900 GeV. The renormalization and factorization scales are set to the mass of the resonance being generated.

The object selection criteria used in this study are similar to those used in the ATLAS $H \rightarrow$
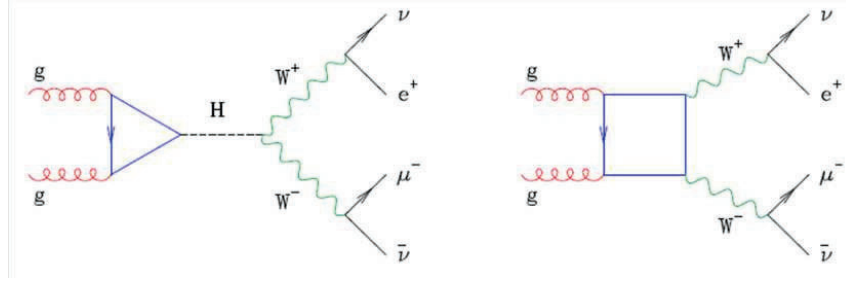
Figure 115: Diagrams for the gg $\to$ H $\to$ WW $\to$ lv$_l$lv$_l$ process (left) and the continuum gg $\to$ WW $\to$ lv$_l$lv$_l$ process (right).

WW $\to$ lv$_l$lv$_l$ analysis [610]. The leptons are required to be within $|\eta| < 2.5$. The leading lepton must have $p_T > 25$ GeV, and the sub-leading lepton $p_T > 15$ GeV. The missing transverse momentum is required to be larger than 45 GeV. No requirement is made on the number of jets in the final state nor on the types of the two leptons.

The interference effect affects the shape of the distributions used in the analysis. The effects of such reweighting are studied for four crucial kinematic variables:

– the dilepton invariant mass $M_{\ell\ell}$
– the transverse momentum of the dilepton system $p_T^{\ell\ell}$
– the dilepton azimuthal opening angle $\Delta\phi_{\ell\ell}$
– the transverse mass M_T

The first three variables are important because the analysis uses them to reject background and define a signal region. The fourth variable, M_T, is the final discriminant [610].

Figures 116 - 119 show distributions of the variables for pure H $\to$ WW, for the process including the interference and for the pure signal process reweighted according to the lineshape distribution (i.e. the invariant mass of the two Ws). For each variable, distributions are shown for three of the six resonance masses corresponding to 400, 600 and 900 GeV. The ratio between the signal distributions including the interference and the reweighted distributions is also plotted. The cross-section σ_{H_i} including the interference effect is not strictly physical, and can be negative (see Eq. 4.1 in [554]), as seen in many of the distributions. From these plots it is clear that the interference has a large impact on both the cross-section and the shape of the distributions, particularly for higher Higgs masses. The plots also show that reweighting by M_{WW} correctly reproduces the effect of interference on the shapes of other distributions.

The same distributions have been obtained before applying any cuts and it has been proven that the shape of the distributions is not affected by the cuts. The difference between the efficiency calculated on samples which include the interference at generation level and on signal reweighted samples, has been used to evaluate the systematic uncertainty associated to the reweighting procedure as reported in table 68.

From this it is clear that the overall effect of the discrepancies between the reweighting and the process including the effect of the interference distributions is a few %. The exact magnitude of the uncertainty depends upon which cuts are applied, and which mass point is being examined - here, it ranges from 1% for the $M_H = 400$ GeV case to 5% for the $M_H = 900$ GeV case.

Having looked at the effect of reweighting at LO, there remains the issue of reweight for higher order effects. This study reweights to NNLO, using the schemes suggested in [102], and the correspondent K factors [559] as discussed in section 12.1.2:
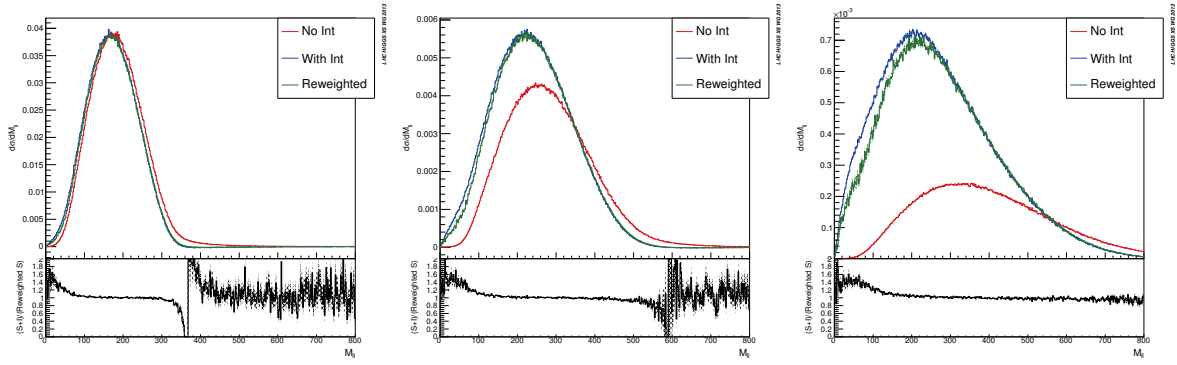
Figure 116: Distributions of the dilepton invariant mass $M_{\ell\ell}$ showing the effect of the interference and the result of the reweighting procedure after cuts, corresponding to a Higgs mass of $M_H = 400\,\text{GeV}$ (left), $600\,\text{GeV}$ (middle), $900\,\text{GeV}$ (right).
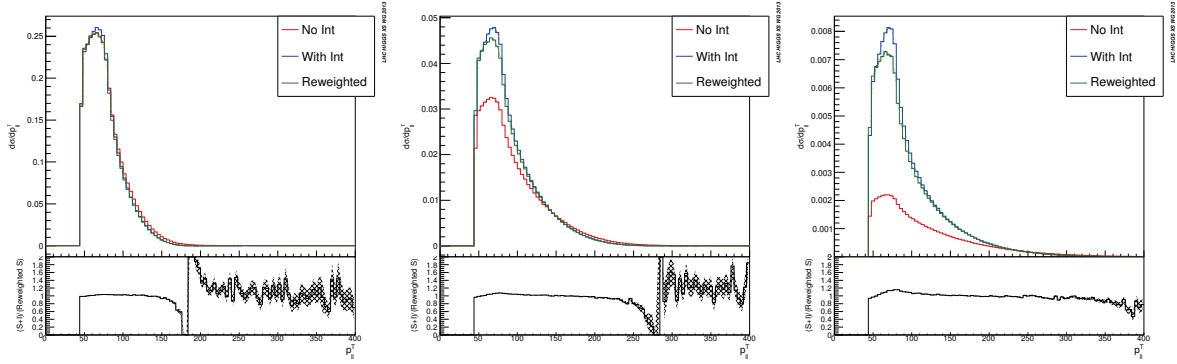
Figure 117: Distributions of the transverse momentum of the dilepton system $p_T^{\ell\ell}$ showing the effect of the interference and the result of the reweighting procedure after cuts, corresponding to a Higgs mass of $M_H = 400\,\text{GeV}$ (left), $600\,\text{GeV}$ (middle), $900\,\text{GeV}$ (right).
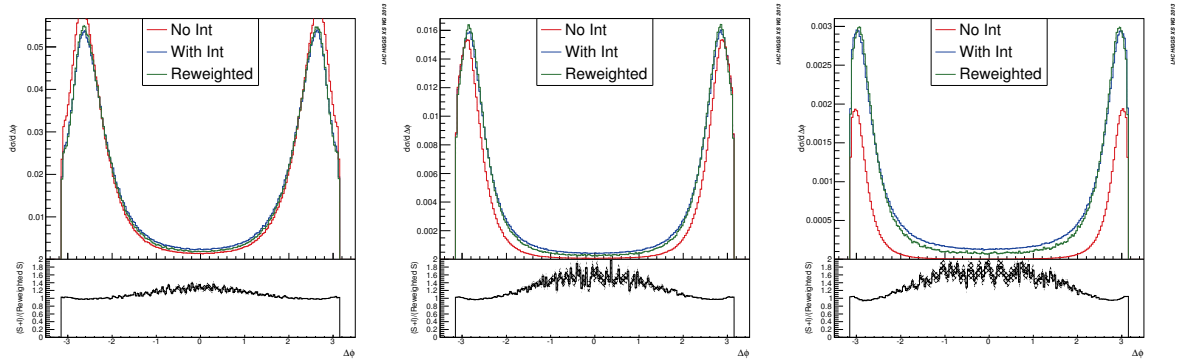
Figure 118: Distributions of the dilepton azimuthal opening angle $\Delta\phi_{\ell\ell}$ showing the effect of the interference and the result of the reweighting procedure after cuts, corresponding to a Higgs mass of $M_H = 400\,\text{GeV}$ (left), $600\,\text{GeV}$ (middle), $900\,\text{GeV}$ (right).

- Additive: $K\,S + I$
- Multiplicative: $K\,S + K\,I$
- Intermediate: $K\,S + \text{sqrt}(K_{\text{gg}})\,I$
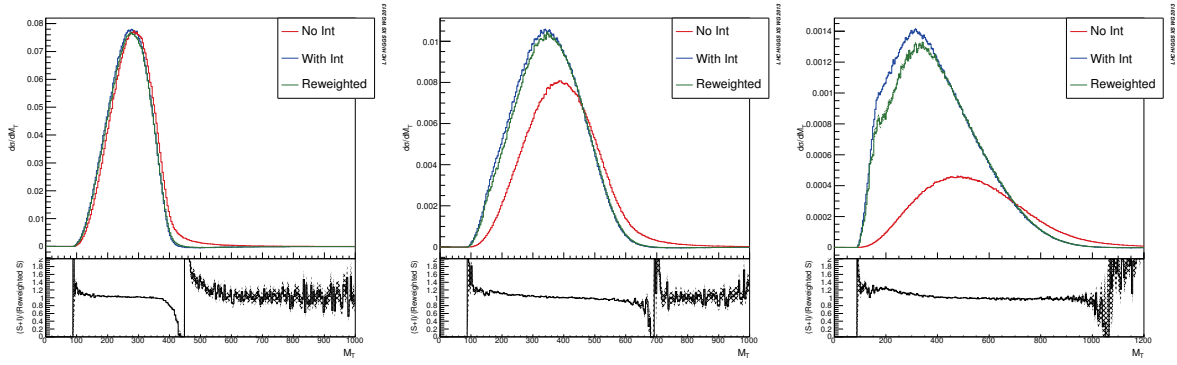
Figure 119: Distributions of the transverse mass M_T showing the effect of the interference and the result of the reweighting procedure after cuts, corresponding to a Higgs mass of $M_H = 400$ GeV (left), 600 GeV (middle), 900 GeV (right).

Table 68: Efficiency of the cuts (fraction of cross section remaining) for the samples generated with the interference effect included and the reweighted samples.

| | $M_H = 400$ GeV | | $M_H = 600$ GeV | | $M_H = 900$ GeV | |
	S+I	Reweighted	S+I	Reweighted	S+I	Reweighted
After Preselection Cuts	0.844945	0.846989	0.876930	0.879919	0.876166	0.881239
After Kinematic Cuts	0.624508	0.619817	0.640973	0.630267	0.661190	0.634992
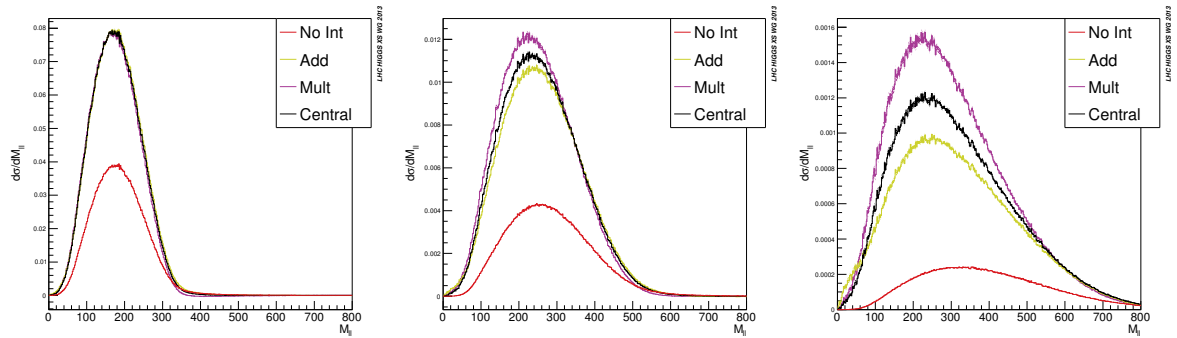
Figure 120: Distributions of the dilepton invariant mass $m_{\ell\ell}$ showing the three schemes for scaling to NNLO, with the LO signal distribution for comparison, at Higgs masses of $M_H = 400$ GeV (left), 600 GeV (middle), 900 GeV (right).

Figures 120 - 123 show these three schemes – together with the LO Signal for comparison – for each of the 4 distributions shown earlier, after the aforementioned cuts have been applied. The Additive (in yellow) and the Multiplicative (in magenta) schemes form bounds for the theory uncertainty in the scaling to NNLO, while the Intermediate scheme (in black) is the nominal NNLO Signal plus Interference distribution.

From these plots, it is evident that the difference between the Intermediate distributions and the Additive or Multiplicative ranges from a negligible amount at $M_H = 400$ GeV, to about $\pm\,25\%$ at $M_H = 900$ GeV. This is a very conservative estimate of the uncertainty in scaling to NNLO, and gives a very large uncertainty for high M_H. The different schemes for scaling to NNLO do not seem to affect
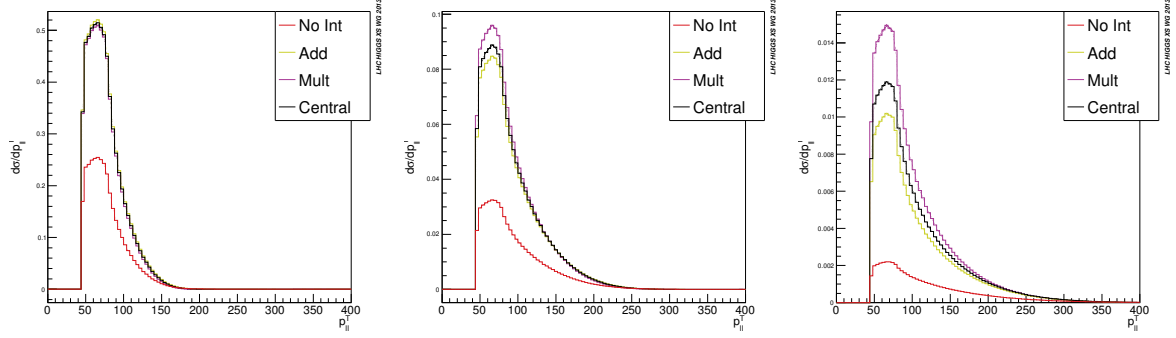
Figure 121: Distributions of the transverse momentum of the dilepton system $p_T^{\ell\ell}$ showing the three schemes for scaling to NNLO, with the LO signal distribution for comparison, at Higgs masses of $M_H = 400$ GeV (left), 600 GeV (middle), 900 GeV (right).
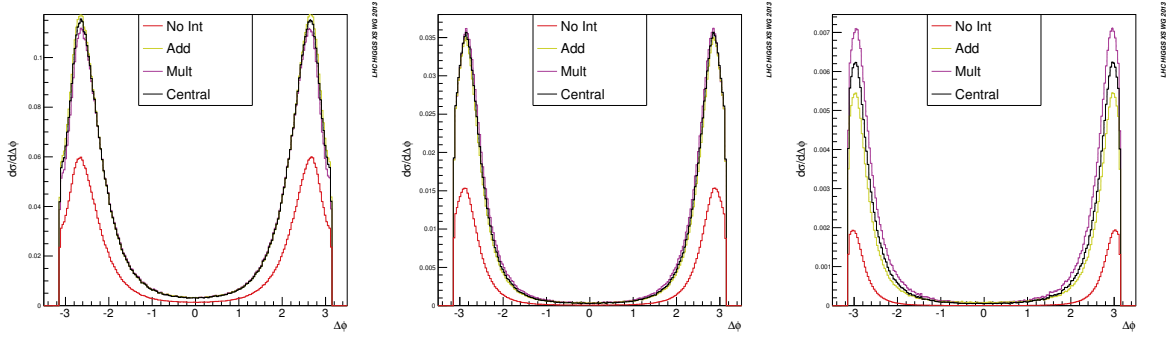
Figure 122: Distributions of the dilepton azimuthal opening angle $\Delta\phi_{\ell\ell}$ showing the three schemes for scaling to NNLO, with the LO signal distribution for comparison, at Higgs masses of $M_H = 400$ GeV (left), 600 GeV (middle), 900 GeV (right).
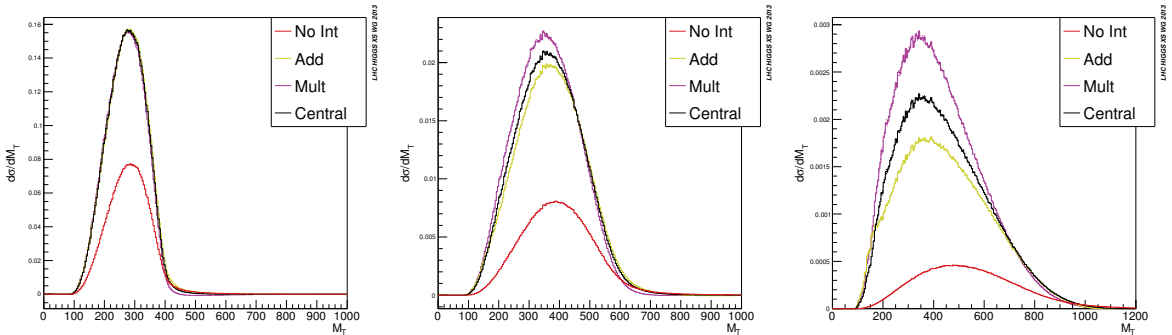
Figure 123: Distributions of the transverse mass M_T showing the three schemes for scaling to NNLO, with the LO signal distribution for comparison, at Higgs masses of $M_H = 400$ GeV (left), 600 GeV (middle), 900 GeV (right).

the shape of the distributions significantly.

In conclusion, event-by-event reweighting by the M_{WW} distribution reproduces the effect of interference fairly closely, though it does introduce some uncertainty, of order 1% for $M_H = 400$ GeV and 5% for $M_H = 900$ GeV. A much larger uncertainty is introduced by the process of reweighting to NNLO, rising to $\pm 25\%$ for $M_H = 900$ GeV, the highest mass point studied.

12.3.3   Studies with gg2VV: gg->ZZ->2l2ν

The effect of the resonance-continuum interference between the SM Higgs signal process $gg \to H \to ZZ$ and the irreducible background process $gg \to ZZ$ has been studied at leading order in pp collision at $\sqrt{s} = 8$ TeV, using the program GG2VV-3.1.0 [85]. Results for a heavy Higgs boson (600 GeV or above) are presented here.

Parton level cross sections for $gg(\to H) \to ZZ \to 2\ell2\nu$ are presented in Table 69 . Results are given for a single lepton flavor combination. Please note when charged leptons and neutrinos are in same flavor, i.e., $2\mu2\nu_\mu$ or $2e2\nu_e$ final states, there also exits interference with $gg \to WW \to 2\ell2\nu$. So the same flavor case is computed separately.

The renormalization and factorization scales are set to $M_H/2$. The PDF set CT10NNLO is used. The following experimental selection cuts are applied: $p_T^\ell > 20$ GeV, $|\eta_\ell| < 2.5$, $|M_{\ell\ell} - 91| < 15$ GeV, $p_T^{\ell\ell} > 55$ GeV, $E_T^{miss} > 90$ GeV, $M_T > 325$ GeV. The M_T variable is the transverse mass of the $ZZ \to 2\ell2\nu$ system, defined as:

$$M_T^2 = \left[\sqrt{p_{T,\ell\ell}^2 + M_{\ell\ell}^2} + \sqrt{E_T^{miss,2} + M_{\ell\ell}^2} \right]^2 - \left[\vec{p}_{T,\ell\ell} + \vec{E}_T^{miss} \right]^2 \tag{303}$$

As shown in the table, for a 600 GeV Higgs signal, the interference effect can be a few percent, and for 1 TeV signal, it can be as large as 90%.

Table 69: Parton level cross sections in fb for a single lepton flavor combination. S is Higgs signal; B is continuum background; Tot is signal and background together, including their interference. R is a ratio of interference effect, defined as (Tot-B)/S.

| M_H (GeV) | $gg(\to H) \to ZZ \to 2\ell2\nu$ | | | | $gg(\to H) \to ZZ/WW \to 2\ell2\nu$ | | | |
	S	B	Tot	R	S	B	Tot	R
600	0.200(1)	0.0633(2)	0.277(1)	1.07	0.202(3)	0.0671(5)	0.283(3)	1.07
700	0.0914(6)	0.0596(2)	0.1681(7)	1.19	0.0920(5)	0.0636(7)	0.171(2)	1.17
800	0.0439(3)	0.0566(2)	0.1159(5)	1.35	0.0441(3)	0.0602(2)	0.1218(7)	1.40
900	0.0224(1)	0.0541(2)	0.0891(3)	1.56	0.0221(3)	0.0567(4)	0.0927(9)	1.63
1000	0.01202(7)	0.05202(2)	0.0741(3)	1.84	0.0121(2)	0.0549(4)	0.0783(3)	1.93

The interference also changes kinematics of signal. A recipe from LHCHXSWG is used [14] to reweight signal lineshapes to account for this change and its uncertainty. Again, GG2VV-3.1.0 is used to generate signal sample, background sample and signal+interference+background sample at each signal mass point. The $2\ell2\nu$ invariant mass distributions of such three samples for 900 GeV signal hypothesis are shown as Fig. 124(left). We can see the interference enhances the mass pole and below, but slightly reduces where above the mass pole. The interference term could be separated by subtracting signal and background distributions from signal+interference+background distribution. Then a set of NNLO K-factors as a function of m_{ZZ} are read from theorists and applied to signal term S and interference term I as below

$$dS_{\mathrm{NNLO}} = K(m)\, dS$$

$$dS_{\mathrm{corr}} = dS_{\mathrm{NNLO}} + (K(m))^n\, dI, n = 0, 0.5, 1$$

Here S_{NNLO} is signal lineshape after NNLO K-factors applied, and S_{corr} is that after including interference. As for the S_{corr}, $n = 0.5$ gives central shape, while $n = 0$ or 1 gives down or up uncertainty band. Fig. 124(right) shows S_{NNLO} and S_{corr} with its uncertainty band, for 900 GeV signal hypothesis. By dividing S_{corr} by S_{NNLO}, we get weights to correct our POWHEG signal lineshapes.
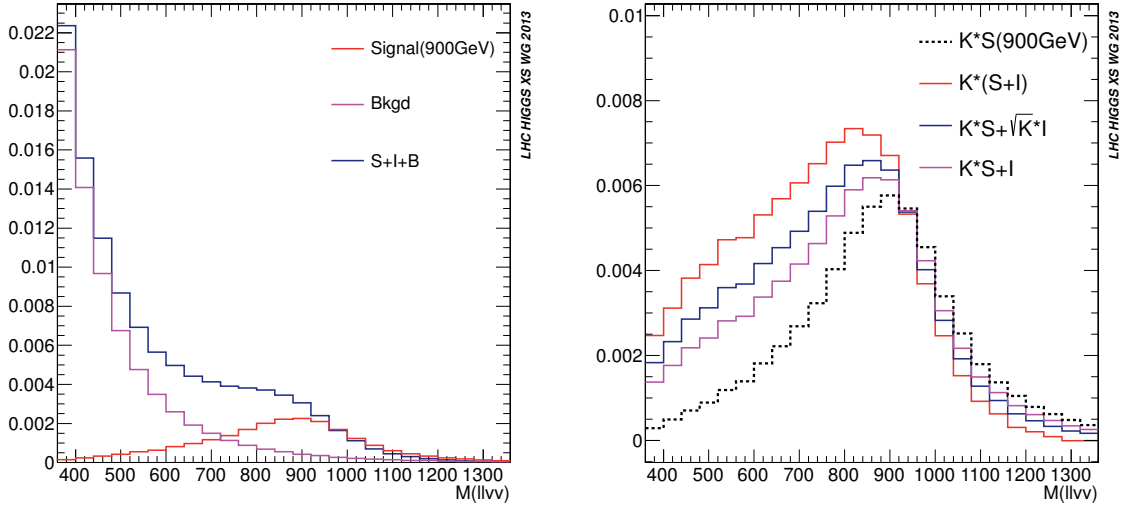
Figure 124: Invariant mass of the $2\ell2\nu$ system for $gg(\rightarrow H) \rightarrow ZZ \rightarrow 2\ell2\nu$ signal, background and signal+background+interference (*left*); Signal lineshape before and after including interference (*right*). A 900 GeV signal hypothesis is used here

12.3.4 Reweighting CPS PowHeg-BOX samples

At high Higgs mass the interference between the Higgs signal and the $gg \rightarrow ZZ$ or $gg \rightarrow WW$ continuum backgrounds becomes very large. It can affect significantly both cross sections and distributions, depending from the final state. More recently, the interference effect at LO has been included in some MC programs as discussed in Section 12.2. Nevertheless the current signal samples used by ATLAS and CMS have been generated with POWHEG BOX [80] which does not include the interference effect. This brings to the needs of a theoretical prescription to reweight such samples in order to account for this effect and associate an uncertainty on this reweighting procedure.

Several reweighting tools based on tables and scale factors provided in [559] have been developed depending from the different final state. They allow to rescale on an event by event basis the CPS PowHeg BOX MC signal samples to account for the interference effect and to include the theoretical uncertainties as described in Section 12.1.2.

The effect of such reweighting on ZZ and WW invariant masses, with the associated uncertainties are shown respectively in Fig. 125 and Fig. 126.
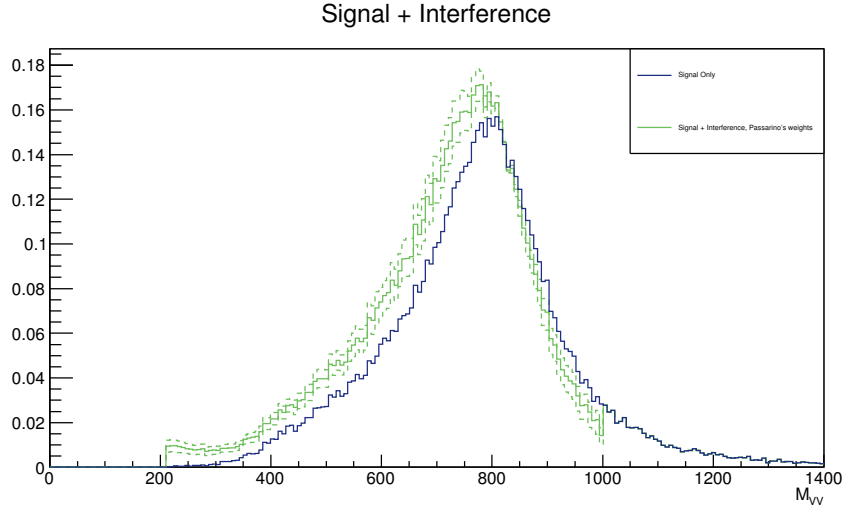
Figure 125: Distribution at generator level for an Higgs mass of 800 GeV before (blue solid line) and after (green solid line) the inclusion of the interference. The shapes to describe the uncertainty are also shown (dot-dashed green lines)
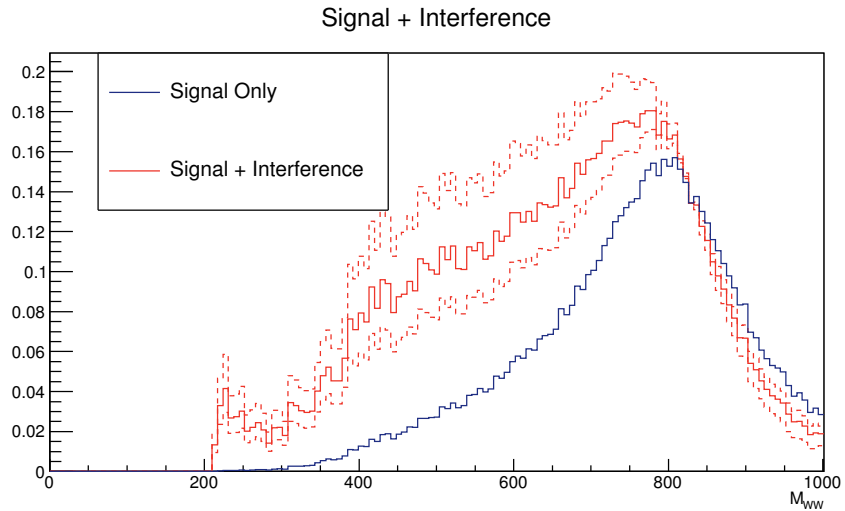
Figure 126: Distribution at generator level for an Higgs mass of 800 GeV before (blue solid line) and after (red solid line) the inclusion of the interference. The shapes to describe the uncertainty are also shown (dot-dashed red lines)

12.4 Interference effects in VBF production

12.4.1 Signal definition

Also in the VBF Higgs production mode, interference effects between the Higgs signal process and the continuum background become increasingly important when going to higher Higgs masses. NLO QCD corrections to the full process $pp \rightarrow VVjj$ have been calculated in Ref. [611, 612] and are available in VBFNLO [110–112] including decays of the vector bosons. We will concentrate on the $pp \rightarrow W^+W^-jj$ process, which can be calculated with both fully leptonic $(l^+\nu_l l^-\bar{\nu}_l)$ as well as semileptonic $(l^+\nu_l jj, l^-\bar{\nu}_l jj)$ decays of the W bosons.
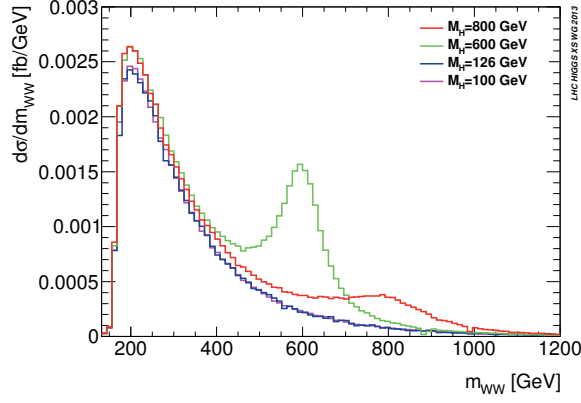
Figure 127: Invariant WW mass distribution for the process $\mathrm{pp} \to \mathrm{WW}jj$ for different Higgs boson masses, intended either as signal (600 and 800 GeV) or as background definition with a light Higgs boson (100 and 126 GeV).

Both Higgs and continuum diagrams are necessary to ensure the correct high-energy behavior. For large invariant masses of the vector-boson pair $\sqrt{s}$, the continuum diagrams $\mathcal{M}_\mathrm{B}$ are proportional to $-\frac{s}{v^2}$, where v denotes the Higgs vacuum expectation value, and would lead to unitarity violation at about 1 TeV. They are canceled by corresponding diagrams with s-, t- and u-channel exchange of a Higgs boson $\mathcal{M}_H \propto \frac{s}{v^2}$ in the leading term. This raises the question of how to best define the signal, or correspondingly the background contribution which is subsequently subtracted from the full process. Naive definitions like only taking the signal plus interference contributions into account or, equivalently, subtracting the contribution coming from background diagrams only will violate unitarity at large center-of-mass energies of the diboson system.

The invariant mass distribution of the WW diboson system is shown in Fig. 127 for various choices of the Higgs boson mass. The distributions have been generated with VBFNLO using standard vector-boson-fusion cuts on the two tagging jets ($m_{jj} > 600$ GeV, $|\eta_{j1} - \eta_{j2}| > 4$, $\eta_{j1} \times \eta_{j2} < 0$) in addition to general detector acceptance cuts ($p_{T,j} > 20$ GeV, $\eta_j < 4.5$, $p_{T,\ell} > 10$ GeV, $\eta_\ell < 2.5$). We show two examples for heavy Higgs bosons of 600 and 800 GeV mass, as well as for two light Higgs masses of 126 and 100 GeV. For the latter, the Higgs peak is outside of the shown range. We see that the two light-mass curves agree very well, with some small remaining mass dependence in the region around the WW production threshold. Therefore, we can use these to define the background

$$\sigma_\mathrm{B} = \int d\Phi |\mathcal{M}_\mathrm{B} + \mathcal{M}_\mathrm{h}(m_\mathrm{h})|^2 \,, \tag{304}$$

where m_h denotes the mass of the light Higgs boson used for subtraction and $d\Phi$ denotes the phase-space integration. This then leads to our definition of the signal+interference contribution

$$\sigma_{S+I} = \int d\Phi |\mathcal{M}_\mathrm{B} + \mathcal{M}_H(M_\mathrm{H})|^2 - \sigma_\mathrm{B} \tag{305}$$

with the heavy Higgs mass M_H. This approach respects the correct high-energy behavior.

12.4.2 Event reweighting

A full simulation of LHC processes, involving NLO events plus parton shower and detector simulation with cuts on the final-state particles, is a time-consuming task. If events in a related scenario with similar kinematic features have already been fully simulated, one can re-use them and apply a reweighting procedure to the events at parton-level. In VBFNLO this is included as an add-on named REPOLO – REweighting POwheg events at Leading Order – and is available on request by the VBFNLO authors.
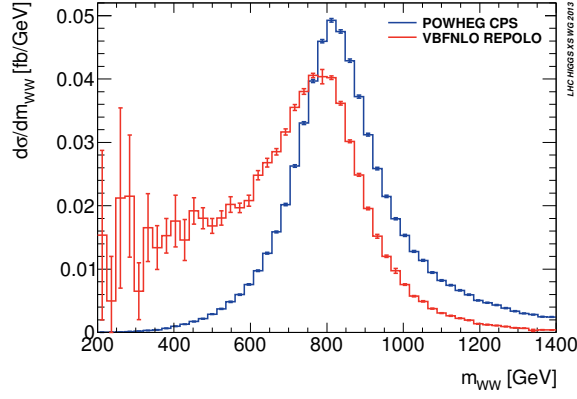
Figure 128: Invariant WW mass distribution for the process $pp \rightarrow WWjj$. The distribution is shown for the signal-only process generated with POWHEG, as well as reweighted by REPOLO to include signal-background interference according to Eq. 306. The branching ratio $H \rightarrow WW$ has been divided out for both curves.

In this subsection we will discuss the reweighting of VBF production of a heavy Higgs boson. The starting point are unweighted events of the signal process only for a Higgs boson of 800 GeV, generated with POWHEG [113]. Using the VBFNLO framework, we then create a new event file where each signal event is reweighted by a factor

$$\frac{|\mathcal{M}_{\mathrm{B}} + \mathcal{M}_{H}(M_{\mathrm{H}})|^2 - |\mathcal{M}_{\mathrm{B}} + \mathcal{M}_{\mathrm{h}}(m_{\mathrm{h}})|^2}{|\mathcal{M}_{H}(M_{\mathrm{H}})|^2} \tag{306}$$

according to Eq. 305. Events are reweighted for heavy Higgs bosons without decay. For the resulting signal+interference contribution, this corresponds to dividing over the Higgs branching into WW. Internally, a decay into $W^+W^- \rightarrow l^+\nu_l l^-\bar{\nu}_l$ is simulated for all matrix elements which appear in the reweighting.

The result of this procedure is shown in Fig. 128 where 900000 POWHEG events have been reweighted. For the background subtraction a Higgs boson with mass 100 GeV has been used. One observes the significant effect of the interference term, which enhances the rate for smaller invariant masses, while at the same time decreasing the rate for larger ones. This corresponds to the constructive and destructive interference, respectively, as expected from theory. The reweighting procedure has its limits in phase-space regions, where the reweighted event weight is significantly larger than the original one. In the shown example this happens for invariant masses below about 400 GeV. The differential signal-only cross section gets very small, while the interference term still yields a relevant contribution. In practice, a possible remedy would be to generate additional events in the region where the process to be reweighted is known to be small.

13 BSM Higgs benchmarks in light of the discovery of a 126 GeV boson [62]

This document provides a first proposition of a framework in which the continuing LHC Higgs searches at masses other than 125 GeV can be interpreted.

13.1 Introduction

After the discovery of a new Higgs-like boson with SM-like properties by the LHC experiments ATLAS and CMS [1, 2, 613] the next step is to determine whether this Higgs-like particle is fully responsible for the generation of the masses of the other SM particles. This means in other words, that it fully unitarizes the high-energy scattering amplitudes for $V_L V_L \to V_L V_L$ (V = W or Z) and $V_L V_L \to f\bar{f}$.

If the Higgs-like particle at 125 GeV is not fully responsible for the unitarization of the scattering amplitudes, then additional new physics must be present to play this role. Here we propose two benchmarks in which a second scalar particle completes the unitarization of the scattering amplitudes. The allowed values of the couplings of this second particle are therefore constrained by the observed production and decay rates of the 125 GeV Higgs-like state.

We try to match these benchmarks to the coupling extraction parameterizations of the Light Mass Higgs Subgroup [306]. For each benchmark we give a model-independent parameterization as well as a particular realization in terms of a specific model. In some cases, the specific model fixes the values of some of the free parameters.

13.2 Relations imposed by unitarity

The couplings to gauge bosons and fermions of the 125 GeV Higgs-like state, denoted by h_1 in the following, and the ones of the second scalar particle, denoted by h_2, are subject to constraints imposed by unitarity. We introduce the scaling factors κ_i and κ_i' ($i = f, W, Z$) for the couplings of h_1 and h_2 to the fermions and gauge bosons. The coupling factors without prime apply for the couplings of the 125 GeV Higgs-like state h_1 and the one with prime for the second state h_2. The coupling factors are defined relative to the corresponding couplings of a SM Higgs boson, as in the coupling-extraction document [306].

The requirement of unitarization of longitudinal gauge boson scattering $V_L V_L \to V_L V_L$ (V = W, Z) leads to the following sum rule[63]:

$$\kappa_V^2 + \kappa_V'^2 = 1. \tag{307}$$

The unitarization of longitudinal gauge boson scattering into a fermion pair, $V_L V_L \to f\bar{f}$, requires that

$$\kappa_V \kappa_f + \kappa_V' \kappa_f' = 1. \tag{308}$$

This equation holds separately for each fermion species. Here κ_f needs not be the same for different kinds of fermions.

In the following we propose two benchmark scenarios. For each of them we give a model-independent parameterization as well as a particular realization in terms of a specific model. In some cases, the specific model fixes the values of some of the free parameters.

13.3 Benchmark 1: One common scaling factor

In this benchmark scenario a common scaling factor is chosen both for the gauge and the fermion couplings of the field h_1 relative to the corresponding SM couplings.

---

[62]S. Bolognesi, S. Diglio, C. Grojean, M. Kadastik, H.E. Logan, M. Muhlleitner K. Peters (eds.)

[63]This expression assumes that $\kappa_W = \kappa_Z$ as imposed by custodial symmetry.

Model-independent parameterization: For the 125 GeV state h_1 we then have

$$\kappa \equiv \kappa_V = \kappa_f. \tag{309}$$

This is equivalent to the overall signal strength scaling $\mu = \kappa^2$.

The corresponding coupling of the second state h_2 is then

$$\kappa' \equiv \kappa'_V = \kappa'_f = \sqrt{1 - \kappa^2}. \tag{310}$$

While κ' can formally be of either sign, we choose the plus sign with no loss of generality because only the relative signs of the couplings of h_2 are physically meaningful.

The only other parameter affecting the rates for production and decay of h_2 is the branching ratio for possible decays into "new" final states, BR_{new}. (For example, this new branching ratio can be due to the decays $h_2 \to h_1 h_1$ for $M_{h_2} \geq 2M_{h_1} \simeq 250$ GeV).

The relevant observables in the search for h_2 are the h_2 production cross section σ', the h_2 total width Γ'_{tot}, and the branching ratio BR' for h_2 into the observable final state of interest. From the expression for the total width Γ' of h_2,

$$\Gamma' = \kappa'^2 \Gamma_{SM} + \Gamma_{new}, \tag{311}$$

it follows that these observables are given in terms of κ' and BR_{new} according to

$$\begin{aligned} \sigma' &= \kappa'^2 \sigma_{SM}, \\ \Gamma' &= \frac{\kappa'^2}{(1 - BR_{new})} \Gamma_{SM}, \\ BR' &= (1 - BR_{new}) BR_{SM}, \end{aligned} \tag{312}$$

where σ_{SM}, Γ_{SM}, and BR_{SM} are the cross section, total width, and branching ratio into the final state of interest as predicted for the SM Higgs when its mass is equal to M_{h_2}. In the narrow width approximation, the signal strength μ' for h_2 can be obtained using

$$\mu' = \frac{\sigma' \times BR'}{\sigma_{SM} \times BR_{SM}} = \kappa'^2 (1 - BR_{new}). \tag{313}$$

In Figure 129 we show the signal strength μ' and the total width Γ' in units of the total width of the SM Higgs boson in the plane (κ'^2, BR_{new}).

Constraints from existing data: ATLAS and CMS have measured $\mu \equiv \sigma/\sigma_{SM}$ for the 125 GeV boson. The results are (as of March 2013) [10, 11]

$$\begin{aligned} \text{ATLAS}: \quad & \mu = 1.30 \pm 0.20 \\ \text{CMS}: \quad & \mu = 0.88 \pm 0.21 \ . \end{aligned} \tag{314}$$

Taking the uncertainty to be Gaussian, these correspond to a 2σ lower bound on μ and hence an upper bound of κ'^2 of

$$\begin{aligned} \text{ATLAS}: \quad & \mu > 0.90 \quad \to \quad \kappa'^2 < 0.10 \\ \text{CMS}: \quad & \mu > 0.46 \quad \to \quad \kappa'^2 < 0.54 \ . \end{aligned} \tag{315}$$

Here we have assumed that the branching ratio of the 125 GeV Higgs h_1 into non-SM final states is zero.

Specific model: This parameterization is realized for the SM Higgs boson mixed with an electroweak singlet. In this case, BR_{new} arises from decays of $h_2 \to h_1 h_1$ for $M_{h_2} > 2M_{h_1} \simeq 250$ GeV. The Lagrangian and Feynman rules, are given in Section 13.3.1.
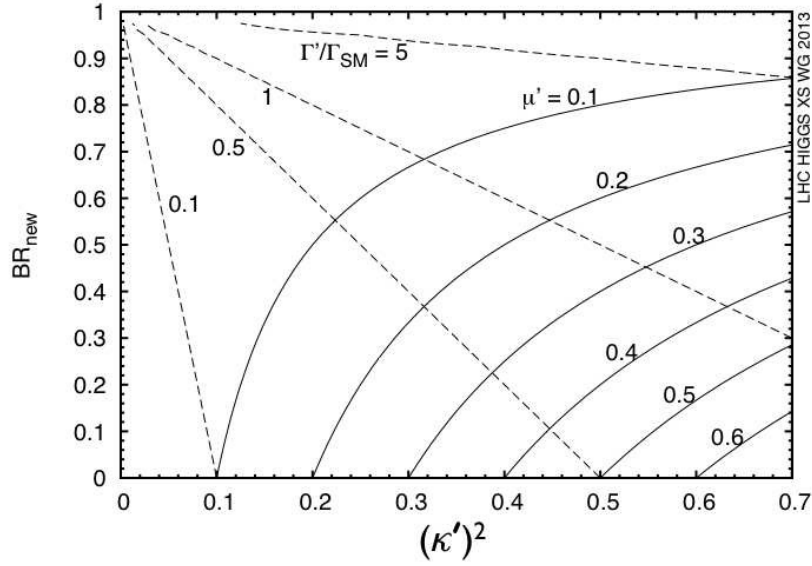
Figure 129: The h_2 signal strength μ' and the h_2 total width Γ' in units of the SM Higgs total width Γ_{SM} for Benchmark 1 (one common scaling factor) in the (κ'^2, BR_{new}) plane.

13.3.1   Specific benchmark model 1: Standard Model plus a Real Singlet Field

The simplest extension of the SM Higgs sector is given by the addition of a singlet field which is neutral under the SM gauge groups [614–618]. This singlet field also acquires a non-vanishing vacuum expectation value. Such models have been discussed in numerous publications [357, 619–633] and we shall give details in the following.

13.3.2   The model

The most general gauge-invariant potential can be written as [617, 619]

$$V = \lambda \left(\Phi^\dagger \Phi - \frac{v^2}{2} \right)^2 + \frac{1}{2}M^2 s^2 + \lambda_1 s^4 + \lambda_2 s^2 \left(\Phi^\dagger \Phi - \frac{v^2}{2} \right) + \mu_1 s^3 + \mu_2 s \left(\Phi^\dagger \Phi - \frac{v^2}{2} \right), \quad (316)$$

where s is the real singlet scalar and in the unitary gauge the SM Higgs doublet can be written as

$$\Phi = \begin{pmatrix} 0 \\ (\phi + v)/\sqrt{2} \end{pmatrix} \quad (317)$$

with $v \simeq 246$ GeV. We have already used the freedom to shift the value of s so that s does not get a vacuum expectation value. As a result, M^2 must be chosen positive in Eq. (316).

To prevent the potential from being unbounded from below, the quartic couplings must satisfy the conditions:

$$\lambda > 0, \qquad \lambda_1 > 0, \qquad \lambda_2 > -2\sqrt{\lambda\lambda_1}. \quad (318)$$

The trilinear couplings μ_1 and μ_2 can have either sign.

13.3.3   Mass eigenstates

After replacing Eq. (317) for Φ in the potential Eq. (316), we obtain

$$V = \frac{\lambda}{4}\phi^4 + \lambda v^2 \phi^2 + \lambda v \phi^3 + \frac{1}{2}M^2 s^2 + \lambda_1 s^4 + \frac{\lambda_2}{2}\phi^2 s^2 + \lambda_2 v \phi s^2 + \mu_1 s^3 + \frac{\mu_2}{2}\phi^2 s + \mu_2 v \phi s . \quad (319)$$

232

The terms quadratic in the fields (that give rise to the mass matrix) are

$$V_2 = \lambda v^2 \phi^2 + \frac{1}{2} M^2 s^2 + \mu_2 v \, \phi s. \tag{320}$$

In particular, the mixing between ϕ and the singlet field s is controlled by the coupling μ_2. The mass eigenvalues are then given by

$$M^2_{h_1, h_2} = \lambda v^2 + \frac{1}{2} M^2 \mp \sqrt{\left(\lambda v^2 - \frac{1}{2} M^2\right)^2 + \mu_2^2 v^2}, \tag{321}$$

where we have defined the mass eigenstates h_1, h_2 as

$$
\begin{aligned}
h_1 &= \phi \cos\theta - s \sin\theta \\
h_2 &= \phi \sin\theta + s \cos\theta,
\end{aligned} \tag{322}
$$

with the mixing angle θ which can be written as

$$\tan 2\theta = \frac{-\mu_2 v}{\lambda v^2 - \frac{1}{2} M^2}. \tag{323}$$

In order to find the domain of θ we can rewrite the masses as follows:

$$M^2_{h_1, h_2} = \left(\lambda v^2 + \frac{1}{2} M^2\right) \mp \left(\frac{1}{2} M^2 - \lambda v^2\right) \sec 2\theta \tag{324}$$

If we require h_1 to be the lighter mass eigenstate and choose $M^2 > 2\lambda v^2$, then $\sec 2\theta > 0$, and hence $\theta \in (-\frac{\pi}{4}, \frac{\pi}{4})$.

Note that in the notation of Eq. (309) and (310) we have in particular

$$
\begin{aligned}
\kappa &\equiv \kappa_V = \kappa_f = \cos\theta \tag{325} \\
\kappa' &\equiv \kappa'_V = \kappa'_f = \sin\theta . \tag{326}
\end{aligned}
$$

13.3.4 The trilinear and quartic interactions

Here, we give the trilinear and quartic interactions among the mass eigenstates h_1 and h_2. The related Feynman rules are necessary for the determination of the Higgs-to-Higgs decays, namely the decay of the heavier state h_2 into two lighter bosons $h_1 h_1$.

The relevant terms for the cubic interactions are

$$V_3 = \lambda v \phi^3 + \lambda_2 v \phi s^2 + \mu_1 s^3 + \frac{\mu_2}{2} \phi^2 s . \tag{327}$$

Using the shorthands $s_\theta \equiv \sin\theta$ and $c_\theta \equiv \cos\theta$ and rewriting the trilinear terms of the potential in terms of the mass eigenstates, we find the following couplings.

After replacing ϕ and s by the mass eigenstates h_1 and h_2, the triple-h_1 coupling comes from the potential term

$$V_{111} = h_1{}^3 \left[\lambda v c_\theta^3 + \lambda_2 v c_\theta s_\theta^2 - \mu_1 s_\theta^3 - \frac{\mu_2}{2} c_\theta^2 s_\theta \right], \tag{328}$$

which yields a Feynman rule

$$h_1 h_1 h_1 : \; -6i \left(\lambda v c_\theta^3 + \lambda_2 v c_\theta s_\theta^2 - \mu_1 s_\theta^3 - \frac{\mu_2}{2} c_\theta^2 s_\theta \right) \equiv -i L_{111}. \tag{329}$$

The $h_2h_1h_1$ coupling, which controls the $h_2 \to h_1h_1$ decay (if kinematically allowed), comes from the potential term

$$V_{211} = h_2h_1{}^2 \left[3\lambda v s_\theta c_\theta - \lambda_2 v s_\theta (3c_\theta^2 - 1) + 3\mu_1 c_\theta s_\theta^2 + \frac{\mu_2}{2} c_\theta (3c_\theta^2 - 2) \right], \tag{330}$$

and yields the Feynman rule

$$h_2h_1h_1 : \quad -2i \left(3\lambda v s_\theta c_\theta - \lambda_2 v s_\theta (3c_\theta^2 - 1) + 3\mu_1 c_\theta s_\theta^2 + \frac{\mu_2}{2} c_\theta (3c_\theta^2 - 2) \right). \equiv -iL_{211}. \tag{331}$$

For the other cubic interactions we have the potential terms and related Feynman rules:

$$\begin{aligned}
V_{122} &= h_1h_2{}^2 \left[-3\lambda v c_\theta s_\theta^2 + \lambda_2 v c_\theta (1 - 3s_\theta^2) - \frac{\mu_2}{2}(2 - 3s_\theta^2) \right], \\
h_1h_2h_2 &: \quad -2i \left(-3\lambda v c_\theta s_\theta^2 + \lambda_2 v c_\theta (1 - 3s_\theta^2) - \frac{\mu_2}{2} s_\theta (2 - 3s_\theta^2) \right); \\
V_{222} &= h_2{}^3 \left[\lambda v s_\theta^3 + \lambda_2 v s_\theta c_\theta^2 + \mu_1 c_\theta^3 - \frac{\mu_2}{2} s_\theta^2 c_\theta \right], \\
h_2h_2h_2 &: \quad -6i \left(\lambda v s_\theta^3 + \lambda_2 v s_\theta c_\theta^2 + \mu_1 c_\theta^3 - \frac{\mu_2}{2} s_\theta^2 c_\theta \right).
\end{aligned} \tag{332}$$

For the quartic interactions, the relevant terms in the Lagrangian are,

$$V_4 = \frac{\lambda}{4}\phi^4 + \lambda_1 s^4 + \frac{\lambda_2}{2}\phi^2 s^2. \tag{333}$$

After inserting the mass eigenstates in terms of the mixing angle θ, we find for the quartic potential terms and the corresponding Feynman rules:

$$\begin{aligned}
V_{1111} &= h_1{}^4 \left[\frac{\lambda}{4}c_\theta^4 + \lambda_1 s_\theta^4 + \frac{\lambda_2}{2}c_\theta^2 s_\theta^2 \right], \\
h_1h_1h_1h_1 &: \quad -24i \left(\frac{\lambda}{4}c_\theta^4 + \lambda_1 s_\theta^4 + \frac{\lambda_2}{2}c_\theta^2 s_\theta^2 \right); \\
V_{2222} &= h_2{}^4 \left[\frac{\lambda}{4}s_\theta^4 + \lambda_1 c_\theta^4 + \frac{\lambda_2}{2}s_\theta^2 c_\theta^2 \right], \\
h_2h_2h_2h_2 &: \quad -24i \left(\frac{\lambda}{4}s_\theta^4 + \lambda_1 c_\theta^4 + \frac{\lambda_2}{2}s_\theta^2 \right); \\
V_{1112} &= h_1{}^3 h_2 \left[\lambda_1 s_\theta c_\theta^3 - 4\lambda_1 c_\theta s_\theta^3 - \frac{\lambda_2}{4}\sin 4\theta \right], \\
h_1h_1h_1h_2 &: \quad -6i \left(\lambda s_\theta c_\theta^3 - 4\lambda_1 c_\theta s_\theta^3 - \frac{\lambda_2}{4}\sin 4\theta \right); \\
V_{1122} &= h_1{}^2 h_2{}^2 \left[\frac{3}{2}\lambda s_\theta^2 c_\theta^2 + 6\lambda_1 s_\theta^2 c_\theta^2 + \frac{\lambda_2}{2}(c_\theta^4 + s_\theta^4 - 4c_\theta^2 s_\theta^2) \right], \\
h_1h_1h_2h_2 &: \quad -4i \left(\frac{3}{2}\lambda s_\theta^2 c_\theta^2 + 6\lambda_1 s_\theta^2 c_\theta^2 + \lambda_2(c_\theta^4 + s_\theta^4 - 4c_\theta^2 s_\theta^2) \right); \\
V_{1222} &= h_1 h_2{}^3 \left[\lambda c_\theta s_\theta^3 - 4\lambda_1 s_\theta c_\theta^3 + \frac{\lambda_2}{4}\sin 4\theta \right], \\
h_1h_2h_2h_2 &: \quad -6i \left(\lambda c_\theta s_\theta^3 - 4\lambda_1 s_\theta c_\theta^3 + \frac{\lambda_2}{4}\sin 4\theta \right).
\end{aligned} \tag{334}$$

13.3.5   Counting of free parameters

The most general scalar potential in Eq. (316) contains six parameters, λ, M^2, λ_1, λ_2, μ_1, and μ_2. The masses of h_1 and h_2 and the mixing angle θ are determined by the three parameters λ, M^2, and μ_2. The physically most interesting trilinear scalar couplings, $h_1 h_1 h_1$ (the triple-Higgs coupling) and $h_2 h_1 h_1$ (which controls $h_2 \rightarrow h_1 h_1$ decays, if kinematically accessible) depend in addition on μ_1 and λ_2. There is enough parameter freedom to choose these two trilinear couplings independently. The remaining parameter λ_1 appears only in quartic scalar interactions.

Two useful bases in which the model can be specified are

$$M_{h_1}, M_{h_2}, \cos\theta, \mu_1, \lambda_2, \lambda_1 \tag{335}$$

and [see Eqs. (329) and (331)]

$$M_{h_1}, M_{h_2}, \cos\theta, L_{111}, L_{211}, \lambda_1. \tag{336}$$

13.4   Benchmark 2: Scaling of vector boson and fermion couplings

In the second benchmark scenario, the couplings of the 125 GeV Higgs boson to the gauge bosons and to the fermions are scaled by two different coupling factors.

Model-independent parameterization: For the 125 GeV state h_1, the production rates in the various channels of observation can be fit to two free parameters,

$$
\begin{aligned}
\kappa_V &\equiv \kappa_W = \kappa_Z\,, \\
\kappa_F &\equiv \kappa_t = \kappa_b = \kappa_\tau\,.
\end{aligned}
\tag{337}
$$

We assume that the h_1 couplings to light fermions are scaled by the same factor κ_F. The couplings of h_1 to gg and $\gamma\gamma$ are also modified by the appropriate scaling factors applied to the fermion and W boson loops.

We assume that there are no new colored particles that contribute to the loop-induced $h_1 gg$ or $h_2 gg$ couplings. In the specific model that we discuss below, there is a charged scalar that can contribute to the loop-induced $h_1\gamma\gamma$, $h_1\gamma Z$ and $h_2\gamma\gamma$, $h_2\gamma Z$ couplings; for this benchmark we assume that its contributions to these loop-induced couplings are negligible.

The corresponding couplings of the second state h_2, as enforced by unitarity, are

$$
\begin{aligned}
\kappa_V' &= \sqrt{1 - \kappa_V^2}, \\
\kappa_F' &= \frac{1 - \kappa_V \kappa_F}{\sqrt{1 - \kappa_V^2}}.
\end{aligned}
\tag{338}
$$

We have chosen the phase of h_2 such that κ_V' is positive. κ_F' can be positive or negative. As in the previous benchmark, there can be additional decays of h_2 with a branching ratio BR_{new} (for example, $h_2 \rightarrow h_1 h_1$ if kinematically allowed).

Constraints from existing data: The allowed ranges of κ_V' and κ_F' are constrained by fits of κ_V and κ_F from measurements of the 125 GeV Higgs h_1, as shown in Fig. 5a of Ref. [11] and Fig. 13a of Ref. [634] (in these figures $\kappa_V \equiv \kappa_V$ and $\kappa_F \equiv \kappa_F$). A theorist-made translation of ATLAS, CMS, and Tevatron Higgs data available in July 2012 (see Ref. [350] for the details of the data used in this analysis) into constraints on κ_V' and κ_F' is shown in Figure 130.

Specific model: This parameterization is realized for the SM Higgs boson mixed with a second scalar electroweak doublet that carries a vacuum expectation value but does not couple to fermions; i.e., the Type-I Two Higgs Doublet Model (2HDM). This model will be specified in the following Section 13.4.1.
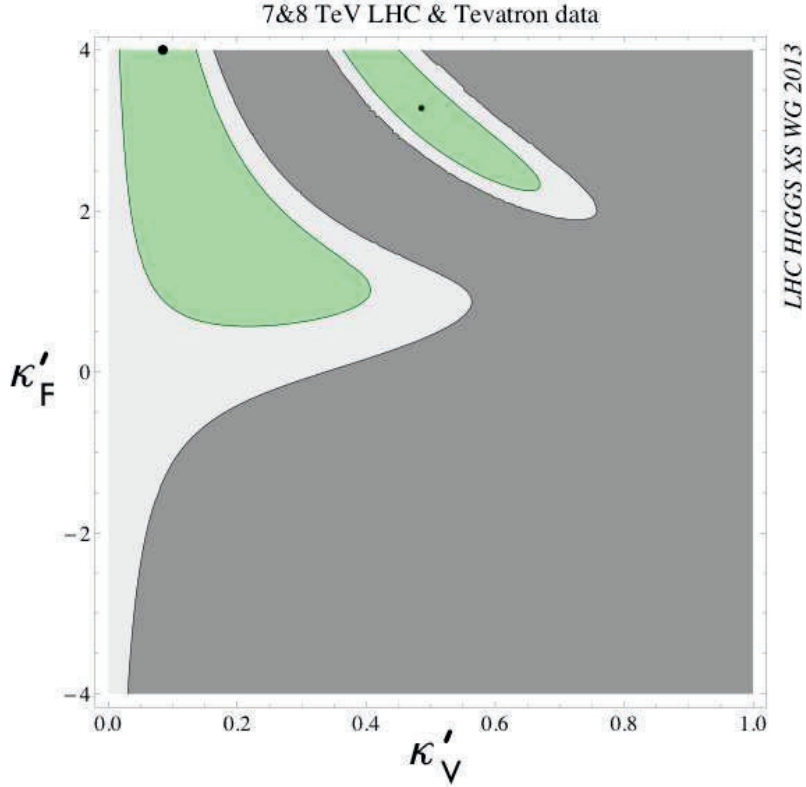
Figure 130: Best-fit points (black dots), 1σ (green) and 2σ (white) allowed regions in the (κ'_V, κ'_F) plane for Benchmark 2 (equivalent to the Type-I two-Higgs-doublet model), based on data available in July 2012 (see Ref. [350]).

13.4.1 *Specific benchmark model 2: Type-I Two-Higgs-Doublet-Model*

The simplest extensions of the SM Higgs sector are given by adding scalar doublet and singlet fields. Thus in two-Higgs-doublet models [635–637] the Higgs sector consists of two Higgs doublet fields.

13.4.2 *The scalar Higgs potential*

In the following we assume CP conservation. Furthermore, we take care to avoid tree-level flavor changing neutral currents. The latter is achieved by imposing a discrete symmetry $\mathbb{Z}_2$ under which one of the doublet fields changes sign, while all the fermion fields remain unchanged. Denoting by Φ_1 and Φ_2 two hypercharge-one weak doublet fields, for the Type-I 2HDM we have in particular:

$$\underline{\text{Type-I 2HDM:}} \qquad \Phi_1 \to -\Phi_1 \quad \text{and} \quad \Phi_2 \to \Phi_2 \,. \tag{339}$$

This ensures that the fermions couple only to Φ_2.

The most general scalar Higgs potential is then given by

$$
\begin{aligned}
V \;=\;& m_{11}^2 \Phi_1^\dagger \Phi_1 + m_{22}^2 \Phi_2^\dagger \Phi_2 - [m_{12}^2 \Phi_1^\dagger \Phi_2 + \text{h.c.}] + \frac{1}{2}\lambda_1 (\Phi_1^\dagger \Phi_1)^2 + \frac{1}{2}\lambda_2 (\Phi_2^\dagger \Phi_2) \\
&+ \lambda_3 (\Phi_1^\dagger \Phi_1)(\Phi_2^\dagger \Phi_2) + \lambda_4 (\Phi_1^\dagger \Phi_2)(\Phi_2^\dagger \Phi_1) + \left\{ \frac{1}{2}\lambda_5 (\Phi_1^\dagger \Phi_2)^2 + \text{h.c.} \right\} \,.
\end{aligned}
\tag{340}
$$

This potential softly violates (by dimension-two terms) the imposed discrete $\mathbb{Z}_2$ symmetry. The parameters m_{12}^2 and λ_5 are taken real to ensure CP conservation. Requiring that the minimum of the potential is

given by a CP-conserving vacuum which does not break the electromagnetic symmetry $U(1)_{em}$, we have for the vacuum expectation values of the neutral components Φ_i^0 ($i = 1, 2$) of the two Higgs doublets,

$$\langle \Phi_i^0 \rangle = \frac{v_i}{\sqrt{2}} \quad \text{with} \quad \tan\beta \equiv \frac{v_2}{v_1} \quad \text{and} \quad v^2 = v_1^2 + v_2^2 = (246 \text{ GeV})^2 . \tag{341}$$

By imposing the minimum conditions of the potential the parameters m_{11}^2 and m_{22}^2 can be eliminated in favor of v^2 and $\tan\beta$, so that we are left with six free parameters, m_{12}^2 and λ_j ($j = 1, ..., 5$). Rotation of the interaction states to the mass eigenstates results in four physical Higgs bosons, two neutral CP-even ones, denoted by h for the lighter and by H for the heavier one, one neutral CP-odd state A and a charged Higgs boson $H^\pm$. The masses of these four particles, together with the neutral CP-even Higgs mixing angle α introduced to diagonalize the neutral CP-even Higgs squared-mass matrix, can be expressed in terms of these six parameters, so that one free parameter is left over. For further discussion on the scalar potential, its symmetries and bounds on the parameters we refer to the literature [636, 637]. Here we content ourselves to give the Higgs couplings to gauge bosons and fermions.

The couplings of the neutral CP-even Higgs bosons h, H to the gauge bosons V (V $= W^\pm$, Z) normalized to the corresponding SM coupling are given by

$$g_{\text{hVV}} = \sin(\beta - \alpha) \qquad \text{and} \qquad g_{\text{HVV}} = \cos(\beta - \alpha) . \tag{342}$$

The pseudoscalar A does not couple to gauge bosons. With the notation of Section 13.2 we identify

$$\kappa_{\text{V}} \equiv g_{\text{hVV}} \qquad \text{and} \qquad \kappa_{\text{V}}' \equiv g_{\text{HVV}} \tag{343}$$

The couplings Eq. (342) fulfill the constraint Eq. (307) imposed by the requirement of unitarity of the longitudinal gauge boson scattering. Furthermore, we recover the SM limit for h in case $\sin(\beta - \alpha) = 1$. Note, that there can also be scenarios where H corresponds to the 125 GeV SM-like Higgs boson, in which case $\cos(\beta - \alpha)$ is close to 1.

As stated above, 2HDMs suffer from possible tree-level flavor-changing neutral currents (FCNC). According to the Paschos–Glashow–Weinberg theorem [638, 639], FCNC are absent if all fermions with the same quantum numbers couple to the same Higgs multiplet. In the 2HDMs this can be achieved by imposing discrete or continuous symmetries. According to the symmetries imposed there are different types of 2HDM, where we discuss here the type-I model, defined in Eq. (339). In this case the Yukawa Lagrangian is given in the mass basis by [640]

$$\mathcal{L}_{\text{Yukawa}} = - \sum_{\text{f=u,d,l}} \frac{m_{\text{f}}}{v} \left(\xi_h^{\text{f}} \bar{\text{f}} \text{fh} + \xi_{\text{H}}^{\text{f}} \bar{\text{f}} \text{fH} - i \xi_{\text{A}}^{\text{f}} \bar{\text{f}} \gamma_5 \text{fA} \right)$$

$$- \left\{ \frac{\sqrt{2} V_{\text{ud}}}{v} \bar{u} (m_{\text{u}} \xi_A^{\text{u}} P_L + m_{\text{d}} \xi_A^{d} P_R) d \, H^+ + \frac{\sqrt{2} m_{\text{l}} \xi_A^{\text{l}}}{v} \bar{\nu}_L \text{l}_R H^+ + \text{h.c.} \right\} , \tag{344}$$

where u, d, l stand generically for up-type quarks, down-type quarks, and charged leptons of all three generations, respectively, $P_{L,R}$ are the projection operators of the left- and right-handed fermions, and V_{ud} denotes the appropriate element of the CKM matrix. We have

$$\text{Type-1 2HDM:} \qquad \xi_h^u = \xi_h^d = \xi_h^l \equiv \xi_h = \frac{\cos\alpha}{\sin\beta} \tag{345}$$

$$\xi_H^u = \xi_H^d = \xi_H^l \equiv \xi_H = \frac{\sin\alpha}{\sin\beta} . \tag{346}$$

In our notation of Section 13.2 we have

$$\kappa_{\text{f}} \equiv \xi_h \qquad \text{and} \qquad \kappa_{\text{f}}' \equiv \xi_H . \tag{347}$$

237

It is easy to verify that the Yukawa couplings Eq. (345), Eq. (346) and the couplings to gauge bosons Eq. (342) fulfill the unitarity conditions Eq. (308).

It is instructive to look the decoupling limit, *i.e.*, when $m_H \gg m_h$ which is obtained for $\alpha \to \beta - \pi/2$:

$$\kappa_V = 1 + \mathcal{O}\left(\frac{M_Z^4}{M_H^4}\right), \tag{348}$$

$$\kappa_f = 1 + 2\,\frac{M_Z^2}{M_H^2}\cos^2\beta\cos 2\beta + \mathcal{O}\left(\frac{M_Z^4}{M_H^4}\right). \tag{349}$$

13.5 Tools

Here we give a short collection of tools which can be exploited in the frameworks of the benchmark models 1 and 2.

Production: As in the proposed benchmark models only the Higgs couplings to the gauge bosons and fermions are modified, the SM production cross sections can be taken over including higher order QCD corrections. They only have to be multiplied by the appropriate scaling factor. Since in both models the fermion modification factors for each of the two Higgs bosons are universal, this is also particularly easy for gluon fusion, as not distinction between top and bottom loops needs to be made. As for electroweak (EW) corrections, however, they cannot be taken over from SM calculations.EW corrections in the BSM models can be substantially different from the SM EW corrections. As long as no dedicated analysis has been performed, no statements about the possible size of these corrections can be made. Hence, we have in benchmark model 1 and 2 for the QCD corrected production cross sections of h_1, h_2 through gluon fusion (gg), vector boson fusion (VBF), Higgs-strahlung (VH) and associated production with heavy quarks (QQH),

$$\sigma_{gg}^h = \bar{\kappa}_f^2\,\sigma_{gg}^{\mathrm{SM,QCD}}\ ,\ \ \sigma_{VBF}^h = \bar{\kappa}_V^2\,\sigma_{VBF}^{\mathrm{SM,QCD}}\ ,\ \ \sigma_{VH}^h = \bar{\kappa}_V^2\,\sigma_{VH}^{\mathrm{SM,QCD}}\ ,\ \ \sigma_{QQH}^h = \bar{\kappa}_f^2\,\sigma_{QQH}^{\mathrm{SM,QCD}}\ , \tag{350}$$

where

$$\bar{\kappa}_f = \kappa_f\ (\kappa_f')\quad \text{for}\quad h = h_1\ (h_2)\qquad \text{and}\qquad \bar{\kappa}_V = \kappa_V\ (\kappa_V')\quad \text{for}\quad h = h_1\ (h_2)\,. \tag{351}$$

For the programs which allow for the calculation of the production cross sections at higher order QCD we refer the reader to YR1.

The program SUSHI [641, 642] has implemented the calculation of neutral Higgs bosons h, H, A within the 2HDM through gluon fusion and bottom quark annihilation. This program can be applied up to NNLO QCD if the Higgs mass stays below twice the top quark mass (this is because the NNLO QCD corrections rely upon an approximation which is valid for $M_h < 2m_t$). The NLO QCD corrections are exact for all Higgs boson masses. Electroweak corrections have to be turned off for consistency reasons, since the electroweak corrections depend on the details of the BSM model (including couplings between scalars that are highly model-dependent) and have not been implemented.

The program GG2VV [85, 86] is a parton-level integrator and event generator for all gg $(\to$ H$) \to$ VV $\to$ 4 leptons processes (V $=$ W, Z/γ^*), which can be used to study Higgs-continuum interference and off-shell effects. It can be used to calculate predictions for BSM scenarios with a SM-like Higgs boson with rescaled Hgg, HWW and HZZ couplings. Full BSM implementations in GG2VV are not public yet. The program has, however, been used already for calculations and checks in models in which all Higgs couplings are modified by a common scaling factor.

Decays: For the calculation of the decay branching ratios in benchmark model 1 the program HDECAY [643] can be used. It has implemented the possibility to turn on modification factors for the SM Higgs couplings to fermions and gauge bosons. This way the branching ratios for h_1 and h_2 can be calculated

separately by specifying in the input file the appropriate scaling factors. The program includes both QCD and EW corrections computed for the SM Higgs, which can only be applied in the vicinity of the SM. The new program EHDECAY [403, 644] has been adapted from HDECAY to implement the calculation of Higgs branching ratios in the framework of effective Lagrangians. EHDECAY provides the possibility to turn off the SM EW corrections, which should be done in the benchmark models described here. By specifying in the input file the appropriate scaling factors and setting the flag for EW corrections to zero, the branching ratios for h_1, h_2 can be separately calculated including the QCD corrections and without the EW corrections. However, neither program has implemented the decays into new states as *e.g.* the decay $h_2 \rightarrow h_1 h_1$. The authors of these programs plan to add this decay in the future.

For the calculation of the branching ratios in the 2HDM there is a dedicated tool, 2HDMC [645, 646]. This program calculates all two-body decay widths and branching ratios at leading order (including FCNC) within different parameterizations which can be specified in the input file. Leading QCD corrections to the decays are included. The program also includes singly off-shell decays into scalar-plus-vector-boson and two-vector-boson final states. Furthermore, theoretical constraints on the 2HDM parameters from perturbativity, unitarity and stability of the scalar potential are included, as are the constraints from EW precision data (via the oblique parameters). Model constraints from Higgs searches and flavor physics can be accessed using external codes. The code provides output in a form similar to the SUSY Les Houches accord [29, 30, 647], which can also be used for Monte Carlo event generation with a supplied model file for MADGRAPH/MADEVENT.

14 Higgs-boson production in the MSSM [64]

14.1 Introduction

The Higgs sector of the Minimal Supersymmetric Standard Model (MSSM) consists of two $SU(2)$ doublets, H_1 and H_2, whose relative contribution to electroweak symmetry breaking is determined by the ratio of vacuum expectation values of their neutral components, $\tan\beta \equiv v_2/v_1$. The spectrum of physical Higgs bosons is richer than in the SM, consisting of two neutral scalars h and H, one neutral pseudoscalar, A, and two charged scalars, $H^\pm$. At the tree level, the mass matrix for the neutral scalars can be expressed in terms of the parameters M_Z, M_A and $\tan\beta$, and the mass of the lightest scalar h is bounded from above by M_Z. However, radiative corrections – especially those involving top and bottom quarks and their supersymmetric partners, the stop and sbottom squarks – can significantly alter the tree-level predictions for the Higgs-boson masses, and bring along a dependence on a large number of free parameters of the MSSM. While the $\mathcal{CP}$ symmetry is conserved at tree level in the MSSM Higgs sector, radiative corrections can also introduce $\mathcal{CP}$-violating phases, and induce mixing among all three neutral states. In this report, however, we will focus on the $\mathcal{CP}$-conserving case, by considering only real values for the parameters in the soft SUSY-breaking Lagrangian and for the Higgs mass μ in the superpotential.

In general, the couplings of the MSSM Higgs bosons to gauge bosons and matter fermions differ from those of the SM Higgs. However, in large regions of the MSSM parameter space one of the scalars has SM-like couplings, while the other Higgs bosons are decoupled from the gauge bosons, and their couplings to down-type (up-type) fermions are enhanced (suppressed) by $\tan\beta$. As in the SM, gluon fusion is one of the most important production mechanisms for the neutral Higgs bosons, whose couplings to the gluons are mediated by the top and bottom quarks and their superpartners. However, for intermediate to large values of $\tan\beta$ the associated production with bottom quarks can become the dominant production mechanism for the neutral Higgs bosons that have enhanced couplings to down-type fermions. The production of the charged Higgs $H^\pm$, on the other hand, proceeds mainly through its coupling to a top-bottom pair. A sufficiently light $H^\pm$ is produced in the decay of a top quark, and it decays dominantly in a tau-neutrino pair. A heavy $H^\pm$ is produced in association with a top quark and it decays dominantly in a top-bottom pair.

The discovery by ATLAS and CMS of what appears to be a neutral scalar with mass around 125.5 GeV [1, 2] puts the studies of the Higgs sector of the MSSM in an entirely new perspective. In order to remain viable, a point in the MSSM parameter space must now not only pass all the (ever stricter) experimental bounds on superparticle masses, but also lead to the prediction of a scalar with mass, production cross section and decay rates compatible with those measured at the LHC. In particular, the relatively large mass of the roughly-SM-like scalar discovered at the LHC implies either very heavy stops, of the order of 3 TeV, or a large value of the left-right stop mixing term (see, e.g., Refs. [648,649]). The "benchmark scenarios" routinely considered in MSSM studies had been devised when the Higgs sector was constrained only by the LEP searches, and many of them, such as the so-called "no-mixing" scenario, are now ruled out because they predict a too-light SM-like scalar. Others, such as the so-called m_h^{max} scenario, are constrained for the opposite reason, i.e. they can predict a too-heavy SM-like scalar. To address the need for new benchmark scenarios to be used in future studies of the MSSM Higgs sector, in Section 14.2 we will define scenarios that are compatible both with the properties of the Higgs boson discovered at the LHC and with the current bounds on superparticle masses.

The fact that information on the Higgs boson mass, production and decays has now become available also puts new emphasis on the need for accurate theoretical predictions of those quantities. In the studies presented in this report, the masses and mixing of the MSSM Higgs bosons are computed with the public code FEYNHIGGS [24–27], which implements the full one-loop radiative corrections together with the dominant two-loop effects. The theoretical accuracy of the prediction of FEYNHIGGS for the

---

[64]M. Flechl, R. Harlander, M. Krämer, S. Lehti, P. Slavich, M. Spira, M. Vazquez Acosta, T. Vickey (eds.); E. Bagnaschi, M. Carena, G. Degrassi, S. Dittmaier, S. Heinemeyer, R. Klees, S. Laurila, S. Liebler, H. Mantler, O. Stål, M. Ubiali, A. Vicini, C. Wagner, G. Weiglein

lightest-scalar mass was estimated to be of the order of 3 GeV [26, 650, 651], i.e., already comparable to the accuracy of the mass measurement at the LHC. Improving the accuracy of the theoretical prediction for the MSSM Higgs masses will require the inclusion in public computer codes of the remaining two-loop effects [652–654] and at least the dominant three-loop effects [655–657].

The production and decay rates of a SM-like Higgs boson in the MSSM are sensitive to contributions from virtual SUSY particles, and their measurement at the LHC – combined with the searches for additional Higgs bosons – can be used to constrain the MSSM parameter space. To this effect, the theoretical predictions for cross section and decays must include precise computations of the SUSY contributions. In Section 14.3 we use the public code SUSHI [641] and the POWHEG implementation of Ref. [77] to compute the total and differential cross sections for neutral Higgs-boson production in gluon fusion, including a NLO-QCD calculation of quark and squark contributions plus higher-order quark contributions adapted from the SM calculation. We show that the SUSY contributions can be sizeable in regions of the MSSM parameter space where the third-generation squarks are relatively light, and discuss the theoretical uncertainty of the predictions for the cross sections.

Finally, we study and update the exclusion limits on light charged MSSM Higgs bosons in the $(M_{H^\pm}, \tan\beta)$-plane in various benchmark scenarios in Section 14.4. Particular emphasis is placed on the dependence of the limits on the variation of SUSY parameters. We also provide improved NLO-QCD cross section predictions for heavy charged Higgs production in the so-called four and five-flavor schemes in Section 14.5. The five-flavor scheme cross section is calculated with a new scheme for setting the factorization scale and takes into account the theoretical uncertainty from scale variation and the PDF, α_s and bottom-mass error. We observe good agreement between the 4FS and 5FS NLO-calculations and provide a combined prediction following the Santander matching.

14.2 New MSSM benchmark scenarios

Within the MSSM an obvious possibility is to interpret the new state at about 125.5 GeV as the light $\mathcal{CP}$-even Higgs boson [334, 338, 648, 649, 658–662]. At the same time, the search for the other Higgs bosons has continued. The non-observation of any additional state in the other Higgs search channels puts by now stringent constraints on the MSSM parameter space, in particular on the values of the tree-level parameters M_A (or $M_{H^\pm}$) and $\tan\beta$. Similarly, the non-observation of supersymmetric (SUSY) particles puts relevant constraints on the masses of the first and second generation scalar quarks and the gluino, and to lesser degree on the stop and sbottom masses (see Refs. [663, 664] for a recent summary).

Due to the large number of free parameters, a complete scan of the MSSM parameter space is impractical in experimental analyses and phenomenological studies. Therefore, the Higgs search results at LEP were interpreted [458] in several benchmark scenarios [16, 665]. In these scenarios only the two parameters that enter the Higgs sector tree-level predictions, M_A and $\tan\beta$, are varied (and the results are usually displayed in the $M_A - \tan\beta$ plane), whereas the other SUSY parameters, entering via radiative corrections, are fixed to particular benchmark values which are chosen to exhibit certain features of the MSSM Higgs phenomenology. These scenarios were also employed for the MSSM Higgs searches at the Tevatron and at the LHC.

By now, most of the parameter space of the original benchmark scenarios [16, 665] has been ruled out by the requirement that one of the $\mathcal{CP}$-even Higgs boson masses should be around 125.5 GeV. Consequently, new scenarios have been proposed [31], which are defined such that over large parts of their available parameter space the observed signal at about 125.5 GeV can be interpreted in terms of one of the (neutral) Higgs bosons, while the scenarios exhibit interesting phenomenology for the MSSM Higgs sector. The benchmark scenarios are all specified using low-energy MSSM parameters, i.e. no particular soft SUSY-breaking scenario was assumed. Constraints from direct searches for Higgs bosons are taken into account, whereas indirect constraints from requiring the correct cold dark matter density, $\mathrm{BR}(b \to s\gamma)$, $\mathrm{BR}(B_s \to \mu^+\mu^-)$ or $(g-2)_\mu$ are neglected. However interesting, those constraints depend to a large extent on other parameters of the theory that are not crucial for Higgs phenomenology.

14.2.1 Definition of parameters

The mass matrices for the stop and sbottom sectors of the MSSM, in the basis of the current eigenstates $\tilde{t}_L, \tilde{t}_R$ and $\tilde{b}_L, \tilde{b}_R$, are given by

$$\mathcal{M}_{\tilde{t}}^2 = \begin{pmatrix} M_{\tilde{t}_L}^2 + m_t^2 + \cos 2\beta(\frac{1}{2} - \frac{2}{3}s_w^2)M_Z^2 & m_t X_t^* \\ m_t X_t & M_{\tilde{t}_R}^2 + m_t^2 + \frac{2}{3}\cos 2\beta s_w^2 M_Z^2 \end{pmatrix}, \qquad (352)$$

$$\mathcal{M}_{\tilde{b}}^2 = \begin{pmatrix} M_{\tilde{b}_L}^2 + m_b^2 + \cos 2\beta(-\frac{1}{2} + \frac{1}{3}s_w^2)M_Z^2 & m_b X_b^* \\ m_b X_b & M_{\tilde{b}_R}^2 + m_b^2 - \frac{1}{3}\cos 2\beta s_w^2 M_Z^2 \end{pmatrix}, \qquad (353)$$

where

$$m_t X_t = m_t(A_t - \mu^* \cot \beta), \quad m_b X_b = m_b(A_b - \mu^* \tan \beta). \qquad (354)$$

Here A_t denotes the trilinear Higgs–stop coupling, A_b denotes the Higgs–sbottom coupling, and μ is the higgsino mass parameter. We furthermore use the notation $s_w = \sqrt{1 - c_w^2}$, with $c_w = M_W/M_Z$. We shall concentrate on the case

$$M_{\tilde{t}_L} = M_{\tilde{b}_L} = M_{\tilde{t}_R} = M_{\tilde{b}_R} =: M_{\text{SUSY}}. \qquad (355)$$

Similarly, the corresponding soft SUSY-breaking parameters in the scalar tau/neutrino sector are denoted as A_τ and $M_{\tilde{l}_3}$, where we assume the diagonal soft SUSY-breaking entries in the stau/sneutrino mass matrices to be equal to each other. For the squarks and sleptons of the first and second generations we also assume equality of the diagonal soft SUSY-breaking parameters, denoted as $M_{\tilde{q}_{1,2}}$ and $M_{\tilde{l}_{1,2}}$, respectively. The off-diagonal A-terms always appear multiplied with the corresponding fermion mass. Hence, for the definition of the benchmark scenarios the A-terms associated with the first and second sfermion generations have a negligible impact and can be set to zero for simplicity.

The Higgs sector depends also on the gaugino masses. For instance, at the two-loop level the gluino mass, $M_{\tilde{g}}$, enters the predictions for the Higgs boson masses. The Higgs sector observables furthermore depend on the SU(2) and U(1) gaugino mass parameters, M_2 and M_1, respectively, which are usually assumed to be related via the GUT relation,

$$M_1 = \frac{5}{3}\frac{s_w^2}{c_w^2}M_2. \qquad (356)$$

Corrections to the MSSM Higgs boson sector have been evaluated in several approaches, see, e.g. Ref. [666]. The leading and subleading parts of the existing two-loop calculations have been implemented into public codes. The program FEYNHIGGS [24–27] is based on results obtained in the Feynman-diagrammatic (FD) approach, while the code CPSUPERH [667–669] is based on results obtained using the renormalization group (RG) improved effective potential approach [666, 670–672].

The FD results have been obtained in the on-shell (OS) renormalization scheme, whereas the RG results have been calculated using the $\overline{\text{MS}}$ scheme. Therefore, the parameters X_t and M_{SUSY} (which are most important for the corrections in the Higgs sector) are scheme-dependent and thus differ in the two approaches, see Ref. [666] for details. The change of scheme induces in general only a minor shift, of the order of 4%, in the parameter M_{SUSY}, but sizable differences can occur between the numerical values of X_t in the two schemes, see Refs. [25, 666, 673].

14.2.2 The benchmark scenarios

In the following several updated benchmark scenarios are proposed, in which the observed LHC signal at ~ 125.5 GeV can be interpreted as one of the (neutral $\mathcal{CP}$-even) states of the MSSM Higgs sector. More details about implications and the phenomenology in these scenarios can be found in Ref. [31].

Concerning the parameters that have only a minor impact on the MSSM Higgs sector predictions, we propose fixing them to the following values.

$$M_{\tilde{q}_{1,2}} = 1500 \text{ GeV}, \tag{357}$$

$$M_{\tilde{l}_{1,2}} = 500 \text{ GeV}, \tag{358}$$

$$A_f = 0 \quad (\text{f} = \text{c}, \text{s}, \text{u}, \text{d}, \mu, e) . \tag{359}$$

M_1 is fixed via the GUT relation, Eq.(356). Motivated by the analysis in Ref. [674] we suggest to investigate for each scenario given in Eqs.(361)–(364), in addition to the default values given there, the following values of μ:

$$\mu = \pm 200, \pm 500, \pm 1000 \text{ GeV}. \tag{360}$$

These values of μ allow for both an enhancement and a suppression of the bottom Yukawa coupling. The illustrative plots shown below have been obtained with FEYNHIGGS 2.9.4 [24–27]. Where relevant, values for the input parameters are quoted both in the on-shell scheme (suitable for FEYNHIGGS), as well as in the $\overline{\text{MS}}$ scheme (that can readily be used by CPSUPERH [667–669]). We also show the exclusion bounds (at 95% C.L.) from direct Higgs searches, evaluated with HIGGSBOUNDS 4.0.0-BETA [675,676] (linked to FEYNHIGGS) using a combined uncertainty on the SM-like Higgs mass of $\Delta M_\text{h} = 3$ GeV ($\Delta M_\text{H} = 3$ GeV in the last scenario) when evaluating the limits. For each benchmark scenario we show the region of parameter space where the mass of the (neutral $\mathcal{CP}$-even) MSSM Higgs boson that is interpreted as the newly discovered state is within the range 125.5 ± 3 GeV and 125.5 ± 2 GeV. The ± 3 GeV uncertainty is meant to represent a combination of the present experimental uncertainty of the determined mass value and of the theoretical uncertainty in the MSSM Higgs mass prediction from unknown higher-order corrections. In particular, in the case that the lightest $\mathcal{CP}$-even Higgs is interpreted as the newly discovered state, the couplings of the h are close to the corresponding SM values (modulo effects from light SUSY particles, see below). Consequently, those rate measurements from the LHC that agree well with the SM are then naturally in good agreement also with the MSSM predictions.

The suggested parameters below refer to recommendations in Ref. [31]. It should be kept in mind that for the evaluations in the LHC Higgs Cross Section Working Group some SM parameters should be adjusted to conform with the respective evaluations. The benchmark scenarios are recommended as follows. The top quark mass is set to its current experimental value, $m_\text{t} = 173.2$ GeV.

– The m_h^max scenario: This scenario can be used to derive conservative lower bounds on M_A, $M_{\text{H}\pm}$ and $\tan\beta$ [648].

$$M_\text{SUSY} = 1000 \text{ GeV}, \mu = 200 \text{ GeV}, M_2 = 200 \text{ GeV},$$
$$X_\text{t}^\text{OS} = 2\,M_\text{SUSY} \text{ (FD calculation)}, X_\text{t}^{\overline{\text{MS}}} = \sqrt{6}\,M_\text{SUSY} \text{ (RG calculation)},$$
$$A_\text{b} = A_\tau = A_\text{t}, M_{\tilde{g}} = 1500 \text{ GeV}, M_{\tilde{l}_3} = 1000 \text{ GeV} . \tag{361}$$

– The m_h^mod scenario:

Departing from the parameter configuration that maximizes M_h, one naturally finds scenarios where in the decoupling region the value of M_h is close to the observed mass of the signal over a wide region of the parameter space. A convenient way of modifying the m_h^max scenario in this way is to reduce the amount of mixing in the stop sector, i.e. to reduce $|X_\text{t}/M_\text{SUSY}|$ compared to the value of ≈ 2 (FD calculation) that gives rise to the largest positive contribution to M_h from the radiative corrections. This can be done for both signs of X_t.

$$m_\text{h}^\text{mod+}: \quad M_\text{SUSY} = 1000 \text{ GeV}, \mu = 200 \text{ GeV}, M_2 = 200 \text{ GeV},$$

$$X_{\mathrm{t}}^{\mathrm{OS}} = 1.5\, M_{\mathrm{SUSY}} \text{ (FD calculation)}, X_{\mathrm{t}}^{\overline{\mathrm{MS}}} = 1.6\, M_{\mathrm{SUSY}} \text{ (RG calculation)},$$

$$A_{\mathrm{b}} = A_{\tau} = A_{\mathrm{t}}, M_{\tilde{\mathrm{g}}} = 1500 \text{ GeV}, M_{\tilde{\mathrm{l}}_3} = 1000 \text{ GeV} . \tag{362}$$

$m_{\mathrm{h}}^{\mathrm{mod}-}$: $M_{\mathrm{SUSY}} = 1000 \text{ GeV}, \mu = 200 \text{ GeV}, M_2 = 200 \text{ GeV},$

$$X_{\mathrm{t}}^{\mathrm{OS}} = -1.9\, M_{\mathrm{SUSY}} \text{ (FD calculation)}, X_{\mathrm{t}}^{\overline{\mathrm{MS}}} = -2.2\, M_{\mathrm{SUSY}} \text{ (RG calculation)},$$

$$A_{\mathrm{b}} = A_{\tau} = A_{\mathrm{t}}, M_{\tilde{\mathrm{g}}} = 1500 \text{ GeV}, M_{\tilde{\mathrm{l}}_3} = 1000 \text{ GeV} . \tag{363}$$

– The light stop scenario:
A light stop may lead to a relevant modification of the gluon fusion rate [16, 677], see the evaluations in Section 14.3.

$$M_{\mathrm{SUSY}} = 500 \text{ GeV}, \mu = 350 \text{ GeV}, M_2 = 350 \text{ GeV},$$

$$X_{\mathrm{t}}^{\mathrm{OS}} = 2.0\, M_{\mathrm{SUSY}} \text{ (FD calculation)}, X_{\mathrm{t}}^{\overline{\mathrm{MS}}} = 2.2\, M_{\mathrm{SUSY}} \text{ (RG calculation)},$$

$$A_{\mathrm{b}} = A_{\mathrm{t}} = A_{\tau}, M_{\tilde{\mathrm{g}}} = 1500 \text{ GeV}, M_{\tilde{\mathrm{l}}_3} = 1000 \text{ GeV} . \tag{364}$$

– The light stau scenario:
It has been shown that light staus, in the presence of large mixing, may lead to important modifications of the di-photon decay width of the lightest $\mathcal{CP}$-even Higgs boson, $\Gamma(h \to \gamma\gamma)$ [321, 334, 338, 365, 661, 662, 678, 679]. Here the parameter definitions depend on whether $\Delta\tau$ corrections are neglected in the stau mass matrix, or not. The latter case is denoted as "$\Delta\tau$ calculation".

$$M_{\mathrm{SUSY}} = 1000 \text{ GeV}, \mu = 500(450) \text{ GeV}, (\Delta\tau \text{ calculation}),$$

$$M_2 = 200(400) \text{ GeV} (\Delta\tau \text{ calculation}),$$

$$X_{\mathrm{t}}^{\mathrm{OS}} = 1.6\, M_{\mathrm{SUSY}} \text{ (FD calculation)}, X_{\mathrm{t}}^{\overline{\mathrm{MS}}} = 1.7\, M_{\mathrm{SUSY}} \text{ (RG calculation)},$$

$$A_{\mathrm{b}} = A_{\mathrm{t}} , A_{\tau} = 0 , M_{\tilde{\mathrm{g}}} = 1500 \text{ GeV}, M_{\tilde{\mathrm{l}}_3} = 245(250) \text{ GeV} (\Delta\tau \text{ calculation}). \tag{365}$$

– The τ-phobic Higgs scenario:
Propagator-type corrections involving the mixing between the two $\mathcal{CP}$-even Higgs bosons of the MSSM can have an important impact. In particular, this type of corrections can lead to relevant modifications of the Higgs couplings to down-type fermions, which can approximately be taken into account via an effective mixing angle α_{eff} (see Refs. [680, 681]).

$$M_{\mathrm{SUSY}} = 1500 \text{ GeV}, \mu = 2000 \text{ GeV}, M_2 = 200 \text{ GeV},$$

$$X_{\mathrm{t}}^{\mathrm{OS}} = 2.45\, M_{\mathrm{SUSY}} \text{ (FD calculation)}, X_{\mathrm{t}}^{\overline{\mathrm{MS}}} = 2.9\, M_{\mathrm{SUSY}} \text{ (RG calculation)},$$

$$A_{\mathrm{b}} = A_{\tau} = A_{\mathrm{t}} , M_{\tilde{\mathrm{g}}} = 1500 \text{ GeV}, M_{\tilde{\mathrm{l}}_3} = 500 \text{ GeV} . \tag{366}$$

– The low-M_{H} scenario:
As it was pointed out in Refs. [345, 648, 682, 683], besides the interpretation of the Higgs-like state at ~ 125.5 GeV in terms of the light $\mathcal{CP}$-even Higgs boson of the MSSM it is also possible, at least in principle, to identify the observed signal with the *heavy $\mathcal{CP}$-even Higgs boson* of the MSSM. In this case instead of M_{A}, which must be given by a relatively small value, μ is suggested to be modified.

$$M_{\mathrm{A}} = 110 \text{ GeV}, M_{\mathrm{SUSY}} = 1500 \text{ GeV}, M_2 = 200 \text{ GeV},$$

$$X_{\mathrm{t}}^{\mathrm{OS}} = 2.45\, M_{\mathrm{SUSY}} \text{ (FD calculation)}, X_{\mathrm{t}}^{\overline{\mathrm{MS}}} = 2.9\, M_{\mathrm{SUSY}} \text{ (RG calculation)},$$

$$A_{\mathrm{b}} = A_{\tau} = A_{\mathrm{t}}, M_{\tilde{\mathrm{g}}} = 1500 \text{ GeV}, M_{\tilde{\mathrm{l}}_3} = 1000 \text{ GeV} . \tag{367}$$

Instead of M_{A} one can also use $M_{\mathrm{H}^{\pm}}$ as input parameter, as it is done, e.g., in CPSUPERH. In this case one should choose as input value $M_{\mathrm{H}^{\pm}} = 132$ GeV, leading to very similar phenomenology.
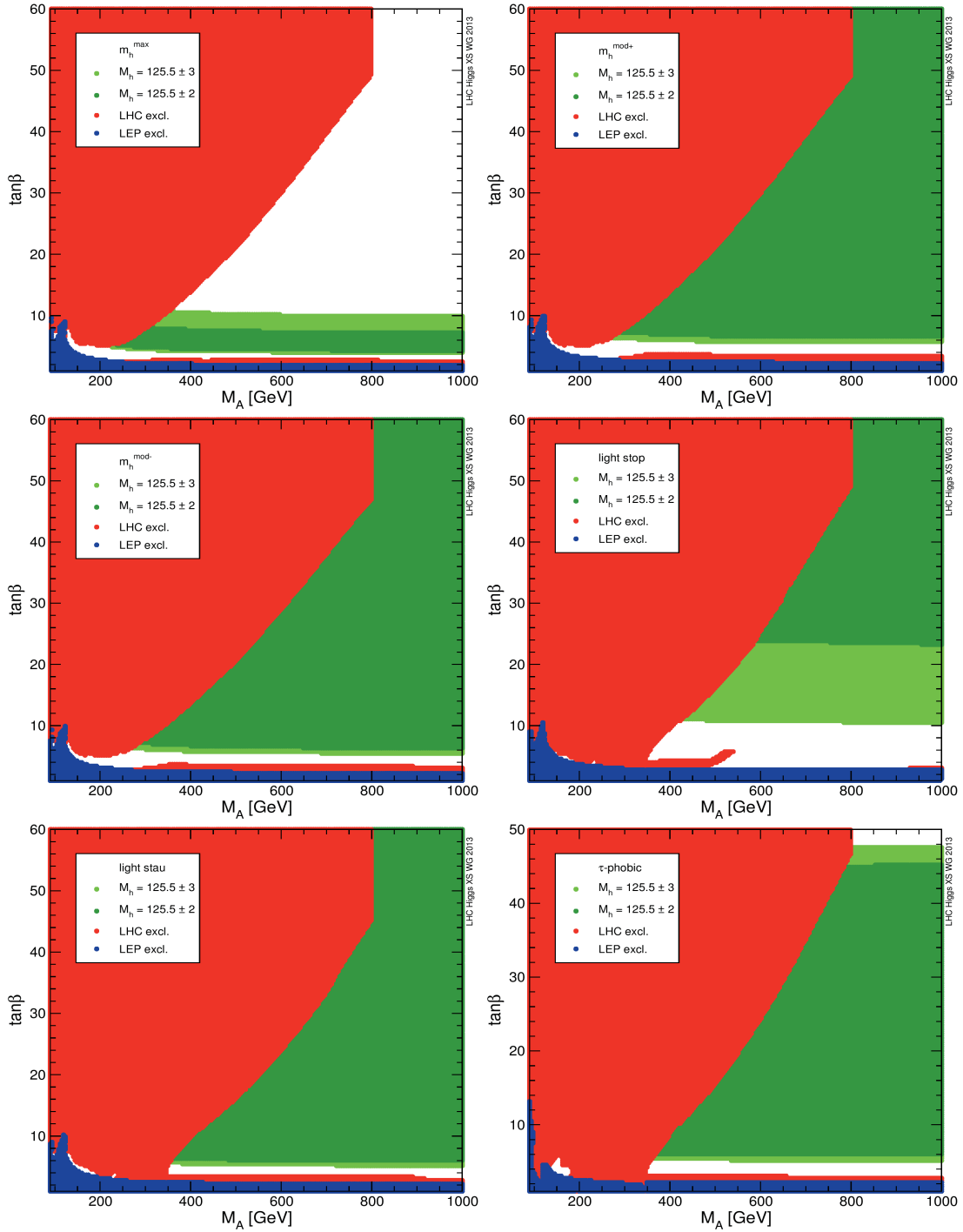
Figure 131: The M_A–$\tan\beta$ plane in the (updated) m_h^{max} (upper left), $m_h^{\mathrm{mod+}}$ (upper right), $m_h^{\mathrm{mod-}}$ (middle left), *light stop* (middle right), *light stau* (lower left), τ-phobic (lower right) scenario, with excluded regions from direct Higgs searches at LEP (blue), and the LHC (solid red). The two green shades correspond to the parameters for which $M_h = 125.5 \pm 2\,(3)$ GeV, see text.

The allowed and excluded regions in the $M_A - \tan\beta$ planes of the benchmark scenarios in which the light $\mathcal{CP}$-even Higgs is interpreted as the new state at 125.5 GeV are shown in Figure 131. The corresponding plot for the *low-M_H* scenario is shown in Figure 132.
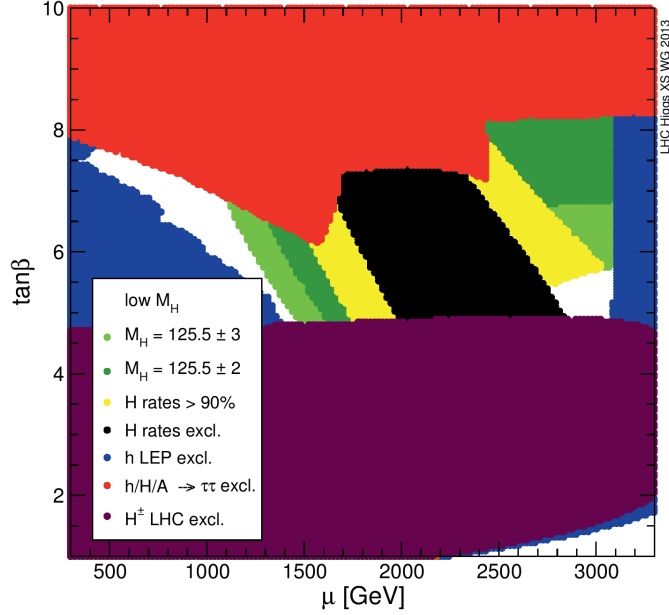
Figure 132: Experimentally favored and excluded regions in the μ–$\tan\beta$ plane in the *low-M_H* scenario. The green shades indicate the region where $M_H = 125.5 \pm 2\,(3)$ GeV. The yellow and black areas also have $M_H = 125.5 \pm 3$ GeV, where the yellow area additionally satisfies the requirement that the rates for the $gg \to H$, $H \to \gamma\gamma$ and $H \to ZZ^*$ channels, are at least at 90% of their SM value for the same Higgs mass. The black region indicates where the rates for H decay to gauge bosons become too high, such that these points are excluded by HIGGSBOUNDS. As before, the blue area is excluded by LEP Higgs searches, whereas the solid red is excluded from LHC searches for the neutral MSSM Higgs bosons, h, H and A in the $\tau^+\tau^-$ decay channel. The purple region is excluded by charged Higgs boson searches at the LHC. The white area at very large values of μ and low $\tan\beta$ is unphysical, i.e. this parameter region is theoretically inaccessible.

14.3 Neutral MSSM Higgs production

The essential features of the theoretical prediction for the production of neutral Higgs bosons within the MSSM have been summarized in Refs. [13, 14] and shall not be repeated here. Suffice it to say that the dominant production mechanisms are gluon fusion and bottom quark annihilation. Theoretical progress concerning the latter process has been marginal, so that the numbers provided in Refs. [13, 14] are still up-to-date. In this report we will present updated computations of the gluon fusion cross section.

In Refs. [13, 14], the numerical results were mostly presented within the so-called "no mixing" and $m_h^{\max}$ scenarios [16, 665], characterized by stop and sbottom masses of the order of one TeV or even heavier. In those scenarios the contributions of diagrams involving squarks to the gluon-fusion process are suppressed, and one can assume that the SUSY effects are well approximated by the non-decoupling corrections to the Higgs-bottom effective couplings, which become relevant at large $\tan\beta$. Therefore, a sufficiently accurate determination of the cross section for MSSM Higgs production in gluon fusion could be achieved with the public code HIGLU [411], including only the top- and bottom-quark contributions rescaled by the appropriate Higgs-quark effective couplings.

However, in scenarios with relatively light squarks such as the *light stop* scenario introduced in Section 14.2 (see Ref. [31] for more details), the squark contributions to the gluon-fusion process are not negligible. Luckily, in the past couple of years significant progress has been made in combining the existing theoretical results for the quark, squark, and gluino contributions into a consistent numerical prediction [77, 641]. In this report we will use the public code SUSHI [641] to provide a state-of-the-art determination of the total inclusive cross section for gluon fusion, as well as for bottom-quark

annihilation. In addition, we will compare differential distributions obtained with SuSHi at the purely partonic level with those obtained via a POWHEG implementation of gluon fusion [77].

14.3.1 Contributions to the gluon-fusion cross section

At LO, the partonic cross section for Higgs production via gluon fusion in the MSSM is induced by quark and squark loops, and we will take into account only the contributions from the top and bottom sectors. For what concerns the first two generations, the quark contributions are negligible due to the smallness of the corresponding Yukawa couplings, while the squarks contribute only via terms suppressed by the ratio $M_Z^2/M_{\tilde{q}}^2$, with significant cancellations among the different contributions in each generation (indeed, the total contribution vanishes for degenerate squark masses). Virtual effects at NLO QCD include gluonic corrections to the LO quark and squark contributions, as well as mixed quark-squark-gluino contributions. While the gluonic corrections to the quark contributions [37, 684] are implemented for generic quark and Higgs-boson masses, for the two-loop contributions involving squarks we use reasonable approximations, valid as long as the Higgs mass does not exceed the lowest threshold for squark production. In particular, for the production of the lightest scalar h we compute the contributions involving stops via a Taylor expansion in M_h^2 [685–687], and those involving sbottoms via an asymptotic expansion in the SUSY masses [688, 689]. For H and A production, on the other hand, we use the asymptotic expansion for both stop and sbottom contributions [690–692]. The validity of these approximations is supported by explicit NLO calculations with full mass dependences of Refs. [608, 693–695]. For the contributions of one-loop diagrams with radiation of a real quark or gluon, which are part of the inclusive cross section at NLO, we include results valid for generic quark and squark masses.

The NNLO-QCD contributions involving top quarks are known on the basis of an effective Lagrangian approach valid for $M_\phi \ll 2\,m_t$ [696–700] where $\phi \in \{h, H, A\}$, and they will be included in our evaluation of the cross section [38–40, 700–702]. For the NNLO contributions involving stop squarks, a pragmatic approximation was presented in Ref. [703]. While this approximation will not enter our prediction for the cross section, we will use it to estimate the uncertainty of the corresponding NLO contributions. In fact, a robust NNLO calculation of the stop contributions was recently presented in Refs. [704, 705]. Since we do not take into account the three-loop corrections to the Higgs boson mass, it is reasonable to neglect these terms in the cross section.

The existence of non-decoupling, $\tan\beta$-enhanced SUSY corrections to the Higgs-bottom couplings, the so-called Δ_b terms, has been known for a long time. These corrections can be taken into account via an effective-Lagrangian approach that resums them to all orders in the perturbative expansion [706–710]. As mentioned above, the Δ_b terms were the only genuine SUSY effects included in previous compilations of the MSSM neutral Higgs cross section by this working group. Since these effects can be numerically dominant in regions of the MSSM parameter space characterized by large $\tan\beta$, we follow the effective-Lagrangian approach and absorb them in a redefinition of the Higgs-bottom Yukawa coupling. As a consequence, we need to shift accordingly the formulae for the two-loop contributions, in order to avoid double counting.

The NLO electro-weak (EW) corrections to the cross section for gluon fusion in the SM have been computed in Refs. [49–51, 711, 712]. For a SM Higgs boson sufficiently lighter than the top threshold, the NLO-EW corrections are well approximated by the contributions coming from two-loop diagrams in which the Higgs couples to EW gauge bosons, which in turn couple to the gluons via a loop of light quarks [50, 712]. The inclusion of these contributions in the MSSM calculation, via an appropriate rescaling of the Higgs-gauge boson couplings, allows us to properly account for the NLO-EW corrections to the production of the lightest scalar h in scenarios where the SUSY particles are heavy. For what concerns the other neutral Higgs bosons, their couplings to gauge bosons are suppressed in most of the parameter space (in the case of the heaviest scalar H) or downright absent (in the case of the pseudoscalar A), therefore the EW light-quark contributions to their production are irrelevant. On the other hand, the NLO-EW corrections involving the bottom Yukawa coupling, which have not yet been computed

because they are negligible for the SM Higgs, could become relevant for the MSSM Higgs bosons whose couplings to bottom quarks are enhanced by $\tan\beta$. In addition, a full computation of the NLO-EW corrections to Higgs production in the MSSM should include the contributions of diagrams involving SUSY particles. The non-decoupling SUSY EW effects that dominate at large $\tan\beta$ are indeed included via the $\Delta_{\rm b}$ resummation, but the remaining contributions, so far un-computed, could become relevant if some of the SUSY particles are relatively light.

14.3.2 Uncertainties

The sources of uncertainty for the gluon fusion cross section in the MSSM include of course the ones already affecting the SM prediction, which are dominated by PDFs, $\alpha_{\rm s}(M_{\rm Z})$, and the scale variation. In addition there are, on the one hand, parametric uncertainties due to the unknown spectrum of SUSY masses and couplings, and, on the other hand, theoretical uncertainties due to the un-computed higher-order SUSY contributions.

Another kind of theoretical uncertainty, which is relatively small in the SM but can become dominant in regions of the MSSM parameter space characterized by large $\tan\beta$, stems from the definition of the Higgs-bottom coupling (for an earlier discussion see Ref. [713]). Indeed, the Yukawa coupling $Y_{\rm b}$ must be extracted from the corresponding quark mass, but the numerical value of the latter depends strongly on the renormalization scheme and scale. For example, a $\overline{\rm MS}$ mass $m_{\rm b}(m_{\rm b}) = 4.16$ GeV corresponds to a pole mass $m_{\rm b}$ of about 4.9 GeV at three-loop level. Evolving $m_{\rm b}(m_{\rm b})$ to a scale of the order of the Higgs mass, on the other hand, can considerably decrease its value, e.g., $m_{\rm b}(M_\phi) = 2.8$ GeV for $M_\phi = 125$ GeV. While any change in the definition of the bottom Yukawa coupling entering the LO part of the calculation is formally compensated for by counterterm contributions in the NLO part, the numerical impact of such strong variations on the result for the cross section can be significant.

Unlike in many other processes where there are theoretical arguments in favor of one or the other renormalization scheme for the bottom Yukawa coupling, for Higgs production in gluon fusion we are not aware of any such arguments that go beyond heuristic.[65] While the options of relating $Y_{\rm b}$ to $m_{\rm b}$ or to $m_{\rm b}(m_{\rm b})$ might seem preferable to the one of using $m_{\rm b}(M_\phi)$ in that they lead to smaller NLO K-factors, it must be kept in mind that this is due to an accidental cancellation between terms of different origin in the contributions of two-loop diagrams with bottom quarks and gluons. There is no argument suggesting that such cancellation persists at higher orders in QCD, or that it is motivated by some physical property of the bottom contribution to the gluon-fusion process. For example, it was noticed already in Ref. [37] that the two-loop bottom-gluon contribution to the amplitude for Higgs decay in two photons is minimized when the bottom mass is defined as $m_{\rm b}(M_\phi/2)$, even if the one-loop bottom contribution has exactly the same structure as the corresponding contribution to gluon fusion. In summary, there is no obvious reason to favor one renormalization scheme for the bottom Yukawa coupling over the others, and it would seem reasonable to consider the difference between the results obtained with the various schemes as a measure of the uncertainty associated with the un-computed higher-order QCD corrections.

14.3.3 Numerical examples

We are now ready to discuss the numerical effect of the contributions that we have included in the computation of the cross section for Higgs production in gluon fusion. As a representative choice for the MSSM parameters, we take the *light stop* scenario discussed in Section 14.2. We use FEYNHIGGS [24–27] to compute the Higgs boson masses and mixing angle, as well as the $\tan\beta$-enhanced correction to the Higgs-bottom coupling, $\Delta_{\rm b}$. To compute the total cross section we use SUSHI [641], and cross-check the results with a private code. It is useful to remark that the two-loop calculations of the Higgs-boson masses

---

[65]In the case of H $\rightarrow \gamma\gamma$ the resummation of leading and subleading logs of the ratio $M_{\rm H}/m_{\rm b}$ has solved this problem for the Abelian case [714, 715].
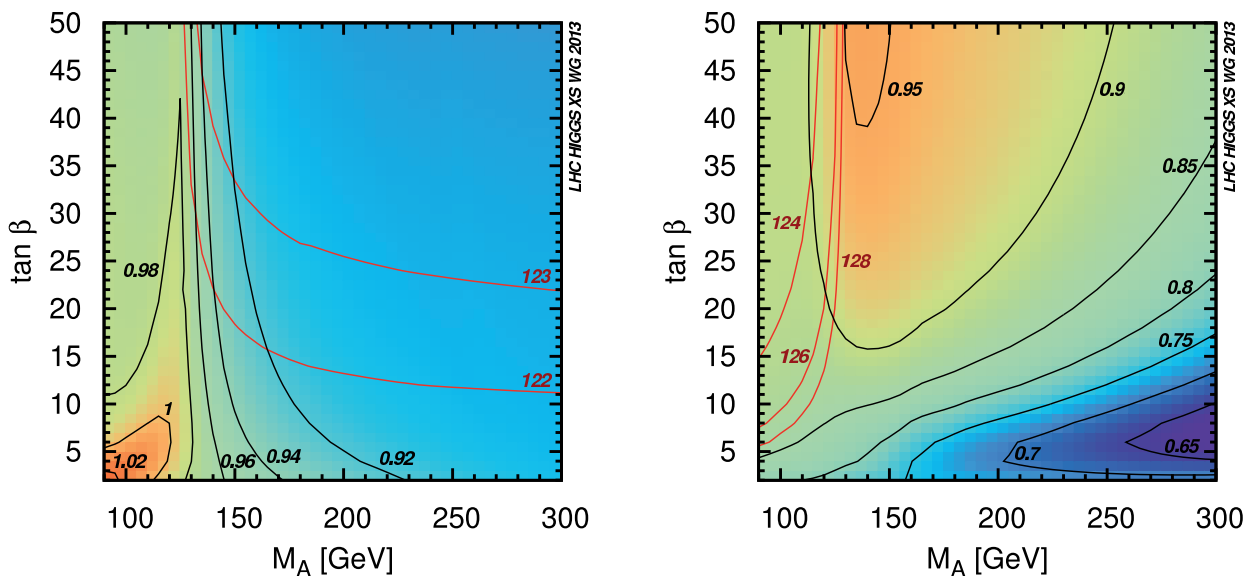
Figure 133: Ratio of the cross section for h (left) and H (right) production in gluon fusion as computed by SUSHI, over the corresponding cross section computed omitting squark contributions and EW corrections. The MSSM parameters are chosen as in the *light stop* scenario of Ref. [31].

and production cross section implemented in FEYNHIGGS and SUSHI, respectively, adopt the same on-shell renormalization scheme for the parameters in the stop and sbottom sectors. As a consequence, the numerical values of the parameters for the *light stop* scenario listed in Section 14.2 can be passed to both codes as they are.

Figure 133 shows the contours in the $M_A - \tan\beta$ plane of equal ratio between the cross section for Higgs-boson production in gluon fusion computed by SUSHI and the corresponding cross section computed as in the earlier LHCHXSWG reports, Refs. [13, 14]. In particular, the former includes the NLO-QCD calculation of both quark and squark contributions plus the dominant NNLO-QCD and NLO-EW effects adapted from the SM calculation, while the latter includes only the NLO-QCD calculation of quark contributions (supplemented with the $\tan\beta$-enhanced SUSY corrections to the Higgs-bottom couplings) and the dominant NNLO-QCD effects from top-quark loops. The latter have been evaluated using NNLO PDFs, while all the NLO terms are obtained with NLO PDFs. The plot on the left in Figure 133 refers to the production of the lightest scalar h, while the plot on the right refers to the production of the heaviest scalar H. The red lines superimposed to each plot are the contours of equal mass for the corresponding scalar (for H we only show the contours between 124 GeV and 128 GeV). The standard LHCHXSWG values for the SM input parameters have been used in these plots (in particular, we set $m_t = 172.5$ GeV and $m_b = 4.75$ GeV).

From the left plot in Figure 133 it can be seen that, in the *light stop* scenario, the combined effect of the squark contributions and the NLO-EW corrections tends to suppress the cross section for h production, with a maximum effect of $8-10\%$ in the region with $M_A \gtrsim 150$ GeV, where h has SM-like couplings to quarks and gauge bosons. It is useful to remark that this results from a partial compensation between the contributions of stop loops, which in this scenario can reduce the cross section of the lightest scalar by up to $14-16\%$, and the NLO-EW light-quark contributions, which increase by approximately 6% the cross section of a SM-like scalar with mass around 125 GeV [712].

The right plot in Figure 133 shows that in the case of H production the effect of the squark contributions can be somewhat larger than in the case of h production (the NLO-EW light-quark contributions, on the other hand, become negligible for sufficiently large M_A, due to the vanishing couplings of H to gauge bosons). However, a suppression of the order of $35-40\%$ is reached only in the lower-right corner

of the plot, where M_A is large and $\tan\beta$ ranges between 5 and 10. In this region, the coupling of H to top quarks is suppressed while the coupling to bottom quarks is not sufficiently enhanced, resulting in very small gluon-fusion cross sections, of the order of tenths of a picobarn.

Concerning uncertainties, we study the dependence of the cross section on the renormalization and factorization scales, μ_R and μ_F, by varying them simultaneously within $\mu_R = \mu_F = [M_\phi/2, 2M_\phi]$. The PDF uncertainty is derived using the MSTW2008 PDF prescription, where, somewhat conservatively, only the NLO set is used for the error estimate, even though the NNLO set enters in the top-quark induced contributions to the cross section. Since scale and PDF variation are purely driven by QCD [13], their effect is expected to be similar for all the three neutral Higgs bosons (differences at the percent level can arise due to the different weight of the bottom- and top-loop contributions, which are included at different orders in perturbation theory). Indeed, for both the lightest and the heaviest scalar, we find that the scale variation is of the order of $\pm10\%$, while the PDF uncertainty amounts to about $\pm2.5\%$.

We estimate the uncertainty associated to the renormalization of the bottom Yukawa coupling by comparing three different options: the first assumes on-shell renormalization of Y_b and employs a value of 4.9 GeV for the pole bottom mass m_b, computed at three-loop accuracy from the $\overline{\text{MS}}$ input value $m_b(m_b) = 4.16$ GeV; the second also assumes on-shell renormalization, but employs $m_b = 4.75$ GeV, consistent with the value used by the MSTW2008 PDF set (this is our default choice); the third option assumes the $\overline{\text{MS}}$ scheme and evaluates the bottom Yukawa coupling at the renormalization scale $\mu_b = m_b$, thus directly employing the input value $m_b(m_b) = 4.16$ GeV. For illustration, we obtain an even more conservative estimate of the uncertainty by relating the bottom Yukawa coupling to the $\overline{\text{MS}}$ mass computed at the scale $\mu_b = M_\phi$.

Since the bottom Yukawa coupling enters the cross-section predictions for h, H, and A with very different weights, the uncertainty due to its renormalization prescription depends significantly on the particle considered and on the SUSY scenario. For example, in the *light stop* scenario with $M_A = 130$ GeV and $\tan\beta = 40$, where both scalars have an enhanced coupling to the bottom quark, the effect of extracting the bottom Yukawa coupling from $m_b = 4.9$ GeV instead of the default $m_b = 4.75$ GeV leads to a 7% increase in the cross section for h production, and a 10% increase in the one for H production. On the other hand, using $\overline{\text{MS}}$ renormalization with $m_b(m_b) = 4.16$ GeV decreases the cross section for h production by 10%, and the one for H production by 19%. Using $m_b(M_\phi)$ instead would decrease the cross section for h production by 27%, and the one for H production by 52%. As a second example, we consider the *light stop* scenario with $M_A = 300$ GeV and $\tan\beta = 10$, where the lightest scalar h has SM-like couplings to quarks. In this case the cross section for h production varies by less than $\pm2\%$ when choosing among the three options for the bottom Yukawa coupling discussed above. For the heaviest scalar H, on the other hand, the changes relative to the value derived with $m_b = 4.75$ GeV amount to $+8\%$, -15% and -45% for a Yukawa coupling extracted from $m_b = 4.9$ GeV, $m_b(m_b)$ and $m_b(M_\phi)$, respectively.

Finally, in order to obtain an estimate of the influence of higher order squark effects, we follow Ref. [703] and find that they typically decrease the cross section by about $2-3\%$.

Let us now turn to kinematical distributions. In regions of the MSSM parameter space where the Higgs coupling to bottom quarks is enhanced, the transverse-momentum distribution of a scalar produced via gluon fusion can be distorted with respect to the corresponding distribution of a SM Higgs boson [716–718]. In order to investigate this effect, we consider again the point in the *light stop* scenario with $M_A = 130$ GeV and $\tan\beta = 40$, characterized by the fact that both scalars have non-standard couplings to quarks and masses in the vicinity of the LHC signal (indeed, FEYNHIGGS predicts $M_h = 122.4$ GeV and $M_H = 129.3$ GeV). This point is likely to be already excluded by the ATLAS and CMS searches for neutral Higgs bosons decaying into $\tau^+\tau^-$ pairs, but it can still provide a useful illustration of the expected size of this kind of effects.

In Figure 134 we show the ratio of the transverse-momentum distribution for a MSSM scalar produced via gluon fusion over the corresponding distribution for a SM Higgs with the same mass. The
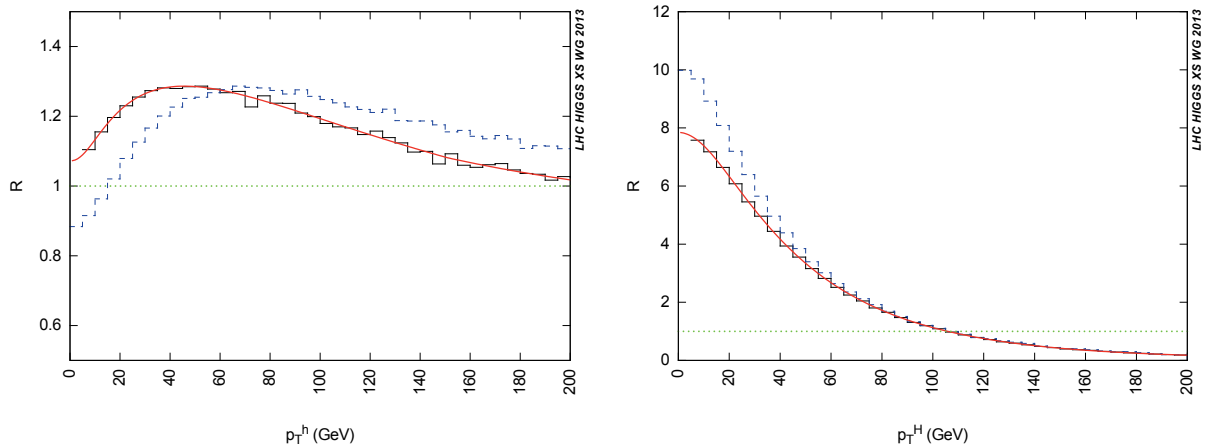
Figure 134: Ratio of the transverse-momentum distribution for the MSSM scalar h (left) or H (right) over the distribution for a SM Higgs with the same mass, in the *light stop* scenario with $M_A = 130 \, \text{GeV}$ and $\tan \beta = 40$. The meaning of the different curves is explained in the text.

plot on the left refers to the lightest scalar h, while the plot on the right refers to the heaviest scalar H. In each plot, the continuous (red) line represents the ratio of distributions computed at NLO by SuSHi, while the two histograms are computed with the POWHEG implementation of gluon fusion of Ref. [77], modified by the adoption of the on-shell renormalization scheme for the squark parameters and the inclusion of the results of Ref. [692] for the squark contributions to H production. In particular, the solid (black) histogram represents the ratio of distributions computed in a pure (i.e., fixed-order) NLO calculation, while in the dashed (blue) histogram the distributions are computed with the POWHEG method [79, 80, 285], in which the potentially large logarithms of the form $\ln(p_T^\phi / M_\phi^2)$ are resummed via the introduction of a Sudakov form factor and a parton-shower generator to describe multiple gluon emission (in this case, we use PYTHIA [81]).

The plots in Figure 134 show that, in this point of the MSSM parameter space, the enhancement of the Higgs-bottom coupling results in both an enhancement of the total cross section and a distortion of the transverse-momentum distribution, in particular for the heaviest scalar H (note the difference in the scale between the left and the right plot). The effect of the resummation in POWHEG and the unitarity constraint implemented in the matching procedure of NLO matrix elements with parton shower make the transverse-momentum distribution of the Higgs bosons harder. The comparison between the solid and dashed histograms shows that for h this effect is somewhat stronger than in the SM, while for H it is somewhat weaker.

It remains to stress that SuSHi also allows for the calculation of the cross section for the pseudoscalar Higgs A, where, however, squark effects are much less important because they are absent at LO. Furthermore, SuSHi includes the production cross section for bottom quark annihilation; we refrain from quoting any numerical results here, as they would not significantly differ from what has already been presented in earlier reports of this working group.

14.4 Light charged Higgs limits as a function of SUSY parameters

The exclusion limits in the ($M_{H^\pm}$, $\tan \beta$) plane are studied for different values of the most relevant SUSY parameters in the Higgs sector: μ, M_2, $M_{\tilde{g}}$, M_{SUSY}, X_t. The model independent limits for the light charged Higgs boson branching ratio [719] are transformed into limits in the ($M_{H^\pm}$, $\tan \beta$) plane with BR($t \to bH^\pm$) and BR($H^\pm \to \tau\nu$) branching ratios calculated with FEYNHIGGS 2.9.4 [24–27]. The studied $M_{H^\pm}$ mass range is $100-160 \, \text{GeV}$ and the $\tan \beta$ range is $5-100$. The exclusion limits

are shown[66] in Figure 135 for the $m_{\mathrm{h}}^{\mathrm{max}}$ scenario [16], $m_{\mathrm{h}}^{\mathrm{mod+}}$, $m_{\mathrm{h}}^{\mathrm{mod-}}$, *light stop*, *light stau* and τ-phobic [31] benchmark scenarios. The effect of varying the SUSY parameters on the exclusion limits are compared with the limits derived for the $m_{\mathrm{h}}^{\mathrm{max}}$ scenario. Since the importance of one parameter may depend on the value of another parameter, the effect of varying also the most significant parameter μ is studied for each parameter variation.

Based on the recent discovery of a Higgs-boson-like particle at the LHC with measured mass of $M_{\Phi} = 126.0 \pm 0.4 \pm 0.4$ GeV [1] (ATLAS) and $M_{\Phi} = 125.8 \pm 0.4 \pm 0.4$ GeV [2] (CMS), an allowed region is derived in the ($M_{\mathrm{H}^{\pm}}$, $\tan\beta$) plane assuming that the discovered particle is the light $\mathcal{CP}$-even MSSM Higgs boson h. The theoretical uncertainty is of the order of 3 GeV [26,650,651], and a ± 3 GeV iso-mass curve around the central value 125.9 GeV is drawn in Figure 135 to indicate the region of the parameter space allowed for the charged Higgs boson in the given scenario. The allowed region depends on the values of the SUSY parameters, but the lower limit for the allowed charged Higgs mass seems to be quite stable against the choice of the SUSY parameter values. The minimum possible value of $\tan\beta$ also varies around $\tan\beta = 10$ for the studied choices of the SUSY parameters up to $M_{\mathrm{H}^{\pm}} = 600$ GeV. The maximum possible value of $\tan\beta$ is more dependent on the choice of the SUSY parameters. For $M_{\mathrm{SUSY}} = 2$ TeV (changing the values of $M_{\tilde{\mathrm{g}}}$ and X_{t} to $0.8 \times M_{\mathrm{SUSY}}$ and $2 \times M_{\mathrm{SUSY}}$, accordingly) and for $X_{\mathrm{t}} = -2000$ GeV the entire high charged Higgs mass, high $\tan\beta$ corner is allowed for all tested values of the μ parameter, shown in Figure 136 (top right). The mass region is extended up to 600 GeV to see the effect of the SUSY parameter variation on the horizontal tail, which in turn gives a prediction for the allowed values of $\tan\beta$ for the heavy charged Higgs boson ($M_{\mathrm{H}^{\pm}} > m_{\mathrm{t}}$).

It is also possible that the discovered Higgs-like particle is the heavy $\mathcal{CP}$-even Higgs boson (or the heavy $\mathcal{CP}$-even and $\mathcal{CP}$-odd Higgs bosons together). In this case the $m_{\mathrm{h}}^{\mathrm{max}}$ scenario is ruled out as the mass of the discovered particle is lower than the minimum possible M_{H} (= $m_{\mathrm{h}}^{\mathrm{max}}$). Figure 136 (bottom) shows the allowed region for the heavy $\mathcal{CP}$-even and $\mathcal{CP}$-odd Higgs bosons when the M_{SUSY} parameter is changed to 2 TeV. The lower edge of the allowed region depends on the choice of the μ parameter, but extends over the high $\tan\beta$ region for all values of the μ parameter studied here. In Figure 136 (bottom left) no bound on M_{A} is used. Figure 136 (bottom right) shows the allowed region if H and A are both assumed to produce the experimental result. With this choice of M_{SUSY} the region with intersecting allowed areas for H and A vanish for positive values of the μ parameter.

14.4.1 Variation of μ, M_{SUSY}, $M_{\tilde{\mathrm{g}}}$, M_2 and X_{t}

As shown in Ref. [720], the μ parameter has a significant effect on the charged Higgs boson production and decay. This is illustrated in Figure 137 (top left) which shows the effect of varying the μ parameter on the observed exclusion region in the ($M_{\mathrm{H}^{\pm}}$, $\tan\beta$) parameter space. The same effect is shown as a function of μ in Figure 137 (top right). The small abs(μ) values are excluded from the plot. The value of μ in the $m_{\mathrm{h}}^{\mathrm{max}}$ scenario is 200 GeV.

The mass scale M_{SUSY} is varied between 500 and 2000 GeV, the $m_{\mathrm{h}}^{\mathrm{max}}$ scenario value being 1000 GeV. The values of $M_{\tilde{\mathrm{g}}}$ and X_{t} are changed to $0.8 \times M_{\mathrm{SUSY}}$ and $2 \times M_{\mathrm{SUSY}}$, accordingly. As shown in Figure 137 (middle), the effect on the exclusion limits are only a fraction of the effect of the μ parameter. If this mass scale is heavier than expected, it has only a small effect on the limits. Figure 137 (bottom) show the μ dependence of the limits with $M_{\mathrm{SUSY}} = 2000$ GeV as a function of $M_{\mathrm{H}^{\pm}}$ and as a function of μ.

Varying $M_{\tilde{\mathrm{g}}}$ has only a small effect on the limits, shown in Figure 138 (top). The variation of M_2 has even a smaller effect. The μ dependence is almost unchanged despite the choice of the M_2 value. For $M_{\tilde{\mathrm{g}}} = 200$ GeV the μ dependence is reduced by about 30% compared to the $m_{\mathrm{h}}^{\mathrm{max}}$ scenario.

The X_{t} parameter is varied in Figure 138 (middle). An effect on the exclusion limits can clearly be seen. The change as a function of X_{t} is close to linear. The μ dependence at $X_{\mathrm{t}} = -2000$ GeV gives

---

[66]Only the region up to $\tan\beta = 65$ is shown for the sake of readability of the plots.
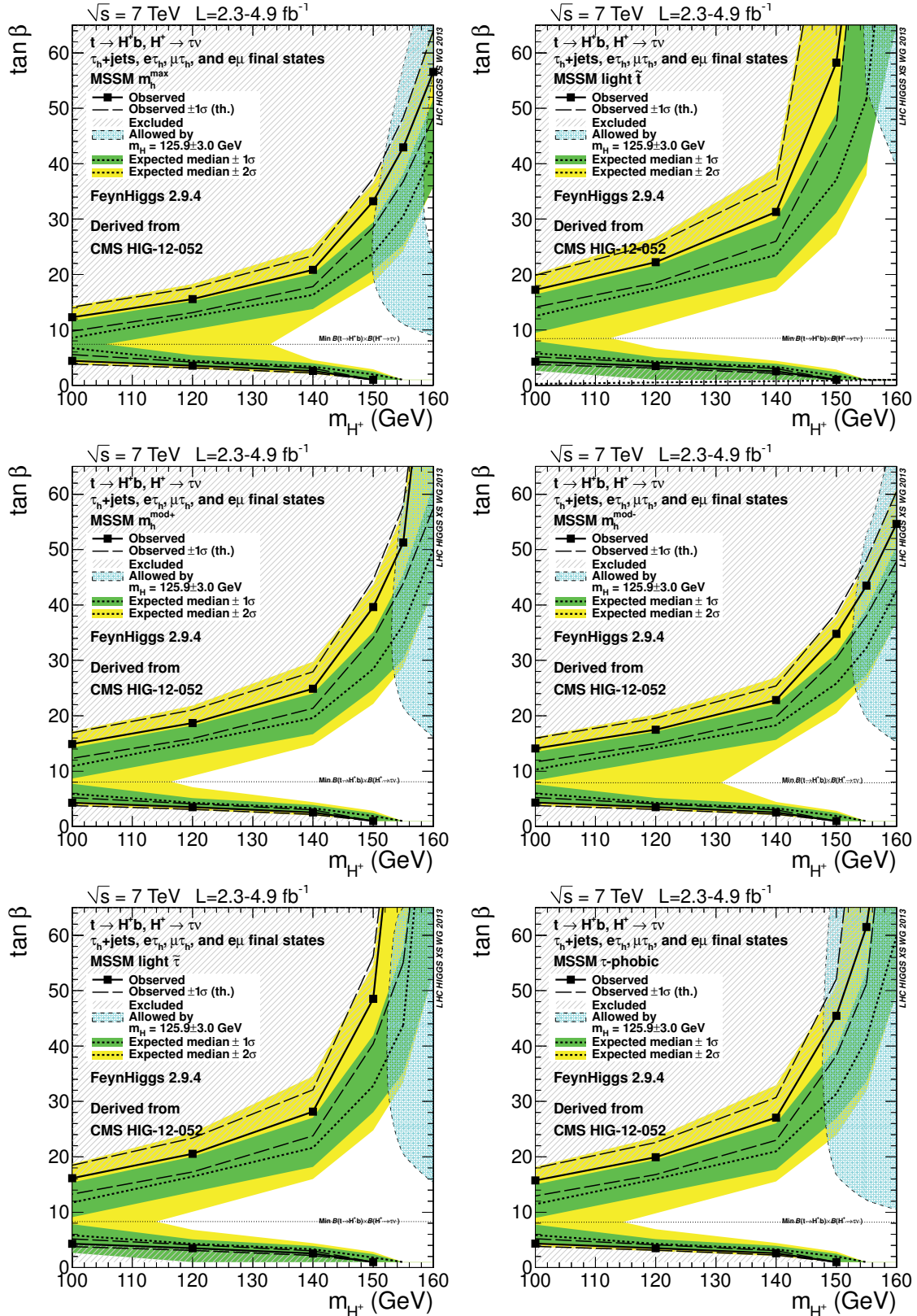
Figure 135: The exclusion limit derived from [719] for the light charged Higgs boson in the $(M_{H^\pm}, \tan\beta)$ plane in the m_h^{max} scenario [16] (top left), in the *light stop* scenario [31] (top right), in the $m_h^{\mathrm{mod+}}$ scenario [31] (middle left) in the $m_h^{\mathrm{mod-}}$ scenario [31] (middle right) in the *light stau* scenario [31] (bottom left) and in the τ-phobic scenario [31] (bottom right).
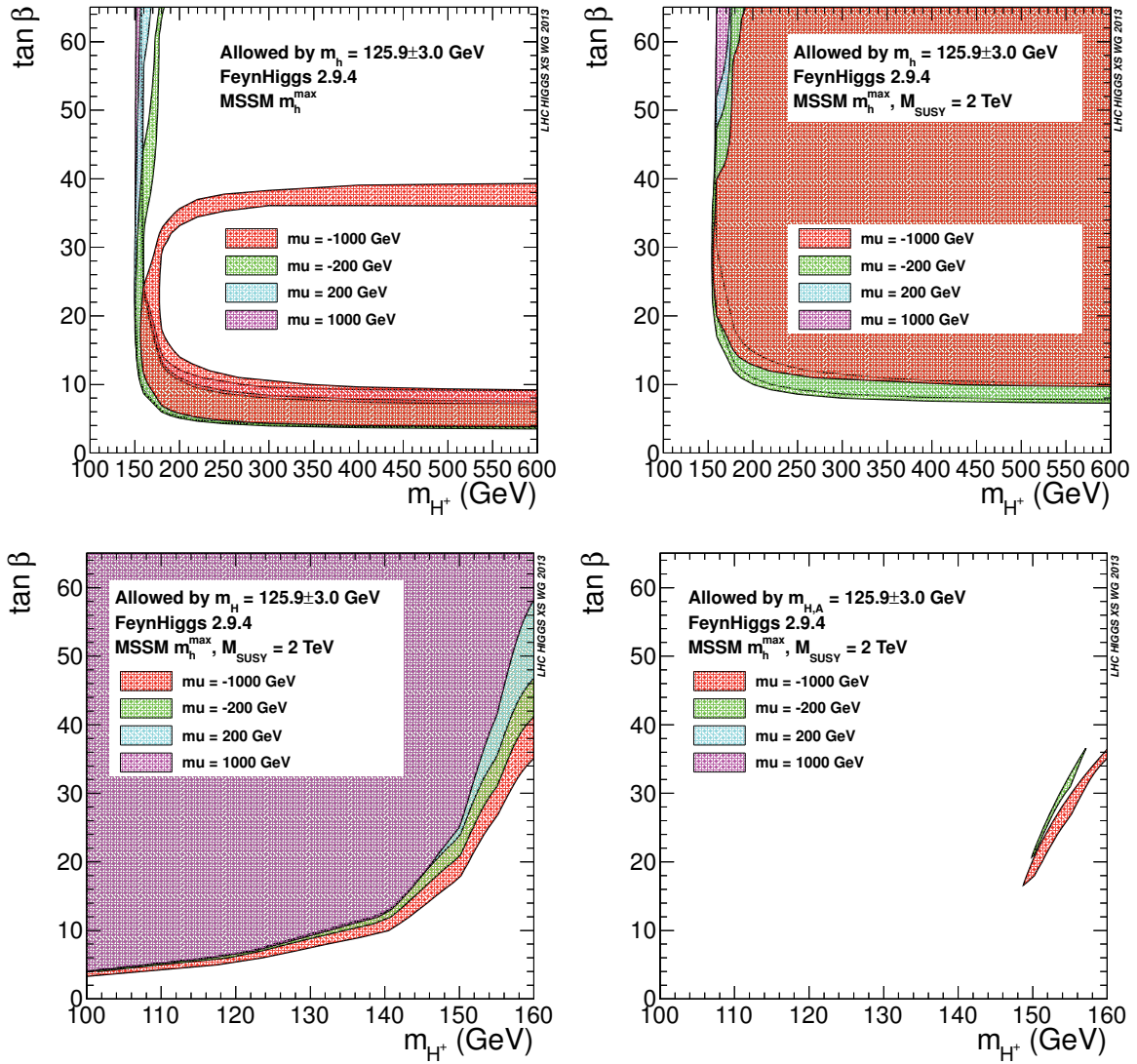
Figure 136: The region allowed by $M_h = 125.9 \pm 3.0\,\text{GeV}$ in the m_h^{max} scenario (top left), in the m_h^{max} scenario with M_{SUSY} set to 2 TeV (top right) and by $M_H = 125.9 \pm 3.0\,\text{GeV}$ (bottom left) and by both H and A, $M_{\text{H,A}} = 125.9 \pm 3.0\,\text{GeV}$ (bottom right). If $\mu > 0$ the allowed regions for H and A do not intersect.

a wave-like behavior, shown in Figure 138 (bottom), which is the reason why the exclusion limits for positive and negative values of the μ parameter are in different order depending on the absolute value.

The experimental 95% CL limits transferred to $(M_{\text{H}^\pm}, \tan\beta)$ parameter space seem to be quite stable against all other parameter variations except the variation of the μ parameter in the mass range $M_{\text{H}^\pm} < 140\,\text{GeV}$. There is a significant dependence on the μ. In the interesting region allowed by $M_h = 125.9 \pm 3.0\,\text{GeV}$ the limits are affected by the choice of M_{SUSY} and X_t in addition to μ. However, although the limits themselves are not too sensitive to the values chosen for M_{SUSY}, $M_{\tilde{g}}$, M_2 and X_t, the choice of the values for these parameters do have a significant effect on the region allowed by the discovery of a Higgs-like particle, whether it is assumed to be h, H or H and A together, as shown in Figure 136. Moreover, the experimental limits are excluding large parts of the allowed regions already. With tighter limits expected from new updated analysis using full integrated luminosity from 2011 and 2012 data taking these allowed regions not experimentally excluded should shrink further, starting to exclude the possibility that the discovered Higgs-like particle could be the heavy $\mathcal{CP}$-even or $\mathcal{CP}$-odd Higgs boson in the studied scenarios.
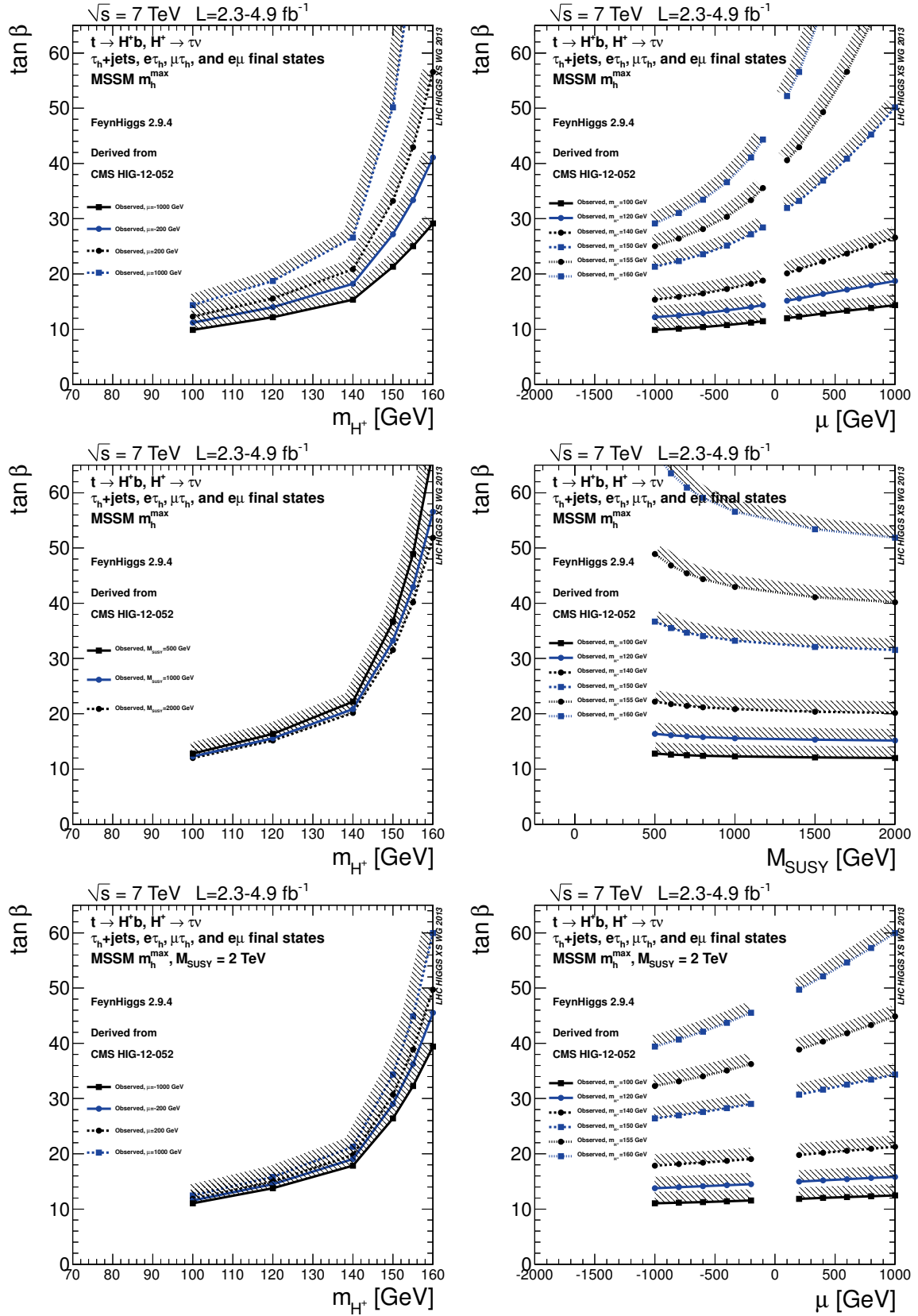
Figure 137: The effect of varying the μ parameter on the experimentally excluded region in the m_h^{max} scenario (top plots), the effect of varying M_{SUSY} (middle plots), and the effect of varying the μ parameter with $M_{\mathrm{SUSY}} = 2\,\mathrm{TeV}$ (bottom plots).
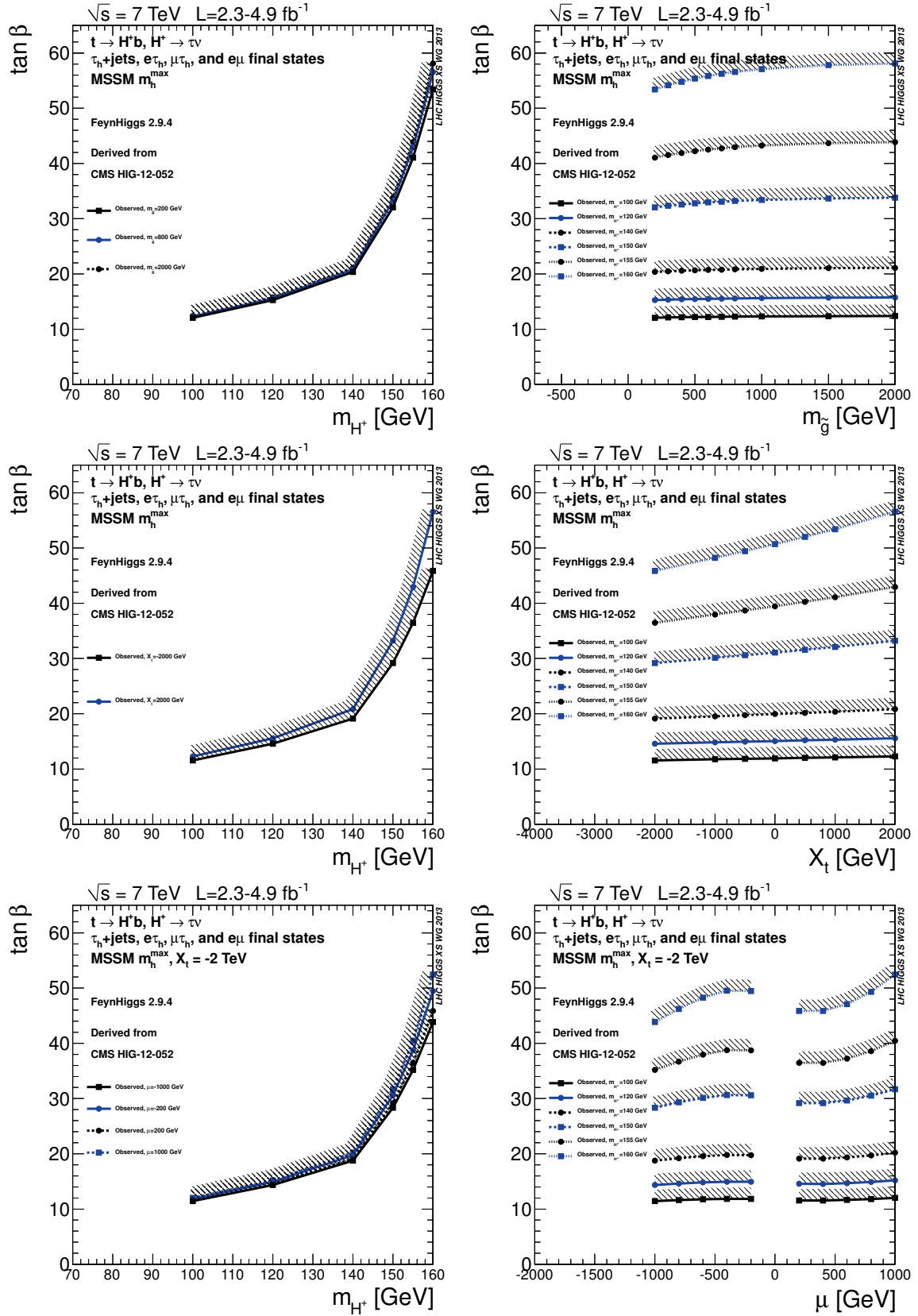
Figure 138: The effect of varying $M_{\tilde{g}}$ on the experimentally excluded region in the m_h^{max} scenario (top left and right), the effect of varying X_t (middle plots), and the effect of varying the μ parameter with $X_t = -2$ TeV (bottom plots).

14.5 Heavy charged Higgs production

Heavy charged Higgs bosons with a mass larger than the top-quark mass would be produced in association with a top quark:

$$\mathrm{pp} \rightarrow \mathrm{tbH}^{\pm} + X.$$

The cross section for associated $\mathrm{tbH}^{\pm}$ production can be computed in the so-called four- and five-flavor schemes. In the four-flavor scheme (4FS) there are no b quarks in the initial state, and therefore the lowest-order QCD production processes are gluon-gluon fusion and quark-antiquark annihilation, $\mathrm{gg} \rightarrow \mathrm{tbH}^{\pm}$ and $\mathrm{q\bar{q}} \rightarrow \mathrm{tbH}^{\pm}$, respectively. Potentially large logarithms of the ratio between the hard scale of the process and the mass of the bottom quark, which arise from the splitting of incoming gluons into nearly collinear $\mathrm{b\bar{b}}$ pairs, can be summed to all orders in perturbation theory by introducing bottom parton densities. This defines the five-flavor scheme (5FS). The use of bottom distribution functions is based on the approximation that the outgoing b quark is at small transverse momentum and massless, and the virtual b quark is quasi on shell. In this scheme, the LO process for the inclusive $\mathrm{tbH}^{\pm}$ cross section is gluon-bottom fusion, $\mathrm{gb} \rightarrow \mathrm{tH}^{\pm}$. The NLO cross section in the 5FS scheme includes $\mathcal{O}(\alpha_{\mathrm{s}})$ corrections to $\mathrm{gb} \rightarrow \mathrm{tH}^{\pm}$, including the tree-level processes $\mathrm{gg} \rightarrow \mathrm{tbH}^{\pm}$ and $\mathrm{q\bar{q}} \rightarrow \mathrm{tbH}^{\pm}$. To all orders in perturbation theory the two schemes are identical, but the way of ordering the perturbative expansion is different, and the results do not match exactly at finite order. For the inclusive production of neutral Higgs bosons with bottom quarks, $\mathrm{pp} \rightarrow \mathrm{b\bar{b}H} + X$, the four- and five-flavor scheme calculations numerically agree within their respective uncertainties, once higher-order QCD corrections are taken into account, see [13, 14] and references therein.

We provide NLO predictions for heavy charged Higgs boson production in a two Higgs doublet model (2HDM) with $\tan\beta = 30$. SUSY effects can be taken into account by rescaling the bottom Yukawa coupling to the proper value. We present results for the 4FS and 5FS schemes, including the theoretical uncertainty, and combine the two schemes according to the Santander matching proposed in [721]. Throughout this report we present results for the $\mathrm{t\bar{b}H}^{-}$ channel.

For the calculation in the 5FS, the program Prospino [722] has been employed, interfaced to the LHAPDF library [723]. The renormalization scale is set to $\mu_{\mathrm{R}} = (M_{\mathrm{H}^{\pm}} + m_{\mathrm{t}})/2$, while the factorization scale $\mu_{\mathrm{F}} = \tilde{\mu}$ is chosen according to the method proposed in [724]. The effective factorization scale entering the initial state logarithms is proportional to the hard scale, but modified by a phase space factor which tends to reduce the size of the logarithms for processes at hadron colliders. The factorization scale $\tilde{\mu}$ is given in Tab. 70 for several Higgs masses, both for 8 and 14 TeV center-of-mass energy. The values of the factorization scale match those proposed in [722].

To estimate the theoretical uncertainty due to missing higher-order contributions, we vary the renormalization and factorization scales by a factor three about their central values. We find scale uncertainties between approximately 10–20%, depending on the Higgs mass and collider energy. In addition to the scale variation, we have computed the uncertainty associated with the PDF set and the values of α_{s} and m_{b} used in PDF fits, following the PDF4LHC [147] recommendation. All uncertainties are given at 68% confidence level (CL). The α_{s} uncertainty corresponds to a variation of ± 0.0012 about the central value [147]. As the uncertainty for the bottom mass we take $m_{\mathrm{b}} = 4.75 \pm 0.25$ GeV, which is a conservative choice compared to the uncertainty given in [725]. The overall PDF+α_{s}+m_{b} uncertainty amounts to approximately 10–15% and is thus comparable to the scale uncertainty. Combining the two sources of uncertainty linearly we obtain an estimate of the overall theoretical uncertainty of approximately 30%. Our 5FS results for heavy charged Higgs production at the LHC with 8 TeV cms energy are displayed in Figure 139, upper panel.

The results for heavy charged Higgs production within the four-flavour scheme (4FS) are based on the calculation presented in Ref. [726]. We adopt the CT10 [145], MRST [727] and NNPDF21 [210] 4FS pdf sets. The renormalization and factorization scales are varied by a factor three about the central scale choice $\mu_0 = (M_{\mathrm{H}^{\pm}} + m_{\mathrm{t}} + m_{\mathrm{b}})/3$. The scale variation in the 4FS is approximately 30%, i.e. somewhat larger than in the 5FS. Note that our estimate of the pdf uncertainty is based on MRST2008

Table 70: Dynamical factorization scale $\tilde{\mu}$ for $pp \to tH^- + X$ for the LHC at 8 and 14 TeV.

	8 TeV		14 TeV	
$M_{H^\pm}$ [GeV]	$\tilde{\mu}$ [GeV]	$(m_t + M_{H^\pm})/\tilde{\mu}$	$\tilde{\mu}$ [GeV]	$(m_t + M_{H^\pm})/\tilde{\mu}$
200	67.3	5.5	74.9	5.0
300	80.3	5.9	90.6	5.2
400	92.1	6.2	105.3	5.4
500	103.1	6.5	119.0	5.7

and NNPDF21 only, as CT10 does not provide eigenvector sets in the 4FS. Furthermore, no uncertainties for α_s and m_b could be calculated, as no pdf collaboration provides 4FS sets with varying α_s and m_b. Our 4FS results for heavy charged Higgs production at the LHC with 8 TeV cms energy are displayed in Figure 139, middle panel.

To arrive at a final prediction for heavy charged Higgs production we combine the NLO 5FS and 4FS cross sections according to the Santander matching [721], analogous to neutral Higgs-bottom associated production. We note that the 4FS and 5FS calculations provide the unique description of the cross section in the asymptotic limits $M_\phi/m_b \to 1$ and $M_\phi/m_b \to \infty$, respectively (here and in the following M_ϕ denotes a generic Higgs boson mass). The 4FS and 5FS are thus combined in such a way that they are given variable weight, depending on the value of the Higgs-boson mass. The difference between the two approaches is formally logarithmic. Therefore, the dependence of their relative importance on the Higgs-boson mass should be controlled by a logarithmic term, i.e.

$$\sigma^{\text{matched}} = \frac{\sigma^{\text{4FS}} + w\,\sigma^{\text{5FS}}}{1 + w} \quad \text{with} \quad w = \ln\frac{M_\phi}{m_b} - 2\,. \tag{368}$$

The theoretical uncertainties are combined according to

$$\Delta\sigma_\pm^{\text{matched}} = \frac{\Delta\sigma_\pm^{\text{4FS}} + w\Delta\sigma_\pm^{\text{5FS}}}{1 + w} \tag{369}$$

where $\Delta\sigma_\pm^{\text{4FS}}$ and $\Delta\sigma_\pm^{\text{5FS}}$ are the upper/lower uncertainty limits of the 4FS and the 5FS, respectively.

The cross section and uncertainty for the Santander matching, together with the results calculated in 4F- and 5F-scheme, for LHC at 8 TeV are presented in Fig. 139, lower panel. We observe that the NLO 4FS and 5FS predictions are in good mutual agreement, with differences of at most $\sim$7%. The dynamical choice for μ_F in the 5FS used here improves the matching of the predictions in the two schemes. The overall theoretical uncertainty of the matched NLO prediction is about 30%.
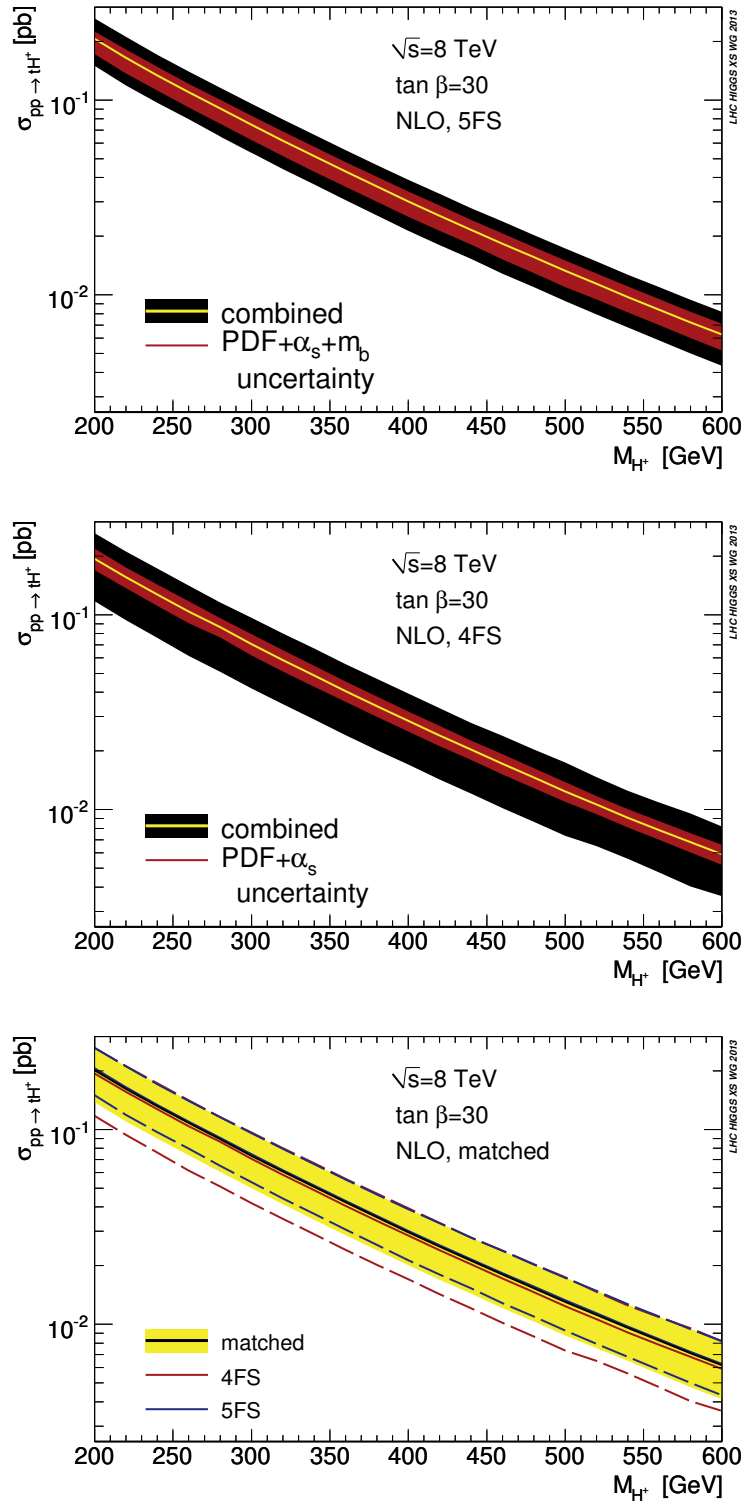
Figure 139: NLO cross section prediction for $pp \to tH^- + X$ at the LHC with 8 TeV for a 2HDM with $\tan\beta = 30$: 5FS (upper panel), 4FS (middle panel) and Santander matched predictions (lower panel). Shown is the central prediction together with an estimate of the theoretical uncertainties as described in the text.

15 Conclusions [67]

The present document is the result of the activities of the LHC Higgs Cross Section Working Group in the year 2012 till spring 2013. The working group, created in January 2010, is a joint effort between ATLAS, CMS and the theory community. Previous reports [13, 14] dealt with the presentation of the main Higgs production cross section and branching ratios of a SM Higgs at the highest available level of accuracy. Similarly, first result for the Higgs bosons of the MSSM were presented. Beyond the level of total cross sections also distributions for the corresponding cross sections were investigated. Most up-to-date results are continuously made public at the TWiki page[68].

The spectacular discovery of a Higgs-boson like resonance with a mass around $\sim 125 - 126$ GeV, which has been announced by ATLAS [1] and CMS [2] on July 4th, 2012, marks a milestone of an effort that has been ongoing for almost half a century and opens up a new era of particle physics.

Having analysed two and a half times more data than was available for the discovery announcement in July 2012, the experiments are finding that the new particle, within the experimental uncertainties, is perfectly compatible with the SM Higgs boson. It remains an open question, however, whether it is indeed the SM Higgs boson, or possibly one of several bosons predicted in some theories that go beyond the SM. It is therefore the highest priority in particle physics research at the moment to examine whether the emerging picture is complete. This entails, in turn, placing increasingly stringent limits on potential new physics scenarios.

Possible deviations from the SM prediction are not statistically significant at present, so that within the uncertainties the results are compatible with the SM. On the other hand, the experimental uncertainties are still rather large and thus also permit non-SM interpretations of the newly discovered Higgs-boson like resonance. If deviations from SM predictions were confirmed in the future, the observed patterns could indicate a first clear step beyond the SM.

With the discovery of a Higgs-boson like resonance the focus of the high-energy physics world, and thus of the LHC Higgs Cross Section Working Group, has shifted. While ever more precise calculation of SM predictions are needed, now corresponding calculations at a similar level of accuracy in BSM models become important. Rules and definitions for the determination of the characteristics of the Higgs-boson like resonance, such as couplings to other particles, quantum numbers, spin etc. are now crucial for the correct interpretation of the experimental data.

Theory uncertainty is becoming more and more relevant than ever before. The experimental accuracy is $\Delta\mu(\sigma/\sigma_{\text{SM}}) = \pm15\%$ (roughly $\pm10\%$ for both statistical and systematic uncertainties) with LHC 2011/2012 data, while the theoretical uncertainty is $\pm(10-15)\%$ dominated by missing higher-order calculations and PDF $+\alpha_{\text{s}}$ in gluon-fusion. This calls for improvements in NNNLO prediction; other important issues are reduction of uncertainty in 1-jet bin and gluon-fusion $+2$-jets versus vector-boson fusion, as well as improvements in parton-luminosity functions with LHC data.

With the present document the LHC Higgs Cross Section Working Group tries to lead the way into the new directions. This volume, correspondingly, provides a wide range of topics: Updated results for Higgs Cross Sections and Higgs Decay Branching Ratios, Jet-bin and Higgs p_{T} Uncertainties, Interference Effects in gg-fusion, NLO Monte Carlo, Higgs Coupling and Spin/Parity and BSM Higgs. Updates of previous results for cross sections and branching ratios of a SM Higgs are refined around the experimentally determined mass range.

Guidelines for the extraction of the couplings have been worked out that can readily applied to the 2011/2012 data set. Results for spin and CP-determinations and refined coupling determinations are outlined. Also in this area more detailed worked out prescriptions will be necessary to cope with the data the LHC will provide in future, toward precision Higgs physics at the LHC.

---

[67]S. Heinemeyer, C. Mariotti, G. Passarino, R. Tanaka

[68]https://twiki.cern.ch/twiki/bin/view/LHCPhysicsCrossSections

Within the MSSM improved cross section calculations were performed, taking into account possible effects of light Supersymmetric particles. Moreover, interpretations in the MSSM (as in any other BSM model) now always must contain at least one Higgs boson at $\sim 125 - 126$ GeV, which is reflected in a new set of MSSM benchmark scenarios. First steps are presented to go to models beyond the SM and the MSSM, where clearly more work, including the calculations of cross sections and branching ratios, are needed in the future.

In conclusion, finding BSM's footsteps should be the primary goal of the Working Group: what are the implications of the newly discovered resonance for BSM scenarios? We can go on to lay out two extreme scenarios. The first one would be nothing but the SM at LHC energies, including no detection of dark matter. In that case it would remain unclear for a long time to come which BSM model is realised in nature. The second scenario is the picture anticipated pre-LHC: detection of non-SM Higgs and possibly of other non-SM particles at the next high-energy run of the LHC. Only experimental data can lead the way.

Finally, no small set of individuals among the hundreds who have worked collaboration to produce this volume can take enough of the credit to single them out, even less the editors.

> Open your mind to what I shall disclose, and hold it fast within you; he who hears, but does
>   not hold what he has heard, learns nothing.

Beatrice - Canto V 40-42

Chiara, Giampiero, Reisaburo and Sven

Acknowledgements

Appendices

A Tables of branching ratios

In this appendix we complete the listing of the branching fractions of the Standard Model Higgs boson discussed in Section 2.

Table A.1: SM Higgs branching ratios to two fermions and their total uncertainties (expressed in percentage). Very-low mass range.

M_H [GeV]	H → bb	H → $\tau^+\tau^-$	H → $\mu^+\mu^-$	H → c$\bar{\text{c}}$
80	$8.24 \cdot 10^{-1}\,^{+1.4}_{-1.5}$	$8.27 \cdot 10^{-2}\,^{+7.0}_{-6.9}$	$2.87 \cdot 10^{-4}\,^{+7.4}_{-7.1}$	$4.18 \cdot 10^{-2}\,^{+12.1}_{-12.1}$
81	$8.23 \cdot 10^{-1}\,^{+1.5}_{-1.5}$	$8.27 \cdot 10^{-2}\,^{+7.0}_{-6.8}$	$2.88 \cdot 10^{-4}\,^{+7.3}_{-7.2}$	$4.17 \cdot 10^{-2}\,^{+12.1}_{-12.1}$
82	$8.21 \cdot 10^{-1}\,^{+1.5}_{-1.5}$	$8.28 \cdot 10^{-2}\,^{+7.0}_{-6.8}$	$2.88 \cdot 10^{-4}\,^{+7.3}_{-7.2}$	$4.16 \cdot 10^{-2}\,^{+12.1}_{-12.1}$
83	$8.20 \cdot 10^{-1}\,^{+1.5}_{-1.5}$	$8.29 \cdot 10^{-2}\,^{+7.0}_{-6.8}$	$2.88 \cdot 10^{-4}\,^{+7.3}_{-7.2}$	$4.16 \cdot 10^{-2}\,^{+12.1}_{-12.1}$
84	$8.19 \cdot 10^{-1}\,^{+1.5}_{-1.5}$	$8.30 \cdot 10^{-2}\,^{+7.0}_{-6.8}$	$2.88 \cdot 10^{-4}\,^{+7.3}_{-7.2}$	$4.15 \cdot 10^{-2}\,^{+12.1}_{-12.1}$
85	$8.17 \cdot 10^{-1}\,^{+1.5}_{-1.5}$	$8.30 \cdot 10^{-2}\,^{+7.0}_{-6.8}$	$2.89 \cdot 10^{-4}\,^{+7.3}_{-7.1}$	$4.14 \cdot 10^{-2}\,^{+12.1}_{-12.1}$
86	$8.16 \cdot 10^{-1}\,^{+1.5}_{-1.6}$	$8.31 \cdot 10^{-2}\,^{+7.0}_{-6.8}$	$2.89 \cdot 10^{-4}\,^{+7.3}_{-7.2}$	$4.13 \cdot 10^{-2}\,^{+12.2}_{-12.1}$
87	$8.15 \cdot 10^{-1}\,^{+1.5}_{-1.6}$	$8.31 \cdot 10^{-2}\,^{+7.0}_{-6.8}$	$2.89 \cdot 10^{-4}\,^{+7.3}_{-7.2}$	$4.13 \cdot 10^{-2}\,^{+12.1}_{-12.1}$
88	$8.13 \cdot 10^{-1}\,^{+1.6}_{-1.6}$	$8.32 \cdot 10^{-2}\,^{+7.0}_{-6.8}$	$2.89 \cdot 10^{-4}\,^{+7.3}_{-7.1}$	$4.12 \cdot 10^{-2}\,^{+12.2}_{-12.1}$
89	$8.12 \cdot 10^{-1}\,^{+1.6}_{-1.6}$	$8.32 \cdot 10^{-2}\,^{+7.0}_{-6.8}$	$2.89 \cdot 10^{-4}\,^{+7.3}_{-7.1}$	$4.11 \cdot 10^{-2}\,^{+12.1}_{-12.1}$
90	$8.10 \cdot 10^{-1}\,^{+1.6}_{-1.6}$	$8.33 \cdot 10^{-2}\,^{+7.0}_{-6.8}$	$2.89 \cdot 10^{-4}\,^{+7.3}_{-7.1}$	$4.10 \cdot 10^{-2}\,^{+12.1}_{-12.1}$
91	$8.09 \cdot 10^{-1}\,^{+1.6}_{-1.6}$	$8.33 \cdot 10^{-2}\,^{+7.0}_{-6.8}$	$2.89 \cdot 10^{-4}\,^{+7.3}_{-7.2}$	$4.09 \cdot 10^{-2}\,^{+12.2}_{-12.1}$
92	$8.07 \cdot 10^{-1}\,^{+1.6}_{-1.7}$	$8.33 \cdot 10^{-2}\,^{+7.0}_{-6.8}$	$2.89 \cdot 10^{-4}\,^{+7.3}_{-7.1}$	$4.08 \cdot 10^{-2}\,^{+12.2}_{-12.1}$
93	$8.05 \cdot 10^{-1}\,^{+1.6}_{-1.7}$	$8.33 \cdot 10^{-2}\,^{+7.0}_{-6.8}$	$2.89 \cdot 10^{-4}\,^{+7.3}_{-7.1}$	$4.07 \cdot 10^{-2}\,^{+12.2}_{-12.1}$
94	$8.03 \cdot 10^{-1}\,^{+1.7}_{-1.7}$	$8.33 \cdot 10^{-2}\,^{+7.0}_{-6.8}$	$2.89 \cdot 10^{-4}\,^{+7.3}_{-7.1}$	$4.06 \cdot 10^{-2}\,^{+12.2}_{-12.1}$
95	$8.01 \cdot 10^{-1}\,^{+1.7}_{-1.7}$	$8.32 \cdot 10^{-2}\,^{+6.9}_{-6.8}$	$2.89 \cdot 10^{-4}\,^{+7.3}_{-7.1}$	$4.05 \cdot 10^{-2}\,^{+12.2}_{-12.1}$
96	$7.99 \cdot 10^{-1}\,^{+1.7}_{-1.7}$	$8.32 \cdot 10^{-2}\,^{+6.9}_{-6.8}$	$2.89 \cdot 10^{-4}\,^{+7.3}_{-7.1}$	$4.04 \cdot 10^{-2}\,^{+12.2}_{-12.1}$
97	$7.97 \cdot 10^{-1}\,^{+1.7}_{-1.8}$	$8.31 \cdot 10^{-2}\,^{+6.9}_{-6.8}$	$2.89 \cdot 10^{-4}\,^{+7.3}_{-7.1}$	$4.03 \cdot 10^{-2}\,^{+12.2}_{-12.2}$
98	$7.95 \cdot 10^{-1}\,^{+1.7}_{-1.8}$	$8.31 \cdot 10^{-2}\,^{+6.9}_{-6.7}$	$2.88 \cdot 10^{-4}\,^{+7.2}_{-7.1}$	$4.02 \cdot 10^{-2}\,^{+12.2}_{-12.2}$
99	$7.92 \cdot 10^{-1}\,^{+1.8}_{-1.8}$	$8.29 \cdot 10^{-2}\,^{+6.9}_{-6.7}$	$2.88 \cdot 10^{-4}\,^{+7.2}_{-7.1}$	$4.00 \cdot 10^{-2}\,^{+12.2}_{-12.2}$
100	$7.89 \cdot 10^{-1}\,^{+1.8}_{-1.8}$	$8.28 \cdot 10^{-2}\,^{+6.9}_{-6.7}$	$2.88 \cdot 10^{-4}\,^{+7.2}_{-7.0}$	$3.99 \cdot 10^{-2}\,^{+12.2}_{-12.2}$
101	$7.86 \cdot 10^{-1}\,^{+1.8}_{-1.9}$	$8.27 \cdot 10^{-2}\,^{+6.9}_{-6.7}$	$2.87 \cdot 10^{-4}\,^{+7.2}_{-7.1}$	$3.97 \cdot 10^{-2}\,^{+12.2}_{-12.2}$
102	$7.83 \cdot 10^{-1}\,^{+1.8}_{-1.9}$	$8.25 \cdot 10^{-2}\,^{+6.8}_{-6.7}$	$2.86 \cdot 10^{-4}\,^{+7.2}_{-7.0}$	$3.96 \cdot 10^{-2}\,^{+12.2}_{-12.2}$
103	$7.79 \cdot 10^{-1}\,^{+1.9}_{-1.9}$	$8.22 \cdot 10^{-2}\,^{+6.8}_{-6.7}$	$2.86 \cdot 10^{-4}\,^{+7.2}_{-7.0}$	$3.94 \cdot 10^{-2}\,^{+12.2}_{-12.2}$
104	$7.75 \cdot 10^{-1}\,^{+1.9}_{-1.9}$	$8.20 \cdot 10^{-2}\,^{+6.8}_{-6.7}$	$2.85 \cdot 10^{-4}\,^{+7.1}_{-7.0}$	$3.92 \cdot 10^{-2}\,^{+12.2}_{-12.2}$
105	$7.71 \cdot 10^{-1}\,^{+1.9}_{-2.0}$	$8.17 \cdot 10^{-2}\,^{+6.8}_{-6.6}$	$2.84 \cdot 10^{-4}\,^{+7.1}_{-7.0}$	$3.90 \cdot 10^{-2}\,^{+12.2}_{-12.2}$
106	$7.66 \cdot 10^{-1}\,^{+2.0}_{-2.0}$	$8.13 \cdot 10^{-2}\,^{+6.8}_{-6.6}$	$2.82 \cdot 10^{-4}\,^{+7.1}_{-6.9}$	$3.87 \cdot 10^{-2}\,^{+12.2}_{-12.2}$
107	$7.61 \cdot 10^{-1}\,^{+2.0}_{-2.0}$	$8.10 \cdot 10^{-2}\,^{+6.7}_{-6.6}$	$2.81 \cdot 10^{-4}\,^{+7.0}_{-6.9}$	$3.85 \cdot 10^{-2}\,^{+12.2}_{-12.2}$
108	$7.56 \cdot 10^{-1}\,^{+2.0}_{-2.1}$	$8.05 \cdot 10^{-2}\,^{+6.7}_{-6.6}$	$2.80 \cdot 10^{-4}\,^{+7.0}_{-6.9}$	$3.82 \cdot 10^{-2}\,^{+12.2}_{-12.2}$
109	$7.50 \cdot 10^{-1}\,^{+2.1}_{-2.1}$	$8.00 \cdot 10^{-2}\,^{+6.7}_{-6.5}$	$2.78 \cdot 10^{-4}\,^{+7.0}_{-6.8}$	$3.79 \cdot 10^{-2}\,^{+12.2}_{-12.2}$
110	$7.44 \cdot 10^{-1}\,^{+2.1}_{-2.2}$	$7.95 \cdot 10^{-2}\,^{+6.6}_{-6.5}$	$2.76 \cdot 10^{-4}\,^{+6.9}_{-6.8}$	$3.76 \cdot 10^{-2}\,^{+12.2}_{-12.2}$
110.5	$7.40 \cdot 10^{-1}\,^{+2.1}_{-2.2}$	$7.92 \cdot 10^{-2}\,^{+6.6}_{-6.5}$	$2.75 \cdot 10^{-4}\,^{+6.9}_{-6.8}$	$3.74 \cdot 10^{-2}\,^{+12.3}_{-12.2}$
111	$7.37 \cdot 10^{-1}\,^{+2.2}_{-2.2}$	$7.89 \cdot 10^{-2}\,^{+6.6}_{-6.5}$	$2.74 \cdot 10^{-4}\,^{+6.9}_{-6.8}$	$3.72 \cdot 10^{-2}\,^{+12.3}_{-12.2}$
111.5	$7.33 \cdot 10^{-1}\,^{+2.2}_{-2.3}$	$7.85 \cdot 10^{-2}\,^{+6.6}_{-6.4}$	$2.73 \cdot 10^{-4}\,^{+6.9}_{-6.7}$	$3.70 \cdot 10^{-2}\,^{+12.3}_{-12.2}$
112	$7.29 \cdot 10^{-1}\,^{+2.2}_{-2.3}$	$7.82 \cdot 10^{-2}\,^{+6.6}_{-6.4}$	$2.71 \cdot 10^{-4}\,^{+6.9}_{-6.7}$	$3.68 \cdot 10^{-2}\,^{+12.2}_{-12.2}$
112.5	$7.25 \cdot 10^{-1}\,^{+2.3}_{-2.3}$	$7.78 \cdot 10^{-2}\,^{+6.5}_{-6.4}$	$2.70 \cdot 10^{-4}\,^{+6.9}_{-6.7}$	$3.66 \cdot 10^{-2}\,^{+12.2}_{-12.2}$
113	$7.21 \cdot 10^{-1}\,^{+2.3}_{-2.3}$	$7.75 \cdot 10^{-2}\,^{+6.5}_{-6.4}$	$2.69 \cdot 10^{-4}\,^{+6.8}_{-6.7}$	$3.64 \cdot 10^{-2}\,^{+12.2}_{-12.2}$
113.5	$7.17 \cdot 10^{-1}\,^{+2.3}_{-2.4}$	$7.71 \cdot 10^{-2}\,^{+6.5}_{-6.4}$	$2.68 \cdot 10^{-4}\,^{+6.8}_{-6.7}$	$3.62 \cdot 10^{-2}\,^{+12.3}_{-12.2}$
114	$7.12 \cdot 10^{-1}\,^{+2.3}_{-2.4}$	$7.67 \cdot 10^{-2}\,^{+6.5}_{-6.4}$	$2.66 \cdot 10^{-4}\,^{+6.8}_{-6.7}$	$3.60 \cdot 10^{-2}\,^{+12.3}_{-12.2}$
114.5	$7.08 \cdot 10^{-1}\,^{+2.4}_{-2.4}$	$7.63 \cdot 10^{-2}\,^{+6.5}_{-6.3}$	$2.65 \cdot 10^{-4}\,^{+6.7}_{-6.6}$	$3.57 \cdot 10^{-2}\,^{+12.3}_{-12.2}$
115	$7.03 \cdot 10^{-1}\,^{+2.4}_{-2.5}$	$7.58 \cdot 10^{-2}\,^{+6.4}_{-6.3}$	$2.63 \cdot 10^{-4}\,^{+6.7}_{-6.6}$	$3.55 \cdot 10^{-2}\,^{+12.2}_{-12.2}$
115.5	$6.98 \cdot 10^{-1}\,^{+2.4}_{-2.5}$	$7.53 \cdot 10^{-2}\,^{+6.4}_{-6.3}$	$2.62 \cdot 10^{-4}\,^{+6.7}_{-6.6}$	$3.53 \cdot 10^{-2}\,^{+12.2}_{-12.2}$
116	$6.93 \cdot 10^{-1}\,^{+2.5}_{-2.5}$	$7.49 \cdot 10^{-2}\,^{+6.4}_{-6.3}$	$2.60 \cdot 10^{-4}\,^{+6.7}_{-6.5}$	$3.50 \cdot 10^{-2}\,^{+12.2}_{-12.2}$
116.5	$6.88 \cdot 10^{-1}\,^{+2.5}_{-2.6}$	$7.44 \cdot 10^{-2}\,^{+6.3}_{-6.2}$	$2.58 \cdot 10^{-4}\,^{+6.6}_{-6.5}$	$3.47 \cdot 10^{-2}\,^{+12.2}_{-12.2}$
117	$6.83 \cdot 10^{-1}\,^{+2.5}_{-2.6}$	$7.39 \cdot 10^{-2}\,^{+6.3}_{-6.2}$	$2.56 \cdot 10^{-4}\,^{+6.6}_{-6.5}$	$3.45 \cdot 10^{-2}\,^{+12.2}_{-12.2}$
117.5	$6.77 \cdot 10^{-1}\,^{+2.6}_{-2.6}$	$7.33 \cdot 10^{-2}\,^{+6.3}_{-6.2}$	$2.54 \cdot 10^{-4}\,^{+6.6}_{-6.5}$	$3.42 \cdot 10^{-2}\,^{+12.2}_{-12.2}$
118	$6.72 \cdot 10^{-1}\,^{+2.6}_{-2.7}$	$7.28 \cdot 10^{-2}\,^{+6.2}_{-6.1}$	$2.53 \cdot 10^{-4}\,^{+6.6}_{-6.4}$	$3.39 \cdot 10^{-2}\,^{+12.2}_{-12.2}$

Table A.2: SM Higgs branching ratios to two fermions and their total uncertainties (expressed in percentage). Very-low mass range.

M_H [GeV]	H → bb	H → $\tau^+\tau^-$	H → $\mu^+\mu^-$	H → c$\bar{\text{c}}$
118.5	$6.66\cdot10^{-1}{}^{+2.6}_{-2.7}$	$7.22\cdot10^{-2}{}^{+6.2}_{-6.1}$	$2.51\cdot10^{-4}{}^{+6.5}_{-6.4}$	$3.36\cdot10^{-2}{}^{+12.3}_{-12.2}$
119	$6.60\cdot10^{-1}{}^{+2.7}_{-2.7}$	$7.16\cdot10^{-2}{}^{+6.2}_{-6.1}$	$2.49\cdot10^{-4}{}^{+6.4}_{-6.4}$	$3.33\cdot10^{-2}{}^{+12.2}_{-12.2}$
119.5	$6.54\cdot10^{-1}{}^{+2.7}_{-2.8}$	$7.10\cdot10^{-2}{}^{+6.1}_{-6.1}$	$2.47\cdot10^{-4}{}^{+6.4}_{-6.4}$	$3.30\cdot10^{-2}{}^{+12.2}_{-12.2}$
120	$6.48\cdot10^{-1}{}^{+2.8}_{-2.8}$	$7.04\cdot10^{-2}{}^{+6.1}_{-6.0}$	$2.44\cdot10^{-4}{}^{+6.4}_{-6.3}$	$3.27\cdot10^{-2}{}^{+12.3}_{-12.2}$
120.1	$6.46\cdot10^{-1}{}^{+2.8}_{-2.8}$	$7.03\cdot10^{-2}{}^{+6.1}_{-6.0}$	$2.44\cdot10^{-4}{}^{+6.4}_{-6.3}$	$3.26\cdot10^{-2}{}^{+12.2}_{-12.2}$
120.2	$6.45\cdot10^{-1}{}^{+2.8}_{-2.8}$	$7.01\cdot10^{-2}{}^{+6.1}_{-6.0}$	$2.43\cdot10^{-4}{}^{+6.3}_{-6.3}$	$3.26\cdot10^{-2}{}^{+12.2}_{-12.2}$
120.3	$6.44\cdot10^{-1}{}^{+2.8}_{-2.8}$	$7.00\cdot10^{-2}{}^{+6.1}_{-6.0}$	$2.43\cdot10^{-4}{}^{+6.4}_{-6.3}$	$3.25\cdot10^{-2}{}^{+12.2}_{-12.2}$
120.4	$6.42\cdot10^{-1}{}^{+2.8}_{-2.9}$	$6.99\cdot10^{-2}{}^{+6.1}_{-6.0}$	$2.43\cdot10^{-4}{}^{+6.4}_{-6.3}$	$3.24\cdot10^{-2}{}^{+12.2}_{-12.2}$
120.5	$6.41\cdot10^{-1}{}^{+2.8}_{-2.9}$	$6.98\cdot10^{-2}{}^{+6.1}_{-6.0}$	$2.42\cdot10^{-4}{}^{+6.4}_{-6.2}$	$3.24\cdot10^{-2}{}^{+12.2}_{-12.2}$
120.6	$6.40\cdot10^{-1}{}^{+2.8}_{-2.9}$	$6.96\cdot10^{-2}{}^{+6.1}_{-6.0}$	$2.42\cdot10^{-4}{}^{+6.3}_{-6.3}$	$3.23\cdot10^{-2}{}^{+12.2}_{-12.2}$
120.7	$6.39\cdot10^{-1}{}^{+2.8}_{-2.9}$	$6.95\cdot10^{-2}{}^{+6.1}_{-6.0}$	$2.41\cdot10^{-4}{}^{+6.4}_{-6.2}$	$3.22\cdot10^{-2}{}^{+12.2}_{-12.2}$
120.8	$6.37\cdot10^{-1}{}^{+2.8}_{-2.9}$	$6.94\cdot10^{-2}{}^{+6.1}_{-6.0}$	$2.41\cdot10^{-4}{}^{+6.3}_{-6.3}$	$3.22\cdot10^{-2}{}^{+12.2}_{-12.2}$
120.9	$6.36\cdot10^{-1}{}^{+2.8}_{-2.9}$	$6.92\cdot10^{-2}{}^{+6.1}_{-6.0}$	$2.40\cdot10^{-4}{}^{+6.3}_{-6.2}$	$3.21\cdot10^{-2}{}^{+12.2}_{-12.2}$
121	$6.35\cdot10^{-1}{}^{+2.8}_{-2.9}$	$6.91\cdot10^{-2}{}^{+6.0}_{-6.0}$	$2.40\cdot10^{-4}{}^{+6.3}_{-6.2}$	$3.20\cdot10^{-2}{}^{+12.2}_{-12.2}$
121.1	$6.33\cdot10^{-1}{}^{+2.9}_{-2.9}$	$6.90\cdot10^{-2}{}^{+6.0}_{-6.0}$	$2.39\cdot10^{-4}{}^{+6.3}_{-6.3}$	$3.20\cdot10^{-2}{}^{+12.2}_{-12.2}$
121.2	$6.32\cdot10^{-1}{}^{+2.9}_{-2.9}$	$6.88\cdot10^{-2}{}^{+6.0}_{-5.9}$	$2.39\cdot10^{-4}{}^{+6.3}_{-6.2}$	$3.19\cdot10^{-2}{}^{+12.2}_{-12.3}$
121.3	$6.31\cdot10^{-1}{}^{+2.9}_{-2.9}$	$6.87\cdot10^{-2}{}^{+6.0}_{-5.9}$	$2.38\cdot10^{-4}{}^{+6.3}_{-6.2}$	$3.18\cdot10^{-2}{}^{+12.2}_{-12.2}$
121.4	$6.29\cdot10^{-1}{}^{+2.9}_{-2.9}$	$6.86\cdot10^{-2}{}^{+6.0}_{-5.9}$	$2.38\cdot10^{-4}{}^{+6.3}_{-6.2}$	$3.18\cdot10^{-2}{}^{+12.2}_{-12.2}$
121.5	$6.28\cdot10^{-1}{}^{+2.9}_{-3.0}$	$6.84\cdot10^{-2}{}^{+6.0}_{-5.9}$	$2.37\cdot10^{-4}{}^{+6.2}_{-6.2}$	$3.17\cdot10^{-2}{}^{+12.2}_{-12.2}$
121.6	$6.27\cdot10^{-1}{}^{+2.9}_{-3.0}$	$6.83\cdot10^{-2}{}^{+6.0}_{-5.9}$	$2.37\cdot10^{-4}{}^{+6.2}_{-6.2}$	$3.16\cdot10^{-2}{}^{+12.2}_{-12.2}$
121.7	$6.25\cdot10^{-1}{}^{+2.9}_{-3.0}$	$6.81\cdot10^{-2}{}^{+6.0}_{-5.9}$	$2.36\cdot10^{-4}{}^{+6.2}_{-6.2}$	$3.16\cdot10^{-2}{}^{+12.2}_{-12.2}$
121.8	$6.24\cdot10^{-1}{}^{+2.9}_{-3.0}$	$6.80\cdot10^{-2}{}^{+6.0}_{-5.9}$	$2.36\cdot10^{-4}{}^{+6.3}_{-6.1}$	$3.15\cdot10^{-2}{}^{+12.2}_{-12.2}$
121.9	$6.22\cdot10^{-1}{}^{+2.9}_{-3.0}$	$6.79\cdot10^{-2}{}^{+6.0}_{-5.9}$	$2.35\cdot10^{-4}{}^{+6.3}_{-6.1}$	$3.14\cdot10^{-2}{}^{+12.2}_{-12.2}$
122	$6.21\cdot10^{-1}{}^{+2.9}_{-3.0}$	$6.77\cdot10^{-2}{}^{+6.0}_{-5.9}$	$2.35\cdot10^{-4}{}^{+6.3}_{-6.2}$	$3.13\cdot10^{-2}{}^{+12.2}_{-12.2}$
122.1	$6.20\cdot10^{-1}{}^{+2.9}_{-3.0}$	$6.76\cdot10^{-2}{}^{+6.0}_{-5.9}$	$2.34\cdot10^{-4}{}^{+6.3}_{-6.1}$	$3.13\cdot10^{-2}{}^{+12.2}_{-12.2}$
122.2	$6.18\cdot10^{-1}{}^{+2.9}_{-3.0}$	$6.74\cdot10^{-2}{}^{+6.0}_{-5.9}$	$2.34\cdot10^{-4}{}^{+6.3}_{-6.1}$	$3.12\cdot10^{-2}{}^{+12.2}_{-12.2}$
122.3	$6.17\cdot10^{-1}{}^{+2.9}_{-3.0}$	$6.73\cdot10^{-2}{}^{+6.0}_{-5.9}$	$2.33\cdot10^{-4}{}^{+6.3}_{-6.1}$	$3.11\cdot10^{-2}{}^{+12.2}_{-12.2}$
122.4	$6.15\cdot10^{-1}{}^{+3.0}_{-3.0}$	$6.72\cdot10^{-2}{}^{+5.9}_{-5.9}$	$2.33\cdot10^{-4}{}^{+6.2}_{-6.1}$	$3.11\cdot10^{-2}{}^{+12.2}_{-12.2}$
122.5	$6.14\cdot10^{-1}{}^{+3.0}_{-3.0}$	$6.70\cdot10^{-2}{}^{+5.9}_{-5.9}$	$2.32\cdot10^{-4}{}^{+6.2}_{-6.1}$	$3.10\cdot10^{-2}{}^{+12.2}_{-12.2}$
122.6	$6.13\cdot10^{-1}{}^{+3.0}_{-3.0}$	$6.69\cdot10^{-2}{}^{+5.9}_{-5.8}$	$2.32\cdot10^{-4}{}^{+6.2}_{-6.1}$	$3.09\cdot10^{-2}{}^{+12.2}_{-12.2}$
122.7	$6.11\cdot10^{-1}{}^{+3.0}_{-3.1}$	$6.67\cdot10^{-2}{}^{+5.9}_{-5.8}$	$2.31\cdot10^{-4}{}^{+6.2}_{-6.1}$	$3.08\cdot10^{-2}{}^{+12.2}_{-12.2}$
122.8	$6.10\cdot10^{-1}{}^{+3.0}_{-3.1}$	$6.66\cdot10^{-2}{}^{+5.9}_{-5.8}$	$2.31\cdot10^{-4}{}^{+6.2}_{-6.1}$	$3.08\cdot10^{-2}{}^{+12.2}_{-12.2}$
122.9	$6.08\cdot10^{-1}{}^{+3.0}_{-3.1}$	$6.64\cdot10^{-2}{}^{+5.9}_{-5.8}$	$2.30\cdot10^{-4}{}^{+6.2}_{-6.1}$	$3.07\cdot10^{-2}{}^{+12.2}_{-12.2}$
123	$6.07\cdot10^{-1}{}^{+3.0}_{-3.1}$	$6.63\cdot10^{-2}{}^{+5.9}_{-5.8}$	$2.30\cdot10^{-4}{}^{+6.1}_{-6.1}$	$3.06\cdot10^{-2}{}^{+12.2}_{-12.2}$
123.1	$6.05\cdot10^{-1}{}^{+3.0}_{-3.1}$	$6.61\cdot10^{-2}{}^{+5.9}_{-5.8}$	$2.29\cdot10^{-4}{}^{+6.1}_{-6.1}$	$3.06\cdot10^{-2}{}^{+12.2}_{-12.2}$
123.2	$6.04\cdot10^{-1}{}^{+3.0}_{-3.1}$	$6.60\cdot10^{-2}{}^{+5.9}_{-5.8}$	$2.29\cdot10^{-4}{}^{+6.1}_{-6.1}$	$3.05\cdot10^{-2}{}^{+12.2}_{-12.2}$
123.3	$6.02\cdot10^{-1}{}^{+3.0}_{-3.1}$	$6.58\cdot10^{-2}{}^{+5.9}_{-5.8}$	$2.28\cdot10^{-4}{}^{+6.2}_{-6.0}$	$3.04\cdot10^{-2}{}^{+12.2}_{-12.2}$
123.4	$6.01\cdot10^{-1}{}^{+3.1}_{-3.1}$	$6.57\cdot10^{-2}{}^{+5.9}_{-5.8}$	$2.28\cdot10^{-4}{}^{+6.1}_{-6.0}$	$3.03\cdot10^{-2}{}^{+12.2}_{-12.2}$
123.5	$6.00\cdot10^{-1}{}^{+3.1}_{-3.1}$	$6.55\cdot10^{-2}{}^{+5.9}_{-5.8}$	$2.27\cdot10^{-4}{}^{+6.1}_{-6.0}$	$3.03\cdot10^{-2}{}^{+12.2}_{-12.2}$
123.6	$5.98\cdot10^{-1}{}^{+3.1}_{-3.1}$	$6.54\cdot10^{-2}{}^{+5.8}_{-5.8}$	$2.27\cdot10^{-4}{}^{+6.1}_{-6.0}$	$3.02\cdot10^{-2}{}^{+12.2}_{-12.2}$
123.7	$5.97\cdot10^{-1}{}^{+3.1}_{-3.1}$	$6.52\cdot10^{-2}{}^{+5.8}_{-5.8}$	$2.26\cdot10^{-4}{}^{+6.1}_{-6.0}$	$3.01\cdot10^{-2}{}^{+12.2}_{-12.2}$
123.8	$5.95\cdot10^{-1}{}^{+3.1}_{-3.2}$	$6.51\cdot10^{-2}{}^{+5.8}_{-5.7}$	$2.26\cdot10^{-4}{}^{+6.1}_{-6.0}$	$3.00\cdot10^{-2}{}^{+12.2}_{-12.2}$
123.9	$5.94\cdot10^{-1}{}^{+3.1}_{-3.2}$	$6.49\cdot10^{-2}{}^{+5.8}_{-5.7}$	$2.25\cdot10^{-4}{}^{+6.1}_{-6.0}$	$3.00\cdot10^{-2}{}^{+12.2}_{-12.2}$
124	$5.92\cdot10^{-1}{}^{+3.1}_{-3.2}$	$6.48\cdot10^{-2}{}^{+5.8}_{-5.7}$	$2.25\cdot10^{-4}{}^{+6.1}_{-6.0}$	$2.99\cdot10^{-2}{}^{+12.2}_{-12.2}$
124.1	$5.91\cdot10^{-1}{}^{+3.1}_{-3.2}$	$6.46\cdot10^{-2}{}^{+5.8}_{-5.7}$	$2.24\cdot10^{-4}{}^{+6.0}_{-6.0}$	$2.98\cdot10^{-2}{}^{+12.2}_{-12.2}$
124.2	$5.89\cdot10^{-1}{}^{+3.1}_{-3.2}$	$6.45\cdot10^{-2}{}^{+5.8}_{-5.7}$	$2.24\cdot10^{-4}{}^{+6.1}_{-6.0}$	$2.97\cdot10^{-2}{}^{+12.2}_{-12.2}$
124.3	$5.88\cdot10^{-1}{}^{+3.1}_{-3.2}$	$6.43\cdot10^{-2}{}^{+5.8}_{-5.7}$	$2.23\cdot10^{-4}{}^{+6.1}_{-6.0}$	$2.96\cdot10^{-2}{}^{+12.2}_{-12.2}$

Table A.3: SM Higgs branching ratios to two fermions and their total uncertainties (expressed in percentage). Low mass range.

M_H [GeV]	$H \to bb$	$H \to \tau^+\tau^-$	$H \to \mu^+\mu^-$	$H \to c\bar{c}$
124.4	$5.86 \cdot 10^{-1}{}^{+3.1}_{-3.2}$	$6.41 \cdot 10^{-2}{}^{+5.8}_{-5.7}$	$2.23 \cdot 10^{-4}{}^{+6.0}_{-6.0}$	$2.96 \cdot 10^{-2}{}^{+12.2}_{-12.2}$
124.5	$5.84 \cdot 10^{-1}{}^{+3.2}_{-3.2}$	$6.40 \cdot 10^{-2}{}^{+5.8}_{-5.7}$	$2.22 \cdot 10^{-4}{}^{+6.0}_{-5.9}$	$2.95 \cdot 10^{-2}{}^{+12.2}_{-12.2}$
124.6	$5.83 \cdot 10^{-1}{}^{+3.2}_{-3.2}$	$6.38 \cdot 10^{-2}{}^{+5.8}_{-5.7}$	$2.22 \cdot 10^{-4}{}^{+6.0}_{-6.0}$	$2.94 \cdot 10^{-2}{}^{+12.2}_{-12.2}$
124.7	$5.81 \cdot 10^{-1}{}^{+3.2}_{-3.2}$	$6.37 \cdot 10^{-2}{}^{+5.7}_{-5.7}$	$2.21 \cdot 10^{-4}{}^{+6.0}_{-5.9}$	$2.93 \cdot 10^{-2}{}^{+12.2}_{-12.2}$
124.8	$5.80 \cdot 10^{-1}{}^{+3.2}_{-3.3}$	$6.35 \cdot 10^{-2}{}^{+5.7}_{-5.7}$	$2.20 \cdot 10^{-4}{}^{+6.0}_{-6.0}$	$2.93 \cdot 10^{-2}{}^{+12.2}_{-12.2}$
124.9	$5.78 \cdot 10^{-1}{}^{+3.2}_{-3.3}$	$6.33 \cdot 10^{-2}{}^{+5.7}_{-5.7}$	$2.20 \cdot 10^{-4}{}^{+6.0}_{-5.9}$	$2.92 \cdot 10^{-2}{}^{+12.2}_{-12.2}$
125	$5.77 \cdot 10^{-1}{}^{+3.2}_{-3.3}$	$6.32 \cdot 10^{-2}{}^{+5.7}_{-5.7}$	$2.19 \cdot 10^{-4}{}^{+6.0}_{-5.9}$	$2.91 \cdot 10^{-2}{}^{+12.2}_{-12.2}$
125.1	$5.75 \cdot 10^{-1}{}^{+3.2}_{-3.3}$	$6.30 \cdot 10^{-2}{}^{+5.7}_{-5.6}$	$2.19 \cdot 10^{-4}{}^{+5.9}_{-5.9}$	$2.90 \cdot 10^{-2}{}^{+12.2}_{-12.2}$
125.2	$5.74 \cdot 10^{-1}{}^{+3.2}_{-3.3}$	$6.29 \cdot 10^{-2}{}^{+5.7}_{-5.6}$	$2.18 \cdot 10^{-4}{}^{+6.0}_{-5.9}$	$2.89 \cdot 10^{-2}{}^{+12.2}_{-12.2}$
125.3	$5.72 \cdot 10^{-1}{}^{+3.2}_{-3.3}$	$6.27 \cdot 10^{-2}{}^{+5.7}_{-5.6}$	$2.18 \cdot 10^{-4}{}^{+5.9}_{-5.9}$	$2.89 \cdot 10^{-2}{}^{+12.2}_{-12.2}$
125.4	$5.71 \cdot 10^{-1}{}^{+3.2}_{-3.3}$	$6.25 \cdot 10^{-2}{}^{+5.7}_{-5.6}$	$2.17 \cdot 10^{-4}{}^{+6.0}_{-5.9}$	$2.88 \cdot 10^{-2}{}^{+12.2}_{-12.2}$
125.5	$5.69 \cdot 10^{-1}{}^{+3.3}_{-3.3}$	$6.24 \cdot 10^{-2}{}^{+5.7}_{-5.6}$	$2.16 \cdot 10^{-4}{}^{+6.0}_{-5.8}$	$2.87 \cdot 10^{-2}{}^{+12.2}_{-12.2}$
125.6	$5.67 \cdot 10^{-1}{}^{+3.3}_{-3.3}$	$6.22 \cdot 10^{-2}{}^{+5.7}_{-5.6}$	$2.16 \cdot 10^{-4}{}^{+5.9}_{-5.9}$	$2.86 \cdot 10^{-2}{}^{+12.2}_{-12.2}$
125.7	$5.66 \cdot 10^{-1}{}^{+3.3}_{-3.3}$	$6.21 \cdot 10^{-2}{}^{+5.6}_{-5.6}$	$2.15 \cdot 10^{-4}{}^{+5.9}_{-5.8}$	$2.85 \cdot 10^{-2}{}^{+12.2}_{-12.2}$
125.8	$5.64 \cdot 10^{-1}{}^{+3.3}_{-3.3}$	$6.19 \cdot 10^{-2}{}^{+5.7}_{-5.6}$	$2.15 \cdot 10^{-4}{}^{+5.9}_{-5.8}$	$2.85 \cdot 10^{-2}{}^{+12.2}_{-12.2}$
125.9	$5.63 \cdot 10^{-1}{}^{+3.3}_{-3.4}$	$6.17 \cdot 10^{-2}{}^{+5.7}_{-5.6}$	$2.14 \cdot 10^{-4}{}^{+5.9}_{-5.8}$	$2.84 \cdot 10^{-2}{}^{+12.2}_{-12.2}$
126	$5.61 \cdot 10^{-1}{}^{+3.3}_{-3.4}$	$6.16 \cdot 10^{-2}{}^{+5.6}_{-5.6}$	$2.14 \cdot 10^{-4}{}^{+5.9}_{-5.8}$	$2.83 \cdot 10^{-2}{}^{+12.2}_{-12.2}$
126.1	$5.59 \cdot 10^{-1}{}^{+3.3}_{-3.4}$	$6.14 \cdot 10^{-2}{}^{+5.6}_{-5.6}$	$2.13 \cdot 10^{-4}{}^{+5.9}_{-5.9}$	$2.82 \cdot 10^{-2}{}^{+12.2}_{-12.2}$
126.2	$5.58 \cdot 10^{-1}{}^{+3.3}_{-3.4}$	$6.12 \cdot 10^{-2}{}^{+5.6}_{-5.5}$	$2.12 \cdot 10^{-4}{}^{+5.9}_{-5.8}$	$2.81 \cdot 10^{-2}{}^{+12.2}_{-12.2}$
126.3	$5.56 \cdot 10^{-1}{}^{+3.3}_{-3.4}$	$6.10 \cdot 10^{-2}{}^{+5.6}_{-5.6}$	$2.12 \cdot 10^{-4}{}^{+5.9}_{-5.8}$	$2.81 \cdot 10^{-2}{}^{+12.2}_{-12.2}$
126.4	$5.55 \cdot 10^{-1}{}^{+3.3}_{-3.4}$	$6.09 \cdot 10^{-2}{}^{+5.6}_{-5.5}$	$2.11 \cdot 10^{-4}{}^{+5.9}_{-5.8}$	$2.80 \cdot 10^{-2}{}^{+12.2}_{-12.2}$
126.5	$5.53 \cdot 10^{-1}{}^{+3.3}_{-3.4}$	$6.07 \cdot 10^{-2}{}^{+5.6}_{-5.5}$	$2.11 \cdot 10^{-4}{}^{+5.9}_{-5.7}$	$2.79 \cdot 10^{-2}{}^{+12.2}_{-12.2}$
126.6	$5.51 \cdot 10^{-1}{}^{+3.4}_{-3.4}$	$6.05 \cdot 10^{-2}{}^{+5.6}_{-5.5}$	$2.10 \cdot 10^{-4}{}^{+5.8}_{-5.7}$	$2.78 \cdot 10^{-2}{}^{+12.2}_{-12.2}$
126.7	$5.50 \cdot 10^{-1}{}^{+3.4}_{-3.4}$	$6.04 \cdot 10^{-2}{}^{+5.6}_{-5.5}$	$2.10 \cdot 10^{-4}{}^{+5.8}_{-5.8}$	$2.77 \cdot 10^{-2}{}^{+12.2}_{-12.2}$
126.8	$5.48 \cdot 10^{-1}{}^{+3.4}_{-3.5}$	$6.02 \cdot 10^{-2}{}^{+5.6}_{-5.5}$	$2.09 \cdot 10^{-4}{}^{+5.8}_{-5.8}$	$2.76 \cdot 10^{-2}{}^{+12.2}_{-12.2}$
126.9	$5.46 \cdot 10^{-1}{}^{+3.4}_{-3.5}$	$6.00 \cdot 10^{-2}{}^{+5.5}_{-5.5}$	$2.08 \cdot 10^{-4}{}^{+5.8}_{-5.8}$	$2.76 \cdot 10^{-2}{}^{+12.2}_{-12.2}$
127	$5.45 \cdot 10^{-1}{}^{+3.4}_{-3.5}$	$5.98 \cdot 10^{-2}{}^{+5.6}_{-5.5}$	$2.08 \cdot 10^{-4}{}^{+5.8}_{-5.7}$	$2.75 \cdot 10^{-2}{}^{+12.2}_{-12.2}$
127.1	$5.43 \cdot 10^{-1}{}^{+3.4}_{-3.5}$	$5.97 \cdot 10^{-2}{}^{+5.5}_{-5.5}$	$2.07 \cdot 10^{-4}{}^{+5.8}_{-5.8}$	$2.74 \cdot 10^{-2}{}^{+12.2}_{-12.2}$
127.2	$5.41 \cdot 10^{-1}{}^{+3.4}_{-3.5}$	$5.95 \cdot 10^{-2}{}^{+5.5}_{-5.5}$	$2.07 \cdot 10^{-4}{}^{+5.7}_{-5.7}$	$2.73 \cdot 10^{-2}{}^{+12.2}_{-12.2}$
127.3	$5.40 \cdot 10^{-1}{}^{+3.4}_{-3.5}$	$5.93 \cdot 10^{-2}{}^{+5.5}_{-5.5}$	$2.06 \cdot 10^{-4}{}^{+5.7}_{-5.7}$	$2.72 \cdot 10^{-2}{}^{+12.1}_{-12.2}$
127.4	$5.38 \cdot 10^{-1}{}^{+3.4}_{-3.5}$	$5.92 \cdot 10^{-2}{}^{+5.5}_{-5.4}$	$2.05 \cdot 10^{-4}{}^{+5.7}_{-5.7}$	$2.71 \cdot 10^{-2}{}^{+12.2}_{-12.1}$
127.5	$5.36 \cdot 10^{-1}{}^{+3.4}_{-3.5}$	$5.90 \cdot 10^{-2}{}^{+5.5}_{-5.5}$	$2.05 \cdot 10^{-4}{}^{+5.7}_{-5.7}$	$2.71 \cdot 10^{-2}{}^{+12.2}_{-12.2}$
127.6	$5.35 \cdot 10^{-1}{}^{+3.5}_{-3.5}$	$5.88 \cdot 10^{-2}{}^{+5.5}_{-5.4}$	$2.04 \cdot 10^{-4}{}^{+5.7}_{-5.7}$	$2.70 \cdot 10^{-2}{}^{+12.2}_{-12.2}$
127.7	$5.33 \cdot 10^{-1}{}^{+3.5}_{-3.5}$	$5.86 \cdot 10^{-2}{}^{+5.5}_{-5.4}$	$2.03 \cdot 10^{-4}{}^{+5.7}_{-5.7}$	$2.69 \cdot 10^{-2}{}^{+12.2}_{-12.2}$
127.8	$5.31 \cdot 10^{-1}{}^{+3.5}_{-3.6}$	$5.85 \cdot 10^{-2}{}^{+5.5}_{-5.4}$	$2.03 \cdot 10^{-4}{}^{+5.8}_{-5.7}$	$2.68 \cdot 10^{-2}{}^{+12.2}_{-12.2}$
127.9	$5.30 \cdot 10^{-1}{}^{+3.5}_{-3.6}$	$5.83 \cdot 10^{-2}{}^{+5.5}_{-5.4}$	$2.02 \cdot 10^{-4}{}^{+5.7}_{-5.6}$	$2.67 \cdot 10^{-2}{}^{+12.2}_{-12.2}$
128	$5.28 \cdot 10^{-1}{}^{+3.5}_{-3.6}$	$5.81 \cdot 10^{-2}{}^{+5.4}_{-5.4}$	$2.02 \cdot 10^{-4}{}^{+5.7}_{-5.6}$	$2.66 \cdot 10^{-2}{}^{+12.2}_{-12.2}$
128.1	$5.26 \cdot 10^{-1}{}^{+3.5}_{-3.6}$	$5.79 \cdot 10^{-2}{}^{+5.4}_{-5.4}$	$2.01 \cdot 10^{-4}{}^{+5.7}_{-5.6}$	$2.66 \cdot 10^{-2}{}^{+12.1}_{-12.2}$
128.2	$5.25 \cdot 10^{-1}{}^{+3.5}_{-3.6}$	$5.77 \cdot 10^{-2}{}^{+5.4}_{-5.4}$	$2.00 \cdot 10^{-4}{}^{+5.6}_{-5.6}$	$2.65 \cdot 10^{-2}{}^{+12.2}_{-12.2}$
128.3	$5.23 \cdot 10^{-1}{}^{+3.5}_{-3.6}$	$5.76 \cdot 10^{-2}{}^{+5.4}_{-5.4}$	$2.00 \cdot 10^{-4}{}^{+5.6}_{-5.6}$	$2.64 \cdot 10^{-2}{}^{+12.1}_{-12.2}$
128.4	$5.21 \cdot 10^{-1}{}^{+3.6}_{-3.6}$	$5.74 \cdot 10^{-2}{}^{+5.4}_{-5.4}$	$1.99 \cdot 10^{-4}{}^{+5.7}_{-5.6}$	$2.63 \cdot 10^{-2}{}^{+12.2}_{-12.2}$
128.5	$5.20 \cdot 10^{-1}{}^{+3.6}_{-3.6}$	$5.72 \cdot 10^{-2}{}^{+5.4}_{-5.4}$	$1.99 \cdot 10^{-4}{}^{+5.6}_{-5.6}$	$2.62 \cdot 10^{-2}{}^{+12.1}_{-12.2}$
128.6	$5.18 \cdot 10^{-1}{}^{+3.6}_{-3.6}$	$5.70 \cdot 10^{-2}{}^{+5.4}_{-5.4}$	$1.98 \cdot 10^{-4}{}^{+5.6}_{-5.6}$	$2.61 \cdot 10^{-2}{}^{+12.2}_{-12.2}$
128.7	$5.16 \cdot 10^{-1}{}^{+3.6}_{-3.6}$	$5.69 \cdot 10^{-2}{}^{+5.4}_{-5.3}$	$1.97 \cdot 10^{-4}{}^{+5.6}_{-5.6}$	$2.60 \cdot 10^{-2}{}^{+12.2}_{-12.1}$
128.8	$5.14 \cdot 10^{-1}{}^{+3.6}_{-3.7}$	$5.67 \cdot 10^{-2}{}^{+5.4}_{-5.3}$	$1.97 \cdot 10^{-4}{}^{+5.6}_{-5.5}$	$2.60 \cdot 10^{-2}{}^{+12.2}_{-12.2}$
128.9	$5.13 \cdot 10^{-1}{}^{+3.6}_{-3.7}$	$5.65 \cdot 10^{-2}{}^{+5.4}_{-5.3}$	$1.96 \cdot 10^{-4}{}^{+5.6}_{-5.5}$	$2.59 \cdot 10^{-2}{}^{+12.2}_{-12.2}$
129	$5.11 \cdot 10^{-1}{}^{+3.6}_{-3.7}$	$5.63 \cdot 10^{-2}{}^{+5.4}_{-5.3}$	$1.95 \cdot 10^{-4}{}^{+5.6}_{-5.5}$	$2.58 \cdot 10^{-2}{}^{+12.2}_{-12.1}$

M_{H} [GeV]	$H \to bb$	$H \to \tau^+\tau^-$	$H \to \mu^+\mu^-$	$H \to c\bar{c}$
129.1	$5.09\cdot10^{-1}{}^{+3.6}_{-3.7}$	$5.61\cdot10^{-2}{}^{+5.3}_{-5.3}$	$1.95\cdot10^{-4}{}^{+5.5}_{-5.5}$	$2.57\cdot10^{-2}{}^{+12.2}_{-12.2}$
129.2	$5.08\cdot10^{-1}{}^{+3.6}_{-3.7}$	$5.60\cdot10^{-2}{}^{+5.3}_{-5.3}$	$1.94\cdot10^{-4}{}^{+5.6}_{-5.5}$	$2.56\cdot10^{-2}{}^{+12.2}_{-12.2}$
129.3	$5.06\cdot10^{-1}{}^{+3.6}_{-3.7}$	$5.58\cdot10^{-2}{}^{+5.3}_{-5.3}$	$1.94\cdot10^{-4}{}^{+5.5}_{-5.5}$	$2.55\cdot10^{-2}{}^{+12.2}_{-12.2}$
129.4	$5.04\cdot10^{-1}{}^{+3.7}_{-3.7}$	$5.56\cdot10^{-2}{}^{+5.3}_{-5.3}$	$1.93\cdot10^{-4}{}^{+5.5}_{-5.5}$	$2.54\cdot10^{-2}{}^{+12.2}_{-12.2}$
129.5	$5.02\cdot10^{-1}{}^{+3.7}_{-3.7}$	$5.54\cdot10^{-2}{}^{+5.3}_{-5.3}$	$1.92\cdot10^{-4}{}^{+5.6}_{-5.4}$	$2.53\cdot10^{-2}{}^{+12.2}_{-12.2}$
129.6	$5.01\cdot10^{-1}{}^{+3.7}_{-3.7}$	$5.52\cdot10^{-2}{}^{+5.3}_{-5.3}$	$1.92\cdot10^{-4}{}^{+5.5}_{-5.5}$	$2.53\cdot10^{-2}{}^{+12.2}_{-12.2}$
129.7	$4.99\cdot10^{-1}{}^{+3.7}_{-3.8}$	$5.50\cdot10^{-2}{}^{+5.3}_{-5.2}$	$1.91\cdot10^{-4}{}^{+5.5}_{-5.5}$	$2.52\cdot10^{-2}{}^{+12.2}_{-12.2}$
129.8	$4.97\cdot10^{-1}{}^{+3.7}_{-3.8}$	$5.49\cdot10^{-2}{}^{+5.3}_{-5.3}$	$1.90\cdot10^{-4}{}^{+5.5}_{-5.5}$	$2.51\cdot10^{-2}{}^{+12.2}_{-12.1}$
129.9	$4.95\cdot10^{-1}{}^{+3.7}_{-3.8}$	$5.47\cdot10^{-2}{}^{+5.3}_{-5.2}$	$1.90\cdot10^{-4}{}^{+5.5}_{-5.5}$	$2.50\cdot10^{-2}{}^{+12.2}_{-12.1}$
130	$4.94\cdot10^{-1}{}^{+3.7}_{-3.8}$	$5.45\cdot10^{-2}{}^{+5.3}_{-5.2}$	$1.89\cdot10^{-4}{}^{+5.5}_{-5.4}$	$2.49\cdot10^{-2}{}^{+12.2}_{-12.1}$
130.5	$4.85\cdot10^{-1}{}^{+3.8}_{-3.8}$	$5.36\cdot10^{-2}{}^{+5.2}_{-5.2}$	$1.86\cdot10^{-4}{}^{+5.5}_{-5.4}$	$2.45\cdot10^{-2}{}^{+12.1}_{-12.2}$
131	$4.76\cdot10^{-1}{}^{+3.8}_{-3.9}$	$5.26\cdot10^{-2}{}^{+5.2}_{-5.1}$	$1.83\cdot10^{-4}{}^{+5.3}_{-5.4}$	$2.40\cdot10^{-2}{}^{+12.1}_{-12.1}$
131.5	$4.67\cdot10^{-1}{}^{+3.9}_{-3.9}$	$5.17\cdot10^{-2}{}^{+5.1}_{-5.1}$	$1.79\cdot10^{-4}{}^{+5.3}_{-5.3}$	$2.36\cdot10^{-2}{}^{+12.2}_{-12.1}$
132	$4.58\cdot10^{-1}{}^{+3.9}_{-4.0}$	$5.07\cdot10^{-2}{}^{+5.1}_{-5.0}$	$1.76\cdot10^{-4}{}^{+5.3}_{-5.2}$	$2.31\cdot10^{-2}{}^{+12.2}_{-12.1}$
132.5	$4.49\cdot10^{-1}{}^{+4.0}_{-4.0}$	$4.98\cdot10^{-2}{}^{+5.0}_{-5.0}$	$1.73\cdot10^{-4}{}^{+5.2}_{-5.2}$	$2.27\cdot10^{-2}{}^{+12.2}_{-12.1}$
133	$4.40\cdot10^{-1}{}^{+4.0}_{-4.1}$	$4.88\cdot10^{-2}{}^{+5.0}_{-5.0}$	$1.69\cdot10^{-4}{}^{+5.2}_{-5.1}$	$2.22\cdot10^{-2}{}^{+12.1}_{-12.2}$
133.5	$4.31\cdot10^{-1}{}^{+4.1}_{-4.1}$	$4.78\cdot10^{-2}{}^{+4.9}_{-4.9}$	$1.66\cdot10^{-4}{}^{+5.1}_{-5.1}$	$2.18\cdot10^{-2}{}^{+12.1}_{-12.1}$
134	$4.22\cdot10^{-1}{}^{+4.2}_{-4.2}$	$4.69\cdot10^{-2}{}^{+4.9}_{-4.8}$	$1.63\cdot10^{-4}{}^{+5.1}_{-5.0}$	$2.13\cdot10^{-2}{}^{+12.1}_{-12.1}$
134.5	$4.13\cdot10^{-1}{}^{+4.2}_{-4.3}$	$4.59\cdot10^{-2}{}^{+4.8}_{-4.8}$	$1.59\cdot10^{-4}{}^{+4.9}_{-5.0}$	$2.08\cdot10^{-2}{}^{+12.1}_{-12.1}$
135	$4.04\cdot10^{-1}{}^{+4.2}_{-4.3}$	$4.49\cdot10^{-2}{}^{+4.8}_{-4.7}$	$1.56\cdot10^{-4}{}^{+5.0}_{-4.9}$	$2.04\cdot10^{-2}{}^{+12.2}_{-12.1}$
135.5	$3.95\cdot10^{-1}{}^{+4.3}_{-4.4}$	$4.39\cdot10^{-2}{}^{+4.7}_{-4.7}$	$1.52\cdot10^{-4}{}^{+4.9}_{-4.9}$	$1.99\cdot10^{-2}{}^{+12.1}_{-12.1}$
136	$3.86\cdot10^{-1}{}^{+4.4}_{-4.4}$	$4.30\cdot10^{-2}{}^{+4.7}_{-4.6}$	$1.49\cdot10^{-4}{}^{+4.9}_{-4.8}$	$1.95\cdot10^{-2}{}^{+12.2}_{-12.1}$
136.5	$3.77\cdot10^{-1}{}^{+4.4}_{-4.5}$	$4.20\cdot10^{-2}{}^{+4.6}_{-4.6}$	$1.46\cdot10^{-4}{}^{+4.7}_{-4.8}$	$1.90\cdot10^{-2}{}^{+12.1}_{-12.1}$
137	$3.68\cdot10^{-1}{}^{+4.5}_{-4.5}$	$4.10\cdot10^{-2}{}^{+4.5}_{-4.5}$	$1.42\cdot10^{-4}{}^{+4.7}_{-4.8}$	$1.86\cdot10^{-2}{}^{+12.1}_{-12.1}$
137.5	$3.59\cdot10^{-1}{}^{+4.5}_{-4.6}$	$4.00\cdot10^{-2}{}^{+4.5}_{-4.5}$	$1.39\cdot10^{-4}{}^{+4.7}_{-4.7}$	$1.81\cdot10^{-2}{}^{+12.2}_{-12.1}$
138	$3.50\cdot10^{-1}{}^{+4.6}_{-4.6}$	$3.91\cdot10^{-2}{}^{+4.4}_{-4.4}$	$1.36\cdot10^{-4}{}^{+4.6}_{-4.6}$	$1.77\cdot10^{-2}{}^{+12.1}_{-12.0}$
138.5	$3.41\cdot10^{-1}{}^{+4.6}_{-4.7}$	$3.81\cdot10^{-2}{}^{+4.4}_{-4.4}$	$1.32\cdot10^{-4}{}^{+4.6}_{-4.5}$	$1.72\cdot10^{-2}{}^{+12.1}_{-12.1}$
139	$3.32\cdot10^{-1}{}^{+4.7}_{-4.7}$	$3.71\cdot10^{-2}{}^{+4.4}_{-4.4}$	$1.29\cdot10^{-4}{}^{+4.5}_{-4.6}$	$1.68\cdot10^{-2}{}^{+12.1}_{-12.1}$
139.5	$3.24\cdot10^{-1}{}^{+4.7}_{-4.8}$	$3.62\cdot10^{-2}{}^{+4.3}_{-4.3}$	$1.26\cdot10^{-4}{}^{+4.4}_{-4.5}$	$1.63\cdot10^{-2}{}^{+12.1}_{-12.1}$
140	$3.15\cdot10^{-1}{}^{+4.8}_{-4.8}$	$3.52\cdot10^{-2}{}^{+4.3}_{-4.3}$	$1.22\cdot10^{-4}{}^{+4.4}_{-4.5}$	$1.59\cdot10^{-2}{}^{+12.1}_{-12.1}$
140.5	$3.06\cdot10^{-1}{}^{+4.8}_{-4.9}$	$3.43\cdot10^{-2}{}^{+4.2}_{-4.2}$	$1.19\cdot10^{-4}{}^{+4.3}_{-4.4}$	$1.54\cdot10^{-2}{}^{+12.1}_{-12.0}$
141	$2.97\cdot10^{-1}{}^{+4.9}_{-4.9}$	$3.33\cdot10^{-2}{}^{+4.2}_{-4.1}$	$1.16\cdot10^{-4}{}^{+4.3}_{-4.3}$	$1.50\cdot10^{-2}{}^{+12.1}_{-12.1}$
141.5	$2.89\cdot10^{-1}{}^{+4.9}_{-5.0}$	$3.24\cdot10^{-2}{}^{+4.1}_{-4.1}$	$1.12\cdot10^{-4}{}^{+4.2}_{-4.2}$	$1.46\cdot10^{-2}{}^{+12.1}_{-12.0}$
142	$2.80\cdot10^{-1}{}^{+5.0}_{-5.0}$	$3.15\cdot10^{-2}{}^{+4.1}_{-4.1}$	$1.09\cdot10^{-4}{}^{+4.1}_{-4.2}$	$1.41\cdot10^{-2}{}^{+12.1}_{-12.0}$
142.5	$2.72\cdot10^{-1}{}^{+5.1}_{-5.1}$	$3.05\cdot10^{-2}{}^{+4.1}_{-4.0}$	$1.06\cdot10^{-4}{}^{+4.1}_{-4.2}$	$1.37\cdot10^{-2}{}^{+12.1}_{-12.1}$
143	$2.64\cdot10^{-1}{}^{+5.0}_{-5.1}$	$2.96\cdot10^{-2}{}^{+4.0}_{-4.0}$	$1.03\cdot10^{-4}{}^{+4.2}_{-4.1}$	$1.33\cdot10^{-2}{}^{+12.1}_{-12.0}$
143.5	$2.56\cdot10^{-1}{}^{+5.1}_{-5.2}$	$2.87\cdot10^{-2}{}^{+3.9}_{-3.9}$	$9.97\cdot10^{-5}{}^{+4.1}_{-4.1}$	$1.29\cdot10^{-2}{}^{+12.1}_{-12.1}$
144	$2.47\cdot10^{-1}{}^{+5.2}_{-5.2}$	$2.78\cdot10^{-2}{}^{+3.9}_{-3.9}$	$9.65\cdot10^{-5}{}^{+4.0}_{-4.0}$	$1.25\cdot10^{-2}{}^{+12.1}_{-12.0}$
144.5	$2.39\cdot10^{-1}{}^{+5.2}_{-5.3}$	$2.69\cdot10^{-2}{}^{+3.8}_{-3.8}$	$9.35\cdot10^{-5}{}^{+3.9}_{-4.0}$	$1.21\cdot10^{-2}{}^{+12.1}_{-12.1}$
145	$2.31\cdot10^{-1}{}^{+5.3}_{-5.3}$	$2.61\cdot10^{-2}{}^{+3.8}_{-3.8}$	$9.04\cdot10^{-5}{}^{+3.9}_{-3.9}$	$1.17\cdot10^{-2}{}^{+12.0}_{-12.1}$
145.5	$2.24\cdot10^{-1}{}^{+5.3}_{-5.4}$	$2.52\cdot10^{-2}{}^{+3.7}_{-3.8}$	$8.74\cdot10^{-5}{}^{+3.8}_{-3.9}$	$1.13\cdot10^{-2}{}^{+12.0}_{-12.0}$
146	$2.16\cdot10^{-1}{}^{+5.4}_{-5.4}$	$2.43\cdot10^{-2}{}^{+3.8}_{-3.7}$	$8.44\cdot10^{-5}{}^{+3.8}_{-3.9}$	$1.09\cdot10^{-2}{}^{+12.1}_{-12.0}$
146.5	$2.08\cdot10^{-1}{}^{+5.4}_{-5.4}$	$2.35\cdot10^{-2}{}^{+3.7}_{-3.6}$	$8.15\cdot10^{-5}{}^{+3.8}_{-3.7}$	$1.05\cdot10^{-2}{}^{+12.1}_{-12.0}$
147	$2.00\cdot10^{-1}{}^{+5.5}_{-5.4}$	$2.26\cdot10^{-2}{}^{+3.6}_{-3.6}$	$7.85\cdot10^{-5}{}^{+3.7}_{-3.7}$	$1.01\cdot10^{-2}{}^{+12.2}_{-12.0}$
147.5	$1.93\cdot10^{-1}{}^{+5.5}_{-5.5}$	$2.18\cdot10^{-2}{}^{+3.5}_{-3.6}$	$7.57\cdot10^{-5}{}^{+3.7}_{-3.7}$	$9.73\cdot10^{-3}{}^{+12.1}_{-12.0}$
148	$1.86\cdot10^{-1}{}^{+5.6}_{-5.5}$	$2.10\cdot10^{-2}{}^{+3.6}_{-3.5}$	$7.28\cdot10^{-5}{}^{+3.7}_{-3.6}$	$9.36\cdot10^{-3}{}^{+12.1}_{-12.0}$
148.5	$1.78\cdot10^{-1}{}^{+5.5}_{-5.6}$	$2.02\cdot10^{-2}{}^{+3.5}_{-3.5}$	$7.00\cdot10^{-5}{}^{+3.6}_{-3.6}$	$8.99\cdot10^{-3}{}^{+12.1}_{-12.0}$

Table A.5: SM Higgs branching ratios to two fermions and their total uncertainties (expressed in percentage). Intermediate mass range.

M_{H} [GeV]	$\mathrm{H} \to \mathrm{bb}$	$\mathrm{H} \to \tau^+\tau^-$	$\mathrm{H} \to \mu^+\mu^-$	$\mathrm{H} \to \mathrm{c\bar{c}}$
149	$1.71 \cdot 10^{-1}{}^{+5.6}_{-5.7}$	$1.94 \cdot 10^{-2}{}^{+3.4}_{-3.5}$	$6.72 \cdot 10^{-5}{}^{+3.5}_{-3.6}$	$8.63 \cdot 10^{-3}{}^{+12.0}_{-12.0}$
149.5	$1.64 \cdot 10^{-1}{}^{+5.7}_{-5.7}$	$1.86 \cdot 10^{-2}{}^{+3.4}_{-3.4}$	$6.45 \cdot 10^{-5}{}^{+3.5}_{-3.5}$	$8.27 \cdot 10^{-3}{}^{+12.1}_{-12.0}$
150	$1.57 \cdot 10^{-1}{}^{+5.7}_{-5.7}$	$1.78 \cdot 10^{-2}{}^{+3.4}_{-3.4}$	$6.18 \cdot 10^{-5}{}^{+3.5}_{-3.5}$	$7.92 \cdot 10^{-3}{}^{+12.0}_{-12.0}$
152	$1.30 \cdot 10^{-1}{}^{+5.8}_{-5.9}$	$1.48 \cdot 10^{-2}{}^{+3.3}_{-3.3}$	$5.13 \cdot 10^{-5}{}^{+3.3}_{-3.3}$	$6.56 \cdot 10^{-3}{}^{+12.1}_{-12.0}$
154	$1.05 \cdot 10^{-1}{}^{+6.0}_{-6.0}$	$1.19 \cdot 10^{-2}{}^{+3.1}_{-3.1}$	$4.13 \cdot 10^{-5}{}^{+3.1}_{-3.2}$	$5.27 \cdot 10^{-3}{}^{+12.0}_{-12.0}$
156	$8.01 \cdot 10^{-2}{}^{+6.1}_{-6.1}$	$9.15 \cdot 10^{-3}{}^{+3.0}_{-3.0}$	$3.17 \cdot 10^{-5}{}^{+3.0}_{-3.0}$	$4.04 \cdot 10^{-3}{}^{+12.0}_{-12.0}$
158	$5.66 \cdot 10^{-2}{}^{+6.3}_{-6.3}$	$6.47 \cdot 10^{-3}{}^{+2.8}_{-2.8}$	$2.24 \cdot 10^{-5}{}^{+2.9}_{-2.9}$	$2.85 \cdot 10^{-3}{}^{+12.0}_{-11.9}$
160	$3.45 \cdot 10^{-2}{}^{+6.4}_{-6.4}$	$3.96 \cdot 10^{-3}{}^{+2.7}_{-2.8}$	$1.37 \cdot 10^{-5}{}^{+2.8}_{-2.7}$	$1.74 \cdot 10^{-3}{}^{+12.0}_{-11.9}$
162	$1.97 \cdot 10^{-2}{}^{+6.5}_{-6.4}$	$2.27 \cdot 10^{-3}{}^{+2.8}_{-2.6}$	$7.87 \cdot 10^{-6}{}^{+2.7}_{-2.7}$	$9.95 \cdot 10^{-4}{}^{+12.0}_{-11.9}$
164	$1.36 \cdot 10^{-2}{}^{+6.5}_{-6.4}$	$1.57 \cdot 10^{-3}{}^{+2.6}_{-2.7}$	$5.43 \cdot 10^{-6}{}^{+2.7}_{-2.6}$	$6.85 \cdot 10^{-4}{}^{+12.0}_{-11.9}$
165	$1.19 \cdot 10^{-2}{}^{+6.5}_{-6.4}$	$1.38 \cdot 10^{-3}{}^{+2.7}_{-2.6}$	$4.78 \cdot 10^{-6}{}^{+2.6}_{-2.6}$	$6.02 \cdot 10^{-4}{}^{+12.0}_{-11.9}$
166	$1.07 \cdot 10^{-2}{}^{+6.6}_{-6.5}$	$1.24 \cdot 10^{-3}{}^{+2.7}_{-2.6}$	$4.30 \cdot 10^{-6}{}^{+2.6}_{-2.7}$	$5.41 \cdot 10^{-4}{}^{+12.0}_{-11.9}$
168	$9.06 \cdot 10^{-3}{}^{+6.5}_{-6.5}$	$1.05 \cdot 10^{-3}{}^{+2.6}_{-2.6}$	$3.63 \cdot 10^{-6}{}^{+2.6}_{-2.7}$	$4.56 \cdot 10^{-4}{}^{+12.0}_{-11.9}$
170	$7.93 \cdot 10^{-3}{}^{+6.5}_{-6.5}$	$9.20 \cdot 10^{-4}{}^{+2.6}_{-2.6}$	$3.19 \cdot 10^{-6}{}^{+2.6}_{-2.6}$	$4.00 \cdot 10^{-4}{}^{+12.0}_{-11.9}$
172	$7.10 \cdot 10^{-3}{}^{+6.5}_{-6.5}$	$8.25 \cdot 10^{-4}{}^{+2.6}_{-2.6}$	$2.86 \cdot 10^{-6}{}^{+2.6}_{-2.6}$	$3.58 \cdot 10^{-4}{}^{+12.0}_{-11.9}$
174	$6.45 \cdot 10^{-3}{}^{+6.5}_{-6.5}$	$7.51 \cdot 10^{-4}{}^{+2.6}_{-2.6}$	$2.60 \cdot 10^{-6}{}^{+2.6}_{-2.6}$	$3.25 \cdot 10^{-4}{}^{+12.0}_{-11.9}$
175	$6.17 \cdot 10^{-3}{}^{+6.6}_{-6.5}$	$7.19 \cdot 10^{-4}{}^{+2.6}_{-2.6}$	$2.49 \cdot 10^{-6}{}^{+2.6}_{-2.6}$	$3.11 \cdot 10^{-4}{}^{+12.0}_{-11.9}$
176	$5.91 \cdot 10^{-3}{}^{+6.5}_{-6.5}$	$6.89 \cdot 10^{-4}{}^{+2.6}_{-2.6}$	$2.39 \cdot 10^{-6}{}^{+2.6}_{-2.7}$	$2.98 \cdot 10^{-4}{}^{+12.0}_{-11.9}$
178	$5.44 \cdot 10^{-3}{}^{+6.6}_{-6.5}$	$6.36 \cdot 10^{-4}{}^{+2.6}_{-2.6}$	$2.21 \cdot 10^{-6}{}^{+2.6}_{-2.7}$	$2.74 \cdot 10^{-4}{}^{+12.0}_{-11.9}$
180	$5.01 \cdot 10^{-3}{}^{+6.6}_{-6.5}$	$5.87 \cdot 10^{-4}{}^{+2.6}_{-2.6}$	$2.03 \cdot 10^{-6}{}^{+2.7}_{-2.6}$	$2.52 \cdot 10^{-4}{}^{+12.0}_{-11.9}$
182	$4.55 \cdot 10^{-3}{}^{+6.6}_{-6.5}$	$5.34 \cdot 10^{-4}{}^{+2.6}_{-2.6}$	$1.85 \cdot 10^{-6}{}^{+2.6}_{-2.6}$	$2.29 \cdot 10^{-4}{}^{+12.0}_{-11.9}$
184	$4.08 \cdot 10^{-3}{}^{+6.6}_{-6.5}$	$4.80 \cdot 10^{-4}{}^{+2.6}_{-2.6}$	$1.67 \cdot 10^{-6}{}^{+2.6}_{-2.6}$	$2.06 \cdot 10^{-4}{}^{+12.0}_{-11.9}$
185	$3.88 \cdot 10^{-3}{}^{+6.6}_{-6.5}$	$4.57 \cdot 10^{-4}{}^{+2.6}_{-2.6}$	$1.59 \cdot 10^{-6}{}^{+2.6}_{-2.6}$	$1.95 \cdot 10^{-4}{}^{+12.0}_{-11.9}$
186	$3.70 \cdot 10^{-3}{}^{+6.6}_{-6.5}$	$4.37 \cdot 10^{-4}{}^{+2.6}_{-2.6}$	$1.51 \cdot 10^{-6}{}^{+2.6}_{-2.7}$	$1.86 \cdot 10^{-4}{}^{+12.0}_{-11.9}$
188	$3.41 \cdot 10^{-3}{}^{+6.6}_{-6.6}$	$4.03 \cdot 10^{-4}{}^{+2.6}_{-2.6}$	$1.40 \cdot 10^{-6}{}^{+2.6}_{-2.7}$	$1.72 \cdot 10^{-4}{}^{+12.0}_{-11.9}$
190	$3.17 \cdot 10^{-3}{}^{+6.6}_{-6.6}$	$3.75 \cdot 10^{-4}{}^{+2.7}_{-2.6}$	$1.30 \cdot 10^{-6}{}^{+2.6}_{-2.5}$	$1.60 \cdot 10^{-4}{}^{+12.0}_{-11.9}$
192	$2.97 \cdot 10^{-3}{}^{+6.6}_{-6.5}$	$3.53 \cdot 10^{-4}{}^{+2.6}_{-2.6}$	$1.22 \cdot 10^{-6}{}^{+2.5}_{-2.6}$	$1.50 \cdot 10^{-4}{}^{+11.9}_{-12.0}$
194	$2.80 \cdot 10^{-3}{}^{+6.6}_{-6.6}$	$3.33 \cdot 10^{-4}{}^{+2.6}_{-2.6}$	$1.15 \cdot 10^{-6}{}^{+2.6}_{-2.5}$	$1.41 \cdot 10^{-4}{}^{+12.0}_{-12.0}$
195	$2.73 \cdot 10^{-3}{}^{+6.6}_{-6.5}$	$3.24 \cdot 10^{-4}{}^{+2.6}_{-2.6}$	$1.13 \cdot 10^{-6}{}^{+2.6}_{-2.6}$	$1.37 \cdot 10^{-4}{}^{+12.0}_{-11.9}$
196	$2.65 \cdot 10^{-3}{}^{+6.6}_{-6.5}$	$3.16 \cdot 10^{-4}{}^{+2.6}_{-2.6}$	$1.10 \cdot 10^{-6}{}^{+2.6}_{-2.6}$	$1.34 \cdot 10^{-4}{}^{+12.1}_{-11.9}$
198	$2.52 \cdot 10^{-3}{}^{+6.6}_{-6.5}$	$3.01 \cdot 10^{-4}{}^{+2.6}_{-2.6}$	$1.04 \cdot 10^{-6}{}^{+2.6}_{-2.6}$	$1.27 \cdot 10^{-4}{}^{+12.1}_{-11.9}$
200	$2.40 \cdot 10^{-3}{}^{+6.6}_{-6.6}$	$2.87 \cdot 10^{-4}{}^{+2.5}_{-2.6}$	$9.95 \cdot 10^{-7}{}^{+2.6}_{-2.6}$	$1.21 \cdot 10^{-4}{}^{+12.0}_{-12.0}$
202	$2.29 \cdot 10^{-3}{}^{+6.6}_{-6.5}$	$2.75 \cdot 10^{-4}{}^{+2.6}_{-2.6}$	$9.52 \cdot 10^{-7}{}^{+2.6}_{-2.6}$	$1.15 \cdot 10^{-4}{}^{+12.1}_{-11.9}$
204	$2.19 \cdot 10^{-3}{}^{+6.6}_{-6.5}$	$2.63 \cdot 10^{-4}{}^{+2.7}_{-2.6}$	$9.12 \cdot 10^{-7}{}^{+2.6}_{-2.6}$	$1.10 \cdot 10^{-4}{}^{+12.0}_{-11.9}$
206	$2.10 \cdot 10^{-3}{}^{+6.6}_{-6.5}$	$2.53 \cdot 10^{-4}{}^{+2.6}_{-2.6}$	$8.76 \cdot 10^{-7}{}^{+2.6}_{-2.6}$	$1.06 \cdot 10^{-4}{}^{+12.0}_{-12.0}$
208	$2.02 \cdot 10^{-3}{}^{+6.6}_{-6.6}$	$2.43 \cdot 10^{-4}{}^{+2.7}_{-2.6}$	$8.42 \cdot 10^{-7}{}^{+2.6}_{-2.6}$	$1.02 \cdot 10^{-4}{}^{+12.0}_{-12.0}$
210	$1.94 \cdot 10^{-3}{}^{+6.6}_{-6.6}$	$2.34 \cdot 10^{-4}{}^{+2.6}_{-2.6}$	$8.11 \cdot 10^{-7}{}^{+2.6}_{-2.6}$	$9.75 \cdot 10^{-5}{}^{+12.0}_{-11.9}$
212	$1.86 \cdot 10^{-3}{}^{+6.6}_{-6.6}$	$2.25 \cdot 10^{-4}{}^{+2.6}_{-2.6}$	$7.82 \cdot 10^{-7}{}^{+2.6}_{-2.6}$	$9.38 \cdot 10^{-5}{}^{+12.0}_{-11.9}$
214	$1.80 \cdot 10^{-3}{}^{+6.6}_{-6.6}$	$2.18 \cdot 10^{-4}{}^{+2.6}_{-2.7}$	$7.54 \cdot 10^{-7}{}^{+2.6}_{-2.6}$	$9.04 \cdot 10^{-5}{}^{+12.0}_{-11.9}$
216	$1.73 \cdot 10^{-3}{}^{+6.6}_{-6.6}$	$2.10 \cdot 10^{-4}{}^{+2.6}_{-2.6}$	$7.28 \cdot 10^{-7}{}^{+2.6}_{-2.6}$	$8.71 \cdot 10^{-5}{}^{+12.0}_{-12.0}$
218	$1.67 \cdot 10^{-3}{}^{+6.7}_{-6.6}$	$2.03 \cdot 10^{-4}{}^{+2.6}_{-2.6}$	$7.04 \cdot 10^{-7}{}^{+2.6}_{-2.6}$	$8.40 \cdot 10^{-5}{}^{+12.0}_{-12.0}$
220	$1.61 \cdot 10^{-3}{}^{+6.7}_{-6.5}$	$1.96 \cdot 10^{-4}{}^{+2.7}_{-2.6}$	$6.81 \cdot 10^{-7}{}^{+2.6}_{-2.6}$	$8.11 \cdot 10^{-5}{}^{+12.1}_{-11.9}$
222	$1.56 \cdot 10^{-3}{}^{+6.6}_{-6.6}$	$1.90 \cdot 10^{-4}{}^{+2.6}_{-2.5}$	$6.59 \cdot 10^{-7}{}^{+2.6}_{-2.6}$	$7.84 \cdot 10^{-5}{}^{+12.1}_{-11.9}$
224	$1.51 \cdot 10^{-3}{}^{+6.6}_{-6.6}$	$1.84 \cdot 10^{-4}{}^{+2.6}_{-2.6}$	$6.38 \cdot 10^{-7}{}^{+2.6}_{-2.6}$	$7.58 \cdot 10^{-5}{}^{+12.1}_{-12.0}$
226	$1.46 \cdot 10^{-3}{}^{+6.7}_{-6.5}$	$1.78 \cdot 10^{-4}{}^{+2.6}_{-2.6}$	$6.18 \cdot 10^{-7}{}^{+2.6}_{-2.6}$	$7.33 \cdot 10^{-5}{}^{+12.1}_{-12.0}$
228	$1.41 \cdot 10^{-3}{}^{+6.6}_{-6.6}$	$1.73 \cdot 10^{-4}{}^{+2.6}_{-2.6}$	$6.00 \cdot 10^{-7}{}^{+2.6}_{-2.6}$	$7.10 \cdot 10^{-5}{}^{+12.1}_{-12.0}$
230	$1.37 \cdot 10^{-3}{}^{+6.7}_{-6.5}$	$1.68 \cdot 10^{-4}{}^{+2.6}_{-2.6}$	$5.82 \cdot 10^{-7}{}^{+2.6}_{-2.6}$	$6.88 \cdot 10^{-5}{}^{+12.1}_{-12.0}$

Table A.6: SM Higgs branching ratios to two fermions and their total uncertainties (expressed in percentage). Intermediate mass range.

M_H [GeV]	H → bb	H → $\tau^+\tau^-$	H → $\mu^+\mu^-$	H → c$\bar{c}$	H → t$\bar{t}$
232	$1.33\cdot10^{-3}{}^{+6.6}_{-6.6}$	$1.63\cdot10^{-4}{}^{+2.6}_{-2.6}$	$5.65\cdot10^{-7}{}^{+2.6}_{-2.6}$	$6.67\cdot10^{-5}{}^{+12.1}_{-12.0}$	$0\cdot10^{0}{}^{+0}_{-0}$
234	$1.29\cdot10^{-3}{}^{+6.6}_{-6.6}$	$1.58\cdot10^{-4}{}^{+2.6}_{-2.6}$	$5.49\cdot10^{-7}{}^{+2.6}_{-2.6}$	$6.47\cdot10^{-5}{}^{+12.1}_{-12.0}$	$0\cdot10^{0}{}^{+0}_{-0}$
236	$1.25\cdot10^{-3}{}^{+6.7}_{-6.6}$	$1.54\cdot10^{-4}{}^{+2.6}_{-2.6}$	$5.33\cdot10^{-7}{}^{+2.6}_{-2.6}$	$6.27\cdot10^{-5}{}^{+12.1}_{-12.0}$	$0\cdot10^{0}{}^{+0}_{-0}$
238	$1.21\cdot10^{-3}{}^{+6.7}_{-6.6}$	$1.50\cdot10^{-4}{}^{+2.6}_{-2.6}$	$5.19\cdot10^{-7}{}^{+2.6}_{-2.6}$	$6.09\cdot10^{-5}{}^{+12.1}_{-12.0}$	$0\cdot10^{0}{}^{+0}_{-0}$
240	$1.18\cdot10^{-3}{}^{+6.7}_{-6.5}$	$1.45\cdot10^{-4}{}^{+2.6}_{-2.6}$	$5.04\cdot10^{-7}{}^{+2.6}_{-2.6}$	$5.91\cdot10^{-5}{}^{+12.1}_{-12.0}$	$0\cdot10^{0}{}^{+0}_{-0}$
242	$1.14\cdot10^{-3}{}^{+6.6}_{-6.7}$	$1.42\cdot10^{-4}{}^{+2.6}_{-2.6}$	$4.91\cdot10^{-7}{}^{+2.6}_{-2.6}$	$5.74\cdot10^{-5}{}^{+12.1}_{-12.0}$	$0\cdot10^{0}{}^{+0}_{-0}$
244	$1.11\cdot10^{-3}{}^{+6.6}_{-6.7}$	$1.38\cdot10^{-4}{}^{+2.6}_{-2.6}$	$4.78\cdot10^{-7}{}^{+2.6}_{-2.6}$	$5.58\cdot10^{-5}{}^{+12.1}_{-12.0}$	$0\cdot10^{0}{}^{+0}_{-0}$
246	$1.08\cdot10^{-3}{}^{+6.7}_{-6.6}$	$1.34\cdot10^{-4}{}^{+2.6}_{-2.6}$	$4.65\cdot10^{-7}{}^{+2.6}_{-2.6}$	$5.43\cdot10^{-5}{}^{+12.1}_{-12.0}$	$0\cdot10^{0}{}^{+0}_{-0}$
248	$1.05\cdot10^{-3}{}^{+6.7}_{-6.6}$	$1.31\cdot10^{-4}{}^{+2.6}_{-2.6}$	$4.53\cdot10^{-7}{}^{+2.6}_{-2.6}$	$5.28\cdot10^{-5}{}^{+12.1}_{-12.0}$	$0\cdot10^{0}{}^{+0}_{-0}$
250	$1.02\cdot10^{-3}{}^{+6.7}_{-6.6}$	$1.27\cdot10^{-4}{}^{+2.6}_{-2.7}$	$4.42\cdot10^{-7}{}^{+2.6}_{-2.6}$	$5.14\cdot10^{-5}{}^{+12.1}_{-12.0}$	$0\cdot10^{0}{}^{+0}_{-0}$
252	$9.95\cdot10^{-4}{}^{+6.7}_{-6.6}$	$1.24\cdot10^{-4}{}^{+2.6}_{-2.6}$	$4.30\cdot10^{-7}{}^{+2.6}_{-2.6}$	$5.00\cdot10^{-5}{}^{+12.1}_{-12.0}$	$0\cdot10^{0}{}^{+0}_{-0}$
254	$9.68\cdot10^{-4}{}^{+6.7}_{-6.6}$	$1.21\cdot10^{-4}{}^{+2.7}_{-2.6}$	$4.20\cdot10^{-7}{}^{+2.6}_{-2.6}$	$4.87\cdot10^{-5}{}^{+12.1}_{-12.0}$	$0\cdot10^{0}{}^{+0}_{-0}$
256	$9.43\cdot10^{-4}{}^{+6.7}_{-6.7}$	$1.18\cdot10^{-4}{}^{+2.6}_{-2.6}$	$4.10\cdot10^{-7}{}^{+2.6}_{-2.6}$	$4.74\cdot10^{-5}{}^{+12.1}_{-12.0}$	$0\cdot10^{0}{}^{+0}_{-0}$
258	$9.19\cdot10^{-4}{}^{+6.7}_{-6.6}$	$1.15\cdot10^{-4}{}^{+2.6}_{-2.6}$	$4.00\cdot10^{-7}{}^{+2.6}_{-2.6}$	$4.62\cdot10^{-5}{}^{+12.1}_{-12.0}$	$0\cdot10^{0}{}^{+0}_{-0}$
260	$8.96\cdot10^{-4}{}^{+6.7}_{-6.6}$	$1.12\cdot10^{-4}{}^{+2.6}_{-2.6}$	$3.90\cdot10^{-7}{}^{+2.6}_{-2.6}$	$4.51\cdot10^{-5}{}^{+12.1}_{-12.0}$	$0\cdot10^{0}{}^{+0}_{-0}$
262	$8.74\cdot10^{-4}{}^{+6.7}_{-6.6}$	$1.10\cdot10^{-4}{}^{+2.6}_{-2.6}$	$3.81\cdot10^{-7}{}^{+2.6}_{-2.6}$	$4.39\cdot10^{-5}{}^{+12.1}_{-12.0}$	$0\cdot10^{0}{}^{+0}_{-0}$
264	$8.52\cdot10^{-4}{}^{+6.7}_{-6.6}$	$1.07\cdot10^{-4}{}^{+2.6}_{-2.6}$	$3.72\cdot10^{-7}{}^{+2.6}_{-2.6}$	$4.28\cdot10^{-5}{}^{+12.1}_{-12.0}$	$0\cdot10^{0}{}^{+0}_{-0}$
266	$8.31\cdot10^{-4}{}^{+6.7}_{-6.6}$	$1.05\cdot10^{-4}{}^{+2.5}_{-2.6}$	$3.63\cdot10^{-7}{}^{+2.6}_{-2.6}$	$4.18\cdot10^{-5}{}^{+12.1}_{-12.0}$	$0\cdot10^{0}{}^{+0}_{-0}$
268	$8.11\cdot10^{-4}{}^{+6.7}_{-6.6}$	$1.02\cdot10^{-4}{}^{+2.6}_{-2.6}$	$3.55\cdot10^{-7}{}^{+2.6}_{-2.6}$	$4.08\cdot10^{-5}{}^{+12.1}_{-12.0}$	$0\cdot10^{0}{}^{+0}_{-0}$
270	$7.92\cdot10^{-4}{}^{+6.7}_{-6.6}$	$1.00\cdot10^{-4}{}^{+2.6}_{-2.6}$	$3.47\cdot10^{-7}{}^{+2.6}_{-2.6}$	$3.98\cdot10^{-5}{}^{+12.1}_{-12.0}$	$0\cdot10^{0}{}^{+0}_{-0}$
272	$7.73\cdot10^{-4}{}^{+6.7}_{-6.6}$	$9.79\cdot10^{-5}{}^{+2.6}_{-2.6}$	$3.39\cdot10^{-7}{}^{+2.6}_{-2.6}$	$3.89\cdot10^{-5}{}^{+12.1}_{-12.0}$	$3.37\cdot10^{-6}{}^{+67.4}_{-48.0}$
274	$7.56\cdot10^{-4}{}^{+6.7}_{-6.6}$	$9.58\cdot10^{-5}{}^{+2.6}_{-2.6}$	$3.32\cdot10^{-7}{}^{+2.6}_{-2.6}$	$3.80\cdot10^{-5}{}^{+12.1}_{-12.0}$	$4.73\cdot10^{-6}{}^{+60.5}_{-44.4}$
276	$7.38\cdot10^{-4}{}^{+6.7}_{-6.6}$	$9.37\cdot10^{-5}{}^{+2.6}_{-2.6}$	$3.25\cdot10^{-7}{}^{+2.6}_{-2.6}$	$3.71\cdot10^{-5}{}^{+12.1}_{-12.0}$	$6.41\cdot10^{-6}{}^{+55.2}_{-41.5}$
278	$7.21\cdot10^{-4}{}^{+6.7}_{-6.6}$	$9.17\cdot10^{-5}{}^{+2.6}_{-2.6}$	$3.18\cdot10^{-7}{}^{+2.6}_{-2.6}$	$3.63\cdot10^{-5}{}^{+12.1}_{-12.0}$	$8.45\cdot10^{-6}{}^{+51.1}_{-39.2}$
280	$7.05\cdot10^{-4}{}^{+6.7}_{-6.7}$	$8.97\cdot10^{-5}{}^{+2.6}_{-2.6}$	$3.11\cdot10^{-7}{}^{+2.6}_{-2.6}$	$3.55\cdot10^{-5}{}^{+12.1}_{-12.0}$	$1.09\cdot10^{-5}{}^{+47.7}_{-37.1}$
282	$6.90\cdot10^{-4}{}^{+6.7}_{-6.6}$	$8.79\cdot10^{-5}{}^{+2.6}_{-2.6}$	$3.05\cdot10^{-7}{}^{+2.6}_{-2.6}$	$3.47\cdot10^{-5}{}^{+12.1}_{-12.0}$	$1.38\cdot10^{-5}{}^{+44.9}_{-35.5}$
284	$6.74\cdot10^{-4}{}^{+6.7}_{-6.6}$	$8.60\cdot10^{-5}{}^{+2.6}_{-2.6}$	$2.98\cdot10^{-7}{}^{+2.6}_{-2.6}$	$3.39\cdot10^{-5}{}^{+12.1}_{-12.0}$	$1.71\cdot10^{-5}{}^{+42.7}_{-34.0}$
286	$6.60\cdot10^{-4}{}^{+6.7}_{-6.7}$	$8.43\cdot10^{-5}{}^{+2.6}_{-2.6}$	$2.92\cdot10^{-7}{}^{+2.6}_{-2.6}$	$3.32\cdot10^{-5}{}^{+12.1}_{-12.0}$	$2.10\cdot10^{-5}{}^{+40.8}_{-32.7}$
288	$6.46\cdot10^{-4}{}^{+6.7}_{-6.7}$	$8.26\cdot10^{-5}{}^{+2.6}_{-2.6}$	$2.86\cdot10^{-7}{}^{+2.6}_{-2.6}$	$3.25\cdot10^{-5}{}^{+12.1}_{-12.0}$	$2.55\cdot10^{-5}{}^{+39.2}_{-31.7}$
290	$6.32\cdot10^{-4}{}^{+6.7}_{-6.7}$	$8.09\cdot10^{-5}{}^{+2.6}_{-2.6}$	$2.80\cdot10^{-7}{}^{+2.6}_{-2.6}$	$3.18\cdot10^{-5}{}^{+12.2}_{-12.0}$	$3.06\cdot10^{-5}{}^{+37.8}_{-30.7}$
292	$6.19\cdot10^{-4}{}^{+6.7}_{-6.7}$	$7.93\cdot10^{-5}{}^{+2.6}_{-2.6}$	$2.75\cdot10^{-7}{}^{+2.6}_{-2.6}$	$3.11\cdot10^{-5}{}^{+12.2}_{-12.0}$	$3.65\cdot10^{-5}{}^{+36.7}_{-29.9}$
294	$6.06\cdot10^{-4}{}^{+6.7}_{-6.7}$	$7.78\cdot10^{-5}{}^{+2.6}_{-2.6}$	$2.70\cdot10^{-7}{}^{+2.6}_{-2.6}$	$3.05\cdot10^{-5}{}^{+12.1}_{-12.0}$	$4.31\cdot10^{-5}{}^{+35.8}_{-29.2}$
296	$5.93\cdot10^{-4}{}^{+6.7}_{-6.6}$	$7.62\cdot10^{-5}{}^{+2.6}_{-2.6}$	$2.64\cdot10^{-7}{}^{+2.6}_{-2.6}$	$2.98\cdot10^{-5}{}^{+12.2}_{-12.0}$	$5.06\cdot10^{-5}{}^{+35.0}_{-28.6}$
298	$5.81\cdot10^{-4}{}^{+6.7}_{-6.7}$	$7.48\cdot10^{-5}{}^{+2.6}_{-2.6}$	$2.59\cdot10^{-7}{}^{+2.6}_{-2.6}$	$2.92\cdot10^{-5}{}^{+12.2}_{-12.0}$	$5.91\cdot10^{-5}{}^{+34.4}_{-28.1}$
300	$5.69\cdot10^{-4}{}^{+6.7}_{-6.7}$	$7.34\cdot10^{-5}{}^{+2.6}_{-2.6}$	$2.54\cdot10^{-7}{}^{+2.6}_{-2.6}$	$2.86\cdot10^{-5}{}^{+12.1}_{-12.0}$	$6.87\cdot10^{-5}{}^{+33.8}_{-27.7}$
305	$5.42\cdot10^{-4}{}^{+6.7}_{-6.7}$	$7.00\cdot10^{-5}{}^{+2.6}_{-2.6}$	$2.43\cdot10^{-7}{}^{+2.6}_{-2.6}$	$2.72\cdot10^{-5}{}^{+12.2}_{-12.0}$	$9.82\cdot10^{-5}{}^{+33.1}_{-26.9}$
310	$5.16\cdot10^{-4}{}^{+6.7}_{-6.7}$	$6.68\cdot10^{-5}{}^{+2.6}_{-2.6}$	$2.32\cdot10^{-7}{}^{+2.6}_{-2.6}$	$2.59\cdot10^{-5}{}^{+12.2}_{-12.0}$	$1.38\cdot10^{-4}{}^{+33.1}_{-26.6}$
315	$4.92\cdot10^{-4}{}^{+6.7}_{-6.7}$	$6.39\cdot10^{-5}{}^{+2.6}_{-2.5}$	$2.22\cdot10^{-7}{}^{+2.6}_{-2.6}$	$2.47\cdot10^{-5}{}^{+12.2}_{-12.0}$	$1.92\cdot10^{-4}{}^{+33.8}_{-26.6}$
320	$4.69\cdot10^{-4}{}^{+6.8}_{-6.6}$	$6.12\cdot10^{-5}{}^{+2.7}_{-2.5}$	$2.12\cdot10^{-7}{}^{+2.7}_{-2.5}$	$2.36\cdot10^{-5}{}^{+12.2}_{-12.0}$	$2.65\cdot10^{-4}{}^{+35.3}_{-27.0}$
325	$4.49\cdot10^{-4}{}^{+6.7}_{-6.7}$	$5.86\cdot10^{-5}{}^{+2.5}_{-2.6}$	$2.03\cdot10^{-7}{}^{+2.5}_{-2.6}$	$2.26\cdot10^{-5}{}^{+12.2}_{-12.1}$	$3.69\cdot10^{-4}{}^{+38.1}_{-28.1}$
330	$4.29\cdot10^{-4}{}^{+6.8}_{-6.7}$	$5.63\cdot10^{-5}{}^{+2.6}_{-2.5}$	$1.95\cdot10^{-7}{}^{+2.6}_{-2.5}$	$2.16\cdot10^{-5}{}^{+12.2}_{-12.1}$	$5.21\cdot10^{-4}{}^{+43.6}_{-29.7}$
335	$4.12\cdot10^{-4}{}^{+6.8}_{-6.7}$	$5.41\cdot10^{-5}{}^{+2.5}_{-2.5}$	$1.87\cdot10^{-7}{}^{+2.5}_{-2.5}$	$2.07\cdot10^{-5}{}^{+12.2}_{-12.0}$	$7.61\cdot10^{-4}{}^{+55.8}_{-32.7}$
340	$3.95\cdot10^{-4}{}^{+6.7}_{-6.7}$	$5.20\cdot10^{-5}{}^{+2.7}_{-2.5}$	$1.80\cdot10^{-7}{}^{+2.7}_{-2.5}$	$1.99\cdot10^{-5}{}^{+12.1}_{-12.1}$	$1.20\cdot10^{-3}{}^{+174.1}_{-38.6}$
345	$3.80\cdot10^{-4}{}^{+6.8}_{-7.0}$	$5.02\cdot10^{-5}{}^{+2.5}_{-4.1}$	$1.74\cdot10^{-7}{}^{+2.5}_{-4.1}$	$1.91\cdot10^{-5}{}^{+12.2}_{-12.2}$	$3.28\cdot10^{-3}{}^{+394.5}_{-67.2}$
350	$3.60\cdot10^{-4}{}^{+7.1}_{-7.4}$	$4.76\cdot10^{-5}{}^{+4.1}_{-5.0}$	$1.65\cdot10^{-7}{}^{+4.1}_{-4.9}$	$1.81\cdot10^{-5}{}^{+12.4}_{-12.5}$	$1.56\cdot10^{-2}{}^{+126.3}_{-84.1}$
360	$3.18\cdot10^{-4}{}^{+7.6}_{-7.5}$	$4.23\cdot10^{-5}{}^{+5.2}_{-5.1}$	$1.47\cdot10^{-7}{}^{+5.2}_{-5.1}$	$1.60\cdot10^{-5}{}^{+12.8}_{-12.6}$	$5.14\cdot10^{-2}{}^{+40.8}_{-41.4}$
370	$2.83\cdot10^{-4}{}^{+7.7}_{-7.6}$	$3.78\cdot10^{-5}{}^{+5.1}_{-5.0}$	$1.31\cdot10^{-7}{}^{+5.2}_{-5.0}$	$1.42\cdot10^{-5}{}^{+12.9}_{-12.7}$	$8.35\cdot10^{-2}{}^{+24.1}_{-25.3}$

Table A.7: SM Higgs branching ratios to two fermions and their total uncertainties (expressed in percentage). High mass range.

M_{H} [GeV]	$H \to b\bar{b}$	$H \to \tau^+\tau^-$	$H \to \mu^+\mu^-$	$H \to c\bar{c}$	$H \to t\bar{t}$
380	$2.54 \cdot 10^{-4}{}^{+7.7}_{-7.6}$	$3.41 \cdot 10^{-5}{}^{+5.0}_{-4.8}$	$1.18 \cdot 10^{-7}{}^{+5.0}_{-4.8}$	$1.27 \cdot 10^{-5}{}^{+13.0}_{-12.8}$	$1.10 \cdot 10^{-1}{}^{+17.1}_{-18.1}$
390	$2.3 \cdot 10^{-4}{}^{+7.7}_{-7.6}$	$3.10 \cdot 10^{-5}{}^{+4.9}_{-4.7}$	$1.07 \cdot 10^{-7}{}^{+4.9}_{-4.7}$	$1.15 \cdot 10^{-5}{}^{+13.0}_{-12.9}$	$1.31 \cdot 10^{-1}{}^{+13.2}_{-14.1}$
400	$2.09 \cdot 10^{-4}{}^{+7.7}_{-7.6}$	$2.84 \cdot 10^{-5}{}^{+4.7}_{-4.4}$	$9.83 \cdot 10^{-8}{}^{+4.6}_{-4.5}$	$1.05 \cdot 10^{-5}{}^{+13.1}_{-12.9}$	$1.48 \cdot 10^{-1}{}^{+10.9}_{-11.5}$
420	$1.78 \cdot 10^{-4}{}^{+7.7}_{-7.6}$	$2.43 \cdot 10^{-5}{}^{+4.3}_{-4.2}$	$8.41 \cdot 10^{-8}{}^{+4.3}_{-4.2}$	$8.93 \cdot 10^{-6}{}^{+13.1}_{-13.0}$	$1.71 \cdot 10^{-1}{}^{+8.1}_{-8.6}$
440	$1.54 \cdot 10^{-4}{}^{+7.7}_{-7.6}$	$2.12 \cdot 10^{-5}{}^{+4.0}_{-3.9}$	$7.35 \cdot 10^{-8}{}^{+4.0}_{-3.9}$	$7.74 \cdot 10^{-6}{}^{+13.2}_{-13.0}$	$1.84 \cdot 10^{-1}{}^{+6.5}_{-6.9}$
450	$1.44 \cdot 10^{-4}{}^{+7.7}_{-7.6}$	$1.99 \cdot 10^{-5}{}^{+3.9}_{-3.8}$	$6.91 \cdot 10^{-8}{}^{+3.9}_{-3.8}$	$7.25 \cdot 10^{-6}{}^{+13.1}_{-13.0}$	$1.88 \cdot 10^{-1}{}^{+6.0}_{-6.4}$
460	$1.36 \cdot 10^{-4}{}^{+7.7}_{-7.7}$	$1.88 \cdot 10^{-5}{}^{+3.8}_{-3.7}$	$6.52 \cdot 10^{-8}{}^{+3.8}_{-3.7}$	$6.81 \cdot 10^{-6}{}^{+13.2}_{-13.0}$	$1.91 \cdot 10^{-1}{}^{+5.6}_{-5.9}$
480	$1.21 \cdot 10^{-4}{}^{+7.8}_{-7.6}$	$1.69 \cdot 10^{-5}{}^{+3.6}_{-3.6}$	$5.85 \cdot 10^{-8}{}^{+3.7}_{-3.5}$	$6.07 \cdot 10^{-6}{}^{+13.2}_{-13.0}$	$1.93 \cdot 10^{-1}{}^{+5.0}_{-5.2}$
500	$1.09 \cdot 10^{-4}{}^{+8.3}_{-8.2}$	$1.53 \cdot 10^{-5}{}^{+4.0}_{-4.1}$	$5.30 \cdot 10^{-8}{}^{+4.1}_{-4.0}$	$5.47 \cdot 10^{-6}{}^{+13.8}_{-13.6}$	$1.92 \cdot 10^{-1}{}^{+5.5}_{-5.8}$
520	$9.88 \cdot 10^{-5}{}^{+8.5}_{-8.4}$	$1.40 \cdot 10^{-5}{}^{+4.1}_{-4.1}$	$4.84 \cdot 10^{-8}{}^{+4.1}_{-4.1}$	$4.96 \cdot 10^{-6}{}^{+13.9}_{-13.8}$	$1.90 \cdot 10^{-1}{}^{+5.8}_{-6.0}$
540	$9.02 \cdot 10^{-5}{}^{+8.6}_{-8.5}$	$1.28 \cdot 10^{-5}{}^{+4.5}_{-4.3}$	$4.45 \cdot 10^{-8}{}^{+4.4}_{-4.3}$	$4.53 \cdot 10^{-6}{}^{+14.1}_{-13.9}$	$1.85 \cdot 10^{-1}{}^{+6.4}_{-6.5}$
550	$8.64 \cdot 10^{-5}{}^{+8.7}_{-8.6}$	$1.23 \cdot 10^{-5}{}^{+4.6}_{-4.4}$	$4.27 \cdot 10^{-8}{}^{+4.5}_{-4.4}$	$4.34 \cdot 10^{-6}{}^{+14.2}_{-14.0}$	$1.83 \cdot 10^{-1}{}^{+6.7}_{-6.8}$
560	$8.28 \cdot 10^{-5}{}^{+8.8}_{-8.7}$	$1.19 \cdot 10^{-5}{}^{+4.6}_{-4.6}$	$4.11 \cdot 10^{-8}{}^{+4.6}_{-4.6}$	$4.15 \cdot 10^{-6}{}^{+14.3}_{-14.1}$	$1.80 \cdot 10^{-1}{}^{+7.0}_{-7.1}$
580	$7.64 \cdot 10^{-5}{}^{+9.0}_{-8.9}$	$1.10 \cdot 10^{-5}{}^{+4.9}_{-4.9}$	$3.81 \cdot 10^{-8}{}^{+4.9}_{-4.9}$	$3.83 \cdot 10^{-6}{}^{+14.4}_{-14.3}$	$1.75 \cdot 10^{-1}{}^{+7.5}_{-7.7}$
600	$7.06 \cdot 10^{-5}{}^{+9.3}_{-9.1}$	$1.02 \cdot 10^{-5}{}^{+5.3}_{-5.0}$	$3.54 \cdot 10^{-8}{}^{+5.2}_{-5.0}$	$3.54 \cdot 10^{-6}{}^{+14.8}_{-14.5}$	$1.69 \cdot 10^{-1}{}^{+8.1}_{-8.2}$
620	$6.56 \cdot 10^{-5}{}^{+9.6}_{-9.4}$	$9.53 \cdot 10^{-6}{}^{+5.4}_{-5.4}$	$3.30 \cdot 10^{-8}{}^{+5.4}_{-5.4}$	$3.29 \cdot 10^{-6}{}^{+15.0}_{-14.8}$	$1.63 \cdot 10^{-1}{}^{+8.7}_{-8.9}$
640	$6.10 \cdot 10^{-5}{}^{+9.9}_{-9.7}$	$8.92 \cdot 10^{-6}{}^{+5.8}_{-5.7}$	$3.09 \cdot 10^{-8}{}^{+5.8}_{-5.7}$	$3.06 \cdot 10^{-6}{}^{+15.3}_{-15.1}$	$1.56 \cdot 10^{-1}{}^{+9.4}_{-9.4}$
650	$5.89 \cdot 10^{-5}{}^{+10.1}_{-9.8}$	$8.63 \cdot 10^{-6}{}^{+6.0}_{-5.8}$	$2.99 \cdot 10^{-8}{}^{+6.0}_{-5.8}$	$2.95 \cdot 10^{-6}{}^{+15.5}_{-15.2}$	$1.53 \cdot 10^{-1}{}^{+9.7}_{-9.7}$
660	$5.69 \cdot 10^{-5}{}^{+10.2}_{-10.0}$	$8.36 \cdot 10^{-6}{}^{+6.1}_{-6.0}$	$2.90 \cdot 10^{-8}{}^{+6.2}_{-6.0}$	$2.85 \cdot 10^{-6}{}^{+15.7}_{-15.4}$	$1.50 \cdot 10^{-1}{}^{+10.1}_{-10.1}$
680	$5.32 \cdot 10^{-5}{}^{+10.6}_{-10.4}$	$7.84 \cdot 10^{-6}{}^{+6.6}_{-6.3}$	$2.72 \cdot 10^{-8}{}^{+6.6}_{-6.3}$	$2.67 \cdot 10^{-6}{}^{+16.1}_{-15.7}$	$1.44 \cdot 10^{-1}{}^{+10.9}_{-10.8}$
700	$4.98 \cdot 10^{-5}{}^{+11.1}_{-10.7}$	$7.38 \cdot 10^{-6}{}^{+7.0}_{-6.7}$	$2.56 \cdot 10^{-8}{}^{+7.0}_{-6.7}$	$2.50 \cdot 10^{-6}{}^{+16.5}_{-16.1}$	$1.38 \cdot 10^{-1}{}^{+11.6}_{-11.5}$
720	$4.67 \cdot 10^{-5}{}^{+11.5}_{-11.1}$	$6.95 \cdot 10^{-6}{}^{+7.5}_{-7.1}$	$2.41 \cdot 10^{-8}{}^{+7.5}_{-7.1}$	$2.34 \cdot 10^{-6}{}^{+17.0}_{-16.5}$	$1.32 \cdot 10^{-1}{}^{+12.6}_{-12.3}$
740	$4.38 \cdot 10^{-5}{}^{+12.1}_{-11.6}$	$6.55 \cdot 10^{-6}{}^{+7.9}_{-7.6}$	$2.27 \cdot 10^{-8}{}^{+8.0}_{-7.5}$	$2.20 \cdot 10^{-6}{}^{+17.5}_{-17.0}$	$1.26 \cdot 10^{-1}{}^{+13.4}_{-13.3}$
750	$4.25 \cdot 10^{-5}{}^{+12.4}_{-11.8}$	$6.36 \cdot 10^{-6}{}^{+8.2}_{-7.8}$	$2.20 \cdot 10^{-8}{}^{+8.3}_{-7.8}$	$2.13 \cdot 10^{-6}{}^{+17.8}_{-17.2}$	$1.23 \cdot 10^{-1}{}^{+13.9}_{-13.7}$
760	$4.12 \cdot 10^{-5}{}^{+12.6}_{-12.1}$	$6.18 \cdot 10^{-6}{}^{+8.5}_{-8.0}$	$2.14 \cdot 10^{-8}{}^{+8.5}_{-8.0}$	$2.06 \cdot 10^{-6}{}^{+18.1}_{-17.5}$	$1.2 \cdot 10^{-1}{}^{+14.4}_{-14.1}$
780	$3.87 \cdot 10^{-5}{}^{+13.3}_{-12.6}$	$5.84 \cdot 10^{-6}{}^{+9.2}_{-8.6}$	$2.02 \cdot 10^{-8}{}^{+9.2}_{-8.5}$	$1.94 \cdot 10^{-6}{}^{+18.8}_{-18.0}$	$1.15 \cdot 10^{-1}{}^{+15.5}_{-15.1}$
800	$3.65 \cdot 10^{-5}{}^{+14.0}_{-13.2}$	$5.52 \cdot 10^{-6}{}^{+9.9}_{-9.1}$	$1.91 \cdot 10^{-8}{}^{+9.9}_{-9.1}$	$1.83 \cdot 10^{-6}{}^{+19.5}_{-18.6}$	$1.10 \cdot 10^{-1}{}^{+16.7}_{-16.1}$
820	$3.43 \cdot 10^{-5}{}^{+14.8}_{-13.7}$	$5.22 \cdot 10^{-6}{}^{+10.7}_{-9.7}$	$1.81 \cdot 10^{-8}{}^{+10.7}_{-9.7}$	$1.72 \cdot 10^{-6}{}^{+20.3}_{-19.1}$	$1.05 \cdot 10^{-1}{}^{+17.9}_{-17.2}$
840	$3.24 \cdot 10^{-5}{}^{+15.6}_{-14.4}$	$4.94 \cdot 10^{-6}{}^{+11.5}_{-10.3}$	$1.71 \cdot 10^{-8}{}^{+11.5}_{-10.4}$	$1.62 \cdot 10^{-6}{}^{+21.1}_{-19.8}$	$9.99 \cdot 10^{-2}{}^{+19.3}_{-18.3}$
850	$3.14 \cdot 10^{-5}{}^{+16.1}_{-14.7}$	$4.80 \cdot 10^{-6}{}^{+12.0}_{-10.6}$	$1.66 \cdot 10^{-8}{}^{+12.0}_{-10.7}$	$1.58 \cdot 10^{-6}{}^{+21.6}_{-20.1}$	$9.75 \cdot 10^{-2}{}^{+20.0}_{-18.9}$
860	$3.05 \cdot 10^{-5}{}^{+16.6}_{-15.1}$	$4.67 \cdot 10^{-6}{}^{+12.5}_{-11.0}$	$1.62 \cdot 10^{-8}{}^{+12.4}_{-11.0}$	$1.53 \cdot 10^{-6}{}^{+22.0}_{-20.5}$	$9.52 \cdot 10^{-2}{}^{+20.8}_{-19.5}$
880	$2.88 \cdot 10^{-5}{}^{+17.6}_{-15.8}$	$4.42 \cdot 10^{-6}{}^{+13.5}_{-11.7}$	$1.53 \cdot 10^{-8}{}^{+13.4}_{-11.7}$	$1.44 \cdot 10^{-6}{}^{+23.1}_{-21.2}$	$9.07 \cdot 10^{-2}{}^{+22.4}_{-20.9}$
900	$2.72 \cdot 10^{-5}{}^{+18.8}_{-16.6}$	$4.19 \cdot 10^{-6}{}^{+14.6}_{-12.5}$	$1.45 \cdot 10^{-8}{}^{+14.6}_{-12.4}$	$1.36 \cdot 10^{-6}{}^{+24.3}_{-22.0}$	$8.64 \cdot 10^{-2}{}^{+24.1}_{-22.2}$
920	$2.57 \cdot 10^{-5}{}^{+20.0}_{-17.4}$	$3.97 \cdot 10^{-6}{}^{+15.8}_{-13.3}$	$1.38 \cdot 10^{-8}{}^{+15.8}_{-13.3}$	$1.29 \cdot 10^{-6}{}^{+25.4}_{-22.8}$	$8.23 \cdot 10^{-2}{}^{+26.0}_{-23.7}$
940	$2.43 \cdot 10^{-5}{}^{+21.4}_{-18.2}$	$3.76 \cdot 10^{-6}{}^{+17.1}_{-14.1}$	$1.30 \cdot 10^{-8}{}^{+17.2}_{-14.1}$	$1.22 \cdot 10^{-6}{}^{+26.8}_{-23.7}$	$7.83 \cdot 10^{-2}{}^{+28.0}_{-25.2}$
950	$2.36 \cdot 10^{-5}{}^{+22.1}_{-18.7}$	$3.66 \cdot 10^{-6}{}^{+17.9}_{-14.5}$	$1.27 \cdot 10^{-8}{}^{+17.9}_{-14.5}$	$1.18 \cdot 10^{-6}{}^{+27.6}_{-24.0}$	$7.64 \cdot 10^{-2}{}^{+29.1}_{-26.0}$
960	$2.29 \cdot 10^{-5}{}^{+22.9}_{-19.1}$	$3.56 \cdot 10^{-6}{}^{+18.6}_{-15.0}$	$1.23 \cdot 10^{-8}{}^{+18.7}_{-14.9}$	$1.15 \cdot 10^{-6}{}^{+28.3}_{-24.5}$	$7.45 \cdot 10^{-2}{}^{+30.2}_{-26.8}$
980	$2.17 \cdot 10^{-5}{}^{+24.5}_{-20.1}$	$3.38 \cdot 10^{-6}{}^{+20.2}_{-15.9}$	$1.17 \cdot 10^{-8}{}^{+20.2}_{-15.9}$	$1.08 \cdot 10^{-6}{}^{+29.9}_{-25.4}$	$7.08 \cdot 10^{-2}{}^{+32.6}_{-28.5}$
1000	$2.05 \cdot 10^{-5}{}^{+26.3}_{-21.1}$	$3.20 \cdot 10^{-6}{}^{+22.0}_{-16.9}$	$1.11 \cdot 10^{-8}{}^{+22.0}_{-16.9}$	$1.02 \cdot 10^{-6}{}^{+31.8}_{-26.4}$	$6.73 \cdot 10^{-2}{}^{+35.2}_{-30.3}$

Table A.8: SM Higgs branching ratios to two gauge bosons and Higgs total width together with their total uncertainties (expressed in percentage). Very-low-mass range.

M_H [GeV]	H → gg	H → γγ	H → Zγ	H → WW	H → ZZ	Total Γ_H [GeV]
80	$4.94\cdot10^{-2}{}^{+12.0}_{-11.6}$	$9.18\cdot10^{-4}{}^{+6.3}_{-6.2}$	$0\cdot10^{0}{}^{+0}_{-0}$	$6.27\cdot10^{-4}{}^{+5.9}_{-5.7}$	$1.64\cdot10^{-4}{}^{+5.8}_{-5.6}$	$1.99\cdot10^{-3}{}^{+5.3}_{-5.2}$
81	$5.05\cdot10^{-2}{}^{+12.0}_{-11.6}$	$9.46\cdot10^{-4}{}^{+6.3}_{-6.1}$	$0\cdot10^{0}{}^{+0}_{-0}$	$6.96\cdot10^{-4}{}^{+5.9}_{-5.7}$	$1.81\cdot10^{-4}{}^{+5.8}_{-5.6}$	$2.01\cdot10^{-3}{}^{+5.3}_{-5.2}$
82	$5.17\cdot10^{-2}{}^{+12.0}_{-11.6}$	$9.74\cdot10^{-4}{}^{+6.3}_{-6.2}$	$0\cdot10^{0}{}^{+0}_{-0}$	$7.74\cdot10^{-4}{}^{+5.9}_{-5.7}$	$1.99\cdot10^{-4}{}^{+5.8}_{-5.6}$	$2.04\cdot10^{-3}{}^{+5.3}_{-5.2}$
83	$5.28\cdot10^{-2}{}^{+12.0}_{-11.5}$	$1.00\cdot10^{-3}{}^{+6.4}_{-6.1}$	$0\cdot10^{0}{}^{+0}_{-0}$	$8.61\cdot10^{-4}{}^{+5.8}_{-5.7}$	$2.18\cdot10^{-4}{}^{+5.8}_{-5.6}$	$2.06\cdot10^{-3}{}^{+5.3}_{-5.2}$
84	$5.40\cdot10^{-2}{}^{+12.0}_{-11.5}$	$1.03\cdot10^{-3}{}^{+6.3}_{-6.1}$	$0\cdot10^{0}{}^{+0}_{-0}$	$9.61\cdot10^{-4}{}^{+5.9}_{-5.7}$	$2.40\cdot10^{-4}{}^{+5.8}_{-5.6}$	$2.08\cdot10^{-3}{}^{+5.3}_{-5.2}$
85	$5.51\cdot10^{-2}{}^{+11.9}_{-11.5}$	$1.06\cdot10^{-3}{}^{+6.3}_{-6.2}$	$0\cdot10^{0}{}^{+0}_{-0}$	$1.08\cdot10^{-3}{}^{+5.9}_{-5.7}$	$2.63\cdot10^{-4}{}^{+5.8}_{-5.6}$	$2.11\cdot10^{-3}{}^{+5.3}_{-5.2}$
86	$5.63\cdot10^{-2}{}^{+11.9}_{-11.5}$	$1.09\cdot10^{-3}{}^{+6.3}_{-6.1}$	$0\cdot10^{0}{}^{+0}_{-0}$	$1.21\cdot10^{-3}{}^{+5.9}_{-5.7}$	$2.88\cdot10^{-4}{}^{+5.8}_{-5.6}$	$2.13\cdot10^{-3}{}^{+5.3}_{-5.2}$
87	$5.75\cdot10^{-2}{}^{+11.9}_{-11.5}$	$1.12\cdot10^{-3}{}^{+6.4}_{-6.1}$	$0\cdot10^{0}{}^{+0}_{-0}$	$1.37\cdot10^{-3}{}^{+5.9}_{-5.7}$	$3.16\cdot10^{-4}{}^{+5.8}_{-5.7}$	$2.15\cdot10^{-3}{}^{+5.3}_{-5.2}$
88	$5.87\cdot10^{-2}{}^{+11.9}_{-11.4}$	$1.15\cdot10^{-3}{}^{+6.3}_{-6.2}$	$0\cdot10^{0}{}^{+0}_{-0}$	$1.56\cdot10^{-3}{}^{+5.9}_{-5.7}$	$3.47\cdot10^{-4}{}^{+5.8}_{-5.6}$	$2.18\cdot10^{-3}{}^{+5.3}_{-5.2}$
89	$5.99\cdot10^{-2}{}^{+11.8}_{-11.4}$	$1.19\cdot10^{-3}{}^{+6.3}_{-6.1}$	$0\cdot10^{0}{}^{+0}_{-0}$	$1.79\cdot10^{-3}{}^{+5.8}_{-5.7}$	$3.80\cdot10^{-4}{}^{+5.7}_{-5.6}$	$2.20\cdot10^{-3}{}^{+5.3}_{-5.2}$
90	$6.12\cdot10^{-2}{}^{+11.8}_{-11.4}$	$1.22\cdot10^{-3}{}^{+6.2}_{-6.2}$	$0\cdot10^{0}{}^{+0}_{-0}$	$2.07\cdot10^{-3}{}^{+5.8}_{-5.7}$	$4.17\cdot10^{-4}{}^{+5.8}_{-5.6}$	$2.22\cdot10^{-3}{}^{+5.2}_{-5.2}$
91	$6.24\cdot10^{-2}{}^{+11.8}_{-11.4}$	$1.25\cdot10^{-3}{}^{+6.2}_{-6.2}$	$0\cdot10^{0}{}^{+0}_{-0}$	$2.41\cdot10^{-3}{}^{+5.8}_{-5.7}$	$4.57\cdot10^{-4}{}^{+5.7}_{-5.6}$	$2.25\cdot10^{-3}{}^{+5.3}_{-5.2}$
92	$6.36\cdot10^{-2}{}^{+11.8}_{-11.4}$	$1.29\cdot10^{-3}{}^{+6.2}_{-6.2}$	$5.09\cdot10^{-8}{}^{+10.3}_{-10.1}$	$2.83\cdot10^{-3}{}^{+5.9}_{-5.6}$	$5.02\cdot10^{-4}{}^{+5.8}_{-5.6}$	$2.27\cdot10^{-3}{}^{+5.2}_{-5.2}$
93	$6.49\cdot10^{-2}{}^{+11.8}_{-11.4}$	$1.32\cdot10^{-3}{}^{+6.3}_{-6.1}$	$5.17\cdot10^{-7}{}^{+10.3}_{-10.1}$	$3.33\cdot10^{-3}{}^{+5.8}_{-5.6}$	$5.50\cdot10^{-4}{}^{+5.8}_{-5.6}$	$2.30\cdot10^{-3}{}^{+5.2}_{-5.2}$
94	$6.61\cdot10^{-2}{}^{+11.7}_{-11.3}$	$1.36\cdot10^{-3}{}^{+6.3}_{-6.1}$	$1.85\cdot10^{-6}{}^{+10.3}_{-10.1}$	$3.94\cdot10^{-3}{}^{+5.8}_{-5.7}$	$6.05\cdot10^{-4}{}^{+5.8}_{-5.6}$	$2.32\cdot10^{-3}{}^{+5.2}_{-5.2}$
95	$6.74\cdot10^{-2}{}^{+11.7}_{-11.3}$	$1.39\cdot10^{-3}{}^{+6.3}_{-6.1}$	$4.48\cdot10^{-6}{}^{+10.3}_{-10.1}$	$4.68\cdot10^{-3}{}^{+5.8}_{-5.6}$	$6.65\cdot10^{-4}{}^{+5.7}_{-5.6}$	$2.35\cdot10^{-3}{}^{+5.2}_{-5.1}$
96	$6.87\cdot10^{-2}{}^{+11.7}_{-11.3}$	$1.43\cdot10^{-3}{}^{+6.2}_{-6.1}$	$8.78\cdot10^{-6}{}^{+10.3}_{-10.1}$	$5.55\cdot10^{-3}{}^{+5.8}_{-5.6}$	$7.33\cdot10^{-4}{}^{+5.8}_{-5.6}$	$2.37\cdot10^{-3}{}^{+5.2}_{-5.2}$
97	$6.99\cdot10^{-2}{}^{+11.7}_{-11.3}$	$1.46\cdot10^{-3}{}^{+6.3}_{-6.0}$	$1.51\cdot10^{-5}{}^{+10.2}_{-10.1}$	$6.6\cdot10^{-3}{}^{+5.8}_{-5.6}$	$8.11\cdot10^{-4}{}^{+5.7}_{-5.6}$	$2.40\cdot10^{-3}{}^{+5.2}_{-5.2}$
98	$7.12\cdot10^{-2}{}^{+11.7}_{-11.3}$	$1.50\cdot10^{-3}{}^{+6.3}_{-6.1}$	$2.38\cdot10^{-5}{}^{+10.2}_{-10.1}$	$7.83\cdot10^{-3}{}^{+5.8}_{-5.6}$	$9.00\cdot10^{-4}{}^{+5.7}_{-5.6}$	$2.43\cdot10^{-3}{}^{+5.2}_{-5.1}$
99	$7.24\cdot10^{-2}{}^{+11.6}_{-11.2}$	$1.54\cdot10^{-3}{}^{+6.3}_{-6.0}$	$3.51\cdot10^{-5}{}^{+10.2}_{-10.0}$	$9.28\cdot10^{-3}{}^{+5.8}_{-5.6}$	$1.00\cdot10^{-3}{}^{+5.7}_{-5.5}$	$2.46\cdot10^{-3}{}^{+5.2}_{-5.2}$
100	$7.37\cdot10^{-2}{}^{+11.6}_{-11.2}$	$1.58\cdot10^{-3}{}^{+6.2}_{-6.1}$	$4.93\cdot10^{-5}{}^{+10.2}_{-10.1}$	$1.1\cdot10^{-2}{}^{+5.7}_{-5.6}$	$1.12\cdot10^{-3}{}^{+5.7}_{-5.5}$	$2.48\cdot10^{-3}{}^{+5.1}_{-5.1}$
101	$7.49\cdot10^{-2}{}^{+11.6}_{-11.2}$	$1.61\cdot10^{-3}{}^{+6.2}_{-6.0}$	$6.67\cdot10^{-5}{}^{+10.2}_{-10.0}$	$1.29\cdot10^{-2}{}^{+5.7}_{-5.6}$	$1.26\cdot10^{-3}{}^{+5.7}_{-5.5}$	$2.51\cdot10^{-3}{}^{+5.1}_{-5.1}$
102	$7.61\cdot10^{-2}{}^{+11.5}_{-11.2}$	$1.65\cdot10^{-3}{}^{+6.2}_{-6.0}$	$8.74\cdot10^{-5}{}^{+10.2}_{-10.0}$	$1.52\cdot10^{-2}{}^{+5.7}_{-5.5}$	$1.43\cdot10^{-3}{}^{+5.6}_{-5.5}$	$2.54\cdot10^{-3}{}^{+5.1}_{-5.1}$
103	$7.73\cdot10^{-2}{}^{+11.5}_{-11.1}$	$1.69\cdot10^{-3}{}^{+6.2}_{-6.0}$	$1.12\cdot10^{-4}{}^{+10.1}_{-10.1}$	$1.78\cdot10^{-2}{}^{+5.7}_{-5.5}$	$1.63\cdot10^{-3}{}^{+5.6}_{-5.5}$	$2.58\cdot10^{-3}{}^{+5.1}_{-5.1}$
104	$7.84\cdot10^{-2}{}^{+11.5}_{-11.1}$	$1.73\cdot10^{-3}{}^{+6.1}_{-6.0}$	$1.40\cdot10^{-4}{}^{+10.1}_{-10.0}$	$2.07\cdot10^{-2}{}^{+5.7}_{-5.5}$	$1.86\cdot10^{-3}{}^{+5.7}_{-5.4}$	$2.61\cdot10^{-3}{}^{+5.1}_{-5.1}$
105	$7.95\cdot10^{-2}{}^{+11.4}_{-11.1}$	$1.77\cdot10^{-3}{}^{+6.1}_{-5.9}$	$1.71\cdot10^{-4}{}^{+10.1}_{-9.9}$	$2.41\cdot10^{-2}{}^{+5.6}_{-5.5}$	$2.13\cdot10^{-3}{}^{+5.6}_{-5.5}$	$2.64\cdot10^{-3}{}^{+5.1}_{-5.0}$
106	$8.06\cdot10^{-2}{}^{+11.4}_{-11.0}$	$1.80\cdot10^{-3}{}^{+6.1}_{-5.9}$	$2.07\cdot10^{-4}{}^{+10.1}_{-10.0}$	$2.78\cdot10^{-2}{}^{+5.6}_{-5.4}$	$2.45\cdot10^{-3}{}^{+5.6}_{-5.4}$	$2.68\cdot10^{-3}{}^{+5.0}_{-5.0}$
107	$8.16\cdot10^{-2}{}^{+11.4}_{-11.0}$	$1.84\cdot10^{-3}{}^{+6.0}_{-5.9}$	$2.47\cdot10^{-4}{}^{+10.0}_{-9.9}$	$3.20\cdot10^{-2}{}^{+5.5}_{-5.4}$	$2.83\cdot10^{-3}{}^{+5.5}_{-5.4}$	$2.72\cdot10^{-3}{}^{+5.0}_{-5.0}$
108	$8.26\cdot10^{-2}{}^{+11.3}_{-10.9}$	$1.88\cdot10^{-3}{}^{+6.0}_{-5.9}$	$2.91\cdot10^{-4}{}^{+10.0}_{-9.9}$	$3.67\cdot10^{-2}{}^{+5.5}_{-5.4}$	$3.26\cdot10^{-3}{}^{+5.5}_{-5.4}$	$2.76\cdot10^{-3}{}^{+5.0}_{-4.9}$
109	$8.36\cdot10^{-2}{}^{+11.3}_{-10.9}$	$1.92\cdot10^{-3}{}^{+6.0}_{-5.9}$	$3.39\cdot10^{-4}{}^{+10.0}_{-9.9}$	$4.19\cdot10^{-2}{}^{+5.5}_{-5.3}$	$3.76\cdot10^{-3}{}^{+5.5}_{-5.3}$	$2.80\cdot10^{-3}{}^{+4.9}_{-4.9}$
110	$8.44\cdot10^{-2}{}^{+11.2}_{-10.9}$	$1.95\cdot10^{-3}{}^{+5.9}_{-5.9}$	$3.91\cdot10^{-4}{}^{+9.9}_{-9.8}$	$4.77\cdot10^{-2}{}^{+5.4}_{-5.3}$	$4.34\cdot10^{-3}{}^{+5.4}_{-5.3}$	$2.85\cdot10^{-3}{}^{+4.9}_{-4.9}$
110.5	$8.48\cdot10^{-2}{}^{+11.2}_{-10.9}$	$1.97\cdot10^{-3}{}^{+5.9}_{-5.8}$	$4.19\cdot10^{-4}{}^{+9.9}_{-9.8}$	$5.08\cdot10^{-2}{}^{+5.4}_{-5.3}$	$4.66\cdot10^{-3}{}^{+5.4}_{-5.2}$	$2.87\cdot10^{-3}{}^{+4.9}_{-4.9}$
111	$8.52\cdot10^{-2}{}^{+11.2}_{-10.8}$	$1.99\cdot10^{-3}{}^{+5.9}_{-5.8}$	$4.47\cdot10^{-4}{}^{+9.9}_{-9.8}$	$5.41\cdot10^{-2}{}^{+5.3}_{-5.3}$	$5.01\cdot10^{-3}{}^{+5.3}_{-5.3}$	$2.89\cdot10^{-3}{}^{+4.9}_{-4.8}$
111.5	$8.56\cdot10^{-2}{}^{+11.2}_{-10.8}$	$2.00\cdot10^{-3}{}^{+5.9}_{-5.8}$	$4.77\cdot10^{-4}{}^{+9.9}_{-9.8}$	$5.75\cdot10^{-2}{}^{+5.3}_{-5.2}$	$5.37\cdot10^{-3}{}^{+5.3}_{-5.2}$	$2.92\cdot10^{-3}{}^{+4.9}_{-4.8}$
112	$8.60\cdot10^{-2}{}^{+11.1}_{-10.8}$	$2.02\cdot10^{-3}{}^{+5.9}_{-5.7}$	$5.07\cdot10^{-4}{}^{+9.9}_{-9.7}$	$6.10\cdot10^{-2}{}^{+5.3}_{-5.2}$	$5.76\cdot10^{-3}{}^{+5.3}_{-5.2}$	$2.95\cdot10^{-3}{}^{+4.8}_{-4.8}$
112.5	$8.63\cdot10^{-2}{}^{+11.1}_{-10.8}$	$2.04\cdot10^{-3}{}^{+5.7}_{-5.7}$	$5.39\cdot10^{-4}{}^{+9.9}_{-9.7}$	$6.48\cdot10^{-2}{}^{+5.3}_{-5.2}$	$6.18\cdot10^{-3}{}^{+5.3}_{-5.2}$	$2.97\cdot10^{-3}{}^{+4.8}_{-4.8}$
113	$8.66\cdot10^{-2}{}^{+11.1}_{-10.7}$	$2.05\cdot10^{-3}{}^{+5.8}_{-5.7}$	$5.71\cdot10^{-4}{}^{+9.8}_{-9.7}$	$6.86\cdot10^{-2}{}^{+5.3}_{-5.2}$	$6.62\cdot10^{-3}{}^{+5.3}_{-5.2}$	$3.00\cdot10^{-3}{}^{+4.8}_{-4.7}$
113.5	$8.69\cdot10^{-2}{}^{+11.0}_{-10.7}$	$2.07\cdot10^{-3}{}^{+5.8}_{-5.7}$	$6.04\cdot10^{-4}{}^{+9.8}_{-9.7}$	$7.27\cdot10^{-2}{}^{+5.3}_{-5.1}$	$7.08\cdot10^{-3}{}^{+5.3}_{-5.1}$	$3.03\cdot10^{-3}{}^{+4.8}_{-4.8}$
114	$8.72\cdot10^{-2}{}^{+11.0}_{-10.7}$	$2.08\cdot10^{-3}{}^{+5.8}_{-5.6}$	$6.39\cdot10^{-4}{}^{+9.8}_{-9.7}$	$7.69\cdot10^{-2}{}^{+5.2}_{-5.1}$	$7.57\cdot10^{-3}{}^{+5.2}_{-5.1}$	$3.06\cdot10^{-3}{}^{+4.7}_{-4.7}$
114.5	$8.74\cdot10^{-2}{}^{+11.0}_{-10.6}$	$2.10\cdot10^{-3}{}^{+5.7}_{-5.6}$	$6.74\cdot10^{-4}{}^{+9.7}_{-9.6}$	$8.13\cdot10^{-2}{}^{+5.2}_{-5.1}$	$8.09\cdot10^{-3}{}^{+5.2}_{-5.1}$	$3.09\cdot10^{-3}{}^{+4.7}_{-4.7}$
115	$8.76\cdot10^{-2}{}^{+11.0}_{-10.6}$	$2.11\cdot10^{-3}{}^{+5.7}_{-5.6}$	$7.10\cdot10^{-4}{}^{+9.7}_{-9.6}$	$8.59\cdot10^{-2}{}^{+5.2}_{-5.0}$	$8.64\cdot10^{-3}{}^{+5.2}_{-5.0}$	$3.12\cdot10^{-3}{}^{+4.7}_{-4.7}$
115.5	$8.78\cdot10^{-2}{}^{+10.9}_{-10.6}$	$2.13\cdot10^{-3}{}^{+5.7}_{-5.5}$	$7.46\cdot10^{-4}{}^{+9.7}_{-9.6}$	$9.06\cdot10^{-2}{}^{+5.1}_{-5.0}$	$9.22\cdot10^{-3}{}^{+5.1}_{-5.0}$	$3.15\cdot10^{-3}{}^{+4.7}_{-4.6}$
116	$8.80\cdot10^{-2}{}^{+10.9}_{-10.6}$	$2.14\cdot10^{-3}{}^{+5.6}_{-5.6}$	$7.84\cdot10^{-4}{}^{+9.7}_{-9.6}$	$9.55\cdot10^{-2}{}^{+5.1}_{-5.0}$	$9.83\cdot10^{-3}{}^{+5.1}_{-5.0}$	$3.19\cdot10^{-3}{}^{+4.6}_{-4.6}$
116.5	$8.81\cdot10^{-2}{}^{+10.9}_{-10.5}$	$2.15\cdot10^{-3}{}^{+5.6}_{-5.6}$	$8.22\cdot10^{-4}{}^{+9.6}_{-9.5}$	$1.01\cdot10^{-1}{}^{+5.0}_{-4.9}$	$1.05\cdot10^{-2}{}^{+5.0}_{-4.9}$	$3.22\cdot10^{-3}{}^{+4.6}_{-4.6}$
117	$8.82\cdot10^{-2}{}^{+10.8}_{-10.5}$	$2.17\cdot10^{-3}{}^{+5.6}_{-5.5}$	$8.61\cdot10^{-4}{}^{+9.6}_{-9.5}$	$1.06\cdot10^{-1}{}^{+5.0}_{-4.9}$	$1.11\cdot10^{-2}{}^{+5.0}_{-4.9}$	$3.26\cdot10^{-3}{}^{+4.6}_{-4.6}$
117.5	$8.83\cdot10^{-2}{}^{+10.8}_{-10.5}$	$2.18\cdot10^{-3}{}^{+5.6}_{-5.5}$	$9.00\cdot10^{-4}{}^{+9.6}_{-9.5}$	$1.11\cdot10^{-1}{}^{+5.0}_{-4.8}$	$1.19\cdot10^{-2}{}^{+5.0}_{-4.8}$	$3.30\cdot10^{-3}{}^{+4.5}_{-4.5}$
118	$8.83\cdot10^{-2}{}^{+10.8}_{-10.5}$	$2.19\cdot10^{-3}{}^{+5.5}_{-5.4}$	$9.41\cdot10^{-4}{}^{+9.5}_{-9.4}$	$1.17\cdot10^{-1}{}^{+4.9}_{-4.8}$	$1.26\cdot10^{-2}{}^{+4.9}_{-4.8}$	$3.33\cdot10^{-3}{}^{+4.5}_{-4.5}$

Table A.9: SM Higgs branching ratios to two gauge bosons and Higgs total width together with their total uncertainties (expressed in percentage). Very-low-mass range.

$M_{\rm H}$ [GeV]	H $\to$ gg	H $\to \gamma\gamma$	H $\to$ Zγ	H $\to$ WW	H $\to$ ZZ	Total $\Gamma_{\rm H}$ [GeV]
118.5	$8.84\cdot10^{-2}{}^{+10.7}_{-10.4}$	$2.20\cdot10^{-3}{}^{+5.5}_{-5.4}$	$9.81\cdot10^{-4}{}^{+9.5}_{-9.4}$	$1.23\cdot10^{-1}{}^{+4.9}_{-4.8}$	$1.34\cdot10^{-2}{}^{+4.9}_{-4.8}$	$3.38\cdot10^{-3}{}^{+4.5}_{-4.5}$
119	$8.84\cdot10^{-2}{}^{+10.7}_{-10.4}$	$2.21\cdot10^{-3}{}^{+5.5}_{-5.4}$	$1.02\cdot10^{-3}{}^{+9.5}_{-9.4}$	$1.29\cdot10^{-1}{}^{+4.8}_{-4.7}$	$1.42\cdot10^{-2}{}^{+4.9}_{-4.7}$	$3.42\cdot10^{-3}{}^{+4.4}_{-4.4}$
119.5	$8.83\cdot10^{-2}{}^{+10.7}_{-10.4}$	$2.22\cdot10^{-3}{}^{+5.5}_{-5.3}$	$1.06\cdot10^{-3}{}^{+9.4}_{-9.4}$	$1.35\cdot10^{-1}{}^{+4.8}_{-4.7}$	$1.50\cdot10^{-2}{}^{+4.8}_{-4.7}$	$3.46\cdot10^{-3}{}^{+4.4}_{-4.4}$
120	$8.82\cdot10^{-2}{}^{+10.6}_{-10.3}$	$2.23\cdot10^{-3}{}^{+5.4}_{-5.3}$	$1.11\cdot10^{-3}{}^{+9.4}_{-9.3}$	$1.41\cdot10^{-1}{}^{+4.8}_{-4.7}$	$1.59\cdot10^{-2}{}^{+4.8}_{-4.7}$	$3.51\cdot10^{-3}{}^{+4.4}_{-4.3}$
120.1	$8.82\cdot10^{-2}{}^{+10.6}_{-10.3}$	$2.23\cdot10^{-3}{}^{+5.4}_{-5.3}$	$1.12\cdot10^{-3}{}^{+9.4}_{-9.2}$	$1.43\cdot10^{-1}{}^{+4.8}_{-4.7}$	$1.61\cdot10^{-2}{}^{+4.8}_{-4.7}$	$3.52\cdot10^{-3}{}^{+4.4}_{-4.3}$
120.2	$8.82\cdot10^{-2}{}^{+10.6}_{-10.3}$	$2.23\cdot10^{-3}{}^{+5.4}_{-5.2}$	$1.12\cdot10^{-3}{}^{+9.3}_{-9.3}$	$1.44\cdot10^{-1}{}^{+4.7}_{-4.7}$	$1.62\cdot10^{-2}{}^{+4.7}_{-4.6}$	$3.52\cdot10^{-3}{}^{+4.4}_{-4.3}$
120.3	$8.82\cdot10^{-2}{}^{+10.6}_{-10.3}$	$2.23\cdot10^{-3}{}^{+5.4}_{-5.3}$	$1.13\cdot10^{-3}{}^{+9.3}_{-9.3}$	$1.45\cdot10^{-1}{}^{+4.7}_{-4.6}$	$1.64\cdot10^{-2}{}^{+4.7}_{-4.6}$	$3.53\cdot10^{-3}{}^{+4.3}_{-4.3}$
120.4	$8.82\cdot10^{-2}{}^{+10.6}_{-10.3}$	$2.24\cdot10^{-3}{}^{+5.4}_{-5.3}$	$1.14\cdot10^{-3}{}^{+9.3}_{-9.3}$	$1.47\cdot10^{-1}{}^{+4.7}_{-4.6}$	$1.66\cdot10^{-2}{}^{+4.7}_{-4.6}$	$3.54\cdot10^{-3}{}^{+4.3}_{-4.3}$
120.5	$8.81\cdot10^{-2}{}^{+10.6}_{-10.3}$	$2.24\cdot10^{-3}{}^{+5.4}_{-5.3}$	$1.15\cdot10^{-3}{}^{+9.4}_{-9.2}$	$1.48\cdot10^{-1}{}^{+4.7}_{-4.6}$	$1.68\cdot10^{-2}{}^{+4.7}_{-4.6}$	$3.55\cdot10^{-3}{}^{+4.3}_{-4.3}$
120.6	$8.81\cdot10^{-2}{}^{+10.6}_{-10.3}$	$2.24\cdot10^{-3}{}^{+5.3}_{-5.3}$	$1.16\cdot10^{-3}{}^{+9.2}_{-9.3}$	$1.49\cdot10^{-1}{}^{+4.7}_{-4.6}$	$1.70\cdot10^{-2}{}^{+4.6}_{-4.7}$	$3.56\cdot10^{-3}{}^{+4.3}_{-4.3}$
120.7	$8.81\cdot10^{-2}{}^{+10.6}_{-10.3}$	$2.24\cdot10^{-3}{}^{+5.4}_{-5.2}$	$1.17\cdot10^{-3}{}^{+9.3}_{-9.2}$	$1.51\cdot10^{-1}{}^{+4.7}_{-4.6}$	$1.72\cdot10^{-2}{}^{+4.7}_{-4.6}$	$3.57\cdot10^{-3}{}^{+4.3}_{-4.3}$
120.8	$8.81\cdot10^{-2}{}^{+10.6}_{-10.3}$	$2.24\cdot10^{-3}{}^{+5.3}_{-5.2}$	$1.18\cdot10^{-3}{}^{+9.3}_{-9.3}$	$1.52\cdot10^{-1}{}^{+4.7}_{-4.6}$	$1.73\cdot10^{-2}{}^{+4.7}_{-4.6}$	$3.58\cdot10^{-3}{}^{+4.3}_{-4.3}$
120.9	$8.80\cdot10^{-2}{}^{+10.6}_{-10.3}$	$2.24\cdot10^{-3}{}^{+5.4}_{-5.2}$	$1.18\cdot10^{-3}{}^{+9.3}_{-9.1}$	$1.53\cdot10^{-1}{}^{+4.7}_{-4.6}$	$1.75\cdot10^{-2}{}^{+4.7}_{-4.6}$	$3.59\cdot10^{-3}{}^{+4.3}_{-4.3}$
121	$8.80\cdot10^{-2}{}^{+10.6}_{-10.3}$	$2.25\cdot10^{-3}{}^{+5.3}_{-5.3}$	$1.19\cdot10^{-3}{}^{+9.3}_{-9.3}$	$1.55\cdot10^{-1}{}^{+4.7}_{-4.6}$	$1.77\cdot10^{-2}{}^{+4.7}_{-4.6}$	$3.60\cdot10^{-3}{}^{+4.3}_{-4.3}$
121.1	$8.80\cdot10^{-2}{}^{+10.5}_{-10.3}$	$2.25\cdot10^{-3}{}^{+5.3}_{-5.2}$	$1.20\cdot10^{-3}{}^{+9.3}_{-9.2}$	$1.56\cdot10^{-1}{}^{+4.7}_{-4.6}$	$1.79\cdot10^{-2}{}^{+4.7}_{-4.6}$	$3.61\cdot10^{-3}{}^{+4.3}_{-4.2}$
121.2	$8.79\cdot10^{-2}{}^{+10.5}_{-10.3}$	$2.25\cdot10^{-3}{}^{+5.3}_{-5.2}$	$1.21\cdot10^{-3}{}^{+9.2}_{-9.2}$	$1.57\cdot10^{-1}{}^{+4.6}_{-4.6}$	$1.81\cdot10^{-2}{}^{+4.6}_{-4.6}$	$3.62\cdot10^{-3}{}^{+4.3}_{-4.2}$
121.3	$8.79\cdot10^{-2}{}^{+10.5}_{-10.2}$	$2.25\cdot10^{-3}{}^{+5.3}_{-5.2}$	$1.22\cdot10^{-3}{}^{+9.4}_{-9.1}$	$1.59\cdot10^{-1}{}^{+4.6}_{-4.6}$	$1.83\cdot10^{-2}{}^{+4.6}_{-4.6}$	$3.63\cdot10^{-3}{}^{+4.3}_{-4.2}$
121.4	$8.79\cdot10^{-2}{}^{+10.5}_{-10.2}$	$2.25\cdot10^{-3}{}^{+5.3}_{-5.2}$	$1.23\cdot10^{-3}{}^{+9.3}_{-9.2}$	$1.60\cdot10^{-1}{}^{+4.7}_{-4.5}$	$1.85\cdot10^{-2}{}^{+4.7}_{-4.5}$	$3.64\cdot10^{-3}{}^{+4.3}_{-4.3}$
121.5	$8.78\cdot10^{-2}{}^{+10.5}_{-10.2}$	$2.25\cdot10^{-3}{}^{+5.3}_{-5.2}$	$1.24\cdot10^{-3}{}^{+9.3}_{-9.2}$	$1.61\cdot10^{-1}{}^{+4.6}_{-4.5}$	$1.87\cdot10^{-2}{}^{+4.6}_{-4.5}$	$3.65\cdot10^{-3}{}^{+4.2}_{-4.2}$
121.6	$8.78\cdot10^{-2}{}^{+10.5}_{-10.2}$	$2.25\cdot10^{-3}{}^{+5.3}_{-5.2}$	$1.24\cdot10^{-3}{}^{+9.3}_{-9.1}$	$1.63\cdot10^{-1}{}^{+4.6}_{-4.5}$	$1.89\cdot10^{-2}{}^{+4.6}_{-4.5}$	$3.66\cdot10^{-3}{}^{+4.3}_{-4.2}$
121.7	$8.78\cdot10^{-2}{}^{+10.5}_{-10.2}$	$2.25\cdot10^{-3}{}^{+5.3}_{-5.2}$	$1.25\cdot10^{-3}{}^{+9.3}_{-9.2}$	$1.64\cdot10^{-1}{}^{+4.6}_{-4.5}$	$1.91\cdot10^{-2}{}^{+4.6}_{-4.5}$	$3.67\cdot10^{-3}{}^{+4.2}_{-4.2}$
121.8	$8.77\cdot10^{-2}{}^{+10.5}_{-10.2}$	$2.26\cdot10^{-3}{}^{+5.3}_{-5.1}$	$1.26\cdot10^{-3}{}^{+9.2}_{-9.2}$	$1.66\cdot10^{-1}{}^{+4.6}_{-4.5}$	$1.93\cdot10^{-2}{}^{+4.6}_{-4.5}$	$3.68\cdot10^{-3}{}^{+4.2}_{-4.2}$
121.9	$8.77\cdot10^{-2}{}^{+10.5}_{-10.2}$	$2.26\cdot10^{-3}{}^{+5.3}_{-5.1}$	$1.27\cdot10^{-3}{}^{+9.2}_{-9.1}$	$1.67\cdot10^{-1}{}^{+4.6}_{-4.5}$	$1.95\cdot10^{-2}{}^{+4.6}_{-4.5}$	$3.69\cdot10^{-3}{}^{+4.2}_{-4.2}$
122	$8.76\cdot10^{-2}{}^{+10.5}_{-10.2}$	$2.26\cdot10^{-3}{}^{+5.2}_{-5.1}$	$1.28\cdot10^{-3}{}^{+9.3}_{-9.2}$	$1.69\cdot10^{-1}{}^{+4.6}_{-4.5}$	$1.97\cdot10^{-2}{}^{+4.6}_{-4.5}$	$3.71\cdot10^{-3}{}^{+4.2}_{-4.2}$
122.1	$8.76\cdot10^{-2}{}^{+10.4}_{-10.2}$	$2.26\cdot10^{-3}{}^{+5.2}_{-5.1}$	$1.29\cdot10^{-3}{}^{+9.3}_{-9.0}$	$1.70\cdot10^{-1}{}^{+4.6}_{-4.5}$	$1.99\cdot10^{-2}{}^{+4.6}_{-4.5}$	$3.72\cdot10^{-3}{}^{+4.2}_{-4.2}$
122.2	$8.75\cdot10^{-2}{}^{+10.4}_{-10.2}$	$2.26\cdot10^{-3}{}^{+5.2}_{-5.1}$	$1.30\cdot10^{-3}{}^{+9.2}_{-9.1}$	$1.71\cdot10^{-1}{}^{+4.6}_{-4.5}$	$2.01\cdot10^{-2}{}^{+4.6}_{-4.5}$	$3.73\cdot10^{-3}{}^{+4.2}_{-4.2}$
122.3	$8.75\cdot10^{-2}{}^{+10.4}_{-10.2}$	$2.26\cdot10^{-3}{}^{+5.2}_{-5.1}$	$1.30\cdot10^{-3}{}^{+9.2}_{-9.1}$	$1.73\cdot10^{-1}{}^{+4.6}_{-4.4}$	$2.03\cdot10^{-2}{}^{+4.6}_{-4.4}$	$3.74\cdot10^{-3}{}^{+4.2}_{-4.2}$
122.4	$8.74\cdot10^{-2}{}^{+10.4}_{-10.2}$	$2.26\cdot10^{-3}{}^{+5.2}_{-5.1}$	$1.31\cdot10^{-3}{}^{+9.2}_{-9.1}$	$1.74\cdot10^{-1}{}^{+4.5}_{-4.4}$	$2.05\cdot10^{-2}{}^{+4.5}_{-4.4}$	$3.75\cdot10^{-3}{}^{+4.2}_{-4.1}$
122.5	$8.74\cdot10^{-2}{}^{+10.4}_{-10.2}$	$2.26\cdot10^{-3}{}^{+5.2}_{-5.1}$	$1.32\cdot10^{-3}{}^{+9.2}_{-9.1}$	$1.76\cdot10^{-1}{}^{+4.5}_{-4.4}$	$2.07\cdot10^{-2}{}^{+4.5}_{-4.4}$	$3.76\cdot10^{-3}{}^{+4.2}_{-4.1}$
122.6	$8.73\cdot10^{-2}{}^{+10.4}_{-10.2}$	$2.26\cdot10^{-3}{}^{+5.2}_{-5.1}$	$1.33\cdot10^{-3}{}^{+9.2}_{-9.1}$	$1.77\cdot10^{-1}{}^{+4.5}_{-4.5}$	$2.10\cdot10^{-2}{}^{+4.5}_{-4.5}$	$3.77\cdot10^{-3}{}^{+4.2}_{-4.1}$
122.7	$8.73\cdot10^{-2}{}^{+10.4}_{-10.1}$	$2.26\cdot10^{-3}{}^{+5.2}_{-5.1}$	$1.34\cdot10^{-3}{}^{+9.3}_{-9.0}$	$1.79\cdot10^{-1}{}^{+4.5}_{-4.4}$	$2.12\cdot10^{-2}{}^{+4.5}_{-4.4}$	$3.78\cdot10^{-3}{}^{+4.1}_{-4.1}$
122.8	$8.72\cdot10^{-2}{}^{+10.4}_{-10.1}$	$2.27\cdot10^{-3}{}^{+5.2}_{-5.1}$	$1.35\cdot10^{-3}{}^{+9.2}_{-9.1}$	$1.80\cdot10^{-1}{}^{+4.5}_{-4.4}$	$2.14\cdot10^{-2}{}^{+4.5}_{-4.4}$	$3.79\cdot10^{-3}{}^{+4.2}_{-4.1}$
122.9	$8.72\cdot10^{-2}{}^{+10.4}_{-10.1}$	$2.27\cdot10^{-3}{}^{+5.2}_{-5.1}$	$1.36\cdot10^{-3}{}^{+9.1}_{-9.1}$	$1.82\cdot10^{-1}{}^{+4.5}_{-4.4}$	$2.16\cdot10^{-2}{}^{+4.5}_{-4.4}$	$3.81\cdot10^{-3}{}^{+4.1}_{-4.1}$
123	$8.71\cdot10^{-2}{}^{+10.4}_{-10.1}$	$2.27\cdot10^{-3}{}^{+5.1}_{-5.1}$	$1.36\cdot10^{-3}{}^{+9.2}_{-9.0}$	$1.83\cdot10^{-1}{}^{+4.5}_{-4.4}$	$2.18\cdot10^{-2}{}^{+4.5}_{-4.4}$	$3.82\cdot10^{-3}{}^{+4.2}_{-4.1}$
123.1	$8.71\cdot10^{-2}{}^{+10.4}_{-10.1}$	$2.27\cdot10^{-3}{}^{+5.1}_{-5.1}$	$1.37\cdot10^{-3}{}^{+9.2}_{-9.0}$	$1.85\cdot10^{-1}{}^{+4.5}_{-4.4}$	$2.20\cdot10^{-2}{}^{+4.4}_{-4.4}$	$3.83\cdot10^{-3}{}^{+4.1}_{-4.1}$
123.2	$8.70\cdot10^{-2}{}^{+10.4}_{-10.1}$	$2.27\cdot10^{-3}{}^{+5.2}_{-5.0}$	$1.38\cdot10^{-3}{}^{+9.1}_{-9.0}$	$1.86\cdot10^{-1}{}^{+4.5}_{-4.4}$	$2.22\cdot10^{-2}{}^{+4.5}_{-4.4}$	$3.84\cdot10^{-3}{}^{+4.1}_{-4.1}$
123.3	$8.69\cdot10^{-2}{}^{+10.4}_{-10.1}$	$2.27\cdot10^{-3}{}^{+5.1}_{-5.0}$	$1.39\cdot10^{-3}{}^{+9.1}_{-9.0}$	$1.88\cdot10^{-1}{}^{+4.5}_{-4.3}$	$2.25\cdot10^{-2}{}^{+4.5}_{-4.3}$	$3.85\cdot10^{-3}{}^{+4.1}_{-4.1}$
123.4	$8.69\cdot10^{-2}{}^{+10.3}_{-10.1}$	$2.27\cdot10^{-3}{}^{+5.1}_{-5.1}$	$1.40\cdot10^{-3}{}^{+9.1}_{-9.0}$	$1.89\cdot10^{-1}{}^{+4.4}_{-4.4}$	$2.27\cdot10^{-2}{}^{+4.4}_{-4.4}$	$3.86\cdot10^{-3}{}^{+4.1}_{-4.1}$
123.5	$8.68\cdot10^{-2}{}^{+10.4}_{-10.1}$	$2.27\cdot10^{-3}{}^{+5.1}_{-5.0}$	$1.41\cdot10^{-3}{}^{+9.1}_{-9.1}$	$1.91\cdot10^{-1}{}^{+4.4}_{-4.3}$	$2.29\cdot10^{-2}{}^{+4.4}_{-4.3}$	$3.88\cdot10^{-3}{}^{+4.1}_{-4.1}$
123.6	$8.68\cdot10^{-2}{}^{+10.3}_{-10.1}$	$2.27\cdot10^{-3}{}^{+5.1}_{-5.0}$	$1.42\cdot10^{-3}{}^{+9.1}_{-9.1}$	$1.92\cdot10^{-1}{}^{+4.4}_{-4.3}$	$2.31\cdot10^{-2}{}^{+4.4}_{-4.3}$	$3.89\cdot10^{-3}{}^{+4.1}_{-4.0}$
123.7	$8.67\cdot10^{-2}{}^{+10.3}_{-10.1}$	$2.27\cdot10^{-3}{}^{+5.1}_{-5.0}$	$1.43\cdot10^{-3}{}^{+9.1}_{-8.9}$	$1.94\cdot10^{-1}{}^{+4.4}_{-4.3}$	$2.34\cdot10^{-2}{}^{+4.4}_{-4.3}$	$3.90\cdot10^{-3}{}^{+4.1}_{-4.0}$
123.8	$8.66\cdot10^{-2}{}^{+10.3}_{-10.1}$	$2.27\cdot10^{-3}{}^{+5.1}_{-5.0}$	$1.44\cdot10^{-3}{}^{+9.1}_{-9.0}$	$1.95\cdot10^{-1}{}^{+4.4}_{-4.3}$	$2.36\cdot10^{-2}{}^{+4.4}_{-4.3}$	$3.91\cdot10^{-3}{}^{+4.1}_{-4.1}$
123.9	$8.65\cdot10^{-2}{}^{+10.3}_{-10.1}$	$2.27\cdot10^{-3}{}^{+5.1}_{-5.0}$	$1.44\cdot10^{-3}{}^{+9.2}_{-8.9}$	$1.97\cdot10^{-1}{}^{+4.4}_{-4.3}$	$2.38\cdot10^{-2}{}^{+4.4}_{-4.3}$	$3.93\cdot10^{-3}{}^{+4.1}_{-4.0}$
124	$8.65\cdot10^{-2}{}^{+10.3}_{-10.0}$	$2.27\cdot10^{-3}{}^{+5.1}_{-5.0}$	$1.45\cdot10^{-3}{}^{+9.1}_{-9.0}$	$1.99\cdot10^{-1}{}^{+4.4}_{-4.3}$	$2.41\cdot10^{-2}{}^{+4.4}_{-4.3}$	$3.94\cdot10^{-3}{}^{+4.0}_{-4.0}$
124.1	$8.64\cdot10^{-2}{}^{+10.3}_{-10.1}$	$2.28\cdot10^{-3}{}^{+5.0}_{-5.0}$	$1.46\cdot10^{-3}{}^{+9.0}_{-9.0}$	$2.00\cdot10^{-1}{}^{+4.4}_{-4.3}$	$2.43\cdot10^{-2}{}^{+4.4}_{-4.3}$	$3.95\cdot10^{-3}{}^{+4.0}_{-4.0}$
124.2	$8.63\cdot10^{-2}{}^{+10.3}_{-10.0}$	$2.28\cdot10^{-3}{}^{+5.1}_{-5.0}$	$1.47\cdot10^{-3}{}^{+9.1}_{-8.9}$	$2.02\cdot10^{-1}{}^{+4.3}_{-4.3}$	$2.45\cdot10^{-2}{}^{+4.3}_{-4.3}$	$3.96\cdot10^{-3}{}^{+4.0}_{-4.0}$
124.3	$8.63\cdot10^{-2}{}^{+10.3}_{-10.0}$	$2.28\cdot10^{-3}{}^{+5.0}_{-5.0}$	$1.48\cdot10^{-3}{}^{+9.0}_{-8.9}$	$2.03\cdot10^{-1}{}^{+4.3}_{-4.3}$	$2.48\cdot10^{-2}{}^{+4.3}_{-4.3}$	$3.98\cdot10^{-3}{}^{+4.0}_{-4.0}$

Table A.10: SM Higgs branching ratios to two gauge bosons and Higgs total width together with their total uncertainties (expressed in percentage). Very-low-mass range.

M_H [GeV]	H → gg	H → γγ	H → Zγ	H → WW	H → ZZ	Total Γ_H [GeV]
124.4	$8.62\cdot10^{-2}{}^{+10.3}_{-10.0}$	$2.28\cdot10^{-3}{}^{+5.0}_{-5.0}$	$1.49\cdot10^{-3}{}^{+9.0}_{-9.0}$	$2.05\cdot10^{-1}{}^{+4.3}_{-4.2}$	$2.5\cdot10^{-2}{}^{+4.3}_{-4.3}$	$3.99\cdot10^{-3}{}^{+4.0}_{-4.0}$
124.5	$8.61\cdot10^{-2}{}^{+10.3}_{-10.0}$	$2.28\cdot10^{-3}{}^{+5.1}_{-4.9}$	$1.50\cdot10^{-3}{}^{+9.0}_{-8.9}$	$2.06\cdot10^{-1}{}^{+4.3}_{-4.3}$	$2.52\cdot10^{-2}{}^{+4.3}_{-4.2}$	$4.00\cdot10^{-3}{}^{+4.0}_{-4.0}$
124.6	$8.60\cdot10^{-2}{}^{+10.3}_{-10.0}$	$2.28\cdot10^{-3}{}^{+5.0}_{-5.0}$	$1.5\cdot10^{-3}{}^{+9.0}_{-9.0}$	$2.08\cdot10^{-1}{}^{+4.3}_{-4.2}$	$2.55\cdot10^{-2}{}^{+4.3}_{-4.2}$	$4.02\cdot10^{-3}{}^{+4.0}_{-4.0}$
124.7	$8.59\cdot10^{-2}{}^{+10.3}_{-10.0}$	$2.28\cdot10^{-3}{}^{+5.0}_{-4.9}$	$1.51\cdot10^{-3}{}^{+9.0}_{-8.9}$	$2.10\cdot10^{-1}{}^{+4.3}_{-4.2}$	$2.57\cdot10^{-2}{}^{+4.3}_{-4.2}$	$4.03\cdot10^{-3}{}^{+4.0}_{-4.0}$
124.8	$8.59\cdot10^{-2}{}^{+10.2}_{-10.0}$	$2.28\cdot10^{-3}{}^{+5.0}_{-4.9}$	$1.52\cdot10^{-3}{}^{+9.0}_{-8.9}$	$2.11\cdot10^{-1}{}^{+4.3}_{-4.2}$	$2.59\cdot10^{-2}{}^{+4.3}_{-4.3}$	$4.04\cdot10^{-3}{}^{+4.0}_{-3.9}$
124.9	$8.58\cdot10^{-2}{}^{+10.2}_{-10.0}$	$2.28\cdot10^{-3}{}^{+5.0}_{-4.9}$	$1.53\cdot10^{-3}{}^{+8.9}_{-8.9}$	$2.13\cdot10^{-1}{}^{+4.3}_{-4.2}$	$2.62\cdot10^{-2}{}^{+4.3}_{-4.2}$	$4.06\cdot10^{-3}{}^{+3.9}_{-3.9}$
125	$8.57\cdot10^{-2}{}^{+10.2}_{-10.0}$	$2.28\cdot10^{-3}{}^{+5.0}_{-4.9}$	$1.54\cdot10^{-3}{}^{+9.0}_{-8.9}$	$2.15\cdot10^{-1}{}^{+4.3}_{-4.2}$	$2.64\cdot10^{-2}{}^{+4.3}_{-4.2}$	$4.07\cdot10^{-3}{}^{+4.0}_{-3.9}$
125.1	$8.56\cdot10^{-2}{}^{+10.2}_{-10.0}$	$2.28\cdot10^{-3}{}^{+4.9}_{-4.9}$	$1.55\cdot10^{-3}{}^{+8.9}_{-8.9}$	$2.16\cdot10^{-1}{}^{+4.2}_{-4.2}$	$2.67\cdot10^{-2}{}^{+4.2}_{-4.2}$	$4.08\cdot10^{-3}{}^{+3.9}_{-3.9}$
125.2	$8.55\cdot10^{-2}{}^{+10.2}_{-10.0}$	$2.28\cdot10^{-3}{}^{+4.9}_{-4.9}$	$1.56\cdot10^{-3}{}^{+9.0}_{-8.8}$	$2.18\cdot10^{-1}{}^{+4.2}_{-4.2}$	$2.69\cdot10^{-2}{}^{+4.2}_{-4.2}$	$4.10\cdot10^{-3}{}^{+3.9}_{-3.9}$
125.3	$8.54\cdot10^{-2}{}^{+10.2}_{-9.9}$	$2.28\cdot10^{-3}{}^{+4.9}_{-4.9}$	$1.56\cdot10^{-3}{}^{+9.0}_{-8.8}$	$2.19\cdot10^{-1}{}^{+4.2}_{-4.2}$	$2.72\cdot10^{-2}{}^{+4.2}_{-4.2}$	$4.11\cdot10^{-3}{}^{+3.9}_{-3.9}$
125.4	$8.53\cdot10^{-2}{}^{+10.2}_{-9.9}$	$2.28\cdot10^{-3}{}^{+4.9}_{-4.9}$	$1.57\cdot10^{-3}{}^{+8.9}_{-8.9}$	$2.21\cdot10^{-1}{}^{+4.2}_{-4.2}$	$2.74\cdot10^{-2}{}^{+4.2}_{-4.1}$	$4.12\cdot10^{-3}{}^{+3.9}_{-3.9}$
125.5	$8.52\cdot10^{-2}{}^{+10.2}_{-9.9}$	$2.28\cdot10^{-3}{}^{+4.9}_{-4.9}$	$1.58\cdot10^{-3}{}^{+8.9}_{-8.8}$	$2.23\cdot10^{-1}{}^{+4.2}_{-4.1}$	$2.76\cdot10^{-2}{}^{+4.2}_{-4.1}$	$4.14\cdot10^{-3}{}^{+3.9}_{-3.9}$
125.6	$8.52\cdot10^{-2}{}^{+10.2}_{-9.9}$	$2.28\cdot10^{-3}{}^{+4.9}_{-4.9}$	$1.59\cdot10^{-3}{}^{+8.9}_{-8.9}$	$2.24\cdot10^{-1}{}^{+4.2}_{-4.1}$	$2.79\cdot10^{-2}{}^{+4.2}_{-4.1}$	$4.15\cdot10^{-3}{}^{+3.9}_{-3.9}$
125.7	$8.51\cdot10^{-2}{}^{+10.2}_{-9.9}$	$2.28\cdot10^{-3}{}^{+4.9}_{-4.9}$	$1.6\cdot10^{-3}{}^{+8.9}_{-8.8}$	$2.26\cdot10^{-1}{}^{+4.2}_{-4.1}$	$2.81\cdot10^{-2}{}^{+4.2}_{-4.1}$	$4.17\cdot10^{-3}{}^{+3.9}_{-3.9}$
125.8	$8.50\cdot10^{-2}{}^{+10.1}_{-9.9}$	$2.28\cdot10^{-3}{}^{+4.9}_{-4.9}$	$1.61\cdot10^{-3}{}^{+8.9}_{-8.9}$	$2.28\cdot10^{-1}{}^{+4.2}_{-4.1}$	$2.84\cdot10^{-2}{}^{+4.1}_{-4.1}$	$4.18\cdot10^{-3}{}^{+3.9}_{-3.8}$
125.9	$8.49\cdot10^{-2}{}^{+10.1}_{-9.9}$	$2.28\cdot10^{-3}{}^{+4.8}_{-4.9}$	$1.62\cdot10^{-3}{}^{+8.9}_{-8.8}$	$2.29\cdot10^{-1}{}^{+4.2}_{-4.1}$	$2.87\cdot10^{-2}{}^{+4.1}_{-4.1}$	$4.20\cdot10^{-3}{}^{+3.9}_{-3.8}$
126	$8.48\cdot10^{-2}{}^{+10.1}_{-9.9}$	$2.28\cdot10^{-3}{}^{+4.9}_{-4.8}$	$1.62\cdot10^{-3}{}^{+8.8}_{-8.8}$	$2.31\cdot10^{-1}{}^{+4.1}_{-4.1}$	$2.89\cdot10^{-2}{}^{+4.1}_{-4.1}$	$4.21\cdot10^{-3}{}^{+3.9}_{-3.8}$
126.1	$8.47\cdot10^{-2}{}^{+10.1}_{-9.9}$	$2.28\cdot10^{-3}{}^{+4.9}_{-4.8}$	$1.63\cdot10^{-3}{}^{+8.8}_{-8.8}$	$2.33\cdot10^{-1}{}^{+4.1}_{-4.1}$	$2.92\cdot10^{-2}{}^{+4.2}_{-4.1}$	$4.23\cdot10^{-3}{}^{+3.9}_{-3.8}$
126.2	$8.46\cdot10^{-2}{}^{+10.1}_{-9.9}$	$2.28\cdot10^{-3}{}^{+4.8}_{-4.8}$	$1.64\cdot10^{-3}{}^{+8.9}_{-8.7}$	$2.35\cdot10^{-1}{}^{+4.1}_{-4.1}$	$2.94\cdot10^{-2}{}^{+4.1}_{-4.1}$	$4.24\cdot10^{-3}{}^{+3.8}_{-3.8}$
126.3	$8.45\cdot10^{-2}{}^{+10.1}_{-9.9}$	$2.28\cdot10^{-3}{}^{+4.8}_{-4.8}$	$1.65\cdot10^{-3}{}^{+8.8}_{-8.8}$	$2.36\cdot10^{-1}{}^{+4.1}_{-4.0}$	$2.97\cdot10^{-2}{}^{+4.1}_{-4.0}$	$4.26\cdot10^{-3}{}^{+3.8}_{-3.8}$
126.4	$8.44\cdot10^{-2}{}^{+10.1}_{-9.9}$	$2.28\cdot10^{-3}{}^{+4.8}_{-4.7}$	$1.66\cdot10^{-3}{}^{+8.9}_{-8.7}$	$2.38\cdot10^{-1}{}^{+4.1}_{-4.0}$	$2.99\cdot10^{-2}{}^{+4.1}_{-4.0}$	$4.27\cdot10^{-3}{}^{+3.8}_{-3.8}$
126.5	$8.42\cdot10^{-2}{}^{+10.1}_{-9.8}$	$2.28\cdot10^{-3}{}^{+4.8}_{-4.7}$	$1.67\cdot10^{-3}{}^{+8.8}_{-8.8}$	$2.40\cdot10^{-1}{}^{+4.1}_{-4.0}$	$3.02\cdot10^{-2}{}^{+4.1}_{-4.0}$	$4.29\cdot10^{-3}{}^{+3.8}_{-3.8}$
126.6	$8.42\cdot10^{-2}{}^{+10.1}_{-9.9}$	$2.28\cdot10^{-3}{}^{+4.8}_{-4.8}$	$1.68\cdot10^{-3}{}^{+8.8}_{-8.8}$	$2.41\cdot10^{-1}{}^{+4.1}_{-4.0}$	$3.04\cdot10^{-2}{}^{+4.1}_{-4.0}$	$4.30\cdot10^{-3}{}^{+3.8}_{-3.8}$
126.7	$8.40\cdot10^{-2}{}^{+10.1}_{-9.8}$	$2.28\cdot10^{-3}{}^{+4.8}_{-4.7}$	$1.68\cdot10^{-3}{}^{+8.8}_{-8.7}$	$2.43\cdot10^{-1}{}^{+4.1}_{-4.0}$	$3.07\cdot10^{-2}{}^{+4.1}_{-4.0}$	$4.32\cdot10^{-3}{}^{+3.8}_{-3.8}$
126.8	$8.39\cdot10^{-2}{}^{+10.1}_{-9.8}$	$2.28\cdot10^{-3}{}^{+4.8}_{-4.7}$	$1.69\cdot10^{-3}{}^{+8.8}_{-8.7}$	$2.45\cdot10^{-1}{}^{+4.1}_{-4.0}$	$3.10\cdot10^{-2}{}^{+4.1}_{-4.0}$	$4.33\cdot10^{-3}{}^{+3.8}_{-3.8}$
126.9	$8.38\cdot10^{-2}{}^{+10.1}_{-9.8}$	$2.27\cdot10^{-3}{}^{+4.8}_{-4.7}$	$1.70\cdot10^{-3}{}^{+8.8}_{-8.7}$	$2.47\cdot10^{-1}{}^{+4.0}_{-4.0}$	$3.12\cdot10^{-2}{}^{+4.0}_{-4.0}$	$4.35\cdot10^{-3}{}^{+3.8}_{-3.7}$
127	$8.37\cdot10^{-2}{}^{+10.1}_{-9.8}$	$2.27\cdot10^{-3}{}^{+4.8}_{-4.7}$	$1.71\cdot10^{-3}{}^{+8.8}_{-8.7}$	$2.48\cdot10^{-1}{}^{+4.0}_{-4.0}$	$3.15\cdot10^{-2}{}^{+4.0}_{-4.0}$	$4.36\cdot10^{-3}{}^{+3.8}_{-3.7}$
127.1	$8.36\cdot10^{-2}{}^{+10.0}_{-9.8}$	$2.27\cdot10^{-3}{}^{+4.8}_{-4.7}$	$1.72\cdot10^{-3}{}^{+8.7}_{-8.7}$	$2.50\cdot10^{-1}{}^{+4.0}_{-4.0}$	$3.18\cdot10^{-2}{}^{+4.0}_{-4.0}$	$4.38\cdot10^{-3}{}^{+3.8}_{-3.7}$
127.2	$8.35\cdot10^{-2}{}^{+10.0}_{-9.8}$	$2.27\cdot10^{-3}{}^{+4.8}_{-4.7}$	$1.73\cdot10^{-3}{}^{+8.8}_{-8.7}$	$2.52\cdot10^{-1}{}^{+4.0}_{-3.9}$	$3.20\cdot10^{-2}{}^{+4.0}_{-3.9}$	$4.40\cdot10^{-3}{}^{+3.8}_{-3.7}$
127.3	$8.34\cdot10^{-2}{}^{+10.0}_{-9.8}$	$2.27\cdot10^{-3}{}^{+4.7}_{-4.7}$	$1.73\cdot10^{-3}{}^{+8.8}_{-8.7}$	$2.54\cdot10^{-1}{}^{+4.0}_{-3.9}$	$3.23\cdot10^{-2}{}^{+4.0}_{-3.9}$	$4.41\cdot10^{-3}{}^{+3.7}_{-3.7}$
127.4	$8.32\cdot10^{-2}{}^{+10.0}_{-9.8}$	$2.27\cdot10^{-3}{}^{+4.8}_{-4.7}$	$1.74\cdot10^{-3}{}^{+8.8}_{-8.6}$	$2.55\cdot10^{-1}{}^{+4.0}_{-3.9}$	$3.26\cdot10^{-2}{}^{+4.0}_{-3.9}$	$4.43\cdot10^{-3}{}^{+3.7}_{-3.7}$
127.5	$8.31\cdot10^{-2}{}^{+10.0}_{-9.8}$	$2.27\cdot10^{-3}{}^{+4.7}_{-4.7}$	$1.75\cdot10^{-3}{}^{+8.7}_{-8.6}$	$2.57\cdot10^{-1}{}^{+4.0}_{-3.9}$	$3.28\cdot10^{-2}{}^{+4.0}_{-3.9}$	$4.45\cdot10^{-3}{}^{+3.7}_{-3.7}$
127.6	$8.30\cdot10^{-2}{}^{+10.0}_{-9.8}$	$2.27\cdot10^{-3}{}^{+4.7}_{-4.7}$	$1.76\cdot10^{-3}{}^{+8.7}_{-8.7}$	$2.59\cdot10^{-1}{}^{+4.0}_{-3.9}$	$3.31\cdot10^{-2}{}^{+4.0}_{-3.9}$	$4.46\cdot10^{-3}{}^{+3.7}_{-3.7}$
127.7	$8.29\cdot10^{-2}{}^{+10.0}_{-9.8}$	$2.27\cdot10^{-3}{}^{+4.7}_{-4.7}$	$1.77\cdot10^{-3}{}^{+8.7}_{-8.7}$	$2.61\cdot10^{-1}{}^{+3.9}_{-3.9}$	$3.34\cdot10^{-2}{}^{+3.9}_{-3.9}$	$4.48\cdot10^{-3}{}^{+3.7}_{-3.7}$
127.8	$8.28\cdot10^{-2}{}^{+10.0}_{-9.7}$	$2.27\cdot10^{-3}{}^{+4.7}_{-4.6}$	$1.77\cdot10^{-3}{}^{+8.7}_{-8.6}$	$2.62\cdot10^{-1}{}^{+4.0}_{-3.9}$	$3.36\cdot10^{-2}{}^{+4.0}_{-3.9}$	$4.50\cdot10^{-3}{}^{+3.7}_{-3.7}$
127.9	$8.26\cdot10^{-2}{}^{+10.0}_{-9.7}$	$2.27\cdot10^{-3}{}^{+4.7}_{-4.6}$	$1.78\cdot10^{-3}{}^{+8.6}_{-8.6}$	$2.64\cdot10^{-1}{}^{+3.9}_{-3.9}$	$3.39\cdot10^{-2}{}^{+3.9}_{-3.9}$	$4.51\cdot10^{-3}{}^{+3.7}_{-3.7}$
128	$8.25\cdot10^{-2}{}^{+10.0}_{-9.7}$	$2.27\cdot10^{-3}{}^{+4.7}_{-4.7}$	$1.79\cdot10^{-3}{}^{+8.7}_{-8.6}$	$2.66\cdot10^{-1}{}^{+3.9}_{-3.8}$	$3.42\cdot10^{-2}{}^{+3.9}_{-3.8}$	$4.53\cdot10^{-3}{}^{+3.7}_{-3.6}$
128.1	$8.24\cdot10^{-2}{}^{+10.0}_{-9.7}$	$2.27\cdot10^{-3}{}^{+4.7}_{-4.6}$	$1.8\cdot10^{-3}{}^{+8.6}_{-8.6}$	$2.68\cdot10^{-1}{}^{+3.9}_{-3.8}$	$3.45\cdot10^{-2}{}^{+3.9}_{-3.8}$	$4.55\cdot10^{-3}{}^{+3.7}_{-3.6}$
128.2	$8.23\cdot10^{-2}{}^{+9.9}_{-9.7}$	$2.27\cdot10^{-3}{}^{+4.7}_{-4.6}$	$1.81\cdot10^{-3}{}^{+8.6}_{-8.6}$	$2.70\cdot10^{-1}{}^{+3.9}_{-3.8}$	$3.47\cdot10^{-2}{}^{+3.9}_{-3.8}$	$4.57\cdot10^{-3}{}^{+3.7}_{-3.6}$
128.3	$8.21\cdot10^{-2}{}^{+9.9}_{-9.7}$	$2.26\cdot10^{-3}{}^{+4.7}_{-4.6}$	$1.81\cdot10^{-3}{}^{+8.6}_{-8.6}$	$2.71\cdot10^{-1}{}^{+3.9}_{-3.8}$	$3.50\cdot10^{-2}{}^{+3.9}_{-3.8}$	$4.58\cdot10^{-3}{}^{+3.6}_{-3.6}$
128.4	$8.20\cdot10^{-2}{}^{+9.9}_{-9.7}$	$2.26\cdot10^{-3}{}^{+4.6}_{-4.6}$	$1.82\cdot10^{-3}{}^{+8.6}_{-8.6}$	$2.73\cdot10^{-1}{}^{+3.9}_{-3.8}$	$3.53\cdot10^{-2}{}^{+3.9}_{-3.8}$	$4.60\cdot10^{-3}{}^{+3.6}_{-3.6}$
128.5	$8.19\cdot10^{-2}{}^{+9.9}_{-9.7}$	$2.26\cdot10^{-3}{}^{+4.6}_{-4.6}$	$1.83\cdot10^{-3}{}^{+8.6}_{-8.6}$	$2.75\cdot10^{-1}{}^{+3.8}_{-3.8}$	$3.56\cdot10^{-2}{}^{+3.8}_{-3.8}$	$4.62\cdot10^{-3}{}^{+3.6}_{-3.6}$
128.6	$8.17\cdot10^{-2}{}^{+9.9}_{-9.7}$	$2.26\cdot10^{-3}{}^{+4.6}_{-4.6}$	$1.84\cdot10^{-3}{}^{+8.6}_{-8.6}$	$2.77\cdot10^{-1}{}^{+3.8}_{-3.8}$	$3.58\cdot10^{-2}{}^{+3.8}_{-3.8}$	$4.64\cdot10^{-3}{}^{+3.6}_{-3.6}$
128.7	$8.16\cdot10^{-2}{}^{+9.9}_{-9.7}$	$2.26\cdot10^{-3}{}^{+4.6}_{-4.6}$	$1.85\cdot10^{-3}{}^{+8.6}_{-8.5}$	$2.79\cdot10^{-1}{}^{+3.8}_{-3.8}$	$3.61\cdot10^{-2}{}^{+3.8}_{-3.8}$	$4.65\cdot10^{-3}{}^{+3.6}_{-3.5}$
128.8	$8.15\cdot10^{-2}{}^{+9.9}_{-9.7}$	$2.26\cdot10^{-3}{}^{+4.6}_{-4.6}$	$1.85\cdot10^{-3}{}^{+8.5}_{-8.6}$	$2.81\cdot10^{-1}{}^{+3.8}_{-3.8}$	$3.64\cdot10^{-2}{}^{+3.8}_{-3.8}$	$4.67\cdot10^{-3}{}^{+3.6}_{-3.6}$
128.9	$8.13\cdot10^{-2}{}^{+9.9}_{-9.7}$	$2.26\cdot10^{-3}{}^{+4.6}_{-4.6}$	$1.86\cdot10^{-3}{}^{+8.6}_{-8.5}$	$2.82\cdot10^{-1}{}^{+3.8}_{-3.7}$	$3.67\cdot10^{-2}{}^{+3.8}_{-3.7}$	$4.69\cdot10^{-3}{}^{+3.6}_{-3.6}$
129	$8.12\cdot10^{-2}{}^{+9.9}_{-9.6}$	$2.26\cdot10^{-3}{}^{+4.6}_{-4.5}$	$1.87\cdot10^{-3}{}^{+8.6}_{-8.5}$	$2.84\cdot10^{-1}{}^{+3.8}_{-3.7}$	$3.70\cdot10^{-2}{}^{+3.8}_{-3.7}$	$4.71\cdot10^{-3}{}^{+3.6}_{-3.5}$

Table A.11: SM Higgs branching ratios to two gauge bosons and Higgs total width together with their total uncertainties (expressed in percentage). Very-low-mass range.

M_H [GeV]	H → gg	H → γγ	H → Zγ	H → WW	H → ZZ	Total Γ_H [GeV]
129.1	$8.10 \cdot 10^{-2}{}^{+9.9}_{-9.6}$	$2.26 \cdot 10^{-3}{}^{+4.6}_{-4.5}$	$1.88 \cdot 10^{-3}{}^{+8.5}_{-8.5}$	$2.86 \cdot 10^{-1}{}^{+3.8}_{-3.7}$	$3.73 \cdot 10^{-2}{}^{+3.8}_{-3.7}$	$4.73 \cdot 10^{-3}{}^{+3.6}_{-3.5}$
129.2	$8.09 \cdot 10^{-2}{}^{+9.8}_{-9.6}$	$2.26 \cdot 10^{-3}{}^{+4.5}_{-4.5}$	$1.89 \cdot 10^{-3}{}^{+8.5}_{-8.5}$	$2.88 \cdot 10^{-1}{}^{+3.8}_{-3.7}$	$3.75 \cdot 10^{-2}{}^{+3.8}_{-3.7}$	$4.75 \cdot 10^{-3}{}^{+3.5}_{-3.5}$
129.3	$8.08 \cdot 10^{-2}{}^{+9.8}_{-9.6}$	$2.25 \cdot 10^{-3}{}^{+4.5}_{-4.5}$	$1.89 \cdot 10^{-3}{}^{+8.5}_{-8.5}$	$2.90 \cdot 10^{-1}{}^{+3.7}_{-3.7}$	$3.78 \cdot 10^{-2}{}^{+3.7}_{-3.7}$	$4.77 \cdot 10^{-3}{}^{+3.5}_{-3.5}$
129.4	$8.06 \cdot 10^{-2}{}^{+9.8}_{-9.6}$	$2.25 \cdot 10^{-3}{}^{+4.6}_{-4.4}$	$1.90 \cdot 10^{-3}{}^{+8.6}_{-8.4}$	$2.92 \cdot 10^{-1}{}^{+3.7}_{-3.7}$	$3.81 \cdot 10^{-2}{}^{+3.7}_{-3.7}$	$4.79 \cdot 10^{-3}{}^{+3.5}_{-3.5}$
129.5	$8.05 \cdot 10^{-2}{}^{+9.8}_{-9.6}$	$2.25 \cdot 10^{-3}{}^{+4.5}_{-4.4}$	$1.91 \cdot 10^{-3}{}^{+8.5}_{-8.5}$	$2.93 \cdot 10^{-1}{}^{+3.7}_{-3.7}$	$3.84 \cdot 10^{-2}{}^{+3.7}_{-3.7}$	$4.81 \cdot 10^{-3}{}^{+3.5}_{-3.5}$
129.6	$8.03 \cdot 10^{-2}{}^{+9.8}_{-9.6}$	$2.25 \cdot 10^{-3}{}^{+4.5}_{-4.5}$	$1.92 \cdot 10^{-3}{}^{+8.5}_{-8.4}$	$2.95 \cdot 10^{-1}{}^{+3.7}_{-3.7}$	$3.87 \cdot 10^{-2}{}^{+3.7}_{-3.7}$	$4.83 \cdot 10^{-3}{}^{+3.5}_{-3.5}$
129.7	$8.02 \cdot 10^{-2}{}^{+9.8}_{-9.6}$	$2.25 \cdot 10^{-3}{}^{+4.5}_{-4.5}$	$1.92 \cdot 10^{-3}{}^{+8.5}_{-8.4}$	$2.97 \cdot 10^{-1}{}^{+3.7}_{-3.6}$	$3.90 \cdot 10^{-2}{}^{+3.7}_{-3.6}$	$4.85 \cdot 10^{-3}{}^{+3.5}_{-3.5}$
129.8	$8.00 \cdot 10^{-2}{}^{+9.8}_{-9.6}$	$2.25 \cdot 10^{-3}{}^{+4.5}_{-4.5}$	$1.93 \cdot 10^{-3}{}^{+8.4}_{-8.5}$	$2.99 \cdot 10^{-1}{}^{+3.7}_{-3.6}$	$3.93 \cdot 10^{-2}{}^{+3.7}_{-3.6}$	$4.87 \cdot 10^{-3}{}^{+3.5}_{-3.5}$
129.9	$7.99 \cdot 10^{-2}{}^{+9.8}_{-9.6}$	$2.25 \cdot 10^{-3}{}^{+4.5}_{-4.4}$	$1.94 \cdot 10^{-3}{}^{+8.5}_{-8.4}$	$3.01 \cdot 10^{-1}{}^{+3.7}_{-3.6}$	$3.95 \cdot 10^{-2}{}^{+3.7}_{-3.6}$	$4.89 \cdot 10^{-3}{}^{+3.5}_{-3.5}$
130	$7.97 \cdot 10^{-2}{}^{+9.8}_{-9.6}$	$2.24 \cdot 10^{-3}{}^{+4.5}_{-4.4}$	$1.95 \cdot 10^{-3}{}^{+8.4}_{-8.5}$	$3.03 \cdot 10^{-1}{}^{+3.7}_{-3.6}$	$3.98 \cdot 10^{-2}{}^{+3.7}_{-3.6}$	$4.91 \cdot 10^{-3}{}^{+3.5}_{-3.4}$
130.5	$7.90 \cdot 10^{-2}{}^{+9.7}_{-9.5}$	$2.24 \cdot 10^{-3}{}^{+4.5}_{-4.4}$	$1.98 \cdot 10^{-3}{}^{+8.4}_{-8.3}$	$3.12 \cdot 10^{-1}{}^{+3.6}_{-3.5}$	$4.13 \cdot 10^{-2}{}^{+3.6}_{-3.5}$	$5.01 \cdot 10^{-3}{}^{+3.4}_{-3.4}$
131	$7.82 \cdot 10^{-2}{}^{+9.7}_{-9.5}$	$2.23 \cdot 10^{-3}{}^{+4.4}_{-4.3}$	$2.02 \cdot 10^{-3}{}^{+8.4}_{-8.3}$	$3.22 \cdot 10^{-1}{}^{+3.5}_{-3.5}$	$4.28 \cdot 10^{-2}{}^{+3.5}_{-3.5}$	$5.12 \cdot 10^{-3}{}^{+3.4}_{-3.3}$
131.5	$7.73 \cdot 10^{-2}{}^{+9.7}_{-9.5}$	$2.22 \cdot 10^{-3}{}^{+4.3}_{-4.2}$	$2.05 \cdot 10^{-3}{}^{+8.3}_{-8.2}$	$3.31 \cdot 10^{-1}{}^{+3.5}_{-3.4}$	$4.42 \cdot 10^{-2}{}^{+3.5}_{-3.4}$	$5.23 \cdot 10^{-3}{}^{+3.3}_{-3.3}$
132	$7.65 \cdot 10^{-2}{}^{+9.6}_{-9.4}$	$2.21 \cdot 10^{-3}{}^{+4.3}_{-4.2}$	$2.09 \cdot 10^{-3}{}^{+8.2}_{-8.2}$	$3.41 \cdot 10^{-1}{}^{+3.4}_{-3.4}$	$4.57 \cdot 10^{-2}{}^{+3.4}_{-3.4}$	$5.35 \cdot 10^{-3}{}^{+3.3}_{-3.2}$
132.5	$7.56 \cdot 10^{-2}{}^{+9.6}_{-9.4}$	$2.19 \cdot 10^{-3}{}^{+4.2}_{-4.2}$	$2.12 \cdot 10^{-3}{}^{+8.2}_{-8.2}$	$3.51 \cdot 10^{-1}{}^{+3.3}_{-3.3}$	$4.72 \cdot 10^{-2}{}^{+3.3}_{-3.4}$	$5.48 \cdot 10^{-3}{}^{+3.2}_{-3.2}$
133	$7.47 \cdot 10^{-2}{}^{+9.5}_{-9.4}$	$2.18 \cdot 10^{-3}{}^{+4.2}_{-4.1}$	$2.15 \cdot 10^{-3}{}^{+8.1}_{-8.1}$	$3.61 \cdot 10^{-1}{}^{+3.3}_{-3.2}$	$4.87 \cdot 10^{-2}{}^{+3.3}_{-3.2}$	$5.60 \cdot 10^{-3}{}^{+3.2}_{-3.1}$
133.5	$7.37 \cdot 10^{-2}{}^{+9.5}_{-9.3}$	$2.17 \cdot 10^{-3}{}^{+4.1}_{-4.1}$	$2.18 \cdot 10^{-3}{}^{+8.1}_{-8.1}$	$3.70 \cdot 10^{-1}{}^{+3.2}_{-3.2}$	$5.02 \cdot 10^{-2}{}^{+3.2}_{-3.2}$	$5.74 \cdot 10^{-3}{}^{+3.1}_{-3.1}$
134	$7.28 \cdot 10^{-2}{}^{+9.4}_{-9.2}$	$2.15 \cdot 10^{-3}{}^{+4.1}_{-4.0}$	$2.21 \cdot 10^{-3}{}^{+8.0}_{-8.0}$	$3.80 \cdot 10^{-1}{}^{+3.1}_{-3.1}$	$5.17 \cdot 10^{-2}{}^{+3.1}_{-3.1}$	$5.88 \cdot 10^{-3}{}^{+3.1}_{-3.0}$
134.5	$7.18 \cdot 10^{-2}{}^{+9.4}_{-9.2}$	$2.14 \cdot 10^{-3}{}^{+4.0}_{-4.0}$	$2.24 \cdot 10^{-3}{}^{+8.0}_{-7.9}$	$3.90 \cdot 10^{-1}{}^{+3.1}_{-3.0}$	$5.32 \cdot 10^{-2}{}^{+3.1}_{-3.0}$	$6.03 \cdot 10^{-3}{}^{+3.0}_{-3.0}$
135	$7.08 \cdot 10^{-2}{}^{+9.3}_{-9.2}$	$2.12 \cdot 10^{-3}{}^{+4.0}_{-3.9}$	$2.27 \cdot 10^{-3}{}^{+7.9}_{-7.9}$	$4.00 \cdot 10^{-1}{}^{+3.0}_{-3.0}$	$5.47 \cdot 10^{-2}{}^{+3.0}_{-3.0}$	$6.18 \cdot 10^{-3}{}^{+2.9}_{-2.9}$
135.5	$6.97 \cdot 10^{-2}{}^{+9.3}_{-9.1}$	$2.11 \cdot 10^{-3}{}^{+3.9}_{-3.9}$	$2.29 \cdot 10^{-3}{}^{+7.9}_{-7.8}$	$4.10 \cdot 10^{-1}{}^{+2.9}_{-2.9}$	$5.62 \cdot 10^{-2}{}^{+2.9}_{-2.9}$	$6.34 \cdot 10^{-3}{}^{+2.9}_{-2.9}$
136	$6.87 \cdot 10^{-2}{}^{+9.2}_{-9.1}$	$2.09 \cdot 10^{-3}{}^{+3.8}_{-3.8}$	$2.32 \cdot 10^{-3}{}^{+7.8}_{-7.8}$	$4.20 \cdot 10^{-1}{}^{+2.9}_{-2.8}$	$5.77 \cdot 10^{-2}{}^{+2.9}_{-2.8}$	$6.51 \cdot 10^{-3}{}^{+2.8}_{-2.8}$
136.5	$6.76 \cdot 10^{-2}{}^{+9.2}_{-9.1}$	$2.07 \cdot 10^{-3}{}^{+3.8}_{-3.8}$	$2.34 \cdot 10^{-3}{}^{+7.8}_{-7.7}$	$4.31 \cdot 10^{-1}{}^{+2.8}_{-2.8}$	$5.91 \cdot 10^{-2}{}^{+2.8}_{-2.8}$	$6.69 \cdot 10^{-3}{}^{+2.8}_{-2.8}$
137	$6.65 \cdot 10^{-2}{}^{+9.2}_{-9.0}$	$2.05 \cdot 10^{-3}{}^{+3.7}_{-3.7}$	$2.36 \cdot 10^{-3}{}^{+7.7}_{-7.7}$	$4.41 \cdot 10^{-1}{}^{+2.7}_{-2.7}$	$6.06 \cdot 10^{-2}{}^{+2.7}_{-2.7}$	$6.87 \cdot 10^{-3}{}^{+2.7}_{-2.7}$
137.5	$6.54 \cdot 10^{-2}{}^{+9.1}_{-9.0}$	$2.03 \cdot 10^{-3}{}^{+3.7}_{-3.7}$	$2.38 \cdot 10^{-3}{}^{+7.6}_{-7.6}$	$4.51 \cdot 10^{-1}{}^{+2.7}_{-2.7}$	$6.20 \cdot 10^{-2}{}^{+2.7}_{-2.7}$	$7.06 \cdot 10^{-3}{}^{+2.7}_{-2.7}$
138	$6.43 \cdot 10^{-2}{}^{+9.1}_{-8.9}$	$2.01 \cdot 10^{-3}{}^{+3.6}_{-3.6}$	$2.40 \cdot 10^{-3}{}^{+7.6}_{-7.6}$	$4.61 \cdot 10^{-1}{}^{+2.6}_{-2.6}$	$6.34 \cdot 10^{-2}{}^{+2.6}_{-2.6}$	$7.26 \cdot 10^{-3}{}^{+2.6}_{-2.6}$
138.5	$6.31 \cdot 10^{-2}{}^{+9.1}_{-8.9}$	$1.99 \cdot 10^{-3}{}^{+3.6}_{-3.5}$	$2.41 \cdot 10^{-3}{}^{+7.6}_{-7.5}$	$4.71 \cdot 10^{-1}{}^{+2.5}_{-2.5}$	$6.48 \cdot 10^{-2}{}^{+2.5}_{-2.5}$	$7.47 \cdot 10^{-3}{}^{+2.6}_{-2.5}$
139	$6.20 \cdot 10^{-2}{}^{+9.0}_{-8.9}$	$1.97 \cdot 10^{-3}{}^{+3.5}_{-3.5}$	$2.43 \cdot 10^{-3}{}^{+7.5}_{-7.5}$	$4.81 \cdot 10^{-1}{}^{+2.5}_{-2.4}$	$6.61 \cdot 10^{-2}{}^{+2.5}_{-2.4}$	$7.70 \cdot 10^{-3}{}^{+2.5}_{-2.5}$
139.5	$6.08 \cdot 10^{-2}{}^{+9.0}_{-8.8}$	$1.95 \cdot 10^{-3}{}^{+3.5}_{-3.4}$	$2.44 \cdot 10^{-3}{}^{+7.4}_{-7.4}$	$4.91 \cdot 10^{-1}{}^{+2.4}_{-2.4}$	$6.75 \cdot 10^{-2}{}^{+2.4}_{-2.4}$	$7.93 \cdot 10^{-3}{}^{+2.5}_{-2.4}$
140	$5.96 \cdot 10^{-2}{}^{+8.9}_{-8.8}$	$1.93 \cdot 10^{-3}{}^{+3.4}_{-3.4}$	$2.45 \cdot 10^{-3}{}^{+7.4}_{-7.4}$	$5.01 \cdot 10^{-1}{}^{+2.4}_{-2.3}$	$6.87 \cdot 10^{-2}{}^{+2.4}_{-2.3}$	$8.17 \cdot 10^{-3}{}^{+2.4}_{-2.4}$
140.5	$5.84 \cdot 10^{-2}{}^{+8.9}_{-8.7}$	$1.90 \cdot 10^{-3}{}^{+3.4}_{-3.3}$	$2.46 \cdot 10^{-3}{}^{+7.3}_{-7.3}$	$5.11 \cdot 10^{-1}{}^{+2.3}_{-2.3}$	$7.00 \cdot 10^{-2}{}^{+2.3}_{-2.3}$	$8.43 \cdot 10^{-3}{}^{+2.3}_{-2.3}$
141	$5.72 \cdot 10^{-2}{}^{+8.9}_{-8.7}$	$1.88 \cdot 10^{-3}{}^{+3.3}_{-3.3}$	$2.47 \cdot 10^{-3}{}^{+7.3}_{-7.3}$	$5.21 \cdot 10^{-1}{}^{+2.2}_{-2.2}$	$7.12 \cdot 10^{-2}{}^{+2.2}_{-2.2}$	$8.70 \cdot 10^{-3}{}^{+2.3}_{-2.3}$
141.5	$5.60 \cdot 10^{-2}{}^{+8.8}_{-8.7}$	$1.85 \cdot 10^{-3}{}^{+3.3}_{-3.2}$	$2.48 \cdot 10^{-3}{}^{+7.2}_{-7.2}$	$5.31 \cdot 10^{-1}{}^{+2.2}_{-2.2}$	$7.24 \cdot 10^{-2}{}^{+2.2}_{-2.2}$	$8.98 \cdot 10^{-3}{}^{+2.2}_{-2.2}$
142	$5.48 \cdot 10^{-2}{}^{+8.8}_{-8.6}$	$1.83 \cdot 10^{-3}{}^{+3.3}_{-3.2}$	$2.48 \cdot 10^{-3}{}^{+7.2}_{-7.2}$	$5.41 \cdot 10^{-1}{}^{+2.1}_{-2.1}$	$7.35 \cdot 10^{-2}{}^{+2.1}_{-2.1}$	$9.28 \cdot 10^{-3}{}^{+2.2}_{-2.2}$
142.5	$5.35 \cdot 10^{-2}{}^{+8.7}_{-8.6}$	$1.80 \cdot 10^{-3}{}^{+3.1}_{-3.1}$	$2.49 \cdot 10^{-3}{}^{+7.1}_{-7.1}$	$5.51 \cdot 10^{-1}{}^{+2.0}_{-2.0}$	$7.46 \cdot 10^{-2}{}^{+2.0}_{-2.0}$	$9.59 \cdot 10^{-3}{}^{+2.2}_{-2.1}$
143	$5.23 \cdot 10^{-2}{}^{+8.7}_{-8.6}$	$1.78 \cdot 10^{-3}{}^{+3.1}_{-3.1}$	$2.49 \cdot 10^{-3}{}^{+7.1}_{-7.0}$	$5.61 \cdot 10^{-1}{}^{+2.0}_{-2.0}$	$7.56 \cdot 10^{-2}{}^{+2.0}_{-2.0}$	$9.92 \cdot 10^{-3}{}^{+2.1}_{-2.1}$
143.5	$5.11 \cdot 10^{-2}{}^{+8.7}_{-8.5}$	$1.75 \cdot 10^{-3}{}^{+3.1}_{-3.1}$	$2.49 \cdot 10^{-3}{}^{+7.0}_{-7.0}$	$5.71 \cdot 10^{-1}{}^{+1.9}_{-1.9}$	$7.66 \cdot 10^{-2}{}^{+1.9}_{-1.9}$	$1.03 \cdot 10^{-2}{}^{+2.0}_{-2.0}$
144	$4.98 \cdot 10^{-2}{}^{+8.6}_{-8.5}$	$1.73 \cdot 10^{-3}{}^{+3.0}_{-3.1}$	$2.49 \cdot 10^{-3}{}^{+7.0}_{-7.0}$	$5.80 \cdot 10^{-1}{}^{+1.8}_{-1.8}$	$7.75 \cdot 10^{-2}{}^{+1.9}_{-1.8}$	$1.06 \cdot 10^{-2}{}^{+2.0}_{-2.0}$
144.5	$4.86 \cdot 10^{-2}{}^{+8.6}_{-8.5}$	$1.70 \cdot 10^{-3}{}^{+2.9}_{-3.0}$	$2.48 \cdot 10^{-3}{}^{+6.9}_{-6.9}$	$5.90 \cdot 10^{-1}{}^{+1.8}_{-1.8}$	$7.84 \cdot 10^{-2}{}^{+1.8}_{-1.8}$	$1.10 \cdot 10^{-2}{}^{+1.9}_{-1.9}$
145	$4.73 \cdot 10^{-2}{}^{+8.6}_{-8.4}$	$1.67 \cdot 10^{-3}{}^{+2.9}_{-2.8}$	$2.48 \cdot 10^{-3}{}^{+6.9}_{-6.9}$	$6.00 \cdot 10^{-1}{}^{+1.7}_{-1.7}$	$7.92 \cdot 10^{-2}{}^{+1.7}_{-1.7}$	$1.14 \cdot 10^{-2}{}^{+1.9}_{-1.9}$
145.5	$4.60 \cdot 10^{-2}{}^{+8.5}_{-8.4}$	$1.64 \cdot 10^{-3}{}^{+2.8}_{-2.9}$	$2.47 \cdot 10^{-3}{}^{+6.8}_{-6.9}$	$6.10 \cdot 10^{-1}{}^{+1.7}_{-1.7}$	$7.99 \cdot 10^{-2}{}^{+1.7}_{-1.7}$	$1.19 \cdot 10^{-2}{}^{+1.8}_{-1.9}$
146	$4.48 \cdot 10^{-2}{}^{+8.5}_{-8.4}$	$1.61 \cdot 10^{-3}{}^{+2.8}_{-2.8}$	$2.46 \cdot 10^{-3}{}^{+6.8}_{-6.8}$	$6.19 \cdot 10^{-1}{}^{+1.6}_{-1.6}$	$8.06 \cdot 10^{-2}{}^{+1.6}_{-1.6}$	$1.23 \cdot 10^{-2}{}^{+1.8}_{-1.8}$
146.5	$4.35 \cdot 10^{-2}{}^{+8.5}_{-8.4}$	$1.58 \cdot 10^{-3}{}^{+2.8}_{-2.7}$	$2.45 \cdot 10^{-3}{}^{+6.7}_{-6.7}$	$6.29 \cdot 10^{-1}{}^{+1.6}_{-1.6}$	$8.11 \cdot 10^{-2}{}^{+1.6}_{-1.6}$	$1.28 \cdot 10^{-2}{}^{+1.8}_{-1.7}$
147	$4.22 \cdot 10^{-2}{}^{+8.4}_{-8.3}$	$1.55 \cdot 10^{-3}{}^{+2.7}_{-2.7}$	$2.43 \cdot 10^{-3}{}^{+6.7}_{-6.7}$	$6.39 \cdot 10^{-1}{}^{+1.5}_{-1.5}$	$8.16 \cdot 10^{-2}{}^{+1.5}_{-1.5}$	$1.33 \cdot 10^{-2}{}^{+1.7}_{-1.7}$
147.5	$4.09 \cdot 10^{-2}{}^{+8.4}_{-8.3}$	$1.52 \cdot 10^{-3}{}^{+2.6}_{-2.6}$	$2.42 \cdot 10^{-3}{}^{+6.6}_{-6.6}$	$6.48 \cdot 10^{-1}{}^{+1.5}_{-1.5}$	$8.20 \cdot 10^{-2}{}^{+1.5}_{-1.5}$	$1.39 \cdot 10^{-2}{}^{+1.7}_{-1.7}$
148	$3.97 \cdot 10^{-2}{}^{+8.4}_{-8.3}$	$1.49 \cdot 10^{-3}{}^{+2.7}_{-2.6}$	$2.40 \cdot 10^{-3}{}^{+6.6}_{-6.6}$	$6.58 \cdot 10^{-1}{}^{+1.4}_{-1.4}$	$8.23 \cdot 10^{-2}{}^{+1.4}_{-1.4}$	$1.45 \cdot 10^{-2}{}^{+1.6}_{-1.6}$
148.5	$3.84 \cdot 10^{-2}{}^{+8.4}_{-8.2}$	$1.46 \cdot 10^{-3}{}^{+2.5}_{-2.6}$	$2.38 \cdot 10^{-3}{}^{+6.5}_{-6.6}$	$6.68 \cdot 10^{-1}{}^{+1.3}_{-1.3}$	$8.25 \cdot 10^{-2}{}^{+1.3}_{-1.3}$	$1.51 \cdot 10^{-2}{}^{+1.6}_{-1.6}$

Table A.12: SM Higgs branching ratios to two gauge bosons and Higgs total width together with their total uncertainties (expressed in percentage). Low-mass range.

M_H [GeV]	H → gg	H → γγ	H → Zγ	H → WW	H → ZZ	Total Γ_H [GeV]
149	$3.71\cdot10^{-2}{}^{+8.3}_{-8.2}$	$1.43\cdot10^{-3}{}^{+2.5}_{-2.5}$	$2.36\cdot10^{-3}{}^{+6.5}_{-6.6}$	$6.77\cdot10^{-1}{}^{+1.3}_{-1.3}$	$8.26\cdot10^{-2}{}^{+1.3}_{-1.3}$	$1.58\cdot10^{-2}{}^{+1.5}_{-1.5}$
149.5	$3.58\cdot10^{-2}{}^{+8.3}_{-8.1}$	$1.39\cdot10^{-3}{}^{+2.5}_{-2.4}$	$2.33\cdot10^{-3}{}^{+6.5}_{-6.4}$	$6.87\cdot10^{-1}{}^{+1.2}_{-1.2}$	$8.26\cdot10^{-2}{}^{+1.2}_{-1.3}$	$1.65\cdot10^{-2}{}^{+1.5}_{-1.5}$
150	$3.46\cdot10^{-2}{}^{+8.3}_{-8.2}$	$1.36\cdot10^{-3}{}^{+2.5}_{-2.4}$	$2.31\cdot10^{-3}{}^{+6.4}_{-6.5}$	$6.96\cdot10^{-1}{}^{+1.2}_{-1.2}$	$8.25\cdot10^{-2}{}^{+1.2}_{-1.2}$	$1.73\cdot10^{-2}{}^{+1.4}_{-1.4}$
152	$2.94\cdot10^{-2}{}^{+8.1}_{-8.1}$	$1.22\cdot10^{-3}{}^{+2.3}_{-2.3}$	$2.18\cdot10^{-3}{}^{+6.3}_{-6.3}$	$7.35\cdot10^{-1}{}^{+1.0}_{-1.0}$	$8.08\cdot10^{-2}{}^{+1.0}_{-1.0}$	$2.11\cdot10^{-2}{}^{+1.3}_{-1.3}$
154	$2.43\cdot10^{-2}{}^{+8.0}_{-8.0}$	$1.08\cdot10^{-3}{}^{+2.2}_{-2.1}$	$2.01\cdot10^{-3}{}^{+6.1}_{-6.1}$	$7.74\cdot10^{-1}{}^{+0.8}_{-0.8}$	$7.66\cdot10^{-2}{}^{+0.8}_{-0.8}$	$2.66\cdot10^{-2}{}^{+1.1}_{-1.1}$
156	$1.92\cdot10^{-2}{}^{+7.9}_{-7.9}$	$9.14\cdot10^{-4}{}^{+2.0}_{-2.0}$	$1.79\cdot10^{-3}{}^{+6.0}_{-6.0}$	$8.16\cdot10^{-1}{}^{+0.6}_{-0.6}$	$6.92\cdot10^{-2}{}^{+0.6}_{-0.6}$	$3.51\cdot10^{-2}{}^{+1.0}_{-1.0}$
158	$1.38\cdot10^{-2}{}^{+7.9}_{-7.8}$	$7.29\cdot10^{-4}{}^{+1.8}_{-1.9}$	$1.50\cdot10^{-3}{}^{+5.8}_{-5.9}$	$8.60\cdot10^{-1}{}^{+0.4}_{-0.4}$	$5.76\cdot10^{-2}{}^{+0.4}_{-0.4}$	$5.02\cdot10^{-2}{}^{+0.8}_{-0.8}$
160	$8.64\cdot10^{-3}{}^{+7.8}_{-7.7}$	$5.32\cdot10^{-4}{}^{+1.7}_{-1.7}$	$1.15\cdot10^{-3}{}^{+5.7}_{-5.7}$	$9.08\cdot10^{-1}{}^{+0.3}_{-0.3}$	$4.15\cdot10^{-2}{}^{+0.3}_{-0.3}$	$8.31\cdot10^{-2}{}^{+0.7}_{-0.7}$
162	$5.04\cdot10^{-3}{}^{+7.9}_{-7.7}$	$3.69\cdot10^{-4}{}^{+1.7}_{-1.6}$	$8.41\cdot10^{-4}{}^{+5.7}_{-5.6}$	$9.43\cdot10^{-1}{}^{+0.2}_{-0.2}$	$2.82\cdot10^{-2}{}^{+0.2}_{-0.2}$	$1.47\cdot10^{-1}{}^{+0.6}_{-0.6}$
164	$3.54\cdot10^{-3}{}^{+7.8}_{-7.7}$	$2.59\cdot10^{-4}{}^{+1.6}_{-1.6}$	$6.06\cdot10^{-4}{}^{+5.6}_{-5.6}$	$9.57\cdot10^{-1}{}^{+0.1}_{-0.1}$	$2.31\cdot10^{-2}{}^{+0.1}_{-0.1}$	$2.15\cdot10^{-1}{}^{+0.6}_{-0.6}$
165	$3.14\cdot10^{-3}{}^{+7.8}_{-7.6}$	$2.30\cdot10^{-4}{}^{+1.6}_{-1.6}$	$5.45\cdot10^{-4}{}^{+5.6}_{-5.6}$	$9.60\cdot10^{-1}{}^{+0.1}_{-0.1}$	$2.22\cdot10^{-2}{}^{+0.1}_{-0.1}$	$2.46\cdot10^{-1}{}^{+0.6}_{-0.6}$
166	$2.85\cdot10^{-3}{}^{+7.8}_{-7.7}$	$2.08\cdot10^{-4}{}^{+1.6}_{-1.6}$	$5.00\cdot10^{-4}{}^{+5.6}_{-5.6}$	$9.62\cdot10^{-1}{}^{+0.1}_{-0.1}$	$2.18\cdot10^{-2}{}^{+0.1}_{-0.1}$	$2.76\cdot10^{-1}{}^{+0.6}_{-0.6}$
168	$2.46\cdot10^{-3}{}^{+7.7}_{-7.7}$	$1.78\cdot10^{-4}{}^{+1.6}_{-1.7}$	$4.39\cdot10^{-4}{}^{+5.6}_{-5.6}$	$9.64\cdot10^{-1}{}^{+0.1}_{-0.1}$	$2.22\cdot10^{-2}{}^{+0.1}_{-0.1}$	$3.30\cdot10^{-1}{}^{+0.6}_{-0.6}$
170	$2.20\cdot10^{-3}{}^{+7.7}_{-7.7}$	$1.58\cdot10^{-4}{}^{+1.6}_{-1.6}$	$4.00\cdot10^{-4}{}^{+5.6}_{-5.6}$	$9.64\cdot10^{-1}{}^{+0.1}_{-0.1}$	$2.36\cdot10^{-2}{}^{+0.1}_{-0.1}$	$3.80\cdot10^{-1}{}^{+0.6}_{-0.6}$
172	$2.02\cdot10^{-3}{}^{+7.7}_{-7.6}$	$1.43\cdot10^{-4}{}^{+1.6}_{-1.6}$	$3.71\cdot10^{-4}{}^{+5.6}_{-5.6}$	$9.63\cdot10^{-1}{}^{+0.1}_{-0.1}$	$2.61\cdot10^{-2}{}^{+0.1}_{-0.1}$	$4.29\cdot10^{-1}{}^{+0.6}_{-0.6}$
174	$1.88\cdot10^{-3}{}^{+7.7}_{-7.7}$	$1.32\cdot10^{-4}{}^{+1.5}_{-1.7}$	$3.48\cdot10^{-4}{}^{+5.6}_{-5.6}$	$9.60\cdot10^{-1}{}^{+0.1}_{-0.1}$	$2.98\cdot10^{-2}{}^{+0.1}_{-0.1}$	$4.77\cdot10^{-1}{}^{+0.6}_{-0.6}$
175	$1.81\cdot10^{-3}{}^{+7.8}_{-7.6}$	$1.27\cdot10^{-4}{}^{+1.6}_{-1.6}$	$3.38\cdot10^{-4}{}^{+5.6}_{-5.6}$	$9.58\cdot10^{-1}{}^{+0.0}_{-0.0}$	$3.23\cdot10^{-2}{}^{+0.1}_{-0.1}$	$5.01\cdot10^{-1}{}^{+0.6}_{-0.6}$
176	$1.76\cdot10^{-3}{}^{+7.7}_{-7.6}$	$1.22\cdot10^{-4}{}^{+1.5}_{-1.7}$	$3.29\cdot10^{-4}{}^{+5.6}_{-5.6}$	$9.55\cdot10^{-1}{}^{+0.0}_{-0.0}$	$3.54\cdot10^{-2}{}^{+0.1}_{-0.1}$	$5.25\cdot10^{-1}{}^{+0.6}_{-0.6}$
178	$1.66\cdot10^{-3}{}^{+7.7}_{-7.6}$	$1.13\cdot10^{-4}{}^{+1.6}_{-1.6}$	$3.12\cdot10^{-4}{}^{+5.6}_{-5.6}$	$9.47\cdot10^{-1}{}^{+0.0}_{-0.1}$	$4.44\cdot10^{-2}{}^{+0.1}_{-0.1}$	$5.75\cdot10^{-1}{}^{+0.6}_{-0.6}$
180	$1.56\cdot10^{-3}{}^{+7.7}_{-7.6}$	$1.05\cdot10^{-4}{}^{+1.6}_{-1.6}$	$2.96\cdot10^{-4}{}^{+5.6}_{-5.5}$	$9.32\cdot10^{-1}{}^{+0.0}_{-0.0}$	$6.02\cdot10^{-2}{}^{+0.1}_{-0.1}$	$6.31\cdot10^{-1}{}^{+0.6}_{-0.6}$
182	$1.44\cdot10^{-3}{}^{+7.7}_{-7.5}$	$9.68\cdot10^{-5}{}^{+1.6}_{-1.6}$	$2.76\cdot10^{-4}{}^{+5.6}_{-5.6}$	$9.03\cdot10^{-1}{}^{+0.0}_{-0.0}$	$9.00\cdot10^{-2}{}^{+0.0}_{-0.1}$	$7.00\cdot10^{-1}{}^{+0.6}_{-0.6}$
184	$1.32\cdot10^{-3}{}^{+7.8}_{-7.6}$	$8.81\cdot10^{-5}{}^{+1.6}_{-1.6}$	$2.54\cdot10^{-4}{}^{+5.6}_{-5.6}$	$8.62\cdot10^{-1}{}^{+0.0}_{-0.0}$	$1.31\cdot10^{-1}{}^{+0.0}_{-0.0}$	$7.88\cdot10^{-1}{}^{+0.6}_{-0.6}$
185	$1.27\cdot10^{-3}{}^{+7.7}_{-7.6}$	$8.43\cdot10^{-5}{}^{+1.6}_{-1.6}$	$2.44\cdot10^{-4}{}^{+5.6}_{-5.6}$	$8.44\cdot10^{-1}{}^{+0.0}_{-0.0}$	$1.50\cdot10^{-1}{}^{+0.0}_{-0.0}$	$8.32\cdot10^{-1}{}^{+0.6}_{-0.6}$
186	$1.23\cdot10^{-3}{}^{+7.7}_{-7.6}$	$8.09\cdot10^{-5}{}^{+1.6}_{-1.6}$	$2.36\cdot10^{-4}{}^{+5.6}_{-5.6}$	$8.28\cdot10^{-1}{}^{+0.0}_{-0.0}$	$1.66\cdot10^{-1}{}^{+0.0}_{-0.0}$	$8.76\cdot10^{-1}{}^{+0.6}_{-0.6}$
188	$1.15\cdot10^{-3}{}^{+7.6}_{-7.6}$	$7.52\cdot10^{-5}{}^{+1.6}_{-1.6}$	$2.22\cdot10^{-4}{}^{+5.6}_{-5.6}$	$8.03\cdot10^{-1}{}^{+0.0}_{-0.0}$	$1.91\cdot10^{-1}{}^{+0.0}_{-0.0}$	$9.60\cdot10^{-1}{}^{+0.6}_{-0.6}$
190	$1.09\cdot10^{-3}{}^{+7.7}_{-7.6}$	$7.05\cdot10^{-5}{}^{+1.6}_{-1.5}$	$2.11\cdot10^{-4}{}^{+5.6}_{-5.5}$	$7.86\cdot10^{-1}{}^{+0.0}_{-0.0}$	$2.09\cdot10^{-1}{}^{+0.0}_{-0.0}$	$1.04\cdot10^{0}{}^{+0.5}_{-0.5}$
192	$1.05\cdot10^{-3}{}^{+7.7}_{-7.6}$	$6.66\cdot10^{-5}{}^{+1.5}_{-1.6}$	$2.02\cdot10^{-4}{}^{+5.5}_{-5.6}$	$7.72\cdot10^{-1}{}^{+0.0}_{-0.0}$	$2.23\cdot10^{-1}{}^{+0.0}_{-0.0}$	$1.12\cdot10^{0}{}^{+0.5}_{-0.5}$
194	$1.01\cdot10^{-3}{}^{+7.7}_{-7.5}$	$6.32\cdot10^{-5}{}^{+1.6}_{-1.6}$	$1.94\cdot10^{-4}{}^{+5.6}_{-5.5}$	$7.61\cdot10^{-1}{}^{+0.0}_{-0.0}$	$2.34\cdot10^{-1}{}^{+0.0}_{-0.0}$	$1.20\cdot10^{0}{}^{+0.5}_{-0.5}$
195	$9.94\cdot10^{-4}{}^{+7.6}_{-7.6}$	$6.17\cdot10^{-5}{}^{+1.6}_{-1.6}$	$1.91\cdot10^{-4}{}^{+5.6}_{-5.6}$	$7.57\cdot10^{-1}{}^{+0.0}_{-0.0}$	$2.39\cdot10^{-1}{}^{+0.0}_{-0.0}$	$1.24\cdot10^{0}{}^{+0.5}_{-0.5}$
196	$9.78\cdot10^{-4}{}^{+7.7}_{-7.6}$	$6.02\cdot10^{-5}{}^{+1.6}_{-1.6}$	$1.87\cdot10^{-4}{}^{+5.5}_{-5.6}$	$7.53\cdot10^{-1}{}^{+0.0}_{-0.0}$	$2.43\cdot10^{-1}{}^{+0.0}_{-0.0}$	$1.28\cdot10^{0}{}^{+0.5}_{-0.5}$
198	$9.50\cdot10^{-4}{}^{+7.7}_{-7.6}$	$5.75\cdot10^{-5}{}^{+1.6}_{-1.6}$	$1.81\cdot10^{-4}{}^{+5.5}_{-5.6}$	$7.46\cdot10^{-1}{}^{+0.0}_{-0.0}$	$2.50\cdot10^{-1}{}^{+0.0}_{-0.0}$	$1.35\cdot10^{0}{}^{+0.5}_{-0.5}$
200	$9.26\cdot10^{-4}{}^{+7.6}_{-7.6}$	$5.51\cdot10^{-5}{}^{+1.6}_{-1.6}$	$1.75\cdot10^{-4}{}^{+5.5}_{-5.6}$	$7.41\cdot10^{-1}{}^{+0.0}_{-0.0}$	$2.55\cdot10^{-1}{}^{+0.0}_{-0.0}$	$1.43\cdot10^{0}{}^{+0.5}_{-0.5}$
202	$9.04\cdot10^{-4}{}^{+7.6}_{-7.6}$	$5.29\cdot10^{-5}{}^{+1.6}_{-1.6}$	$1.70\cdot10^{-4}{}^{+5.5}_{-5.6}$	$7.36\cdot10^{-1}{}^{+0.0}_{-0.0}$	$2.60\cdot10^{-1}{}^{+0.0}_{-0.0}$	$1.51\cdot10^{0}{}^{+0.5}_{-0.5}$
204	$8.84\cdot10^{-4}{}^{+7.7}_{-7.5}$	$5.08\cdot10^{-5}{}^{+1.6}_{-1.6}$	$1.65\cdot10^{-4}{}^{+5.5}_{-5.5}$	$7.32\cdot10^{-1}{}^{+0.0}_{-0.0}$	$2.65\cdot10^{-1}{}^{+0.0}_{-0.0}$	$1.59\cdot10^{0}{}^{+0.5}_{-0.5}$
206	$8.66\cdot10^{-4}{}^{+7.6}_{-7.5}$	$4.89\cdot10^{-5}{}^{+1.6}_{-1.6}$	$1.61\cdot10^{-4}{}^{+5.6}_{-5.6}$	$7.28\cdot10^{-1}{}^{+0.0}_{-0.0}$	$2.68\cdot10^{-1}{}^{+0.0}_{-0.0}$	$1.68\cdot10^{0}{}^{+0.5}_{-0.5}$
208	$8.50\cdot10^{-4}{}^{+7.6}_{-7.5}$	$4.71\cdot10^{-5}{}^{+1.6}_{-1.6}$	$1.56\cdot10^{-4}{}^{+5.7}_{-5.5}$	$7.25\cdot10^{-1}{}^{+0.0}_{-0.0}$	$2.71\cdot10^{-1}{}^{+0.0}_{-0.0}$	$1.76\cdot10^{0}{}^{+0.5}_{-0.5}$
210	$8.36\cdot10^{-4}{}^{+7.6}_{-7.5}$	$4.54\cdot10^{-5}{}^{+1.7}_{-1.6}$	$1.52\cdot10^{-4}{}^{+5.6}_{-5.6}$	$7.23\cdot10^{-1}{}^{+0.0}_{-0.0}$	$2.74\cdot10^{-1}{}^{+0.0}_{-0.0}$	$1.85\cdot10^{0}{}^{+0.5}_{-0.5}$
212	$8.22\cdot10^{-4}{}^{+7.6}_{-7.5}$	$4.39\cdot10^{-5}{}^{+1.6}_{-1.7}$	$1.48\cdot10^{-4}{}^{+5.5}_{-5.6}$	$7.20\cdot10^{-1}{}^{+0.0}_{-0.0}$	$2.76\cdot10^{-1}{}^{+0.0}_{-0.0}$	$1.93\cdot10^{0}{}^{+0.5}_{-0.5}$
214	$8.10\cdot10^{-4}{}^{+7.6}_{-7.5}$	$4.24\cdot10^{-5}{}^{+1.6}_{-1.6}$	$1.45\cdot10^{-4}{}^{+5.6}_{-5.6}$	$7.18\cdot10^{-1}{}^{+0.0}_{-0.0}$	$2.78\cdot10^{-1}{}^{+0.0}_{-0.0}$	$2.02\cdot10^{0}{}^{+0.5}_{-0.5}$
216	$7.98\cdot10^{-4}{}^{+7.6}_{-7.5}$	$4.10\cdot10^{-5}{}^{+1.6}_{-1.7}$	$1.41\cdot10^{-4}{}^{+5.6}_{-5.6}$	$7.17\cdot10^{-1}{}^{+0.0}_{-0.0}$	$2.80\cdot10^{-1}{}^{+0.0}_{-0.0}$	$2.12\cdot10^{0}{}^{+0.5}_{-0.5}$
218	$7.87\cdot10^{-4}{}^{+7.6}_{-7.5}$	$3.96\cdot10^{-5}{}^{+1.6}_{-1.6}$	$1.38\cdot10^{-4}{}^{+5.6}_{-5.5}$	$7.15\cdot10^{-1}{}^{+0.0}_{-0.0}$	$2.82\cdot10^{-1}{}^{+0.0}_{-0.0}$	$2.21\cdot10^{0}{}^{+0.5}_{-0.5}$
220	$7.77\cdot10^{-4}{}^{+7.6}_{-7.5}$	$3.84\cdot10^{-5}{}^{+1.6}_{-1.6}$	$1.34\cdot10^{-4}{}^{+5.6}_{-5.6}$	$7.14\cdot10^{-1}{}^{+0.0}_{-0.0}$	$2.84\cdot10^{-1}{}^{+0.0}_{-0.0}$	$2.31\cdot10^{0}{}^{+0.5}_{-0.5}$
222	$7.68\cdot10^{-4}{}^{+7.6}_{-7.5}$	$3.72\cdot10^{-5}{}^{+1.6}_{-1.6}$	$1.31\cdot10^{-4}{}^{+5.5}_{-5.6}$	$7.12\cdot10^{-1}{}^{+0.0}_{-0.0}$	$2.85\cdot10^{-1}{}^{+0.0}_{-0.0}$	$2.40\cdot10^{0}{}^{+0.5}_{-0.5}$
224	$7.59\cdot10^{-4}{}^{+7.6}_{-7.5}$	$3.60\cdot10^{-5}{}^{+1.6}_{-1.6}$	$1.28\cdot10^{-4}{}^{+5.6}_{-5.6}$	$7.11\cdot10^{-1}{}^{+0.0}_{-0.0}$	$2.86\cdot10^{-1}{}^{+0.0}_{-0.0}$	$2.50\cdot10^{0}{}^{+0.5}_{-0.5}$
226	$7.50\cdot10^{-4}{}^{+7.6}_{-7.5}$	$3.49\cdot10^{-5}{}^{+1.6}_{-1.6}$	$1.25\cdot10^{-4}{}^{+5.6}_{-5.6}$	$7.10\cdot10^{-1}{}^{+0.0}_{-0.0}$	$2.87\cdot10^{-1}{}^{+0.0}_{-0.0}$	$2.61\cdot10^{0}{}^{+0.5}_{-0.5}$
228	$7.43\cdot10^{-4}{}^{+7.6}_{-7.5}$	$3.39\cdot10^{-5}{}^{+1.6}_{-1.6}$	$1.22\cdot10^{-4}{}^{+5.5}_{-5.6}$	$7.09\cdot10^{-1}{}^{+0.0}_{-0.0}$	$2.88\cdot10^{-1}{}^{+0.0}_{-0.0}$	$2.71\cdot10^{0}{}^{+0.5}_{-0.5}$
230	$7.35\cdot10^{-4}{}^{+7.6}_{-7.5}$	$3.28\cdot10^{-5}{}^{+1.6}_{-1.6}$	$1.19\cdot10^{-4}{}^{+5.6}_{-5.5}$	$7.08\cdot10^{-1}{}^{+0.0}_{-0.0}$	$2.89\cdot10^{-1}{}^{+0.0}_{-0.0}$	$2.82\cdot10^{0}{}^{+0.5}_{-0.5}$

Table A.13: SM Higgs branching ratios to two gauge bosons and Higgs total width together with their total uncertainties (expressed in percentage). Intermediate-mass range.

M_H [GeV]	$H \to gg$	$H \to \gamma\gamma$	$H \to Z\gamma$	$H \to WW$	$H \to ZZ$	Total Γ_H [GeV]
232	$7.29\cdot10^{-4}{}^{+7.6}_{-7.5}$	$3.19\cdot10^{-5}{}^{+1.6}_{-1.6}$	$1.17\cdot10^{-4}{}^{+5.5}_{-5.6}$	$7.07\cdot10^{-1}{}^{+0.0}_{-0.0}$	$2.90\cdot10^{-1}{}^{+0.0}_{-0.0}$	$2.93\cdot10^{0}{}^{+0.5}_{-0.5}$
234	$7.22\cdot10^{-4}{}^{+7.6}_{-7.5}$	$3.09\cdot10^{-5}{}^{+1.6}_{-1.6}$	$1.14\cdot10^{-4}{}^{+5.6}_{-5.6}$	$7.06\cdot10^{-1}{}^{+0.0}_{-0.0}$	$2.91\cdot10^{-1}{}^{+0.0}_{-0.0}$	$3.04\cdot10^{0}{}^{+0.5}_{-0.5}$
236	$7.16\cdot10^{-4}{}^{+7.6}_{-7.5}$	$3.01\cdot10^{-5}{}^{+1.6}_{-1.6}$	$1.11\cdot10^{-4}{}^{+5.5}_{-5.5}$	$7.06\cdot10^{-1}{}^{+0.0}_{-0.0}$	$2.92\cdot10^{-1}{}^{+0.0}_{-0.0}$	$3.16\cdot10^{0}{}^{+0.5}_{-0.5}$
238	$7.10\cdot10^{-4}{}^{+7.6}_{-7.5}$	$2.92\cdot10^{-5}{}^{+1.6}_{-1.7}$	$1.09\cdot10^{-4}{}^{+5.6}_{-5.5}$	$7.05\cdot10^{-1}{}^{+0.0}_{-0.0}$	$2.93\cdot10^{-1}{}^{+0.0}_{-0.0}$	$3.27\cdot10^{0}{}^{+0.5}_{-0.5}$
240	$7.05\cdot10^{-4}{}^{+7.6}_{-7.5}$	$2.84\cdot10^{-5}{}^{+1.7}_{-1.6}$	$1.07\cdot10^{-4}{}^{+5.5}_{-5.6}$	$7.04\cdot10^{-1}{}^{+0.0}_{-0.0}$	$2.94\cdot10^{-1}{}^{+0.0}_{-0.0}$	$3.40\cdot10^{0}{}^{+0.5}_{-0.5}$
242	$7.00\cdot10^{-4}{}^{+7.6}_{-7.5}$	$2.76\cdot10^{-5}{}^{+1.7}_{-1.7}$	$1.04\cdot10^{-4}{}^{+5.6}_{-5.5}$	$7.04\cdot10^{-1}{}^{+0.0}_{-0.0}$	$2.94\cdot10^{-1}{}^{+0.0}_{-0.0}$	$3.52\cdot10^{0}{}^{+0.5}_{-0.5}$
244	$6.95\cdot10^{-4}{}^{+7.6}_{-7.5}$	$2.68\cdot10^{-5}{}^{+1.7}_{-1.7}$	$1.02\cdot10^{-4}{}^{+5.6}_{-5.5}$	$7.03\cdot10^{-1}{}^{+0.0}_{-0.0}$	$2.95\cdot10^{-1}{}^{+0.0}_{-0.0}$	$3.64\cdot10^{0}{}^{+0.5}_{-0.5}$
246	$6.90\cdot10^{-4}{}^{+7.6}_{-7.5}$	$2.61\cdot10^{-5}{}^{+1.7}_{-1.7}$	$9.96\cdot10^{-5}{}^{+5.6}_{-5.6}$	$7.02\cdot10^{-1}{}^{+0.0}_{-0.0}$	$2.96\cdot10^{-1}{}^{+0.0}_{-0.0}$	$3.77\cdot10^{0}{}^{+0.5}_{-0.5}$
248	$6.86\cdot10^{-4}{}^{+7.6}_{-7.5}$	$2.54\cdot10^{-5}{}^{+1.7}_{-1.7}$	$9.75\cdot10^{-5}{}^{+5.6}_{-5.6}$	$7.02\cdot10^{-1}{}^{+0.0}_{-0.0}$	$2.96\cdot10^{-1}{}^{+0.0}_{-0.0}$	$3.91\cdot10^{0}{}^{+0.5}_{-0.5}$
250	$6.82\cdot10^{-4}{}^{+7.6}_{-7.5}$	$2.47\cdot10^{-5}{}^{+1.7}_{-1.7}$	$9.54\cdot10^{-5}{}^{+5.6}_{-5.6}$	$7.01\cdot10^{-1}{}^{+0.0}_{-0.0}$	$2.97\cdot10^{-1}{}^{+0.0}_{-0.0}$	$4.04\cdot10^{0}{}^{+0.5}_{-0.5}$
252	$6.78\cdot10^{-4}{}^{+7.6}_{-7.5}$	$2.41\cdot10^{-5}{}^{+1.6}_{-1.7}$	$9.33\cdot10^{-5}{}^{+5.6}_{-5.6}$	$7.01\cdot10^{-1}{}^{+0.0}_{-0.0}$	$2.97\cdot10^{-1}{}^{+0.0}_{-0.0}$	$4.18\cdot10^{0}{}^{+0.5}_{-0.5}$
254	$6.75\cdot10^{-4}{}^{+7.6}_{-7.5}$	$2.34\cdot10^{-5}{}^{+1.7}_{-1.7}$	$9.13\cdot10^{-5}{}^{+5.6}_{-5.6}$	$7.00\cdot10^{-1}{}^{+0.0}_{-0.0}$	$2.98\cdot10^{-1}{}^{+0.0}_{-0.0}$	$4.32\cdot10^{0}{}^{+0.5}_{-0.5}$
256	$6.72\cdot10^{-4}{}^{+7.6}_{-7.5}$	$2.28\cdot10^{-5}{}^{+1.6}_{-1.7}$	$8.94\cdot10^{-5}{}^{+5.6}_{-5.6}$	$7.00\cdot10^{-1}{}^{+0.0}_{-0.0}$	$2.98\cdot10^{-1}{}^{+0.0}_{-0.0}$	$4.46\cdot10^{0}{}^{+0.5}_{-0.5}$
258	$6.69\cdot10^{-4}{}^{+7.6}_{-7.5}$	$2.22\cdot10^{-5}{}^{+1.7}_{-1.7}$	$8.75\cdot10^{-5}{}^{+5.6}_{-5.6}$	$6.99\cdot10^{-1}{}^{+0.0}_{-0.0}$	$2.99\cdot10^{-1}{}^{+0.0}_{-0.0}$	$4.61\cdot10^{0}{}^{+0.5}_{-0.5}$
260	$6.66\cdot10^{-4}{}^{+7.6}_{-7.5}$	$2.16\cdot10^{-5}{}^{+1.7}_{-1.7}$	$8.57\cdot10^{-5}{}^{+5.6}_{-5.6}$	$6.99\cdot10^{-1}{}^{+0.0}_{-0.0}$	$2.99\cdot10^{-1}{}^{+0.0}_{-0.0}$	$4.76\cdot10^{0}{}^{+0.5}_{-0.5}$
262	$6.63\cdot10^{-4}{}^{+7.7}_{-7.5}$	$2.11\cdot10^{-5}{}^{+1.7}_{-1.7}$	$8.39\cdot10^{-5}{}^{+5.6}_{-5.6}$	$6.98\cdot10^{-1}{}^{+0.0}_{-0.0}$	$3.00\cdot10^{-1}{}^{+0.0}_{-0.0}$	$4.91\cdot10^{0}{}^{+0.5}_{-0.5}$
264	$6.61\cdot10^{-4}{}^{+7.7}_{-7.6}$	$2.06\cdot10^{-5}{}^{+1.7}_{-1.7}$	$8.21\cdot10^{-5}{}^{+5.6}_{-5.6}$	$6.98\cdot10^{-1}{}^{+0.0}_{-0.0}$	$3.00\cdot10^{-1}{}^{+0.0}_{-0.0}$	$5.07\cdot10^{0}{}^{+0.5}_{-0.5}$
266	$6.59\cdot10^{-4}{}^{+7.7}_{-7.6}$	$2.01\cdot10^{-5}{}^{+1.7}_{-1.7}$	$8.05\cdot10^{-5}{}^{+5.6}_{-5.6}$	$6.98\cdot10^{-1}{}^{+0.0}_{-0.0}$	$3.01\cdot10^{-1}{}^{+0.0}_{-0.0}$	$5.23\cdot10^{0}{}^{+0.5}_{-0.5}$
268	$6.57\cdot10^{-4}{}^{+7.7}_{-7.6}$	$1.96\cdot10^{-5}{}^{+1.7}_{-1.7}$	$7.88\cdot10^{-5}{}^{+5.6}_{-5.6}$	$6.97\cdot10^{-1}{}^{+0.0}_{-0.0}$	$3.01\cdot10^{-1}{}^{+0.0}_{-0.0}$	$5.39\cdot10^{0}{}^{+0.5}_{-0.5}$
270	$6.55\cdot10^{-4}{}^{+7.7}_{-7.6}$	$1.91\cdot10^{-5}{}^{+1.7}_{-1.7}$	$7.72\cdot10^{-5}{}^{+5.6}_{-5.6}$	$6.97\cdot10^{-1}{}^{+0.0}_{-0.0}$	$3.02\cdot10^{-1}{}^{+0.0}_{-0.0}$	$5.55\cdot10^{0}{}^{+0.5}_{-0.5}$
272	$6.54\cdot10^{-4}{}^{+7.7}_{-7.6}$	$1.86\cdot10^{-5}{}^{+1.7}_{-1.7}$	$7.56\cdot10^{-5}{}^{+5.6}_{-5.6}$	$6.96\cdot10^{-1}{}^{+0.0}_{-0.0}$	$3.02\cdot10^{-1}{}^{+0.0}_{-0.0}$	$5.72\cdot10^{0}{}^{+0.5}_{-0.5}$
274	$6.52\cdot10^{-4}{}^{+7.7}_{-7.6}$	$1.82\cdot10^{-5}{}^{+1.7}_{-1.7}$	$7.41\cdot10^{-5}{}^{+5.6}_{-5.6}$	$6.96\cdot10^{-1}{}^{+0.0}_{-0.0}$	$3.02\cdot10^{-1}{}^{+0.0}_{-0.0}$	$5.89\cdot10^{0}{}^{+0.5}_{-0.5}$
276	$6.51\cdot10^{-4}{}^{+7.7}_{-7.6}$	$1.77\cdot10^{-5}{}^{+1.7}_{-1.7}$	$7.26\cdot10^{-5}{}^{+5.6}_{-5.6}$	$6.96\cdot10^{-1}{}^{+0.0}_{-0.0}$	$3.03\cdot10^{-1}{}^{+0.0}_{-0.0}$	$6.07\cdot10^{0}{}^{+0.5}_{-0.5}$
278	$6.50\cdot10^{-4}{}^{+7.7}_{-7.6}$	$1.73\cdot10^{-5}{}^{+1.8}_{-1.7}$	$7.12\cdot10^{-5}{}^{+5.6}_{-5.6}$	$6.95\cdot10^{-1}{}^{+0.0}_{-0.0}$	$3.03\cdot10^{-1}{}^{+0.0}_{-0.0}$	$6.25\cdot10^{0}{}^{+0.5}_{-0.5}$
280	$6.50\cdot10^{-4}{}^{+7.7}_{-7.6}$	$1.69\cdot10^{-5}{}^{+1.8}_{-1.8}$	$6.98\cdot10^{-5}{}^{+5.6}_{-5.6}$	$6.95\cdot10^{-1}{}^{+0.0}_{-0.0}$	$3.04\cdot10^{-1}{}^{+0.0}_{-0.0}$	$6.43\cdot10^{0}{}^{+0.5}_{-0.5}$
282	$6.49\cdot10^{-4}{}^{+7.8}_{-7.6}$	$1.65\cdot10^{-5}{}^{+1.8}_{-1.8}$	$6.84\cdot10^{-5}{}^{+5.6}_{-5.6}$	$6.95\cdot10^{-1}{}^{+0.0}_{-0.0}$	$3.04\cdot10^{-1}{}^{+0.0}_{-0.0}$	$6.61\cdot10^{0}{}^{+0.5}_{-0.5}$
284	$6.49\cdot10^{-4}{}^{+7.8}_{-7.7}$	$1.61\cdot10^{-5}{}^{+1.7}_{-1.8}$	$6.71\cdot10^{-5}{}^{+5.6}_{-5.6}$	$6.94\cdot10^{-1}{}^{+0.0}_{-0.0}$	$3.04\cdot10^{-1}{}^{+0.0}_{-0.0}$	$6.80\cdot10^{0}{}^{+0.5}_{-0.5}$
286	$6.49\cdot10^{-4}{}^{+7.8}_{-7.7}$	$1.57\cdot10^{-5}{}^{+1.7}_{-1.8}$	$6.57\cdot10^{-5}{}^{+5.6}_{-5.6}$	$6.94\cdot10^{-1}{}^{+0.0}_{-0.0}$	$3.05\cdot10^{-1}{}^{+0.0}_{-0.0}$	$6.99\cdot10^{0}{}^{+0.5}_{-0.5}$
288	$6.49\cdot10^{-4}{}^{+7.8}_{-7.7}$	$1.54\cdot10^{-5}{}^{+1.7}_{-1.8}$	$6.45\cdot10^{-5}{}^{+5.6}_{-5.6}$	$6.93\cdot10^{-1}{}^{+0.0}_{-0.0}$	$3.05\cdot10^{-1}{}^{+0.0}_{-0.0}$	$7.19\cdot10^{0}{}^{+0.5}_{-0.5}$
290	$6.49\cdot10^{-4}{}^{+7.9}_{-7.7}$	$1.50\cdot10^{-5}{}^{+1.8}_{-1.8}$	$6.32\cdot10^{-5}{}^{+5.6}_{-5.6}$	$6.93\cdot10^{-1}{}^{+0.0}_{-0.0}$	$3.05\cdot10^{-1}{}^{+0.0}_{-0.0}$	$7.39\cdot10^{0}{}^{+0.5}_{-0.5}$
292	$6.49\cdot10^{-4}{}^{+7.9}_{-7.7}$	$1.47\cdot10^{-5}{}^{+1.8}_{-1.8}$	$6.20\cdot10^{-5}{}^{+5.6}_{-5.6}$	$6.93\cdot10^{-1}{}^{+0.0}_{-0.0}$	$3.06\cdot10^{-1}{}^{+0.0}_{-0.0}$	$7.59\cdot10^{0}{}^{+0.5}_{-0.5}$
294	$6.50\cdot10^{-4}{}^{+7.9}_{-7.7}$	$1.44\cdot10^{-5}{}^{+1.7}_{-1.8}$	$6.08\cdot10^{-5}{}^{+5.6}_{-5.6}$	$6.93\cdot10^{-1}{}^{+0.0}_{-0.0}$	$3.06\cdot10^{-1}{}^{+0.0}_{-0.0}$	$7.79\cdot10^{0}{}^{+0.5}_{-0.5}$
296	$6.51\cdot10^{-4}{}^{+7.9}_{-7.8}$	$1.41\cdot10^{-5}{}^{+1.7}_{-1.8}$	$5.97\cdot10^{-5}{}^{+5.6}_{-5.6}$	$6.92\cdot10^{-1}{}^{+0.0}_{-0.0}$	$3.06\cdot10^{-1}{}^{+0.0}_{-0.0}$	$8.00\cdot10^{0}{}^{+0.5}_{-0.5}$
298	$6.52\cdot10^{-4}{}^{+8.0}_{-7.8}$	$1.37\cdot10^{-5}{}^{+1.8}_{-1.8}$	$5.86\cdot10^{-5}{}^{+5.6}_{-5.6}$	$6.92\cdot10^{-1}{}^{+0.0}_{-0.0}$	$3.07\cdot10^{-1}{}^{+0.0}_{-0.0}$	$8.22\cdot10^{0}{}^{+0.5}_{-0.5}$
300	$6.53\cdot10^{-4}{}^{+8.0}_{-7.8}$	$1.34\cdot10^{-5}{}^{+1.8}_{-1.8}$	$5.75\cdot10^{-5}{}^{+5.6}_{-5.6}$	$6.92\cdot10^{-1}{}^{+0.0}_{-0.0}$	$3.07\cdot10^{-1}{}^{+0.0}_{-0.0}$	$8.43\cdot10^{0}{}^{+0.5}_{-0.5}$
305	$6.58\cdot10^{-4}{}^{+8.1}_{-7.9}$	$1.27\cdot10^{-5}{}^{+1.8}_{-1.8}$	$5.48\cdot10^{-5}{}^{+5.6}_{-5.6}$	$6.91\cdot10^{-1}{}^{+0.0}_{-0.0}$	$3.08\cdot10^{-1}{}^{+0.0}_{-0.0}$	$8.99\cdot10^{0}{}^{+0.5}_{-0.5}$
310	$6.64\cdot10^{-4}{}^{+8.2}_{-8.0}$	$1.21\cdot10^{-5}{}^{+1.9}_{-1.9}$	$5.24\cdot10^{-5}{}^{+5.6}_{-5.6}$	$6.90\cdot10^{-1}{}^{+0.0}_{-0.0}$	$3.08\cdot10^{-1}{}^{+0.0}_{-0.0}$	$9.57\cdot10^{0}{}^{+0.5}_{-0.5}$
315	$6.71\cdot10^{-4}{}^{+8.4}_{-8.1}$	$1.14\cdot10^{-5}{}^{+1.9}_{-1.8}$	$5.00\cdot10^{-5}{}^{+5.6}_{-5.6}$	$6.90\cdot10^{-1}{}^{+0.0}_{-0.0}$	$3.09\cdot10^{-1}{}^{+0.0}_{-0.0}$	$1.02\cdot10^{1}{}^{+0.5}_{-0.5}$
320	$6.80\cdot10^{-4}{}^{+8.6}_{-8.2}$	$1.09\cdot10^{-5}{}^{+1.9}_{-1.9}$	$4.78\cdot10^{-5}{}^{+5.7}_{-5.5}$	$6.89\cdot10^{-1}{}^{+0.0}_{-0.0}$	$3.09\cdot10^{-1}{}^{+0.0}_{-0.0}$	$1.08\cdot10^{1}{}^{+0.5}_{-0.5}$
325	$6.93\cdot10^{-4}{}^{+8.8}_{-8.4}$	$1.03\cdot10^{-5}{}^{+1.9}_{-1.9}$	$4.58\cdot10^{-5}{}^{+5.5}_{-5.5}$	$6.88\cdot10^{-1}{}^{+0.0}_{-0.0}$	$3.10\cdot10^{-1}{}^{+0.0}_{-0.1}$	$1.14\cdot10^{1}{}^{+0.5}_{-0.5}$
330	$7.07\cdot10^{-4}{}^{+9.1}_{-8.6}$	$9.83\cdot10^{-6}{}^{+1.9}_{-2.0}$	$4.38\cdot10^{-5}{}^{+5.6}_{-5.5}$	$6.88\cdot10^{-1}{}^{+0.0}_{-0.0}$	$3.10\cdot10^{-1}{}^{+0.1}_{-0.1}$	$1.21\cdot10^{1}{}^{+0.5}_{-0.6}$
335	$7.26\cdot10^{-4}{}^{+9.6}_{-9.0}$	$9.37\cdot10^{-6}{}^{+1.9}_{-2.0}$	$4.21\cdot10^{-5}{}^{+5.5}_{-5.5}$	$6.87\cdot10^{-1}{}^{+0.0}_{-0.0}$	$3.11\cdot10^{-1}{}^{+0.1}_{-0.1}$	$1.28\cdot10^{1}{}^{+0.6}_{-0.6}$
340	$7.50\cdot10^{-4}{}^{+10.8}_{-9.4}$	$8.91\cdot10^{-6}{}^{+2.1}_{-2.5}$	$4.03\cdot10^{-5}{}^{+5.6}_{-5.5}$	$6.87\cdot10^{-1}{}^{+0.0}_{-0.2}$	$3.11\cdot10^{-1}{}^{+0.1}_{-0.3}$	$1.35\cdot10^{1}{}^{+0.7}_{-0.7}$
345	$7.83\cdot10^{-4}{}^{+9.5}_{-10.2}$	$8.44\cdot10^{-6}{}^{+3.4}_{-6.1}$	$3.88\cdot10^{-5}{}^{+5.5}_{-7.5}$	$6.85\cdot10^{-1}{}^{+0.2}_{-1.3}$	$3.11\cdot10^{-1}{}^{+0.3}_{-1.4}$	$1.42\cdot10^{1}{}^{+2.0}_{-0.5}$
350	$8.14\cdot10^{-4}{}^{+9.4}_{-10.5}$	$7.73\cdot10^{-6}{}^{+6.0}_{-8.0}$	$3.65\cdot10^{-5}{}^{+7.6}_{-8.7}$	$6.76\cdot10^{-1}{}^{+1.3}_{-2.0}$	$3.07\cdot10^{-1}{}^{+1.4}_{-2.1}$	$1.52\cdot10^{1}{}^{+3.0}_{-2.0}$
360	$8.51\cdot10^{-4}{}^{+8.2}_{-8.6}$	$6.25\cdot10^{-6}{}^{+9.0}_{-8.9}$	$3.17\cdot10^{-5}{}^{+9.1}_{-9.0}$	$6.51\cdot10^{-1}{}^{+2.2}_{-2.2}$	$2.97\cdot10^{-1}{}^{+2.3}_{-2.2}$	$1.76\cdot10^{1}{}^{+3.1}_{-3.1}$
370	$8.64\cdot10^{-4}{}^{+7.8}_{-8.0}$	$5.03\cdot10^{-6}{}^{+9.8}_{-9.3}$	$2.76\cdot10^{-5}{}^{+9.2}_{-9.0}$	$6.28\cdot10^{-1}{}^{+2.3}_{-2.2}$	$2.87\cdot10^{-1}{}^{+2.3}_{-2.2}$	$2.02\cdot10^{1}{}^{+3.0}_{-3.0}$

Table A.14: SM Higgs branching ratios to two gauge bosons and Higgs total width together with their total uncertainties (expressed in percentage). High-mass range.

M_H [GeV]	H → gg	H → $\gamma\gamma$	H → Zγ	H → WW	H → ZZ	Total Γ_H [GeV]
380	$8.61\cdot10^{-4}{}^{+7.7}_{-7.7}$	$4.06\cdot10^{-6}{}^{+10.0}_{-9.6}$	$2.42\cdot10^{-5}{}^{+9.1}_{-8.9}$	$6.09\cdot10^{-1}{}^{+2.2}_{-2.1}$	$2.80\cdot10^{-1}{}^{+2.2}_{-2.1}$	$2.31\cdot10^{1}{}^{+2.8}_{-2.9}$
390	$8.50\cdot10^{-4}{}^{+7.7}_{-7.7}$	$3.27\cdot10^{-6}{}^{+10.4}_{-9.7}$	$2.14\cdot10^{-5}{}^{+9.0}_{-8.7}$	$5.94\cdot10^{-1}{}^{+2.1}_{-2.0}$	$2.74\cdot10^{-1}{}^{+2.1}_{-2.0}$	$2.61\cdot10^{1}{}^{+2.6}_{-2.7}$
400	$8.32\cdot10^{-4}{}^{+7.8}_{-7.7}$	$2.65\cdot10^{-6}{}^{+10.4}_{-9.8}$	$1.90\cdot10^{-5}{}^{+8.7}_{-8.5}$	$5.82\cdot10^{-1}{}^{+2.0}_{-1.9}$	$2.69\cdot10^{-1}{}^{+2.0}_{-1.9}$	$2.92\cdot10^{1}{}^{+2.5}_{-2.5}$
420	$7.89\cdot10^{-4}{}^{+7.9}_{-7.9}$	$1.74\cdot10^{-6}{}^{+10.6}_{-9.8}$	$1.53\cdot10^{-5}{}^{+8.3}_{-8.2}$	$5.65\cdot10^{-1}{}^{+1.8}_{-1.7}$	$2.63\cdot10^{-1}{}^{+1.7}_{-1.6}$	$3.59\cdot10^{1}{}^{+2.1}_{-2.2}$
440	$7.42\cdot10^{-4}{}^{+8.1}_{-8.0}$	$1.15\cdot10^{-6}{}^{+10.7}_{-10.1}$	$1.26\cdot10^{-5}{}^{+8.0}_{-7.8}$	$5.55\cdot10^{-1}{}^{+1.6}_{-1.5}$	$2.60\cdot10^{-1}{}^{+1.5}_{-1.4}$	$4.30\cdot10^{1}{}^{+1.9}_{-2.0}$
450	$7.18\cdot10^{-4}{}^{+8.1}_{-8.1}$	$9.28\cdot10^{-7}{}^{+10.9}_{-10.0}$	$1.15\cdot10^{-5}{}^{+7.8}_{-7.6}$	$5.51\cdot10^{-1}{}^{+1.5}_{-1.4}$	$2.59\cdot10^{-1}{}^{+1.4}_{-1.3}$	$4.68\cdot10^{1}{}^{+1.8}_{-1.8}$
460	$6.94\cdot10^{-4}{}^{+8.2}_{-8.1}$	$7.50\cdot10^{-7}{}^{+10.8}_{-10.1}$	$1.05\cdot10^{-5}{}^{+7.7}_{-7.5}$	$5.49\cdot10^{-1}{}^{+1.3}_{-1.3}$	$2.59\cdot10^{-1}{}^{+1.3}_{-1.3}$	$5.08\cdot10^{1}{}^{+1.7}_{-1.7}$
480	$6.47\cdot10^{-4}{}^{+8.3}_{-8.1}$	$4.86\cdot10^{-7}{}^{+11.0}_{-9.7}$	$8.88\cdot10^{-6}{}^{+7.4}_{-7.2}$	$5.46\cdot10^{-1}{}^{+1.3}_{-1.2}$	$2.60\cdot10^{-1}{}^{+1.2}_{-1.1}$	$5.91\cdot10^{1}{}^{+1.5}_{-1.6}$
500	$6.04\cdot10^{-4}{}^{+8.9}_{-8.8}$	$3.11\cdot10^{-7}{}^{+11.0}_{-9.5}$	$7.59\cdot10^{-6}{}^{+7.7}_{-7.6}$	$5.46\cdot10^{-1}{}^{+1.4}_{-1.3}$	$2.61\cdot10^{-1}{}^{+1.4}_{-1.3}$	$6.8\cdot10^{1}{}^{+2.0}_{-2.0}$
520	$5.62\cdot10^{-4}{}^{+9.1}_{-9.0}$	$1.96\cdot10^{-7}{}^{+9.9}_{-8.2}$	$6.54\cdot10^{-6}{}^{+7.6}_{-7.5}$	$5.47\cdot10^{-1}{}^{+1.4}_{-1.3}$	$2.63\cdot10^{-1}{}^{+1.4}_{-1.4}$	$7.75\cdot10^{1}{}^{+2.2}_{-2.2}$
540	$5.24\cdot10^{-4}{}^{+9.3}_{-9.2}$	$1.24\cdot10^{-7}{}^{+7.3}_{-5.2}$	$5.67\cdot10^{-6}{}^{+7.6}_{-7.5}$	$5.49\cdot10^{-1}{}^{+1.5}_{-1.4}$	$2.65\cdot10^{-1}{}^{+1.5}_{-1.5}$	$8.77\cdot10^{1}{}^{+2.4}_{-2.4}$
550	$5.06\cdot10^{-4}{}^{+9.4}_{-9.3}$	$9.89\cdot10^{-8}{}^{+5.1}_{-3.7}$	$5.30\cdot10^{-6}{}^{+7.6}_{-7.5}$	$5.50\cdot10^{-1}{}^{+1.5}_{-1.5}$	$2.66\cdot10^{-1}{}^{+1.6}_{-1.5}$	$9.30\cdot10^{1}{}^{+2.5}_{-2.6}$
560	$4.88\cdot10^{-4}{}^{+9.5}_{-9.5}$	$8.10\cdot10^{-8}{}^{+7.8}_{-4.1}$	$4.96\cdot10^{-6}{}^{+7.6}_{-7.5}$	$5.52\cdot10^{-1}{}^{+1.6}_{-1.6}$	$2.67\cdot10^{-1}{}^{+1.6}_{-1.6}$	$9.86\cdot10^{1}{}^{+2.7}_{-2.7}$
580	$4.55\cdot10^{-4}{}^{+9.7}_{-9.7}$	$5.92\cdot10^{-8}{}^{+14.3}_{-11.2}$	$4.35\cdot10^{-6}{}^{+7.8}_{-7.7}$	$5.55\cdot10^{-1}{}^{+1.6}_{-1.6}$	$2.70\cdot10^{-1}{}^{+1.7}_{-1.6}$	$1.10\cdot10^{2}{}^{+2.9}_{-2.9}$
600	$4.24\cdot10^{-4}{}^{+10.2}_{-9.9}$	$5.03\cdot10^{-8}{}^{+19.8}_{-16.8}$	$3.84\cdot10^{-6}{}^{+8.2}_{-8.0}$	$5.58\cdot10^{-1}{}^{+1.7}_{-1.6}$	$2.72\cdot10^{-1}{}^{+1.7}_{-1.7}$	$1.23\cdot10^{2}{}^{+3.2}_{-3.2}$
620	$3.96\cdot10^{-4}{}^{+10.4}_{-10.2}$	$4.82\cdot10^{-8}{}^{+23.3}_{-19.9}$	$3.40\cdot10^{-6}{}^{+8.6}_{-8.4}$	$5.62\cdot10^{-1}{}^{+1.7}_{-1.7}$	$2.75\cdot10^{-1}{}^{+1.7}_{-1.7}$	$1.36\cdot10^{2}{}^{+3.5}_{-3.5}$
640	$3.69\cdot10^{-4}{}^{+10.7}_{-10.6}$	$5.29\cdot10^{-8}{}^{+27.2}_{-23.6}$	$3.03\cdot10^{-6}{}^{+9.0}_{-8.8}$	$5.66\cdot10^{-1}{}^{+1.7}_{-1.7}$	$2.77\cdot10^{-1}{}^{+1.8}_{-1.8}$	$1.50\cdot10^{2}{}^{+3.8}_{-3.8}$
650	$3.57\cdot10^{-4}{}^{+10.9}_{-10.7}$	$5.82\cdot10^{-8}{}^{+27.1}_{-24.6}$	$2.86\cdot10^{-6}{}^{+9.3}_{-9.1}$	$5.68\cdot10^{-1}{}^{+1.8}_{-1.8}$	$2.79\cdot10^{-1}{}^{+1.8}_{-1.8}$	$1.58\cdot10^{2}{}^{+3.9}_{-3.9}$
660	$3.45\cdot10^{-4}{}^{+11.1}_{-10.9}$	$6.60\cdot10^{-8}{}^{+26.3}_{-23.9}$	$2.70\cdot10^{-6}{}^{+9.5}_{-9.3}$	$5.7\cdot10^{-1}{}^{+1.8}_{-1.8}$	$2.80\cdot10^{-1}{}^{+1.8}_{-1.8}$	$1.65\cdot10^{2}{}^{+4.1}_{-4.1}$
680	$3.22\cdot10^{-4}{}^{+11.6}_{-11.2}$	$8.65\cdot10^{-8}{}^{+21.8}_{-20.9}$	$2.42\cdot10^{-6}{}^{+10.0}_{-9.7}$	$5.73\cdot10^{-1}{}^{+1.8}_{-1.8}$	$2.82\cdot10^{-1}{}^{+1.8}_{-1.8}$	$1.82\cdot10^{2}{}^{+4.5}_{-4.5}$
700	$3.01\cdot10^{-4}{}^{+11.9}_{-11.7}$	$1.11\cdot10^{-7}{}^{+19.3}_{-17.8}$	$2.18\cdot10^{-6}{}^{+10.5}_{-10.2}$	$5.77\cdot10^{-1}{}^{+1.9}_{-1.9}$	$2.85\cdot10^{-1}{}^{+1.9}_{-1.9}$	$1.99\cdot10^{2}{}^{+4.9}_{-4.9}$
720	$2.81\cdot10^{-4}{}^{+12.5}_{-12.2}$	$1.38\cdot10^{-7}{}^{+16.8}_{-16.0}$	$1.96\cdot10^{-6}{}^{+11.1}_{-10.7}$	$5.81\cdot10^{-1}{}^{+1.9}_{-1.9}$	$2.87\cdot10^{-1}{}^{+1.9}_{-1.9}$	$2.17\cdot10^{2}{}^{+5.3}_{-5.3}$
740	$2.63\cdot10^{-4}{}^{+13.1}_{-12.6}$	$1.65\cdot10^{-7}{}^{+15.6}_{-14.7}$	$1.77\cdot10^{-6}{}^{+11.7}_{-11.3}$	$5.84\cdot10^{-1}{}^{+1.9}_{-1.9}$	$2.89\cdot10^{-1}{}^{+1.9}_{-1.9}$	$2.37\cdot10^{2}{}^{+5.8}_{-5.8}$
750	$2.55\cdot10^{-4}{}^{+13.3}_{-12.9}$	$1.79\cdot10^{-7}{}^{+15.2}_{-14.2}$	$1.69\cdot10^{-6}{}^{+12.1}_{-11.6}$	$5.86\cdot10^{-1}{}^{+1.9}_{-2.0}$	$2.90\cdot10^{-1}{}^{+1.9}_{-2.0}$	$2.47\cdot10^{2}{}^{+6.1}_{-6.1}$
760	$2.46\cdot10^{-4}{}^{+13.6}_{-13.1}$	$1.92\cdot10^{-7}{}^{+14.8}_{-13.9}$	$1.61\cdot10^{-6}{}^{+12.4}_{-11.8}$	$5.88\cdot10^{-1}{}^{+1.9}_{-2.0}$	$2.91\cdot10^{-1}{}^{+1.9}_{-2.0}$	$2.58\cdot10^{2}{}^{+6.3}_{-6.3}$
780	$2.31\cdot10^{-4}{}^{+14.3}_{-13.7}$	$2.18\cdot10^{-7}{}^{+14.3}_{-13.6}$	$1.46\cdot10^{-6}{}^{+13.1}_{-12.5}$	$5.91\cdot10^{-1}{}^{+2.0}_{-2.0}$	$2.94\cdot10^{-1}{}^{+2.0}_{-2.0}$	$2.80\cdot10^{2}{}^{+6.9}_{-6.9}$
800	$2.16\cdot10^{-4}{}^{+15.0}_{-14.3}$	$2.44\cdot10^{-7}{}^{+14.4}_{-13.3}$	$1.33\cdot10^{-6}{}^{+14.0}_{-13.1}$	$5.94\cdot10^{-1}{}^{+2.0}_{-2.1}$	$2.96\cdot10^{-1}{}^{+2.0}_{-2.1}$	$3.04\cdot10^{2}{}^{+7.5}_{-7.5}$
820	$2.03\cdot10^{-4}{}^{+15.9}_{-14.9}$	$2.69\cdot10^{-7}{}^{+14.4}_{-13.2}$	$1.22\cdot10^{-6}{}^{+14.8}_{-13.8}$	$5.98\cdot10^{-1}{}^{+2.0}_{-2.1}$	$2.97\cdot10^{-1}{}^{+2.0}_{-2.1}$	$3.30\cdot10^{2}{}^{+8.2}_{-8.2}$
840	$1.90\cdot10^{-4}{}^{+16.7}_{-15.6}$	$2.93\cdot10^{-7}{}^{+14.6}_{-13.4}$	$1.12\cdot10^{-6}{}^{+15.7}_{-14.5}$	$6.01\cdot10^{-1}{}^{+2.0}_{-2.2}$	$2.99\cdot10^{-1}{}^{+2.0}_{-2.1}$	$3.57\cdot10^{2}{}^{+8.9}_{-8.9}$
850	$1.84\cdot10^{-4}{}^{+17.3}_{-15.8}$	$3.04\cdot10^{-7}{}^{+14.9}_{-13.4}$	$1.07\cdot10^{-6}{}^{+16.3}_{-14.9}$	$6.02\cdot10^{-1}{}^{+2.1}_{-2.2}$	$3.00\cdot10^{-1}{}^{+2.0}_{-2.2}$	$3.71\cdot10^{2}{}^{+9.3}_{-9.3}$
860	$1.78\cdot10^{-4}{}^{+17.7}_{-16.3}$	$3.15\cdot10^{-7}{}^{+15.3}_{-13.5}$	$1.02\cdot10^{-6}{}^{+16.7}_{-15.3}$	$6.04\cdot10^{-1}{}^{+2.1}_{-2.2}$	$3.01\cdot10^{-1}{}^{+2.0}_{-2.2}$	$3.86\cdot10^{2}{}^{+9.7}_{-9.7}$
880	$1.67\cdot10^{-4}{}^{+18.9}_{-16.9}$	$3.37\cdot10^{-7}{}^{+15.8}_{-13.9}$	$9.44\cdot10^{-7}{}^{+17.9}_{-16.0}$	$6.06\cdot10^{-1}{}^{+2.1}_{-2.2}$	$3.03\cdot10^{-1}{}^{+2.1}_{-2.2}$	$4.16\cdot10^{2}{}^{+10.6}_{-10.6}$
900	$1.57\cdot10^{-4}{}^{+20.0}_{-17.7}$	$3.58\cdot10^{-7}{}^{+16.2}_{-14.4}$	$8.72\cdot10^{-7}{}^{+19.0}_{-16.9}$	$6.09\cdot10^{-1}{}^{+2.1}_{-2.3}$	$3.04\cdot10^{-1}{}^{+2.1}_{-2.3}$	$4.49\cdot10^{2}{}^{+11.5}_{-11.5}$
920	$1.48\cdot10^{-4}{}^{+21.2}_{-18.6}$	$3.77\cdot10^{-7}{}^{+17.9}_{-14.7}$	$8.07\cdot10^{-7}{}^{+20.3}_{-17.8}$	$6.12\cdot10^{-1}{}^{+2.1}_{-2.3}$	$3.06\cdot10^{-1}{}^{+2.1}_{-2.3}$	$4.84\cdot10^{2}{}^{+12.4}_{-12.4}$
940	$1.39\cdot10^{-4}{}^{+22.5}_{-19.4}$	$3.93\cdot10^{-7}{}^{+18.6}_{-15.6}$	$7.49\cdot10^{-7}{}^{+21.7}_{-18.6}$	$6.14\cdot10^{-1}{}^{+2.2}_{-2.4}$	$3.07\cdot10^{-1}{}^{+2.1}_{-2.4}$	$5.21\cdot10^{2}{}^{+13.5}_{-13.5}$
950	$1.34\cdot10^{-4}{}^{+23.3}_{-19.9}$	$4.00\cdot10^{-7}{}^{+19.2}_{-15.9}$	$7.22\cdot10^{-7}{}^{+22.5}_{-19.1}$	$6.16\cdot10^{-1}{}^{+2.2}_{-2.4}$	$3.08\cdot10^{-1}{}^{+2.1}_{-2.4}$	$5.40\cdot10^{2}{}^{+14.0}_{-14.0}$
960	$1.30\cdot10^{-4}{}^{+24.1}_{-20.4}$	$4.08\cdot10^{-7}{}^{+19.9}_{-16.2}$	$6.97\cdot10^{-7}{}^{+23.3}_{-19.6}$	$6.17\cdot10^{-1}{}^{+2.2}_{-2.4}$	$3.09\cdot10^{-1}{}^{+2.1}_{-2.4}$	$5.60\cdot10^{2}{}^{+14.6}_{-14.6}$
980	$1.23\cdot10^{-4}{}^{+25.7}_{-21.4}$	$4.27\cdot10^{-7}{}^{+21.3}_{-16.9}$	$6.50\cdot10^{-7}{}^{+24.9}_{-20.5}$	$6.19\cdot10^{-1}{}^{+2.2}_{-2.5}$	$3.10\cdot10^{-1}{}^{+2.2}_{-2.5}$	$6.02\cdot10^{2}{}^{+15.8}_{-15.8}$
1000	$1.15\cdot10^{-4}{}^{+27.5}_{-22.4}$	$4.39\cdot10^{-7}{}^{+23.0}_{-17.7}$	$6.08\cdot10^{-7}{}^{+26.8}_{-21.6}$	$6.21\cdot10^{-1}{}^{+2.2}_{-2.6}$	$3.11\cdot10^{-1}{}^{+2.2}_{-2.5}$	$6.47\cdot10^{2}{}^{+17.1}_{-17.1}$

B   Tables of cross sections

Tables with the cross section values for the various production modes follow.

Table B.1: ggF cross sections at the LHC at 7 TeV and corresponding scale and PDF+α_s uncertainties computed according to the PDF4LHC recommendation.

M_{H}[GeV]	σ [pb]	QCD Scale [%]	PDF+α_{s} [%]
80.0	36.59	+8.3 −8.8	+7.8 −6.7
81.0	35.71	+8.3 −8.8	+7.8 −6.7
82.0	34.86	+8.3 −8.8	+7.8 −6.7
83.0	34.04	+8.3 −8.8	+7.8 −6.7
84.0	33.25	+8.3 −8.8	+7.8 −6.7
85.0	32.49	+8.3 −8.8	+7.8 −6.7
86.0	31.75	+8.3 −8.8	+7.8 −6.7
87.0	31.04	+8.3 −8.8	+7.8 −6.7
88.0	30.35	+8.3 −8.7	+7.8 −6.7
89.0	29.69	+8.2 −8.7	+7.8 −6.7
90.0	29.03	+8.2 −8.7	+7.8 −6.7
91.0	28.42	+8.2 −8.7	+7.8 −6.7
92.0	27.81	+8.1 −8.7	+7.8 −6.7
93.0	27.23	+8.1 −8.6	+7.8 −6.7
94.0	26.65	+8.1 −8.6	+7.8 −6.7
95.0	26.10	+8.0 −8.6	+7.8 −6.7
96.0	25.56	+8.0 −8.6	+7.8 −6.7
97.0	25.06	+7.9 −8.5	+7.8 −6.7
98.0	24.56	+7.9 −8.5	+7.8 −6.8
99.0	24.07	+7.8 −8.5	+7.7 −6.8
100.0	23.64	+7.8 −8.4	+7.7 −6.8
101.0	23.17	+7.8 −8.4	+7.7 −6.8
102.0	22.73	+7.8 −8.4	+7.7 −6.8
103.0	22.29	+7.7 −8.3	+7.7 −6.9
104.0	21.87	+7.7 −8.3	+7.7 −6.9
105.0	21.45	+7.7 −8.3	+7.7 −6.9
106.0	21.05	+7.7 −8.3	+7.7 −6.9
107.0	20.67	+7.6 −8.2	+7.7 −6.9
108.0	20.29	+7.6 −8.2	+7.7 −6.9
109.0	19.92	+7.6 −8.2	+7.7 −6.9
110.0	19.56	+7.5 −8.1	+7.7 −6.9
110.5	19.38	+7.5 −8.1	+7.7 −6.9
111.0	19.21	+7.5 −8.1	+7.7 −6.9
111.5	19.03	+7.5 −8.1	+7.7 −6.9
112.0	18.87	+7.5 −8.1	+7.7 −6.9
112.5	18.70	+7.4 −8.0	+7.7 −6.9
113.0	18.53	+7.4 −8.0	+7.7 −7.0
113.5	18.37	+7.4 −8.0	+7.7 −7.0
114.0	18.21	+7.4 −8.0	+7.7 −7.0
114.5	18.05	+7.4 −8.0	+7.7 −7.0
115.0	17.89	+7.4 −8.0	+7.7 −7.0
115.5	17.74	+7.4 −8.0	+7.7 −7.0
116.0	17.59	+7.4 −8.0	+7.7 −7.0
116.5	17.44	+7.4 −8.0	+7.7 −7.0
117.0	17.29	+7.3 −8.0	+7.7 −7.0
117.5	17.14	+7.3 −8.0	+7.7 −7.0
118.0	16.99	+7.3 −7.9	+7.7 −7.0

Table B.2: ggF cross sections at the LHC at 7 TeV and corresponding scale and PDF+α_s uncertainties computed according to the PDF4LHC recommendation.

M_H[GeV]	σ [pb]	QCD Scale [%]	PDF+α_s [%]
118.5	16.85	+7.3 −7.9	+7.6 −7.0
119.0	16.71	+7.3 −7.9	+7.6 −7.0
119.5	16.57	+7.2 −7.9	+7.6 −7.0
120.0	16.43	+7.2 −7.9	+7.6 −7.0
120.1	16.40	+7.2 −7.9	+7.6 −7.0
120.2	16.37	+7.2 −7.9	+7.6 −7.0
120.3	16.35	+7.2 −7.9	+7.6 −7.0
120.4	16.32	+7.2 −7.9	+7.6 −7.0
120.5	16.29	+7.2 −7.9	+7.6 −7.0
120.6	16.27	+7.2 −7.9	+7.6 −7.0
120.7	16.24	+7.2 −7.9	+7.6 −7.0
120.8	16.21	+7.2 −7.9	+7.6 −7.0
120.9	16.18	+7.2 −7.9	+7.6 −7.0
121.0	16.16	+7.2 −7.9	+7.6 −7.0
121.1	16.13	+7.2 −7.9	+7.6 −7.0
121.2	16.10	+7.2 −7.9	+7.6 −7.0
121.3	16.08	+7.2 −7.9	+7.6 −7.0
121.4	16.05	+7.2 −7.9	+7.6 −7.0
121.5	16.02	+7.2 −7.9	+7.6 −7.0
121.6	16.00	+7.2 −7.9	+7.6 −7.0
121.7	15.97	+7.2 −7.9	+7.6 −7.0
121.8	15.94	+7.2 −7.9	+7.6 −7.0
121.9	15.92	+7.2 −7.9	+7.6 −7.0
122.0	15.89	+7.2 −7.9	+7.6 −7.0
122.1	15.87	+7.2 −7.9	+7.6 −7.0
122.2	15.84	+7.2 −7.9	+7.6 −7.0
122.3	15.81	+7.1 −7.9	+7.6 −7.0
122.4	15.79	+7.1 −7.9	+7.6 −7.0
122.5	15.76	+7.1 −7.9	+7.6 −7.0
122.6	15.73	+7.1 −7.9	+7.6 −7.0
122.7	15.71	+7.1 −7.9	+7.6 −7.0
122.8	15.68	+7.1 −7.8	+7.6 −7.1
122.9	15.66	+7.1 −7.8	+7.6 −7.1
123.0	15.63	+7.1 −7.8	+7.6 −7.1
123.1	15.61	+7.1 −7.8	+7.6 −7.1
123.2	15.58	+7.1 −7.8	+7.6 −7.1
123.3	15.56	+7.1 −7.8	+7.6 −7.1
123.4	15.53	+7.1 −7.8	+7.6 −7.1
123.5	15.51	+7.1 −7.8	+7.6 −7.1
123.6	15.48	+7.1 −7.8	+7.6 −7.1
123.7	15.46	+7.1 −7.8	+7.6 −7.1
123.8	15.43	+7.1 −7.8	+7.6 −7.1
123.9	15.40	+7.1 −7.8	+7.6 −7.1
124.0	15.38	+7.1 −7.8	+7.6 −7.1
124.1	15.35	+7.1 −7.8	+7.6 −7.1
124.2	15.33	+7.1 −7.8	+7.6 −7.1
124.3	15.31	+7.1 −7.8	+7.6 −7.1

Table B.3: ggF cross sections at the LHC at 7 TeV and corresponding scale and PDF+α_s uncertainties computed according to the PDF4LHC recommendation.

M_H[GeV]	σ [pb]	QCD Scale [%]	PDF+α_s [%]
124.4	15.28	+7.1 −7.8	+7.6 −7.1
124.5	15.26	+7.1 −7.8	+7.6 −7.1
124.6	15.23	+7.1 −7.8	+7.6 −7.1
124.7	15.21	+7.1 −7.8	+7.6 −7.1
124.8	15.18	+7.1 −7.8	+7.6 −7.1
124.9	15.16	+7.1 −7.8	+7.6 −7.1
125.0	15.13	+7.1 −7.8	+7.6 −7.1
125.1	15.11	+7.1 −7.8	+7.6 −7.1
125.2	15.08	+7.1 −7.8	+7.6 −7.1
125.3	15.06	+7.1 −7.8	+7.6 −7.1
125.4	15.04	+7.1 −7.8	+7.6 −7.1
125.5	15.01	+7.1 −7.8	+7.6 −7.1
125.6	14.99	+7.1 −7.8	+7.6 −7.1
125.7	14.96	+7.1 −7.8	+7.6 −7.1
125.8	14.94	+7.1 −7.8	+7.6 −7.1
125.9	14.91	+7.1 −7.8	+7.6 −7.1
126.0	14.89	+7.1 −7.8	+7.6 −7.1
126.1	14.87	+7.1 −7.8	+7.6 −7.1
126.2	14.84	+7.1 −7.8	+7.6 −7.1
126.3	14.82	+7.1 −7.8	+7.6 −7.1
126.4	14.80	+7.1 −7.8	+7.6 −7.1
126.5	14.77	+7.1 −7.8	+7.6 −7.1
126.6	14.75	+7.1 −7.8	+7.6 −7.1
126.7	14.73	+7.1 −7.8	+7.6 −7.1
126.8	14.70	+7.1 −7.8	+7.6 −7.1
126.9	14.68	+7.1 −7.8	+7.6 −7.1
127.0	14.65	+7.1 −7.8	+7.6 −7.1
127.1	14.63	+7.1 −7.8	+7.6 −7.1
127.2	14.62	+7.1 −7.8	+7.6 −7.1
127.3	14.59	+7.1 −7.8	+7.6 −7.2
127.4	14.56	+7.1 −7.8	+7.6 −7.2
127.5	14.54	+7.1 −7.8	+7.6 −7.2
127.6	14.52	+7.1 −7.8	+7.6 −7.2
127.7	14.49	+7.1 −7.8	+7.6 −7.2
127.8	14.47	+7.0 −7.7	+7.6 −7.2
127.9	14.45	+7.0 −7.7	+7.6 −7.2
128.0	14.42	+7.0 −7.7	+7.6 −7.2
128.1	14.40	+7.0 −7.7	+7.6 −7.2
128.2	14.38	+7.0 −7.7	+7.6 −7.2
128.3	14.36	+7.0 −7.7	+7.6 −7.2
128.4	14.33	+7.0 −7.7	+7.6 −7.2
128.5	14.31	+7.0 −7.7	+7.6 −7.2
128.6	14.29	+7.0 −7.7	+7.6 −7.2
128.7	14.27	+7.0 −7.7	+7.6 −7.2
128.8	14.24	+7.0 −7.7	+7.6 −7.2
128.9	14.22	+7.0 −7.7	+7.6 −7.2
129.0	14.20	+7.0 −7.7	+7.6 −7.2

Table B.4: ggF cross sections at the LHC at 7 TeV and corresponding scale and PDF+α_s uncertainties computed according to the PDF4LHC recommendation.

M_H[GeV]	σ [pb]	QCD Scale [%]	PDF+α_s [%]
129.1	14.18	+7.0 −7.7	+7.6 −7.2
129.2	14.15	+7.0 −7.7	+7.6 −7.2
129.3	14.13	+7.0 −7.7	+7.6 −7.2
129.4	14.11	+7.0 −7.7	+7.6 −7.2
129.5	14.09	+7.0 −7.7	+7.6 −7.2
129.6	14.07	+7.0 −7.7	+7.6 −7.2
129.7	14.04	+7.0 −7.7	+7.6 −7.2
129.8	14.02	+7.0 −7.7	+7.6 −7.2
129.9	14.00	+7.0 −7.7	+7.6 −7.2
130.0	13.98	+7.0 −7.7	+7.6 −7.2
130.5	13.87	+7.0 −7.7	+7.6 −7.2
131.0	13.76	+7.0 −7.7	+7.6 −7.2
131.5	13.66	+7.0 −7.7	+7.6 −7.2
132.0	13.55	+7.0 −7.7	+7.6 −7.2
132.5	13.45	+7.0 −7.7	+7.6 −7.3
133.0	13.35	+6.9 −7.6	+7.6 −7.3
133.5	13.24	+6.9 −7.6	+7.6 −7.3
134.0	13.14	+6.9 −7.6	+7.6 −7.3
134.5	13.05	+6.9 −7.6	+7.6 −7.3
135.0	12.95	+6.9 −7.6	+7.6 −7.3
135.5	12.85	+6.9 −7.6	+7.6 −7.3
136.0	12.75	+6.9 −7.6	+7.6 −7.3
136.5	12.66	+6.9 −7.6	+7.6 −7.3
137.0	12.57	+6.9 −7.6	+7.6 −7.3
137.5	12.47	+6.9 −7.6	+7.6 −7.3
138.0	12.38	+6.8 −7.5	+7.6 −7.3
138.5	12.29	+6.8 −7.5	+7.6 −7.3
139.0	12.20	+6.8 −7.5	+7.6 −7.3
139.5	12.11	+6.8 −7.5	+7.6 −7.3
140.0	12.02	+6.8 −7.5	+7.6 −7.3
140.5	11.93	+6.8 −7.5	+7.6 −7.3
141.0	11.89	+6.8 −7.5	+7.6 −7.3
141.5	11.81	+6.8 −7.5	+7.6 −7.3
142.0	11.73	+6.8 −7.5	+7.6 −7.3
142.5	11.64	+6.8 −7.5	+7.6 −7.3
143.0	11.56	+6.7 −7.5	+7.6 −7.4
143.5	11.48	+6.7 −7.5	+7.6 −7.4
144.0	11.40	+6.7 −7.5	+7.6 −7.4
144.5	11.32	+6.7 −7.5	+7.6 −7.4
145.0	11.24	+6.7 −7.5	+7.6 −7.4
145.5	11.17	+6.7 −7.5	+7.6 −7.4
146.0	11.09	+6.7 −7.5	+7.6 −7.4
146.5	11.02	+6.7 −7.5	+7.6 −7.4
147.0	10.94	+6.7 −7.5	+7.6 −7.4
147.5	10.87	+6.7 −7.5	+7.6 −7.5
148.0	10.80	+6.6 −7.5	+7.6 −7.5
148.5	10.72	+6.6 −7.5	+7.6 −7.5

Table B.5: ggF cross sections at the LHC at 7 TeV and corresponding scale and PDF+α_s uncertainties computed according to the PDF4LHC recommendation.

M_{H}[GeV]	σ [pb]	QCD Scale [%]	PDF+α_s [%]
149.0	10.65	+6.6 −7.4	+7.6 −7.5
149.5	10.58	+6.6 −7.4	+7.6 −7.5
150.0	10.51	+6.6 −7.4	+7.6 −7.5
152.0	10.24	+6.6 −7.4	+7.6 −7.5
154.0	9.978	+6.5 −7.3	+7.5 −7.5
156.0	9.723	+6.5 −7.3	+7.5 −7.5
158.0	9.473	+6.4 −7.2	+7.5 −7.6
160.0	9.223	+6.4 −7.2	+7.5 −7.6
162.0	8.930	+6.4 −7.2	+7.5 −7.6
164.0	8.586	+6.4 −7.2	+7.5 −7.7
165.0	8.434	+6.4 −7.2	+7.5 −7.7
166.0	8.292	+6.4 −7.2	+7.5 −7.7
168.0	8.029	+6.4 −7.2	+7.5 −7.8
170.0	7.801	+6.3 −7.1	+7.5 −7.8
172.0	7.585	+6.3 −7.1	+7.5 −7.8
174.0	7.385	+6.2 −7.0	+7.5 −7.8
175.0	7.291	+6.2 −7.0	+7.5 −7.8
176.0	7.199	+6.2 −7.0	+7.5 −7.8
178.0	7.026	+6.2 −7.0	+7.5 −7.8
180.0	6.856	+6.2 −7.0	+7.5 −7.8
182.0	6.677	+6.2 −7.0	+7.5 −7.8
184.0	6.477	+6.1 −6.9	+7.5 −7.8
185.0	6.384	+6.1 −6.9	+7.5 −7.8
186.0	6.291	+6.1 −6.9	+7.5 −7.8
188.0	6.124	+6.1 −6.9	+7.5 −7.8
190.0	5.971	+6.1 −6.9	+7.5 −7.8
192.0	5.823	+6.1 −6.9	+7.5 −7.8
194.0	5.684	+6.1 −6.8	+7.5 −7.8
195.0	5.614	+6.1 −6.8	+7.5 −7.8
196.0	5.547	+6.1 −6.8	+7.5 −7.8
198.0	5.441	+6.1 −6.8	+7.6 −7.8
200.0	5.356	+6.0 −6.8	+7.6 −7.8
202.0	5.242	+6.0 −6.8	+7.6 −7.8
204.0	5.169	+6.0 −6.8	+7.6 −7.8
206.0	5.078	+6.0 −6.8	+7.6 −7.8
208.0	4.982	+6.0 −6.7	+7.6 −7.9
210.0	4.895	+6.0 −6.7	+7.5 −7.9
212.0	4.806	+6.1 −6.7	+7.5 −7.9
214.0	4.731	+6.1 −6.7	+7.5 −7.9
216.0	4.668	+6.2 −6.6	+7.5 −7.9
218.0	4.581	+6.4 −6.6	+7.6 −7.9
220.0	4.502	+6.5 −6.6	+7.6 −7.9
222.0	4.424	+6.5 −6.6	+7.6 −7.9
224.0	4.357	+6.4 −6.6	+7.6 −7.9
226.0	4.299	+6.3 −6.5	+7.7 −8.0
228.0	4.224	+6.1 −6.5	+7.7 −8.0
230.0	4.157	+5.9 −6.5	+7.7 −8.0

Table B.6: ggF cross sections at the LHC at 7 TeV and corresponding scale and PDF+α_s uncertainties computed according to the PDF4LHC recommendation.

M_H[GeV]	σ [pb]	QCD Scale [%]	PDF+α_s [%]
232.0	4.094	+5.9 −6.5	+7.7 −8.0
234.0	4.036	+5.8 −6.5	+7.7 −8.0
236.0	3.971	+5.8 −6.4	+7.7 −8.0
238.0	3.904	+5.9 −6.4	+7.7 −8.0
240.0	3.835	+5.9 −6.4	+7.7 −8.0
242.0	3.771	+5.9 −6.4	+7.7 −8.0
244.0	3.709	+5.9 −6.4	+7.7 −8.0
246.0	3.651	+5.9 −6.3	+7.8 −8.1
248.0	3.596	+5.8 −6.3	+7.8 −8.1
250.0	3.540	+5.8 −6.3	+7.8 −8.1
252.0	3.486	+5.8 −6.3	+7.8 −8.1
254.0	3.434	+5.8 −6.3	+7.8 −8.1
256.0	3.383	+5.8 −6.3	+7.8 −8.1
258.0	3.335	+5.8 −6.3	+7.8 −8.1
260.0	3.288	+5.8 −6.3	+7.8 −8.1
262.0	3.243	+5.8 −6.3	+7.8 −8.1
264.0	3.199	+5.8 −6.3	+7.8 −8.1
266.0	3.155	+5.8 −6.3	+7.9 −8.1
268.0	3.113	+5.8 −6.2	+7.9 −8.1
270.0	3.072	+5.8 −6.2	+7.9 −8.1
272.0	3.033	+5.8 −6.2	+7.9 −8.1
274.0	2.995	+5.8 −6.2	+7.9 −8.1
276.0	2.959	+5.8 −6.1	+7.9 −8.2
278.0	2.923	+5.8 −6.1	+7.9 −8.2
280.0	2.889	+5.8 −6.1	+7.9 −8.2
282.0	2.856	+5.8 −6.1	+7.9 −8.2
284.0	2.824	+5.8 −6.1	+7.9 −8.2
286.0	2.794	+5.8 −6.1	+8.0 −8.3
288.0	2.764	+5.8 −6.1	+8.0 −8.3
290.0	2.736	+5.8 −6.1	+8.0 −8.3
292.0	2.708	+5.8 −6.1	+8.0 −8.3
294.0	2.681	+5.8 −6.1	+8.0 −8.3
296.0	2.656	+5.8 −6.1	+8.0 −8.3
298.0	2.632	+5.8 −6.0	+8.0 −8.3
300.0	2.608	+5.8 −6.0	+8.0 −8.3
305.0	2.555	+5.8 −6.0	+8.0 −8.3
310.0	2.509	+5.8 −6.0	+8.1 −8.3
315.0	2.470	+5.8 −6.0	+8.1 −8.4
320.0	2.436	+5.8 −6.0	+8.2 −8.4
325.0	2.411	+5.8 −6.0	+8.2 −8.4
330.0	2.397	+5.8 −6.0	+8.3 −8.4
335.0	2.392	+5.8 −5.9	+8.3 −8.4
340.0	2.402	+5.8 −5.9	+8.3 −8.4
345.0	2.426	+5.8 −5.9	+8.3 −8.4
350.0	2.423	+5.8 −5.9	+8.4 −8.4
360.0	2.404	+5.8 −5.9	+8.4 −8.5
370.0	2.359	+5.8 −5.8	+8.4 −8.6

Table B.7: ggF cross sections at the LHC at 7 TeV and corresponding scale and PDF+$\alpha_{\rm s}$ uncertainties computed according to the PDF4LHC recommendation.

$M_{\rm H}$[GeV]	σ [pb]	QCD Scale [%]	PDF+$\alpha_{\rm s}$ [%]
380.0	2.280	+5.9 −5.6	+8.4 −8.6
390.0	2.172	+5.9 −5.5	+8.6 −8.6
400.0	2.047	+5.9 −5.4	+8.8 −8.6
420.0	1.775	+5.9 −5.3	+9.1 −8.6
440.0	1.506	+5.9 −5.3	+9.2 −8.7
450.0	1.380	+5.9 −5.3	+9.2 −8.7
460.0	1.262	+5.9 −5.3	+9.3 −8.7
480.0	1.050	+5.9 −5.2	+9.4 −8.8
500.0	0.8704	+6.0 −5.2	+9.5 −8.9
520.0	0.7208	+6.0 −5.2	+9.6 −9.0
540.0	0.5974	+6.0 −5.2	+9.7 −9.0
550.0	0.5441	+6.0 −5.2	+9.7 −9.0
560.0	0.4958	+6.0 −5.2	+9.8 −9.1
580.0	0.4126	+6.0 −5.2	+9.9 −9.2
600.0	0.3445	+6.1 −5.2	+10.1 −9.4
620.0	0.2884	+6.1 −5.2	+10.2 −9.5
640.0	0.2422	+6.2 −5.2	+10.4 −9.7
650.0	0.2224	+6.2 −5.2	+10.4 −9.7
660.0	0.2043	+6.2 −5.2	+10.5 −9.8
680.0	0.1729	+6.3 −5.3	+10.6 −9.8
700.0	0.1469	+6.3 −5.3	+10.7 −9.9
720.0	0.1253	+6.3 −5.3	+10.8 −10.0
740.0	0.1072	+6.4 −5.4	+10.9 −10.1
750.0	0.0993	+6.4 −5.4	+10.9 −10.1
760.0	0.0920	+6.4 −5.4	+11.0 −10.2
780.0	0.0794	+6.5 −5.4	+11.1 −10.3
800.0	0.0687	+6.5 −5.4	+11.2 −10.4
820.0	0.0596	+6.5 −5.4	+11.4 −10.6
840.0	0.0519	+6.5 −5.5	+11.7 −10.9
850.0	0.0485	+6.5 −5.5	+11.8 −11.0
860.0	0.0454	+6.5 −5.5	+11.9 −11.1
880.0	0.0398	+6.6 −5.6	+12.3 −11.5
900.0	0.0350	+6.7 −5.6	+12.6 −11.8
920.0	0.0309	+6.8 −5.6	+13.0 −12.2
940.0	0.0273	+6.8 −5.7	+13.3 −12.5
950.0	0.0257	+6.8 −5.7	+13.5 −12.7
960.0	0.0242	+6.8 −5.7	+13.7 −12.9
980.0	0.0216	+6.9 −5.7	+14.0 −13.2
1000.0	0.0192	+7.0 −5.7	+14.2 −13.5

Table B.8: ggF cross sections at the LHC at 8 TeV and corresponding scale and PDF+α_s uncertainties computed according to the PDF4LHC recommendation.

M_H[GeV]	σ [pb]	QCD Scale [%]	PDF+α_s [%]
80.0	45.37	+8.8 −9.2	+7.9 −6.7
81.0	44.31	+8.8 −9.1	+7.9 −6.7
82.0	43.28	+8.7 −9.1	+7.9 −6.6
83.0	42.29	+8.7 −9.0	+7.9 −6.6
84.0	41.33	+8.6 −9.0	+7.9 −6.6
85.0	40.41	+8.6 −9.0	+7.9 −6.6
86.0	39.52	+8.5 −8.9	+7.9 −6.6
87.0	38.66	+8.5 −8.9	+7.9 −6.6
88.0	37.83	+8.4 −8.8	+7.9 −6.6
89.0	37.02	+8.4 −8.8	+7.8 −6.6
90.0	36.23	+8.3 −8.8	+7.8 −6.6
91.0	35.49	+8.3 −8.7	+7.8 −6.6
92.0	34.75	+8.2 −8.7	+7.8 −6.5
93.0	34.04	+8.2 −8.7	+7.8 −6.5
94.0	33.36	+8.1 −8.6	+7.8 −6.5
95.0	32.69	+8.1 −8.6	+7.8 −6.5
96.0	32.04	+8.1 −8.6	+7.8 −6.5
97.0	31.41	+8.0 −8.5	+7.8 −6.5
98.0	30.80	+8.0 −8.5	+7.8 −6.5
99.0	30.21	+8.0 −8.5	+7.8 −6.5
100.0	29.68	+7.9 −8.4	+7.8 −6.5
101.0	29.12	+7.9 −8.4	+7.8 −6.5
102.0	28.57	+7.9 −8.4	+7.8 −6.5
103.0	28.04	+7.8 −8.4	+7.8 −6.5
104.0	27.52	+7.8 −8.3	+7.8 −6.5
105.0	27.01	+7.8 −8.3	+7.7 −6.5
106.0	26.52	+7.7 −8.3	+7.7 −6.6
107.0	26.05	+7.7 −8.3	+7.7 −6.6
108.0	25.59	+7.7 −8.2	+7.7 −6.6
109.0	25.14	+7.6 −8.2	+7.7 −6.7
110.0	24.70	+7.6 −8.2	+7.7 −6.7
110.5	24.48	+7.6 −8.2	+7.7 −6.7
111.0	24.27	+7.6 −8.2	+7.6 −6.7
111.5	24.06	+7.5 −8.1	+7.6 −6.7
112.0	23.85	+7.5 −8.1	+7.6 −6.7
112.5	23.64	+7.5 −8.1	+7.6 −6.7
113.0	23.44	+7.5 −8.1	+7.6 −6.7
113.5	23.24	+7.5 −8.1	+7.6 −6.8
114.0	23.05	+7.5 −8.1	+7.6 −6.8
114.5	22.85	+7.5 −8.1	+7.6 −6.8
115.0	22.66	+7.4 −8.1	+7.6 −6.8
115.5	22.47	+7.4 −8.0	+7.6 −6.8
116.0	22.28	+7.4 −8.0	+7.5 −6.8
116.5	22.10	+7.4 −8.0	+7.5 −6.8
117.0	21.91	+7.4 −8.0	+7.5 −6.8
117.5	21.73	+7.4 −8.0	+7.5 −6.8
118.0	21.55	+7.4 −8.0	+7.5 −6.8

Table B.9: ggF cross sections at the LHC at 8 TeV and corresponding scale and PDF+α_s uncertainties computed according to the PDF4LHC recommendation.

$M_{\rm H}$[GeV]	σ [pb]	QCD Scale [%]		PDF+$\alpha_{\rm s}$ [%]	
118.5	21.38	+7.3	−8.0	+7.5	−6.8
119.0	21.20	+7.3	−8.0	+7.5	−6.8
119.5	21.03	+7.3	−8.0	+7.5	−6.8
120.0	20.86	+7.3	−7.9	+7.5	−6.9
120.1	20.83	+7.3	−7.9	+7.5	−6.9
120.2	20.80	+7.3	−7.9	+7.5	−6.9
120.3	20.76	+7.3	−7.9	+7.5	−6.9
120.4	20.73	+7.3	−7.9	+7.5	−6.9
120.5	20.69	+7.3	−7.9	+7.5	−6.9
120.6	20.66	+7.3	−7.9	+7.5	−6.9
120.7	20.63	+7.3	−7.9	+7.5	−6.9
120.8	20.59	+7.3	−7.9	+7.5	−6.9
120.9	20.56	+7.3	−7.9	+7.5	−6.9
121.0	20.53	+7.3	−7.9	+7.5	−6.9
121.1	20.50	+7.3	−7.9	+7.5	−6.9
121.2	20.46	+7.3	−7.9	+7.5	−6.9
121.3	20.43	+7.3	−7.9	+7.5	−6.9
121.4	20.40	+7.3	−7.9	+7.5	−6.9
121.5	20.36	+7.3	−7.9	+7.5	−6.9
121.6	20.33	+7.3	−7.9	+7.5	−6.9
121.7	20.30	+7.3	−7.9	+7.5	−6.9
121.8	20.27	+7.3	−7.9	+7.5	−6.9
121.9	20.23	+7.3	−7.9	+7.5	−6.9
122.0	20.20	+7.3	−7.9	+7.5	−6.9
122.1	20.17	+7.3	−7.9	+7.5	−6.9
122.2	20.14	+7.3	−7.9	+7.5	−6.9
122.3	20.11	+7.2	−7.9	+7.5	−6.9
122.4	20.07	+7.2	−7.9	+7.5	−6.9
122.5	20.04	+7.2	−7.9	+7.5	−6.9
122.6	20.01	+7.2	−7.9	+7.5	−6.9
122.7	19.98	+7.2	−7.9	+7.5	−6.9
122.8	19.95	+7.2	−7.9	+7.5	−6.9
122.9	19.92	+7.2	−7.9	+7.5	−6.9
123.0	19.88	+7.2	−7.9	+7.5	−6.9
123.1	19.85	+7.2	−7.9	+7.5	−6.9
123.2	19.82	+7.2	−7.9	+7.5	−6.9
123.3	19.79	+7.2	−7.9	+7.5	−6.9
123.4	19.76	+7.2	−7.9	+7.5	−6.9
123.5	19.73	+7.2	−7.9	+7.5	−6.9
123.6	19.70	+7.2	−7.9	+7.5	−6.9
123.7	19.67	+7.2	−7.9	+7.5	−6.9
123.8	19.63	+7.2	−7.9	+7.5	−6.9
123.9	19.60	+7.2	−7.9	+7.5	−6.9
124.0	19.57	+7.2	−7.9	+7.5	−6.9
124.1	19.54	+7.2	−7.9	+7.5	−6.9
124.2	19.51	+7.2	−7.9	+7.5	−6.9
124.3	19.48	+7.2	−7.9	+7.5	−6.9

Table B.10: ggF cross sections at the LHC at 8 TeV and corresponding scale and PDF+α_s uncertainties computed according to the PDF4LHC recommendation.

M_H[GeV]	σ [pb]	QCD Scale [%]	PDF+α_s [%]
124.4	19.45	+7.2 −7.9	+7.5 −6.9
124.5	19.42	+7.2 −7.9	+7.5 −6.9
124.6	19.39	+7.2 −7.9	+7.5 −6.9
124.7	19.36	+7.2 −7.9	+7.5 −6.9
124.8	19.33	+7.2 −7.8	+7.5 −6.9
124.9	19.30	+7.2 −7.8	+7.5 −6.9
125.0	19.27	+7.2 −7.8	+7.5 −6.9
125.1	19.24	+7.2 −7.8	+7.5 −6.9
125.2	19.21	+7.2 −7.8	+7.5 −6.9
125.3	19.18	+7.2 −7.8	+7.5 −6.9
125.4	19.15	+7.2 −7.8	+7.5 −6.9
125.5	19.12	+7.2 −7.8	+7.5 −6.9
125.6	19.09	+7.2 −7.8	+7.5 −6.9
125.7	19.06	+7.2 −7.8	+7.5 −6.9
125.8	19.03	+7.2 −7.8	+7.5 −6.9
125.9	19.00	+7.2 −7.8	+7.5 −6.9
126.0	18.97	+7.2 −7.8	+7.5 −6.9
126.1	18.94	+7.2 −7.8	+7.5 −6.9
126.2	18.91	+7.2 −7.8	+7.5 −6.9
126.3	18.88	+7.2 −7.8	+7.5 −6.9
126.4	18.85	+7.2 −7.8	+7.5 −6.9
126.5	18.82	+7.2 −7.8	+7.5 −6.9
126.6	18.80	+7.2 −7.8	+7.5 −6.9
126.7	18.77	+7.2 −7.8	+7.5 −6.9
126.8	18.74	+7.1 −7.8	+7.5 −6.9
126.9	18.71	+7.1 −7.8	+7.5 −6.9
127.0	18.68	+7.1 −7.8	+7.5 −6.9
127.1	18.65	+7.1 −7.8	+7.5 −6.9
127.2	18.62	+7.1 −7.8	+7.5 −6.9
127.3	18.59	+7.1 −7.8	+7.5 −6.9
127.4	18.57	+7.1 −7.8	+7.5 −6.9
127.5	18.54	+7.1 −7.8	+7.5 −6.9
127.6	18.51	+7.1 −7.8	+7.5 −6.9
127.7	18.48	+7.1 −7.8	+7.5 −6.9
127.8	18.45	+7.1 −7.8	+7.5 −6.9
127.9	18.42	+7.1 −7.8	+7.5 −6.9
128.0	18.40	+7.1 −7.8	+7.5 −6.9
128.1	18.37	+7.1 −7.8	+7.5 −6.9
128.2	18.34	+7.1 −7.8	+7.5 −6.9
128.3	18.31	+7.1 −7.8	+7.5 −6.9
128.4	18.28	+7.1 −7.8	+7.5 −6.9
128.5	18.26	+7.1 −7.8	+7.5 −6.9
128.6	18.23	+7.1 −7.8	+7.5 −6.9
128.7	18.20	+7.1 −7.8	+7.5 −6.9
128.8	18.17	+7.1 −7.8	+7.5 −6.9
128.9	18.15	+7.1 −7.8	+7.5 −6.9
129.0	18.12	+7.1 −7.8	+7.5 −6.9

Table B.11: ggF cross sections at the LHC at 8 TeV and corresponding scale and PDF+α_s uncertainties computed according to the PDF4LHC recommendation.

M_{H}[GeV]	σ [pb]	QCD Scale [%]	PDF+α_{s} [%]
129.1	18.09	+7.1 −7.8	+7.5 −6.9
129.2	18.06	+7.1 −7.8	+7.5 −6.9
129.3	18.04	+7.1 −7.8	+7.5 −6.9
129.4	18.01	+7.1 −7.8	+7.5 −6.9
129.5	17.98	+7.1 −7.8	+7.5 −6.9
129.6	17.95	+7.1 −7.8	+7.5 −6.9
129.7	17.93	+7.1 −7.8	+7.5 −6.9
129.8	17.90	+7.1 −7.7	+7.5 −6.9
129.9	17.87	+7.1 −7.7	+7.5 −6.9
130.0	17.85	+7.1 −7.7	+7.5 −6.9
130.5	17.71	+7.1 −7.7	+7.5 −6.9
131.0	17.58	+7.1 −7.7	+7.5 −7.0
131.5	17.45	+7.0 −7.7	+7.5 −7.0
132.0	17.32	+7.0 −7.7	+7.5 −7.0
132.5	17.19	+7.0 −7.7	+7.5 −7.0
133.0	17.07	+7.0 −7.7	+7.4 −7.0
133.5	16.94	+7.0 −7.7	+7.4 −7.0
134.0	16.82	+7.0 −7.7	+7.4 −7.0
134.5	16.69	+7.0 −7.7	+7.4 −7.0
135.0	16.57	+7.0 −7.7	+7.4 −7.0
135.5	16.45	+7.0 −7.6	+7.4 −7.0
136.0	16.33	+6.9 −7.6	+7.4 −7.0
136.5	16.22	+6.9 −7.6	+7.4 −7.0
137.0	16.10	+6.9 −7.6	+7.4 −7.0
137.5	15.98	+6.9 −7.6	+7.4 −7.0
138.0	15.87	+6.9 −7.6	+7.4 −6.9
138.5	15.76	+6.9 −7.6	+7.4 −6.9
139.0	15.64	+6.9 −7.6	+7.4 −6.9
139.5	15.53	+6.9 −7.6	+7.4 −6.9
140.0	15.42	+6.9 −7.6	+7.4 −6.9
140.5	15.32	+6.9 −7.6	+7.4 −6.9
141.0	15.27	+6.8 −7.6	+7.3 −6.9
141.5	15.16	+6.8 −7.5	+7.3 −6.9
142.0	15.06	+6.8 −7.5	+7.3 −6.9
142.5	14.96	+6.8 −7.5	+7.3 −6.9
143.0	14.86	+6.8 −7.5	+7.3 −6.9
143.5	14.76	+6.8 −7.5	+7.3 −6.9
144.0	14.66	+6.8 −7.5	+7.3 −6.9
144.5	14.56	+6.8 −7.5	+7.3 −6.9
145.0	14.46	+6.8 −7.5	+7.3 −6.9
145.5	14.37	+6.8 −7.5	+7.3 −6.9
146.0	14.27	+6.7 −7.5	+7.3 −6.9
146.5	14.18	+6.7 −7.5	+7.3 −6.9
147.0	14.09	+6.7 −7.5	+7.3 −6.9
147.5	14.00	+6.7 −7.5	+7.3 −7.0
148.0	13.91	+6.7 −7.4	+7.3 −7.0
148.5	13.82	+6.7 −7.4	+7.3 −7.0

Table B.12: ggF cross sections at the LHC at 8 TeV and corresponding scale and PDF+α_s uncertainties computed according to the PDF4LHC recommendation.

M_H[GeV]	σ [pb]	QCD Scale [%]	PDF+α_s [%]
149.0	13.73	+6.7 −7.4	+7.4 −7.0
149.5	13.64	+6.7 −7.4	+7.4 −7.0
150.0	13.55	+6.7 −7.4	+7.4 −7.0
152.0	13.22	+6.6 −7.4	+7.4 −7.1
154.0	12.89	+6.6 −7.3	+7.5 −7.1
156.0	12.58	+6.6 −7.3	+7.5 −7.1
158.0	12.27	+6.5 −7.3	+7.5 −7.1
160.0	11.96	+6.5 −7.3	+7.5 −7.1
162.0	11.60	+6.5 −7.2	+7.5 −7.2
164.0	11.17	+6.4 −7.2	+7.5 −7.2
165.0	10.97	+6.4 −7.2	+7.5 −7.2
166.0	10.79	+6.4 −7.2	+7.5 −7.3
168.0	10.46	+6.4 −7.2	+7.5 −7.3
170.0	10.17	+6.4 −7.1	+7.5 −7.4
172.0	9.897	+6.3 −7.1	+7.5 −7.4
174.0	9.645	+6.3 −7.1	+7.4 −7.4
175.0	9.526	+6.3 −7.1	+7.4 −7.4
176.0	9.410	+6.3 −7.1	+7.4 −7.4
178.0	9.194	+6.3 −7.0	+7.4 −7.5
180.0	8.980	+6.2 −7.0	+7.4 −7.5
182.0	8.755	+6.2 −7.0	+7.4 −7.5
184.0	8.501	+6.2 −7.0	+7.4 −7.5
185.0	8.383	+6.2 −7.0	+7.4 −7.5
186.0	8.266	+6.1 −6.9	+7.4 −7.5
188.0	8.053	+6.1 −6.9	+7.4 −7.5
190.0	7.858	+6.1 −6.9	+7.4 −7.5
192.0	7.671	+6.1 −6.9	+7.4 −7.6
194.0	7.494	+6.1 −6.9	+7.4 −7.6
195.0	7.405	+6.0 −6.8	+7.4 −7.6
196.0	7.320	+6.0 −6.8	+7.4 −7.6
198.0	7.187	+6.0 −6.8	+7.4 −7.7
200.0	7.081	+6.0 −6.8	+7.4 −7.7
202.0	6.937	+6.0 −6.8	+7.4 −7.7
204.0	6.846	+6.0 −6.8	+7.4 −7.7
206.0	6.731	+6.0 −6.7	+7.4 −7.7
208.0	6.609	+6.0 −6.7	+7.4 −7.8
210.0	6.500	+6.0 −6.7	+7.4 −7.8
212.0	6.387	+6.0 −6.7	+7.4 −7.7
214.0	6.293	+6.0 −6.7	+7.4 −7.7
216.0	6.214	+5.9 −6.6	+7.4 −7.7
218.0	6.104	+5.9 −6.6	+7.4 −7.6
220.0	6.003	+5.9 −6.6	+7.3 −7.6
222.0	5.905	+5.9 −6.6	+7.3 −7.6
224.0	5.821	+5.9 −6.6	+7.4 −7.6
226.0	5.748	+5.9 −6.6	+7.4 −7.6
228.0	5.653	+5.9 −6.5	+7.4 −7.7
230.0	5.567	+5.9 −6.5	+7.4 −7.7

Table B.13: ggF cross sections at the LHC at 8 TeV and corresponding scale and PDF+α_s uncertainties computed according to the PDF4LHC recommendation.

M_{H}[GeV]	σ [pb]	QCD Scale [%]	PDF+α_s [%]
232.0	5.487	+5.9 −6.5	+7.4 −7.7
234.0	5.413	+5.9 −6.5	+7.3 −7.7
236.0	5.327	+5.9 −6.5	+7.3 −7.7
238.0	5.247	+5.9 −6.5	+7.3 −7.7
240.0	5.159	+5.9 −6.4	+7.3 −7.7
242.0	5.078	+5.9 −6.4	+7.3 −7.7
244.0	4.999	+5.9 −6.4	+7.3 −7.7
246.0	4.924	+5.8 −6.4	+7.4 −7.7
248.0	4.854	+5.8 −6.4	+7.4 −7.7
250.0	4.783	+5.8 −6.4	+7.4 −7.7
252.0	4.714	+5.8 −6.4	+7.4 −7.7
254.0	4.647	+5.8 −6.3	+7.5 −7.6
256.0	4.582	+5.8 −6.3	+7.5 −7.5
258.0	4.521	+5.8 −6.3	+7.5 −7.4
260.0	4.461	+5.8 −6.3	+7.6 −7.4
262.0	4.405	+5.8 −6.3	+7.6 −7.5
264.0	4.350	+5.8 −6.3	+7.6 −7.6
266.0	4.292	+5.8 −6.3	+7.6 −7.7
268.0	4.237	+5.8 −6.2	+7.6 −7.8
270.0	4.184	+5.8 −6.2	+7.6 −7.9
272.0	4.134	+5.8 −6.2	+7.6 −7.9
274.0	4.086	+5.8 −6.2	+7.6 −7.9
276.0	4.040	+5.8 −6.2	+7.6 −8.0
278.0	3.994	+5.7 −6.2	+7.6 −8.0
280.0	3.950	+5.7 −6.2	+7.6 −8.0
282.0	3.908	+5.7 −6.2	+7.6 −8.0
284.0	3.867	+5.7 −6.1	+7.6 −8.0
286.0	3.829	+5.7 −6.1	+7.6 −8.0
288.0	3.792	+5.7 −6.1	+7.6 −8.0
290.0	3.755	+5.7 −6.1	+7.6 −8.0
292.0	3.720	+5.7 −6.1	+7.6 −8.0
294.0	3.687	+5.7 −6.1	+7.6 −8.0
296.0	3.654	+5.7 −6.1	+7.6 −8.0
298.0	3.624	+5.7 −6.1	+7.7 −7.9
300.0	3.594	+5.7 −6.1	+7.7 −7.9
305.0	3.529	+5.7 −6.0	+7.7 −7.9
310.0	3.472	+5.7 −6.0	+7.7 −8.0
315.0	3.425	+5.7 −6.0	+7.7 −8.0
320.0	3.383	+5.7 −6.0	+7.7 −8.0
325.0	3.355	+5.7 −6.0	+7.7 −8.1
330.0	3.341	+5.7 −6.0	+7.8 −8.1
335.0	3.341	+5.7 −5.9	+7.9 −8.1
340.0	3.359	+5.7 −5.9	+7.9 −8.1
345.0	3.399	+5.7 −5.9	+7.9 −8.2
350.0	3.401	+5.7 −5.9	+8.0 −8.2
360.0	3.385	+5.8 −5.9	+8.0 −8.2
370.0	3.332	+5.8 −5.8	+8.1 −8.2

Table B.14: ggF cross sections at the LHC at 8 TeV and corresponding scale and PDF+α_{s} uncertainties computed according to the PDF4LHC recommendation.

M_{H}[GeV]	σ [pb]	QCD Scale [%]	PDF+α_{s} [%]
380.0	3.231	$+5.8$ -5.6	$+8.1$ -8.2
390.0	3.089	$+5.8$ -5.5	$+8.2$ -8.2
400.0	2.921	$+5.8$ -5.4	$+8.2$ -8.2
420.0	2.550	$+5.8$ -5.3	$+8.3$ -8.3
440.0	2.178	$+5.8$ -5.3	$+8.5$ -8.4
450.0	2.002	$+5.8$ -5.2	$+8.6$ -8.4
460.0	1.837	$+5.8$ -5.2	$+8.7$ -8.4
480.0	1.538	$+5.8$ -5.2	$+8.9$ -8.5
500.0	1.283	$+5.8$ -5.1	$+9.1$ -8.5
520.0	1.069	$+5.8$ -5.1	$+9.2$ -8.6
540.0	0.8913	$+5.8$ -5.1	$+9.4$ -8.6
550.0	0.8144	$+5.8$ -5.1	$+9.4$ -8.7
560.0	0.7442	$+5.9$ -5.1	$+9.4$ -8.7
580.0	0.6228	$+5.9$ -5.1	$+9.5$ -8.7
600.0	0.5230	$+5.9$ -5.0	$+9.5$ -8.8
620.0	0.4403	$+5.9$ -5.0	$+9.6$ -8.9
640.0	0.3719	$+5.9$ -5.0	$+9.7$ -9.0
650.0	0.3424	$+5.9$ -5.0	$+9.7$ -9.0
660.0	0.3153	$+5.9$ -5.1	$+9.8$ -9.1
680.0	0.2682	$+6.0$ -5.1	$+9.9$ -9.2
700.0	0.2290	$+6.0$ -5.1	$+10.1$ -9.3
720.0	0.1964	$+6.0$ -5.1	$+10.2$ -9.5
740.0	0.1689	$+6.1$ -5.1	$+10.4$ -9.6
750.0	0.1568	$+6.1$ -5.1	$+10.4$ -9.7
760.0	0.1457	$+6.1$ -5.2	$+10.5$ -9.7
780.0	0.1262	$+6.1$ -5.2	$+10.5$ -9.8
800.0	0.1097	$+6.1$ -5.2	$+10.6$ -9.8
820.0	0.0957	$+6.2$ -5.2	$+10.7$ -9.8
840.0	0.0837	$+6.2$ -5.2	$+10.8$ -9.9
850.0	0.0784	$+6.2$ -5.3	$+10.9$ -9.9
860.0	0.0735	$+6.2$ -5.3	$+10.9$ -10.0
880.0	0.0647	$+6.3$ -5.3	$+11.0$ -10.1
900.0	0.0571	$+6.3$ -5.3	$+11.1$ -10.2
920.0	0.0506	$+6.3$ -5.3	$+11.2$ -10.4
940.0	0.0450	$+6.4$ -5.4	$+11.4$ -10.6
950.0	0.0424	$+6.4$ -5.4	$+11.5$ -10.7
960.0	0.0400	$+6.4$ -5.4	$+11.6$ -10.8
980.0	0.0357	$+6.5$ -5.4	$+11.8$ -11.0
1000.0	0.0320	$+6.9$ -5.4	$+12.0$ -11.2

Table B.15: VBF cross sections at 7 TeV. Central values at NNLO QCD, NNLO QCD + NLO EW, relative EW corrections, and uncertainties from PDF+α_s (according to the PDF4LHC prescription) and from QCD scale.

M_H [GeV]	$\sigma_{\text{VBF@NNLO}}^{\text{NNLO}}$ [fb]	$\sigma^{\text{NNLO+EW}}$ [fb]	$\delta_{\text{HAWK}}^{\text{EW}}$ [%]	PDF4LHC [%]		QCD Scale [%]	
80.0	2002	1914	−4.4	+2.1	−2.1	+0.6	−0.2
81.0	1981	1894	−4.4	+2.1	−2.1	+0.6	−0.2
82.0	1957	1871	−4.4	+2.1	−2.1	+0.6	−0.2
83.0	1938	1853	−4.4	+2.1	−2.1	+0.6	−0.2
84.0	1916	1833	−4.4	+2.1	−2.1	+0.6	−0.2
85.0	1897	1814	−4.4	+2.1	−2.1	+0.6	−0.2
86.0	1876	1794	−4.4	+2.1	−2.1	+0.6	−0.2
87.0	1857	1776	−4.4	+2.1	−2.1	+0.6	−0.2
88.0	1839	1759	−4.4	+2.1	−2.1	+0.6	−0.2
89.0	1818	1738	−4.4	+2.1	−2.1	+0.6	−0.2
90.0	1801	1723	−4.4	+2.1	−2.1	+0.6	−0.2
91.0	1782	1705	−4.4	+2.1	−2.1	+0.6	−0.2
92.0	1766	1689	−4.4	+2.1	−2.1	+0.5	−0.3
93.0	1744	1668	−4.4	+2.1	−2.1	+0.5	−0.3
94.0	1730	1654	−4.4	+2.1	−2.1	+0.4	−0.4
95.0	1714	1639	−4.4	+2.1	−2.1	+0.4	−0.4
96.0	1691	1617	−4.4	+2.1	−2.1	+0.4	−0.4
97.0	1673	1600	−4.4	+2.1	−2.1	+0.4	−0.4
98.0	1654	1582	−4.4	+2.2	−2.1	+0.4	−0.3
99.0	1640	1568	−4.3	+2.2	−2.1	+0.4	−0.3
100.0	1628	1557	−4.3	+2.2	−2.1	+0.4	−0.3
101.0	1611	1541	−4.3	+2.2	−2.1	+0.4	−0.3
102.0	1595	1526	−4.3	+2.2	−2.1	+0.4	−0.3
103.0	1578	1509	−4.3	+2.2	−2.1	+0.3	−0.3
104.0	1560	1492	−4.3	+2.2	−2.1	+0.3	−0.3
105.0	1545	1478	−4.4	+2.2	−2.1	+0.3	−0.3
106.0	1531	1465	−4.3	+2.2	−2.1	+0.3	−0.3
107.0	1517	1452	−4.3	+2.2	−2.1	+0.4	−0.3
108.0	1503	1438	−4.3	+2.3	−2.1	+0.4	−0.2
109.0	1487	1423	−4.3	+2.3	−2.1	+0.5	−0.2
110.0	1473	1410	−4.3	+2.3	−2.1	+0.5	−0.2
110.5	1467	1404	−4.3	+2.3	−2.1	+0.5	−0.2
111.0	1459	1396	−4.3	+2.3	−2.1	+0.4	−0.2
111.5	1454	1391	−4.3	+2.3	−2.1	+0.4	−0.2
112.0	1445	1382	−4.3	+2.3	−2.1	+0.4	−0.2
112.5	1438	1375	−4.3	+2.3	−2.1	+0.3	−0.2
113.0	1431	1369	−4.4	+2.3	−2.1	+0.3	−0.2
113.5	1425	1363	−4.4	+2.3	−2.1	+0.3	−0.2
114.0	1418	1356	−4.4	+2.3	−2.1	+0.3	−0.2
114.5	1410	1349	−4.4	+2.3	−2.1	+0.2	−0.2
115.0	1405	1344	−4.4	+2.3	−2.1	+0.2	−0.2
115.5	1396	1335	−4.4	+2.3	−2.1	+0.2	−0.2
116.0	1391	1330	−4.4	+2.3	−2.1	+0.2	−0.2
116.5	1384	1324	−4.4	+2.3	−2.1	+0.2	−0.3
117.0	1378	1317	−4.4	+2.3	−2.1	+0.2	−0.3
117.5	1369	1310	−4.4	+2.3	−2.1	+0.2	−0.3
118.0	1363	1304	−4.4	+2.4	−2.1	+0.3	−0.3

Table B.16: VBF cross sections at 7 TeV. Central values at NNLO QCD, NNLO QCD + NLO EW, relative EW corrections, and uncertainties from PDF+α_s (according to the PDF4LHC prescription) and from QCD scale.

M_H [GeV]	$\sigma_{\text{VBF@NNLO}}^{\text{NNLO}}$ [fb]	$\sigma^{\text{NNLO+EW}}$ [fb]	$\delta_{\text{HAWK}}^{\text{EW}}$ [%]	PDF4LHC [%]		QCD Scale [%]	
118.5	1356	1297	−4.4	+2.4	−2.1	+0.3	−0.3
119.0	1351	1292	−4.4	+2.4	−2.1	+0.3	−0.4
119.5	1345	1286	−4.3	+2.4	−2.1	+0.3	−0.4
120.0	1337	1279	−4.3	+2.4	−2.1	+0.3	−0.4
120.1	1338	1280	−4.3	+2.4	−2.1	+0.3	−0.4
120.2	1337	1279	−4.3	+2.4	−2.1	+0.3	−0.4
120.3	1336	1278	−4.3	+2.4	−2.1	+0.3	−0.4
120.4	1334	1277	−4.3	+2.4	−2.1	+0.3	−0.4
120.5	1333	1275	−4.3	+2.4	−2.1	+0.3	−0.4
120.6	1330	1272	−4.3	+2.4	−2.1	+0.3	−0.4
120.7	1330	1272	−4.3	+2.4	−2.1	+0.3	−0.4
120.8	1330	1272	−4.3	+2.4	−2.1	+0.3	−0.4
120.9	1326	1269	−4.3	+2.4	−2.1	+0.3	−0.4
121.0	1326	1269	−4.3	+2.4	−2.1	+0.3	−0.4
121.1	1326	1268	−4.3	+2.4	−2.1	+0.3	−0.4
121.2	1324	1267	−4.3	+2.4	−2.1	+0.3	−0.4
121.3	1323	1266	−4.3	+2.4	−2.1	+0.3	−0.4
121.4	1322	1265	−4.3	+2.4	−2.1	+0.3	−0.4
121.5	1320	1263	−4.3	+2.4	−2.1	+0.3	−0.4
121.6	1319	1262	−4.3	+2.4	−2.1	+0.3	−0.4
121.7	1317	1260	−4.3	+2.4	−2.1	+0.3	−0.4
121.8	1315	1259	−4.3	+2.4	−2.1	+0.3	−0.4
121.9	1313	1256	−4.3	+2.4	−2.1	+0.3	−0.4
122.0	1314	1257	−4.3	+2.4	−2.1	+0.3	−0.4
122.1	1313	1256	−4.3	+2.4	−2.1	+0.3	−0.4
122.2	1310	1253	−4.3	+2.4	−2.1	+0.3	−0.4
122.3	1310	1253	−4.3	+2.4	−2.1	+0.3	−0.4
122.4	1308	1252	−4.3	+2.4	−2.1	+0.3	−0.4
122.5	1307	1251	−4.3	+2.5	−2.1	+0.3	−0.3
122.6	1307	1251	−4.3	+2.5	−2.1	+0.3	−0.3
122.7	1303	1247	−4.3	+2.5	−2.1	+0.3	−0.3
122.8	1305	1249	−4.3	+2.5	−2.1	+0.3	−0.3
122.9	1304	1248	−4.3	+2.5	−2.1	+0.3	−0.3
123.0	1302	1246	−4.3	+2.5	−2.1	+0.3	−0.3
123.1	1301	1245	−4.3	+2.5	−2.1	+0.3	−0.3
123.2	1298	1242	−4.3	+2.5	−2.1	+0.3	−0.3
123.3	1298	1242	−4.3	+2.5	−2.1	+0.3	−0.3
123.4	1297	1241	−4.3	+2.5	−2.1	+0.3	−0.3
123.5	1297	1241	−4.3	+2.5	−2.1	+0.3	−0.3
123.6	1294	1239	−4.3	+2.5	−2.1	+0.3	−0.3
123.7	1293	1237	−4.3	+2.5	−2.1	+0.3	−0.3
123.8	1291	1236	−4.3	+2.5	−2.1	+0.3	−0.3
123.9	1292	1236	−4.3	+2.5	−2.1	+0.3	−0.3
124.0	1289	1234	−4.3	+2.5	−2.1	+0.3	−0.3
124.1	1289	1234	−4.3	+2.5	−2.1	+0.3	−0.3
124.2	1287	1231	−4.3	+2.5	−2.1	+0.3	−0.3
124.3	1286	1231	−4.3	+2.5	−2.1	+0.3	−0.3

Table B.17: VBF cross sections at 7 TeV. Central values at NNLO QCD, NNLO QCD + NLO EW, relative EW corrections, and uncertainties from PDF+α_s (according to the PDF4LHC prescription) and from QCD scale.

M_H [GeV]	$\sigma_{VBF@NNLO}^{NNLO}$ [fb]	$\sigma^{NNLO+EW}$ [fb]	δ_{HAWK}^{EW} [%]	PDF4LHC [%]	QCD Scale [%]
124.4	1283	1228	−4.3	+2.5 −2.1	+0.3 −0.3
124.5	1282	1227	−4.3	+2.5 −2.1	+0.3 −0.3
124.6	1283	1228	−4.3	+2.5 −2.1	+0.3 −0.3
124.7	1280	1225	−4.3	+2.5 −2.1	+0.3 −0.3
124.8	1281	1225	−4.3	+2.5 −2.1	+0.3 −0.3
124.9	1281	1226	−4.3	+2.5 −2.1	+0.3 −0.3
125.0	1277	1222	−4.3	+2.5 −2.1	+0.3 −0.3
125.1	1277	1222	−4.3	+2.5 −2.1	+0.3 −0.3
125.2	1276	1221	−4.3	+2.5 −2.1	+0.3 −0.3
125.3	1274	1219	−4.3	+2.5 −2.1	+0.3 −0.3
125.4	1273	1219	−4.3	+2.5 −2.1	+0.3 −0.3
125.5	1274	1219	−4.3	+2.5 −2.1	+0.3 −0.3
125.6	1269	1214	−4.3	+2.5 −2.1	+0.3 −0.3
125.7	1270	1215	−4.3	+2.5 −2.1	+0.3 −0.3
125.8	1267	1213	−4.3	+2.5 −2.1	+0.3 −0.3
125.9	1268	1213	−4.3	+2.5 −2.1	+0.3 −0.3
126.0	1266	1211	−4.3	+2.5 −2.1	+0.3 −0.3
126.1	1263	1209	−4.3	+2.5 −2.1	+0.3 −0.3
126.2	1264	1210	−4.3	+2.5 −2.1	+0.3 −0.3
126.3	1262	1208	−4.3	+2.5 −2.1	+0.3 −0.3
126.4	1261	1207	−4.3	+2.5 −2.1	+0.3 −0.3
126.5	1260	1206	−4.3	+2.5 −2.1	+0.3 −0.3
126.6	1260	1206	−4.3	+2.5 −2.1	+0.3 −0.3
126.7	1257	1203	−4.3	+2.5 −2.1	+0.3 −0.3
126.8	1256	1202	−4.3	+2.5 −2.1	+0.3 −0.3
126.9	1256	1202	−4.3	+2.5 −2.1	+0.3 −0.3
127.0	1253	1199	−4.3	+2.5 −2.1	+0.3 −0.3
127.1	1253	1199	−4.3	+2.5 −2.1	+0.3 −0.3
127.2	1252	1198	−4.3	+2.5 −2.1	+0.3 −0.3
127.3	1251	1197	−4.3	+2.5 −2.1	+0.3 −0.3
127.4	1250	1196	−4.3	+2.5 −2.1	+0.3 −0.3
127.5	1247	1194	−4.3	+2.5 −2.1	+0.3 −0.2
127.6	1247	1194	−4.3	+2.5 −2.1	+0.3 −0.2
127.7	1247	1194	−4.3	+2.5 −2.1	+0.3 −0.2
127.8	1246	1192	−4.3	+2.5 −2.1	+0.3 −0.2
127.9	1243	1190	−4.3	+2.5 −2.1	+0.3 −0.2
128.0	1241	1187	−4.3	+2.5 −2.1	+0.3 −0.2
128.1	1242	1189	−4.3	+2.5 −2.1	+0.3 −0.2
128.2	1240	1187	−4.3	+2.5 −2.1	+0.3 −0.2
128.3	1240	1187	−4.3	+2.5 −2.1	+0.3 −0.2
128.4	1239	1186	−4.3	+2.5 −2.1	+0.3 −0.2
128.5	1237	1184	−4.3	+2.5 −2.1	+0.3 −0.2
128.6	1236	1183	−4.3	+2.5 −2.1	+0.3 −0.2
128.7	1236	1183	−4.3	+2.5 −2.1	+0.3 −0.2
128.8	1234	1181	−4.3	+2.5 −2.1	+0.3 −0.2
128.9	1231	1178	−4.3	+2.5 −2.1	+0.3 −0.2
129.0	1230	1178	−4.3	+2.5 −2.1	+0.3 −0.2

Table B.18: VBF cross sections at 7 TeV. Central values at NNLO QCD, NNLO QCD + NLO EW, relative EW corrections, and uncertainties from PDF+$\alpha_{\rm s}$ (according to the PDF4LHC prescription) and from QCD scale.

$M_{\rm H}$ [GeV]	$\sigma^{\rm NNLO}_{\rm VBF@NNLO}$ [fb]	$\sigma^{\rm NNLO+EW}$ [fb]	$\delta^{\rm EW}_{\rm HAWK}$ [%]	PDF4LHC [%]	QCD Scale [%]
129.1	1230	1178	−4.3	+2.5 −2.1	+0.3 −0.2
129.2	1229	1177	−4.3	+2.5 −2.1	+0.3 −0.2
129.3	1227	1175	−4.3	+2.5 −2.1	+0.3 −0.2
129.4	1226	1174	−4.3	+2.5 −2.1	+0.3 −0.2
129.5	1225	1173	−4.3	+2.5 −2.1	+0.3 −0.2
129.6	1225	1173	−4.3	+2.5 −2.1	+0.3 −0.2
129.7	1223	1171	−4.3	+2.5 −2.1	+0.3 −0.2
129.8	1222	1170	−4.3	+2.5 −2.1	+0.3 −0.2
129.9	1221	1169	−4.3	+2.5 −2.1	+0.3 −0.2
130.0	1219	1168	−4.2	+2.5 −2.1	+0.3 −0.2
130.5	1213	1161	−4.2	+2.5 −2.1	+0.3 −0.2
131.0	1208	1157	−4.2	+2.5 −2.1	+0.3 −0.2
131.5	1203	1152	−4.2	+2.5 −2.1	+0.4 −0.2
132.0	1197	1147	−4.2	+2.5 −2.1	+0.4 −0.2
132.5	1192	1142	−4.2	+2.5 −2.1	+0.4 −0.2
133.0	1186	1136	−4.2	+2.6 −2.1	+0.4 −0.1
133.5	1183	1133	−4.2	+2.6 −2.1	+0.4 −0.1
134.0	1176	1127	−4.2	+2.6 −2.1	+0.5 −0.1
134.5	1170	1121	−4.2	+2.6 −2.1	+0.5 −0.1
135.0	1165	1117	−4.2	+2.6 −2.1	+0.5 −0.1
135.5	1161	1112	−4.2	+2.6 −2.1	+0.5 −0.1
136.0	1156	1107	−4.2	+2.6 −2.1	+0.4 −0.1
136.5	1152	1103	−4.2	+2.6 −2.1	+0.4 −0.1
137.0	1145	1097	−4.2	+2.6 −2.1	+0.4 −0.1
137.5	1140	1092	−4.2	+2.6 −2.1	+0.3 −0.1
138.0	1135	1087	−4.2	+2.6 −2.1	+0.3 −0.2
138.5	1130	1082	−4.2	+2.6 −2.1	+0.3 −0.2
139.0	1126	1078	−4.2	+2.6 −2.1	+0.3 −0.2
139.5	1121	1074	−4.2	+2.6 −2.1	+0.2 −0.2
140.0	1116	1069	−4.2	+2.6 −2.1	+0.2 −0.2
140.5	1110	1063	−4.2	+2.6 −2.1	+0.2 −0.2
141.0	1105	1059	−4.2	+2.6 −2.1	+0.2 −0.2
141.5	1101	1055	−4.2	+2.6 −2.1	+0.3 −0.1
142.0	1096	1050	−4.2	+2.6 −2.1	+0.3 −0.1
142.5	1092	1046	−4.2	+2.7 −2.1	+0.3 −0.1
143.0	1086	1040	−4.2	+2.7 −2.1	+0.3 −0.1
143.5	1083	1037	−4.2	+2.7 −2.1	+0.3 −0.1
144.0	1077	1032	−4.2	+2.7 −2.1	+0.4 −0.0
144.5	1073	1028	−4.2	+2.7 −2.1	+0.4 −0.0
145.0	1068	1023	−4.2	+2.7 −2.1	+0.4 −0.0
145.5	1064	1019	−4.2	+2.7 −2.1	+0.4 −0.0
146.0	1059	1015	−4.2	+2.7 −2.1	+0.4 −0.0
146.5	1055	1010	−4.2	+2.7 −2.1	+0.3 −0.0
147.0	1050	1005	−4.2	+2.7 −2.1	+0.3 −0.0
147.5	1046	1002	−4.2	+2.7 −2.1	+0.3 −0.0
148.0	1042	998	−4.2	+2.7 −2.1	+0.3 −0.1
148.5	1037	993	−4.2	+2.7 −2.1	+0.3 −0.1

Table B.19: VBF cross sections at 7 TeV. Central values at NNLO QCD, NNLO QCD + NLO EW, relative EW corrections, and uncertainties from PDF+α_s (according to the PDF4LHC prescription) and from QCD scale.

M_H [GeV]	$\sigma^{NNLO}_{VBF@NNLO}$ [fb]	$\sigma^{NNLO+EW}$ [fb]	δ^{EW}_{HAWK} [%]	PDF4LHC [%]	QCD Scale [%]
149.0	1032	988	−4.2	+2.7 −2.1	+0.2 −0.1
149.5	1029	985	−4.2	+2.7 −2.1	+0.2 −0.1
150.0	1024	980	−4.2	+2.7 −2.1	+0.2 −0.1
152.0	1007	964	−4.3	+2.7 −2.1	+0.2 −0.1
154.0	991.4	948.7	−4.3	+2.8 −2.1	+0.3 −0.0
156.0	976.5	933.9	−4.4	+2.8 −2.1	+0.3 −0.0
158.0	962.5	919.9	−4.4	+2.8 −2.1	+0.2 −0.1
160.0	946.8	904.3	−4.5	+2.8 −2.1	+0.1 −0.2
162.0	927.5	890.6	−4.0	+2.8 −2.1	+0.1 −0.2
164.0	906.9	875.5	−3.5	+2.9 −2.1	+0.2 −0.1
165.0	898.3	869.4	−3.2	+2.9 −2.1	+0.2 −0.1
166.0	889.8	861.3	−3.2	+2.9 −2.1	+0.2 −0.1
168.0	875.1	847.3	−3.2	+3.0 −2.1	+0.2 −0.2
170.0	861.0	833.8	−3.2	+3.0 −2.1	+0.2 −0.2
172.0	847.4	820.1	−3.2	+3.0 −2.1	+0.2 −0.2
174.0	833.7	806.3	−3.3	+3.0 −2.1	+0.2 −0.1
175.0	827.2	799.8	−3.3	+3.0 −2.1	+0.2 −0.1
176.0	821.1	793.4	−3.4	+3.0 −2.1	+0.2 −0.1
178.0	809.1	780.9	−3.5	+3.1 −2.1	+0.1 −0.2
180.0	797.2	768.4	−3.6	+3.1 −2.1	+0.0 −0.3
182.0	782.7	756.1	−3.4	+3.1 −2.1	+0.1 −0.2
184.0	767.8	743.3	−3.2	+3.1 −2.0	+0.2 −0.1
185.0	760.9	737.5	−3.1	+3.1 −2.0	+0.3 −0.1
186.0	754.4	731.4	−3.0	+3.1 −2.0	+0.3 −0.1
188.0	741.7	719.5	−3.0	+3.2 −2.0	+0.2 −0.2
190.0	729.4	708.0	−2.9	+3.2 −2.0	+0.1 −0.2
192.0	717.3	696.0	−3.0	+3.2 −2.0	+0.1 −0.3
194.0	705.7	684.5	−3.0	+3.2 −2.0	+0.2 −0.4
195.0	700.2	679.0	−3.0	+3.2 −2.0	+0.2 −0.4
196.0	694.7	673.5	−3.0	+3.2 −2.0	+0.2 −0.4
198.0	684.1	662.9	−3.1	+3.3 −2.0	+0.1 −0.3
200.0	673.7	652.4	−3.2	+3.3 −2.0	+0.1 −0.2
202.0	664.3	642.9	−3.2	+3.3 −2.0	+0.1 −0.2
204.0	655.7	634.3	−3.3	+3.3 −2.0	+0.1 −0.2
206.0	647.6	626.2	−3.3	+3.4 −2.0	+0.1 −0.3
208.0	639.8	618.4	−3.4	+3.4 −2.0	+0.1 −0.3
210.0	632.4	610.8	−3.4	+3.4 −2.0	+0.1 −0.3
212.0	624.8	603.3	−3.4	+3.4 −2.0	+0.1 −0.3
214.0	617.0	595.5	−3.5	+3.4 −2.0	+0.1 −0.3
216.0	609.4	587.9	−3.5	+3.5 −2.0	+0.0 −0.4
218.0	601.6	580.2	−3.6	+3.5 −2.0	+0.0 −0.4
220.0	593.8	572.4	−3.6	+3.5 −2.0	+0.0 −0.4
222.0	586.0	564.6	−3.6	+3.5 −2.0	+0.0 −0.4
224.0	578.3	557.0	−3.7	+3.5 −2.0	+0.0 −0.4
226.0	570.5	549.3	−3.7	+3.6 −2.0	+0.1 −0.4
228.0	562.7	541.6	−3.7	+3.6 −2.0	+0.1 −0.4
230.0	555.1	534.1	−3.8	+3.6 −2.0	+0.1 −0.4

Table B.20: VBF cross sections at 7 TeV. Central values at NNLO QCD, NNLO QCD + NLO EW, relative EW corrections, and uncertainties from PDF+α_s (according to the PDF4LHC prescription) and from QCD scale.

M_H [GeV]	$\sigma^{\mathrm{NNLO}}_{\mathrm{VBF@NNLO}}$ [fb]	$\sigma^{\mathrm{NNLO+EW}}$ [fb]	$\delta^{\mathrm{EW}}_{\mathrm{HAWK}}$ [%]	PDF4LHC [%]	QCD Scale [%]
232.0	547.5	526.6	−3.8	+3.6 −2.0	+0.1 −0.4
234.0	539.8	519.0	−3.9	+3.6 −2.0	+0.1 −0.4
236.0	532.1	511.4	−3.9	+3.7 −2.0	+0.1 −0.5
238.0	524.4	503.8	−3.9	+3.7 −2.0	+0.1 −0.5
240.0	516.3	495.9	−4.0	+3.7 −2.0	+0.1 −0.5
242.0	508.5	488.2	−4.0	+3.7 −2.0	+0.1 −0.5
244.0	500.8	480.7	−4.0	+3.7 −2.0	+0.1 −0.5
246.0	493.1	473.3	−4.0	+3.8 −2.0	+0.1 −0.6
248.0	485.6	465.9	−4.1	+3.8 −2.0	+0.1 −0.6
250.0	478.3	458.8	−4.1	+3.8 −2.0	+0.1 −0.6
252.0	471.2	451.9	−4.1	+3.8 −2.0	+0.1 −0.6
254.0	464.3	445.2	−4.1	+3.8 −2.0	+0.2 −0.5
256.0	457.5	438.5	−4.1	+3.9 −2.0	+0.2 −0.5
258.0	450.7	432.0	−4.2	+3.9 −2.0	+0.3 −0.4
260.0	444.1	425.6	−4.2	+3.9 −2.0	+0.3 −0.4
262.0	437.6	419.3	−4.2	+3.9 −2.0	+0.3 −0.4
264.0	431.3	413.1	−4.2	+3.9 −2.0	+0.2 −0.5
266.0	425.0	406.9	−4.2	+4.0 −2.0	+0.2 −0.5
268.0	418.8	401.0	−4.3	+4.0 −2.0	+0.1 −0.6
270.0	412.8	395.1	−4.3	+4.0 −2.0	+0.1 −0.6
272.0	406.9	389.4	−4.3	+4.0 −2.0	+0.1 −0.6
274.0	401.0	383.7	−4.3	+4.1 −2.0	+0.1 −0.6
276.0	395.4	378.3	−4.3	+4.1 −2.0	+0.2 −0.7
278.0	389.9	372.9	−4.3	+4.2 −2.0	+0.2 −0.7
280.0	384.3	367.6	−4.4	+4.2 −2.0	+0.2 −0.7
282.0	378.9	362.3	−4.4	+4.2 −2.0	+0.2 −0.7
284.0	373.7	357.2	−4.4	+4.2 −2.0	+0.2 −0.7
286.0	368.4	352.1	−4.4	+4.3 −2.0	+0.2 −0.7
288.0	363.3	347.1	−4.5	+4.3 −2.0	+0.2 −0.7
290.0	358.3	342.2	−4.5	+4.3 −2.0	+0.2 −0.7
292.0	353.2	340.8	−3.5	+4.3 −2.0	+0.2 −0.7
294.0	348.4	339.4	−2.6	+4.3 −2.0	+0.2 −0.7
296.0	343.6	337.9	−1.6	+4.4 −2.0	+0.2 −0.8
298.0	338.8	336.5	−0.7	+4.4 −2.0	+0.2 −0.8
300.0	334.2	335.0	+0.3	+4.4 −2.0	+0.2 −0.8
305.0	322.9	323.7	+0.2	+4.5 −2.0	+0.2 −0.8
310.0	312.3	313.0	+0.2	+4.5 −1.9	+0.2 −0.8
315.0	302.2	302.8	+0.2	+4.5 −1.9	+0.3 −0.7
320.0	292.2	292.9	+0.2	+4.6 −1.9	+0.3 −0.7
325.0	282.8	283.4	+0.2	+4.6 −1.9	+0.3 −0.8
330.0	274.0	274.5	+0.2	+4.7 −1.9	+0.3 −0.8
335.0	265.6	266.1	+0.2	+4.8 −1.9	+0.3 −0.9
340.0	258.1	258.5	+0.2	+4.8 −1.9	+0.3 −0.9
345.0	251.5	251.9	+0.1	+4.8 −1.9	+0.3 −1.0
350.0	242.1	238.0	−1.7	+4.9 −1.9	+0.3 −1.0
360.0	226.3	214.2	−5.3	+5.0 −1.9	+0.3 −1.1
370.0	213.9	203.9	−4.7	+5.1 −1.9	+0.4 −1.1

Table B.21: VBF cross sections at 7 TeV. Central values at NNLO QCD, NNLO QCD + NLO EW, relative EW corrections, and uncertainties from PDF+α_s (according to the PDF4LHC prescription) and from QCD scale.

M_H [GeV]	$\sigma_{\text{VBF@NNLO}}^{\text{NNLO}}$ [fb]	$\sigma^{\text{NNLO+EW}}$ [fb]	$\delta_{\text{HAWK}}^{\text{EW}}$ [%]	PDF4LHC [%]	QCD Scale [%]
380.0	203.0	194.9	-4.0	$+5.2$ -1.9	$+0.4$ -1.1
390.0	192.4	185.9	-3.4	$+5.3$ -1.9	$+0.4$ -1.1
400.0	182.3	177.2	-2.8	$+5.5$ -1.9	$+0.4$ -1.2
420.0	163.3	160.1	-2.0	$+5.7$ -1.9	$+0.5$ -1.2
440.0	145.9	144.2	-1.1	$+5.9$ -1.8	$+0.6$ -1.3
450.0	137.8	136.8	-0.7	$+6.0$ -1.8	$+0.6$ -1.3
460.0	130.1	129.6	-0.4	$+6.1$ -1.8	$+0.6$ -1.4
480.0	116.1	116.4	$+0.2$	$+6.4$ -1.8	$+0.7$ -1.5
500.0	103.7	104.6	$+0.9$	$+6.6$ -1.8	$+0.7$ -1.6
520.0	92.67	94.03	$+1.5$	$+6.8$ -1.8	$+0.7$ -1.6
540.0	82.95	84.63	$+2.0$	$+7.0$ -1.8	$+0.8$ -1.7
550.0	78.52	80.34	$+2.3$	$+7.1$ -1.8	$+0.8$ -1.7
560.0	74.37	76.31	$+2.6$	$+7.2$ -1.8	$+0.8$ -1.8
580.0	66.8	68.94	$+3.2$	$+7.4$ -1.7	$+0.9$ -1.9
600.0	60.13	62.42	$+3.8$	$+7.6$ -1.7	$+1.0$ -2.0
620.0	54.24	56.65	$+4.4$	$+7.8$ -1.7	$+1.0$ -2.1
640.0	49.01	51.51	$+5.1$	$+8.1$ -1.7	$+1.1$ -2.2
65.00	46.62	49.15	$+5.4$	$+8.2$ -1.7	$+1.1$ -2.2
66.00	44.37	46.93	$+5.8$	$+8.3$ -1.7	$+1.1$ -2.2
680.0	40.24	42.86	$+6.5$	$+8.5$ -1.6	$+1.2$ -2.3
700.0	36.56	39.21	$+7.3$	$+8.7$ -1.6	$+1.2$ -2.4
720.0	33.28	35.97	$+8.1$	$+8.9$ -1.6	$+1.3$ -2.5
740.0	30.32	33.03	$+8.9$	$+9.2$ -1.6	$+1.4$ -2.6
750.0	28.99	31.70	$+9.3$	$+9.3$ -1.6	$+1.4$ -2.6
760.0	27.71	30.44	$+9.8$	$+9.4$ -1.6	$+1.4$ -2.6
780.0	25.35	28.09	$+10.8$	$+9.6$ -1.6	$+1.5$ -2.7
800.0	23.24	25.98	$+11.8$	$+9.8$ -1.6	$+1.5$ -2.8
820.0	21.33	24.08	$+12.9$	$+10.0$ -1.6	$+1.5$ -2.9
840.0	19.61	22.36	$+14.0$	$+10.3$ -1.5	$+1.6$ -3.0
850.0	18.81	21.56	$+14.6$	$+10.4$ -1.5	$+1.6$ -3.0
860.0	18.05	20.81	$+15.3$	$+10.5$ -1.5	$+1.6$ -3.0
880.0	16.64	19.41	$+16.6$	$+10.7$ -1.5	$+1.7$ -3.1
900.0	15.36	18.13	$+18.0$	$+10.9$ -1.5	$+1.7$ -3.2
920.0	14.21	16.97	$+19.4$	$+11.1$ -1.5	$+1.8$ -3.2
940.0	13.14	15.89	$+20.9$	$+11.4$ -1.4	$+1.9$ -3.3
950.0	12.65	15.38	$+21.6$	$+11.5$ -1.4	$+2.0$ -3.3
960.0	12.18	14.93	$+22.5$	$+11.6$ -1.4	$+2.0$ -3.3
98.00	11.30	14.04	$+24.3$	$+11.8$ -1.4	$+2.1$ -3.4
1000	10.49	13.22	$+26.0$	$+12.0$ -1.4	$+2.2$ -3.5

Table B.22: VBF cross sections at 8 TeV. Central values at NNLO QCD, NNLO QCD + NLO EW, relative EW corrections, and uncertainties from PDF+α_s (according to the PDF4LHC prescription) and from QCD scale.

M_H [GeV]	$\sigma^{NNLO}_{VBF@NNLO}$ [fb]	$\sigma^{NNLO+EW}$ [fb]	δ^{EW}_{HAWK} [%]	PDF4LHC [%]	QCD Scale [%]
80.0	2542	2424	−4.6	+2.7 −3.0	+0.2 −0.3
81.0	2515	2399	−4.6	+2.6 −3.0	+0.4 −0.3
82.0	2479	2364	−4.6	+2.6 −2.8	+0.3 −0.3
83.0	2461	2346	−4.6	+2.6 −2.8	+0.4 −0.2
84.0	2439	2326	−4.6	+2.6 −2.8	+0.3 −0.2
85.0	2412	2300	−4.6	+2.6 −2.8	+0.3 −0.2
86.0	2394	2283	−4.6	+2.6 −2.8	+0.3 −0.2
87.0	2368	2258	−4.6	+2.6 −2.9	+0.3 −0.3
88.0	2349	2240	−4.6	+2.6 −2.9	+0.2 −0.3
89.0	2316	2209	−4.6	+2.6 −2.9	+0.3 −0.3
90.0	2297	2191	−4.6	+2.6 −2.7	+0.3 −0.2
91.0	2276	2170	−4.6	+2.6 −2.7	+0.3 −0.2
92.0	2258	2153	−4.6	+2.6 −2.9	+0.2 −0.3
93.0	2232	2129	−4.6	+2.6 −2.7	+0.3 −0.2
94.0	2211	2108	−4.6	+2.6 −2.7	+0.3 −0.2
95.0	2186	2084	−4.6	+2.6 −2.9	+0.2 −0.2
96.0	2168	2068	−4.6	+2.6 −2.9	+0.3 −0.2
97.0	2145	2046	−4.6	+2.6 −2.7	+0.3 −0.3
98.0	2126	2027	−4.6	+2.6 −2.9	+0.3 −0.2
99.0	2102	2004	−4.6	+2.6 −2.9	+0.2 −0.2
100.0	2085	1988	−4.6	+2.6 −2.9	+0.2 −0.2
101.0	2062	1967	−4.6	+2.6 −2.9	+0.3 −0.2
102.0	2040	1945	−4.6	+2.5 −2.8	+0.2 −0.2
103.0	2027	1933	−4.6	+2.6 −2.8	+0.2 −0.2
104.0	2006	1914	−4.6	+2.6 −2.9	+0.2 −0.2
105.0	1989	1897	−4.6	+2.5 −2.8	+0.3 −0.2
106.0	1967	1877	−4.6	+2.5 −2.8	+0.3 −0.2
107.0	1952	1862	−4.6	+2.5 −2.8	+0.2 −0.2
108.0	1930	1841	−4.6	+2.5 −2.8	+0.2 −0.2
109.0	1915	1826	−4.6	+2.5 −2.8	+0.3 −0.2
110.0	1896	1809	−4.6	+2.5 −2.8	+0.2 −0.2
110.5	1886	1799	−4.6	+2.5 −2.6	+0.2 −0.2
111.0	1878	1791	−4.6	+2.5 −2.8	+0.2 −0.2
111.5	1870	1784	−4.6	+2.5 −2.8	+0.2 −0.2
112.0	1866	1780	−4.6	+2.5 −2.8	+0.2 −0.2
112.5	1856	1771	−4.6	+2.6 −2.8	+0.2 −0.2
113.0	1848	1764	−4.6	+2.5 −2.8	+0.3 −0.2
113.5	1837	1753	−4.6	+2.6 −2.8	+0.2 −0.2
114.0	1827	1743	−4.6	+2.5 −2.8	+0.2 −0.2
114.5	1819	1735	−4.6	+2.5 −2.8	+0.2 −0.2
115.0	1812	1729	−4.6	+2.5 −2.8	+0.2 −0.2
115.5	1802	1719	−4.6	+2.6 −2.8	+0.2 −0.2
116.0	1796	1714	−4.6	+2.6 −2.8	+0.2 −0.2
116.5	1786	1704	−4.6	+2.6 −2.8	+0.2 −0.2
117.0	1780	1699	−4.6	+2.5 −2.8	+0.2 −0.2
117.5	1769	1688	−4.6	+2.6 −2.8	+0.2 −0.2
118.0	1764	1683	−4.6	+2.6 −2.8	+0.3 −0.2

Table B.23: VBF cross sections at 8 TeV. Central values at NNLO QCD, NNLO QCD + NLO EW, relative EW corrections, and uncertainties from PDF+$\alpha_{\rm s}$ (according to the PDF4LHC prescription) and from QCD scale.

$M_{\rm H}$ [GeV]	$\sigma^{\rm NNLO}_{\rm VBF@NNLO}$ [fb]	$\sigma^{\rm NNLO+EW}$ [fb]	$\delta^{\rm EW}_{\rm HAWK}$ [%]	PDF4LHC [%]		QCD Scale [%]	
118.5	1755	1675	−4.6	+2.6	−2.8	+0.2	−0.2
119.0	1745	1666	−4.6	+2.6	−2.8	+0.3	−0.2
119.5	1738	1659	−4.6	+2.6	−2.8	+0.2	−0.2
120.0	1728	1649	−4.6	+2.6	−2.8	+0.2	−0.2
120.1	1728	1650	−4.5	+2.6	−2.8	+0.2	−0.2
120.2	1726	1648	−4.5	+2.6	−2.8	+0.2	−0.2
120.3	1724	1646	−4.5	+2.6	−2.8	+0.2	−0.1
120.4	1725	1647	−4.5	+2.6	−2.8	+0.2	−0.1
120.5	1722	1643	−4.6	+2.6	−2.8	+0.2	−0.1
120.6	1722	1645	−4.5	+2.6	−2.8	+0.2	−0.1
120.7	1721	1643	−4.5	+2.6	−2.8	+0.2	−0.1
120.8	1716	1638	−4.5	+2.6	−2.8	+0.2	−0.2
120.9	1716	1638	−4.5	+2.6	−2.8	+0.2	−0.2
121.0	1714	1636	−4.6	+2.6	−2.8	+0.2	−0.2
121.1	1711	1634	−4.5	+2.6	−2.8	+0.2	−0.2
121.2	1712	1634	−4.5	+2.6	−2.8	+0.2	−0.2
121.3	1711	1634	−4.5	+2.6	−2.8	+0.2	−0.2
121.4	1710	1633	−4.5	+2.6	−2.8	+0.2	−0.2
121.5	1708	1631	−4.6	+2.6	−2.8	+0.2	−0.2
121.6	1705	1628	−4.5	+2.6	−2.8	+0.2	−0.2
121.7	1704	1627	−4.5	+2.6	−2.8	+0.2	−0.2
121.8	1703	1627	−4.5	+2.6	−2.8	+0.3	−0.2
121.9	1703	1627	−4.5	+2.6	−2.8	+0.3	−0.2
122.0	1700	1623	−4.5	+2.6	−2.8	+0.3	−0.2
122.1	1699	1622	−4.5	+2.6	−2.8	+0.3	−0.2
122.2	1697	1621	−4.5	+2.6	−2.8	+0.3	−0.2
122.3	1698	1622	−4.5	+2.6	−2.8	+0.2	−0.2
122.4	1694	1618	−4.5	+2.6	−2.8	+0.2	−0.2
122.5	1692	1615	−4.5	+2.6	−2.8	+0.2	−0.2
122.6	1691	1614	−4.5	+2.6	−2.8	+0.2	−0.2
122.7	1690	1614	−4.5	+2.6	−2.8	+0.2	−0.2
122.8	1688	1611	−4.5	+2.6	−2.8	+0.2	−0.2
122.9	1685	1609	−4.5	+2.6	−2.8	+0.2	−0.2
123.0	1685	1608	−4.5	+2.6	−2.8	+0.2	−0.2
123.1	1682	1606	−4.5	+2.6	−2.8	+0.2	−0.2
123.2	1680	1605	−4.5	+2.6	−2.8	+0.2	−0.2
123.3	1678	1603	−4.5	+2.6	−2.8	+0.2	−0.2
123.4	1679	1603	−4.5	+2.6	−2.8	+0.2	−0.2
123.5	1674	1598	−4.5	+2.6	−2.8	+0.2	−0.2
123.6	1679	1603	−4.5	+2.6	−2.8	+0.2	−0.2
123.7	1675	1600	−4.5	+2.6	−2.8	+0.2	−0.2
123.8	1673	1598	−4.5	+2.6	−2.8	+0.3	−0.2
123.9	1671	1596	−4.5	+2.6	−2.8	+0.3	−0.2
124.0	1671	1595	−4.5	+2.6	−2.8	+0.3	−0.2
124.1	1666	1591	−4.5	+2.6	−2.8	+0.3	−0.2
124.2	1666	1591	−4.5	+2.6	−2.8	+0.3	−0.2
124.3	1665	1590	−4.5	+2.6	−2.8	+0.2	−0.2

Table B.24: VBF cross sections at 8 TeV. Central values at NNLO QCD, NNLO QCD + NLO EW, relative EW corrections, and uncertainties from PDF+α_s (according to the PDF4LHC prescription) and from QCD scale.

M_H [GeV]	$\sigma^{NNLO}_{VBF@NNLO}$ [fb]	$\sigma^{NNLO+EW}$ [fb]	δ^{EW}_{HAWK} [%]	PDF4LHC [%]	QCD Scale [%]
124.4	1663	1589	-4.5	$+2.6$ -2.8	$+0.2$ -0.2
124.5	1662	1587	-4.5	$+2.6$ -2.8	$+0.2$ -0.2
124.6	1661	1586	-4.5	$+2.6$ -2.8	$+0.2$ -0.2
124.7	1665	1590	-4.5	$+2.6$ -2.8	$+0.2$ -0.2
124.8	1659	1584	-4.5	$+2.6$ -2.8	$+0.2$ -0.2
124.9	1656	1582	-4.5	$+2.6$ -2.8	$+0.2$ -0.2
125.0	1653	1578	-4.5	$+2.6$ -2.8	$+0.2$ -0.2
125.1	1653	1579	-4.5	$+2.6$ -2.8	$+0.2$ -0.2
125.2	1651	1576	-4.5	$+2.6$ -2.8	$+0.2$ -0.2
125.3	1650	1576	-4.5	$+2.6$ -2.8	$+0.2$ -0.2
125.4	1647	1573	-4.5	$+2.6$ -2.8	$+0.2$ -0.2
125.5	1647	1573	-4.5	$+2.6$ -2.8	$+0.2$ -0.2
125.6	1646	1572	-4.5	$+2.6$ -2.8	$+0.2$ -0.2
125.7	1644	1570	-4.5	$+2.6$ -2.8	$+0.2$ -0.2
125.8	1642	1568	-4.5	$+2.6$ -2.8	$+0.3$ -0.1
125.9	1642	1568	-4.5	$+2.6$ -2.8	$+0.3$ -0.1
126.0	1643	1568	-4.5	$+2.6$ -2.8	$+0.3$ -0.1
126.1	1639	1565	-4.5	$+2.6$ -2.8	$+0.3$ -0.1
126.2	1638	1565	-4.5	$+2.6$ -2.8	$+0.3$ -0.1
126.3	1637	1564	-4.5	$+2.6$ -2.7	$+0.2$ -0.2
126.4	1634	1561	-4.5	$+2.6$ -2.7	$+0.2$ -0.2
126.5	1632	1558	-4.5	$+2.6$ -2.7	$+0.2$ -0.2
126.6	1633	1560	-4.5	$+2.6$ -2.7	$+0.2$ -0.2
126.7	1630	1557	-4.5	$+2.6$ -2.7	$+0.2$ -0.2
126.8	1628	1555	-4.5	$+2.6$ -2.7	$+0.3$ -0.2
126.9	1627	1554	-4.5	$+2.6$ -2.7	$+0.3$ -0.2
127.0	1625	1552	-4.5	$+2.6$ -2.7	$+0.3$ -0.2
127.1	1621	1548	-4.5	$+2.6$ -2.7	$+0.3$ -0.2
127.2	1621	1548	-4.5	$+2.6$ -2.7	$+0.3$ -0.2
127.3	1622	1549	-4.5	$+2.6$ -2.7	$+0.2$ -0.2
127.4	1619	1547	-4.5	$+2.6$ -2.7	$+0.2$ -0.2
127.5	1616	1543	-4.5	$+2.6$ -2.7	$+0.2$ -0.2
127.6	1618	1545	-4.5	$+2.6$ -2.7	$+0.2$ -0.2
127.7	1616	1544	-4.5	$+2.6$ -2.7	$+0.2$ -0.2
127.8	1613	1541	-4.5	$+2.6$ -2.7	$+0.2$ -0.2
127.9	1613	1541	-4.5	$+2.6$ -2.7	$+0.2$ -0.2
128.0	1612	1540	-4.5	$+2.6$ -2.7	$+0.2$ -0.2
128.1	1609	1537	-4.5	$+2.6$ -2.7	$+0.2$ -0.2
128.2	1608	1536	-4.5	$+2.6$ -2.7	$+0.2$ -0.2
128.3	1608	1535	-4.5	$+2.6$ -2.7	$+0.2$ -0.2
128.4	1605	1533	-4.5	$+2.6$ -2.7	$+0.2$ -0.2
128.5	1604	1531	-4.5	$+2.6$ -2.7	$+0.2$ -0.2
128.6	1602	1531	-4.5	$+2.6$ -2.7	$+0.2$ -0.2
128.7	1601	1529	-4.5	$+2.6$ -2.7	$+0.2$ -0.2
128.8	1600	1529	-4.5	$+2.6$ -2.7	$+0.2$ -0.2
128.9	1599	1527	-4.5	$+2.6$ -2.7	$+0.2$ -0.2
129.0	1598	1525	-4.5	$+2.6$ -2.7	$+0.2$ -0.2

Table B.25: VBF cross sections at 8 TeV. Central values at NNLO QCD, NNLO QCD + NLO EW, relative EW corrections, and uncertainties from PDF+α_s (according to the PDF4LHC prescription) and from QCD scale.

M_H [GeV]	$\sigma^\text{NNLO}_\text{VBF@NNLO}$ [fb]	$\sigma^\text{NNLO+EW}$ [fb]	$\delta^\text{EW}_\text{HAWK}$ [%]	PDF4LHC [%]		QCD Scale [%]	
129.1	1597	1526	−4.5	+2.6	−2.7	+0.2	−0.2
129.2	1594	1523	−4.5	+2.6	−2.7	+0.2	−0.2
129.3	1593	1522	−4.5	+2.6	−2.7	+0.2	−0.2
129.4	1595	1523	−4.5	+2.6	−2.7	+0.2	−0.2
129.5	1585	1513	−4.5	+2.6	−2.7	+0.2	−0.2
129.6	1587	1516	−4.5	+2.6	−2.7	+0.2	−0.2
129.7	1588	1517	−4.5	+2.6	−2.7	+0.2	−0.2
129.8	1586	1515	−4.5	+2.6	−2.7	+0.2	−0.2
129.9	1586	1515	−4.5	+2.6	−2.7	+0.2	−0.2
130.0	1583	1511	−4.5	+2.6	−2.7	+0.2	−0.2
130.5	1575	1504	−4.5	+2.6	−2.7	+0.2	−0.2
131.0	1568	1497	−4.5	+2.6	−2.7	+0.2	−0.2
131.5	1563	1492	−4.5	+2.6	−2.7	+0.2	−0.2
132.0	1556	1485	−4.5	+2.6	−2.7	+0.2	−0.1
132.5	1549	1479	−4.5	+2.6	−2.7	+0.2	−0.2
133.0	1542	1473	−4.5	+2.6	−2.7	+0.2	−0.2
133.5	1536	1466	−4.5	+2.6	−2.7	+0.2	−0.2
134.0	1530	1462	−4.5	+2.6	−2.7	+0.2	−0.2
134.5	1524	1455	−4.5	+2.6	−2.7	+0.2	−0.2
135.0	1516	1448	−4.5	+2.6	−2.7	+0.2	−0.2
135.5	1512	1444	−4.5	+2.6	−2.7	+0.2	−0.2
136.0	1503	1436	−4.5	+2.5	−2.7	+0.3	−0.2
136.5	1496	1429	−4.5	+2.6	−2.7	+0.2	−0.2
137.0	1490	1423	−4.5	+2.5	−2.7	+0.2	−0.2
137.5	1483	1417	−4.5	+2.5	−2.7	+0.2	−0.2
138.0	1478	1412	−4.5	+2.6	−2.7	+0.2	−0.2
138.5	1474	1407	−4.5	+2.6	−2.7	+0.2	−0.2
139.0	1466	1400	−4.5	+2.5	−2.7	+0.2	−0.2
139.5	1461	1396	−4.5	+2.5	−2.7	+0.2	−0.2
140.0	1454	1389	−4.5	+2.5	−2.7	+0.2	−0.2
140.5	1448	1384	−4.4	+2.5	−2.7	+0.2	−0.2
141.0	1441	1377	−4.5	+2.5	−2.7	+0.2	−0.2
141.5	1436	1372	−4.4	+2.5	−2.7	+0.2	−0.2
142.0	1429	1365	−4.5	+2.5	−2.7	+0.2	−0.2
142.5	1424	1361	−4.4	+2.5	−2.7	+0.2	−0.2
143.0	1417	1354	−4.5	+2.5	−2.7	+0.2	−0.2
143.5	1413	1350	−4.4	+2.5	−2.7	+0.2	−0.2
144.0	1406	1344	−4.5	+2.5	−2.7	+0.2	−0.2
144.5	1400	1337	−4.4	+2.5	−2.7	+0.2	−0.2
145.0	1395	1333	−4.5	+2.5	−2.7	+0.3	−0.1
145.5	1389	1327	−4.4	+2.5	−2.7	+0.3	−0.1
146.0	1383	1321	−4.5	+2.5	−2.7	+0.2	−0.1
146.5	1379	1317	−4.4	+2.5	−2.7	+0.2	−0.1
147.0	1372	1311	−4.5	+2.5	−2.7	+0.2	−0.1
147.5	1367	1307	−4.4	+2.5	−2.7	+0.2	−0.1
148.0	1363	1302	−4.5	+2.5	−2.7	+0.3	−0.1
148.5	1357	1296	−4.5	+2.5	−2.7	+0.2	−0.1

Table B.26: VBF cross sections at 8 TeV. Central values at NNLO QCD, NNLO QCD + NLO EW, relative EW corrections, and uncertainties from PDF+α_s (according to the PDF4LHC prescription) and from QCD scale.

M_H [GeV]	$\sigma_{\text{VBF@NNLO}}^{\text{NNLO}}$ [fb]	$\sigma^{\text{NNLO+EW}}$ [fb]	$\delta_{\text{HAWK}}^{\text{EW}}$ [%]	PDF4LHC [%]	QCD Scale [%]
149.0	1351	1291	−4.5	+2.5 −2.7	+0.2 −0.1
149.5	1345	1285	−4.5	+2.5 −2.7	+0.2 −0.2
150.0	1341	1280	−4.5	+2.5 −2.7	+0.3 −0.2
152.0	1319	1259	−4.5	+2.5 −2.7	+0.2 −0.1
154.0	1299	1240	−4.6	+2.5 −2.7	+0.2 −0.1
156.0	1282	1222	−4.6	+2.5 −2.6	+0.2 −0.1
158.0	1264	1204	−4.8	+2.5 −2.6	+0.2 −0.2
160.0	1244	1185	−4.7	+2.5 −2.6	+0.2 −0.1
162.0	1220	1171	−4.0	+2.5 −2.6	+0.2 −0.1
164.0	1194	1152	−3.5	+2.5 −2.6	+0.2 −0.1
165.0	1182	1141	−3.5	+2.6 −2.6	+0.2 −0.1
166.0	1172	1132	−3.4	+2.6 −2.6	+0.2 −0.1
168.0	1153	1114	−3.4	+2.6 −2.6	+0.2 −0.1
170.0	1136	1098	−3.4	+2.6 −2.6	+0.2 −0.1
172.0	1119	1080	−3.5	+2.6 −2.6	+0.2 −0.1
174.0	1101	1062	−3.5	+2.6 −2.6	+0.2 −0.1
175.0	1094	1055	−3.6	+2.6 −2.6	+0.2 −0.1
176.0	1086	1047	−3.6	+2.6 −2.6	+0.2 −0.1
178.0	1071	1031	−3.7	+2.6 −2.6	+0.2 −0.1
180.0	1056	1015	−3.9	+2.6 −2.6	+0.3 −0.1
182.0	1037	998	−3.8	+2.5 −2.6	+0.3 −0.1
184.0	1018	983	−3.5	+2.5 −2.6	+0.2 −0.1
185.0	1010	976	−3.3	+2.5 −2.6	+0.2 −0.1
186.0	1001	969	−3.2	+2.5 −2.6	+0.2 −0.1
188.0	985.1	953.6	−3.2	+2.5 −2.6	+0.3 −0.1
190.0	969.7	938.7	−3.2	+2.5 −2.5	+0.3 −0.1
192.0	954.6	923.8	−3.2	+2.5 −2.5	+0.2 −0.1
194.0	939.7	909.0	−3.3	+2.5 −2.5	+0.3 −0.1
195.0	932.5	901.8	−3.3	+2.5 −2.5	+0.2 −0.1
196.0	926.1	895.3	−3.3	+2.5 −2.7	+0.3 −0.1
198.0	912.6	881.9	−3.4	+2.5 −2.5	+0.3 −0.1
200.0	899.3	868.5	−3.4	+2.5 −2.7	+0.3 −0.1
202.0	887.5	856.8	−3.5	+2.5 −2.7	+0.2 −0.1
204.0	876.5	845.6	−3.5	+2.5 −2.7	+0.3 −0.1
206.0	866.5	835.6	−3.6	+2.5 −2.7	+0.3 −0.1
208.0	856.9	825.9	−3.6	+2.5 −2.7	+0.3 −0.1
210.0	847.4	816.3	−3.7	+2.5 −2.6	+0.2 −0.1
212.0	837.8	806.7	−3.7	+2.5 −2.7	+0.2 −0.1
214.0	828.1	797.0	−3.8	+2.5 −2.6	+0.2 −0.1
216.0	818.4	787.3	−3.8	+2.5 −2.6	+0.2 −0.1
218.0	808.7	777.6	−3.8	+2.4 −2.6	+0.2 −0.1
220.0	798.7	767.7	−3.9	+2.5 −2.6	+0.2 −0.1
222.0	788.9	757.9	−3.9	+2.6 −2.6	+0.3 −0.1
224.0	779.0	748.1	−4.0	+2.6 −2.6	+0.2 −0.1
226.0	768.8	738.1	−4.0	+2.6 −2.6	+0.2 −0.1
228.0	759.4	728.7	−4.0	+2.5 −2.6	+0.3 −0.1
230.0	749.5	719.0	−4.1	+2.5 −2.6	+0.3 −0.1

Table B.27: VBF cross sections at 8 TeV. Central values at NNLO QCD, NNLO QCD + NLO EW, relative EW corrections, and uncertainties from PDF+α_s (according to the PDF4LHC prescription) and from QCD scale.

M_H [GeV]	$\sigma^{NNLO}_{VBF@NNLO}$ [fb]	$\sigma^{NNLO+EW}$ [fb]	δ^{EW}_{HAWK} [%]	PDF4LHC [%]	QCD Scale [%]
232.0	739.8	709.5	−4.1	+2.5 −2.6	+0.3 −0.1
234.0	730.1	699.9	−4.1	+2.5 −2.6	+0.2 −0.1
236.0	720.2	690.3	−4.2	+2.5 −2.6	+0.3 −0.1
238.0	710.4	680.6	−4.2	+2.5 −2.6	+0.2 −0.1
240.0	699.9	670.3	−4.2	+2.5 −2.6	+0.3 −0.1
242.0	689.8	660.4	−4.3	+2.5 −2.6	+0.3 −0.1
244.0	679.7	650.6	−4.3	+2.5 −2.6	+0.2 −0.1
246.0	669.8	641.0	−4.3	+2.5 −2.6	+0.3 −0.1
248.0	660.5	631.9	−4.3	+2.5 −2.6	+0.2 −0.1
250.0	650.9	622.5	−4.4	+2.5 −2.6	+0.3 −0.1
252.0	641.7	613.6	−4.4	+2.5 −2.6	+0.3 −0.1
254.0	632.9	605.0	−4.4	+2.5 −2.6	+0.3 −0.1
256.0	624.0	596.4	−4.4	+2.5 −2.5	+0.2 −0.1
258.0	615.3	587.9	−4.4	+2.5 −2.5	+0.3 −0.1
260.0	606.8	579.7	−4.5	+2.5 −2.5	+0.3 −0.1
262.0	598.3	571.4	−4.5	+2.5 −2.5	+0.3 −0.1
264.0	590.2	563.6	−4.5	+2.5 −2.5	+0.3 −0.1
266.0	581.8	555.4	−4.5	+2.5 −2.5	+0.3 −0.1
268.0	573.8	547.7	−4.6	+2.5 −2.5	+0.2 −0.1
270.0	566.0	540.1	−4.6	+2.5 −2.5	+0.3 −0.1
272.0	558.4	532.8	−4.6	+2.5 −2.5	+0.3 −0.1
274.0	550.9	525.5	−4.6	+2.5 −2.5	+0.3 −0.1
276.0	543.5	518.4	−4.6	+2.4 −2.5	+0.3 −0.1
278.0	536.4	511.5	−4.6	+2.4 −2.5	+0.2 −0.1
280.0	529.2	504.5	−4.7	+2.4 −2.5	+0.3 −0.1
282.0	522.2	497.8	−4.7	+2.4 −2.5	+0.3 −0.1
284.0	515.2	491.1	−4.7	+2.5 −2.5	+0.3 −0.1
286.0	508.4	484.5	−4.7	+2.5 −2.6	+0.2 −0.1
288.0	501.7	478.0	−4.7	+2.5 −2.6	+0.3 −0.1
290.0	495.1	471.6	−4.7	+2.5 −2.6	+0.3 −0.2
292.0	488.6	465.4	−4.8	+2.5 −2.6	+0.3 −0.2
294.0	482.2	459.1	−4.8	+2.5 −2.6	+0.3 −0.2
296.0	476.0	453.0	−4.8	+2.5 −2.6	+0.3 −0.2
298.0	469.8	446.9	−4.9	+2.5 −2.6	+0.3 −0.2
300.0	463.7	440.8	−4.9	+2.5 −2.6	+0.3 −0.2
305.0	449.0	426.6	−5.0	+2.5 −2.6	+0.3 −0.2
310.0	435.0	413.1	−5.0	+2.5 −2.6	+0.3 −0.2
315.0	421.6	399.9	−5.1	+2.5 −2.6	+0.3 −0.2
320.0	408.6	387.5	−5.2	+2.5 −2.6	+0.3 −0.2
325.0	396.3	375.3	−5.3	+2.4 −2.6	+0.3 −0.2
330.0	384.5	363.7	−5.4	+2.5 −2.6	+0.3 −0.3
335.0	373.7	352.6	−5.6	+2.5 −2.5	+0.3 −0.3
340.0	363.7	342.2	−5.9	+2.5 −2.5	+0.3 −0.3
345.0	355.0	330.3	−7.0	+2.5 −2.5	+0.3 −0.3
350.0	342.5	320.0	−6.6	+2.5 −2.6	+0.3 −0.3
360.0	321.3	302.8	−5.8	+2.5 −2.7	+0.3 −0.3
370.0	305.0	289.6	−5.1	+2.5 −2.7	+0.3 −0.3

Table B.28: VBF cross sections at 8 TeV. Central values at NNLO QCD, NNLO QCD + NLO EW, relative EW corrections, and uncertainties from PDF+α_s (according to the PDF4LHC prescription) and from QCD scale.

M_H [GeV]	$\sigma^{\text{NNLO}}_{\text{VBF@NNLO}}$ [fb]	$\sigma^{\text{NNLO+EW}}$ [fb]	$\delta^{\text{EW}}_{\text{HAWK}}$ [%]	PDF4LHC [%]	QCD Scale [%]
380.0	290.4	277.6	−4.4	+2.6 −2.8	+0.3 −0.3
390.0	276.5	266.0	−3.8	+2.6 −2.8	+0.3 −0.4
400.0	263.0	254.3	−3.3	+2.6 −2.8	+0.3 −0.4
420.0	237.3	231.7	−2.4	+2.8 −2.8	+0.3 −0.4
440.0	213.6	210.3	−1.5	+2.8 −2.9	+0.3 −0.4
450.0	202.6	200.2	−1.2	+2.8 −3.1	+0.3 −0.5
460.0	192.0	190.5	−0.8	+2.9 −3.1	+0.3 −0.5
480.0	172.7	172.4	−0.2	+2.9 −3.1	+0.3 −0.5
500.0	155.4	156.1	+0.5	+3.1 −3.2	+0.3 −0.5
520.0	139.9	141.4	+1.1	+3.1 −3.3	+0.3 −0.6
540.0	126.3	128.3	+1.6	+3.2 −3.5	+0.3 −0.6
550.0	120.0	122.3	+1.9	+3.2 −3.5	+0.3 −0.6
560.0	114.1	116.6	+2.2	+3.2 −3.5	+0.3 −0.6
580.0	103.3	106.2	+2.8	+3.4 −3.6	+0.3 −0.7
600.0	93.69	96.88	+3.4	+3.5 −3.6	+0.4 −0.7
620.0	85.18	88.61	+4.0	+3.5 −3.7	+0.4 −0.7
640.0	77.58	81.21	+4.7	+3.6 −3.8	+0.4 −0.8
650.0	74.12	77.84	+5.0	+3.6 −4.0	+0.4 −0.8
660.0	70.79	74.59	+5.4	+3.8 −4.0	+0.4 −0.8
680.0	64.71	68.65	+6.1	+3.9 −4.1	+0.4 −0.8
700.0	59.26	63.30	+6.8	+4.0 −4.2	+0.4 −0.8
720.0	54.37	58.53	+7.7	+4.0 −4.4	+0.4 −0.9
740.0	49.97	54.20	+8.5	+4.1 −4.3	+0.4 −0.9
750.0	48.05	52.35	+9.0	+4.3 −4.3	+0.4 −0.9
760.0	46.00	50.32	+9.4	+4.3 −4.5	+0.5 −0.9
780.0	42.42	46.82	+10.4	+4.4 −4.6	+0.5 −1.0
800.0	39.18	43.65	+11.4	+4.5 −4.7	+0.5 −1.0
820.0	36.25	40.78	+12.5	+4.5 −4.9	+0.5 −1.1
840.0	33.59	38.15	+13.6	+4.6 −5.1	+0.6 −1.0
850.0	32.45	37.06	+14.2	+4.8 −4.9	+0.6 −1.1
860.0	31.17	35.79	+14.8	+4.9 −5.1	+0.6 −1.1
880.0	28.96	33.63	+16.1	+4.9 −5.2	+0.6 −1.1
900.0	26.95	31.64	+17.4	+5.0 −5.3	+0.6 −1.2
920.0	25.11	29.86	+19.0	+5.1 −5.6	+0.6 −1.2
940.0	23.41	28.20	+20.5	+5.2 −5.7	+0.6 −1.2
950.0	22.63	27.45	+21.3	+5.4 −5.5	+0.6 −1.3
960.0	21.86	26.69	+22.1	+5.4 −5.8	+0.7 −1.2
980.0	20.42	25.24	+23.6	+5.5 −5.8	+0.7 −1.3
1000.0	19.10	23.99	+25.6	+5.6 −5.9	+0.7 −1.3

Table B.29: WH production cross section and its scale and PDF uncertainties for various Higgs-boson masses at the LHC with CM energy $\sqrt{s} = 7$ TeV.

M_H [GeV]	σ_WH [fb]	Scale [%]	PDF [%]	Total [%]
80.00	2341	±1.0	±2.3	±3.2
81.00	2258	±0.9	±2.3	±3.2
82.00	2179	±0.9	±2.3	±3.2
83.00	2104	±0.9	±2.3	±3.2
84.00	2031	±0.9	±2.3	±3.2
85.00	1963	±0.9	±2.3	±3.2
86.00	1896	±0.9	±2.3	±3.2
87.00	1831	±1.0	±2.3	±3.2
88.00	1770	±1.0	±2.3	±3.3
89.00	1711	±1.0	±2.3	±3.3
90.00	1654	±1.0	±2.2	±3.3
91.00	1600	±1.0	±2.3	±3.3
92.00	1548	±1.0	±2.3	±3.2
93.00	1498	±1.0	±2.3	±3.2
94.00	1450	±1.0	±2.3	±3.2
95.00	1404	±0.9	±2.3	±3.2
96.00	1359	±0.9	±2.3	±3.2
97.00	1315	±0.9	±2.3	±3.2
98.00	1274	±0.9	±2.3	±3.2
99.00	1234	±0.9	±2.3	±3.2
100.0	1195	±0.9	±2.3	±3.2
101.0	1159	±0.9	±2.3	±3.2
102.0	1125	±0.9	±2.4	±3.3
103.0	1091	±0.9	±2.4	±3.3
104.0	1058	±0.9	±2.4	±3.3
105.0	1029	±0.9	±2.4	±3.4
106.0	996.4	±0.9	±2.4	±3.4
107.0	967.4	±0.9	±2.4	±3.4
108.0	938.4	±0.9	±2.4	±3.3
109.0	910.9	±0.9	±2.4	±3.3
110.0	884.7	±0.9	±2.4	±3.3
110.5	872.0	±0.9	±2.4	±3.3
111.0	858.7	±0.9	±2.4	±3.3
111.5	845.8	±1.0	±2.4	±3.4
112.0	833.3	±1.0	±2.4	±3.4
112.5	821.3	±1.0	±2.4	±3.4
113.0	809.3	±1.0	±2.4	±3.4
113.5	797.3	±0.9	±2.4	±3.4
114.0	785.8	±0.9	±2.4	±3.4
114.5	774.3	±0.9	±2.4	±3.3
115.0	762.6	±0.9	±2.4	±3.3
115.5	751.7	±0.9	±2.4	±3.3
116.0	741.5	±0.9	±2.4	±3.4
116.5	730.9	±0.9	±2.5	±3.4
117.0	720.3	±0.9	±2.5	±3.4
117.5	710.2	±0.9	±2.5	±3.4
118.0	700.2	±0.9	±2.5	±3.4

Table B.30: WH production cross section and its scale and PDF uncertainties for various Higgs-boson masses at the LHC with CM energy $\sqrt{s} = 7$ TeV.

M_H [GeV]	σ_{WH} [fb]	Scale [%]	PDF [%]	Total [%]
118.5	690.7	±0.9	±2.5	±3.5
119.0	680.8	±0.9	±2.6	±3.5
119.5	671.2	±0.9	±2.6	±3.5
120.0	661.7	±0.9	±2.6	±3.5
120.1	660.3	±0.9	±2.6	±3.5
120.2	658.5	±0.9	±2.5	±3.5
120.3	656.7	±0.9	±2.5	±3.5
120.4	654.9	±0.9	±2.5	±3.4
120.5	653.3	±0.9	±2.5	±3.4
120.6	651.4	±0.9	±2.5	±3.4
120.7	649.6	±0.9	±2.5	±3.4
120.8	647.9	±0.9	±2.5	±3.4
120.9	646.3	±0.9	±2.5	±3.5
121.0	644.8	±0.9	±2.6	±3.5
121.1	643.0	±0.9	±2.5	±3.4
121.2	641.2	±0.9	±2.5	±3.4
121.3	639.7	±0.9	±2.4	±3.4
121.4	637.9	±0.9	±2.4	±3.3
121.5	636.3	±0.9	±2.4	±3.3
121.6	633.9	±0.9	±2.4	±3.3
121.7	632.4	±0.9	±2.4	±3.4
121.8	630.7	±0.9	±2.5	±3.4
121.9	628.8	±0.9	±2.5	±3.4
122.0	626.8	±0.9	±2.5	±3.5
122.1	625.1	±0.9	±2.5	±3.5
122.2	623.6	±0.9	±2.5	±3.5
122.3	621.8	±0.9	±2.6	±3.5
122.4	620.2	±0.9	±2.6	±3.5
122.5	618.5	±0.9	±2.6	±3.5
122.6	616.8	±0.9	±2.6	±3.5
122.7	615.3	±0.9	±2.6	±3.5
122.8	613.4	±0.9	±2.6	±3.5
122.9	611.6	±0.9	±2.6	±3.6
123.0	610.0	±0.9	±2.6	±3.6
123.1	608.4	±0.9	±2.6	±3.6
123.2	606.9	±0.9	±2.6	±3.5
123.3	605.0	±0.9	±2.6	±3.5
123.4	603.5	±0.9	±2.6	±3.5
123.5	602.1	±0.9	±2.5	±3.5
123.6	600.3	±0.9	±2.5	±3.5
123.7	599.0	±0.9	±2.5	±3.5
123.8	597.6	±0.9	±2.5	±3.5
123.9	595.9	±0.9	±2.5	±3.4
124.0	594.4	±0.9	±2.5	±3.4
124.1	592.6	±0.9	±2.5	±3.5
124.2	590.9	±0.9	±2.5	±3.5
124.3	589.4	±0.9	±2.6	±3.5

Table B.31: WH production cross section and its scale and PDF uncertainties for various Higgs-boson masses at the LHC with CM energy $\sqrt{s} = 7$ TeV.

M_H [GeV]	σ_{WH} [fb]	Scale [%]	PDF [%]	Total [%]
124.4	587.7	±0.9	±2.6	±3.5
124.5	585.8	±0.9	±2.6	±3.5
124.6	584.4	±0.9	±2.6	±3.5
124.7	582.9	±0.9	±2.6	±3.5
124.8	581.2	±0.9	±2.6	±3.5
124.9	579.8	±0.9	±2.6	±3.5
125.0	578.5	±0.9	±2.6	±3.5
125.1	577.0	±0.9	±2.6	±3.5
125.2	575.1	±0.9	±2.6	±3.5
125.3	573.6	±0.9	±2.6	±3.5
125.4	571.8	±1.0	±2.6	±3.5
125.5	570.3	±1.0	±2.6	±3.5
125.6	568.8	±1.0	±2.6	±3.5
125.7	567.3	±1.0	±2.5	±3.5
125.8	566.0	±1.0	±2.5	±3.5
125.9	564.3	±1.0	±2.5	±3.5
126.0	562.9	±1.0	±2.5	±3.4
126.1	561.2	±1.0	±2.5	±3.4
126.2	559.9	±1.0	±2.5	±3.5
126.3	558.5	±1.0	±2.5	±3.5
126.4	556.9	±1.0	±2.5	±3.5
126.5	555.5	±1.0	±2.5	±3.5
126.6	553.9	±1.0	±2.5	±3.5
126.7	552.3	±1.0	±2.6	±3.5
126.8	550.8	±1.0	±2.6	±3.6
126.9	549.2	±1.0	±2.6	±3.6
127.0	547.6	±1.0	±2.6	±3.6
127.1	546.3	±1.0	±2.6	±3.6
127.2	544.9	±1.0	±2.6	±3.5
127.3	543.4	±1.0	±2.5	±3.5
127.4	542.0	±1.0	±2.5	±3.5
127.5	540.6	±1.0	±2.5	±3.4
127.6	538.9	±1.0	±2.5	±3.4
127.7	537.3	±1.0	±2.5	±3.5
127.8	536.1	±1.0	±2.5	±3.5
127.9	534.8	±1.0	±2.5	±3.5
128.0	533.2	±1.0	±2.5	±3.5
128.1	531.9	±0.9	±2.5	±3.5
128.2	530.3	±0.9	±2.5	±3.5
128.3	528.8	±0.9	±2.5	±3.5
128.4	527.5	±0.9	±2.6	±3.5
128.5	525.8	±0.9	±2.6	±3.5
128.6	524.5	±0.9	±2.6	±3.5
128.7	523.3	±0.9	±2.6	±3.5
128.8	521.9	±0.9	±2.6	±3.5
128.9	520.4	±0.9	±2.6	±3.5
129.0	518.9	±0.9	±2.6	±3.5

Table B.32: WH production cross section and its scale and PDF uncertainties for various Higgs-boson masses at the LHC with CM energy $\sqrt{s} = 7$ TeV.

M_{H} [GeV]	σ_{WH} [fb]	Scale [%]	PDF [%]	Total [%]
129.1	517.6	± 0.9	± 2.6	± 3.5
129.2	516.4	± 0.9	± 2.6	± 3.5
129.3	515.0	± 0.9	± 2.6	± 3.5
129.4	513.7	± 0.9	± 2.5	± 3.5
129.5	512.2	± 0.9	± 2.5	± 3.5
129.6	511.2	± 0.9	± 2.5	± 3.5
129.7	509.6	± 0.9	± 2.6	± 3.5
129.8	508.4	± 0.9	± 2.6	± 3.5
129.9	507.2	± 0.9	± 2.6	± 3.5
130.0	505.9	± 0.9	± 2.6	± 3.6
130.5	498.9	± 0.9	± 2.6	± 3.6
131.0	492.2	± 1.0	± 2.6	± 3.6
131.5	485.8	± 1.0	± 2.6	± 3.5
132.0	479.5	± 1.0	± 2.6	± 3.5
132.5	473.0	± 1.0	± 2.6	± 3.5
133.0	466.8	± 1.0	± 2.6	± 3.5
133.5	460.8	± 1.0	± 2.6	± 3.5
134.0	454.9	± 1.0	± 2.6	± 3.5
134.5	449.1	± 1.0	± 2.6	± 3.5
135.0	443.1	± 1.0	± 2.6	± 3.5
135.5	437.4	± 1.0	± 2.6	± 3.5
136.0	431.8	± 1.0	± 2.6	± 3.5
136.5	426.1	± 1.0	± 2.6	± 3.5
137.0	420.7	± 1.0	± 2.6	± 3.5
137.5	415.2	± 1.0	± 2.6	± 3.6
138.0	409.8	± 1.0	± 2.6	± 3.5
138.5	404.6	± 1.0	± 2.6	± 3.5
139.0	399.6	± 1.0	± 2.6	± 3.5
139.5	394.5	± 0.9	± 2.6	± 3.5
140.0	389.6	± 0.9	± 2.6	± 3.5
140.5	384.6	± 0.9	± 2.6	± 3.5
141.0	379.9	± 1.0	± 2.6	± 3.6
141.5	375.2	± 1.0	± 2.6	± 3.6
142.0	370.4	± 1.0	± 2.6	± 3.6
142.5	365.8	± 1.0	± 2.6	± 3.6
143.0	361.1	± 1.0	± 2.7	± 3.6
143.5	356.7	± 1.0	± 2.7	± 3.6
144.0	352.4	± 1.0	± 2.7	± 3.6
144.5	348.0	± 1.0	± 2.7	± 3.6
145.0	343.7	± 1.0	± 2.7	± 3.7
145.5	339.4	± 1.0	± 2.7	± 3.7
146.0	335.1	± 1.0	± 2.7	± 3.7
146.5	331.0	± 1.0	± 2.7	± 3.7
147.0	326.9	± 1.0	± 2.7	± 3.7
147.5	322.8	± 1.0	± 2.8	± 3.8
148.0	319.0	± 1.0	± 2.7	± 3.8
148.5	314.9	± 1.0	± 2.7	± 3.7

Table B.33: WH production cross section and its scale and PDF uncertainties for various Higgs-boson masses at the LHC with CM energy $\sqrt{s} = 7$ TeV.

M_H [GeV]	σ_{WH} [fb]	Scale [%]	PDF [%]	Total [%]
149.0	310.9	±1.0	±2.7	±3.7
149.5	307.1	±1.0	±2.7	±3.7
150.0	303.4	±1.0	±2.7	±3.7
152.0	288.3	±1.0	±2.8	±3.8
154.0	274.2	±1.0	±2.8	±3.8
156.0	259.7	±1.0	±2.8	±3.8
158.0	245.2	±1.0	±2.8	±3.8
160.0	231.6	±1.0	±2.8	±3.9
162.0	224.1	±1.0	±2.9	±3.9
164.0	216.8	±1.0	±2.9	±3.9
165.0	213.3	±1.0	±2.9	±3.9
166.0	208.5	±1.0	±2.9	±3.9
168.0	199.4	±1.1	±2.9	±4.0
170.0	190.8	±1.0	±2.9	±4.0
172.0	182.6	±1.1	±2.9	±4.0
174.0	174.8	±1.1	±2.9	±4.0
175.0	170.9	±1.1	±2.9	±4.0
176.0	167.4	±1.1	±2.9	±4.0
178.0	160.5	±1.1	±3.0	±4.0
180.0	153.8	±1.1	±3.0	±4.0
182.0	148.2	±1.1	±3.0	±4.1
184.0	142.7	±1.1	±3.0	±4.1
185.0	140.1	±1.1	±3.0	±4.1
186.0	137.4	±1.1	±3.0	±4.1
188.0	132.0	±1.1	±3.0	±4.2
190.0	126.9	±1.1	±3.0	±4.2
192.0	122.0	±1.1	±3.1	±4.2
194.0	117.3	±1.1	±3.1	±4.2
195.0	115.1	±1.2	±3.1	±4.2
196.0	112.9	±1.1	±3.1	±4.3
198.0	108.6	±1.1	±3.1	±4.3
200.0	104.5	±1.1	±3.2	±4.3
202.0	100.6	±1.1	±3.2	±4.3
204.0	96.89	±1.2	±3.2	±4.4
206.0	93.32	±1.2	±3.2	±4.4
208.0	89.93	±1.2	±3.2	±4.4
210.0	86.65	±1.2	±3.2	±4.4
212.0	83.56	±1.2	±3.3	±4.5
214.0	80.56	±1.2	±3.3	±4.5
216.0	77.72	±1.2	±3.3	±4.5
218.0	74.99	±1.2	±3.3	±4.5
220.0	72.38	±1.2	±3.3	±4.5
222.0	69.85	±1.2	±3.4	±4.6
224.0	67.45	±1.2	±3.4	±4.6
226.0	65.14	±1.3	±3.4	±4.7
228.0	62.94	±1.3	±3.4	±4.7
230.0	60.82	±1.3	±3.4	±4.7

Table B.34: WH production cross section and its scale and PDF uncertainties for various Higgs-boson masses at the LHC with CM energy $\sqrt{s} = 7$ TeV.

M_H [GeV]	σ_{WH} [fb]	Scale [%]	PDF [%]	Total [%]
232.0	58.77	±1.3	±3.5	±4.8
234.0	56.81	±1.3	±3.5	±4.8
236.0	54.96	±1.3	±3.5	±4.8
238.0	53.14	±1.3	±3.5	±4.8
240.0	51.41	±1.3	±3.5	±4.8
242.0	49.73	±1.3	±3.5	±4.8
244.0	48.12	±1.3	±3.6	±4.9
246.0	46.58	±1.3	±3.6	±4.9
248.0	45.07	±1.3	±3.6	±4.9
250.0	43.65	±1.3	±3.6	±5.0
252.0	42.27	±1.3	±3.7	±5.0
254.0	40.95	±1.3	±3.7	±5.0
256.0	39.66	±1.3	±3.7	±5.0
258.0	38.42	±1.3	±3.7	±5.1
260.0	37.24	±1.3	±3.7	±5.1
262.0	36.09	±1.3	±3.8	±5.1
264.0	34.99	±1.4	±3.8	±5.1
266.0	33.93	±1.4	±3.8	±5.2
268.0	32.89	±1.4	±3.8	±5.2
270.0	31.91	±1.4	±3.8	±5.2
272.0	30.95	±1.4	±3.8	±5.2
274.0	30.02	±1.4	±3.9	±5.3
276.0	29.12	±1.4	±3.9	±5.3
278.0	28.26	±1.4	±3.9	±5.3
280.0	27.41	±1.4	±3.9	±5.4
282.0	26.61	±1.4	±4.0	±5.4
284.0	25.83	±1.4	±4.0	±5.4
286.0	25.08	±1.4	±4.0	±5.4
288.0	24.35	±1.4	±4.0	±5.5
290.0	23.66	±1.4	±4.0	±5.5
292.0	22.98	±1.5	±4.1	±5.5
294.0	22.32	±1.5	±4.1	±5.5
296.0	21.69	±1.5	±4.1	±5.6
298.0	21.07	±1.5	±4.1	±5.6
300.0	20.47	±1.5	±4.1	±5.6
305.0	19.09	±1.5	±4.2	±5.7
310.0	17.81	±1.5	±4.3	±5.8
315.0	16.61	±1.5	±4.3	±5.9
320.0	15.51	±1.6	±4.4	±5.9
325.0	14.47	±1.6	±4.4	±6.0
330.0	13.53	±1.6	±4.5	±6.1
335.0	12.63	±1.6	±4.5	±6.2
340.0	11.80	±1.6	±4.6	±6.2
345.0	11.00	±1.7	±4.6	±6.3
350.0	10.26	±1.7	±4.6	±6.3
360.0	9.127	±1.7	±4.9	±6.6
370.0	8.106	±1.8	±5.0	±6.8
380.0	7.225	±1.8	±5.1	±6.9
390.0	6.457	±1.8	±5.2	±7.0
400.0	5.783	±1.8	±5.1	±6.9

Table B.35: WH production cross section and its scale and PDF uncertainties for various Higgs-boson masses at the LHC with CM energy $\sqrt{s} = 8$ TeV.

M_{H} [GeV]	σ_{WH} [fb]	Scale [%]	PDF [%]	Total [%]
80.00	2808	±1.1	±2.2	±3.3
81.00	2711	±1.1	±2.2	±3.3
82.00	2619	±1.0	±2.2	±3.3
83.00	2528	±1.0	±2.2	±3.2
84.00	2442	±1.0	±2.2	±3.2
85.00	2359	±1.0	±2.1	±3.2
86.00	2279	±1.0	±2.2	±3.2
87.00	2203	±1.0	±2.2	±3.2
88.00	2129	±1.0	±2.2	±3.2
89.00	2058	±1.0	±2.2	±3.2
90.00	1990	±1.0	±2.2	±3.2
91.00	1929	±1.0	±2.2	±3.2
92.00	1866	±1.0	±2.2	±3.2
93.00	1806	±1.0	±2.2	±3.2
94.00	1749	±1.0	±2.2	±3.2
95.00	1695	±1.0	±2.2	±3.2
96.00	1641	±1.0	±2.2	±3.2
97.00	1589	±1.0	±2.3	±3.3
98.00	1540	±1.0	±2.3	±3.3
99.00	1495	±1.0	±2.3	±3.3
100.0	1447	±1.0	±2.3	±3.3
101.0	1403	±1.0	±2.3	±3.3
102.0	1360	±1.0	±2.3	±3.3
103.0	1319	±1.0	±2.3	±3.3
104.0	1280	±1.0	±2.3	±3.3
105.0	1242	±1.0	±2.3	±3.3
106.0	1204	±1.0	±2.3	±3.3
107.0	1169	±1.0	±2.3	±3.4
108.0	1135	±1.0	±2.3	±3.4
109.0	1103	±1.0	±2.4	±3.4
110.0	1071	±1.0	±2.4	±3.4
110.5	1056	±1.0	±2.3	±3.4
111.0	1040	±1.0	±2.3	±3.3
111.5	1026	±1.0	±2.3	±3.3
112.0	1010	±1.0	±2.3	±3.3
112.5	995.9	±1.0	±2.3	±3.3
113.0	981.3	±1.0	±2.3	±3.3
113.5	967.6	±1.0	±2.3	±3.3
114.0	953.5	±1.0	±2.3	±3.3
114.5	939.5	±1.0	±2.3	±3.2
115.0	926.6	±1.0	±2.3	±3.2
115.5	913.5	±1.0	±2.3	±3.2
116.0	900.2	±1.0	±2.3	±3.2
116.5	888.0	±1.0	±2.3	±3.2
117.0	875.8	±1.0	±2.3	±3.3
117.5	864.2	±1.0	±2.3	±3.3
118.0	851.5	±1.0	±2.3	±3.3

Table B.36: WH production cross section and its scale and PDF uncertainties for various Higgs-boson masses at the LHC with CM energy $\sqrt{s} = 8$ TeV.

M_H [GeV]	σ_{WH} [fb]	Scale [%]	PDF [%]	Total [%]
118.5	840.3	±1.0	±2.4	±3.3
119.0	828.4	±1.0	±2.4	±3.3
119.5	817.0	±1.0	±2.4	±3.4
120.0	805.2	±1.0	±2.5	±3.4
120.1	803.4	±1.0	±2.4	±3.4
120.2	800.9	±1.0	±2.4	±3.4
120.3	799.2	±1.0	±2.4	±3.3
120.4	796.7	±1.0	±2.4	±3.3
120.5	794.6	±0.9	±2.3	±3.3
120.6	792.8	±1.0	±2.3	±3.3
120.7	790.2	±1.0	±2.3	±3.3
120.8	788.1	±1.0	±2.3	±3.3
120.9	786.3	±1.0	±2.3	±3.3
121.0	784.4	±1.0	±2.3	±3.3
121.1	782.5	±1.0	±2.3	±3.3
121.2	780.2	±1.0	±2.3	±3.3
121.3	778.2	±1.0	±2.3	±3.3
121.4	775.8	±1.0	±2.4	±3.3
121.5	773.7	±1.0	±2.4	±3.3
121.6	771.3	±1.0	±2.4	±3.3
121.7	769.7	±1.0	±2.3	±3.3
121.8	767.5	±1.0	±2.3	±3.3
121.9	765.3	±1.0	±2.3	±3.3
122.0	763.1	±1.0	±2.3	±3.3
122.1	761.2	±1.0	±2.3	±3.3
122.2	758.9	±1.0	±2.3	±3.3
122.3	757.3	±1.0	±2.4	±3.3
122.4	755.5	±1.0	±2.4	±3.4
122.5	753.3	±1.0	±2.4	±3.4
122.6	751.0	±1.0	±2.4	±3.4
122.7	749.3	±1.0	±2.4	±3.4
122.8	747.5	±1.0	±2.4	±3.4
122.9	745.3	±1.0	±2.4	±3.4
123.0	743.4	±1.0	±2.4	±3.3
123.1	741.4	±1.0	±2.4	±3.3
123.2	739.3	±1.0	±2.4	±3.4
123.3	737.4	±1.0	±2.4	±3.4
123.4	735.2	±1.0	±2.4	±3.4
123.5	733.4	±1.0	±2.4	±3.4
123.6	731.7	±1.0	±2.4	±3.3
123.7	729.4	±1.0	±2.3	±3.3
123.8	727.7	±1.0	±2.3	±3.3
123.9	725.9	±1.0	±2.3	±3.3
124.0	723.9	±0.9	±2.3	±3.2
124.1	721.8	±0.9	±2.3	±3.2
124.2	720.1	±1.0	±2.3	±3.2
124.3	718.1	±1.0	±2.3	±3.3

Table B.37: WH production cross section and its scale and PDF uncertainties for various Higgs-boson masses at the LHC with CM energy $\sqrt{s} = 8$ TeV.

M_H [GeV]	σ_{WH} [fb]	Scale [%]	PDF [%]	Total [%]
124.4	715.9	±1.0	±2.3	±3.3
124.5	714.3	±1.0	±2.3	±3.3
124.6	712.5	±1.0	±2.3	±3.3
124.7	710.5	±1.0	±2.3	±3.3
124.8	708.6	±1.0	±2.3	±3.3
124.9	706.5	±1.0	±2.3	±3.3
125.0	704.6	±1.0	±2.3	±3.4
125.1	702.7	±1.0	±2.3	±3.4
125.2	700.5	±1.0	±2.4	±3.4
125.3	698.8	±1.0	±2.4	±3.4
125.4	697.0	±1.0	±2.4	±3.4
125.5	695.1	±1.0	±2.4	±3.4
125.6	693.1	±1.0	±2.4	±3.4
125.7	691.3	±1.0	±2.3	±3.3
125.8	689.5	±1.0	±2.3	±3.3
125.9	687.8	±1.0	±2.3	±3.3
126.0	686.0	±1.0	±2.3	±3.3
126.1	683.8	±1.0	±2.3	±3.3
126.2	681.8	±1.0	±2.3	±3.3
126.3	680.2	±1.0	±2.3	±3.3
126.4	678.4	±1.0	±2.3	±3.4
126.5	676.7	±1.0	±2.3	±3.4
126.6	674.7	±1.0	±2.3	±3.4
126.7	673.1	±1.0	±2.3	±3.4
126.8	671.1	±1.0	±2.3	±3.4
126.9	669.3	±1.0	±2.3	±3.4
127.0	667.6	±1.0	±2.3	±3.4
127.1	665.8	±1.0	±2.3	±3.3
127.2	664.0	±1.0	±2.3	±3.3
127.3	662.3	±1.0	±2.4	±3.3
127.4	660.5	±1.0	±2.4	±3.3
127.5	658.8	±1.0	±2.4	±3.3
127.6	657.2	±1.0	±2.4	±3.3
127.7	655.3	±1.0	±2.4	±3.3
127.8	653.5	±1.0	±2.4	±3.3
127.9	651.8	±1.0	±2.4	±3.3
128.0	650.1	±1.0	±2.4	±3.3
128.1	648.5	±1.0	±2.4	±3.3
128.2	647.0	±1.0	±2.4	±3.4
128.3	644.8	±1.0	±2.4	±3.4
128.4	643.0	±1.0	±2.4	±3.4
128.5	641.5	±1.0	±2.4	±3.4
128.6	639.8	±1.0	±2.4	±3.4
128.7	638.0	±1.0	±2.4	±3.4
128.8	636.4	±1.0	±2.3	±3.3
128.9	634.4	±1.0	±2.3	±3.3
129.0	632.9	±1.0	±2.3	±3.3

Table B.38: WH production cross section and its scale and PDF uncertainties for various Higgs-boson masses at the LHC with CM energy $\sqrt{s} = 8$ TeV.

M_H [GeV]	σ_{WH} [fb]	Scale [%]	PDF [%]	Total [%]
129.1	631.0	±1.0	±2.3	±3.3
129.2	629.4	±1.0	±2.3	±3.3
129.3	627.8	±1.0	±2.4	±3.3
129.4	626.4	±1.0	±2.4	±3.4
129.5	624.7	±1.0	±2.4	±3.4
129.6	623.3	±1.0	±2.4	±3.4
129.7	621.6	±0.9	±2.4	±3.4
129.8	620.1	±0.9	±2.4	±3.4
129.9	618.5	±0.9	±2.4	±3.3
130.0	616.9	±0.9	±2.4	±3.3
130.5	608.5	±0.9	±2.4	±3.4
131.0	600.5	±1.0	±2.4	±3.4
131.5	592.9	±1.0	±2.4	±3.4
132.0	585.6	±1.0	±2.4	±3.4
132.5	577.8	±1.0	±2.5	±3.5
133.0	570.3	±1.0	±2.5	±3.5
133.5	563.2	±1.0	±2.5	±3.5
134.0	555.6	±1.0	±2.5	±3.5
134.5	548.7	±1.0	±2.5	±3.5
135.0	541.6	±1.0	±2.5	±3.4
135.5	534.7	±1.0	±2.5	±3.4
136.0	527.7	±1.0	±2.5	±3.4
136.5	521.0	±1.0	±2.5	±3.4
137.0	514.5	±1.0	±2.4	±3.4
137.5	508.0	±1.0	±2.4	±3.4
138.0	501.8	±1.0	±2.4	±3.4
138.5	495.5	±1.0	±2.4	±3.4
139.0	489.0	±1.0	±2.4	±3.4
139.5	482.9	±1.0	±2.4	±3.4
140.0	476.8	±1.0	±2.4	±3.3
140.5	470.9	±1.0	±2.4	±3.4
141.0	465.1	±1.0	±2.4	±3.4
141.5	459.6	±1.0	±2.4	±3.4
142.0	454.0	±1.0	±2.5	±3.4
142.5	448.4	±1.0	±2.5	±3.5
143.0	442.6	±1.0	±2.5	±3.5
143.5	437.6	±1.0	±2.5	±3.4
144.0	432.0	±1.0	±2.5	±3.4
144.5	426.6	±1.0	±2.5	±3.4
145.0	421.6	±1.0	±2.4	±3.4
145.5	416.4	±1.0	±2.5	±3.4
146.0	411.2	±1.0	±2.5	±3.5
146.5	406.1	±1.0	±2.5	±3.5
147.0	401.4	±1.0	±2.5	±3.5
147.5	396.2	±1.0	±2.6	±3.5
148.0	391.3	±1.0	±2.6	±3.5
148.5	386.8	±1.0	±2.6	±3.5

Table B.39: WH production cross section and its scale and PDF uncertainties for various Higgs-boson masses at the LHC with CM energy $\sqrt{s} = 8$ TeV.

M_H [GeV]	σ_{WH} [fb]	Scale [%]	PDF [%]	Total [%]
149.0	382.1	±1.0	±2.6	±3.5
149.5	377.4	±1.0	±2.6	±3.5
150.0	372.8	±1.0	±2.6	±3.5
152.0	354.6	±1.0	±2.6	±3.6
154.0	337.6	±1.0	±2.6	±3.6
156.0	320.2	±1.0	±2.6	±3.6
158.0	302.4	±1.0	±2.5	±3.5
160.0	285.5	±1.0	±2.5	±3.5
162.0	276.3	±1.0	±2.6	±3.6
164.0	267.5	±1.0	±2.6	±3.6
165.0	263.0	±1.0	±2.6	±3.6
166.0	257.5	±1.0	±2.6	±3.6
168.0	246.6	±1.0	±2.7	±3.7
170.0	236.2	±1.0	±2.7	±3.7
172.0	226.1	±1.0	±2.7	±3.7
174.0	216.5	±1.0	±2.7	±3.7
175.0	211.8	±1.0	±2.7	±3.7
176.0	207.6	±1.0	±2.7	±3.7
178.0	199.1	±1.0	±2.7	±3.7
180.0	191.1	±1.0	±2.7	±3.7
182.0	184.1	±1.0	±2.7	±3.8
184.0	177.4	±1.0	±2.8	±3.8
185.0	174.1	±1.0	±2.8	±3.9
186.0	170.7	±1.0	±2.8	±3.9
188.0	164.2	±1.1	±2.8	±3.9
190.0	157.9	±1.1	±2.9	±3.9
192.0	152.0	±1.1	±2.9	±3.9
194.0	146.4	±1.1	±2.9	±3.9
195.0	143.6	±1.1	±2.9	±3.9
196.0	140.9	±1.1	±2.9	±4.0
198.0	135.6	±1.1	±2.9	±4.0
200.0	130.5	±1.1	±2.9	±4.0
202.0	125.7	±1.1	±2.9	±4.0
204.0	121.1	±1.1	±2.9	±4.0
206.0	116.8	±1.1	±2.9	±4.0
208.0	112.7	±1.1	±2.9	±4.1
210.0	108.7	±1.1	±3.0	±4.1
212.0	104.8	±1.1	±3.0	±4.1
214.0	101.1	±1.1	±3.0	±4.1
216.0	97.61	±1.1	±3.0	±4.1
218.0	94.27	±1.1	±3.0	±4.2
220.0	90.98	±1.1	±3.0	±4.2
222.0	87.92	±1.1	±3.1	±4.2
224.0	84.96	±1.2	±3.1	±4.2
226.0	82.12	±1.2	±3.1	±4.3
228.0	79.40	±1.2	±3.1	±4.3
230.0	76.78	±1.2	±3.1	±4.3

Table B.40: WH production cross section and its scale and PDF uncertainties for various Higgs-boson masses at the LHC with CM energy $\sqrt{s} = 8$ TeV.

M_H [GeV]	σ_{WH} [fb]	Scale [%]	PDF [%]	Total [%]
232.0	74.24	±1.2	±3.1	±4.3
234.0	71.81	±1.2	±3.1	±4.3
236.0	69.44	±1.2	±3.1	±4.4
238.0	67.18	±1.2	±3.2	±4.4
240.0	65.01	±1.2	±3.1	±4.4
242.0	62.94	±1.2	±3.2	±4.4
244.0	60.94	±1.2	±3.2	±4.4
246.0	59.02	±1.2	±3.2	±4.4
248.0	57.19	±1.2	±3.2	±4.5
250.0	55.40	±1.2	±3.3	±4.5
252.0	53.67	±1.2	±3.3	±4.5
254.0	52.00	±1.2	±3.3	±4.6
256.0	50.40	±1.3	±3.3	±4.6
258.0	48.86	±1.3	±3.4	±4.6
260.0	47.38	±1.3	±3.4	±4.7
262.0	45.98	±1.3	±3.4	±4.7
264.0	44.61	±1.3	±3.4	±4.7
266.0	43.31	±1.3	±3.4	±4.7
268.0	42.05	±1.3	±3.4	±4.7
270.0	40.83	±1.3	±3.5	±4.8
272.0	39.64	±1.3	±3.5	±4.8
274.0	38.47	±1.3	±3.5	±4.8
276.0	37.33	±1.3	±3.5	±4.8
278.0	36.24	±1.3	±3.5	±4.9
280.0	35.19	±1.3	±3.5	±4.9
282.0	34.17	±1.3	±3.6	±4.9
284.0	33.20	±1.3	±3.6	±4.9
286.0	32.26	±1.3	±3.6	±4.9
288.0	31.34	±1.3	±3.6	±4.9
290.0	30.46	±1.3	±3.6	±4.9
292.0	29.60	±1.4	±3.6	±5.0
294.0	28.79	±1.4	±3.7	±5.0
296.0	27.99	±1.4	±3.7	±5.1
298.0	27.23	±1.4	±3.7	±5.1
300.0	26.49	±1.4	±3.7	±5.1
305.0	24.74	±1.4	±3.8	±5.2
310.0	23.13	±1.4	±3.8	±5.3
315.0	21.60	±1.5	±3.9	±5.3
320.0	20.19	±1.5	±3.9	±5.4
325.0	18.89	±1.5	±3.9	±5.4
330.0	17.69	±1.5	±4.0	±5.5
335.0	16.55	±1.5	±4.1	±5.6
340.0	15.50	±1.5	±4.1	±5.6
345.0	14.47	±1.6	±4.2	±5.7
350.0	13.52	±1.6	±4.2	±5.7
360.0	12.07	±1.6	±4.4	±6.0
370.0	10.76	±1.7	±4.5	±6.2
380.0	9.627	±1.7	±4.6	±6.3
390.0	8.629	±1.7	±4.6	±6.3
400.0	7.765	±1.7	±4.6	±6.2

Table B.41: ZH production cross section and its scale and PDF uncertainties for various Higgs-boson masses at the LHC with CM energy $\sqrt{s} = 7$ TeV. The gluon-fusion contribution is also given separately.

M_H [GeV]	σ_{ZH} [fb]	Scale [%]	PDF [%]	Total [%]	$\sigma_{gg \to ZH}$ [fb]
80.00	1244	±1.8	±2.3	±4.1	36.64
81.00	1203	±1.8	±2.3	±4.2	36.29
82.00	1163	±1.8	±2.4	±4.2	35.94
83.00	1125	±1.8	±2.4	±4.2	35.61
84.00	1087	±1.8	±2.4	±4.2	35.27
85.00	1052	±1.8	±2.4	±4.2	34.93
86.00	1019	±1.9	±2.4	±4.2	34.59
87.00	985.8	±1.9	±2.4	±4.3	34.26
88.00	954.8	±1.9	±2.4	±4.3	33.92
89.00	924.4	±2.0	±2.4	±4.4	33.59
90.00	895.9	±2.0	±2.4	±4.4	33.26
91.00	868.2	±2.0	±2.4	±4.5	32.92
92.00	841.7	±2.0	±2.4	±4.5	32.60
93.00	816.2	±2.1	±2.4	±4.5	32.27
94.00	791.7	±2.1	±2.4	±4.5	31.94
95.00	767.8	±2.1	±2.4	±4.5	31.62
96.00	744.7	±2.1	±2.4	±4.6	31.31
97.00	723.2	±2.1	±2.5	±4.6	30.99
98.00	701.1	±2.2	±2.5	±4.7	30.67
99.00	681.4	±2.2	±2.5	±4.7	30.34
100.0	661.6	±2.2	±2.5	±4.7	30.03
101.0	642.5	±2.2	±2.5	±4.8	29.72
102.0	624.0	±2.3	±2.5	±4.8	29.41
103.0	606.3	±2.3	±2.6	±4.9	29.09
104.0	589.5	±2.3	±2.6	±4.9	28.77
105.0	572.4	±2.3	±2.6	±4.9	28.47
106.0	556.4	±2.4	±2.6	±4.9	28.15
107.0	541.2	±2.4	±2.6	±5.0	27.86
108.0	526.1	±2.4	±2.6	±5.0	27.57
109.0	511.6	±2.4	±2.6	±5.0	27.31
110.0	497.8	±2.4	±2.6	±5.0	27.05
110.5	490.9	±2.5	±2.6	±5.1	26.90
111.0	484.5	±2.5	±2.6	±5.1	26.75
111.5	477.5	±2.6	±2.6	±5.2	26.63
112.0	471.0	±2.6	±2.7	±5.3	26.41
112.5	464.7	±2.7	±2.7	±5.3	26.26
113.0	458.6	±2.6	±2.7	±5.3	26.11
113.5	452.2	±2.6	±2.7	±5.3	25.95
114.0	446.0	±2.6	±2.7	±5.4	25.79
114.5	440.2	±2.6	±2.7	±5.4	25.69
115.0	434.5	±2.6	±2.7	±5.4	25.54
115.5	428.7	±2.6	±2.7	±5.4	25.39
116.0	423.2	±2.7	±2.7	±5.4	25.32
116.5	417.4	±2.7	±2.7	±5.4	25.17
117.0	411.9	±2.7	±2.7	±5.4	25.00
117.5	406.3	±2.7	±2.7	±5.4	24.85
118.0	401.3	±2.7	±2.7	±5.4	24.77

Table B.42: ZH production cross section and its scale and PDF uncertainties for various Higgs-boson masses at the LHC with CM energy $\sqrt{s} = 7$ TeV. The gluon-fusion contribution is also given separately.

M_H [GeV]	σ_{ZH} [fb]	Scale [%]	PDF [%]	Total [%]	$\sigma_{gg \to ZH}$ [fb]
118.5	396.0	± 2.7	± 2.7	± 5.5	24.62
119.0	390.9	± 2.7	± 2.8	± 5.5	24.48
119.5	385.8	± 2.8	± 2.8	± 5.5	24.34
120.0	380.8	± 2.8	± 2.8	± 5.6	24.19
120.1	379.8	± 2.8	± 2.8	± 5.6	24.17
120.2	378.9	± 2.8	± 2.8	± 5.5	24.14
120.3	377.9	± 2.8	± 2.7	± 5.5	24.11
120.4	376.9	± 2.8	± 2.7	± 5.5	24.08
120.5	375.9	± 2.8	± 2.7	± 5.5	24.05
120.6	374.9	± 2.8	± 2.7	± 5.5	24.03
120.7	373.9	± 2.8	± 2.7	± 5.5	24.00
120.8	373.0	± 2.8	± 2.7	± 5.5	23.97
120.9	372.0	± 2.8	± 2.7	± 5.5	23.94
121.0	371.1	± 2.8	± 2.7	± 5.5	23.91
121.1	370.2	± 2.8	± 2.7	± 5.6	23.89
121.2	369.2	± 2.8	± 2.7	± 5.6	23.86
121.3	368.2	± 2.8	± 2.7	± 5.6	23.83
121.4	367.3	± 2.8	± 2.8	± 5.6	23.80
121.5	366.4	± 2.8	± 2.8	± 5.6	23.77
121.6	365.5	± 2.8	± 2.8	± 5.6	23.75
121.7	364.5	± 2.8	± 2.8	± 5.6	23.72
121.8	363.6	± 2.8	± 2.8	± 5.6	23.68
121.9	362.6	± 2.8	± 2.8	± 5.6	23.66
122.0	361.8	± 2.8	± 2.8	± 5.6	23.63
122.1	360.9	± 2.8	± 2.8	± 5.6	23.60
122.2	359.9	± 2.8	± 2.7	± 5.6	23.57
122.3	359.0	± 2.9	± 2.7	± 5.6	23.54
122.4	358.0	± 2.9	± 2.7	± 5.6	23.52
122.5	357.1	± 2.9	± 2.7	± 5.6	23.49
122.6	356.2	± 2.9	± 2.7	± 5.6	23.45
122.7	355.2	± 2.9	± 2.7	± 5.6	23.43
122.8	354.2	± 2.9	± 2.7	± 5.6	23.40
122.9	353.5	± 2.9	± 2.7	± 5.6	23.37
123.0	352.5	± 2.9	± 2.7	± 5.6	23.34
123.1	351.6	± 2.9	± 2.7	± 5.6	23.31
123.2	350.8	± 2.9	± 2.7	± 5.6	23.28
123.3	349.8	± 2.9	± 2.7	± 5.6	23.25
123.4	349.0	± 2.9	± 2.7	± 5.6	23.22
123.5	348.0	± 2.9	± 2.7	± 5.6	23.19
123.6	347.1	± 2.9	± 2.7	± 5.6	23.16
123.7	346.2	± 2.9	± 2.8	± 5.7	23.12
123.8	345.4	± 2.9	± 2.8	± 5.7	23.10
123.9	344.5	± 2.9	± 2.8	± 5.7	23.07
124.0	343.6	± 2.9	± 2.8	± 5.7	23.05
124.1	342.7	± 2.9	± 2.8	± 5.7	23.01
124.2	341.9	± 2.9	± 2.8	± 5.7	22.99
124.3	341.1	± 2.9	± 2.8	± 5.7	22.96

Table B.43: ZH production cross section and its scale and PDF uncertainties for various Higgs-boson masses at the LHC with CM energy $\sqrt{s} = 7$ TeV. The gluon-fusion contribution is also given separately.

M_H [GeV]	σ_{ZH} [fb]	Scale [%]	PDF [%]	Total [%]	$\sigma_{gg \to ZH}$ [fb]
124.4	340.2	±2.9	±2.8	±5.7	22.93
124.5	339.3	±2.9	±2.8	±5.7	22.90
124.6	338.4	±2.9	±2.8	±5.7	22.88
124.7	337.6	±2.9	±2.8	±5.7	22.85
124.8	336.8	±2.9	±2.7	±5.7	22.82
124.9	335.9	±2.9	±2.7	±5.6	22.80
125.0	335.1	±2.9	±2.7	±5.6	22.78
125.1	334.1	±2.9	±2.7	±5.6	22.75
125.2	333.3	±2.9	±2.7	±5.6	22.72
125.3	332.5	±2.9	±2.7	±5.6	22.70
125.4	331.7	±2.9	±2.6	±5.6	22.68
125.5	330.9	±2.9	±2.6	±5.6	22.65
125.6	329.9	±3.0	±2.7	±5.6	22.63
125.7	329.1	±3.0	±2.7	±5.6	22.60
125.8	328.3	±3.0	±2.7	±5.6	22.58
125.9	327.5	±3.0	±2.7	±5.7	22.56
126.0	326.7	±3.0	±2.7	±5.7	22.53
126.1	325.8	±2.9	±2.7	±5.7	22.50
126.2	325.0	±2.9	±2.7	±5.6	22.47
126.3	324.3	±2.9	±2.7	±5.6	22.45
126.4	323.5	±2.9	±2.6	±5.6	22.42
126.5	322.7	±2.9	±2.6	±5.6	22.39
126.6	321.9	±2.9	±2.7	±5.6	22.36
126.7	321.0	±2.9	±2.7	±5.6	22.34
126.8	320.1	±2.9	±2.7	±5.7	22.31
126.9	319.2	±2.9	±2.7	±5.7	22.28
127.0	318.4	±2.9	±2.8	±5.7	22.26
127.1	317.5	±3.0	±2.8	±5.7	22.23
127.2	316.9	±3.0	±2.8	±5.7	22.21
127.3	316.1	±3.0	±2.8	±5.7	22.17
127.4	315.3	±3.0	±2.7	±5.7	22.15
127.5	314.5	±3.0	±2.7	±5.7	22.12
127.6	313.7	±3.0	±2.7	±5.7	22.10
127.7	312.9	±3.0	±2.7	±5.7	22.07
127.8	312.2	±2.9	±2.8	±5.7	22.04
127.9	311.4	±2.9	±2.8	±5.7	22.02
128.0	310.6	±2.9	±2.8	±5.7	21.99
128.1	309.9	±3.0	±2.8	±5.7	21.97
128.2	309.0	±3.0	±2.8	±5.7	21.94
128.3	308.3	±3.0	±2.8	±5.7	21.91
128.4	307.5	±3.0	±2.8	±5.8	21.89
128.5	306.8	±3.0	±2.8	±5.8	21.86
128.6	306.0	±3.0	±2.8	±5.8	21.84
128.7	305.4	±3.0	±2.8	±5.8	21.81
128.8	304.6	±3.0	±2.8	±5.8	21.79
128.9	303.9	±3.0	±2.8	±5.8	21.76
129.0	303.1	±3.0	±2.8	±5.8	21.73

Table B.44: ZH production cross section and its scale and PDF uncertainties for various Higgs-boson masses at the LHC with CM energy $\sqrt{s} = 7$ TeV. The gluon-fusion contribution is also given separately.

M_H [GeV]	σ_ZH [fb]	Scale [%]	PDF [%]	Total [%]	$\sigma_{\mathrm{gg}\to\mathrm{ZH}}$ [fb]
129.1	302.3	±3.0	±2.8	±5.8	21.71
129.2	301.7	±3.0	±2.8	±5.8	21.68
129.3	301.0	±3.0	±2.8	±5.8	21.65
129.4	300.2	±3.0	±2.8	±5.8	21.63
129.5	299.4	±3.0	±2.7	±5.8	21.60
129.6	298.6	±3.0	±2.8	±5.8	21.58
129.7	297.9	±3.0	±2.8	±5.8	21.55
129.8	297.2	±3.0	±2.8	±5.8	21.52
129.9	296.5	±3.0	±2.8	±5.8	21.50
130.0	295.7	±3.0	±2.8	±5.8	21.47
130.5	292.0	±3.0	±2.8	±5.8	21.33
131.0	288.3	±3.1	±2.8	±5.8	21.20
131.5	284.8	±3.1	±2.8	±5.8	21.07
132.0	281.3	±3.1	±2.8	±5.8	20.93
132.5	278.0	±3.1	±2.8	±5.9	20.81
133.0	274.6	±3.1	±2.8	±5.9	20.68
133.5	271.2	±3.1	±2.8	±5.9	20.50
134.0	268.0	±3.1	±2.8	±5.9	20.39
134.5	264.7	±3.2	±2.8	±6.0	20.26
135.0	261.6	±3.2	±2.8	±6.0	20.11
135.5	258.5	±3.2	±2.8	±6.0	19.98
136.0	255.5	±3.2	±2.8	±6.1	19.92
136.5	252.5	±3.2	±2.9	±6.1	19.80
137.0	249.5	±3.3	±2.9	±6.1	19.67
137.5	246.4	±3.3	±2.9	±6.2	19.54
138.0	243.6	±3.3	±2.9	±6.2	19.42
138.5	240.6	±3.3	±2.9	±6.2	19.21
139.0	237.7	±3.3	±2.9	±6.2	19.09
139.5	235.0	±3.3	±2.9	±6.2	18.98
140.0	232.2	±3.3	±2.9	±6.2	18.86
140.5	229.4	±3.3	±2.9	±6.2	18.75
141.0	226.9	±3.3	±2.9	±6.2	18.64
141.5	224.3	±3.3	±2.9	±6.2	18.55
142.0	221.6	±3.4	±2.9	±6.2	18.43
142.5	219.0	±3.4	±2.9	±6.3	18.32
143.0	216.5	±3.4	±2.9	±6.3	18.22
143.5	214.2	±3.4	±2.9	±6.3	18.11
144.0	211.7	±3.4	±2.9	±6.3	18.02
144.5	209.1	±3.4	±2.9	±6.3	17.80
145.0	206.8	±3.4	±2.9	±6.3	17.68
145.5	204.2	±3.5	±2.9	±6.4	17.57
146.0	201.9	±3.5	±2.9	±6.4	17.46
146.5	199.6	±3.5	±2.9	±6.4	17.35
147.0	197.3	±3.5	±3.0	±6.4	17.24
147.5	195.1	±3.5	±3.0	±6.5	17.13
148.0	192.8	±3.5	±3.0	±6.5	17.01
148.5	190.6	±3.5	±3.0	±6.5	16.90

Table B.45: ZH production cross section and its scale and PDF uncertainties for various Higgs-boson masses at the LHC with CM energy $\sqrt{s} = 7$ TeV. The gluon-fusion contribution is also given separately.

M_H [GeV]	σ_ZH [fb]	Scale [%]	PDF [%]	Total [%]	$\sigma_{\mathrm{gg}\to\mathrm{ZH}}$ [fb]
149.0	188.4	±3.5	±3.0	±6.5	16.79
149.5	186.2	±3.6	±3.0	±6.6	16.68
150.0	184.2	±3.6	±3.0	±6.6	16.57
152.0	175.8	±3.6	±3.0	±6.7	16.11
154.0	168.0	±3.7	±3.1	±6.8	15.66
156.0	159.9	±3.8	±3.1	±6.9	15.22
158.0	151.8	±3.9	±3.1	±7.0	14.79
160.0	144.2	±3.9	±3.1	±7.1	14.38
162.0	139.7	±3.9	±3.1	±7.1	13.97
164.0	135.4	±3.9	±3.1	±7.1	13.56
165.0	133.4	±3.9	±3.1	±7.0	13.36
166.0	130.5	±3.9	±3.1	±7.1	13.15
168.0	125.2	±4.0	±3.2	±7.2	12.75
170.0	120.0	±4.1	±3.2	±7.3	12.37
172.0	115.1	±4.1	±3.2	±7.3	11.99
174.0	110.3	±4.2	±3.2	±7.3	11.60
175.0	108.0	±4.2	±3.2	±7.4	11.41
176.0	105.6	±4.2	±3.2	±7.4	11.23
178.0	101.2	±4.2	±3.2	±7.4	10.86
180.0	96.86	±4.2	±3.3	±7.5	10.50
182.0	93.36	±4.2	±3.3	±7.5	10.15
184.0	90.00	±4.3	±3.3	±7.5	9.816
185.0	88.36	±4.3	±3.3	±7.6	9.651
186.0	86.65	±4.3	±3.3	±7.6	9.486
188.0	83.41	±4.3	±3.4	±7.7	9.163
190.0	80.26	±4.3	±3.4	±7.7	8.846
192.0	77.27	±4.3	±3.4	±7.7	8.539
194.0	74.43	±4.4	±3.4	±7.8	8.300
195.0	73.05	±4.4	±3.4	±7.8	8.158
196.0	71.69	±4.4	±3.4	±7.8	8.013
198.0	69.06	±4.4	±3.4	±7.8	7.737
200.0	66.51	±4.4	±3.5	±7.9	7.436
202.0	64.11	±4.4	±3.5	±7.9	7.193
204.0	61.78	±4.4	±3.5	±7.9	6.921
206.0	59.50	±4.4	±3.5	±7.9	6.624
208.0	57.33	±4.4	±3.5	±7.9	6.361
210.0	55.27	±4.4	±3.5	±7.9	6.108
212.0	53.27	±4.4	±3.5	±8.0	5.859
214.0	51.40	±4.4	±3.6	±8.0	5.614
216.0	49.57	±4.4	±3.6	±8.0	5.380
218.0	47.82	±4.4	±3.6	±8.0	5.152
220.0	46.12	±4.3	±3.6	±8.0	4.930
222.0	44.50	±4.3	±3.7	±8.0	4.713
224.0	42.94	±4.3	±3.7	±8.0	4.504
226.0	41.44	±4.3	±3.7	±8.0	4.300
228.0	40.01	±4.3	±3.7	±8.0	4.105
230.0	38.60	±4.3	±3.8	±8.0	3.917

Table B.46: ZH production cross section and its scale and PDF uncertainties for various Higgs-boson masses at the LHC with CM energy $\sqrt{s} = 7$ TeV. The gluon-fusion contribution is also given separately.

M_H [GeV]	σ_{ZH} [fb]	Scale [%]	PDF [%]	Total [%]	$\sigma_{gg \to ZH}$ [fb]
232.0	37.28	±4.2	±3.8	±8.0	3.738
234.0	36.00	±4.2	±3.8	±8.0	3.566
236.0	34.78	±4.2	±3.8	±8.0	3.397
238.0	33.59	±4.1	±3.9	±8.0	3.232
240.0	32.45	±4.1	±3.9	±7.9	3.073
242.0	31.35	±4.0	±3.9	±7.9	2.921
244.0	30.30	±4.0	±3.9	±7.9	2.780
246.0	29.29	±4.0	±3.9	±7.9	2.641
248.0	28.31	±3.9	±4.0	±7.9	2.512
250.0	27.38	±3.9	±4.0	±7.8	2.382
252.0	26.47	±3.8	±4.0	±7.8	2.261
254.0	25.60	±3.8	±4.0	±7.8	2.148
256.0	24.76	±3.8	±4.0	±7.8	2.038
258.0	23.96	±3.7	±4.1	±7.8	1.933
260.0	23.18	±3.7	±4.1	±7.8	1.834
262.0	22.43	±3.7	±4.1	±7.8	1.743
264.0	21.71	±3.6	±4.1	±7.8	1.655
266.0	21.01	±3.6	±4.2	±7.8	1.568
268.0	20.34	±3.6	±4.2	±7.7	1.485
270.0	19.69	±3.5	±4.2	±7.7	1.408
272.0	19.07	±3.5	±4.2	±7.7	1.334
274.0	18.48	±3.5	±4.3	±7.7	1.265
276.0	17.90	±3.4	±4.3	±7.7	1.199
278.0	17.34	±3.4	±4.3	±7.7	1.136
280.0	16.81	±3.4	±4.3	±7.7	1.076
282.0	16.30	±3.3	±4.3	±7.7	1.019
284.0	15.79	±3.3	±4.4	±7.7	0.9655
286.0	15.32	±3.3	±4.4	±7.6	0.9147
288.0	14.85	±3.2	±4.4	±7.6	0.8678
290.0	14.41	±3.2	±4.4	±7.6	0.8205
292.0	13.98	±3.2	±4.4	±7.6	0.7770
294.0	13.56	±3.1	±4.5	±7.6	0.7354
296.0	13.15	±3.1	±4.5	±7.6	0.6962
298.0	12.76	±3.1	±4.5	±7.6	0.6590
300.0	12.39	±3.0	±4.5	±7.5	0.6237
305.0	11.50	±3.0	±4.6	±7.6	0.5427
310.0	10.68	±2.9	±4.7	±7.6	0.4721
315.0	9.930	±2.9	±4.7	±7.6	0.4117
320.0	9.241	±2.8	±4.8	±7.6	0.3588
325.0	8.604	±2.7	±4.8	±7.5	0.3137
330.0	8.017	±2.7	±4.9	±7.6	0.2747
335.0	7.463	±2.7	±5.0	±7.6	0.2408
340.0	6.955	±2.7	±5.0	±7.7	0.2123
345.0	6.473	±2.6	±5.0	±7.7	0.1892
350.0	6.035	±2.6	±5.0	±7.7	0.1721
360.0	5.338	±2.7	±5.3	±7.9	0.1466
370.0	4.734	±2.7	±5.4	±8.2	0.1284
380.0	4.212	±2.8	±5.5	±8.3	0.1149
390.0	3.757	±2.8	±5.6	±8.4	0.1048
400.0	3.357	±2.8	±5.5	±8.3	0.09677

Table B.47: ZH production cross section and its scale and PDF uncertainties for various Higgs-boson masses at the LHC with CM energy $\sqrt{s} = 8$ TeV. The gluon-fusion contribution is also given separately.

M_H [GeV]	σ_{ZH} [fb]	Scale [%]	PDF [%]	Total [%]	$\sigma_{gg \to ZH}$ [fb]
80.00	1508	±1.9	±2.1	±4.1	51.69
81.00	1459	±1.9	±2.1	±4.1	51.20
82.00	1411	±2.0	±2.1	±4.1	50.71
83.00	1366	±2.0	±2.1	±4.1	50.22
84.00	1321	±2.0	±2.1	±4.1	49.74
85.00	1281	±2.0	±2.1	±4.1	49.28
86.00	1238	±2.1	±2.1	±4.2	48.65
87.00	1200	±2.1	±2.1	±4.2	48.20
88.00	1163	±2.1	±2.2	±4.3	47.75
89.00	1126	±2.1	±2.2	±4.3	47.28
90.00	1092	±2.1	±2.2	±4.4	46.85
91.00	1059	±2.2	±2.2	±4.4	46.41
92.00	1028	±2.2	±2.2	±4.4	45.99
93.00	996.5	±2.2	±2.2	±4.5	45.72
94.00	967.0	±2.2	±2.3	±4.5	45.11
95.00	938.3	±2.3	±2.3	±4.5	44.67
96.00	910.9	±2.3	±2.3	±4.6	44.22
97.00	884.0	±2.3	±2.3	±4.6	43.79
98.00	859.2	±2.3	±2.3	±4.6	43.36
99.00	834.0	±2.4	±2.3	±4.7	42.94
100.0	810.2	±2.4	±2.3	±4.7	42.51
101.0	787.6	±2.4	±2.3	±4.8	42.09
102.0	765.0	±2.4	±2.3	±4.8	41.66
103.0	743.6	±2.5	±2.3	±4.8	41.23
104.0	722.6	±2.5	±2.3	±4.8	40.81
105.0	702.2	±2.5	±2.3	±4.9	40.39
106.0	683.3	±2.6	±2.4	±4.9	39.97
107.0	664.6	±2.6	±2.4	±5.0	39.58
108.0	646.9	±2.6	±2.4	±5.0	39.20
109.0	629.6	±2.7	±2.4	±5.1	38.81
110.0	612.5	±2.7	±2.4	±5.1	38.40
110.5	604.0	±2.7	±2.4	±5.1	38.20
111.0	596.0	±2.7	±2.4	±5.1	37.99
111.5	588.0	±2.8	±2.4	±5.1	37.79
112.0	580.3	±2.8	±2.4	±5.2	37.58
112.5	572.5	±2.8	±2.4	±5.2	37.38
113.0	564.6	±2.8	±2.4	±5.2	37.18
113.5	557.3	±2.8	±2.4	±5.2	36.98
114.0	550.1	±2.8	±2.4	±5.2	36.76
114.5	542.7	±2.8	±2.4	±5.2	36.55
115.0	535.8	±2.8	±2.5	±5.3	36.34
115.5	528.6	±2.8	±2.5	±5.3	36.11
116.0	521.8	±2.9	±2.5	±5.3	35.84
116.5	515.2	±2.9	±2.5	±5.4	35.75
117.0	508.3	±2.9	±2.5	±5.4	35.56
117.5	502.0	±3.0	±2.5	±5.4	35.37
118.0	495.6	±3.0	±2.5	±5.4	35.17

Table B.48: ZH production cross section and its scale and PDF uncertainties for various Higgs-boson masses at the LHC with CM energy $\sqrt{s} = 8$ TeV. The gluon-fusion contribution is also given separately.

M_H [GeV]	σ_{ZH} [fb]	Scale [%]	PDF [%]	Total [%]	$\sigma_{gg \to ZH}$ [fb]
118.5	489.3	±3.0	±2.5	±5.4	34.97
119.0	482.9	±3.0	±2.5	±5.4	34.77
119.5	477.2	±3.0	±2.5	±5.4	34.58
120.0	471.0	±3.0	±2.5	±5.5	34.39
120.1	469.8	±3.0	±2.5	±5.5	34.34
120.2	468.5	±3.0	±2.5	±5.5	34.30
120.3	467.5	±3.0	±2.5	±5.5	34.27
120.4	466.1	±3.0	±2.5	±5.5	34.23
120.5	464.8	±3.0	±2.5	±5.5	34.19
120.6	463.6	±3.0	±2.5	±5.5	34.15
120.7	462.5	±3.0	±2.5	±5.5	34.11
120.8	461.3	±3.0	±2.5	±5.5	34.07
120.9	460.1	±3.0	±2.5	±5.5	34.04
121.0	458.9	±3.0	±2.5	±5.4	34.00
121.1	458.0	±3.0	±2.5	±5.4	33.95
121.2	456.7	±3.0	±2.5	±5.4	33.92
121.3	455.6	±3.0	±2.5	±5.4	33.88
121.4	454.5	±3.0	±2.4	±5.4	33.84
121.5	453.5	±3.0	±2.4	±5.4	33.80
121.6	452.2	±3.0	±2.4	±5.4	33.76
121.7	450.9	±3.0	±2.4	±5.4	33.73
121.8	449.8	±3.0	±2.5	±5.5	33.69
121.9	448.8	±3.0	±2.5	±5.5	33.65
122.0	447.8	±3.0	±2.5	±5.5	33.61
122.1	446.8	±3.0	±2.5	±5.5	33.58
122.2	445.7	±3.0	±2.5	±5.5	33.53
122.3	444.4	±3.0	±2.5	±5.6	33.49
122.4	443.4	±3.0	±2.6	±5.6	33.45
122.5	442.1	±3.0	±2.6	±5.6	33.41
122.6	440.9	±3.0	±2.6	±5.6	33.37
122.7	439.6	±3.0	±2.6	±5.6	33.33
122.8	438.5	±3.1	±2.6	±5.6	33.30
122.9	437.6	±3.1	±2.5	±5.6	33.26
123.0	436.6	±3.1	±2.5	±5.6	33.22
123.1	435.6	±3.1	±2.6	±5.6	33.19
123.2	434.6	±3.1	±2.6	±5.6	33.15
123.3	433.5	±3.1	±2.6	±5.7	33.11
123.4	432.5	±3.1	±2.6	±5.7	33.07
123.5	431.1	±3.1	±2.6	±5.7	33.03
123.6	430.1	±3.1	±2.6	±5.7	32.99
123.7	429.2	±3.1	±2.6	±5.6	32.95
123.8	428.0	±3.1	±2.5	±5.6	32.92
123.9	427.1	±3.1	±2.5	±5.6	32.88
124.0	426.0	±3.1	±2.4	±5.5	32.84
124.1	424.9	±3.1	±2.4	±5.6	32.80
124.2	423.8	±3.1	±2.4	±5.6	32.77
124.3	422.8	±3.1	±2.4	±5.6	32.73

Table B.49: ZH production cross section and its scale and PDF uncertainties for various Higgs-boson masses at the LHC with CM energy $\sqrt{s} = 8$ TeV. The gluon-fusion contribution is also given separately.

M_H [GeV]	σ_{ZH} [fb]	Scale [%]	PDF [%]	Total [%]	$\sigma_{gg \to ZH}$ [fb]
124.4	421.7	±3.2	±2.5	±5.6	32.70
124.5	420.6	±3.2	±2.5	±5.6	32.66
124.6	419.4	±3.2	±2.5	±5.6	32.62
124.7	418.5	±3.1	±2.5	±5.6	32.58
124.8	417.4	±3.1	±2.5	±5.6	32.54
124.9	416.4	±3.1	±2.5	±5.6	32.50
125.0	415.3	±3.1	±2.5	±5.6	32.46
125.1	414.2	±3.1	±2.5	±5.6	32.43
125.2	413.3	±3.1	±2.5	±5.6	32.39
125.3	412.3	±3.1	±2.5	±5.6	32.35
125.4	411.2	±3.1	±2.5	±5.6	32.31
125.5	410.2	±3.1	±2.5	±5.6	32.27
125.6	409.1	±3.2	±2.5	±5.6	32.23
125.7	408.2	±3.2	±2.5	±5.6	32.20
125.8	407.0	±3.2	±2.5	±5.7	32.16
125.9	406.1	±3.2	±2.5	±5.7	32.12
126.0	405.0	±3.2	±2.5	±5.7	32.08
126.1	404.2	±3.2	±2.5	±5.7	32.05
126.2	403.0	±3.2	±2.5	±5.7	32.01
126.3	402.0	±3.2	±2.5	±5.7	31.97
126.4	401.0	±3.2	±2.5	±5.7	31.93
126.5	400.0	±3.2	±2.5	±5.7	31.90
126.6	399.0	±3.2	±2.5	±5.7	31.86
126.7	398.0	±3.2	±2.5	±5.8	31.82
126.8	397.0	±3.2	±2.5	±5.8	31.78
126.9	396.2	±3.2	±2.6	±5.8	31.75
127.0	395.3	±3.2	±2.6	±5.8	31.71
127.1	394.3	±3.2	±2.6	±5.8	31.67
127.2	393.2	±3.2	±2.5	±5.8	31.63
127.3	392.1	±3.2	±2.5	±5.7	31.59
127.4	391.2	±3.2	±2.5	±5.7	31.56
127.5	390.1	±3.2	±2.5	±5.7	31.52
127.6	389.2	±3.2	±2.5	±5.7	31.48
127.7	388.3	±3.2	±2.5	±5.7	31.44
127.8	387.4	±3.2	±2.4	±5.7	31.40
127.9	386.3	±3.2	±2.4	±5.7	31.37
128.0	385.6	±3.3	±2.4	±5.7	31.33
128.1	384.7	±3.3	±2.5	±5.7	31.29
128.2	383.8	±3.2	±2.5	±5.7	31.26
128.3	383.0	±3.2	±2.5	±5.8	31.22
128.4	381.9	±3.2	±2.6	±5.8	31.18
128.5	380.9	±3.2	±2.6	±5.8	31.14
128.6	379.9	±3.2	±2.6	±5.8	31.11
128.7	379.0	±3.3	±2.6	±5.8	31.07
128.8	378.0	±3.3	±2.6	±5.8	31.04
128.9	377.0	±3.3	±2.6	±5.8	31.00
129.0	376.2	±3.3	±2.6	±5.8	30.96

Table B.50: ZH production cross section and its scale and PDF uncertainties for various Higgs-boson masses at the LHC with CM energy $\sqrt{s} = 8$ TeV. The gluon-fusion contribution is also given separately.

$M_{\rm H}$ [GeV]	$\sigma_{\rm ZH}$ [fb]	Scale [%]	PDF [%]	Total [%]	$\sigma_{\rm gg \to ZH}$ [fb]
129.1	375.1	±3.3	±2.6	±5.8	30.92
129.2	374.1	±3.3	±2.6	±5.8	30.89
129.3	373.1	±3.3	±2.6	±5.9	30.85
129.4	372.3	±3.3	±2.6	±5.9	30.81
129.5	371.4	±3.3	±2.6	±5.9	30.78
129.6	370.5	±3.3	±2.5	±5.8	30.74
129.7	369.6	±3.3	±2.5	±5.8	30.70
129.8	368.8	±3.3	±2.5	±5.8	30.67
129.9	367.9	±3.3	±2.5	±5.7	30.63
130.0	367.1	±3.3	±2.4	±5.7	30.60
130.5	362.6	±3.3	±2.5	±5.8	30.42
131.0	358.3	±3.3	±2.5	±5.8	30.23
131.5	353.9	±3.3	±2.5	±5.8	30.04
132.0	349.8	±3.3	±2.5	±5.9	29.86
132.5	345.7	±3.4	±2.6	±5.9	29.68
133.0	341.8	±3.4	±2.6	±6.0	29.50
133.5	337.6	±3.4	±2.6	±6.0	29.33
134.0	333.7	±3.4	±2.6	±6.0	29.14
134.5	329.7	±3.4	±2.6	±6.1	28.97
135.0	325.9	±3.5	±2.7	±6.1	28.79
135.5	322.1	±3.5	±2.6	±6.1	28.62
136.0	318.4	±3.5	±2.6	±6.1	28.44
136.5	314.5	±3.5	±2.6	±6.1	28.27
137.0	310.9	±3.5	±2.6	±6.1	28.10
137.5	307.3	±3.6	±2.6	±6.1	27.93
138.0	303.6	±3.6	±2.6	±6.2	27.75
138.5	300.3	±3.6	±2.6	±6.2	27.59
139.0	296.6	±3.6	±2.7	±6.2	27.41
139.5	293.3	±3.6	±2.7	±6.3	27.25
140.0	289.8	±3.6	±2.7	±6.3	27.07
140.5	286.5	±3.6	±2.7	±6.3	26.90
141.0	283.1	±3.6	±2.7	±6.3	26.73
141.5	279.9	±3.6	±2.7	±6.3	26.56
142.0	276.9	±3.6	±2.7	±6.3	26.39
142.5	273.6	±3.6	±2.7	±6.3	26.23
143.0	270.5	±3.7	±2.7	±6.3	26.07
143.5	267.4	±3.7	±2.7	±6.4	25.91
144.0	264.4	±3.7	±2.7	±6.4	25.73
144.5	261.3	±3.8	±2.7	±6.4	25.56
145.0	258.3	±3.8	±2.7	±6.5	25.39
145.5	255.4	±3.8	±2.7	±6.5	25.22
146.0	252.7	±3.8	±2.7	±6.5	25.05
146.5	249.7	±3.8	±2.7	±6.5	24.88
147.0	246.9	±3.8	±2.7	±6.5	24.71
147.5	244.2	±3.8	±2.7	±6.5	24.54
148.0	241.5	±3.8	±2.7	±6.5	24.38
148.5	238.7	±3.8	±2.7	±6.5	24.22

Table B.51: ZH production cross section and its scale and PDF uncertainties for various Higgs-boson masses at the LHC with CM energy $\sqrt{s} = 8$ TeV. The gluon-fusion contribution is also given separately.

M_H [GeV]	σ_{ZH} [fb]	Scale [%]	PDF [%]	Total [%]	$\sigma_{gg \to ZH}$ [fb]
149.0	236.1	±3.8	±2.7	±6.5	24.06
149.5	233.4	±3.9	±2.7	±6.6	23.90
150.0	230.8	±3.9	±2.7	±6.6	23.73
152.0	220.7	±3.9	±2.7	±6.7	23.09
154.0	210.9	±4.0	±2.8	±6.8	22.47
156.0	201.0	±4.1	±2.8	±6.8	21.86
158.0	191.1	±4.1	±2.8	±6.9	21.24
160.0	181.6	±4.2	±2.8	±7.0	20.59
162.0	176.2	±4.2	±2.8	±7.0	20.03
164.0	170.8	±4.2	±2.8	±7.0	19.43
165.0	168.3	±4.2	±2.8	±7.0	19.14
166.0	164.9	±4.2	±2.8	±7.1	18.87
168.0	158.2	±4.3	±2.8	±7.1	18.33
170.0	151.8	±4.3	±2.9	±7.2	17.79
172.0	145.7	±4.3	±2.9	±7.2	17.24
174.0	139.8	±4.4	±2.9	±7.3	16.69
175.0	136.9	±4.4	±2.9	±7.3	16.43
176.0	134.0	±4.4	±2.9	±7.4	16.17
178.0	128.4	±4.5	±2.9	±7.4	15.65
180.0	123.1	±4.6	±2.9	±7.5	15.14
182.0	118.7	±4.6	±2.9	±7.5	14.64
184.0	114.5	±4.6	±2.9	±7.5	14.16
185.0	112.5	±4.5	±2.9	±7.5	13.93
186.0	110.3	±4.6	±3.0	±7.5	13.70
188.0	106.2	±4.6	±3.0	±7.6	13.24
190.0	102.2	±4.6	±3.0	±7.6	12.79
192.0	98.48	±4.6	±3.0	±7.6	12.36
194.0	94.89	±4.6	±3.0	±7.6	11.92
195.0	93.14	±4.6	±3.0	±7.6	11.70
196.0	91.46	±4.6	±3.0	±7.6	11.49
198.0	88.13	±4.6	±3.0	±7.7	11.08
200.0	84.91	±4.7	±3.1	±7.7	10.67
202.0	81.92	±4.7	±3.1	±7.8	10.28
204.0	78.96	±4.7	±3.1	±7.8	9.894
206.0	76.13	±4.7	±3.1	±7.8	9.515
208.0	73.44	±4.6	±3.2	±7.8	9.145
210.0	70.82	±4.6	±3.2	±7.8	8.785
212.0	68.34	±4.6	±3.2	±7.8	8.434
214.0	65.93	±4.6	±3.2	±7.8	8.094
216.0	63.66	±4.6	±3.2	±7.8	7.766
218.0	61.45	±4.6	±3.2	±7.8	7.445
220.0	59.33	±4.6	±3.2	±7.8	7.130
222.0	57.27	±4.5	±3.3	±7.8	6.825
224.0	55.29	±4.5	±3.3	±7.8	6.528
226.0	53.39	±4.5	±3.3	±7.9	6.241
228.0	51.56	±4.5	±3.4	±7.9	5.965
230.0	49.86	±4.5	±3.4	±7.9	5.760

Table B.52: ZH production cross section and its scale and PDF uncertainties for various Higgs-boson masses at the LHC with CM energy $\sqrt{s} = 8$ TeV. The gluon-fusion contribution is also given separately.

M_H [GeV]	σ_ZH [fb]	Scale [%]	PDF [%]	Total [%]	$\sigma_{\mathrm{gg}\to\mathrm{ZH}}$ [fb]
232.0	48.16	±4.5	±3.4	±7.9	5.493
234.0	46.52	±4.4	±3.4	±7.9	5.226
236.0	44.94	±4.4	±3.5	±7.8	4.984
238.0	43.44	±4.3	±3.5	±7.8	4.745
240.0	41.99	±4.3	±3.5	±7.7	4.517
242.0	40.60	±4.2	±3.5	±7.7	4.319
244.0	39.26	±4.2	±3.5	±7.7	4.107
246.0	37.97	±4.2	±3.5	±7.7	3.906
248.0	36.72	±4.1	±3.5	±7.7	3.715
250.0	35.52	±4.1	±3.5	±7.6	3.532
252.0	34.37	±4.0	±3.6	±7.6	3.355
254.0	33.25	±4.0	±3.6	±7.6	3.190
256.0	32.15	±4.0	±3.6	±7.6	3.018
258.0	31.12	±3.9	±3.7	±7.6	2.864
260.0	30.12	±3.9	±3.7	±7.5	2.719
262.0	29.16	±3.8	±3.7	±7.5	2.581
264.0	28.23	±3.8	±3.7	±7.5	2.452
266.0	27.36	±3.7	±3.8	±7.5	2.333
268.0	26.49	±3.7	±3.8	±7.5	2.208
270.0	25.68	±3.7	±3.8	±7.4	2.094
272.0	24.88	±3.6	±3.8	±7.4	1.987
274.0	24.11	±3.6	±3.8	±7.4	1.884
276.0	23.37	±3.5	±3.8	±7.4	1.788
278.0	22.66	±3.5	±3.9	±7.4	1.696
280.0	21.98	±3.5	±3.9	±7.3	1.609
282.0	21.31	±3.4	±3.9	±7.3	1.530
284.0	20.66	±3.4	±3.9	±7.3	1.447
286.0	20.04	±3.4	±3.9	±7.3	1.372
288.0	19.45	±3.3	±4.0	±7.3	1.300
290.0	18.87	±3.3	±4.0	±7.3	1.231
292.0	18.30	±3.2	±4.0	±7.3	1.167
294.0	17.77	±3.2	±4.0	±7.2	1.107
296.0	17.25	±3.2	±4.1	±7.2	1.049
298.0	16.75	±3.1	±4.1	±7.2	0.9953
300.0	16.27	±3.1	±4.1	±7.2	0.9462
305.0	15.13	±3.0	±4.2	±7.2	0.8255
310.0	14.08	±2.9	±4.2	±7.2	0.7207
315.0	13.11	±2.9	±4.3	±7.2	0.6296
320.0	12.21	±2.8	±4.3	±7.1	0.5500
325.0	11.39	±2.8	±4.3	±7.1	0.4818
330.0	10.63	±2.7	±4.4	±7.1	0.4229
335.0	9.912	±2.7	±4.4	±7.1	0.3722
340.0	9.251	±2.7	±4.5	±7.1	0.3288
345.0	8.625	±2.6	±4.5	±7.2	0.2943
350.0	8.056	±2.6	±4.5	±7.1	0.2680
360.0	7.150	±2.7	±4.7	±7.4	0.2290
370.0	6.364	±2.7	±4.9	±7.6	0.2010
380.0	5.684	±2.8	±5.0	±7.7	0.1810
390.0	5.090	±2.8	±5.0	±7.8	0.1653
400.0	4.568	±2.8	±5.0	±7.8	0.1531

Table B.53: NLO QCD cross sections of $pp \to t\bar{t}H$ for $\sqrt{s} = 7$ TeV including both scale and PDF+α_s errors obtained according to the envelope method of the PDF4LHC goup.

M_H [GeV]	NLO QCD [fb]	scale [%]	PDF+α_s [%]
80.0	289.7	$+4.3 - 9.8$	± 8.3
81.0	281.2	$+4.3 - 9.8$	± 8.3
82.0	272.9	$+4.3 - 9.8$	± 8.3
83.0	265.0	$+4.3 - 9.8$	± 8.4
84.0	257.3	$+4.2 - 9.8$	± 8.4
85.0	249.8	$+4.2 - 9.8$	± 8.4
86.0	242.6	$+4.2 - 9.7$	± 8.4
87.0	235.7	$+4.2 - 9.7$	± 8.4
88.0	229.0	$+4.1 - 9.7$	± 8.4
89.0	222.5	$+4.1 - 9.7$	± 8.4
90.0	216.2	$+4.1 - 9.7$	± 8.4
91.0	210.2	$+4.1 - 9.7$	± 8.4
92.0	204.4	$+4.0 - 9.7$	± 8.4
93.0	198.8	$+4.0 - 9.7$	± 8.4
94.0	193.3	$+4.0 - 9.6$	± 8.4
95.0	188.0	$+3.9 - 9.6$	± 8.4
96.0	182.8	$+3.9 - 9.6$	± 8.4
97.0	177.8	$+3.9 - 9.6$	± 8.4
98.0	173.0	$+3.9 - 9.6$	± 8.4
99.0	168.3	$+3.8 - 9.6$	± 8.4
100.0	163.7	$+3.8 - 9.6$	± 8.4
101.0	159.3	$+3.8 - 9.6$	± 8.4
102.0	155.1	$+3.8 - 9.5$	± 8.4
103.0	151.0	$+3.7 - 9.5$	± 8.4
104.0	147.1	$+3.7 - 9.5$	± 8.4
105.0	143.2	$+3.7 - 9.5$	± 8.4
106.0	139.5	$+3.7 - 9.5$	± 8.4
107.0	135.9	$+3.6 - 9.5$	± 8.4
108.0	132.4	$+3.6 - 9.5$	± 8.4
109.0	129.0	$+3.6 - 9.5$	± 8.4
110.0	125.7	$+3.6 - 9.4$	± 8.4
110.5	124.0	$+3.6 - 9.4$	± 8.4
111.0	122.4	$+3.5 - 9.4$	± 8.4
111.5	120.9	$+3.5 - 9.4$	± 8.4
112.0	119.3	$+3.5 - 9.4$	± 8.4
112.5	117.8	$+3.5 - 9.4$	± 8.4
113.0	116.3	$+3.5 - 9.4$	± 8.4
113.5	114.8	$+3.5 - 9.4$	± 8.4
114.0	113.3	$+3.5 - 9.4$	± 8.4
114.5	111.9	$+3.5 - 9.4$	± 8.4
115.0	110.5	$+3.5 - 9.4$	± 8.4
115.5	109.1	$+3.4 - 9.4$	± 8.4
116.0	107.8	$+3.4 - 9.4$	± 8.4
116.5	106.4	$+3.4 - 9.4$	± 8.4
117.0	105.1	$+3.4 - 9.4$	± 8.4
117.5	103.8	$+3.4 - 9.4$	± 8.4
118.0	102.5	$+3.4 - 9.4$	± 8.4

Table B.54: NLO QCD cross sections of $pp \rightarrow t\bar{t}H$ for $\sqrt{s} = 7$ TeV including both scale and PDF+α_s errors obtained according to the envelope method of the PDF4LHC goup.

M_H [GeV]	NLO QCD [fb]	scale [%]	PDF+α_s [%]
118.5	101.3	$+3.4 - 9.3$	± 8.4
119.0	100.0	$+3.4 - 9.3$	± 8.4
119.5	98.79	$+3.4 - 9.3$	± 8.4
120.0	97.58	$+3.4 - 9.3$	± 8.4
120.1	97.34	$+3.4 - 9.3$	± 8.4
120.2	97.10	$+3.3 - 9.3$	± 8.4
120.3	96.86	$+3.3 - 9.3$	± 8.4
120.4	96.62	$+3.3 - 9.3$	± 8.4
120.5	96.38	$+3.3 - 9.3$	± 8.4
120.6	96.14	$+3.3 - 9.3$	± 8.4
120.7	95.90	$+3.3 - 9.3$	± 8.4
120.8	95.67	$+3.3 - 9.3$	± 8.4
120.9	95.43	$+3.3 - 9.3$	± 8.4
121.0	95.20	$+3.3 - 9.3$	± 8.4
121.1	94.96	$+3.3 - 9.3$	± 8.4
121.2	94.73	$+3.3 - 9.3$	± 8.4
121.3	94.49	$+3.3 - 9.3$	± 8.4
121.4	94.26	$+3.3 - 9.3$	± 8.4
121.5	94.03	$+3.3 - 9.3$	± 8.4
121.6	93.80	$+3.3 - 9.3$	± 8.4
121.7	93.57	$+3.3 - 9.3$	± 8.4
121.8	93.34	$+3.3 - 9.3$	± 8.4
121.9	93.11	$+3.3 - 9.3$	± 8.4
122.0	92.88	$+3.3 - 9.3$	± 8.4
122.1	92.65	$+3.3 - 9.3$	± 8.4
122.2	92.43	$+3.3 - 9.3$	± 8.4
122.3	92.20	$+3.3 - 9.3$	± 8.4
122.4	91.97	$+3.3 - 9.3$	± 8.4
122.5	91.75	$+3.3 - 9.3$	± 8.4
122.6	91.52	$+3.3 - 9.3$	± 8.4
122.7	91.30	$+3.3 - 9.3$	± 8.4
122.8	91.07	$+3.3 - 9.3$	± 8.4
122.9	90.85	$+3.3 - 9.3$	± 8.4
123.0	90.63	$+3.3 - 9.3$	± 8.4
123.1	90.41	$+3.3 - 9.3$	± 8.4
123.2	90.19	$+3.3 - 9.3$	± 8.4
123.3	89.97	$+3.3 - 9.3$	± 8.4
123.4	89.75	$+3.3 - 9.3$	± 8.4
123.5	89.53	$+3.3 - 9.3$	± 8.4
123.6	89.31	$+3.3 - 9.3$	± 8.4
123.7	89.09	$+3.3 - 9.3$	± 8.4
123.8	88.88	$+3.3 - 9.3$	± 8.4
123.9	88.66	$+3.3 - 9.3$	± 8.4
124.0	88.44	$+3.3 - 9.3$	± 8.4
124.1	88.23	$+3.3 - 9.3$	± 8.4
124.2	88.01	$+3.3 - 9.3$	± 8.4
124.3	87.80	$+3.3 - 9.3$	± 8.4

Table B.55: NLO QCD cross sections of $pp \to t\bar{t}H$ for $\sqrt{s} = 7$ TeV including both scale and PDF+α_s errors obtained according to the envelope method of the PDF4LHC goup.

M_H [GeV]	NLO QCD [fb]	scale [%]	PDF+α_s [%]
124.4	87.59	$+3.3 - 9.3$	± 8.4
124.5	87.37	$+3.3 - 9.3$	± 8.4
124.6	87.16	$+3.3 - 9.3$	± 8.4
124.7	86.95	$+3.3 - 9.3$	± 8.4
124.8	86.74	$+3.3 - 9.3$	± 8.4
124.9	86.53	$+3.3 - 9.3$	± 8.4
125.0	86.32	$+3.2 - 9.3$	± 8.4
125.1	86.11	$+3.2 - 9.3$	± 8.4
125.2	85.90	$+3.2 - 9.3$	± 8.4
125.3	85.70	$+3.2 - 9.3$	± 8.4
125.4	85.49	$+3.2 - 9.3$	± 8.4
125.5	85.28	$+3.2 - 9.3$	± 8.4
125.6	85.08	$+3.2 - 9.3$	± 8.4
125.7	84.87	$+3.2 - 9.3$	± 8.4
125.8	84.67	$+3.2 - 9.3$	± 8.4
125.9	84.46	$+3.2 - 9.3$	± 8.4
126.0	84.26	$+3.2 - 9.3$	± 8.4
126.1	84.06	$+3.2 - 9.3$	± 8.4
126.2	83.86	$+3.2 - 9.3$	± 8.4
126.3	83.66	$+3.2 - 9.3$	± 8.4
126.4	83.46	$+3.2 - 9.3$	± 8.4
126.5	83.26	$+3.2 - 9.3$	± 8.4
126.6	83.06	$+3.2 - 9.3$	± 8.4
126.7	82.86	$+3.2 - 9.3$	± 8.4
126.8	82.66	$+3.2 - 9.3$	± 8.4
126.9	82.46	$+3.2 - 9.3$	± 8.4
127.0	82.26	$+3.2 - 9.3$	± 8.4
127.1	82.07	$+3.2 - 9.3$	± 8.4
127.2	81.87	$+3.2 - 9.3$	± 8.4
127.3	81.68	$+3.2 - 9.3$	± 8.4
127.4	81.48	$+3.2 - 9.3$	± 8.4
127.5	81.29	$+3.2 - 9.3$	± 8.4
127.6	81.09	$+3.2 - 9.3$	± 8.4
127.7	80.90	$+3.2 - 9.3$	± 8.4
127.8	80.71	$+3.2 - 9.3$	± 8.4
127.9	80.51	$+3.2 - 9.3$	± 8.4
128.0	80.32	$+3.2 - 9.3$	± 8.4
128.1	80.13	$+3.2 - 9.3$	± 8.4
128.2	79.94	$+3.2 - 9.3$	± 8.4
128.3	79.75	$+3.2 - 9.3$	± 8.4
128.4	79.56	$+3.2 - 9.3$	± 8.4
128.5	79.37	$+3.2 - 9.3$	± 8.4
128.6	79.18	$+3.2 - 9.3$	± 8.5
128.7	79.00	$+3.2 - 9.3$	± 8.5
128.8	78.81	$+3.2 - 9.2$	± 8.5
128.9	78.62	$+3.2 - 9.2$	± 8.5
129.0	78.44	$+3.2 - 9.2$	± 8.5

Table B.56: NLO QCD cross sections of $pp \to t\bar{t}H$ for $\sqrt{s} = 7$ TeV including both scale and PDF+α_s errors obtained according to the envelope method of the PDF4LHC goup.

M_H [GeV]	NLO QCD [fb]	scale [%]	PDF+α_s [%]
129.1	78.25	$+3.2 - 9.2$	± 8.5
129.2	78.07	$+3.2 - 9.2$	± 8.5
129.3	77.88	$+3.2 - 9.2$	± 8.5
129.4	77.70	$+3.2 - 9.2$	± 8.5
129.5	77.51	$+3.2 - 9.2$	± 8.5
129.6	77.33	$+3.2 - 9.2$	± 8.5
129.7	77.15	$+3.2 - 9.2$	± 8.5
129.8	76.96	$+3.2 - 9.2$	± 8.5
129.9	76.78	$+3.2 - 9.2$	± 8.5
130.0	76.60	$+3.2 - 9.2$	± 8.5
130.5	75.70	$+3.1 - 9.2$	± 8.5
131.0	74.82	$+3.1 - 9.2$	± 8.5
131.5	73.94	$+3.1 - 9.2$	± 8.5
132.0	73.08	$+3.1 - 9.2$	± 8.5
132.5	72.23	$+3.1 - 9.2$	± 8.5
133.0	71.40	$+3.1 - 9.2$	± 8.5
133.5	70.57	$+3.1 - 9.2$	± 8.5
134.0	69.75	$+3.1 - 9.2$	± 8.5
134.5	68.95	$+3.1 - 9.2$	± 8.5
135.0	68.16	$+3.1 - 9.2$	± 8.5
135.5	67.38	$+3.1 - 9.2$	± 8.5
136.0	66.60	$+3.0 - 9.2$	± 8.5
136.5	65.84	$+3.0 - 9.2$	± 8.5
137.0	65.09	$+3.0 - 9.2$	± 8.5
137.5	64.35	$+3.0 - 9.2$	± 8.5
138.0	63.62	$+3.0 - 9.2$	± 8.5
138.5	62.90	$+3.0 - 9.2$	± 8.5
139.0	62.19	$+3.0 - 9.2$	± 8.5
139.5	61.48	$+3.0 - 9.2$	± 8.5
140.0	60.79	$+3.0 - 9.2$	± 8.5
140.5	60.10	$+3.0 - 9.2$	± 8.5
141.0	59.42	$+3.0 - 9.1$	± 8.5
141.5	58.75	$+3.0 - 9.1$	± 8.5
142.0	58.08	$+2.9 - 9.1$	± 8.5
142.5	57.43	$+2.9 - 9.1$	± 8.5
143.0	56.78	$+2.9 - 9.1$	± 8.5
143.5	56.15	$+2.9 - 9.1$	± 8.5
144.0	55.52	$+2.9 - 9.1$	± 8.5
144.5	54.90	$+2.9 - 9.1$	± 8.5
145.0	54.29	$+2.9 - 9.1$	± 8.5
145.5	53.69	$+2.9 - 9.1$	± 8.5
146.0	53.10	$+2.9 - 9.1$	± 8.5
146.5	52.52	$+2.9 - 9.1$	± 8.5
147.0	51.95	$+2.9 - 9.1$	± 8.5
147.5	51.38	$+2.9 - 9.1$	± 8.5
148.0	50.82	$+2.9 - 9.1$	± 8.5
148.5	50.27	$+2.9 - 9.1$	± 8.5

Table B.57: NLO QCD cross sections of $\mathrm{pp} \rightarrow \mathrm{t\bar{t}H}$ for $\sqrt{s} = 7$ TeV including both scale and PDF+α_s errors obtained according to the envelope method of the PDF4LHC goup.

M_H [GeV]	NLO QCD [fb]	scale [%]	PDF+α_s [%]
149.0	49.73	$+2.9 - 9.1$	± 8.5
149.5	49.20	$+2.8 - 9.1$	± 8.5
150.0	48.67	$+2.8 - 9.1$	± 8.5
152.0	46.63	$+2.8 - 9.1$	± 8.5
154.0	44.70	$+2.8 - 9.1$	± 8.5
156.0	42.85	$+2.8 - 9.1$	± 8.5
158.0	41.08	$+2.8 - 9.1$	± 8.5
160.0	39.40	$+2.7 - 9.0$	± 8.5
162.0	37.81	$+2.7 - 9.0$	± 8.5
164.0	36.30	$+2.7 - 9.0$	± 8.6
165.0	35.57	$+2.7 - 9.0$	± 8.6
166.0	34.86	$+2.7 - 9.0$	± 8.6
168.0	33.49	$+2.7 - 9.0$	± 8.6
170.0	32.18	$+2.7 - 9.0$	± 8.6
172.0	30.93	$+2.6 - 9.0$	± 8.6
174.0	29.74	$+2.6 - 9.0$	± 8.6
175.0	29.16	$+2.6 - 9.0$	± 8.6
176.0	28.60	$+2.6 - 9.0$	± 8.6
178.0	27.52	$+2.6 - 9.0$	± 8.6
180.0	26.50	$+2.6 - 9.0$	± 8.6
182.0	25.52	$+2.6 - 9.0$	± 8.7
184.0	24.60	$+2.6 - 9.0$	± 8.7
185.0	24.15	$+2.6 - 9.0$	± 8.7
186.0	23.71	$+2.6 - 9.0$	± 8.7
188.0	22.86	$+2.6 - 9.0$	± 8.7
190.0	22.05	$+2.6 - 9.0$	± 8.7
192.0	21.27	$+2.6 - 9.0$	± 8.7
194.0	20.53	$+2.6 - 9.0$	± 8.7
195.0	20.17	$+2.6 - 9.0$	± 8.7
196.0	19.82	$+2.6 - 9.0$	± 8.7
198.0	19.13	$+2.6 - 9.0$	± 8.8
200.0	18.48	$+2.6 - 9.1$	± 8.8
202.0	17.85	$+2.6 - 9.1$	± 8.8
204.0	17.25	$+2.7 - 9.1$	± 8.8
206.0	16.68	$+2.7 - 9.1$	± 8.8
208.0	16.13	$+2.7 - 9.1$	± 8.8
210.0	15.61	$+2.7 - 9.1$	± 8.8
212.0	15.11	$+2.8 - 9.2$	± 8.8
214.0	14.62	$+2.8 - 9.2$	± 8.8
216.0	14.16	$+2.8 - 9.2$	± 8.8
218.0	13.72	$+2.9 - 9.2$	± 8.9
220.0	13.29	$+2.9 - 9.2$	± 8.9
222.0	12.89	$+3.0 - 9.3$	± 8.9
224.0	12.49	$+3.0 - 9.3$	± 8.9
226.0	12.12	$+3.1 - 9.3$	± 8.9
228.0	11.76	$+3.1 - 9.4$	± 8.9
230.0	11.41	$+3.1 - 9.4$	± 9.0

Table B.58: NLO QCD cross sections of pp → t̄tH for $\sqrt{s} = 7$ TeV including both scale and PDF+α_s errors obtained according to the envelope method of the PDF4LHC goup.

M_H [GeV]	NLO QCD [fb]	scale [%]	PDF+α_s [%]
232.0	11.08	$+3.1 - 9.4$	± 9.0
234.0	10.76	$+3.1 - 9.4$	± 9.0
236.0	10.46	$+3.1 - 9.4$	± 9.0
238.0	10.16	$+3.2 - 9.4$	± 9.0
240.0	9.876	$+3.2 - 9.5$	± 9.0
242.0	9.600	$+3.2 - 9.5$	± 9.0
244.0	9.333	$+3.3 - 9.5$	± 9.1
246.0	9.077	$+3.4 - 9.6$	± 9.1
248.0	8.830	$+3.4 - 9.6$	± 9.1
250.0	8.592	$+3.5 - 9.7$	± 9.2
252.0	8.365	$+3.6 - 9.7$	± 9.2
254.0	8.145	$+3.7 - 9.7$	± 9.2
256.0	7.934	$+3.7 - 9.8$	± 9.2
258.0	7.730	$+3.8 - 9.8$	± 9.2
260.0	7.533	$+3.9 - 9.9$	± 9.2
262.0	7.342	$+4.0 - 9.9$	± 9.2
264.0	7.157	$+4.1 - 10.0$	± 9.2
266.0	6.979	$+4.1 - 10.0$	± 9.2
268.0	6.806	$+4.2 - 10.1$	± 9.2
270.0	6.640	$+4.3 - 10.1$	± 9.3
272.0	6.478	$+4.4 - 10.2$	± 9.3
274.0	6.322	$+4.5 - 10.2$	± 9.3
276.0	6.172	$+4.6 - 10.3$	± 9.4
278.0	6.026	$+4.6 - 10.3$	± 9.4
280.0	5.886	$+4.7 - 10.4$	± 9.5
282.0	5.752	$+4.8 - 10.4$	± 9.5
284.0	5.622	$+4.9 - 10.5$	± 9.5
286.0	5.496	$+5.0 - 10.5$	± 9.6
288.0	5.374	$+5.1 - 10.6$	± 9.7
290.0	5.257	$+5.2 - 10.6$	± 9.7
292.0	5.142	$+5.3 - 10.7$	± 9.8
294.0	5.031	$+5.4 - 10.7$	± 9.8
296.0	4.924	$+5.5 - 10.8$	± 9.9
298.0	4.819	$+5.6 - 10.9$	± 9.9
300.0	4.718	$+5.6 - 10.9$	± 10.0
305.0	4.478	$+5.7 - 10.9$	± 10.1
310.0	4.255	$+5.6 - 11.0$	± 10.3
315.0	4.047	$+5.5 - 11.0$	± 10.4
320.0	3.853	$+5.5 - 11.0$	± 10.5
325.0	3.672	$+5.6 - 11.1$	± 10.7
330.0	3.501	$+5.7 - 11.2$	± 10.9
335.0	3.342	$+5.9 - 11.3$	± 11.0
340.0	3.192	$+6.1 - 11.4$	± 11.2
345.0	3.053	$+6.2 - 11.5$	± 11.3
350.0	2.921	$+6.4 - 11.6$	± 11.5
360.0	2.680	$+6.7 - 11.8$	± 11.8
370.0	2.466	$+6.9 - 12.0$	± 12.2
380.0	2.273	$+7.2 - 12.2$	± 12.6
390.0	2.100	$+7.5 - 12.3$	± 13.0
400.0	1.943	$+7.8 - 12.5$	± 13.5

Table B.59: NLO QCD cross sections of $pp \to t\bar{t}H$ for $\sqrt{s} = 8$ TeV including both scale and PDF+α_s errors obtained according to the envelope method of the PDF4LHC goup.

M_H [GeV]	NLO QCD [fb]	scale [%]	PDF+α_s [%]
80.0	427.7	$+4.7 - 9.7$	± 8.0
81.0	415.2	$+4.7 - 9.7$	± 8.0
82.0	403.2	$+4.7 - 9.7$	± 8.0
83.0	391.5	$+4.7 - 9.7$	± 8.0
84.0	380.3	$+4.7 - 9.7$	± 8.0
85.0	369.4	$+4.6 - 9.7$	± 8.0
86.0	358.9	$+4.6 - 9.7$	± 8.0
87.0	348.7	$+4.6 - 9.7$	± 8.0
88.0	338.9	$+4.6 - 9.6$	± 8.0
89.0	329.4	$+4.5 - 9.6$	± 8.0
90.0	320.2	$+4.5 - 9.6$	± 8.0
91.0	311.3	$+4.5 - 9.6$	± 8.0
92.0	302.7	$+4.5 - 9.6$	± 8.0
93.0	294.4	$+4.4 - 9.6$	± 8.0
94.0	286.4	$+4.4 - 9.6$	± 8.0
95.0	278.6	$+4.4 - 9.6$	± 8.0
96.0	271.1	$+4.4 - 9.6$	± 8.0
97.0	263.8	$+4.3 - 9.5$	± 8.0
98.0	256.7	$+4.3 - 9.5$	± 8.0
99.0	249.9	$+4.3 - 9.5$	± 8.0
100.0	243.3	$+4.3 - 9.5$	± 8.0
101.0	236.9	$+4.3 - 9.5$	± 8.0
102.0	230.8	$+4.2 - 9.5$	± 8.0
103.0	224.8	$+4.2 - 9.5$	± 8.1
104.0	219.0	$+4.2 - 9.5$	± 8.1
105.0	213.3	$+4.2 - 9.5$	± 8.1
106.0	207.7	$+4.1 - 9.4$	± 8.1
107.0	202.3	$+4.1 - 9.4$	± 8.1
108.0	197.1	$+4.1 - 9.4$	± 8.1
109.0	192.0	$+4.1 - 9.4$	± 8.1
110.0	187.1	$+4.1 - 9.4$	± 8.1
110.5	184.7	$+4.1 - 9.4$	± 8.1
111.0	182.4	$+4.0 - 9.4$	± 8.1
111.5	180.1	$+4.0 - 9.4$	± 8.1
112.0	177.9	$+4.0 - 9.4$	± 8.1
112.5	175.7	$+4.0 - 9.4$	± 8.1
113.0	173.5	$+4.0 - 9.4$	± 8.1
113.5	171.3	$+4.0 - 9.4$	± 8.1
114.0	169.2	$+4.0 - 9.4$	± 8.1
114.5	167.1	$+4.0 - 9.4$	± 8.1
115.0	165.1	$+4.0 - 9.4$	± 8.1
115.5	163.0	$+4.0 - 9.4$	± 8.1
116.0	161.0	$+3.9 - 9.4$	± 8.1
116.5	159.0	$+3.9 - 9.3$	± 8.1
117.0	157.1	$+3.9 - 9.3$	± 8.1
117.5	155.2	$+3.9 - 9.3$	± 8.1
118.0	153.3	$+3.9 - 9.3$	± 8.1

Table B.60: NLO QCD cross sections of $pp \rightarrow t\bar{t}H$ for $\sqrt{s} = 8$ TeV including both scale and PDF+α_s errors obtained according to the envelope method of the PDF4LHC goup.

M_H [GeV]	NLO QCD [fb]	scale [%]	PDF+α_s [%]
118.5	151.4	$+3.9 - 9.3$	± 8.1
119.0	149.5	$+3.9 - 9.3$	± 8.1
119.5	147.7	$+3.9 - 9.3$	± 8.1
120.0	145.9	$+3.9 - 9.3$	± 8.1
120.1	145.6	$+3.9 - 9.3$	± 8.1
120.2	145.2	$+3.9 - 9.3$	± 8.1
120.3	144.9	$+3.9 - 9.3$	± 8.1
120.4	144.5	$+3.9 - 9.3$	± 8.1
120.5	144.1	$+3.9 - 9.3$	± 8.1
120.6	143.8	$+3.9 - 9.3$	± 8.1
120.7	143.4	$+3.9 - 9.3$	± 8.1
120.8	143.1	$+3.9 - 9.3$	± 8.1
120.9	142.7	$+3.9 - 9.3$	± 8.1
121.0	142.4	$+3.9 - 9.3$	± 8.1
121.1	142.0	$+3.9 - 9.3$	± 8.1
121.2	141.7	$+3.9 - 9.3$	± 8.1
121.3	141.4	$+3.8 - 9.3$	± 8.1
121.4	141.0	$+3.8 - 9.3$	± 8.1
121.5	140.7	$+3.8 - 9.3$	± 8.1
121.6	140.3	$+3.8 - 9.3$	± 8.1
121.7	140.0	$+3.8 - 9.3$	± 8.1
121.8	139.6	$+3.8 - 9.3$	± 8.1
121.9	139.3	$+3.8 - 9.3$	± 8.1
122.0	139.0	$+3.8 - 9.3$	± 8.1
122.1	138.6	$+3.8 - 9.3$	± 8.1
122.2	138.3	$+3.8 - 9.3$	± 8.1
122.3	138.0	$+3.8 - 9.3$	± 8.1
122.4	137.6	$+3.8 - 9.3$	± 8.1
122.5	137.3	$+3.8 - 9.3$	± 8.1
122.6	137.0	$+3.8 - 9.3$	± 8.1
122.7	136.6	$+3.8 - 9.3$	± 8.1
122.8	136.3	$+3.8 - 9.3$	± 8.1
122.9	136.0	$+3.8 - 9.3$	± 8.1
123.0	135.6	$+3.8 - 9.3$	± 8.1
123.1	135.3	$+3.8 - 9.3$	± 8.1
123.2	135.0	$+3.8 - 9.3$	± 8.1
123.3	134.7	$+3.8 - 9.3$	± 8.1
123.4	134.3	$+3.8 - 9.3$	± 8.1
123.5	134.0	$+3.8 - 9.3$	± 8.1
123.6	133.7	$+3.8 - 9.3$	± 8.1
123.7	133.4	$+3.8 - 9.3$	± 8.1
123.8	133.0	$+3.8 - 9.3$	± 8.1
123.9	132.7	$+3.8 - 9.3$	± 8.1
124.0	132.4	$+3.8 - 9.3$	± 8.1
124.1	132.1	$+3.8 - 9.3$	± 8.1
124.2	131.8	$+3.8 - 9.3$	± 8.1
124.3	131.4	$+3.8 - 9.3$	± 8.1

Table B.61: NLO QCD cross sections of $pp \rightarrow t\bar{t}H$ for $\sqrt{s} = 8$ TeV including both scale and PDF+α_s errors obtained according to the envelope method of the PDF4LHC goup.

M_H [GeV]	NLO QCD [fb]	scale [%]	PDF+α_s [%]
124.4	131.1	$+3.8 - 9.3$	± 8.1
124.5	130.8	$+3.8 - 9.3$	± 8.1
124.6	130.5	$+3.8 - 9.3$	± 8.1
124.7	130.2	$+3.8 - 9.3$	± 8.1
124.8	129.9	$+3.8 - 9.3$	± 8.1
124.9	129.6	$+3.8 - 9.3$	± 8.1
125.0	129.3	$+3.8 - 9.3$	± 8.1
125.1	129.0	$+3.8 - 9.3$	± 8.1
125.2	128.6	$+3.8 - 9.3$	± 8.1
125.3	128.3	$+3.8 - 9.3$	± 8.1
125.4	128.0	$+3.8 - 9.3$	± 8.1
125.5	127.7	$+3.8 - 9.3$	± 8.1
125.6	127.4	$+3.8 - 9.3$	± 8.1
125.7	127.1	$+3.8 - 9.3$	± 8.1
125.8	126.8	$+3.8 - 9.3$	± 8.1
125.9	126.5	$+3.8 - 9.3$	± 8.1
126.0	126.2	$+3.8 - 9.3$	± 8.1
126.1	125.9	$+3.8 - 9.3$	± 8.1
126.2	125.6	$+3.8 - 9.3$	± 8.1
126.3	125.3	$+3.8 - 9.3$	± 8.1
126.4	125.0	$+3.8 - 9.3$	± 8.1
126.5	124.7	$+3.8 - 9.3$	± 8.1
126.6	124.5	$+3.8 - 9.3$	± 8.1
126.7	124.2	$+3.8 - 9.3$	± 8.1
126.8	123.9	$+3.8 - 9.3$	± 8.1
126.9	123.6	$+3.8 - 9.3$	± 8.1
127.0	123.3	$+3.8 - 9.3$	± 8.1
127.1	123.0	$+3.8 - 9.3$	± 8.1
127.2	122.7	$+3.7 - 9.3$	± 8.1
127.3	122.4	$+3.7 - 9.3$	± 8.1
127.4	122.1	$+3.7 - 9.3$	± 8.1
127.5	121.8	$+3.7 - 9.3$	± 8.1
127.6	121.6	$+3.7 - 9.3$	± 8.1
127.7	121.3	$+3.7 - 9.3$	± 8.1
127.8	121.0	$+3.7 - 9.3$	± 8.1
127.9	120.7	$+3.7 - 9.3$	± 8.1
128.0	120.4	$+3.7 - 9.3$	± 8.1
128.1	120.1	$+3.7 - 9.3$	± 8.1
128.2	119.9	$+3.7 - 9.3$	± 8.1
128.3	119.6	$+3.7 - 9.3$	± 8.1
128.4	119.3	$+3.7 - 9.3$	± 8.1
128.5	119.0	$+3.7 - 9.2$	± 8.1
128.6	118.7	$+3.7 - 9.2$	± 8.1
128.7	118.5	$+3.7 - 9.2$	± 8.1
128.8	118.2	$+3.7 - 9.2$	± 8.1
128.9	117.9	$+3.7 - 9.2$	± 8.1
129.0	117.6	$+3.7 - 9.2$	± 8.1

Table B.62: NLO QCD cross sections of $pp \rightarrow t\bar{t}H$ for $\sqrt{s} = 8$ TeV including both scale and PDF+α_s errors obtained according to the envelope method of the PDF4LHC goup.

M_H [GeV]	NLO QCD [fb]	scale [%]	PDF+α_s [%]
129.1	117.4	$+3.7 - 9.2$	± 8.1
129.2	117.1	$+3.7 - 9.2$	± 8.1
129.3	116.8	$+3.7 - 9.2$	± 8.1
129.4	116.6	$+3.7 - 9.2$	± 8.1
129.5	116.3	$+3.7 - 9.2$	± 8.1
129.6	116.0	$+3.7 - 9.2$	± 8.1
129.7	115.7	$+3.7 - 9.2$	± 8.1
129.8	115.5	$+3.7 - 9.2$	± 8.1
129.9	115.2	$+3.7 - 9.2$	± 8.1
130.0	114.9	$+3.7 - 9.2$	± 8.1
130.5	113.6	$+3.7 - 9.2$	± 8.1
131.0	112.3	$+3.7 - 9.2$	± 8.1
131.5	111.0	$+3.7 - 9.2$	± 8.1
132.0	109.7	$+3.7 - 9.2$	± 8.1
132.5	108.5	$+3.7 - 9.2$	± 8.1
133.0	107.2	$+3.7 - 9.2$	± 8.1
133.5	106.0	$+3.6 - 9.2$	± 8.1
134.0	104.8	$+3.6 - 9.2$	± 8.1
134.5	103.6	$+3.6 - 9.2$	± 8.1
135.0	102.4	$+3.6 - 9.2$	± 8.1
135.5	101.3	$+3.6 - 9.2$	± 8.1
136.0	100.1	$+3.6 - 9.2$	± 8.1
136.5	98.98	$+3.6 - 9.2$	± 8.2
137.0	97.87	$+3.6 - 9.2$	± 8.2
137.5	96.77	$+3.6 - 9.2$	± 8.2
138.0	95.69	$+3.6 - 9.2$	± 8.2
138.5	94.62	$+3.6 - 9.2$	± 8.2
139.0	93.56	$+3.6 - 9.2$	± 8.2
139.5	92.52	$+3.6 - 9.2$	± 8.2
140.0	91.50	$+3.6 - 9.2$	± 8.2
140.5	90.49	$+3.5 - 9.2$	± 8.2
141.0	89.49	$+3.5 - 9.2$	± 8.2
141.5	88.51	$+3.5 - 9.2$	± 8.2
142.0	87.54	$+3.5 - 9.2$	± 8.2
142.5	86.59	$+3.5 - 9.2$	± 8.2
143.0	85.64	$+3.5 - 9.2$	± 8.2
143.5	84.71	$+3.5 - 9.2$	± 8.2
144.0	83.79	$+3.5 - 9.2$	± 8.2
144.5	82.89	$+3.5 - 9.2$	± 8.2
145.0	81.99	$+3.5 - 9.2$	± 8.2
145.5	81.11	$+3.5 - 9.2$	± 8.2
146.0	80.23	$+3.5 - 9.1$	± 8.2
146.5	79.37	$+3.5 - 9.1$	± 8.2
147.0	78.51	$+3.5 - 9.1$	± 8.2
147.5	77.67	$+3.5 - 9.1$	± 8.2
148.0	76.84	$+3.5 - 9.1$	± 8.2
148.5	76.02	$+3.5 - 9.1$	± 8.2

Table B.63: NLO QCD cross sections of $pp \rightarrow t\bar{t}H$ for $\sqrt{s} = 8$ TeV including both scale and PDF+α_s errors obtained according to the envelope method of the PDF4LHC goup.

M_H [GeV]	NLO QCD [fb]	scale [%]	PDF+α_s [%]
149.0	75.21	$+3.5 -9.1$	± 8.2
149.5	74.40	$+3.4 -9.1$	± 8.2
150.0	73.61	$+3.4 -9.1$	± 8.2
152.0	70.53	$+3.4 -9.1$	± 8.2
154.0	67.60	$+3.4 -9.1$	± 8.2
156.0	64.85	$+3.4 -9.1$	± 8.2
158.0	62.25	$+3.4 -9.1$	± 8.3
160.0	59.78	$+3.4 -9.1$	± 8.3
162.0	57.43	$+3.4 -9.1$	± 8.3
164.0	55.19	$+3.3 -9.1$	± 8.3
165.0	54.11	$+3.3 -9.1$	± 8.3
166.0	53.04	$+3.4 -9.1$	± 8.3
168.0	50.99	$+3.4 -9.1$	± 8.3
170.0	49.04	$+3.4 -9.1$	± 8.3
172.0	47.19	$+3.4 -9.1$	± 8.3
174.0	45.43	$+3.4 -9.1$	± 8.3
175.0	44.58	$+3.4 -9.1$	± 8.3
176.0	43.75	$+3.4 -9.1$	± 8.3
178.0	42.15	$+3.4 -9.1$	± 8.4
180.0	40.61	$+3.3 -9.1$	± 8.4
182.0	39.13	$+3.3 -9.1$	± 8.4
184.0	37.72	$+3.3 -9.1$	± 8.4
185.0	37.04	$+3.3 -9.1$	± 8.4
186.0	36.38	$+3.3 -9.1$	± 8.4
188.0	35.11	$+3.4 -9.1$	± 8.4
190.0	33.90	$+3.4 -9.1$	± 8.4
192.0	32.74	$+3.4 -9.2$	± 8.4
194.0	31.64	$+3.4 -9.2$	± 8.4
195.0	31.10	$+3.4 -9.2$	± 8.5
196.0	30.58	$+3.4 -9.2$	± 8.5
198.0	29.56	$+3.4 -9.2$	± 8.5
200.0	28.58	$+3.4 -9.2$	± 8.5
202.0	27.65	$+3.5 -9.2$	± 8.5
204.0	26.76	$+3.5 -9.2$	± 8.5
206.0	25.91	$+3.5 -9.3$	± 8.5
208.0	25.09	$+3.5 -9.3$	± 8.6
210.0	24.30	$+3.6 -9.3$	± 8.6
212.0	23.54	$+3.6 -9.3$	± 8.6
214.0	22.81	$+3.6 -9.4$	± 8.6
216.0	22.11	$+3.7 -9.4$	± 8.6
218.0	21.44	$+3.7 -9.4$	± 8.6
220.0	20.80	$+3.8 -9.4$	± 8.6
222.0	20.18	$+3.8 -9.5$	± 8.7
224.0	19.59	$+3.9 -9.5$	± 8.7
226.0	19.03	$+3.9 -9.5$	± 8.7
228.0	18.48	$+4.0 -9.6$	± 8.7
230.0	17.96	$+4.0 -9.6$	± 8.7

Table B.64: NLO QCD cross sections of pp → t̄tH for $\sqrt{s} = 8$ TeV including both scale and PDF+α_s errors obtained according to the envelope method of the PDF4LHC goup.

M_H [GeV]	NLO QCD [fb]	scale [%]	PDF+α_s [%]
232.0	17.45	$+4.0 - 9.6$	± 8.8
234.0	16.96	$+4.0 - 9.6$	± 8.8
236.0	16.49	$+4.0 - 9.6$	± 8.8
238.0	16.04	$+4.0 - 9.6$	± 8.8
240.0	15.61	$+4.1 - 9.7$	± 8.8
242.0	15.19	$+4.1 - 9.7$	± 8.8
244.0	14.79	$+4.2 - 9.7$	± 8.8
246.0	14.41	$+4.3 - 9.8$	± 8.9
248.0	14.04	$+4.3 - 9.8$	± 8.9
250.0	13.68	$+4.4 - 9.9$	± 8.9
252.0	13.33	$+4.5 - 9.9$	± 8.9
254.0	13.00	$+4.6 - 10.0$	± 8.9
256.0	12.68	$+4.6 - 10.0$	± 9.0
258.0	12.37	$+4.7 - 10.0$	± 9.0
260.0	12.06	$+4.8 - 10.1$	± 9.0
262.0	11.77	$+4.9 - 10.1$	± 9.0
264.0	11.49	$+4.9 - 10.2$	± 9.0
266.0	11.21	$+5.0 - 10.2$	± 9.0
268.0	10.95	$+5.1 - 10.3$	± 9.1
270.0	10.70	$+5.2 - 10.3$	± 9.1
272.0	10.45	$+5.3 - 10.4$	± 9.1
274.0	10.21	$+5.4 - 10.4$	± 9.1
276.0	9.984	$+5.4 - 10.5$	± 9.1
278.0	9.762	$+5.5 - 10.5$	± 9.2
280.0	9.547	$+5.6 - 10.6$	± 9.2
282.0	9.337	$+5.7 - 10.6$	± 9.2
284.0	9.133	$+5.8 - 10.7$	± 9.2
286.0	8.936	$+5.9 - 10.7$	± 9.2
288.0	8.744	$+6.0 - 10.8$	± 9.3
290.0	8.559	$+6.1 - 10.8$	± 9.3
292.0	8.381	$+6.2 - 10.9$	± 9.3
294.0	8.208	$+6.2 - 11.0$	± 9.3
296.0	8.041	$+6.3 - 11.0$	± 9.3
298.0	7.879	$+6.4 - 11.1$	± 9.4
300.0	7.721	$+6.5 - 11.1$	± 9.4
305.0	7.347	$+6.5 - 11.1$	± 9.5
310.0	6.999	$+6.4 - 11.1$	± 9.6
315.0	6.675	$+6.2 - 11.1$	± 9.7
320.0	6.371	$+6.1 - 11.1$	± 9.8
325.0	6.087	$+6.2 - 11.1$	± 10.0
330.0	5.821	$+6.3 - 11.2$	± 10.1
335.0	5.571	$+6.5 - 11.3$	± 10.2
340.0	5.337	$+6.7 - 11.4$	± 10.4
345.0	5.116	$+6.8 - 11.5$	± 10.5
350.0	4.909	$+6.9 - 11.6$	± 10.7
360.0	4.529	$+7.2 - 11.8$	± 10.9
370.0	4.192	$+7.4 - 12.0$	± 11.2
380.0	3.889	$+7.7 - 12.1$	± 11.4
390.0	3.615	$+7.9 - 12.3$	± 11.7
400.0	3.366	$+8.1 - 12.5$	± 12.0

Table B.65: SM Higgs-boson production cross sections at $\sqrt{s} = 7$ TeV: light Higgs boson.

M_{H} [GeV]	ggF σ [pb]	VBF σ [pb]	WH σ [pb]	ZH σ [pb]	ttH σ [pb]	Total σ [pb]
80.0	36.59	1.914	2.341	1.244	0.2897	42.38
81.0	35.71	1.894	2.258	1.203	0.2812	41.35
82.0	34.86	1.871	2.179	1.163	0.2729	40.35
83.0	34.04	1.853	2.104	1.125	0.2650	39.39
84.0	33.25	1.833	2.031	1.087	0.2573	38.46
85.0	32.49	1.814	1.963	1.052	0.2498	37.57
86.0	31.75	1.794	1.896	1.019	0.2426	36.71
87.0	31.04	1.776	1.831	0.9858	0.2357	35.87
88.0	30.35	1.759	1.770	0.9548	0.2290	35.06
89.0	29.69	1.738	1.711	0.9244	0.2225	34.28
90.0	29.03	1.723	1.654	0.8959	0.2162	33.52
91.0	28.42	1.705	1.600	0.8682	0.2102	32.80
92.0	27.81	1.689	1.548	0.8417	0.2044	32.09
93.0	27.23	1.668	1.498	0.8162	0.1988	31.41
94.0	26.65	1.654	1.450	0.7917	0.1933	30.74
95.0	26.10	1.639	1.404	0.7678	0.1880	30.10
96.0	25.57	1.617	1.359	0.7447	0.1828	29.47
97.0	25.06	1.600	1.315	0.7232	0.1778	28.87
98.0	24.56	1.582	1.274	0.7011	0.1730	28.29
99.0	24.07	1.568	1.234	0.6814	0.1683	27.72
100.0	23.64	1.557	1.195	0.6616	0.1637	27.21
101.0	23.17	1.541	1.159	0.6425	0.1593	26.68
102.0	22.73	1.526	1.125	0.6240	0.1551	26.16
103.0	22.29	1.509	1.091	0.6063	0.1510	25.65
104.0	21.87	1.492	1.058	0.5895	0.1471	25.15
105.0	21.45	1.478	1.029	0.5724	0.1432	24.68
106.0	21.05	1.465	0.9964	0.5564	0.1395	24.21
107.0	20.67	1.452	0.9674	0.5412	0.1359	23.76
108.0	20.29	1.438	0.9384	0.5261	0.1324	23.32
109.0	19.92	1.423	0.9109	0.5116	0.1290	22.89
110.0	19.56	1.410	0.8847	0.4978	0.1257	22.48
110.5	19.38	1.404	0.8720	0.4909	0.1240	22.27
111.0	19.21	1.396	0.8587	0.4845	0.1224	22.07
111.5	19.03	1.391	0.8458	0.4775	0.1209	21.87
112.0	18.87	1.382	0.8333	0.4710	0.1193	21.67
112.5	18.70	1.375	0.8213	0.4647	0.1178	21.48
113.0	18.53	1.369	0.8093	0.4586	0.1163	21.29
113.5	18.37	1.363	0.7973	0.4522	0.1148	21.10
114.0	18.21	1.356	0.7858	0.4460	0.1133	20.91
114.5	18.05	1.349	0.7743	0.4402	0.1119	20.73
115.0	17.89	1.344	0.7626	0.4345	0.1105	20.55
115.5	17.74	1.335	0.7517	0.4287	0.1091	20.36
116.0	17.59	1.330	0.7415	0.4232	0.1078	20.19
116.5	17.44	1.324	0.7309	0.4174	0.1064	20.01
117.0	17.29	1.317	0.7203	0.4119	0.1051	19.84
117.5	17.14	1.310	0.7102	0.4063	0.1038	19.67
118.0	16.99	1.304	0.7002	0.4013	0.1025	19.50

Table B.66: SM Higgs-boson production cross sections at $\sqrt{s} = 7$ TeV: light Higgs boson.

M_H [GeV]	ggF σ [pb]	VBF σ [pb]	WH σ [pb]	ZH σ [pb]	ttH σ [pb]	Total σ [pb]
118.5	16.85	1.297	0.6907	0.3960	0.1013	19.34
119.0	16.71	1.292	0.6808	0.3909	0.1000	19.17
119.5	16.57	1.286	0.6712	0.3858	0.0988	19.01
120.0	16.43	1.279	0.6617	0.3808	0.0976	18.85
120.1	16.40	1.280	0.6603	0.3798	0.0973	18.82
120.2	16.37	1.279	0.6585	0.3789	0.0971	18.79
120.3	16.35	1.278	0.6567	0.3779	0.0969	18.76
120.4	16.32	1.277	0.6549	0.3769	0.0966	18.73
120.5	16.29	1.275	0.6533	0.3759	0.0964	18.69
120.6	16.27	1.272	0.6514	0.3749	0.0961	18.66
120.7	16.24	1.272	0.6496	0.3739	0.0959	18.63
120.8	16.21	1.272	0.6479	0.3730	0.0957	18.60
120.9	16.18	1.269	0.6463	0.3720	0.0954	18.57
121.0	16.16	1.269	0.6448	0.3711	0.0952	18.54
121.1	16.13	1.268	0.6430	0.3702	0.0950	18.51
121.2	16.10	1.267	0.6412	0.3692	0.0947	18.48
121.3	16.08	1.266	0.6397	0.3682	0.0945	18.45
121.4	16.05	1.265	0.6379	0.3673	0.0943	18.42
121.5	16.02	1.263	0.6363	0.3664	0.0940	18.38
121.6	16.00	1.262	0.6339	0.3655	0.0938	18.35
121.7	15.97	1.260	0.6324	0.3645	0.0936	18.32
121.8	15.94	1.259	0.6307	0.3636	0.0933	18.29
121.9	15.92	1.256	0.6288	0.3626	0.0931	18.26
122.0	15.89	1.257	0.6268	0.3618	0.0929	18.23
122.1	15.87	1.256	0.6251	0.3609	0.0927	18.20
122.2	15.84	1.253	0.6236	0.3599	0.0924	18.17
122.3	15.81	1.253	0.6218	0.3590	0.0922	18.14
122.4	15.79	1.252	0.6202	0.3580	0.0920	18.11
122.5	15.76	1.251	0.6185	0.3571	0.0918	18.08
122.6	15.74	1.251	0.6168	0.3562	0.0915	18.05
122.7	15.71	1.247	0.6153	0.3552	0.0913	18.02
122.8	15.68	1.249	0.6134	0.3542	0.0911	17.99
122.9	15.66	1.248	0.6116	0.3535	0.0909	17.96
123.0	15.63	1.246	0.6100	0.3525	0.0906	17.93
123.1	15.61	1.245	0.6084	0.3516	0.0904	17.90
123.2	15.58	1.242	0.6069	0.3508	0.0902	17.87
123.3	15.56	1.242	0.6050	0.3498	0.0900	17.84
123.4	15.53	1.241	0.6035	0.3490	0.0898	17.81
123.5	15.51	1.241	0.6021	0.3480	0.0895	17.79
123.6	15.48	1.239	0.6003	0.3471	0.0893	17.76
123.7	15.46	1.237	0.5990	0.3462	0.0891	17.73
123.8	15.43	1.236	0.5976	0.3454	0.0889	17.70
123.9	15.40	1.236	0.5959	0.3445	0.0887	17.67
124.0	15.38	1.234	0.5944	0.3436	0.0884	17.64
124.1	15.35	1.234	0.5926	0.3427	0.0882	17.61
124.2	15.33	1.231	0.5909	0.3419	0.0880	17.58
124.3	15.31	1.231	0.5894	0.3411	0.0878	17.55

Table B.67: SM Higgs-boson production cross sections at $\sqrt{s} = 7$ TeV: light Higgs boson.

$M_{\rm H}$ [GeV]	ggF σ [pb]	VBF σ [pb]	WH σ [pb]	ZH σ [pb]	ttH σ [pb]	Total σ [pb]
124.4	15.28	1.228	0.5877	0.3402	0.0876	17.52
124.5	15.26	1.227	0.5858	0.3393	0.0874	17.50
124.6	15.23	1.228	0.5844	0.3384	0.0872	17.47
124.7	15.21	1.225	0.5829	0.3376	0.0870	17.44
124.8	15.18	1.225	0.5812	0.3368	0.0867	17.41
124.9	15.16	1.226	0.5798	0.3359	0.0865	17.39
125.0	15.13	1.222	0.5785	0.3351	0.0863	17.35
125.1	15.11	1.222	0.5770	0.3341	0.0861	17.33
125.2	15.08	1.221	0.5751	0.3333	0.0859	17.30
125.3	15.06	1.219	0.5736	0.3325	0.0857	17.27
125.4	15.04	1.219	0.5718	0.3317	0.0855	17.24
125.5	15.01	1.219	0.5703	0.3309	0.0853	17.22
125.6	14.99	1.214	0.5688	0.3299	0.0851	17.18
125.7	14.96	1.215	0.5673	0.3291	0.0849	17.16
125.8	14.94	1.213	0.5660	0.3283	0.0847	17.13
125.9	14.91	1.213	0.5643	0.3275	0.0845	17.10
126.0	14.89	1.211	0.5629	0.3267	0.0843	17.08
126.1	14.87	1.209	0.5612	0.3258	0.0841	17.05
126.2	14.84	1.210	0.5599	0.3250	0.0839	17.02
126.3	14.82	1.208	0.5585	0.3243	0.0837	16.99
126.4	14.80	1.207	0.5569	0.3235	0.0835	16.97
126.5	14.77	1.206	0.5555	0.3227	0.0833	16.94
126.6	14.75	1.206	0.5539	0.3219	0.0831	16.91
126.7	14.73	1.203	0.5523	0.3210	0.0829	16.88
126.8	14.70	1.202	0.5508	0.3201	0.0827	16.86
126.9	14.68	1.202	0.5492	0.3192	0.0825	16.83
127.0	14.65	1.199	0.5476	0.3184	0.0823	16.80
127.1	14.63	1.199	0.5463	0.3175	0.0821	16.78
127.2	14.61	1.198	0.5449	0.3169	0.0819	16.75
127.3	14.59	1.197	0.5434	0.3161	0.0817	16.72
127.4	14.56	1.196	0.5420	0.3153	0.0815	16.70
127.5	14.54	1.194	0.5406	0.3145	0.0813	16.67
127.6	14.52	1.194	0.5389	0.3137	0.0811	16.64
127.7	14.49	1.194	0.5373	0.3129	0.0809	16.62
127.8	14.47	1.192	0.5361	0.3122	0.0807	16.59
127.9	14.45	1.190	0.5348	0.3114	0.0805	16.56
128.0	14.42	1.187	0.5332	0.3106	0.0803	16.54
128.1	14.40	1.189	0.5319	0.3099	0.0801	16.51
128.2	14.38	1.187	0.5303	0.3090	0.0799	16.48
128.3	14.36	1.187	0.5288	0.3083	0.0798	16.46
128.4	14.33	1.186	0.5275	0.3075	0.0796	16.43
128.5	14.31	1.184	0.5258	0.3068	0.0794	16.41
128.6	14.29	1.183	0.5245	0.3060	0.0792	16.38
128.7	14.27	1.183	0.5233	0.3054	0.0790	16.36
128.8	14.24	1.181	0.5219	0.3046	0.0788	16.33
128.9	14.22	1.178	0.5204	0.3039	0.0786	16.30
129.0	14.20	1.178	0.5189	0.3031	0.0784	16.28

Table B.68: SM Higgs-boson production cross sections at $\sqrt{s} = 7$ TeV: light Higgs boson.

M_H [GeV]	ggF σ [pb]	VBF σ [pb]	WH σ [pb]	ZH σ [pb]	ttH σ [pb]	Total σ [pb]
129.1	14.18	1.178	0.5176	0.3023	0.0783	16.25
129.2	14.15	1.177	0.5164	0.3017	0.0781	16.23
129.3	14.13	1.175	0.5150	0.3010	0.0779	16.20
129.4	14.11	1.174	0.5137	0.3002	0.0777	16.18
129.5	14.09	1.173	0.5122	0.2994	0.0775	16.15
129.6	14.07	1.173	0.5112	0.2986	0.0773	16.13
129.7	14.04	1.171	0.5096	0.2979	0.0772	16.10
129.8	14.02	1.170	0.5084	0.2972	0.0770	16.07
129.9	14.00	1.169	0.5072	0.2965	0.0768	16.05
130.0	13.98	1.168	0.5059	0.2957	0.0766	16.02
130.5	13.87	1.161	0.4989	0.2920	0.0757	15.90
131.0	13.76	1.157	0.4922	0.2883	0.0748	15.77
131.5	13.66	1.152	0.4858	0.2848	0.0739	15.65
132.0	13.55	1.147	0.4795	0.2813	0.0731	15.53
132.5	13.45	1.142	0.4730	0.2780	0.0722	15.41
133.0	13.35	1.136	0.4668	0.2746	0.0714	15.30
133.5	13.24	1.133	0.4608	0.2712	0.0706	15.18
134.0	13.14	1.127	0.4549	0.2680	0.0698	15.06
134.5	13.05	1.121	0.4491	0.2647	0.0690	14.95
135.0	12.95	1.117	0.4431	0.2616	0.0682	14.84
135.5	12.85	1.112	0.4374	0.2585	0.0674	14.73
136.0	12.75	1.107	0.4318	0.2555	0.0666	14.62
136.5	12.66	1.103	0.4261	0.2525	0.0658	14.51
137.0	12.57	1.097	0.4207	0.2495	0.0651	14.40
137.5	12.47	1.092	0.4152	0.2464	0.0644	14.29
138.0	12.38	1.087	0.4098	0.2436	0.0636	14.18
138.5	12.29	1.082	0.4046	0.2406	0.0629	14.08
139.0	12.20	1.078	0.3996	0.2377	0.0622	13.98
139.5	12.11	1.074	0.3945	0.2350	0.0615	13.87
140.0	12.02	1.069	0.3896	0.2322	0.0608	13.77
140.5	11.93	1.063	0.3846	0.2294	0.0601	13.67
141.0	11.89	1.059	0.3799	0.2269	0.0594	13.62
141.5	11.81	1.055	0.3752	0.2243	0.0588	13.52
142.0	11.73	1.050	0.3704	0.2216	0.0581	13.43
142.5	11.64	1.046	0.3658	0.2190	0.0574	13.33
143.0	11.56	1.040	0.3611	0.2165	0.0568	13.24
143.5	11.48	1.037	0.3567	0.2142	0.0562	13.15
144.0	11.40	1.032	0.3524	0.2117	0.0555	13.05
144.5	11.32	1.028	0.3480	0.2091	0.0549	12.96
145.0	11.24	1.023	0.3437	0.2068	0.0543	12.87
145.5	11.17	1.019	0.3394	0.2042	0.0537	12.78
146.0	11.09	1.015	0.3351	0.2019	0.0531	12.70
146.5	11.02	1.010	0.3310	0.1996	0.0525	12.61
147.0	10.94	1.005	0.3269	0.1973	0.0520	12.52
147.5	10.87	1.002	0.3228	0.1951	0.0514	12.44
148.0	10.80	0.9980	0.3190	0.1928	0.0508	12.36
148.5	10.72	0.9930	0.3149	0.1906	0.0503	12.27

Table B.69: SM Higgs-boson production cross sections at $\sqrt{s} = 7$ TeV: light Higgs boson.

M_{H} [GeV]	ggF σ [pb]	VBF σ [pb]	WH σ [pb]	ZH σ [pb]	ttH σ [pb]	Total σ [pb]
149.0	10.65	0.9880	0.3109	0.1884	0.0497	12.19
149.5	10.58	0.9850	0.3071	0.1862	0.0492	12.11
150.0	10.51	0.9800	0.3034	0.1842	0.0487	12.02
152.0	10.24	0.9640	0.2883	0.1758	0.0466	11.71
154.0	9.978	0.9487	0.2742	0.1680	0.0447	11.41
156.0	9.723	0.9339	0.2597	0.1599	0.0429	11.12
158.0	9.473	0.9199	0.2452	0.1518	0.0411	10.83
160.0	9.223	0.9043	0.2316	0.1442	0.0394	10.54
162.0	8.930	0.8906	0.2241	0.1397	0.0378	10.22
164.0	8.586	0.8755	0.2168	0.1354	0.0363	9.850
165.0	8.434	0.8694	0.2133	0.1334	0.0356	9.686
166.0	8.292	0.8613	0.2085	0.1305	0.0349	9.528
168.0	8.029	0.8473	0.1994	0.1252	0.0335	9.234
170.0	7.801	0.8338	0.1908	0.1200	0.0322	8.977
172.0	7.585	0.8201	0.1826	0.1151	0.0309	8.734
174.0	7.385	0.8063	0.1748	0.1103	0.0297	8.506
175.0	7.291	0.7998	0.1709	0.1080	0.0292	8.399
176.0	7.199	0.7934	0.1674	0.1056	0.0286	8.294
178.0	7.026	0.7809	0.1605	0.1012	0.0275	8.096
180.0	6.856	0.7684	0.1538	0.0969	0.0265	7.901
182.0	6.677	0.7561	0.1482	0.0934	0.0255	7.700
184.0	6.477	0.7433	0.1427	0.0900	0.0246	7.478
185.0	6.384	0.7375	0.1401	0.0884	0.0242	7.374
186.0	6.292	0.7314	0.1374	0.0867	0.0237	7.271
188.0	6.124	0.7195	0.1320	0.0834	0.0229	7.081
190.0	5.971	0.7080	0.1269	0.0803	0.0221	6.908
192.0	5.823	0.6960	0.1220	0.0773	0.0213	6.740
194.0	5.684	0.6845	0.1173	0.0744	0.0205	6.581
195.0	5.614	0.6790	0.1151	0.0731	0.0202	6.501
196.0	5.547	0.6735	0.1129	0.0717	0.0198	6.425
198.0	5.441	0.6629	0.1086	0.0691	0.0191	6.301
200.0	5.356	0.6524	0.1045	0.0665	0.0185	6.198
202.0	5.242	0.6429	0.1006	0.0641	0.0179	6.068
204.0	5.169	0.6343	0.0969	0.0618	0.0173	5.979
206.0	5.078	0.6262	0.0933	0.0595	0.0167	5.874
208.0	4.982	0.6184	0.0899	0.0573	0.0161	5.764
210.0	4.895	0.6108	0.0867	0.0553	0.0156	5.663
212.0	4.806	0.6033	0.0836	0.0533	0.0151	5.561
214.0	4.731	0.5955	0.0806	0.0514	0.0146	5.473
216.0	4.668	0.5879	0.0777	0.0496	0.0142	5.397
218.0	4.581	0.5802	0.0750	0.0478	0.0137	5.298
220.0	4.502	0.5724	0.0724	0.0461	0.0133	5.206
222.0	4.424	0.5646	0.0699	0.0445	0.0129	5.116
224.0	4.357	0.5570	0.0675	0.0429	0.0125	5.037
226.0	4.299	0.5493	0.0651	0.0414	0.0121	4.967
228.0	4.224	0.5416	0.0629	0.0400	0.0118	4.880
230.0	4.157	0.5341	0.0608	0.0386	0.0114	4.802

Table B.70: SM Higgs-boson production cross sections at $\sqrt{s} = 7$ TeV: light Higgs boson.

$M_{\rm H}$ [GeV]	ggF σ [pb]	VBF σ [pb]	WH σ [pb]	ZH σ [pb]	ttH σ [pb]	Total σ [pb]
232.0	4.094	0.5266	0.0588	0.0373	0.0111	4.728
234.0	4.036	0.5190	0.0568	0.0360	0.0108	4.658
236.0	3.971	0.5114	0.0550	0.0348	0.0105	4.582
238.0	3.904	0.5038	0.0531	0.0336	0.0102	4.505
240.0	3.835	0.4959	0.0514	0.0325	0.0099	4.425
242.0	3.771	0.4882	0.0497	0.0314	0.0096	4.350
244.0	3.709	0.4807	0.0481	0.0303	0.0093	4.278
246.0	3.651	0.4733	0.0466	0.0293	0.0091	4.209
248.0	3.596	0.4659	0.0451	0.0283	0.0088	4.144
250.0	3.540	0.4588	0.0437	0.0274	0.0086	4.078
252.0	3.486	0.4519	0.0423	0.0265	0.0084	4.015
254.0	3.434	0.4452	0.0410	0.0256	0.0081	3.954
256.0	3.383	0.4385	0.0397	0.0248	0.0079	3.894
258.0	3.335	0.4320	0.0384	0.0240	0.0077	3.837
260.0	3.288	0.4256	0.0372	0.0232	0.0075	3.782
262.0	3.243	0.4193	0.0361	0.0224	0.0073	3.728
264.0	3.199	0.4131	0.0350	0.0217	0.0072	3.676
266.0	3.155	0.4069	0.0339	0.0210	0.0070	3.624
268.0	3.113	0.4010	0.0329	0.0203	0.0068	3.574
270.0	3.072	0.3951	0.0319	0.0197	0.0066	3.525
272.0	3.033	0.3894	0.0310	0.0191	0.0065	3.479
274.0	2.996	0.3837	0.0300	0.0185	0.0063	3.434
276.0	2.959	0.3783	0.0291	0.0179	0.0062	3.391
278.0	2.924	0.3729	0.0283	0.0173	0.0060	3.348
280.0	2.889	0.3676	0.0274	0.0168	0.0059	3.307
282.0	2.856	0.3623	0.0266	0.0163	0.0058	3.267
284.0	2.824	0.3572	0.0258	0.0158	0.0056	3.228
286.0	2.794	0.3521	0.0251	0.0153	0.0055	3.192
288.0	2.764	0.3471	0.0244	0.0149	0.0054	3.156
290.0	2.736	0.3422	0.0237	0.0144	0.0053	3.121
292.0	2.708	0.3408	0.0230	0.0140	0.0051	3.091
294.0	2.681	0.3394	0.0223	0.0136	0.0050	3.062
296.0	2.656	0.3379	0.0217	0.0132	0.0049	3.033
298.0	2.632	0.3365	0.0211	0.0128	0.0048	3.007
300.0	2.608	0.3350	0.0205	0.0124	0.0047	2.981
305.0	2.555	0.3237	0.0191	0.0115	0.0045	2.914
310.0	2.510	0.3130	0.0178	0.0107	0.0043	2.855
315.0	2.470	0.3028	0.0166	0.0099	0.0040	2.804
320.0	2.436	0.2929	0.0155	0.0092	0.0039	2.757
325.0	2.411	0.2834	0.0145	0.0086	0.0037	2.722
330.0	2.397	0.2745	0.0135	0.0080	0.0035	2.696
335.0	2.392	0.2661	0.0126	0.0075	0.0033	2.682
340.0	2.402	0.2585	0.0118	0.0070	0.0032	2.682
345.0	2.426	0.2519	0.0110	0.0065	0.0031	2.698
350.0	2.423	0.2380	0.0103	0.0060	0.0029	2.680
360.0	2.404	0.2142	0.0091	0.0053	0.0027	2.635
370.0	2.359	0.2039	0.0081	0.0047	0.0025	2.578
380.0	2.280	0.1949	0.0072	0.0042	0.0023	2.488
390.0	2.172	0.1859	0.0065	0.0038	0.0021	2.371
400.0	2.047	0.1772	0.0058	0.0034	0.0019	2.235

Table B.71: SM Higgs-boson production cross sections at $\sqrt{s} = 7$ TeV: heavy Higgs boson.

M_H [GeV]	ggF σ [pb]	VBF σ [pb]	Total σ [pb]
420.0	1.775	0.1601	1.935
440.0	1.506	0.1442	1.651
450.0	1.380	0.1368	1.517
460.0	1.262	0.1296	1.392
480.0	1.050	0.1164	1.166
500.0	0.8704	0.1046	0.9750
520.0	0.7208	0.0940	0.8148
540.0	0.5974	0.0846	0.6820
550.0	0.5441	0.0803	0.6244
560.0	0.4958	0.0763	0.5721
580.0	0.4126	0.0689	0.4815
600.0	0.3445	0.0624	0.4069
620.0	0.2884	0.0567	0.3451
640.0	0.2422	0.0515	0.2937
650.0	0.2224	0.0492	0.2716
660.0	0.2043	0.0469	0.2512
680.0	0.1729	0.0429	0.2158
700.0	0.1469	0.0392	0.1861
720.0	0.1253	0.0360	0.1613
740.0	0.1072	0.0330	0.1402
750.0	0.0993	0.0317	0.1310
760.0	0.0920	0.0304	0.1224
780.0	0.0794	0.0281	0.1075
800.0	0.0687	0.0260	0.0947
820.0	0.0596	0.0241	0.0837
840.0	0.0519	0.0224	0.0743
850.0	0.0485	0.0216	0.0701
860.0	0.0454	0.0208	0.0662
880.0	0.0398	0.0194	0.0592
900.0	0.0350	0.0181	0.0531
920.0	0.0309	0.0170	0.0479
940.0	0.0273	0.0159	0.0432
950.0	0.0257	0.0154	0.0411
960.0	0.0242	0.0149	0.0391
980.0	0.0216	0.0140	0.0356
1000.0	0.0192	0.0132	0.0324

Table B.72: SM Higgs-boson production cross sections at $\sqrt{s} = 8$ TeV: light Higgs boson.

M_{H} [GeV]	ggF σ [pb]	VBF σ [pb]	WH σ [pb]	ZH σ [pb]	ttH σ [pb]	Total σ [pb]
80.0	45.37	2.424	2.808	1.508	0.4277	52.54
81.0	44.31	2.399	2.711	1.459	0.4152	51.29
82.0	43.28	2.364	2.619	1.411	0.4032	50.08
83.0	42.29	2.346	2.528	1.366	0.3915	48.92
84.0	41.33	2.326	2.442	1.321	0.3803	47.80
85.0	40.41	2.300	2.359	1.281	0.3694	46.72
86.0	39.52	2.283	2.279	1.238	0.3589	45.68
87.0	38.66	2.258	2.203	1.200	0.3487	44.67
88.0	37.83	2.240	2.129	1.163	0.3389	43.70
89.0	37.02	2.209	2.058	1.126	0.3294	42.74
90.0	36.23	2.191	1.990	1.092	0.3202	41.82
91.0	35.49	2.170	1.929	1.059	0.3113	40.95
92.0	34.75	2.153	1.866	1.028	0.3027	40.10
93.0	34.04	2.129	1.806	0.9965	0.2944	39.27
94.0	33.36	2.108	1.749	0.9670	0.2864	38.47
95.0	32.69	2.084	1.695	0.9383	0.2786	37.68
96.0	32.04	2.068	1.641	0.9109	0.2711	36.93
97.0	31.41	2.046	1.589	0.8840	0.2638	36.19
98.0	30.80	2.027	1.540	0.8592	0.2567	35.48
99.0	30.21	2.004	1.495	0.8340	0.2499	34.79
100.0	29.68	1.988	1.447	0.8102	0.2433	34.17
101.0	29.12	1.967	1.403	0.7876	0.2369	33.51
102.0	28.57	1.945	1.360	0.7650	0.2308	32.87
103.0	28.04	1.933	1.319	0.7436	0.2248	32.26
104.0	27.52	1.914	1.280	0.7226	0.2190	31.66
105.0	27.01	1.897	1.242	0.7022	0.2133	31.06
106.0	26.52	1.877	1.204	0.6833	0.2077	30.49
107.0	26.05	1.862	1.169	0.6646	0.2023	29.95
108.0	25.59	1.841	1.135	0.6469	0.1971	29.41
109.0	25.14	1.826	1.103	0.6296	0.1920	28.89
110.0	24.70	1.809	1.071	0.6125	0.1871	28.38
110.5	24.48	1.799	1.056	0.6040	0.1847	28.13
111.0	24.27	1.791	1.040	0.5960	0.1824	27.88
111.5	24.06	1.784	1.026	0.5880	0.1801	27.64
112.0	23.85	1.780	1.010	0.5803	0.1779	27.40
112.5	23.64	1.771	0.9959	0.5725	0.1757	27.16
113.0	23.44	1.764	0.9813	0.5646	0.1735	26.93
113.5	23.24	1.753	0.9676	0.5573	0.1713	26.69
114.0	23.05	1.743	0.9535	0.5501	0.1692	26.46
114.5	22.85	1.735	0.9395	0.5427	0.1671	26.23
115.0	22.66	1.729	0.9266	0.5358	0.1651	26.02
115.5	22.47	1.719	0.9135	0.5286	0.1630	25.79
116.0	22.28	1.714	0.9002	0.5218	0.1610	25.58
116.5	22.10	1.704	0.8880	0.5152	0.1590	25.36
117.0	21.91	1.699	0.8758	0.5083	0.1571	25.15
117.5	21.73	1.688	0.8642	0.5020	0.1552	24.94
118.0	21.55	1.683	0.8515	0.4956	0.1533	24.74

Table B.73: SM Higgs-boson production cross sections at $\sqrt{s} = 8$ TeV: light Higgs boson.

M_{H} [GeV]	ggF σ [pb]	VBF σ [pb]	WH σ [pb]	ZH σ [pb]	ttH σ [pb]	Total σ [pb]
118.5	21.38	1.675	0.8403	0.4893	0.1514	24.53
119.0	21.20	1.666	0.8284	0.4829	0.1495	24.33
119.5	21.03	1.659	0.8170	0.4772	0.1477	24.13
120.0	20.86	1.649	0.8052	0.4710	0.1459	23.93
120.1	20.83	1.650	0.8034	0.4698	0.1456	23.90
120.2	20.80	1.648	0.8009	0.4685	0.1452	23.86
120.3	20.76	1.646	0.7992	0.4675	0.1449	23.82
120.4	20.73	1.647	0.7967	0.4661	0.1445	23.78
120.5	20.69	1.643	0.7946	0.4648	0.1441	23.74
120.6	20.66	1.645	0.7928	0.4636	0.1438	23.71
120.7	20.63	1.643	0.7902	0.4625	0.1434	23.67
120.8	20.59	1.638	0.7881	0.4613	0.1431	23.63
120.9	20.56	1.638	0.7863	0.4601	0.1427	23.59
121.0	20.53	1.636	0.7844	0.4589	0.1424	23.55
121.1	20.50	1.634	0.7825	0.4580	0.1420	23.51
121.2	20.46	1.634	0.7802	0.4567	0.1417	23.48
121.3	20.43	1.634	0.7782	0.4556	0.1414	23.44
121.4	20.40	1.633	0.7758	0.4545	0.1410	23.40
121.5	20.36	1.631	0.7737	0.4535	0.1407	23.36
121.6	20.33	1.628	0.7713	0.4522	0.1403	23.32
121.7	20.30	1.627	0.7697	0.4509	0.1400	23.29
121.8	20.27	1.627	0.7675	0.4498	0.1396	23.25
121.9	20.23	1.627	0.7653	0.4488	0.1393	23.22
122.0	20.20	1.623	0.7631	0.4478	0.1390	23.18
122.1	20.17	1.622	0.7612	0.4468	0.1386	23.14
122.2	20.14	1.621	0.7589	0.4457	0.1383	23.10
122.3	20.11	1.622	0.7573	0.4444	0.1380	23.07
122.4	20.07	1.618	0.7555	0.4434	0.1376	23.03
122.5	20.04	1.615	0.7533	0.4421	0.1373	22.99
122.6	20.01	1.614	0.7510	0.4409	0.1370	22.95
122.7	19.98	1.614	0.7493	0.4396	0.1366	22.92
122.8	19.95	1.611	0.7475	0.4385	0.1363	22.88
122.9	19.92	1.609	0.7453	0.4376	0.1360	22.84
123.0	19.88	1.608	0.7434	0.4366	0.1356	22.81
123.1	19.85	1.606	0.7414	0.4356	0.1353	22.77
123.2	19.82	1.605	0.7393	0.4346	0.1350	22.73
123.3	19.79	1.603	0.7374	0.4335	0.1347	22.70
123.4	19.76	1.603	0.7352	0.4325	0.1343	22.66
123.5	19.73	1.598	0.7334	0.4311	0.1340	22.62
123.6	19.70	1.603	0.7317	0.4301	0.1337	22.59
123.7	19.67	1.600	0.7294	0.4292	0.1334	22.56
123.8	19.63	1.598	0.7277	0.4280	0.1330	22.52
123.9	19.60	1.596	0.7259	0.4271	0.1327	22.48
124.0	19.57	1.595	0.7239	0.4260	0.1324	22.45
124.1	19.54	1.591	0.7218	0.4249	0.1321	22.41
124.2	19.51	1.591	0.7201	0.4238	0.1318	22.38
124.3	19.48	1.590	0.7181	0.4228	0.1314	22.34

Table B.74: SM Higgs-boson production cross sections at $\sqrt{s} = 8$ TeV: light Higgs boson.

$M_{\rm H}$ [GeV]	ggF σ [pb]	VBF σ [pb]	WH σ [pb]	ZH σ [pb]	ttH σ [pb]	Total σ [pb]
124.4	19.45	1.589	0.7159	0.4217	0.1311	22.31
124.5	19.42	1.587	0.7143	0.4206	0.1308	22.27
124.6	19.39	1.586	0.7125	0.4194	0.1305	22.24
124.7	19.36	1.590	0.7105	0.4185	0.1302	22.21
124.8	19.33	1.584	0.7086	0.4174	0.1299	22.17
124.9	19.30	1.582	0.7065	0.4164	0.1296	22.13
125.0	19.27	1.578	0.7046	0.4153	0.1293	22.10
125.1	19.24	1.579	0.7027	0.4142	0.1290	22.06
125.2	19.21	1.576	0.7005	0.4133	0.1286	22.03
125.3	19.18	1.576	0.6988	0.4123	0.1283	21.99
125.4	19.15	1.573	0.6970	0.4112	0.1280	21.96
125.5	19.12	1.573	0.6951	0.4102	0.1277	21.92
125.6	19.09	1.572	0.6931	0.4091	0.1274	21.89
125.7	19.06	1.570	0.6913	0.4082	0.1271	21.86
125.8	19.03	1.568	0.6895	0.4070	0.1268	21.82
125.9	19.00	1.568	0.6878	0.4061	0.1265	21.79
126.0	18.97	1.568	0.6860	0.4050	0.1262	21.76
126.1	18.94	1.565	0.6838	0.4042	0.1259	21.72
126.2	18.91	1.565	0.6818	0.4030	0.1256	21.69
126.3	18.88	1.564	0.6802	0.4020	0.1253	21.65
126.4	18.85	1.561	0.6784	0.4010	0.1250	21.62
126.5	18.82	1.558	0.6767	0.4000	0.1247	21.58
126.6	18.80	1.560	0.6747	0.3990	0.1245	21.55
126.7	18.77	1.557	0.6731	0.3980	0.1242	21.52
126.8	18.74	1.555	0.6711	0.3970	0.1239	21.48
126.9	18.71	1.554	0.6693	0.3962	0.1236	21.45
127.0	18.68	1.552	0.6676	0.3953	0.1233	21.42
127.1	18.65	1.548	0.6658	0.3943	0.1230	21.38
127.2	18.62	1.548	0.6640	0.3932	0.1227	21.35
127.3	18.59	1.549	0.6623	0.3921	0.1224	21.32
127.4	18.57	1.547	0.6605	0.3912	0.1221	21.29
127.5	18.54	1.543	0.6588	0.3901	0.1218	21.25
127.6	18.51	1.545	0.6572	0.3892	0.1216	21.22
127.7	18.48	1.544	0.6553	0.3883	0.1213	21.19
127.8	18.45	1.541	0.6535	0.3874	0.1210	21.16
127.9	18.42	1.541	0.6518	0.3863	0.1207	21.12
128.0	18.40	1.540	0.6501	0.3856	0.1204	21.09
128.1	18.37	1.537	0.6485	0.3847	0.1201	21.06
128.2	18.34	1.536	0.6470	0.3838	0.1199	21.03
128.3	18.31	1.535	0.6448	0.3830	0.1196	20.99
128.4	18.28	1.533	0.6430	0.3819	0.1193	20.96
128.5	18.26	1.531	0.6415	0.3809	0.1190	20.93
128.6	18.23	1.531	0.6398	0.3799	0.1187	20.90
128.7	18.20	1.529	0.6380	0.3790	0.1185	20.87
128.8	18.17	1.529	0.6364	0.3780	0.1182	20.83
128.9	18.15	1.527	0.6344	0.3770	0.1179	20.80
129.0	18.12	1.525	0.6329	0.3762	0.1176	20.77

Table B.75: SM Higgs-boson production cross sections at $\sqrt{s} = 8$ TeV: light Higgs boson.

M_H [GeV]	ggF σ [pb]	VBF σ [pb]	WH σ [pb]	ZH σ [pb]	ttH σ [pb]	Total σ [pb]
129.1	18.09	1.526	0.6310	0.3751	0.1174	20.74
129.2	18.06	1.523	0.6294	0.3741	0.1171	20.71
129.3	18.04	1.522	0.6278	0.3731	0.1168	20.68
129.4	18.01	1.523	0.6264	0.3723	0.1166	20.65
129.5	17.98	1.513	0.6247	0.3714	0.1163	20.61
129.6	17.95	1.516	0.6233	0.3705	0.1160	20.58
129.7	17.93	1.517	0.6216	0.3696	0.1157	20.55
129.8	17.90	1.515	0.6201	0.3688	0.1155	20.52
129.9	17.87	1.515	0.6185	0.3679	0.1152	20.49
130.0	17.85	1.511	0.6169	0.3671	0.1149	20.46
130.5	17.71	1.504	0.6085	0.3626	0.1136	20.30
131.0	17.58	1.497	0.6005	0.3583	0.1123	20.15
131.5	17.45	1.492	0.5929	0.3539	0.1110	20.00
132.0	17.32	1.485	0.5856	0.3498	0.1097	19.85
132.5	17.19	1.479	0.5778	0.3457	0.1085	19.70
133.0	17.07	1.473	0.5703	0.3418	0.1072	19.56
133.5	16.94	1.466	0.5632	0.3376	0.1060	19.41
134.0	16.82	1.462	0.5556	0.3337	0.1048	19.27
134.5	16.69	1.455	0.5487	0.3297	0.1036	19.13
135.0	16.57	1.448	0.5416	0.3259	0.1024	18.99
135.5	16.45	1.444	0.5347	0.3221	0.1013	18.85
136.0	16.33	1.436	0.5277	0.3184	0.1001	18.71
136.5	16.22	1.429	0.5210	0.3145	0.0990	18.58
137.0	16.10	1.423	0.5145	0.3109	0.0979	18.44
137.5	15.98	1.417	0.5080	0.3073	0.0968	18.31
138.0	15.87	1.412	0.5018	0.3036	0.0957	18.18
138.5	15.76	1.407	0.4955	0.3003	0.0946	18.05
139.0	15.64	1.400	0.4890	0.2966	0.0936	17.92
139.5	15.53	1.396	0.4829	0.2933	0.0925	17.80
140.0	15.42	1.389	0.4768	0.2898	0.0915	17.67
140.5	15.32	1.384	0.4709	0.2865	0.0905	17.55
141.0	15.27	1.377	0.4651	0.2831	0.0895	17.48
141.5	15.16	1.372	0.4596	0.2799	0.0885	17.36
142.0	15.06	1.365	0.4540	0.2769	0.0875	17.24
142.5	14.96	1.361	0.4484	0.2736	0.0866	17.13
143.0	14.86	1.354	0.4426	0.2705	0.0856	17.01
143.5	14.76	1.350	0.4376	0.2674	0.0847	16.90
144.0	14.66	1.344	0.4320	0.2644	0.0838	16.78
144.5	14.56	1.337	0.4266	0.2613	0.0829	16.67
145.0	14.46	1.333	0.4216	0.2583	0.0820	16.56
145.5	14.37	1.327	0.4164	0.2554	0.0811	16.45
146.0	14.27	1.321	0.4112	0.2527	0.0802	16.34
146.5	14.18	1.317	0.4061	0.2497	0.0794	16.23
147.0	14.09	1.311	0.4014	0.2469	0.0785	16.13
147.5	14.00	1.307	0.3962	0.2442	0.0777	16.02
148.0	13.91	1.302	0.3913	0.2415	0.0768	15.92
148.5	13.82	1.296	0.3868	0.2387	0.0760	15.82

Table B.76: SM Higgs-boson production cross sections at $\sqrt{s} = 8$ TeV: light Higgs boson.

M_{H} [GeV]	ggF σ [pb]	VBF σ [pb]	WH σ [pb]	ZH σ [pb]	ttH σ [pb]	Total σ [pb]
149.0	13.73	1.291	0.3821	0.2361	0.0752	15.71
149.5	13.64	1.285	0.3774	0.2334	0.0744	15.61
150.0	13.55	1.280	0.3728	0.2308	0.0736	15.51
152.0	13.22	1.259	0.3546	0.2207	0.0705	15.12
154.0	12.89	1.240	0.3376	0.2109	0.0676	14.75
156.0	12.58	1.222	0.3202	0.2010	0.0649	14.39
158.0	12.27	1.204	0.3024	0.1911	0.0623	14.03
160.0	11.96	1.185	0.2855	0.1816	0.0598	13.67
162.0	11.60	1.171	0.2763	0.1762	0.0574	13.28
164.0	11.17	1.152	0.2675	0.1708	0.0552	12.81
165.0	10.97	1.141	0.2630	0.1683	0.0541	12.60
166.0	10.79	1.132	0.2575	0.1649	0.0530	12.40
168.0	10.46	1.114	0.2466	0.1582	0.0510	12.03
170.0	10.17	1.098	0.2362	0.1518	0.0490	11.70
172.0	9.897	1.080	0.2261	0.1457	0.0472	11.40
174.0	9.645	1.062	0.2165	0.1398	0.0454	11.11
175.0	9.526	1.055	0.2118	0.1369	0.0446	10.97
176.0	9.410	1.047	0.2076	0.1340	0.0438	10.84
178.0	9.194	1.031	0.1991	0.1284	0.0422	10.59
180.0	8.980	1.015	0.1911	0.1231	0.0406	10.35
182.0	8.755	0.9980	0.1841	0.1187	0.0391	10.09
184.0	8.501	0.9830	0.1774	0.1145	0.0377	9.814
185.0	8.383	0.9760	0.1741	0.1125	0.0370	9.682
186.0	8.266	0.9690	0.1707	0.1103	0.0364	9.552
188.0	8.053	0.9536	0.1642	0.1062	0.0351	9.312
190.0	7.858	0.9387	0.1579	0.1022	0.0339	9.091
192.0	7.671	0.9238	0.1520	0.0985	0.0327	8.878
194.0	7.494	0.9090	0.1464	0.0949	0.0316	8.676
195.0	7.405	0.9018	0.1436	0.0931	0.0311	8.575
196.0	7.320	0.8953	0.1409	0.0915	0.0306	8.478
198.0	7.187	0.8819	0.1356	0.0881	0.0296	8.322
200.0	7.081	0.8685	0.1305	0.0849	0.0286	8.193
202.0	6.937	0.8568	0.1257	0.0819	0.0277	8.029
204.0	6.846	0.8456	0.1211	0.0790	0.0268	7.918
206.0	6.731	0.8356	0.1168	0.0761	0.0259	7.785
208.0	6.609	0.8259	0.1127	0.0734	0.0251	7.646
210.0	6.500	0.8163	0.1087	0.0708	0.0243	7.520
212.0	6.387	0.8067	0.1048	0.0683	0.0235	7.390
214.0	6.293	0.7970	0.1011	0.0659	0.0228	7.279
216.0	6.214	0.7873	0.0976	0.0637	0.0221	7.185
218.0	6.104	0.7776	0.0943	0.0615	0.0214	7.059
220.0	6.003	0.7677	0.0910	0.0593	0.0208	6.942
222.0	5.905	0.7579	0.0879	0.0573	0.0202	6.828
224.0	5.821	0.7481	0.0850	0.0553	0.0196	6.729
226.0	5.748	0.7381	0.0821	0.0534	0.0190	6.641
228.0	5.653	0.7287	0.0794	0.0516	0.0185	6.531
230.0	5.567	0.7190	0.0768	0.0499	0.0180	6.431

Table B.77: SM Higgs-boson production cross sections at $\sqrt{s} = 8$ TeV: light Higgs boson.

M_H [GeV]	ggF σ [pb]	VBF σ [pb]	WH σ [pb]	ZH σ [pb]	ttH σ [pb]	Total σ [pb]
232.0	5.487	0.7095	0.0742	0.0482	0.0175	6.337
234.0	5.413	0.6999	0.0718	0.0465	0.0170	6.248
236.0	5.327	0.6903	0.0694	0.0449	0.0165	6.148
238.0	5.247	0.6806	0.0672	0.0434	0.0160	6.054
240.0	5.159	0.6703	0.0650	0.0420	0.0156	5.952
242.0	5.078	0.6604	0.0629	0.0406	0.0152	5.857
244.0	4.999	0.6506	0.0609	0.0393	0.0148	5.764
246.0	4.924	0.6410	0.0590	0.0380	0.0144	5.676
248.0	4.854	0.6319	0.0572	0.0367	0.0140	5.594
250.0	4.783	0.6225	0.0554	0.0355	0.0137	5.510
252.0	4.714	0.6136	0.0537	0.0344	0.0133	5.429
254.0	4.647	0.6050	0.0520	0.0333	0.0130	5.350
256.0	4.582	0.5964	0.0504	0.0322	0.0127	5.274
258.0	4.521	0.5879	0.0489	0.0311	0.0124	5.202
260.0	4.461	0.5797	0.0474	0.0301	0.0121	5.130
262.0	4.405	0.5714	0.0460	0.0292	0.0118	5.063
264.0	4.350	0.5636	0.0446	0.0282	0.0115	4.998
266.0	4.292	0.5554	0.0433	0.0274	0.0112	4.929
268.0	4.237	0.5477	0.0421	0.0265	0.0110	4.864
270.0	4.184	0.5401	0.0408	0.0257	0.0107	4.801
272.0	4.134	0.5328	0.0396	0.0249	0.0105	4.742
274.0	4.086	0.5255	0.0385	0.0241	0.0102	4.684
276.0	4.040	0.5184	0.0373	0.0234	0.0100	4.629
278.0	3.994	0.5115	0.0362	0.0227	0.0098	4.574
280.0	3.950	0.5045	0.0352	0.0220	0.0095	4.522
282.0	3.908	0.4978	0.0342	0.0213	0.0093	4.471
284.0	3.867	0.4911	0.0332	0.0207	0.0091	4.421
286.0	3.829	0.4845	0.0323	0.0200	0.0089	4.374
288.0	3.792	0.4780	0.0313	0.0195	0.0087	4.330
290.0	3.755	0.4716	0.0305	0.0189	0.0086	4.284
292.0	3.720	0.4654	0.0296	0.0183	0.0084	4.242
294.0	3.687	0.4591	0.0288	0.0178	0.0082	4.200
296.0	3.654	0.4530	0.0280	0.0173	0.0080	4.160
298.0	3.624	0.4469	0.0272	0.0168	0.0079	4.122
300.0	3.594	0.4408	0.0265	0.0163	0.0077	4.086
305.0	3.529	0.4267	0.0247	0.0151	0.0073	4.003
310.0	3.472	0.4132	0.0231	0.0141	0.0070	3.930
315.0	3.425	0.4000	0.0216	0.0131	0.0067	3.866
320.0	3.383	0.3875	0.0202	0.0122	0.0064	3.809
325.0	3.355	0.3753	0.0189	0.0114	0.0061	3.767
330.0	3.341	0.3638	0.0177	0.0106	0.0058	3.739
335.0	3.341	0.3526	0.0166	0.0099	0.0056	3.726
340.0	3.359	0.3422	0.0155	0.0093	0.0053	3.732
345.0	3.399	0.3305	0.0145	0.0086	0.0051	3.757
350.0	3.401	0.3200	0.0135	0.0081	0.0049	3.747
360.0	3.385	0.3028	0.0121	0.0072	0.0045	3.711
370.0	3.332	0.2896	0.0108	0.0064	0.0042	3.643
380.0	3.231	0.2776	0.0096	0.0057	0.0039	3.528
390.0	3.089	0.2660	0.0086	0.0051	0.0036	3.373
400.0	2.921	0.2543	0.0078	0.0046	0.0034	3.191

Table B.78: SM Higgs-boson production cross sections at $\sqrt{s} = 8$ TeV: heavy Higgs boson.

M_H [GeV]	ggF σ [pb]	VBF σ [pb]	Total σ [pb]
420.0	2.550	0.2317	2.782
440.0	2.178	0.2103	2.389
450.0	2.002	0.2002	2.203
460.0	1.837	0.1905	2.027
480.0	1.538	0.1724	1.710
500.0	1.283	0.1561	1.439
520.0	1.069	0.1414	1.210
540.0	0.8913	0.1283	1.020
550.0	0.8144	0.1223	0.9367
560.0	0.7442	0.1166	0.8608
580.0	0.6228	0.1062	0.7290
600.0	0.5230	0.0969	0.6199
620.0	0.4403	0.0886	0.5289
640.0	0.3719	0.0812	0.4531
650.0	0.3424	0.0778	0.4202
660.0	0.3153	0.0746	0.3899
680.0	0.2682	0.0687	0.3369
700.0	0.2290	0.0633	0.2923
720.0	0.1964	0.0585	0.2549
740.0	0.1689	0.0542	0.2231
750.0	0.1568	0.0524	0.2092
760.0	0.1457	0.0503	0.1960
780.0	0.1262	0.0468	0.1730
800.0	0.1097	0.0437	0.1534
820.0	0.0957	0.0408	0.1365
840.0	0.0837	0.0382	0.1219
850.0	0.0784	0.0371	0.1155
860.0	0.0735	0.0358	0.1093
880.0	0.0647	0.0336	0.0983
900.0	0.0571	0.0316	0.0887
920.0	0.0506	0.0299	0.0805
940.0	0.0450	0.0282	0.0732
950.0	0.0424	0.0275	0.0699
960.0	0.0400	0.0267	0.0667
980.0	0.0357	0.0252	0.0609
1000.0	0.0320	0.0240	0.0560

References

[1] ATLAS Collaboration, G. Aad et al., *Observation of a new particle in the search for the Standard Model Higgs boson with the ATLAS detector at the LHC*, Phys. Lett. B **716** (2012) 1–29, `arXiv:1207.7214 [hep-ex]`.

[2] CMS Collaboration, S. Chatrchyan et al., *Observation of a new boson at a mass of 125 GeV with the CMS experiment at the LHC*, Phys. Lett. B **716** (2012) 30–61, `arXiv:1207.7235 [hep-ex]`.

[3] F. Englert and R. Brout, *Broken symmetry and the mass of gauge vector mesons*, Phys. Rev. Lett. **13** (1964) 321–323.

[4] P. W. Higgs, *Broken symmetries, massless particles and gauge fields*, Phys. Lett. B **12** (1964) 132–133.

[5] P. W. Higgs, *Broken symmetries and the masses of gauge bosons*, Phys. Rev. Lett. **13** (1964) 508–509.

[6] G. Guralnik, C. Hagen, and T. Kibble, *Global conservation laws and massless particles*, Phys. Rev. Lett. **13** (1964) 585–587.

[7] P. W. Higgs, *Spontaneous symmetry breakdown without massless bosons*, Phys. Rev. **145** (1966) 1156–1163.

[8] T. Kibble, *Symmetry breaking in non-Abelian gauge theories*, Phys. Rev. **155** (1967) 1554–1561.

[9] ATLAS Collaboration, *Combined measurements of the mass and signal strength of the Higgs-like boson with the ATLAS detector using up to 25 fb^{-1} of proton-proton collision data*, ATLAS-CONF-2013-014 (2013). `https://cds.cern.ch/record/1523727`.

[10] CMS Collaboration, *Combination of standard model Higgs boson searches and measurements of the properties of the new boson with a mass near 125 GeV*, CMS-PAS-HIG-13-005 (2013). `https://cds.cern.ch/record/1542387`.

[11] ATLAS Collaboration, *Combined coupling measurements of the Higgs-like boson with the ATLAS detector using up to 25 fb^{-1} of proton-proton collision data*, ATLAS-CONF-2013-034 (2013). `https://cds.cern.ch/record/1528170`.

[12] CMS Collaboration, S. Chatrchyan et al., *On the mass and spin-parity of the Higgs boson candidate via its decays to Z boson pairs*, Phys. Rev. Lett. **110** (2013) 081803, `arXiv:1212.6639 [hep-ex]`.

[13] LHC Higgs Cross Section Working Group, S. Dittmaier, C. Mariotti, G. Passarino, and R. Tanaka (Eds.), *Handbook of LHC Higgs Cross Sections: 1. Inclusive Observables*, CERN-2011-002 (CERN, Geneva, 2011), `arXiv:1101.0593 [hep-ph]`.

[14] LHC Higgs Cross Section Working Group, S. Dittmaier, C. Mariotti, G. Passarino, and R. Tanaka (Eds.), *Handbook of LHC Higgs Cross Sections: 2. Differential Distributions*, CERN-2012-002 (CERN, Geneva, 2012), `arXiv:1201.3084 [hep-ph]`.

[15] A. Denner, S. Heinemeyer, I. Puljak, D. Rebuzzi, and M. Spira, *Standard Model Higgs-boson branching ratios with uncertainties*, Eur. Phys. J. **C71** (2011) 1753, `arXiv:1107.5909 [hep-ph]`.

[16] M. S. Carena, S. Heinemeyer, C. E. M. Wagner, and G. Weiglein, *Suggestions for benchmark scenarios for MSSM Higgs boson searches at hadron colliders*, Eur. Phys. J. **C26** (2003) 601–607, `arXiv:hep-ph/0202167`.

[17] A. Djouadi, J. Kalinowski, and M. Spira, *HDECAY: A program for Higgs boson decays in the Standard Model and its supersymmetric extension*, Comput. Phys. Commun. **108** (1998) 56–74, `arXiv:hep-ph/9704448`.

[18] M. Spira, *QCD effects in Higgs physics*, Fortschr. Phys. **46** (1998) 203–284, `arXiv:hep-ph/9705337`.

[19] A. Djouadi, J. Kalinowski, M. Mühlleitner, and M. Spira, *An update of the program HDECAY*, in

The Les Houches 2009 workshop on TeV colliders: The tools and Monte Carlo working group summary report. 2010. `arXiv:1003.1643 [hep-ph]`.

[20] A. Bredenstein, A. Denner, S. Dittmaier, and M. M. Weber, *Precise predictions for the Higgs-boson decay H → WW/ZZ → 4 leptons*, Phys. Rev. D **74** (2006) 013004, `arXiv:hep-ph/0604011`.

[21] A. Bredenstein, A. Denner, S. Dittmaier, and M. M. Weber, *Radiative corrections to the semileptonic and hadronic Higgs-boson decays H → W W / Z Z→ 4 fermions*, JHEP **02** (2007) 080, `arXiv:hep-ph/0611234 [hep-ph]`.

[22] A. Bredenstein, A. Denner, S. Dittmaier, A. Mück, and M. M. Weber, *Prophecy4f: A Monte Carlo generator for a proper description of the Higgs decay into 4 fermions*, `http://omnibus.uni-freiburg.de/~sd565/programs/prophecy4f/prophecy4f.ht%ml`, 2010.

[23] S. Narison, *A Fresh look into the heavy quark mass values*, Phys. Lett. B **341** (1994) 73–83, `arXiv:hep-ph/9408376 [hep-ph]`.

[24] S. Heinemeyer, W. Hollik, and G. Weiglein, *FeynHiggs: A program for the calculation of the masses of the neutral CP-even Higgs bosons in the MSSM*, Comput. Phys. Commun. **124** (2000) 76–89, `arXiv:hep-ph/9812320`.

[25] S. Heinemeyer, W. Hollik, and G. Weiglein, *The masses of the neutral CP-even Higgs bosons in the MSSM: Accurate analysis at the two loop level*, Eur. Phys. J. **C9** (1999) 343–366, `arXiv:hep-ph/9812472`.

[26] G. Degrassi, S. Heinemeyer, W. Hollik, P. Slavich, and G. Weiglein, *Towards high-precision predictions for the MSSM Higgs sector*, Eur. Phys. J. **C28** (2003) 133–143, `arXiv:hep-ph/0212020`.

[27] M. Frank, T. Hahn, S. Heinemeyer, W. Hollik, H. Rzehak, et al., *The Higgs boson masses and mixings of the complex MSSM in the Feynman-diagrammatic approach*, JHEP **02** (2007) 047, `arXiv:hep-ph/0611326 [hep-ph]`.

[28] T. Hahn, S. Heinemeyer, W. Hollik, H. Rzehak, and G. Weiglein, *FeynHiggs: A program for the calculation of MSSM Higgs-boson observables - Version 2.6.5*, Comput. Phys. Commun. **180** (2009) 1426–1427.

[29] P. Z. Skands, B. Allanach, H. Baer, C. Balazs, G. Belanger, et al., *SUSY Les Houches accord: Interfacing SUSY spectrum calculators, decay packages, and event generators*, JHEP **07** (2004) 036, `arXiv:hep-ph/0311123 [hep-ph]`.

[30] B. Allanach, C. Balazs, G. Belanger, M. Bernhardt, F. Boudjema, et al., *SUSY Les Houches Accord 2*, Comput. Phys. Commun. **180** (2009) 8–25, `arXiv:0801.0045 [hep-ph]`.

[31] M. Carena, S. Heinemeyer, O. Stal, C. Wagner, and G. Weiglein, *MSSM Higgs Boson Searches at the LHC: Benchmark Scenarios after the Discovery of a Higgs-like Particle*, `arXiv:1302.7033 [hep-ph]`.

[32] S. AbdusSalam, B. Allanach, H. Dreiner, J. Ellis, U. Ellwanger, et al., *Benchmark Models, Planes, Lines and Points for Future SUSY Searches at the LHC*, Eur. Phys. J. **C71** (2011) 1835, `arXiv:1109.3859 [hep-ph]`.

[33] *Higgs Branching Ratios in the MSSM can be found at the LHC Higgs Cross Section Working Group*, `https://twiki.cern.ch/twiki/bin/view/LHCPhysics/BRs`.

[34] H. M. Georgi, S. L. Glashow, M. E. Machacek, and D. V. Nanopoulos, *Higgs bosons from two gluon annihilation in proton proton collisions*, Phys. Rev. Lett. **40** (1978) 692.

[35] S. Dawson, *Radiative corrections to Higgs boson production*, Nucl. Phys. B **359** (1991) 283–300.

[36] A. Djouadi, M. Spira, and P. M. Zerwas, *Production of Higgs bosons in proton colliders: QCD corrections*, Phys. Lett. B **264** (1991) 440–446.

[37] M. Spira, A. Djouadi, D. Graudenz, and P. M. Zerwas, *Higgs boson production at the LHC*, Nucl. Phys. B **453** (1995) 17–82, `arXiv:hep-ph/9504378 [hep-ph]`.

[38] R. V. Harlander and W. B. Kilgore, *Next-to-next-to-leading order Higgs production at hadron colliders*, Phys. Rev. Lett. **88** (2002) 201801, `arXiv:hep-ph/0201206`.

[39] C. Anastasiou and K. Melnikov, *Higgs boson production at hadron colliders in NNLO QCD*, Nucl. Phys. B **646** (2002) 220–256, `arXiv:hep-ph/0207004`.

[40] V. Ravindran, J. Smith, and W. L. van Neerven, *NNLO corrections to the total cross section for Higgs boson production in hadron hadron collisions*, Nucl. Phys. B **665** (2003) 325–366, `arXiv:hep-ph/0302135`.

[41] C. Anastasiou, K. Melnikov, and F. Petriello, *Fully differential Higgs boson production and the di-photon signal through next-to-next-to-leading order*, Nucl. Phys. B **724** (2005) 197–246, `arXiv:hep-ph/0501130 [hep-ph]`.

[42] C. Anastasiou, G. Dissertori, and F. Stöckli, *NNLO QCD predictions for the $H \to WW \to \ell\nu\ell\nu$ signal at the LHC*, JHEP **09** (2007) 018, `arXiv:0707.2373 [hep-ph]`.

[43] S. Catani and M. Grazzini, *An NNLO subtraction formalism in hadron collisions and its application to Higgs boson production at the LHC*, Phys. Rev. Lett. **98** (2007) 222002, `arXiv:hep-ph/0703012 [hep-ph]`.

[44] M. Grazzini, *NNLO predictions for the Higgs boson signal in the $H \to WW \to l\nu l\nu$ and $H \to ZZ \to 4l$ decay channels*, JHEP **02** (2008) 043, `arXiv:0801.3232 [hep-ph]`.

[45] C. Anastasiou, R. Boughezal, and F. Petriello, *Mixed QCD-electroweak corrections to Higgs boson production in gluon fusion*, JHEP **04** (2009) 003, `arXiv:0811.3458 [hep-ph]`.

[46] D. de Florian and M. Grazzini, *Higgs production through gluon fusion: Updated cross sections at the Tevatron and the LHC*, Phys. Lett. B **674** (2009) 291–294, `arXiv:0901.2427 [hep-ph]`.

[47] D. De Florian and M. Grazzini, *Higgs production at the LHC: updated cross sections at $\sqrt{s} = 8$ TeV*, Phys. Lett. B **718** (2012) 117, `arXiv:1206.4133 [hep-ph]`.

[48] S. Catani, D. de Florian, M. Grazzini, and P. Nason, *Soft gluon resummation for Higgs boson production at hadron colliders*, JHEP **07** (2003) 028, `arXiv:hep-ph/0306211 [hep-ph]`.

[49] S. Actis, G. Passarino, C. Sturm, and S. Uccirati, *NLO electroweak corrections to Higgs boson production at hadron colliders*, Phys. Lett. B **670** (2008) 12–17, `arXiv:0809.1301 [hep-ph]`.

[50] U. Aglietti, R. Bonciani, G. Degrassi, and A. Vicini, *Two-loop light fermion contribution to Higgs production and decays*, Phys. Lett. B **595** (2004) 432–441, `arXiv:hep-ph/0404071`.

[51] G. Degrassi and F. Maltoni, *Two-loop electroweak corrections to Higgs production at hadron colliders*, Phys. Lett. B **600** (2004) 255–260, `arXiv:hep-ph/0407249`.

[52] U. Aglietti, R. Bonciani, G. Degrassi, and A. Vicini, *Two-loop electroweak corrections to Higgs production in proton-proton collisions*, `arXiv:hep-ph/0610033 [hep-ph]`.

[53] C. Anastasiou, S. Buehler, F. Herzog, and A. Lazopoulos, *Inclusive Higgs boson cross-section for the LHC at 8 TeV*, JHEP **04** (2012) 004, `1202.3638 [hep-ph]`.

[54] R. Boughezal, F. Caola, K. Melnikov, F. Petriello, and M. Schulze, *Higgs boson production in association with a jet at next-to-next-to-leading order in perturbative QCD*, JHEP **06** (2013) 072, `arXiv:1302.6216 [hep-ph]`.

[55] C. F. Berger, C. Marcantonini, I. W. Stewart, F. J. Tackmann, and W. J. Waalewijn, *Higgs Production with a Central Jet Veto at NNLL+NNLO*, JHEP **04** (2011) 092, `arXiv:1012.4480 [hep-ph]`.

[56] A. Banfi, G. P. Salam, and G. Zanderighi, *NLL+NNLO predictions for jet-veto efficiencies in Higgs-boson and Drell-Yan production*, JHEP **06** (2012) 159, `arXiv:1203.5773 [hep-ph]`.

[57] T. Becher and M. Neubert, *Factorization and NNLL Resummation for Higgs Production with a Jet Veto*, JHEP **07** (2012) 108, `arXiv:1205.3806 [hep-ph]`.

[58] F. J. Tackmann, J. R. Walsh, and S. Zuberi, *Resummation Properties of Jet Vetoes at the LHC*, Phys. Rev. D **86** (2012) 053011, `arXiv:1206.4312 [hep-ph]`.

[59] A. Banfi, P. F. Monni, G. P. Salam, and G. Zanderighi, *Higgs and Z-boson production with a jet veto*, Phys. Rev. Lett. **109** (2012) 202001, `arXiv:1206.4998 [hep-ph]`.

[60] X. Liu and F. Petriello, *Resummation of jet-veto logarithms in hadronic processes containing jets*, Phys. Rev. D **87** (2013) 014018, `arXiv:1210.1906 [hep-ph]`.

[61] X. Liu and F. Petriello, *Reducing theoretical uncertainties for exclusive Higgs plus one-jet production at the LHC*, `arXiv:1303.4405 [hep-ph]`.

[62] T. Gehrmann, M. Jaquier, E. Glover, and A. Koukoutsakis, *Two-Loop QCD Corrections to the Helicity Amplitudes for $H \to 3$ partons*, JHEP **02** (2012) 056, `arXiv:1112.3554 [hep-ph]`.

[63] J. M. Campbell and R. Ellis, *MCFM for the Tevatron and the LHC*, Nucl. Phys. Proc. Suppl. **205-206** (2010) 10–15, `arXiv:1007.3492 [hep-ph]`.

[64] S. Frixione, Z. Kunszt, and A. Signer, *Three jet cross-sections to next-to-leading order*, Nucl. Phys. B **467** (1996) 399–442, `arXiv:hep-ph/9512328 [hep-ph]`.

[65] M. Czakon, *A novel subtraction scheme for double-real radiation at NNLO*, Phys. Lett. B **693** (2010) 259–268, `arXiv:1005.0274 [hep-ph]`.

[66] S. Catani and M. Grazzini, *Infrared factorization of tree level QCD amplitudes at the next-to-next-to-leading order and beyond*, Nucl. Phys. B **570** (2000) 287–325, `arXiv:hep-ph/9908523 [hep-ph]`.

[67] NNPDF Collaboration, R. D. Ball et al., *Unbiased global determination of parton distributions and their uncertainties at NNLO and at LO*, Nucl. Phys. B **855** (2012) 153–221, `arXiv:1107.2652 [hep-ph]`.

[68] R. D. Ball, V. Bertone, S. Carrazza, C. S. Deans, L. Del Debbio, et al., *Parton distributions with LHC data*, Nucl. Phys. B **867** (2013) 244–289, `arXiv:1207.1303 [hep-ph]`.

[69] D. De Florian, G. Ferrera, M. Grazzini, and D. Tommasini, *Higgs boson production at the LHC: transverse momentum resummation effects in the $H \to 2\gamma$, $H \to WW \to \ell\nu\ell\nu$ and $H \to ZZ \to 4\ell$ decay modes*, JHEP **06** (2012) 132, `1203.6321 [hep-ph]`.

[70] D. de Florian, G. Ferrera, M. Grazzini, and D. Tommasini, *Transverse-momentum resummation: Higgs boson production at the Tevatron and the LHC*, JHEP **11** (2011) 064, `arXiv:1109.2109 [hep-ph]`.

[71] *HqT program*, `http://theory.fi.infn.it/grazzini/codes.html`.

[72] S. Catani and B. Webber, *Infrared safe but infinite: Soft gluon divergences inside the physical region*, JHEP **10** (1997) 005, `arXiv:hep-ph/9710333 [hep-ph]`.

[73] J. M. Campbell, R. K. Ellis, R. Frederix, P. Nason, C. Oleari, et al., *NLO Higgs Boson Production Plus One and Two Jets Using the POWHEG BOX, MadGraph4 and MCFM*, JHEP **07** (2012) 092, `arXiv:1202.5475 [hep-ph]`.

[74] ATLAS Collaboration, *Observation of an excess of events in the search for the Standard Model Higgs boson in the $\gamma\gamma$ channel with the ATLAS detector*, ATLAS-CONF-2012-091 (2012) . `http://cds.cern.ch/record/1460410`.

[75] S. Frixione, P. Nason, and B. R. Webber, *Matching NLO QCD and parton showers in heavy flavour production*, JHEP **08** (2003) 007, `arXiv:hep-ph/0305252`.

[76] G. Corcella et al., *HERWIG 6: An event generator for hadron emission reactions with interfering gluons (including supersymmetric processes)*, JHEP **01** (2001) 010, `arXiv:hep-ph/0011363`.

[77] E. Bagnaschi, G. Degrassi, P. Slavich, and A. Vicini, *Higgs production via gluon fusion in the POWHEG approach in the SM and in the MSSM*, JHEP **02** (2012) 088, `arXiv:1111.2854 [hep-ph]`.

[78] P. Nason, *A New method for combining NLO QCD with shower Monte Carlo algorithms*, JHEP

11 (2004) 040, arXiv:hep-ph/0409146 [hep-ph].

[79] S. Frixione, P. Nason, and C. Oleari, *Matching NLO QCD computations with parton shower simulations: The POWHEG method*, JHEP **11** (2007) 070, arXiv:0709.2092 [hep-ph].

[80] S. Alioli, P. Nason, C. Oleari, and E. Re, *A general framework for implementing NLO calculations in shower Monte Carlo programs: The POWHEG BOX*, JHEP **06** (2010) 043, arXiv:1002.2581 [hep-ph].

[81] T. Sjöstrand, S. Mrenna, and P. Z. Skands, *PYTHIA 6.4 physics and manual*, JHEP **05** (2006) 026, arXiv:hep-ph/0603175 [hep-ph].

[82] T. Sjöstrand, S. Mrenna, and P. Z. Skands, *A brief Introduction to PYTHIA 8.1*, Comput. Phys. Commun. **178** (2008) 852–867, arXiv:0710.3820 [hep-ph].

[83] J. Butterworth, J. R. Forshaw, and M. Seymour, *Multiparton interactions in photoproduction at HERA*, Z. Phys. C **72** (1996) 637–646, arXiv:hep-ph/9601371 [hep-ph].

[84] ATLAS Collaboration, *New ATLAS event generator tunes to 2010 data*, ATL-PHYS-PUB-2011-008, (2011). https://cds.cern.ch/record/1345343.

[85] N. Kauer and G. Passarino, *Inadequacy of zero-width approximation for a light Higgs boson signal*, JHEP **08** (2012) 116, arXiv:1206.4803 [hep-ph].

[86] *gg2VV*, http://gg2VV.hepforge.org/.

[87] S. Goria, G. Passarino, and D. Rosco, *The Higgs Boson Lineshape*, Nucl. Phys. B **864** (2012) 530–579, arXiv:1112.5517 [hep-ph].

[88] D. de Florian, N. Fidanza, R. HernǦndez-Pinto, J. Mazzitelli, Y. R. Habarnau, et al., *A complete $O(\alpha_s^2)$ calculation of the signal-background interference for the Higgs diphoton decay channel*, Eur. Phys. J. **C73** (2013) 2387, arXiv:1303.1397 [hep-ph].

[89] S. P. Martin, *Interference of Higgs diphoton signal and background in production with a jet at the LHC*, arXiv:1303.3342 [hep-ph].

[90] S. Martin, *Shift in the LHC Higgs diphoton mass peak from interference with background*, Phys. Rev. D **86** (2012) 073016, 1208.1533.

[91] H.-Q. Zheng and D.-D. Wu, *First order QCD corrections to the decay of the Higgs boson into two photons*, Phys. Rev. D **42** (1990) 3760–3763.

[92] A. Djouadi, M. Spira, J. J. van der Bij, and P. M. Zerwas, *QCD corrections to $\gamma\gamma$ decays of Higgs particles in the intermediate mass range*, Phys. Lett. B **257** (1991) 187–190.

[93] S. Dawson and R. Kauffman, *QCD corrections to $H \to \gamma\gamma$*, Phys. Rev. D **47** (1993) 1264–1267.

[94] A. Djouadi, M. Spira, and P. M. Zerwas, *Two photon decay widths of Higgs particles*, Phys. Lett. B **311** (1993) 255–260, arXiv:hep-ph/9305335 [hep-ph].

[95] K. Melnikov and O. I. Yakovlev, *Higgs $\to$ two photon decay: QCD radiative correction*, Phys. Lett. B **312** (1993) 179–183, arXiv:hep-ph/9302281 [hep-ph].

[96] M. Inoue, R. Najima, T. Oka, and J. Saito, *QCD corrections to two photon decay of the Higgs boson and its reverse process*, Mod. Phys. Lett. **A9** (1994) 1189–1194.

[97] S. Catani, L. Cieri, D. de Florian, G. Ferrera, and M. Grazzini, *Diphoton production at hadron colliders: a fully-differential QCD calculation at NNLO*, Phys. Rev. Lett. **108** (2012) 072001, arXiv:1110.2375 [hep-ph].

[98] L. J. Dixon and M. S. Siu, *Resonance-continuum interference in the di-photon Higgs signal at the LHC*, Phys. Rev. Lett. **90** (2003) 252001, arXiv:hep-ph/0302233.

[99] D. A. Dicus and S. S. D. Willenbrock, *Photon pair production and the intermediate mass Higgs boson*, Phys. Rev. D **37** (1988) 1801.

[100] A. D. Martin, W. J. Stirling, R. S. Thorne, and G. Watt, *Parton distributions for the LHC*, Eur. Phys. J. **C63** (2009) 189–285, arXiv:0901.0002 [hep-ph].

[101] D. de Florian and Z. Kunszt, *Two photons plus jet at LHC: The NNLO contribution from the g g*

initiated process, Phys. Lett. B **460** (1999) 184–188, `arXiv:hep-ph/9905283 [hep-ph]`.

[102] G. Passarino, *Higgs Interference Effects in gg → ZZ and their Uncertainty*, JHEP **08** (2012) 146, `arXiv:1206.3824 [hep-ph]`.

[103] ATLAS Collaboration, *Measurements of the properties of the Higgs-like boson in the $WW^* → \ell\nu\ell\nu$ decay channel with the ATLAS detector using 25 fb^{-1} of proton-proton collision data*, ATLAS-CONF-2013-030 (2013) . `https://cds.cern.ch/record/1527126`.

[104] M. Ciccolini, A. Denner, and S. Dittmaier, *Strong and electroweak corrections to the production of Higgs + 2-jets via weak interactions at the LHC*, Phys. Rev. Lett. **99** (2007) 161803, `arXiv:0707.0381 [hep-ph]`.

[105] M. Ciccolini, A. Denner, and S. Dittmaier, *Electroweak and QCD corrections to Higgs production via vector-boson fusion at the LHC*, Phys. Rev. D **77** (2008) 013002, `arXiv:0710.4749 [hep-ph]`.

[106] A. Denner, S. Dittmaier, and A. Mück, *HAWK: A Monte Carlo generator for the production of Higgs bosons Attached to WeaK bosons at hadron colliders*, `http://omnibus.uni-freiburg.de/~sd565/programs/hawk/hawk.html`, 2010.

[107] A. Denner, S. Dittmaier, S. Kallweit, and A. Muck, *Electroweak corrections to Higgs-strahlung off W/Z bosons at the Tevatron and the LHC with HAWK*, JHEP **03** (2012) 075, `arXiv:1112.5142 [hep-ph]`.

[108] G. Passarino, C. Sturm, and S. Uccirati, *Higgs pseudo-observables, second Riemann sheet and all that*, Nucl. Phys. B **834** (2010) 77–115, `arXiv:1001.3360 [hep-ph]`.

[109] C. Anastasiou, S. Buehler, F. Herzog, and A. Lazopoulos, *Total cross-section for Higgs boson hadroproduction with anomalous Standard Model interactions*, JHEP **12** (2011) 058, `arXiv:1107.0683 [hep-ph]`.

[110] K. Arnold, J. Bellm, G. Bozzi, F. Campanario, C. Englert, et al., *Release Note – Vbfnlo-2.6.0*, `arXiv:1207.4975 [hep-ph]`.

[111] K. Arnold, J. Bellm, G. Bozzi, M. Brieg, F. Campanario, et al., *VBFNLO: A parton level Monte Carlo for processes with electroweak bosons – Manual for Version 2.5.0*, `arXiv:arXiv:1107.4038 [hep-ph]`.

[112] K. Arnold et al., *VBFNLO: A parton level Monte Carlo for processes with electroweak bosons*, Comput. Phys. Commun. **180** (2009) 1661–1670, `arXiv:0811.4559 [hep-ph]`.

[113] P. Nason and C. Oleari, *NLO Higgs boson production via vector-boson fusion matched with shower in POWHEG*, JHEP **02** (2010) 037, `arXiv:0911.5299 [hep-ph]`.

[114] P. Bolzoni, F. Maltoni, S.-O. Moch, and M. Zaro, *Higgs production via vector-boson fusion at NNLO in QCD*, Phys. Rev. Lett. **105** (2010) 011801, `arXiv:1003.4451 [hep-ph]`.

[115] P. Bolzoni, F. Maltoni, S.-O. Moch, and M. Zaro, *Vector boson fusion at NNLO in QCD: SM Higgs and beyond*, Phys. Rev. D **85** (2012) 035002, `arXiv:1109.3717 [hep-ph]`.

[116] T. Han, G. Valencia, and S. Willenbrock, *Structure function approach to vector boson scattering in pp collisions*, Phys. Rev. Lett. **69** (1992) 3274–3277, `arXiv:hep-ph/9206246`.

[117] W. A. Bardeen, A. J. Buras, D. W. Duke, and T. Muta, *Deep inelastic scattering beyond the leading order in asymptotically free gauge theories*, Phys. Rev. D **18** (1978) 3998.

[118] D. I. Kazakov, A. V. Kotikov, G. Parente, O. A. Sampayo, and J. Sanchez Guillen, *Complete quartic (α_s^2) correction to the deep inelastic longitudinal structure function F(L) in QCD*, Phys. Rev. Lett. **65** (1990) 1535–1538.

[119] E. B. Zijlstra and W. L. van Neerven, *Order α_s^2 correction to the structure function F3 (x, Q^2) in deep inelastic neutrino-hadron scattering*, Phys. Lett. B **297** (1992) 377–384.

[120] E. B. Zijlstra and W. L. van Neerven, *Order α_s^2 QCD corrections to the deep inelastic proton structure functions F2 and F(L)*, Nucl. Phys. B **383** (1992) 525–574.

[121] S. Moch and J. A. M. Vermaseren, *Deep inelastic structure functions at two loops*, Nucl. Phys. B **573** (2000) 853–907, `arXiv:hep-ph/9912355`.

[122] W. L. van Neerven and J. A. M. Vermaseren, *The role of the five point function in radiative corrections to two photon physics*, Phys. Lett. B **142** (1984) 80.

[123] J. Blümlein, G. J. van Oldenborgh, and R. Rückl, *QCD and QED corrections to Higgs boson production in charged current ep scattering*, Nucl. Phys. B **395** (1993) 35–59, `arXiv:hep-ph/9209219`.

[124] T. Figy, V. Hankele, and D. Zeppenfeld, *Next-to-leading order QCD corrections to Higgs plus three jet production in vector-boson fusion*, JHEP **02** (2008) 076, `arXiv:0710.5621 [hep-ph]`.

[125] R. V. Harlander, J. Vollinga, and M. M. Weber, *Gluon-induced weak boson fusion*, Phys. Rev. D **77** (2008) 053010, `arXiv:0801.3355 [hep-ph]`.

[126] J. Alwall, R. Frederix, S. Frixione, V. Hirschi, F. Maltoni, et al., *to appear*, .

[127] *aMC@NLO*, `http://amcatnlo.web.cern.ch/amcatnlo/`.

[128] S. Frixione and B. R. Webber, *Matching NLO QCD computations and parton shower simulations*, JHEP **06** (2002) 029, `arXiv:hep-ph/0204244 [hep-ph]`.

[129] J. Alwall, M. Herquet, F. Maltoni, O. Mattelaer, and T. Stelzer, *MadGraph 5: Going beyond*, JHEP **06** (2011) 128, `arXiv:1106.0522 [hep-ph]`.

[130] R. Frederix, S. Frixione, F. Maltoni, and T. Stelzer, *Automation of next-to-leading order computations in QCD: The FKS subtraction*, JHEP **10** (2009) 003, `arXiv:0908.4272 [hep-ph]`.

[131] S. Frixione, *A General approach to jet cross-sections in QCD*, Nucl. Phys. B **507** (1997) 295–314, `arXiv:hep-ph/9706545 [hep-ph]`.

[132] V. Hirschi et al., *Automation of one-loop QCD corrections*, JHEP **05** (2011) 044, `arXiv:1103.0621 [hep-ph]`.

[133] G. Ossola, C. G. Papadopoulos, and R. Pittau, *Reducing full one-loop amplitudes to scalar integrals at the integrand level*, Nucl. Phys. B **763** (2007) 147–169, `arXiv:hep-ph/0609007 [hep-ph]`.

[134] G. Ossola, C. G. Papadopoulos, and R. Pittau, *CutTools: A Program implementing the OPP reduction method to compute one-loop amplitudes*, JHEP **03** (2008) 042, `arXiv:0711.3596 [hep-ph]`.

[135] J. Alwall et al., *MadGraph/MadEvent v4: The new web generation*, JHEP **09** (2007) 028, `arXiv:0706.2334 [hep-ph]`.

[136] R. Frederix et al., *Scalar and pseudoscalar Higgs production in association with a top-antitop pair*, Phys. Lett. B **701** (2011) 427–433, `arXiv:1104.5613 [hep-ph]`.

[137] R. Frederix, S. Frixione, V. Hirschi, F. Maltoni, R. Pittau, et al., *W and Z/γ^* boson production in association with a bottom-antibottom pair*, JHEP **09** (2011) 061, `arXiv:1106.6019 [hep-ph]`.

[138] R. Frederix, S. Frixione, V. Hirschi, F. Maltoni, R. Pittau, et al., *Four-lepton production at hadron colliders: aMC@NLO predictions with theoretical uncertainties*, JHEP **02** (2012) 099, `arXiv:1110.4738 [hep-ph]`.

[139] R. Frederix, S. Frixione, V. Hirschi, F. Maltoni, R. Pittau, et al., *aMC@NLO predictions for Wjj production at the Tevatron*, JHEP **02** (2012) 048, `arXiv:1110.5502 [hep-ph]`.

[140] R. Frederix, E. Re, and P. Torrielli, *Single-top t-channel hadroproduction in the four-flavour scheme with POWHEG and aMC@NLO*, JHEP **09** (2012) 130, `arXiv:1207.5391 [hep-ph]`.

[141] R. Frederix, M. K. Mandal, P. Mathews, V. Ravindran, S. Seth, et al., *Diphoton production in the ADD model to NLO+parton shower accuracy at the LHC*, JHEP **12** (2012) 102, `arXiv:1209.6527 [hep-ph]`.

[142] R. Frederix and S. Frixione, *Merging meets matching in MC@NLO*, JHEP **12** (2012) 061,

`arXiv:1209.6215 [hep-ph]`.

[143] S. Frixione, F. Stoeckli, P. Torrielli, and B. R. Webber, *NLO QCD corrections in Herwig++ with MC@NLO*, JHEP **01** (2011) 053, `arXiv:1010.0568 [hep-ph]`.

[144] P. Torrielli and S. Frixione, *Matching NLO QCD computations with PYTHIA using MC@NLO*, JHEP **04** (2010) 110, `arXiv:1002.4293 [hep-ph]`.

[145] H.-L. Lai, M. Guzzi, J. Huston, Z. Li, P. M. Nadolsky, et al., *New parton distributions for collider physics*, Phys. Rev. D **82** (2010) 074024, `arXiv:1007.2241 [hep-ph]`.

[146] F. Cerutti, *The NNPDF2.1 parton set*, `arXiv:1107.1095 [hep-ph]`.

[147] M. Botje, J. Butterworth, A. Cooper-Sarkar, A. de Roeck, J. Feltesse, et al., *The PDF4LHC Working Group Interim Recommendations*, `arXiv:1101.0538 [hep-ph]`.

[148] S. Frixione, P. Torrielli, and M. Zaro, *Higgs production through vector-boson fusion at the NLO matched with parton showers*, `arXiv:1304.7927 [hep-ph]`.

[149] M. Bahr et al., *Herwig++ physics and manual*, Eur. Phys. J. **C58** (2008) 639–707, `arXiv:0803.0883 [hep-ph]`.

[150] O. Brein, A. Djouadi, and R. Harlander, *NNLO QCD corrections to the Higgs-strahlung processes at hadron colliders*, Phys. Lett. B **579** (2004) 149–156, `arXiv:hep-ph/0307206`.

[151] G. Ferrera, M. Grazzini, and F. Tramontano, *Associated WH production at hadron colliders: a fully exclusive QCD calculation at NNLO*, Phys. Rev. Lett. **107** (2011) 152003, `arXiv:1107.1164 [hep-ph]`.

[152] G. Ferrera, M. Grazzini, and F. Tramontano. In preparation, 2013.

[153] L. Altenkamp, S. Dittmaier, R. V. Harlander, H. Rzehak, and T. J. Zirke, *Gluon-induced Higgs-strahlung at next-to-leading order QCD*, JHEP **02** (2013) 078, `arXiv:1211.5015 [hep-ph]`.

[154] O. Brein, R. Harlander, M. Wiesemann, and T. Zirke, *Top-quark mediated effects in hadronic Higgs-strahlung*, Eur. Phys. J. **C72** (2012) 1868, `arXiv:1111.0761 [hep-ph]`.

[155] M. L. Ciccolini, S. Dittmaier, and M. Krämer, *Electroweak radiative corrections to associated WH and ZH production at hadron colliders*, Phys. Rev. D **68** (2003) 073003, `arXiv:hep-ph/0306234`.

[156] O. Brein, R. V. Harlander, and T. J. Zirke, *vh@nnlo - Higgs Strahlung at hadron colliders*, Comput. Phys. Commun. **184** (2013) 998–1003, `arXiv:1210.5347 [hep-ph]`.

[157] W. Beenakker et al., *Higgs radiation off top quarks at the Tevatron and the LHC*, Phys. Rev. Lett. **87** (2001) 201805, `arXiv:hep-ph/0107081`.

[158] W. Beenakker et al., *NLO QCD corrections to t$\bar{t}$H production in hadron collisions*, Nucl. Phys. B **653** (2003) 151–203, `arXiv:hep-ph/0211352`.

[159] L. Reina and S. Dawson, *Next-to-leading order results for t$\bar{t}$h production at the Tevatron*, Phys. Rev. Lett. **87** (2001) 201804, `arXiv:hep-ph/0107101`.

[160] S. Dawson, L. H. Orr, L. Reina, and D. Wackeroth, *Associated top quark Higgs boson production at the LHC*, Phys. Rev. D **67** (2003) 071503, `arXiv:hep-ph/0211438`.

[161] M. Garzelli, A. Kardos, C. Papadopoulos, and Z. Trocsanyi, *Standard Model Higgs boson production in association with a top anti-top pair at NLO with parton showering*, Europhys. Lett. **96** (2011) 11001, `arXiv:1108.0387 [hep-ph]`.

[162] T. Gleisberg, S. Hoeche, F. Krauss, M. Schonherr, S. Schumann, et al., *Event generation with SHERPA 1.1*, JHEP **02** (2009) 007, `arXiv:0811.4622 [hep-ph]`.

[163] P. Artoisenet, R. Frederix, O. Mattelaer, and R. Rietkerk, *Automatic spin-entangled decays of heavy resonances in Monte Carlo simulations*, Journal of High Energy Physics **03** (2013) 3, `arXiv:1212.3460 [hep-ph]`.

[164] F. Cascioli, P. Maierhofer, and S. Pozzorini, *Scattering Amplitudes with Open Loops*, Phys. Rev.

Lett. **108** (2012) 111601, `arXiv:1111.5206 [hep-ph]`.

[165] F. Krauss, R. Kuhn, and G. Soff, *AMEGIC++ 1.0: A Matrix element generator in C++*, JHEP **02** (2002) 044, `arXiv:hep-ph/0109036 [hep-ph]`.

[166] T. Gleisberg and F. Krauss, *Automating dipole subtraction for QCD NLO calculations*, Eur. Phys. J. **C53** (2008) 501–523, `arXiv:0709.2881 [hep-ph]`.

[167] A. Kardos and Z. Trócsányi, *Hadroproduction of t anti-t pair with a b anti-b pair with PowHel*, `arXiv:1303.6291 [hep-ph]`.

[168] A. D. Martin, W. J. Stirling, R. S. Thorne, and G. Watt, *Uncertainties on α_s in global PDF analyses and implications for predicted hadronic cross sections*, Eur. Phys. J. **C64** (2009) 653–680, `arXiv:0905.3531 [hep-ph]`.

[169] J. Pumplin et al., *New generation of parton distributions with uncertainties from global QCD analysis*, JHEP **07** (2002) 012, `arXiv:hep-ph/0201195`.

[170] R. D. Ball et al., *A first unbiased global NLO determination of parton distributions and their uncertainties*, Nucl. Phys. B **838** (2010) 136–206, `arXiv:1002.4407 [hep-ph]`.

[171] A. Denner and S. Dittmaier, *Reduction of one-loop tensor 5-point integrals*, Nucl. Phys. B **658** (2003) 175–202, `arXiv:hep-ph/0212259`.

[172] A. Denner and S. Dittmaier, *Reduction schemes for one-loop tensor integrals*, Nucl. Phys. B **734** (2006) 62–115, `arXiv:hep-ph/0509141`.

[173] A. Denner and S. Dittmaier, *Scalar one-loop 4-point integrals*, Nucl. Phys. B **844** (2011) 199–242, `arXiv:1005.2076 [hep-ph]`.

[174] S. Schumann and F. Krauss, *A Parton shower algorithm based on Catani-Seymour dipole factorisation*, JHEP **03** (2008) 038, `arXiv:0709.1027 [hep-ph]`.

[175] S. Catani and M. H. Seymour, *A general algorithm for calculating jet cross sections in NLO QCD*, Nucl. Phys. B **485** (1997) 291–419, `arXiv:hep-ph/9605323`.

[176] Z. Nagy and D. E. Soper, *Matching parton showers to NLO computations*, JHEP **10** (2005) 024, `arXiv:hep-ph/0503053 [hep-ph]`.

[177] S. Hoeche, F. Krauss, M. Schonherr, and F. Siegert, *A critical appraisal of NLO+PS matching methods*, JHEP **09** (2012) 049, `arXiv:1111.1220 [hep-ph]`.

[178] A. Buckley, J. Butterworth, L. Lonnblad, H. Hoeth, J. Monk, et al., *Rivet user manual*, `arXiv:1003.0694 [hep-ph]`.

[179] M. Cacciari, G. P. Salam, and G. Soyez, *FastJet User Manual*, Eur. Phys. J. **C72** (2012) 1896, `arXiv:1111.6097 [hep-ph]`.

[180] ATLAS Collaboration, *Search for the Standard Model Higgs boson produced in association with top quarks in proton-proton collisions at $\sqrt{s} = 7$ TeV using the ATLAS detector*, ATLAS-CONF-2012-135 (2012) . `https://cds.cern.ch/record/1478423`.

[181] CMS Collaboration, *Search for Higgs boson production in association with top quark pairs in pp collisions*, CMS-PAS-HIG-12-025 (2012) . `http://cds.cern.ch/record/1460423`.

[182] CMS Collaboration Collaboration, S. Chatrchyan et al., *Search for the standard model Higgs boson produced in association with a top-quark pair in pp collisions at the LHC*, JHEP **05** (2013) 145, `arXiv:1303.0763 [hep-ex]`.

[183] A. Bredenstein, A. Denner, S. Dittmaier, and S. Pozzorini, *NLO QCD corrections to $t\bar{t}b\bar{b}$ production at the LHC: 1. quark-antiquark annihilation*, JHEP **08** (2008) 108, `arXiv:0807.1248 [hep-ph]`.

[184] A. Bredenstein, A. Denner, S. Dittmaier, and S. Pozzorini, *NLO QCD corrections to $pp \to t\bar{t}b\bar{b} + X$ at the LHC*, Phys. Rev. Lett. **103** (2009) 012002, `arXiv:0905.0110 [hep-ph]`.

[185] A. Bredenstein, A. Denner, S. Dittmaier, and S. Pozzorini, *NLO QCD corrections to $t\bar{t}b\bar{b}$ production at the LHC: 2. full hadronic results*, JHEP **03** (2010) 021, `arXiv:1001.4006`

```
[hep-ph].
```

[186] G. Bevilacqua, M. Czakon, C. G. Papadopoulos, R. Pittau, and M. Worek, *Assault on the NLO wishlist: $pp \to t\bar{t}b\bar{b}$*, JHEP **09** (2009) 109, `arXiv:0907.4723` `[hep-ph]`.

[187] G. Bevilacqua, M. Czakon, C. G. Papadopoulos, and M. Worek, *Dominant QCD backgrounds in Higgs boson analyses at the LHC: A study of $pp \to t\bar{t}$ + 2 jets at next-to-leading order*, Phys. Rev. Lett. **104** (2010) 162002, `arXiv:1002.4009` `[hep-ph]`.

[188] G. Bevilacqua, M. Czakon, C. Papadopoulos, and M. Worek, *Hadronic top-quark pair production in association with two jets at Next-to-Leading Order QCD*, Phys. Rev. D **84** (2011) 114017, `arXiv:1108.2851` `[hep-ph]`.

[189] S. Hoeche, F. Krauss, M. Schonherr, and F. Siegert, *QCD matrix elements + parton showers: The NLO case*, JHEP **04** (2013) 027, `arXiv:1207.5030` `[hep-ph]`.

[190] M. Cacciari, G. P. Salam, and G. Soyez, *The Anti-k_t jet clustering algorithm*, JHEP **04** (2008) 063, `arXiv:0802.1189` `[hep-ph]`.

[191] G. Bevilacqua, M. Czakon, M. Garzelli, A. van Hameren, A. Kardos, et al., *HELAC-NLO*, Comput. Phys. Commun. **184** (2013) 986–997, `arXiv:1110.1499` `[hep-ph]`.

[192] G. Bevilacqua, M. Czakon, M. Garzelli, A. van Hameren, Y. Malamos, et al., *NLO QCD calculations with HELAC-NLO*, Nucl. Phys. Proc. Suppl. **205-206** (2010) 211–217, `arXiv:1007.4918` `[hep-ph]`.

[193] J. Alwall et al., *A standard format for Les Houches event files*, Comput. Phys. Commun. **176** (2007) 300–304, `arXiv:hep-ph/0609017`.

[194] A. Kardos, C. Papadopoulos, and Z. Trocsanyi, *Top quark pair production in association with a jet with NLO parton showering*, Phys. Lett. B **705** (2011) 76–81, `arXiv:1101.2672` `[hep-ph]`.

[195] M. Garzelli, A. Kardos, C. Papadopoulos, and Z. Trocsanyi, *Z0 - boson production in association with a top anti-top pair at NLO accuracy with parton shower effects*, Phys. Rev. D **85** (2012) 074022, `arXiv:1111.1444` `[hep-ph]`.

[196] M. Garzelli, A. Kardos, C. Papadopoulos, and Z. Trocsanyi, *$t\bar{t}W^{+-}$ and $t\bar{t}Z$ Hadroproduction at NLO accuracy in QCD with Parton Shower and Hadronization effects*, JHEP **11** (2012) 056, `arXiv:1208.2665` `[hep-ph]`.

[197] *PowHel*, `http://grid.kfki.hu/twiki/bin/view/DbTheory/`.

[198] G. Ossola, C. G. Papadopoulos, and R. Pittau, *On the Rational Terms of the one-loop amplitudes*, JHEP **05** (2008) 004, `arXiv:0802.1876` `[hep-ph]`.

[199] M. Whalley, D. Bourilkov, and R. Group, *The Les Houches accord PDFs (LHAPDF) and LHAGLUE*, `arXiv:hep-ph/0508110` `[hep-ph]`.

[200] ATLAS Collaboration, G. Aad et al., *Combined search for the Standard Model Higgs boson using up to 4.9 fb^{-1} of pp collision data at $\sqrt{s}$ = 7 TeV with the ATLAS detector at the LHC*, Phys. Lett. B **710** (2012) 49–66, `arXiv:1202.1408` `[hep-ex]`.

[201] CMS Collaboration, S. Chatrchyan et al., *Combined results of searches for the standard model Higgs boson in pp collisions at $\sqrt{s}$ = 7 TeV*, Phys. Lett. B **710** (2012) 26–48, `arXiv:1202.1488` `[hep-ex]`.

[202] P. Nason and C. Oleari, *Generation cuts and Born suppression in POWHEG*, `arXiv:1303.3922` `[hep-ph]`.

[203] *PDF4LHC steering committee*, `http://www.hep.ucl.ac.uk/pdf4lhc/`.

[204] J. Gao, M. Guzzi, J. Huston, H.-L. Lai, Z. Li, et al., *The CT10 NNLO Global Analysis of QCD*, `arXiv:1302.6246` `[hep-ph]`.

[205] SM and NLO Multileg Working Group Collaboration, J. Andersen et al., *The SM and NLO Multileg Working Group: Summary report*, `arXiv:1003.1241` `[hep-ph]`.

[206] G. Watt and R. Thorne, *Study of Monte Carlo approach to experimental uncertainty propagation*

with MSTW 2008 PDFs, JHEP **08** (2012) 052, `arXiv:1205.4024 [hep-ph]`.

[207] NNPDF Collaboration, R. D. Ball et al., *Reweighting NNPDFs: the W lepton asymmetry*, Nucl. Phys. B **849** (2011) 112–143, `arXiv:1012.0836 [hep-ph]`.

[208] R. D. Ball, V. Bertone, F. Cerutti, L. Del Debbio, S. Forte, et al., *Reweighting and Unweighting of Parton Distributions and the LHC W lepton asymmetry data*, Nucl. Phys. B **855** (2012) 608–638, `arXiv:1108.1758 [hep-ph]`.

[209] A. Martin, A. T. Mathijssen, W. Stirling, R. Thorne, B. Watt, et al., *Extended Parameterisations for MSTW PDFs and their effect on Lepton Charge Asymmetry from W Decays*, Eur. Phys. J. **C73** (2013) 2318, `arXiv:1211.1215 [hep-ph]`.

[210] R. D. Ball et al., *Impact of heavy quark masses on parton distributions and LHC phenomenology*, Nucl. Phys. B **849** (2011) 296–363, `arXiv:1101.1300 [hep-ph]`.

[211] S. Forte and G. Watt, *Progress in the Determination of the Partonic Structure of the Proton*, `arXiv:1301.6754 [hep-ph]`.

[212] S. Alekhin, J. Blumlein, and S. Moch, *Parton Distribution Functions and Benchmark Cross Sections at NNLO*, Phys. Rev. D **86** (2012) 054009, `arXiv:1202.2281 [hep-ph]`.

[213] H1 and ZEUS Collaboration, F. Aaron et al., *Combined Measurement and QCD Analysis of the Inclusive e+- p Scattering Cross Sections at HERA*, JHEP **01** (2010) 109, `arXiv:0911.0884 [hep-ex]`.

[214] S. Alekhin, J. Blümlein, S. Klein, and S. Moch, *The 3-, 4-, and 5-flavor NNLO parton from deep-inelastic-scattering data and at hadron colliders*, Phys. Rev. D **81** (2010) 014032, `arXiv:0908.2766 [hep-ph]`.

[215] S. Alekhin, J. Bluemlein, and S.-O. Moch, *Statistical issues in the parton distribution analysis of the Tevatron jet data*, `arXiv:1211.2642 [hep-ph]`.

[216] H1 and ZEUS Collaboration, V. Radescu, *Combination and QCD analysis of the HERA inclusive cross sections*, PoS **ICHEP2010** (2010) 168.

[217] ZEUS and H1 Collaboration, A. Cooper-Sarkar, *PDF Fits at HERA*, PoS **EPS-HEP2011** (2011) 320, `arXiv:1112.2107 [hep-ph]`.

[218] H1 Collaboration, F. Aaron et al., *Inclusive Deep Inelastic Scattering at High Q^2 with Longitudinally Polarised Lepton Beams at HERA*, JHEP **09** (2012) 061, `arXiv:1206.7007 [hep-ex]`.

[219] ZEUS Collaboration, H. Abramowicz, *Measurement of high-Q2 neutral current deep inelastic e+p scattering cross sections with a longitudinally polarised positron beam at HERA*, `arXiv:1208.6138 [hep-ex]`.

[220] ATLAS Collaboration, G. Aad et al., *Determination of the strange quark density of the proton from ATLAS measurements of the $W \to l\nu$ and $Z \to ll$ cross sections*, Phys. Rev. Lett. **109** (2012) 012001, `arXiv:1203.4051 [hep-ex]`.

[221] ATLAS Collaboration, G. Aad et al., *Measurement of the inclusive $W^{\pm}$ and Z/gamma cross sections in the electron and muon decay channels in pp collisions at $\sqrt{s} = 7$ TeV with the ATLAS detector*, Phys. Rev. D **85** (2012) 072004, `arXiv:1109.5141 [hep-ex]`.

[222] A. Kusina, T. Stavreva, S. Berge, F. Olness, I. Schienbein, et al., *Strange Quark PDFs and Implications for Drell-Yan Boson Production at the LHC*, Phys. Rev. D **85** (2012) 094028, `arXiv:1203.1290 [hep-ph]`.

[223] J. Owens, A. Accardi, and W. Melnitchouk, *Global parton distributions with nuclear and finite-Q^2 corrections*, `arXiv:1212.1702 [hep-ph]`.

[224] The NNPDF Collaboration Collaboration, R. D. Ball et al., *Theoretical issues in PDF determination and associated uncertainties*, Phys.Lett. **B723** (2013) 330–339, `arXiv:1303.1189 [hep-ph]`.

[225] P. Jimenez-Delgado, *The role of the input scale in parton distribution analyses*, Phys. Lett. B **714** (2012) 301–305, `arXiv:1206.4262 [hep-ph]`.

[226] R. Thorne, *Effect of changes of variable flavor number scheme on parton distribution functions and predicted cross sections*, Phys. Rev. D **86** (2012) 074017, `arXiv:1201.6180 [hep-ph]`.

[227] A. Martin, R. Roberts, W. Stirling, and R. Thorne, *Uncertainties of predictions from parton distributions. 2. Theoretical errors*, Eur. Phys. J. **C35** (2004) 325–348, `arXiv:hep-ph/0308087 [hep-ph]`.

[228] J. Gao, Z. Liang, D. E. Soper, H.-L. Lai, P. M. Nadolsky, et al., *MEKS: a program for computation of inclusive jet cross sections at hadron colliders*, Comput.Phys.Commun. **184** (2013) 1626–1642, `arXiv:1207.0513 [hep-ph]`.

[229] R. D. Ball, S. Carrazza, L. Del Debbio, S. Forte, J. Gao, et al., *Parton Distribution Benchmarking with LHC Data*, JHEP **04** (2013) 125, `arXiv:1211.5142 [hep-ph]`.

[230] S. D. Ellis, Z. Kunszt, and D. E. Soper, *Two jet production in hadron collisions at order α_s^3 in QCD*, Phys. Rev. Lett. **69** (1992) 1496–1499.

[231] Z. Nagy, *Three jet cross-sections in hadron hadron collisions at next-to-leading order*, Phys. Rev. Lett. **88** (2002) 122003, `arXiv:hep-ph/0110315 [hep-ph]`.

[232] T. Carli, D. Clements, A. Cooper-Sarkar, C. Gwenlan, G. P. Salam, et al., *A posteriori inclusion of parton density functions in NLO QCD final-state calculations at hadron colliders: The APPLGRID Project*, Eur. Phys. J. **C66** (2010) 503–524, `arXiv:0911.2985 [hep-ph]`.

[233] T. Kluge, K. Rabbertz, and M. Wobisch, *FastNLO: Fast pQCD calculations for PDF fits*, `arXiv:hep-ph/0609285 [hep-ph]`.

[234] J. M. Campbell, J. Huston, and W. Stirling, *Hard Interactions of Quarks and Gluons: A Primer for LHC Physics*, Rept. Prog. Phys. **70** (2007) 89, `arXiv:hep-ph/0611148 [hep-ph]`.

[235] S. Catani, D. de Florian, and M. Grazzini, *Direct Higgs production and jet veto at the Tevatron and the LHC in NNLO QCD*, JHEP **01** (2002) 015, `arXiv:hep-ph/0111164 [hep-ph]`.

[236] I. W. Stewart and F. J. Tackmann, *Theory Uncertainties for Higgs and Other Searches Using Jet Bins*, Phys. Rev. D **85** (2012) 034011, `arXiv:1107.2117 [hep-ph]`.

[237] C. Anastasiou, G. Dissertori, F. Stockli, and B. R. Webber, *QCD radiation effects on the $H \to WW \to l\nu l\nu$ signal at the LHC*, JHEP **03** (2008) 017, `arXiv:0801.2682 [hep-ph]`.

[238] C. Anastasiou, G. Dissertori, M. Grazzini, F. Stockli, and B. R. Webber, *Perturbative QCD effects and the search for a $H \to WW \to \ell\nu\ell\nu$ signal at the Tevatron*, JHEP **08** (2009) 099, `arXiv:0905.3529 [hep-ph]`.

[239] SM AND NLO MULTILEG and SM MC Working Groups Collaboration, J. Alcaraz Maestre et al., *The SM and NLO Multileg and SM MC Working Groups: Summary Report*, `arXiv:1203.6803 [hep-ph]`.

[240] G. Bozzi, S. Catani, D. de Florian, and M. Grazzini, *The q_T spectrum of the Higgs boson at the LHC in QCD perturbation theory*, Phys. Lett. B **564** (2003) 65–72, `arXiv:hep-ph/0302104 [hep-ph]`.

[241] G. Bozzi, S. Catani, D. de Florian, and M. Grazzini, *Transverse-momentum resummation and the spectrum of the Higgs boson at the LHC*, Nucl. Phys. B **737** (2006) 73–120, `arXiv:hep-ph/0508068 [hep-ph]`.

[242] T. Becher and M. Neubert, *Drell-Yan production at small q_T, transverse parton distributions and the collinear anomaly*, Eur. Phys. J. **C71** (2011) 1665, `arXiv:1007.4005 [hep-ph]`.

[243] J.-Y. Chiu, A. Jain, D. Neill, and I. Z. Rothstein, *A Formalism for the Systematic Treatment of Rapidity Logarithms in Quantum Field Theory*, JHEP **05** (2012) 084, `arXiv:1202.0814 [hep-ph]`.

[244] J. Wang, C. S. Li, Z. Li, C. Yuan, and H. T. Li, *Improved Resummation Prediction on Higgs*

Production at Hadron Colliders, Phys. Rev. D **86** (2012) 094026, `arXiv:1205.4311 [hep-ph]`.

[245] T. Becher, M. Neubert, and D. Wilhelm, *Higgs-boson production at small transverse momentum*, JHEP **05** (2013) 110, `arXiv:1212.2621 [hep-ph]`.

[246] I. W. Stewart, F. J. Tackmann, and W. J. Waalewijn, *Factorization at the LHC: From PDFs to Initial State Jets*, Phys. Rev. D **81** (2010) 094035, `arXiv:0910.0467 [hep-ph]`.

[247] S. Catani, Y. L. Dokshitzer, M. Seymour, and B. Webber, *Longitudinally invariant K_t clustering algorithms for hadron hadron collisions*, Nucl. Phys. B **406** (1993) 187–224.

[248] S. D. Ellis and D. E. Soper, *Successive combination jet algorithm for hadron collisions*, Phys. Rev. D **48** (1993) 3160–3166, `arXiv:hep-ph/9305266 [hep-ph]`.

[249] Y. L. Dokshitzer, G. Leder, S. Moretti, and B. Webber, *Better jet clustering algorithms*, JHEP **08** (1997) 001, `arXiv:hep-ph/9707323 [hep-ph]`.

[250] M. Wobisch and T. Wengler, *Hadronization corrections to jet cross-sections in deep inelastic scattering*, `arXiv:hep-ph/9907280 [hep-ph]`.

[251] C. W. Bauer, S. Fleming, and M. E. Luke, *Summing Sudakov logarithms in $B \rightarrow X_s\gamma$ in effective field theory*, Phys. Rev. D **63** (2000) 014006, `arXiv:hep-ph/0005275 [hep-ph]`.

[252] C. W. Bauer, S. Fleming, and I. W. Pirjol, Dan a nd Stewart, *An Effective field theory for collinear and soft gluon s: Heavy to light decays*, Phys. Rev. D **63** (2001) 114020, `arXiv:hep-ph/0011336 [hep-ph]`.

[253] C. W. Bauer and I. W. Stewart, *Invariant operators in collinear effective theory*, Phys. Lett. B **516** (2001) 134–142, `arXiv:hep-ph/0107001 [hep-ph]`.

[254] C. W. Bauer, D. Pirjol, and I. W. . Stewart, *Soft collinear factorization in effective field theory* , Phys. Rev. D **65** (2002) 054022, `arXiv:hep-ph/0109045 [hep-ph]`.

[255] C. W. Bauer, S. Fleming, I. Z. Pirjol, Dan a nd Rothstein, and I. W. Stewart, *Hard scattering factorization from effective field the ory*, Phys. Rev. D **66** (2002) 014017, `arXiv:hep-ph/0202088 [hep-ph]`.

[256] M. Beneke, A. Chapovsky, M. Diehl, and T. Feldmaňn, *Soft collinear effective theory and heavy to light cur rents beyond leading power*, Nucl. Phys. B **643** (2002) 431–476, `arXiv:hep-ph/0206152 [hep-ph]`.

[257] J. Campbell and R. K. Ellis, *Next-to-leading order corrections to W +2jet and Z +2jet production at hadron colliders*, Phys. Rev. D **65** (2002) 113007, `arXiv:hep-ph/0202176`.

[258] J. M. Campbell, R. K. Ellis, and G. Zanderighi, *Next-to-leading order Higgs + 2-jet production via gluon fusion*, JHEP **10** (2006) 028, `arXiv:hep-ph/0608194`.

[259] J. M. Campbell, R. Ellis, and C. Williams, *Hadronic production of a Higgs boson and two jets at next-to-leading order*, Phys. Rev. D **81** (2010) 074023, `arXiv:1001.4495 [hep-ph]`.

[260] A. Banfi, P. F. Monni, G. P. Salam, and G. Zanderighi, *JetVHeto*, `http://jetvheto.hepforge.org`, 2012.

[261] M. Dasgupta and G. Salam, *Resummation of nonglobal QCD observables*, Phys. Lett. B **512** (2001) 323–330, `arXiv:hep-ph/0104277 [hep-ph]`.

[262] S. Gangal and F. J. Tackmann, *NLO uncertainties in Higgs + 2 jets from gluon fusion*, `arXiv:1302.5437 [hep-ph]`.

[263] ATLAS Collaboration, *Observation and study of the Higgs boson candidate in the two photon decay channel with the ATLAS detector at the LHC*, ATLAS-CONF-2012-168 (2012) . `https://cds.cern.ch/record/1499625`.

[264] CMS Collaboration, *Evidence for a new state decaying into two photons in the search for the standard model Higgs boson in pp collisions*, CMS-PAS-HIG-12-015 (2012) . `http://cds.cern.ch/record/1460419`.

[265] A. Hocker, J. Stelzer, F. Tegenfeldt, H. Voss, K. Voss, et al., *TMVA - Toolkit for multivariate data*

analysis, PoS **ACAT** (2007) 040, `arXiv:physics/0703039` `[PHYSICS]`.

[266] ATLAS Collaboration, *Measurements of the properties of the Higgs-like boson in the two photon decay channel with the ATLAS detector using 25* fb^{-1} *of proton-proton collision data*, ATLAS-CONF-2013-012 (2013) `.https://cds.cern.ch/record/1523698`.

[267] CMS Collaboration, *Updated measurements of the Higgs boson at 125 GeV in the two photon decay channel*, CMS-PAS-HIG-13-001 (2013) `.http://cds.cern.ch/record/1530524`.

[268] R. Field, *Min-Bias and the Underlying Event at the LHC*, Acta Phys. Polon. **42** (2011) 2631–2656, `arXiv:1110.5530` `[hep-ph]`.

[269] T. Sjöstrand and M. van Zijl, *A multiple interaction model for the event structure in hadron collisions*, Phys. Rev. D **36** (1987) 2019.

[270] T. Sjostrand and P. Z. Skands, *Multiple interactions and the structure of beam remnants*, JHEP **03** (2004) 053, `arXiv:hep-ph/0402078` `[hep-ph]`.

[271] ATLAS Collaboration, *Summary of ATLAS Pythia 8 tunes*, ATL-PHYS-PUB-2012-003 (2012) . `https://cds.cern.ch/record/1474107`.

[272] TeV4LHC QCD Working Group Collaboration, M. G. Albrow et al., *Tevatron-for-LHC Report of the QCD Working Group*, `arXiv:hep-ph/0610012` `[hep-ph]`.

[273] P. Z. Skands, *Tuning Monte Carlo generators: The Perugia tunes*, Phys. Rev. D **82** (2010) 074018, `arXiv:1005.3457` `[hep-ph]`.

[274] R. Corke and T. Sjostrand, *Interleaved Parton Showers and Tuning Prospects*, JHEP **03** (2011) 032, `arXiv:1011.1759` `[hep-ph]`.

[275] A. Buckley, H. Hoeth, H. Lacker, H. Schulz, and J. E. von Seggern, *Systematic event generator tuning for the LHC*, Eur. Phys. J. **C65** (2010) 331–357, `arXiv:0907.2973` `[hep-ph]`.

[276] CMS Collaboration, S. Chatrchyan et al., *Forward Energy Flow, Central Charged-Particle Multiplicities, and Pseudorapidity Gaps in W and Z Boson Events from pp Collisions at 7 TeV*, Eur. Phys. J. **C72** (2012) 1839, `arXiv:1110.0181` `[hep-ex]`.

[277] J. R. Andersen and J. M. Smillie, *Constructing All-Order Corrections to Multi-Jet Rates*, JHEP **01** (2010) 039, `arXiv:0908.2786` `[hep-ph]`.

[278] J. R. Andersen and J. M. Smillie, *The Factorisation of the t-channel Pole in Quark-Gluon Scattering*, Phys. Rev. D **81** (2010) 114021, `arXiv:0910.5113` `[hep-ph]`.

[279] J. R. Andersen and J. M. Smillie, *Multiple Jets at the LHC with High Energy Jets*, JHEP **06** (2011) 010, `arXiv:1101.5394` `[hep-ph]`.

[280] J. R. Andersen and C. D. White, *A New Framework for Multijet Predictions and its application to Higgs Boson production at the LHC*, Phys. Rev. D **78** (2008) 051501, `arXiv:0802.2858` `[hep-ph]`.

[281] J. R. Andersen, V. Del Duca, and C. D. White, *Higgs Boson Production in Association with Multiple Hard Jets*, JHEP **02** (2009) 015, `arXiv:0808.3696` `[hep-ph]`.

[282] J. R. Andersen and J. M. Smillie, *HEJ framework*, `http://cern.ch/hej`.

[283] J. Campbell and K. Ellis, *MCFM-Monte Carlo for FeMtobarn processes*, `http://mcfm.fnal.gov`, 2010.

[284] P. M. Nadolsky et al., *Implications of CTEQ global analysis for collider observables*, Phys. Rev. D **78** (2008) 013004, `arXiv:0802.0007` `[hep-ph]`.

[285] S. Alioli, P. Nason, C. Oleari, and E. Re, *NLO Higgs boson production via gluon fusion matched with shower in POWHEG*, JHEP **04** (2009) 002, `arXiv:0812.0578` `[hep-ph]`.

[286] K. Hamilton, P. Nason, and G. Zanderighi, *MINLO: Multi-Scale Improved NLO*, JHEP **10** (2012) 155, `arXiv:1206.3572` `[hep-ph]`.

[287] K. Hamilton, P. Nason, C. Oleari, and G. Zanderighi, *Merging H/W/Z + 0 and 1 jet at NLO with no merging scale: a path to parton shower + NNLO matching*, JHEP **05** (2013) 082,

arXiv:1212.4504 [hep-ph].

[288] T. Gehrmann, S. Hoche, F. Krauss, M. Schonherr, and F. Siegert, *NLO QCD matrix elements + parton showers in $e^+e^- \to hadrons$*, JHEP **01** (2013) 144, arXiv:1207.5031 [hep-ph].

[289] S. Dawson, *Radiative corrections to Higgs boson production*, Nucl. Phys. B **359** (1991) 283–300.

[290] V. Ravindran, J. Smith, and W. Van Neerven, *Next-to-leading order QCD corrections to differential distributions of Higgs boson production in hadron hadron collisions*, Nucl. Phys. B **634** (2002) 247–290, arXiv:hep-ph/0201114 [hep-ph].

[291] C. R. Schmidt, *H → g g g (g q anti-q) at two loops in the large M(t) limit*, Phys. Lett. B **413** (1997) 391–395, arXiv:hep-ph/9707448 [hep-ph].

[292] H. van Deurzen, N. Greiner, G. Luisoni, P. Mastrolia, E. Mirabella, et al., *NLO QCD corrections to the production of Higgs plus two jets at the LHC*, Phys. Lett. B **721** (2013) 74–81, arXiv:1301.0493 [hep-ph].

[293] T. Binoth, F. Boudjema, G. Dissertori, A. Lazopoulos, A. Denner, et al., *A Proposal for a standard interface between Monte Carlo tools and one-loop programs*, Comput. Phys. Commun. **181** (2010) 1612–1622, arXiv:1001.1307 [hep-ph].

[294] S. Höche, F. Krauss, S. Schumann, and F. Siegert, *QCD matrix elements and truncated showers*, JHEP **05** (2009) 053, arXiv:0903.1219 [hep-ph].

[295] M. Guzzi, P. Nadolsky, E. Berger, H.-L. Lai, F. Olness, et al., *CT10 parton distributions and other developments in the global QCD analysis*, arXiv:1101.0561 [hep-ph].

[296] J. R. Andersen, K. Arnold, and D. Zeppenfeld, *Azimuthal Angle Correlations for Higgs Boson plus Multi-Jet Events*, JHEP **06** (2010) 091, arXiv:1001.3822 [hep-ph].

[297] S. Hoeche, F. Krauss, M. Schonherr, and F. Siegert, *W+n-jet predictions at the Large Hadron Collider at next-to-leading order matched with a parton shower*, Phys. Rev. Lett. **110** (2013) 052001, arXiv:1201.5882 [hep-ph].

[298] CMS Collaboration, *Evidence for a particle decaying to W^+W^- in the fully leptonic final state in a standard model Higgs boson search in pp collisions at the LHC*, CMS-PAS-HIG-13-003 (2013). http://cds.cern.ch/record/1523673.

[299] G. Cullen, N. Greiner, G. Heinrich, G. Luisoni, P. Mastrolia, et al., *Automated one-loop calculations with GoSam*, arXiv:1111.2034 [hep-ph].

[300] R. K. Ellis, W. Giele, and Z. Kunszt, *A Numerical Unitarity Formalism for Evaluating One-Loop Amplitudes*, JHEP **03** (2008) 003, arXiv:0708.2398 [hep-ph].

[301] P. Mastrolia, E. Mirabella, G. Ossola, and T. Peraro, *Scattering Amplitudes from Multivariate Polynomial Division*, Phys. Lett. B **718** (2012) 173–177, arXiv:1205.7087 [hep-ph].

[302] P. Mastrolia, G. Ossola, T. Reiter, and F. Tramontano, *Scattering Amplitudes from Unitarity-based Reduction Algorithm at the Integrand-level*, JHEP **08** (2010) 080, arXiv:1006.0710 [hep-ph].

[303] P. Mastrolia, E. Mirabella, and T. Peraro, *Integrand reduction of one-loop scattering amplitudes through Laurent series expansion*, JHEP **06** (2012) 095, arXiv:1203.0291 [hep-ph].

[304] R. K. Ellis, W. Giele, and G. Zanderighi, *Virtual QCD corrections to Higgs boson plus four parton processes*, Phys. Rev. D **72** (2005) 054018, arXiv:hep-ph/0506196 [hep-ph].

[305] CDF and D0 Collaboration, T. Aaltonen et al., *Evidence for a particle produced in association with weak bosons and decaying to a bottom-antibottom quark pair in Higgs boson searches at the Tevatron*, Phys. Rev. Lett. **109** (2012) 071804, arXiv:1207.6436 [hep-ex].

[306] LHC Higgs Cross Section Working Group, A. David, A. Denner, M. Duehrssen, M. Grazzini, et al., *LHC HXSWG interim recommendations to explore the coupling structure of a Higgs-like particle*, arXiv:1209.0040 [hep-ph].

[307] D. Zeppenfeld, R. Kinnunen, A. Nikitenko, and E. Richter-Was, *Measuring Higgs boson*

couplings at the LHC, Phys. Rev. D **62** (2000) 013009, `arXiv:hep-ph/0002036`.

[308] M. Dührssen, *Prospects for the measurement of Higgs boson coupling parameters in the mass range from 110 - 190 GeV*, ATL-PHYS-2003-030 (2003) .

[309] M. Dührssen et al., *Extracting Higgs boson couplings from LHC data*, Phys. Rev. D **70** (2004) 113009, `arXiv:hep-ph/0406323`.

[310] R. Lafaye, T. Plehn, M. Rauch, D. Zerwas, and M. Dührssen, *Measuring the Higgs Sector*, JHEP **08** (2009) 009, `arXiv:0904.3866 [hep-ph]`.

[311] K. Hagiwara, R. Szalapski, and D. Zeppenfeld, *Anomalous Higgs boson production and decay*, Phys. Lett. B **318** (1993) 155–162, `arXiv:hep-ph/9308347 [hep-ph]`.

[312] M. Gonzalez-Garcia, *Anomalous Higgs couplings*, Int. J. Mod. Phys. A **14** (1999) 3121–3156, `arXiv:hep-ph/9902321 [hep-ph]`.

[313] V. Barger, T. Han, P. Langacker, B. McElrath, and P. Zerwas, *Effects of genuine dimension-six Higgs operators*, Phys. Rev. D **67** (2003) 115001, `arXiv:hep-ph/0301097 [hep-ph]`.

[314] A. V. Manohar and M. B. Wise, *Modifications to the properties of the Higgs boson*, Phys. Lett. B **636** (2006) 107–113, `arXiv:hep-ph/0601212 [hep-ph]`.

[315] G. Giudice, C. Grojean, A. Pomarol, and R. Rattazzi, *The Strongly-Interacting Light Higgs*, JHEP **06** (2007) 045, `arXiv:hep-ph/0703164 [hep-ph]`.

[316] I. Low, R. Rattazzi, and A. Vichi, *Theoretical Constraints on the Higgs Effective Couplings*, JHEP **04** (2010) 126, `arXiv:0907.5413 [hep-ph]`.

[317] J. Espinosa, C. Grojean, and M. Mühlleitner, *Composite Higgs Search at the LHC*, JHEP **05** (2010) 065, `arXiv:1003.3251 [hep-ph]`.

[318] D. Carmi, A. Falkowski, E. Kuflik, and T. Volansky, *Interpreting LHC Higgs Results from Natural New Physics Perspective*, `arXiv:1202.3144 [hep-ph]`.

[319] A. Azatov, R. Contino, and J. Galloway, *Model-Independent Bounds on a Light Higgs*, JHEP **04** (2012) 127, `arXiv:1202.3415 [hep-ph]`.

[320] J. Espinosa, C. Grojean, M. Mühlleitner, and M. Trott, *Fingerprinting Higgs Suspects at the LHC*, JHEP **05** (2012) 097, `arXiv:1202.3697 [hep-ph]`.

[321] J.-J. Cao, Z.-X. Heng, J. M. Yang, Y.-M. Zhang, and J.-Y. Zhu, *A SM-like Higgs near 125 GeV in low energy SUSY: a comparative study for MSSM and NMSSM*, JHEP **03** (2012) 086, `arXiv:1202.5821 [hep-ph]`.

[322] F. Boudjema and G. D. La Rochelle, *Beyond the MSSM Higgs bosons at 125 GeV*, Phys. Rev. D **86** (2012) 015018, `arXiv:1203.3141 [hep-ph]`.

[323] V. Barger, M. Ishida, and W.-Y. Keung, *Total Width of 125 GeV Higgs Boson*, Phys. Rev. Lett. **108** (2012) 261801, `arXiv:1203.3456 [hep-ph]`.

[324] M. T. Frandsen and F. Sannino, *Discovering a light scalar or pseudoscalar at the large hadron collider*, `arXiv:1203.3988 [hep-ph]`.

[325] P. P. Giardino, K. Kannike, M. Raidal, and A. Strumia, *Reconstructing Higgs boson properties from the LHC and Tevatron data*, JHEP **06** (2012) 117, `arXiv:1203.4254 [hep-ph]`.

[326] J. Ellis and T. You, *Global Analysis of Experimental Constraints on a Possible Higgs-Like Particle with Mass   125 GeV*, JHEP **06** (2012) 140, `arXiv:1204.0464 [hep-ph]`.

[327] P. Draper and D. McKeen, *Diphotons from Tetraphotons in the Decay of a 125 GeV Higgs at the LHC*, Phys. Rev. D **85** (2012) 115023, `arXiv:1204.1061 [hep-ph]`.

[328] A. Azatov, R. Contino, D. Del Re, J. Galloway, M. Grassi, et al., *Determining Higgs couplings with a model-independent analysis of $H \to \gamma\gamma$*, JHEP **06** (2012) 134, `arXiv:1204.4817 [hep-ph]`.

[329] M. Farina, C. Grojean, and E. Salvioni, *(Dys)Zphilia or a custodial breaking Higgs at the LHC*, JHEP **07** (2012) 012, `arXiv:1205.0011 [hep-ph]`.

[330] C. Englert, D. G. Netto, M. Spannowsky, and J. Terning, *Constraining the unhiggs with LHC data*, Phys. Rev. D **86** (2012) 035010, `arXiv:1205.0836 [hep-ph]`.

[331] C. Degrande, J. Gerard, C. Grojean, F. Maltoni, and G. Servant, *Probing top-Higgs non-standard interactions at the LHC*, JHEP **07** (2012) 036, `arXiv:1205.1065 [hep-ph]`.

[332] M. Klute, R. Lafaye, T. Plehn, M. Rauch, and D. Zerwas, *Measuring Higgs Couplings from LHC Data*, Phys. Rev. Lett. **109** (2012) 101801, `arXiv:1205.2699 [hep-ph]`.

[333] A. Arhrib, R. Benbrik, and C.-H. Chen, $H \rightarrow \gamma\gamma$ *in the complex two Higgs doublet model*, `arXiv:1205.5536 [hep-ph]`.

[334] M. Carena, S. Gori, N. R. Shah, C. E. M. Wagner, and L.-T. Wang, *Light Stau Phenomenology and the Higgs $\gamma\gamma$ Rate*, JHEP **07** (2012) 175, `arXiv:1205.5842 [hep-ph]`.

[335] J. R. Espinosa, M. Mühlleitner, C. Grojean, and M. Trott, *Probing for invisible Higgs decays with global fits*, JHEP **09** (2012) 126, `arXiv:1205.6790 [hep-ph]`.

[336] A. Akeroyd and S. Moretti, *Enhancement of $H \rightarrow \gamma\gamma$ from doubly charged scalars in the Higgs Triplet Model*, Phys. Rev. D **86** (2012) 035015, `arXiv:1206.0535 [hep-ph]`.

[337] A. Azatov, S. Chang, N. Craig, and J. Galloway, *Higgs fits preference for suppressed down-type couplings: Implications for supersymmetry*, Phys. Rev. D **86** (2012) 075033, `arXiv:1206.1058 [hep-ph]`.

[338] M. Carena, I. Low, and C. E. Wagner, *Implications of a Modified Higgs to Diphoton Decay Width*, JHEP **08** (2012) 060, `arXiv:1206.1082 [hep-ph]`.

[339] R. S. Gupta, H. Rzehak, and J. D. Wells, *How well do we need to measure Higgs boson couplings?*, Phys. Rev. D **86** (2012) 095001, `arXiv:1206.3560 [hep-ph]`.

[340] K. Blum, R. T. D'Agnolo, and J. Fan, *Natural SUSY Predicts: Higgs Couplings*, JHEP **01** (2013) 057, `arXiv:1206.5303 [hep-ph]`.

[341] J. Chang, K. Cheung, P.-Y. Tseng, and T.-C. Yuan, *Distinguishing various models of the 125 GeV boson in vector boson fusion*, JHEP **12** (2012) 058, `arXiv:1206.5853 [hep-ph]`.

[342] M. Gillioz, R. Grober, C. Grojean, M. Muhlleitner, and E. Salvioni, *Higgs Low-Energy Theorem (and its corrections) in Composite Models*, JHEP **10** (2012) 004, `arXiv:1206.7120 [hep-ph]`.

[343] S. Chang, C. A. Newby, N. Raj, and C. Wanotayaroj, *Revisiting theories with enhanced Higgs couplings to weak gauge bosons*, Phys. Rev. D **86** (2012) 095015, `arXiv:1207.0493 [hep-ph]`.

[344] I. Low, J. Lykken, and G. Shaughnessy, *Have we observed the Higgs (imposter)?*, Phys. Rev. **D86** (2012) 093012, `arXiv:1207.1093 [hep-ph]`.

[345] R. Benbrik, M. Gomez Bock, S. Heinemeyer, O. Stal, G. Weiglein, et al., *Confronting the MSSM and the NMSSM with the Discovery of a Signal in the two Photon Channel at the LHC*, Eur. Phys. J. **C72** (2012) 2171, `arXiv:1207.1096 [hep-ph]`.

[346] T. Corbett, O. Eboli, J. Gonzalez-Fraile, and M. Gonzalez-Garcia, *Constraining anomalous Higgs interactions*, Phys. Rev. D **86** (2012) 075013, `arXiv:1207.1344 [hep-ph]`.

[347] P. P. Giardino, K. Kannike, M. Raidal, and A. Strumia, *Is the resonance at 125 GeV the Higgs boson?*, Phys.Lett. **B718** (2012) 469–474, `arXiv:1207.1347 [hep-ph]`.

[348] J. Ellis and T. You, *Global Analysis of the Higgs Candidate with Mass 125 GeV*, JHEP **09** (2012) 123, `arXiv:1207.1693 [hep-ph]`.

[349] M. Montull and F. Riva, *Higgs discovery: the beginning or the end of natural EWSB?*, JHEP **11** (2012) 018, `arXiv:1207.1716 [hep-ph]`.

[350] J. Espinosa, C. Grojean, M. Muhlleitner, and M. Trott, *First Glimpses at Higgs' face*, JHEP **12** (2012) 045, `arXiv:1207.1717 [hep-ph]`.

[351] D. Carmi, A. Falkowski, E. Kuflik, T. Volansky, and J. Zupan, *Higgs after the discovery: A status report*, JHEP **10** (2012) 196, `arXiv:1207.1718 [hep-ph]`.

[352] M. E. Peskin, *Comparison of LHC and ILC capabilities for higgs boson coupling measurements*, `arXiv:1207.2516 [hep-ph]`.

[353] S. Banerjee, S. Mukhopadhyay, and B. Mukhopadhyaya, *New Higgs interactions and recent data from the LHC and the Tevatron*, JHEP **10** (2012) 062, `arXiv:1207.3588 [hep-ph]`.

[354] T. Abe, N. Chen, and H.-J. He, *LHC Higgs Signatures from Extended Electroweak Gauge Symmetry*, JHEP **01** (2013) 082, `arXiv:1207.4103 [hep-ph]`.

[355] J. Cao, Z. Heng, J. M. Yang, and J. Zhu, *Status of low energy SUSY models confronted with the LHC 125 GeV Higgs data*, JHEP **10** (2012) 079, `arXiv:1207.3698 [hep-ph]`.

[356] A. Joglekar, P. Schwaller, and C. E. Wagner, *Dark Matter and Enhanced Higgs to Di-photon Rate from Vector-like Leptons*, JHEP **12** (2012) 064, `arXiv:1207.4235 [hep-ph]`.

[357] D. Bertolini and M. McCullough, *The Social Higgs*, JHEP **12** (2012) 118, `arXiv:1207.4209 [hep-ph]`.

[358] N. Arkani-Hamed, K. Blum, R. T. D'Agnolo, and J. Fan, *2:1 for Naturalness at the LHC?*, JHEP **01** (2013) 149, `arXiv:1207.4482 [hep-ph]`.

[359] F. Bonnet, T. Ota, M. Rauch, and W. Winter, *Interpretation of precision tests in the Higgs sector in terms of physics beyond the Standard Model*, Phys. Rev. D **86** (2012) 093014, `arXiv:1207.4599 [hep-ph]`.

[360] S. Dawson and E. Furlan, *A Higgs Conundrum with Vector Fermions*, Phys. Rev. D **86** (2012) 015021, `arXiv:1205.4733 [hep-ph]`.

[361] N. Craig and S. Thomas, *Exclusive signals of an extended Higgs sector*, JHEP **11** (2012) 083, `arXiv:1207.4835 [hep-ph]`.

[362] L. G. Almeida, E. Bertuzzo, P. A. Machado, and R. Z. Funchal, *Does $H \to \gamma\gamma$ Taste like vanilla New Physics?*, JHEP **11** (2012) 085, `arXiv:1207.5254 [hep-ph]`.

[363] D. S. Alves, P. J. Fox, and N. J. Weiner, *Higgs Signals in a Type I 2HDM or with a Sister Higgs*, `arXiv:1207.5499 [hep-ph]`.

[364] T. Plehn and M. Rauch, *Higgs Couplings after the discovery*, Europhys.Lett. **100** (2012) 11002, `arXiv:1207.6108 [hep-ph]`.

[365] M. A. Ajaib, I. Gogoladze, and Q. Shafi, *Higgs Boson Production and Decay: Effects from Light Third Generation and Vectorlike Matter*, Phys. Rev. D **86** (2012) 095028, `arXiv:1207.7068 [hep-ph]`.

[366] J. R. Espinosa, C. Grojean, V. Sanz, and M. Trott, *NSUSY fits*, `arXiv:1207.7355 [hep-ph]`.

[367] E. Accomando, L. Fedeli, S. Moretti, S. De Curtis, and D. Dominici, *Charged di-boson production at the LHC in a 4-site model with a composite Higgs boson*, Phys. Rev. D **86** (2012) 115006, `arXiv:1208.0268 [hep-ph]`.

[368] D. Elander and M. Piai, *The decay constant of the holographic techni-dilaton and the 125 GeV boson*, Nucl.Phys. **B867** (2013) 779Ð809, `arXiv:1208.0546 [hep-ph]`.

[369] M. Reece, *Vacuum instabilities with a wrong-sign Higgs-gluon-gluon amplitude*, New J.Phys. **15** (2013) 043003, `arXiv:1208.1765 [hep-ph]`.

[370] A. Djouadi, *Precision Higgs coupling measurements at the LHC through ratios of production cross sections*, `arXiv:1208.3436 [hep-ph]`.

[371] A. Kobakhidze, *Standard Model with a distorted Higgs sector and the enhanced Higgs diphoton decay rate*, `arXiv:1208.5180 [hep-ph]`.

[372] C. Englert, M. Spannowsky, and C. Wymant, *Partially (in)visible Higgs decays at the LHC*, Phys. Lett. B **718** (2012) 538–544, `arXiv:1209.0494 [hep-ph]`.

[373] Z. Chacko, R. Franceschini, and R. K. Mishra, *Resonance at 125 GeV: Higgs or Dilaton/Radion?*, JHEP **04** (2013) 015, `arXiv:1209.3259 [hep-ph]`.

[374] B. Bellazzini, C. Csaki, J. Hubisz, J. Serra, and J. Terning, *A Higgslike Dilaton*, Eur. Phys. J. **C73**

(2013) 2333, `arXiv:1209.3299` `[hep-ph]`.

[375] G. Passarino, *NLO Inspired Effective Lagrangians for Higgs Physics*, Nucl. Phys. B **868** (2013) 416–458, `arXiv:1209.5538` `[hep-ph]`.

[376] W. Huang, J. Shu, and Y. Zhang, *On the Higgs Fit and Electroweak Phase Transition*, JHEP **03** (2013) 164, `arXiv:1210.0906` `[hep-ph]`.

[377] B. A. Dobrescu and J. D. Lykken, *Coupling spans of the Higgs-like boson*, JHEP **02** (2013) 073, `arXiv:1210.3342` `[hep-ph]`.

[378] S. Chang, S. K. Kang, J.-P. Lee, K. Y. Lee, S. C. Park, et al., *Comprehensive study of two Higgs doublet model in light of the new boson with mass around 125 GeV*, JHEP **05** (2013) 075, `arXiv:1210.3439` `[hep-ph]`.

[379] G. Moreau, *Constraining extra-fermion(s) from the Higgs boson data*, Phys. Rev. D **87** (2013) 015027, `arXiv:1210.3977` `[hep-ph]`.

[380] T. Han and Z. Liu, *Direct Measurement of the Higgs Boson Total Width at a Muon Collider*, Phys. Rev. D **87** (2013) 033007, `arXiv:1210.7803` `[hep-ph]`.

[381] G. Cacciapaglia, A. Deandrea, G. D. La Rochelle, and J.-B. Flament, *Higgs couplings beyond the Standard Model*, JHEP **03** (2013) 029, `arXiv:1210.8120` `[hep-ph]`.

[382] S. Biswas, E. Gabrielli, and B. Mele, *Single top and Higgs associated production as a probe of the Htt coupling sign at the LHC*, JHEP **01** (2013) 088, `arXiv:1211.0499` `[hep-ph]`.

[383] E. Masso and V. Sanz, *Limits on Anomalous Couplings of the Higgs to Electroweak Gauge Bosons from LEP and LHC*, Phys. Rev. D **87** (2013) 033001, `arXiv:1211.1320` `[hep-ph]`.

[384] C. Petersson, A. Romagnoni, and R. Torre, *Liberating Higgs couplings in supersymmetry*, Phys. Rev. D **87** (2013) 013008, `arXiv:1211.2114` `[hep-ph]`.

[385] J. R. Andersen, C. Englert, and M. Spannowsky, *Extracting precise Higgs couplings by using the matrix element method*, Phys. Rev. D **87** (2013) 015019, `arXiv:1211.3011` `[hep-ph]`.

[386] M. Farina, C. Grojean, F. Maltoni, E. Salvioni, and A. Thamm, *Lifting degeneracies in Higgs couplings using single top production in association with a Higgs boson*, JHEP **05** (2013) 022, `arXiv:1211.3736` `[hep-ph]`.

[387] J. Chang, K. Cheung, P.-Y. Tseng, and T.-C. Yuan, *Various Models Mimicking the SM Higgs Boson*, Int. J. Mod. Phys. A **27** (2012) 1230030, `arXiv:1211.6823` `[hep-ph]`.

[388] R. T. D'Agnolo, E. Kuflik, and M. Zanetti, *Fitting the Higgs to Natural SUSY*, JHEP **03** (2013) 043, `arXiv:1212.1165` `[hep-ph]`.

[389] A. Azatov and J. Galloway, *Electroweak Symmetry Breaking and the Higgs Boson: Confronting Theories at Colliders*, Int. J. Mod. Phys. A **28** (2013) 1330004, `arXiv:1212.1380` `[hep-ph]`.

[390] R. Alonso, M. Gavela, L. Merlo, S. Rigolin, and J. Yepes, *The effective chiral Lagrangian for a light dynamical 'Higgs'*, Phys.Lett. **B722** (2013) 330–335, `arXiv:1212.3305` `[hep-ph]`.

[391] G. Bhattacharyya, D. Das, and P. B. Pal, *Modified Higgs couplings and unitarity violation*, Phys. Rev. D **87** (2013) 011702, `arXiv:1212.4651` `[hep-ph]`.

[392] D. Choudhury, R. Islam, A. Kundu, and B. Mukhopadhyaya, *Anomalous Higgs Couplings as a Window to New Physics*, `arXiv:1212.4652` `[hep-ph]`.

[393] R. S. Gupta, M. Montull, and F. Riva, *SUSY faces its Higgs couplings*, JHEP **04** (2013) 132, `arXiv:1212.5240` `[hep-ph]`.

[394] G. Belanger, B. Dumont, U. Ellwanger, J. Gunion, and S. Kraml, *Higgs Couplings at the End of 2012*, JHEP **02** (2013) 053, `arXiv:1212.5244` `[hep-ph]`.

[395] J. Reuter and M. Tonini, *Can the 125 GeV Higgs be the Little Higgs?*, JHEP **02** (2013) 077, `arXiv:1212.5930` `[hep-ph]`.

[396] M. Klute, R. Lafaye, T. Plehn, M. Rauch, and D. Zerwas, *Measuring Higgs Couplings at a Linear Collider*, Europhys. Lett. **101** (2013) 51001, `arXiv:1301.1322` `[hep-ph]`.

[397] F. Goertz, A. Papaefstathiou, L. L. Yang, and J. Zurita, *Higgs Boson self-coupling measurements using ratios of cross sections*, JHEP **06** (2013) 016, `arXiv:1301.3492 [hep-ph]`.

[398] C. Cheung, S. D. McDermott, and K. M. Zurek, *Inspecting the Higgs for new weakly interacting particles*, JHEP **04** (2013) 074, `arXiv:1302.0314 [hep-ph]`.

[399] K. Cheung, J. S. Lee, and P.-Y. Tseng, *Higgs precision (Higgcision) era begins*, JHEP **05** (2013) 134, `arXiv:1302.3794 [hep-ph]`.

[400] G. Belanger, B. Dumont, U. Ellwanger, J. Gunion, and S. Kraml, *Status of invisible Higgs decays*, Phys.Lett. **B723** (2013) 340–347, `arXiv:1302.5694 [hep-ph]`.

[401] A. Falkowski, F. Riva, and A. Urbano, *Higgs at last*, `arXiv:1303.1812 [hep-ph]`.

[402] P. P. Giardino, K. Kannike, I. Masina, M. Raidal, and A. Strumia, *The universal Higgs fit*, `arXiv:1303.3570 [hep-ph]`.

[403] R. Contino, M. Ghezzi, C. Grojean, M. Muhlleitner, and M. Spira, *Effective Lagrangian for a light Higgs-like scalar*, `arXiv:1303.3876 [hep-ph]`.

[404] J. Ellis and T. You, *Updated Global Analysis of Higgs Couplings*, JHEP **06** (2013) 103, `arXiv:1303.3879 [hep-ph]`.

[405] A. Djouadi and G. Moreau, *The couplings of the Higgs boson and its CP properties from fits of the signal strengths and their ratios at the 7+8 TeV LHC*, `arXiv:1303.6591 [hep-ph]`.

[406] W.-F. Chang, W.-P. Pan, and F. Xu, *An effective gauge-Higgs operators analysis of new physics associated with the Higgs*, `arXiv:1303.7035 [hep-ph]`.

[407] S. Biswas, E. Gabrielli, F. Margaroli, and B. Mele, *Direct constraints on the top-Higgs coupling from the 8 TeV LHC data*, `arXiv:1304.1822 [hep-ph]`.

[408] B. Dumont, S. Fichet, and G. von Gersdorff, *A Bayesian view of the Higgs sector with higher dimensional operators*, `arXiv:1304.3369 [hep-ph]`.

[409] LHC Higgs Cross Section Working Group, *LHC Higgs cross section TWiki*, `https://twiki.cern.ch/twiki/bin/view/LHCPhysics/CrossSections`, 2010.

[410] K. Arnold et al., *VBFNLO: A parton level Monte Carlo for processes with electroweak bosons*, `http://www-itp.particle.uni-karlsruhe.de/~vbfnloweb`, 2009.

[411] M. Spira, *HIGLU: A program for the calculation of the total Higgs production cross-section at hadron colliders via gluon fusion including QCD corrections*, `arXiv:hep-ph/9510347 [hep-ph]`.

[412] M. Spira, *HIGLU and HDECAY: Programs for Higgs boson production at the LHC and Higgs boson decay widths*, Nucl. Instrum. Meth. A **389** (1997) 357–360, `arXiv:hep-ph/9610350`.

[413] M. Spira, A. Djouadi, and P. M. Zerwas, *QCD corrections to the $HZ\gamma$ coupling*, Phys. Lett. B **276** (1992) 350–353.

[414] A. Falkowski, S. Rychkov, and A. Urbano, *What if the Higgs couplings to W and Z bosons are larger than in the Standard Model?*, JHEP **04** (2012) 073, `arXiv:1202.1532 [hep-ph]`.

[415] W. Buchmüller and D. Wyler, *Effective Lagrangian Analysis of New Interactions and Flavor Conservation*, Nucl. Phys. B **268** (1986) 621.

[416] B. Grzadkowski, M. Iskrzynski, M. Misiak, and J. Rosiek, *Dimension-Six Terms in the Standard Model Lagrangian*, JHEP **10** (2010) 085, `arXiv:1008.4884 [hep-ph]`.

[417] K. Hagiwara, S. Ishihara, R. Szalapski, and D. Zeppenfeld, *Low-energy effects of new interactions in the electroweak boson sector*, Phys. Rev. D **48** (1993) 2182–2203.

[418] O. J. Eboli, M. Gonzalez-Garcia, S. . Lietti, and S. Novaes, *Probing intermediate mass Higgs interactions at the CERN Large Hadron Collider*, Phys. Lett. B **478** (2000) 199–207, `arXiv:hep-ph/0001030 [hep-ph]`.

[419] V. Hankele, G. Klamke, D. Zeppenfeld, and T. Figy, *Anomalous Higgs boson couplings in vector boson fusion at the CERN LHC*, Phys. Rev. D **74** (2006) 095001, `arXiv:hep-ph/0609075`.

[420] S. Kanemura and K. Tsumura, *Effects of the anomalous Higgs couplings on the Higgs boson production at the Large Hadron Collider*, Eur. Phys. J. **C63** (2009) 11–21, `arXiv:0810.0433` `[hep-ph]`.

[421] F. Bonnet, M. Gavela, T. Ota, and W. Winter, *Anomalous Higgs couplings at the LHC, and their theoretical interpretation*, Phys. Rev. D **85** (2012) 035016, `arXiv:1105.5140` `[hep-ph]`.

[422] T. Corbett, O. Eboli, J. Gonzalez-Fraile, and M. Gonzalez-Garcia, *Robust Determination of the Higgs Couplings: Power to the Data*, Phys. Rev. D **87** (2013) 015022, `arXiv:1211.4580` `[hep-ph]`.

[423] C. Arzt, M. Einhorn, and J. Wudka, *Patterns of deviation from the standard model*, Nucl. Phys. B **433** (1995) 41–66, `arXiv:hep-ph/9405214` `[hep-ph]`.

[424] R. Contino, C. Grojean, M. Moretti, F. Piccinini, and R. Rattazzi, *Strong Double Higgs Production at the LHC*, JHEP **05** (2010) 089, `arXiv:1002.1011` `[hep-ph]`.

[425] ATLAS Collaboration, *Measurements of the properties of the Higgs-like boson in the four lepton decay channel with the ATLAS detector using 25 fb^{-1} of proton-proton collision data*, ATLAS-CONF-2013-013 (2013) . `https://cds.cern.ch/record/1523699`.

[426] CMS Collaboration, *Properties of the Higgs-like boson in the decay $H \to ZZ \to 4l$ in pp collisions at $\sqrt{s}$=7 and 8 TeV*, CMS-PAS-HIG-13-002 (2013) . `http://cds.cern.ch/record/1523673`.

[427] L. Landau, *On the angular momentum of a two-photon system*, Dokl. Akad. Nauk Ser. Fiz. **60** (1948) 207–209.

[428] C.-N. Yang, *Selection Rules for the Dematerialization of a Particle Into Two Photons*, Phys. Rev. **77** (1950) 242–245.

[429] G. Velo and D. Zwanziger, *Propagation and quantization of Rarita-Schwinger waves in an external electromagnetic potential*, Phys. Rev. **186** (1969) 1337–1341.

[430] G. Velo and D. Zwanziger, *Noncausality and other defects of interaction lagrangians for particles with spin one and higher*, Phys. Rev. **188** (1969) 2218–2222.

[431] M. Porrati and R. Rahman, *Intrinsic Cutoff and Acausality for Massive Spin 2 Fields Coupled to Electromagnetism*, Nucl. Phys. B **801** (2008) 174–186, `arXiv:0801.2581` `[hep-th]`.

[432] J. Ellis, V. Sanz, and T. You, *Prima facie evidence against spin-two Higgs impostors*, `arXiv:1211.3068` `[hep-ph]`.

[433] R. Plano, A. Prodell, N. Samios, M. Schwartz, and J. Steinberger, *Parity of the Neutral Pion*, Phys. Rev. Lett. **3** (1959) 525–527.

[434] J. R. Dell'Aquila and C. A. Nelson, *P or CP determination by sequential decays: v1 v2 modes with decays into anti-lepton (A) lepton (B) and/or anti-q (A) q (B)*, Phys. Rev. D **33** (1986) 80.

[435] S. Y. Choi, . Miller, D. J., M. M. Muhlleitner, and P. M. Zerwas, *Identifying the Higgs spin and parity in decays to Z pairs*, Phys. Lett. B **553** (2003) 61–71, `arXiv:hep-ph/0210077` `[hep-ph]`.

[436] A. De Rujula, J. Lykken, M. Pierini, C. Rogan, and M. Spiropulu, *Higgs look-alikes at the LHC*, Phys. Rev. D **82** (2010) 013003, `arXiv:1001.5300` `[hep-ph]`.

[437] Y. Gao et al., *Spin determination of single-produced resonances at hadron colliders*, Phys. Rev. D **81** (2010) 075022, `arXiv:1001.3396` `[hep-ph]`.

[438] P. Avery, D. Bourilkov, M. Chen, T. Cheng, A. Drozdetskiy, et al., *Precision Studies of the Higgs Golden Channel $H \to ZZ \to 4\ell$ Part I. Kinematic discriminants from leading order matrix elements*, journal (2012) , `arXiv:1210.0896` `[hep-ph]`.

[439] ATLAS Collaboration, *Study of the spin of the Higgs-like boson in the two photon decay channel using 20.7 fb^{-1} of pp collisions collected at $\sqrt{s} = 8$ TeV with the ATLAS detector*, ATLAS-CONF-2013-029 (2013) . `https://cds.cern.ch/record/1527124`.

[440] ATLAS Collaboration, *Study of the spin properties of the Higgs-like particle in the $H \to WW^{(*)} \to e\nu\mu\nu$ channel with 21 fb^{-1} of $\sqrt{s} = 8$ TeV data collected with the ATLAS detector.*, ATLAS-CONF-2013-031 (2013) . https://cds.cern.ch/record/1527127.

[441] J. Ellis, D. S. Hwang, V. Sanz, and T. You, *A Fast Track towards the 'Higgs' Spin and Parity*, JHEP **11** (2012) 134, arXiv:1208.6002 [hep-ph].

[442] J. Ellis, V. Sanz, and T. You, *Associated Production Evidence against Higgs Impostors and Anomalous Couplings*, arXiv:1303.0208 [hep-ph].

[443] A. Djouadi, R. Godbole, B. Mellado, and K. Mohan, *Probing the spin-parity of the Higgs boson via jet kinematics in vector boson fusion*, Phys.Lett. **B723** (2013) 307–313, arXiv:1301.4965 [hep-ph].

[444] T. Plehn, D. L. Rainwater, and D. Zeppenfeld, *Determining the structure of Higgs couplings at the LHC*, Phys. Rev. Lett. **88** (2002) 051801, arXiv:hep-ph/0105325 [hep-ph].

[445] J. Frank, M. Rauch, and D. Zeppenfeld, *Spin-2 resonances in vector-boson-fusion processes at NLO QCD*, Phys. Rev. D **87** (2013) 055020, arXiv:1211.3658 [hep-ph].

[446] C. Englert, D. Goncalves-Netto, K. Mawatari, and T. Plehn, *Higgs quantum numbers in weak boson fusion*, JHEP **01** (2013) 148, arXiv:1212.0843 [hep-ph].

[447] J. F. Gunion and X.-G. He, *Determining the CP nature of a neutral Higgs boson at the LHC*, Phys. Rev. Lett. **76** (1996) 4468–4471, arXiv:hep-ph/9602226 [hep-ph].

[448] J. F. Gunion and J. Pliszka, *Determining the relative size of the CP even and CP odd Higgs boson couplings to a fermion at the LHC*, Phys. Lett. B **444** (1998) 136–141, arXiv:hep-ph/9809306 [hep-ph].

[449] B. Field, *Distinguishing scalar from pseudoscalar Higgs production at the CERN LHC*, Phys. Rev. D **66** (2002) 114007, arXiv:hep-ph/0208262 [hep-ph].

[450] S. Weinberg, *Implications of Dynamical Symmetry Breaking*, Phys. Rev. D **13** (1976) 974–996.

[451] S. Weinberg, *Implications of Dynamical Symmetry Breaking: An Addendum*, Phys. Rev. D **19** (1979) 1277–1280.

[452] L. Susskind, *Dynamics of Spontaneous Symmetry Breaking in the Weinberg-Salam Theory*, Phys. Rev. D **20** (1979) 2619–2625.

[453] W. Bernreuther, P. Gonzalez, and M. Wiebusch, *Pseudoscalar Higgs Bosons at the LHC: Production and Decays into Electroweak Gauge Bosons Revisited*, Eur. Phys. J. **C69** (2010) 31–43, arXiv:1003.5585 [hep-ph].

[454] T. Figy, S. Palmer, and G. Weiglein, *Higgs Production via Weak Boson Fusion in the Standard Model and the MSSM*, JHEP **02** (2012) 105, arXiv:1012.4789 [hep-ph].

[455] N. Arkani-Hamed, A. G. Cohen, and H. Georgi, *Electroweak symmetry breaking from dimensional deconstruction*, Phys. Lett. B **513** (2001) 232–240, arXiv:hep-ph/0105239 [hep-ph].

[456] N. Arkani-Hamed, A. G. Cohen, T. Gregoire, and J. G. Wacker, *Phenomenology of electroweak symmetry breaking from theory space*, JHEP **08** (2002) 020, arXiv:hep-ph/0202089 [hep-ph].

[457] N. Arkani-Hamed, A. Cohen, E. Katz, and A. Nelson, *The Littlest Higgs*, JHEP **07** (2002) 034, arXiv:hep-ph/0206021 [hep-ph].

[458] ALEPH, DELPHI, L3 and OPAL Collaborations, LEP Working Group for Higgs Boson Searches, *Search for neutral MSSM Higgs bosons at LEP*, Eur. Phys. J. **C47** (2006) 547–587, arXiv:hep-ex/0602042 [hep-ex].

[459] S. Dimopoulos, S. Raby, and G. L. Kane, *Experimental Predictions from Technicolor Theories*, Nucl. Phys. B **182** (1981) 77–103.

[460] J. R. Ellis, M. K. Gaillard, D. V. Nanopoulos, and P. Sikivie, *Can One Tell Technicolor from a*

Hole in the Ground?, Nucl. Phys. B **182** (1981) 529–545.

[461] R. S. Chivukula, R. Rosenfeld, E. H. Simmons, and J. Terning, *Strongly coupled electroweak symmetry breaking: Implication of models*, arXiv:hep-ph/9503202 [hep-ph].

[462] S. L. Adler, *Axial vector vertex in spinor electrodynamics*, Phys. Rev. **177** (1969) 2426–2438.

[463] J. Bell and R. Jackiw, *A PCAC puzzle: $\pi^0 \to \gamma\gamma$ in the sigma model*, Nuovo Cim. A **60** (1969) 47–61.

[464] C. T. Hill, *Topcolor assisted technicolor*, Phys. Lett. B **345** (1995) 483–489, arXiv:hep-ph/9411426 [hep-ph].

[465] S. Bolognesi, Y. Gao, A. V. Gritsan, K. Melnikov, M. Schulze, et al., *On the spin and parity of a single-produced resonance at the LHC*, Phys. Rev. D **86** (2012) 095031, arXiv:1208.4018 [hep-ph].

[466] Y. Chen, N. Tran, and R. Vega-Morales, *Scrutinizing the Higgs Signal and Background in the $2e2\mu$ Golden Channel*, JHEP **01** (2013) 182, arXiv:1211.1959 [hep-ph].

[467] J. Ellis and D. S. Hwang, *Does the 'Higgs' have Spin Zero?*, JHEP **09** (2012) 071, arXiv:1202.6660 [hep-ph].

[468] J. Ellis, R. Fok, D. S. Hwang, V. Sanz, and T. You, *Distinguishing 'Higgs' Spin Hypotheses using $\gamma\gamma$ and WW^* Decays*, arXiv:1210.5229 [hep-ph].

[469] A. Alves, *Is the New Resonance Spin 0 or 2? Taking a Step Forward in the Higgs Boson Discovery*, Phys. Rev. D **86** (2012) 113010, arXiv:1209.1037 [hep-ph].

[470] S. Y. Choi, M. M. Muhlleitner, and P. M. Zerwas, *Theoretical Basis of Higgs-Spin Analysis in $H \to \gamma\gamma$ and $Z\gamma$ Decays*, Phys. Lett. B **718** (2013) 1031–1035, arXiv:1209.5268 [hep-ph].

[471] A. Soni and R. M. Xu, *Probing CP violation via Higgs decays to four leptons*, Phys. Rev. D **48** (1993) 5259–5263, arXiv:hep-ph/9301225 [hep-ph].

[472] D. Chang, W.-Y. Keung, and I. Phillips, *CP odd correlation in the decay of neutral Higgs boson into ZZ, W^+W^-, or $t\bar{t}$*, Phys. Rev. D **48** (1993) 3225–3234, arXiv:hep-ph/9303226 [hep-ph].

[473] R. M. Godbole, D. J. Miller, and M. M. Muhlleitner, *Aspects of CP violation in the H ZZ coupling at the LHC*, JHEP **12** (2007) 031, arXiv:0708.0458 [hep-ph].

[474] C. A. Nelson, *CP / P determination and other application of tau lepton and t quark polarimetry*, Phys. Rev. D **41** (1990) 2805.

[475] B. Grzadkowski and J. F. Gunion, *Using decay angle correlations to detect CP violation in the neutral Higgs sector*, Phys. Lett. B **350** (1995) 218–224, arXiv:hep-ph/9501339 [hep-ph].

[476] K. Hagiwara, Q. Li, and K. Mawatari, *Jet angular correlation in vector-boson fusion processes at hadron colliders*, JHEP **07** (2009) 101, arXiv:0905.4314 [hep-ph].

[477] V. D. Barger, K.-m. Cheung, A. Djouadi, B. A. Kniehl, and P. M. Zerwas, *Higgs bosons: Intermediate mass range at e+ e- colliders*, Phys. Rev. D **49** (1994) 79–90, arXiv:hep-ph/9306270 [hep-ph].

[478] D. J. Miller, S. Y. Choi, B. Eberle, M. M. Muhlleitner, and P. M. Zerwas, *Measuring the spin of the Higgs boson*, Phys. Lett. B **505** (2001) 149–154, arXiv:hep-ph/0102023 [hep-ph].

[479] M. E. Rose, *Elementary Theory of Angular Momentum.* Dover Publications, 1995.

[480] C. A. Nelson, *Correlation between decay planes in Higgs boson decays into W pair (into Z pair)*, Phys. Rev. D **37** (1988) 1220.

[481] K. Hagiwara and M. L. Stong, *Probing the scalar sector in $e^+e^- \to f\bar{f}H$*, Z. Phys. C **62** (1994) 99–108, arXiv:hep-ph/9309248 [hep-ph].

[482] K. Hagiwara, S. Ishihara, J. Kamoshita, and B. A. Kniehl, *Prospects of measuring general Higgs couplings at e^+e^- linear colliders*, Eur. Phys. J. **C14** (2000) 457–468, arXiv:hep-ph/0002043 [hep-ph].

380

[483] B. Grzadkowski, J. F. Gunion, and J. Pliszka, *How valuable is polarization at a muon collider? A Test case: Determining the CP nature of a Higgs boson*, Nucl. Phys. B **583** (2000) 49–75, `arXiv:hep-ph/0003091 [hep-ph]`.

[484] T. Han and J. Jiang, *CP violating Z Z H coupling at e+ e- linear colliders*, Phys. Rev. D **63** (2001) 096007, `arXiv:hep-ph/0011271 [hep-ph]`.

[485] M. Kramer, J. H. Kuhn, M. L. Stong, and P. M. Zerwas, *Prospects of measuring the parity of Higgs particles*, Z. Phys. C **64** (1994) 21–30, `arXiv:hep-ph/9404280 [hep-ph]`.

[486] A. Skjold and P. Osland, *Angular and energy correlations in Higgs decay*, Phys. Lett. B **311** (1993) 261–265, `arXiv:hep-ph/9303294 [hep-ph]`.

[487] T. Arens and L. M. Sehgal, *Energy spectra and energy correlations in the decay* $H \to ZZ \to \mu^+\mu^-\mu^+\mu^-$, Z. Phys. C **66** (1995) 89–94, `arXiv:hep-ph/9409396 [hep-ph]`.

[488] K. Odagiri, *On azimuthal spin correlations in Higgs plus jet events at LHC*, JHEP **03** (2003) 009, `arXiv:hep-ph/0212215 [hep-ph]`.

[489] C. P. Buszello, I. Fleck, P. Marquard, and J. J. van der Bij, *Prospective analysis of spin- and CP-sensitive variables in* $H \to ZZ \to \ell_1^+\ell_1^-\ell_2^+\ell_2^-$ *at the LHC*, Eur. Phys. J. **C32** (2004) 209–219, `arXiv:hep-ph/0212396 [hep-ph]`.

[490] C. P. Buszello and P. Marquard, *Determination of spin and CP of the Higgs boson from WBF*, `arXiv:hep-ph/0603209 [hep-ph]`.

[491] W.-Y. Keung, I. Low, and J. Shu, *Landau-Yang theorem and decays of a* Z' *boson into two Z bosons*, Phys. Rev. Lett. **101** (2008) 091802, `arXiv:0806.2864 [hep-ph]`.

[492] P. Bhupal Dev, A. Djouadi, R. M. Godbole, M. Muhlleitner, and S. D. Rindani, *Determining the CP properties of the Higgs boson*, Phys. Rev. Lett. **100** (2008) 051801, `arXiv:0707.2878 [hep-ph]`.

[493] N. D. Christensen, T. Han, and Y. Li, *Testing CP Violation in ZZH Interactions at the LHC*, Phys. Lett. B **693** (2010) 28–35, `arXiv:1005.5393 [hep-ph]`.

[494] C. Englert, C. Hackstein, and M. Spannowsky, *Measuring spin and CP from semi-hadronic ZZ decays using jet substructure*, Phys. Rev. D **82** (2010) 114024, `arXiv:1010.0676 [hep-ph]`.

[495] U. De Sanctis, M. Fabbrichesi, and A. Tonero, *Telling the spin of the 'Higgs boson' at the LHC*, Phys. Rev. D **84** (2011) 015013, `arXiv:1103.1973 [hep-ph]`.

[496] R. M. Godbole, C. Hangst, M. Muhlleitner, S. D. Rindani, and P. Sharma, *Model-independent analysis of Higgs spin and CP properties in the process* $e^+e^- \to t\bar{t}\Phi$, Eur. Phys. J. **C71** (2011) 1681, `arXiv:1103.5404 [hep-ph]`.

[497] R. Boughezal, T. J. LeCompte, and F. Petriello, *Single-variable asymmetries for measuring the 'Higgs' boson spin and CP properties*, `arXiv:1208.4311 [hep-ph]`.

[498] D. Stolarski and R. Vega-Morales, *Directly Measuring the Tensor Structure of the Scalar Coupling to Gauge Bosons*, Phys. Rev. D **86** (2012) 117504, `arXiv:1208.4840 [hep-ph]`.

[499] C. Englert, M. Spannowsky, and M. Takeuchi, *Measuring Higgs CP and couplings with hadronic event shapes*, JHEP **06** (2012) 108, `arXiv:1203.5788 [hep-ph]`.

[500] A. Freitas and P. Schwaller, *Higgs CP properties from early LHC data*, Phys. Rev. D **87** (2013) , `arXiv:1211.1980 [hep-ph]`.

[501] T. Modak, D. Sahoo, R. Sinha, and H.-Y. Cheng, *Inferring the nature of the boson at 125-126 GeV*, `arXiv:1301.5404 [hep-ph]`.

[502] R. Godbole, D. J. Miller, K. Mohan, and C. D. White, *Boosting Higgs CP properties via VH production at the large hadron collider*, `arXiv:1306.2573 [hep-ph]`.

[503] J. Ellis, M. Gaillard, and D. Nanopoulos, *A Phenomenological Profile of the Higgs Boson*, Nucl. Phys. B **106** (1976) 292.

[504] D. Boer, W. J. d. Dunnen, C. Pisano, and M. Schlegel, *Determining the Higgs spin and parity in*

the diphoton decay channel, arXiv:1304.2654 [hep-ph].

[505] M. Bengtsson and P. M. Zerwas, *Four Jet Events in e+ e- Annihilation: Testing the Three Gluon Vertex*, Phys. Lett. B **208** (1988) 306.

[506] M. S. Carena and H. E. Haber, *Higgs boson theory and phenomenology*, Prog. Part. Nucl. Phys. **50** (2003) 63–152, arXiv:hep-ph/0208209 [hep-ph].

[507] A. Djouadi, *The anatomy of electro-weak symmetry breaking. II: The Higgs bosons in the minimal supersymmetric model*, Phys. Rep. **459** (2008) 1–241, arXiv:hep-ph/0503173.

[508] E. Accomando, A. G. Akeroyd, E. Akhmetzyanova, J. Albert, A. Alves, et al., *Workshop on CP Studies and Non-Standard Higgs Physics*, arXiv:hep-ph/0608079 [hep-ph].

[509] S. Berge, W. Bernreuther, and J. Ziethe, *Determining the CP parity of Higgs bosons at the LHC in their tau decay channels*, Phys. Rev. Lett. **100** (2008) 171605, arXiv:0801.2297 [hep-ph].

[510] S. Berge and W. Bernreuther, *Determining the CP parity of Higgs bosons at the LHC in the tau to 1-prong decay channels*, Phys. Lett. B **671** (2009) 470–476, arXiv:0812.1910 [hep-ph].

[511] S. Berge, W. Bernreuther, B. Niepelt, and H. Spiesberger, *How to pin down the CP quantum numbers of a Higgs boson in its tau decays at the LHC*, Phys. Rev. D **84** (2011) 116003, arXiv:1108.0670 [hep-ph].

[512] A. Pilaftsis, *CP odd tadpole renormalization of Higgs scalar - pseudoscalar mixing*, Phys. Rev. D **58** (1998) 096010, arXiv:hep-ph/9803297 [hep-ph].

[513] A. Pilaftsis and C. E. M. Wagner, *Higgs bosons in the minimal supersymmetric standard model with explicit CP violation*, Nucl. Phys. B **553** (1999) 3–42, arXiv:hep-ph/9902371 [hep-ph].

[514] S. Choi, M. Drees, and J. S. Lee, *Loop corrections to the neutral Higgs boson sector of the MSSM with explicit CP violation*, Phys. Lett. B **481** (2000) 57–66, arXiv:hep-ph/0002287 [hep-ph].

[515] M. S. Carena, J. R. Ellis, A. Pilaftsis, and C. E. M. Wagner, *Higgs boson pole masses in the MSSM with explicit CP violation*, Nucl. Phys. B **625** (2002) 345–371, arXiv:hep-ph/0111245 [hep-ph].

[516] J. R. Ellis, J. S. Lee, and A. Pilaftsis, *CERN LHC signatures of resonant CP violation in a minimal supersymmetric Higgs sector*, Phys. Rev. D **70** (2004) 075010, arXiv:hep-ph/0404167 [hep-ph].

[517] S. Choi, J. Kalinowski, Y. Liao, and P. M. Zerwas, *H/A Higgs mixing in CP-noninvariant supersymmetric theories*, Eur. Phys. J. **C40** (2005) 555–564, arXiv:hep-ph/0407347 [hep-ph].

[518] Y.-S. Tsai, *Decay correlations of heavy leptons in $e^+e^- \to l^+l^-$*, Phys. Rev. D **4** (1971) 2821.

[519] K. Hagiwara, A. D. Martin, and D. Zeppenfeld, *Tau Polarization Measurements at LEP and SLC*, Phys. Lett. B **235** (1990) 198–202.

[520] A. Rouge, *Polarization observables in the $3\pi\nu$ neutrino decay mode of the τ*, Z. Phys. C **48** (1990) 75–78.

[521] S. Jadach, Z. Was, R. Decker, and J. H. Kuhn, *The tau decay library TAUOLA: Version 2.4*, Comput. Phys. Commun. **76** (1993) 361–380.

[522] K. Hagiwara, T. Li, K. Mawatari, and J. Nakamura, *TauDecay: a library to simulate polarized tau decays via FeynRules and MadGraph5*, arXiv:1212.6247 [hep-ph].

[523] CMS Collaboration, *Updated results on the new boson discovered in the search for the standard model Higgs boson in the ZZ to 4 leptons channel in pp collisions at $\sqrt{s}$=7 and 8 TeV*, CMS-PAS-HIG-12-041 (2012). https://cds.cern.ch/record/1494488.

[524] *The JHU Monte Carlo generator, the manual and supporting material can be downloaded from http://www.pha.jhu.edu/spin/*, .

[525] N. D. Christensen and C. Duhr, *FeynRules - Feynman rules made easy*, Comput. Phys. Commun.

180 (2009) 1614–1641, `arXiv:0806.4194` `[hep-ph]`.

[526] *FeynRules*, `http://feynrules.irmp.ucl.ac.be`.

[527] C. Degrande, C. Duhr, B. Fuks, D. Grellscheid, O. Mattelaer, et al., *UFO - The Universal FeynRules Output*, Comput. Phys. Commun. **183** (2012) 1201–1214, `arXiv:1108.2040` `[hep-ph]`.

[528] P. Artoisenet, P. de Aquino, F. Demartin, R. Frederix, S. Frixione, et al., *A framework for Higgs characterisation*, `arXiv:1306.6464` `[hep-ph]`.

[529] K. Hagiwara, R. Peccei, D. Zeppenfeld, and K. Hikasa, *Probing the Weak Boson Sector in $e^+e^- \to W^+W^-$*, Nucl. Phys. B **282** (1987) 253.

[530] G. F. Giudice, R. Rattazzi, and J. D. Wells, *Quantum gravity and extra dimensions at high-energy colliders*, Nucl. Phys. B **544** (1999) 3–38, `arXiv:hep-ph/9811291` `[hep-ph]`.

[531] T. Han, J. D. Lykken, and R.-J. Zhang, *On Kaluza-Klein states from large extra dimensions*, Phys. Rev. D **59** (1999) 105006, `arXiv:hep-ph/9811350` `[hep-ph]`.

[532] K. Hagiwara, J. Kanzaki, Q. Li, and K. Mawatari, *HELAS and MadGraph/MadEvent with spin-2 particles*, Eur. Phys. J. **C56** (2008) 435–447, `arXiv:0805.2554` `[hep-ph]`.

[533] M. J. G. Veltman, *Unitarity and causality in a renormalizable field theory with unstable particles*, Physica **29** (1963) 186–207.

[534] R. Jacob and R. Sachs, *Mass and lifetime of unstable particles*, Phys. Rev. **121** (1961) 350–356.

[535] G. Valent, *Renormalization and second sheet poles in unstable particle theory*, Nucl. Phys. B **65** (1973) 445–459.

[536] J. Lukierski, *Field operator for unstable particle and complex mass description in local QFT*, Fortsch. Phys. **28** (1980) 259.

[537] C. Bollini and L. Oxman, *Unitarity and complex mass fields*, Int. J. Mod. Phys. A **8** (1993) 3185–3198.

[538] P. A. Grassi, B. A. Kniehl, and A. Sirlin, *Width and partial widths of unstable particles in the light of the Nielsen identities*, Phys. Rev. D **65** (2002) 085001, `arXiv:hep-ph/0109228` `[hep-ph]`.

[539] P. A. Grassi, B. A. Kniehl, and A. Sirlin, *Width and partial widths of unstable particles*, Phys. Rev. Lett. **86** (2001) 389–392, `arXiv:hep-th/0005149`.

[540] B. A. Kniehl and A. Sirlin, *Mass and width of a heavy Higgs boson*, Phys. Lett. B **440** (1998) 136–140, `arXiv:hep-ph/9807545` `[hep-ph]`.

[541] B. A. Kniehl and A. Sirlin, *Differences between the pole and on-shell masses and widths of the Higgs boson*, Phys. Rev. Lett. **81** (1998) 1373–1376, `arXiv:hep-ph/9805390` `[hep-ph]`.

[542] R. G. Stuart, *Gauge invariance, analyticity and physical observables at the Z0 resonance*, Phys. Lett. B **262** (1991) 113–119.

[543] E. N. Argyres, W. Beenakker, G. J. van Oldenborgh, A. Denner, S. Dittmaier, et al., *Stable calculations for unstable particles: Restoring gauge invariance*, Phys. Lett. B **358** (1995) 339–346, `arXiv:hep-ph/9507216` `[hep-ph]`.

[544] W. Beenakker, G. J. van Oldenborgh, A. Denner, S. Dittmaier, J. Hoogland, et al., *The Fermion loop scheme for finite width effects in e^+e^- annihilation into four fermions*, Nucl. Phys. B **500** (1997) 255–298, `arXiv:hep-ph/9612260` `[hep-ph]`.

[545] S. Actis, G. Passarino, C. Sturm, and S. Uccirati, *Two-loop threshold singularities, unstable particles and complex masses*, Phys. Lett. B **669** (2008) 62–68, `arXiv:0809.1302` `[hep-ph]`.

[546] A. Ghinculov and T. Binoth, *On the position of a heavy Higgs pole*, Phys. Lett. B **394** (1997) 139–146, `arXiv:hep-ph/9611357` `[hep-ph]`.

[547] A. Frink, B. A. Kniehl, D. Kreimer, and K. Riesselmann, *Heavy Higgs lifetime at two loops*, Phys. Rev. D **54** (1996) 4548–4560, `arXiv:hep-ph/9606310` `[hep-ph]`.

[548] M. Cacciari and N. Houdeau, *Meaningful characterisation of perturbative theoretical uncertainties*, JHEP **09** (2011) 039, arXiv:1105.5152 [hep-ph].

[549] ATLAS Collaboration, G. Aad et al., *Search for the Standard Model Higgs boson in the decay channel $H \to ZZ^* \to 4l$ with $4.8\,fb^{-1}$ of pp collision data at $\sqrt{s} = 7\,TeV$ with ATLAS*, Phys. Lett. B **710** (2012) 383–402, arXiv:1202.1415 [hep-ex].

[550] ATLAS Collaboration, G. Aad et al., *Search for the Standard Model Higgs boson in the $H \to WW(*) \to l\nu l\nu$ decay mode with $4.7\,fb^{-1}$ of ATLAS data at $\sqrt{s} = 7\,TeV$*, arXiv:1206.0756 [hep-ex].

[551] CMS Collaboration, S. Chatrchyan et al., *Search for the standard model Higgs boson decaying to a W pair in the fully leptonic final state in pp collisions at $\sqrt{s} = 7\,TeV$*, Phys. Lett. B **710** (2012) 91–113, arXiv:1202.1489 [hep-ex].

[552] ATLAS Collaboration, G. Aad et al., *Search for a Standard Model Higgs boson in the $H \to ZZ \to ll\nu\nu$ decay channel using $4.7\,fb^{-1}$ of $\sqrt{s} = 7\,TeV$ data with the ATLAS detector*, arXiv:1205.6744 [hep-ex].

[553] CMS Collaboration, S. Chatrchyan et al., *Search for the standard model Higgs boson in the $H \to ZZ \to 2l2\nu$ channel in pp collisions at $\sqrt{s} = 7\,TeV$*, arXiv:1202.3478 [hep-ex].

[554] J. M. Campbell, R. Ellis, and C. Williams, *Gluon-Gluon Contributions to W^+W^- Production and Higgs Interference Effects*, JHEP **10** (2011) 005, arXiv:1107.5569 [hep-ph].

[555] N. Kauer, *Signal-background interference in $gg \to H \to VV$*, PoS **RADCOR2011** (2011) 027, arXiv:1201.1667 [hep-ph].

[556] T. Binoth, M. Ciccolini, N. Kauer, and M. Kramer, *Gluon-induced W-boson pair production at the LHC*, JHEP **12** (2006) 046, arXiv:hep-ph/0611170 [hep-ph].

[557] E. Glover and J. J. van der Bij, *Z Boson Pair Production vai Gluon Fusion*, Nucl. Phys. B **321** (1989) 561.

[558] M. Bonvini, F. Caola, S. Forte, K. Melnikov, and G. Ridolfi, *Signal-background interference effects for $gg \to H \to W^+W^-$ beyond leading order*, arXiv:1304.3053 [hep-ph].

[559] G. Passarino, *THU for $gg \to H$ and interference for $gg \to ZZ$*, http://personalpages.to.infn.it/ giampier/CPHTO.html, 2012.

[560] S. Actis, G. Passarino, C. Sturm, and S. Uccirati, *NNLO computational techniques: The cases $H \to \gamma\gamma$ and $H \to gg$*, Nucl. Phys. B **811** (2009) 182–273, arXiv:0809.3667 [hep-ph].

[561] G. Passarino, C. Sturm, and S. Uccirati, *Complete Two-Loop Corrections to $H \to \gamma\gamma$*, Phys.Lett. **B655** (2007) 298–306, arXiv:0707.1401 [hep-ph].

[562] G. Passarino, C. Sturm, and S. Uccirati, *EW grid for $gg \to H$*, http://personalpages.to.infn.it/ giampier/ngridc.dat, 2012.

[563] R. D. Ball, M. Bonvini, S. Forte, S. Marzani, and G. Ridolfi, *Higgs production in gluon fusion beyond NNLO*, arXiv:1303.3590 [hep-ph].

[564] W. Beenakker, F. A. Berends, and A. Chapovsky, *An Effective Lagrangian approach for unstable particles*, Nucl. Phys. B **573** (2000) 503–535, arXiv:hep-ph/9909472 [hep-ph].

[565] W. Beenakker, A. Chapovsky, A. Kanaki, C. Papadopoulos, and R. Pittau, *Towards an effective Lagrangian approach to fermion loop corrections*, Nucl. Phys. B **667** (2003) 359–393, arXiv:hep-ph/0303105 [hep-ph].

[566] G. Valencia and S. Willenbrock, *The goldstone boson equivalence theorem and the Higgs resonance*, Phys. Rev. D **42** (1990) 853–859.

[567] G. Valencia and S. Willenbrock, *The Heavy Higgs resonance*, Phys. Rev. D **46** (1992) 2247–2251.

[568] A. Aeppli, G. J. van Oldenborgh, and D. Wyler, *Unstable particles in one loop calculations*, Nucl. Phys. B **428** (1994) 126–146, arXiv:hep-ph/9312212 [hep-ph].

[569] H. G. Veltman, *Mass and width of unstable gauge bosons*, Z. Phys. C **62** (1994) 35–52.

[570] A. Sirlin, *Observations concerning mass renormalization in the electroweak theory*, Phys. Lett. B **267** (1991) 240–242.

[571] S. Willenbrock and G. Valencia, *On the definition of the Z boson mass*, Phys. Lett. B **259** (1991) 373–376.

[572] M. Passera and A. Sirlin, *Analysis of the Z^0 resonant amplitude in the general R_ξ gauges*, Phys. Rev. Lett. **77** (1996) 4146–4149, `arXiv:hep-ph/9607253 [hep-ph]`.

[573] F. Jegerlehner, M. Y. Kalmykov, and O. Veretin, *MS versus pole masses of gauge bosons: Electroweak bosonic two loop corrections*, Nucl. Phys. B **641** (2002) 285–326, `arXiv:hep-ph/0105304 [hep-ph]`.

[574] F. Jegerlehner, M. Y. Kalmykov, and O. Veretin, *MS-bar versus pole masses of gauge bosons. 2. Two loop electroweak fermion corrections*, Nucl. Phys. B **658** (2003) 49–112, `arXiv:hep-ph/0212319 [hep-ph]`.

[575] P. Gambino and P. A. Grassi, *The Nielsen identities of the SM and the definition of mass*, Phys. Rev. D **62** (2000) 076002, `arXiv:hep-ph/9907254 [hep-ph]`.

[576] B. A. Kniehl, C. P. Palisoc, and A. Sirlin, *Elimination of threshold singularities in the relation between on shell and pole widths*, Phys. Rev. D **66** (2002) 057902, `arXiv:hep-ph/0205304 [hep-ph]`.

[577] J. M. Cornwall, *Dynamical Mass Generation in Continuum QCD*, Phys. Rev. D **26** (1982) 1453.

[578] J. M. Cornwall and J. Papavassiliou, *Gauge Invariant Three Gluon Vertex in QCD*, Phys. Rev. D **40** (1989) 3474.

[579] J. Papavassiliou, *Gauge Invariant Proper Selfenergies and Vertices in Gauge Theories with Broken Symmetry*, Phys. Rev. D **41** (1990) 3179.

[580] G. Degrassi and A. Sirlin, *Gauge invariant selfenergies and vertex parts of the Standard Model in the pinch technique framework*, Phys. Rev. D **46** (1992) 3104–3116.

[581] J. Papavassiliou and A. Pilaftsis, *Gauge invariance and unstable particles*, Phys. Rev. Lett. **75** (1995) 3060–3063, `arXiv:hep-ph/9506417 [hep-ph]`.

[582] J. Papavassiliou and A. Pilaftsis, *Gauge invariant resummation formalism for two point correlation functions*, Phys. Rev. D **54** (1996) 5315–5335, `arXiv:hep-ph/9605385 [hep-ph]`.

[583] J. Papavassiliou and A. Pilaftsis, *A Gauge independent approach to resonant transition amplitudes*, Phys. Rev. D **53** (1996) 2128–2149, `arXiv:hep-ph/9507246 [hep-ph]`.

[584] J. Papavassiliou and A. Pilaftsis, *Effective charge of the Higgs boson*, Phys. Rev. Lett. **80** (1998) 2785–2788, `arXiv:hep-ph/9710380 [hep-ph]`.

[585] J. Papavassiliou, *The Pinch technique approach to the physics of unstable particles*, `arXiv:hep-ph/9905328 [hep-ph]`.

[586] J. Papavassiliou and A. Pilaftsis, *Gauge and renormalization group invariant formulation of the Higgs boson resonance*, Phys. Rev. D **58** (1998) 053002, `arXiv:hep-ph/9710426 [hep-ph]`.

[587] G. 't Hooft and M. J. G. Veltman, *Scalar one loop integrals*, Nucl. Phys. B **153** (1979) 365–401.

[588] G. Passarino and M. J. G. Veltman, *One loop corrections for e^+e^- annihilation into $\mu^+\mu^-$ in the Weinberg model*, Nucl. Phys. B **160** (1979) 151.

[589] A. Denner, G. Weiglein, and S. Dittmaier, *Gauge invariance of green functions: Background field method versus pinch technique*, Phys. Lett. B **333** (1994) 420–426, `arXiv:hep-ph/9406204 [hep-ph]`.

[590] S. Hashimoto, J. Kodaira, Y. Yasui, and K. Sasaki, *The Background field method: Alternative way of deriving the pinch technique's results*, Phys. Rev. D **50** (1994) 7066–7076, `arXiv:hep-ph/9406271 [hep-ph]`.

[591] J. Papavassiliou, *On the connection between the pinch technique and the background field*

method, Phys. Rev. D **51** (1995) 856–861, `arXiv:hep-ph/9410385 [hep-ph]`.

[592] J. Papavassiliou, E. de Rafael, and N. Watson, *Electroweak effective charges and their relation to physical cross-sections*, Nucl. Phys. B **503** (1997) 79–116, `arXiv:hep-ph/9612237 [hep-ph]`.

[593] B. Grinstein, D. O'Connell, and M. B. Wise, *The Lee-Wick standard model*, Phys. Rev. D **77** (2008) 025012, `arXiv:0704.1845 [hep-ph]`.

[594] M. H. Seymour, *The Higgs boson line shape and perturbative unitarity*, Phys. Lett. B **354** (1995) 409–414, `arXiv:hep-ph/9505211 [hep-ph]`.

[595] S. Weinberg, *Phenomenological Lagrangians*, Physica A **96** (1979) 327.

[596] A. Denner, S. Dittmaier, M. Roth, and L. Wieders, *Electroweak corrections to charged-current $e^+e^- \to 4$ fermion processes: Technical details and further results*, Nucl. Phys. B **724** (2005) 247–294, `arXiv:hep-ph/0505042 [hep-ph]`.

[597] A. Denner and S. Dittmaier, *The complex-mass scheme for perturbative calculations with unstable particles*, Nucl. Phys. Proc. Suppl. **160** (2006) 22–26, `arXiv:hep-ph/0605312`.

[598] T. Binoth, M. Ciccolini, N. Kauer, and M. Krämer, *Gluon-induced WW background to Higgs boson searches at the LHC*, JHEP **03** (2005) 065, `arXiv:hep-ph/0503094 [hep-ph]`.

[599] T. Binoth, N. Kauer, and P. Mertsch, *Gluon-induced QCD corrections to $pp \to ZZ \to \ell\bar{\ell}\ell'\bar{\ell}'$*, Proc. of XVI Int. Workshop on Deep-Inelastic Scattering and Related Topics, London, England, April 2008, `arXiv:0807.0024 [hep-ph]`.

[600] T. Hahn, *Generating Feynman diagrams and amplitudes with FeynArts 3*, Comput. Phys. Commun. **140** (2001) 418–431, `arXiv:hep-ph/0012260`.

[601] T. Hahn and M. Perez-Victoria, *Automatized one-loop calculations in four and D dimensions*, Comput. Phys. Commun. **118** (1999) 153–165, `arXiv:hep-ph/9807565`.

[602] *Dvegas*, `http://Dvegas.hepforge.org/`.

[603] N. Kauer and D. Zeppenfeld, *Finite width effects in top quark production at hadron colliders*, Phys. Rev. D **65** (2002) 014021, `arXiv:hep-ph/0107181 [hep-ph]`.

[604] N. Kauer, *Top pair production beyond double pole approximation: pp, $p\bar{p} \to$ six fermions and zero, one or two additional partons*, Phys. Rev. D **67** (2003) 054013, `arXiv:hep-ph/0212091 [hep-ph]`.

[605] T. Melia, P. Nason, R. Rontsch, and G. Zanderighi, *W^+W^-, WZ and ZZ production in the POWHEG BOX*, JHEP **11** (2011) 078, `arXiv:1107.5051 [hep-ph]`.

[606] J. M. Campbell, R. K. Ellis, and C. Williams, *Vector boson pair production at the LHC*, JHEP **07** (2011) 018, `arXiv:1105.0020 [hep-ph]`.

[607] U. Aglietti, R. Bonciani, G. Degrassi, and A. Vicini, *Analytic results for virtual QCD corrections to Higgs production and decay*, JHEP **01** (2007) 021, `arXiv:hep-ph/0611266 [hep-ph]`.

[608] R. Bonciani, G. Degrassi, and A. Vicini, *Scalar particle contribution to Higgs production via gluon fusion at NLO*, JHEP **11** (2007) 095, `arXiv:0709.4227 [hep-ph]`.

[609] CMS Collaboration, *Search for the Standard Model Higgs boson in the H to WW to $\ell\nu jj$ decay channel in pp collisions at the LHC*, CMS-PAS-HIG-12-046 (2012) . `http://cds.cern.ch/record/1494573`.

[610] ATLAS Collaboration, G. Aad et al., *Search for the Standard Model Higgs boson in the $H \to WW^{(*)} \to \ell\nu\ell\nu$ decay mode with 4.7 /fb of ATLAS data at $\sqrt{s} = 7$ TeV*, Phys. Lett. B **716** (2012) 62–81, `arXiv:1206.0756 [hep-ex]`.

[611] B. Jager, C. Oleari, and D. Zeppenfeld, *Next-to-leading order QCD corrections to W^+W^- production via vector-boson fusion*, JHEP **07** (2006) 015, `arXiv:hep-ph/0603177 [hep-ph]`.

[612] B. Jager, C. Oleari, and D. Zeppenfeld, *Next-to-leading order QCD corrections to Z boson pair production via vector-boson fusion*, Phys. Rev. D **73** (2006) 113006, `arXiv:hep-ph/0604200 [hep-ph]`.

[613] CMS Collaboration, S. Chatrchyan et al., *Observation of a new boson with mass near 125 GeV in pp collisions at $\sqrt{s}$ = 7 and 8 TeV*, `arXiv:1303.4571` `[hep-ex]`.

[614] A. Hill and J. van der Bij, *Strongly interacting singlet - doublet Higgs model*, Phys. Rev. D **36** (1987) 3463–3473.

[615] M. Veltman and F. Yndurain, *Radiative corrections to WW scattering*, Nucl.Phys. **B325** (1989) 1.

[616] T. Binoth and J. van der Bij, *Influence of strongly coupled, hidden scalars on Higgs signals*, Z.Phys. **C75** (1997) 17–25, `arXiv:hep-ph/9608245` `[hep-ph]`.

[617] R. Schabinger and J. D. Wells, *A Minimal spontaneously broken hidden sector and its impact on Higgs boson physics at the large hadron collider*, Phys. Rev. D **72** (2005) 093007, `arXiv:hep-ph/0509209` `[hep-ph]`.

[618] B. Patt and F. Wilczek, *Higgs-field portal into hidden sectors*, `arXiv:hep-ph/0605188` `[hep-ph]`.

[619] M. Bowen, Y. Cui, and J. D. Wells, *Narrow trans-TeV Higgs bosons and H to hh decays: Two LHC search paths for a hidden sector Higgs boson*, JHEP **03** (2007) 036, `arXiv:hep-ph/0701035` `[hep-ph]`.

[620] V. Barger, P. Langacker, M. McCaskey, M. J. Ramsey-Musolf, and G. Shaughnessy, *LHC Phenomenology of an Extended Standard Model with a Real Scalar Singlet*, Phys. Rev. D **77** (2008) 035005, `arXiv:0706.4311` `[hep-ph]`.

[621] V. Barger, P. Langacker, M. McCaskey, M. Ramsey-Musolf, and G. Shaughnessy, *Complex Singlet Extension of the Standard Model*, Phys. Rev. D **79** (2009) 015018, `arXiv:0811.0393` `[hep-ph]`.

[622] G. Bhattacharyya, G. C. Branco, and S. Nandi, *Universal Doublet-Singlet Higgs Couplings and phenomenology at the CERN Large Hadron Collider*, Phys. Rev. D **77** (2008) 117701, `arXiv:0712.2693` `[hep-ph]`.

[623] S. Dawson and W. Yan, *Hiding the Higgs Boson with Multiple Scalars*, Phys. Rev. D **79** (2009) 095002, `arXiv:0904.2005` `[hep-ph]`.

[624] S. Bock, R. Lafaye, T. Plehn, M. Rauch, D. Zerwas, et al., *Measuring Hidden Higgs and Strongly-Interacting Higgs Scenarios*, Phys. Lett. B **694** (2010) 44–53, `arXiv:1007.2645` `[hep-ph]`.

[625] P. J. Fox, D. Tucker-Smith, and N. Weiner, *Higgs friends and counterfeits at hadron colliders*, JHEP **06** (2011) 127, `arXiv:1104.5450` `[hep-ph]`.

[626] C. Englert, T. Plehn, D. Zerwas, and P. M. Zerwas, *Exploring the Higgs portal*, Phys. Lett. B **703** (2011) 298–305, `arXiv:1106.3097` `[hep-ph]`.

[627] C. Englert, J. Jaeckel, E. Re, and M. Spannowsky, *Evasive Higgs Maneuvers at the LHC*, Phys. Rev. D **85** (2012) 035008, `arXiv:1111.1719` `[hep-ph]`.

[628] B. Batell, S. Gori, and L.-T. Wang, *Exploring the Higgs Portal with 10/fb at the LHC*, JHEP **06** (2012) 172, `arXiv:1112.5180` `[hep-ph]`.

[629] C. Englert, T. Plehn, M. Rauch, D. Zerwas, and P. M. Zerwas, *LHC: Standard Higgs and Hidden Higgs*, Phys. Lett. B **707** (2012) 512–516, `arXiv:1112.3007` `[hep-ph]`.

[630] R. S. Gupta and J. D. Wells, *Higgs boson search significance deformations due to mixed-in scalars*, Phys. Lett. B **710** (2012) 154–158, `arXiv:1110.0824` `[hep-ph]`.

[631] M. J. Dolan, C. Englert, and M. Spannowsky, *New Physics in LHC Higgs boson pair production*, Phys. Rev. D **87** (2013) 055002, `arXiv:1210.8166` `[hep-ph]`.

[632] B. Batell, D. McKeen, and M. Pospelov, *Singlet Neighbors of the Higgs Boson*, JHEP **10** (2012) 104, `arXiv:1207.6252` `[hep-ph]`.

[633] G. M. Pruna and T. Robens, *The Higgs Singlet extension parameter space in the light of the LHC discovery*, `arXiv:1303.1150` `[hep-ph]`.

[634] CMS Collaboration, *Combination of standard model Higgs boson searches and measurements of the properties of the new boson with a mass near 125 GeV*, CMS-PAS-HIG-12-045 (2012) . `http://cds.cern.ch/record/1494149`.

[635] T. Lee, *A Theory of Spontaneous T Violation*, Phys. Rev. D **8** (1973) 1226–1239.

[636] J. F. Gunion and H. E. Haber, *The CP conserving two Higgs doublet model: The Approach to the decoupling limit*, Phys. Rev. D **67** (2003) 075019, `arXiv:hep-ph/0207010 [hep-ph]`.

[637] G. Branco, P. Ferreira, L. Lavoura, M. Rebelo, M. Sher, et al., *Theory and phenomenology of two-Higgs-doublet models*, Phys. Rept. **516** (2012) 1–102, `arXiv:1106.0034 [hep-ph]`.

[638] S. L. Glashow and S. Weinberg, *Natural Conservation Laws for Neutral Currents*, Phys. Rev. D **15** (1977) 1958.

[639] E. Paschos, *Diagonal Neutral Currents*, Phys. Rev. D **15** (1977) 1966.

[640] M. Aoki, S. Kanemura, K. Tsumura, and K. Yagyu, *Models of Yukawa interaction in the two Higgs doublet model, and their collider phenomenology*, Phys. Rev. D **80** (2009) 015017, `arXiv:0902.4665 [hep-ph]`.

[641] R. V. Harlander, S. Liebler, and H. Mantler, *SusHi: A program for the calculation of Higgs production in gluon fusion and bottom-quark annihilation in the Standard Model and the MSSM*, Comput. Phys. Commun. **184** (2013) 1605–1617, `arXiv:1212.3249 [hep-ph]`.

[642] *ShsHi*, `http://sushi.hepforge.org/`.

[643] *HDECAY*, `http://people.web.psi.ch/spira/hdecay/`.

[644] *eHDECAY*, `http://www.itp.kit.edu/~maggie/eHDECAY/`.

[645] D. Eriksson, J. Rathsman, and O. Stal, *2HDMC: Two-Higgs-Doublet Model Calculator Physics and Manual*, Comput. Phys. Commun. **181** (2010) 189–205, `arXiv:0902.0851 [hep-ph]`.

[646] *2HDMC*, `http://2hdmc.hepforge.org/`.

[647] F. Mahmoudi, S. Heinemeyer, A. Arbey, A. Bharucha, T. Goto, et al., *Flavour Les Houches Accord: Interfacing Flavour related Codes*, Comput. Phys. Commun. **183** (2012) 285–298, `arXiv:1008.0762 [hep-ph]`.

[648] S. Heinemeyer, O. Stal, and G. Weiglein, *Interpreting the LHC Higgs Search Results in the MSSM*, Phys. Lett. B **710** (2012) 201–206, `arXiv:1112.3026 [hep-ph]`.

[649] A. Arbey, M. Battaglia, A. Djouadi, F. Mahmoudi, and J. Quevillon, *Implications of a 125 GeV Higgs for supersymmetric models*, Phys. Lett. B **708** (2012) 162–169, `arXiv:1112.3028 [hep-ph]`.

[650] B. Allanach, A. Djouadi, J. Kneur, W. Porod, and P. Slavich, *Precise determination of the neutral Higgs boson masses in the MSSM*, JHEP **09** (2004) 044, `arXiv:hep-ph/0406166 [hep-ph]`.

[651] S. Heinemeyer, W. Hollik, and G. Weiglein, *Electroweak precision observables in the minimal supersymmetric Standard Model*, Phys. Rep. **425** (2006) 265–368, `arXiv:hep-ph/0412214`.

[652] S. P. Martin, *Two loop effective potential for the minimal supersymmetric standard model*, Phys. Rev. D **66** (2002) 096001, `arXiv:hep-ph/0206136 [hep-ph]`.

[653] S. P. Martin, *Complete two loop effective potential approximation to the lightest Higgs scalar boson mass in supersymmetry*, Phys. Rev. D **67** (2003) 095012, `arXiv:hep-ph/0211366 [hep-ph]`.

[654] S. P. Martin, *Strong and Yukawa two-loop contributions to Higgs scalar boson self-energies and pole masses in supersymmetry*, Phys. Rev. D **71** (2005) 016012, `arXiv:hep-ph/0405022 [hep-ph]`.

[655] S. P. Martin, *Three-loop corrections to the lightest Higgs scalar boson mass in supersymmetry*, Phys. Rev. D **75** (2007) 055005, `arXiv:hep-ph/0701051 [hep-ph]`.

[656] R. Harlander, P. Kant, L. Mihaila, and M. Steinhauser, *Higgs boson mass in supersymmetry to three loops*, Phys. Rev. Lett. **100** (2008) 191602, `arXiv:0803.0672 [hep-ph]`.

[657] P. Kant, R. Harlander, L. Mihaila, and M. Steinhauser, *Light MSSM Higgs boson mass to three-loop accuracy*, JHEP **08** (2010) 104, `arXiv:1005.5709` [`hep-ph`].

[658] L. J. Hall, D. Pinner, and J. T. Ruderman, *A Natural SUSY Higgs Near 126 GeV*, JHEP **04** (2012) 131, `arXiv:1112.2703` [`hep-ph`].

[659] H. Baer, V. Barger, and A. Mustafayev, *Implications of a 125 GeV Higgs scalar for LHC SUSY and neutralino dark matter searches*, Phys. Rev. D **85** (2012) 075010, `arXiv:1112.3017` [`hep-ph`].

[660] P. Draper, P. Meade, M. Reece, and D. Shih, *Implications of a 125 GeV Higgs for the MSSM and Low-Scale SUSY Breaking*, Phys. Rev. D **85** (2012) 095007, `arXiv:1112.3068` [`hep-ph`].

[661] M. Carena, S. Gori, N. R. Shah, and C. E. M. Wagner, *A 125 GeV SM-like Higgs in the MSSM and the $\gamma\gamma$ rate*, JHEP **03** (2012) 014, `arXiv:1112.3336` [`hep-ph`].

[662] M. Carena, S. Gori, I. Low, N. R. Shah, and C. E. M. Wagner, *Vacuum Stability and Higgs Diphoton Decays in the MSSM*, JHEP **02** (2013) 114, `arXiv:1211.6136` [`hep-ph`].

[663] J. Marrouche, *Talk given at "Rencontres de Moriond EW 2013"*, `https://indico.in2p3.fr/getFile.py/access?contribId=17&sessionId=8&resId= 0&m%aterialId=slides&confId=7411`.

[664] A. Mann, *Talk given at "Moriond QCD and High Energy Interactions 2013"*, `http://moriond.in2p3.fr/QCD/2013/MondayMorning/Mann.pdf`.

[665] M. S. Carena, S. Heinemeyer, C. E. M. Wagner, and G. Weiglein, *Suggestions for improved benchmark scenarios for Higgs- boson searches at LEP2*, `arXiv:hep-ph/9912223`.

[666] M. S. Carena et al., *Reconciling the two-loop diagrammatic and effective field theory computations of the mass of the lightest CP-even Higgs boson in the MSSM*, Nucl. Phys. B **580** (2000) 29–57, `arXiv:hep-ph/0001002`.

[667] J. S. Lee et al., *CPsuperH: A computational tool for Higgs phenomenology in the minimal supersymmetric Standard Model with explicit CP violation*, Comput. Phys. Commun. **156** (2004) 283–317, `arXiv:hep-ph/0307377`.

[668] J. S. Lee, M. Carena, J. Ellis, A. Pilaftsis, and C. E. M. Wagner, *CPsuperH2.0: An improved computational tool for Higgs phenomenology in the MSSM with explicit CP violation*, Comput. Phys. Commun. **180** (2009) 312–331, `arXiv:0712.2360` [`hep-ph`].

[669] J. Lee, M. Carena, J. Ellis, A. Pilaftsis, and C. E. M. Wagner, *CPsuperH2.3: an Updated Tool for Phenomenology in the MSSM with Explicit CP Violation*, Comput. Phys. Commun. **184** (2013) 1220–1233, `arXiv:1208.2212` [`hep-ph`].

[670] J. Casas, J. Espinosa, M. Quiros, and A. Riotto, *The Lightest Higgs boson mass in the minimal supersymmetric standard model*, Nucl. Phys. B **436** (1995) 3–29, `arXiv:hep-ph/9407389` [`hep-ph`].

[671] M. S. Carena, J. Espinosa, M. Quiros, and C. E. M. Wagner, *Analytical expressions for radiatively corrected Higgs masses and couplings in the MSSM*, Phys. Lett. B **355** (1995) 209–221, `arXiv:hep-ph/9504316` [`hep-ph`].

[672] M. S. Carena, M. Quiros, and C. E. M. Wagner, *Effective potential methods and the Higgs mass spectrum in the MSSM*, Nucl. Phys. B **461** (1996) 407–436, `arXiv:hep-ph/9508343` [`hep-ph`].

[673] K. E. Williams, H. Rzehak, and G. Weiglein, *Higher order corrections to Higgs boson decays in the MSSM with complex parameters*, Eur. Phys. J. **C71** (2011) 1669, `arXiv:1103.1335` [`hep-ph`].

[674] M. S. Carena, S. Heinemeyer, C. E. M. Wagner, and G. Weiglein, *MSSM Higgs boson searches at the Tevatron and the LHC: Impact of different benchmark scenarios*, Eur. Phys. J. **C45** (2006) 797–814, `arXiv:hep-ph/0511023`.

[675] P. Bechtle, O. Brein, S. Heinemeyer, G. Weiglein, and K. E. Williams, *HiggsBounds: Confronting Arbitrary Higgs Sectors with Exclusion Bounds from LEP and the Tevatron*, Comput. Phys. Commun. **181** (2010) 138–167, `arXiv:0811.4169 [hep-ph]`.

[676] P. Bechtle, O. Brein, S. Heinemeyer, G. Weiglein, and K. E. Williams, *HiggsBounds 2.0.0: Confronting Neutral and Charged Higgs Sector Predictions with Exclusion Bounds from LEP and the Tevatron*, Comput. Phys. Commun. **182** (2011) 2605–2631, `arXiv:1102.1898 [hep-ph]`.

[677] A. Djouadi, *Squark effects on Higgs boson production and decay at the LHC*, Phys. Lett. B **435** (1998) 101–108, `arXiv:hep-ph/9806315 [hep-ph]`.

[678] K. Hagiwara, J. S. Lee, and J. Nakamura, *Properties of 125 GeV Higgs boson in non-decoupling MSSM scenarios*, JHEP **10** (2012) 002, `arXiv:1207.0802 [hep-ph]`.

[679] G. F. Giudice, P. Paradisi, A. Strumia, and A. Strumia, *Correlation between the Higgs Decay Rate to Two Photons and the Muon g - 2*, JHEP **10** (2012) 186, `arXiv:1207.6393 [hep-ph]`.

[680] A. Dabelstein, *Fermionic decays of neutral MSSM Higgs bosons at the one loop level*, Nucl. Phys. B **456** (1995) 25–56, `arXiv:hep-ph/9503443 [hep-ph]`.

[681] S. Heinemeyer, W. Hollik, and G. Weiglein, *Decay widths of the neutral CP even MSSM Higgs bosons in the Feynman diagrammatic approach*, Eur. Phys. J. **C16** (2000) 139–153, `arXiv:hep-ph/0003022 [hep-ph]`.

[682] A. Bottino, N. Fornengo, and S. Scopel, *Phenomenology of light neutralinos in view of recent results at the CERN Large Hadron Collider*, Phys. Rev. D **85** (2012) 095013, `arXiv:1112.5666 [hep-ph]`.

[683] M. Drees, *A Supersymmetric Explanation of the Excess of Higgs–Like Events at the LHC and at LEP*, Phys. Rev. D **86** (2012) 115018, `arXiv:1210.6507 [hep-ph]`.

[684] R. Harlander and P. Kant, *Higgs production and decay: Analytic results at next-to-leading order QCD*, JHEP **12** (2005) 015, `arXiv:hep-ph/0509189 [hep-ph]`.

[685] R. V. Harlander and M. Steinhauser, *Hadronic Higgs production and decay in supersymmetry at next-to-leading order*, Phys. Lett. B **574** (2003) 258–268, `arXiv:hep-ph/0307346 [hep-ph]`.

[686] R. V. Harlander and M. Steinhauser, *Supersymmetric Higgs production in gluon fusion at next-to-leading order*, JHEP **09** (2004) 066, `arXiv:hep-ph/0409010 [hep-ph]`.

[687] G. Degrassi and P. Slavich, *On the NLO QCD corrections to Higgs production and decay in the MSSM*, Nucl. Phys. B **805** (2008) 267–286, `arXiv:0806.1495 [hep-ph]`.

[688] G. Degrassi and P. Slavich, *NLO QCD bottom corrections to Higgs boson production in the MSSM*, JHEP **11** (2010) 044, `arXiv:1007.3465 [hep-ph]`.

[689] R. V. Harlander, F. Hofmann, and H. Mantler, *Supersymmetric Higgs production in gluon fusion*, JHEP **02** (2011) 055, `arXiv:1012.3361 [hep-ph]`.

[690] R. V. Harlander and F. Hofmann, *Pseudo-scalar Higgs production at next-to-leading order SUSY-QCD*, JHEP **03** (2006) 050, `arXiv:hep-ph/0507041 [hep-ph]`.

[691] G. Degrassi, S. Di Vita, and P. Slavich, *NLO QCD corrections to pseudoscalar Higgs production in the MSSM*, JHEP **08** (2011) 128, `arXiv:1107.0914 [hep-ph]`.

[692] G. Degrassi, S. Di Vita, and P. Slavich, *On the NLO QCD Corrections to the Production of the Heaviest Neutral Higgs Scalar in the MSSM*, Eur. Phys. J. **C72** (2012) 2032, `arXiv:1204.1016 [hep-ph]`.

[693] M. Mühlleitner and M. Spira, *Higgs boson production via gluon fusion: squark loops at NLO QCD*, Nucl. Phys. B **790** (2008) 1–27, `arXiv:hep-ph/0612254 [hep-ph]`.

[694] M. Mühlleitner, H. Rzehak, and M. Spira, *SUSY-QCD corrections to MSSM Higgs boson production via gluon fusion*, PoS **RADCOR2009** (2010) 043, `arXiv:1001.3214 [hep-ph]`.

[695] C. Anastasiou, S. Beerli, and A. Daleo, *The two-loop QCD amplitude gg → h, H in the minimal supersymmetric Standard Model*, Phys. Rev. Lett. **100** (2008) 241806, `arXiv:0803.3065`

`[hep-ph]`.

[696] S. Marzani, R. D. Ball, V. Del Duca, S. Forte, and A. Vicini, *Higgs production via gluon-gluon fusion with finite top mass beyond next-to-leading order*, Nucl. Phys. B **800** (2008) 127–145, `arXiv:arXiv:0801.2544 [hep-ph]`.

[697] R. V. Harlander, H. Mantler, S. Marzani, and K. J. Ozeren, *Higgs production in gluon fusion at next-to-next-to-leading order QCD for finite top mass*, Eur. Phys. J. **C66** (2010) 359–372, `arXiv:0912.2104 [hep-ph]`.

[698] R. V. Harlander and K. J. Ozeren, *Finite top mass effects for hadronic Higgs production at next-to-next-to-leading order*, JHEP **11** (2009) 088, `arXiv:0909.3420 [hep-ph]`.

[699] A. Pak, M. Rogal, and M. Steinhauser, *Finite top quark mass effects in NNLO Higgs boson production at LHC*, JHEP **02** (2010) 025, `arXiv:0911.4662 [hep-ph]`.

[700] A. Pak, M. Rogal, and M. Steinhauser, *Production of scalar and pseudo-scalar Higgs bosons to next-to-next-to-leading order at hadron colliders*, JHEP **09** (2011) 088, `arXiv:1107.3391 [hep-ph]`.

[701] R. V. Harlander and W. B. Kilgore, *Production of a pseudoscalar Higgs boson at hadron colliders at next-to-next-to leading order*, JHEP **10** (2002) 017, `arXiv:hep-ph/0208096 [hep-ph]`.

[702] C. Anastasiou and K. Melnikov, *Pseudoscalar Higgs boson production at hadron colliders in NNLO QCD*, Phys. Rev. D **67** (2003) 037501, `arXiv:hep-ph/0208115 [hep-ph]`.

[703] R. Harlander and M. Steinhauser, *Effects of SUSY QCD in hadronic Higgs production at next-to-next-to-leading order*, Phys. Rev. D **68** (2003) 111701, `arXiv:hep-ph/0308210 [hep-ph]`.

[704] A. Pak, M. Steinhauser, and N. Zerf, *Supersymmetric next-to-next-to-leading order corrections to Higgs boson production in gluon fusion*, JHEP **09** (2012) 118, `arXiv:1208.1588 [hep-ph]`.

[705] A. Pak, M. Steinhauser, and N. Zerf, *Towards Higgs boson production in gluon fusion to NNLO in the MSSM*, Eur. Phys. J. **C71** (2011) 1602, `arXiv:1012.0639 [hep-ph]`.

[706] M. S. Carena, D. Garcia, U. Nierste, and C. E. M. Wagner, *Effective Lagrangian for the $\bar{t}bH^+$ interaction in the MSSM and charged Higgs phenomenology*, Nucl. Phys. B **577** (2000) 88–120, `arXiv:hep-ph/9912516`.

[707] J. Guasch, P. Häfliger, and M. Spira, *MSSM Higgs decays to bottom quark pairs revisited*, Phys. Rev. D **68** (2003) 115001, `arXiv:hep-ph/0305101`.

[708] D. Noth and M. Spira, *Higgs boson couplings to bottom quarks: Two-loop supersymmetry-QCD corrections*, Phys. Rev. Lett. **101** (2008) 181801, `arXiv:0808.0087 [hep-ph]`.

[709] D. Noth and M. Spira, *Supersymmetric Higgs Yukawa couplings to bottom quarks at next-to-next-to-leading order*, JHEP **06** (2011) 084, `arXiv:1001.1935 [hep-ph]`.

[710] L. Mihaila and C. Reisser, *$O(\alpha_s^2)$ corrections to fermionic Higgs decays in the MSSM*, JHEP **08** (2010) 021, `arXiv:arXiv:1007.0693 [hep-ph]`.

[711] A. Djouadi and P. Gambino, *Leading electroweak correction to Higgs boson production at proton colliders*, Phys. Rev. Lett. **73** (1994) 2528–2531, `arXiv:hep-ph/9406432 [hep-ph]`.

[712] R. Bonciani, G. Degrassi, and A. Vicini, *On the generalized harmonic polylogarithms of one complex variable*, Comput. Phys. Commun. **182** (2011) 1253–1264, `arXiv:1007.1891 [hep-ph]`.

[713] J. Baglio and A. Djouadi, *Higgs production at the lHC*, JHEP **03** (2011) 055, `arXiv:1012.0530 [hep-ph]`.

[714] M. Kotsky and O. I. Yakovlev, *On the resummation of double logarithms in the process $H \rightarrow \gamma\gamma$*, Phys. Lett. B **418** (1998) 335–344, `arXiv:hep-ph/9708485 [hep-ph]`.

[715] R. Akhoury, H. Wang, and O. I. Yakovlev, *On the Resummation of large QCD logarithms in $H \rightarrow \gamma\gamma$ decay*, Phys. Rev. D **64** (2001) 113008, `arXiv:hep-ph/0102105 [hep-ph]`.

[716] U. Langenegger, M. Spira, A. Starodumov, and P. Trueb, *SM and MSSM Higgs boson production: Spectra at large transverse momentum*, JHEP **06** (2006) 035, `arXiv:hep-ph/0604156 [hep-ph]`.

[717] O. Brein and W. Hollik, *MSSM Higgs bosons associated with high-p_T jets at hadron colliders*, Phys. Rev. D **68** (2003) 095006, `arXiv:hep-ph/0305321 [hep-ph]`.

[718] O. Brein and W. Hollik, *Distributions for MSSM Higgs boson + jet production at hadron colliders*, Phys. Rev. D **76** (2007) 035002, `arXiv:0705.2744 [hep-ph]`.

[719] CMS Collaboration, *Updated search for a light charged Higgs boson in top quark decays in pp collisions at $\sqrt{s} = 7$ TeV*, CMS-PAS-HIG-12-052 (2012) . `http://cds.cern.ch/record/1502246`.

[720] M. Hashemi, S. Heinemeyer, R. Kinnunen, A. Nikitenko, and G. Weiglein, *Charged Higgs bosons in the MSSM at CMS: Discovery reach and parameter dependence*, `arXiv:0804.1228 [hep-ph]`.

[721] R. Harlander, M. Kramer, and M. Schumacher, *Bottom-quark associated Higgs-boson production: reconciling the four- and five-flavour scheme approach*, `arXiv:1112.3478 [hep-ph]`.

[722] T. Plehn, *Charged Higgs boson production in bottom gluon fusion*, Phys. Rev. D **67** (2003) 014018, `arXiv:hep-ph/0206121`.

[723] D. Bourilkov, R. C. Group, and M. R. Whalley, *LHAPDF: PDF use from the Tevatron to the LHC*, `arXiv:hep-ph/0605240 [hep-ph]`.

[724] F. Maltoni, G. Ridolfi, and M. Ubiali, *b-initiated processes at the LHC: a reappraisal*, JHEP **07** (2012) 022, `arXiv:1203.6393 [hep-ph]`.

[725] Particle Data Group Collaboration, J. Beringer et al., *Review of Particle Physics (RPP)*, Phys. Rev. D **86** (2012) 010001.

[726] S. Dittmaier, M. Kramer, M. Spira, and M. Walser, *Charged-Higgs-boson production at the LHC: NLO supersymmetric QCD corrections*, Phys. Rev. D **83** (2011) 055005, `arXiv:0906.2648 [hep-ph]`.

[727] A. Martin, W. Stirling, R. Thorne, and G. Watt, *Heavy-quark mass dependence in global PDF analyses and 3- and 4-flavour parton distributions*, Eur. Phys. J. **C70** (2010) 51–72, `arXiv:1007.2624 [hep-ph]`.